LTE Baseband DSP/FPGA for Beamspace MIMO RF Antenna

Uooyeol Yoon and Dang-Oh Kim
Wireless Power Transfer Research Center
KAIST (Korea Advanced Institute of Science and Technology), Daejeon, Republic of Korea

Abstract— As the MIMO processing gets popular in LTE wireless mobile communication, the number of RF chains of eNodeB for MIMO processing gets increased, which results in the increase of cost and the volume of eNodeB base-station. In order to solve this problem, the Beamspace MIMO RF Antenna has been proposed. The advantage of Beam-space MIMO RF Antenna is to reduce the RF chain which results in the cost reduction of LTE RF module. In order to support Beam-space MIMO RF Antenna, the LTE baseband signal from LTE modem should be transformed. This transformation includes the matrix and trigonometric computation which is complex to be performed by FPGA. From this observation, authors have implemented baseband algorithm in DSP processor which enables the complex matrix computation efficiently. The requirement of DSP processing is 300 Mbps in 33 MHz band which supports 4 streams. While DSP processor is very efficient for the matrix computation, there should be interface module between baseband DSP and the impedance loading module for Beam-space MIMO RF Antenna. Authors have implemented this interface module with FPGA. The interface between DSP processor and FPGA has been implemented PCIe (PCI Express) to support high-speed serial IO. The integration system has been designed with LTE modem that supports 4×4 MIMO. The testing of full integration system consists of baseband DSP, FPGA, LTE modem and Beam-space MIMO RF Antenna module. Various spectrum analyzers have been used to validate the design of Beamspace MIMO RF baseband system during the test procedure.

1. INTRODUCTION

As the MIMO processing gets popular in LTE wireless mobile communication, the number of RF chains of eNodeB for MIMO processing gets increased, which results in the increase of cost and the volume of eNodeB basestation. In order to solve this problem, the Beam-space MIMO RF Antenna has been proposed. The advantage of Beam-space MIMO RF Antenna is to reduce the RF chain which results in the cost reduction of LTE RF module. In order to support Beamspace MIMO RF Antenna, the LTE baseband signal from LTE modem should be modified. This modification includes the matrix and trigonometric computation which is complex to be performed by FPGA. From this observation, authors have implemented baseband algorithm in DSP processor which enables the complex matrix computation efficiently. The requirement of DSP processing is 300 Mbps in 33 MHz band which supports 4 streams. While DSP processor is very efficient for the matrix computation, there should be interface module between baseband DSP and the impedance loading module for Beam-space MIMO RF Antenna.

In the following Section 2, the current trends and problems of Beamspace MIMO RF researches are described. In Section 3, the architecture of LTE baseband processing for Beamspace MIMO RF to handle the problems of the current Beamspace MIMO RF researches is described. In Section 4, the implementation of the proposed architecture is described. In Section 5, conclusion follows.

2. BEAMSPACE MIMO RF

In the single-RF MIMO transmitter, each of spatially multiplexed streams is mapped into the respective basis beam pattern, which is contrast to conventional MIMO transmitters where symbol streams are driven to different antenna elements. The radiated beam pattern of this beam-space multiplexing with a two-element antenna can be decomposed.

The main advantage of ESPAR (Electronically Steerable Parasitic Array Radiator) antenna is that ESPAR antenna requires only a single RF chain for reducing the complexity of transmitter's complexity, as compared to the current MIMO system. In the current MIMO system, each symbol is mapped to each antenna. But, each symbol is mapped to each orthogonal basis pattern in ESPAR system. The critical problem of beam-space MIMO system using ESPAR antenna with single RF chain for MIMO system is that the impedance to induce the radiation current between parasitic elements antenna is uncontrollable. In order to make parasitic elements antenna induce the current for radiation, it is very essential to implement the controllable impedance matrix between parasitic elements antennas. In Figure 1, the Beamspace MIMO ESPAR Antenna system is shown.
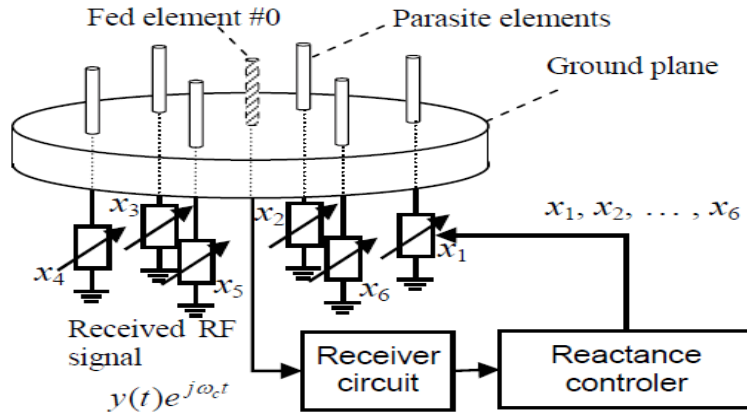
Figure 1: Beamspace MIMO ESPAR Antenna system.

3. LTE BASEBAND PROCESSING FOR BEAMSPACE MIMO RF

In Figure 2, the diagram of current 2×2 LTE downlink system (150 Mbps capacity) is shown. The IQ Signal from LTE modem through QAM modulation will go through 2 RF chains with DACs and PAs.
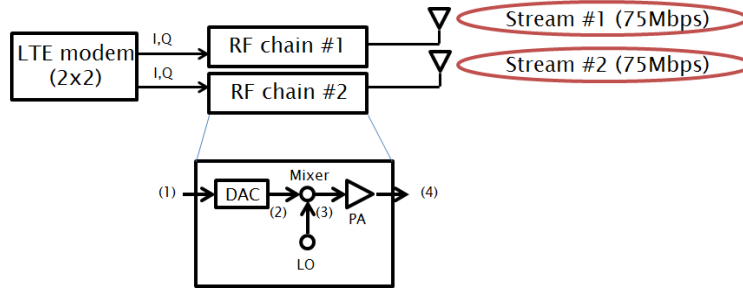

Figure 2: Current 2×2 LTE Downlink system (150 Mbps capacity).

As described in the previous chapter, it is very necessary to make impedance matrix at parasitic elements antenna in Beamspace MIMO system controllable. For that reason, the IQ signals from LTE modem should be transformed into the impedance value for making impedance matrix controllable. From this consideration, the following architecture for Baseband processing for Beamspace MIMO RF in 4×4 LTE downlink system (300 Mbps capacity) is shown Figure 3.
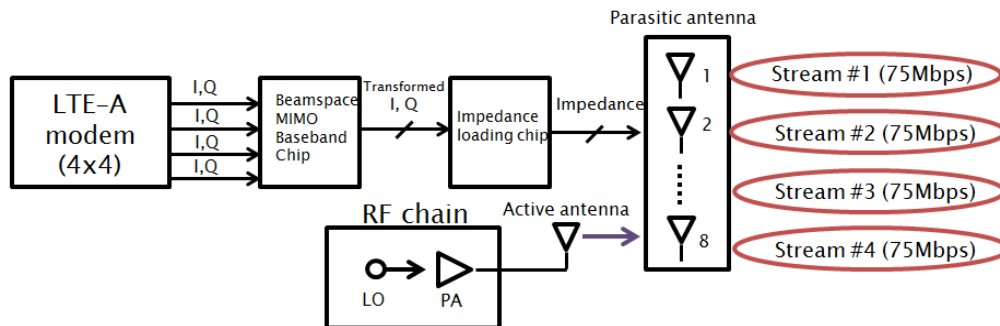

Figure 3: Proposed Beamspace MIMO Baseband system with 4×4 LTE Downlink (300 Mbps).

The purpose of Impedance loading chip is to provide impedance to Parasitic elements Antenna. In Impedance loading chip module, it is very essential to make impedance matric to Parasitic elements Antenna controllable.

4. IMPLEMENTATION

In order to realize the function of baseband processing to the impedance loading module, the following architecture in Figure 4 is proposed. For DSP processor, Texas Instruments DSP is used. For FPGA, Xilinx FPGA is used. For the Downlink of LTE system, IQ signal from LTE modem is transferred from LTE eNodeB through Optic SFP interface. The transformation of IQ signal to Impedance loading value is performed in DSP processor. Algorithm and DSP SW are designed considering LTE system capacity 300 Mbps. Part of Impedance loading transformation is performed in Xilinx Virtex FPGA. The interface between Beamspace MIMO Baseband system and Impedance loading chip is handled in FPGA. The interface between DSP processor and FPGA is designed with PCIe (PCI Express) using high speed Serial IO. The Interface between FPGA and Impedance loading chip is implemented with SMA, GPIO and FMC interface. The SW in DSP processor is implanted using TI CCS (Code Composer Studio). Xilinx FPGA is implemented using Verilog HDL. Depending on the complexity of transformation algorithms, all algorithms can be implemented in FPGA.
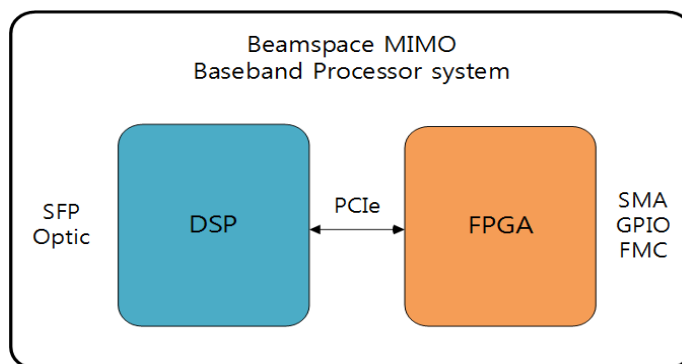

Figure 4: Proposed DSP/FPGA architecture for Baseband processing in Beamspace MIMO.

5. CONCLUSION

In MIMO processing, the number of RF chains of eNodeB for MIMO processing gets increased, which results in the increase of cost and the volume of eNodeB base-station. In order to solve this problem, the Beamspace MIMO RF Antenna has been proposed. The advantage of Beam-space MIMO RF Antenna is to reduce the RF chain which results in the cost reduction of LTE RF module. In order to support Beam-space MIMO RF Antenna, the LTE baseband signal from LTE modem should be transformed. This transformation includes the matrix and trigonometric computation which is complex to be performed by FPGA. From this observation, authors have implemented baseband algorithm in DSP processor which enables the complex matrix computation efficiently. The requirement of DSP processing is 300 Mbps in 33 MHz band which supports 4 streams. While DSP processor is very efficient for the matrix computation, there should be interface module between baseband DSP and the impedance loading module for Beam-space MIMO RF Antenna. Authors have implemented this interface module with FPGA. The interface between DSP processor and FPGA has been implemented PCIe (PCI Express) to support high-speed serial IO. The integration system has been designed with LTE modem that supports 4×4 MIMO. The testing of full integration system consists of baseband DSP, FPGA, LTE modem and Beamspace MIMO RF Antenna module. Various spectrum analyzers have been used to validate the design of Beamspace MIMO RF baseband system during the test procedure. From the test performed so far, it is shown that the Baseband processing system for Beamspace MIMO RF Antenna works correctly to provide the controllability of impedance matrix parasitic elements antennas.

REFERENCES

1. Kalis, A., A. G. Kanatas, and C. B. Papadias, *Parasitic Antenna Arrays for Wireless MIMO Systems*, Springer, New York; Heidelberg; Dordrecht; London, 2014, ISBN 978-1-4614-7998-7.

2. Hong, S.-E. and K.-S. Oh, "Load-modulated single-RF MIMO transmission for spatially multiplexed QAM signals," arxiv, 2015.
3. Han, B., V. Barousis, C. Papadias, A. Kalis, and R. Prasad, "MIMO over ESPAR with 16-QAM modulation," *IEEE Wireless Commun. Lett.*, Vol. 2, No. 6, 687–690, Dec. 2013.
4. Muller, R. R., M. A. Sedaghat, and G. Fisher, "Load modulated massive MIMO," *Proc. CTW2014*, May 2014.
5. Sedaghat, M., R. Muller, and G. Fisher, "A novel single-RF transmitter for massive MIMO," *Proc. ITG Workshop on Smart Antennas*, 1–8, Mar. 2014.

Dynamical and Stochastic Approach to Non-linear Polarization Optics

Satoshi Tuchida and Hiroshi Kuratsuji

Department of Physics, Ritsumeikan University-BKC, Kusatsu City 525-8577, Shiga, Japan

Abstract— We develop the dynamical as well as stochastic aspects for the polarized light transmitting the non-linear media. The central concept is the non-linear birefringence, which is realized for the two-component non-linear Schrödinger equation (NLSE). We put an ansatz: $\psi = (\psi_1, \ \psi_2) = (a(z), \ b(z))F(\mathbf{x})$, where $F(\mathbf{x})$ is the single component scalar wave, which is given as the "soliton" solution for the NLSE. The parameter z is the coordinate of propagation direction, and the $\mathbf{x} = (x, y)$ is that of polarized plane. By substituting this ansatz into the action function $S = \int \psi^*(i\lambda\frac{\partial}{\partial z} - \mathcal{H})\psi d\mathbf{x}dz$, where λ is the wave length for traveling wave, and $\mathcal{H}$ is the Hamiltonian which is written by 2×2 matrix, and using the variation principle, we derive the coupled equation for $a(z)$ and $b(z)$, which can be reduced to the equation of motion for the Stokes parameters. Taking into account of randomness and dissipation contained in the birefringent media, we derive the Langevin equation for the Stokes parameters. From this equation, we can obtain the Fokker-Planck (FP) equation for the probability distribution with respect to Stokes parameters. In order to derive the FP equation, we employ the technique of functional integral, which is based on the assumption of the Gaussian white noise for the random fluctuation arising from birefringence.

1. INTRODUCTION

The polarization is a characteristic property inherent in transversal nature of light wave (or electromagnetic field). This gives rise to a variety of phenomena when the light transmits optically anisotropic medium [1, 2]. The anisotropy of medium is complement to polarization degree of freedom and this complementary nature provides a strong motivation to investigate the evolutional behavior of polarized light in various linear as well as non-linear optical substances (see, e.g., [3–5]).

The standard procedure to describe the evolution of polarization is based on *para-axial scheme* [3–5] (assisted by an envelope approximation). This describes the light propagation along a prescribed direction that is perpendicular to the polarization plane. Two polarization components are mixed each other owing to the dielectric tensor which causes a polarization change. The central concept to describe the change of polarization is the Stokes parameter.

From the applicational point of view, there have been a great deal of studies of polarization phenomena from the microscopic level to cosmological scale. Especially mentioned is that the recent development in the observations of the cosmic microwave background (CMB) polarization, which may connect with the substructure of the Universe [6, 7]. In addition, the characteristic polarization mode, so-called "B-mode", which are generated by gravitational lens effect [8] and primordial gravitational waves [9, 10], is hot topic in cosmology and astrophysics.

What we are going to develop in what follows is concerning the dynamical as well as stochastic aspect for the polarized light transmitting the non-linear media. We need to develop the stochastic aspect, because it plays a crucial role in actual problems concerning the birefringent phenomena. This can be realized as the dynamics of the Stokes parameters, which is reduced to the Fokker-Planck (FP) equation [11, 12] via the Langevin equation by using the functional integral. We expect this attempt may provide a possible basis for problems of CMB polarization above mentioned.

2. FIELD EQUATION FOR THE POLARIZED LIGHT

The polarization characterizes the light propagation in anisotropic materials. This is orthogonal to traveling direction and is described by two component (complex) wave function.

We start with the brief sketch for the two components non-linear Schrödinger equation (NLSE) for the light wave traveling through the non-linear substance [13–15]. We put electric field as

$$\mathbf{E}(\mathbf{x}, z) = \mathbf{f}(\mathbf{x}, z)e^{ikn_0 z} \tag{1}$$

where n_0 refractive index in isotropic media, and $\mathbf{f}(\mathbf{x}, z)$ is a modified wave function. The parameter z is the coordinate of propagation direction, and the $\mathbf{x} = (x, y)$ is the coordinate of polarized plane. The $k = \frac{\omega}{c}$, and $n_0(\equiv \sqrt{\varepsilon_0})$ means the refractive index for the case as if the medium is isotropic.

The amplitude $\mathbf{f}(\mathbf{x}, z)$ is written as $\mathbf{f} = {}^t(f_1, f_2) = f_1\mathbf{e}_1 + f_2\mathbf{e}_2$, where $\mathbf{e}_1$ and $\mathbf{e}_2$ denotes the basis of linear polarization.

Here we adopt the para-axial approximation [5, 15]: We assume that $\mathbf{f}$ is slowly varying function of z, that means $|\frac{\partial^2 \mathbf{f}}{\partial z^2}| \ll k|\frac{\partial \mathbf{f}}{\partial z}|$. The circular basis instead of the linear polarization $(\mathbf{e}_1, \mathbf{e}_2)$, which is written as

$$ {}^t(\mathbf{e}_+, \mathbf{e}_-) = \frac{1}{\sqrt{2}} \begin{pmatrix} 1 & i \\ 1 & -i \end{pmatrix} \cdot {}^t(\mathbf{e}_1, \mathbf{e}_2) \equiv T {}^t(\mathbf{e}_1, \mathbf{e}_2) \tag{2} $$

By introducing the wave function

$$ \psi = T\mathbf{f} = {}^t(\psi_1, \psi_2), \tag{3} $$

we have the two component Schrödinger-type equation for ψ:

$$ i\lambda \frac{\partial \psi}{\partial z} = \mathcal{H}\psi \tag{4} $$

with the transformed "Hamiltonian"

$$ \mathcal{H} = -\frac{\lambda^2}{2n_0}\nabla_\perp^2 + V. \tag{5} $$

where λ is wave length of the polarized wave, $\nabla_\perp^2 = \frac{\partial^2}{\partial x^2} + \frac{\partial^2}{\partial y^2}$ means the Laplacian respect to the polarized plane. and $V = V_{\mathrm{NL}} + V_{\mathrm{L}}$ (V_{NL} and V_{L} represent potential of non-linear and linear, respectively) is defined as following:

$$ V_{\mathrm{NL}} = \frac{g_0}{2}|\psi|^2 + g \begin{pmatrix} -\frac{|\psi_1|^2 - |\psi_2|^2}{2} & \psi_2^\dagger \psi_1 \\ \psi_1^\dagger \psi_2 & \frac{|\psi_1|^2 - |\psi_2|^2}{2} \end{pmatrix}, \quad V_{\mathrm{L}} = \begin{pmatrix} \gamma & \alpha - i\beta \\ \alpha + i\beta & -\gamma \end{pmatrix} \tag{6} $$

Here, the first term of V_{NL} describes the scalar type non-linear interaction with the coupling constant g_0, whereas the second term represents the non-linear birefringence with g [16, 17]. The parameters α, β and γ in V_{L} are described by the effects of external fields, for example, electric and magnetic fields.

3. THE EVOLUTION OF THE STOKES PARAMETERS

In the following, we consider a specific solution of the two-component NLSE such that the solution incorporates the polarization degree of freedom in a simple way. In order to realize this we put ansatz for ψ by using the spinor form:

$$ \psi = F(\mathbf{x}) \begin{pmatrix} a(z) \\ b(z) \end{pmatrix} = F(\mathbf{x}) \begin{pmatrix} \cos\frac{\theta(z)}{2} \\ \sin\frac{\theta(z)}{2}e^{i\phi(z)} \end{pmatrix} \tag{7} $$

where (θ, ϕ) represents the angular coordinate characterizing the polarization, namely, that of the Poincare Sphere, and $F(\mathbf{x})$ is the single component scalar wave which becomes the "soliton" solution of NLSE;

$$ \left[-\frac{\lambda^2}{2n_0}\nabla_\perp^2 + \frac{g_0}{2}|\psi|^2 + k \right] F(\mathbf{x}) = 0 $$

We substitute this ansatz into the action function;

$$ S = \int \psi^\dagger \left(i\lambda\frac{\partial}{\partial z} - \mathcal{H} \right) \psi d^2x dz = \int \mathcal{L}dz \tag{8} $$

where the $\mathcal{L}$ is the Lagrangian. By using the variation principle $\delta S = 0$, we can obtain the coupled equation for $a(z)$ and $b(z)$, which is reduced to the equation of motion for the Stokes parameters. The Stokes parameters are defined as

$$ \mathbf{S}_i = \psi^\dagger \sigma_i \psi, \quad \mathbf{S} = (\sin\theta\cos\phi, \sin\theta\sin\phi, \cos\theta) \tag{9} $$

Then we can get the equation satisfied by Stokes variables

$$\frac{d\mathbf{S}}{dz} = -\mathbf{S} \times \frac{\partial H}{\partial \mathbf{S}} \tag{10}$$

where H is the Hamiltonian; $H = \psi^\dagger \mathcal{H} \psi$. This is just an analogy with the equation of motion of real spin. The concrete expression of H is given as

$$H = \frac{A}{\lambda} [\alpha S_x + \beta S_y + \gamma S_z] - \frac{1}{2} B \left(2S_z^2 - 1\right) - C \tag{11}$$

where the parameters A, B and C are defined by the soliton solution $F(\mathbf{x})$.

The next problem takes into account of randomness contained in the birefringence media. Besides the random fluctuations, we have to take into account of an another effect coming from dissipation, that is caused by the inevitable effect of absorption. This can be given in a phenomenological form; $\frac{\partial H}{\partial \mathbf{S}} \to \frac{\partial H}{\partial \mathbf{S}} + \mu \frac{d\mathbf{S}}{dz}$. Thus we have

$$\frac{d\mathbf{S}}{dz} = \frac{1}{1 + \mu^2} \left[\mu \frac{\partial H}{\partial \mathbf{S}} - \mu \left(\mathbf{S} \cdot \frac{\partial H}{\partial \mathbf{S}} \right) - \mathbf{S} \times \frac{\partial H}{\partial \mathbf{S}} \right] = -\mathbf{A} \tag{12}$$

This is an analogy of the "Landau-Lifschitz equation", that is well known in the ferromagnetic theory [18].

An example — We assume the non-dissipation state ($\mu = 0$) and $\alpha = \beta = 0$, we can simply derive the equation for the Stokes parameters:

$$S_x = S_0 \sin \zeta \cos(Dz), \quad S_y = S_0 \sin \zeta \sin(Dz), \quad S_z = S_0 \cos \zeta \tag{13}$$

where the parameter ζ is the angle respect to S_z, and $D = \frac{A}{\lambda}\gamma - BS_z$. This represents the uniform rotation of the elliptic polarization characterized by the constant angle ζ. This can be regarded as a generalization of the Faraday effect.

4. THE LANGEVIN EQUATION AND FUNCTIONAL INTEGRAL

In what follows we have a mind of the case that the fluctuation effect gives rise to the randomness for the "pseudo-magnetic field", which is written as ξ, so we replace $\frac{\partial H}{\partial \mathbf{S}} \to \frac{\partial H}{\partial \mathbf{S}} + \xi$. Here $\xi(z)$ is assumed to be the Gaussian white noise as a random magnetic field. Hence we have

$$\frac{d\mathbf{S}}{dz} = -\mathbf{A} + \eta \tag{14}$$

Here η stands for a random torque, $\eta = \mathbf{S} \times \xi$. From this Langevin equation, we can derive the FP equation for the probability distribution respect to Stokes parameter. In order to get the FP equation, we employ the technique of functional path integral.

As a result of the randomly uncorrelated nature of the function ξ, η can be also expected to obey the Gaussian white noise, which is expressed as $\langle \eta_i(z) \rangle = 0$, $\langle \eta_i(z) \eta_j(z+u) \rangle = h \delta_{ij} \delta(u)$ with $\delta(u)$ is the delta function, and the h means the diffusion constant. It is assumed that $\langle \eta^2 \rangle = 2h$, and its probability distribution may be given by the standard Gaussian functional form:

$$P[\eta(z)] = \exp\left[-\frac{1}{2h} \int_0^z \eta^2(z) dz \right]. \tag{15}$$

Using this distribution, the propagator K, which is connected between two end points of pseudo-spin, is given by the functional integral:

$$K[\mathbf{S}(z)|\mathbf{S}(0)] = \int \prod_z \delta \left[\frac{d\mathbf{S}}{dz} + \mathbf{A}(\mathbf{S}(z)) - \eta(z) \right] \times \exp\left[-\int \frac{\eta^2(z)}{2h} dz \right] \mathcal{D}[\mathbf{S}] J(\mathbf{S}) \mathcal{D}[\eta(z)] \tag{16}$$

with δ being the Dirac delta-functional, and $J(\mathbf{S})$ is the functional Jacobian. By carrying out the Gaussian functional integral with respect to $\eta(z)$, one obtains

$$K[\mathbf{S}(z)|\mathbf{S}(0)] = \int \exp\left[-\frac{1}{2h} \int_0^z \left(\frac{d\mathbf{S}}{dz} + \mathbf{A}(\mathbf{S}) \right)^2 dz \right] J(\mathbf{S}) \mathcal{D}[\mathbf{S}]. \tag{17}$$

where $J(\mathbf{S})$ is given as

$$J(\mathbf{S}) = \exp\left[\int_0^z M dz\right] \tag{18}$$

and we see that M is determined as $M = -\frac{1}{2}\frac{\partial}{\partial \mathbf{S}} \cdot \mathbf{A}$ [19].

5. THE FOKKER-PLANCK EQUATION

The derivation of the FP equation is carried out most directly by using the above path integral. For this purpose, we use the "imaginary time trick", that is, we define $\tau = iz$, so introduce the "wave function" $\Psi(\mathbf{S}, \tau)$, then we have the integral equation:

$$\Psi(\mathbf{S}, \tau) = \int K[\mathbf{S}(\tau)|\mathbf{S}(0)]\Psi(\mathbf{S}, 0)d\mathbf{S}(0). \tag{19}$$

Following the standard procedure of Feynman path integral, we obtain the Schrödinger equation:

$$ih\frac{\partial \Psi}{\partial \tau} = -\frac{1}{2}(\mathbf{p} - i\mathbf{A})^2 \Psi + W\Psi \tag{20}$$

where

$$\mathbf{p} = -ih\frac{\partial}{\partial \mathbf{S}}, \quad W = \frac{\mathbf{A}^2}{2} + Mh \tag{21}$$

By using Eq. (21), replacing the imaginary time τ with the original real coordinate z, namely $\tau \to iz$, and getting "wave function" Ψ back to the original probability distribution P. Thus, we can obtain the FP equation:

$$\frac{\partial P}{\partial z} = \frac{h}{2}\left(\frac{\partial}{\partial \mathbf{S}}\right)^2 P + \frac{\partial}{\partial \mathbf{S}} \cdot (\mathbf{A}P) \tag{22}$$

The detailed analyses for this FP equation will be given near-future.

6. SUMMARY

We have developed the theory of evolution of the polarization inherent in the non-linear birefringent media. This can be realized as the dynamics of the Stokes parameters. The equation of the Stokes parameters is reduced to the Langevin equation. The Langevin equation is naturally converted to the FP equation by using the functional integral based on the Gaussian white noise for the random fluctuations inherent in the birefringent media.

REFERENCES

1. Landau, L. D., E. M. Lifshitz, and L. P. Pitaevskii, "Electrodynamics of continuous media," *Course of Theoretical Physics*, Vol. 8, Butterworth-Heinemann, 1984.
2. Born, M. and E. Wolf, *Principle of Optics* Pergamon, Oxford, 1975.
3. Sala, K., "Nonlinear refractive-index phenomena in isotropic media subjected to a dc electric field: Exact solutions," *Phys. Rev. A*, Vol. 29, 1944–1956, 1984.
4. Tratnik, M. V. and J. E. Sipe, "Nonlinear polarization dynamics. I. The single-pulse equations," *Phys. Rev. A*, Vol. 35, 2965–2975, 1986.
5. Kuratsuji, H. and S. Kakigi, "Maxwell-Schrödinger equation for polarized light and evolution of the stokes parameters," *Phys. Rev. Lett.*, Vol. 80, 1888–1891, 1998, and references cited therein.
6. Ade, P. A. R., et al., "Evidence for gravitational lensing of the cosmic microwave background polarization from cross-correlation with the cosmic infrared background," *Phys. Rev. Lett.*, Vol. 112, 131302-1–131302-6, 2014.
7. Ade, P. A. R., et al., "Measurement of the cosmic microwave background polarization lensing power spectrum with the POLARBEAR experiment," *Phys. Rev. Lett.*, Vol. 113, 021301-1–021301-7, 2014.
8. Zaldarriaga, M. and U. Seljak, "Gravitational lensing effect on cosmic microwave background polarization," *Phys. Rev. D*, Vol. 58, 023003-1–023003-6, 1998.

9. Seljak, U. and M. Zaldarriaga, "Signature of gravity waves in the polarization of the microwave background," *Phys. Rev. Lett.*, Vol. 78, 2054–2057, 1997.

10. Kamionkowski, M., A. Kosowsky, and A. Stebbins, "A probe of primordial gravity waves and vorticity," *Phys. Rev. Lett.*, Vol. 78, 2058–2061, 1997.

11. Chandrasekhar, S., "Stochastic problems in physics and astronomy," *Rev. Mod. Phys.*, Vol. 15, 1–89, 1943.

12. Kubo, R., M. Toda, and N. Hashitsume, *Statistical Physics II, Nonequilibrium Statistical Mechanics*, 2nd Edition, Springer-Verlag, Heidelberg, 1991.

13. Chiao, R. Y., E. Gamire, and C. H. Townes, "Self-trapping of optical beams," *Phys. Rev. Lett.*, Vol. 13, 479–482, 1964; Erratum, *Phys. Rev. Lett.*, Vol. 14, 1056, 1965.

14. Swartzlander, Jr., G. A. and C. T. Law, "Optical vortex solitons observed in kerr nonlinear media," *Phys. Rev. Lett.*, Vol. 69, 2503–2506, 1992.

15. Kuratsuji, H., "A field equation of the stokes parameters — Spin texture of light polarization," *J. Phys. Soc. Jpn.*, Vol. 77, 044403-1–044403-5, 2008.

16. Maker, P. D., R. W. Terhune, and C. M. Savage, "Intensity-dependent changes in the refractive index of liquids," *Phys. Rev. Lett.*, Vol. 12, 507–509, 1964; Erratum, *Phys. Rev. Lett.*, Vol. 16, 832, 1966.

17. Kuratsuji, H., R. Botet, and R. Seto, "Electromagnetic Gyration-Hamiltonian dynamics of the stokes parameters," *Prog. Theor. Phys.*, Vol. 117, 195–217, 2007.

18. Lischitz, E. M. and L. P. Pitaevski, *Statistical Physics; Part 2, Course of Theoretical Physics*, Vol. 9, Butterworth-Heinemann, 1986.

19. Tsuchida, S. and H. Kuratsuji, under Submission for Publication.

Calculations of Inductance and Induced EMF in a Planar Pickup Coil

G. A. Topasna and D. M. Topasna

Department of Physics and Astronomy, Virginia Military Institute, Lexington, VA, USA

Abstract— We present derivations of the equations and numerical solutions for the inductance and induced emf in a rectangular pickup loop in the presence of a current-carrying short straight wire. We explore three orientations of the loop with respect to the wire: in the plane of the wire with one edge of the loop parallel to the wire, in the plane of the wire with one edge of the loop at an arbitrary angle with respect to the wire, and with the loop at an arbitrary angle in three-space with respect to the wire. Solutions in closed-form are presented for the simple cases. This work has applications related to pickup coils in general.

1. INTRODUCTION

Electromagnetic calculations involving the ideal situations typically make for easier calculation that are covered in most introductory textbooks [1, 2], but are usually not indicative of practical, working conditions of a device. In more complex configurations the equations typically take closed-form solutions and approximations for specific geometrical shapes and arrangements of conductors [3, 4] but integral equations are not usually given.

For example, consider the calculation of the flux through a rectangular loop adjacent to the an infinitely long, current carrying straight wire. The rectangular loop acts as a pick-up coil since it is flux-linked to the straight wire. By making the straight wire infinitely long, the calculation is easier because of the constant flux inside an infinitesimally thin rectangular box that has its long side parallel to the wire. Consider the arrangement shown in Figure 1 (with the wire's z axis infinite in both directions). Using the dimensions shown in Figure 1, the flux is easily given by the integral

$$\Phi = \int_a^{a+b} \int_0^c \frac{\mu_0 I}{2\pi y} dz dy = \frac{\mu_0 I c}{2\pi} \ln\left[1 + \frac{b}{a}\right]. \tag{1}$$

However, the problem becomes more difficult when the infinitely long restriction is lifted since the magnetic field is no longer symmetric in the rectangular loop. Additionally, the orientation of the loop may vary with respect to the wire. In these cases, finding closed-form algebraic expressions are typically not practical and numerical solutions are usually sufficient. In this article we show how the induced emf can be calculated for various geometries for this wire-loop combination.

2. DERIVATION I: SIMPLIFIED GEOMETRY OF A PLANAR LOOP

Consider the single-turn rectangular loop parallel to the straight wire as shown in Figure 1. The straight wire carries a time varying current $I(t)$ and the magnetic field intensity at locations x and y and time t is given by the expression

$$\vec{B}(y, z, t) = \frac{\mu_0 I(t)}{4\pi y} \left[\frac{(z - L)}{\sqrt{y^2 + (z - L)^2}} - \frac{z}{\sqrt{y^2 + z^2}}\right](-\hat{i}) \tag{2}$$

where y and z are the coordinates measured from the bottom of the wire (taken as the origin). The expression, integrated over the area of the loop $[d\vec{A} = dy dz(-\hat{i})]$, is the time rate of change of flux $\Phi(z, t)$ and is

$$\Phi(z, t) = \frac{\mu_0 I(t)}{4\pi} \int_{z_0}^{z_0+c} \int_a^{a+b} \left[\frac{(z - L)}{y\sqrt{y^2 + (z - L)^2}} - \frac{z}{y\sqrt{y^2 + z^2}}\right] dy dz. \tag{3}$$

This equation can be written as

$$\Phi(z_0, t) = \frac{\mu_0 I(t)}{4\pi} \left[\bar{I}(z_0 - L) - \bar{I}(z_0)\right] \tag{4}$$
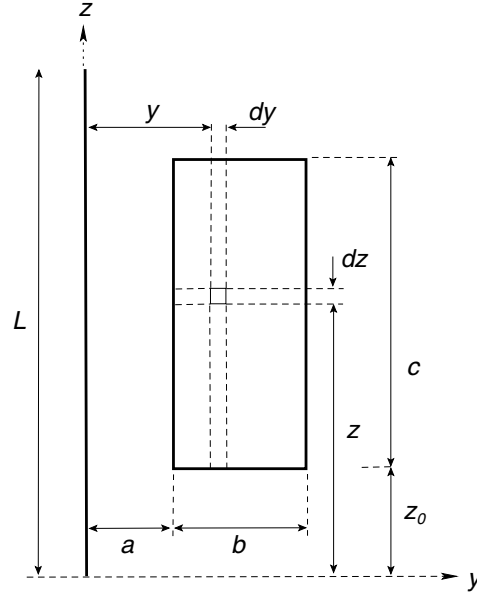
Figure 1: Configuration of loop parallel to straight wire.

where the integrals differ only in the replacement of $z_0 - L$ for z_0 which simplifies the closed-form solution to

$$
\begin{aligned}
\bar{I}(z_0) = {} & \sqrt{(a+b)^2 + (z_0+c)^2} - \sqrt{a^2 + (z_0+c)^2} \\
& -(z_0+c)\ln\frac{a}{a+b}\frac{(z_0+c)+\sqrt{(a+b)^2+(z_0+c)^2}}{(z_0+c)+\sqrt{a^2+(z_0+c)^2}} \\
& -\sqrt{(a+b)^2+z_0^2} + \sqrt{a^2+z_0^2} + z_0\ln\frac{a}{a+b}\frac{z_0+\sqrt{(a+b)^2+z_0^2}}{z_0+\sqrt{a^2+z_0^2}}
\end{aligned}
\tag{5}
$$

with the expression for $\bar{I}(z_0 - L)$ given as the same expression above but with $z_0 - L$ substituted for z_0. While the above expression does show that the time-varying flux can be expressed in closed-form, its actual use in calculations can be un-wielding. It can be shown that in the proper limits, this expression reduces to Equation (1). Since numerical results are sufficient for experimental comparisons, we include the above expression only for completeness and will use only integral expressions for the rest of our calculations.

Since mutual inductance is defined as $M \equiv \Phi/I$ the expression for the mutual inductance between the straight wire and the rectangular loop is $M = \mu_0/4\pi[\bar{I}(z_0 - L) - \bar{I}(z_0)]$ where it is noted that the integral expressions contain only geometric terms, consistent with the fact that inductance is determined only by geometry. Using Faraday's law, the induced emf that appears as $V(t)$ across the terminals of the loop is very closely approximated at $V(t) = -\dot{\Phi} = -M\dot{I}(t)$ when the gap in the loop is very small.

Consider a sinusoidal time-varying current in the straight wire $I(t) = I_0\cos\omega t$ where I_0 is the maximum current in the wire and $\omega = 2\pi f$ is the angular frequency. The instantaneous value of the induced emf is $V(t) = \omega M I_0 \sin\omega t$. Since the *rms* value is what is physically measurable it is easily calculated using the time-average integral over one period for the previous expression

$$
V_{rms} = \frac{\mu_0\omega I_0}{8\pi}\left[\bar{I}(z_0 - L) - \bar{I}(z_0)\right]
\tag{6}
$$

where $[\bar{I}(z_0 - L) - \bar{I}(z_0)]$ is numerically calculated for various loop-wire geometries.

3. DERIVATION II: GENERAL CASE OF A PLANAR LOOP AT ANGLE θ

Consider the single-turn rectangular loop shown in Figure 2(a). In this configuration the loop's angle with respect to the finite straight wire is given by the parameter θ (measured parallel to the length of the finite wire). We first note that there is a critical angle for the loop's orientation with
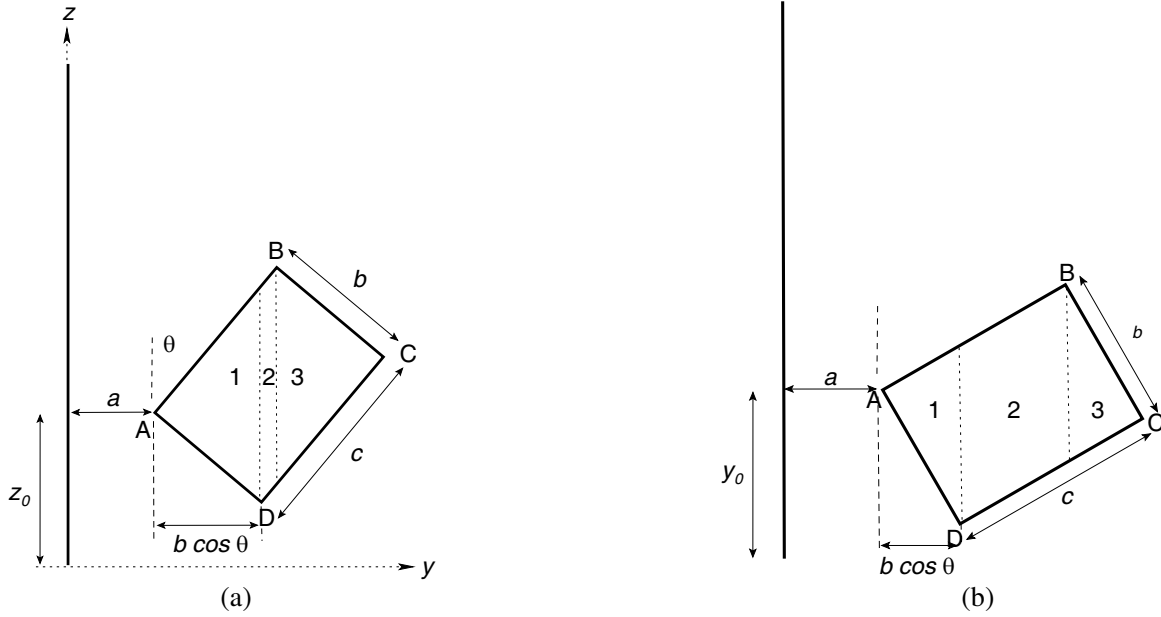
Figure 2: Configuration of straight wire with loop at angle (a) less than the critical angle and (b) greater than the critical angle.

respect to the straight wire. It occurs when a line drawn from the corner angle A to corner angle B is perpendicular to the straight wire. The critical angle is then given by $\tan \theta_c = b/c$. This will split the rectangle into two equal triangles with a common hypotenuse and integration over the loop is a little more straightforward. However, at any other angle there will be three regions to integrate over (two triangular regions and the parallelogram region between them as seen in the figure and labeled as 1, 2, and 3).

There are two cases to consider. One is when the loop is at an angle less than the critical angle θ_c and the other is when it is greater than the critical angle. The case for when the loop is exactly at the critical angle is then either of these cases and both results are the same when evaluated at this critical angle.

Angle less than θ_c

The first case we consider is when the angle is less than the critical angle. The three regions of the loop lend themselves to three separate integrals for $I(\theta < \theta_c) = I_1 + I_2 + I_3$ which gives

$$
\begin{aligned}
I(\theta) = & \int_{a}^{a+c\sin\theta} \int_{z_0-(x-a)\tan\theta}^{z_0+\frac{y-a}{\tan\theta}} B(y,z,t)dydz + \int_{a+c\sin\theta}^{a+b\cos\theta} \int_{z_0-(c\sin\theta+y)\tan\theta}^{z_0+c\cos\theta-y\tan\theta} B(y,z,t)dydz \\
& + \int_{a+b\cos\theta}^{a+b\cos\theta+c\sin\theta} \int_{z_0+\alpha-\frac{c\sin\theta-(y-a-b\cos\theta)}{\tan\theta}}^{z_0+\alpha+[c\sin\theta-(y-a-b\cos\theta)]\tan\theta} B(y,z,t)dydz
\end{aligned} \tag{7}
$$

where $\alpha = c/\cos\theta - b\sin\theta - c\sin\theta\tan\theta$.

Angle greater than θ_c

The second case we consider is when the angle is greater than the critical angle. The three regions of the loop for giving $I(\theta > \theta_c) = I_1 + I_2 + I_3$ then yields

$$
\begin{aligned}
I(\theta) = & \int_{a}^{a+b\cos\theta} \int_{z_0-(x-a)\tan\theta}^{z_0+\frac{y-a}{\tan\theta}} B(y,z,t)dydz + \int_{a+b\cos\theta}^{a+c\sin\theta} \int_{z_0-(b\sin\theta)+\frac{y-a-b\cos\theta}{\tan\theta}}^{z_0+\frac{y-a}{\tan\theta}} B(y,z,t)dydz \\
& + \int_{a+c\sin\theta}^{a+c\sin\theta+b\cos\theta} \int_{z_0+\alpha\frac{b\cos\theta-(y-a-c\sin\theta)}{\tan\theta}}^{z_0+\alpha+[b\cos\theta-(y-a-c\sin\theta)]\tan\theta} B(y,z,t)dydz
\end{aligned} \tag{8}
$$

where now $\alpha = (c - b\tan\theta)\cos\theta$ and the total integration giving $I(\theta > \theta_c) = I_1 + I_2 + I_3$.

4. DERIVATION III: ARBITRARY ORIENTATION

Consider the single-turn rectangular loop shown in Figure 3. The single loop is located in the (x, y, z) coordinate system with integration carried out over the (y, z) plane of the loop. The finite wire is oriented along z' axis of a coordinate system that is rotated about the (x, y, z) axes with the two origins coincident.
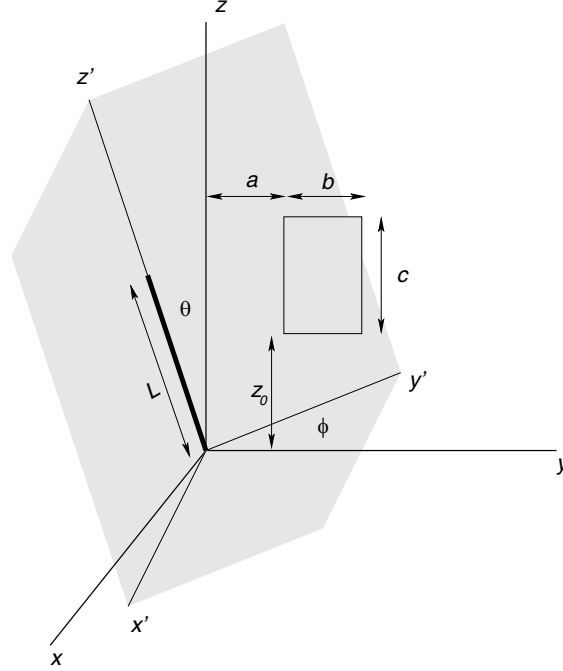

Figure 3: General rotation figure.

Using the Biot-Savart Law, the integral in the primed coordinate system

$$\vec{B}(\vec{r'}, t) = \frac{\mu_0 I(t)}{4\pi\epsilon_0} \int_0^L \frac{\left(y'\hat{i'} - x'\hat{j'}\right) d\zeta'}{\left(x'^2 + y'^2 + (z' - \zeta)^2\right)^{3/2}} \tag{9}$$

can be solved in a straightforward manner to yield

$$\vec{B}(\vec{r'}, t) = \frac{\mu_0 I(t)}{4\pi\epsilon_0} \frac{(y'\hat{i'} - x'\hat{j'})}{(x'^2 + y'^2)} \left[\frac{z'}{\sqrt{x'^2 + y'^2 + z'^2}} - \frac{z' - L}{\sqrt{x'^2 + y'^2 + (z' - \zeta)^2}} \right] \tag{10}$$

for a closed-form solution of the magnetic field. Now, the integration to determine the flux is easier to carry out over the unprimed coordinate system,

$$\Phi(t) = \int_a^{a+b} \int_{z_0}^{z_0+c} \vec{B}(\vec{r}, t) \cdot d\vec{A} \tag{11}$$

but this requires the magnetic field equation to map from $\vec{B}(\vec{r'}, t)$ to $\vec{B}(\vec{r}, t)$. This is easily accomplished using the transformation equation $\mathbf{x} = \boldsymbol{\lambda}\mathbf{x'}$ where the transformation matrix $\boldsymbol{\lambda}$ transforms coordinates in the primed frame $\mathbf{x'}$ to those in the unprimed frame $\mathbf{x}$ using the matrix equation

$$\mathbf{x_i} = \sum_{i,j} \lambda_{i,j} \mathbf{x'_i} \tag{12}$$

where the elements of matrix (λ_{ij}) are the direction cosines of the $x'_i - x_j$ axis (i.e., $\lambda_{ij} = \cos(x'_i, x_j)$). Additionally, the transformation matrix is used to transform the unit vectors from the primed to

unprimed coordinate system therefore allowing the complete transformation $\mathbf{B}(\vec{r'}, t) \mapsto \mathbf{B}(\vec{r}, t)$ that is given by

$$
\begin{aligned}
\mathbf{B}(\vec{r}, t) \;=\; & \frac{\mu_0 I(t)}{4\pi\epsilon_0} \frac{1}{(\lambda_{12}y + \lambda_{13}z)^2 + (\lambda_{22}y + \lambda_{23}z)^2} \\
& \times \Bigg[\frac{(\lambda_{32}y + \lambda_{33}z)}{\sqrt{(\lambda_{12}y + \lambda_{13}z)^2 + (\lambda_{22}y + \lambda_{23}z)^2 + (\lambda_{32}y + \lambda_{33}z)^2}} \\
& \quad - \frac{(\lambda_{32}y + \lambda_{33}z - L)}{\sqrt{(\lambda_{12}y + \lambda_{13}z)^2 + (\lambda_{22}y + \lambda_{23}z)^2 + (\lambda_{32}y + \lambda_{33}z - L)^2}} \Bigg] \\
& \times \Big[\lambda_{11}(\lambda_{22}y + \lambda_{23}z) - \lambda_{21}(\lambda_{12}y + \lambda_{13}z) \Big].
\end{aligned}
\tag{13}
$$

With the appropriate direction cosines, this equation is substituted into Equation (11) and the flux integral carried out over $d\vec{A} = dydz\hat{i}$, which can then be used to calculate the mutual inductance and induced emf in the loop.

5. CONCLUSION

We have derived numerical expressions for the mutual inductance and emf for a pick-up coil in the presence of a current-carrying finite length wire. Three geometries were considered and typical numerical results were presented. The expressions lend themselves to easy implementation by programs such as Mathcad, Mathematica, or other programming languages.

REFERENCES

1. Cheng, D. K., *Field and Wave Electromagnetics*, Addison-Wesley, New York, 1992.
2. Reitz, J. R., F. J. Milford, and R. W. Christy, *Foundations of Electromagnetic Theory*, 3rd Edition, Addison-Wesley, New York, 1980.
3. Grover, F. W., *Inductance Calculations*, Dover Publications, Inc., New York, 2009.
4. Thompson, M. T., *Inductance Calculation Techniques — Part II: Approximations and Handbook Methods, Power Control and Intelligent Motion*, Dec. 1999, http://www.pcim.com.

Time Delay Module Design, Simulation and Synthesis Based on FPGA for Dielectric Dispersion Logging

Changqi Yang, **Simin Liu**, **Liuyi Yang**, **and Cheng Yang**

School of Science, Xi'an Shiyou University, Xi'an 710065, China

Abstract— A few years ago, a kind of dielectric scanning imaging logging instrument emerged in the foreign markets. That instrument scanned the earth at different frequency electromagnetic wave. It can measure the dielectric constant at different frequencies of the layer. There is not any similar instrument developed at home. Xi'an Shiyou University has launched a project to develop a comparable instrument. This paper introduces the basic principle of dielectric dispersion logging. A general layout is given for the dielectric dispersion logging. The time delay module is simulated and synthesized based on FPGA. This laid the foundation for the development of comparable instruments gradually.

1. INTRODUCTION

Dielectric logging is known for a group of logging method by using the rock dielectric constant to distinguish between different strata. It is currently the most potential one of the logging technologies. It uses a transmitting coil and two receiving coils. The coil center is in the well shaft. A transmitting antenna transmits electromagnetic (EM) wave to the layer. Because of the influence of EM wave propagation, there is phase change and amplitude attenuation in the propagation process. It leads to a difference in the signals' phase and amplitude of the two coils. The two receiving antennae can be used to received the layer's EM wave phase difference and amplitude ratio. The phase difference and amplitude ratio are functions of the layer's resistivity and dielectric constant. It can be used to inversely calculate the layer's resistivity and dielectric constant.

The relevant research of dielectric logging is started from the former Soviet Union. In 1966, a new kind of method of high-frequency logging was proposed in the former Soviet Union. Its principle is putting two receiving coils nearby the transmitting one, and detecting the EM wave's phase difference between the two receiving coils. When the detection frequency is nearly tens of MHz, the phase difference mainly depends on the rock dielectric constant. Thus far, the Soviet Union completed the relevant theoretical research, manufactured a prototype, and tested the prototype in the well smoothly. As a result, high-frequency logging is used in the production [1–3]. In America, the most well-known instrument is Schlumberger's Electromagnetic Wave Propagation Tool. Its operation frequency is 1.1 GHz [4]. In 2010, high frequency dielectric logging tool with 1 GHz frequency that developed by Halliburton is put into commercial application [5].

In China, many institutes have developed this technique. Nowadays dielectric logging tools have been successfully put into markets [6]. Their function is equivalent to Schlumberger's instrument.

All the above is about the dielectric logging technology of a single frequency. The dielectric dispersion logging technology is to emit different frequencies of EM waves into the stratum. Different frequencies mean different dielectric constant. According to the analysis result of the scanning information, it can reverse the stratum's structure.

In 2010, Schlumberger released the dielectric dispersion logging instrument. The instrument can measure the stratum's water saturation and rock structure [7]. Field test results show that it provides a new method to find oil and gas. But its current price in China is extremely expensive. Xi'an Shiyou University has launched a project to develop dielectric dispersion logging equipment. As an early work, the authors have carried on the corresponding research. This paper introduces the basic principle of dielectric dispersion logging and its framework design, and the time delay module has been simulated and synthesized based on FPGA.

2. TIME DELAY DIFFERENCE OF DIELECTRIC LOGGING

If emit EM wave into the stratum, the stratum's EM parameters will be reflected in the amplitude and phase of EM waves, such as the stratum's dielectric constant, resistivity and magnetic conductivity. Generally speaking, there exist great differences of the dielectric constant among oil, water, and rock matrix. For example, at normal temperature the relative dielectric constant of water is about 80, while the oil's is about 2.0–2.4, and the rock matrix' is about 3–9. Thus far, in

some logging circumstances it has great advantages to using dielectric constant parameter instead of resistivity parameters.

The dielectric constant of strata can usually be expressed in a complex form as below: $\varepsilon = \varepsilon' - j\varepsilon''$, where, the real part $\varepsilon' = t_{p1}/\mu_{0} = \alpha/(\omega^2\mu_0)$, the imaginary part $\varepsilon'' = 2\alpha t_{p1}/(\omega\mu_0)$, t_{p1} is EM wave's propagation time delay per meter, μ_0 is the magnetic permeability of vacuum, α is EM wave's propagation attenuation coefficient per meter, ω is the EM wave's angular frequency, j is the imaginary unit. Usually the so-called dielectric constant refers to the real part, while the imaginary part comes from the EM wave's attenuation when propagating in the medium. The imaginary part is not zero means that the medium absorbs the EM energy and converts it into heat. Since ω and μ_0 are known, the complex dielectric constant ε can be reached as long as t_{p1} and α are measured.

Usually dual-frequency technique is used to detect dielectric constant. Then reverse the stratum information. The so-called "dual frequency" is to change the detection depth by using two different working frequencies, such as Western Atlas's dual-frequency dielectric logging instrument. The deep detector uses 47 MHz operating frequency, and the shallow detector uses 200 MHz operating frequency.

And Schlumberger's dielectric dispersion logging instrument can use EM wave to scan the stratum with a band from 1 MHz–1 GHz. It can depict the dielectric constant of the entire frequency band. For us, our approach is selecting 4 frequency points to detect the dielectric constant in the 1 MHz–1 GHz frequency range. It is enough.

As shown in Figure 1, it is the principle of the dielectric dispersion logging instrument designed by the authors.
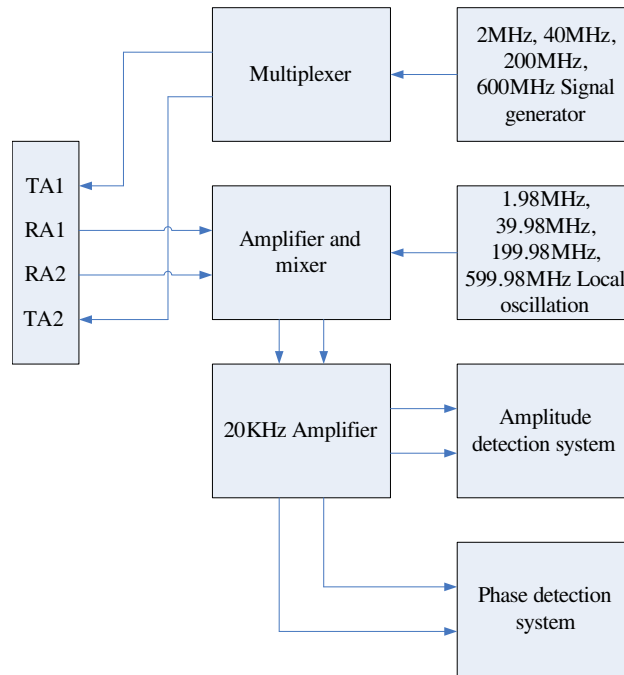

Figure 1: Principle of the dielectric dispersion logging instrument.

In Figure 1, there are 2 transmitting antennas TA1 and TA2, and 2 receiving antennas RA1 and RA2. The signal source can respectively emit 4 EM waves of different frequency: 2 MHz, 40 MHz, 200 MHz and 600 MHz. It uses double transceiver working mode. This paper mainly studies the module of time delay. Assuming that the frequency of the emitting signal $S(t)$ is $\omega = 600$ MHz, then the output of receiver RA1 is $R_1(t) = A_1\sin(\omega t + \varphi_1)$, the output of receiver RA2 is $R_2(t) = A_2\sin(\omega t + \varphi_2)$. The frequency of the local oscillation signal $S_L(t) = A_L\sin(\omega_L t + \varphi_L)$ is $\omega_L = 599.98$ MHz. The local oscillation signal mixes with the output of the first receiver, and the result is $M_1(t) = S_L(t) * R_1(t) = A_L\sin(\omega_L t + \varphi_L) * A_1\sin(\omega t + \varphi_1)$. Passing through the low-pass filter, filtering out the sum frequency term, taking into account the transmission coefficient of the filter K_1, we arrive at the difference frequency term as below: $M_1(t) = 0.5 * K_1 A_L A_1 \cos[(\omega - \omega_L)t + \varphi_1\varphi_L]$. Similarly, the output of the second mixer is $M_2(t) = 0.5 * K_2 A_L A_2 \cos[(\omega - \omega_L)t + \varphi_2\varphi_L]$. Suppose that $K_1 = K_2$, therefore the time delay difference of the two mixer's output can be calculated as

$\Delta\varphi = (\varphi_2 - \varphi_L) - (\varphi_1 - \varphi_L) = \varphi_2 - \varphi_1$. Accordingly, it provides a reference for the inversion of the dielectric constant.

3. SIMULATION AND SYNTHESIS BASED ON FPGA

As to the time delay module, the authors write source codes based on the Verilog HDL. The time delay module is simulated by Modelsim software. As shown in Figure 2, it is the simulation result. In Figure 2, clk is the system clock, and CP is the input signal. CP consists of CP1 and CP2. CP1 and CP2 are differential frequency signals. When the rising edge of CP1 comes, it generates a rising edge at the output Qout; when the rising edge of CP2 comes, it generates a falling edge at the output Qout. The high level width of Qout is the time delay difference of CP1 and CP2.

Using the clock signal clk to count in the time of high level of Qout, we can know the length of time delay difference.
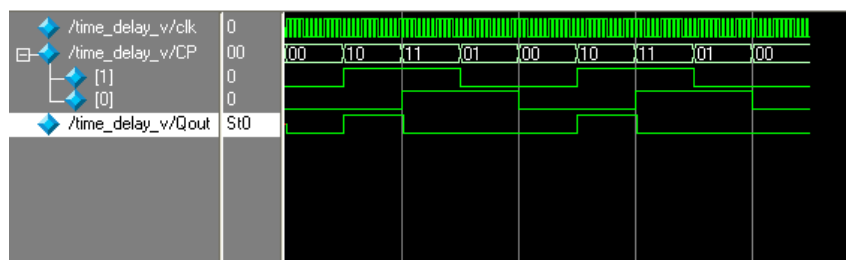

Figure 2: Simulation result of the time delay module.

As shown in Figure 3, it is the hardware synthesis result of this module. The hardware synthesis is based on Synplify software. The hardware structure of the system is very simple. It mainly consists of a multiplexer and a D flip-flop. The output of the multiplexer is used as the input of the D flip-flop. The CP signal is used to control the multiplexer. The synchronous clock clk is used to control the D flip-flop.
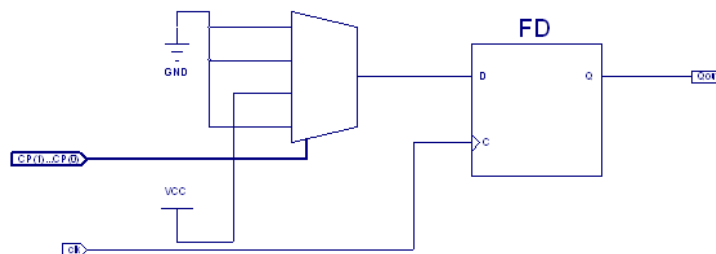

Figure 3: Synthesis result of the time delay module.

4. DISCUSSION

The dielectric dispersion logging technology is reviewed in this paper. The principle of the dielectric dispersion logging is introduced. The authors establish a model on how to extract the time delay signal. Software simulation and hardware synthesis are carried on this model. The simulation results accord with the theoretical expectations. The next step goes to study the amplitude attenuation module.

REFERENCES

1. Daqing Oilfield, "Research on the dielectric logging," *Petroleum Exploration and Development*, Vol. 02, 60–64, 1974.

2. Zhao, S., "Relationship between rock dielectric constant and other factors," *WLT*, Vol. 04, 36–47, 1982.

3. Shang, Z., "EM wave propagation logging," *Logging Technology*, Vol. 04, 73–83, 1982.

4. Wu, X. and W. Pan, "Lateral wave propagation in EM wave logging," *Chinese Journal of Geophysics*, Vol. 35, No. 1, 93–101, 1992.

5. David, "New development of logging while drilling and stratum evaluation," *Overseas Oilfield Engineering*, Vol. 4, 2–5, 1999.

6. Liu, S., "Numerical and experimental study on multi-frequency EM wave well logging," *WLT*, Vol. 27, No. 4, 278–282, 2003.

7. "New technology and application of dielectric logging," *New Technology in Oilfield*, Vol. 23, No. 1, 36–52, 2011.

Geometry and Its Physical Meaning

S. L. Vesely[1] and A. A. Vesely[2]

[1]I.T.B. — C.N.R., Italy
[2]Via L. Anelli 13, Milano, Italy

Abstract— Until the end of 1800s, the graphical aspect of geometry used to be compared to the external world, called "physical space", and justified on the basis of mechanics. As a consequence of the foundational crisis of mathematics, geometry switched to axiomatic programs and disengaged from the physical intuition of space. Its logical structure was formalized and further developed, neglecting geometrical constructions. Endorser of formalist programs, physics evolved toward more and more sophisticated interpretations of the world, also supported by advancements of surveying and measurement techniques. Physical laws are regarded as interpretative algorithms tied to recurring process patterns, no longer as interpretations of a code that Nature is written in the language of. What got lost during that transition, in our opinion, is the ability to avail of both experience and deduction in geometrical models of field theories, so as to provide a logical foundation for interpreting the extent in a physically meaningful way. In particular, (1) irrespectively of whatever code, the optical channel does convey a huge amount of the data, which our experience consists of, and (2) geometry allows to model non-optical electromagnetic signals consistently with the optical ones, so as to analyze them uniformly. In this paper, we stem from models entailed by geometrical optics and discuss the relationships among them, imaging based on projective geometry, and mathematical analysis.

1. INTRODUCTION

Euclid's contribution to geometry as we know it consisted in setting logical reasoning apart from cosmological conceptions, sensory perceptions, and empirically gathered methods to assess properties of physical objects.[1] His distinction between postulates and axioms, problems and theorems[2] suggest that he regarded the drawings constructed to illustrate theorems as proofs of existence [1].[3] Newton diverged from that mindset. In his Principia, he combines cosmology and Euclidean geometry, originating the concept of a space devoid of matter. In the early 1900s, as a consequence of the uptake of non-Euclidean geometry, the whole discipline, including Euclidean, non-Euclidean, affine and projective geometries, was restated on an axiomatic basis. Today implicit designations of terms such as point and straight line,[4] given through axioms, supersede explicit definitions of graphical elements endowed with geometrical meaning. Logical principles of geometrical thinking introduce abstraction via isomorphisms, such as that between real numbers and a straight line.

Based on isomorphisms, analytical representations of axiomatic structures bear a semantical meaning different from that of traditional geometrical constructions. For an idea of the meaning of constructions, consider how Mach verified the parallelogram of forces by probing Galileo's and Stevin's experiences on inclined planes [2]. His graphical construction does neither suggest what inertia is, nor prove laws of forces or mathematical parallelogram identity. However, it shows how Varignon's construction applies to Galileo's and Stevin's mechanics. On the other hand, to say that vectors *realize* linear algebra is a statement which does not depend on any application or graphical symbol.[5] Suppression of geometrical constructions has eventually implied waiver of real world modeling.

---

[1]We mean geometry as a deductive process, not as Platonic ideas ($\iota\delta\epsilon\alpha$ = archetypal image) like Proclus does.

[2]It is difficult, today, to estimate what Euclid meant by his porisms. According to pre-Socratic philosophers, through whom the idea of Cosmos came, it made no sense to attribute a shape to a vacuum, as shapes belonged to the four elements, earth, air, water, and fire. Celestial maps of the time display the vault of sky held up by the ocean around the flat Earth. Later, ∼350 BC, at Plato's and Aristotle's time, Earth shape became spherical, and the wheels, which used to trail celestial bodies around the Earth in the earlier, groundbreaking model of Anaximander-Thales' disciple-, were replaced by armillary spheres. The cutting-edge cosmological problem was "Why doesn't the Earth fall down?" By contrast, Euclid's Elements, Book XI, which dates back to that time, introduces solids without referring to physical space. Indeed, it neither defines a "space".

[3]While a theorem's statement establishes a universal quantification ($\forall$), a geometrical construction gives an existential one ($\exists$).

[4]In his sixth problem, Hilbert proposed to treat physics substituting the basic objects of the axiomatically formulated geometry with a different system of objects put in a one-to-one relationship with it.

[5]Valid mathematical statements don't imply the existence of the entities that they refer to, except where explicitly noted. Furthermore, mathematical existence does not imply any corresponding physical object.

2. CONSTRUCTIVE GEOMETRICAL APPROACH TO OPTICS

The geometric framework of electromagnetism results mainly from two approaches. (1) The electrodynamic approach which, thanks to Lagrange's analytical mechanics formulation, evolved into the unified theories of space-time geometry with quantum theoretical principles. (2) The graphical ray-optics approach, which is dual to Huygens' wave fronts. In the latter approach, constructions are borrowed from the so-called *mechanical geometry*, where optical instruments play the role of ray tracer, a kind of geometric construction tool. In the rest of this section we give a critical account of the way approach (2) describes magnification M as obtained by optical systems without taking defects and apertures into account. The fundamental assumption of geometrical optics is that the angular magnification is the same as the linear one, so that an image is similar to the corresponding object.[6] A light ray emitted by a source point P_1 is plotted as a straight line having a slope α_0 with respect to the optical axis x.[7] The optical instrument provides for tracing the ray to the final image point, say P_{N+1}. Analytical geometry provides a method to convert the resulting construction to an analytical expression, as we do next [3].

Let's denote by S_1, ..., S_N a coaxial array of thin lenses; by d_j the distances (S_j, S_{j+1}); by P_1 the object point, and by P_2, ..., P_{N+1} its images; by s_i the distances between any two of those, so that s_0 is the distance (S_1, P_1), s_1 the distance (S_1, P_2) and so forth.[8] As images are formed, the system traces open, monotone polygonal chains, whereby the image point after S_j works as an object point for for the next lens. In the one-simple-lens case, the correspondence between graphics and experiment can easily be verified. A normal congruence of traced rays can be visualized as a beam, e.g., by spreading around some smoke. That beam may suggest to consider a ray as a light trajectory. The lens first F and second F' focal points can be identified that way. The focal length is $f = FS_1 = S_1F'$. Let's call n the air-glass refractive index, and $1/r$, $1/r'$ the curvatures, then the power is defined as: $p := \frac{1}{s_1} - \frac{1}{s_0} = (n-1)(\frac{1}{r} - \frac{1}{r'}) = \frac{1}{f}$.

For a system composed of N lenses, let's compute the abscissa of the image point P_{N+1} formed at a distance s_{2N-1} behind the last lens, S_N. Starting from the identities $f_1(1/s_1 - 1/s_0) = f_2(1/s_3 - 1/s_2) = \ldots = 1$ valid for each lens, a system of N equations is build up solving for even s_i: $s_0 = \frac{-f_1}{1-f_1/s_1} = \frac{-f_1}{1-\frac{f_1}{d_1+s_2}}, s_2 = \frac{-f_2}{1-\frac{f_2}{d_2+s_4}}, \ldots, s_{2N-2} = \frac{-f_N}{1-\frac{f_N}{s_{2N-1}}}$. By substitution, we get the descending continued fraction: $s_{2N-1} = \frac{f_N}{1-} \frac{f_N}{d_{N-1}-} \frac{f_{N-1}}{1-} \frac{f_{N-1}}{d_{N-2}-} \frac{f_{N-2}}{1-} \frac{f_{N-2}}{d_{N-3}-} \cdots \frac{f_2}{1-} \frac{f_2}{d_1-} \frac{f_1}{1+f_1/s_0}$. That expression consists of simple terms, and resembles an *amplitude function* of ladder networks [4, 5].[9] In geometrical optics it is derived from the physical laws that light-related phenomena obey to.

If the object has an extent in a plane $x = const$, and diffuses light toward the glass-work as a whole, the size h' of the image is magnified relative to the size h of the object. In order to determine the transverse magnification $M = h'/h$ choose a point P_1 of the object and trace a ray from there toward S_1, such that the ray meets its vertex with height $y_0 = 0$ and slope $y_{S_1} = s_0\alpha_0$. As the lens has a power, the ray leaves with an increased slope $p_1 y_{S_1} = \alpha_1 - \alpha_0$, resulting in a ratio of $\alpha_1/\alpha_0 = 1 + p_1 s_0$. The outgoing ray has equation $y = \alpha_1(x - x_{S_2}) + \alpha_1 d_1$. The ordinate undergoes a further increment $y_{S_2} - y_{S_1} = \alpha_1 d_1$ along the subsequent segment d_1 between S_1 and S_2.[10] Repeating the procedure for each lens, one obtains a system of equations with parameters α_j and $y_{S_{j+1}}$:[11]

---

[6]Euclidean geometry defines similarity as an admissible transformation. In optics, similarity applies to objects perpendicular to the optical axis. It is confined to paraxial approximation and thin lenses, not dioptric systems such as eyes.

[7]The so called divergence angle α_0 (with sign) of the ray is related to the incidence angle i in Snell's sine law by $i = \theta - \alpha_0$. $\pm\theta$ is the angle between x and the normal to the refractive surface meeting that light ray. For consistence $-\theta$ is used for a convergent lens.

[8]Here, we follow the Cartesian sign convention. The x axis is oriented toward increasing indexes; S_1 is in $x = 0$. Intermediate distances with odd subscripts are oriented as x, while $s_{2j} = s_{2j-1} - d_{2j-1}$ have the opposite orientation.

[9]Lenses form more than one image, if all reflections and refractions are taken into account. Here we are dealing with the geometric refraction of a point object located on the x-axis, disregarding diffraction and aberrations, frequency dispersion included, as well as the diffraction effects of apertures. The system's ray-transfer matrix reduces to a quotient of polynomials like a transfer function of a passive linear filter. When Cauer's mathematical development is carried over to optics, the dichotomy between (diffraction) frequency- and space-domain can be abandoned. In fact, Stieltjes showed how to express equivalently any holomorphic function either by a possibly infinite continued fraction, or by a definite integral. Hence, the frequently encountered linear functional transform $\int_0^\infty \psi(u)e^{zg(u)} du$ of an analytical function $\phi(z)$, $z \in \mathbb{C}$ can be represented as a continued fraction. Continued fractions converge in instances where the corresponding series do not. For an alternative treatment of filters, see, e.g., Bloomfield.

[10]Lens S_j contributes $\Delta_j\alpha = \alpha_j - \alpha_{j-1} = p_j y_{S_j}$ and $\Delta_{S_j}y = d_{j-1}\alpha_{j-1}$. If the j-th segment is inside a medium having refractive index n_j, one replaces d_j with $t_j = d_j/n_j$.

[11]Given $y_{S_1} = s_0\alpha_0$, The tridiagonal matrix is formed from the rays' parameters: $(\alpha_1 = \alpha_0 + p_1 y_{S_1}, y_{S_2} = y_{S_1} + d_1\alpha_1)$,

$$
\begin{array}{rllllll}
\alpha_1 & & & & = & \alpha_0 & +p_1 y_{S_1} \\
-d_1\alpha_1 & +y_{S_2} & & & = & & y_{S_1} \\
-\alpha_1 & -p_2 y_{S_2} & +\alpha_2 & & = & 0 & \\
0 & -y_{S_2} & -d_2\alpha_2 & +y_{S_3} & = & 0 & \\
0 & 0 & -\alpha_2 & -p_3 y_{S_3} & +\alpha_3 = & 0 & \\
\dots & \dots & \dots & \dots & \dots \ \dots \ \dots & \dots &
\end{array}
$$

The parameters (α_N, y_N) belong to the ray which leaves S_N to form the final image. Expressing them as a function of the input ray parameters $(\alpha_0, 0)$, by substitution, gives a continued fraction like the one obtained above for s_{2N-1}. In fact, the total power p could have been obtained from the above continued fraction by solving it for f_i. In Gauss' description, the magnification is given by the determinant of the coefficient matrix as $h/h' = \alpha_m/\alpha_0 = ps_0 + \partial p/\partial p_1$, where the latter expression is the cofactor expansion, in which the coefficient of the second term is the formal derivative with respect to p_1 of the first one.[12]

Since both abscissa and magnification are built in an Euclidean space, and each ray used for the pointwise construction can be visualized, the image made up of a point from each ray should be similarly traceable in the same space, as if it got off the object as an empty form and proceeded through the glass-work [6][13]. In fact, a splotch of light can be visualized on a cloud of smoke or a screen, but no propagation of an ethereal, object-like image is experimentally substantiated. The "extent", a term used to mean *that* property of the external world, is not modeled. Hence, interest turned from the homogeneous and isotropic space of Euclidean geometry toward the algebraic program of Lagrangian mechanics and Gauss' differential geometry.[14] Consequently, algebraic geometry applied to optics turned to formulating just the theoretical framework. Concepts such as light rays remain as relics of the previous theories and are only used to understand what we're talking about.

3. GEOMETRY AS A MODEL OF THE EXTENT

Geometry owes its name to the fact that, since the times of King Scorpion, Egyptians used tools equivalent to straightedges and compasses to parcel out the terrain after Nile floods. As Greek symbols hardly lent themselves to numerical computing, in Books V and VI Euclid developed compass-and-straightedge constructions to compute ratios between quantities.[15] Today, we associate continuous numerical variables to geometric objects — in an analytic, algebraic, or other context — considering metric as an integral part of geometry. Instead, geometrical shapes model plots of land as long as the same tools are used, at least theoretically, in both cases.[16]

Mechanical geometry (kinematics), which we touched upon about geometrical optics constructions, is a geometry different from Euclid's in that it originated for squaring the circle, and related Delian problems which could not be solved using only straightedge and collapsible compass [7]. It deploys gears motion to trace curves so that their measures depend on an algorithm of motion rather than on deductive reasoning and Euclid's construction tools.[17] When the Helmholtz-Lie problem of generating space by means of motion was put forward, the transformations performed

---

$(\alpha_2 = \alpha_1 + p_2 y_{S_2}, y_{S_3} = y_{S_2} + \alpha_2 d_2)$, ..., whose determinant of the coefficients is a continuant polynomial.

[12]The formal derivative is obtained by removing from p the row and column which contain coefficient p_1. The magnification $M = h'/h$ of the system, expressed as a function of the powers of the lenses and their separation, varies inversely as the distance s_0 of the object. This result makes use of the Lagrange invariant $n'h'\alpha' = nh\alpha$.

[13]Lucretius (deceased in 55 BC) tells that the image detaches itself from a body like a pellicle. He would not have admitted that a pinhole camera yields a clear image. Since then, there have been huge experimental and mathematical developments. However, the geometric theory of aberrations still recurs to the Gaussian image to determine the light intensity distribution. The wave-fronts proceeding from each element of a body orthogonally to the beams — whose departure from the spherical shape determines aberrations — quite resemble Lucretian pellicles.

[14]Originally, Hamilton derived the laws of reflection and refraction of light rays from the principle of least action given in Jacobi's form $A = \int_1^2 \sqrt{(E_{TOT} - V)\sum_{i,j} a_{ij}\, dq_i\, dq_j}$, where V is a suitable potential energy, q_k $(k = 1, \dots, n)$ are generalized coordinates, and the initial and final configurations have subscripts 1 and 2 respectively. In a differential geometric interpretation of the principle, q_k are intrinsic coordinates on a Riemann surface, and the differential element of a geodesic on it is the infinitesimal path length of a light ray $ds^2 = (E_{TOT} - V)\sum_{i,j} a_{ij}\, dq_i\, dq_j$. By substituting $ds \to nds$, where n is the refractive index of an isotropic homogeneous medium, a surface orthogonal to a rays congruence can be interpreted as Hamilton's characteristic function *applied to optics* on that bidimensional manifold having said metric. If one considers wave fronts instead of rays, A must be interpreted as time (Fermat's principle of stationary action). Expressing the action of N point particles in that framework, Lipschitz contributed a dynamical foundation to Hamilton's formulation. The geometrical representation in the configuration space is due to him.

[15]Euclid used to draw upon geometry to treat problems of algebraic or computational nature (in modern conception).

[16]A measurement of length presupposes a measuring rod and a surface plate. Along a rough path, a straight line "drawn" by theodolite likely yields a different length value then that drawn using a tape.

[17]Roulettes, the curves generated by a point on a rolling gear, have been Newton's starting point.

by optical instruments were written as differentials for light propagation, and were interpreted according to intrinsic geometry. It isn't allowed, though, to identify the means of representation — the light rays — with the represented object — the image.

Consistently with the Erlangen Program, Klein's model presents Maxwell's field equations as an invariant under geometric transformations of *projective space*. Once the aether medium has been relinquished, it accounts for the input-output transformations typical of electromagnetic signals.[18] Projective geometry is a theoretical framework consisting of deductive reasoning and a construction tool — the straightedge. Graphically, it gives views of a space constructible by straightedge, whereas geometrical optics generates its space by ray tracing. In order to allow consistent interpretations, the geometric framework of electromagnetism should be the same for all signals in every frequency range.[19] In the rest of this section, we try to justify the choice of a projective-space model.

According to Maxwell, most of the relations between an object and its image formed by an optical instrument may be deduced from the purely geometrical theory of homographic figures [8, 9].[20] Abscissa x of a source point is transformed into the corresponding sink point abscissa $t(x) = \frac{\alpha x + \beta}{\gamma x + \delta} = \frac{\alpha}{\gamma} - \frac{D/\gamma^2}{\frac{\delta}{\gamma} + x}$, where $D = \alpha\delta - \beta\gamma$. Parameters α, β, γ, and δ are related to the instrument, which is considered a black box, and are independent of the source point. The projective transformation — a generalization of perspective — is obtained, as previously, as the sum of simple terms. For example, if the j-th term has the form $t_j(x) = \frac{a_j}{b_j + x}$, by letting $T_0(x) = t_0(x) = s_0 + x$ and $T_j(x) = T_0(t_1 t_2 \ldots t_j(x))$, we have the successive convergents $T_1(x) = T_0(t_1(x)) = s_0 + t_1(x) = s_0 + \frac{a_1}{b_1 + x}$, $T_2(x) = T_1(t_2(x)) = s_0 + \frac{a_1}{b_1 + \frac{a_2}{b_2 + x}}$, and so forth.

The expression for the transformation of the object-point (source) into the image-point (sink) is similar to those obtained previously [10].[21] The projective transformation group is a proper superset of point-to-point transformations (homographies), so the transformations could be extended from systems composed of N lenses to general linear receivers, and projective *models* of the extent could help interpreting small signals in any frequency range [11].[22]

Ancient geometry had a secular propensity for visual models. Euclid is considered the (probable) author of a pamphlet where the Greek knowledge on vision was summarized in the form of notions and theorems on perspective. It was the starting point of relevant arts and crafts upon its rediscovery at the dawn of Renaissance. Painters conceived central projection as a means to render the illusion of a spatial disposition of objects to an observer looking at the painting from a predetermined position.[23] Sculptural reliefs and architectonic structures were also studied. Modern science of vision, by contrast, concedes to ethereal images only a perceptual space internal to the mind, and no extent in the outer world. It arouses research interest rather about psychological facets of optical impressions than geometric models [12]. Accordingly, the topology of the visual space is intermingled with statements on physiological structures and functions. Geometry of position exists, along with other legacy achievements. Some projective constructions were investigated as to how they match their Euclidean counterparts, but research purely on projective constructions was never

---

[18]Plücker's line complex — the null system — belongs to projective geometry. The transformations of his complex were connected to the system of partial differential equations that summarizes the behavior of electromagnetic fields in a vacuum. As those fields are defined over the whole space, the logical framework provided by a geometric model is by far more important for their representations than it is for point particle dynamics.

[19]The oneness of the geometric framework sounds obvious. Projective geometry models the extent if it is agreed upon that visual images are phenomena, and as such pertain to the *external* world. However, images viewed in the light frequency range are not to be confused with projected silhouettes. In other frequency ranges, signals received are often reconstructed as if they were slide shows. In our opinion, rendering them in a way homogeneous with optical images would allow to compare the data on the same logical basis. Comparing contours would be a different model.

[20]In "Draft on the methods of geometrical optics. Appendix: Homographic figures and projective geometry", 1874.

[21]The transform T results from successive iterations. It can be expressed by a definite integral $T(\phi) = \int_a^b \phi(u)K(u)\,du$, where the part K describing the performance of the receiver is a well behaved function. See also note 9. Volterra introduced his *functions of a line* $T(\phi)$ as classes of scalar valued functions which depend on the shape of a curve, construed as the limit of functions defined on polygons as the number of vertices approaches infinity, pioneering functional calculus. His work can be generalized by considering correspondences between elements of the same space which contain additional parameters $\phi(x, y, z) \xrightarrow{T} \psi(x, y, z)$, thereby expressing the received signal as a transformation of the space onto itself. For a different approach, Fredholm's definition of the integral equation is rather oriented toward the solution of differential equations, and generalizes linear algebraic systems by providing for infinitely many variables. Both methods can use continued fractions to obtain approximated solutions of integral equations in the framework of Helmholtz-von Neumann spectral theory.

[22]An imaging problem is how to represent *signals* geometrically when the frequency range is not visually perceivable. In fact, human visual experience is integrated with knowledge originated from the other senses, while non-visible electromagnetic signals, however well rendered, can hardly be endowed with an equivalent evocative power.

[23]Photographic techniques meet the same demand as painting.

undertaken. In an attempt to elicit technical interest, let's mention two facts about images. One, a subject in daylight forms a sharp image whether it projects on a flat screen through a pinhole, or it appears inside a crystal sphere as a 3D image.[24] Two, Fourier optics lacks a geometric model for the observed Fraunhofer diffraction pattern, although Abbe showed that such patterns are images at finite of subjects at the optical system's infinity, or vice-versa.

4. AT THE ROOTS OF PROJECTIVE GEOMETRY

The roots of displaying forms in projective geometry are twofold. One is the theory of perspective, a theorization of artistic painting. It links back to Euclid's and Apollonius' methods, but, as a theory, it does not even cover all of constructions actually used by architects.[25] The other root — geometry of position — is traced back to Desargues and Pascal about 1600. They conceived constructions independent of any projection point; that is, figures with no metric properties. However, a logical-deductive system to back their constructions was missing. Toward the end of 1700s, the critical review of the parallel postulate and the mathematical foundations research it triggered determined the convergence of graphical perspective with Desargues' and Pascal's constructions, which resulted in a new *synthetic geometry* approach, entirely different from Euclid's one. Finally, F. Klein proved that the projective logical-deductive system is self-standing, as it can be stated independently of the Euclidean one. Unfortunately, since its foundation, that new geometry was progressively derailed toward *analytic geometry*.[26] The resulting formalism is homogeneous across all geometries, but does not recognize any more the differences between a system that only avails of a straightedge and the one formalized by Euclid. Since projective transformations can be handled with algebraic methods, their group structure can be interpreted in a manifold. However projective configurations can be contrasted against Euclidean figures.[27] Having dealt with projective models of non-Euclidean geometries, Klein concluded that a non-Euclidean surface is endowed with a curvature only if it is immersed in an Euclidean space; the geodesics of the same surface are straight lines in projective geometry.[28] He suggested that physical models can be built upon projective geometry just like mathematical ones. That suggestion anticipated image reconstruction techniques, as well as all the problems related to sampling, storage, and recovery of information. Nowadays, backed up by considerable experience in treating and rendering encoded signals, the idea of modeling electromagnetic signals directly upon projective geometry could be taken up again. Geometric modeling can supersede — and surpass — nomograms, for example the Smith chart, bringing forth the power of a full blown hypothetico-deductive system in stead of specifically tailored graphical aids.

5. CONCLUSIONS

Geometry attained mathematical rigor by neglecting the relationship between modeling of the display and geometrical constructions, both of which hence lack mathematical support. Our analysis suggests that, restoring that relationship, projective geometry can lend itself to modeling the extent in electromagnetism, in linear approximation. "Linear" in both ways: (1) geometrical, as geometric space is homogeneous and isotropic, and (2) electromagnetic, according to the so-called "small signal" approximation of fields. Since the axiomatization of mathematics, little progress was made which would be useful to physics in this respect. Notwithstanding today's technical achievements, modeling based on projective geometry has remained in a somewhat rudimentary state. In our opinion, modeling of received signals could provide a common ground for information theories applied to telecommunications and information-based complexity theories. In fact, the huge advancements in electromagnetics and computer sciences make it also possible to gradually broaden the frequency ranges that we can interpret visually, under varying illumination conditions.

---

[24] The image we refer to appears right inside the sphere, and is not the only one being formed. The imaged subject is always the whole world, not just the detail of interest.

[25] Panoramic drawings use multiple projection points to correct perspective, so as to take into account binocular visual effects at a slant. We underline this detail because, when the geometric construction itself is the subject under investigation, the ability to represent projective spaces in homogeneous coordinates deserves (re)consideration.

[26] Hilbert solved definitively the consistency problem by reducing all geometries to a unique Cartesian geometry.

[27] Projective constructions differ from Euclidean ones in how elements at infinity are conceived and in the duality principle. As for Seidel aberrations, observed in optics, projective transformations of a straight line range all conics. In fact, any conic can be construed using only a straightedge, according to Steiner.

[28] Projective geometry provides models of non-Euclidean geometries. They are not the only models. Poincaré represented hyperbolic geometry on a disc in the complex plane. In his model, conformal but not projective, the unit disc in $\mathbb{C}$ results from the mapping of the Riemannian surface generated by the group of automorphic functions by tiling of their fundamental domains.

REFERENCES

1. Rodin, A., "On constructive axiomatic method," *Specific Sciences — Mathematics*, arXiv: 1408.3591v2, 2014.
2. Mach, E., *The Science of Mechanics*, The Open Court Publishing Co., Chicago, 1919.
3. Herman, R. A., *A Treatise on Geometrical Optics*, University Press, Cambridge, 1900.
4. Cauer, W., *Synthesis of Linear Communication Networks*, McGraw-Hill, New York, 1958.
5. Bloomfield, P., *Fourier Analysis of Time Series. An Introduction*, Wiley-Interscience, New York, 2000.
6. Pfeil, A., F. Wyrowsky, A. Drauschke, and H. Aagendahl, "Analysis of optical elements with the local plane-interface approximation," *Appl. Opt.*, Vol. 39, No. 19, 3304–3313, 2000.
7. Braunmühl, A., "Historische Studien über die organische Erzeugung ebener Curven von den ältesten Zeiten bis zum 18. Jahrhundert," *Katalog Mathematischer und Mathematisch-physikalischer Modelle, Apparate und Instrumente*, C. Wolf & Sohn, München, 1892.
8. Harman, P. M., *The Natural Philosophy of James Clerk Maxwell*, Cambridge University Press, Cambridge, 2001.
9. Whittaker, E. T., *The Theory of Optical Instruments*, Cambridge University Press, Cambridge, 1907.
10. Fantappiè, L., "Überblick über die theorie der analytischen funktionale und ihre Anwendungen," *DMV-Jahresbericht*, Vol. 43, 1–25, 1934.
11. Biederman, I., "Human image understanding. Recent research and theory," *Comput. Vision Graph.*, Vol. 30, No. 1, 29–73, 1985.
12. Ronchi, V., "Classical optics is a mathematical science," *Arch. Hist. Exact Sci.*, Vol. 1, No. 2, 160–171, 1960.

Efficient Analysis of EM Scattering from Rotating Structures Using a Fast Iterative Physical Optics Method

E. Pascual, **G. Gutierrez**, and **F. J. Jimenez**

EMC & MW Department, AIRBUS DS, Spain

Abstract— Analysis of the electromagnetic fields scattering from rotating structures such as aerogenerators, aircraft propellers, turbojet and turbofan, helicopter rotors, etc. has an increased interest due to the influence in civil and military radars efficiency and in radiation characteristics of on-board antennas. In this paper an Iterative Physical Optics method accelerated by a fast Far Field Approximation is presented. It has been developed in such a way that the computation time is reduced by means of a multilevel Far Field Approximation, a preprocessing of the parameters that are invariant with the rotations, a fast calculation of the rotation transformations of the parameters affected by the movement and a parallelization schema based on Fortran Coarrays.

1. INTRODUCTION

The interaction of EM fields with rotating structures such as wind turbines, aircraft propellers, turbojet and turbofan, helicopter rotors, etc. can produce Doppler effects [1] and spatial modulations [2] degrading the performances of radars and antennas. To predict accurately the scattering is necessary to compute the interaction of EM fields with the rotating and fixed parts and the interaction of scattered fields from one part with the others for each relative position between them taking into account also the different electromagnetic material properties. In the case of complex rotating structures such as turbofan or turbojet with hundreds of blades rotating at different speeds and directions, it is necessary to analyze efficiently thousands of relative positions in order to obtain useful results. Previous works use Method of Moments [2], Physical Optics [3] or Finite Elements [4] to perform this analysis. This paper presents an Iterative Physical Optics (IPO) method [5, 6] accelerated by a fast Far Field Approximation (FFA) [7] in order to analyze accurately and efficiently this problem. It has been developed in such a way that the computation time is reduced by means of a multilevel FFA (MLFFA), a preprocessing of the parameters that are invariant with the rotations, a fast calculation of the rotation transformations of the parameters affected by the movement [8] and a parallelization schema based on FORTRAN co-arrays [9]. Cross comparison with Multilevel Fast Multipole Method (MLFMM) results of several test cases shows an excellent agreement at a much lower computational cost. Complex cases such as time-variant radar cross section of a large aircraft with four rotating propellers have also been computed in affordable time.
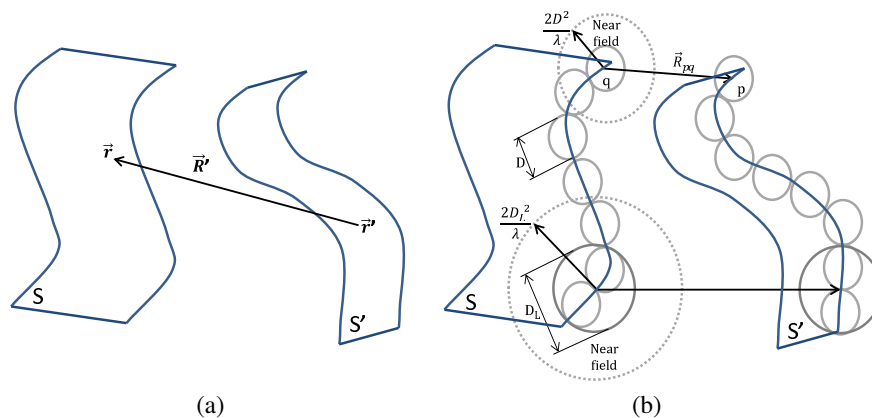
2. IPO AND MLFFA

Figure 1: Geometry of the problem: (a) The integral equation is discretized using point sampling, the surfaces are assumed to be locally flat at the sample points and two orthogonal current directions are defined at each point. (b) FFA and MLFFA grouping.

Using the approximate Magnetic Field Integral Equation (MFIE), the electric current at point $\vec{r}$ on a target surface S due to an incident magnetic field $\vec{H}^i$ in presence of other surface S' (Fig. 1(a))

can be calculated by

$$\vec{J}(\vec{r}) = 2\hat{n} \times \vec{H}^i(\vec{r}) + 2\hat{n} \times \int_{S'} \vec{J}(\vec{r}') \times \vec{R}' \frac{e^{-jkR'}}{4\pi R'} (jk + \frac{1}{R'}) dS' \tag{1}$$

being $\hat{n}$ the unitary normal vector at point $\vec{r}$, $\vec{r}'$ a point on surface S', $\vec{R}' = \vec{r} - \vec{r}'$ and $R' = |\vec{R}'|$.

The next iterative formula can be used to find J for the n iteration

$$\vec{J}^{(n)}(\vec{r}) = 2\hat{n} \times \vec{H}^i(\vec{r}) + 2\hat{n} \times \int_{S'} \vec{J}^{(n-1)}(\vec{r}') \times \vec{R}' \frac{e^{-jkR'}}{4\pi R'} (jk + \frac{1}{R'}) dS' \tag{2}$$

with an initial guess of

$$\vec{J}^{(0)}(\vec{r}) = 2\hat{n} \times \vec{H}^i(\vec{r}) \tag{3}$$

Each iteration step adds another reflection between surfaces. The iteration halts after a pre-specified number of steps based on the number of expected reflections or when the relative change in the currents becomes small enough to neglect subsequent iterations. An iterative schema is presented in [5] in order to converge to a stable solution by defining a residual error for each iteration and minimizing this residual error using an iterative algorithm. The complexity of such schema is driven by the computation of operator $\bar{Z}$ with a cost of $O(N^2)$.

$$\bar{Z}\vec{J}^{(n)}(\vec{r}) = \vec{J}^{(n)}(\vec{r}) - 2\hat{n} \times \int_{S'} \vec{J}^{(n-1)}(\vec{r}') \times \vec{R}' \frac{e^{-jkR'}}{4\pi R'} \left(jk + \frac{1}{R'} \right) dS' \tag{4}$$

Far Field Approximation is used to reduce the computational cost. FFA is similar to Fast Multipole Method (FMM) in that the unknown current elements are spatially grouped and the radiation integral is evaluated one pair of groups at a time. For groups which are separated by less than the far field distance $\frac{2D^2}{\lambda}$, being D the size of the groups and λ the wavelength, the integral is computed using direct numerical integration. For groups separated by more than the far field distance (Fig. 1(b)), the FFA is used

$$\vec{H}_{pq}(\vec{r}) \approx \vec{H}_{pq}(\vec{r}_q) e^{-jk(\vec{r}-\vec{r}_q)\cdot\hat{R}_{pq}} \tag{5}$$

where $\vec{H}_{pq}$ is the magnetic field radiated from source group p to far field group q, $\vec{r}_p$ and $\vec{r}_q$ are the center of groups p and q respectively, $\vec{R}_{pq} = \vec{r}_q - \vec{r}_p$ and $\hat{R}_{pq} = \frac{\vec{R}_{pq}}{|\vec{R}_{pq}|}$. In this way, $\vec{H}_{pq}(\vec{r}_q)$ is calculated first by integrating over the elements of group p, them FFA is used to find $\vec{H}_{pq}(\vec{r})$ for all the sample points within group q. Using FFA the complexity of IPO is reduced to $O(N^{\frac{3}{2}})$. Considering groups with at least a sampling point inside, these groups can be spatially grouped again in higher level groups with a size $D_L > D$ (Fig. 1(b)), being able to apply the FFA between these more populated groups if they are separated at least by a far field distance $\frac{2D_L^2}{\lambda}$. This grouping process can be continued until a level with only one group, obtaining a multilevel FFA. Applying the FFA for each couple of groups at the adequate level, it is possible to reduce the complexity of the operator $\bar{Z}$ to $O(N \log(N))$. Several techniques can be used to perform the space partition, in particular it has being used an octree partition as in most of MLFMM implementations.

3. PRE-PROCESSING OF INVARIANT DATA

All those geometrical data that are invariant with the rotation transformation can be computed only once before the rotation loop. These data include the values of vector $\vec{R}'$ and its module in (1), (2) and (4) when $\vec{r}$ and $\vec{r}'$ are both in the fixed part or in the same rotating part of the target and $\hat{R}_{pq}$ in (5) when group p and q are also in those parts. Other parameters related with PO, as the curvature of surfaces to calculate its reflection coefficients or the relationship between surfaces of the same fixed or rotating part to determine the shadow zones, are also pre-computed previously to the rotation loop.

4. FAST COMPUTATION OF ROTATIONS

Many other parameters (sampling points, normals, MLFFA groups geometry, ...) are affected by rotations and must be computed efficiently. A rotation around an arbitrary axis can be defined by

an origin point (a, b, c) plus a unitary direction vector $\langle u, v, w \rangle$ to build the axis and an angular speed to determine the angle θ rotated at each time step. The rotation can be decomposed in the following transformations of the affected structure: T_P to move the axis origin point to $(0, 0, 0)$, T_{xz} to move the axis to xz plane, T_z to move the axis to z axis, $R_z(\theta)$ to rotate around the z axis, T_z^{-1}, T_{xz}^{-1} and T_P^{-1}. The total transformation matrix $T_{tot} = T_P^{-1} T_{xz}^{-1} T_z^{-1} R_z(\theta) T_z T_{xz} T_P$ is presented in [8], multiplying it by vector $\langle x, y, z, 1 \rangle$ yields the result of rotating the point (x, y, z). When the time steps are uniforms, the angle θ is a constant and the matrix T_{tot} is computed only once. For each time step, the affected parameters are rotated using T_{tot} by means of a very efficient vector-matrix product routine.

5. PARALLELIZATION USING COARRAYS

Fortran programming language includes since its 2008 standard version a new parallelization schema named Coarray Fortran. It uses the model of single-program multiple-data (SPMD) where a single program runs on multiple machines with different local data that is occasionally shared across machines. Each execution context is called an "image". In Coarray Fortran, variables can have the CODIMENSION attribute, which is similar to an array dimension. This means that such a variable not only exists on all the images, but also that the content of this variable on any given image can be accessed by all other images. This feature can be used to parallelize at a high level the IPO, MLFFA and rotation algorithms by distributing the different surfaces of the structure between images, so that each one computes all data relative to their own surfaces and accessing the data of the rest of surfaces to calculate the interaction between them. As point sampling is a function of the area of surfaces, work and memory load is balanced distributing surfaces among images in a way that total area is similar for all of them.

6. RESULTS

IPO, MLFFA and fast computation of rotations have been implemented in an existing PO solver parallelized using coarrays. A first case was analyzed consisting in the monostatic radar cross section (RCS) computation of a time-varying target comprised of several coaxial wheels of planar blades rotating around Z axis. The test-case definition was originally submitted by MBDA France as part of the 2014 ISAE EM Workshop [10]. Fig. 2 shows the results of time varying RCS computed at 10 GHz illuminating the structure with a plane wave from $Z = +\infty$ polarized with the electric field along X axis. Lower wheel is fixed, middle wheel is rotating clockwise with an angular speed of 1 degree/second and upper wheel is rotating counterclockwise at 2 degree/second. Time step is 0.1 seconds with a total time of 360 seconds and 3601 different relative positions. For this test-case with most of the surfaces rotating, the computational cost of IPO+MLFFA is three times lower than MLFFM one and the difference between both methods is lower than 1 dBsm. For cases where the amount of rotating surfaces is much smaller than the fixed ones the pre-processing of invariant
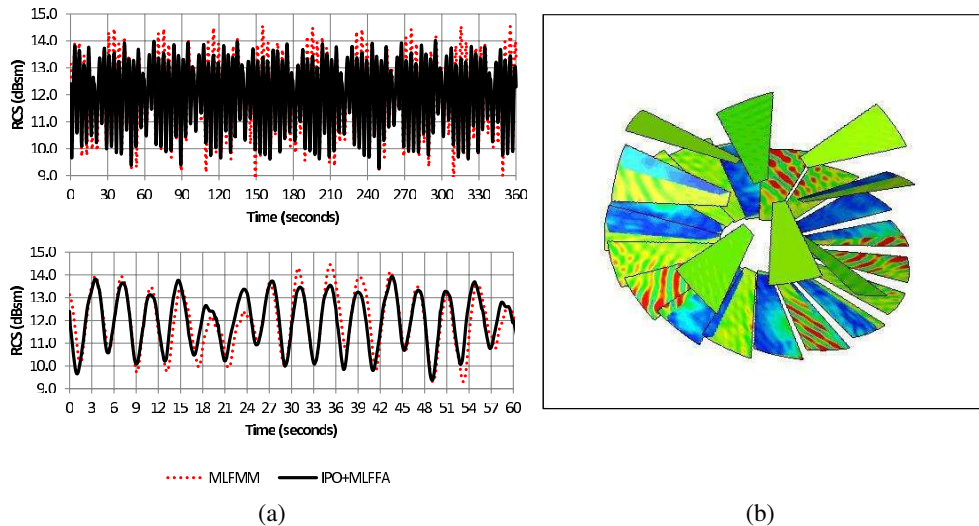

Figure 2: Rotating blades test-case: (a) Comparison of IPO+MLFFA and MLFMM results. (b) Current distribution at time zero.

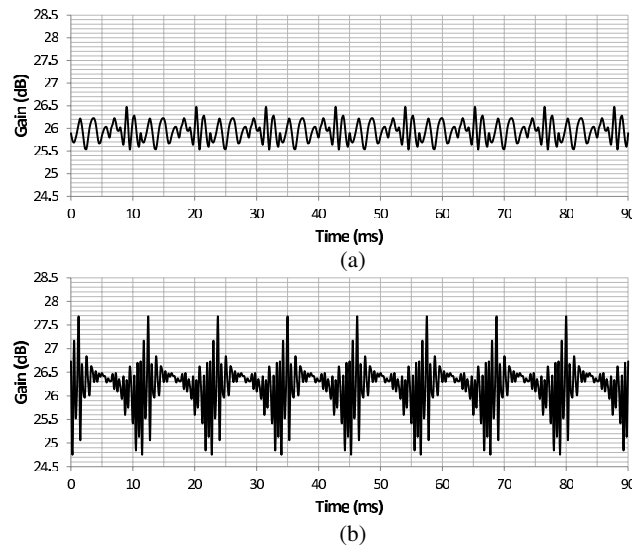parts made IPO+MLFFA even more efficient.

Figure 3: Time variation of GPS antenna gain: (a) Direction with minimum effect. (b) Direction with maximum effect.

Rotating structures were demonstrated to introduce a periodic modulation onto the Global Positioning System (GPS) satellite signals [11]. Fig. 3 shows the time variation of the gain of a GPS antenna on-board a large transport turboprop aircraft due to the rotation of their four propellers. The antenna is located in the upper fuselage between the propellers, the frequency is 1575 MHz corresponding to an aircraft electrical length of 225 wavelengths. The propellers are rotating at 655 revolutions per minute, the considered time step is 0.25 milliseconds with a total time of 90 milliseconds and 360 different relative positions of the propellers. A gain variation of about 1 dB is observed in the direction where the effect of the propellers rotation is minimum (Fig. 3(a)) while in the direction where the effect is maximum, the gain variation is about 3 dB (Fig. 3(b)).

7. CONCLUSIONS

An efficient method to analyze the EM scattering from rotating structures based on a fast iterative PO is presented. The traditional iterative PO schema is accelerated by mean of a multilevel far field approximation reducing the complexity of the iteration computation. Pre-processing of data not varying with the rotations and the use of a matrix algorithm to compute efficiently the rotations reduce even more the computational cost. Finally a parallel schema based on Coarray Fortran has been used to implement the code in an easy way with a very good scalability. The solver including all these features has been tested through the computation of simple and complex cases comparing with MLFMM results obtaining an excellent agreement with a calculation cost several times lower.

REFERENCES

1. Matthews, J. C. G., C. Sarno, and R. Herring, "Interaction of wind turbines with radar systems," *Proceedings of the 2008 Loughborough Antennas and Propagation Conference*, 461–464, Loughborough, UK, 17–18 March 2008, 2008.

2. Somers, G. A. and D. M. Bruno, "Spectral characteristics of electromagnetic wave scattering by rotating propellers and its effect on clutter discrimination," *Antennas and Propagation Society International Symposium, 1994*, Vol. 1, 144–147, Seattle, WA, USA, 20–24 June 1994.

3. Tardy, I., G. P. Piau, P. Chabrat, and J. Rouch, "Computational and experimental analysis of the scattering by rotating fans," *IEEE Trans. Antennas Propag.*, Vol. 44, No. 10, 1414–1421, 1996

4. Graglia, R., A. Freni, and G. Pelosi, "A finite element approach to the electromagnetic interaction with rotating penetrable cylinders of arbitrary cross section," *IEEE Trans. Antennas Propag.*, Vol. 41, 635–650, 1993

5. Obelleiro, F., J. L. Rodriguez, and R. J. Burkholder, "An iterative physical optics approach for analyzing the electromagnetic scattering by large open-ended cavities," *IEEE Trans. Antennas and Propag.*, Vol. 43, No. 4, 356–361, 1995.

6. Burkholder, R. J., Ç Tokgz, C. J. Reddy, and P. H. Pathak, "Iterative physical optics: It's not just for cavities anymore," *Proc. IEEE Antennas and Propag. Soc. Int. Symp.*, Vol. 1A, 18–21, 2005.

7. Lu, C. C. and W. C. Chew, "Fast far-field approximation for calculating the RCS of large objects," *Microwave Opt. Tech. Lett.*, Vol. 8, No. 5, 238–241, 1995.

8. Murray, G., "Rotation about an arbitrary axis in 3 dimensions," [Online] http://inside.mines.edu, 2013.

9. Fortran 2008 Standard ISO/IEC 1539-1:2010.

10. (2014, Nov.) *ISAE EM Workshop* Organizers: ISAE, DGA and SEE-Midi Pyrnes [Online], Available: http://websites.isae.fr/workshop-em-isae-2014.

11. UK Civil Aviation Authority "Effect of helicopter rotors on GPS reception," *CAA PAPER 2003-7*, December 2003.

Modeling the Scattering by Small Holes

R. Solimene, **P. Piccolo**, and **R. Pierri**

Dipartimento di Ingegneria Industriale e dell'Informazione, Seconda Università degli studi di Napoli, Italy

Abstract— The scattering by a hole/aperture within a perfect electric conducing (PEC) plane is a classical electromagnetic problem. As is well known, this scattering can be formulated as the solution of an integral equation where the unknown aperture electric field (or equivalently the magnetic source) is to be retrieved once the incident field is known. When the aperture becomes a hole small in terms of the wavelength, Bethe's diffraction theory [1] or the low frequency approximation (Stevensons series low order terms) [2] can be invoked to approximate the mentioned integral equation. This allows getting analytical results for simple hole's shape, for example in the case of circular hole. For such a case, in this paper, analytical results are compared with numerical simulations obtained by a commercial FDTD forward solver. It is shown that in near zone, low-frequency approximation fits numerical simulations better than the Bethe's theory does. By contrary, Bethe's theory works fairly well in predicting the radiated field in far-zone and allows to obtain a more handling field expression which in principle permits to more easily considering the role of the incident field polarization and the hole's shape. Finally, the case of a hole over the faces of a rectangular waveguide located at different points is analyzed as well. It is found out that Bethe's theory works also in these cases.

1. MATHEMATICAL BACKGROUND

In this section the mathematical notation is introduced and the Bethe's theory as well as the Stevenson approximation are briefly recalled.

Let us consider the scattering experiment described in Figure 1.
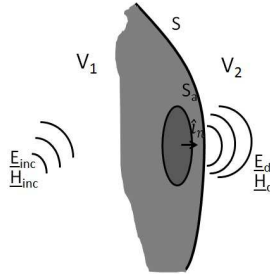

Figure 1: Illustrating the scattering experiment under consideration. A hole in a PEC surface is probed by an impinging field.

A PEC surface divides the whole space in two regions addressed as V_1 and V_2. On such a surface an aperture S_a occurs and the overall structure is illuminated by the impinging field $\underline{H}_{inc}$. The integral equation describing the scattering by such an aperture is:

$$\hat{i}_n \times \underline{H}_0(\underline{r}) = \hat{i}_n \times \iint_{S_a} (\underline{\underline{G}}^{(2)}_{HJ_m}(\underline{r},\underline{r}') + \underline{\underline{G}}^{(1)}_{HJ_m}(\underline{r},\underline{r}')) \cdot \underline{J}_{ms}(\underline{r}')\, d\underline{r}' \qquad \underline{r} \in S_a \tag{1}$$

where $\hat{i}_n$ is the normal vector to the surface pointing from the space V_1 to V_2, $\underline{H}_0$ is the unperturbed magnetic field, (i.e., the solution of Maxwell's equations in absence of the aperture), $\underline{\underline{G}}^{(2)}_{HJ_m}(\underline{r},\underline{r}')$ and $\underline{\underline{G}}^{(1)}_{HJ_m}(\underline{r},\underline{r}')$ are the dyadic Green functions in the space V_2 and V_1, respectively, and $\underline{J}_{ms}$ is the surface density distribution of the equivalent magnetic current related to the electric field $\underline{E}_d$ scattered by the aperture according to the equation:

$$\underline{J}_{ms}(\underline{r}) = -\hat{i}_n \times \underline{E}_d(\underline{r}) \qquad \underline{r} \in S_a \tag{2}$$

Equation (1) was obtained through the equivalent theorem and by enforcing the continuity of tangential components of the electric and magnetic field on the aperture. When S is a plane, image theory allow us simplifying (1) as:

$$\tfrac{1}{2}\hat{i}_n \times \underline{H}_0(\underline{r}) = \hat{i}_n \times \iint_{S_a} \underline{\underline{G}}^{fs}_{HJ_m}(\underline{r},\underline{r}') \cdot \underline{J}_{ms}(\underline{r}')\, d\underline{r}' \qquad \underline{r} \in S_a \tag{3}$$

where $\underline{\underline{G}}_{HJ_m}^{fs}(\underline{r},\underline{r}')$ is the free space dyadic Green function and $\underline{J}_{ms}$ is doubled with respect to the magnetic current (2).

In [1], when the aperture is small as compared to the wavelength, Equation (3) can be approximated and split in two easier equations such as:

$$-\frac{1}{2}\underline{H}_0 \cdot \underline{r} = \iint_{S_a} \eta(\underline{r}')\frac{1}{4\pi\mu|\underline{r}-\underline{r}'|}\,d\underline{r}' \qquad \underline{r} \in S_a \tag{4}$$

$$-\frac{1}{4}\underline{E}_0 \times \underline{r} = \iint_{S_a} \underline{J}_{msE}(\underline{r}')\frac{1}{4\pi|\underline{r}-\underline{r}'|}\,d\underline{r}' \qquad \underline{r} \in S_a \tag{5}$$

where η is the surface magnetic charge density that is related to the magnetic currents by the equation:

$$\nabla_t \cdot \underline{J}_{msH}(\underline{r}) = -j\omega\eta(\underline{r}) \tag{6}$$

and $\underline{J}_{msE}$ and $\underline{J}_{msH}$ are the two contributions to the total magnetic currents $\underline{J}_{ms}$.

Furthermore, for the case of circular aperture of radius a, an analytical solution is given as:

$$\underline{J}_{msH}(\underline{r}) = -\frac{4j\omega\mu}{\pi}(a^2-r^2)^{\frac{1}{2}}\underline{H}_0 \tag{7}$$

$$\underline{J}_{msE}(\underline{r}) = \frac{2}{\pi(a^2-r^2)^{\frac{1}{2}}}\underline{r}\times\underline{E}_0 \tag{8}$$

The far field radiated by the first contribution can be approximated as the field radiated by an elementary **magnetic dipole**, whereas the second one as the field radiated by a magnetic loop or equivalently by an **electric dipole** perpendicular to the surface S_a. This is the approximation coming from Bethe's theory.

In [2] a series of integral equations is obtained by expanding Equation (3) in terms of wave number k powers. According to Stevenson, analytical solution for the first two terms of that expansion is given in the case of circular aperture and with an incident plane wave $\underline{E}_i = \tilde{\underline{E}}_i e^{-jk\hat{i}_k\cdot\underline{r}}$:

$$\underline{J}_{ms\rho}^{(0)} = 0 \tag{9}$$

$$\underline{J}_{ms\theta}^{(0)} = \frac{2\rho}{\pi(a^2-\rho^2)^{\frac{1}{2}}}\tilde{E}_{iz} \tag{10}$$

$$\underline{J}_{ms\rho}^{(1)} = -\frac{8j}{3\pi}(\hat{i}_k\cdot\hat{i}_z)(\tilde{E}_{iy}\cos\theta - \tilde{E}_{ix}\sin\theta)(a^2-\rho^2)^{\frac{1}{2}}$$
$$-\frac{4j}{3\pi}\left[(\hat{i}_k\cdot\hat{i}_x)\sin\theta - (\hat{i}_k\cdot\hat{i}_y)\cos\theta\right](a^2-\rho^2)^{\frac{1}{2}}\tilde{E}_{iz} \tag{11}$$

$$\underline{J}_{ms\theta}^{(1)} = \frac{2j}{3\pi}(\hat{i}_k\cdot\hat{i}_z)(\tilde{E}_{ix}\cos\theta + \tilde{E}_{iy}\sin\theta)\left[4(a^2-\rho^2)^{\frac{1}{2}} + \frac{2\rho^2}{(a^2-\rho^2)^{\frac{1}{2}}}\right]$$
$$-\frac{4j}{3\pi}\left[(\hat{i}_k\cdot\hat{i}_x)\cos\theta + (\hat{i}_k\cdot\hat{i}_y)\sin\theta\right]\frac{\rho^2+a^2}{(a^2-\rho^2)^{\frac{1}{2}}}\tilde{E}_{iz} \tag{12}$$

with ρ and θ being the polar coordinates.

2. APERTURES IN PEC PLANE

In Figure 2, it is represented the electric field on an aperture in a PEC plane with a normally incident plane wave, calculated by FDTD software. It can be noted that it is not in agreement with Bethe's solution (7) because the latter is a function that is null on the edge. Instead, results from (9)–(12) are more in agreement since in (12) there is a term that diverges on the edge even in the case of normal incidence.

However, Bethe's theory predicts that the far field scattered by that aperture can be attributed to the field radiated by an elementary magnetic dipole and Figures 4–5 confirm this prediction.
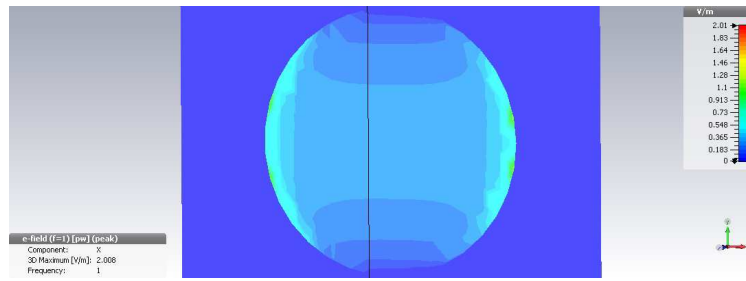
Figure 2: x component of the electric field on the aperture with normal incidence. The radius of the aperture is $\lambda/10$.
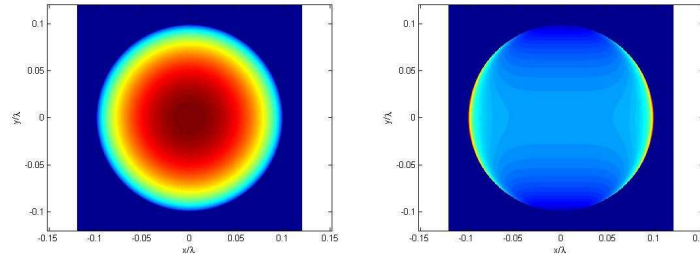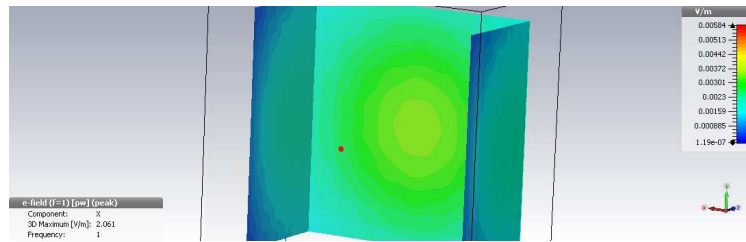

Figure 3: x component of the electric field on the aperture with normal incidence predicted by Equations (9)–(12) (left side) and Equations (7)–(8) (right side). The plots show the electric field for a circle of radius radius $0.99 \times \lambda/10$ to avoid the singularity in Equation (12). By comparison with Figure 2, it can be argued that Stevenson's theory works better than Bethe's theory for the near zone field.

Figure 4: x component of the electric field scattered by an aperture on a PEC plane with normal incidence. The radius of the aperture is $\lambda/10$ and the field is plotted on 3 surfaces: one parallel to the PEC plane distant 5λ from it and the other two perpendicular to it distant 4λ from the aperture.
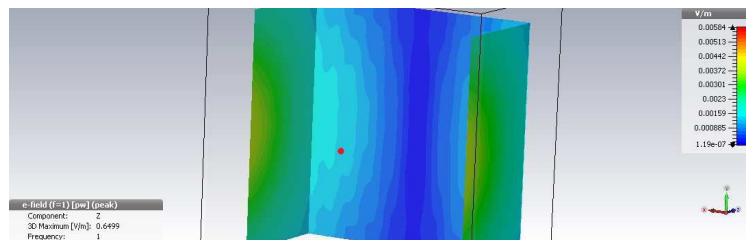
Figure 5: z component of the electric field scattered by an aperture on a PEC plane with normal incidence and in the same configuration as in Figure 4.

3. APERTURES IN RECTANGULAR PEC WAVEGUIDE

Although Bethe's theory was developed from the integral equation relative to a CEP plane, it is reasonable to check if it works for apertures made in more complex PEC structures. Here, we consider the hole occurring in rectangular waveguide still by considering the apertures being small with respect to the structure and the wavelength. The following figures of the fields scattered outside the guide are obtained thanks to a FDTD software. Figure 6 shows the amplitude of y component of the electric field radiated by an aperture in the centre of the waveguide's upper surface over three different plane located at 1.5, 3.5 and 5.5 times the wavelength from the waveguide's upper surface. In this case the unperturbed field $\underline{E}_0$ and $\underline{H}_0$ corresponds to the waveguide fundamental mode and are directed respectively along y and x directions. As can be noted, the scattered field
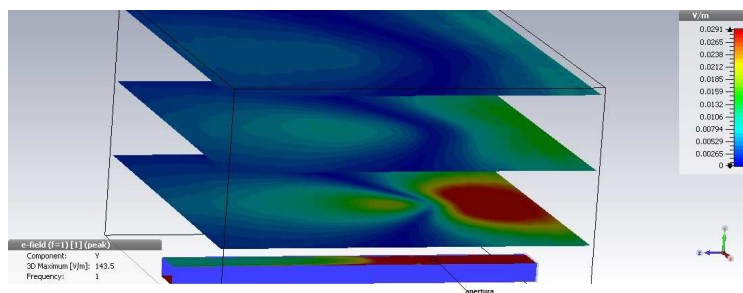
Figure 6: y component's amplitude of electric field radiated by an aperture in the centre of rectangular waveguide's upper surface. The waveguide (in the lower side of the figure) has a section wich dimensions are $1\lambda \times 0.5\lambda$, whereas the aperture's radius is $\lambda/20$.
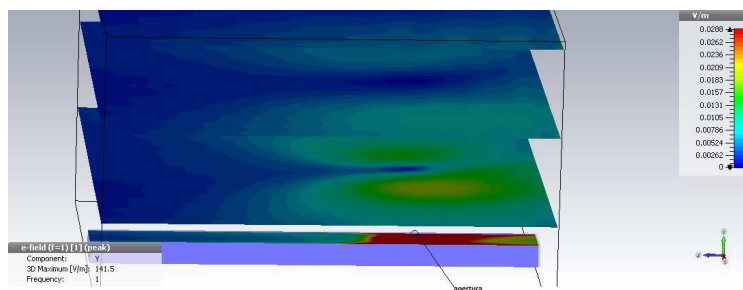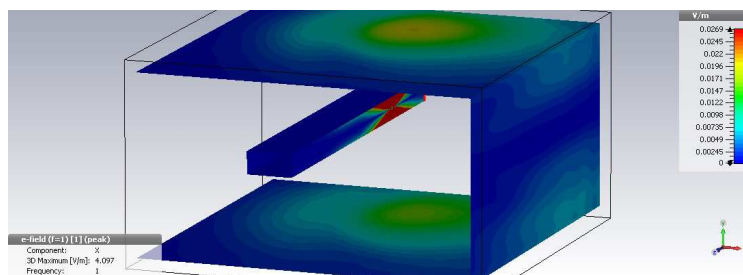

Figure 7: y component's amplitude of electric field radiated by an aperture near the edge of rectangular waveguide's upper surface. The dimensions are the same as in the Figure 6. The aperture's centre is $\lambda/10$ from the upper surface's edge.

Figure 8: x component's amplitude of electric field radiated by an aperture on rectangular waveguide's side surface. The dimensions are the same as in the Figure 6.
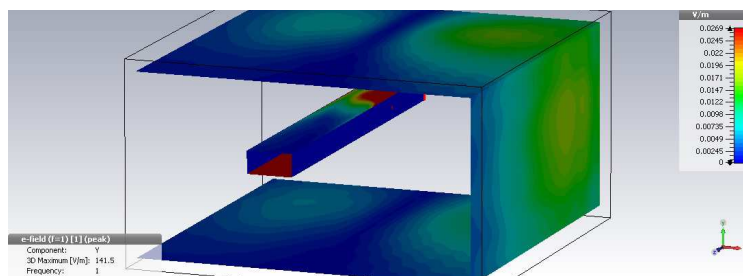

Figure 9: y component's amplitude of electric field radiated by an aperture with the same configuration as in Figure 8.

is similar to that radiated by a Huygens source radiating toward negative direction of z axis. That is in strict accordance to the Bethe's theory.

Figure 7 reports the scattered field when the aperture is moved near the edge of the upper

waveguide surface. In this case $\underline{H}_0$ has a z component, so the Huygens source is rotated and the propagation's direction is mainly along the x axis. Once again in accordance to the Bethe's theory.

If the aperture is placed on the lateral waveguide surface, $\underline{E}_0$ is equal to zero and $\underline{H}_0$ is directed along z direction. So the field radiated is that one of an elementary magnetic dipole directed along z (see Figures 8–9).

4. CONCLUSION

The scattering by small holes in PEC surface have been dealt with. Two approches have been shown, one developed by the german physicist Hans Albrecht Bethe and one based on series expansions. Numerical simulations of far-field have shown great agreement with Bethe's theory, but this fails to predict the near-field. For the last the "low frequency expansion" theory is more adequate.

REFERENCES

1. Bethe, H. A., "Theory of diffraction by small holes," *Physical Review*, Vol. 66, 163–182, 1944.
2. Butler, C. M., Y. Rahamat-Sami, and R. Mittra, "Electromagnetic penetration through apertures in conducting surfaces," *IEEE Transactions on Antennas and Propagation*, Vol. 26, 82–93, 1978.
3. Stevenson, A. F., "Solution of electromagnetic scattering problems as power series in the ratio (dimension of scatter)/wavelength," *J. Appl. Phys.*, Vol. 24, No. 9, 1134–1142, 1953.

Compact Circularly Polarized RFID Tag Antenna with an Embedded L-shaped Feedline for Metallic Objects

Cheng Liu, **Zhibin He**, **Hui Liu**, **Yoichi Okuno, and Sailing He**

Centre for Optical and Electromagnetic Research, Academy of Advanced Optoelectronics
South China Normal University, Guangzhou, China

Abstract— An ultra-high frequency (UHF) passive radio frequency identification (RFID) tag antenna with circular polarization for metallic objects is proposed. Using a novel and embedded L shape microstrip line to feed, a good performance of impedance matching is achieved. The proposed antenna can cover the whole operating frequency of UHF RFID system from 860 MHz to 960 MHz. The 3-dB circular polarization bandwidth is 7 MHz (from 916 to 923 MHz). The optimized antenna has a high gain of -5.5 dBi in 0 degree direction. The main parameters of the antenna are also discussed.

1. INTRODUCTION

In recent years, the applications of radio frequency identification (RFID) operating in the ultrahigh frequency (UHF) become more and more extensive. Long reading distance, high data rate transfer, and small tag size are needed to achieve a good RFID system. As the majority of reader antennas are designed with circular polarization (CP) for orientation diversity in a commercial RFID application, the polarization mismatch occurs if the tag antenna uses a linear polarization (LP) such as in [1] and [2]. The polarization mismatch will result in that only half of the transmitted power can be received by the LP tag and the reading range decreases. To provide high directivity and narrow beamwidth in certain areas, some RFID readers are designed with linear polarization. In this case, if the LP tag is attached inadequately to the targeted object with different direction, the polarization will mismatch, and the RFID reader will not identify the targeted object. Thus, to resolve the polarization mismatch problem, the study of CP tag antenna is necessary.

Many studies have been done about the CP tag antenna. In [3–5], the tag antenna is designed with a good circular polarization, impedance matching and an excellent performance when the tag antenna is mounted on metallic plates. However, all the feedlines are outside the radiator and consequently the size of the tag antenna is big.

A center frequency of 920 MHz broadband RFID tag antenna with circular polarization for metallic objects is proposed in this paper. The antenna is used a novel L-shape feedline embedded in two cross rectangular slots of unequal lengths. To get a smaller size of antenna, another two L-shape slots are designed in opposite corner of patch. The parameters of this antenna are simulated and discussed in this paper.

2. ANTENNA DESIGN

The substrate we used is FR4 layer (relative permittivity of 4.4, loss tangent of 0.02) with a thickness of $h = 1.6$ mm. The two L-shaped slots with width of 2 mm, length of $S1$ and $S2$ in opposite corners are etched on the 60 mm $\times$ 60 mm radiating patch to produce CP. The ground plane size is 86 mm $\times$ 86 mm and the operating frequency band is from 695 MHz to 1060 MHz. A terminal grounded L-shaped feedline is embedded in two cross rectangular slots to couple and excite the patch antenna. The impedance of the welded Monza4 tag chip is $11 + j143K$ at 920 MHz. The length of the feedline should be set to 27.9 mm according to the theory of short-circuited transmission line in [6]. Considering the electromagnetic coupling effect [7], the feed line length should be slightly tuned to 37.5 mm to ensure the antenna impedance is matched to the impedance of the tag chip. The geometry of the proposed tag antenna is shown in Fig. 1. Table 1 shows the detailed dimension of the designed antenna.

3. RESULTS AND DISCUSSIONS

In this paper, the tag antenna is simulated and optimized by the ANSYS HFSS. Since the tag chip has the feature of low impedance and high reactance, the impedance matching is an important part of the tag antenna design. Fig. 2 shows the simulated input impedance. At 920 MHz, the input impedance is $37 + j142 \, \Omega$, which matches to the tag chip impedance. As shown in Fig. 3, the return
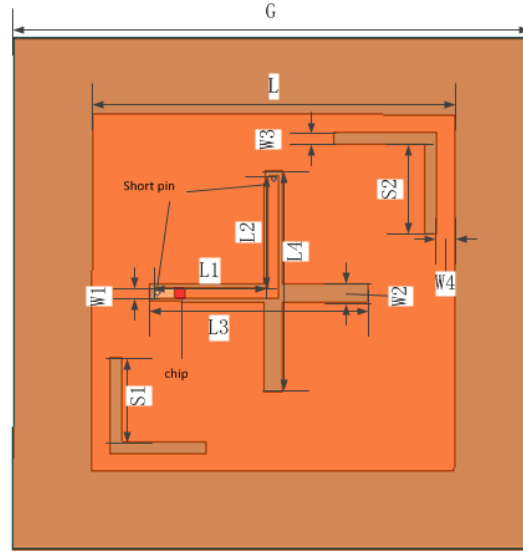
Figure 1: Geometry of the tag antenna.

Table 1: Detailed dimensions of the proposed antenna (Unit: mm).

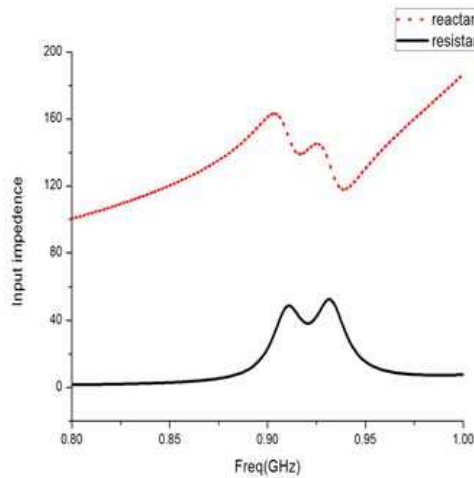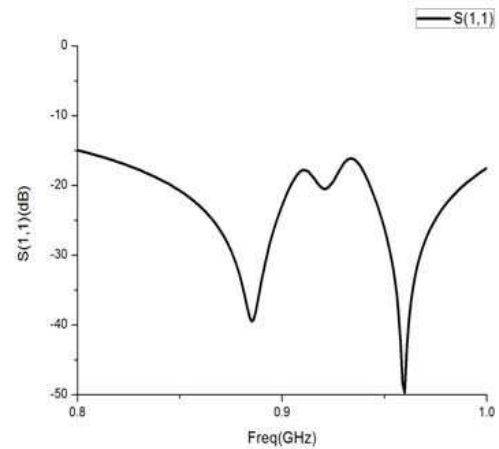| G	L	$L1$	$L2$	$L3$	$L4$
86	60	18.75	18.75	36.2	37.2
$W1$	$W2$	$W3$	$W4$	$S1$	$S2$
1.7	3	2	3	14	15

Figure 2: Input impedance of the antenna.

Figure 3: The S_{11} of the antenna.

loss (S_{11} parameter) of the antenna in the entire RFID ultra-high frequency $860\,\text{MHz} \sim 960\,\text{MHz}$ are below $-10\,\text{dB}$, and the return loss parameter is below $-21\,\text{dB}$ at $920\,\text{MHz}$.

Figure 4 shows the simulated CP radiation patterns at $920\,\text{MHz}$. In Fig. 4, the 3-dB axial ratio is from $916\,\text{MHz}$ to $923\,\text{MHz}$. Compared the situation without the two L-shaped slots, the center frequency of the axial ratio moves from $955\,\text{MHz}$ (without L-shaped slots) to move $920\,\text{MHz}$ (with the L-shaped slots). Fig. 5 also shows the simulated gains of our tag antenna in different placement environment (mounted on metal plates of various sizes). On the metal surface, our tag antenna still has a good gain characteristic. Since the metal surface of the antenna can increase the current area, it also plays a role in increasing the antenna gain. Fig. 6 shows the simulated 2-D and 3-D
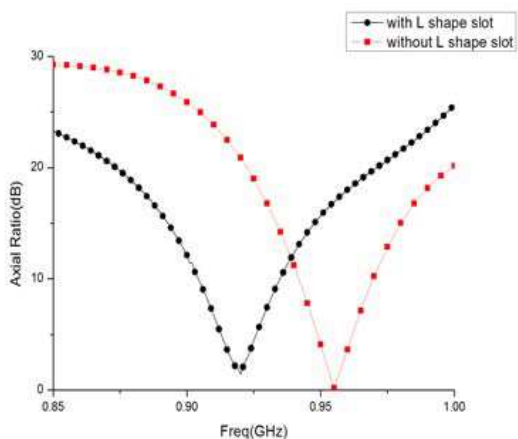
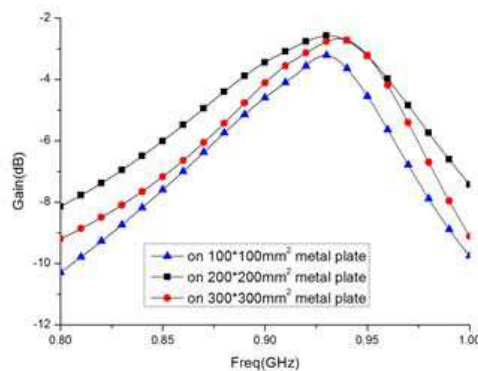Figure 4: Simulated axial ratio of the antenna.

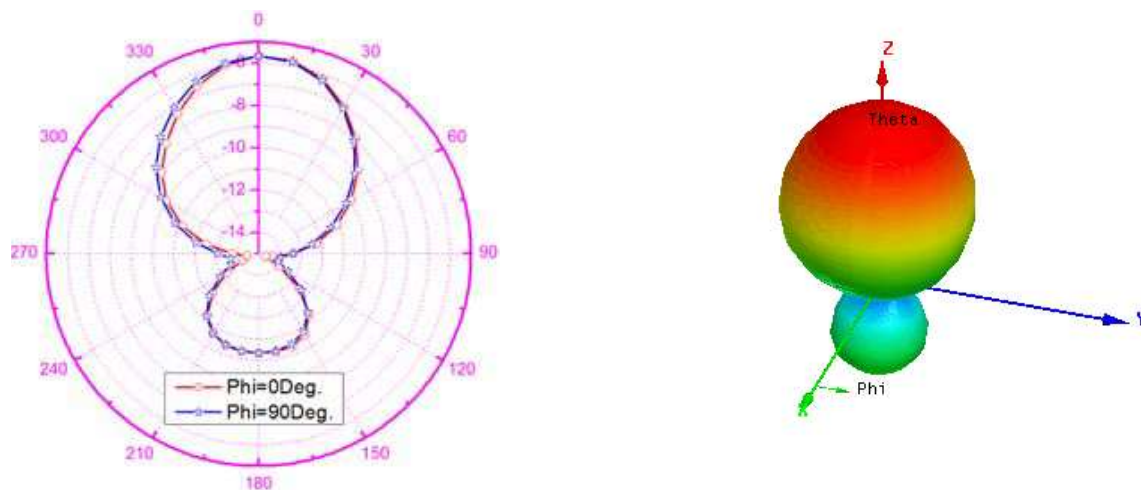Figure 5: Simulated gains of the antenna mounted on a metal plate of various sizes.

Figure 6: Simulated radiation patterns at 920 MHz.

Table 2: Comparison of antenna performances between the proposed antenna and the antennas in [4] and [8].

Proposed optimal antennas with different ground plane sizes (mm^2)	Simulated Gain (Gr)	AR bandwidth
Proposed antenna (80×80)	-6.15 dBic	7 MHz
[4] (80×80)	-11.4 dBic	6 MHz
Proposed antenna (100×100)	-3.22 dBic	8 MHz
[8] (100×100)	-8 dBic	8 MHz

radiation pattern of the antenna at 920 MHz, and the max gains is about -5.5 dBi in 0 degree direction. The radiation gains on the XOY and YOZ planes are good.

To further illustrate the advantages of our antenna compared to [8] and [9], we discuss in detail the differences in gain and AR bandwidth with the same ground size. As we can see from Table 2, our optimized antenna has a higher gain and a wider AR bandwidth.

4. CONCLUSION

A compact circularly polarized RFID tag antenna was proposed with an embedded L-shaped feedline for metallic objects. The impedance matching, return loss, axial ratio and gain of the proposed

antenna had been analyzed and discussed. The Monza4 tag chip was selected. The proposed antenna can achieve a good impedance conjugate matching at the 920 MHz, realize circular polarization at 920 MHz and also has a stable gain on a metal surface of different size.

ACKNOWLEDGMENT

REFERENCES

1. Marrocco, G., "The art of UHF RFID antenna design impedance-matching and size-reduction techniques," *IEEE Antennas Propag. Mag.*, Vol. 50, No. 1, 66–79, Feb. 2008.
2. Koskinen, T. V., H. Rajagopalan, and Y. Rahmat-Samii, "A thin multi-slotted dual patch UHF-band metal-mountable RFID tag antenna," *Microw. Opt. Technol. Lett.*, Vol. 53, No. 1, 40–47, Jan. 2011.
3. Tseng, Y. M., S. H. Kuo, H. D. Chen, and C. Y. D. Sim, "Circularly polarized circular microstrip RFID tag antenna," *2012 Proceedings of APMC*, 1142–1144, Kaohsiung, Taiwan, Dec. 2012.
4. Chen, H. D., S. H. Kuo, and J. L. Jheng, "Design of compact circularly polarized radio frequency identification tag antenna for metallic object application," *Microw. Opt. Technol. Lett.*, Vol. 55, No. 7, 1481–1485, Jul. 2013.
5. Chen, H. D., S. H. Kuo, C. Y. D. Sim, and C. H. Tsai, "Coupling-feed circularly polarized RFID tag antenna mountable on metallic surface," *IEEE Trans. Antennas Propag.*, Vol. 60, No. 5, 2066–2174, May 2012.
6. Pozar, D. M., *Microwave Engineering*, 3rd Edition, Wiley, New York, 2005.
7. Son, H. W. and C. S. Pyo, "Design of RFID tag antennas using an inductively coupled feed," *Electron. Lett.*, Vol. 41, No. 18, 994–996, Sep. 2005.
8. Chen, H. D., C. Y. D. Sim, and S. H. Kuo, "Compact broadband dual coupling-feed circularly polarized RFID microstrip tag antenna mountable on metallic surface," *IEEE Trans. Antennas Propag.*, Vol. 60, No. 12, 5571–5577, Dec. 2012.

Microwave Dielectric Properties of BiNbO$_4$ Ceramics

C. S. Ferreira, **M. P. F. Graça**, **T. Santos**, and **L. C. Costa**

I3N and Physics Department, University of Aveiro, Aveiro 3810-193, Portugal

Abstract— BiNbO$_4$ ceramics were prepared by the solid state reaction, and the as-prepared samples were treated at temperatures between 600 and 1200°C. The samples structure was analyzed by X-Ray Diffraction and the morphology was studied using Scanning Electron Microscopy. The low-perturbation resonant cavity method was used to calculate the dielectric properties of the ceramic material. The samples heat treated at temperatures above 800°C present the BiNbO$_4$ crystal phase, being the predominant phase on the samples treated above 950°C. The samples treated below 900°C present the Bi$_5$Nb$_3$O$_{15}$ secondary phase, which seems to be responsible for the highest dielectric constant values observed at room temperature. The dielectric losses of all samples are always lower than 10^{-4}. The electromagnetic fields, inside the cavity, without and with the cylindrical sample were simulated using the COMSOL Multiphysics software.

1. INTRODUCTION

The progress in communications technology led to extensive researches for the development of miniaturized electronic devices. The study of the properties of potential materials and the development of new materials with specific properties have been the subject of interest [1]. One of the most promising is the bismuth niobate (BiNbO$_4$), that presents good properties in the microwave range [2, 3], with applications in multilayer capacitors [4].

Several authors have studied the influence of the preparation process of BiNbO$_4$, the influence of sintering temperatures and the addition of different oxides [5–7]. The method of solid state reaction has been the most used in the preparation of bismuth niobate.

The measurement of the materials dielectric properties at microwave frequencies can be done in a resonant cavity, using the small perturbation theory [8, 9]. In this method, the changes in the resonance peak frequency and in the quality factor of the cavity, due to the insertion of a sample, can be used to obtain the complex dielectric permittivity of the material, $\varepsilon^* = \epsilon' - i\epsilon''$. The shift in the resonant frequency of the cavity, Δf, can be related to the real part of the complex permittivity, ε', and the change in the inverse of the quality factor of the cavity, $\Delta(1/Q)$, gives the imaginary part, ε''. The relations are simple when can be considered only the first order perturbation in the electric field caused by the sample [10].

In this work, the dielectric properties were measured at 2.7 GHz, using a resonant cavity.

X-Ray diffraction (XRD) and scanning electron microscopy (SEM) were used to find the influence of the microstructures in the microwave dielectric properties.

2. EXPERIMENTAL

Bismuth niobate (BiNbO$_4$) powders were prepared by the solid state method. The raw materials used were bismuth oxide (Bi$_2$O$_3$) and niobium pentoxide (Nb$_2$O$_5$). After weighting the raw materials in the stoichiometry amount, they were mixed, in agata vessels with agata balls during 2 hours at 250 rpm using the same volume of powders and balls in a Fritsch planetary ball mill.

The obtained powder was thermally analysed by differential thermal analysis (DTA), using a Linseis apparatus, from room temperature until 1200°C, with heating rates of 10 and 20°C/min. The obtained results allowed us to define the treatment temperatures. Therefore, pellets from the base powder were made in cylinders with 4 mm in diameter and 8 mm in height, and heat-treated at 200, 500, 600, 700, 800, 900, 1100 and 1200°C, using a dwell time of 4 hours. The heating rate used in the treatments was 5°C/min.

The X-Ray diffraction (XRD) patterns were obtained on a X'Pert MPD Philips difractometer (CuKα radiation, $\lambda = 1.54060$ Å) at 45 kV, and 40 mA, with a curved graphite monochromator, an automatic divergence slit (irradiated length 20.00 mm), a progressive receiving slit (height 0.05 mm) and a flat plane sample holder in a Bragg-Brentano parafocusing optic configuration. Intensity data were collected by the step counting method (step 0.02° in 1 s), in the 2θ angle range from 10 to 60°.

The morphology of the obtained samples was analyzed by scanning electron microscopy (SEM). The measurements were performed on a Hitachi S4100-1, on free and fracture surfaces. The samples were covered with carbon before microscopic observation.

The measurement of the complex permittivity, was made by using a cavity, operating in TE_{015} mode, with a resonant frequency of $2.7\,GHz$. The cavity transmission was measured using an HP 8753D Network Analyzer.

The COMSOL RF module was used to simulate the electromagnetic field inside the cavity, with and without a material sample.

3. RESULTS AND DISCUSSION

Figure 1 shows the most relevant diffraction patterns of the heat treated samples. The one treated at 600°C presents the $Bi_5Nb_3O_{15}$ phase, which is maintained in the highest treatment temperatures. The orthorhombic α-$BiNbO_4$ phase is mostly presented in the sample treated at 900°C, and for higher temperatures it is observed the triclinic β-$BiNbO_4$ phase.

Figure 2 shows SEM images of heat treated samples at different temperatures. At the lowest temperature treatment we can see stacked rods of the $Bi_5Nb_3O_{15}$ phase. For 900°C of temperature, a kind of aggregation of particles is observed and for the highest temperature, the coalescence and high densification is then detected.

Figure 3 shows the resonant cavity, which was used to measure the dielectric properties, and the simulated electric field inside it, when a small sample is introduced in its center.

The measurement of the complex permittivity, $\varepsilon^* = \epsilon' - i\epsilon''$, was made by using the small perturbation theory. When we consider only the first order perturbation in the electric field caused

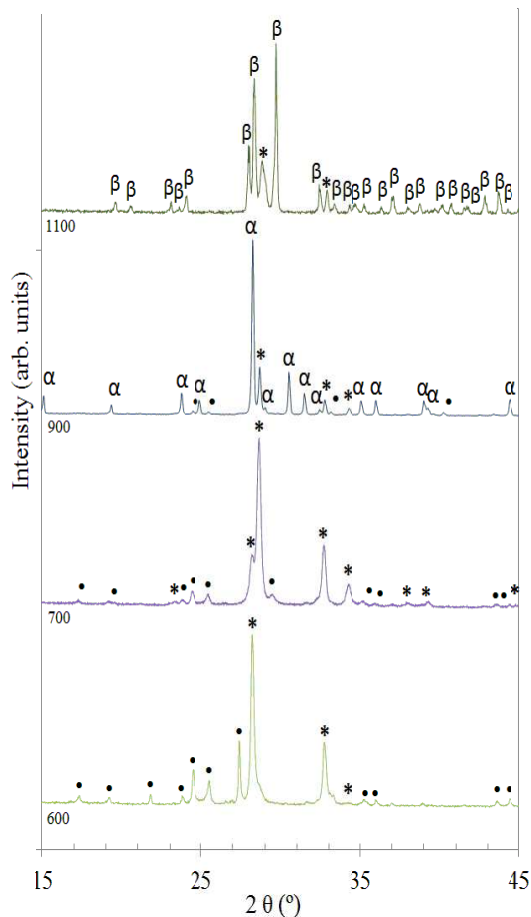Figure 1: X-Ray diffraction patterns of different samples (●: Nb_2O_5; ∗: $Bi_5Nb_3O_{15}$; α: α-$BiNbO_4$; β: β-$BiNbO_4$).
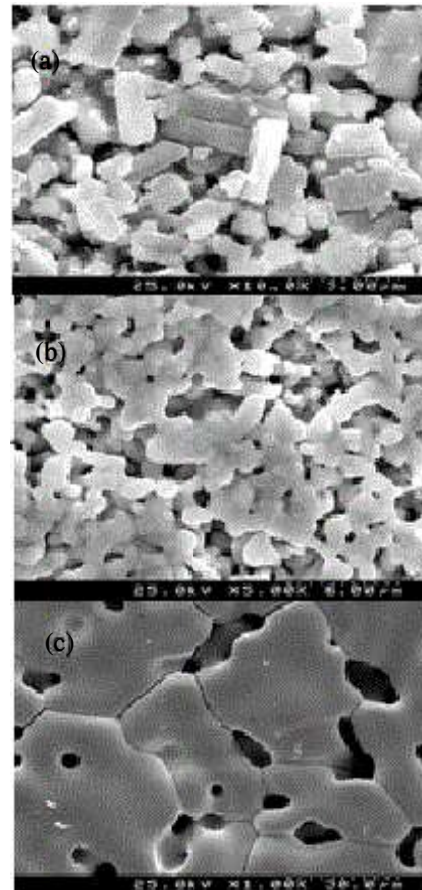

Figure 2: SEM images of heat treated samples: (a) 600°C; (b) 900°C; (c) 1200°C.
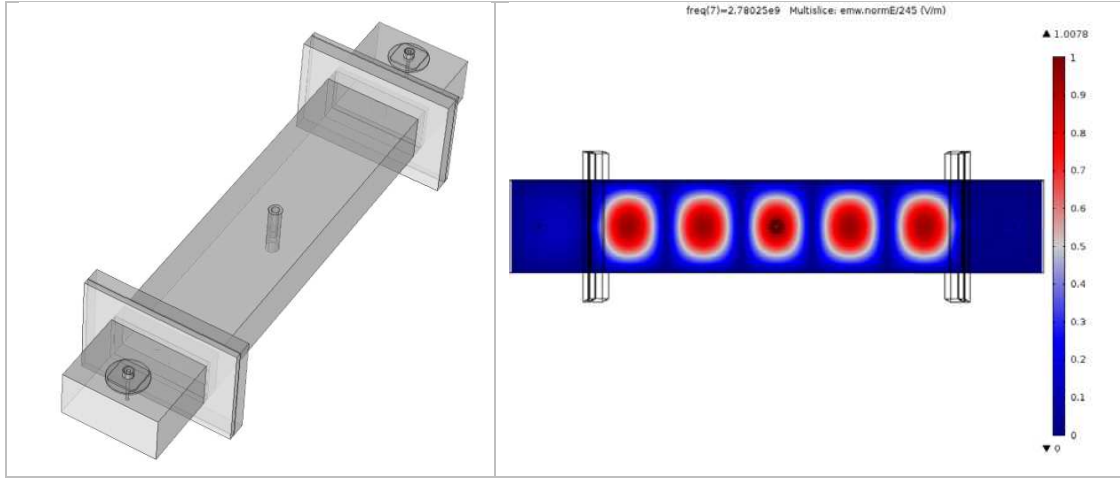
Figure 3: 2.7 GHz resonant cavity and simulated electric field inside it, when a small sample is introduced in its center.
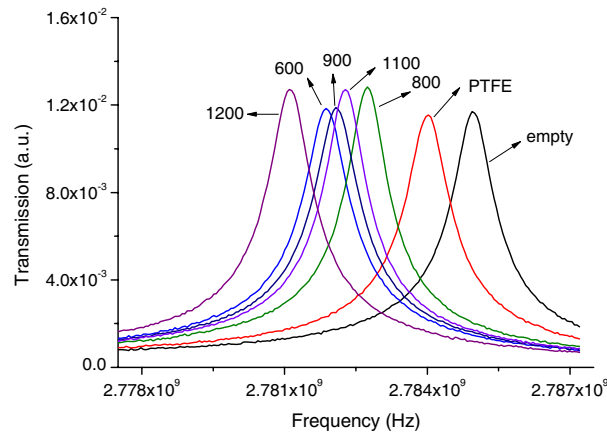

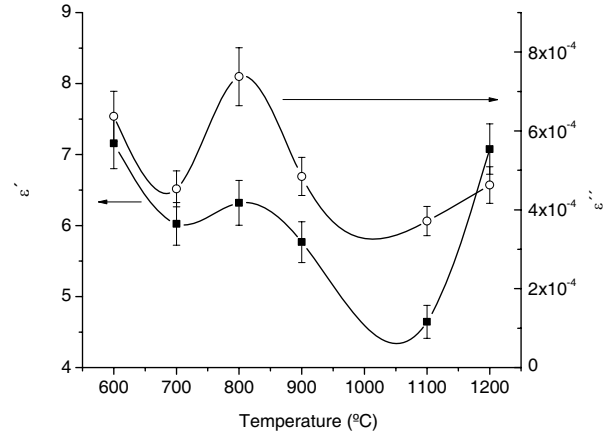Figure 4: Transmission of the cavity, empty and with different samples.

Figure 5: Calculated values of the complex permittivity, for the different samples.

by the sample [11],

$$\varepsilon' = K \frac{\Delta f}{f_0} \frac{V}{v} + 1 \tag{1}$$

$$\varepsilon'' = \frac{K}{2} \Delta \left(\frac{1}{Q} \right) \frac{V}{v} \tag{2}$$

where f_0 is the resonance frequency of the cavity, v the volume of the sample, V the volume of the cavity, and K is a constant related to the depolarization factor, which depends upon the geometric parameters. Using a sample of known complex permittivity we can calculate K. In our case we used a polytetrafluoroethylene (PTFE) cylinder, with the same size and shape of the samples.

Figure 4 shows the transmission of the cavity, empty and with different samples. The most perturbing sample is the 1200°C, indicating that the dielectric constant is high.

Figure 5 shows the calculated values of the complex permittivity. The highest value for the dielectric constant is observed for the sample heat treated at 600°C, which can be assigned to $Bi_5Nb_3O_{15}$ phase, the one that is predominant in this sample. It is also observable that the 1200°C treated sample shows high value for ε'. The triclinic β-$BiNbO_4$ phase and the particular morphology can justify this behavior. However, this sample also shows very low ε'', and consequently low loss tangent, $tg\delta = \varepsilon''/\varepsilon'$. This fact is relevant for technological applications.

4. CONCLUSIONS

$BiNbO_4$ ceramics were prepared by the solid state reaction, and treated at temperatures between 600 and 1200°C. The samples heat treated at higher temperatures present the $BiNbO_4$ crystal phase, being the predominant phase on the samples treated above 950°C. The samples treated at lower temperatures present the $Bi_5Nb_3O_{15}$ phase, which seems to be responsible for the highest dielectric constant values. The 1200°C heat treated samples present the lower dielectric losses, with high dielectric constant, which make them useful for electronic applications.

REFERENCES

1. Cao, G., *Nanostructures and Nanomaterials, Synthesis, Properties and Applications*, World Scientific Publishing Co., London, 2004.
2. Plonska, M. and D. Czeka, "Studies of temperature and fabrication methods influence on structure of $BiNbO_4$ microwave electroceramics," *Arch. of Metall. Mater.*, Vol. 58, 1169–1175, 2011.
3. Radha, R., H. Muthurajan, N. Rao, S. Pradhan, U. Gupta, R. Jha, S. Mirji, and V. Ravi, "Low temperature synthesis and characterization of $BiNbO_4$ powders," *Mater. Charact.*, Vol. 59, 1083–1087, 2008.
4. Kim, E. and W. Choi, "Effect of phase transition on the microwave dielectric properties of $BiNbO_4$," *J. Eur. Ceram. Soc.*, Vol. 26, 1761–1766, 2006.
5. Carneiro, R., J. Araújo, M. F. Gianani, A. G. Assunção, R. A. Martins, and L. M. Mendonça, "Simulation and measurement of insetfed microstrip patch antennas on $BiNbO_4$ substrates," *Opt. Technol. Lett.*, Vol. 52, No. 5, 1034–1036, 2010.
6. Almeida, C., H. Andrade, A. Mascarenhas, and L. Silva, "Synthesis of nanosized β-$BiTaO_4$ by the polymeric precursor method," *Mater. Lett.*, Vol. 64, 1088–1090, 2010.
7. Brinker, C. J. and G. W. Scherer, *Sol-Gel Science: The Physics and Chemistry of Sol-Gel Processing*, Academic Press, New York, 1989.
8. Henry, F. and A. J. Berteaud, "New measurement technique for the dielectric study of solutions and suspensions," *J. Micr. Power*, Vol. 15, 235–242, 1980.
9. Costa, L. C., S. Devesa, and F. Henry, "Microwave dielectric properties of polybutylene terephtalate (PBT) with carbon black particles," *Micr. Opt. Tech. Lett.*, Vol. 46, 61–63, 2005.
10. Costa, L. C. and F. Henry, "The impact of blue inorganic pigments on the microwave electrical properties of polymer composites," *Inter. J. Micr. Sci. Tech.*, Vol. 2012, 2012.
11. Henry, F., "Contribution à l'étude des processus d'hydratation en milieu solide et liquide par relaxation diélectrique en micro-ondes. Développement de la métrologie," PhD Thesis, France, 1982.

Chaos Generation Utilizing Optically Square-wave-injected Semiconductor Lasers

Chen-Wei Fu, **Shao-Wei Peng**, **and Yu-Shan Juan**

Department of Photonics Engineering, Yuan Ze University
No. 135, Yuandong Rd., Zhongli Dist., Taoyuan City 32003, Taiwan

Abstract— Benefiting from a non-zero value of the linewidth enhancement factor which leads to a variety of dynamics different from any other lasers, the broad bandwidth of chaos can be easily generated. There are several applications in chaotic laser, such as broadband random-bit generation, ranging, and secured communications. In the past two decays, most studies of the chaos generations focused on the nonlinear dynamics of the traditional continuous wave (cw) injection and dynamical pulse and sine wave injection. In this work, we study chaos generation utilizing an optically square-wave-injected semiconductor laser with tunable duty cycle. By injecting a slave laser with periodic optical square-wave at specific parameters, chaos oscillation and chaos pulsing can be generated individually. Compared with continuous wave injection with the same injected conditions, the chaos oscillation generated by square-wave injection shows larger bandwidth and more complex behaviors. Furthermore, if the operating variables are adjusted to the center of the chaos area in the dynamical mapping, the waveforms of power spectra of the generated chaos are much smoother and broader. In this paper, the distribution map of chaos oscillation and pulsing oscillation are investigated. When the duty cycle is operated at high level, chaos oscillation is observed. On the other hand, if we operate the condition at high repetition rate and strong injection strength, nonlinear dynamics is driven into the chaos pulsing states and the bandwidth of chaos pulsing is two times larger than chaos oscillation which is operated in week injection strength. The three parameters, duty cycle, repetition rate, and injection strength, all play important roles in chaos generation utilizing optical square-wave injection system.

1. INTRODUCTION

Nonlinear dynamics of semiconductor lasers have been widely investigated in recent years. Subject to different types of perturbations, such as optical feedback [1], optical injection [2], optoelectronic feedback [3], and dual-beam injection [4], rich dynamical behaviors can be easily generated. The main reasons which lead to a variety of dynamics in semiconductor lasers are the low reflectivity of the internal mirrors in the laser cavity and a non-zero value of the linewidth enhancement factor. The variety of dynamics are including stable locking, periodic oscillation, chaos pulsing, and chaos oscillation [5, 6]. Chaos pulsing and chaos oscillation are the phenomena of irregular variations of system outputs. Potential applications utilizing chaotic states have been extensively explored, such as secured communications [7], ranging [8, 9], and broadband random-bit generation [10]. In the past two decays, most studies utilized traditional continuous wave injection and dynamical pulse and sine wave injection to generate chaos, in this work, we focused on the chaos which is generated by an optically square-wave-injected semiconductor laser with tunable duty cycle. Compared with continuous wave injection with the same injected conditions, the chaos oscillation generated by square-wave injection shows larger bandwidth and more complex behaviors. Additionally, when the conditions are operated at high repetition rate and strong injection strength, the nonlinear dynamics is driven into the chaos pulsing states and the bandwidth is larger than that is operated at low repetition rate and week injection strength.
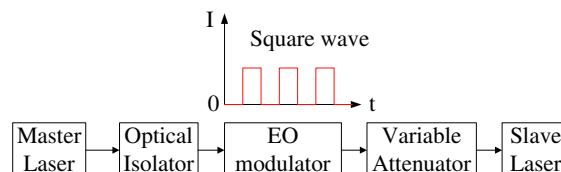
2. SCHEMATIC SETUP

Figure 1: Schematic setup of a semiconductor laser under repetitive optical square wave injection.

Figure 1 is the schematic setup of the semiconductor laser under repetitive optical square-wave injection. In Fig. 1, EO modulator is an optical device in which a signal-controlled element exhibiting the electro-optic effect is used to make continuous wave change into square-wave and variable attenuator is to control the injection strength of square-wave input. The dynamics of the slave laser is controlled by adjusting the operational parameters. The nonlinear behavior of the optically injected slave laser can be derived by normalizing three coupled rate equations [11]:

$$\frac{da}{dt} = \frac{1}{2}\left[\frac{\gamma_c\gamma_n}{\gamma_s\tilde{J}}\tilde{n} - \gamma_p(2a+a^2)\right](1+a) + \xi_i(t)\gamma_c\cos(\Omega t + \phi) \tag{1}$$

$$\frac{d\phi}{dt} = -\frac{b}{2}\left[\frac{\gamma_c\gamma_n}{\gamma_s\tilde{J}}\tilde{n} - \gamma_p(2a+a^2)\right] - \frac{\xi_i(t)\gamma_c}{1+a}\sin(\Omega t + \phi) \tag{2}$$

$$\frac{d\tilde{n}}{dt} = -\gamma_s\tilde{n} - \gamma_n(1+a)^2\tilde{n} - \gamma_s\tilde{J}(2a+a^2) + \frac{\gamma_s\gamma_p}{\gamma_c}\tilde{J}(2a+a^2)(1+a)^2 \tag{3}$$

where ϕ, a, and $\tilde{n}$ representing the optical phase difference, normalized optical field and normalized carrier density, respectively. γ_c is the cavity decay rate, γ_n is the differential carrier relaxation rate, γ_p is the nonlinear carrier relaxation rate, γ_s is the spontaneous carrier relaxation rate, b is the linewidth enhancement factor, $\tilde{J}$ is the normalized dimensionless injection current parameter, Ω is the detuning frequency, and n is the effective refractive index. The dimensionless injection parameter $\xi_i(t)$ is the normalized strength of the injection field received by the injected laser. The injection profile of each Square wave is described as:

$$\xi_i(t) = \begin{cases} \xi_{sq}, & \text{if } T \leq D \times \tau \\ 0, & \text{otherwise} \end{cases}$$

Here ξ_{sq} is the normalized injection strength of the square wave. T is the period of function, D is the duty cycle of the square wave, and τ is the duration that the function are active. The relaxation resonance frequency of the laser used in this simulation is $f_r = 2.47\,\text{GHz}$. By adjusting the controllable operational parameters including the normalized injection strength of square wave ξ_{sq}, the detuning frequency Ω between the master laser and the slaver laser, the duty cycle D of square wave, and repetition frequency f_{rep} of the repetitive square waves, various dynamical states including frequency-locked state, periodic oscillation, and chaos states can be observed.

3. RESULTS

Figure 2 shows the chaos oscillation generated by continuous wave injection and square-wave injection. The red and black curves indicate the input and output of slave laser, respectively. Figs. 2(a)–(b) show the time series and the corresponding power spectra under traditional continuous wave injection which is operated at the boundary between chaos oscillation and period-doubling oscillation area. The dynamics in Fig. 2(a) shows a period-doubling oscillation and the power spectra in Fig. 2(b) displays high intensity signal at specific frequency which gives rise to a narrow bandwidth. The bandwidth at this condition is about 4.36 GHz. It is obvious that this waveform is not a good choice to be applied to the application in chaotic lidar. However, instead of traditional continuous wave injection, we used square-wave injection with duty cycle $D = 50\%$ under the same conditions of detuning frequency and injection strength. The chaos oscillation became more complex, as shown in Figs. 2(c)–(d). Figs. 2(c)–(d) show time series and power spectra at the repetition rate $f_{rep} = 200\,\text{MHz}$, respectively. Compared with continuous wave injection, square-wave injection at repetition rate $f_{rep} = 200\,\text{MHz}$ demonstrate a smoother power spectra, this chaos oscillation still displays a distinguish peak at 8 GHz in the power spectra caused by the slow repetition rate. High quality chaos waveform can be achieved if the repetition rate is operated at the center of the chaos area, and nonlinear dynamics could be more complicated than the fixed repetition rate at 200 MHz.

Moreover, the distribution map of chaos oscillation and pulsing oscillation is investigated. Fig. 3 shows the chaos map and corresponding bandwidth with various injection strength and repetition rate at fixed duty cycle of $D = 50\%$. The red dots in Fig. 3(a) represent chaos oscillation and the black dots represent chaos pulsing. As shown in Fig. 3(a), chaos pulsing occurs at high injection strength and high repetition rate area and almost all of chaos pulsing demonstrate better bandwidth than chaos oscillation, as can be seen in Fig. 3(b). The definition of bandwidth here is the 80% of total energy from the DC in power spectra. When the repetition rate is fixed at 4.8 GHz, operating
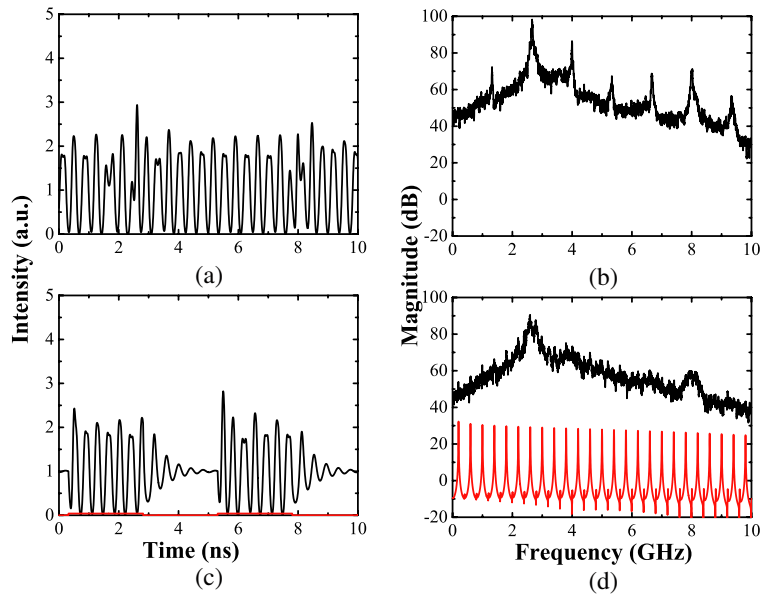
Figure 2: Comparison between continuous wave injection and square-wave injection. (a)–(b) Chaos oscillation generated by continuous wave injection operated at the boundary between period-2 and chaos with injection strength $\xi_i = 0.04$ and detuning frequency $\Omega = -0.7\,\text{GHz}$. (c)–(d) chaos oscillation generated by square-wave injection with duty cycle $D = 50\%$ and repetition rate $f_{rep} = 200\,\text{MHz}$. The red curves are the input of slave laser and the black curves are the output of slave laser.
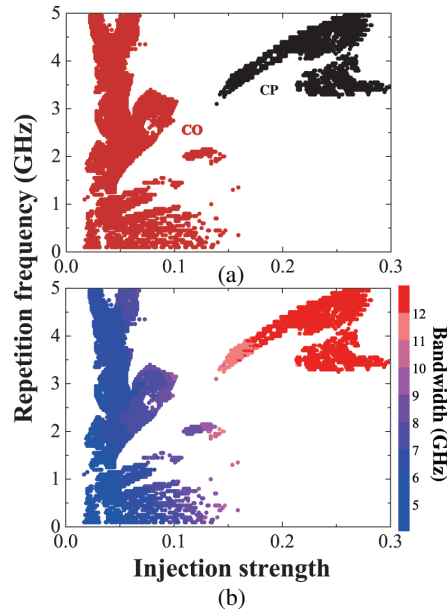

Figure 3: (a) The map of chaos and (b) the map of bandwidth with square-wave injection operated at duty cycle $D = 50\%$ and detuning frequency $\Omega = -0.7\,\text{GHz}$. The red dots and the black dots in Fig. 3(a) represent chaos oscillation and chaos pulsing, respectively.

the injection strength $\xi_{sq} = 0.05$ and $\xi_{sq} = 0.273$ to generate chaos oscillation and chaos pulsing with the bandwidths of $7.1\,\text{GHz}$ and $14.5\,\text{GHz}$ are demonstrated, respectively. As the result, the bandwidth of chaos pulsing is two times larger than chaos oscillation. Except the repetition rate and injection strength, duty cycle is also an key parameter for chaos generation. Chaos oscillation is usually found at high duty cycle condition and chaos pulsing is easily observed when operating at low duty cycle.

4. CONCLUSION

In this work, we have numerically investigated chaos oscillation and chaos pulsation generated by square-wave injection. Under the same conditions of detuning frequency and injection strength, the waveforms of chaos oscillation generated by square-wave injection are more complex than traditional continuous wave injection. Furthermore, when increasing the repetition rate of square-wave injection, the chaos waveforms show more smoother than operating at low repetition rate. In this paper, the distribution map of chaos oscillation and chaos pulsing is also obtained and studied. Chaos oscillation is usually observed at the conditions of low repetition rate and low injection strength. In addition, due to the bandwidth enhancement effect, chaos with larger bandwidth is easily found under strong injection strength.

ACKNOWLEDGMENT

REFERENCES

1. Mork, J., B. Tromborg, and J. Mark, "Chaos in semiconductor lasers with optical feedback: Theory and experiment," *IEEE J. Quantum Electron.*, Vol. 28, 93–108, 1992.
2. Simpson, T. B., J. M. Liu, A. Gavrielides, V. Kovanis, and P. M. Alsing, "Period-doubling cascades and chaos in a semiconductor laser with optical injection," *Phys. Rev. A*, Vol. 51, 4181–4185, 1995.
3. Lin, F. Y. and J. M. Liu, "Nonlinear dynamics of a semiconductor laser with delayed negative optoelectronic feedback," *IEEE J. Quantum Electron.*, Vol. 39, 562–568, 2003.
4. Liao, Y. H., J. M. Liu, and F. Y. Lin, "Dynamical characteristics of a dual-beam optically injected semiconductor laser," *IEEE J. of Sel. Top. Quantum Electron*, Vol. 19, No. 4, 1500606, 2013.
5. Mogensen, F., H. Olesen, and G. Jacobsen, "Locking conditions and stability properties for a semiconductor laser with external light injection," *IEEE J. Quantum Electron.*, Vol. QE21, No. 7, 784–793, 1985.
6. Mukai, T. and K. Otsuka, "New route to optical chaos: successive-subharmonic-oscillation cascade in a semiconductor laser coupled to an external cavity," *Phys. Rev. Lett.*, Vol. 55, 1711–1714, 1985.
7. Lin, F. Y. and M. C. Tsai, "Chaotic communication in radio-over-fiber transmission based on optoelectronic feedback semiconductor lasers," *Opt. Express*, Vol. 15, 302–311, 2007.
8. Lin, F. Y. and J. M. Liu, "Chaotic radar using nonlinear laser dynamics," *IEEE J. Quantum Electron.*, Vol. 40, No. 6, 815–820, 2004.
9. Lin, F. Y. and J. M. Liu, "Chaotic lidar," *IEEE J. Select. Topics Quantum Electron.*, Vol. 10, No. 5, 991–997, 2004.
10. Hirano, K., T. Yamazaki, S. Morikatsu, H. Okumura, H. Aida, A. Uchida, S. Yoshimori, K. Yoshimura, T. Harayama, and P. Davis, "Fast random bit generation with bandwidth-enhanced chaos in semiconductor lasers," *Opt. Exp.*, Vol. 18, 5512–5524, 2010.
11. Simpson, T. B., J. M. Liu, A. Gavrielides, V. Kovanis, and P. M. Alsing, "Period-doubling cascades and chaos in a semiconductor laser with optical injection," *Phys. Rev. A*, Vol. 173, 4181–4185, 1995.

Photonic Band Structure and Field Distribution for TE Polarization. High Plasmon Concentration in the Corners of Metallic Rods of a 2D Photonic Crystal

D. M. Calvo-Velasco and N. Porras-Montenegro

Departamento de Física, Universidad del Valle, A. A. 25.360, Cali, Colombia

Abstract— In this work we calculated the photonic band structure (PBS) of a square 2D photonic crystal (PC) made of square metallic rods embedded in air, considering a Drude type dielectric function without loss for different values of the rod plasma frequency, ω_p. The PBS was calculated for TE polarization in the Γ-X direction using the revised plane wave method (RPWM), considering the Li's rules for the product of two periodic functions. We found that the PBS presents flat bands below and above the surface plasmon frequency (SPF), and by means of the distribution of the square module of the magnetic component of the electromagnetic radiation, $|H_z|^2$, in the crystal unit cell, we found that these bands are related with the existence of plasmons in the surface of the rods, as it has been discussed and published in previous works. Besides these findings, we found a high concentration of the square module of the electric component of the electromagnetic radiation, $|E|^2$, close to the rod corners, which is a signature of the existence of localize surface plasmons, due to the geometry of the PCs structure. On the other hand, we found that $|H_z|^2$ presents a distribution which does not change in passing from the metallic regime to the dielectric one for frequencies close to ω_p, while $|E|^2$ is distributed only inside the rods for frequencies below ω_p, and essentially in the whole unit cell above this value.

1. INTRODUCTION

In recent years the study of photonic crystals (PCs) and their optical properties [1–3], aroused the interest of the scientific community, thanks to the discovery of the photonic band gaps present in these structures, that is, frequency ranges where the propagation of the electromagnetic field is prohibited, allowing the development of new technologies [4].

PCs are an arrangement of materials with different refraction index, which allow light behaviors not present in the bulk materials that form the PC. The photonic band structure (PBS) and the band gaps in the PCs depend on the difference between the refractive index of the components of the PC, their geometry disposition, and the filling fraction. The different studies on these structures rang from multiple slabs of different materials for 1D systems up to 3D structures [1–8], including fractal disposition of a dielectric material in air in a limited region of the space [9, 10]. Also, some studies are related to defects which modify the translation symmetry of PCs which allows the existence of high localized modes used in the construction of wave guides.

Maxwell equations are used to study the light behavior in PCs. To solve them several techniques have been developed such as plane waves, finite difference time domain (FDTD), revised plane wave method (RPWM), and others [11], and have been applied to several systems in order to study their optical response [12–14].

For PCs formed by dispersive materials it is possible to locate the incident radiation thanks to the existence of surface plasmon polaritons, that are related with the collective motion of coupled charges with the electromagnetic field [15].

Kusmiak et al. [12] studied a 2D system made of an arrange of parallel metallic rods in air using the plane wave method, reducing the PBS calculation to a standard eigenvalue problem. They show the existences of localized modes for TE polarization that must correspond to the interaction of the rod isolated excitations that overlap in the PC to form flat bands. This observation was corrected by Ito et al. [16], who presented a calculation based in a dipolar radiation implemented on the FDTD method to study the PBS, showing a strong distribution of the electromagnetic field on the surface of the rods, near to the resonant frequencies of a single rod under normal incidence for the electromagnetic radiation, that corresponds to the excitation of localized plasmon polariton in the metallic rod. Esteban Moreno et al. [17], demonstrated that the hypothesis by Ito et al. about the dipolar radiation for the excitation of surface localized modes in the crystal is not enough for another geometry of the rods, being necessary a generalization of the FDTD method using a set of dipoles in the unitary cell. It is important to note that the location shown by Ito et al., as well as the results obtained by Esteban Moreno et al., show that the field at the surface of the metal bars is

distributed satisfying any of the symmetries of the metal cross section, also they show that the PBS for the circular cross section has bands with low dispersion below the surface plasmon frequency (SPF). These flat bands are distributed around frequencies which correspond to the resonant modes of the metal rods. Now that Esteban Moreno et al. also presents the study of a PC formed by bars with triangular cross section, showing the existence of flat bands above and below the SPF, demonstrating that the flat bands are distributed around the resonant modes of the rods, but the bands distribution above the SPF depends strongly on the geometry of the cross section of the rods.

In this work we study a 2D PC formed by an square arrangement of square metal rods embedded in air without dispersion in the materials. We calculate the PBS and some distributions of $|H_z|^2$ and $|E|^2$ in the unitary cell defined for the crystal using the RPWM method in order to elucidate the existence of surface plasmons in these systems.

2. THEORETICAL FRAMEWORK

We use the RPWM [18], for the calculation of the PBS of the PC proposed in the introduction. Considering square rods made of metallic material with dielectric function ϵ_m in a square lattice embedded in air, whose axes are parallel to z direction, it is possible to show that for TE polarization, $(\vec{H} = (0, 0, H_z), \vec{E} = (E_x, E_y, 0))$, and with a plane wave representations for the electrical and magnetic field, the Maxwell equations can be organized in the form

$$k_x \begin{bmatrix} [E_y] \\ [H_z] \end{bmatrix} = \frac{1}{k_0} \begin{bmatrix} -k_0\,[[G_x]] & k_0^2 - (k_y + [[G_y]])\,[[\epsilon_{xx}]]^{-1}\,(k_y + [[G_y]]) \\ k_0^2\,[[\epsilon_{yy}]] & -k_0\,[[G_x]] \end{bmatrix} \begin{bmatrix} [E_y] \\ [H_z] \end{bmatrix}, \quad (1)$$

where $k_0 = \frac{\omega}{c}$ with ω the frequency of the radiation, and $[[G_{x(y)}]]_{G,G'} = G_{x(y)}\delta_{G,G'}$, are diagonal matrices of order N formed with the components of reciprocal lattice vector $\vec{G} = (G_x, G_y, 0)$. $[E_y]$ and $[H_z]$ are column vectors of order N constructed by the coefficients of the plane wave representation of the electrical and magnetic fields. k_x and k_y are the components of the radiation wave vector $\vec{k} = (k_x, k_y, 0)$ in the plane x-y.

The matrices $[[\epsilon_{xx}]]$, $[[\epsilon_{yy}]]$ are matrices of order N constructed following the Li's rules for the
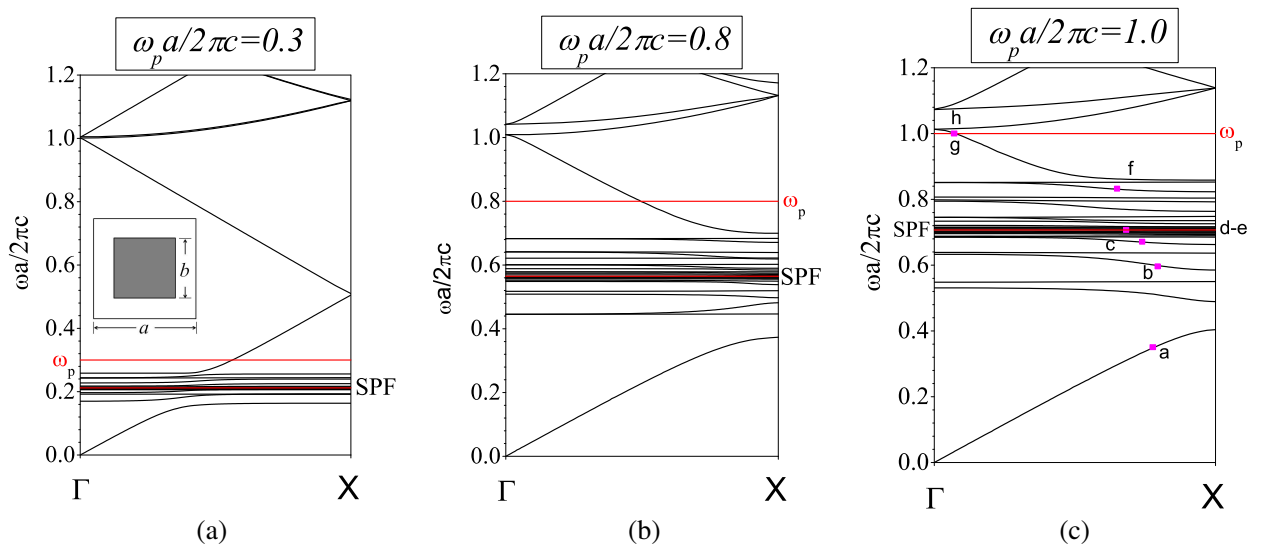

Figure 1: Photonic band structure for TE polarization in the Γ-X direction of a square lattice of square metallic rods embedded in air (inset in Fig. 1(a)), with $b/a = 0.25$, being a the lattice parameter and b the side size of the square rod. The value of plasma frequency is: (a) $\omega_p a/2\pi c = 0.3$, (b) $\omega_p a/2\pi c = 0.8$, (c) $\omega_p a/2\pi c = 1.0$. Red lines show the ω_p frequency and the value of the SPF. The purple marked squares a–h in Fig. 1(c) are to display $|H_z|^2$ and $|E|^2$ as it is presented in Fig. 2.

product of two periodic functions [19, 20]. In our case we have

$$[[\epsilon_{xx}]]_{mn,m'n'} = \frac{1}{a} \int_{-a/2}^{a/2} [[A_x^{-1}]]_{m,m'} \, e^{-i(n-n')g_y y} dy, \tag{2}$$

$$[[A_x]]_{m,m'} = \frac{1}{a} \int_{-a/2}^{a/2} \frac{1}{\epsilon} e^{-i(m-m')g_x x} dx, \tag{3}$$

where $g_i = |\vec{b_i}|$ are the elementary translation vectors of the reciprocal lattice, a is the lattice parameter and ϵ is a periodic function that takes the value of ϵ_m in the rods and is 1 in air. The coefficients of the matrix are relating the term $\vec{G} = m\vec{b}_x + n\vec{b}_y$ with $\vec{G}' = m'\vec{b}_x + n'\vec{b}_y$. A similar construction follows for $[[\epsilon_{yy}]]$.

The calculation of the PBS in Γ-X direction, that is with $k_y = 0$, is obtained solving the eigen values of Eq. (1).

3. RESULTS

By means of Eq. (1), we calculate the PBS of a 2D square PC made of square rods of metal embedded in air for three values of plasma frequency, which in practice corresponds to different
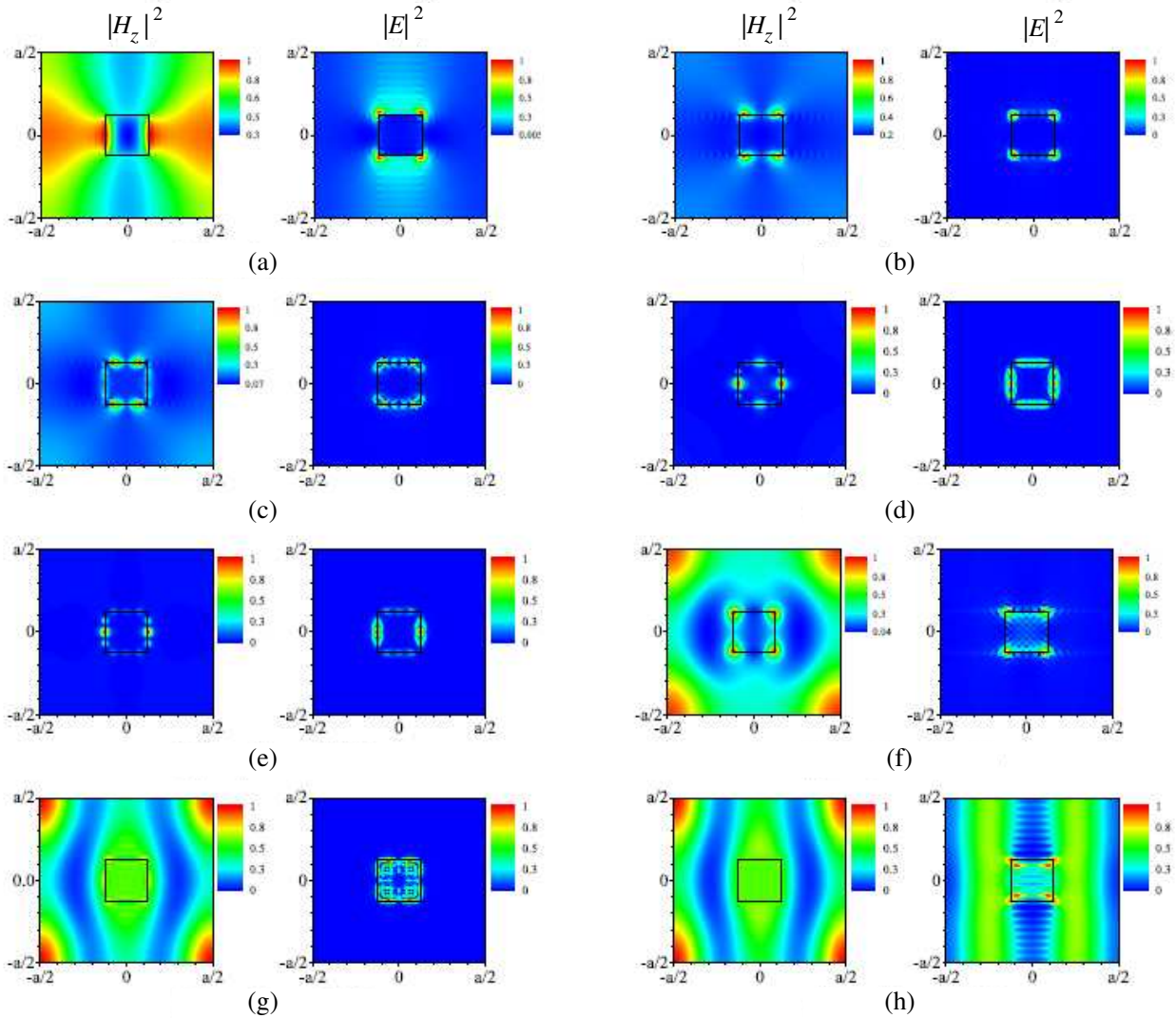
Figure 2: Some distributions of $|H_z|^2$ and $|E|^2$ in the unitary cell of a PC made of square metallic rods in air with $\omega_p a/2\pi c = 1.0$ and $b/a = 0.25$. The intensity distribution is in arbitrary units. (a) $\omega a/2\pi c = 0.361$, (b) $\omega a/2\pi c = 0.595$, (c) $\omega a/2\pi c = 0.670$, (d) $\omega a/2\pi c = 0.706$, (e) $\omega a/2\pi c = 0.708$, (f) $\omega a/2\pi c = 0.835$, (g) $\omega a/2\pi c = 0.999$, (h) $\omega a/2\pi c = 1.001$.

metals. We consider squares rods with $b/a = 0.25$, where b is the length of the square side and a is the lattice parameter. The dielectric function of the rod material is assumed as [21]

$$\epsilon_m = 1 - \frac{\omega_p^2}{\omega^2}, \tag{4}$$

where ω_p is the plasma frequency.

In Fig. 1, we observe the PBS characterized with flat bands localized below ω_p, behavior just reported by Ito et al. [16], due to the characteristic resonance frequencies associated with the existence of surface plasmons on the rod surface. Also, we found that for higher values of the ω_p, not only flat bands, but also new dispersive bands appear above the ω_p.

Figure 2 displays some field $|H_z|^2 - |E|^2$ distributions in the unitary cell for $\omega_p a/2\pi c = 1.0$. For low frequencies and in the dispersive band, Fig. 2(a), we observe that $|H_z|^2$ and $|E|^2$ are distributed outside the rod, and $|E|^2$ presents a strong concentration close to the corners of the rod, related with the movement of charge over the surface of the rod, but localized in their corners. On the other hand for higher frequencies, Figs. 2(b) and 2(c), show a high localization in the rod region, due to the smaller absolute values of the dielectric function of the metal, which promote the entering of radiation into the rod, while the distribution $|E|^2$ shows the formation of surface plasmons.

Figures 2(d) and 2(e), present the field distribution for higher and lower frequencies, close to the SPF, showing strong plasmon localization in the rod sides, in agreement with the low group velocity of radiation. For frequencies above the SPF, Fig. 2(f), the $|H_z|^2 - |E|^2$ distributions show the presence of radiation in the rod regions, because of the metal has the lower absolute value of the dielectric function. With respect to $|E|^2$ distribution, we observe that the field is highly concentrated in the corners. For frequencies below and above to ω_p, Figs. 2(g) and 2(h), present a similar $|H_z|^2$ distribution in the unitary cell, differently to the case for the $|E|^2$ distribution, which below ω_p forces the electric field to enter into the rod, due to the low absolute value of its refractive index, while for frequencies above ω_p the electric field is mainly distributed into the rod, but also with a strong presence in the air region. In these case, both materials present a positive refractive index, but the metallic rod is the material with the lower one, which makes the radiation to concentrate inside the rod.

4. CONCLUSION

In this work, using the RPWM we calculate the PBS in the Γ-X direction of a 2D square PC formed of square metallic rods embedded in air for the TE polarization. We found that the PBS of the PC depends markedly on the value of the ω_p, which modifies and shifts it to lower or higher frequencies. For all values of ω_p the PBS is characterized by the existence of flat bands below the plasma frequency related with the existence of localized surface plasmons in the rod surfaces, bands which are distribute around the SPF. By means of $|H_z|^2$ we encounter that for frequencies which make ϵ large negative in the rod region, the field is expelled out of the rods, behavior that also occurs for $|E|^2$, with a strong concentration of the field in the corners of the rods, due to the movement of charge in the metal caused by the electric field. For frequencies very close to the SPF we observe a strong localization of the fields on the surface of the rods. As $|\epsilon|$ decreases in the metal we encounter a distribution that is characterized by the existence of localized surface plasmons. On the other hand for frequencies between the SPF and ω_p, the field enters inside the rod, being more evident in the $|E|^2$ distribution just below ω_p. Above ω_p we found the common behavior of localization of the radiation, presenting a discontinuity of $|E|^2$ across the surface of the rod due to its discontinuity in the metal surface.

ACKNOWLEDGMENT

REFERENCES

1. Joannopoulos, J. D., S. G. Johnson, J. N. Winn, and R. D. Meade, *Photonic Crystals: Molding the Flow of Light*, Pricenton University Press, Pricenton, 2008.

2. Sakoda, K., *Optical Properties of Photonic Cristals*, 2nd Edition, Springer-Verlag, Berlin, Heidelberg, 2005.

3. Ramakrishna, S. A. and T. M. Grzegorczyk, *Physics and Applications of Negative Refractive Index Materials*, Taylos & Francis Group, Bellingham, Washington, 2009.

4. Engheta, N. and R. W. Ziolkoshowski, *Metamaterials: Physics and Engineering Explorations*, IEEE Press, Wiley-Interscience, 2006.

5. Cavalcanti, S. B., M. de Dios-Leyva, E. Reyes-Gomez, and L. E. Oliveira, "Band structure and band-gap control in photonic superlattices," *Phys. Rev. B*, Vol. 74, 153102, 2006.

6. González, L. E. and N. Porras Montenegro, "Pressure, temperature and plasma frequency effects on the band structure of a 1D semiconductor photonic cristal," *Physica E*, Vol. 44, 773, 2012.

7. Díaz-Valencia, B. F. and J. M. Calero, "Photonic band gaps of a two-dimensional square lattice composed by superconducting hollow rods," *Physica C*, Vol. 505, 74, 2014.

8. López, J., L. E. González, M. F. Quiñónez, M. E. Gómez, N. Porras-Montenegro, and G. Zambrano, "Magnetic field role on the structure and optical response of photonic crystals based on ferrofluids containing $Co_{0.25}Zn_{0.75}Fe_2O_4$ nanoparticles," *Journal of Applied Physics*, Vol. 115, 193502, 2014.

9. Sakoda, K., "Electromagnetic eigenmodes of a three-dimensional photonic fractal," *Phys. Rev. B*, Vol. 72, 184201, 2005.

10. Mejia, J. R., N. Porras-Montenegro, E. Reyes, S. B. Cavalcanti, and L. E. Oliveira, "Plasmon polaritons in 1D Cantor-like fractal photonic superlattices containing a left-handed material," *Europhys. Lett.*, Vol. 95, 24004, 2011.

11. Veselago, V., L. Braginsky, V. Shklover, and C. Hafner, "Negative refractive index materials," *J. Comput. Theor. Nanosci.*, Vol. 3, 1, 2006.

12. Kuzmiak, V., A. A. Maradudin, and F. Pincemin, "Photonic band structures of two-dimensional systems containing metallic components," *Phys. Rev. B*, Vol. 50, 16835, 1994.

13. Sakoda, K., N. Kawai, T. Ito, A. Chutinan, S. Noda, T. Mitsuyu, and K. Hirao, "Photonic bands of metallic systems. I. Principle of calculation and accuracy," *Phys. Rev. B*, Vol. 64, 045116, 2001.

14. Huang, K. C., P. Bienstman, J. D. Joannopoulos, K. A. Nelson, and S. Fan, "Phonon-polariton excitations in photonic crystals," *Phys. Rev. B*, Vol. 68, 075209, 2003.

15. Maier, S., *Plasmonics: Fundamentals and Applications*, Springer Science+Business Media LLC, 2007.

16. Ito, T. and K. Sakoda, "Photonic bands of metallic systems. II. Features of surface plasmon polaritons," *Phys. Rev. B*, Vol. 64, 045117, 2001.

17. Moreno, E., D. Erni, and C. Hafner, "Band structure computations of metallic photonic crystals with the multiple multipole method," *Phys. Rev. B*, Vol. 65, 155120, 2002.

18. Shi, S., C. Chen, and D. W. Prather, "Revised plane wave method for dispersive material and its application to band structure calculations of photonic crystal slabs," *Appl. Phys. Lett.*, Vol. 86, 043104, 2005.

19. Li, L., "Use of Fourier series in the analysis of discontinuous periodic structures," *J. Opt. Soc. Am. A*, Vol. 13, 1870, 1996.

20. Lalanne, P., "Effective properties and band structure of lamellar subwavelength crystals: Plane-wave method revisited," *Phys. Rev. B*, Vol. 58, 9801, 1998.

21. Kitell, C., *Introduction to Solid States Physics*, 7th Edition, Wiley, New York, 1966.

The Dispersion Properties of Three-dimensional Magnetized Plasma Photonic Crystals as the Mixed Polarized Waves Considered

Hai-Feng Zhang[1, 2], Yi-Bing Lin[2], Yu-Qing Chen[2], and Guo-Wen Ding[1]

[1]College of Electronic and Information Engineering
Nanjing University of Aeronautics and Astronautics, Nanjing 210016, China
[2]Nanjing Artillery Academy, Nanjing 211132, China

Abstract— In this paper, the dispersion properties of three-dimensional (3D) magnetized plasma photonic crystals (MPPCs) with face-centered-cubic (fcc) lattices are theoretically investigated based on the modified plane wave expansion (PWE) method, in which the homogeneous magnetized plasma spheres are immersed in the homogeneous and isotropic dielectric background, as the mixed polarized waves and magneto-optical Voigt effects are considered. The more general case has been studied, and the photonic band gap (PBG) of such MPPCs is not only for the left and right circular polarized waves but also for the mixed polarized waves. The equations for calculating the PBG for all of the electromagnetic waves in such 3D MPPCs also are theoretically deduced. Theoretical computing results show that one PBG and two flatbands regions can be observed. Compared to the conventional dielectric-air photonic crystals with similar structure, the larger PBG can be obtained in such 3D MPPCs. However, the narrower PBG can be achieved compared to the PBG for the extraordinary mode, but the larger upper edge frequency of flatbands region can be obtained.

1. INTRODUCTION

In 2004, the concept of plasma photonic crystals (PPCs) is firstly proposed by Hojo and co-worker [1]. Compared to the conventional dielectric PCs, the PPCs can display the strong spatial dispersion [1] since the physical properties of plasma can be easily tuned by many parameters, such as the plasma density, the temperature of electron and the external magnetic field [2]. If the external magnetic field is introduced into the PPCs, the magnetized plasma photonic crystals (MPPCs) can be obtained. Compared to the PPCs, the more complicated EM modes can be found in the MPPCs [2]. If the external magnetic field is perpendicular to the EM wave vector, the Voigt effects can be observed in the magnetized plasma [2]. In this configuration, two basic EM modes can be found [2], which are named the extraordinary and ordinary modes, respectively. If the external magnetic field is parallel to the EM wave vector, the magneto-optical Faraday effects can be obtained. Therefore, the MPPCs become a new research field. Up to the present, a lot of reports on the MPPCs have been published. Especially, one- and two-dimensional (2D) MPPCs and PPCs have been investigated in detail [3–8]. However, there are a few reports of 3D PPCs and MPPCs until Zhang et al. [9–14] studied the dispersive properties of 3D PPCs and MPPCs. Compared to the 1D and 2D PCs, the 3D case can produce the complete PBGs and may be closer to the real applications. However, all of the reports on 3D MPPCs only focused on the dispersive properties of one kind of EM modes, which is the extraordinary mode for the Voigt effects or the right circular polarized wave for Faraday effects. In those reports, not all of the EM modes in 3D MPPCs are considered. Especially, the properties of mixed polarized modes in 3D MPPCs are not investigated. As mentioned above, the aims of this paper are to investigate the properties of PBG and surface plasmon modes in the 3D MPPCs with face-centered-cubic (fcc) lattices, which are composed of the homogeneous magnetized plasma spheres inserted in the dielectric background by the modified plane wave expansion (PWE) method, as the Voigt effects are considered.

2. THEORETICAL MODEL AND NUMERICAL METHOD

As shown in Fig. 1(a), we consider the radius of the sphere and lattice constant are R and a respectively; the relative dielectric function for magnetized plasma and dielectric background are ε_p and ε_a, respectively. We assume the incidence EM wave vector $\mathbf{k}$ is perpendicular to the external magnetic field $\mathbf{B}$ at any time (the Voigt effects of magnetized plasma are considered). As shown in Fig. 1(b). The high symmetry points for the fcc lattices have the coordinate as $X = (2\pi/a, 0, 0)$, $U = (2\pi/a, 0.5\pi/a, 0.5\pi/a)$, $L = (\pi/a, \pi/a, \pi/a)$, $\Gamma = (0, 0, 0)$, $W = (2\pi/a, \pi/a, 0)$ and $K = (1.5\pi/a, 1.5\pi/a, 0)$. It is well known that the expression of the relative dielectric function ε_p is
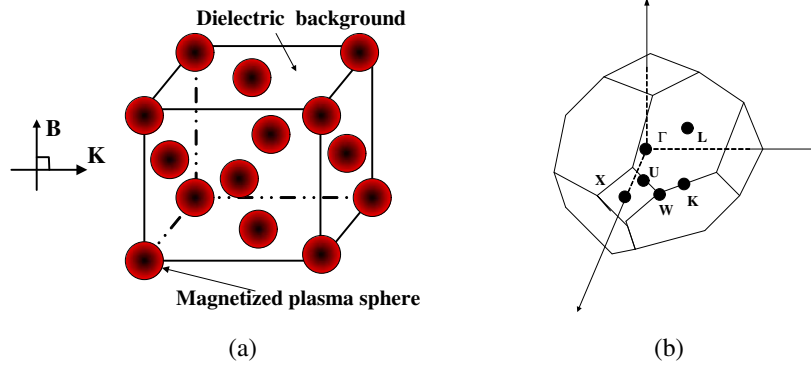
Figure 1: Schematic structure of 3D MPPCs with fcc lattices. (a) 3D MPPCs structure, and (b) the first irreducible Brillouin zone showing symmetry point used for computing the PBG.

determined by the angle between the wave vector and the external magnetic field [2]. Thus, the effective dielectric function ε_p can be written as [2]:

$$\boldsymbol{\varepsilon_p}(\omega) = \begin{pmatrix} 1 - \frac{\omega_p^2(\omega+j\nu_c)}{\omega[(\omega+j\nu_c)^2-\omega_c^2]} & 0 & \frac{-j\omega_p^2\omega_c}{\omega[(\omega+j\nu_c)^2-\omega_c^2]} \\ 0 & 1 - \frac{\omega_p^2}{\omega(\omega+j\nu_c)} & 0 \\ \frac{j\omega_p^2\omega_c}{\omega[(\omega+j\nu_c)^2-\omega_c^2]} & 0 & 1 - \frac{\omega_p^2(\omega+j\nu_c)}{\omega[(\omega+j\nu_c)^2-\omega_c^2]} \end{pmatrix} \quad (1)$$

In this expression, ω_p, ν_c, ω_c and ω are the plasma frequency, the electron collision frequency, plasma cyclotron frequency and the angular frequency, respectively. According to the PWE method, the dispersion properties of such MPPCs can be obtained by computing the flowing following equation,

$$\zeta^8 \overleftrightarrow{\mathbf{I}} - \zeta^7 \overleftrightarrow{\mathbf{X}}_7 - \zeta^6 \overleftrightarrow{\mathbf{X}}_6 - \zeta^5 \overleftrightarrow{\mathbf{X}}_5 - \zeta^4 \overleftrightarrow{\mathbf{X}}_4 - \zeta^3 \overleftrightarrow{\mathbf{X}}_3 - \zeta^2 \overleftrightarrow{\mathbf{X}}_2 - \zeta \overleftrightarrow{\mathbf{X}}_1 - \overleftrightarrow{\mathbf{X}}_0 = 0 \quad (2)$$

where

$$\overleftrightarrow{\mathbf{X}}_7(\mathbf{G}|\mathbf{G}') = -3j\frac{\nu_c}{c}\delta_{\mathbf{G}\cdot\mathbf{G}'}, \quad \overleftrightarrow{\mathbf{X}}_6(\mathbf{G}|\mathbf{G}') = \frac{(2\nu_c^2+\omega_p^2+A)}{c^2}\delta_{\mathbf{G}\cdot\mathbf{G}'} + \overleftrightarrow{\mathbf{M}_1} + \overleftrightarrow{\mathbf{M}_2} + \overleftrightarrow{\mathbf{M}_3} + \overleftrightarrow{\mathbf{M}_4},$$

$$\overleftrightarrow{\mathbf{X}}_5(\mathbf{G}|\mathbf{G}') = \frac{j\left(4\nu_c\omega_p^2+A\cdot\nu_c\right)}{c^3}\delta_{\mathbf{G}\cdot\mathbf{G}'} + 3j\frac{\nu_c}{c}\cdot\left(\overleftrightarrow{\mathbf{M}_1} + \overleftrightarrow{\mathbf{M}_2} + \overleftrightarrow{\mathbf{M}_3}\right),$$

$$\overleftrightarrow{\mathbf{X}}_4(\mathbf{G}|\mathbf{G}') = \frac{-\left(2\nu_c^2\omega_p^2+\omega_p^4+A\cdot\omega_p^2\right)}{c^4}\delta_{\mathbf{G}\cdot\mathbf{G}'} - \frac{\left(2\nu_c^2+\omega_p^2+A\right)}{c^2}\cdot\overleftrightarrow{\mathbf{M}_1} - \frac{\left(2\nu_c^2+\omega_p^2+B\right)}{c^2}\overleftrightarrow{\mathbf{M}_2}$$
$$- \frac{\left(2\nu_c^2+A\right)}{c^2}\overleftrightarrow{\mathbf{M}_3},$$

$$\overleftrightarrow{\mathbf{X}}_3(\mathbf{G}|\mathbf{G}') = \frac{-3j\nu_c^2\omega_p^4}{c^5}\delta_{\mathbf{G}\cdot\mathbf{G}'} - j\frac{\left(4\nu_c\omega_p^2+A\cdot\nu_c\right)}{c^3}\cdot\overleftrightarrow{\mathbf{M}_1} - j\frac{\left(3\nu_c\omega_p^2+B\cdot\nu_c\right)}{c^3}\overleftrightarrow{\mathbf{M}_2}$$
$$- j\frac{\left(2\nu_c\omega_p^2+A\cdot\nu_c\right)}{c^3}\overleftrightarrow{\mathbf{M}_3} + j\frac{\omega_c\omega_p^2}{c^3}\overleftrightarrow{\mathbf{M}_4},$$

$$\overleftrightarrow{\mathbf{X}}_2(\mathbf{G}|\mathbf{G}') = \frac{\omega_p^6}{c^6}\delta_{\mathbf{G}\cdot\mathbf{G}'} + \frac{\left(2\nu_c^2\omega_p^2+\omega_p^4+A\cdot\omega_p^2\right)}{c^4}\cdot\overleftrightarrow{\mathbf{M}_1} + \frac{\left(\nu_c^2\omega_p^2+B\cdot\omega_p^2\right)}{c^4}\overleftrightarrow{\mathbf{M}_2}$$
$$+ j\frac{\left(2\nu_c^2\omega_p^2+\omega_p^4\right)}{c^4}\overleftrightarrow{\mathbf{M}_3} - \frac{\nu_c\omega_c\omega_p^2}{c^4}\overleftrightarrow{\mathbf{M}_4},$$

$$\overleftrightarrow{\mathbf{X}}_1(\mathbf{G}|\mathbf{G}') = j\frac{3\nu_c\omega_p^4}{c^5}\cdot\overleftrightarrow{\mathbf{M}_1} + j\frac{\nu_c\omega_p^4}{c^5}\overleftrightarrow{\mathbf{M}_2} + j\frac{\nu_c\omega_p^4}{c^5}\overleftrightarrow{\mathbf{M}_3} - j\frac{\omega_c\omega_p^4}{c^5}\overleftrightarrow{\mathbf{M}_4}, \quad \overleftrightarrow{\mathbf{X}}_0(\mathbf{G}|\mathbf{G}') = -\frac{\omega_p^6}{c^6}\overleftrightarrow{\mathbf{M}_1},$$

The parameters of Eq. (2) can be found in Ref. [15].

3. NUMERICAL RESULTS AND DISCUSSION

Without loss of generality, we use $\omega a/2\pi c$ to normalize the frequency region. We use a variable $\omega_{p0} = 2\pi c/a$ to define the plasma frequency, the plasma collision frequency and the plasma cyclotron

frequency, as $\omega_p = 0.35\omega_{p0}$, $\omega_{pl} = 0.15\omega_{p0}$, $\nu_c = 0.02\omega_{pl}$ and $\omega_c = 0.6\omega_{pl}$, respectively. Obviously, ω_{p0} and ω_{pl} are the symbols to define the constants and have not any physical meanings. We also consider $\mu_a = 1$, and $\mu_p = 1$, respectively. In our calculation, we use 729 plane waves to make the convergence accuracy is better than 1% for the lower bands [9].
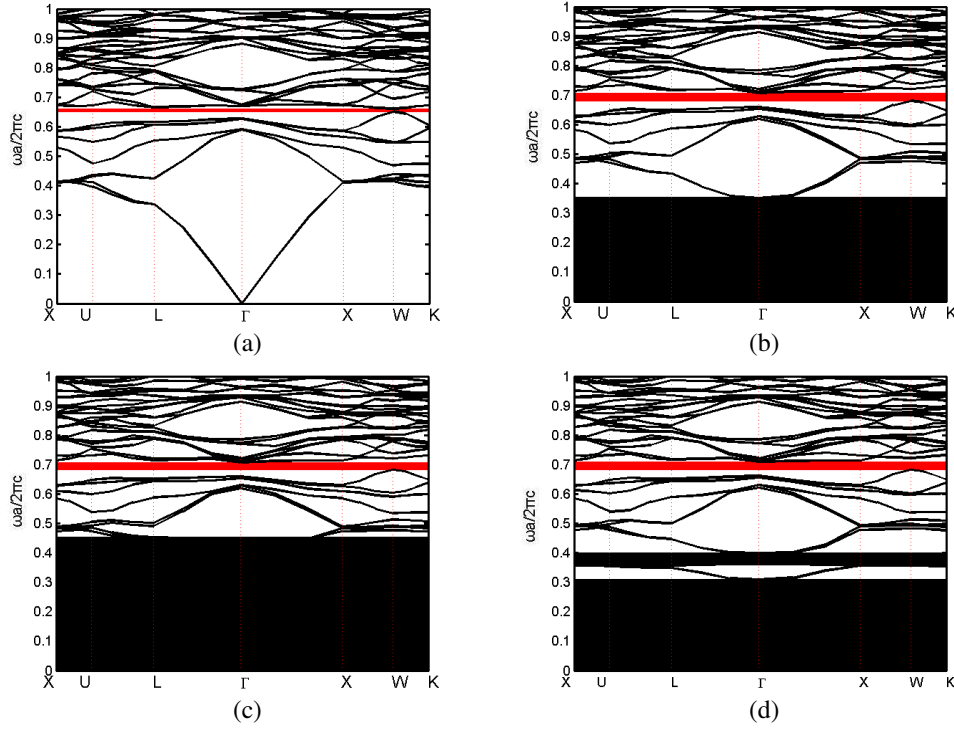

Figure 2: The band structures for such 3D MPPCs with $\varepsilon_a = 13.9$ and $f = 0.63$ but with different ω_p, ν_c and ω_c. (a) $\omega_p = \nu_c = \omega_c = 0$; (b) $\omega_p = 0.35\omega_{p0}$, $\nu_c = 0.02\omega_{pl}$ and $\omega_c = 0$; (c) $\omega_p = 0.35\omega_{p0}$, $\nu_c = 0.02\omega_{pl}$ and $\omega_c = 0.6\omega_{pl}$; (d) the band structures for the extraordinary mode in such 3D MPPCs with same parameters as Fig. 1(c). The red shaded regions indicate the PBGs.

As shown in Fig. 2(a), if $\omega_p = \omega_c = \nu_c = 0$, the magnetized plasma spheres can be looked as the air, and one complete PBG can be observed, which can be found at 0.6515–0.6611 $(2\pi c/a)$. If $\omega_p = 0.35\omega_{p0}$, $\nu_c = 0.02\omega_{pl}$, $\omega_c = 0$, the inserted spheres can be looked as the plasma, and a complete PBG and a flatbands region can be obtained. Obviously, the edges of PBG shift to higher frequency region. In this case, the PBG is located at 0.6808–0.7074 $(2\pi c/a)$. Compared to the results in Fig. 2(a), the bandwidth of PBG is enlarged obviously. The flatbands can be observed in the flatbands region, which spans from 0 to 0.35 $(2\pi c/a)$. The existence of surface plasmon modes produces the flatbands region. Fig. 2(c) demonstrates that, if the external magnetic field is introduced (Voigt effects are considered), one flatbands region can be obtained. The PBG also can be found at 0.6814–0.7067 $(2\pi c/a)$, whose edges shift to higher frequency region. The upper edge frequency of flatbands region is 0.4499 $(2\pi c/a)$. Compared to Fig. 2(a), the bandwidth of PBG is enhanced, which is 0.0253 $(2\pi c/a)$. Obviously, in Fig. 2(c), the PBG is for all of the EM modes (including the mixed polarized modes) in such 3D MPPCs. As a comparison, in Fig. 2(d), we plot the band structures for extraordinary mode in such 3D MPPCs with similar parameters as mentioned in Fig. 2(c). As shown in Fig. 2(d), one PBG and two flatbands regions can be obtained. The PBG runs from 0.6819 to 0.7082 $(2\pi c/a)$, and bandwidth is 0.0263 $(2\pi c/a)$. Two flatbands regions are located at 0–0.3072 $(2\pi c/a)$ and 0.361–0.3971 $(2\pi c/a)$, respectively. As we know, the upper edge frequencies of two flatbands regions and the lower edge of second flatbands region are nearly corresponding to the cutoff frequencies for left and the right circular polarization, and the upper hybrid frequency, respectively. Compared Fig. 2(c) to Fig. 2(d), the frequency range of PBG is narrowed, and only one flatbands region can be observed. The upper edge of flatbands region is upward to higher frequency region. It is noticed that Fig. 2(b) is the band structures for the ordinary mode in such 3D MPPCs. Compared to Fig. 2(c), the PBG for ordinary mode has a larger bandwidth. As mentioned above, the PBG for all of the EM modes in such 3D MPPCs can be achieved as the Voigt effects of magnetized plasma are considered, and the larger PBG can

be obtained compared to the conventional isotropic 3D dielectric-air PCs with similar structure. Compared to band structures for the extraordinary and ordinary modes, the PBG for all of the EM modes has a narrower bandwidth, and only one flatbands region can be found. Here, we only focus on the first PBG in the frequency domain 0–$2\pi c/a$.

4. CONCLUSIONS

In summary, the properties of PBG and surface plasmon modes in the 3D MPPCs with fcc lattices are theoretically investigated based on the modified PWE method, in which the homogeneous magnetized plasma spheres are immersed in the homogeneous dielectric background, as the Voigt effects of magnetized plasma are considered (the incidence electromagnetic wave vector is perpendicular to the external magnetic field at any time). The equations for calculating the PBG for all of the EM modes in such 3D MPPCs are theoretically deduced. Based on the calculated results, some conclusions can be drawn. Compared to the conventional dielectric-air PCs, the larger PBG and one flatbands region can be obtained as the magnetized plasma is introduced. It is worth to be noticed that such PBG is not only for the extraordinary and ordinary modes but also can prohibit the mixed polarized modes. The flatbands are caused by the existence of surface plasmon modes which stem from the coupling effects between the magnetized plasma spheres.

ACKNOWLEDGMENT

REFERENCES

1. Hojo, H. and A. Mase, "Dispersion relation of electromagnetic waves in one dimensional plasma photonic crystals," *Plasma Fusion Res.*, Vol. 80, No. 2, 89–90, 2004.
2. Ginzburg, V. L., *The Propagation of Electromagnetic Wave in Plasma*, Pergamon, Oxford, UK, 1970.
3. Zhang, H. F., M. Li, and S. B. Liu, "Defect mode properties of magnetized plasma photonic crystals," *Acta Phys. Sin.*, Vol. 58, No. 2, 1071–1076, 2009.
4. Qi, L., Z. Yang, and T. Fu, "Defect modes in one-dimensional magnetized plasma photonic crystals with a dielectric defect layer," *Phys. Plasma*, Vol. 19, No. 1, 012509, 2012.
5. Hamidi, S. M., "Optcal and magneto-optical properties of one-dimensional magnetized coupled resoner plasma photonic crystals," *Phys. Plasma*, Vol. 19, No. 1, 012503, 2012.
6. Qi, L., "Photonic band structures of two-dimensional magnetized plasma photonic crystals," *J. Appl. Phys.*, Vol. 111, No. 7, 073301, 2012.
7. Zhang, H. F., S. B. Liu, X. K. Kong, B. R. Bian, and Y. N. Guo, "Dispersion properties of two-dimensioanl plasma photonic crystals with periodically external magnetic field," *Solid State Commun.*, Vol. 152, No. 7, 1221–1229, 2012.
8. Qi, L. and X. Zhang, "Band gap characteristics of plasma with periodically varying external magnetic field," *Solid State Commun.*, Vol. 151, 1838–1841, 2011.
9. Zhang, H. F., S. B. Liu, X. K. Kong, C. Chen, and B. R. Bian, "The characteristics of photonic band gaps for three-dimensional unmagnetized dielectric plasma photonic crystals with simple-cubic lattice," *Optic Commun.*, Vol. 288, 82–90, 2013.
10. Zhang, H. F., S. B. Liu, and X. K. Kong, "Photonic band gaps in one-dimensional magnetized plasma photonic crystals with arbitrary magnetic declination," *Phys. Plasma*, Vol. 19, No. 12, 122103, 2012.
11. Zhang, H. F., S. B. Liu, H. Yang, and X. K. Kong, "Analysis of band gap in dispersive properties of tunable three-dimensional photonic crystals doped by magnetized plasma," *Phys. Plasma*, Vol. 20, No. 3, 032118, 2013.
12. Zhang, H. F., S. B. Liu, and X. K. Kong, "Dispersion properties of three-dimensional plasma photonic crystals in Diamond lattice arrangement," *J. Lightwave Technol.*, Vol. 17, No. 11, 1694–1702, 2013.
13. Zhang, H. F., S. B. Liu, X. K. Kong, C. Chen, and B. R. Bian, "The properties of photonic band gaps for three-dimensional plasma photonic crystals in a diamond structure," *Phys. Plasma*, Vol. 20, No. 4, 042110, 2013.
14. Zhang, H. F., S. B. Liu, and B. X. Li, "The properties of photonic band gaps for three-dimensional tunable photonic crystals with simple-cubic lattices doped by magnetized plasma," *Optics & Laser Technol.*, Vol. 50, 93–102, 2013.

15. Zhang, H. F., S. B. Liu, and Y. C. Jiang, "The properties of photonic band gap and surface plasmon modes in the three-dimensional magnetized photonic crystals as the mixed polarized modes considered," *J. Plasma Physics*, doi:10.1017/S0022377814001238, 2014.

Zn Concentration, Shape and Size Effects on the Band Structure of Photonic Crystals Based on Ferrofluids with $(\mathbf{Co_{1-x}Zn_xFe_2O_4})$ Nanoparticles

Luz E. González and N. Porras-Montenegro

Departamento de Física, Universidad del Valle, A.A. 25360, Cali, Colombia

Abstract— In this work using the transfer matrix technique we study the Zn concentration, nanoparticles size and shape effects on the band structure of a 1D photonic crystal (PC), made of alternating layers of air and a ferrofluid containing $(Co_{1-x}Zn_xFe_2O_4)$ nanoparticles, coated by oleic acid suspended in ethanol. We found that the photonic band structure (PBS) is shifted to higher frequencies with the increasing of the Zn concentration, size of the nanoparticles and with ferrofluids containing ellipsoidal instead of spherical nanoparticles. However, the difference in the shifting of the PBS due to oblate or prolate ellipsoidal nanoparticles, is negligible. The effects of the Zn concentration, the width of the ferrofluid and air layers, as well as their dielectric constant on the PBS, allow us to propose photonic quantum wells (QWs) by means of which we can have very well defined frequency regions to transmit or reflect electromagnetic waves to be used in technologycal applications. We also extend our analysis considering disipative effects in the ferrofluid layers, and we found a considerable reduction of the transmission power as the number N of layer period is increased.

1. INTRODUCTION

After works by Yablonovitch [1] and John [2] in which the photonic crystals were proposed, many experimental and theoretical works have been devoted to the understanding of the physical properties of these crystals. PCs are periodic structures characterized by the periodic variation of refractive index and the consequently periodic spacial variation of the dielectric constant, thus allowing the appearance of define frequency ranges and address for which the propagation of the electromagnetic waves is prohibited or permitted [3]. As a consequence, the tunability of PCs opens a new perspective in the scientific research and in technological applications. To obtain a tunable PC, the dielectric constant or the magnetic permeability of one of the constituents materials must depend on some external parameters, such as electric or applied magnetic fields [4, 5], temperature and hydrostatic pressure [6], applying mechanical force, stress, etc., which can modify the structure of this systems and consequently the optical response function of the PC.

In this work using the transfer matrix technique we study the photonic band structure of the 1D PCs made of alternating layers of air (layer 1) and ferrofluid (layer 2), which consists of cobalt-zinc ferrite nanoparticles $(Co_{1-x}Zn_xFe_2O_4)$ coated by oleic acid suspended in the host liquid (ethanol), as a function of the Zn concentration, size and shape of the nanoparticles in the ferrofluid, which can be ellipsoids or spheres; we also study the optical response of photonic quantum wells [7] constructed using this type of ferrofluids.

2. THEORETICAL FRAMEWORK

In Figure 1(a) we display a scheme of a 1D photonic superlattice studied in this work.

The effective dielectric constant ε_{eff} of the whole suspension was obtain by the Maxwell-Garnett approximation (MGA) wich describes a three-component composite where many particles are randomly embedded in a host medium. To characterize the electromagnetic properties of the composite media, it is important to know the electromagnetic parameters of both the host material and the inclusions (nanoparticles). For a mixture of a base material with permittivity ε_e (ethanol), spherical nanoparticles with permittivity ε_f (cobalt-zinc ferrite), and coated with oleic acid of permittivity ε_a, the effective permittivity is [8]

$$\frac{\varepsilon_2 - \varepsilon_e}{\varepsilon_2 - 2\varepsilon_e} = (f_1 + f_2)\frac{f_1\left(\varepsilon_a - \varepsilon_e\right) + f_2 t_{12}\left(\varepsilon_f - \varepsilon_e\right)}{f_1\left(\varepsilon_a + 2\varepsilon_e\right) + f_2 t_{12}\left(\varepsilon_f - 2\varepsilon_e\right)}, \tag{1}$$

where $t_{12} = \frac{3\varepsilon_a}{\varepsilon_f + 2\varepsilon_a}$, f_1 and f_2 are the volume fractions of the coating and the core materials, respectively.
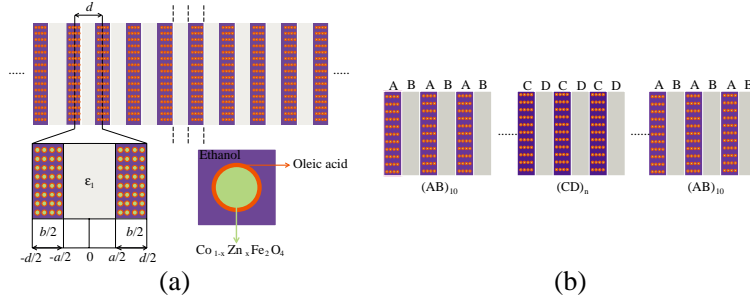
Figure 1: (Color online). (a) Pictoral view of the 1D photonic crystal, composed of alternating layers of air (layer 1) and ferrofluid (layer 2). In the ferrofluid layers, ferromagnetic spherical nanoparticles are embedded in a carrier fluid. For the model calculations, we take layer 1 to be air, the carrier fluid, ethanol, and the suspended nanoparticles, cobalt-zinc ferrites (core) coated by oleic acid (shell). (b) Esquematic view of a 1D photonic quantum well, $(AB)_{10}/(CD)_n/(AB)_{10}$, made of two different 1D photonic crystals with differents Zn concentrations. The subindex 10 and n correspond to the number of repeated periods in the barriers and wells respectively.

For the three-phase mixtures we follow the MGA for two confocal inclusion phases (ε_f and ε_a) contained in a background representing the third phase (ε_e). The effective permittivity of an isotropic three-phases confocal system of ellipsoids was derived by Sihvola and Lindell [9] for any number of confocal ellipsoids, in the isotropic case as

$$\varepsilon_{\text{eff}} = \varepsilon_e + \frac{\frac{\varepsilon_e}{3}\Sigma_{i=a,b,c}\left(\frac{n_\nu\alpha^i}{\varepsilon_e}\right)}{1 - \frac{1}{3}\Sigma_{i=a,b,c}N_1^i\left(\frac{n_\nu\alpha^i}{\varepsilon_e}\right)}, \tag{2}$$

where

$$\frac{n_\nu\alpha^i}{\varepsilon_e} = (f_1 + f_2)\left[(\varepsilon_a - \varepsilon_e) + \left[\varepsilon_a + N_1^i(\varepsilon_e - \varepsilon_a)\right]\frac{(\varepsilon_f - \varepsilon_a)\frac{f_2}{f_1+f_2}}{\left[\varepsilon_a + N_2^i(\varepsilon_f - \varepsilon_a)\right]}\right]$$

$$\cdot\left[\left[\varepsilon_e + N_1^i(\varepsilon_a - \varepsilon_e)\right] + N_1^i(1 - N_1^i)(\varepsilon_a - \varepsilon_e)\cdot\frac{(\varepsilon_f - \varepsilon_a)\frac{f_2}{f_1+f_2}}{\left[\varepsilon_a + N_2^i(\varepsilon_f - \varepsilon_a)\right]}\right]^{-1}, \tag{3}$$

a, b, and c are the three orthogonal axial directions of the ellipsoid, and N_i are the corresponding depolarization factors of the ellipsoid. For simplicity, we consider ellipsoids generated by the rotation of an ellipse around its major of minor axes, which produces prolate or oblate spheroids, correspondingly. These relations are ploted in the inset in Figure 2 as a function of the aspect ratio $m = \frac{a}{b}$. Similarly, the formulas used to calculate the effective permittivity ε are employed to calculate the effective permeability, owing to the separability of the electrostatic and magnetostatic problems which can be derived from Maxwell's equations [10].

3. RESULTS

In our calculations we have taken the ethanol dielectric constant and its refractive index to be 25.3 and 1.36, and the oleic acid dielectric constant and its refractive index equal to 2.34, and 1.44 respectively. For the dielectric constant of the cobalt-zinc ferrites nanoparticles as a function of the Zn concentration we have used the data given in reference [11], and for the magnetic permeability the date in reference [12].

Firstly, Figure 2(a) is devoted to show the PBS dependence with the radius of the nanoparticles, calculated by using Eq. (1). Note that for larger values of the radius, the PBS is shifted to higher frequencies except for the lower energy band, which means that the ferrofluid acquires higher values of the dielectric constant.

The shape effects of the nanoparticles on the PBS is presented in Figure 2(b), where we compare the results obtained for ferrofluids containing spherical, and ellipsoidal nanoparticles. According with Eq. (2), the dielectric constant of ferrofluids based on ellipsoids depends on the depolarization factor, which in turn depends on the aspect ratio $m = \frac{a}{b}$. It is noticeable that the PBS is shifted to higher energies in PC with ferrrofluids containing ellipsoidal than spherical nanoparticles. On the
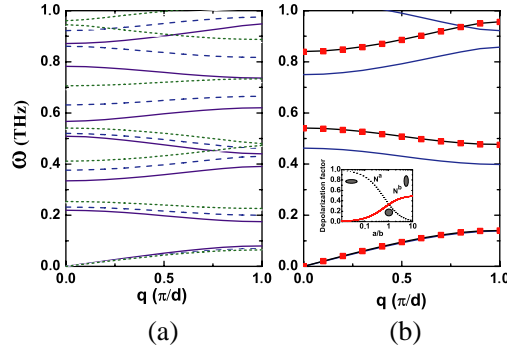
Figure 2: (Color online). (a) PBS of the PC varing the nanoparticles radius. The purple line (solid) is for $a_2 = 1.5\,\text{nm}$ with $f_2 = 0.2$, the blue line (dash) is for $a_2 = 3\,\text{nm}$ with $f_2 = 0.3$, and the green line (dot) is for $a_2 = 7.5\,\text{nm}$ with $f_2 = 0.4$. (b) PBS of the PC varing the nanoparticles shape. The blue line (solid) is for ferrofluids with spherical nanoparticles, the black line (solid) and red squares which superimpose themselves, are for ferrofluids with oblate and prolate ellipsoidal nanoparticles, respectively. The inset shows the depolarization factors N^a and N^b, of spheroidal nanoparticles as a function of the axial ratio of the spheroids, $m = \frac{a}{b}$.
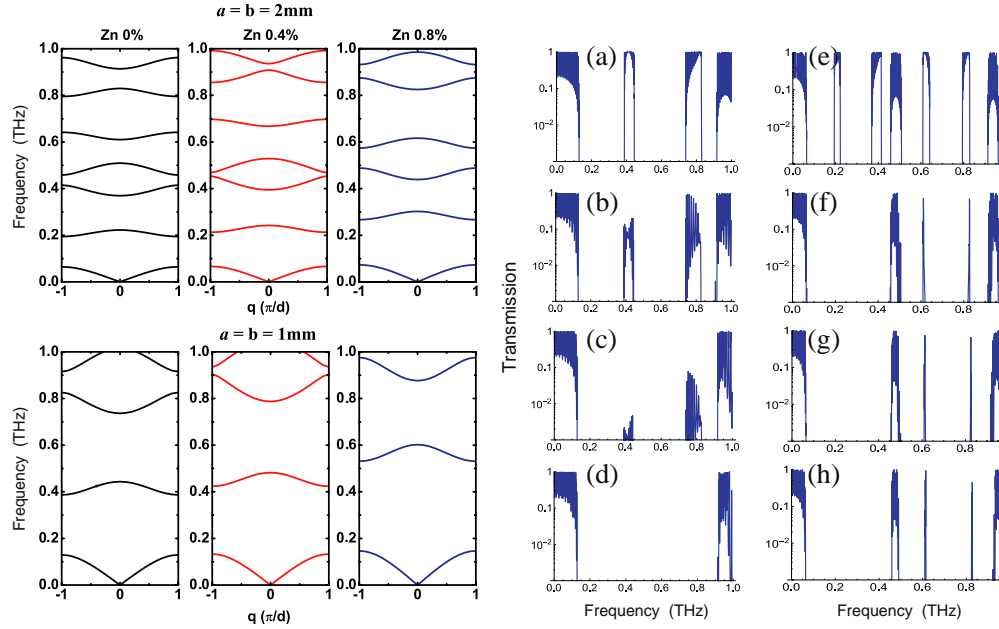

Figure 3: (Color online). Photonic band structure with alternating layers of air and ferrofluid, with different Zn concentration. The above panels are for $a = b = 2\,\text{mm}$ and down panels are for $a = b = 1\,\text{mm}$. In panels (a)–(d), transmission in a photonic QW structures, $(AB)_{10}/(CD)_n/(AB)_{10}$, as a function of frequency with (a) $n = 0$, (b) $n = 1$, (c) $n = 2$, and (d) $n = 5$. $(CD)_n$ is the superlayer made of alternating layers of air and ferrofluid with $x = 0.8$ and $(AB)_m$ with $x = 0$, with $a = b = 1\,\text{mm}$, and In panels (e)–(h), transmission in a photonic QW structures, $(AB)_{10}/(CD)_n/(AB)_{10}$, as a function of frequency with (a) $n = 0$, (b) $n = 5$, (c) $n = 7$, and (d) $n = 10$. In this case $(CD)_n$ and $(AB)_m$ are constructed with $a = b = 2\,\text{mm}$.

other hand, no changes are observed between the PBS of PC with ferrofluids containing prolate or oblate ellipsoidal nanoparticles, due to the fact that the ferrofluid layer has the same filling factor in each case of the nanoparticles ordering.

   In Figure 3, we investigate the effects of the Zn concentration (x) on the PBS of 1D photonic crystals taking into account the variation of the dielectric constant with the Zn concentration in the nanoparticles, as it is displayed in Table 1. The dielectric constant of the ferrofluid layer decreases with the increment of the Zn concentration, shifting the PBS to higher frequencies, in agreement with the electromagnetic variational theorem [3]. Otherwise, it is observed that for a given Zn concentration the PBS is shifted to higher frequencies with the diminishing of the layer widths.

   As observed in Figure 3, the second and third band of the PBS with $x = 0$ for $a = b = 1\,\text{mm}$ are

just inside the first and second photonic band gap (PBGs) of the PBS with $x = 0.8$, respectively, while the second band of the PC with $x = 0.8$ is just inside the second band gap (BG) of the PBS with $x = 0$. Also, it is noitced that the second, third, fourth and sixth band of the PBS with $x = 0$ and $(a = b = 2\,\text{mm})$ fall within the first and second BG of the PBS with $x = 0.8$ for $a = b = 1\,\text{mm}$. We use these findings to propose photonic QW structures, which may present large forbidden PBGs with weak transmission, or at the contrary, frequency regions where the transmission is sharp but very high. This opens the prospect of applications of these PC in the design of new optical devices.

In what follows, we name $(AB)_m$ the superlayer made of m alternating layers of air and ferrofluid with $x = 0$, and $(CD)_n$ the superlayer made of n alternating layers of air and ferrofluid with $x = 0.8$, both with $a = b = 1\,\text{mm}$. The constructed structure is $(AB)_m/(CD)_n/(AB)_m$, where the CD layer can play the role of barrier or well. As mentioned above, in these structures some well bands for photonic propagation are inside the photonic gap of the barriers.

The transmission spectra of a photonic QW structure as a function of frequency is presented in Figures 3(a)–(h). As the band gaps of the $(CD)_n$ superlattice cannot sustain the propagation of electromagnetic waves with frequencies inside its PBGs, the transmission falls to zero with the increasing of the penetration depth, that is, increasing the number of layers in this region. In this case, the photon is not allowed to propagate through the barrier slab of the PC. In the absence of CD layers [Figure 3(a)] there is a large transmission through all bands of the $(AB)_m$ superlattice, whereas the transmission is reduced to zero for frequencies between 0.15 THz to 0.93 THz with the increase of the $(CD)_n$ superlattice width, as depicted in Figures 3(b)–3(d). Also, in Figure 3 it is important to note that in absence of the CD superlattice, the $(AB)_m$ one presents a complete transmission between 0.91 THz and 1.1 THz in its last band (Figure 3(a)), by increasing the number of CD layers, this transmission finding with the last transmission band of CD layers that go from 0.84 THz to 0.99 THz as shown in the PBS, the final result when increasing the CD layers is a transmission band between 0.91 THz and 0.99 THz of Figure 3(d) where the bands overlap in frequency rang.

In addition, when the thickness of the layers is varied, namely, taking $(AB)_m$ and $(CD)_n$ as the superlattices made of alternating layer of air and ferrofluid whit $x = 0$ and $x = 0.8$ respectively, both with $a = b = 2\,\text{mm}$, it is found the same behavior, that is, zero transmission coefficient for frequencies in the gap region. In Figures 3(g) and 3(h), two maximum-transmission sharp peaks close to 0.61 THz and 0.83 THz are observed, which can be used as high-quality filters.

Finally, In Figure 4, we present results considering disipative effects in the ferrofluid layers by adding a complex term in the dielectric constant, finding a considerable reduction of the transmission power as the number N of layer period is increased. We obtain these results by taking the
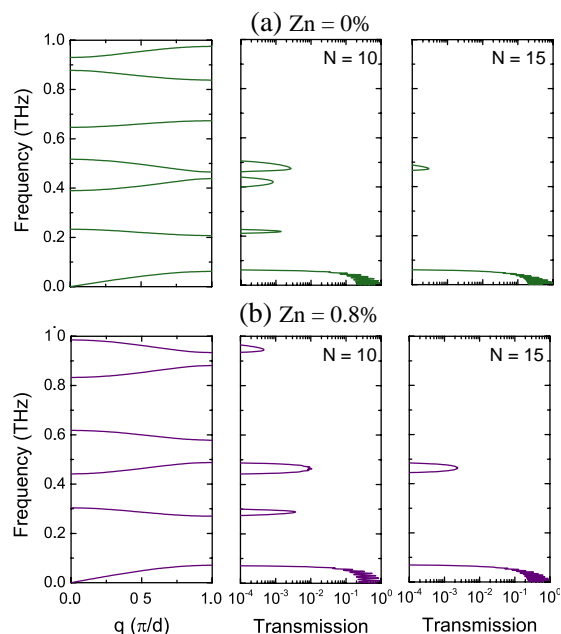

Figure 4: (Color online). PBS and transmittance in 1D PC with $a = b = 2\,\text{mm}$, calculated including the complex term in the ferrite dielectric constant. Panels (a) are for $x = 0$, and (b) are for $x = 0.8$, respectively.

complex dielectric constants of $CoFe_2O_4$ and $Co_{0.2}Zn_{0.8}Fe_2O_4$ from reference [11], where the former is higher than the latter, result which is in agreement with the high dissipative energy effects in the $CoFe_2O_4$.

4. CONCLUSION

In summary, based on the transfer matrix method, we theoretically studied the PBS in 1D PCs, composed of alternating layers of air and a ferrofluid containing $(Co_{1-x}Zn_xFe_2O_4)$ nanoparticles coated by oleic acid suspended in ethanol. We have found that the PBGs are shifted to higher frequencies with the increase of the Zn concentration and the size of the nanoparticles. In addition, we found that in PCs containing ferrofluids the PBS is shifted to higher frequencies in those containing ellipsoidal instead of spherical nanoparticles, however the difference in the shifting of the PBS due to oblate or prolate ellipsoidal nanoparticles, is negligible. Also, taking into account the effects of the Zn concentration on the PBS, we proposed photonic QWs, which depending on their composition can offer large forbidden gaps, but with sharp transmission peaks, with very well defined frequency ranges which can be used in several technologycal application. We also extend our analysis considering disipative effects in the ferrofluid layers, finding a considerable reduction of the transmission power as the number N of layer period is increased. We hope experimental work on these subjects confirm our findings, which certainly can be taken into account to be used in future technological applications.

REFERENCES

1. Yablonovitch, E., "Inhibited spontaneuos emission in solid-state physics and electronics," *Phys. Rev. Lett.*, Vol. 58, 2059–2062, 1987.
2. John, S., "Strong localization of photons in certain disordered dielectric superlattices," *Phys. Rev. Lett.*, Vol. 58, 2486–2489, 1987.
3. Joannopoulos, J. D., et al., *Photonic Crystals: Molding the Flow of Light*, Princeton University Press, Princeton, 1995.
4. Lopez, J., L. E. González, M. F. Quiñonez, M. E. Gómez, N. Porras-Montenegro, and G. Zambrano, "Magnetic field role on the structure and optical response of photonic crystals based on ferrofluids containing $Co_{1-x}Zn_xFe_2O_4$ nanoparticles," *J. Appl. Phys.*, Vol. 115, 193502, 2014.
5. Lopez, J., L. E. González, M. F. Quiñonez, M. E. Gómez, N. Porras-Montenegro, and G. Zambrano, "Band structure of a 2D photonic crystals based on ferrofluids of $Co_{0.8}Zn_{0.2}Fe_2O_4$ nanoparticles under perpendicular applied magnetic fields," *J. Phys.: Conf. Ser.*, Vol. 480, 012033, 2014.
6. González, L. E. and N. Porras-Montenegro, "Pressure, temperature and plasma frequency effects on the band structure of a 1D semiconductor photonic crystal," *Physica E*, Vol. 44, 773–777, 2012.
7. Zi, J., J. Wan, and C. Zhang, "Large frequency range of negligible transmission in 1D photonic quantum well structures," *Appl. Phys. Lett.*, Vol. 73, 2084–2086, 1998.
8. Sihvola, A. H. and I. V. Lindell, "Polarizability modeling of heterogeneous media," *Progress In Electromagnetics Research*, Vol. 6, 101–151, 1992.
9. Sihvola, A. and I. V. Lindell, "Polarizability and effective permitivity of layered and continuously inhomogeneous dielectric ellipsoids," *Journal of Electromagnetic Waves and Applications*, Vol. 4, No. 1, 1–26, 1990.
10. Sihvola, A. H. and I. V. Lindell "Effective permeability of mixtures," *Progress In Electromagnetics Research*, Vol. 6, 153–180, 1992.
11. Ramana Murty, S., "Dielectric behaviour of cobalt-zinc ferrites," *J. Mater. Sci. Lett.*, Vol. 3, 1049–1051, 1984.
12. Dong, H., A. Meininger, H. Jiang, K.-S. Moon, and C. P. Wong, "Magnetic nanocomposite for potencial ultrahigh frequency microelectronic application," *J. Electron. Mater.*, Vol. 36, 593–597, 2007.

Analysis on the Aperture Averaging Weight Factor for Equidistant Dual-aperture Receiver

Changqi Yang and Simin Liu

School of Science, Xi'an Shiyou University, Xi'an 710065, China

Abstract— Free-space optical communication receiver aperture is usually a single circular aperture. When the aperture size is large, its cost will be high. This paper proposes a new receiver aperture structure: equidistant dual-aperture receiver. The authors analyze its performance. Aperture Averaging Weight Factors of the two kinds of receiver structures are compared. The analysis results show that: Equidistant dual-aperture receiver can obviously decrease the Aperture Averaging Weight Factor, and reduce the optical scintillation.

1. INTRODUCTION

The research on free-space optical(FSO) communication has been sustained for a very long time [1, 2]. In the design of a FSO system, usually it only uses a singular large aperture. When the receiver aperture diameter increases, it can receive more optical flux, and the aperture averaging effect is also more obvious [3, 4]. However, as the receiver aperture size gets larger, its cost gets higher. For the civil FSO, cost factor is of great importance. When the receiver aperture is small, the optical signal can be collected by a single lens. When the receiver aperture increases, because of the influence of aberrations produced by gravity, an aspherical reflecting mirror must be used as the primary mirror. But the aspherical reflecting mirror is very expensive. Generally speaking, when the receiver aperture diameter is larger than $15\,\mathrm{cm}$, it must use an aspherical mirror as the primary mirror. However, if we use 2 or 3 10-cm diameter lens to replace it, the cost reduces significantly. This paper concerns on such an issue: when use an equidistant dual-aperture receiver, how does the aperture averaging effect change?

2. PRINCIPLE OF APERTURE AVERAGING

At the end of the FSO receiver, the normalized log-signal variance is shown as below [3]:

$$
\begin{aligned}
\sigma_\vartheta^2 &= \frac{1}{S_{receiver}^2} \int d\boldsymbol{\rho} \int d\boldsymbol{\rho}' W\left(\frac{1}{2}\boldsymbol{\rho} + \boldsymbol{\rho}', D\right) W\left(-\frac{1}{2}\boldsymbol{\rho} + \boldsymbol{\rho}', D\right) \sigma_l^2\left(\boldsymbol{\rho}\right) \\
&= \frac{1}{S_{receiver}^2} \int_0^\infty \rho d\rho \int_0^{2\pi} d\varphi K_0\left(\rho, \varphi, D\right) \sigma_l^2\left(\rho\right) \\
&= \frac{1}{S_{receiver}^2} \int_0^\infty \rho d\rho \int_0^{2\pi} d\varphi \cdot S_{overlap} \cdot \sigma_l^2\left(\rho\right).
\end{aligned}
\tag{1}
$$

where, $W(\mathbf{r}, D)$ is a function used to depict the aperture. When $|\mathbf{r}| \leq D/2$, $W = 1$; when $|\mathbf{r}| > D/2$, $W = 0$. $\boldsymbol{\rho} = \mathbf{r} - \mathbf{r}'$, $\boldsymbol{\rho}' = (\mathbf{r} + \mathbf{r}')/2$, $\rho = |\boldsymbol{\rho}|$ (ρ means the distance between two arbitrary points at the wave-front). $K_0(\rho, \varphi, D)$ is a result that integrates over $\boldsymbol{\rho}'$. It is function including variables $\boldsymbol{\rho}$, D and φ. It is called as the K function. It means the overlap area when moves the aperture centroid to a distance $\boldsymbol{\rho}$. Fried gave its result [3]. In the case of singular aperture, because of the rotational symmetry, $K_0(\rho, \varphi, D)$ is independent of the angle φ. We define a parameter $A(\rho, D) = \int_0^{2\pi} d\varphi \cdot S_{overlap}$. Function A is called as Aperture Averaging Weight Factor. Thus

$$
\sigma_\vartheta^2 = \frac{1}{S_{receiver}^2} \int_0^\infty \rho d\rho \cdot A\left(\rho, D\right) \cdot \sigma_l^2\left(\rho\right) \approx \frac{1}{S_{receiver}^2} \sum_{i=1}^\infty \rho_i A\left(\rho_i, D\right) \sigma_l^2\left(\rho_i\right) \Delta\rho_i.
\tag{2}
$$

As a result, the log-signal variance is changed to a sigma summation. It consists of products at many points. $A(\rho_i, D)$ is seemed to be the weight factor of $\sigma_l^2(\rho_i)$.
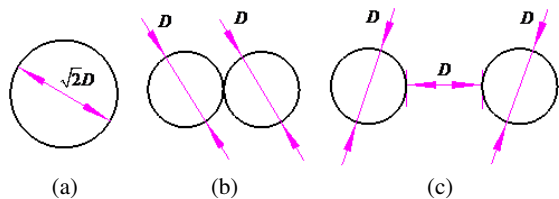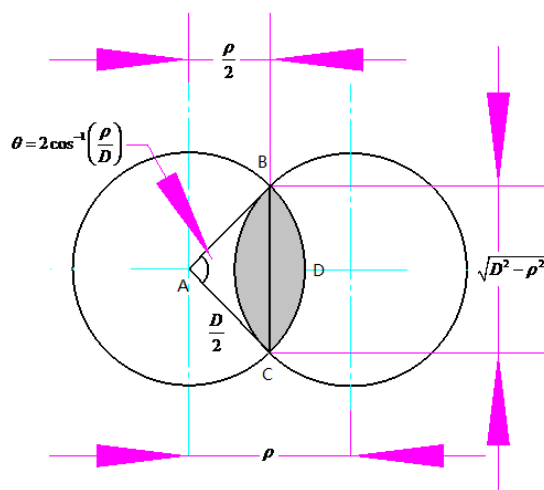
Figure 1: Three kinds of aperture configurations.

Figure 2: Diagram for calculating the K function.

Because $\sigma_l^2(\rho_i)$ cannot be controlled, if want to reduce σ_ϑ^2, $A(\rho_i, D)$ should be reduced. If want to reduce $A(\rho_i, D)$, the overlapping area of the aperture function should be reduced.

As shown in Figure 1(a), we can use a receiver aperture with diameter $\sqrt{2}D$. As shown in Figure 1(b), we also can use 2 receiver apertures with diameter D. Figure 1(a) and Figure 1(b) have the same light receiving area. Assuming that the receiver aperture D is $10\,\mathrm{cm}$, diameter $\sqrt{2}D$ is too large to use lens as the primary mirror. It can only use aspherical mirror. So the cost is too high. As a result, we can use the aperture layout in Figure 1(b). But is it the best choice? No. We find out from our research that the layout in Figure 1(c) is much better that in Figure 1(b). Let's go back to the calculation process of K function. It is actually gotten through by calculating the overlap area of two apertures when two graphics center spacing is ρ. The calculation process is given in Figure 2 and Equation (3).

$$S_{shade} = 2\left(S_{arcABDC} - S_{\Delta ABC}\right) = \frac{D^2}{2}\left\{\cos^{-1}\left(\frac{\rho}{D}\right) - \frac{\rho}{D}\left[1 - \left(\frac{\rho}{D}\right)^2\right]^{1/2}\right\}. \qquad (3)$$

3. APERTURE AVERAGING WEIGHT FACTOR

In the next part the authors will analyze the k function of that in Figure 1(c). As shown in Figure 3, when $0 < \rho < D$, the moving region of the stacking ring is limited in the green line area. No one arbitrary stacking ring will stack two stacked rings at the same time.

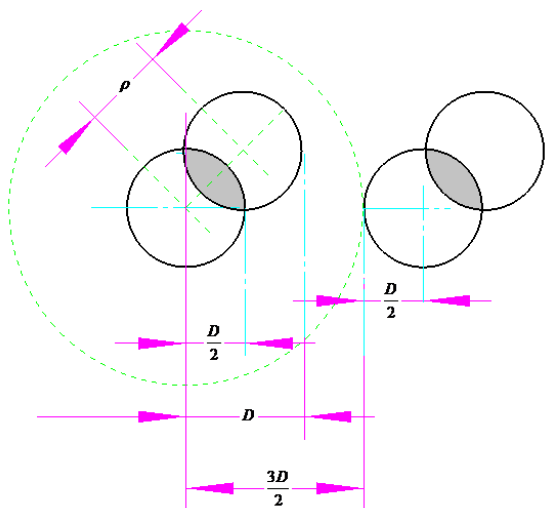As shown in Figure 4, when $\rho > 3D$, there is not any possibility of overlapping. K function is

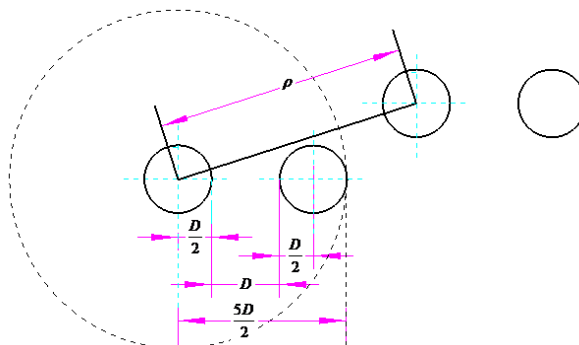Figure 3: Diagram for calculating the K function in the case of $0 < \rho < D$.

Figure 4: Diagram for calculating the K function in the case of $\rho > 3D$.

0. As shown in Figure 5, when $D < \rho < 3D$ and $\pi/6 < \varphi < 11\pi/6$, there is not any possibility of overlapping. K function is 0.
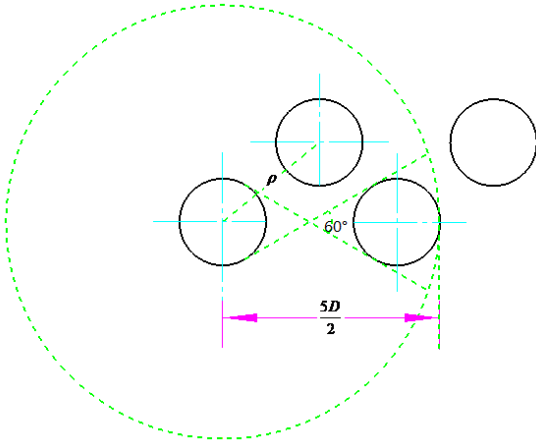

Figure 5: Diagram for calculating the K function in the case of $D < \rho < 3D$ and $\pi/6 < \varphi < 11\pi/6$.
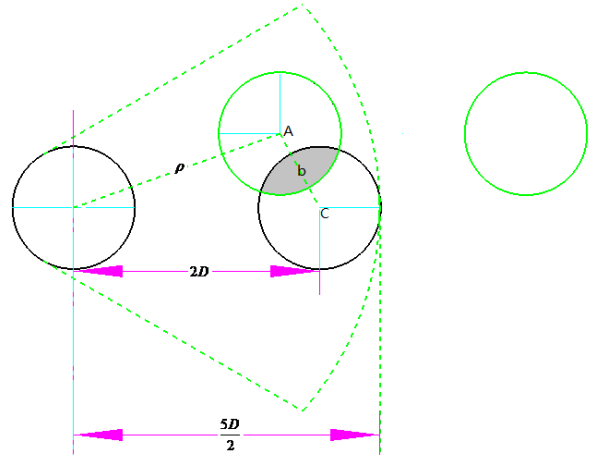
Figure 6: Diagram for calculating the K function in the case of $D < \rho < 3D$ and $-\pi/6 < \varphi < \pi/6$.

As shown in Figure 6, when $D < \rho < 3D$ and $-\pi/6 < \varphi < \pi/6$, the first stacking ring can only move in the green line range. $\overline{AC} = b$. According to a simple trigonometry and a series expansion, it changes into $b \approx |2D - \rho \cos \varphi + \frac{1}{4D}\rho^2 \sin^2 \varphi|$. To sum it up:

$$A(\rho, D) = \begin{cases} 2\pi D^2 \left\{ \cos^{-1}\left(\frac{\rho}{D}\right) - \left(\frac{\rho}{D}\right)\left[1 - \left(\frac{\rho}{D}\right)^2\right]^{1/2} \right\}, & 0 < \rho \leq D, \ \varphi \in (0, 2\pi) \\ \dfrac{D^2}{2} \displaystyle\int_{-\pi/6}^{\pi/6} d\varphi \left\{ \cos^{-1}\left(\frac{b}{D}\right) - \frac{b}{D}\left[1 - \left(\frac{b}{D}\right)^2\right]^{1/2} \right\}, & \\ \text{where, } b \approx \left|2D - \rho \cos \varphi + \dfrac{1}{4D}\rho^2 \sin^2 \varphi\right|, & D < \rho < 3D, \\ 0, \ \rho \geq 3D, \ \varphi \in (0, 2\pi) \end{cases} \tag{4}$$
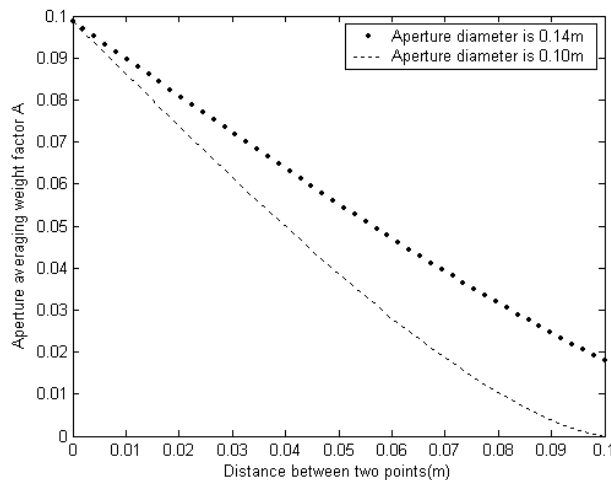

Figure 7: Aperture averaging weight factors of two different receiver structures.

4. CONCLUSIONS

In this paper, the authors propose a new kind of receiver structure for FSO. The comparison result is shown in Figure 7. Obviously the equidistant dual-aperture receiver has a significant decrease of Aperture Averaging Weight Factor. Next step work will concerns on an experiment with this kind of new aperture.

ACKNOWLEDGMENT

REFERENCES

1. Yura, H. T. and W. G. McKinley, "Optical scintillation statistics for IR ground-to-space laser communication systems," *Appl. Opt.*, Vol. 22, No. 21, 3353–3358, 1983.
2. Yang, C., W. Jiang, and C. Rao, "Bit-error rate for free-space optical communication with tip-tilt compensation," *Waves in Random and Complex Media*, Vol. 16, No. 3, 281–292, 2006.
3. Fried, D. L., "Aperture Averaging of scintillation," *J. Opt. Soc. Am.*, Vol. 57, No. 2, 169–175, 1967.
4. Yang, C., W. Jiang, and C. Rao, "Impact of aperture averaging on bit-error rate for free-space optical communication," *Acta Optica Sinica*, Vol. 27, No. 2, 212–218, 2007.

Trend Technology's Theory Model and Experiment Verification for Atmospheric Optical Scintillation

Changqi Yang

School of Science, Xi'an Shiyou University, Xi'an 710065, China

Abstract— Trend technology's theoretical model for atmospheric optical scintillation is establishes in this paper. For many years, people have always thought that atmospheric optics is completely random. In the previous paper, the author has used several experiments to overturn the traditional view. In this paper, the author will put forward a model to explain the author's point of view theoretically. It will demonstrate the process how does the optical scintillation evolve according to the trend. In this paper, the author will give the second batch of the experimental data to verify the theory model.

1. INTRODUCTION

When laser is transmitted through atmospheric turbulence, because of the influence of temperature, pressure, wind speed and other factors, the optical wavefront distorts. The light intensity varies. It is called as scintillation. For many years, scientific communities have made efforts in this field [1, 2]. Almost all of the experiments concern only with changes between one or two data points. The changes reflect a completely random shape.

In the field of atmospheric optics, adaptive optics (AO) system is usually used to correct wavefront [3]. For example, in an optical imaging system, firstly a beam is transmitted along the path. Then the wavefront distortion resulting from atmospheric turbulence is measured. A conjugation shape of wavefront distortion is produced on the deformable mirror to compensate the wavefront. Finally a clear picture can be seen at the image terminal. Because the traditional view treats the atmospheric turbulence is totally random, AO system is designed to passively follow the wavefront variation. When optical scintillation is strong, AO system usually fails to keep pace with the change of the turbulence. At this time, AO system is paralysed.

However, in a preceding study, the author discovered that optical scintillation is not completely random [4]. The author has used experimental data from three different links to prove it. This actually provides us with a new method for AO wavefront correction. In other words, it means to predict scintillation according to the previous turbulent trend.

In the second part of this paper, the author will establish a model to demonstrate how does scintillation evolve with the trend. In the third part, the author will continue to disclose the second batch of experimental data to support this model.

2. MODEL OF OPTICAL SCINTILLATION EVOLVES WITH TREND

Suppose that there is a laser beam fleets across a four-quadrant detector along the positive X axis. As shown in Figure 1, they are 4 consecutive frames of sampled data. The intensities in the 1st and 4th quadrants are more and more strong, and intensities in the 2 and the 3 quadrants are more and more weak. Use the time (frame number) as the horizontal axis. Use the total intensity in every quadrant as the vertical axis. Plot the pictures for every quadrants. We can observe signal patterns as shown in Figure 2.

If we lessen the observation time scale, considering the randomness of turbulence, actually we will observe the similar signal behaviors as shown in Figure 3. The signals move along large-scale trends. At the same time, it displays small-scale fluctuations.

Thus, we can observe the four quadrants of data as a whole. Estimate the signals' running trend. According to the running trend of signals, we can predict in the next few frames how does the signals will run.

3. THE SECOND BATCH OF EXPERIMENTAL DATA

In [4], the author introduced 3 kinds of different optical propagation experimental links. In the three links, image is sampled by a high speed camera. One frame of received optical pattern is shown in Figure 4. The receiving aperture is made up of a number of sub-aperture. Colorful values at its right side are used to evaluate the strength of the optical intensities.
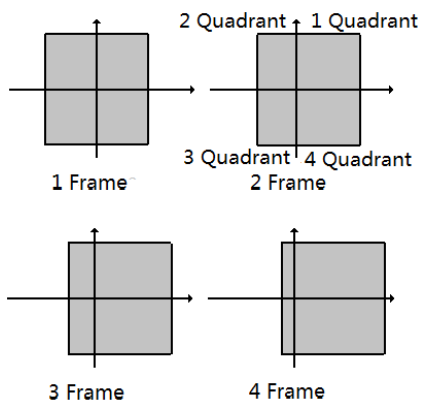
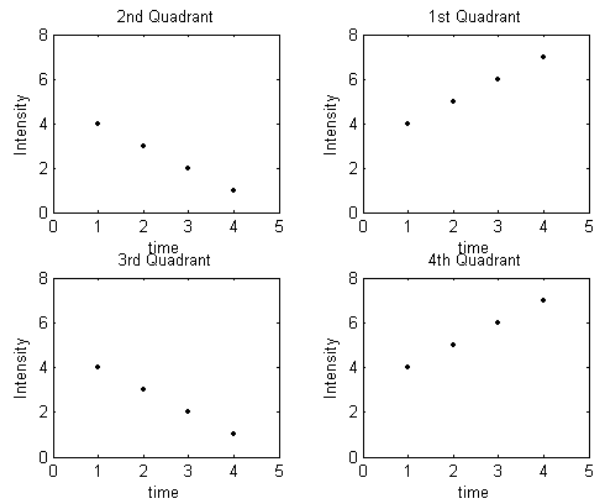Figure 1: Four frames of data.

Figure 2: Total intensities of every quadrant.
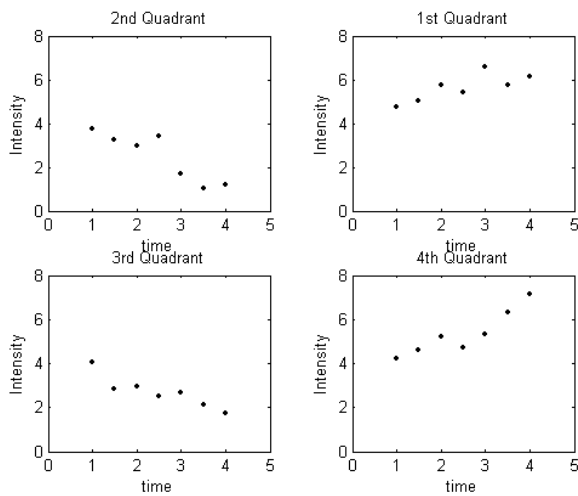

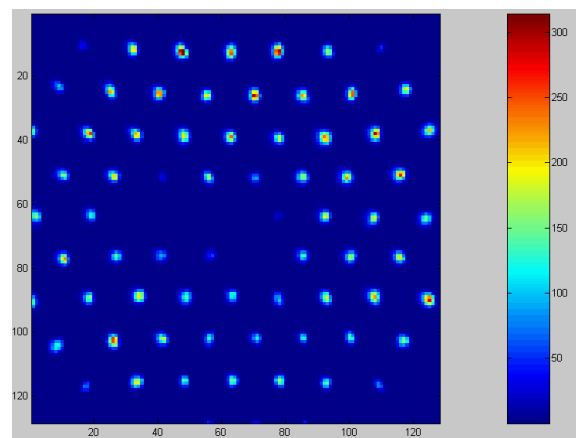Figure 3: Signal behaviors when considering small-period random fluctuations.

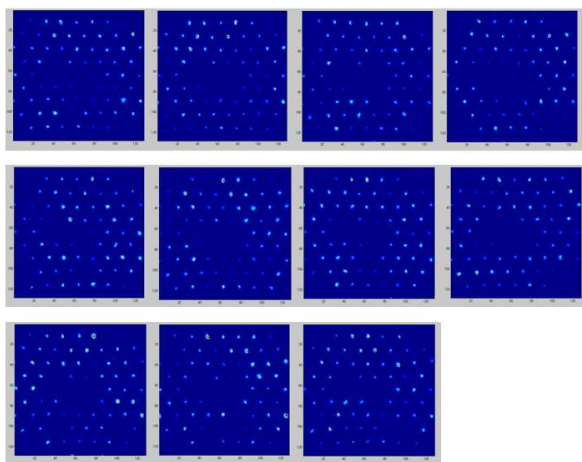Figure 4: Speckle pattern of sub-apertures.

Figure 5: 11 frames of continuous images in an active laser illumination experiment.
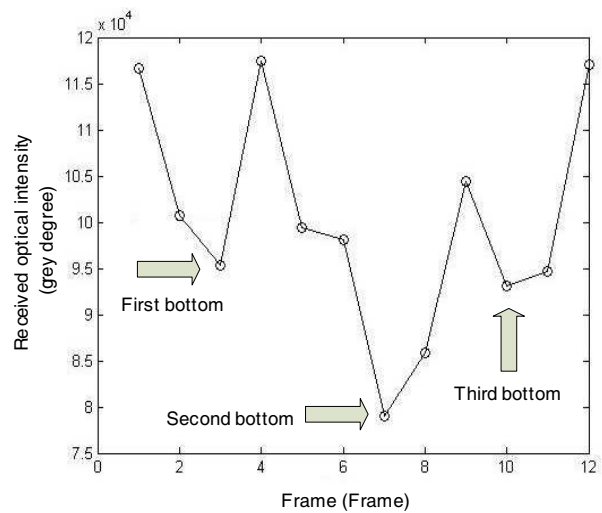

Figure 6: Processed data of Figure 5.

3.1. Active Laser Illumination Experiment

One of the active laser illumination experimental data is shown in Figure 5. The experimental conditions are introduced in [4]. Figure 5 includes 11 frames of images.

Figure 5 displays an obvious triple-bottom trend.

3.2. Downlink

In Figure 7, it is a group of data for stellar observation. The signal is limited in an uptrend and a horizontal fluctuation.
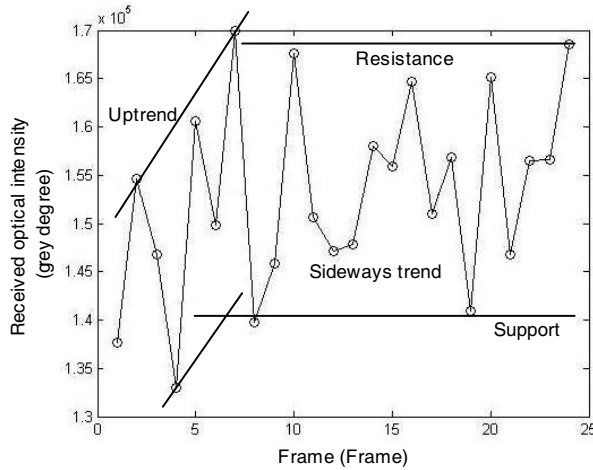
Figure 7: A group of data of a downlink.
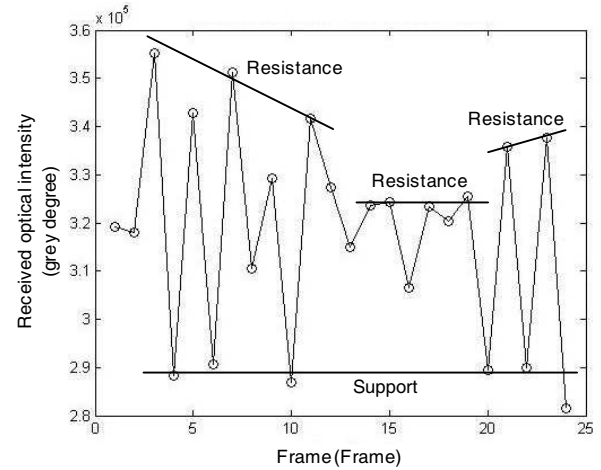
Figure 8: The other group of data of the downlink.

In Figure 8, it is the other group of data in the downlink. The signals move in horizontal fluctuations.

4. CONCLUSIONS

In this paper, the author establishes a theory model to describe how does optical scintillation fluctuate. The signals move according to the order of the trend, and there are some small fluctuations twist the trend. The author also discloses the second batch of experimental data to confirm the trend theory.

ACKNOWLEDGMENT

REFERENCES

1. Ishimaru, A., *Wave Propagation and Scattering in Random Media*, IEEE Press and Oxford University Press, London, 1997.
2. Andrews, L. C. and R. L. Phillips, *Laser Beam Propagation through Random Media*, SPIE Press, Washington, 2005.
3. Murphy, D. V., "Atmospheric-turbulence compensation experiments using cooperative beacons," *The Lincoln Laboratory Journal*, Vol. 5, No. 1, 25–44, 1992.
4. Yang, C., et al., "Experimental validation that optical scintillation obeys the same rules of share price fluctuations," *PIERS Proceedings*, 750–753, Suzhou, China, September 12–16, 2011.

Electromagnetic Simulation of Coupled Silicon and Diamond Microdisks and Slab Waveguides in the Mid-infrared

Muhammad Rehan Chaudhry[1], **Zeeshan Rashid**[1], **Yiğit Uysallı**[2],
Adnan Kurt[3], **Ulaş Sabahattin Gökay**[1], and **Ali Serpengüzel**[1]

[1]Microphotonics Research Laboratory, Department of Physics
Koç University, Rumelifeneri Yolu, Sarıyer, Istanbul 34450, Turkey
[2]Department of Physics, Middle East Technical University, Ankara 06531, Turkey
[3]Teknofil Limited, Vişne 2 Mahallesi, 3. Cadde
Market Blok No. 8, Zekeriyaköy, Sarıyer, Istanbul 34450, Turkey

Abstract— Electromagnetic numerical studies of silicon and diamond microdisks coupled with silicon and diamond slab waveguides are performed in the CO_2 laser emission region in the mid-infrared. Microdisk is the 2D analog of the microsphere and the slab waveguide is the 2D analog of the rectangular optical waveguide. The evanescent coupling between the waveguide and the microdisk results in efficient pumping of the whispering gallery modes of the microdisk. On-resonant and off-resonant studies are performed by tuning the laser wavelength to the microdisk whispering gallery modes.

1. INTRODUCTION

Photonic devices such as optical fibers, integrated photonic circuits, and lasers are great innovations, and played an important part in revolutionizing the modern world, because of their immunity to electromagnetic interference (EMI), low loss transmission at longer distances, and higher bandwidths [1]. Silicon photonics [2] is the current state-of-art, and photonics devices such as silicon Raman lasers have already been demonstrated in the near-infrared [3]. The concept of whispering gallery modes (WGMs) is not new, as it was first described by Lord Rayleigh in 1910 [4]. The WGMs rely greatly on the geometry of the resonator [5]. WGMs are favored due to their high quality factors [6], on the order of 10^6 [7] and 10^7 [8]. Here, we present electromagnetic numerical simulation results of microdisks coupled with optical waveguides, the on- and off-resonance conditions for silicon and diamond microdisks in air placed on silicon and diamond slab waveguides excited with tunable mid-infrared lasers operating at wavelengths of 9.2–10.7 micrometers. We demonstrate our approach by performing a simulation of the out of plane electric field strength of evanescently coupled silicon and diamond microdisks (the 2D analog of the microspheres) with silicon and diamond slab waveguides (the 2D analog of optical waveguides) [9]. We adopted MIT electromagnetic equation propagation (MEEP) tool based on finite difference time domain (FDTD) method to perform simulations [10].

2. PROPOSED EXPERIMENTAL SETUP

The overall proposed experimental setup is shown in Figure 1. A tunable CO_2 laser with wavelength range of 9.2–10.7 μm can be used to excite the WGMs in microdisks with radius $a = 15$ μm and refractive index $n = 3.41$ for silicon, and $n = 2.38$ for diamond, respectively. The input laser is coupled to a slab waveguide. The width of the slab waveguide is $w = 3$ μm. There is a beam splitter (BS) placed in the path of transmitted light at $45°$ to reduce the intensity of light falling on the passive infrared (PIR) sensor 3. The transmission at $0°$ and scattering at $90°$ and $270°$ from the microsphere can be collected by PIR sensors, whose signals can be sent to a data acquisition (DAQ) box, which is connected to a computer through universal serial bus (USB) interface.

3. ELECTROMAGNETIC SIMULATION GEOMETRY

The FDTD electromagnetic numerical simulation geometry is shown in Figure 2. The microdisk resonator placed on the area near the evanescent field of the slab waveguide will enable light to couple from the waveguide to the microdisk resonator, at the WGMs of the microdisk resonator. In the simulations, the excitation port is at the left hand side of the slab waveguide. The incident light wave is oscillating in the z-direction (out of the plane) and the amplitude of the E_z component is calculated everywhere on the xy plane.
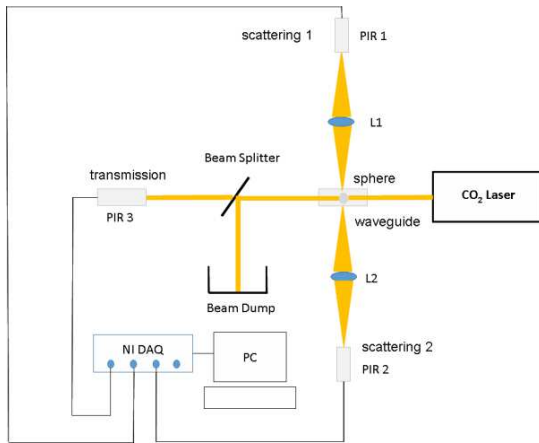
Figure 1: Proposed experimental setup for coupling of silicon microdisk to a slab waveguide.
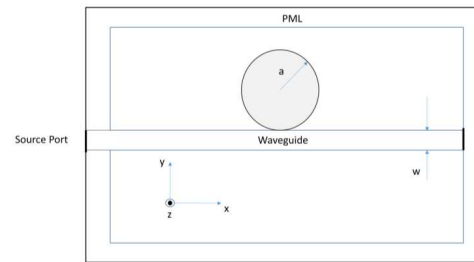
Figure 2: Geometry of the electromagnetic FDTD simulation.

4. SIMULATION RESULTS AND DISCUSSION

Figure 3(a) shows the off-resonance, and 3(b) the on-resonance condition for silicon waveguide ($m = 3.41$) and silicon microdisk ($m = 3.41$) coupling. The off-resonance wavelength is $10.325\,\mu$m, while the on-resonance wavelength is $10.5\,\mu$m. For the on-resonance case, the angular mode number is $n = 26$ and radial mode order is $l = 1$. Figure 4(a) shows the off-resonance, and 4(b) the on-resonance condition for diamond waveguide ($m = 2.38$) and silicon microdisk ($m = 3.41$) coupling. The off-resonance wavelength is $10.2\,\mu$m, while the on-resonance wavelength is $10.62\,\mu$m. For the on-resonance case the angular mode number is $n = 18$ and radial mode order is $l = 3$. Figure 5(a) shows the off-resonance, and 5(b) the on-resonance condition for diamond waveguide ($m = 2.38$) and diamond microdisk ($m = 2.38$) coupling. The off-resonance wavelength is $10.30\,\mu$m, while the on-resonance wavelength is $10.62\,\mu$m. For the on-resonance case the angular mode number is $n = 17$ and radial mode order is $l = 1$. Figure 6 shows silicon waveguide ($m = 3.41$) and diamond microdisk ($m = 2.38$) coupling. The on-resonance amplitude in Figure 6 is negligible, because of the smaller refractive index of diamond microdisk as compared to the silicon waveguide.

(a)   (b)

Figure 3: (a) The off-resonance and (b) on-resonance for a silicon microdisk on a silicon slab waveguide.

(a)   (b)

Figure 4: (a) The off-resonance and (b) on-resonance for a silicon microdisk on a diamond slab waveguide.

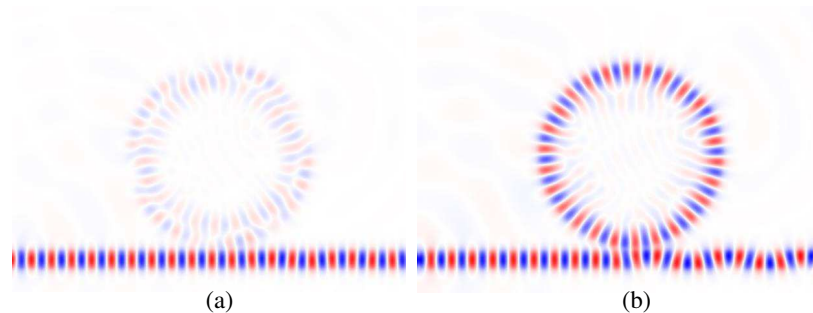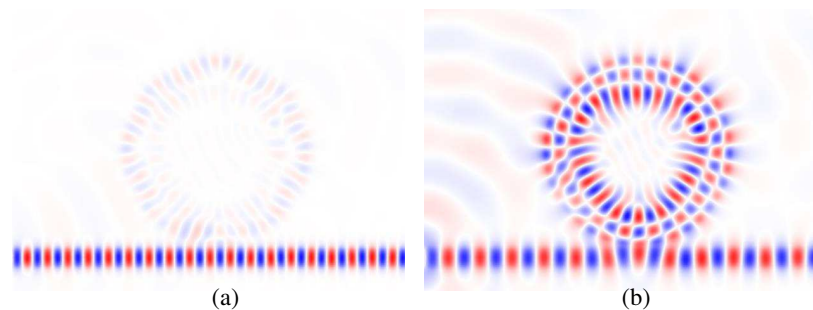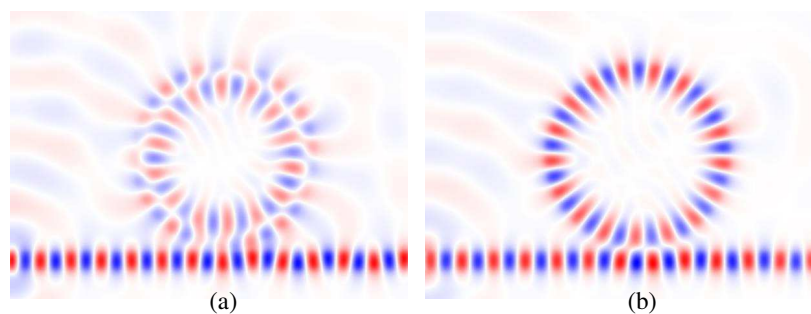Figure 5: (a) The off-resonance and (b) on-resonance for a diamond microdisk on a diamond slab waveguide.

Figure 6: The case for a diamond microdisk on a silicon slab waveguide.

5. CONCLUSIONS

We numerically simulated the amplitude of the z component of the electric field in silicon and diamond waveguides coupled to silicon and diamond microdisks in the mid-infrared wavelength range of 9.2–10.7 μm of CO_2 lasers. The microdisk is the 2D analog of the microsphere and the slab waveguide is the 2D analog of the rectangular optical waveguide. The evanescent coupling between the waveguide and the microdisk results in efficient pumping of the whispering gallery modes of the microdisk. The on-resonant and off-resonant studies are performed by tuning the CO_2 laser wavelength to the microdisk whispering gallery mode. Silicon microsphere on silicon and diamond waveguides shows very strong resonances, whereas diamond microsphere resonances on diamond and silicon waveguides are not as strong.

ACKNOWLEDGMENT

REFERENCES

1. Matsko, A. B., A. A. Savchenkov, D. Strekalov, V. S. Ilchenko, and L. Maleki, "Review of applications of whispering-gallery mode resonators in photonics and nonlinear optics," IPN Progress Report 42-162, 1–51, Aug. 2005.

2. Chen, X., C. Li, and H. K. Tsang, "Device engineering for silicon photonics," *NPG Asia Materials*, Vol. 3, No. 1, 34–40, Jan. 2011.

3. Boyraz, O. and B. Jalali, "Demonstration of a silicon Raman laser," *Optics Express*, Vol. 12, 5269–5273, Oct. 2004.

4. Rayleigh, L., "The problem of the whispering Gallery," *Philosophical Magazine*, Vol. 20, 1001–1004, 1910.

5. Féron, P., "Whispering Gallery mode lasers in Erbium doped fluoride glasses," *Annales de la Fondation Louis de Broglie*, Vol. 29, 317–329, 2004.

6. Vahala, K. J., "Optical microcavities," *Nature*, Vol. 424, No. 6950, 839–846, 2003.

7. Murib, M. S., E. Yüce, O. Gürlü, and A. Serpengüzel, "Polarization behavior of elastic scattering from a silicon microsphere coupled to an optical fiber," *Photonics Research*, Vol. 2, No. 2, 45–50, Apr. 2014.

8. Cai, M., O. Painter, and K. J. Vahala, "Observation of critical coupling in a fiber taper to a silica-microsphere whispering-gallery mode system," *Physical Review Letters*, Vol. 85, No. 1, 74, 2000.

9. Eryürek, M., "Hydrogen gas sensor based on a polymer optical microdisk resonator," Koç University, 2013.

10. Oskooi, A. F., D. Roundy, M. Ibanescu, P. Bermel, J. D. Joannopoulos, and S. G. Johnson, "MEEP: A flexible free-software package for electromagnetic simulations by the FDTD method," *Computer Physics Communications*, Vol. 181, 687–702, 2010.

A Photonic QPSK Modulator Aimed at Space Applications

J. Panasiewicz[1,2], **D. M. S. Morais**[2], **and G. M. Pacheco**[2]

[1]National Institute for Space Research, Brazil
[2]Aeronautics Technical Institute, Brazil

Abstract— This paper addresses the subject of the satellite payload signal transmission and the digital-microwave link. Usually, the carrier modulation data transmitter (DT) employs in-phase (I) and quadrature-phase (Q) processing to achieve phase shift keying (M-PSK). Typically, this I/Q processing is obtained by multiplying a low-frequency reference signal. Such systems usually have many stages of multipliers, amplifiers and filters. As a result the microwave transmitter is complicated, bulky and costly. The results presented are based on a photonic circuit that achieves QPSK modulation directly at the microwave frequency carrier. The QPSK modulation was performed using a carrier frequency of 2 GHz and 2 Mbps I/Q signal from a pattern generator using a photonic circuit with a pair of Mach-Zehnder optical modulators arranged in a parallel configuration. The source of the photonic circuit is a DFB diode laser with a wavelength equal to 1550 nm. The modulated optical signal direct detection comes from an InGaAs photo detector. The optical modulator circuit output can be directly connected to the high power amplifier (HPA) and the transmission antenna. The resulting system enables one to achieve a microwave data transmitter with a reduced mass and volume, further lowering power consumption. These achievements are very important for spacecraft engineering teams during the conception of the satellite payloads when starting a new satellite project. Gamma radiation and thermal effects of the space environment are also discussed.

1. INTRODUCTION

Microwave photonic technology has attracted significant interest in many applications, such as wireless communications, RF up-conversion, optical oscillator, etc. [1]. Photonic technologies have many advantages over traditional electrical systems, such as high data rates, low weight and size. They are immune and do not induce electromagnetic interference (EMI), as well as being galvanically isolated and transparent to any modulation format.

In satellite engineering these advantages are desired due to the special economic and technical aspects related to building and operating satellite [2].

In this manner, much work has been direct towards the use of photonic technologies for spacecraft [3]. Since 2002 the European Space Agency (ESA) has been conducting a program of Research and Development to study the application of photonics in spacecraft [2]. As an example, it is possible to point out the on board optical fiber distribution of RF signal inside a satellite [4].

The Low Earth Orbit (LEO) satellite operates at altitudes from 160 to 2500 km and with proper inclination, has a restricted operation period from 8 to 10 minutes from a fixed location on earth, because the satellite is not a fixed location in the sky [5]. The satellites of National Institute for Space Research (INPE) are used to collect data from remote stations and image the Earth for deforestation control. The communication link of such satellites operates in the S and X bands for tracking, telemetry, command (TT&C) and image transmission. In the X band, the link operates using QPSK modulation. This technique is the preferred form of digital modulation due to the relatively simple implementation, high powered efficiency, the relatively narrow main lobe width and half bandwidth when compared to the BPSK modulation [6].

For the China-Brazil Earth Resources Satellite (CBERS) program, a QPSK transmitter in X band and data rate of 68 Mbps [7] that utilizes modular components with microwave technology was developed at INPE. The I/Q processing is obtained by multiplying a low-frequency reference signal and to reach the X band such a system has stages of multipliers, amplifiers and filters. Due to the many subsystems the microwave data transmitter is complicated, bulky and costly.

Thus, taking advantage of the advent of photonic technology and its use in space environment, we investigate a QPSK modulator using an external modulation technique and direct detection IM/DD. Utilizing photonic technology it is possible to eliminate spurious emissions and filtering requirements associated with the multiplication of the frequency in the electric domain, resulting in a potential increase of the carrier modulation bandwidth [8]. This article shows the first results and discusses its use in space environment.

2. SYSTEM DESCRIPTION

Actually, the photonic vector modulator generation employs different techniques. Usually it is 1 — a parallel structure [9], where two Mach-Zehnder intensity modulator, MZIM, are embedded in a main modulator dual-parallel MZIM (DPMZIM). A phase shift of $\pi/2$ is introduced in one arm making the optical signals orthogonal to each other; 2 — serial or cascade structure [10], where the first MZIM modulates the in-phase signal, I, and the second one modulates the quadrature signal, Q. These two modulators are connected in cascade; 3 — a dual-drive Mach-Zehnder (MZDD) [11], where the I and Q signals are connected to each port.

The system implemented in this study is based on the parallel configuration mentioned above. Instead of an embedded modulator, two separated MZIMs connected by an optical splitter were used. A single CW laser was used. Previous authors used two separated laser source [8]. The block diagram is shown in Figure 1. The microwave signal is split by a 90 degree hybrid to generate the $\cos(wt)$ and $\sin(wt)$ components. The binary data signal is provided by a pseudo random bit sequence (PRBS) separated into two data channels I and Q. The system configuration is similar to a photonic phase shifter for phased array antenna [12].
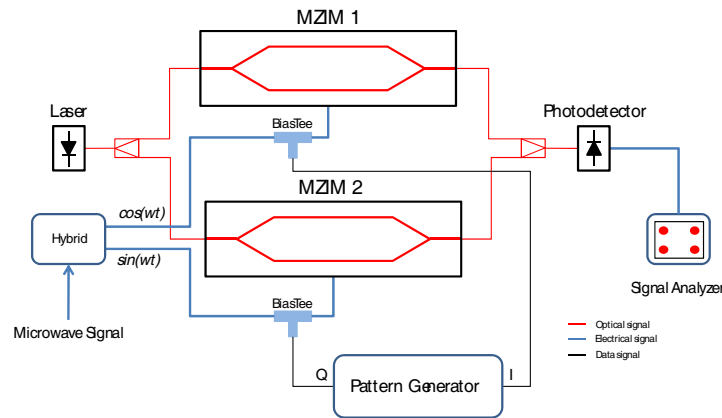
Figure 1: System block diagram.

The MZIM used a chirp free (push-pull modulators) [13]. The output optical field of each MZIM can be expressed as:

$$E_{out1}(t) = \frac{E_0}{2}\cos\left(\pi\left[\frac{Vd}{V\pi}Data(t) + \frac{Vm}{V\pi}\cos(w_{rf}t)\right]\right)\cos(w_0 t) \tag{1}$$

$$E_{out2}(t) = \frac{E_0}{2}\cos\left(\pi\left[\frac{Vd}{V\pi}Data(t) + \frac{Vm}{V\pi}\sin(w_{rf}t)\right]\right)\cos(w_0 t) \tag{2}$$

where $Data(t)$ is the transmitted data "0" and "1" and Vd is the amplitude of NRZ signal of $Data(t)$, $V\pi$ is the MZIM half-wave voltage, Vm and w_{rf} are the amplitude and the angular frequency of the electrical driving signal while E_0 and w_0 are the amplitude and angular frequency of the optical carrier.

From Equations (1) and (2), it can be noted that switching the amplitude data signal between the values of $-V\pi/4$ and $3V\pi/4$ the modulation BPSK is performed on each MZIM. As the transfer function of an MZIM is a periodic function, the phase of the optical field changes its sign but it is equal in magnitude, i.e., two equal intensity points of the transmission function separated by the modulator bias voltage have opposite optical phase, nearing perfect $180°$ [8, 14].

The optical signals of the each MZIM output when combined using a 50/50 optical coupler and detected by a photodetector results in a QPSK modulated microwave carrier. As the output of the photodectector had an impedance of 50 ohms, the signal can be connected directly in a high power amplifier (HPA) and after in a digital filter.

3. EXPERIMENTAL RESULTS

In order to verify the proposed scheme, a 2 GHz microwave carrier was applied to both MZIM by a bias tee. The MZIM are a Lucent 2623NA LiNbO$_3$ devices with $V\pi = 3.2V$. They are driven by

a DFB laser diode with wavelength of 1550 nm and power of 16 mW. The PRBS was provided by an Agilent 81130A with a code rate equal to 1 Mbps and length of $2^{15} - 1$. The signal was injected into the bias tee DC connector of each MZIM. The photodetector used was a Thorlabs InGaAs 5 GHz photodiode.

Figure 2(a) show the constellation diagram and transmission statistics measured with the Agilent N9020A Signal Analyzer for BPSK modulation at 1 Mbps on one channel. Figure 2(b) show the spectrum of BPSK signal where the main lobe width of 2 MHz correlates exactly to a modulation of 1 Mbps.
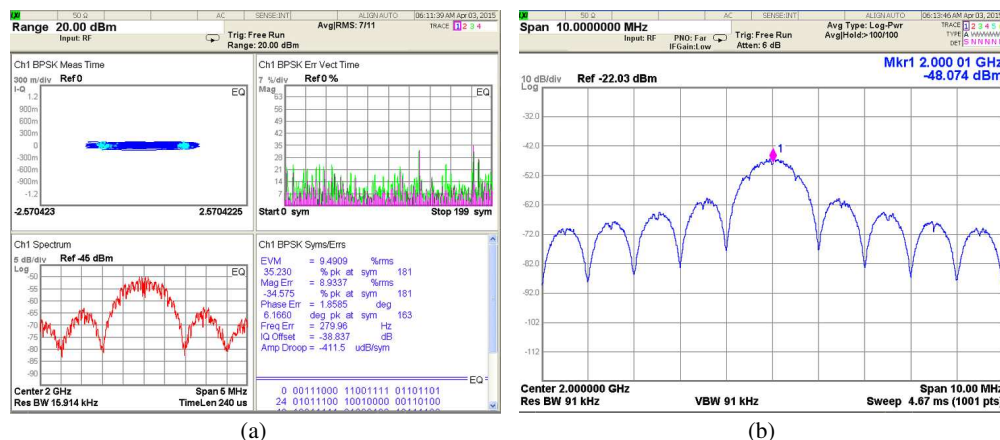
Figure 2: (a) BPSK constellation. (b) BPSK spectrum.

To perform the QPSK modulation, both BPSK channels have to have good performance on EVM. But, one of the MZIM channel had an EVM of 18%. A modulation with 1 Mbps on each channels (I and Q) totalizing one modulation of 2 Mbps was performed. Figures 3(a) and 3(b) show the QPSK constellation and spectrum of the modulation. The width of main lobe is 2 MHz, corresponding to a 2 Mbps QPSK modulation.
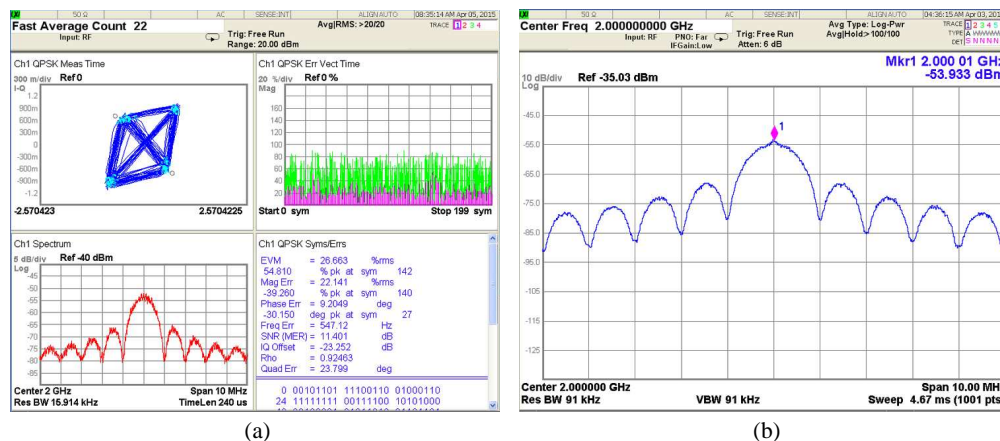
Figure 3: (a) QPSK constellation. (b) QPSK spectrum.

The data rate was incremented from 500 kbps to 2.5 Mbps and was limited by the frequency response of the bias tee. Although the International Telecommunications Union (ITU) assigned X band downlink frequency from 8025 to 8400 MHz, with the bandwidth of 375 MHZ by channel [15], no attempt was made to increase the microwave carrier since the photodetector is limited to 5 GHZ.

4. SPACE ENVIRONMENTAL

In the conception of a spaceflight mission and consequently in the design of payloads, the space environmental factors should be considered. In LEO, this environment includes many hazards such as UV radiation, ionizing radiation, atomic oxygen, plasma, radiation belts, high vacuum (induces material outgassing), orbital debris, as well as severe temperature cycles [16, 17].

Considering the ionizing radiation, space environment has a low dose rate of 10^{-4} to 10^2 rad/s. Although large accumulated doses can be reached as the duration of a mission may last years, total ionizing dose (TID) levels on the order of 10^5 rad, can be easily accumulated over the life of a spacecraft mission [18]. Therefore, devices, such as lasers, photodetectors, optical fibers, optical amplifiers, Mach Zehnder modulators need to be qualified considering performance against the requirements of a spacecraft mission. A theoretical study was carried out regarding the performance of eletro-optic modulators under neutrons irradiation [19] and provided good results.

5. CONCLUSION

This study presents a direct carrier modulation with the use of a photonic vector modulator suitable for radio digital communications of LEO satellites. A set of two Mach-Zehnder optical modulators in parallel and a common laser source and unique photodetector were used. Operating at 1550 nm and with control voltage between -0.85 V to 2.5 V the setup was tested with a pseudo random signal sequence of data.

Digital modulation, BPSK and QPSK were experimentally demonstrated with a carrier frequency of 2 GHz and a data rate limited to the 2.5 Mbps. The results suggest some MZIM modulators criteria selection and enable us to consider the construction of a higher frequency system for real satellite data transmission tests operating at around 8 GHz.

ACKNOWLEDGMENT

REFERENCES

1. Yao, J. P. "A tutorial on microwave photonics," *IEEE Photon. Soc. Newsletter*, Vol. 26, No. 2, 412, 2012.
2. Karafolas, N., J. P. Armengol, and I. Mckenzie, "Introducing photonics in spacecraft engineering: ESA's strategic approach," *Aerospace Conference*, 1–15, IEEE, 2009.
3. Ressia, J. H. and J. L. Peck, "Fiber optics demonstrated use in space vehicles," *RAST'03. International Conference on. Proceedings of Recent Advances in Space Technologies*, 321–324, IEEE, 2003.
4. Bénazet, B., M. Sotom, M. Maignan, and J. Berthon, "Optical distribution of local oscillators in future telecommunication satellite payloads," *5th International Conference on Space Optics*, Vol. 554, 589–594, 2004,
5. Ippolito, Jr, L. J., *Satellite Communications Systems Engineering: Atmospheric Effects, Satellite Link Design and System Performance*, Vol. 6, John Wiley & Sons, 2008.
6. Bokulic, R. S., C. C. DeBoy, S. W. Enger, J. P. Schneider, and J. K. McDermott, *Spacecraft Subsystems IV Communications and Power. Space Mission Engineering: The New SMAD*, Microcosm Press, 2011.
7. Tosetto, I., L. Cividanes, B. Santos, L. Silva, and R. Araújo, "Transmissor QPSK em Banda X para Aplicação Espacial," *XXV Simpósio Brasileiro de Telecomunicações*, 2007.
8. Jemison, W. D., A. J. Kreuzberger, and E. Funk. "Microwave photonic vector modulator for high-speed wireless digital communications," *IEEE Microwave and Wireless Components Letters*, Vol. 12, No. 4, 125–127, 2002.
9. Jiang, Jr., W., et al., "Photonic vector signal generation employing a novel optical direct-detection in-phase/quadrature-phase upconversion," *Optics Letters*, Vol. 35, No. 23, 4069–4071, 2010.
10. Loayssa, A. and D. Benito, "All-optical implementation of broadband QPSK subcarrier modulator," *Electronics Letters*, Vol. 40, No. 21, 1362–1364, 2004.
11. Binh, L. N., "Generation and transmission of multilevel quadrature amplitude modulation formats using only one optical modulator: MATLAB Simulink simulation models," *Optical Engineering*, Vol. 48, No. 4, 5005, 2009.
12. Coward, J. F., et al., "A photonic integrated-optic RF phase shifter for phased array antenna beam-forming applications," *Journal of lightwave technology*, Vol. 11, No. 12, 2201–2205, 1993.
13. Li, G. L. and P. K. L. Yu, "Optical intensity modulators for digital and analog applications," *Journal of Lightwave Technology*, Vol. 21, No. 9, 2010, 2003.

14. Gnauck, A. H. and P. J. Winzer, "Optical phase-shift-keyed transmission," *Journal of Lightwave Technology*, Vol. 23, No. 1, 115, 2005.

15. International Telecommunication Union (ITU) Handbook EESS, 2011.

16. Teichman, L. A. and B. A. Stein, "NASA/SDIO Space Environmental Effects on Materials Workshop", Part 1. No. NASA-L-16575, "National aeronautics and space administration hampton va langley research center", Hampton Virginia, June 28–July 1, 1988.

17. Tobiska, W. K., *The Space Environment. Space Mission Engineering: The New SMAD*, Microcosm Press, 2011.

18. Maurer, R. H., M. E. Fraeman, M. N. Martin, and D. R. Roth, "Harsh environments: Space radiation environment, effects, and mitigation," *Johns Hopkins APL Technical Digest*, Vol. 28, No. 1, 17, 2008.

19. Rashed, A. N. Z., "Speed performance degradation of electro-optic modulator devices by neutrons irradiations at high temperature effects," *IJCEM International Journal of Computational Engineering & Management*, Vol. 14, No. 1, 1–8, 2011.

Optoelectronic Applications of Sapphire Microspheres

Muhammad Zakwan, Muhammad Sohail Anwar,
Syed Sultan Shah Bukhari, Ulaş Sabahattin Gökay, and Ali Serpengüzel
Microphotonics Research Laboratory, Department of Physics, Koç University
Rumelifeneri Yolu, Sarıyer, Istanbul 34450, Turkey

Abstract— The sphere with its highly symmetric geometrical shape enhances the efficiency of optical effects with its high quality factor morphology dependent resonances (MDRs). We report here on numerical studies of elastic light scattering in a sapphire microdisk coupled to slab waveguides, i.e., the 2D analog of a microsphere coupled to the 2D analog of an optical waveguide. The numerical electromagnetic simulations for the surface electric field strength are performed at 800 nm. The experimental elastic light scattering measurements are also proposed in the near-infrared from sapphire microspheres. 800 nm operation with sapphire microspheres is suitable for local area networks (LANs) applications such as channel dropping, filtering, switching, modulation, and monitoring.

1. INTRODUCTION

Over the past few decades light interaction with microspheres composed of various materials has been studied towards the observation of novel photonic effects. The whispering gallery modes (WGMs) are optical resonances excited in dielectric and semiconductor resonators [1]. The WGMs take advantage of 3-dimensional state of light trapped inside the resonator medium and offer very narrow optical linewidths, as well as specific resonance lineshapes, and high quality factors. WGMs can be used in various applications such as biosensing [2, 3], nano-particle sizing [4], optical switching [5], and optoelectronics [6]. WGMs of circular microresonators can be excited with an optical waveguide [7] using evanescent coupling [8, 9]. In this work, modeling and analysis of WGMs excited in a dielectric microsphere with a waveguide is studied. Here, we perform numerical simulation of the out of plane electric field strength of an evanescently coupled sapphire microdisk (the 2D analogue of the sapphire microsphere) and various slab waveguides (the 2D analogue of optical waveguide) [10]. We utilized finite difference time domain (FDTD) technique of the MIT electromagnetic equation propagation (MEEP) tool for the numerical simulations [11].

2. PROPOSED EXPERIMENTAL SETUP

The overall proposed experimental setup diagram is shown in Figure 1. A sapphire (refractive index 1.764) microsphere can be used as an optical resonator with radius $a = 1.5\,\mu\text{m}$. An optical waveguide with a width $w = 0.4\,\mu\text{m}$ can be used for the excitation of the sapphire sphere placed at an impact parameter of $b = 1.9\,\mu\text{m}$. A continuous wave (CW) tunable laser diode operating at 800 nm can be used for the excitation of the WGMs of the microsphere resonator. The evanescent coupling of the near-IR laser to the sapphire microsphere can be achieved with an optical waveguide [9]. The 0° transmission and 90° elastic scattering intensities from the microsphere can be measured with photodiodes (PD1 and PD2), which can be connected to a digital storage oscilloscope. The 90° elastic scattering can be collected with the optical microscope (L1, L2 and L3).

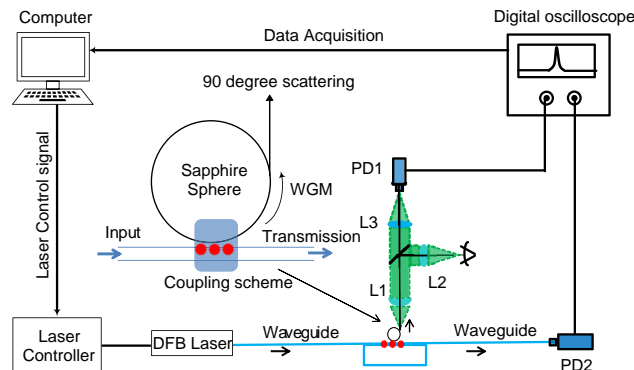

Figure 1: Proposed experimental setup with the inset showing the coupling region of the sphere.

3. SIMULATION GEOMETRY, RESULTS, AND DISCUSSION

In the numerical electromagnetic simulations, we studied the effect of the waveguide material on the 'waveguide to sphere coupling' by changing the material of the slab waveguide, exciting the sapphire microdisk. The slab waveguide was coupled to a sapphire microdisk with a radius of $a = 1.5\,\mu\mathrm{m}$ and refractive index 1.764. The excitation wavelegth was set in the near-IR region from 795 nm to 855 nm. Four different materials were used in the waveguide: glass with a refractive index of 1.455, sapphire with a refractive index of 1.764, diamond with a refractive index of 2.419, and silicon with a refractive index of 3.681. The excitation beam was placed at an impact parameter of $b = 1.9\,\mu\mathrm{m}$. The width of the waveguide $w = 400\,\mathrm{nm}$ was chosen such that, the waveguide would be single mode for operation at 800 nm for the case of glass, sapphire, and diamond. Ideally, the waveguide should have both a core and a cladding for evanescent coupling to the microdisk. The radial mode order l, and the angular mode number n will be specified for each numerical simulation. By changing the impact parameter b or the wavelength λ, it is possible to address various mode orders l or mode numbers n. The mode spacing is given by $\lambda^2/2a\pi m = 43.5\,\mathrm{nm}$ at 850 nm and 38.5 nm at 800 nm. The excitation from the left port of the waveguide is in the z direction (perpendicular to the paper) and the following figures show the electric field (perpendicular to the paper) strength everywhere in the xy plane.

Figure 2 shows off/on resonance condition for sapphire microdisk coupled to a glass waveguide. The off-resonance wavelength is at 819 nm, while the on resonance wavelength is at 800 nm. For the on resonance case the angular mode number is $n = 17$ and radial mode order is $l = 1$. Figure 3 shows the off/on-resonance condition for sapphire microdisk coupled to a sapphire waveguide. The off-resonance wavelength is 820.6 nm, while the on-resonance wavelength is 795.6 nm. For the on-
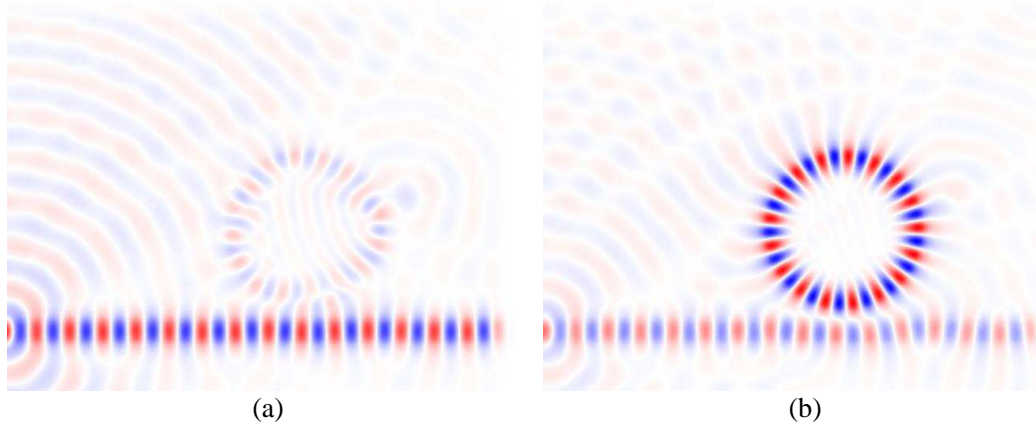
Figure 2: (a) The off-resonance at 819 nm and (b) on-resonance at 800 nm excitation for sapphire microdisc on glass slab waveguide.
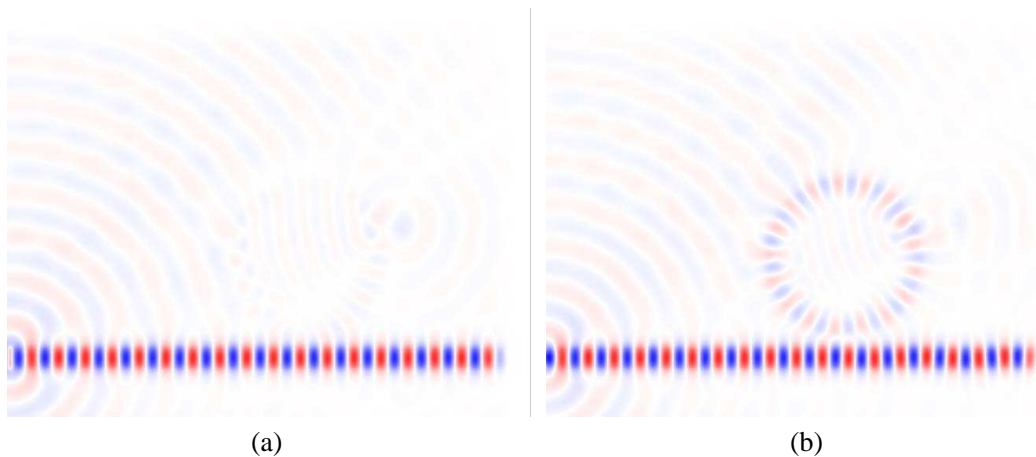
Figure 3: (a) The off-resonance at 820.6 nm and (b) on-resonance at 795.6 nm sapphire microdisk on sapphire slab waveguide excitation.
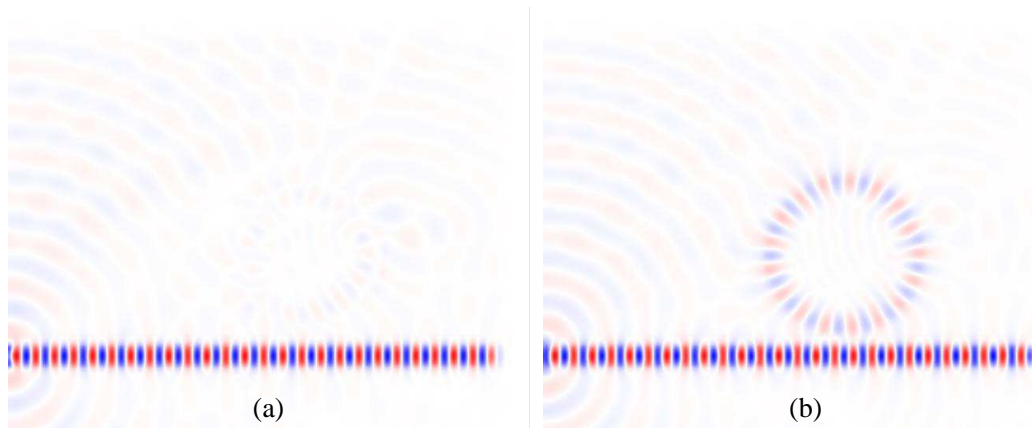
Figure 4: (a) The off-resonance at 820 nm and (b) on-resonance at 799.6 nm sapphire microdisk on diamond slab waveguide excitation.
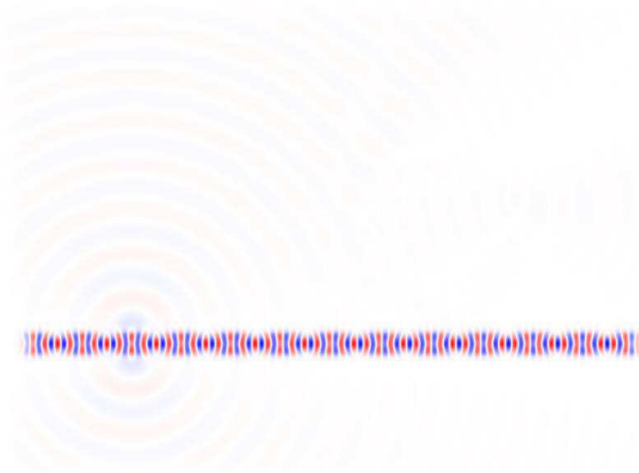
Figure 5: Sapphire microdisk on silicon slab waveguide at a wavelength of 800 nm. There is no evanescent excitation to the microdisk.

resonance case the angular mode number is $n = 17$ and radial mode order is $l = 1$. Figure 4 shows the off/on-resonance condition for sapphire microdisk on a diamond waveguide. The off-resonance wavelength is 820 nm, while the on-resonance wavelength is 799.6 nm. For the on-resonance case the angular mode number is again $n = 17$ and radial mode order is $l = 1$. Figure 5 shows the excitation of sapphire microdisk by a silicon slab waveguide excited with a wavelength of 800 nm. As the refractive index of silicon is bigger than sapphire, there is no appreciable evanescent coupling from the waveguide to the sapphire microdisk.

4. CONCLUSIONS

We have shown that the sapphire microdisks can be used as optical resonators, which eventually can be used for applications such as biosensing, and optical communication. We demonstrated our approach by numerically calculating the electric field strengths of an evanescently coupled sapphire microdisk (the 2D analogue of the sapphire microsphere) and various slab waveguides (the 2D analogue of the optical waveguide) of glass, sapphire, diamond, and silicon. As the refractive index of silicon is higher than sapphire, there is no significant evanescent coupling from the silicon waveguide to the sapphire microdisk.

would like to thank Mustafa Eryürek for his valuable input with the FDTD simulations.

REFERENCES

1. Serpengüzel, A., G. Griffel, and S. Arnold, "Excitation of resonances of microspheres on an optical fiber," *Optics Letters*, Vol. 20, 654–656, 1995.
2. Cheema, M. I., S. Mehrabani, A. A. Hayat, F. Vanier, Y.-A. Peter, A. M. Armani, and A. G. Kirk, "Experimental demonstration of application of ring down measurement approach to microcavities for biosensing," *Proceedings of SPIE on Frontiers in Biological Detection: From Nanosensors to Systems IV*, 82120B-1–82120B-6, San Francisco, California, USA, 2012.
3. Gökay, U. S., M. Zakwan, and A. Serpengüzel, "Spherical silicon optical resonators: Possible applications to biosensing," *The European Physical Journal Special Topics*, Vol. 223, 2003–2008, 2014.
4. Keng, D., X. Tan, and S. Arnold, "Whispering gallery micro-global positioning system for nanoparticle sizing in real time," *Applied Physics Letters*, Vol. 105, 071105, 2014.
5. O'Shea, D., C. Junge, M. Pöllinger, A. Vogler, and A. Rauschenbeutel, "All-optical switching and strong coupling using tunable whispering-gallery-mode microresonators," *Applied Physics B*, Vol. 105, 129–148, 2011.
6. Benson, T., S. Boriskina, P. Sewell, A. Vukovic, S. Greedy, and A. Nosich, "Micro-optical resonators for microlasers and integrated optoelectronics," *Frontiers in Planar Lightwave Circuit Technology*, Vol. 216, 39–70, S. Janz, J. Ctyroky, and S. Tanev, Eds., Springer, Netherlands, 2006.
7. Yariv, A., "Critical coupling and its control in optical waveguide-ring resonator systems," *IEEE Photonics Technology Letters*, Vol. 14, 483–485, 2002.
8. Blair, S. and Y. Chen, "Resonant-enhanced evanescent-wave fluorescence biosensing with cylindrical optical cavities," *Applied Optics*, Vol. 40, 570–582, 2001.
9. Spillane, S. M., T. J. Kippenberg, and K. J. Vahala, "Ultralow-threshold Raman laser using a spherical dielectric microcavity," *Nature*, Vol. 415, 621–623, 2002.
10. Eryürek, M., "Hydrogen gas sensor based on a polymer optical microdisk resonator," Koç University, 2013.
11. Oskooi, A. F., D. Roundy, M. Ibanescu, P. Bermel, J. D. Joannopoulos, and S. G. Johnson, "MEEP: A flexible free-software package for electromagnetic simulations by the FDTD method," *Computer Physics Communications*, Vol. 181, 687–702, 2010.

Silicon Microspheres in Metrology

Muhammad Hamza Humayun, **Farhan Azeem**, **Imran Khan**,
Ulaş Sabahattin Gökay, **and Ali Serpengüzel**
Microphotonics Research Laboratory, Department of Physics, Koç University
Rumelifeneri Yolu, Sarıyer, Istanbul 34450, Turkey

Abstract— The Système International unit of mass is the kilogram. The present definition of the kg is based on a prototype dating back to 1880s. New approaches to define the unit of mass are being investigated. Avogadro Project uses 10 cm diameter single crystal silicon spheres. The technique commonly observed to measure the radius of the silicon sphere is optical interferometry. Here, we propose an alternate method of measuring the diameter of the single crystal silicon sphere using near-infrared spectroscopy. We demonstrate our approach by numerically simulating the electromagnetic coupling of a silicon microdisk of radius 5 μm to an optical waveguide of width 0.5 μm, thereby approximating the coupling of a microsphere to a rectangular optical waveguide. It might be possible to have a precise technique for determining the radius of the sphere, which can be used for the definition of the kilogram.

1. INTRODUCTION

The kilogram (kg) is defined as the mass of international prototype made of platinum-iridium alloy kept at Bureau International des Poids et des Measures (BIPM) [1]. The kg is the only base unit, which uses a material artifact in Système International (SI) [2]. Three other base units are affected by the definition of mass: the ampere, whose definition depends on force (newton) acting between current carrying wires; the mole, whose definition refers to 12 grams of carbon-12, and the candela, whose definition refers to the watt.

Currently, there are efforts to replace the definition of the kg based on the mass artifact by a definition based on physical constants. The kg can be defined as the mass of certain number of silicon atoms. For the definition of a base unit, the quantity used should be a true invariant of nature i.e., invariant under translation in space and time [3, 4]. The need for redefinition surfaced because of the long-term stability problem with the old platinum–iridium artifact [5, 6]. The appropriate quantities for the redefinition are the Planck constant, h or the Avogadro number, N_A. Perfect silicon single crystals are used [7] to find N_A. Calculating N_A requires an accurate measurement of the radius of the silicon crystal spheres. For this aim, interferometric methods are used to measure the diameter [8] of single crystal silicon spheres. Spheres possess whispering gallery modes (WGMs) with narrow linewidths [9] and quality factors (Q) as high as 8×10^9 [10]. Exciting the WGMs of the spheres with a tunable laser results in the measurement of the spectral parameters such as the resonant wavelengths, Q's, and mode spacing. We propose the measurement of the radius of the silicon microspheres by using the optical resonance condition $x < n < xm_{sphere}$, where $x = 2\pi a/\lambda$ is the size parameter, n the angular mode number, λ the resonant wavelength, a the radius of the sphere, and m_{sphere} the refractive index of the sphere. In our approach, we can calculate N_A by measuring the silicon spheres radius with near-infared (near-IR) spectroscopy. Here we demonstrate our approach by performing a simulation of the out of plane electric field strength of an evanescently coupled silicon microdisk (the 2D analogue of the microsphere) and various slab waveguides (the 2D analogue of optical waveguide) [11]. We utilize finite difference time domain (FDTD) method by using the MIT electromagnetic equation propagation (MEEP) tool for the simulations [12].

2. SPECTROSCOPIC GEOMETRY

The geometry of the simulations for the spectrocopic measurments is given as follows: a slab waveguide with a width $w = 0.5$ μm is coupled to a silicon microdisk with a radius of $a = 5$ μm at a wavelength of 1550 nm. The materials for the slab waveguides are silicon ($m_{silicon} = 3.4757$), diamond ($m_{diamond} = 2.4$), sapphire ($m_{sapphire} = 1.746$) and silica ($m_{silica} = 1.44$). The silicon microdisk is placed at an impact parameter $b = 5.35$ μm. The waveguide width is chosen to operate in single mode at a wavelength of $\lambda_{laser} = 1550$ nm, where the left end of the waveguide is chosen to be the excitation port. Ideally, the waveguide should have a core and a cladding layer for evanescent coupling to the microdisk, but for the sake of simplicity the cladding part is omitted.

The overall proposed experimental setup diagram is given in Figure 1 where a silicon microsphere will be used instead of a microdisk. A distributed feedback (DFB) diode laser in the near-IR
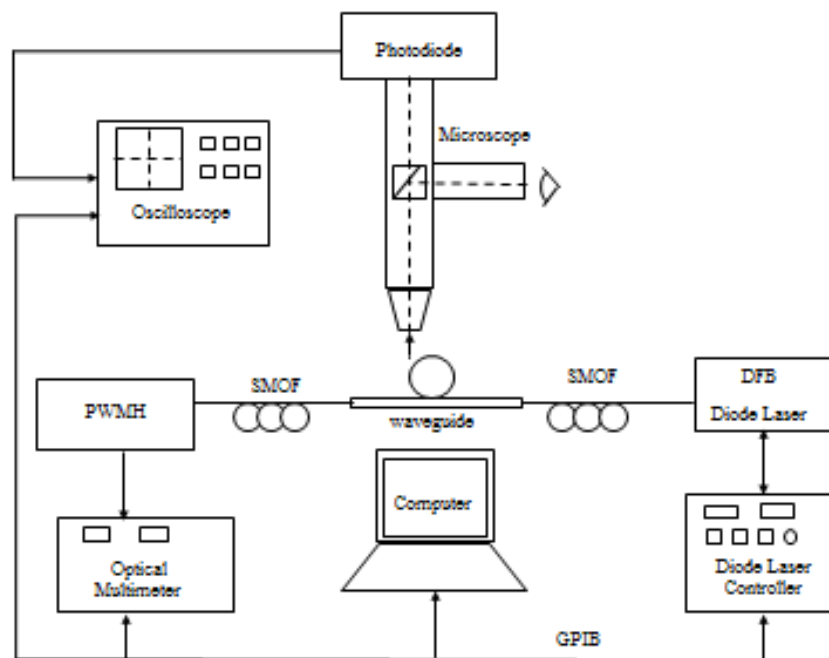
Figure 1: Proposed experimental setup for evanescent coupling of silicon sphere to an optical slab waveguide.

operating at $\lambda_{laser} = 1550\,\text{nm}$ can be used for the excitation of the WGMs in the microsphere. The input laser is coupled to a single mode optical waveguide. The evanescent coupling of the near-IR laser to the microsphere can be achieved with a rectangular waveguide. The 90° elastic scattering intensity from the microsphere can be collected with an optical microscope and can be measured with a photodiode which is connected to an oscilloscope. The 0° transmission can be measured with an optical multimeter with a power/wavelength measurement head (PWMH).

3. SIMULATION RESULTS AND DISCUSSION

Polarization of the source electric field at the left port is vertical, and the propagation of the elecgtromagnetic wave is in the x-y plane and we are calculating the out of plane component of the electric field strength everywhere on the x-y plane in z direction. The impact parameter b is always set to the radius a of the microdisk plus the half width of the waveguide, and the air-gap between the resonator and the waveguide. By changing the impact parameter b, or the wavelength λ, it is possible to address various mode orders (l) and mode numbers (n) of the WGMs.

Figure 2(a) shows off resonance and Figure 2(b) shows on resonance condition for a silica waveguide and silicon microdisk coupling. In the off-resonance case, we can see that the intensity of the

| (a) | (b) |

| (a) | (b) |
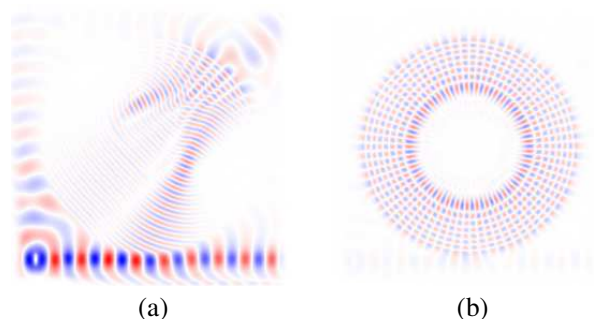
Figure 2: (a) The off-resonance and (b) on-resonance condition for a silicon disk on a glass slab waveguide.
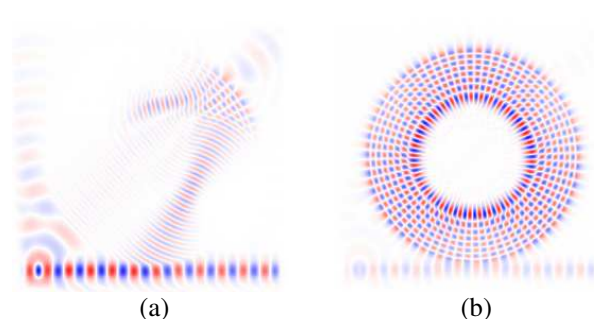
Figure 3: (a) The off-resonance and (b) on-resonance condition for a silicon disk on a sapphire slab waveguide.
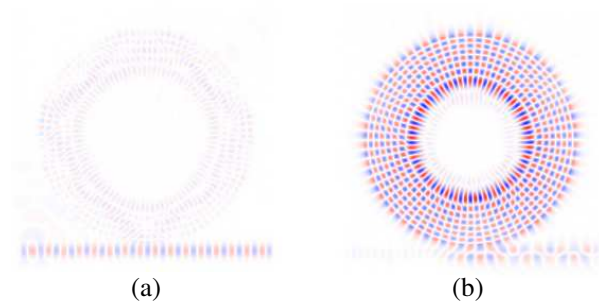
Figure 4: (a) The off-resonance and (b) on-resonance condition for a silicon disk on a diamond slab waveguide.
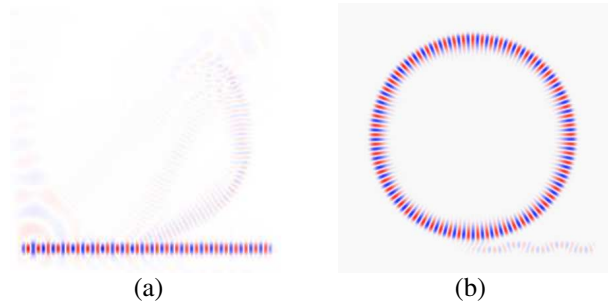
Figure 5: (a) The off-resonance and (b) on-resonance condition for a silicon disk on a silicon slab waveguide.

waveguide is high, but no WGMs can be observed inside the microdisk. The wavelength for the on-resonance case is $\lambda_{laser} = 1550\,\text{nm}$, the angular mode number is $n = 37$ and radial mode order is $l = 8$. Figure 3(a) shows the off-resonance and Figure 3(b) shows the on-resonance condition for sapphire waveguide and silicon microdisk coupling. Similar pattern is observed for off-resonance case, while the on-resonance wavelength is $\lambda_{laser} = 1550\,\text{nm}$. For the on-resonance case the angular mode number is $n = 37$ and radial mode order is $l = 8$.

Figure 4(a) shows off resonance and Figure 4(b) shows the on resonance condition for diamond waveguide and silicon microdisk coupling. The off-resonance wavelength is 1560 nm while the on resonance wavelength is 1550 nm. The mode number and mode orders observed are same as that of the silica and sapphire waveguides. Figure 5(a) shows the off resonance and Figure 5(b) shows the on-resonance condition for silicon waveguide and silicon microdisk coupling. The off-resonance wavelength is 1552 nm, while the on-resonance wavelength is 1548 nm. For the on-resonance case the angular mode number is $n = 65$ and radial mode order is $l = 8$. As for the resonance condition i.e., $x \leq n \leq m_{sphere}x$, n should lie between 22 and 76, and our numerical analysis has confirmed this condition in all of the cases considered above.

4. CONCLUSIONS

We have shown that, in addition to the commonly used interferometric method, near-IR spectroscopy can also be used to measure the radius of the silicon Avogadro sphere. We demonstrated our approach by numerically calculating the electric field strengths of an evanescently coupled silicon microdisk (the 2D analog of the microsphere) and various slab waveguides (the 2D analog of the optical waveguide) of glass, sapphire, diamond, and silicon.

ACKNOWLEDGMENT

REFERENCES

1. Davis, R., "The SI unit of mass," *Metrologia*, Vol. 40, 299, 2003.
2. Quinn, T. J., "The kilogram: The present state of our knowledge," *IEEE Transactions on Instrumentation and Measurement*, Vol. 40, 81–85, 1991.
3. Mills, I. M., P. J. Mohr, T. J. Quinn, B. N. Taylor, and E. R. Williams, "Redefinition of the kilogram, ampere, kelvin and mole: A proposed approach to implementing CIPM recommendation 1 (CI-2005)," *Metrologia*, Vol. 43, 227–246, 2006.
4. Becker, P., P. D. Bièvre, K. Fujii, M. Glaeser, B. Inglis, H. Luebbig, and G. Mana, "Considerations on future redefinitions of the kilogram, the mole and of other units," *Metrologia*, Vol. 44, 1–14, 2007.
5. Becker, P., "Tracing the definition of the kilogram to the Avogadro constant using a silicon single crystal," *Metrologia*, Vol. 40, 366, 2003.
6. Mills, I. M., P. J. Mohr, T. J. Quinn, B. N. Taylor, and E. R. Williams, "Redefinition of the kilogram: a decision whose time has come," *Metrologia*, Vol. 42, 71–80, 2005.

7. Becker, P., H. Bettin, H. Danzebrink, M. Gläser, U. Kuetgens, A. Nicolaus, D. Schiel, P. De Bievre, S. Valkiers, and P. Taylor, "Determination of the Avogadro constant via the silicon route," *Metrologia*, Vol. 40, 271, 2003.

8. Fujii, K., M. Tanaka, Y. Nezu, K. Nakayama, R. Masui, and G. Zosi, "Interferometric measurements of the diameters of a single-crystal silicon sphere," *Review of Scientific Instruments*, Vol. 63, 5320, 1992.

9. Righini, G. C., Y. Dumeige, P. Féron, M. Ferrari, G. Nunzi Conti, D. Ristic, and S. Soria, "Whispering gallery mode microresonators: Fundamentals and applications," *Rivista del Nuovo Cimento*, Vol. 34, 435–488, 2011.

10. Murib, M. S., E. Yüce, O. Gürlü, and A. Serpengüzel, "Polarization behavior of elastic scattering from a silicon microsphere coupled to an optical fiber," *Photonics Research*, Vol. 2, 45–50, 2014.

11. Eryürek, M., "Hydrogen gas sensor based on a polymer optical microdisk resonator," Koç University, 2013.

12. Oskooi, A. F., D. Roundy, M. Ibanescu, P. Bermel, J. D. Joannopoulos, and S. G. Johnson, "MEEP: A flexible free-software package for electromagnetic simulations by the FDTD method," *Computer Physics Communications*, Vol. 181, 687–702, 2010.

A Moment-method Analysis of a Thin-wire Chireix-coil Antenna

A. A. Ayorinde[1], S. A. Adekola[1, 2], and A. Ike Mowete[1]

[1]Department of Electrical and Electronics Engineering
Faculty of Engineering, University of Lagos, Nigeria
[2]Department of Electrical and Electronics Engineering
Niger Delta University, Wilberforce Island, Yenegoa, Nigeria

Abstract— Using a moment-method solution technique in an Electric-Field Integral Equation (EFIE) formulation approach, this presentation examines certain performance characteristics of the electrically thin-wire variety of the Chireix-coil antenna, whose geometry as defined by [2] is given by $C_\lambda = \sqrt{1 + 2S_\lambda}$, where the parameters (C_λ, S_λ), respectively symbolize helix circumference and turn spacing, measured in units of wavelength at the operating frequency.

Computational results obtained for the Chireix coil with 4-, 6-, 8-, and 10-turns suggest that the maximum value of magnitude of current distributed along the axis of the antenna is more or less independent of number of antenna turns. And the results also indicate that when S_λ is less than 0.9, the radiation field (E_θ, E_φ) patterns on the azimuthal plane consist of two diametrically directed majors; which degenerate into four distinct lobes (with relative maxima along $\varphi = 0°$, $90°$, $180°$, and $270°$ axes) for values of S_λ in excess of 1.0. A particularly remarkable feature of these radiation field pattern characteristics is that they appear to be independent of the number of coil turns.

1. INTRODUCTION

When, for the thin-wire circular helical antenna, size of circumference (denoted by (C_λ) and measured in units of wavelength) lies between 0.75 and 1.3, the antenna radiates maximally in its axial direction, and is consequently commonly referred to as the axial-mode helix [2]. On the other hand, for values of C_λ less than 0.75, the helix antenna directs its radiation principally in the plane perpendicular to the helix axis, which is why it is designated as the normal-mode helix [4]. Although these two modes represent the principal radiation modes of the helical antenna, a few other important radiation modes such as octafilar-axial, quadrifilar-axial, backfire, and four-lobed (Chireix coil) have been developed and put to practical applications [2]. The focus of this presentation is on the Chireix coil (four-lobed mode), which as far as we can ascertain, has received little analytical attention in the open literature, and whose geometry, according to [2], is defined by $C_\lambda = \sqrt{1 + 2S_\lambda}$, making the simple realization of helical antennas with dimension C_λ greater than 1.3, a possibility.

The Chireix coil is modeled as an electrically thin structure and the approximate distribution of current along its axis is determined through a moment-method solution of the Electric Field Integral Equation (EFIE) formulated for the antenna problem. This current profile is then introduced in the radiation field integrals for the antenna, to determine the radiation field patterns, with emphasis solely on the azimuthal plane patterns following [5], who treated the case of a centre-fed microstrip helical antenna. Computational results generated for 4-, 6-, 8-, and 10-turn Chireix coils operating at the frequency of 3 GHz, and the Chireix coils physical parameters in the ranges $1.10 \leq C_\lambda \leq 2.15$ and $0.10 \leq S_\lambda \leq 1.80$ are displayed in graphical formats. A particularly interesting observation arising from these results is that they clearly suggest that the Chireix coil antenna's current profiles and associated azimuthal-plane radiation patterns are somewhat independent of the number of coil turns.

2. ELECTRIC-FIELD INTEGRAL EQUATION (EFIE) FORMULATION

Figure 1(a) depicts a Chireix-coil antenna which is essentially a thin-wire helix of circular cross-section excited at its geometrical centre, in which the position vector $\bar{r}'$ from the coordinate system origin to any point on the helical wire axis is expressible as:

$$\bar{r}' = a \cos \varphi' \hat{a}_x + a \sin \varphi' \hat{a}_y + (a \tan \alpha) \varphi' \hat{a}_z \qquad (1)$$

where a represents the radius of the circular helix, α the helix pitch angle, and φ' the running variable along the helical wire axis. Figure 1(b) shows a complete turn of the coil of total length L_λ.
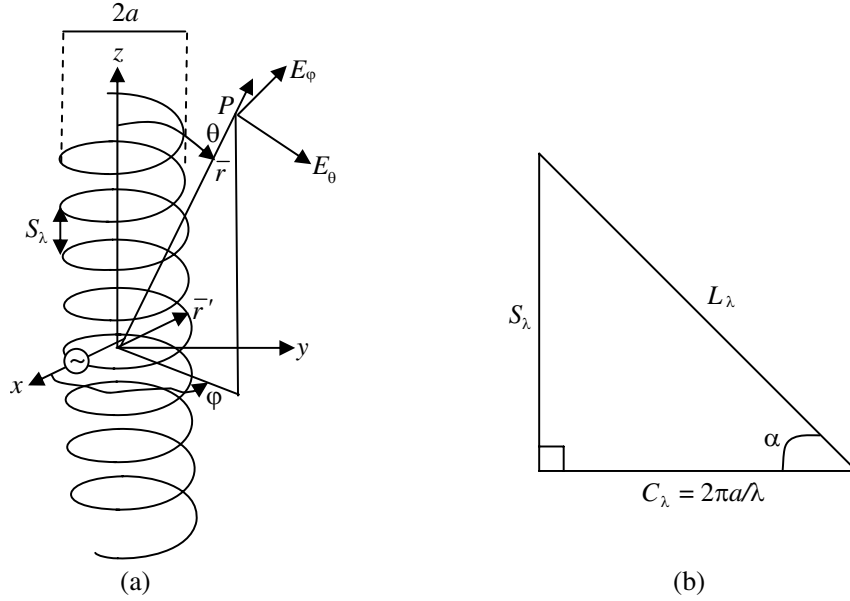
Figure 1: (a) A Chireix coil antenna excited at its geometrical centre; (b) a complete turn of the coil.

If it is assumed that the helical wire is perfectly conducting, then the total electric field on the helical wire surface, that is, the sum of incident electric field $\bar{E}^i$ and scattered electric field $\bar{E}^s$, satisfies the following boundary condition:

$$\hat{a}_n \times \left(\bar{E}^i + \bar{E}^s \right) = \bar{0} \tag{2}$$

in which $\hat{a}_n$ stands for the unit vector normal to the wire surface. Because the scattered electric field depends on the retarded scalar and vector potentials which can be expressed in terms of the induced current $I(\varphi')$, and upon the restriction of $I(\varphi')$ to the helical wire axis, it can be shown that the Electric Field Integral Equation (EFIE) governing the Chireix coil antenna problem posed here admits the form:

$$E_\varphi^i = L\left[I(\varphi') \right] \tag{3}$$

where

$$L[*] = \int_{-\pi N}^{\pi N} \left\{ \left[\cos\alpha\cos(\varphi - \varphi') + \tan\alpha\sin\alpha \right] \left[\frac{j\omega\mu_o a}{4\pi} \right] [*] - \frac{1}{j4\pi\omega\varepsilon_o a \sec\alpha} \frac{d[*]}{d\varphi'} \frac{d}{d\varphi} \right\} \frac{e^{-jk_o R}}{R} d\varphi', \tag{4a}$$

and

$$R = a\sqrt{\left(\frac{r_w}{a}\right)^2 + 4\sin^2\left(\frac{\varphi - \varphi'}{2}\right) + \tan^2\alpha(\varphi - \varphi')^2} \tag{4b}$$

provided that the observation point φ is specified on the helical wire surface, r_w denotes the wire radius and N the number of coil turns. It should be remarked that the limits of the line integral $[-\pi N, \pi N]$ are the consequence of the fact that the helical antenna is excited at its geometrical centre which corresponds to the coordinate system origin. Of course the only unknown quantity in the EFIE above is $I(\varphi')$, the determination of which is effected via the moment-method technique in what follows.

3. MOMENT-METHOD SOLUTION OF THE EFIE

Towards the numerical solution of $I(\varphi')$ in the EFIE formulated above using the method of moments, we segment the helical structure into short lengths, and model the unknown quantity $I(\varphi')$ by the series representation:

$$I(\varphi') = \sum_{k=1}^{K} I_k T_k(\varphi') \tag{5}$$

where $T_k(\varphi')$ stands for triangular expansion functions of unit height, each defined over four consecutive segments, and I_k the unknown superposition coefficients. The substitution of Equation (5) in Equation (3) and taking the inner product of the resulting equation with the weighting functions $W_j(\varphi)$ defined over the helical surface and in the same manner as the expansion functions, we ultimately transform the EFIE into a matrix equation:

$$[V_j] = [Z_{jk}][I_k] \tag{6}$$

in which $[Z_{jk}]$ is the generalized impedance matrix of the helical structure, $[V_j]$ the generalized voltage matrix which, in this case, has only one non-zero entry at the middle, and $[I_k]$ the generalized current matrix whose entries are the unknown superposition coefficients. The matrix inversion of $[Z_{jk}]$ and subsequent multiplication by the voltage matrix $[V_j]$ give the solution of $[I_k]$, that is,

$$I(\varphi'_k) = \sum_{k=1}^{K} [T_k(\varphi'_k)][Z_{jk}]^{-1}[V_j] \tag{7}$$

which readily facilitates the computation of the electric fields radiated by the Chireix coil antenna. Using the vector potential approach, the radiated electric fields by the Chireix coil antenna are given by

$$E_\theta(\theta, \varphi) = \frac{-j\omega\mu_o a e^{-jk_o r}}{4\pi r} \int_{-\pi N}^{\pi N} I(\varphi')[\cos\theta\sin(\varphi - \varphi') - \sin\theta\tan\alpha]e^{jk_o a\zeta\sin\theta}d\varphi', \tag{8a}$$

$$E_\varphi(\theta, \varphi) = \frac{-j\omega\mu_o a e^{-jk_o r}}{4\pi r} \int_{-\pi N}^{\pi N} I(\varphi')[\cos(\varphi - \varphi')]e^{jk_o a\zeta\sin\theta}d\varphi', \tag{8b}$$

where

$$\zeta = \cos(\varphi - \varphi') + (\tan\alpha\cot\theta)\varphi'. \tag{8c}$$

For the numerical evaluation of the electric field components, we replace $I(\varphi')$ by Equation (7), and accordingly, change the integrals to summation in the following manner:

$$E_\theta(\theta, \varphi) = \frac{-j\omega\mu_o a e^{-jk_o r}}{4\pi r}\sum_{k=1}^{K}[T_k(\varphi'_k)][Z_{jk}]^{-1}[V_j][\cos\theta\sin(\varphi - \varphi'_k) - \sin\theta\tan\alpha]e^{jk_o a\zeta\sin\theta}\Delta\varphi'_k, \tag{9a}$$

$$E_\varphi(\theta, \varphi) = \frac{-j\omega\mu_o a e^{-jk_o r}}{4\pi r}\sum_{k=1}^{K}[T_k(\varphi'_k)][Z_{jk}]^{-1}[V_j][\cos(\varphi - \varphi'_k)]e^{jk_o a\xi\sin\theta}\Delta\varphi'_k \tag{9b}$$

$$\zeta = \cos(\varphi - \varphi'_k) + (\tan\alpha\cot\theta)\varphi'_k. \tag{9c}$$

Of main interest in this presentation is the radiated electric fields of the chireix coil antenna in the azimuthal plane where $\theta = \pi/2$ because of the remarkable radiation characteristics of centre-fed microstrip helix in that plane [5]. Consequently, upon the substitution of $\theta = \pi/2$ in Equations (9a)–(9c) we readily obtained the following simplified expressions:

$$E_\theta(\pi/2, \varphi) = \frac{-j\omega\mu_o a e^{-jk_o r}}{4\pi r}\sum_{k=1}^{K}[T_k(\varphi'_k)][Z_{jk}]^{-1}[V_j][-\tan\alpha]e^{jk_o a\zeta}\Delta\varphi'_k, \tag{10a}$$

$$E_\varphi(\pi/2, \varphi) = \frac{-j\omega\mu_o a e^{-jk_o r}}{4\pi r}\sum_{k=1}^{K}[T_k(\varphi'_k)][Z_{jk}]^{-1}[V_j][\cos(\varphi - \varphi'_k)]e^{jk_o a\xi}\Delta\varphi'_k, \tag{10b}$$

$$\zeta = \cos(\varphi - \varphi'_k). \tag{10c}$$

The computational results obtained based on the above equations will now be discussed.

4. COMPUTATIONAL RESULTS

Before discussing the computational results generated for the chireix coil antenna, a comparison is made between the current distribution computed from Equation (7) at operating frequency of 500 MHz with the published theoretical and experimental results of [3] who provided a Fourier series solution of the current along a centre-fed thin-wire helix. The results of the comparative exercise for a 6-turn centre-fed helix are displayed in Figures 2(a) and (b), which clearly reveal

(a)   (b)
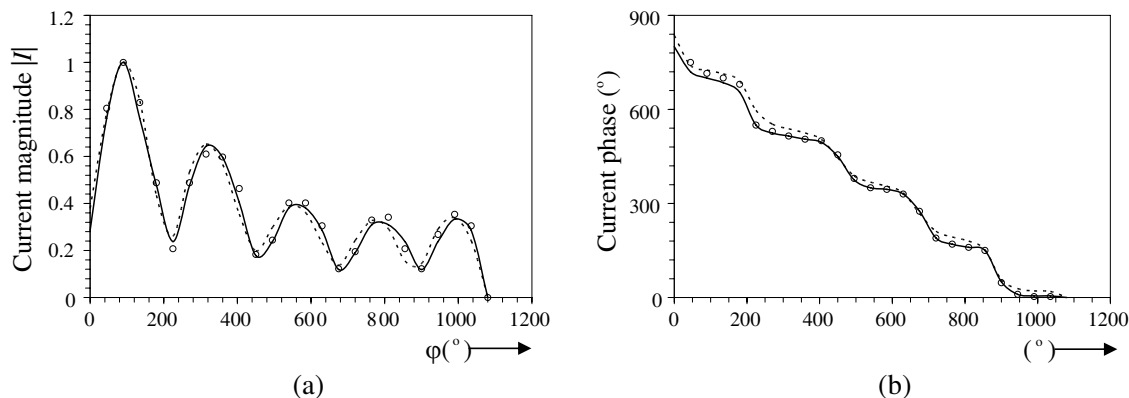
Figure 2: Comparison of current magnitude and phase of a centre-fed helical antenna at 500 MHz: $-\,-\,-\,-$: MoM; ———: Chen's theory and ∘ ∘ ∘∘: Experimental results at 500 MHz of Figure 6(a) [3].

(a)

(b)

(c)

(d)
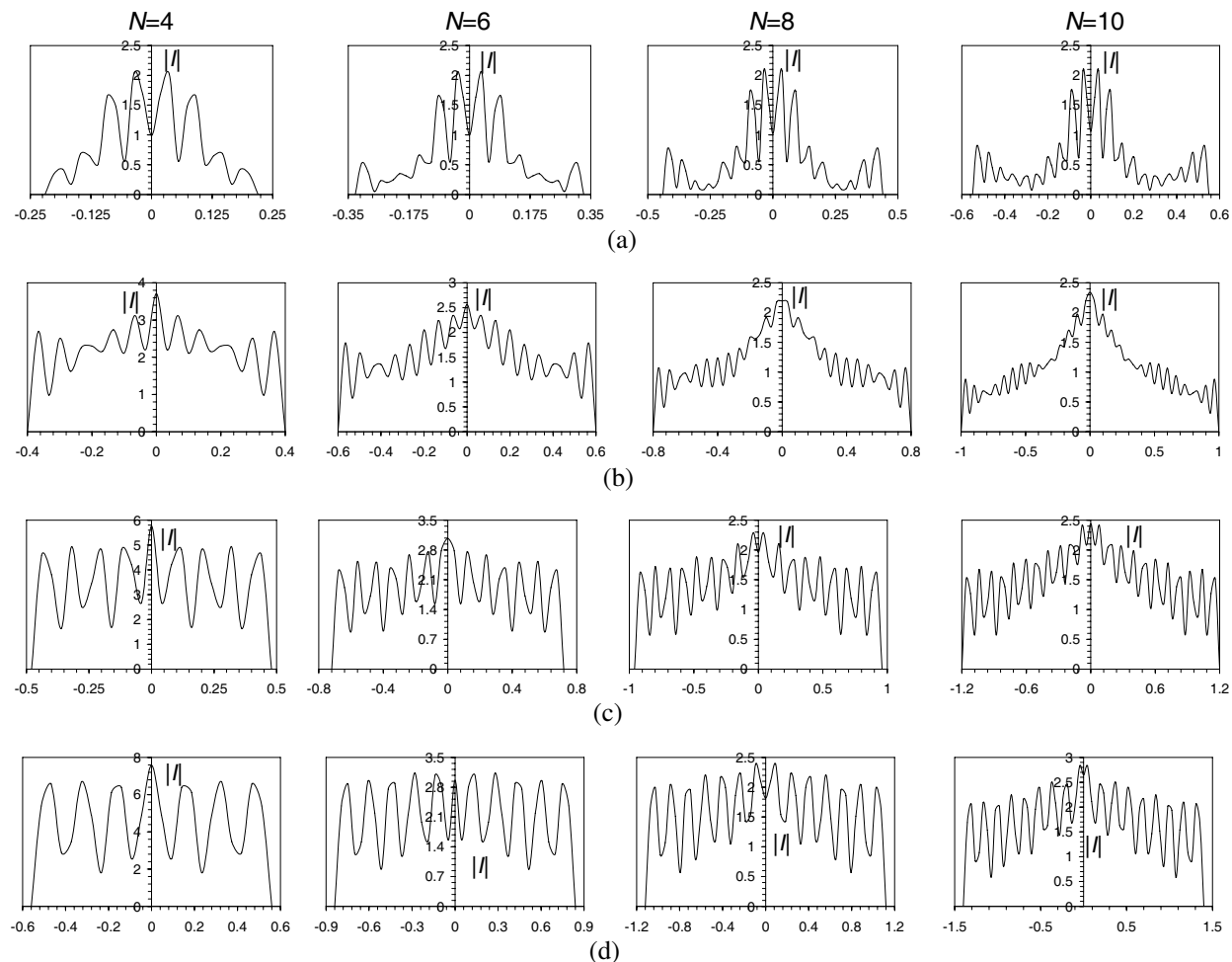
Figure 3: Current distributions along the arm length of Chireix coil antenna: $0.1 \leq S_\lambda \leq 1.8$. The horizontal axis represents the coil arm length. (a) $S_\lambda = 0.10$, (b) $S_\lambda = 1.0$, (c) $S_\lambda = 1.4$, (d) $S_\lambda = 1.8$.

good agreement between our MoM results and the Chen's results, and invariably lends credence to the MoM solution of the centre-fed helical antenna problem addressed in this paper.

The Chiriex coil geometry is mathematically defined by $C_\lambda = \sqrt{1 + 2S_\lambda}$ [2] where (C_λ, S_λ) symbolize helix circumference and turn-spacing expressed in wavelengths at the operating frequency, respectively. Consequently, the length of one turn of the helix is given by $L_\lambda = \sqrt{(1 + 2S_\lambda)^2 + S_\lambda^2} = 1 + S_\lambda$ based on Figure 1(b). For numerical computations, the following values of relevant parameters
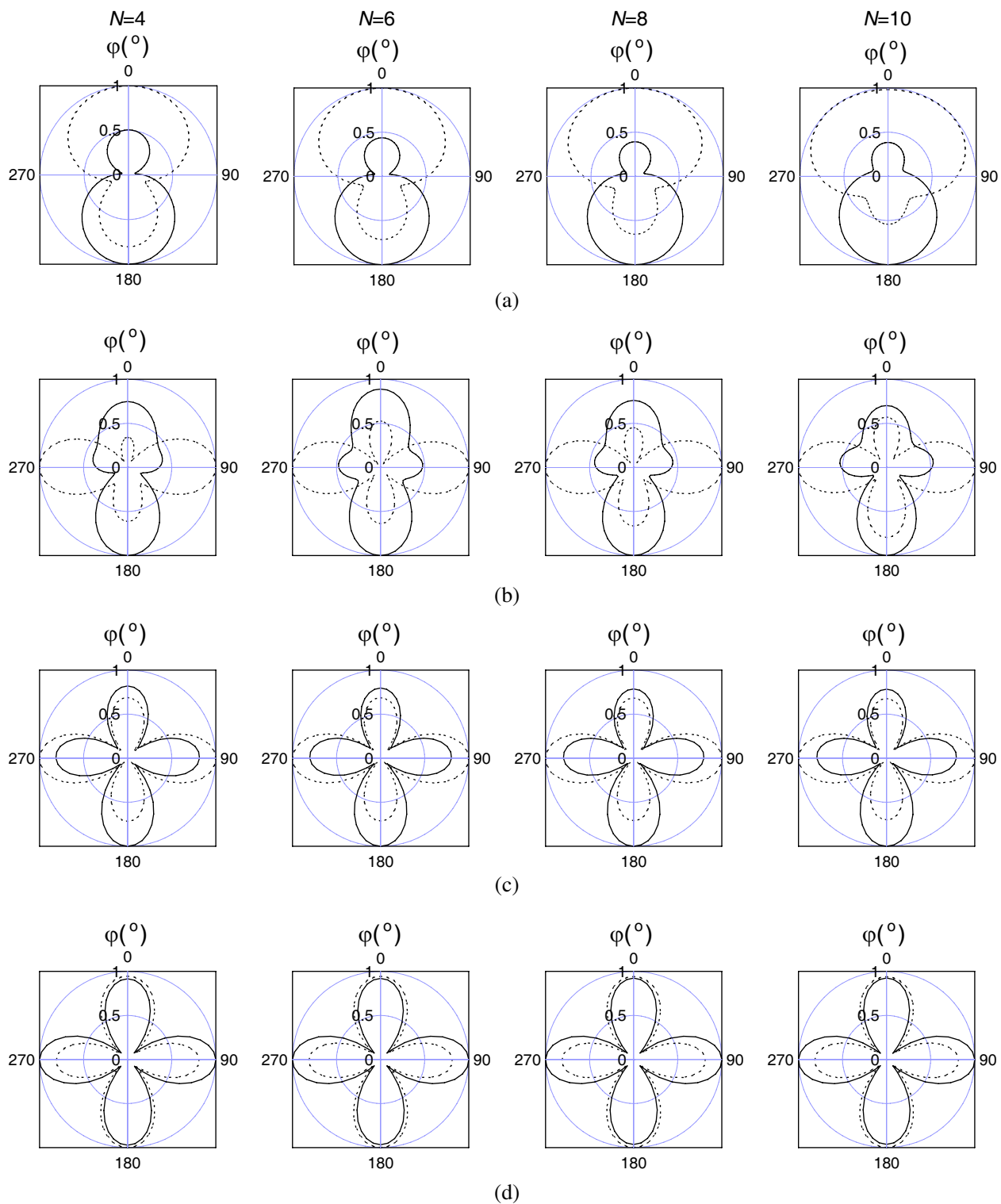
Figure 4: Electric field patterns on the azimuthal plane: ———: E_θ; - - - - - - -: E_φ. (a) $S_\lambda = 0.1$, (b) $S_\lambda = 1.0$, (c) $S_\lambda = 1.4$, (d) $S_\lambda = 1.8$.

are utilized: $0.1 \leq S_\lambda \leq 1.8$, $1.095 \leq C_\lambda \leq 2.145$, $5.2° \leq \alpha \leq 40°$, $N = 4, 6, 8$, and 10, operating frequency $= 3\,\mathrm{GHz}$, wire radius $(r_w) = 0.3\,\mathrm{mm}$ and the excitation voltage $= 1.0\,\mathrm{V}$.

4.1. Current Distributions

A cursory examination of Figure 3 clearly shows that the current profiles along the helical arm length are symmetrical about the feed-point which corresponds to the geometrical centre of the chiriex coil. It is also noticed that the maximum value of the magnitude of current distribution along the arm length is, to a large extent, independent of number of coil turns. Except for the scenario $S_\lambda = 1.0$ and $C_\lambda = \sqrt{3}$ that the current peaks occur at the feed-point regardless of the number of chireix coil turns, the other scenarios reported $S_\lambda = 0.1$, 1.4 and 1.8 are characterized by current peaks at or off the feed-point. In addition, for S_λ less than 1.0, the maximum value of current which is about $2.1\,\mathrm{mA}$ remains fairly unchanged irrespective of the number of coil turns. It is further observed that only the 4-turn coil enjoys steady increase in the current maximum as S_λ increases, other coil antennas (6-, 8- and 10-turn helices) have relatively constant maximum current of about $2.5\,\mathrm{mA}$, perhaps this observation may be attributed to substantial reflections from the open ends due to the shortness of the 4-turn coil. And characteristic of all the current distributions is the several undulations along the helical arm regardless of the number of coil turns, a consequence of reflections from the two open ends of the antenna. Finally, it is worth remarking that for helix of several turns mounted on a large ground plane, its current is typified by a travelling wave that decays exponentially towards the open end [1]. Next, the corresponding electric field patterns in the azimuthal plane generated by the current distributions of Figure 3 are given consideration.

4.2. Electric Fields

Although only the E_θ and E_φ patterns for $S_\lambda = 0.1$ are displayed in Figure 4(a), it is noted that for $S_\lambda < 1.0$, the radiation field (E_θ, E_φ) patterns on the azimuthal plane $(\theta = \pi/2)$ are characterized by two diametrically directed major lobes along $\varphi = 0°$ and $180°$ irrespective of the number of coil turns. However, when S_λ equals 1.0, the degeneration of the aforementioned two majors into four major lobes begins for the 4-, 6-, 8-, and 10-turn Chireix coils investigated here. Remarkably at S_λ greater than 1.4, the four lobes have been fully developed and distinct with relative maxima along $\varphi = 0°$, $90°$, $180°$ and $270°$ axes. In general, these radiation field pattern features seem to be independent of the number of Chiriex coil turns. Thus, the Chiriex coil antenna may enjoy practical applications where multilobed radiation patterns are desirable.

5. CONCLUDING REMARKS

Presented here is the method of moment solution of the electric field integral equation (EFIE) governing the Chiriex coil antenna problem. In the main, attention was focused on the current distributions and associated azimuthal plane radiation characteristics of the antenna. It is found that the maximum value of current distributed along the antenna axis is somewhat independent of the number of coil turns, and when turn spacing is 1.8 wavelengths, the E_θ and E_φ patterns are characterized by four distinct lobes with relative maxima along $\varphi = 0°$, $90°$, $180°$ and $270°$ axes, which suggest possible deployment of the coil antenna for multi-lobed radiation patterns applications.

REFERENCES

1. Nakano, H. and J. Yamauchi, "Radiation characteristics of helix antenna with parasitic elements," *Electronics Letters*, Vol. 16, No. 18, 687–688, 1980.
2. Kraus, J. D., *Antennas*, 2nd Edition, 265–339, McGraw-Hill, Inc., USA, 1988.
3. Chen, C. L., "Theory of the balanced helical wire antenna," *Radio Science*, Vol. 2, No. 2, 167–190, 1967.
4. Roy, M. N., "Investigations on normal mode helices," *Int. J. Electronics*, Vol. 26, No. 6, 573–578, 1969.
5. Martin, R. A. and D. H. Werner, "A reciprocity approach for calculating the far-field radiation patterns of a centre-fed helical microstrip antenna mounted on a dielectric-coated circular cylinder," *IEEE Trans. Ant. & Prog.*, Vol. 49, No. 12, 1754–1762, 2001.
6. Harrington, R. F., *Field Computation by Moment Methods*, 125, The Macmillian Book Company, New York, 1968.

A Frequency Reconfigurable PIFA Design for Wireless Communication Applications

S. C. Basaran and E. Dokuzlar

Department of Electrical-Electronics Engineering
Akdeniz University, Antalya 07058, Turkey

Abstract— A novel design of dual-band reconfigurable Planar Inverted F Antenna (PIFA) is proposed in the paper. Primary radiator of the antenna consists of concentric split-ring (SR)resonators and metallic loadings appropriately placed between the rings. The compact design fed by vertical probe provides two independent dual-band operations by means of an integrated switch inserted between the rings. Dual-band reconfigurable operation of antenna is studied and demonstrated for GPS at 1.575 GHz, DCS at 1.8 GHz, WiMAX at 3.5 GHz and WLAN at 5.2 GHz applications. Also, the proposed design exhibits uniform radiation patterns at the frequency band of interests. Analysis and design of the antenna is carried out Ansoft HFSS v.13.

1. INTRODUCTION

Reconfigurable antennas, with the ability to radiate more than one pattern at different frequencies and polarizations, are necessary in modern wireless telecommunication systems. Compared to conventional wideband antennas that can cover multiple communications bands, reconfigurable antennas have become an important and desired feature of modern, agile, radio-frequency systems for wireless communications, sensing, and imaging. In addition, they provide much needed agility to dynamically tune into sub-bands for improved noise, crosstalk, and jamming suppression without using external filters, thus also reducing the size, cost, and power requirements of wireless mobile devices. Thus, various types of reconfigurable antenna design have been proposed in the literature [1–4].

In this paper, we propose a novel frequency reconfigurable PIFA design based on printed split-ring elements. As it well known, PIFA is evolved from a quarter-wavelength monopole antenna and is now widely used in mobile and portable applications due to its simple design, lightweight, low cost, conformal nature, attractive radiation pattern, and reliable performance [5, 6]. On the other hand, split-ring resonators were introduced as the building blocks of metamaterial structures and they were utilized in various electrically small antenna designs [7–9] thanks to their resonant behavior. The proposed antenna in this study has typically PIFA structure and primary radiator of the antenna consists of two concentric split-ring resonators and six metallic loadings appropriately placed between the rings as depicted in Fig. 1. The antenna is fed by a current-probe placed in between the feeding plate and the ground plane in the simulations. In addition, a conductive switch standing for SW in Fig. 1, implemented as a small metallic pad in the numerical design, is integrated between a straight patch and inner split-ring element. The proposed design provides two independent dual-band performances depending on the switch being in ON or OFF states. When the switch is ON state, the antenna provides a dual-band performance at 1.8 GHz and 5.2 GHz. On the other hand, a dual band operation at 1.75 GHz and 3.65 GHz is achieved when the switch is OFF state. Analysis and design of the antenna is carried out by means of Ansoft HFFS v.13. Here, we present predicted return loss and radiation pattern/gain results for the proposed frequency reconfigurable antenna while the actual antenna performance is going to be discussed in the conference.

2. FREQUENCY RECONFIGURABLE SPLIT RING PIFA DESIGN

The proposed design with novel configuration is depicted in Fig. 1. As seen, the antenna is fabricated on the Rogers RO3006(tm) substrate with 0.64 mm thickness and dielectric constant of $\varepsilon_r = 6.15$. The radiating top plate consists of two concentric split-ring elements and six metallic loadings (s_1–s_6) appropriately placed between the rings. The antenna height is 10 mm, and the space between the top plate and the substrate is filled with air. The shorting plate has dimensions of 3 mm, and the feed plate has dimensions of 7 mm. The shorting plate is placed under the top corner of the top plate. The horizontal distance between shorting and feed plates is 22 mm. The proposed antenna is fed by a current-probe placed between the feeding plate and the ground plane in the simulations.
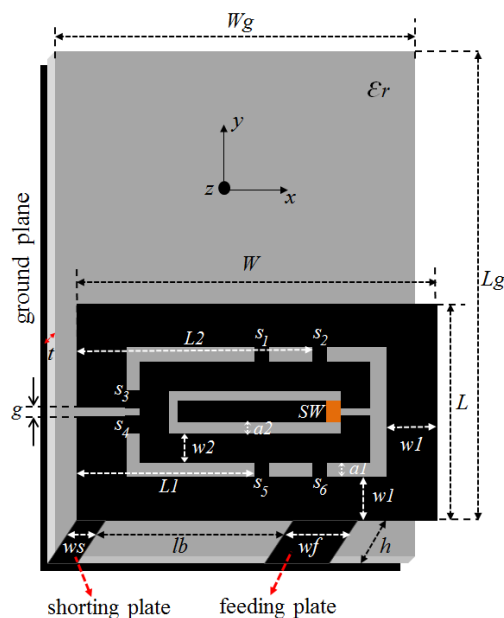
Figure 1: Configuration of proposed antenna with its design parameters: $W_g = 40$, $L_g = 60$, $W = 40$, $L = 20$, $w_1 = 4$, $w_2 = 3$, $w_s = 3$, $w_f = 7$, $lb = 22$, $a = 1$, $g = 1$, $h = 10$, $L1 = 22$, $L2 = 26$, $t = 0.64$, $S_1 - S_6 = 1 \times 1$ (all in mm), $\varepsilon_r = 6.15$.
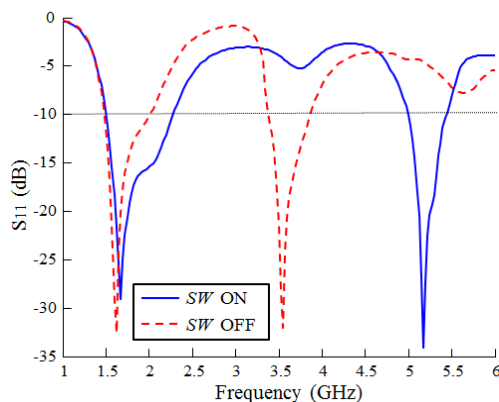
Figure 2: Return loss of the dual-mode SR-PIFA.

In addition, a conductive switch, implemented as a small metallic pad in the numerical design, is integrated into astraight patch and inner split-ring element.

Computed return loss characteristic of the proposed antenna is shown in Fig. 2 for the two states of the switch (SW). When the switch is in OFF state, a dual band operation at 1.75 GHz and 3.65 GHz with 28% and 18% bandwidths, respectively is achieved. On the other hand, the antenna provides a dual band performance at 1.85 GHZ and 5.2 GHz with 38% and 8% bandwidths, respectively when the switch is the ON state. Hence, the proposes antenna covers 1.575 GHz GPS/1.8 GHz DCS/5.2 GHz WLAN bands or 1.575 GHz GPS/3.5 GHz WiMAX bands depending on switch being in ON or OFF state, respectively.

The simulated radiation patterns on the y-z plane and x-y plane of the SR-PIFA design for OFF and ON statuses of the switch at 1.5 GHz, OFF state of the switch at 3.5 GHz and ON state of the switch at 5.2 GHz are shown in Figs. 3(a), (b), (c) and (d), respectively.As seen, the SR-PIFA exhibits relatively uniform radiation pattern at the desired frequency bands. Computed realized antenna gains of the antenna in the H-plane are also displayed in Fig. 4. As seen, when the switch is OFF state, the predicted gain at 1.5 GHz and 3.5 GHz are about 3 and 1 dBi, respectively. When the diode is ON state, the gain at the frequencies 1.5 GHz and 5.2 GHz are about 6 and 7 dBi, respectively
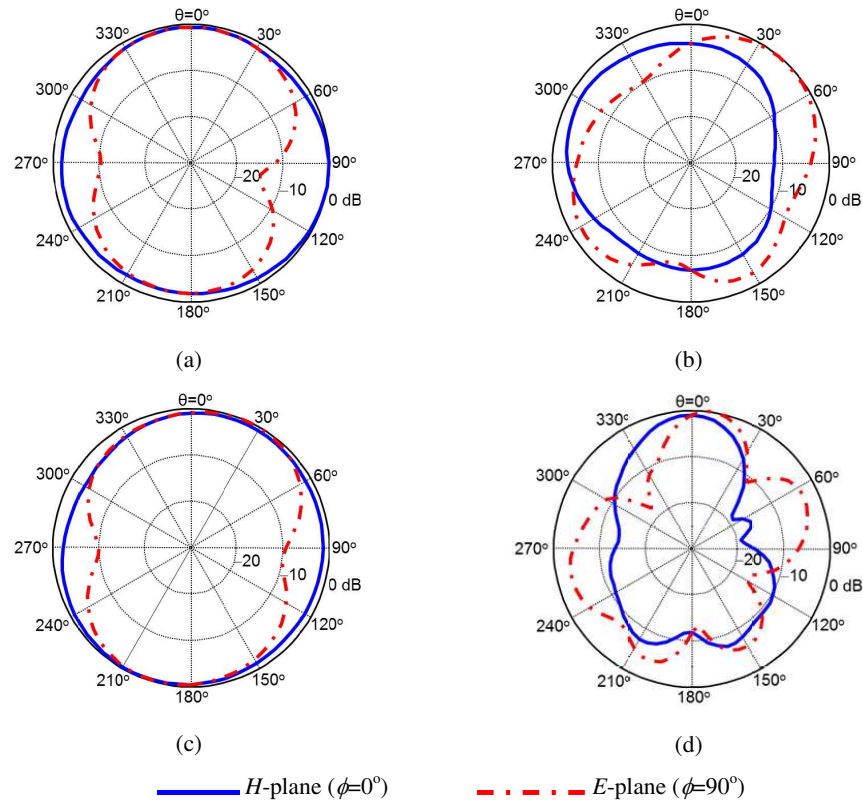
Figure 3: Radiation patterns of the proposed antenna. (a) $f = 1.5\,\text{GHz}$, switch OFF, (b) $f = 3.5\,\text{GHz}$, switch OFF, (c) $f = 1.5\,\text{GHz}$, switch ON, (d) $f = 5.2\,\text{GHz}$, switch ON.
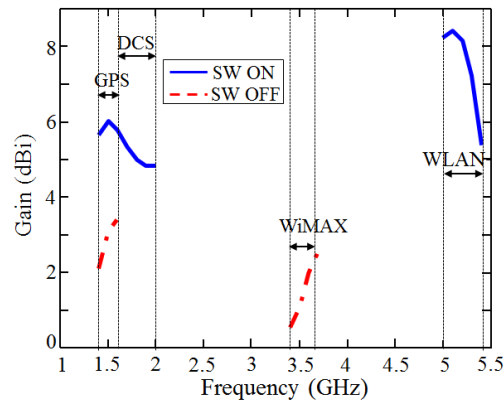
Figure 4: Predicted realized gain of the proposed antenna for frequency across.

3. CONCLUSION

We presented a novel frequency reconfigurable PIFA for wireless communication applications. In order to keep the antenna size small, two concentric split ring resonators are used as main radiator of the proposed antenna. The antenna provides either a dual band operation at $1.5/3.5\,\text{GHz}$ or dual-band coverage of the $1.5\,\text{GHz}$ and $5.2\,\text{GHz}$ bands by means of an integrated switch placed between one of the split ring elements and the microstrip line being between the inner rings. In addition, a good radiation pattern as well as gain performance is achieved for the frequency bands considered.

ACKNOWLEDGMENT

REFERENCES

1. White, C. R. and G. M. Rebeiz, "Single and dual-polarized tunable slot-ring antennas," *IEEE Trans. Antennas Propag.*, Vol. 57, No. 1, 19–26, Jan. 2009.
2. Chen, S.-H., J.-S. Row, and K.-L. Wong, "Reconfigurable square-ring patch antenna with pattern diversity," *IEEE Trans. Antennas Propag.*, Vol. 55, No. 2, 472–475, Feb. 2007.
3. Basaran, S. C. and K. Sertel, "Dual-band frequency reconfigurable monopole antenna for WLAN applications," *Microwave and Optical Technology Letters*, Vol. 57, No. 1 55–58, 2015.
4. Başaran, S. C., "Design of a frequency reconfigurable monopole antenna with complementary split ring resonators," *Microwave and Optical Technology Letters*, Vol. 56, No. 4, 977–979, 2014.
5. Kokkinos, T., E. Liakou, and A. P. Feresidis, "Decoupling antennaelements of PIFA arrays on handheld devices," *Electronics Letters*, Vol. 44, No. 25, 1442–1444, Dec. 2008.
6. Nepa, P., G. Manara, A. A. Serra, and G. Nenna, "Multiband PIFA for WLAN mobile terminals," *IEEE Antennas Wireless Propag. Lett.*, Vol. 4, 349–350, 2005.
7. Başaran, S. C. and K. Sertel, "Dual wideband CPW-fed split-ring monopole antenna with split-ring resonators," *Microwave and Optical Technology Letters*, Vol. 55, No. 9, 2088–2092, 2013.
8. Basaran, S. C., "Compact Dual-Band Split-Ring Antenna for 2.4/5.2 GHz WLAN Applications," *Turkish J. Elec. Engin. Comp. Sci.*, Vol. 20, No. 3, 347–352, 2012.
9. Basaran, S. C. and Y. E. Erdemli, "A dual-band split-ring monopole antenna for WLAN applications," *Microwave and Optical Technology Letters*, Vol. 51, No. 11, 2685–2688, 2009.

An Accurate Technique to Model the Substrate of Wearable Textile Antennas

Ghufran M. Hatem, **Ali J. Salim**, **and Jawad K. Ali**

Microwave Research Group, Department of Electrical Engineering, University of Technology, Iraq

Abstract— The utilization of wearable textiles in the antennas has shown a dramatic increase due to the recent challenges imposed on wireless devices to be miniaturized. For RFID purposes, a wearable antenna is meant to be a part of the clothing used. This includes tracking and navigation, mobile computing and public safety applications. Investigating the wearable textile antennas reported in the literature, it has been noted that when modeling the antenna using the commercially available EM simulators, the substrate (textile) has been dealt with as a solid homogenous material. This is fact is not the case, since the textile as a substrate is composed of woven threads (fibers). As a result, this adds some inaccuracy when comparing the simulated results with measured ones. In this paper, the textile antenna material, as a substrate, has been modeled in a way closer to the real practice. It has been modeled as horizontal and vertical fibers with different thread levels. A case study, representing a wearable textile antenna structure, has been investigated and the relevant textile material is being modeled using the proposed modeling technique. Simulation results of the antenna return loss responses using the proposed modeling technique; have shown to be more accurate than those obtained using the conventional modelling technique in that they are more close to measured results relevant to the antennas involved in the case study.

1. INTRODUCTION

Wearable and textile-based antennas have attracted more attention for the use in body-centric communications because of the ease to be integrated into clothes. The electromagnetic properties of the textiles play important roles in antenna design and performance [1]. This will include the adopted woven threads and the concentration of threads. The dielectric behaviour of textile materials are highly dependent on the properties of their contained fibers and polymers, and on fiber packing density in the fibrous materials. However, textiles fabrics are rough, porous and heterogeneous having air in between the fibers, making their characterization difficult [2].

Investigating the wearable textile antennas reported in the literature, it has been noted that when modeling the antenna using the commercially available EM simulators, the substrate (textile) has been dealt with as a solid homogenous material. This fact is not the case in the real practice, since the textile as a substrate is composed of woven threads (fibers). As the results, this adds some inaccuracy when comparing the simulated results with measured ones.

In this work simulated the textile material has been modeled and built as horizontal and vertical threads woven as textile with a suitable radius for each thread which will results in the electromagnetic features for the material. In order to make insure the efficiency of the proposed method for modeling the wearable antenna printed on a textile substrate, and because of the disability to make the measurement on the proposed antenna, use of the proposed antenna simulation technique has been applied to modeling one of the wearable textile antennas reported in literature.

2. THE PROPOSED TEXTILE MODELING

The proposed method for modeling the textile material of a wearable antenna is demonstrated in Figure 1, where a dual-band E-shaped textile antenna for wearable applications is depicted [3]. The substrate has been considered to be felt fabric for the antenna to offer dual-band resonant response. Figure 1(b) shows a magnified portion of the substrate in the form of textile. The magnified portion of the substrate reveals how the textile material has to be modeled using the commercially available Finite Integration Technique (FIT) based EM simulator, CST Microwave Studio (CST MWS) [4]. In addition to the woven vertical and horizontal threads that compose the textile material, there will be some air gaps thoroughly distributed amongst the threads.

The proposed modeling technique of the textile materials, as being prescribed, will add some reality to the modeling process in that the textile is composed of threads and air. Consequently, simulation results are expected to be more close to the measured ones as compared with those based on the conventional modeling of textile as a homogenous solid material.
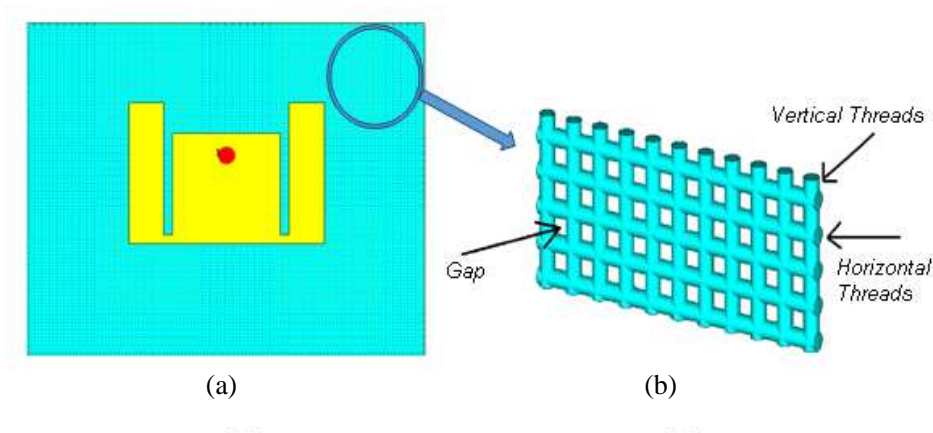
Figure 1: (a) The layout of the modeled antenna, and (b) a magnified portion of the modeled textile substrate material.
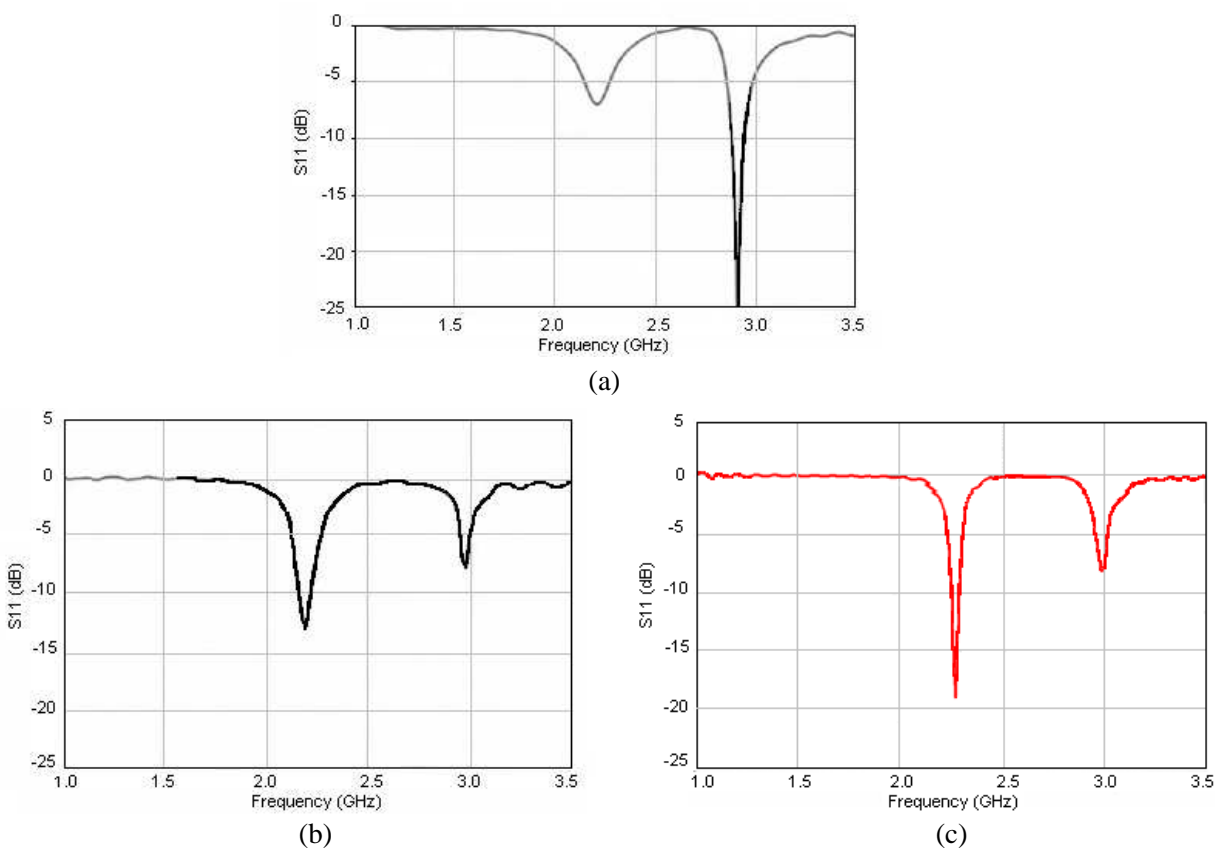
Figure 2: The modeled antenna performance: (a) simulated results using the conventional modeling technique, (b) measured results, and (c) simulated results using the proposed modeling technique.

This antenna has been simulated by a conventional method where the substrate is considered solid and homogenous material, as shown in Figure 2(a). Measured results of the antenna return loss are depicted in Figure 2(b). Simulation results of the antenna return loss, using the proposed textile modeling technique are shown in Figure 2(c).

3. VALIDATION OF THE PROPOSED METHOD

Figure 2 summarizes the adopted dual-band wearable antenna performance in terms of its input reflection coefficient. Simulated results using the conventional method are shown in Figure 2(a), while Figure 2(b) demonstrates the measured results of the fabricated prototype. Results depicted in Figure 2(c) represent the antenna performance as simulated using the proposed modeling tech-

nique. In an attempt of comparison, Table 1 presents the main features of the antenna performance in terms positions of the dual-band resonant frequencies and the relevant reflection coefficient levels. It is quite clear that simulated results using the proposed modeling technique are in better agreement with the measured one the those simulated using the conventional modeling technique in both the positions of the resonant bands and the corresponding reflection coefficient levels.

Table 1: Summary of the antenna performance evaluation.

Parameters	f_1 (GHz)	S_{11} (dB)	f_2 (GHz)	S_{11} (dB)
Measured [3]	2.23	-12.5	2.9	-7.5
Simulated [3]	2.20	-7.0	2.8	-25
Simulated (proposed)	2.24	-19.0	2.9	-8.5

4. CONCLUSIONS

In this paper, the substrate material of a wearable antenna has been modeled as horizontal and vertical threads woven as textile with suitable radii, in an attempt to obtain more accurate results as compared with the case where the textile material is considered as a solid homogenous material. The proposed technique has been applied to assess the performance of a fabricated antenna reported in the literature. Simulation results, using the proposed modeling technique, are found better than those obtained using the conventional method. The results using the presented technique are more close to the measured ones in both the positions of the resonant frequencies and the levels of the antenna input reflection coefficient. To gain more insight about the validity of the proposed modeling technique, it has to be justified in terms of the other antenna parameters such the antenna gain and radiation characteristic in addition to the input reflection coefficient.

REFERENCES

1. Lui, N., Y. Lu, S. Qui, and P. Li, "Electromagnetic properties of electro-textiles for wearable antennas applications," *Frontiers of Electrical and Electronics Engineering in China*, Vol. 6, 563–566, 2011.
2. Salvado, R., C. Loss, R. Gonçalves, and P. Pinho, "Textile materials for the design of wearable antennas: A survey," *Sensors*, Vol. 12, No. 11, 15841–15857, 2012.
3. Salonen, P., J. Kim, and Y. Rahmat-Samii, "Dual-band E-shaped patch wearable textile antenna," *IEEE Antennas and Propagation Society International Symposium*, Vol. 1A, 466–469, 2005.
4. CST, Available Online: www.cst.com.

A CMOS I/Q Up-conversion Mixer and a Power Pre-amplifier for UHF RFID Reader Systems

C. C. Zhang[1,2], **L. S. Gao**[1,2], **C. H. Dong**[1,2], **Y. F. Guo**[1,2],
D. B. Wang[1,2], **and Y. Zhang**[1,2]

[1]Jiangsu Provincial Engineering Laboratory of RF Integration and Micro-assembly
Nanjing University of Posts and Telecommunications, Nanjing 210023, China
[2]College of Electronics Science & Engineering
Nanjing University of Posts and Telecommunications, Nanjing 210023, China

Abstract— A high gain, high linearity, low noise I/Q up-conversion mixer and a programmable gain power pre-amplifier are designed in a standard $0.18\,\mu m$ CMOS process, which are both the critical building blocks in a transmitter for UHF RFID reader systems. To comply with the system specifications, both low noise figure (NF) and high LO-IF isolation for the up-conversion mixer are required, so the I/Q mixer topology based on two coupled double-balanced Gilbert cells is applied. Besides, other techniques such as the pseudo-differential structure and the active load are also used to improve its linearity, gain, etc.. As for the power pre-amplifier, a programmable gain fully differential cascode configuration is employed to satisfy the emission spectrum requirements from various application environments. A 3-bit control word is used to switch the three parallel trans-conductance transistors in each side to change the output power flexibly. And the source inductance negative feedback technique is adopted to achieve a good trade-off among noise matching, impedance matching, linearity and gain. From a single $1.8\,V$ power supply, simulation results show that the up-conversion mixer has a total conversion gain of $4\,dB$, an input 1 dB compression point (IP1 dB) of $4.84\,dBm$, and an input NF of less than $20.9\,dB$. The power pre-amplifier has an output 1 dB compression point (OP1 dB) of better than $2.8\,dBm$, a gain of above $7\,dB$, and a good input impedance matching.

1. INTRODUCTION

UHF radio frequency identification (RFID) is a remote auto-identification technology with many advantages such as a relatively long recognition range, anti-collision characteristics for multi-tag scenarios, a high data rate and a small antenna size [1]. Nowadays, UHF RFID reader is evolving towards miniaturization and low cost with integration in CMOS technology.

For the transmitter of the RFID reader, which is shown in Figure 1, one of the most important building blocks is the up-conversion mixer, which converts the base-band signal to an RF signal mostly based on a double sideband (DSB) up-conversion. In view of this, it should have high linearity and low NF to comply with the specifications of the UHF RFID communication standard [2–5]. Besides, a programmable gain power pre-amplifier (PA) is designed after the mixer to match the reader, which can change the output power of the pre-amplifier flexibly.

Different DC and AC signals can be combined in the quadrature two I/Q circuits of the RF transmitter. In addition, different modulation according to protocol requirements of the system can be achieved through digital baseband filter.

To date, several excellent CMOS up-conversion mixers have been reported [6–8]. For example, in [6], a 1.9 GHz high linearity up-conversion mixer was designed. Though the IP1 dB of 0 dBm is achieved, its 19.8 mW power consumption and $0.35\,\mu m$ process are not good enough. In [7], a 2.4 GHz up-conversion mixer on wireless sensor networks SoC chip was demonstrated. In spite of
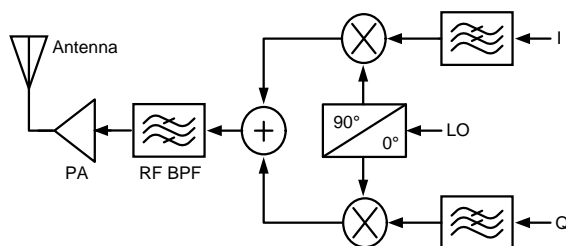
Figure 1: Architecture diagram of the up-conversion transmitter system.

the power consumption of $5.4\,\text{mW}$ achieved in $0.18\,\mu\text{m}$ process, its IP1 dB of $-4.6\,\text{dBm}$ is not good enough. In [8], a CMOS up-conversion mixer with adaptive bias circuit for UHF RFID reader was demonstrated. Although the IP1 dB of $9\,\text{dBm}$ is achieved, the CG of $-3.7\,\text{dB}$ is not good enough. In view of the disadvantages of the above design, a high gain, high linearity, low power and excellent LO-IF isolation quadrature up-conversion mixer is designed in the paper. And a programmable gain power pre-amplifier is designed to match the UHF RFID reader systems simultaneously.

2. CIRCUIT DESIGN AND ANALYSIS

2.1. Up-conversion Mixer

As we all know, the key part to improve the linearity of the circuit is the trans-conductance stage. The Pseudo Differential Trans-conductance (PDT) stage can increase the output swing of the mixer [9]. Therefore, the PDT is picked out as the trans-conductance stage of the mixer. In this case, linearity of the mixer can achieve the optimization to the maximum extent, for that the nonlinearity introduced by the trans-conductance can be neglected.

The mixer includes an output load stage, a switching stage, a trans-conductance stage and a resistance stage in the paper, as is shown in Figure 2. In the circuit, transistors M1–M4 and resistors R1–R4 are composed of the PDT to increase the linearity. And the input voltage is converted to a small signal current by trans-conductors M1–M4. Then this current is switched in the role of local oscillation signals by switches M5–M12, which can reduce the low-frequency flicker noise injection of active mixer. As the active output load, the transistors M13–M14 and resistors R5–R6 can ensure the necessary CG as well as a suitable output voltage level.

In the positive half cycle of the LO signal, the switching stage M5, M6 and M11, M12 are conducted, M7, M8 and M9, M10 are disconnected, then the IF output signal voltage is gmvRFRL. While the negative half exactly appears the opposite state, the IF output of -gmvRFRL is obtained. Therefore, the CG of the mixer is given by

$$\text{CG} = \frac{2}{\pi} g_m R_L \tag{1}$$

In fact, two single-balanced mixers are connected in anti-parallel, so the LO voltage in the output is zero, so as to solve the problem of LO-IF port isolation. The output single current is given by Eq. (2).

$$I_{\text{mixer}} = I_{C1} \cdot \tanh\left(\frac{v_{\text{LO}}}{2V_T}\right) - I_{C2} \cdot \tanh\left(\frac{v_{\text{LO}}}{2V_T}\right) \tag{2}$$

Furthermore, in a common mixer, there is a voltage fluctuation with a frequency of $2\omega\text{LO}$ in the drain of tube M1M2, and the voltage fluctuation can leak to the IF input through the parasitic capacitance between the gate and the drain of tube M1M2. But in the circuit configuration in this paper, the voltage fluctuation becomes common mode interference signal of the IF input for the symmetry between M1, M2 and M3, M4, and therefore can also be suppressed.

2.2. Power Pre-amplifier

Figure 3 shows the schematic diagram of the programmable gain power pre-amplifier. In order to achieve the output P1 dB point of $0\,\text{dB}$ to satisfy the emission spectrum of dense and multi-
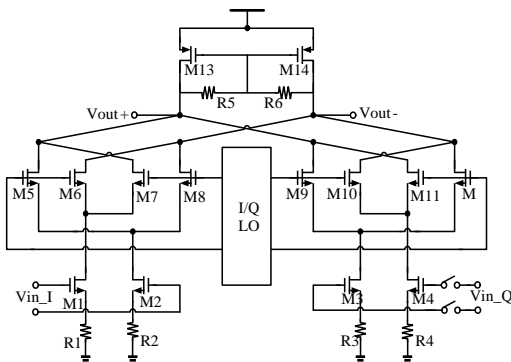
Figure 2: Schematic diagram of the up-conversion mixer.
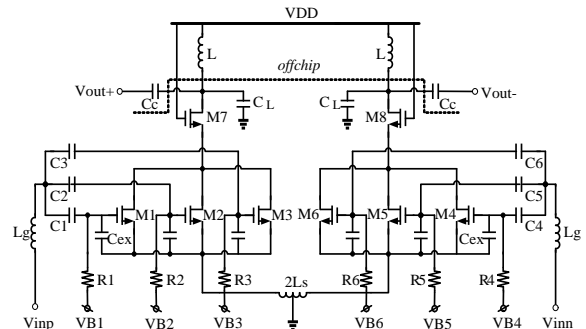
Figure 3: Schematic diagram of the power pre-amplifier.

reader systems, the programmable gain fully differential cascode circuit is chosen for the power pre-amplifier. The circuit can be divided into two stages: the common-source amplifier with inductance negative feedback circuit and the common-gate amplifier.

As the circuit is completely symmetrical, any half to be analyzed is enough. As input tubes, M1–M3 are all controlled by a digital circuit, which is connected in parallel. In order to achieve the simultaneous match between input impedance and the noise, circuit uses source inductance LS negative feedback technology. However, if the inductance value is excessive, the CG of the pre-amplifier will be reduced. Therefore, there is a tradeoff between the CG and the circuit match. Then, the input impedance of the half circuit can be expressed as Eq. (3)

$$Z_{\text{in,single}} = s\left(L_g + L_s\right) + \frac{1}{sC_{\text{gs}}} + \omega_T L_s \tag{3}$$

M7 as a second stage can reduce the interaction between the input and output terminal of the pre-amplifier as well as the influence of the Miller effect. At the same time, the output terminal uses the off-chip inductor as the load.

In real applications, the distance between the tag and reader is always changing, thence the input terminal use three amplifier input NMOS transistors connected in parallel. When 3 bit digital control switch turned on, the CG of the pre-amplifier can be expressed as Eq. (4)

$$A = (g_{\text{m1}} + g_{\text{m2}} + g_{\text{m3}}) \cdot Q_{\text{in}} \cdot R_{\text{out}} \tag{4}$$

where Q_{in} is quality factor of the input resonant network, and Rout is equivalent output impedance of the pre-amplifier.

3. SIMULATION RESULTS

3.1. Up-conversion Mixer

The quadrature up-conversion mixer is designed and simulated in a standard $0.18\,\mu\text{m}$ RF CMOS process. The supply voltage is $1.8\,\text{V}$. Figure 4 shows the CG, IP1 dB, NF and DSB-ASK modulation of the mixer, respectively.

As is seen in Figure 4(a), the amplitude of the mixer is $-14.01\,\text{dB}$ when the fundamental frequency is $10\,\text{MHz}$. After the conversion, at the center frequency of $910\,\text{MHz}$, the amplitude is $-10.07\,\text{dB}$, so the total CG is $4\,\text{dB}$. The power amplifier stage to reduce the difficulty of the design can be seen from Figure 4(b), the IP1 dB of the mixer is $4.84\,\text{dBm}$. That means the circuit has a good linearity. When comes to Figure 4(c), input NF is less than $20.9\,\text{dB}$, while Figure 4(d) shows the DSB-ASK output waveform modulation of the mixer. And Table 1 shows the total simulation results of the proposed mixer.

3.2. Power Pre-amplifier

The power pre-amplifier is also designed in a standard $0.18\,\mu\text{m}$ process and simulated. Figure 5 shows the match characteristic between input and output terminal, transmission characteristic, NF and output linearity of the power amplifier under different conditions of the gain settings, respectively.

As is seen in the figures, the simulation results show that the worst output linearity OP1 dB is better than $2.8\,\text{dBm}$ when the power amplifier has a gain of $7\,\text{dB}$, and a match characteristic of $50\,\Omega$.

Table 1: Simulation results of the mixer.

Parameters	Simulation Results	Units
Operating Voltage	1.80	V
Input IF Frequency	35.452	MHz
Output RF Frequency	150~950	MHz
Consumed Current	29.49 (core current: 7.54)	mA
Conversion Gain	3.94	dB
Noise Figure	20.9	dB
Input $P_{1\,\text{dB}}$ point	4.84	dBm

(a)   (b)

(c)   (d)
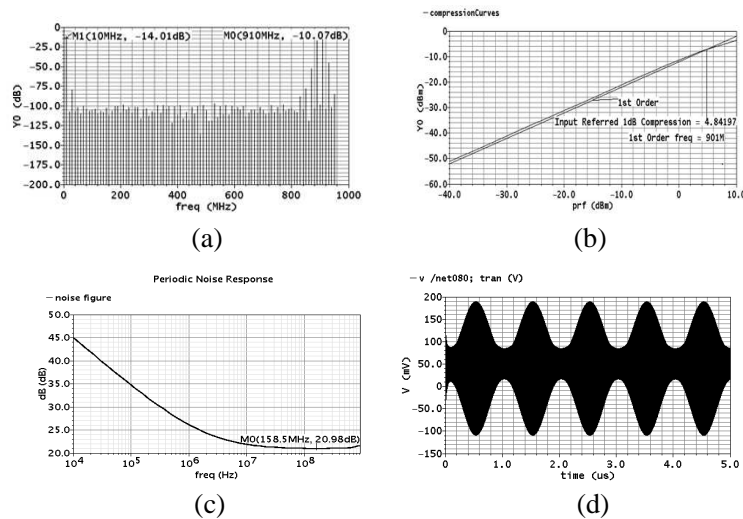
Figure 4: Simulated results of the mixer (a) CG, (b) IP$_{1\,dB}$, (c) NF, and (d) DSB-ASK modulation.

(a)   (b)

(c)
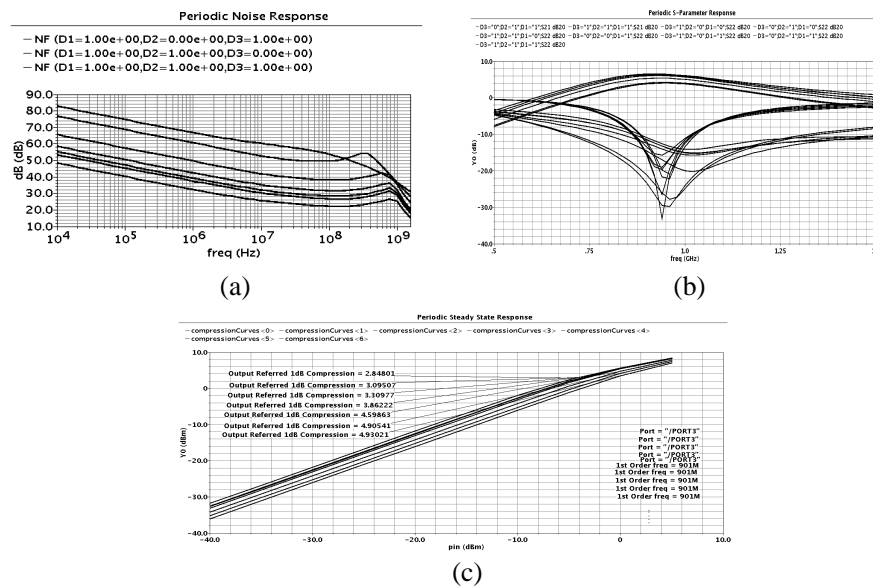
Figure 5: Simulated results of the power pre-amplifier, (a) noise factor, (b) transmission and match characteristics, and (c) output linearity.

4. CONCLUSIONS

A high performance quadrature up-conversion mixer along with a programmable gain power pre-amplifier for the RF front-end transmitter of UHF RFID reader system are designed in 0.18 μm CMOS process. Considering the stringent requirements of the system, Gilbert double-balanced circuit configuration is picked out for the mixer. In addition, in order to satisfy the emission spectrum of dense and multi-reader system, the programmable gain fully differential cascade circuit configuration is applied to the power pre-amplifier. Simulation results show that they can meet the requirement of the UHF RFID reader system.

REFERENCES

1. "EPC UHf radio frequency identity protocols: Class 1 Generation 2 UHF RFID," Ver. 1.2.0, EPC Global, 2007.
2. "EPCTM radio-frequency identity protocols Class-1 Generation-2 UHF RFID protocol for communications at 860 MHz–960 MHz," EPC, Sep. 2004.
3. Maas, S., "Mixer technologies for modern microwave and wireless systems," *IEEE Gallium Arsenide Applications Symp., Dig.*, 23–27, Sep. 2002.
4. Terrovitis, M. T. and R. G. Meyer, "Noise in current commutating CMOS mixers," *IEEE J. Solid-State Circuits*, Vol. 34, No. 6, 772–783, Jun. 1999.
5. Zhang, F., E. Skasidas, W. Shieh, et al., "A 60-GHz double-balanced mixer for direct up-conversion transmitter on 130-nm CMOS," *IEEE Compound Semiconductor Integrated Circuits Symp.*, 1–4, Monterey, CA, 2008.
6. Xi, Z. G., Y. J. Qin, Y. F. Su, et al., "A 1.9 GHz high linearity up-conversion mixer," *Research & Progress of Solid State Electronics*, 49–53, 2007.
7. Zhang, L. and X. N. Fan, "A 2.4 GHz up-conversion mixer on wireless sensor networks SoC ship," *Electronic Devices*, 361–363, 2009.
8. Cho, K., M. Kim, H. C. Kim, et al., "CMOS up-conversion mixer with adaptive bias circuit for UHF RFID reader," *IEEE Int. Sym. on Radio-Frequency Identification Technology*, 20–23, 2009.
9. Chi, B. Y., Z. P. Yu, and B. X. Shi, *Analysis and Design of CMOS RFIC*, Tsinghua University Press, Beijing, China, 2006.

A UHF RFID Reader Receiver SoC in 0.18 μm CMOS Technology

C. C. Zhang[1, 2], **Y. Q. Qian**[1, 2], **J. Zhao**[1, 2], **Y. Zhang**[1, 2], **D. B. Wang**[1, 2], and **Y. F. Guo**[1, 2]

[1]Jiangsu Provincial Engineering Laboratory of RF Integration and Micro-assembly
Nanjing University of Posts and Telecommunications, Nanjing 210023, China
[2]College of Electronics Science & Engineering
Nanjing University of Posts and Telecommunications, Nanjing 210023, China

Abstract— A fully-integrated single-chip receiver for an 860–960 MHz UHF RFID reader is designed in 0.18 μm CMOS technology. It is mainly composed of an RF front-end, a DC offset cancellation (DCOC) block, and an analogue baseband. The RF front-end consists of a double-mode low noise amplifier (LNA) and an I/Q mixer. The LNA can operate under two different modes, which correspond to the listen-before-talk (LBT) mode and the normal mode specified by UHF RFID protocols, respectively. The common-gate structure and the dynamic current injection technique are used for the mixer to achieve high linearity and low 1/f noise. The analogue baseband comprises a programmable gain amplifier (PGA) and a low-pass filter (LPF). The opamp-based PGA is composed of a fine gain stage with a gain step of 1 dB, and a coarse gain stage with three fixed gain, corresponding to 6 dB, 12 dB and 24 dB, respectively. The LPF is a fourth-order Butterworth active RC one, whose bandwidth can be adjusted between 480 kHz and 1.68 MHz. Simulation results show that the receiver achieves $P_{1\,\mathrm{dB}}$ of -2.1 dB in LBT mode and sensitivity of -88 dBm in normal mode, with power dissipation of 95.72 mW from a 1.8 V power supply.

1. INTRODUCTION

Radio frequency identification (RFID) techniques have found rapidly-growing applications in many areas, such as supply chain managements and object tracking systems, which present diverse and demanding needs for application-specific and sophisticated design techniques [1]. The direct-conversion architecture along with standard CMOS technologies is widely preferred for RF readers among various solutions because of the reducing cost and improving integration level [2]. As for a UHF RFID system, one of the most challenging issues within the reader receiver design is to make a proper tradeoff between linearity and noise figure [3].

In this paper, a fully-integrated 860∼960 MHz CMOS RFID reader receiver system on a chip (SoC) is presented in 0.18 μm CMOS technology. The simulated $P_{1\,\mathrm{dB}}$ is -2.1 dB in the listen-before-talk (LBT) mode, and the simulated sensitivity is -88 dBm in normal mode. Compared with the previous works in standard 0.18 μm CMOS technology [1–3], this receiver shows high linearity with similar gain and power consumption.

2. RECEIVER ARCHITECTURE

The highly-integrated direct-conversion receiver architecture is employed for the RFID reader receiver, shown in Fig. 1. The receiver consists mainly of an RF front-end, an analogue baseband, and a DC offset cancellation (DCOC) bock. The RF front-end comprises a low noise amplifier (LNA) and a I/Q down-conversion mixer. The analog baseband is composed of baseband programmable gain amplifiers (PGA), and low pass filters (LPF). Due to its many advantages over a single-ended one, the fully-differential topology is applied here.

The LNA is designed specifically to improve sensitivity in the listen-before-talk (LBT) mode, and in the meanwhile, to achieve high linearity in the normal mode. And then, the amplified RF signal is fed into the I/Q mixer, by which it is demodulated to produce two I/Q baseband signals. The local I/Q clocks are generated by an external frequency synthesizer.

Owing to the diversified application environments, the amplitude of the RF signal coming to the antenna before the receiver varies largely. The PGA is aimed to amplify adaptively the incoming analog signal to one with a proper amplitude level for the downstream analog-digital converter (ADC). The LPF is used to filter out out-of-band noises to improve the signal-to-noise ratio (SNR) of the signal which will come into the ADC. The LPF is also programmable to accommodate different transmission data rates.

It's well known that the DC offset issue is one of the trickiest issues, which, as for a UHF RFID receiver, becomes more complicated, because both transmitter and receiver operate on a

same frequency. In order to overcome the DC offset issue, a DCOC block is inserted between the RF front-end and the analog baseband.
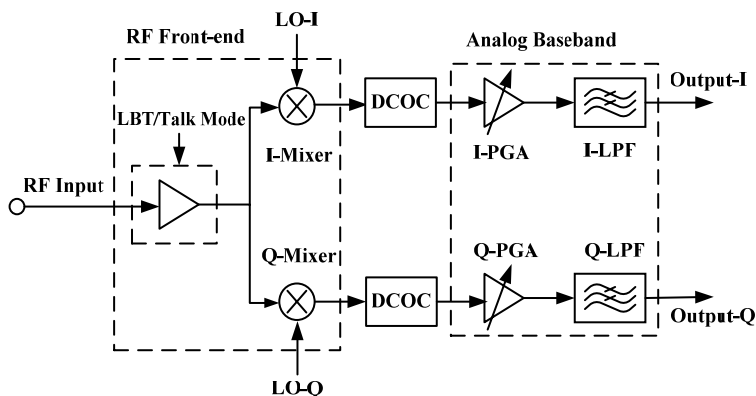
Figure 1: Block diagram of the UHF RFID reader receiver architecture.

3. KEY BUILDING BLOCKS

3.1. Low Noise Amplifier

According to the LNA shown in Fig. 2, by changing the bias voltage Vb2, the MOS transistors M1 and M2 can operate in two different regions. Usually, M1 and M2 operate in saturation region, and then the LNA has higher gain, which is fit for the normal mode. However, if Vb2 is set to a higher voltage, M1 and M2 can operate in triode region, and then the LNA has higher linearity, which is fit for the LBT mode.

The introduction of the coupling capacitors (C3 and C4) will improve both gain and noise performance of the LNA [4]. The tradeoff among impedance matching, gain, noise and linearity is made carefully when the optimization is executed.

3.2. Down-conversion Mixer

Indicated in Fig. 3, the common-gate structure and the dynamic current injection technique are used for the mixer to achieve high linearity and low 1/f noise.

Compared to the traditional Gilbert mixer, the common-gate configuration of input stage (M1-M2) will provide more voltage headroom for the pre-stage driver, and also higher linearity can be obtained for the mixer. The dynamic current injection technique used in the switching stage injects current when nearly all of the transistors are turned on, which can greatly reduce 1/f noise while white noise performance are almost unaffected.

Two mixers shown in Fig. 3 can comprise an I/Q mixer, when two I/Q local clocks are provided for the two mixers, respectively.
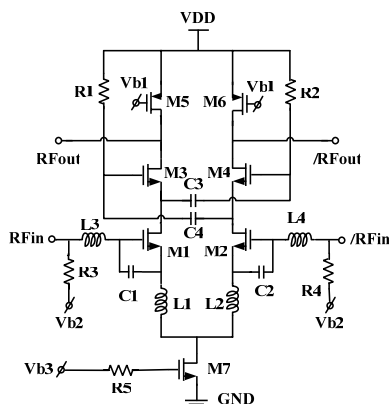
Figure 2: Schematic diagram of the LNA.
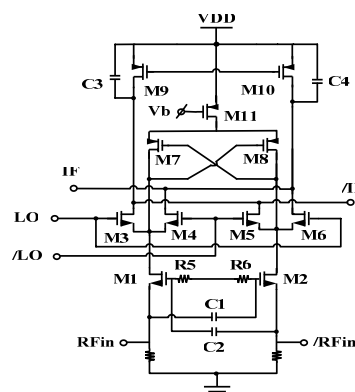
Figure 3: Schematic diagram of the mixer.

3.3. DC Offset Cancellation Block

A DC offset cancellation (DCOC) block, shown in Fig. 4, is applied after the output of the mixer to remove the annoying DC offset. The pre-amplifier has a gain of 10 dB to suppress the noise afterwards.
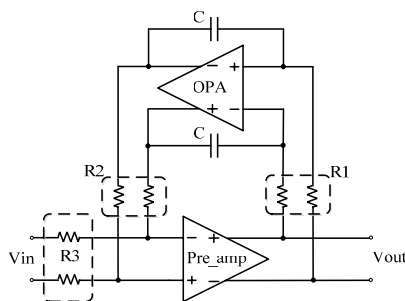
Figure 4: Topology diagram for the DC offset cancellation (DCOC).
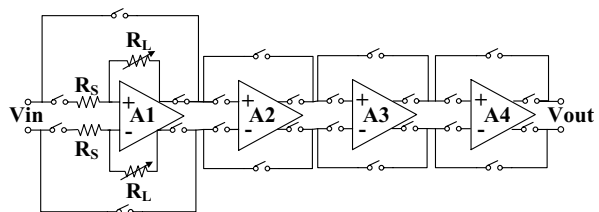
Figure 5: Illustration diagram for the PGA.

3.4. Programmable Gain Amplifier

The PGA is depicted in Fig. 5. The opamp-based PGA is used for good linearity performance. The operational amplifier A1 has a maximum gain of 6 dB, which can tuned in gain step of 1 dB by the resistance ratio of variable resistor arrays R_L and R_S. The fixed-gain amplifiers A2-A4, all adopting the source negative feedback technique to improve their linearity performance, have gains of 24 dB, 12 dB and 6 dB, respectively.

3.5. Programmable Baseband Filter

The baseband low-pass filter is used as a channel selection filter to reject out-of-band interferers and noise. The filter is illustrated in Fig. 6, which is a fourth-order Butterworth active-RC differential one.
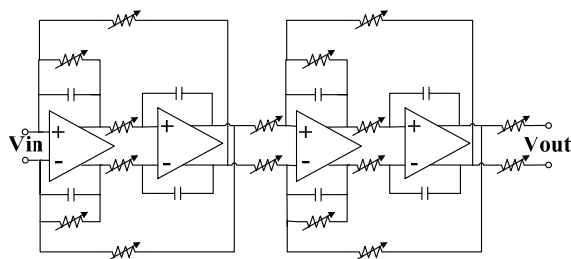
Figure 6: Illustration diagram for the programmable LPF.

In order to meet the channel bandwidth requirements from the UHF RFID direct conversion receiver, the cutoff frequency, that is, the bandwidth of the LPF is adjustable between 480 kHz ∼ 1.68 MHz, by controlling the relevant resistor sizes. The design scheme allows the receiver to accommodate a variety of different transmission rates from 40 kb/s to 640 kb/s, and adapt to the LBT mode and normal mode respectively.

4. SIMULATION RESULTS

The simulated $P_{1\,dB}$ of the proposed RF front-end in the normal mode is shown in Fig. 7 (a). It could be seen from this figure that the $P_{1\,dB}$ is as high as -2.1 dBm. Fig. 7(b) shows the noise figure characteristic of the LBT mode. The NF characteristic achieves 11.8 dB at 900 MHz.

Figure 8 depicts the measured gain error of the PGA and the channel select characteristics of the LPF. The gain control range is from 0 dB to 48 dB in a step of 3 dB and the maximum gain error is less than 0.9 dB as shown in Fig. 9(a). The frequency response characteristic is shown in Fig. 9(b). The cut-off frequency is 489 kHz, 595 kHz, 696 kHz, 910 kHz, 1.09 MHz, 1.61 MHz adjustable. The out-of-band rejection achieves 50 dB.

(a)   (b)
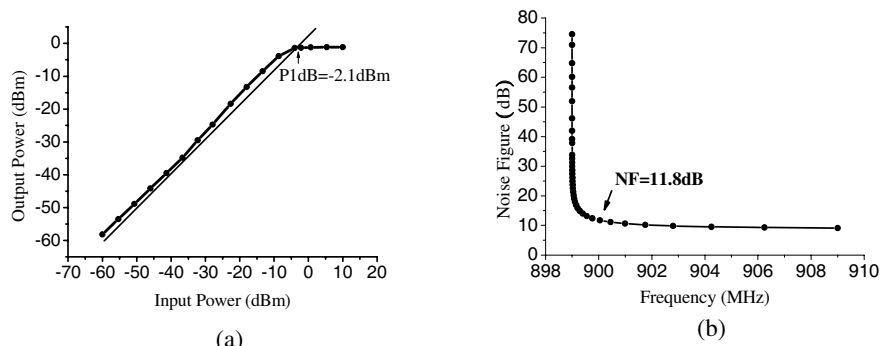
Figure 7: Simulated results of RF front-end (a) $P_{1\,\mathrm{dB}}$ in the normal mode (b) noise figure in the LBT mode.

(a)   (b)
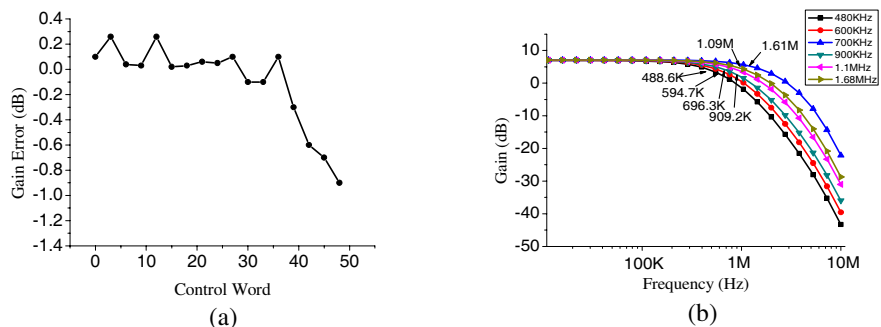
Figure 8: Simulated results of (a) PGA gain error (b) LPF frequency response.

The major chip performance is summarized in Table 1. The sensitivity of the receiver could achieve $-88\,\mathrm{dBm}$ with the bandwidth of $1\,\mathrm{MHz}$ in the normal mode. When working in the LBT mode, the sensitivity of the receiver improves. The comparison between state-of-the-art works and this work is given in Table 2, in which all the works are designed in $0.18\,\mu\mathrm{m}$ CMOS technology.

Table 1: Summary of receiver performance.

Parameters	Simulated Results	
	Normal	LBT
Operation Frequency	860–960 MHz	
$P_{1\,\mathrm{dB}}$(RF front-end)	$-2.1\,\mathrm{dB}$	$-9.8\,\mathrm{dB}$
Gain(RF front-end)	3 dB	12 dB
Sensitivity	$-77\,\mathrm{dBm}$	$-88\,\mathrm{dBm}$
Gain Range	3–51 dB	12–60 dB
Power Consumption	95.72 mW	
Supply Voltage	1.8 V	

Table 2: Comparison with state-of-the-art works.

Parameter		[1]	[2]	[3]	This Work
$\mathbf{P_{1\,dB}}$	Normal	3.5 dBm	$-8\,\mathrm{dBm}$	7 dBm	$-2.1\,\mathrm{dB}$
(RF front-end)	LBT	$-9.4\,\mathrm{dBm}$	NA	$-7\,\mathrm{dBm}$	$-9.8\,\mathrm{dB}$
Sensitivity	Normal	$-70\,\mathrm{dBm}$	NA	$-77\,\mathrm{dBm}$	$-77\,\mathrm{dBm}$
(RF front-end)	LBT	$-90\,\mathrm{dBm}$	$-81\,\mathrm{dBm}$	$-87\,\mathrm{dBm}$	$-88\,\mathrm{dBm}$
Gain Range		10 dB–94 dB	3.6 dB–86.5 dB	NA	3 dB–60 dB
Power	Normal	105.6 mW	135 mW	74 mW	95.72 mW
Consumption	LBT			122 mW	

5. CONCLUSIONS

A direct-conversion receiver has been designed for a UHF RFID reader. The double-mode RF front-end achieves high linearity in normal mode and high sensitivity in LBT mode. The bandwidth of the LPF and the gain of PGA are programmable. Simulations of the receiver are done with a standard $0.18\,\mu$m CMOS technology in CADENCE.

ACKNOWLEDGMENT

REFERENCES

1. Wang, W., S. Lou, K. Chui, et al., "Single-chip UHF RFID reader in 0.18- μm CMOS," *IEEE Custom Integrated Circuits Conference*, 111–114, 2007.
2. Ye, L., H. Liao, F. Song, et al., "A 900 MHz UHF RFID reader transceiver in 0.18 μm CMOS technology," *IEEE 9th International Conference on Solid-State and Integrated-Circuit Technology*, 1569–1572, 2008.
3. Sun, X., B. Chi, C. Zhang, et al., "A 1.8 V 74 mW UHF RFID reader receiver with 18.5 dBm IIP3 and −77 dBm sensitivity in 0.18 μm CMOS," *Radio Frequency Integrated Circuits Symposium*, 597–600, 2010.
4. Koo, K., et al., "Noise figure degradation analysis of power ground noise on 900 MHz LNA for UHF RFID," *IEEE Electronics Packaging Technology Conference*, 416–420, Singapore, 2007.
5. Kwon, I., Y. Eo, H. Bang, et al., "A single-chip CMOS transceiver for UHF mobile RFID reader," *IEEE Journal of Solid-State Circuits*, Vol. 43, No. 3, 729–738, 2008.

Compact Substrate Integrated Waveguide BPF for Wideband Communication Applications

Aya N. Alkhafaji[1], Ali J. Salim[2], and Jawad K. Ali[2]

[1]Department of Electrical Engineering, University of Technology, Baghdad, Iraq
[2]Microwave Research Group, Department of Electrical Engineering
University of Technology, Baghdad, Iraq

Abstract— A new compact substrate integrated waveguide (SIW) bandpass filter (BPF) is presented in this paper as a candidate for use in wide bandwidth X-band applications. The proposed filter is constructed by embedding two semi-circular slots have been in the SIW structure from the input and the output sides. The simulation and performance evaluation of the proposed filter have been carried out using Microwave Studio Suite of Computer Simulation Technology CST. A parametric study reveals that the insertion of these slots has successfully led to the compact size and the wide bandwidth. The cavity dimensions are $13.6 \times 10.6 \, \text{mm}^2$ while the overall filter dimensions are $28.5 \times 16 \, \text{mm}^2$ using a substrate with relative permittivity of 2.2 and thickness of 0.245 mm. The resulting filter exhibits a return loss less than $-15 \, \text{dB}$ and insertion loss approaching to 0 dB over the passband. The proposed filter offers a $-3 \, \text{dB}$ fractional bandwidth of about 68.4% centered at 11.7 GHz. The compact size offered by this filter makes it a suitable for use in designing microwave and millimeter-wave circuits.

1. INTRODUCTION

The features that characterize the waveguide, which is the possibility of dealing with handling high power capacity, high quality factor and a few losses, but this does not enough to make waveguides familiar in planar devices environment due to their large size, difficulty of manufacturing and the difficulty of compatibility with integrated applications that are widely spread and have become popular in wireless applications. On the contrary, we find that the planar structures characterized by their small size and ease of manufacturing and ease of compatibility with integrated circuits and other tools. However, we still encounter the difficulty of dealing with high capacity and high losses. The introduction of the substrate integrated waveguide, SIW, represents a planar structure which combines the good features of the previous structures.

An SIW is a synthesized non-planar waveguide that is transformed into planar form. It can then be integrated into any planar dielectric substrate with any planar fabrication or processing technique. This will include the printed circuit boards (PCBs), and low-temperature co-fired ceramic (LTCC) technologies, among others [1]. The basic idea of the substrate integrated waveguide technique is the allocation of rows of cylindrical holes with certain radius and specific spacing. This led to emerging guided-wave structure and it looks like two parallel walls that have a specific spacing in which EM waves are well confined [1]. The purpose of the application of this technique is to make the planar structures behave as a waveguide. Therefore; all the concepts of waveguide theory can be applied to these planar structures. It is worth mentioning that SIW technique has been applied to many of microwave structures such as antennas, filters, power dividers, couplers, etc..

Due to the advantages offered by the SIW techniques, it has been attractive for microwave circuits and antenna designers. To illustrate more, the published research works can be classified into more than one category depending on how this technique has been applied. The first category includes distribution of via holes linearly on the sides of the substrate [2–5]. The second category included via holes distribution in particular certain pattern on the top layer of the planar structure [6–11]. While in the third category, defected ground structures, DGSs, and complementary single split resonators CSSRs have been applied in the ground planes of the SIW structures included in the previous two categories [12–16].

In this paper, a semi-circular slots loaded SIW based BPF is presented. The proposed BPF offers a compact size and wide bandwidth.

2. THE PROPOSED FILTER DESIGN

The structure of the proposed SIW BPF represents an improvement of that adopting the bow-tie resonator, reported in the literature [17], as a starting step. The relationship between the cut-off

frequency, f_c, and the dimensions of any waveguide filled with a dielectric material can be related together, and this relationship can be considered as the starting points of a SIW design. For a rectangular waveguide, the cut-off frequency of a dominant TE mode is given by [18]:

$$f_c = \frac{c}{2\pi} \sqrt{\left(\frac{m\pi}{a}\right)^2 + \left(\frac{n\pi}{b}\right)^2} \tag{1}$$

where c is the speed of light in free space, m and n are mode numbers, a and b are the longer and the shorter dimensions of the waveguide respectively. For the dominant TE_{10} mode, Equation (1) is simplified to:

$$f_c = \frac{c}{2a} \tag{2}$$

For dielectric filled waveguide with same cut off frequency, dimension "a_d" is found to be:

$$a_d = \frac{a}{\sqrt{\varepsilon_R}} \tag{3}$$

where ε_{eff} is the effective dielectric constant, and can be calculated by empirical expressions reported in the literature [19].

Having determined the dimension "a" for the dielectric filled waveguide; we can now pass to an empirical design equation of the SIW correlating its width, a_s, and is given by [20]:

$$a_s = a_d + \frac{d^2}{0.95p} \tag{4}$$

where d is the diameter of the vias, and p is the center to center separation between the vias along the longitudinal direction. A general rule of thumb for the choice of d and p is given in (5) and (6), respectively [20]:

$$d < \lambda_g/5 \tag{5}$$
$$p < 2d \tag{6}$$

where λ_g is the guided wavelength [21] which is given by:

$$\lambda_g = \frac{2\pi}{\sqrt{\left(\frac{\varepsilon_r (2\pi f)^2}{c^2}\right) - \left(\frac{\pi}{a}\right)^2}} \tag{7}$$

The proposed filter is constructed by embedding two semi-circular slots in the SIW structure from the input and the output sides as shown Figure 1.

3. PARAMETRIC STUDY AND SIMULATION RESULTS

The proposed filter is constructed by embedding two half-circular slots in the SIW structure from the input and the output sides as shown in Figure 1. The proposed SIW cavity dimensions are $13.09 \times 9.945\,\text{mm}^2$ while the overall dimensions are $26.625 \times 14\,\text{mm}^2$ using a substrate with relative permittivity of 2.2 and thickness of 0.245 mm. The complete parameters are finely tuned by using Microwave Studio Suite of Computer Simulation Technology CST. The detailed and optimum dimensions of the proposed filter are illustrated in Table 1.

Many parameters have studied to get more insight about their effects on the proposed filter performance. For this it is found that the most influential of these factors is the radius of the half-circular slot in the resonator. A parametric study has been conducted to explore the effect of the embedded semi-circular slot radius, r, on the presented filter performance. The effect of varying the slot radius r, while keeping the other filter parameters unchanged, has been shown in Figures 2(a) and (b).

Table 1: Summary of the dimensions of the proposed filter structure.

Parameters	l	w	a_s	r	b	y	d	p
Values (mm)	10.63	26.63	13.09	5	0.76	6.12	0.50	0.765
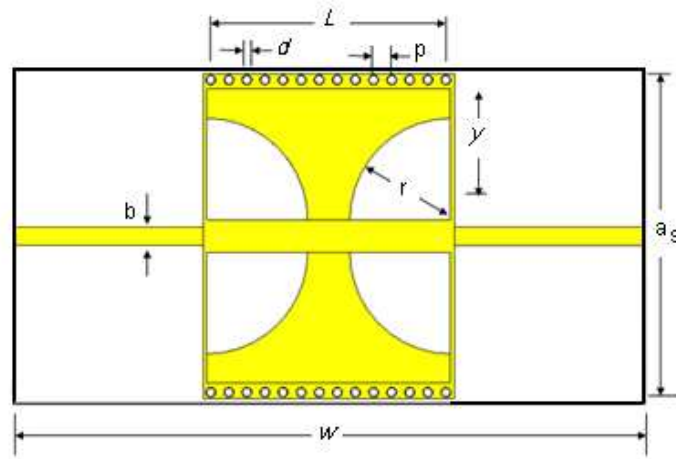
Figure 1: The front view of the simulated BPF.
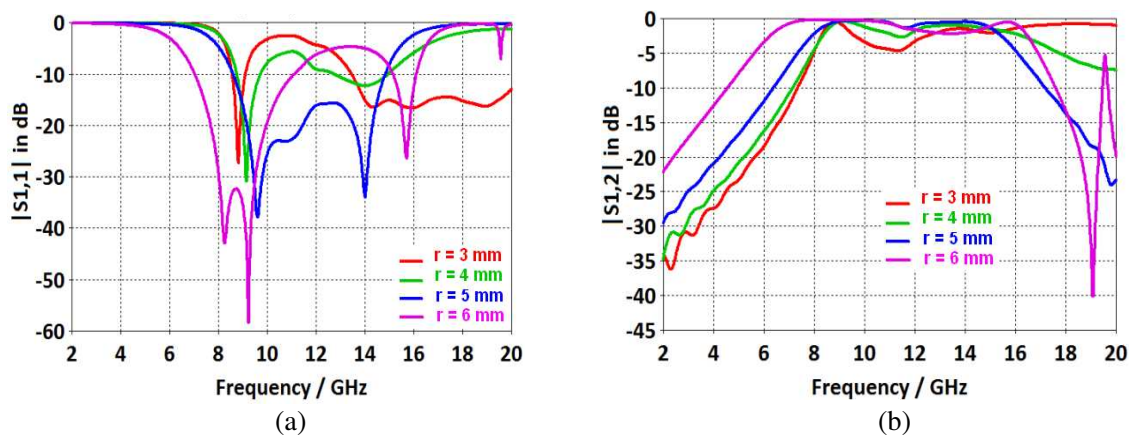
Figure 2: The simulated S_{11} and S_{12} responses of the proposed BPF with r as a parameter.
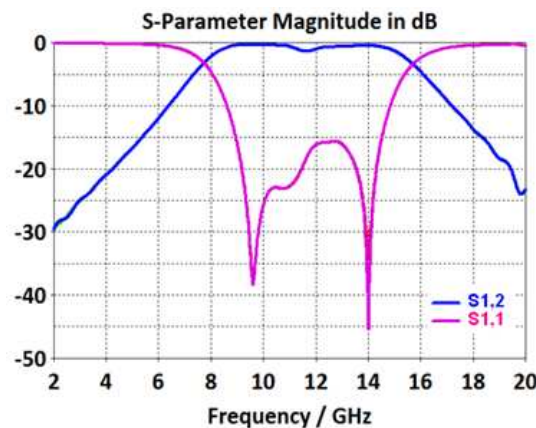
Figure 3: The simulated S_{11} and S_{12} responses of the proposed BPF with $r = 5$ mm.

Examining the results of Figure 2, it is clear that the increase of r leads to reduce the lower cut-off frequency. As r becomes larger, up to r equal to 5 mm, this will expand the filter bandwidth. Beyond this value reduction of lower cut-off frequency continues. However, the effect of varying r on the filter performance can be described as follows. As r increases, the position of the lower transmission zero has been shifted away from the lower edge cut-off frequency resulting in a low selectivity and roll-off rate. Furthermore, the increase of r makes the upper transmission zero approaches the upper edge cut-off frequency resulting in higher selectivity and higher roll-off rate at the upper passband. The resulting increase in the filter bandwidth is at the expense of the in-band performance.

There must be some compromise between the various requirements of the wide bandwidth, higher selectivity at both the lower and the upper edges of the passband, besides the low ripple in the filter passband. Figure 3 shows the performance responses of the resulting filter responses with the dimensions summarized in Table 1. The filter have exhibited a return loss less than $-15\,\mathrm{dB}$ at the center of the passband, insertion loss approaching to $0\,\mathrm{dB}$ over the passband and offers a $-3\,\mathrm{dB}$ fractional bandwidth of about 68.4% centered at $11.7\,\mathrm{GHz}$. The results reveal that the dimensions of the proposed filter represent only (69.9%) lower than those reported in [17].

4. CONCLUSIONS

A new compact substrate integrated waveguide (SIW) bandpass filter (BPF) is presented in this paper as a candidate for use in wide bandwidth X-band applications. Two semi-circular slots have been embedded in the structure from the input and the output sides. The simulation and performance evaluation of the proposed filter have been exhibited a return loss less than $-15\,\mathrm{dB}$, insertion loss approaching to $0\,\mathrm{dB}$ over the passband and offers a $-3\,\mathrm{dB}$ fractional bandwidth of about 68.4% centered at $11.7\,\mathrm{GHz}$. A parametric study reveals that the insertion of these slots has successfully led to the compact size and the wide bandwidth. The results reveal that the dimensions of the proposed filter represent a considerable size reduction as compared with those reported in the relevant literature. The compact size offered by this filter makes it a suitable for use in designing microwave and millimeter-wave circuits.

REFERENCES

1. Chen, X. and K. Wu, "Substrate integrated waveguide filters: Practical aspects and design considerations," *IEEE Microwave Magazine*, Vol. 15, No. 7, 75–83, 2014.

2. Liu, C. and K. Huang, "A compact substrate integrated waveguide band-pass filter," *PIERS Proceedings*, 1135–1138, Cambridge USA, Jul. 5–8, 2010.

3. Xu, Z., G. Zhang, H. Xia, and M. Xu, "Novel hexagonal dual-mode substrate integrated waveguide filter with source-load coupling," *The Scientific World Journal*, Vol. 2014, Article ID 915740, Apr. 2014.

4. Xu, Z., Y. Shi, C. Xu, and P. Wang, "A novel dual mode substrate integrated waveguide filter with mixed source-load coupling (MSLC)," *Progress In Electromagnetics Research*, Vol. 136, 595–606, 2013.

5. Huang, Y., Z. Shao, and L. Liu, "A substrate integrated waveguide bandpass filter using novel defected ground structure shape," *Progress In Electromagnetics Research*, Vol. 135, 201–213, 2013.

6. Dong, Y., W. Hong, H. Tang, J. Chen, and K. Wu, "Planar realization of a Q-band triple-mode filter using high order resonances," *Microwave and Optical Technology Letters*, Vol. 51, No. 3, 600–603, 2009.

7. Shen, K., G.-M. Wang, S.-H. Fu, and G.-D. Gu, "Highly selective bandpass filter based on substrate integrated waveguide," *Electronics Letters*, Vol. 45, No. 14, 746–748, 2009.

8. Zheng, B., Z. Zhao, and Y. Lv, "A K-band SIW filter with bypass coupling substrate integrated circular cavity (SICC) to improved stopband performance for satellite communication," *Progress In Electromagnetics Research C*, Vol. 17, 95–104, 2010.

9. Zou, X., C. Tong, and D. Yu, "Design of an X-band symmetrical window bandpass filter based on substrate integrated waveguide," *Proceedings of Cross Strait Quad-Regional Radio Science and Wireless Technology Conference*, Harbin, China, Jul. 2011.

10. Chen, L.-N., Y.-C. Jiao, Z. Zhang, and F.-S. Zhang, "Miniaturized substrate integrated waveguide dual-mode filters loaded by a series of cross-slot structures," *Progress In Electromagnetics Research C*, Vol. 29, 29–39, 2012.

11. Zhu, X., W. Hong, and K. Wu, "Design and implementation of a triple-mode planar filter," *IEEE Microwave and Wireless Components Letters*, Vol. 23, No. 5, 243–245, 2013.

12. Deng, K., Z. Guo, C. Li, and W. Che, "A compact planar bandpass filter with wide out-of-band rejection implemented by substrate integrated waveguide and complementary split-ring resonator," *Microwave and Optical Technology Letters*, Vol. 53, No. 7, 1483–1487, 2011.

13. Guo, Z., K. Chin, W. Che, and C. Chang, "Substrate integrated waveguide quasi-elliptic bandpass filter with meander-slot coupling structures," *Proceedings of 2012 Asia Pacific Microwave Conference, APMC 2012*, Kaohsiung, Taiwan, Dec. 2012.

14. Guo, Z., K.-S. Chin, W. Che, and C. Chang, "Cross-coupled bandpass filters using QMSIW cavities and S-shaped slot coupling structures," *Journal of Electromagnetic Waves and Applications*, Vol. 27, No. 2, 160–167, 2013.

15. Zhang, Q., W.-Y. Yin, and S. He, "Evanescent-mode substrate integrated waveguide (SIW) filters implemented with complementary split ring resonators," *Progress In Electromagnetics Research*, Vol. 111, 419–432, 2011.

16. Szydlowski, L., A. Jedrzejewski, and M. Mrozowski, "A trisection filter design with negative slope of frequency-dependent cross coupling implemented in substrate integrated waveguide (SIW)," *IEEE Microwave and Wireless Components Letters*, Vol. 23, No. 9, 456–458, 2013.

17. Zhang, X., J. Xu, Z. Yu, and Y. Dong, "Microstrip wide band-pass filter based on substrate integrated waveguide (SIW)," *Proceedings of IEEE International Symposium on Microwave, Antenna, Propagation, and EMC Technologies for Wireless Communications*, Hangzhou, China, Aug. 2007.

18. Pozar, D. M., *Microwave Engineering*, John Wiley & Sons, New York, 2005.

19. Hong, J. S., *Microstrip Filters for RF/Microwave Application*, Wiley, New York, 2001.

20. Wu, K., D. Deslandes, and Y. Cassivi, "The substrate integrated circuits — A new concept for high-frequency electronics and optoelectronics," *Proceedings of 6th International Conference on Telecommunications in Modern Satellite, Cable and Broadcasting Service, TELSKIS 2003*, Nis, Serbia and Montenegro, Oct. 2003.

21. Rayas-Sanchez, J. E. and V. Gutierrez-Ayala, "A general EM-based design procedure for single-layer substrate integrated waveguide interconnects with microstrip transitions," *IEEE MTT-S International Microwave Symposium Digest*, 983–986, Atlanta, USA, Jun. 2008.

A Compact Dual-band Bandstop Filter Based on Fractal Microstrip Resonators

Hayder S. Ahmed, **Ali J. Salim**, and **Jawad K. Ali**

Microwave Research Group, Department of Electrical Engineering, University of Technology, Iraq

Abstract— Fractal geometries are found attractive to designers seeking for compact size microwave circuits and antennas. In this paper, Peano fractal based open-loop resonators are adopted to design dual-band microstrip band-stop filters (PSFs). The suggested filter structure is essentially based on that of the conventional open-loop rectangular microstrip resonators. The resonators of the proposed PSF structure are made in the form of Peano fractal geometry with different iteration levels. Many filters have been modeled, and their performances have been evaluated using a commercially available full-wave electromagnetic simulator. Each of the modeled filter structures contains two pairs of open loop fractal based resonators with different iteration levels. The lower frequency band-stop performance is attributed to the resonators with higher iteration level while the higher frequency band-stop performance is due to the resonators with lower iteration level. Simulation results for the proposed microstrip filters have confirmed the validity to realize compact dual-band narrow-stopband microstrip filters. A comparative study implies that higher size reduction of the realized filter has taken place as the iteration level of the fractal microstrip open-loop resonators becomes higher. The results presented show that the fractal-based resonators can be used to construct compact narrow-stopband filters suitable for a wide variety of the recently available communication applications.

1. INTRODUCTION

Fractal geometries are characterized by two unique properties; space-filling and self-similarity. These properties have opened new and essential approaches for antennas and electronic solutions in the course of the most recent 25 years. This preliminary stage gives a prologue to the benefits given by fractal geometry in antennas, resonators, and related structures. Such profits incorporate, among numerous, wider bandwidths, littler sizes, part-less electronic parts, and better performance. Additionally, fractals give another era of optimized design tools, initially utilized effectively in antennas but applicable in a general manner [1].

Various fractal geometries have been applied to the conventional microstrip resonators that are successfully adopted to design compact microwave microstrip filters and planar circuits. Based on the conventional square patch, Sierpinski fractal curve has been applied to design a dual-mode microstrip bandpass filter [2, 3]. Other fractal geometries, such as Hilbert, Moore, have been also adopted to design miniaturized bandpass filters [4, 5]. Minkowski fractal based microstrip resonators have more attracted microwave filter designers to be successfully applied to produce compact dual-mode microstrip bandpass filters [6–11]. However, research works dealt with the application of fractal based structures to design microstrip BSFs have been seldom reported in the literature [12], where a Peano fractal shaped open stub microstrip resonator has been proposed to reduce the second harmonics of a dual-mode bandpass filter. On the other hand, Peano fractal geometries have been successfully applied to the conventional resonators to produce high-performance miniaturized single-mode and dual-mode microstrip bandpass filters [13–16]. The high space-filling property of this fractal geometry makes it an attractive choice to design bandpass filters with high size reduction levels.

In this paper, a compact DBBSF with Peano fractal based resonators is presented. Peano fractal curve, with different iteration levels, has been applied to shape microstrip resonators. The proposed filter structure is composed of two groups of microstrip resonators with different iteration levels. This will result in more compact microstrip BSFs with dual stopband responses.

2. THE PROPOSED FILTER CONFIGURATION

The structure of the proposed BSF represents an improvement of that of the conventional BSF with open-loop square ring resonators depicted in Figure 1. In this filter, the resonant frequency of the stopband is dependent on the perimeter of the open-loop square ring resonator [17, 18].

An interesting feature the Peano fractal curve has, as shown in Figure 2, is that it has a relatively higher compression rate than the other space-filling fractal curves such as Hilbert, Moore

Figure 1: The structure of the microstrip of the open-loop resonator BSF reported in [17, 18].
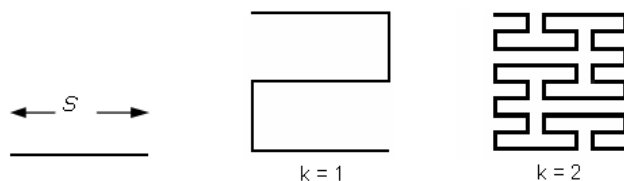
Figure 2: The steps of the growth of the Peano pre-fractal structure [12].
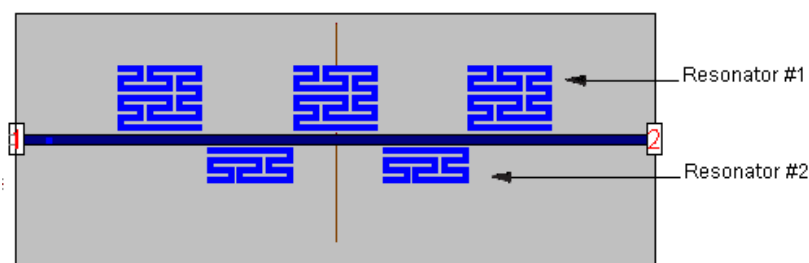
Figure 3: The proposed dual-band BSF configuration with fractal based resonators.

geometries. This suggests that the Peano resonator may resonate at a lower fundamental resonant frequency. The length included, $L(k)$, in the kth iteration pre-fractal structure in terms of the initial line segment, S, is given as [12]:

$$L(k) = \left(3^k + 1\right) S \tag{1}$$

Theoretically, as k goes to infinity, the resulting length goes to infinity. The ability of the resulting structure to increase its perimeter in the successive iterations was found very triggering for examining its size reduction capability as a BSF.

The proposed BSF configuration will constitute two groups of fractal based resonators, located at both sides of the feed line; each with different iteration level of Peano pre-fractal structures shown in Figure 3. Therefore, each group will create its own resonant band as each will have different length.

3. THE FILER DESIGN AND PERFORMANCE EVALUATION

To validate the idea of the proposed filter, three BSFs have been modeled; each with resonators based on Peano fractal geometry of the 2nd iteration level depicted in Figure 2. Two types of resonators, resonator #1 and resonator #2, are used with different length; representing fractions of the Peano fractal geometry of the 2nd iteration as demonstrated in Figure 3. The first filter uses only resonator #1, the second filter only resonator #2 while the third filter uses both resonators. These filter structures have been modeled and analyzed using the commercially available EM simulator, IE3D [19] using a substrate material with a relative dielectric constant of 10.8 and substrate thickness of 1.27 mm. This simulator performs electromagnetic analysis using the method of moments (MoM). The input/output ports have $50 \, \Omega$ characteristic impedance. This corresponds to a microstrip line width of about 1.2 mm.

The side length of all the resonators of the modeled filter has been kept unchanged with S equal to 8.60 mm with trace width of about 0.6 mm. The enclosed lengths of the resonators #1 and 2 are 79.57 mm and 47.20 mm respectively. The resulting responses of the modeled filters are depicted in Figures 4–6. It is clear that the results in Figures 4 and 5 imply that the filters with single type resonator offer a single band stopband dependent on the resonator length. Consequently, the lower
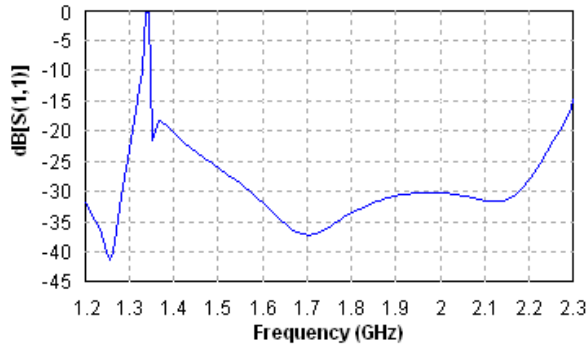
Figure 4: The simulated S_{11} response of the modeled BSF with resonators #1 alone.
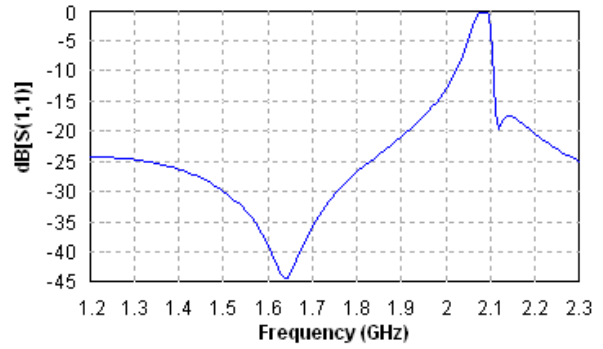
Figure 5: The simulated S_{11} response of the modeled BSF with resonators #2 alone.
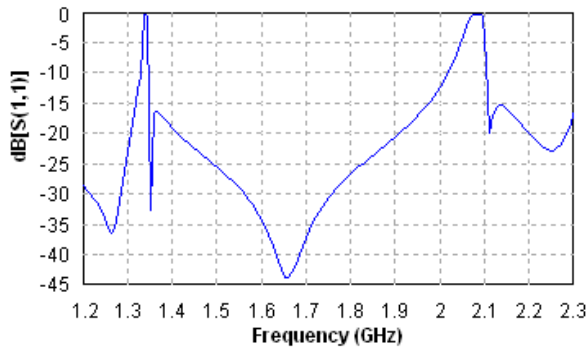
Figure 6: The simulated S_{11} response of the proposed dual-band BSF.
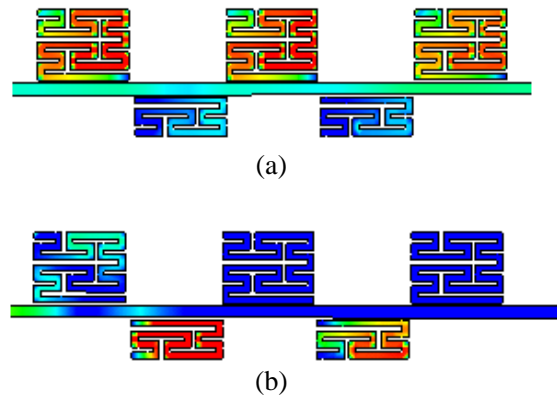
Figure 7: Current distribution on the surface of the proposed dual-band BSF at: (a) 1.34 GHz and (b) 2.08 GHz

stopband, centered at 1.34 GHz, is attributed by the resonator #1 and the higher one, centered at 2.08 GHz, is attributed by resonator #2. In terms of the corresponding guided wavelength, λ_{g1} and λ_{g2}, the side lengths of the two resonators represents about $0.10\lambda_{g1}$ and $0.16\lambda_{g2}$ respectively, where λ_g;

$$\lambda_g = \frac{\lambda_0}{\sqrt{\varepsilon_{eff}}} \tag{2}$$

where ε_{eff} is the effective dielectric constant and can be calculated by empirical expressions reported in the literature [17]. This length has been found to be more compact as compared with that reported in [17]. The BSF that uses the resonator #1 has higher selectivity response with steep roll-off rate as compared with that using resonator #1. This is because the former is a 3rd order filter while the latter is a second order one.

On the other hand, Figure 6 implies that when the two resonators are employed in the filter structure, the resulting response has two stop bands; exactly at the same frequency and shape as if each resonator works alone. This suggests that; using pairs of resonators with different lengths the positions of the stopband could be varied as required for certain applications. In addition, the frequency ratio of the two stop bands can be adjusted by choosing the appropriate resonators length ratio. To a certain extent, the proposed filter can be suggested to be a candidate for use in a wide variety of dual-band wireless applications.

Figure 7 demonstrates the surface current distribution on the proposed filter structure at 1.34 GHz and 2.08 GHz. The resulting current distribution confirms the results of Figures 4 and 5 in that each resonator works independently as if it exists alone. In Figure 7(a), the resonator #1 resonates at 1.34 GHz, while in Figure 7(a), the resonator #2 resonates at 2.08 GHz.

4. CONCLUSIONS

A compact size dual-band microstrip BSF has been presented in this paper. The application of two pairs of Peano fractal based resonators, with different length enclosed, results in compact dual-band BSF. The use of different length fractal shaped resonators could be used to vary the frequency ratio of the two stop bands which can be determined by the two resonators enclosed lengths. To a certain extent, the proposed filter can be suggested to be a candidate for use in a wide variety of dual-band wireless applications.

REFERENCES

1. Cohen, N., "Fractal antenna and fractal resonator primer," *Fractals and Dynamics in Mathematics, Science, and the Arts: Theory and Applications*, Vol. 1, Chapter 8, J. A. Rock and M. van Frankenhuijsen, Eds., World Scientific Publishing Co. Pte. Ltd., Singapore, 2015.

2. Weng, M. H., D. S. Lee, R. Y. Yang, H. W. Wu, and C. L. Liu, "A Sierpinski fractal-based dual-mode bandpass filter," *Microwave and Optical Technology Letters*, Vol. 50, No. 9, 2287–2289, 2008.

3. Weng, M. H., L. S. Jang, and W. Y. Chen, "A Sierpinski-based resonator applied for low loss and miniaturized bandpass filters," *Microwave and Optical Technology Letters*, Vol. 51, No. 2, 411–413, 2009.

4. Mezaal, Y. S., H. T. Eyyuboglu, and J. K. Ali, "New microstrip bandpass filter designs based on stepped impedance Hilbert fractal resonators," *IETE Journal of Research*, Vol. 60, No. 3, 257–264, 2014.

5. Mezaal, Y. S., J. K. Ali, and H. T. Eyyuboglu, "Miniaturised microstrip bandpass filters based on Moore fractal geometry," *International Journal of Electronics*, 1–14, ahead-of-print, 2014.

6. Ali, J. K., "A new miniaturized fractal bandpass filter based on dual-mode microstrip square ring resonator," *Proceedings of the 5th International Multi-Conference on Signals, Systems and Devices, IEEE SSD' 08*, Amman, Jordan, Jul. 2008.

7. Ali, J. K. and N. N. Hussain, "A new fractal microstrip bandpass filter design based on dual-mode square ring resonator for wireless communication systems," *Iraqi Journal of Applied Physics*, Vol. 5, No. 1, 7–14, 2009.

8. Ali, J. K. and N. N. Hussain, "An extra reduced size dual-mode bandpass filter for wireless communication systems," *PIERS Proceedings*, 1467–1470, Suzhou, China, Sep. 12–16, 2011.

9. Liu, J.-C., H.-H. Liu, K.-D. Yeh, C.-Y. Liu, B.-H. Zeng, and C.-C. Chen, "Miniaturized dual-mode resonators with Minkowski-island-based fractal patch for WLAN dual-band systems," *Progress In Electromagnetics Research C*, Vol. 26, 229–243, 2012.

10. Alqaisy, M., C. Chakrabraty, J. Ali, and A. R. H. Alhawari, "A miniature fractal-based dual-mode dual-band microstrip bandpass filter design," *International Journal of Microwave and Wireless Technologies*, Vol. 7, 127–133, 2015.

11. Lalbakhsh, A., A. A. L. Neyestanak, and M. Naser-Moghaddasi, "Microstrip hairpin bandpass filter using modified minkowski fractal-shape for suppression of second harmonic," *IEICE Transactions on Electronics*, Vol. E95C, No. 3, 378–381, 2012.

12. Ali, J. K. and Y. S. Miz'el "A new miniature Peano fractal-based bandpass filter design with 2nd harmonic suppression," *Proceedings of 3rd IEEE International Symposium on Microwave, Antenna, Propagation and EMC Technologies for Wireless Communications*, Beijing, China, Oct. 2009.

13. Ali, J. K. and Y. S. Mezaal, "A new miniature narrowband microstrip bandpass filter design based on Peano fractal geometry," *Iraqi Journal of Applied Physics*, Vol. 5, No. 4, 3–9, 2009.

14. Ali, J. K., H. Alsaedi, M. F. Hasan, and H. A. Hammas, "A Peano fractal-based dual-mode microstrip bandpass filters for wireless communication systems," *PIERS Proceedings*, 888–892, Moscow, Russia, Aug. 19–23, 2012.

15. Mezaal, Y. S., H. T. Eyyuboglu, and J. K. Ali, "A new design of dual band microstrip bandpass filter based on Peano fractal geometry: Design and simulation results," *Proceedings of the 13th IEEE Mediterranean Microwave Symposium, MMS'2013*, Saida, Lebanon, Sep. 2013.

16. Ali, J. K. and H. Alsaedi, "Second harmonic reduction of miniaturized dual-mode microstrip bandpass filters using fractal shaped open stub resonators," *PIERS Proceedings*, 1266–1269, Kuala Lumpur, Malaysia, Mar. 27–30, 2012.

17. Hong, J. S., *Microstrip Filters for RF/Microwave Application*, Wiley, New York, 2001.

18. Joubert, J., "Spiral microstrip resonator for narrow-stopband filters," *IEE Proceedings on Microwave Antennas and Propagation*, Vol. 150, 493–496, 2003.
19. *IE3D User's Manual*, Release 12.3, Zeland Software, Inc., Fremont, CA, 2007.

Design of Evaluation Board with a Built-in 25 Gb/s PRBS Source for Testing High-frequency Probe

Wei Wang, **Hong-Lu Lin**, **Jau-Ji Jou**, **Yaw-Dong Wu**, **and Tien-Tsorng Shih**

Department of Electronic Engineering, National Kaohsiung University of Applied Sciences
415 Chien Kung Road, Sanmin District, Kaohsiung 80778, Taiwan

Abstract— In this paper, an evaluation board with a built-in 25 Gb/s PRBS source was developed for testing high frequency probe (pogo pin) in time domain. The high frequency probes in semiconducting testing field are one of convincing contact elements selections. A commercial clock-data-recovery (CDR) chip was used to design the PRBS source. The 25 Gb/s PRBS signal with 14.2 ps rise time, 15.6 ps fall time, and 14.2 ps time jitter can be generated from our evaluation board. Some printed circuit board (PCB) layout techniques were used to design the 25 Gb/s evaluation board. The advantages of our 25 Gb/s evaluation board for testing high frequency probe have low cost, small size, and light weight.

1. INTRODUCTION

There are more and more internet applications, such as internet TV, multimedia network, online games, social networking sites and cloud computing. We need to decrease the time of the data processing and increase the quality of the data transmission. For higher data rate applications, the 40/100 Gigabit Ethernet standards was proposed in 2010 [1]. The 100GBase can use four parallel 25 Gb/s channels to achieve the transmission rate [2]. Therefore, the performance of the high data rate products, modules, devices, or testing kits need be measured over 25 GHz frequency range.

The time domain measurement of high-speed signal needs generally an expensive pattern generator to provide a pseudo-random binary sequence (PRBS) signal and the volume of the high-speed measurement system is bulky. Therefore, we will design an evaluation board including PRBS source and microcontroller unit (MCU) for reducing the volume, weight, and cost of high-speed measurement system.

Some printed circuit board (PCB) layout techniques were used to design the 25 Gb/s evaluation board The differential traces were designed to reduce noise interference, and the length of signal traces was short as possible for improving the transmission bandwidth. Using a clock-data-recovery (CDR) chip, our 25 Gb/s PRBS generator was designed. The CDR chip can be controlled by a MCU chip through firmware. The graphical user interface (GUI) software was also developed to conveniently control MCU and read/write data. The communication between the firmware and the software is through the universal serial bus (USB) interface because the USB is a popularity connector between computers and electronic devices. The high frequency probe (pogo pin) is tested through our evaluation board with a built-in 25 Gb/s PRBS source and through a commercial PRBS generator, the results are compared and discussed.

2. DESIGN OF MODULE CIRCUITS

The PRBS generator on our evaluation board used Gennum GN2425 chip, and the circuit diagram is shown in Figure 1(a). The MCU on our evaluation board used Atmel ATmega328P chip, and the circuit diagram is shown in Figure 1(b). The surge protection device IC was also used on our evaluation board to avoid large transient voltage to damage the PRBS generator and the MCU. The π-type filter circuits were also designed on our evaluation board to filter out noise from the power supply.

3. DESIGN OF PCB LAYOUT

On our evaluation board the impedance match of differential trace and single-end trace is taken into account and designed carefully. Under the coupling capacitor, the anti-pad is designed for the impedance match of signal trace [3]. The differential traces were designed to reduce noise interference, and the length of signal traces was short as possible for improving the transmission bandwidth.

Because the high-frequency signal traces are on the top and bottom layers of our PCB, the dielectric material of the top and bottom layers used Rogers 4350B with dielectric constant 3.66. The dielectric material of other layers used FR-4 or Polypropylene (PP), and our evaluation board

is designed as a six-layer PCB. Special K connectors with 40 GHz bandwidth were used in signal input and output interfaces.

Figure 2 shows the PCB layout of the top and bottom layers of our evaluation board. Our evaluation board with a built-in 25 Gb/s PRBS source for testing high frequency probe was fabricated and is shown in Figure 3.

(a)   (b)
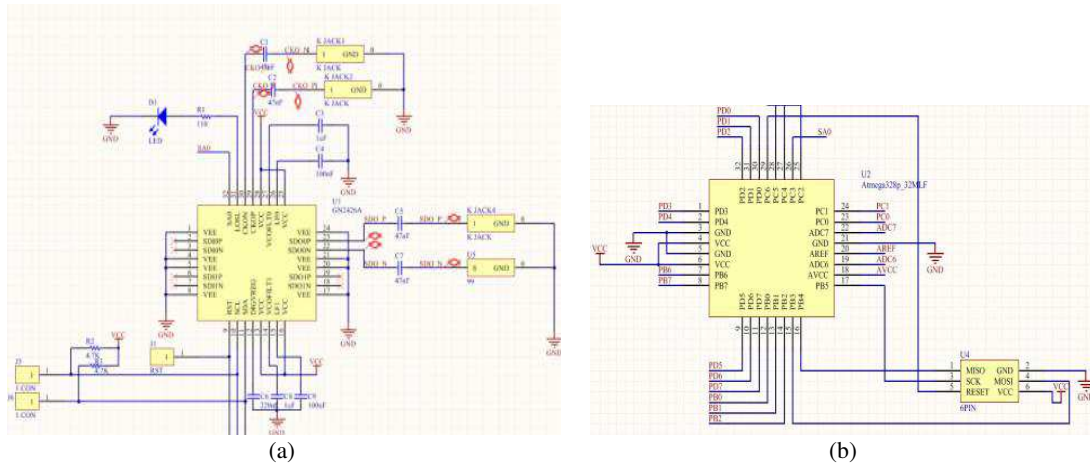
Figure 1: (a) The circuit of PRBS generator (GN2425) and (b) the circuit of MCU (ATmega328P).

(a)   (b)
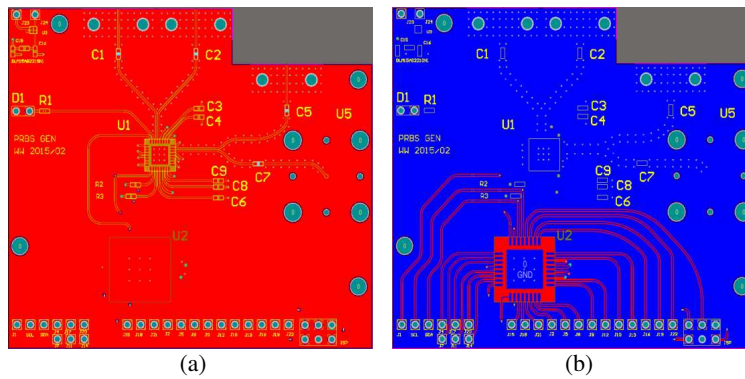
Figure 2: The PCB layout of the (a) top and (b) bottom layers of our evaluation board.
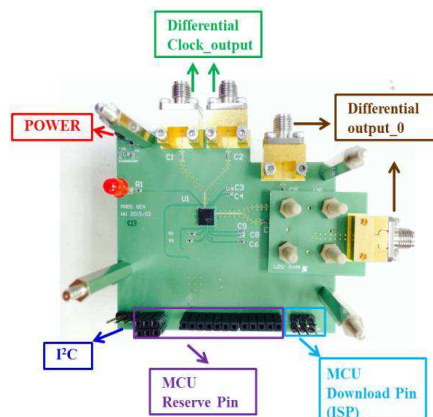
Figure 3: The evaluation board with a built-in 25 Gb/s PRBS source for testing high frequency probe.
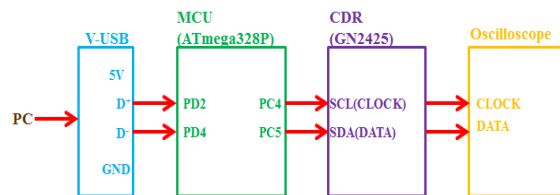
Figure 4: Flow chart from PC command to PRBS signal.

4. DESIGN OF SOFTWARE AND FIRMWARE

The USB is a popularity connector between computers and electronic devices, so the USB is considered to use as an interface between the firmware and the software on our evaluation board. Because the Atmel MCU is used, we used the V-USB [4] to develop USB hardware. The V-USB is a software-only implementation of a low-speed USB device for Atmel AVR MCU, making it possible to build USB hardware with almost any AVR MCU, not requiring any additional chip.

The communication between MCU and GN2425 chip is through I^{2}C (Inter-Integrated Circuit) [5], the I^{2}C is a serial communication bus developed by Philips. I^{2}C uses only two bidirectional open-drain lines, serial data line (SDA) and serial clock line (SCL). I^{2}C provides every devices with 7-bit address but retains 16 addresses, so it can allow 2^7-16 devices on bus.

Atmel Studio 6 is the integrated development platform for developing and debugging Atmel AVR MCU based applications. Using Atmel Studio 6 the firmware can be burned into the MCU Atmega328P through Atmel's AVRISP mkII burner.

Using computer GUI, the command of personal computer (PC) can be sent to control the MCU through V-USB. The MCU can control the CDR chip to generate PRBS signal through I^{2}C. The PRBS and clock signals can be sent into a digital oscilloscope to measure eye diagram. Figure 4 shows a flow chart from PC command to PRBS signal on our evaluation board.

5. RESULTS OF MEASUREMENT

Figure 5 shows the eye diagrams of 25 Gb/s PRBS signals from our evaluation board and Anristu pulse pattern generator MT1810A. The parameters of 25 Gb/s original eye diagrams are shown in Table 1. The quality of PRBS signal from Anristu pulse pattern generator is better than from our evaluation board, but the quality of our PRBS signal is still desirable

Using our evaluation board and Anristu pulse pattern generator, the performance of high frequency probe (pogo pin) is measured in time domain and the eye diagrams of 25 Gb/s PRBS through the pogo pin is shown in Figure 6. The parameters of 25 Gb/s eye diagrams of pogo pin testing are shown in Table 2. The rise time and fall time of the eye diagram from our evaluation board are similar to from Anristu pulse pattern generator, because the transmission bandwidth is limited by the high frequency pogo pin. Because of the attenuation of the pogo pin, the eye highs of both eye diagrams are attenuated about 42% from our evaluation board and Anristu pulse pattern generator Therefore the 25 Gb/s high frequency probe can be tested through our evaluation board with built-in PRBS source.
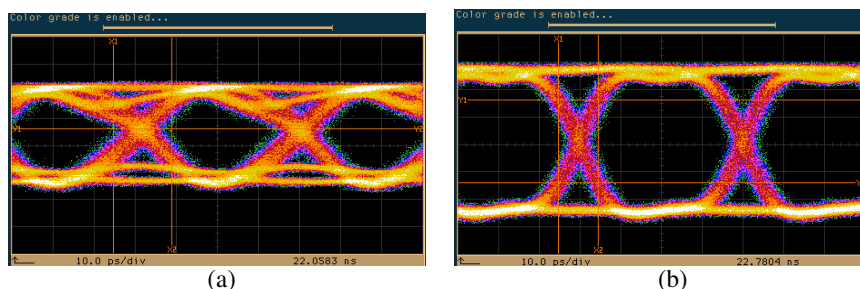
Figure 5: 25 Gb/s original eye diagrams from (a) our evaluation board and (b) Anritsu (MT1810A).

Table 1: Parameters of 25 Gb/s original eye diagrams.

	Jitter	Rise time	Fall time	Eye width	Eye high	Q factor
Our evaluation board	14.2 ps	14.2 ps	15.7 ps	24.3 ps	100.4 mV	8.0
Anristu (MT1810A)	9.0 ps	9.5 ps	9.7 ps	31.2 ps	405.8 mV	16.0

Table 2: Parameters of 25 Gb/s eye diagrams of pogo pin testing.

	Jitter	Rise time	Fall time	Eye width	Eye high	Q factor
Our evaluation board	18.7 ps	38.9 ps	51.3 ps	20.2 ps	42.4 mV	4.6
Anristu (MT1810A)	11.1 ps	42.0 ps	40.6 ps	41.1 ps	172.7 mV	5.4

(a)   (b)
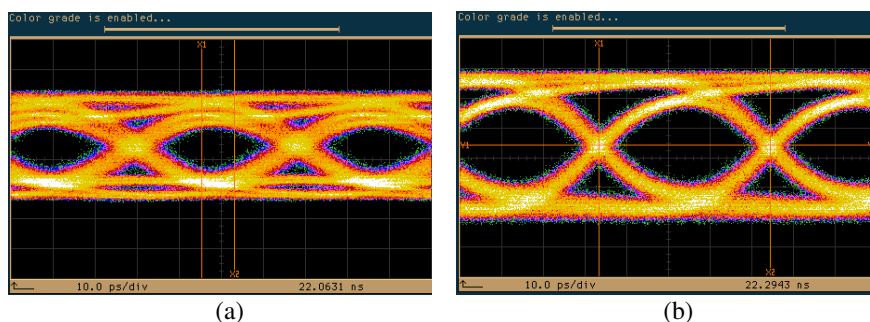
Figure 6: 25 Gb/s eye diagrams of pogo pin testing using (a) our evaluation board and (b) Anritsu (MT1810A).

6. CONCLUSION

We has successfully used Gennum GN2425 chip to develop a built-in 25 Gb/s PRBS generator on our evaluation board. Some PCB layout techniques have been used to design the 25 Gb/s evaluation board. The differential traces were designed to reduce noise interference, and the length of signal traces was short as possible for improving the transmission bandwidth. Our evaluation board with a built-in 25 Gb/s PRBS source has been also applied to measure the performance of the high-frequency probe (pogo pin) in time domain Although the performance of eye diagram from our evaluation board is not as good as from the commercial pulse pattern generator, but the advantages of our evaluation board have low cost, small size and light weight. In the future, we can use a better PRBS generator chip and improve PCB layout to design the better evaluation board, and our evaluation board can also apply to test the other electronic device in high-speed time domain

REFERENCES

1. IEEE Standards Association. "IEEE Standard 802.3ba"
2. Arima, R., T. Hatano, K. Hiramoto, and H. Irie, "Demonstration of world-first 112 Gbit/s 1310 nm LAN-WDM optical transceiver for 100GbE and 100GbE over OTN applications," *Optical Fiber Communication Conference*, paper PDPD3, Mar. 2010.
3. Yee, C. F., "Methods of optimized via design for higher channel bandwidth," IEEE, 2013.
4. V-USB, http://www.obdev.at/products/vusb/index.html.
5. Semiconductors, N. X. P., "I2C-bus specification and user manual," Rev, 3, 19, 2007.

The Optimized Electrode between a SMPM Connector and a Microstrip for High Frequency Applications

Cheng-Ying Wu, **Hong-Lu Lin**, **Jau-Ji Jou**, **Yaw-Dong Wu**, **and Tien-Tsorng Shih**

Department of Electronic Engineering, National Kaohsiung University of Applied Sciences
Kaohsiung, No. 415 Chien Kung Road, Kaohsiung City, Taiwan

Abstract— In this paper, a smaller and cheaper novel Subminiature Modular Plug-in Mini (SMPM) connector has been used to replace a K-type connector. The SMPM connector is installed on the top of printed circuit board (PCB) and soldering with an electrode to reduce the trace of a microstrip and to maintain the high frequency performance. Three designs of the PCB electrode have been simulated and verified experimentally. The optimized impedance mismatch of the soldering point between a SMPM connector and the PCB electrode is controlled within a range of ± 2-Ohm. The 3-dB bandwidth of the whole setup including two SMPM connectors and a 2.5-cm long microstrip is above 25-GHz. This optimization can be used in designing high-speed PCB for the application of 100GBASE Ethernet.

1. INTRODUCTION

Due to the advent of the cloud computing, a high data rate transmission is greatly demand. The data traffic between servers inside a data center becomes busy. The data rate of the servers will be mainly 100 Gb/s for the Ethernet in the future. In IEEE 802.3bm Ethernet standard the 100GBaseSR4 (4×25 Gb/s) technology has been proposed. According to the requirement of a 100GBASE Ethernet, the transmitted data rate of a single channel is 25-Gb/s and the aggregated data rate is 100-Gb/s by adopting 4-channel transmission simultaneously [1–3]. The testing setup and connection for a 100-Gb/s environment is very essential. Signal integrity and impedance match are key points in designing either the transmission line on a printed circuit board (PCB) and the connector [4–6].

For high-frequency PCB design, the issue of connection with the connector is investigated worthily. Usually, a K-type connector is generally adopting and soldering with PCB. However, the size of a K-type connector 1.3-cm × 1.7-cm × 1.5-cm (diameter × width × height) is large The K-type connectors are arranged on PCB and the pitch between two connectors is also larger. It makes a difficulty in minimizing the length of a microstrip of a PCB. Therefore, the PCB needs larger area, the trace of microstripe line becomes also longer, and the transmission bandwidth will be limited.

In this paper, the Subminiature Modular Plug-in Mini (SMPM) connector is considered to use on PCB. The size of a SMPM connector, 0.4-cm × 0.4-cm × 0.3-cm (diameter × width × height) is smaller than a K-type connector. Figure 1 shows the schematic of a SMPM connector. Because the smaller connectors are used, the pitch between two connectors can be reduced, the area of PCB is also reduced, and the trace of transmission line can becomes shorter on PCB. Therefore, the high-frequency performance of high-speed PCB becomes better, and the cost can be lower. It will be analyzed that the SMPM connector contacts with high-speed PCB. Using the SMPM connector, the 25-Gb/s operation on PCB will be also verified.
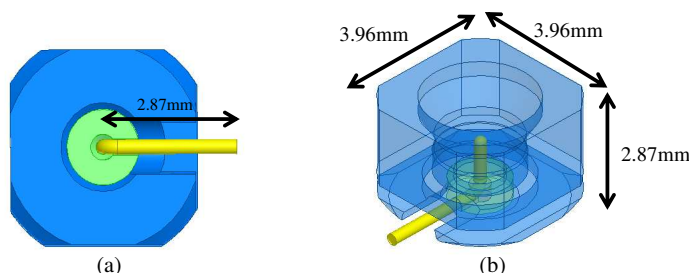
Figure 1: Schematic of a SMPM connector (a) bottom of connector (b) 3D perspective drawing.

2. DESIGN OF ELECTRODE BETWEEN SMPM CONNECTOR AND MICROSTRIP LINE ON PCB

Figure 2 shows the simulated reflection loss and insertion loss of a SMPM connector. The simulated bandwidth of the SMPM connector can be over 30-GHz, so the SMPM connector should be able to use in 25-Gb/s applications. However, the contact between SMPM connector and PCB could induce the transmission bandwidth reducing, so it must be analyzed that the SMPM connector contacts with high-speed PCB.
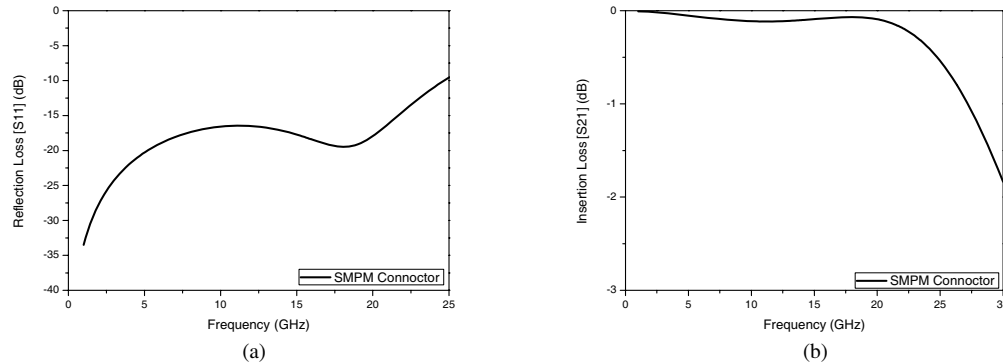
Figure 2: Simulated (a) reflection loss and (b) insertion loss of a SMPM connector.

In our high-frequency PCB, the insulation material uses Rogers 4350B with dielectric constant 366 and the length of the microstrip line is 2.5-cm. We design and analyze three kinds of connects between SMPM connector and microstrip line, as shown in Figure 3. The first kind connect is that the signal pin of SMPM connector contacts with the original microstrip line. The second kind connect is like the first kind but an anti-pad is set on the ground plane under the SMPM connector. The third kind contact has no the anti-pad, but the length of microstrip line is reduced and the contact area of SMPM pin and microstrip line becomes small.
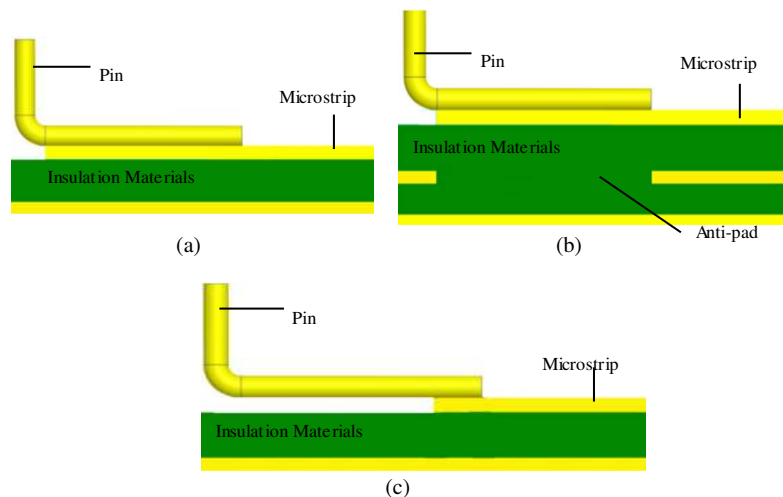
Figure 3: Three kinds of contacts between SMPM connector and microstrip line (a) for original, (b) with anti-pad, and (c) with small contact area.

3. SIMULATION AND MEASUREMENT RESULTS

The S-parameters of transmission with three kinds of contacts are simulated through the 3D electro-magnetic simulation software Ansoft HFSS. The S-parameters are also measured using the vector network analyzer Agilent 8522ES, and the experiment setup is shown in Figure 4. In this mea-surement architecture a SMPM to K-type cable must be used between input/output port of the network analyzer and a device under test (DUT). The loss of the cable must also be considered. Therefore, the circuit model of SMPM to K-type cable is also established. The HFSS simulation

results of three kinds of contacts combine the circuit model of SMPM to K-type cable to simulate the insertion loss of complete transmission through the Agilent ADS simulator, as shown in Figure 5. The insertion loss is also measured using the vector network analyzer, as shown in Figure 6. The simulations with SMPM to K-type cable show good agreement with the measured results. The simulations of the testing without SMPM to K-type cable are also simulated, as shown in Figure 7, and the insertion loss is lower than with SMPM to K-type cable. The loss of our K to SMPM-type cable is large. If the lower loss cable can be used in our experiment, the better performance of SMPM connector testing can be obtained. According to the results, using anti-pad or small contact area, the electrode between SMPM connector and microstrip line can have about 20-GHz transmission bandwidth.
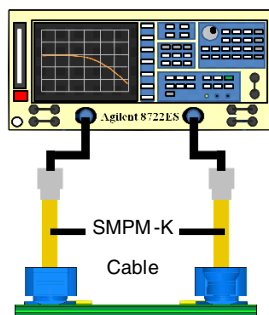
Figure 4: Experiment setup for the SMPM connector testing.
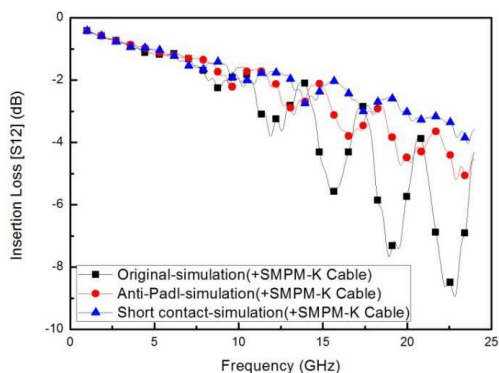
Figure 5: Simulated insertion loss with SMPM-K cable for the SMPM connector testing.
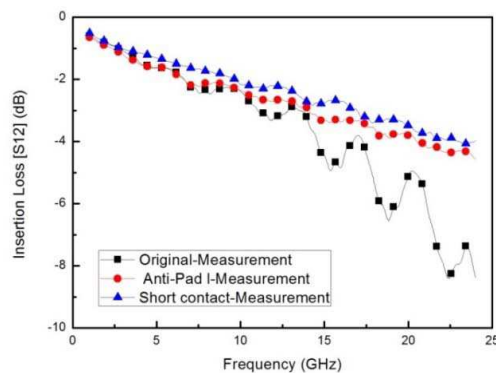
Figure 6: Measured insertion loss with SMPM-K cable for the SMPM connector testing.
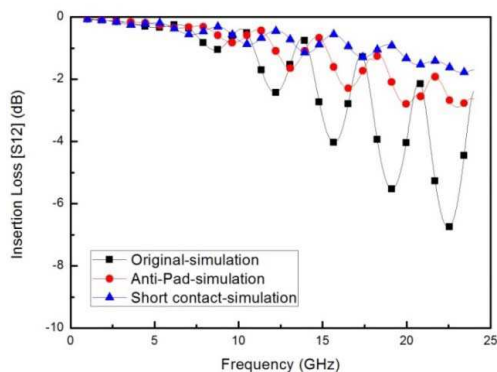
Figure 7: Simulated insertion loss without SMPM-K cable for the SMPM connector testing.
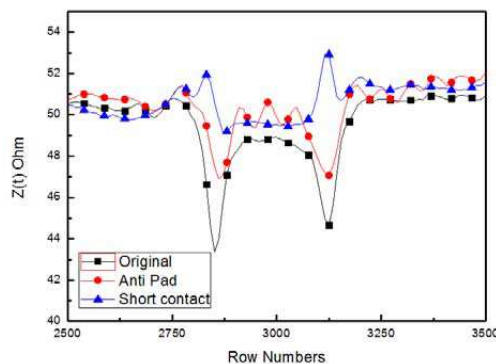
Figure 8: Measured impedance variation using TDR for the SMPM connector testing.

The impedance variations of transmission are also measured by time-domain reflectometer (TDR) for three kinds of contacts, as shown in Figure 8. The transmission impedance has a larger variation in the original testing. However, the transmission impedances can keep around $50\,\Omega$ in the cases with anti-pad and small contact area.

4. CONCLUSIONS

The contact electrode between SMPM connector and transmission line had been analyze for high-frequency transmission. Which an anti-pad is set on the ground plane under the contact and the contact area of SMPM pin and microstrip line is reduced, the two kinds of contacts can improve the transmission performance. The high-speed PCB with SMPM connector is verified to be able to operate within 20-GHz, so the SMPM connector can be suitable to apply for 100GBase-SR4 Ethernet technology

ACKNOWLEDGMENT

REFERENCES

1. Ishida, O, "40/100GbE technologies and related activities of IEEE standardization," *Proc. of OFC'2009*, OWR5, 2009.
2. Duelk M. and S. Member, "4 × 25-Gb/s 40-km PHY at 1310 nm for 100 GbE using SOA-based preamplifier," *Journal of Lightwave Technology*, Vol. 26, No. 12, 1681–1689, June, 2008.
3. Sinsky, J. and P. Winzer, "100-Gb/s optical communications" *IEEE Microwave Mag.*, Vol. 10, No. 2, 44, April 2009.
4. Magerl, M., T. Mandic, and A. Baric, "Broadband characterization of SMA connectors by measurements," *MIPRO 2014*, Opatija, Croatia, May 2014
5. McMorrow S. and A. Neves, "A hybrid measurement and electromagnetic field solver approach for the design of high-performance interconnects: An investigation of traces and SMA transitions," *DesignCon 2004 Conference Proceedings*, January 2004.
6. Uesugi, T., N. Okada, T. Saito, T. Yamatoya, Y. Morita, and A. Sugitatsu, "1.3 μm EML TOSA for serial 40 Gbps ethernet solution," *OFC/NFOEC 2010*, OThC2, March 2010.

High Frequency Performance Comparison among Three Kinds of Board to Wire Connectors

Ruei-Nian Wang, **Li-Wei Chen**, **Jau-Ji Jou**, **Yaw-Dong Wu**, and **Tien-Tsorng Shih**

Department of Electronic Engineering, National Kaohsiung University of Applied Sciences
Kaohsiung No. 415 Chien Kung Road, Kaohsiung City, Taiwan

Abstract— In this paper, we analyze and compare the properties of three kinds of high frequency board to wire connectors which are horizontal K-type connector vertical K-type connector, and subminiature modular plug-in mini (SMPM) connector. The S-parameters of these connectors were simulated through the High Frequency Structure Simulator (HFSS) software. Using these connectors, three kinds of evaluation boards (EVB) were designed for measuring the high frequency performance of the connectors. The S-parameters of these EVBs were measured and verified through the network analyzer, and the impedances were also measured through the time domain reflector (TDR) The bandwidth of the SMPM connector is about 19 GHz, the bandwidth of the vertical K-type connector is about 23 GHz, and the bandwidth of the horizontal K-type connector is above 25 GHz. The board to wire horizontal K-type connector is more suitable than the other two connectors for 25 Gb/s transmission applications.

1. INTRODUCTION

In recent years, due to the vigorous develop of information and communication technology, it makes the popularization of the internet broadband applications, such as bandwidth internet games, online teaching platform, network conference, and cloud applications. The 100 Gigabit Ethernet can use four parallel 25 Gb/s channels to achieve the transmission rate [1]. The 400GBase SR4 is currently defined 16 parallel 25 Gb/s channels in IEEE P802.3bs [2]. Therefore, the bandwidth of the related device, module, equipment, and network must increase to near 25 GHz. For the high-speed modules, the signal integrity and impedance match between the printed circuit board (PCB) and connector have to be investigated [3–5].

For the 25 Gb/s transmissions on PCB, it has to analyze and verify that the high-speed performances of board to wire connectors can be suitable. We select three kinds of high frequency connectors, which are horizontal K-type connector, vertical K-type connector, and subminiature modular plug-in mini (SMPM) connector, as shown in Figure 1, to analyze and compare. The vertical and horizontal K-type connectors can be easily assembled and reused, and they can be screwed on PCB. However, the size of vertical K-type connector is bigger and it must be fixed on the edge of PCB. For the vertical K-type connector, the length of signal trace is difficultly reduced on PCB, and the area of PCB becomes larger. The horizontal K-type connector can be fixed on the surface of PCB, so the length of signal trace and the area of PCB can be reduced. The SMPM connector can be also fixed on the surface of PCB, but it must be welded on PCB. The size of SMPM connector is smaller than horizontal K-type connector, so the length of signal trace and the area of PCB can be reduced substantially. The high frequency of three kinds of connectors will be simulated through Ansoft HFSS software, and be measured through network analyzer and time-domain reflectometer (TDR).
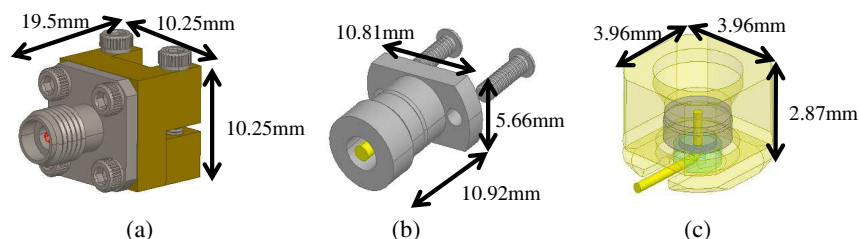
Figure 1: Schematics of three kinds of connectors. (a) Horizontal K-type connector, (b) vertical K-type connector, and (c) SMPM connector.

2. HIGH FREQUENCY SIMULATION OF CONNECTOR

Because the high performance of only connector is measured difficultly, the high performance of only connector is analyzed through simulation software. The reflection and insertion losses of three kinds of connectors were simulated through HFSS software, as shown in Figure 2, and the PCB was not considered in the simulations of connectors. According to the simulations, the reflection losses of three kinds of connectors are below -10 dB within 25 GHz bandwidth, but the reflection losses of K-type connectors are lower than SMPM connector. According to the insertion losses, the bandwidths of three kinds of connectors can be over 25 GHz, but the frequency responses of K-type connectors are flatter than SMPM connector.
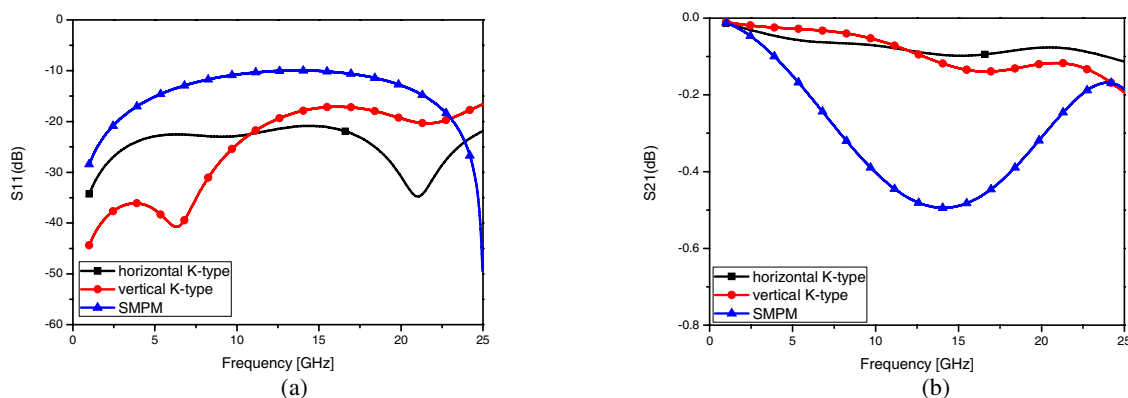
Figure 2: Simulated (a) reflection and (b) insertion losses for three kinds of connectors.

3. SIMULATION AND MEASUREMENT OF HIGH-SPEED PCB WITH CONNECTOR

For verifying the high frequency performance of connector through measurement, a test PCB was designed including three connectors. In our high-frequency test PCB, the insulation material uses Rogers 4350B with dielectric constant 3.66 and the length of the microstrip line is 2.5 cm. For three kinds of connectors, the reflection and insertion losses of PCB were also simulated through HFSS software, as shown in Figure 3. The reflection loss of our test PCB is higher than only connector. The insertion loss of our test PCB is lower than only connector, but the bandwidths of three kinds of connectors can be still over 25 GHz.
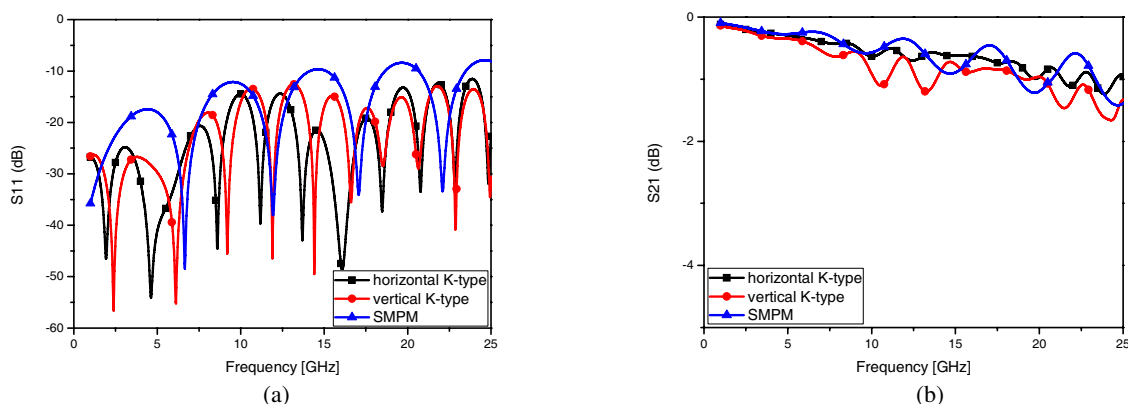
Figure 3: Simulated (a) reflection and (b) insertion losses of PCB for three kinds of connectors.

The reflection and insertion losses of PCB were measured using Agilent 8722ES vector network analyzer, as shown in Figure 4. The performance of PCB with horizontal K-type connectors is better than with other two kinds of connectors. However, the measured insertion losses are higher than the simulations, so the measured -3 dB bandwidth is also lower than the simulations. The bandwidth of vertical K-type connector can be still over 25 GHz, the bandwidth of horizontal K-type connector is about 23 GHz, and the bandwidth of SMPM connector is just about 19 GHz. The simulations of the reflection and insertion losses still show agreement with the measured results.
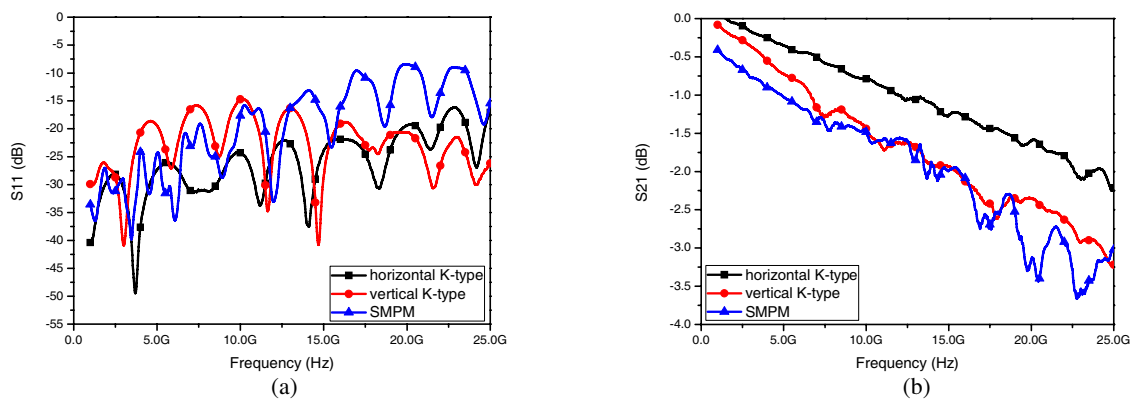
Figure 4: Simulated (a) reflection and (b) insertion losses of PCB for three kinds of connectors.
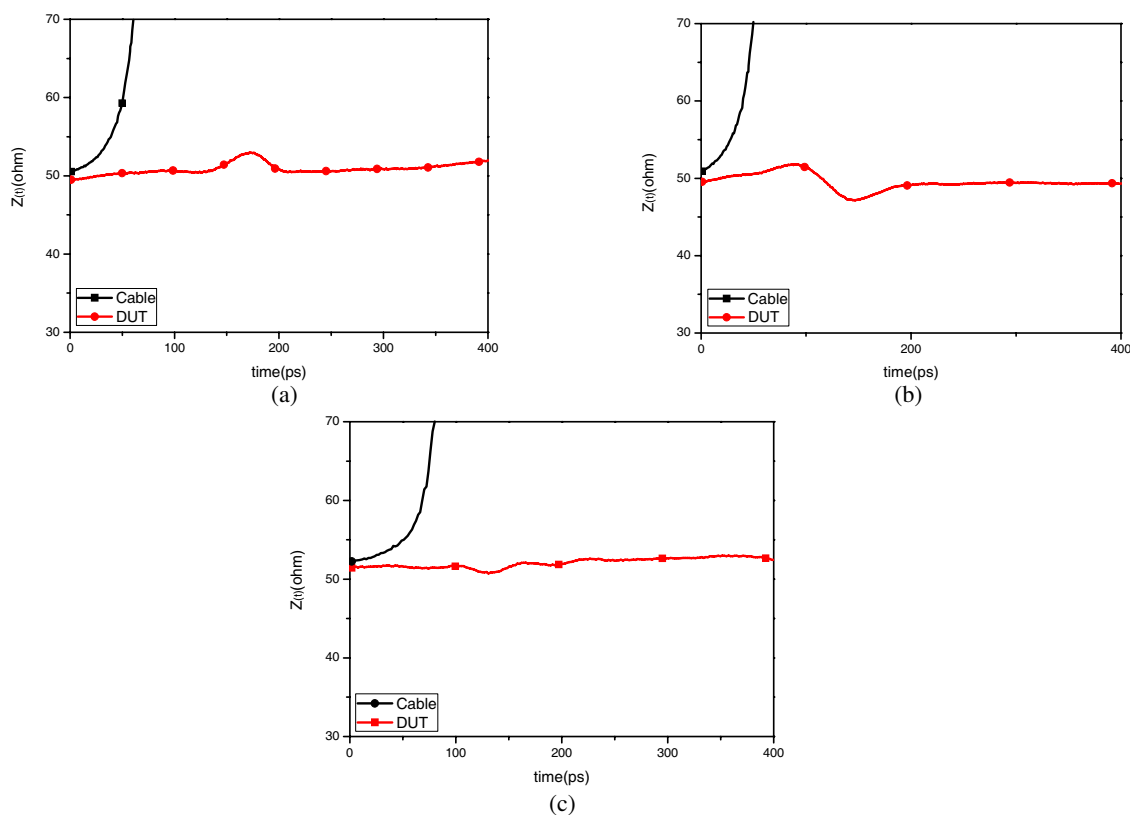
Figure 5: Measured impedance variation using TDR for three kinds of connectors. (a) Horizontal K-type connector, (b) vertical K-type connector, and (c) SMPM connector.

The higher measured insertion losses could be influenced by the fabrication of PCB, the contact between connector and PCB, or the testing cable.

For three kinds of connectors, the impedance variations of transmission were also measured by Agilent 86100A and 54754A TDR module, as shown in Figure 5. The transmission impedances can be kept around 50 Ohm for three kinds of connectors, but the little mismatch of impedance appears at the contact between connector and PCB.

4. CONCLUSION

The high frequency performances of three kinds of board to wire connectors which are horizontal K-type connector, vertical K-type connector, and subminiature modular plug-in mini (SMPM) connector, have been simulated and measure. The performance of the horizontal K-type connector is the best and its bandwidth can be over 25 GHz, but its size is the biggest. The performance of the

SMPM connector is the worst and its bandwidth just is about 19 GHz, but its size is the smallest. The three kinds of connector could be able to be used in 25 G/bs transmission applications. The size of connector is bigger, then the length of trace is longer and the area of PCB is larger. According to the size or cost requirements of PCB, the most suitable 25 G/bs connector can be selected from the three kinds of connectors.

ACKNOWLEDGMENT

REFERENCES

1. http://www.ieee802.org/3/bm/index.html
2. http://www.ieee802.org/3/bs/index.html
3. Duelk, M. and S. Member, "4 × 25-Gb/s 40-km PHY at 1310 nm for 100 GbE using SOA-based preamplifier," *Journal of Lightwave Technology*, Vol. 26, No. 12, 1681–1689, June 2008.
4. Sinsky, J. and P. Winzer, "100-Gb/s optical communications," *IEEE Microwave Mag.*, Vol. 10, No. 2, 44, Apr. 2009.
5. D'Ambrosia, J., "100 Gigabit ethernet and beyond," *IEEE Communications Mag.*, Vol. 48, No. 3, S6–S13, Mar. 2010.

An Investigation of Equatorial Ionospheric Irregularities under Solar Maximum in the 24th Solar Cycle in Middle and East Africa Using GPS

Fang-Dar Chu[1], Wei-Sheng Chen[2], and Chien-Chih Lee[2]

[1]National Standard Time and Frequency Laboratory, Chunghwa Telecom Co., Ltd., Taiwan
[2]General Education Center, Chien Hsin University of Science and Technology, Taiwan

Abstract— Ionospheric irregularities exert scintillations on electromagnetic waves when the waves pass through them. So they are interesting for satellite signal propagation in the ionosphere at the magnetic equator and low latitudes. The global navigation satellite system (GNSS) observations recorded at ground-based tracking sites have been a convenient database for investigating ionospheric irregularities. The irregularities over Africa during solar maximum years of 2013–2014 in the 24th solar cycle were investigated in this study by employing the Global Positioning System (GPS), which is a GNSS system. Six African GPS tracking sites of the International GNSS Service (IGS) network were adopted. First three sites were located at low latitudes close to the geomagnetic equator, in Middle and East Africa (from the Atlantic coast to the Indian coast). The other three were located at middle latitudes and at about the same longitudes as the aforementioned low-latitude sites. Equatorial irregularities were characterized by hourly GPS phase-fluctuation index. This index categorized irregularities into three levels: they are background, moderate, and strong irregularities. The important climatological results have been obtained as followings. First: The equinoctial irregularity occurrence rates over the three low-latitude sites decreased slowly from Middle to East Africa (94%, 89%, 83% and 87%, 73%, 64% for moderate and strong irregularities, respectively). Likewise, the June solstitial rates were also decreased similarly (90%, 88%, 74% and 67%, 58%, 37%). However, the December solstitial rates decreased faster (55%, 24%, 28% and 26%, 10%, 7%). Thus, the equinoctial and June solstitial occurrence rates were also high in East Africa (83% and 64%; 74% and 37%), while the December solstitial one was low (only 28% and 7%). Second: Although moderate and strong irregularities occurred very frequently over the low latitude sites (e.g., 94% and 87%), they over the three middle latitude sites all were nearly at the background level (i.e., nearly 0% and 0%). This indicates the irregularities did indeed come from the equator. Third: Although the equinoctial irregularities were dominant, the June solstitial irregularities also occurred frequently and their occurrence rates were comparable to the equinoctial ones, especially in Middle Africa. As for the December solstitial irregularities, they were obviously of minor importance when compared to both the equinoctial and June solstitial ones. The prominent June solstitial rates in Middle Africa may be due to the northward shifted geomagnetic equator (located in the northern hemisphere) and small declination angles.

1. INTRODUCTION

Ionospheric irregularities can exert amplitude and phase scintillations on electromagnetic waves if the waves traverse them [1]. This effect may cause severe signal fading and loss of lock at a receiver. Therefore, ionospheric irregularities are interesting for satellite radio signal propagation.

Ionospheric irregularities usually occur in the F region of the ionosphere, and can be observed by high frequency (HF) radio sounding as spread F, which is a spread of HF echo trace on the ionogram [2]. In addition, the irregularities can also be observed by global navigation satellite systems (GNSS), such as the Global Positioning System (GPS), and the observation result is consistent with that of spread-F echoes [3]. Furthermore, some strong irregularities can reach the top of the ionosphere and can be observed in situ by satellite [4].

Owing to lack of appropriate observation data over the low-latitude Africa, the climatology study of African equatorial irregularities is few. There was a study used slant total electron contents to study equatorial bubbles during the first 6 month of 2004 (a solar minimum year) and showed that the bubbles tends to occur during spring equinox and has obviously less occurrence in East Africa [5]. Nowadays, the GPS geodetic database has become more completed than before. This offers a good opportunity to study the climatology of equatorial irregularities over Africa, especially during solar maximum period. The purpose of this paper is to investigate equatorial irregularities under solar maximum in the 24th solar cycle in Middle and East Africa Using GPS.
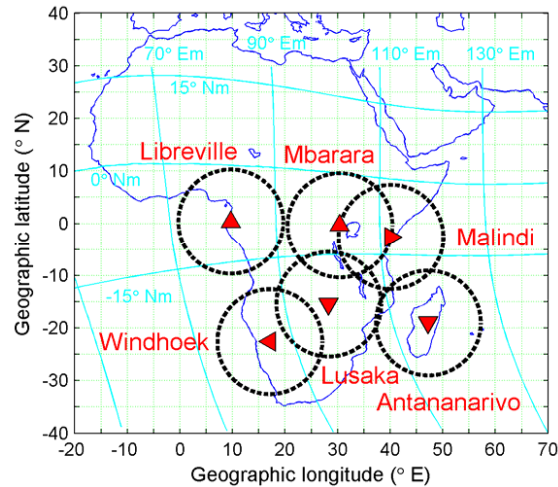
Figure 1: Locations and view fields of GPS tracking sites in Middle and East Africa.

2. DATABASE AND METHOD

The just past 2013–2014 are high solar activity years in the 24th solar cycle, with moderate smoothed yearly sun spot number of 64.9 and 78.9, respectively (both > 50). Six GPS tracking sites of the International GNSS Service (IGS, http://www.igs.org) were found in the middle-east African sector. Their marker names were NKLG, MBAR, MAL2, WIND, ZAMB, and ABPO, which are located in Libreville (Gabon), Mbarara (Uganda), Malindi (Kenya), Windhoek (Namibia), Lusaka (Zambia), and Antananarivo (Madagascar), respectively. For the sake of readability, these sites are represented by the city names at which they are located. The locations of the sites and the fields of view at the height of 400 km with 15° elevation angle over the sites are shown in Figure 1 as triangle symbols and dash circles, respectively. Libreville, Windhoek, Mbarara and Lusaka are in Middle Africa; likewise, Malindi and Antananarivo are in East Africa. The background smooth cyan lines in Figure 1 are auxiliary geomagnetic grid lines, which are in corrected geomagnetic latitude (°Nm) and longitude (°Em). Libreville, Mbarara, and Malindi are at low geomagnetic latitudes (within ±15° Nm) close to the geomagnetic equator (0° Nm); likewise, Windhoek, Lusaka, and Antananarivo are at middle latitudes (outside ±15° Nm). The relations between local time (LT) and universal time (UT) are as the following: for Libreville and Windhoek: LT = UT + 1; for Mbarara and Lusaka: LT = UT + 2; for Malindi and Antananarivo: LT = UT + 3.

The nocturnal ionospheric irregularities are detected using hourly GPS phase-fluctuation index during 1800-0600 LT at each site. GPS phase fluctuations, which were practically high-pass filtered time variation of total electron contents with cutoff period of 25 minutes, were used as an indicator to detect ionospheric irregularities [6]. For quantitatively characterizing GPS phase fluctuations, the hourly phase-fluctuation index F_p is defined as the average of all the quarterly index f_p of satellites available to a site in an hour multiplied by 1000, and the index f_p is the median value of absolute phase fluctuations of a satellite in a 15-minute interval [7,8]. The magnitude of F_p indicates the strength of existing irregularities: $F_p \leq 50$ represents the GPS phase fluctuations come from background noise of irregularities; $F_p > 200$ means the GPS signal is severe influenced by strong irregularities; $50 < F_p \leq 200$ stands for the existence of moderate irregularities.

3. RESULTS AND DISCUSSION

Figure 2 demonstrates an example of comparison for ionospheric irregularity strengths between low and middle latitudes on 2 March 2014. Over Mbarara (low latitudes), irregularities occurred during 17-24 UT (19-02 LT) and caused severe disturbances for vertical total electron contents and phase fluctuations. The hourly index $F_p > 200$ indicated that there occurred strong irregularities during 17-23 UT. However, there were only moderate irregularities ($F_p > 50$) over Lusaka (middle latitudes) during 19-22 UT. The irregularities over Lusaka is considerable weaker than that over Mbarara. Besides, the irregularities over Mbarara occurred earlier than those over Lusaka. Therefore, it seemed that the irregularities were generated at the geomagnetic equator or at low latitudes and then expanded to middle latitudes (i.e., they were equatorial irregularities).

Figure 3 depicts the monthly occurrence rates of nocturnal ionospheric irregularities over Libre-
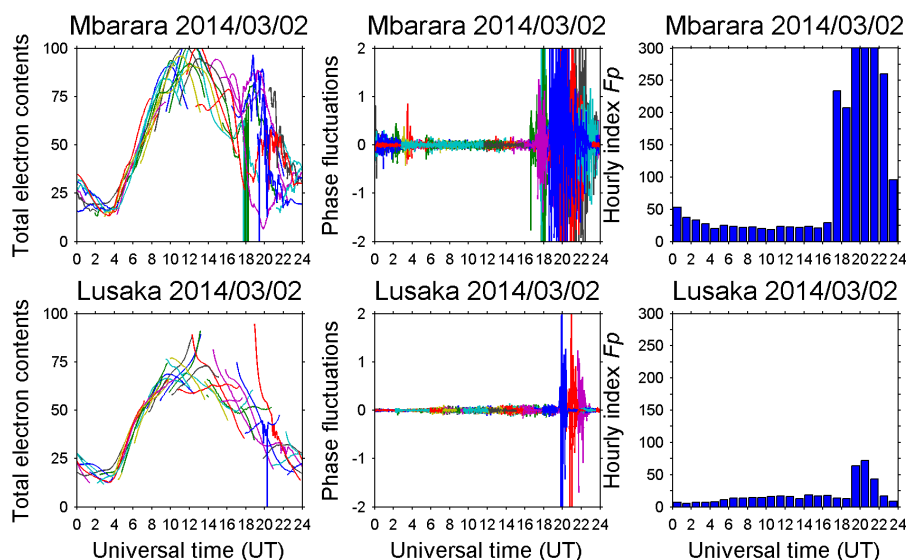
Figure 2: Examples of GPS derived total electron contents, phase fluctuations, and hourly phase fluctuation index F_p over Mbarara and Lusaka for comparison.
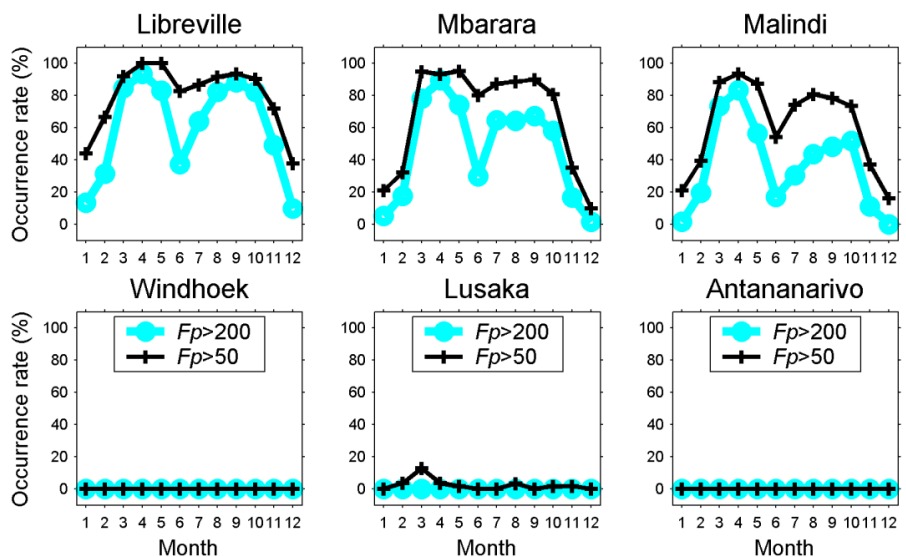
Figure 3: Monthly occurrence rates of nocturnal ionospheric irregularities.

ville, Mbarara, Malindi, Windhoek, Lusaka, and Antananarivo. First, the monthly occurrence rates at middle latitudes (Windhoek, Lusaka, and Antananarivo) were low (nearly 0%) and obviously smaller than those at low latitudes (Libreville, Mbarara and Malindi). This confirms the aforementioned assumption that the irregularities origined at the geomagnetic equator or low latitudes rather than at middle latitudes. By the way, the equatorial irregularities have a narrow latitudinal extent, but are extended in longitude. Second, the patterns of monthly occurrence rate at low latitudes are similar each other, despite that the rates seemed slightly decreasing from west (the Atlantic coast) to east (the Indian coast).

Figure 4 shows the seasonal occurrence rates of nocturnal ionospheric irregularities, which is another aspect of Figure 3. The equinoctial irregularity occurrence rates over the three low-latitude sites decreased slowly from Middle to East Africa (94%, 89%, 83% and 87%, 73%, 64% for moderate and strong irregularities, respectively). Likewise, the June solstitial rates also decreased similarly (90%, 88%, 74% and 67%, 58%, 37%). However, the December solstitial rates decreased faster (55%, 24%, 28% and 26%, 10%, 7%). Thus, the equinoctial and June solstitial occurrence rates were also high in East Africa (83% and 64%; 74% and 37%), while the December solstitial one
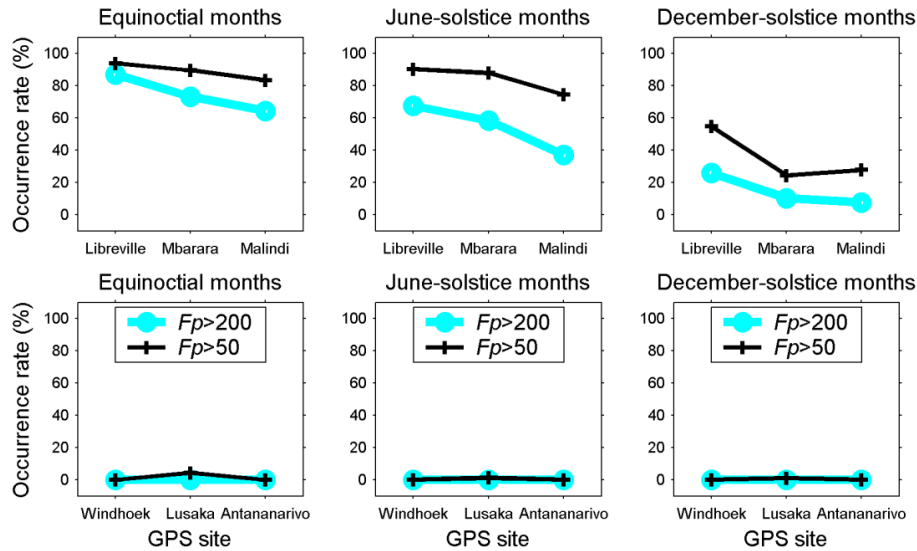
Figure 4: Seasonal occurrence rates of nocturnal ionospheric irregularities.

was low (only 28% and 7%). Although the equinoctial irregularities were dominant, the June solstitial irregularities also occurred frequently and the occurrence rates were comparable to those of equinoctial ones. The June solstitial irregularity occurrence rates have a peak in Middle Africa which nearly catches up with the equinoctial occurrence rate. As for the December solstitial irregularities, they were obviously of minor importance when compared to both the equinoctial and June solstitial ones.

In general, the seasonal climatology of low-latitude ionospheric irregularities can be adequately explained by the alignment of the solar terminator and local geomagnetic meridian [9, 10]. For Middle and East Africa, although the declination angles (the angle between the geomagnetic and geographic meridians) are small (compared to those over the Atlantic Ocean as shown in Figure 1), it still can be expected that the best alignment of the solar terminator and local geomagnetic meridian occurs in December-solstice months. So the December-solstice occurrence rate should be larger than the June-solstice one. However, this expectation doesn't meet the result. Another mechanism proposed by [11] can perhaps be considered here: The magnitude of the $E \times B$ upward drift velocity of pre-reversal enhancement (PRE) at the magnetic equator plays a dominant role on the variability of F region irregularities. Additionally, the late reversal time of the PRE velocity at the magnetic equator would also help the generation of F region irregularities in the equatorial ionosphere. The latest and the earliest reversal times occur in the magnetic equator's local summer and winter, respectively. In Africa, because the magnetic equator is located in the northern hemisphere (as shown in Figure 1), so the June-solstice occurrence rate is larger than the December-solstice one.

Equatorial ionospheric irregularities are plasma bubbles, which often occur in the F region of the ionosphere after sunset near the geomagnetic equator. The irregularities are originally formed on the bottom side of the F region by linear Rayleigh-Taylor instability and then rise and may up to the top of the ionosphere by nonlinear Rayleigh-Taylor instability [12]. They also elongate along geomagnetic fields off the equator to low and even middle latitudes. High equinoctial irregularity occurrence rate is due to large $E \times B$ upward drift in equinoctial months. Both the northward shifted geomagnetic equator (located in the northern hemisphere) and small declination angles in low latitudes may make irregularities occur frequently in June-solstice months but seldom in December-solstice months.

4. CONCLUSIONS

This study has investigated the nocturnal ionospheric irregularities in Middle and East Africa during solar maximum period using the GPS. The aforementioned results and discussion can lead to the following conclusions. (1) The low latitude irregularities come from the geomagnetic equator. (2) The low latitude irregularities often develop in equinoctial and June-solstice months but less develop in December-solstice months. (3) The June solstitial irregularity occurrence rates have a crest in Middle Africa which nearly catches up with the equinoctial occurrence rate. (4) The

solstitial irregularity occurrences may be due to the northward shifted geomagnetic equator and small declination angles in low latitudes.

REFERENCES

1. Yeh, K. C. and C. H. Liu, "Radio wave scintillations in the ionosphere," *Proc. IEEE*, Vol. 70, No. 4, 324–360, 1982.
2. Davies, K., *Ionospheric Radio*, Peter Peregrinus Ltd., London, UK, 1990.
3. Chen, W. S., C. C. Lee, J. Y. Liu, F. D. Chu, and B. W. Reinisch, "Digisonde spread F and GPS phase fluctuations in the equatorial ionosphere during solar maximum," *J. Geophys. Res.*, Vol. 111, A12305, 2006.
4. Su, S.-Y., C. H. Liu, H. H. Ho, and C. K. Chao, "Distribution characteristics of topside ionospheric density irregularities: Equatorial versus midlatitude regions," *J. Geophys. Res.*, Vol. 111, A06305, 2006.
5. Portillo, A., M. Herraiz, S. M. Radicella, and L. Ciraolo, "Equatorial plasma bubbles studied using African slant total electron content observations," *J. Atmos. Solar. Terr. Phys.*, Vol. 70, 907–917, 2008.
6. Aarons, J., M. Mendillo, R. Yantosca, and E. Kudeki, "GPS phase fluctuations in the equatorial region during the MISETA 1994 campaign," *J. Geophys. Res.*, Vol. 101, 26851–26862, 1996.
7. Mendillo, M., B. Lin, and J. Aarons, "The application of GPS observations to equatorial aeronomy," *Radio Sci.*, Vol. 35, No. 3, 885–904, 2000.
8. Tiwari, R., H. J. Strangeways, S. Tiwari, and A. Ahmed, "Investigation of ionospheric irregularities and scintillation using TEC at high latitude," *Adv. Space Res.*, Vol. 52, 1111–1124, 2013.
9. Tsunoda, R. T., "Control of the seasonal and longitudinal occurrenceof equatorial scintillations by the longitudinal gradient inintegrated E region Pedersen conductivity," *J. Geophys. Res.*, Vol. 90, 447–456, 1985.
10. Tsunoda, R. T., "On seeding equatorial spread F during solstices," *Geophys. Res. Lett.*, Vol. 37, L05102, 2010.
11. Fejer, B. G., L. Scherliess, and E. R. de Paula, "Effects of the verticalplasma drift velocity on the generation and evolution of equatorial spreadF," *J. Geophys. Res.*, Vol. 104, 19,859–19,869, 1999.
12. Kelley, M. C., *The Earth's Ionosphere*, Elsevier, San Diego, California, USA, 2009.

Assessment of the Forest Disturbances Rate Caused by Windthrow Using Remote Sensing Techniques

Paula Furtuna[1], I. Haidu[2], I. H. Holobaca[1], M. Alexe[1],
Cristina Rosca[1], and D. Petrea[1]

[1]Faculty of Geography, "Babes Bolyai" University, Cluj Napoca, Romania
[2]Laboratoire LOTERR, Université de Lorraine, France

Abstract— Change detection using multi-temporal satellite images data is an important domain with various applications in forestry and can allow an evaluation of areas extended to the same spatial temporal scale. The focus of the study is to assess the changes occurring after catastrophic wind events using Landsat time series data. Estimates of disturbance rates are derived using 8 sample sites selected across the Apuseni Mountains during 2000–2014 periods. Multi-temporal analysis on annual basis has detected the patterns of the changing forest ecosystem and the trends that are occurring and give more accurate results. The satellite images have been calibrated and the root mean square error has been made The satellite images preprocessing is made in order to transform the DN values into the surface reflectance. The approach requires images during the peak growing season. Local knowledge and available ancillary data about windthrow occurrence are required in order to fully understand the nature of these trends. The statistical algorithms are applied to characterize the magnitude of the disturbance. We found evidence of systematic change in the forest ecosystem of the Apuseni Mountains by analyzing multi-temporal surface data. The accuracy of forest disturbance detection diminishes with the decrease of the temporal resolution. Therefore, the approach described in this paper demonstrates that the Landsat time series data can be used operationally for assessing forest cover changes analysis after a windthrow occurrence across a large area.

1. INTRODUCTION

Forests are one of the most important components of the global biosphere and have critical influences on the Earth's ecological balance, [11]. The forest vegetation is constantly changing [6]. The changes causes can be determined by anthropic or natural factors. Natural disturbances play an important role in forest ecosystem, but they can cause huge economic damage. Forest disturbance by wind varies from large-scale to small scale perturbations operating at the scale of individual trees [4]. According to [1] storms are responsible for more than 50 % of all primary abiotic and biotic damage by volume to European forests from catastrophic events. In the Romanian Carpathians, recent statistics shows that about 28% from the Romanian afforested surface is vulnerable to windthrow phenomena, [9].

The overall aim of this research is to detect and assess the forest disturbances rate over Apuseni Mountains by using Landsat multi-temporal images and by calculating spectral indices, including the red-edge band and other commonly used vegetation indices. Based on the differences of histograms among different forests we obtained the 2000–2014 forests distribution for Apuseni Mountains at a spatial resolution of 30-m × 30-m.

2. METHODS

2.1. Study Sites and Data Used

The study area is located in the Western Romanian Carpathians, Apuseni Mountains-which lies between the Pannonian Plain and Transylvanian Plateau, (Fig. 1). It encompasses $10750 \, \text{km}^2$, with geographic center located at 46°21' N and 23°02'E. The mountains are of no great height except for a central area where there are several peaks higher than 1800 m.

The mean annual air temperature is 6–10°C and means annual precipitation is 700–1000 mm [5]. The air circulation is predominantly westerly and the mean annual values of air temperature are generally lower on the western slopes, compared to the eastern ones at the same altitude, as a result of the interaction processes between the surface of the slopes and the moving air. Prevailing winds in the region generally came from the west, on the eastern side of the Apuseni Mountains the föehn is felt as a local wind. In certain synoptic conditions the wind may reach maximum speeds of over 40 m/s in the area with high altitudes. On the eastern slopes of the Apuseni the maximum wind speeds reach 28 m/s and 16–27 m/s in the rest of the areas.

The potential natural vegetation is formed by zonal mixed beech (Fagus sylvatica)-fir (Abies alba)-spruce (Picea abies) forests and spruce (Picea abies) forest.
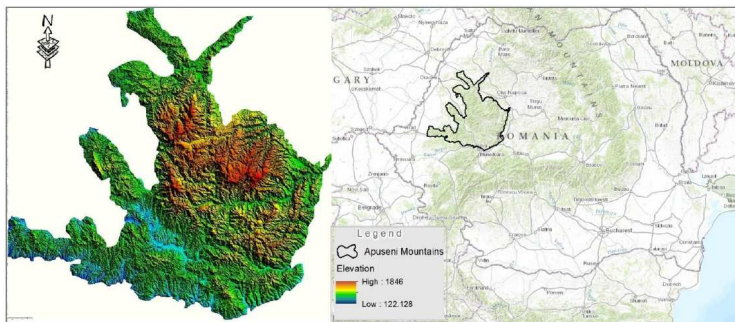
Figure 1: Location of study area.

Assessment of the windthrow occurrence using the remote sensing data requires satellite images from the year before and the year after the windfall event. At the same time the estimation of rate disturbance requires the use of scenes covering a longer period of time to achieve better results and representation of changes in the forest environment and to determine trends. Use of dense image acquisitions is therefore necessary in order to minimize potential omission errors in derived disturbance products [3].

To conclude the study we used database which contain Landsat satellite imagery and forestry data. Forestry data is represented by inventory tables of windthrow occurrence for the years 2002, 2004, 2006 2007, 2011 and 2013.

The satellite images was obtained for 2000-2014 period and corresponding for Path 185/Row 28 and were acquired during the growing season. The Landsat sensors are particularly appropriate for providing the imagery used to generate change information for assessing and monitoring natural resources, [10].

2.2. Spectral Indices

The pre-processing operation was made in order to calculate the root mean square error (RMSE) and to convert the digital number into surface reflectance, necessary to carry out the following operations. A low pass filter (kernel size: 3×3) was applied to the images to reduce radiometric noise as well as enhance the effectiveness in detection process.

The main workflow steps of windthrow analysis include: (i) detecting the disturbance pixels; (ii) calculate the spectral index; (iii) filtering training data and disturbances pixel through a number of statistical filters; (iv) mapping forest disturbance.

We generated indices to evaluate the optical properties of disturbance in forest ecosystem. The spectral indices used in this paper including: NDVI, NDVI 750, GI, and NNIR, (Table 1).

NDVI was used because is positively correlated with total green biomass [8] and is useful because it shows spatial and temporal trends in vegetation dynamics, productivity and distribution [7]. The NDVI 750 index was found to show maximum sensitivity to a wide range of chlorophyll contents [2].

Table 1: Vegetation indices used for the performance evaluation.

Name	Formula	Application	References
NDVI (Normalized Difference Vegetation Index)	(NIR–Red)/(NIR + Red)	Biomass, stress, vitality	[12]
NDVI 750 (Red-edge Normalized Difference Vegetation Index)	(R750-R750)/(R750+R750)	Changes in leaf and canopy structures	[2]
GI (Greenness Index)	Green/Red	Chlorophyll activity	[5]
NNIR (Normalized Near Infrared)	NIR/(NIR + Red + Green)	Biomass, chlorophyll activity	[11]

3. RESULTS

The forestry area was analyzed by first masking out the non-forest land cover classes and the spectral indices were standardized around the scene mean forest value to obtain better results. The windthrow detection was made based on the relationship between the spectral indexes. Tracing the polygons for affected areas (Fig. 3) was made automatically by establishing the difference between the spectral indices calculates for each year's corresponding for before and after period of each windthrow.

Next step consisted in delineating of windthrow concentrations. The separability filters allowed us to determine how distinct and separable the vegetation indices for the disturbed surface are from each other. The frequency filter was applied to spectral indices used for 2000–2014 period to show the spatial frequencies of each pixel for disturbed areas. Also to determine the number of pixels associated with the major disturbance and to characterize the temporal trajectory for a change pixel. The scatter plots were used to locate the disturbed pixels and capturing change
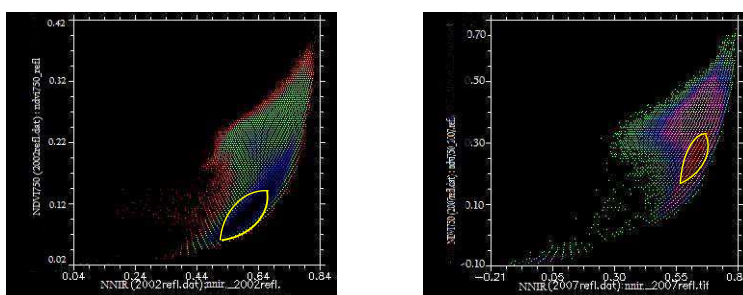
Figure 2: Scatter plots used to locate the disturbed pixels (example for year 2002 and 2007).
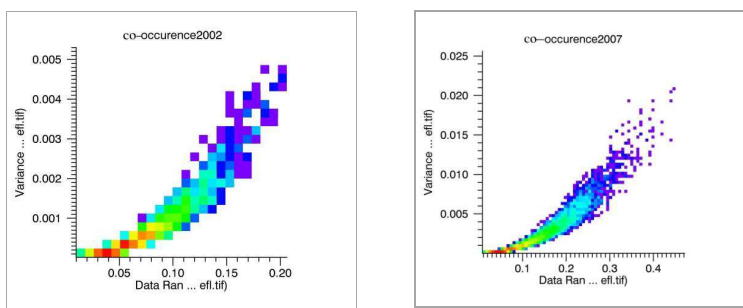
Figure 3: Relationship between the co-occurrence variance and the vegetation indices (example year 2002 and 2007).
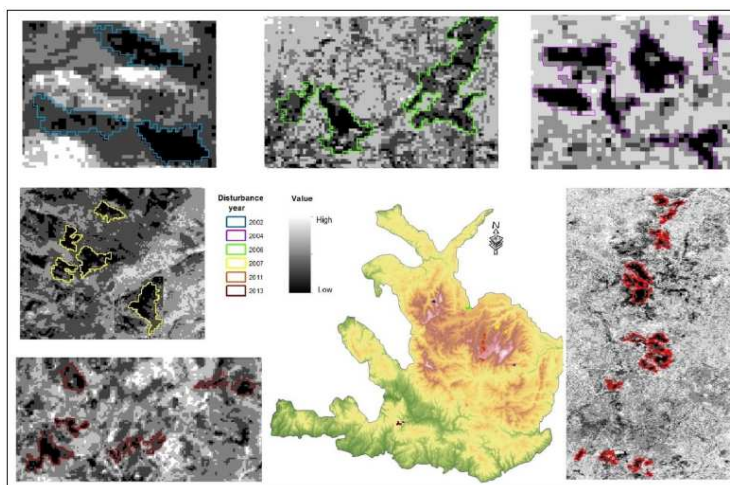
Figure 4: Windthrows area detected for 2000–2014 period.

events, (Fig. 2).

The co-occurrence filters were used to generate, based on disturbed area vegetation indices value, features for each disturbed area. The relationships between the images for before and after windthrow were "texturally" distinct when the disturbance occurred. Therefore the images were classified in three classes constant forest, disturbed area and constant other classes. Spectrally two stands can be confused, but the difference in structure and the resulting texture by applying a filter allow distinguishing between them. This filter includes mean, variance, homogeneity and correlation. Monotonic relationships were observed between the variable for these filter and vegetation indices (Fig. 3).

The synchronicity of each windthrow detected was evaluated by consulting the meteorological information to confirm the occurrence of a storm in the area and by consulting forest company archives.

4. CONCLUSION

Through analysis of multi-temporal Landsat data, we found evidence of systematic change in forest ecosystem from Apuseni Mountains. The similarities of the vegetation indices in near-infrared limit the ability to distinguish between windthrow area and harvest, therefore the windthrow area have been established by using forestry and meteorological data.

The approach described in this paper demonstrates that Landsat data can be used operationally for assessing forest cover changes analysis after a windthrow occurrence but the local knowledge and available ancillary data about windthrow occurrence are required in order to fully understand the nature of these trends.

Further investigations are, still, required into how the relationship can be modeled between the disturbance probability values obtained from this approach and the results obtained from forest monitoring on ground truth data.

REFERENCES

1. Gardiner, B., K. Blennow, J. M. Carnus, P. Fleischer, F. Ingemarson, G. Landmann, M. Lindner, M. Marzano, B. Nicoll, C. Orazia, J. L. Peyron, M. P. Reviron, M. J. Schelhaas, A. Schuck, M. Spielmann, and T. Usbeck, "Destructive storms in European forests: Past and forthcoming impacts," *European Forest Institute, Final Report to European Commission*, 138, 2011, Online: http://www.sifi.se/wp-content/uploads/2011/01.

2. Gitelson, A. A. and M. N. Merzlyak, "Spectral reflectance changes associated with autumn senescence of Aesculus hippocastanum L and Acer platanoides L leaves-spectral features and relation to chlorophyll estimation," *J. Plant Physiol.*, Vol. 143, 286–292, 1994.

3. Huang, C., S. N. Goward, J. G. Masek, F. Gao, E. F. Vermote, N. Thomas, K. Scleewies, R. E. Kennedy, Z. Zhu, J. C. Eidenshink, and J. R. G. Townshend, "Development of time series stacks of Landsat images for reconstructing forest disturbance history," *International Journal of Digital Earth*, Vol. 2, No. 3, 195–218, 2009.

4. Kuuluvainen, T. and P. Juntunen, "Seedling establishment in relation to microhabitat variation in a windthrow gap in a boreal Pinus sylvestris forest," *J. Veg. Sci.*, Vol. 9, No. 4, 551–562, 1998.

5. Le Maire, G., Franc, C. Francois, and E. Dufrene, "Towards universal broad leaf chlorophyll indices using PROSPECT simulated database and hyperspectral reflectance measurements,"*Remote Sensing Environment*, Vol. 89, No. 1, 1–28, 2004.

6. Maier, N., "Studiul instabilităţii atmosferice şi a ecourilor radar în scopul realizării prognozei de tip "Now casting" a precipitaţiilor din Munţii Apuseni," Phd thesis, 2011.

7. Manning, A. D., J. Fischer, A. Felton, B. Newll, W. Steffen, and D. B.Lindenmayer, "Landscape fluidity — A unifying perspective for understanding and adapting to global change," *Journal of Biogeography*, Vol. 36, 193–199, 2009.

8. Nemani, R. R., C. D. Keeling, H. Hashimoto, W. M. Jolly, S. C. Piper, C. J. Tucker, R. B. Myneni, and S. W. Running, "Climate-driven increases in global terrestrial net primary production from 1982 to 1999," *Science*, Vol. 300, 1560–1563, 2003.

9. Pettorelli, N., J. Vik, A. Mysterud, J. M. Gaillard, C. Tucker, and N. Stenseth, "Using the satellite-derived NDVI to assess ecological responses to environmental change," *Trends Ecol. Evol.*, Vol. 20, 503–510, 2005.

10. Savulescu, I. and B. Mihai, "Geographic information system (GIS) application for windthrow mapping and management in Iezer Mountains, Southern Carpathians," *Journal of Forestry Research*, Vol. 23, No. 2, 175–184, 2012.

11. Sripada, R. P., R. W. Heiniger, J. G. White, and A. D. Meijer, "Aerial color infrared photography for determining early in-season nitrogen requirements in corn," *Agronomy Journal*, Vol. 98, 968–977, 2006.

12. Tucker, C. J., "Red and photographic infrared linear combinations for monitoring vegetation," *Remote Sensing of Environment*, Vol. 8, 127–150, 1979.

13. Vogelmann, J. E., G. Xian, C. Homer, and B. Tolk, "Monitoring gradual ecosystem change using Landsat time series analyses: Case studies in selected forest and rangeland ecosystems," *Remote Sensing of Environment*, Vol. 122, 92–105, 2012.

14. Zhao, X., P. Xu, T. Zhou, Q. Li, and D. Wu, "Distribution and variation of forests in China from 2001 to 2011: A study based on remotely sensed data," *Forests*, Vol. 4, 632–649, 2013.

Monitoring Land Use Change in South-west Romania Using Multi-temporal Landsat Remote Sensing Imagery

Cristina Rosca[1], I. Holobaca[1], M. Alexe[1], D. Petrea[1], Paula Furtuna[1], and I. Haidu[2]

[1]Faculty of Geography, Babeş-Bolyai University, Cluj-Napoca, Romania
[2]Laboratoire LOTERR, Université de Lorraine, Ile du Saulcy, Metz 57000, France

Abstract— The changes in land cover in south-west Romania could affect the low frequency cycle of precipitation regime through changes in ground water stress and atmospheric circulation. Monitoring these changes using satellite images has been proved less expensive, as well as more reliable compared to conventional methods. The 50 ha of walnuts plantation, which were meant to strengthen the dunes in the area, have been deforested since 2013. This analysis to detect the deforestation was done using GIS, ENVI and ERDAS software and the method was made based on NDVI. The entire study was made with Landsat remote sensing imagery, choosing the month July. The change is quantified via spectral (image) or thematic (characterization) contrast. The percentage of vegetation losses after deforestation was 85.7%.

1. INTRODUCTION

Early detection of land use changes is important for environments with a frail ecological equilibrium like the ones affected by drought or having a sandy soil. Sudden changes are caused by modifications in landscape alteration, disturbing events, deforestation being the main phenomena in this case study. In general, these types of events radically alter the spectral properties of the land surface, and are readily discernible in Landsat imagery [7]. Human-made forcings result from, for example, the gases and aerosols produced by fossil fuel burning, and alterations of Earth's surface from various changes in land use, such as the conversion of forests into agricultural land [1]. GIS and Remote Sensing have the potential to support such models, by providing data and analytical tools for the study of environment. The literature is replete with examples of mapping and monitoring major disruptive changes using remotely sensed data [2–5, 8].
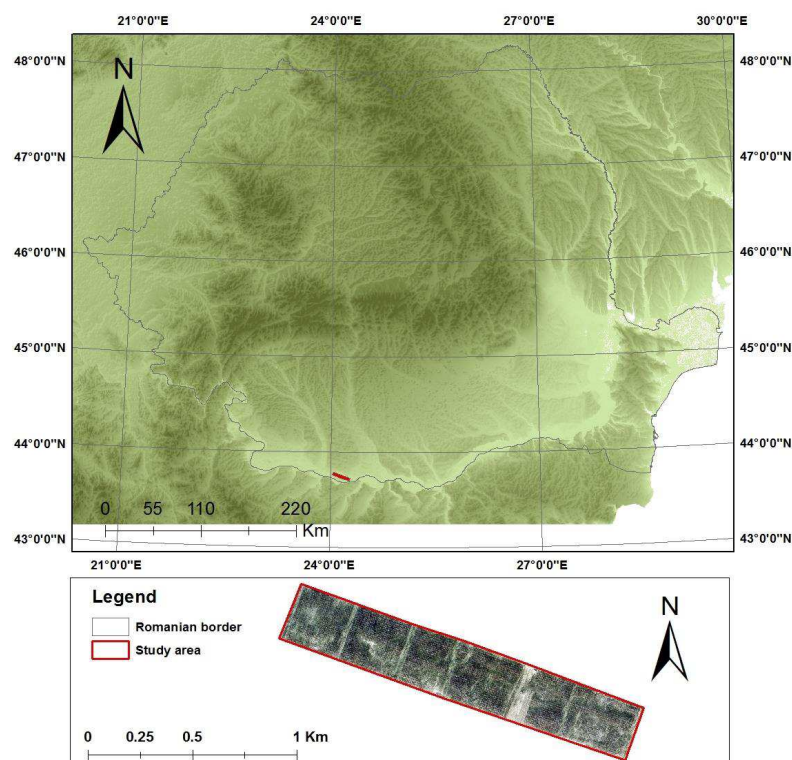
Figure 1: Walnut plantatin location.
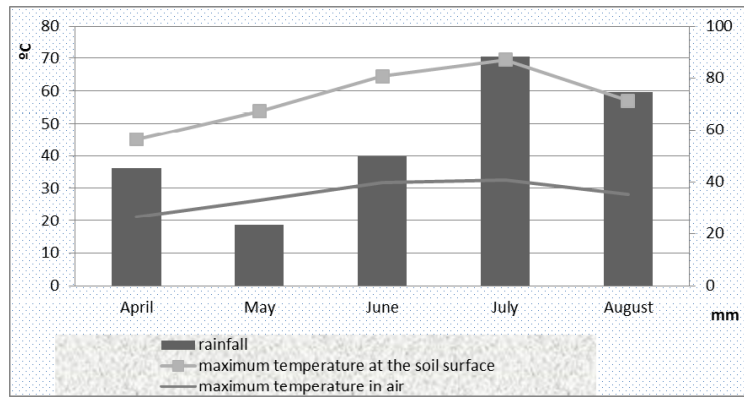
Figure 2: Climatic parameters for growing season — Bechet weather station (1987–2013).
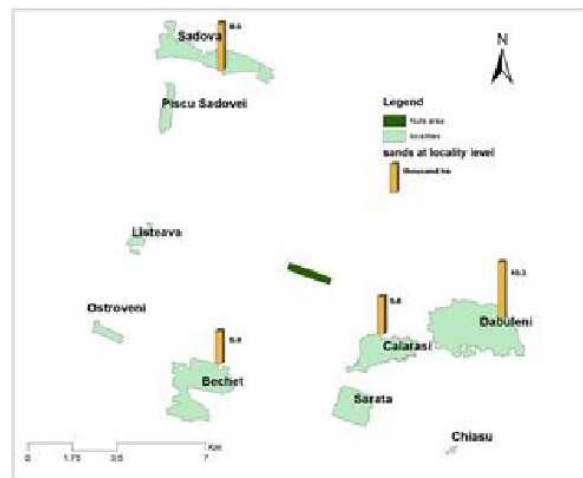
Figure 3: Sands at locality level according with Research Development Center for Agricultural Plants on Sands Dăbuleni, 2009.

2. STUDY AREA

The study area from Romanian Plain with a frail equilibrium also has a sandy soil and was covered by a walnut plantation which has now been affected by deforestation (Figure 1). Regarding the meteorological aspect, during the summer time, the area is not affected only by atmospheric drought but even pedological, with maximum temperatures up to 40°C in the air and 50–70°C at ground level. Rainfall records have a negative trend. July monthly rainfall average is 90 mm (Figure 2) which usually falls in only 5 to 7 days. Prevailing wind direction is the same as the sand dunes exposure, from West to East, with a frequency of 27.6%.

The walnut tree has been chosen for the fixation of the sand dunes (sands soils at the locality level is shown in Figure 3) due to its profound radicular system. The plantation started since 1977, but it has been gradually deforestated since the fall of 2012 onwards. A favourable plantation and development would be almost impossible due to non-operating irigation system and the pronounced pedological drought.

3. SURFACE DATA

The study area is covered by 5 satellite images from years 1987, 1993, 2006, 2009 and 2014. We used a multi-temporal imagery of Landsat Thematic Mapper (TM) and Landsat 8 (OLI) images for Path 184 and Row 29. The study area has the geographical coordinates: 43°49″17′ lat. N and 24°01″08′ long. E. The polygon corresponding with the studied area, walnuts plantation from the S-W Romania, was created using Google Earth, because the precise location was determined using GPS. In order to ensure comparability of data, it was chosen the month July, because in the full vegetation season the crowning is very developed. We chose July because then it is produced a large NDVI response. Preprocessing procedures can be expressed as: (1) radiometric calibration, each

imagine was calibrated using Radiometric Calibration tools from ENVI software, (2) clipping the imagines used to get a subset where the test site is located, (3) RMSE (horizontal root mean square error) calculation by Erdas software, (4) NDVI calculation using Raster Calculator by ArcMap 10.1, (5) mathematical operation (report, difference) using NDVI product corresponding to each year of study.

4. CHANGE DETECTION

For this case study we've used remote sensing techniques integrated in a surface analysis in order to identify the walnut plantation areas affected by deforestation. This disturbing event was caused by human interference. Starting with the fall of 2012 the deforestation took place gradually until the fall of 2013. All six allotments have been cut gradually, but started from only branch cutting and ended with cutting the trunks. Due to its temporal profile with different types of seasonal coverages, we have calculated the NDVI using a common extraction data, the value thresholds method, based on the idea that the disturbing phenomena occured in the same time with the decrease of NDVI
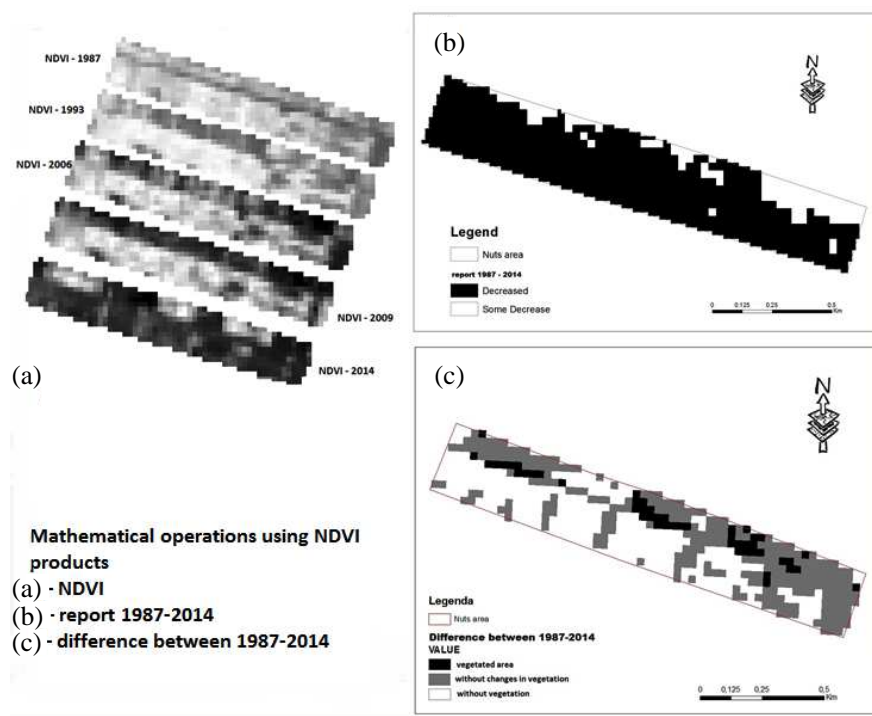
Figure 4: Walnut plantation — change detection (tool models).
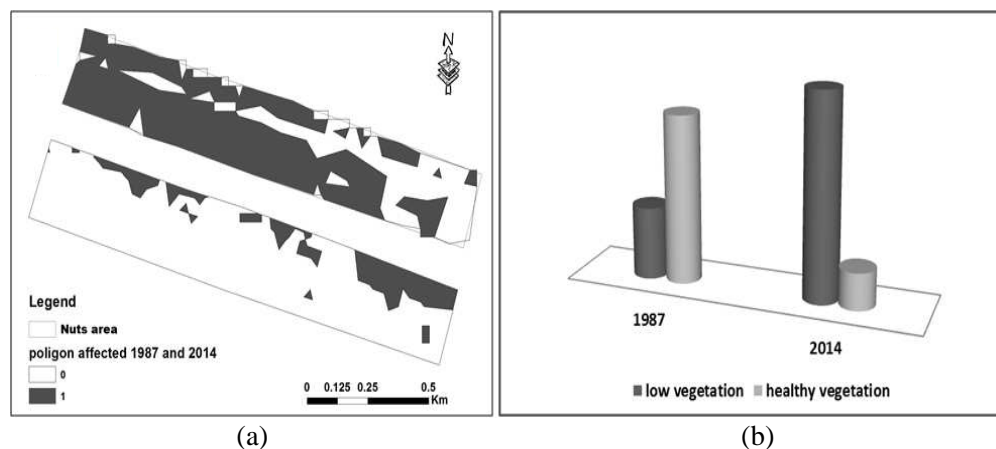
Figure 5: (a) Raster to vector conversion. (b) NDVI — quantitative analysis.

values, under the threshold. Thus we have graphically represented reality (Figure 4). Horizontally it means square error calculated for the satellite images used is situated between 0.3–0.35. The analysis required crossing from raster to vector representation, thus 0 values are polygons with a scattered vegetation and 1 values are dense vegetation polygons (Figure 5(a)). The negative and positive pixel values from 1987 and 2014 are acacia curtains that separate walnut plantation allotments and walnut trunks which weren't effectively ground cut so they grew new branches in the vegetation period of July. Surface analysis indicated a growth in deforestated areas, so if in July 1987, scattered vegetation areas had a low value of 15,05%, in July 2014 affected areas reached 42.7% (Figure 5(b)).

5. CONCLUSIONS

South-West Romania is facing major transformations regarding its land use. Human interference has higher and higher levels given that climate variability is corelated with a faulty management in maitaining and improving mitigation methods. GIS and remote sensing instruments like multi-temporal analysis of preprocessed Landsat satellite imagery followed by applying NDVI mathematic equations provided the data and analytical instruments which led to the disturbing phenomena detection. Quantitative analysis highlighted the high percentage of vegetation loss, of 85.7%, the rest of 14.3% being insignificant reported to the protection factors of that area's degree of necessity. Applying this change detection method, in this area with a frail equilibrium, led to findings which can be materialized in reorganising land use methods.

ACKNOWLEDGMENT

REFERENCES

1. Committee on the Science of Climate Change, National Research Council, *Climate Change Science – An Analysis of Some Key Questions*, 6, National Academy Press, Washington, DC, 2001.
2. Ding, Y., K. Zhao, X. Zheng, and T. Jiang, "Temporal dynamics of spatial hetero-geneity over cropland quantified by time-series NDVI, near infrared and redreflectance of Landsat 8 OLI imagery," *Int. J. Appl. Earth Observ. Geoinf.*, Vol. 30, 139–145, 2014.
3. Hansen, M. C. and T. R. Loveland, "A review of large area monitoring of land cover change using Landsat data," *Remote Sens. Environ.*, Vol. 122, 66–74, 2012.
4. Huang, C., S. N. Goward, J. G. Masek, N. Thomas, Z. Zhu, and J. E.Vogelmann, "An automated approach for reconstructing recent forest disturbance historyusing dense Landsat time series stacks," *Remote Sens. Environ.*, Vol. 114, 183–198, 2010.
5. Masek, J. G., C. Huang, R. Wolfe, W. Cohen, F. Hall,, J. Kutler, and P. Nelson, "North American forest disturbance mapped from a decadal Landsat record," *Remote Sensing of Environment*, Vol. 112, 2914–2926, 2008.
6. *Annals of Research Development Center for Agricultural Plants on Sands Dăbuleni*, Editura Sitech, Craiova, 2009.
7. Vogelmann, J. E., S. M. Howard, L. Yang, C. R. Larson, B. K. Wylie, and J. N. Van Driel, "Completion of the 1990's national land cover data set for the conterminous United States," *Photogrammetric Engineering and Remote Sensing*, Vol. 67, 650–662, 2001.
8. Wulder, M. A., C. R. Butson, and J. C. White, "Cross-sensor change detection over a forested landscape: Options to enable continuity of medium spatial resolution measures," *Remote Sensing of Environment*, Vol. 112, 796–809, 2008.

Looking for a Biophysical Approach to Early Stages of Chronic Kidney Disease

Alberto Foletti[1, 2] and Mario Cozzolino[3]

[1]Institute of Translational Pharmacology, National Research Council-CNR, Rome, Italy
[2]Clinical Biophysics International Research Group, Lugano, Switzerland
[3]Department of Health Sciences, University of Milan, Italy

Abstract— Chronic Kidney Disease (CKD) and its subsequent complications and consequences are an increasing concern in general population. A biophysical integrated approach in early stages of CKD was investigated in 30 patients with a 12-month follow-up. A clinical approach based on the use of an electro medical device (Medselect 729) was employed following previous reports as well as the procedure of electromagnetic information transfer through aqueous systems. Interestingly, we observed a significant increase in the estimated glomerular filtration rate (e GFR) according to CKD-EPI formula ($+11.57$ ml/min; $+18.43\%$, $p < 0.0001$). Beside further studies are certainly recommended, a biophysical integrated approach in the management of early stages of Chronic Kidney Disease seems actually to be feasible, effective, and promising.

1. INTRODUCTION

Chronic Kidney Disease (CKD) and its subsequent complications and consequences are an increasing concern in general population. Moreover, CKD is very likely related to aging. CKD contributes also to the general increase of allostatic load, as consequence of adaptive stress [1], and frailty in elderly people [2]. According to the allostatic load theory, CKD is a result of the increasing rate of chronic stress-related syndromes in both young and elderly people [3]. Successful management of CKD may play an important role on successful aging strategies together with the management of other emerging chronic diseases.

Biophysical methods are emerging tools in clinical practice and several studies have shown their potential use in preventing chemotherapy induced mielotoxicity [4], in treatment of gonarthrosis [5], and rheumatoid arthritis [6], in improvement of renal function in a case of autoimmune nephritic syndrome [7], in relieving from chronic constipation or diarrhoea [8], and as an effective alternative to pharmacological treatments of chronic pain [9–11]. Biophysical therapies are thought to be effective due to a resonance effect [12]. Resonance occurs between therapeutically delivered signals and target tissues, which allows the achievement of local and/or systemic effects [13]. In this pilot study, we integrated the current CKD treatment of early stages of CKD with a biophysical procedure to assess whether it could be of some support.

2. MATERIAL AND METHODS

2.1. Study Design

This was an open-label prospective cohort study.

2.2. Study Population

30 patients aged 63.60 ± 11.83 (13 Males, age 61.92 ± 12.69 and 17 Females, age 64.88 ± 11.35), with early stages of CKD (CKD stages I and II, estimated Glomerular Filtration Rate, eGFR > 60 ml/min) were enrolled. After being informed about the aim, methods, and timing of the study, all patients provided a signed written informed consent form. This study was performed in accordance with the declaration of Helsinki.

2.3. Evaluation of Estimated Glomerular Filtration Rate

After considering which method should be simple, useful, and reliable among those available in clinical use for estimation of the glomerular filtration rate [14] we decide to employ the CKD-EPI formula [15]. Serum creatinine was sampled every three months in order to calculate CKDEPI values before each administration of the biophysical procedure.

2.4. Biophysical therapy procedure

A 2-step treatment was administered to each patient. The 1st step consisted of selecting the program "regulation therapy" on the touch screen of the Med Select 729 device (Wegamed, GmbH, Essen, Germany) to record the endogenous input signals at the low back region of each patient and of delivering the therapeutic electromagnetic output signals on an electromagnetic, full body, carpet on which the patient laid on for 10 minutes. The program "basic drainage therapy" was next selected from the touch screen of the Med Select 729 device to record the endogenous input signals at the renal region and deliver the therapeutic output signals at the kidney's site for 10 minutes. These output therapeutic signals were meanwhile recorded on a commercial available aqueous system (Nomabit Base, Named SRL, MB Italy) by placing the solution into a special output coil, built-in for this aim in the Med Select 729 device. This medical device operates in the low frequency range (between 0 and 20 KHz) using a magnetic field with an intensity similar to the Earth's magnetic field with a maximum of 50 μT. It allows to record input signals using two electrodes and to send output signals to the patient through two magnetic electrodes for local use, for example, on the pain site, or through a magnetic carpet where the patient can lay down (in this way the entire body of the patient can be treated). Therefore, the device can simultaneously deliver a local and systemic treatment. The recording circuit and procedures are described in detail in a previous study as Electromagnetic Information Transfer Through Aqueous System [16] . The Nomabit Base aqueous solution was subsequently self-administered by the patient in order to allow the therapeutic information recorded to be delivered according to a weekly plan beginning on Monday with a single drop and increasing by one drop/day up to 6 drops on Saturday; no therapy was administered on Sunday [7, 9–11]. The Nomabit Base solution is composed of oligominerals and is currently used as a food supplement. It is provided with a dropper and stored in an aluminum-shielded container, which ensures that the signals are preserved on the aqueous solution and are protected from environmental thermal and electromagnetic pollution. This is an "off label" use of a common dietary supplement, which is already suited to be stored for a long period of time (up to three months after opening, as indicated by the manufacturer, which avoids the risk of alteration of its characteristics).

2.5. Statistical Analysis

Statistics was performed with Student's t-test. A p-value < 0.05 was considered statistically significant.

3. RESULTS

All patients who enrolled completed the study. No side effects were reported. At baseline, mean eGFR, according to the CKD-EPI formula, was 67.80 ± 12.75 ml/min. After 12 months, mean eGFR score was 79.37 ± 14.71 ml/min. There was a 18.43% increase in eGFR ($p < 0.01$) (Figure 1).
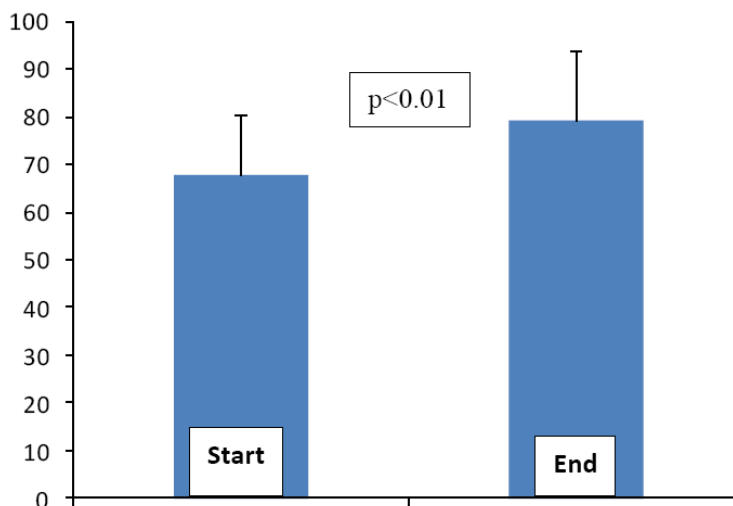
Figure 1: Variation in the estimated Glomerurar Filtration Rate eGFR (on the left column) from the start to the end of the study after 1 year.

4. DISCUSSION

The aim of this pilot study was to identify a novel potential synergistic strategy for early stages CKD patients. The use of the electromagnetic information transfer of endogenously produced therapeutic signals seems to represents a very promising therapeutic tool since only a single treatment needs to be performed by the physician on each patient every three months. A total of four treatment were therefore delivered during the study. This approach may represent a novel approach to improve quality of life for patients and save clinical resources. A significant increase of eGFR has been observed, with no side effects. This preliminary study provides substantial evidence that a biophysical approach to early stages CKD patients is feasible, effective, safe, and long lasting. Since, CKD is progressively increasing in general population [17], in adults [18], and especially in elderly [19], these results may contribute to delay the progression of CKD. eGFR reduction associates with all-cause mortality and cardiovascular even in a low risk population [20]. Therefore, any synergistic strategy aimed to manage effectively early stage CKD patients, through maintenance or increase eGFR should be considered as a complementary and useful tool to manage public health and to support successful aging [21, 22].

5. CONCLUSIONS

In conclusion, the integration of a biophysical approach in current management of early stages of CKD appears to be feasible, safe, and effective. A biophysical integrated approach may also represent a synergistic and personalized tool to reduce age-related global functional decline [21, 22]. Beside further studies are certainly recommended, a biophysical integrated approach in the management of early stages of Chronic Kidney Disease could probably represent a valuable integrative tool in the field of preventive medicine.

ACKNOWLEDGMENT

REFERENCES

1. McEwen,B. S. "Stress, adaptation and disease. Allostasis and allostatic load," *Ann. N.Y. Acad. Sci.*, Vol. 840, 33–44, 1998.
2. Grunewald, T. L., T. E. Seeman, A. S. Karlamangla, and C. A. Sarkisian, "Allostatic load and frailty in older adults," *J Am Geriatr Soc.*, Vol. 57, NO. 9, 1525–1531, 2009.
3. Glein, D. A., N. Goldman, Y.-L. Chuang, and M. Weinstein, "Do chronic stressors lead to physiological dysregulation? Testing the theory of allostatic load," *Psychosomatic Med.*, Vol. 69, No. 8, 769–776, 2007.
4. Rossi, E., M. T. Corsetti, S. Sukkar, and C. Poggi, "Extremely low frequency electromagnetic fields prevent chemotherapy induced myelotoxicity," *Electromagn Biol Med.*, Vol. 26, No. 4, 277–281, 2007.
5. Maiko, O. and E. F. Gogoleva, "Outpatient bioresonance treatment of gonarthrosis," *Ter Arkh.*, Vol. 72, No. 12, 50–53, 2000, Article in Russian.
6. Islamov, B. I., V. A. Funtikov, R. V. Bobrovski, Y. V. Gotovskii, "Bioresonance therapy in rheumatoid arthritis and heat shock proteins," *Bull Exp Biol Med.*, Vol. 128, No. 11, 525–528, 1999.
7. Foletti, A. and M. Cozzolino, "A biophysical integrated approach to autoimmune nephrotic syndrome: Case report," *Recenti Prog Med.*, Vol. 104, No. 9, 488–489, 2013, Article in Italian.
8. Bokkon, I., A. Erdöfi-Szabó, A. Till, T. Lukacs, and E. Erdöfi-Nagy, "EMOST: Elimination of chronic constipation and diarrhea by low-frequency and intensity electromagnetic fields," *Electromagn Biol Med.*, Vol. 33, No. 1, 68–74, 2014.
9. Baron, P., G. Bucci, A. Rinaudo, R. Rocco, E. Sclauzero, and A. Foletti, "System information therapy in the management of pain: a pilot study," *PIERS Proceedings*, 1698–1702, Stockholm, Sweden, August 12–15, 2013.
10. Foletti, A., P. Baron, E. Sclauzero, G. Bucci, A. Rinaudo, and R. Rocco, "Assessment of biophysical therapy in the management of pain in current medical practice compared with ibuprofen and placebo: A pilot study," *J. Biol. Regul. Homeostat. Agents*, Vol. 28, No. 3, 431–439, 2014.
11. Foletti, A. and J. Pokorny, "Biophysical approach to low back pain: A pilot report," *Electromagn. Biol. Med.*, in press, 2015.

12. Foletti, A., S. Grimaldi, A. Lisi, M. Ledda, and A. R. Liboff, "Bioelectromagnetic medicine: The role of resonance signaling," *Electromagn. Biol. Med.*, Vol. 32, No. 4, 484–499, 2013.

13. Liboff, A. R., "Local and holistic electromagnetic therapies," *Electromagn. Biol. Med.*, Vol. 26, No. 4, 315–325, 2007.

14. Yildiz, G., K. Mağden, Y. Abdulkerim, F. Ozcicek, E. Hur, and F. Candan, "Glomerular filtration rate: Which method should we measure in daily clinical practice?," *Minerva Med.*, Vol. 104. No. 6, 613–623, 2013.

15. Levey, A. S., L. A. Stevens, C. H. Schmid, Y. L. Zhang, A. F. Castro, H. I. Feldman, J. W. Kusek, P. Eggers, F. Van Lente, T. Greene, and J. Coresh, CKD-EPI (Chronic Kidney Disease Epidemiology Collaboration), "A new equation to estimate glomerular filtration rate," *Ann. Intern. Med.*, Vol. 150, No. 9, 604–612, 2009.

16. Foletti, A., M. Ledda, E. D'Emilia, S. Grimaldi, and A. Lisi, "Experimental finding on the electromagnetic information transfer of specific molecular signals mediated through aqueous system on two human cellular models," *J. Altern. Complement. Med.*, Vol. 18, No. 3, 258–261, 2012.

17. Mitchell, T., N. Hadlow, and A. Chakera, "The impact of routine reporting of estimated glomerular filtration rate using the CKD-EPI formula in a community population: A cross-sectional cohort study," *Nephrology (Carlton)*, Vol. 19, No. 9, 581–6, 2014.

18. Cueto-Manzano, A. M., L. Cortes-Sanabria, H. R. Martinez-Ramirez, E. Rojas-Campos, B. Gomez-Navarro, and M. Castillero-Manzano, "Prevalence of chronic Kidney disease in an adult population," *Arch Med Res.*, pii: S0188-4409(14)00130-1, 2014.

19. Nitta, K., K. Okada, M. Yanai, and S. Takahashi, "Aging and chronic kidney disease," *Kidney Blood Press Res.*, Vol. 38, No. 1, 109–120, 2013.

20. Levey, A. S., L. A. Inker, and J. Coresh, "GFR estimation: From physiology to public health," *Am. J. Kidney. Dis.*, Vol. 63, No. 5, 820–834, Review, 2014.

21. Henney, A. M., "The promise and challenge of personalized medicine: aging populations, complex diseases, and unmet medical need," *Croat. Med. J.*, Vol. 53, No. 3, 207–210, 2012.

22. Foletti, A., "Toward a personalized biophysical approach to stress related diseases and successful aging," *Proceedings of the 3rd International Symposium "Biophysical Aspects of Complexity in Health and Disease"*, 19–21, Lugano, Switzerland, October 4, 2014.

Steps towards a Biophysical Approach to Refractory Gynecological Infections

Ida Ferrara[1] and Alberto Foletti[1, 2]

[1]Clinical Biophysics International Research Group, Lugano, Switzerland
[2]Institute of Translational Pharmacology, National Research Council-CNR, Rome, Italy

Abstract— Refractory gynecological infections are often very difficult to treat. The need for new strategies in their management is therefore continuously increasing. Some researchers have recently pointed up that microorganisms could emit specific electromagnetic signals. Moreover electromagnetic signals could be able to yield response from immune system. The aim of this study was to assess the possibility to employ electromagnetic signals from swabs of refractory gynecological infections to rise a response of the immune system able to erase them. Twenty-two consecutive patients with refractory gynecological infections, since at least 3 months, participate into this study employing an electro medical device (Med Matrix) to perform the electromagnetic information delivery procedure. Vaginal swabs was picked up for microbiological assessment at baseline and after 7 days. Out of 22 swabs performed, 15 were positive for microbiological assessment at baseline. Out of the 15 positive at baseline only 2 were still positive after one week of biophysical treatment ($p < 0.0031$). Biophysical treatment of refractory gynecological infections seems to be an useful and promising second line clinical tool.

1. INTRODUCTION

Refractory gynecological infections are often very difficult to treat both with local or systemic drugs. The need for new strategies of coping with them is therefore continuously increasing. Some researchers have recently pointed up that microorganisms could emit specific electromagnetic signals [1–3] they probably use to communicate each others. Moreover electromagnetic signals are hypothesized to be able to yield response from immune system [4, 5] even when mediated through an aqueous system recording procedure [6–8]. The aim of this study was to assess the possibility to employ electromagnetic signals from swabs of refractory gynecological infections to rise a response of the immune system able to erase them.

2. MATERIAL AND METHODS

2.1. Study Design

Twenty-two consecutive patients with refractory gynecological infections, with duration since at least 3 months, participate into this study after delivering their informed consent. Vaginal swab was picked up for microbiological assessment at baseline and after 7 days.

2.2. Study Population

The average age of the 22 patients with refractory gynecological infections was $33, 4 \pm 14.5$ years (range 71–21). Inclusion criteria was a gynecological symptomatology such as vaginal itching or vaginal burning lasting since at least 3 months. The average duration of the symptomatology was 15.7 ± 15.9 months (range 3–36). Patients should also be not responder to common pharmacological therapies and do not assume other treatments during the week duration of the assessment.

2.3. Electromagnetic Information Delivery through Aqueous System

An electro medical device (Med Matrix-Wegamed, GmbH, Essen, Germany) was used to perform the electromagnetic information delivery procedure placing the swab into the input coil of the device and placing an aqueous system (Nomabit Base -Named SRL, Lesmo, Italy) into a special output coil, built-in for this aim in the device as reported in previous works [9, 10]. This medical device operates in the low frequency range (between 0 and 20 kHz) using a magnetic field with an intensity similar to the Earth's magnetic field with a maximum of 50 μT. The aqueous solution (Nomabit base) was self-administered by the patient in order to allow the therapeutic information recorded to be delivered according to a weekly plan beginning on Monday with a single drop and increasing by one drop/day up to 6 drops on Saturday; no therapy was administered on Sunday [11].

2.4. Microbiological Assessment

The samples of vaginal swabs was sent for microbiological assessment at baseline, at enrollment, and after 7 days of treatment with electromagnetic information delivery procedure through aqueous system (Nomabit Base) following a weekly administration protocol [11]. Microbiological Assessment was carried out for: Mycoplasma Hominis, Ureaplasma Urealyticum, Trichomonas Vaginalis, Escherichia Coli, Proteus species, Pseudomonas Aeruginosa, Gardnerella Vaginalis, Staphylococcus Aureus, Enterococcus Faecalis, Streptococcus Agalactiae, Neisseria Gonorrhea, Streptococcus Beta Aemoliticus, Chlamydia species.

2.5. Statistical Analysis

Statistics was performed with Student's t-test. A p-value of < 0.05 was considered statistically significant.

3. RESULTS

All patients who enrolled completed the study. No side effects were reported. Out of the 22 swabs sample performed 15 were positive for microbiological assessment at baseline, $15/22 = 68,18\%$. Out of the 15 positive at baseline only 2 were still positive after one week of biophysical treatment, $2/15 = 13,33\%$ ($p < 0.0031$).

4. DISCUSSION

The need for new strategies to cope with refractory gynecological infections has been Our starting point. We also want to evaluate if the hypothesis of yielding a systemic response through activation of a selective immune response originated from a biophysical infectious mimicry could be useful into a clinical application. The background of our working hypothesis was from one side some evidence that microorganisms could emit specific electromagnetic signals [1–3] and from the other side previous report of the possibility to achieve biological evidence of the transfer of specific electromagnetic pattern of signal through aqueous systems both in vitro [6–8] and in clinical applications [9–14]. If any infectious agents has its own characteristic electromagnetic pattern of signals it could be possible to record it by means of an electronic device and transferring it to an aqueous system to be stored and subsequently re-delivered to cell culture as for in vitro studies [6–8] or to the entire organism as for clinical studies [9–14]. Electromagnetic Information Delivery through Aqueous System has been confirmed to be feasible and effective even when applied to pattern of signals from biological sample like vaginal swabs in this study. These preliminary data are in agreement with the hypothesis of an electromagnetic vaccination as described recently by Abraham Liboff [4]. Bio-electromagnetic therapies could deliver local and systemic signals at once [15] relying on the resonance effect as their main effective principle [16]. Resonance can both explain the transfer of the information pattern from the source input, like biological samples from vaginal swab, to an aqueous system [8] and from the aqueous system to the whole organism [9–14]. We assume that both the systemic and local effect giving rise to disappearance of infection at the control microbiological assessment of vaginal swab are very lily due to the activation of the immune system [4, 5]. Activation of the immune system response through biophysical procedure could be probably used in other clinical condition as reported in some work on refractory infectious disease [13], autoimmune disease [10, 13, 18], and allergic disease [13]. Biophysical methods could also represent a promising practical tool in personalized medicine since the treatment is unique for each person at each time [19]. In the case of recurrent gynecological infections, for instance, they represent a way to overcome drug resistance yielding the direct response of the individual immune system of each patient allowing somehow to amplifying the physiological inner resource of self-defense and self-regulation that was for some reasons ineffective and lead to recurrence or persistence of the disease.

5. CONCLUSIONS

This preliminary study support the hypotheses of the so called "electromagnetic vaccination" as proposed by Abraham Liboff [4]. The biophysical paradigm proposed for biology and medicine [16, 17] could enrich both basic and clinical researches disclosing new avenue especially in chronic and refractory disease that are emerging concern in almost any department of clinical medicine. A biophysical treatment of refractory gynecological infections [20] seems, therefore, to be an useful and promising second line clinical tool for gynecologists and practitioners.

6. DECLARATION OF INTEREST

The authors reports no declarations of interest.

REFERENCES

1. Reguera, G., "When microbial conversation get physical," *Trends Microbiol.*, Vol. 19, No. 3, 105–103, 2011.
2. Montagnier, L., J. Aissa, S. Ferris, J.-L. Montagnier, and C. Lavallée, "Electromagnetic signals are produced by aqueous nanostructures derived from bacterial DNA sequences," *Interdiscip. Sci.*, Vol. 1, No. 2, 81–90, 2009.
3. Montagnier, L., J. Aissa, C. Lavallée, M. Mbamy, J. Varon, and H. Chenal, "Electromagnetic detection of HIV DNA in the blood of AIDS patients treated by retroviral therapy," *Interdiscip. Sci.*, Vol. 1, No. 4, 245–253, 2009.
4. Liboff, A. R., "Electromagnetic vaccination," *Med. Hypotheses*, Vol. 79, No. 3, 331–333, 2012.
5. Simkó, M. and M. O. Mattsson, "Extremely low frequency electromagnetic fields as effectors of cellular responses in vitro: possible immune cell activation," *J. Cell Biochem.*, Vol. 93, No. 1, 83–92, 2004.
6. Jerman, I., R. Ruźic, R. Krasovec, M. Skarja, and L. Mogilnicki, "Electrical transfer of molecule information into water, its storage, and bioeffects on plants and bacteria," *Electromagn. Biol. Med.*, Vol. 24, No. 3, 341–353, 2005.
7. Jerman, I., M. Berden, and R. Ruźic, "Biological influence of ultraweak supposedly EM radiation from organisms mediated through water," *Electro and Magnetobiology*, Vol. 15, No. 3, 229–244, 1996.
8. Foletti, A., M. Ledda, S. Piccirillo, S. Grimaldi, and A. Lisi, "Electromagnetic Information Delivery as a new tool in translational medicine," *Int. J. Clin. Exp. Med.*, Vol. 7, No. 9, 2550–2556, 2014.
9. Foletti, A., P. Baron, E. Sclauzero, G. Bucci, A. Rinaudo, and R. Rocco, "Assessment of biophysical therapy in the management of pain in current medical practice compared with ibuprofen and placebo: A pilot study," *J. Biol. Regul Homeostat Agents*, Vol. 28, No. 3, 431–439, 2014.
10. Foletti, A. and M. Cozzolino, "A biophysical integrated approach to autoimmune nephrotic syndrome: case report," *Recenti Prog. Med.*, Vol. 104, No. 9, 488–489, 2013.
11. Baron, P., G. Bucci, A. Rinaudo, R. Rocco, E. Sclauzero, and A. Foletti, "System Information Therapy in the management of pain: A pilot study," *PIERS Proceedings*, 1698–1702, Stockholm, August 12–15, 2013.
12. Smith, C. W., "Quanta and coherence effects in water and living systems," *J. Altern Complement Med.*, Vol. 10, No. 1, 69–78, 2004.
13. Herrmann, E. and M. Galle, "Retrospective surgery study of the therapeutic effectiveness of the MORA bioresonance therapy with conventional therapy resistant patients suffering from allergies, pain and infection diseases," *Eur. J. Integrative Med.*, Vol. 2, No. 4, 257–258, 2010.
14. Foletti, A. and J. Pokorný, "Biophysical approach to low back pain: A pilot report," *Electromagn. Biol. Med.*, 2015 (in press).
15. Liboff, A. R., "Local and holistic electromagnetic therapies," *Electromagn. Biol. Med.*, Vol. 26, No. 4, 315–325, 2007.
16. Foletti, A., S. Grimaldi, A. Lisi, M. Ledda, and A. R. Liboff, "Bioelectromagnetic medicine: The role of resonance signaling," *Electromagn. Biol. Med.*, Vol. 32, No. 4, 484–499, 2013.
17. Liboff, A. R., "Toward an electromagnetic paradigm for biology and medicine," *J. Altern Complement Med.*, Vol. 10, No. 1, 41–47, 2004 (Review).
18. Foletti, A., "Simplexity and the possible integrative role of system information therapy in autoimmune diseases management," *Proceedings of the 2nd International Symposium "Biophysical Aspects of Complexity in Health and Disease"*, 44–45, Lugano, Switzerland, May 18–19, 2012.

19. Foletti, A. and S. Grimaldi, "System information therapy as a tool in personalized medicine," *Progress In Electromagnetics Research Symposium Abstracts*, Stockholm, Sweden, August 12–15, 2013.

20. Ferrara, I. and M. Salvi, "Biophysical therapies in gynaecology: Clinical applications and future perspectives," *Proceedings of the 3rd International Symposium "Biophysical Aspects of Complexity in Health and Disease"*, 18, Lugano, Switzerland, October 4, 2014.

FEM Evaluation of the Novel Cardiac Defibrillation Electrode Placement

Elham Khosrowshahli[1] and Aleksandar Jeremic[2]

[1]School of Biomedical Engineering, McMaster University, Canada
[2]Department of Electrical and Computer Engineering, McMaster University, Canada

Abstract— Defibrillation is used to treat patients with certain heart malfunctions. Different external defibrillation systems use two electrodes to deliver current to heart to regain normal beat. Successful defibrillation is determined by the amount of current delivered to myocardium, the amplitude of which depends on the impedance seen by defibrillator. Therefore, in order to gain higher current in the heart, this impedance should be minimized. All attempts to reduce this impedance is focused on decreasing external components like pad-skin impedance. But, in this paper the goal is the reduction of the internal component which is the impedance of the current path in torso by adding additional electrode according to parallel impedance rule of electric circuit theory. The new proposed defibrillation electrode placement is analyzed using developed electric circuit and Finite Element Method models.

1. INTRODUCTION

Defibrillation along with artificial breathing and certain medications is an important part of the process of treating patients with heart dysfunctions, such as ventricular fibrillation and ventricular tachycardia which may lead to death if the patient does not receive proper attention immediately. Investigation of current influence on heart beat started after the invention of glass capacitor in 1745, which is capable of storing electric charge and delivering it as a static shock. Several fibrillation and defibrillation experiments were conducted on animals and humans without the knowledge of the phenomenon at early time [1, 2]. The first documented report on the effect of electric current on ventricular fibrillation was published in 1849 by Carl Friedrich Wilhelm Ludwig and his student Moritz Hoffa [3]. Later, in 1899 Jean-Louis Prevost and Frederic Battelli noticed that although certain amount of electrical current can cause ventricular fibrillation, larger levels of current can reverse the damage and restore normal heart beat [4]. The first documented defibrillation on a human was conducted by Dr. Claude S. Beck in 1947. He applied the electric shock directly to the heart when the chest cavity was open during a surgery, and could regain young patient's heart beat [5]. The first reported closed chest defibrillation was performed by Paul Zoll in 1955 using defibrillator built by Electrodyne [6]. Since then several variations to the classic defibrillation method like automated external defibrillators (AED) [7], implantable cardiovascular defibrillators (ICD) [8] and wearable cardiac defibrillators [9] have been proposed. Also, the waveform of defibrillator voltage has been changed during this period. At first, alternative voltage was used for defibrillation. Later, in 1946 Gurvich and Yuniev introduced the use of DC voltage in defibrillation and reported that applying a single discharge of a capacitor is more effective than the application of alternative voltage [10]. Following this finding, Gurvich also introduced the biphasic waveform for defibrillation in 1967 for the first time [11]. Few years later, this waveform became the standard waveform of defibrillation in Soviet Union. But, it took some time to be verified and used in western countries as well. Now, biphasic is the preferred waveform for defibrillation.

Successful defibrillation depends on the voltage gradient or current density in myocardium [12, 13] which is determined by total current delivered to chest and current distribution in torso according to the impedance profile of it. The current is the function of defibrillator's voltage and the total impedance seen by defibrillator. The impedance consists of several components, one of which is the impedance between the pad or paddle and skin. This element may be reduced by the application of appropriate available gels and/or increasing the pad size. But, practical issues and reducing current density and hence, current delivered to torso prevent from increasing electrode size beyond the optimum value, which is 8–12 cm in diameter for human applications [14, 15]. Another component of this impedance is the impedance of current path between two points on the skin under pads on the chest. It is not easy to calculate this impedance because of the presence of several organs with complicated shapes and diverse electrical properties in torso which results in highly inhomogeneous medium and therefore complex current profile. Despite of this complexity, transthoracic impedance can be reduced using a simple rule of electrical circuit theory which says

that the equivalent impedance of two parallel impedances would be smaller than each of them. This can be achieved by introducing the third electrode to defibrillation system. The role of this electrode is to create parallel current paths to the existing ones in torso and decrease the equivalent impedance seen by defibrillator which results in higher current delivered to the chest when the same defibrillator voltage is applied. Consequently, smaller voltage and energy is needed to deliver certain amount of current to the heart.

In this paper, the proposed method is analyzed by two approaches. A circuit model of defibrillation system is used to show how the extra pad decreases the applied voltage to deliver the same current to heart by creating parallel impedances. Also, a Finite Element Method (FEM) model is developed to investigate the method considering more details of the body. Effects of several configurations of the new pad placement on the current passing through heart is also analyzed using FEM model.

2. THEORY AND MODELING

There are four paddle/pad placements with no significant reported difference in results used in defibrillation which are anterior-apex, anteriorposterior, anterior-left infrascapular, anterior-right infrascapular [16]. The common feature of all methods, which are called conventional methods in this paper, is that all of them use two electrodes to apply defibrillator voltage to the patient's chest, that makes current to pass through the path created in torso between them, and consequently through the heart to achieve desired level of voltage gradient/current density in myocardium to reverse fibrillation. This phenomenon can be modeled with an electrical circuit consisting of a voltage source with the amplitude of defibrillator's voltage and the combination of number of impedances which resemble different components of the impedance seen by defibrillator. This model is shown in Fig. 1. In this model, V_c is defibrillator's voltage, Z_c resembles all impedances between defibrillator and skin, including impedances of cables, electrodes and pads, impedance between pad and skin and also part of the body impedance, Z_p is the impedance of parallel current path to the heart, Z_{s1} and Z_{s2} are body impedances in series with heart, and finally Z_{heart} is the impedance of heart. This model is a simplified explanation of defibrillation, since impedances of complicated current paths in torso are modeled as few single impedances, and used to describe the concepts of the new method. More precise models developed to confirm the results of this model, is presented in subsequent parts. Defibrillator's voltage needed to deliver desired current I_{heart} to the heart is calculated using (1).

$$V_c = I_{\text{heart}} Z_c \left(1 + (Z_{s1} + Z_{\text{heart}} + Z_{s2}) \left(\frac{1}{Z_p} + \frac{1}{Z_c} \right) \right) \tag{1}$$

(1) shows that desired heart current depends on defibrillator's voltage, and equivalent impedances of current paths in the body and the impedances of equipments outside the body. Therefore, in order to reduce required defibrillation voltage to achieve desired current in heart, impedances in the circuit should be decreased or the arrangement is changed to gain smaller equivalent impedance. Body impedances cannot be changed, but some techniques such as larger pad size and lotion application between pad and skin can be useful and have already been used to reduce pad and pad-skin impedances [14, 15]. Impedances of body is a considerable part of the impedance seen by defibrillator. The idea of the new method is to reduce this impedance which is employed in addition to already used strategies.
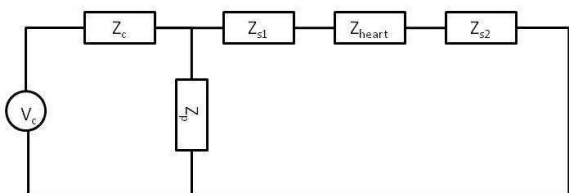
Figure 1: Circuit model of conventional defibrillation method.
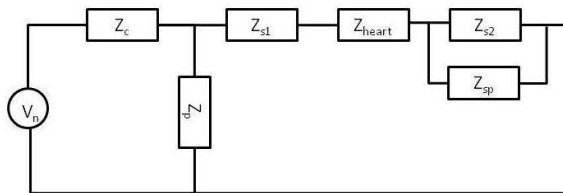
Figure 2: Circuit model of new defibrillation method.

Using parallel impedances rule in electrical circuit theory, the equivalent impedance of two parallel impedances is smaller than each of them, substantiates adding a parallel current path to

the existing ones in conventional defibrillation methods to decrease the resulting impedance, and consequently voltage required to deliver the same current to the heart. Parallel current paths can be created by adding another electrode to the defibrillation system. The circuit model of the new technique is shown in Fig. 2. Here Z_{sp} is the impedance of new current path created by the third electrode. According this model, if I_{heart} is the desired current passing through heart, defibrillator voltage of the new method can be calculated using (2).

$$V_n = I_{\text{heart}} Z_c \left(1 + (Z_{s1} + Z_{\text{heart}} + Z_{s2} \parallel Z_{sp}) \left(\frac{1}{Z_p} + \frac{1}{Z_c} \right) \right) \tag{2}$$

Comparing (1) and (2), shows that since the equivalent impedance of $Z_{s2} \parallel Z_{sp}$ is smaller than Z_{s2} in conventional method, required defibrillator voltage is smaller in the new system. In addition, total power of defibrillator needed to deliver the same amount of current to the heart is smaller in this method, due to smaller voltage with the same current. Lower defibrillator voltage and power is mainly desired in portable and wearable cardiac defibrillators, where the battery size and life time are of great importance.

As it is stated before, circuit modeling of defibrillation is not precise enough to study exact effect of new electrode placement on current distribution in human body. Since differential equation which governs this phenomenon should be solved for an inhomogeneous medium containing several tissues with complex shapes and different electrical properties, numerical methods are practical for defibrillation studies. Finite Element Method (FEM) is one of these methods, that is used in this paper for further studies of the new technique. FEM solves following equation in conjunction with proper boundary conditions to obtain voltage profile in torso.

$$\nabla \cdot (\overline{\sigma} \nabla V) = 0 \tag{3}$$

where $\overline{\sigma}$ is electrical conductivity tensor and V is electric potential. Recall that the purpose of this study is to compare two methods of defibrillation and the exact FEM model of human's upper body which includes every single detail restricts simulation flexibility to study different electrode placements, a geometrically simplified FEM model is developed. In this model, although complicated anatomy is avoided, most of organs including lungs, heart, skletalmuscle, liver, small intestine, fat and skin are incorporated. The model of torso and different included organs are shown in Fig. 3. Dirichlet boundary condition is applied to areas which resemble pads and needed electrical properties are taken from [12, 13, 17].

Because this is not a model based on real images from MRI or CT like models in [12, 13, 18], actual threshold level of current density and voltage gradient for successful defibrillation cannot be assessed. But, simple geometry allows simulating several electrode placements of both conventional and proposed method, and investigating the effect of variant third electrode placement on defibrillation current.

To investigate the efficacy of the new technique, total current density in heart is calculated for two conventional electrode placements and is compared to the new method when the third

(a)   (b)   (c)
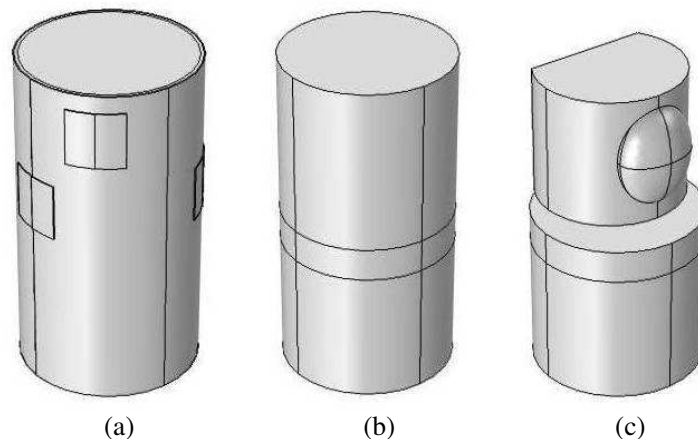
Figure 3: FEM model of torso for defibrillation (a) pads, skin, fat (b) skeletal muscle, liver, small intestine (c) lung, heart.

pad is added to the existing ones in different locations. For better interpretation of results, each pad position is determined by its height from the bottom of the model which is shown by z and measured in centimeters and the angle between body's sagittal plane and the pad counterclockwise. The angle is measured in degrees and shown by $theta$. z and $theta$ axes and their directions are shown in Fig. 4.
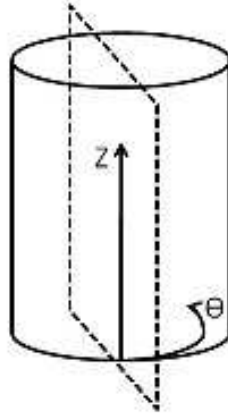
Figure 4: z and $theta$ axes.

3. RESULTS

FEM simulation is performed for two conventional pad placements, where pads are placed at $(z_1, theta_1, z_2, theta_2) = (40, 0, 30, 90)$ and $(z_1, theta_1, z_2, theta_2) = (45, 315, 30, 90)$ to obtain the total current density in heart due to the defibrillator's voltage. To study the performance of the new method, the third pad is added to each conventional layouts, and total current density in heart is calculated. The additional pad is placed on $z = 30$ and $z = 40$ at eight different $theta$s at 45 degrees steps, except where it overlaps the already placed pads of conventional system. Simulations are done with same defibrillator voltage for both conventional and new method. The arrow diagrams of current density for conventional pad placement at $(z_1, theta_1, z_2, theta_2) = (40, 0, 30, 90)$ and one of the simulated new method pad configuration where the third pad is located at $(z_3, theta_3) = (30, 135)$, are plotted in Fig. 5. In this figure arrows show the paths of the current in torso, and

| (a) | (b) |
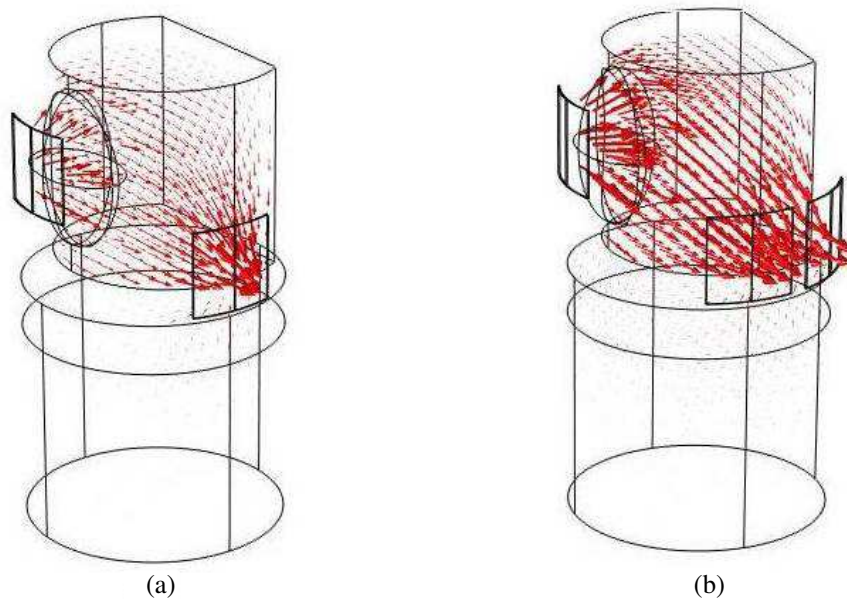
Figure 5: Arrow diagram of current density in torso. (a) Conventional method, (b) novel method.
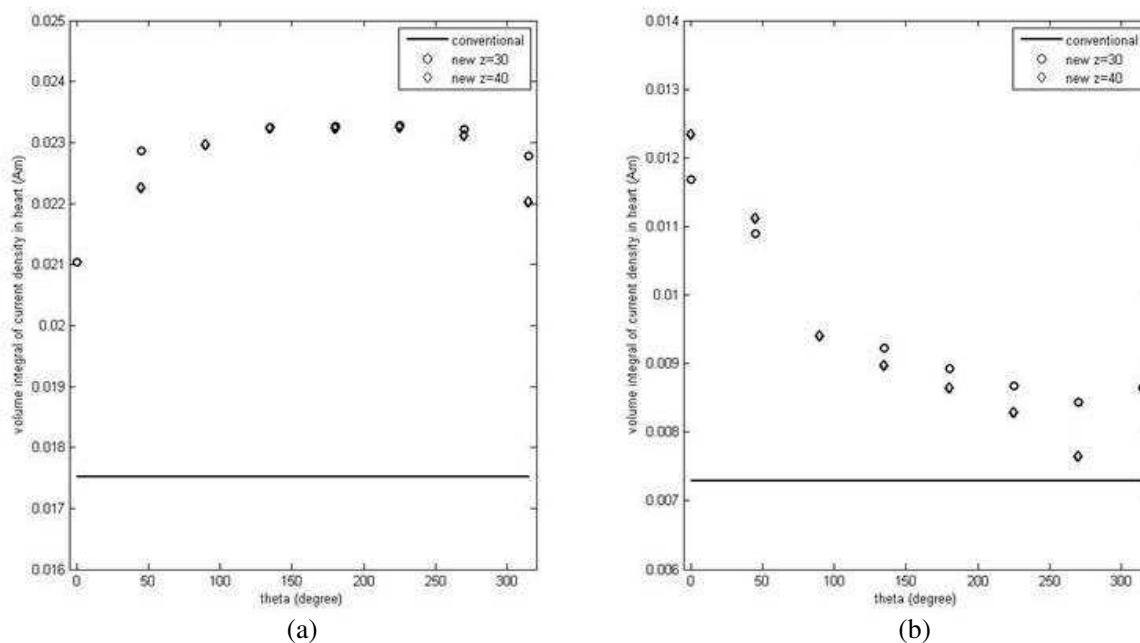
Figure 6: Total current density in heart for different conventional and novel method configurations. (a) $(z_1, theta_1, z_2, theta_2) = (40, 0, 30, 90)$, (b) $(z_1, theta_1, z_2, theta_2) = (45, 315, 30, 90)$.

it is seen that in new method new current paths are created towards the third pad, parallel to the paths in Fig. 5(a). Total current density in heart for all simulated pad layouts summarized in Fig. 6 shows that including additional electrode increases current density in heart as predicted by circuit model due to creating new current paths parallel to the existing ones in torso, and results in the decrease of the impedance seen by defibrillator. As seen in Fig. 6, the position of the third pad affects the amount of heart current increase, such that in first conventional placement, the current is increased by almost 30% neglecting where the third pad is placed. While, when the second conventional layout is used, the location of the third pad affects dramatically the amount of current increase from almost zero in $theta = 270$ to 50% in $theta = 0$.

Therefore, it is verified that the new technique can be considered as a more efficient defibrillation method by reducing the needed voltage and power to send the proper amount of current to the heart comparing to conventional methods. Using this technique can lead to reduce the battery size of portable and wearable defibrillators and increase their life time. However, further studies must be done using more precise models derived from actual MRI or CT images which consider more anatomical details to determine the best positions of pads to get the desired heart current with the application of smaller voltage.

4. CONCLUSION

A novel electrode placement for external defibrillation is proposed. Based on electric circuit theory, the new method increases the current sent to the heart with the application of the same voltage by creating parallel impedances in torso, and consequently reducing the total impedance seen by defibrillator. A circuit model of defibrillation is used for preliminary study of proposed method. Also, for more comprehensive investigation, a FEM model of torso is developed, and several electrode layouts are analyzed. The results are in agree with the outcomes of the circuit model. Therefore, this method can reduce required voltage to deliver the same amount of current to the heart for successful defibrillation. It is desirable in situations when electric power supply is limited, like portable or wearable external defibrillators, where new method could help to increase battery life time or decrease the battery size.

REFERENCES

1. Akselrod, H., et al., "History of defibrillation," I. R. Efimov, *Cardiac Bioelectric Therapy: Mechanisms and Practical Implications*, 15–40, Springer Scicncc+Busincss Media LLC, New York, 2009.

2. Cakulev, I., et al., "Cardioversion past, present, and future," *Circulation*, Vol. 120, No. 16, 1623–1632, 2009.

3. Hoffa, M., et al., "Einige neue versuche UBER herzbewegung," *Zeitschrift Rationelle Medizin*, Vol. 9, 107–144, 1850.

4. Prevost, J. L. and Battelli, F., "Physiologie pathologique: La mort par les décharges électriques," *Compt. Rend. Acad. Sci.*, Vol. 129, 651–654, 1899.

5. Beck, C. S., "Ventricular fibrillation of long duration abolished by electric shock," *JAMA*, Vol. 135, No. 15, 985–986, 1947.

6. Zoll, P. M., "Termination of ventricular fibrillation in man by externally applied electric countershock," *NEJM*, Vol. 254, No. 16, 727–732, 1956.

7. Bocka, J. J., "Automatic external defibrillators," *Ann. Emerg. Med.*, Vol. 18, No. 12, 1264–1268, 1989.

8. Pinski, S. L. and G. J. Fahy, "Implantable cardioverter-defibrillators," *Am. J. Med.*, Vol. 106, No. 4, 446–458, 1999.

9. Feldman, A. M., "Use of a wearable defibrillator in terminating tachyarrhythmias in patients at high risk for sudden death," *Pacing Clin. Electrophysiol.*, Vol. 27, No. 1, 4–9, 2004.

10. Gurvich, N. L. and G. S. Yuniev, "Restoration of regular rhythm in the mammalian fibrillating heart," *Amer. Rev. Soviet Med.*, Vol. 3, 236–236, 1946.

11. Gurvich, N. L. and V. A. Makarychev, "Defibrillation of the heart with biphasic electric impulsation," *Kardiologiia*, Vol. 7, No. 7, 109–112, 1967.

12. Camacho, M. A., et al., "A three-dimensional finite element model of human transthoracic defibrillation: Paddle placement and size," *IEEE Trans. Biomed. Eng.*, Vol. 42, No. 6, 572–578, 1995.

13. Jorgenson, D. S., et al., "Computational studies of transthoracic and transvenous defibrillation in a detailed 3-D human thorax model," *IEEE Trans. Biomed. Eng*, Vol. 42, No. 2, 172–184, 1995.

14. Dalzell, G. W. N., et al., "Electrode pad size, transthoracic impedance and success of external ventricular defibrillation," *Am. J. Cardiol.*, Vol. 64, No. 12, 741–744, 1989.

15. Samson, R. A., "Use of automated external defibrillators for children: An update an advisory statement from the pediatric advanced life support task force, international liaison committee on resuscitation," *Circulation*, Vol. 107, No. 25, 3250–3255, 2003.

16. Sayre, "Part 5: Adult basic life support: 2010 international consensus on cardiopulmonary resuscitation and emergency cardiovascular care science with treatment recommendations," *Circulation*, Vol. 128, No. 19, E393–E393, 2013.

17. http://niremf.ifac.cnr.it/tissprop.

18. Johnson, C. R., "A computer model for the study of electrical current flow in the human thorax," *Comput. Biol. Med.*, Vol. 22, No. 5, 305–323, 1992.

Conductivity Estimation of Breast Cancer Using Stochastic Optimization

A. Jeremic[1] and E. Khosrowshahli[2]

[1]Department of Electrical and Computer Engineering, McMaster University, Canada
[2]School of Biomedical Engineering, McMaster University, Canada

Abstract— Breast cancer detection is one of the most important problems in health care as it is second most frequent cancer according to WHO. Breast cancer is among cancers which are most probably curable, only if it is diagnosed at early stages. To this purpose it has been recently proposed that microwave imaging could be used as a cheaper and safer alternative to the commonly used combination of mammography. From a physical standpoint breast cancer can be modelled as a scatterer with a significantly (tenfold) larger conductivity than a healthy tissue. In our previous work we proposed a maximum likelihood based method for detection of cancer which estimates the unknown parameters by minimizing the residual error vector assuming that the error can be modelled as a multivariate (multiple antennas) random variable. In this paper we utilize stochastic optimization technique and evaluate its applicability to the detection of cancer using numerical models. Although these models have significant limitations they are potentially useful as they provide insight in required levels of noise in order to achieve desirable detection rates.

1. INTRODUCTION

According to breast cancer society , breast cancer is the most frequently diagnosed cancer in women with over 232,670 new cases expected in 2014 [1]. Due to the progressive nature of the disease early detection is extremely important and can potentially significantly improve survival of patients. Currently clinical procedures are commonly based on mammography which is routinely prescribed for older women who tend to be more susceptible to the disease [2]. Although mammography is extremely important diagnostic technique, it suffers from some limitations such as false negative and positive results, using ionizing radiation and patients discomfort [2, 3]. The number of false positives is rather significant in the case of so called dense breasts in which healthy tissue may be mistaken for malignant and as a consequence unnecessary biopsies are prescribed. Furthermore, complicating the matter is the fact that mammography is a two-dimensional technique and hence the reconstruction techniques which are needed to obtain three-dimensional images can lead to false positives.

Microwave imaging has been recently proposed as an additional medical imaging technique which can potentially overcome some of the shortcomings of the mammography. Essentially the technique is based on illuminating breast with electromagnetic-wave(s) in microwave range. From the physical point of view this can be represented as a wave propagation in medium (breast) that contains scatterers (both healthy and malignant tissue). Due to the fact that malignant tissue has larger conductivity the measurements obtained by receiving array of antennas will be different if the scatterers are present. Therefore once the wave propagates through the breast the received signal is analyzed in order to obtain permittivity map using appropriately selected image reconstruction technique [4]. Most of the image reconstruction techniques minimize a particular cost function (e.g., mean-square error). In most cases the number of unknowns (e.g., number of pixels in the map) is much larger than the number of available measurements which requires an additional constraint.

In this paper we propose a simplified parametric inverse 3D model which enables us detection of tumour presence and estimation of its size and/or position. Most of the existing solutions [7] employ non-parametric image reconstruction techniques. In our previous work we proposed a maximum likelihood based method for detection of cancer which estimates the unknown parameters by minimizing the residual error vector assuming that the error can be modelled as a multivariate (multiple antennas) random variable. In this paper we utilize stochastic optimization which is based on the minimization of the variance of the expected value rather than on the gradient of the partial-differential equations based model. Namely the scattering models utilize multiple PDEs in order to calculate scattering parameters from a transmitting to receiving antenna. We propose to utilize recently proposed algorithm for stochastic optimization which achieves smaller computational time but can suffer from estimation accuracy. However detection performance is

often somewhat robust to estimation results and to this purpose we investigate the accuracy of detection algorithms based on stochastic optimization results. In Section 2 we present computational models of electromagnetic wave propagation in breast when tumours are absent and present and discuss how the aforementioned models were implemented using COMSOL finite element solver. In Section 3 we present the statical models and present estimation algorithm. In Section 4 we present simulation results and discuss their potential use for inverse problems. Finally, Section 5 concludes the paper.

2. PHYSICAL MODEL

In this Section we develop mathematical model describing the measured signals. The imaging system consists of several antennas which can both serve as transmitting and receiving antennas. These antennas in principle can be distributed over the breast surface thus allowing for a three-dimensional scan whose resolution depends only on number of antennas. Obviously the number of antennas is determined by their size which may be constrained by technical requirements such as antenna-to-antenna noise (interference). Once the microwave is generated it propagates through the volume of the breast according to Maxwell's equations which in this particular case can be reduced to the phasor form since microwave antennas operate in a single-frequency mode.

It should be observed that any non-homogeneity in the object can be modelled as a scatterer and thus in the presence of multiple scatterers the resulting electromagnetic field becomes very complex superposition of reflected and refracted waves. Since malignant tissue has significantly larger permittivity than healthy tissue it can also be modelled as a scatterer (see Figure 1). The reflection/refraction from scatterers can then be modelled as described in Figure 2.

In the remainder of the paper we will assume that in the absence of cancer the scattering in the breast is due only to small non-homogeneities which will be included as the modelling noise. Of course if a particular patient is submitted to continuous monitoring in a regular intervals the previous images can be used a reference signal and thus "healthy scattering" can be properly recorded and modelled. In this paper we assume that the tumours can be modelled as spheres and therefore are uniquely defined by location vector and radius. In general, arbitrarily shaped tumours can be represented by spatial Fourier transform and corresponding spatial frequency amplitudes and phases. As we stated before, the electromagnetic properties of the malignant tissue is significantly different than breast tissue and thus proper boundary conditions must be considered in order to ensure continuity (see Figure 2).

In order to solve the above equations we utilize finite-element method by developing three-dimensional model using RF module in COMSOL Multiphysics software. In this paper we model the breast as a sphere with radius of 100 mm as shown in Figure 3 immersed into the cubical structure representing microwave imaging system. Antennas are equally spaced on all the sides of the imaging structure. These antennas are modelled as slim cubes which are centred on the surface of the sphere. Three boundary conditions are used to send waves in the medium. Electric
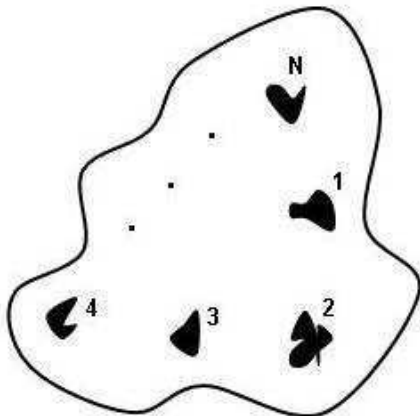
Figure 1: Medium with multiple scatterers.
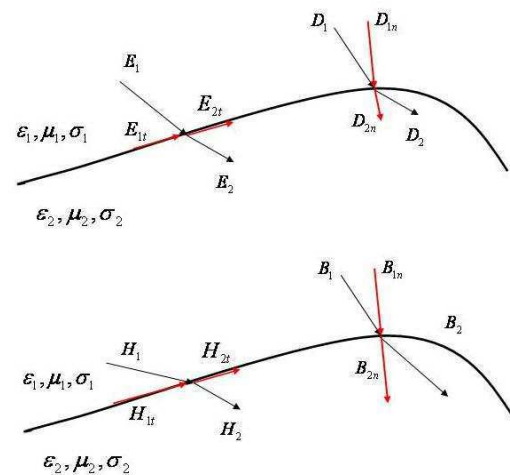
Figure 2: Boundary conditions.

Table 1: Tissue properties.

Tissue	Relative permittivity	Condutcitivty
Immersion Liquid	9	0
Chest Wall	50	7
Skin	36	4
Breast Tissue	9	0.4
Tumour	50	4
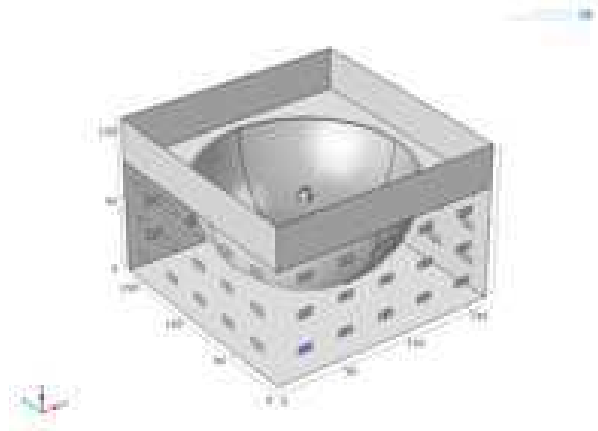
Figure 3: Geometry of the breast.
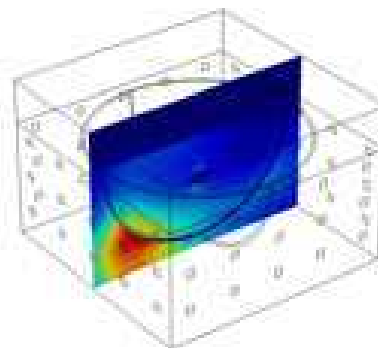
Figure 4: Sample result for the field.

field is applied to transmitter antenna. Perfect electric conductor boundary condition is applied to sides of antennas in order to guide wave through them, and scattering boundary condition is applied to the rest of surfaces to let waves propagate freely. Afterward, for different studies one or multiple tumours with arbitrary shapes can be modelled. In this study tumour is considered as a sphere inside the breast with an arbitrary size and in arbitrary position. The actual values for physiological parameters are outlined in the Table 1.

3. STATISTICAL MODEL

Most of the existing methods describe the above physical model using Maxwell equations in order to model the electromagnetic wave propagation. Consequently for the transmitting antenna located at position $\mathbf{r}_0$ and the receiving antenna located at location $\mathbf{r}_i$ the scattering parameter can be obtained either by solving Maxwell's equation with adequately defined boundary conditions related to the transmitting antenna and finding the solution at the location of the receiving antenna. Due to irregular geometry and non-homogeneus parameters the solution can be obtained only numerically using finite-element method. In order to define non-linear transfer functions we utilize COMSOL finite-element solver and consequently describe the measurements as

$$y_{ij} = f(i, j, \theta_s, \theta_g) + e_{ij} \tag{1}$$

where y_{ij} is scattering parameter when the i-th antenna is transmitter and the j-th antenna receiver. The parameters θ_s and θ_g are scatterers parameters (number, radiuses and permittivity/conductivity parameters) and θ_g are the geometry parameters. In this paper we simplify the problem by removing the geometry parameters, i.e., they are fixed for a particular breast model. The residual errors/noise e_{ij} is assumed to be zero-mean Gaussian uncorrelated in space. Note the correlated noise can be easily addressed using any of the existing techniques based on the growth-curve model by Pothoff and Roy [9]. Our main focus in this paper is to demonstrate applicability of stochastic optimization and hence we choose the simplest possible noise model.

It has been recently proposed [8] that a set of multiple PDE equations can be inverted, i.e., the unknown parameters can be estimated without the need of solving multiple PDEs at each iteration. Let q_i be the power of the transmitting antenna and let y_{ij} be the $n-1$ scattering parameters obtained on all the other antennas (note that each antenna can serve as transmitting and receiving but we need n PDEs in order to utilize all n antenna's as transmitters). The main

idea of stochastic optimization is based on so called simultaneous random sources in which a new source is obtained using a linear combination of the existing sources, i.e., $\hat{q} = \Sigma w_i q_i$ and new data are obtained as $\hat{y}_{i\cdot} = \sum w_j y_{ij}$ in which the weighting coefficients are chosen from appropriately defined probability density function, i.e., they are random. In that case it can be shown that the optimization problem reduces to minimizing the expected value

$$\frac{1}{2} E_w \left\| \left(A^{-1}(\theta_s) \mathbf{q} - \mathbf{y} \right) w \right\|^2 \tag{2}$$

where A is the transfer matrix obtained from non-linear functions f which represent finite-element solutions in which the discretized/linear formulation results in antenna-to-antenna transfer matrix, $\mathbf{y}$ and $\mathbf{q}$ are the lumped vectors of scattering parameters and sources respectively.

In order to solve the above stochastic optimization problem there are two general techniques: a) sample average approximation in which the expected value is approximated by a Monte-Carlo sum with the constraint that the number of realizations should be smaller than the number of PDEs and b) stochastic approximation technique in which a single realization is used to compute the stochastic gradient. In order to reduce the computational complexity and due to a smaller number of antennas (16) in this paper we choose the stochastic approximation technique and investigate its applicability to our problem.

The structure of SA approximation is given by:

- Initialize the solution, i.e., set the scatterer parameters to $\theta_s = \theta_s^0$;
- while convergence is not reached do;
- draw a random sample for weighting coefficients;
- approximately solve the optimization problem by calculating the gradient at the given point — note due to random mixing it requires only single solution to PDE;
- obtains the new value of $\hat{\theta}_s^{i+1}$ calculated using the gradient from the previous step;
- average the new value with the previous values and obtain the new value of parameter, i.e., $\theta_s^{i+1} = \frac{1}{i+1}(\sum_{j=1}^{i} \theta_s^j + \hat{\theta}_s^{i+1})$;
- end while.

It has been empirically shown [8] that the above technique shows acceptable performance when the random weight are drawn from binary distribution $(-1, 1)$ as in this case the minimization of the expected value yields mean with the smallest variance. In this preliminary work we use the same pdf for the weights and leave for future work to examine the possibility of selecting the pdf according to a particular problem.

In order to determine whether the estimated scatterer can potentially represent a cancer we need to perform a classification/detection algorithm which determines the probability (likelihood) that the conductivity and permittivity of the tissue are comparable to the values from Table 1. In general the likelihood ratio tests result in ratio of variances (or determinants of covariance matrices in the presence of correlated noise). In this preliminary approach we propose a simplified algorithm in which the estimated value of conductivity is compared to the healthy tissue value (9). Obviously the resulting test is comparable to T-test as it is similar to comparing the sample mean to a priori known value.

4. NUMERICAL RESULTS

In order to evaluate the applicability of the proposed technique we perform the following experiment. For a fixed geometry of the breast we insert 10 scatterers of random size at random locations. In order to simulate so called dense breasts in which the fat tissue can have slightly larger conductivity we choose to select conductivity of scatterers to be uniformly distributed in range (9, 25) where the lower boundary is chosen to equal healthy tissue and the upper one is arbitrarily set to half of the cancerous tissue. Then we insert a tumour located in the center of the breast with a radius of 0.5 cm. For a simplicity we assume that the location is known (note that other imaging techniques such as ultrasound and MRI could be used to detect suspicious regions and hence these locations can be known). Our main goal at this stage is to demonstrate ability to non-invasively estimate unknown conductivity and hence potentially detect breast cancer. An additional unknown parameter would most likely decrease performance but we believe that this issue could be addressed by utilizing more advanced techniques. In this preliminary work we want to examine applicability of model-based

scatterer detection. We perform the proposed experiment 2000 times and in half of the experiments we use cancerous tissue as the scatterer in the centre and half of the times we insert healthy tissue in the center location. As discussed previously to account for the errors we add zero-mean Gaussian noise.

In order to evaluate the proposed the applicability of the proposed estimation algorithm we count the number of false positives and negatives in these 2000 runs. In Figure 5 we show the mean square error of the proposed stochastic optimization algorithm as a function of signal-to-noise ratio defined with respect to the scattering parameter values. In future work we will improve the noise models and include additive noise directly to the values of the scattered electromagnetic field. As expected we see that the error decreases as the SNR improves which may be used in order to understand what noise levels are needed in order to have an algorithm that can function in the clinical setting. In Figure 6 we illustrate the detection performance calculated using empirical values of probabilities based on the count of false decisions. The preliminary results indicate that the error is not symmetric and thus we expect to be able to achieve better performance by investigating the properties of error residual vector in more details.
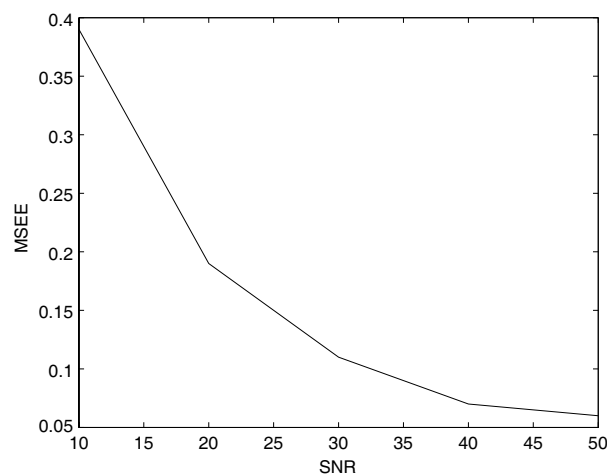
Figure 5: Mean square error for the stochastic optimization algorithm.
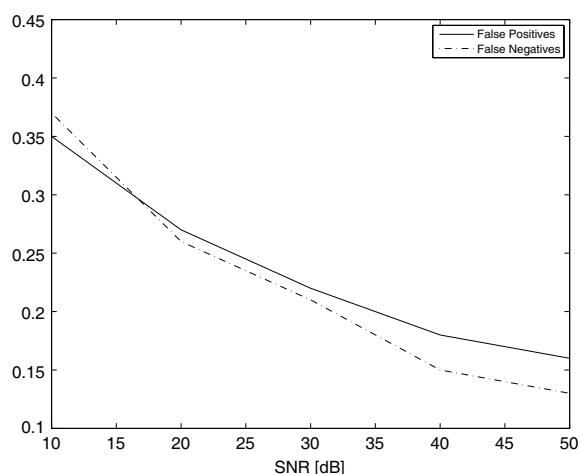
Figure 6: Detection performance as a function of SNR.

5. CONCLUSIONS AND FUTURE WORKS

In this paper we proposed a model based algorithm for estimating the conductivity of unknown scatterer in the breast tissue and implemented the decision making algorithm which can potentially be used for making decisions if the scatterers have conductivity similar to that of cancerous tissue. We developed a computational algorithm based on the stochastic optimization and finite-element model in order to decrease computational time without significant losses in accuracy. In future work we plan to compare the performance of stochastic algorithms and maximum likelihood based algorithms for different noise models. This is especially important in microwave settings as the noise levels can have significant impact. Furthermore we plan to investigate the effects that probability density functions of weighting coefficients have on the overall performance of the proposed algorithms.

REFERENCES

1. http://www.breastcancer.org/symptoms/understand_bc/statistics.

2. Gemignani, M. L., "Breast cancer screening: Why, when, and how many?," *Clinical Obstetrics and Gynecology*, Vol. 54, No. 1, 125–132, 2011.

3. Tice, J. and K. Kerlikowske, "Screening and prevention of breast cancer in primary care," *Primary Care: Clinics in Office Practice*, Vol. 36, No. 3, 533–558, 2009.

4. Fear, E. C., "Enhancing breast tumor detection with near-field imaging," *IEEE Microwave Magazine*, Vol. 3, No. 1, 48–56, 2002.

5. Cheng, D. K., *Field and Wave Electromagnetics*, Addison-Wesley Publishing Company, 1983.

6. Semenov, S., et al., "Microwave-tomographic imaging of the high dielectric-contrast objects using different image reconstruction approaches," *IEEE Transactions on Microwave Theory and Techniques*, Vol. 53, No. 7, 2284–2294, 2005.

7. Pastorino, M., "Stochastic optimization methods applied to microwave imaging: A review," *IEEE Transactions on Antennas and Propagation*, Vol. 55, No. 3, 538–548, 2007.

8. Haber, E., et al., "An effective method for parameter estimation with PDE constraints with multiple right hand sides," 2010.

9. Pothoff, R. and S. Roy, "A generalized multivariate analysis of variance model useful especially for growth curve problems," *Biometrika*, Vol. 51, 313–326, 1964.

EM Exposure System with Well Defined Dosimetry

J. Vrba[1], **L. Vísek**[1], **L. Oppl**[1], **D. Vrba**[2], **J. Vrba, Jr.**[2], **F. Vožeh**[3], **J. Barcal**[3], **and L. Vannucci**[4]

[1]Department of EM Field, Faculty of Electrical Engineering
Czech Technical University in Prague, Prague, Czech Republic
[2]Department of Biomedical Technique, Faculty of Biomedical Engineering
Czech Technical University in Prague, Kladno, Czech Republic
[3]Department of Patophysiology, Medical Faculty in Pilsen
Charles University in Prague, Pilsen, Czech Republic
[4]Institute of Microbiology, Czech Academy of Sciences, Prague, Czech Republic

Abstract— The whole-body exposure system for unrestrained mice was designed in order to analyze the influence of electromagnetic field. The setup operating at 900 MHz was designed with respect to induced uniform field, external radiation elimination, absorbed power determination, sufficient space for mice movement together with even mice exposure and costs. The main aim of this paper is to assure that the dosimetry results reached by computer simulations can be used for determination of absorbed power in the unrestrained mouse. The whole-body exposure chamber with anatomical mouse model was simulated by two different numerical methods: finite-difference-time-domain method (FDTD) and Finite Integration Technique (FIT) and its dosimetry results were compared by computed SAR values. In our contribution we will describe our first results dealing with observed biological effects of EM field, obtained by real exposures of experimental animals.

1. INTRODUCTION

In our modern world various sophisticated devices emitting microwave electromagnetic field are ubiquitous. These devices are used in many branches such as industry, medicine and particularly communication. The advent of a wide penetration of mobile communications has arisen the concern whether the exposure to electromagnetic field could be adverse to the exposed users. The increasing daily exposure has raised the research activities in order to determine the effects of exposure to the electromagnetic radiation of mobile phones. Although a lot of researches have been accomplished, no adverse health effects of cellular phones have been confirmed yet. The main aim of this work was to design exposure chamber for in vivo studies where the impact of electromagnetic field on biological organisms is analysed. In our contribution we will describe our first results dealing with observed biological effects of EM field, obtained by real exposures of experimental animals.

2. METHODS

The whole-body exposure system for unrestrained mice was designed in order to analyze the influence of electromagnetic field. The setup operating at 900 MHz has been designed with respect to following conditions:

- induced uniform field,
- external radiation elimination,
- accurate absorbed power determination,
- sufficient space for mice.

These conditions are grounded on requirements for exposure system from [1]. Such conditions assure an accurate determination of Specific absorption rate (SAR) together with the elimination of stress induced in mice. The major advantage of the system is the capability of direct measurement the whole-body averaged SAR which is performed by analysis of measured scattering parameters.

As the basic structure of the exposure chamber a waveguide was chosen. The advantage of the waveguide structure is a shielding of electromagnetic field generated inside in order to protect the operators and also generated outside the system in order to eliminate outer radiation. Dimensions of the exposure chamber were calculated in order to use desired frequency of operation and the volume needed to exposed mice. The exposure chamber is made of copper plate with dimensions of 1650 mm length and 240 mm diameter. The chamber is terminated by matched loads at both ends. In order to avoid reflection and assure an attenuation of power the loads must be made of lossy

dielectric material and must have a suitable shape. The electrical resistance of the shape should grow linearly in a direction of the wave propagation. The designed matched loads are conical, 500 mm long and are made of RF absorber. The reflection loss of the matched load is more than −20 dB at 900 MHz. The circular polarized wave TE_{11} is excited in the waveguide (Figure 1).

This wave is comprised by two monopoles which have mutually orthogonal orientation and the distance between them is equal to one-fourth of wavelength. Circular polarized wave provides relatively constant coupling of the field to each mouse regardless of its position, posture or movement.

The exposed mice are kept in a box which is made of Styrofoam. Styrofoam has a dielectric constant of 1.03, i.e., very close to that of air, and thus the disturbance of exposure and measurements is negligible. The box provides space for two separated mice. Punctured slit-like holes are set on the cover and side of the box for air ventilation. In the study the mice are hold in the chamber only during RF exposures and therefore, no food or drinking water is necessary.

Efficient ventilation is necessary to maintain constant temperature and good air quality in the chamber. The air exchange is realized by a ventilation system which consisted of a fan installed outside the chamber and a tube attached to the ventilation hole. The exchange air come towards mice through the ventilation hole placed below the styrofoam box and flow towards the second opposite ventilation hole placed above the box.

Basic properties such as electromagnetic field distribution and impedance matching of the designed chamber were optimized and verified by a 3D electromagnetic field simulator SEMCAD X [5].

Dosimetry is an inherent task for exposure setups. Dosimetry is the quantification of the magnitude and distribution of absorbed electromagnetic energy within biological objects that are exposed to electromagnetic fields. At RF, the dosimetric quantity, which is called the specific absorption rate, is defined as the rate at which energy is absorbed per unit mass. The SAR is determined not only by the incident electromagnetic waves but also by the electrical and geometric characteristics of the irradiated subject and nearby objects. It is related to the internal electric field strength as well as to the electric conductivity and the density of tissues. Therefore, it is a suitable dosimetric parameter, even when a mechanism is determined to be "athermal." SAR distributions are usually determined from measurements in animal tissues or from calculations. It generally is difficult to measure the SAR directly in a living biological body, and therefore dosimetry efforts are forced to rely on computer simulations [2].

An anatomically based biological model is essential for numerical dosimetry. Such a numerical model is developed commonly from MRI or CT scans. In order to develop a model for numerical dosimetry original gray-scale data must be interpreted into tissue types which is known as a process of segmentation. Segmentation is the task of partitioning the data into contiguous regions representing individual anatomical objects. Segmentation is a difficult task because in most cases
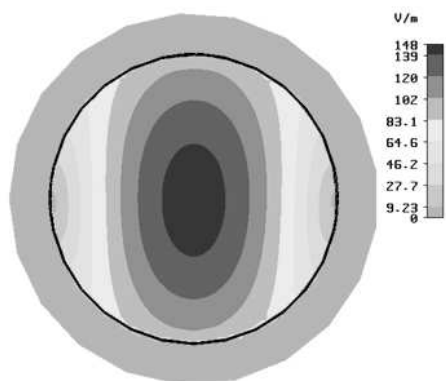
Figure 1: Distribution of electric field strength of TE_{11}.
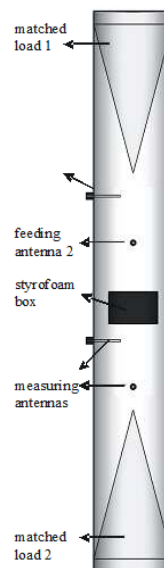
Figure 2: Exposure chamber.

it is very hard to separate the object from the image background. This is due to the characteristics of the imaging process as well as the grey-value mappings of the objects themselves. The most common medical image acquisition modalities include computer tomography (CT) and magnetic resonance imaging images (MRI).

MRI or CT provides gray-scale image data as many transverse slices, at a designated spacing, from the head to the feet of the biological body. The resolution in each slice is on the order of several millimeters.

CT scans for mouse model development were obtained from the project Digimouse [3, 4]. The CT raw data can be downloaded directly from the web site http://neuroimage.usc.edu/Digimouse_download.html. The mouse model (Figure 3) has the resolution 0.1 mm, meaning voxel size 0.1 × 0.1 × 0.1 mm. Each voxel was assigned to one of 14 different tissue types, such as bone, muscle, brain, etc..

For dosimetry with the numerical voxel models, proper permittivity and conductivity values must be assigned to each tissue. The data from 10 MHz to 6 GHz, which were derived from 4-Cole-Cole extrapolation based on measurements for small animals [7], constitutes the most widely accepted database for this information. The data are recommended by various international standardization organizations and can be accessed from the web site http://www.fcc.gov/fcc-bin/dielec.sh.

3. RESULTS

In order to verify and rely on numerical dosimetry results, the simulations of exposure chamber is desired to be performed in different electromagnetic field simulators using different numerical methods. As 3D simulators using different numerical methods were chosen SEMCAD X [5] which uses Finite Difference Time Domain (FDTD) method and CST Microwave Studio [6] which uses Finite Integration Technique (FIT) method. For the purpose of results comparison the model of the mouse was chosen homogenous phantom with anatomical shape of the mouse. The model dielectric parameters were set the same like muscle tissue. The simulations were performed for three positions

Figure 3: The numerical mouse model based on CT scans.
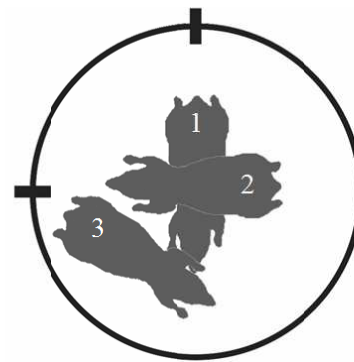
Figure 4: Positions of mouse inside the box.
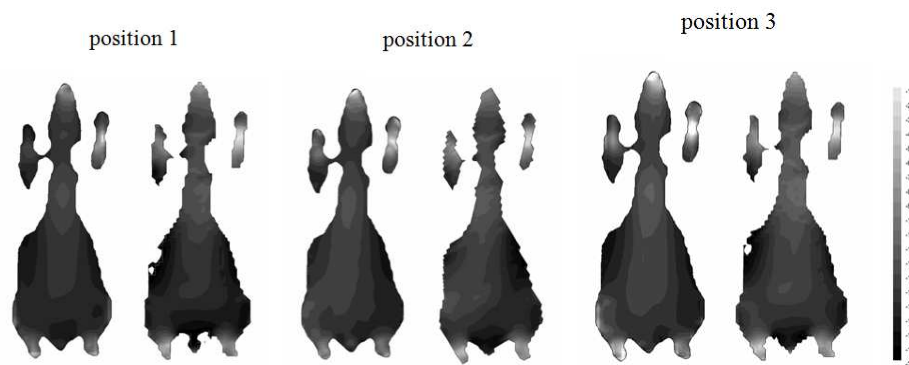
Figure 5: SAR distribution in middle cutting plane (top view) for three positions of mouse.

of mouse in order to verify an even exposure which should be assured by circular polarized wave. The first and the second position of the mouse was chosen perpendicularly to one of the feeding antenna and the third position was chosen generally (Figure 4.).

From the Figure 5, it is obvious that the reached simulation results for both numerical methods are in a good agreement. Further, it was verified that the circular polarization provides constant coupling of the field to each mouse regardless of its position or movement.

4. CONCLUSION

It was designed the exposure chamber working at 900 MHz serving for researches of effects of electromagnetic field. The chamber was optimized by aid 3D simulator of electromagnetic field. In order to verify simulation results, the numerical dosimetry was computed in two different electromagnetic field simulators with two different numerical method. The simulation results were compared and reached results were in a good agreement. The designed exposure chamber is suitable for researches of effects of electromagnetic field. In our contribution we will describe our first results dealing with observed biological effects of EM field, obtained by real exposures of experimental animals.

ACKNOWLEDGMENT

REFERENCES

1. Kuster, N. and F. Shonborn, "Recommended minimal requirements and development guidelines for exposure setups of bio-experiments addressing the health risk concern of wireless communications," *Bioelectromagnetics*, Vol. 21, 508–514; Vol. 40, 16–19, Jan. 2000.
2. Fujiwara, O. and J. Wang, *Electromagnetics in Biology*, Springer, Japan, 2006.
3. Dogdas, B., D. Stout, A. Chatziionnou, and R. M. Leathy, "Digimouse: A 3D whole body mouse atlas from CT and cryosection data," *Phys. Med. Biol.*, Vol. 52, No. 3, 577–587, 2007.
4. Stout, D., P. Chow, R. Silverman, R. M. Leathy, X. Lewis, S. Gambhir, and A. Chatziionnou, "Creating a whole body digital mouse atlas with PET, CT and cryosection images," *Molecular Imaging and Biology*, Vol. 4, No. 4, S27, 2002.
5. Schmid & Partner Engineering AG, 2010, Online: http://www.semcad.com/.
6. Computer Simulation Technology, 2010, Online: http://www.cst.com/.
7. Gabriel, C., "Compilation of the dielectric properties of body tissues at RF and microwave frequencies," Brooks Air Force Technical Report, AL/OE-TR-1996-0037, 1996.

Mutual Coupling Evaluation within Waveguide Slotted Antennas

Giovanni Leone and Domenico Russo

Dipartimento di Ingegneria Industriale e dell'Informazione
Seconda Università degli Studi di Napoli, Italy

Abstract— Mutual coupling in an array of different sized narrow rectangular waveguide slots embedded within an infinite PEC plane is estimated by computing the generalized admittance matrix, connecting the coefficients of the modal expansion of the magnetic field to the ones of the electric field. The generic element of the above matrix requires the numerical evaluation of a quadruple integral. In this paper a singularity cancellation approach is used to remove the singularity of the Green's function and the order of integration is reduced by a suitable changes of variables. In this way self and mutual admittances can be estimated by computing double integrals. A further approximation is introduced in order to compute the latter ones by single integrals saving computational time and resources. The results of such approach are then compared with the ones provided by a commercial numerical simulation tool showing good agreement.

1. INTRODUCTION

Planar arrays of waveguide fed slotted antennas [1] find many applications in telecommunication because they show low cost and weight, do not change the structure aerodynamic properties and have a very narrow beam. The principal limit is the relatively narrow band. For both analysis and synthesis purposes, evaluation of the mutual coupling between the slots is fundamental since it affects in a non-negligible way the array factor. In literature many works offer a phenomenon approximate analysis while a more accurate one could be carried out by using a commercial numerical simulation tool. However, both computational time and resources rise considerably when the array dimensions increase and such tools become unusable. So, the problem arises of both an efficient and accurate analysis.

We assume that the slots are embedded within an infinite PEC plane and mutual coupling is estimated by computing the generalized admittance matrix (GAM) [2, 3]. We start from the integral relationship connecting the magnetic equivalent currents to the magnetic field that can be obtained by means of the vector potential. Then tangential fields are expanded into rectangular waveguide mode functions and the GAM is built by connecting the coefficients of the modal expansion of the magnetic field to the ones of the electric field. The resulting integral relationship are simplified and numerically evaluated accounting exactly for the singular behavior of self-admittance.

2. FORMULATION

N rectangular slots are considered within an infinite PEC plane at $z = 0$ as shown in Fig. 1 (right panel highlights two of them for the sake of illustration). The infinite PEC plane assumption is well verified because the antenna radiates mainly around the direction orthogonal at the plane so the electrical field tangential components can be assumed vanishing everywhere at $z = 0$ except than within the slots.

By invoking the equivalence theorem and introducing the vector potential, the following integral relationship connecting the tangential magnetic field over the i-th slot with the tangential electric field over the k-th slot is established:

$$\underline{H}_t^{(i)}(\underline{r}) = j\frac{1}{2\pi\omega\mu_0}\left(k^2 + \nabla_t\nabla_t\right) \cdot \left(\hat{z} \times \sum_{k=1}^{N} \iint_{S_k} \underline{E}_t^{(k)}(\underline{r}')G\left(\left|\underline{r} - \underline{r}'\right|\right)ds'\right) \tag{1}$$

where $G(\cdot)$ is the free space scalar Green's function and $\underline{r} \in S_i$.

As mentioned before, the tangential fields are expanded into M modes over each slot:

$$\underline{H}_t^{(i)}(\underline{r}) = \sum_{m=1}^{M} I_{mi}\underline{h}_{mi}(\underline{r})$$

$$\underline{E}_t^{(k)}(\underline{r}) = \sum_{p=1}^{M} V_{pk}\underline{e}_{pk}(\underline{r}) \tag{2}$$
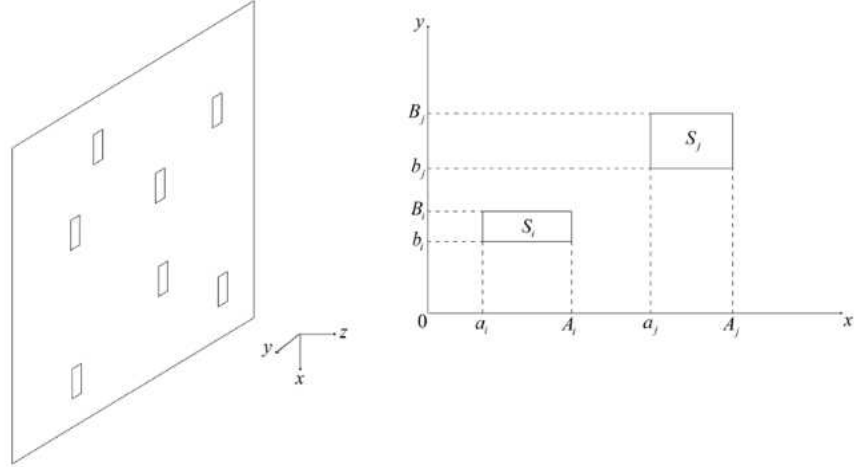
Figure 1: Problem geometry.

For slots, only the TE_{no} modes are considered because $B_k - b_k \ll \lambda$ and, so, the others are in cut-off. By inserting (2) into (1) we obtain the formulation of the GAM matrix

$$\sum_{m=1}^{M} I_{mi} \underline{h}_{mi}(\underline{r}) = j \frac{1}{2\pi\omega\mu_0} \left(k^2 + \nabla_t\nabla_t\right) \cdot \left(\sum_{k=1}^{N} \iint_{S_k} \sum_{p=1}^{M} V_{pk} \underline{h}_{pk}(\underline{r}')G ds'\right) \tag{3}$$

whose elements are provided by:

$$y_{mn}^{(ij)} = \frac{I_{mi}}{V_{nj}} = j\frac{\omega\varepsilon}{2\pi}\left[\iint_{S_i}\iint_{S_j} \underline{h}_{mi}(\underline{r})\cdot\underline{h}_{nj}(\underline{r}')G ds'ds - \frac{k_{tmi}k_{tnj}}{k_z^2}\iint_{S_i}\iint_{S_j}\Psi_{mi}(\underline{r})\Psi_{nj}(\underline{r}')G ds'ds\right] \tag{4}$$

As it can be appreciated, the numerical evaluation of a quadruple integral would be required. However the slots are narrow, so, to save computational time, after a first change of variables, we can approximate (4) by three single integral:

$$y_{mn}^{(ij)} = j\frac{\omega\varepsilon_0 K_i K_j}{4\pi}(B_i - b_i)(B_j - b_j)\left[\int_{A_1}^{B_1} F_1\left(\sigma, \frac{B_i - b_i}{2}, \frac{B_j - b_j}{2}\right)\gamma_1(\sigma)d\sigma\right.$$
$$\left. + \int_{A_2}^{B_2} F_1\left(\sigma, \frac{B_i - b_i}{2}, \frac{B_j - b_j}{2}\right)\gamma_2(\sigma)d\sigma + \int_{A_3}^{B_3} F_1\left(\sigma, \frac{B_i - b_i}{2}, \frac{B_j - b_j}{2}\right)\gamma_3(\sigma)d\sigma\right] \tag{5}$$

where γ_1, γ_2 and γ_3 are linear combinations of sinusoidal functions and F_1 is an exponential function.

Such approach can be pursued for the mutual admittances but it cannot be used for the self-admittance because the Green's function is singular. In this paper a singularity cancellation approach [4] is used to overcome such problem. After other two changes of variables we obtain:

$$y_{mn}^{(ii)} = j\frac{\omega\varepsilon_0 K_i K_j}{4\pi}\left\{\int_{-D_{ai}}^{0}\gamma_1(v)\left[\int_{\frac{-D_{bi}}{v}}^{0} F_3(u,v) * (\nu u + D_{bi})du + \int_{0}^{\frac{D_{bi}}{v}} F_3(u,v)(D_{bi} - \nu u)du\right]\text{sign}(v)dv\right.$$
$$\left. + \int_{0}^{D_{ai}}\gamma_3(v)\left[\int_{\frac{-D_{bi}}{v}}^{0} F_3(u,v)(\nu u + D_{bi})du + \int_{0}^{\frac{D_{bi}}{v}} F_3(u,v)(D_{bi} - \nu u)du\right]\text{sign}(v)dv\right\} \tag{6}$$

where F_3 is again an exponential function.

3. NUMERICAL RESULTS

The results of such approach are now compared with the ones provided by a commercial numerical simulation tool (CST).

First a single slot of dimension $0.5\,\text{m} \times 0.1\,\text{m}$ in an infinite PEC plane is considered and $y_{11}^{(11)}$, $y_{22}^{(11)}$ and $y_{12}^{(11)}$ are computed and shown in Figs. 2–6.

A good agreement between the two results is observed. (Numerical evaluation of $y_{12}^{(11)}$ provides zero).

Mutual coupling is now evaluated. Two horizontally and vertically, respectively, aligned slots
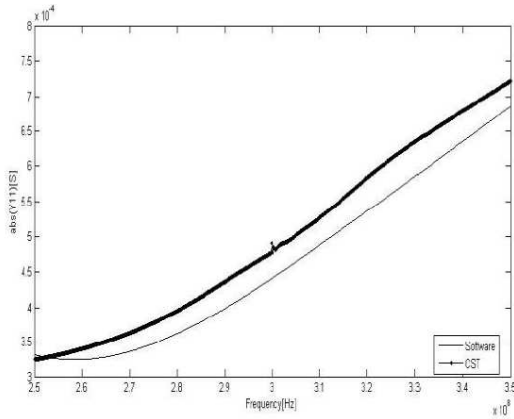
Figure 2: Module of $Y_{11}^{(11)}$.
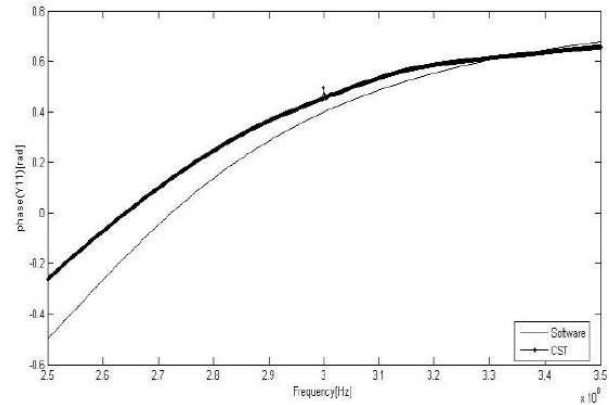
Figure 3: Phase of $Y_{11}^{(11)}$.
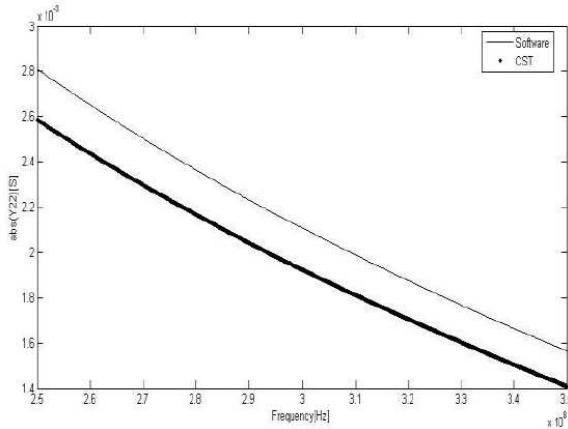
Figure 4: Modulus of $Y_{22}^{(11)}$.
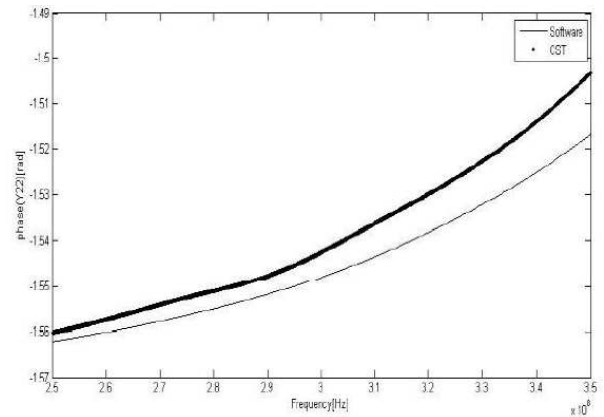
Figure 5: Phase of $Y_{22}^{(11)}$.
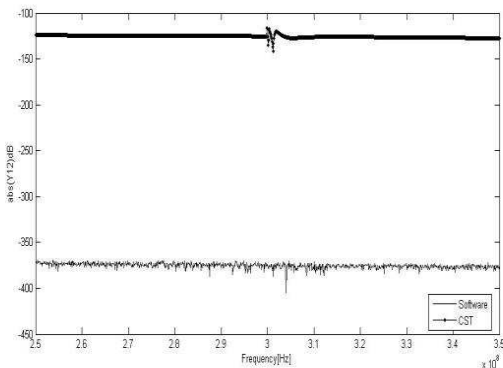
Figure 6: Module of $Y_{12}^{(11)}$.
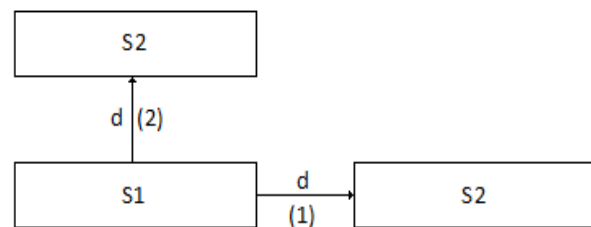
Figure 7: Example geometry.
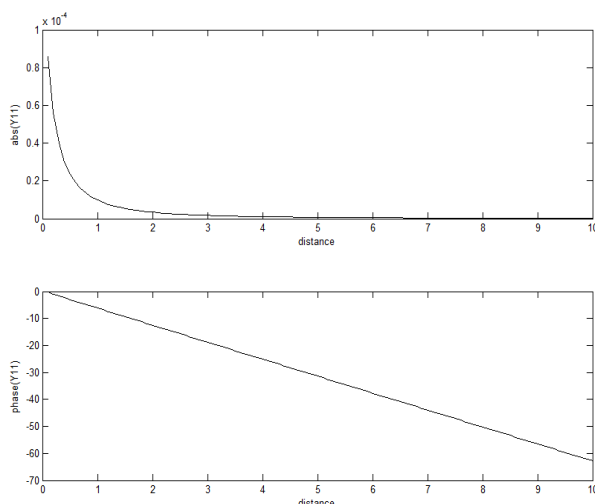
Figure 8: Modulus and phase of $Y_{11}^{(12)}$.
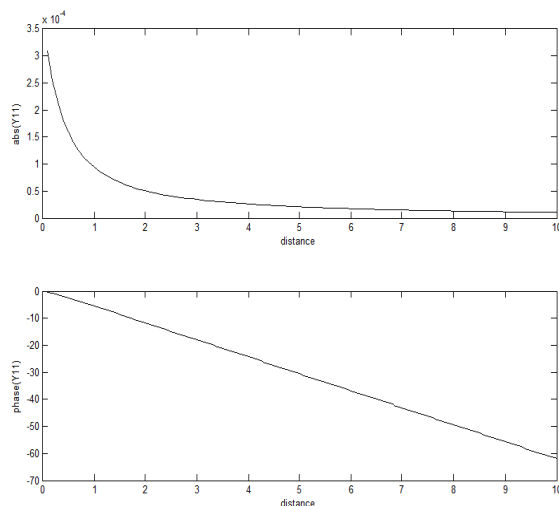
Figure 9: Module and phase of $Y_{11}^{(12)}$.

Figure 10: Geometry.

Slot	Auto-admittance	Active admittance
S1	6.46e-4 + i8.64e-4	5.58e-4 + i7.04e-4
S2	2.78e-4 + i4.45e-4	2.71e-4 + i4.46e-4
S3	1.05e-3 + i1.14e-3	9.57e-4 + i9.90e-4

Table 1: Slots admittances.
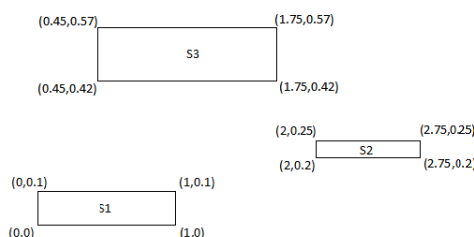
are considered (Fig. 7) and $y_{11}^{(12)}$ has been computed versus relative distance function and shown in Fig. 8, exhibiting the typical decay.

Finally in order to estimate the mutual coupling effect we consider the geometry of Fig. 10, composed of 3 slots of different dimensions where we assume only the fundamental mode on each slot to exist.

The following table shows the auto and active admittances values for each slot when the equivalent voltage is assumed equal to 1 V on each slot.

So, without taking into account the mutual coupling, a radiated power of $P_i = 0.99$ mW would be obtained. In turn, the mutual coupling leads to a value of 0.89 mW with about 10% decrease.

ACKNOWLEDGMENT

REFERENCES

1. Elliot, R. S., *Antenna Theory and Design*, IEEE Wiley, 2003.
2. Bird, T. S., "Analysis of mutual coupling in finite arrays of different-sized rectangular waveguides," *IEEE Trans. Antennas Propagat.*, Vol. 38, No. 2, 166–172, Feb. 1990.
3. Bird, T. S., "Mutual coupling in arrays of coaxial waveguides and horns," *IEEE Trans. Antennas Propagat.*, Vol. 52, No. 3, 821–829, Mar. 2004.
4. Duffy, M. G., "Quadrature over a pyramid or cube of integrands with a singularity at a vertex," *SIAM J. Num. Anal.*, Vol. 19, No. 6, 1260–1262, 1982.

An Adaptive Spectroellipsometric Technology for the Diagnosis of Water Ecosystems

F. A. Mkrtchyan, **V. F. Krapivin**, and **V. V. Klimov**

Institute of Radioengineering & Electronics RAS
1 Vvedensky Sq., Fryazino, Moscow reg. 141190, Russia

Abstract— Ellipsometry is an optical technique that uses the change in the state of polarization of light upon reflection and refraction for the in-situ and real-time characterization of surfaces, interfaces, liquid solutions in the hydrochemical investigations. Spectroellipsometry methods are used for the undestroying investigation of chemical and physical characteristics of liquid solutions. The diagnostics of liquids gives possibility to assess the concentration of chemicals dissolved and weighed in the liquid as well as to determine the spots of pollutants on the water surface.

A compact measuring — information multi-channel spectroellipsometric system for monitoring the quality of aquatic environment, that is based on the combined use of spectroellipsometry and training, classification, and identification algorithms is described. This system is differed from modern analogues by the use of a new and very promising method of ellipsometric measurements, an original element base of polarization optics and a complex mathematical approach to estimating the quality of a water object subjected to anthropogenic influence. The spectroellipsometric system can be used in different fields where the water quality should be estimated or the presence of a particular set of chemical elements should be revealed.

1. INTRODUCTION

Problem of the aquatic environment operative diagnostics is arisen practically in many human base including agriculture, medicine, industry and service. The development of these anthropogenic processes poses the problem of water pollution control and synthesizing monitoring system for water quality assessment in active regime.

Pollutant sources can have different structures and classes. Therefore, monitoring system is to be multi-purpose and mobile. It can be realized with the use of spectroellipsometric technology that gives possibility to have the spectrums with the sensitivity of 0.01% [1, 2].

The creation of multi-channel polarization optical instrumentation and use of spectroellipsometric technology are very important for the real-time ecological control of aquatic environment. It should be mentioned that efficient solution of this multi-parametric problem greatly depends on the precision and simplicity of ellipsometric devices. A technology of combined use of spectroellipsometry and algorithms of optical spectrums identification and recognition allows the creation of a standard integral complex of instrumental, algorithmic, modular and software tools for the collection and processing of data on the aquatic environment quality with forecasting and decision — making functions [2–4].

This paper describes new version of spectroellipsometric system that develops and realizes the functions of contaminant identification for multi-component solutions. It is realized by means of combined use of cluster analysis and algorithms for inverse task solution.

2. METHODOLOGY

Spectroellipsometric expert system for the aquatic environment diagnostics (SESAED) consists of measuring subsystem and software. The system's structure includes a compact multi-channel spectroellipsometer (MCS), information interface with computer (IIC), software (STW), and extending database (EDB). The STW realizes a number of algorithms to process data fluxes from the MCS and provides the service functions of visualization and control of measurements. The EDB consists of sets of standard spectral images of aquatic environments represented by points in the multi-dimensional vector space of indicators, pre-calculated on the basis of learning samples.

The principle behind the SESAED is based on fixing changes in light flux the MCS and digitizing them in IIC. Further processing of these data to make them more efficient is determined by STW with algorithms capable of recognizing spectral images. The degree of adaptability of the recognition procedure is determined by the level of accumulated knowledge about intensity fluctuations and the polarizing properties of light reflected from the water surface or dispersed and refracted within the water environment. The STW enables, in case of uncertain identification of spectral images, to

make an expert decision based on the visual analysis of a spectral image. This procedure is realized in dialog mode with the SESAED and, if a decision is made, the operator can fix it in the database in the form of a standard for subsequent appearances of similar spectral images.

Spectroellipsometric measurements deliver spectrums that are considered as spectral images of water solutions. Space of spectral images is formed during the learning procedure realized in laboratory conditions when spectral images and chemical analysis are performed at the same time. Identification procedure to recognize spectral image of water solution is carried out with the use of the EDB where spectrums and their derivatives are storage during learning procedure. Standard of the EDB item is given in Table 1.

Table 1: Structure of standard spectral image of water solution. Notation: A_1 is the square occupied by spectral curve, A_2 is the maximal value of spectral curve, A_3 is the minimal value of spectral curve, A_4 is the distance between wavelengths with minimal and maximal values of spectral curve, respectively; A_5 is the maximal derivative of spectral curve; A_6 is the maximal value of second derivative of spectral curve; A_7 is the number of spectral curve maximums; A_8 is the average value of spectral curve; A_9 is the wavelength corresponded to average value of spectral curve; B is the chemical element concentration.

Etalon number	A_1	A_2	A_3	A_4	A_5	A_6	A_7	A_8	A_9	B
1	A_{11}	A_{21}	A_{31}	A_{41}	A_{51}	A_{61}	A_{71}	A_{81}	A_{91}	B_1
...										
n	A_{1n}	A_{2n}	A_{3n}	A_{4n}	A_{5n}	A_{6n}	A_{7n}	A_{8n}	A_{9n}	B_n

An identification of spectral image for unknown water solution is realized by means of comparison his vector — identifier with elements of the EDB. Depending from used optical device spectral image of water solution can be represented by one or two vector-identifiers calculated with the use of rule described in Table 2. Final identification is realized by means of search in the EDB of vector — identifiers which are minimal distance from considered vector-identifier $Q = \{X_1, \ldots, X_n\}$ of given water solution. Distance between vector-identifiers is calculated with the use of the following formula:

$$\delta = \min_n \rho \left(Q - Q_n \right) = \frac{1}{2n} \min_i \left[\sum_{j=1}^n \left| X_j - A_j^i \right| + \sqrt{\sum_{j=1}^n \left(X_j - A_j^i \right)^2} \right] \tag{1}$$

Use of (1) gives better result in comparison with the application of other known criteria of closeness between spectral curves. That is why in this case there is minimal risk to miss the situation with dangerous pollution of water reservoir. In common case, usually the following methods are used:

•*Cluster analysis.* In this case two types of clusters are formed for $\cos \Delta$ and $\tan \Psi$ where Δ and Ψ are ellipsometric angles corresponding to complex amplitude reflection coefficients for two different polarizations. Decision is made by weighted values (1) or independently for each polarization.

•*Algorithm of discrepancy between spectra.* It is assessed average distance between the ordinates for both spectra and spectrum of studied case and decision is made taking into account minimal value of this distance.

•A*lgorithm of discrepancy between etalon vectors.* In this case, decision is made taking into consideration of minimal δ.

•*Inverse task solution.* This algorithm is based on linear dependence of optical spectrum on the concentration of chemical elements in water solution. In this case, sub-definite system of linear algebraic equations is solved.

3. RESULTS

The SESAED was used in different laboratory and in-situ conditions. Table 2 shows example of vector-identifiers calculated for $CuSO_4$ 10% solution with use of Table 1 procedure. Table 3 gives experimental results which give possibility to compare above mention algorithms. Dependence of risk assessment as function of solution concentration is represented in Fig. 1. As it follows from these results risk to have high error under the solution identification is reduced when algorithm of Table 1 is used. We see that risk to have high error is growth with increase of chemical element concentration. It is caused that discrepancy between spectra is decreased with increase of chemicals concentration. In this case it is necessary to extend the database of spectral etalons.

Table 2: An example of the SESAEC database element.

Solution	Q	Vector-identifiers								
CuSO$_4$ (10%)	Q_Δ	21.6	0.17	0.1	143	0.67	0.12	2	0.16	0.21
	Q_Ψ	43.1	0.89	0.04	201	0.59	0.09	3	0.65	0.01

Table 3: Comparatively assessment of algorithms for recognition of spectral images of water solutions.

Object for study	Identification algorithm and its error (%)			
	Cluster analysis	Discrepancy between spectra	Discrepancy between vector-etalons with the use Equation (1)	Inverse task solution
CuSO$_4$	15	12	8	7
NaCl	17	11	7	5
NaHCO$_3$	16	10	5	5
NH$_4$OH	21	13	9	6
ZnSO$_4$	22	12	8	6
Potassium iodite	13	10	6	4
Na + Cu + Zn + Mn + glu	18	9	9	8
cose	23	11	5	5
Furaciline	14	10	4	4
Bifidumbacterium				

Figure 1: Dependence of spectral image identification on the solution concentration.

4. CONCLUSION

The main objective of work is to create in future the compact information systems for monitoring the quality of aquatic environment and to investigate their potential efficiency. These systems are based on the combined application of spectroellipsometry methods and algorithms of training, classification, and identification. The realization of this objective will require the combined use of engineering and algorithmic tools providing real — time measurements and data processing. The technology of combined use of spectroellipsometry and algorithms of detection and classification

will allow the creation of an original system of instrumental, algorithmic, modular and software tools for the collection and processing of data on the aquatic environment with forecasting and decision-making functions. The theoretical part of the work will include the use of methods of polarization optics, mathematical statistics, the theory of pattern recognition and mathematical modeling.

ACKNOWLEDGMENT

REFERENCES

1. Perov, P. I., V. I. Kovalev, A. I. Rukovishnikov, N. M. Rossukanyi, and W. H. Johnson, "Hydrogen-sensitive palladium film study with precise and fast ellipsometers," *Int. J. Electronics*, Vol. 76, No. 5, 797–803, 1994.

2. Mkrtchyan, F. A., V. F. Krapivin, V. I. Kovalev, and V. V. Klimov, "An adaptive spectroellipsometer for ecological monitoring," *Microwave and Optical Technology Letters*, Vol. 51, No. 11, 2792–2795, 2009.

3. Mkrtchyan, F. A. and V. F. Krapivin, "An adaptive monitoring system for identify the spots of pollutants on the water surface," *World Environment*, Vol. 3, No. 5, 165–169, 2013.

4. Krapivin, V. F. and F. A. Mkrtchyan, "Multichannel spectroellipsometric technology for aguatic environment diagnostic," *Environment and Ecology Research*, Vol. 2, No. 2, 91–96, 2014.

Wideband Dual-mode Dielectric Waveguide with Applications in Millimeter-wave Interconnects and Wireless Links

Nemat Dolatsha and Amin Arbabian

Center of Integrated Systems (CIS), EE Department, Stanford University, Stanford, CA, USA

Abstract— Millimeter and submillimeter wave dielectric waveguides are receiving increasing attention for high capacity communication links due to the low transmission loss over a large bandwidth. In this paper, a new single-side multi-mode coupler for efficient excitation of two fundamental and polarization-orthogonal modes of a rectangular dielectric waveguide is presented. This technique doubles the available bandwidth of the waveguide without sacrificing the performance The effect of bending the waveguide is also investigated. Finally, the proposed multi-mode coupler is used to feed a high gain dual-polarized dielectric rod antenna. This also doubles the available *wireless* capacity of conventional singlepolarized rod antennas.

1. INTRODUCTION

With the exponential growth in data traffic arising from new subscriptions and emerging web and mobile applications, there is a significant need for efficient and extremely high-throughput wired and wireless links that can provide similar gains in network capacity at all levels. To this end, a substantial improvement in bandwidth and communication energy efficiency is required.

Conventional electrical links, based on TEM waveguide interconnects, are limited to a short range, especially for high-data rate applications. This is mainly due to the fundamental limitations of these links, namely the conductive loss at higher frequencies leading to adverse channel properties, the cross talk and impedance mismatch on these lines [1]. Non-TEM metal interconnects, such as the Substrate Integrated Waveguides (SIW) [2] have been proposed due to superior channel characteristics, but they are still limited to short range applications for high data rates due to the inherent high conductive losses. On the other side of the spectrum, optical links have been extensively used for long-range ultra-high data rate communication and are gradually entering the short/medium range space as well. However system cost and power efficiency of the entire link remain as major obstacles for optical interconnects in the short to medium range ($< 50\,\mathrm{m}$). This is due to the large over-head power consumption in the electro-optic convertors and the high complexity/precision needed for packaging and implementation.

On another front, recent progress in the development of low-power CMOS millimeter/submillimeter wave transceivers opens the way for energy efficient and high throughout links operating in this relatively unexplored frequency range [3]. Coupled with the very low loss characteristics of dielectric waveguides [4], these silicon-based mm-wave transceivers can open the way to a new class of wired links that bridge the gap between conventional TEM electrical interconnects and optical fiber [5–8]. In this paper we introduce a low-loss dual-mode wideband waveguide coupling scheme for the transceiver interface without adding significant packaging complexities.

Millimeter-wave dielectric waveguides have been investigated for the low transmission loss properties that can be exploited as an effective channel in high-speed interconnects [7–9]. In addition to losses, the maximum achievable data-rate in these interconnects is also limited by the dispersive channel characteristics, especially when utilizing a single carrier in order to increase the energy efficiency of the entire system. The available capacity of the waveguide channel can be further boosted by multi-mode excitation of the guide. This enables either higher throughput in the same bandwidth, or, alternatively, the same throughput on a narrower bandwidth that is less affected by the dispersive behavior of the channel. Here, the challenge is the efficient excitation of appropriate modes and polarizations in the waveguides. To this aim, we have recently proposed an all-electrical, low-cost and easy-to-package structure based on millimeter-wave dielectric waveguides for high-throughput interconnects (see Figure 1(a)) [9]. A planar feed structure excites two *polarization-orthogonal* modes of the waveguide, namely the E_x^{11} and E_y^{11} modes (Figure 1(b)). This doubles the available capacity of the waveguide.

In the current paper, we have modified the proposed multi-mode excitation structure to improve the coupling efficiency and further simplify the packaging and implementation. As opposed to the prior work [9], the couplers are now integrated together in a single two-layer PCB placed on one side of the dielectric waveguide (instead of on both sides). This eliminates the routing of the RF
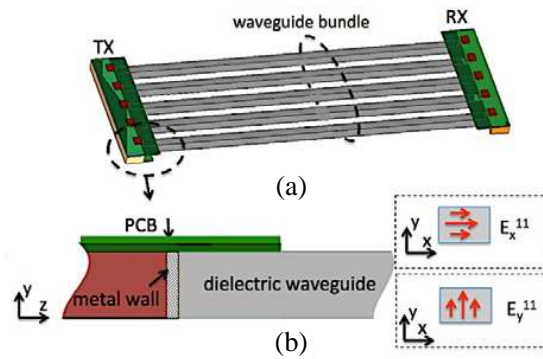
Figure 1: (a) Dielectric waveguide bundle for high-throughput wired links. (b) Conceptual drawing (side view) of the multi-mode excitation structure for a rectangular dielectric waveguide.

signal from transceiver ICs to both printed couplers and then the waveguide. The effect of bending of the waveguide carrying both modes is also investigated. Eventually, the proposed feed structure is also used for realizing a high gain millimeter-wave dielectric rod antenna with dual-polarization, which doubles the capacity for wireless communications.

2. DIELECTRIC WAVEGUIDE CHARACTERISTICS

Dielectric waveguides shaped in rectangular, circular, and hollow circular cross sections have been studied for various applications [4]. They provide a very low insertion loss medium for millimeter/sub-millimeter waves. Due to the recent progress in developing efficient CMOS transceivers at millimeter/sub-millimeter waves, they are receiving increasing attentions for high-speed interconnects.

In [9], we have investigated the *transmission loss* and *bandwidth per pitch* of the rectangular waveguide for different dielectric properties. In rectangular dielectric waveguides, the low permittivity along with the small loss tangent results in a low transmission loss [4, 9]. In this paper, a low-permittivity and mechanically flexible HDPE polyethylene dielectric with $?_r = 2.25$ and $\tan \delta = 0.001$ is used to realize the waveguide ($?_r$ and $\tan \delta$ are measured at $40\,\mathrm{GHz}$ using a 900 T model cavity resonator setup made by Damaskos Inc.). The waveguide is designed for operation at the center frequency of $75\,\mathrm{GHz}$. This results in $2.3 \times 2.3\,\mathrm{mm}^2$ waveguide cross-section. Simulations show a transmission loss of $10\,\mathrm{dB/m}$ at $75\,\mathrm{GHz}$.

In many applications, mechanically flexible waveguides are desirable to enable effective routing and distribution of a long line. Although the HDPE Polyethylene lines are flexible, the electromagnetic properties of the waveguide at bends should be carefully examined with focus on power leakage and mode conversion. Due to reduced field confinement, the former effect is more severe in waveguides with low permittivity. Figure 2 shows the bending loss of two polarization-orthogonal modes for different bending radii. As expected, the bending loss decreases with increasing the radius or the frequency. The latter is partly due to the fact that at higher frequencies, the effective electrical bending radius is larger (i.e., at higher frequencies the waveguide is effectively closer to a straight waveguide). In addition, at higher frequencies, fields are more confined inside the waveguide. Simulations show that the mode cross-coupling, from one polarization to the other, is less than $-40\,\mathrm{dB}$ in the entire range for all of the above cases.

3. MULTI-MODE COUPLER

In [9], a printed electric dipole placed on top of the waveguide launches the E_x^{11} mode (with electric field in x direction) into the waveguide. The E_y^{11} mode is coupled into the waveguide using a printed slot dipole placed on the bottom side of the waveguide. In the current paper, to simplify the implementation, the feed structure is modified and both mode couplers are mounted on the single side of the waveguide (see Figure 3(a)). Due to difficulties in co-integration of electric and slot dipoles on a single side, the slot dipole is replaced by a planar horn-like structure realized in a substrate-integrated waveguide (SIW). In addition, a printed Vivaldi antenna, instead of a simple electric dipole, couples the E_x^{11} mode efficiently into the waveguide.

The couplers are made on a two-layer RO3003 PCB ($?_r = 3$, with thicknesses of $100\,\mu\mathrm{m}$ and $150\,\mu\mathrm{m}$) with three printed metal layers (shown in Figure 3(b), from top M_1, M_2, M_3). As shown
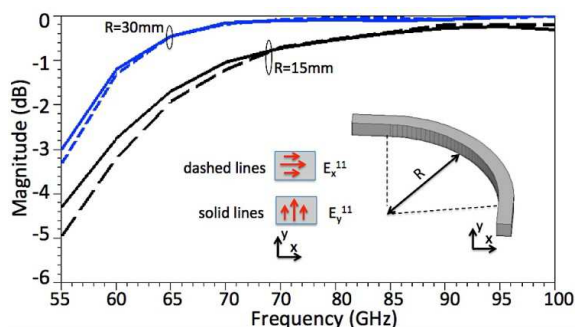
Figure 2: Bending loss of two polarization-orthogonal modes for different bending radii.
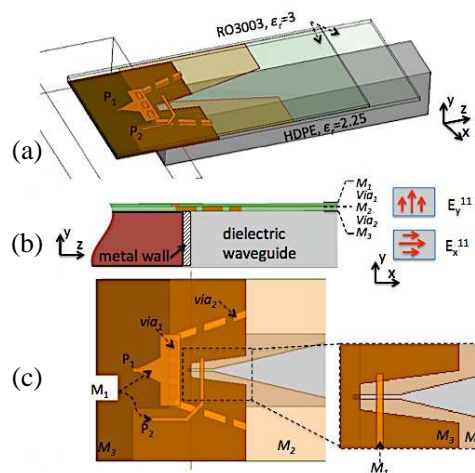
Figure 3: (a) Drawing of the multi-mode excitation structure. P_1 and P_2 launch the fields from ICs into E_y^{11} and E_x^{11} modes of the dielectric waveguide. (b) Side view, a two layer RO3003 PCB made of M_1, M_2 and M_3 metal patterns. (c) Top view of the planar multimode excitation structure, Vivaldi antenna realized on M_2 excites the E_x^{11} mode and the SIW horn (between M_2 and M_3) excites the E_y^{11} mode.
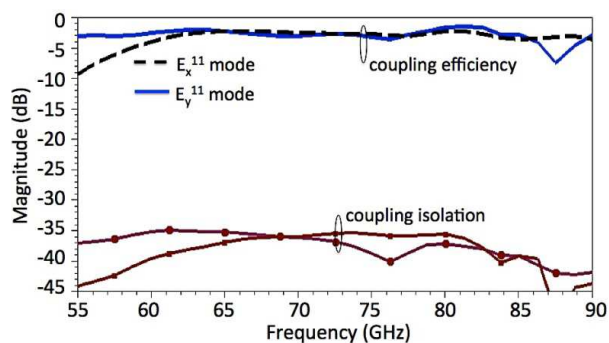
Figure 4: Coupling efficiency of E_y^{11} and E_x^{11} modes and isolation to their unwanted cross-polarized modes.
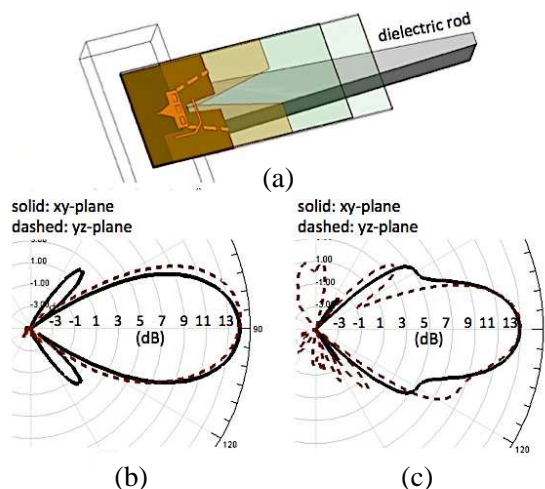
Figure 5: (a) Dual polarize dielectric rod antenna fed by the proposed planar multi-mode coupler. (b) Radiation pattern of the E_x^{11} mode. (c) Radiation pattern of the E_y^{11} mode.

in Figure 3(c), the horn-like SIW is realized by two rows of via_2 connecting M_2 and M_3. The horn-like opening along with tapered opening slot on M_3 gradually couples the TE_{10} mode (with electric field in y direction) of the SIW into the E_y^{11} mode of the dielectric waveguide. These result in a higher coupling efficiency. Eventually, the input of the SIW section (at M_2) is connected to a microstrip transition on M_1 through via_1.

The Vivaldi antenna printed on the M_2 excites the E_x^{11} mode (see Figure 3(c)). Here, the signals with electric field components, mainly in x direction, traveling along the tapered slot on M_2 smoothly and efficiently couple into the E_x^{11} mode of dielectric waveguide. A microstrip line printed on M_1 feeds the Vivaldi antenna.

The coupling efficiency and the amount of leakage to the unwanted cross-polarized mode are plotted in Figure 4. A coupling efficiency of better than 2.5 dB is achieved in the range of 60–

85 GHz. The isolation to the unwanted mode is significant and better than 35 dB for both couplers. A large transmission bandwidth of 50 GHz (2×25 GHz) is available for a single line. When exploited in aggregated lines, the proposed multi-mode waveguide has a great potential for ultra-high throughput interconnects.

The proposed multi-mode feed can be modified to also realize a dual-polarization antenna offering a larger capacity for wireless links. The details are discussed in the next section.

4. DUAL-POLARIZED DIELECTRIC ROD ANTENNA

Dual-polarized antennas, due to the doubling of the available bandwidth, have been extensively used for different applications. Conventional dual-polarized printed antennas such as microstrip patches or electric/slot dipoles offer easy manufacturing and implementation at the expense of a limited gain. Printed Vivaldi antennas, exhibit higher gain, at the expenses of significant difficulties for feeding and implementation for dual-polarization radiation [10]. In this section, employing the proposed planar feed structure based on the dielectric waveguide, we present the dual-polarized rod antenna shown in Figure 5(a). Compared to the printed Vivaldi, the proposed antenna not only exhibits a higher gain but also its implementation and feed network in larger arrays is significantly simplified. The gain of the rod antenna increases with the length of the tapered section [11]. However, due to required mechanical strength, the length is limited to 13 mm. Figures 5(b) and 5(c) show the simulated radiation pattern for both modes. The antenna gain at 75 GHz is 14 dBi and 13 dBi for E_x^{11} and E_y^{11} modes, respectively. The unwanted cross-polarization level for each of modes is less than -40 dB at the maximum directivity.

5. CONCLUSION

A low-cost planar coupler for multi-mode excitation of a rectangular dielectric waveguide is presented. The proposed method boosts the large available bandwidths of dielectric waveguides applicable for ultra-high data rate communication in interconnects and wireless links. Simulations also confirm efficient guiding of the two polarization-orthogonal modes along the waveguide bends.

REFERENCES

1. Naeemi, A., A. V. Mule, and J. D. Meindel, "Partition length between board-level electrical and optical interconnects," *IEEE Intern. Tech. Conf.*, 230–232, Jun. 2003.
2. Asanee, S. and R. Abhari, "Ultra-high-speed multichannel data transmission using hybrid substrate integrated waveguides," *IEEE Trans. Microw. Theory Tech.*, Vol. 56, No. 8, 1973–1984, 2008.
3. Marcu, C., et al., "A 90 nm CMOS low-power 60 GHz transceiver with integrated baseband circuitry," *IEEE Jour. Solid-State Circuits*, Vol. 44, No. 12, 3434–3447, 2009.
4. Koul, S. K., *Millimeter Wave and Optical Dielectric Integrated Guides and Circuits*, J. Wiley & Sons, New York, 1997.
5. Kim, Y., et al., "High-speed mm-wave data-link based on hollow plastic cable and CMOS transceiver," *IEEE Microw. Wireless Component Lett.*, Vol. 23, No. 12, 674–676, Dec. 2013.
6. Dolatsha, N. and J. Hesselbarth, "Millimeter-wave chip-to-chip transmission using an insulated image guide excited by an on-chip dipole antenna at 90 GHz," *IEEE Microw. Wireless Component Lett.*, Vol. 22, No. 5, 266–268, May 2012.
7. Haroun, B. S., et al., "Chip-to-dielectric waveguide interface for sub-millimeter-wave communication link," US Patent Application Filed, Sep. 2010.
8. Fukuda, S., et al., "A 12.5 + 12.5 Gb/s full-duplex plastic waveguide interconnect," *IEEE J. Solid-State Circuits*, Vol. 46, No. 12, 3113–3125, Dec. 2011.
9. Dolatsha, N. and A. Arbabian, "Dielectric waveguide with planar multi-mode excitation for high data-rate chip-to-chip interconnects," *IEEE Intern. Conf. UWB*, 184–188, Sep. 2013.
10. Veidt, B., et al., "Demonstration of a dual-polarized phased-array feed," *IEEE Trans. Antennas Propag.*, Vol. 59, No. 6, 2047–2057, 2011.
11. Mueller, G. E. and W. A. Tyrrell, "Polyrod antennas," *Bell. Syst. Tech. J.*, Vol. 26, 851–837, Oct. 1947.

Development of Wireless Power Induction Cooker Using Magnetic Induction-based Technology

Wonho Jang[1], Seonghun Lee[2], Jeongsug Yeom[3], Byungduk Min[4],
Goonyeon Kim[1], and Sangho Choi[1]

[1]Electromagnetic Wave Technology Institute of RAPA, Seoul, Korea
[2]Creative Innovation Center of LGE, Seoul, Korea
[3]Komatech, Seoul, Korea
[4]R&D Department of Green Power, Suwon, Korea

Abstract— -Magnetic induction technology offers higher power transmission and higher efficiency of power transmission than magnetic resonance technology in the wireless power transmission. We have developed a wireless power induction range which has over 90% dc-to-dc wireless power transmission efficiency and transmission power up to 2.4 kW. We used 20 kHz frequency to resonate between transmission coil and reception coil. EMF level is below 30% according to the ICNIRP 2010 measured by the IEC 62233 measurement method.

1. INTRODUCTION

The growth of the wireless power transmission technology is propelled by the increased demand in smartphones, the consumer goods industry, and consumers' inclination toward wireless connectivity. The market is further driven by the increasing efficiency in technologies as well as new emerging application areas. Wireless power transmission (WPT) systems are becoming ubiquitous with applications in powering smartphones, transportation and a range of kitchen appliance devices such as induction cooker. In Korean kitchen appliances, induction cooker sales increase dramatically in the last five years. The second is a deep-fat fryer and the third is electric grill. IH (Induction Heating) range is new product in the induction cooker up to now. We had noticed that IH + WPT cooker is new integrated product for the kitchen appliance. We call it is WPIC (Wireless Power induction cooker) In the 2020 the wireless power revenue will expect 13 billion USD and the consumer electronics including appliances will project 4 billion USD as well.

2. DESIGN PROCEDURE

WPIC is required to meet wider margin of alignment to cook conveniently and to prepare foreign object detection mode to avoid fire and harmful damage to the human body. The level of EMC is limited by the CISPR 11 regulation and the level of EMF is limited by the ICNIRP guideline.

2.1. Resonator Design

We made disk type resonators, two transmission coils and one reception coil. Figure 1 shows the simulation picture of the electromagnetic field distribution between transmission and reception coils. Figure 2 shows the prototype resonators.

Figure 3 shows the shielding ferrite construction to minimize the leakage of the magnetic field.

2.2. Inverter Design

We selected a full-bridge inverter to get higher power output and higher efficiency.

2.3. Communication Part Design

We have developed both an out-of-band communication and a time multiplexing (in-band) communication method. We used a Bluetooth Low Energy (BLE) for out-of-band communication.
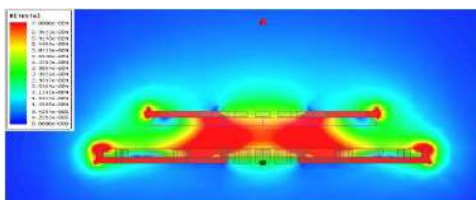
Figure 1: Coil shielding part simulation by Maxwell.
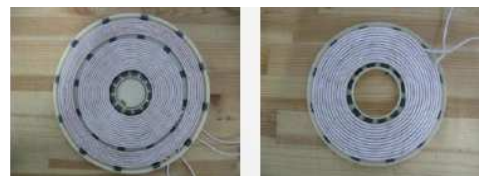
Figure 2: Transmission and reception resonators.
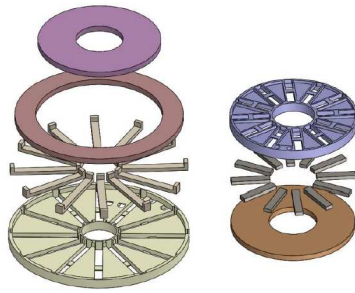
Figure 3: Tx and Rx coil & ferrite assembly.
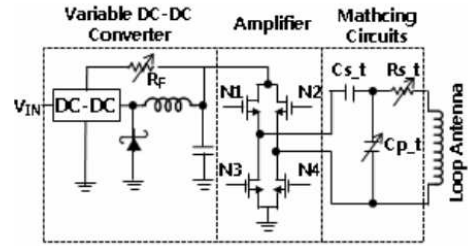
Figure 4: The circuit diagram of the Full-bridge Inverter
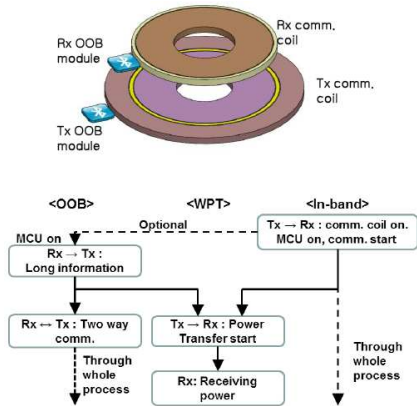
Figure 5: The configuration of out-of-band (OOB) and time multiplexing communication.
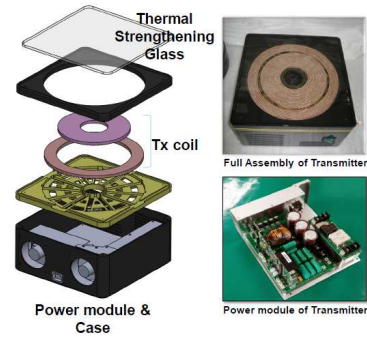
Figure 6: The configuration of 3D modeling of transmitter and picture of prototype transmitter and power module.

Figure 7: The pictures of WPT kettle and WPT blender.
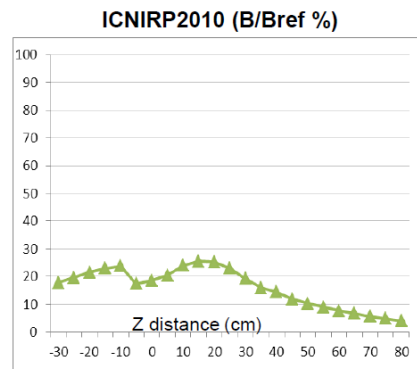
Figure 8: The measured result of the EMF levels.

2.4. Prototype-transmitter

We made the transmitter for a stand-alone and a built-in type in the kitchen countertop. We designed the heat dissipation structure in the transmitter such as fins, fans and a ventilation duct. The transmitter is compatible as an IH (Induction Heating) type and a Wireless Power Transmission (WPT) type with a thermal strengthen glass. Both the wireless power kitchen appliances and IH appliances can use the transmitter at the same time.

2.5. Prototype-receiver

We made a receiver as a module type for several appliances. Heat dissipation structure is designed such as a fin and a duct. DC power output from the reception coil in the appliances could be changed to AC power output to feed to the receiver heating coil in the kettle or to drive the motor in the mixers.
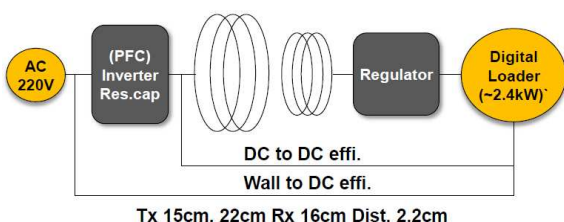
Figure 9: The efficiency test setup.
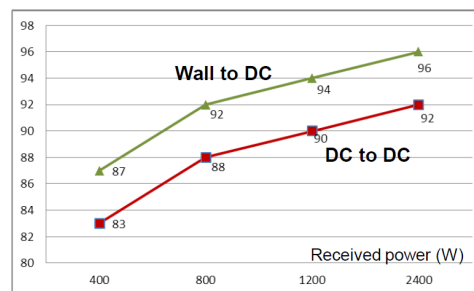
Figure 10: The measured efficiency result.

3. EMF AND EFFICIENCY MEASUREMENT

WPIC systems are ISM equipment, and are required to meet free-space electric and magnetic-field levels to conform to limits provided by CISPR 11 standard on wanted emissions at the operating frequency and its harmonics, and also on unwanted (spurious) emissions up to 18 GHz.

We measured EMF based on IEC 62233 with Narda EHP-200A, 9 kHz∼100 kHz frequency measurement bandwidth. Sweep the probe from −50 cm to 100 cm in z-direction at 30 cm apart from Transmission coil. Reference the guideline ICNIRP 2010. At 2 kW received power condition, the EMF level compared to the ICNIRP guideline is below 30%.

We configured the efficiency test set as a Figure 9. The Wall to DC efficiency is 96% maximum at the 2.4 kW power transmission point.

4. CONCLUSION

We made a prototype wireless power transmission induction cooker. It is a new product of wireless kitchen appliance. We achieved good wireless power transmission efficiency, 96% maximum at the 2.4 kW. We also conform to the CISPR 11 standard and ICNIRP guideline. The standardization process of the product is working at the Wireless Power Consortium.

ACKNOWLEDGMENT

REFERENCES

1. "Industrial, scientific and medical equipment — Radio-frequency disturbance characteristics — Limits and methods of measurement," International Special Committee on Radio Interference CISPR Std. CISPR 11, 2010.
2. Balanis, C. A., *Antenna Theory: Analysis and Design*, John Wiley and Sons, Inc., Chichester, Brisbane, New York, Toronto, Signapore, 2005.
3. ICNIRP, "Guidelines for limiting exposure to time-varying electric, magnetic and electromagnetic fields (up to 300 GHz)," *Health Physics*, Vol. 74, No. 4, 494–522, Apr. 1998.
4. ICNIRP, "Guidelines for limiting exposure to time-varying electric and magnetic fields (1 Hz to 100 kHz)," *Health Physics*, Vol. 99, No. 6, 818–836, Dec. 2010.
5. IEEE Standard for Safety Levels with Respect to Human Exposure to Radio Frequency Electromagnetic Fields, 3 kHz to 300 GHz, IEEE Std. C95.1, 1992.
6. IEEE Standard for Safety Levels with Respect to Human Exposure to Radio Frequency Electromagnetic Fields, 3 kHz to 300 GHz, IEEE Std. C95.1, 2005.
7. ICNIRP, "Response to questions and comments on guidelines for limiting exposure to time-varying electric, magnetic and electromagnetic fields (up to 300 GHz)," *Health Physics*, Vol. 75, No. 4, 438–439, 1998.

Miniaturized Transmitter in Digital Modulation System with Non-constant Envelope for VHF Band

Heon-Kook Kwon, Sung Jun Lee, Byung-Su Kang, and Bong-Hyuk Park

Electronics and Telecommunications Research Institute (ETRI), Korea

Abstract— In this paper, compact transmitter included power amplifier linearization in digital modulation with non-constant envelope for VHF band using cartesian feedback loop is presented. The digital modulation(QPSK/16-QAM/64-QAM) signal is non-constant envelope with constant peak to average power ratio. Digital modulation signal used when linearizing PA is 64-QAM, 70 ksps symbol rate, 0.35 of roll-off factor, and 7.5 dB PAPR. We used the Mitsubishi's Silicon power module, RA60H1317M1A, as a results, obtained an Adjacent Channel Power Ratio(ACPR) of less than -72 dBc, Error Vector Magnitude (EVM) of 2.8% at $+39$ dBm in VHF band. This technique is utilized to achieve miniaturization of transmitter with high linearity.

1. INTRODUCTION

Today, digital modulation rather than analog has been primarily used in wireless communication. The primary reason is to transfer more data without error since information to be transmitted via the wireless communication has changed from voice to data. However, QPSK and QAMs which is higher order digital modulation for large amounts of data transmission have a non-constant envelope due to the modulation using both of phase and amplitude. In addition, non-constant envelope signal has a high PAPR, the signal give a heavy load on the power amplifier of the transmitter. That is, to achieve high linearity, power amplifier should be as much as or more back-off than PAPR. Therefore, power amplifier should be designed with power higher than the specified transmit power [1].

In using a power amplifier, a high linearity and efficiency transmitter configuration through a small back-off is relatively simple. In general, to obtain high linearity of the power amplifier without the use of excessively high power amplifier, linearization techniques are used. These techniques allow that the output power of the power amplifier is used close to its saturated power while maintaining high linearity. In addition, a highly efficient performance of the power amplifier can be achieved. That is, a highly linear and efficient power amplifier is capable of reducing the size of the transmitter [2, 3].

Cartesian feedback which is one of linearization techniques adopt quadrature modulator as up-converter. A coupled signal of the power amplifier output in quadrature transmitter is demodulated in quadrature phase, and the demodulated signal is fed back to pre-distort baseband I/Q signal for the linearization [2–4].

In this paper, in order to obtain a high linearity of a power amplifier, we implemented a miniature transmitter using the cartesian feedback linearization technique. The implemented transmitter has high linearity at the maximum output power which is backoff power less than PAPR of non-constant envelope digital modulation signals such as QPSK, 16QAM, 64QAM and this is the same result with the signals of different bandwidths.

2. THE CONFIGURATION OF THE MINIATURIZED TRANSMITTER

Figure 1 shows a block diagram of a transmitter for digital modulation in the VHF band, which can transmit more than a 8 W average power. The transmitter consists of quadrature modulator/demodulator, driving amplifier, and power amplifier. CML Microcircuits' CMX998 is used as a quadrature modulator, which is up-converts baseband analog In-phase and Quadrature signals to the VHF band. In addition, it has a demodulator for cartesian feedback. To output more than a 8 W average power, up-converted signal is amplified by the amplifier which is used BEREX's BIF7 as a driving amplifier, and Mitsubishi's RA60H1317M1A as a power amplifier.

3. THE MEASURED PERFORMANCE OF THE TRANSMITTER

Figure 2 shows test results of RA60H1317M1A biased $Vd = 12$ V and $Vg = 4.5$ V with a 1-tone and digital modulation signal. As shown in the Figure 2, gain and 1 dB gain compression point $(P_{1\,\text{dB,out}})$ of power amplifier are $+39$ dB and $+43.6$ dBm respectively. Also, ACLR(Adjacent Channel Leakage Ratio) of the power amplifier is -41 dBc at $+39$ dBm of average power with digital
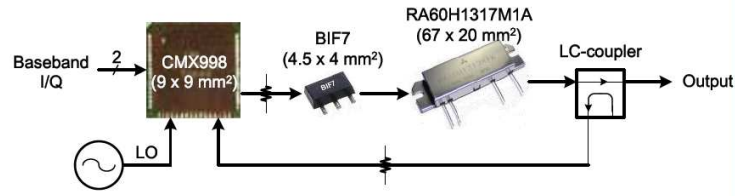
Figure 1: The configuration of the miniaturized transmitter.

(a)   (b)
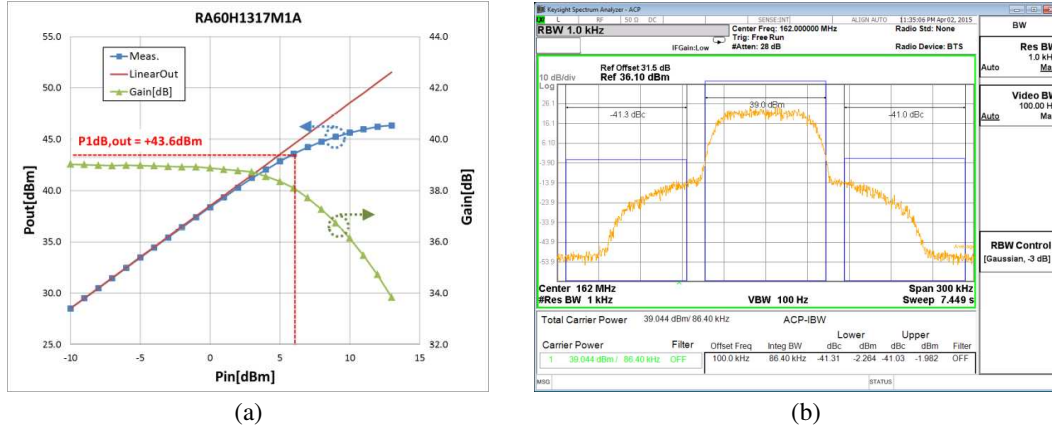
Figure 2: The characteristic of the power amplifier(RA60H1317M1A). (a) Gain and $P_{1\,\text{dB}}$. (b) ACLR.

modulation signal, which is 64-QAM, 70 ksps symbol rate, 0.35 of roll-off factor, and 7.5 dB PAPR.

To verify the performance of the implemented transmitter for the digital modulation, the test environment was configured as shown in Figure 3. Digital modulation signals which are QPSK, 16QAM, and 64QAM are generated by signal generator. Digital filter has 0.35 of roll-off factor, and Null to Null bandwidth of digital modulated signals is 25 kHz, 50 kHz, and 100 kHz. By this test configuration, we measured the maximum output power of the transmitter corresponding to each signal. Also, we observed ACLR and EVM at the maximum power.
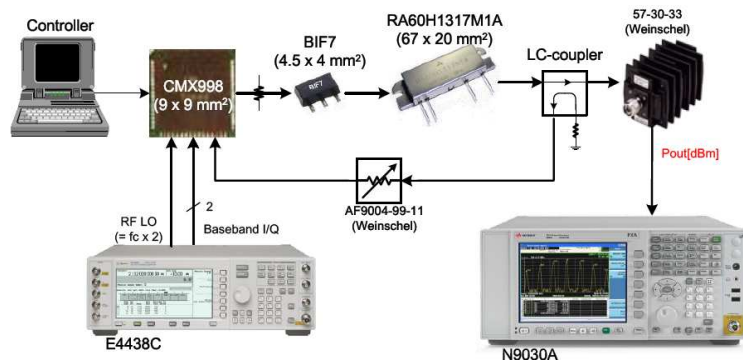
Figure 3: Test configuration of the transmitter for digital modulation.

As one of the results, Figure 4 shows results using 64QAM, 100 kHz bandwidth signal. The signal's PAPR is 7.5 dB. With this signal, we obtained an Adjacent Channel Power Ratio(ACPR) of less than -72 dBc, Error Vector Magnitude(EVM) of 2.8% at $+39$ dBm which is the maximum output power of the transmitter.

Generally, maximum output power of the transmitter is backed off as much as or more than PAPR from $P_{1\,\text{dB,out}}$ of the power amplifier [4]. This is expressed by Equation (1).

$$P_{\text{OUT,MAX}}\,[\text{dBm}] = P_{1\,\text{dB,OUT}}\,[\text{dBm}] - PAPR\,[\text{dB}] + K\,[\text{dB}] \tag{1}$$

where, K represents the degree of improvement compared to the PAPR back-off, $P_{1\,\text{dB,out}}$ denotes

(a)   (b)

(c)
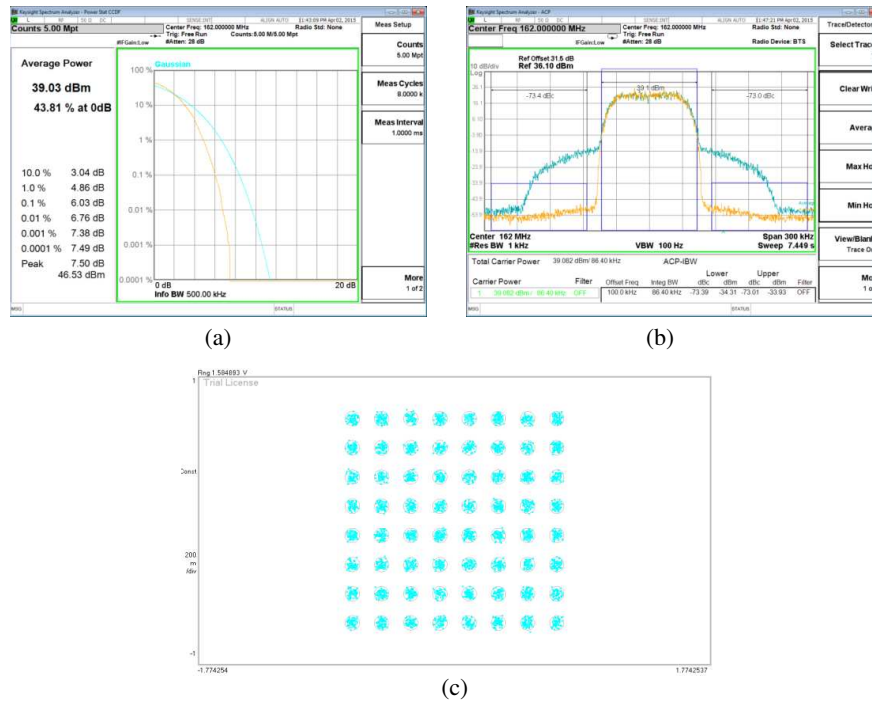
Figure 4: Measured performance of the transmitter with 64-QAM, 100 kHz bandwidth signal. (a) CCDF. (b) ACLR before and after linearization. (c) EVM (= 2.8%) on constellation.

maximum output power available in transmitter, and $P_{1\,dB,out}$ means 1dB Gain compression point at output of power amplifier.

Table 1 summarizes the measured results of the implemented transmitter for the various bandwidth and digital modulation. As shown in the Table 1, the maximum transmitter output power of this study are results of backoff smaller than PAPR from the $P_{1\,dB,out}$. That is, The amount of the back-off is 2.6 to 3.9 dB smaller than the PAPR. Also, we can be seen that ACLR is less than -75 dBc, EVM is less than 1% corresponding to the digital modulation (QPSK/16QAM/64QAM) signal with 25 kHz and 50 kHz bandwidth. Even for 100 kHz bandwidth signal, ACLR is less than -72 dBc, and this represents high linearity. However, EVM is slightly higher than different bandwidth as 2.8 to 4.4%. This is because the bandwidth of the baseband block is designed narrower than 100 kHz.

Table 1: Performance of the transmitter to the different bandwidth and modulation.

Bandwidth (Null to Null)	Modulation	PAPR [dB]	Max. output Power [dBm]	**K** **[dB]**	ACLR [dB]	EVM [%]
25 kHz	QPSK	5.0	+42.5	**3.9**	< -78.0	0.43
	16QAM	6.8	+40.5	**3.7**	< -77.5	0.32
	64QAM	7.4	+39.5	**3.3**	< -78.0	0.28
50 kHz	QPSK	5.3	+41.0	**2.7**	< -77.0	0.68
	16QAM	6.8	+40.0	**3.2**	< -76.5	0.32
	64QAM	7.5	+39.0	**2.9**	< -77.0	0.42
100 kHz	QPSK	5.2	+41.0	**2.6**	< -70.2	4.40
	16QAM	6.9	+40.0	**3.3**	< -70.7	3.30
	64QAM	7.5	+39.0	**2.9**	< -719	2.80

4. CONCLUSION

A transmitter using the linearization technique of the power amplifier for non-constant envelope, such as QPSK, 16QAM, and 64QAM digital modulation signal, is implemented. The transmitter performance shows wide bandwidth, high linearity compared to previous result[5]. Also, Back-off is smaller than PAPR was used to make output power close to $P_{1\,dB}$ of its power amplifier in VHF band, while maintaining high linearity.

We obtained the maximum output power of the transmitter up to $+39$ ($= 8\,W$) to $+42.5\,dBm$ ($= 17.8\,W$) through power amplifier with $P_{1\,dB,out}$ of $+43.6\,dBm$ ($= 22.9\,W$), while achieving high linearity as ACLR of $-70\,dBc$ or less. The maximum output power are results of backoff smaller than PAPR of non-constant envelope signal from the $P_{1\,dB,out}$. The amount of the back-off is 2.6 to $3.9\,dB$ smaller than the PAPR. Output power is close to $P_{1\,dB,out}$ of power amplifier as much as that.

In the future, we are going to modify the baseband block to improve EVM of transmitter for the signals of $100\,kHz$ bandwidth

ACKNOWLEDGMENT

REFERENCES

1. Razavi, B., *RF Microelectronics*, 2nd Edition, Prentice-Hall, Upper Saddle River, NJ, USA, 2011.
2. Kim, B., J. Moon, and I. Kim, "Efficiently amplified," *IEEE Microw. Mag.*, Vol. 11, No. 5, 89–100, 2010
3. Bruss, S., "Linearization methods," 23 Apr. 2003.
4. Ali, S., Z. Chen, and F. Yin, "Peak-to-average power ratio reduction using N-tuple selective mapping method for MC-CDMA," *ETRI Journal*, Vol. 37, No. 2, 338–347, Apr. 2015.
5. Narendra, K., L. Anand, P. Sangaran, S. Anbalagan, and G. Boeck, "RF power amplifier with Cartesian feedback for TETRA modulation," *ICECS 2007*, 262–265, 11–14 Dec. 2007.

Nonlocality in Discrete Metamaterials

M. A. Gorlach[1, 2] **and P. A. Belov**[1]

[1]ITMO University, Russia
[2]Belarusian State University, Belarus

Abstract— We discuss spatial dispersion effects in three-dimensional discrete metamaterials. In the present work, we consider two examples of metamaterials whose behavior can not be described properly by means of the effective medium model and where nonlocality is important. These examples are (i) discrete structure consisting of the uniaxial dipoles operating in the vicinity of the transition from elliptic to the hyperbolic dispersion regime and (ii) structure composed of isotropic particles with electric polarizability where spatial-dispersion-induced birefringence can arise.

1. INTRODUCTION

One of the exciting perspectives provided by the field of metamaterials is a possibility to tailor metamaterial electromagnetic response choosing proper constituent elements of artificial structure as well as the geometry of their arrangement. Engineering composite materials' local material parameters (e.g., permittivity and permeability) is widely discussed in the literature [1, 2]. Besides that, the use of metamaterials provides a novel degree of freedom in material science, namely, a possibility to tailor metamaterial spatially dispersive response. Spatial dispersion or nonlocality of material electromagnetic response means that the polarization of a physically small volume is influenced not only by the field in a given volume but also by the electric field existing in the neighbouring regions of space [3, 4]. Strong spatial dispersion effects are quite uncommon in natural materials [4]. However, there exists a class of metamaterials where nonlocality is important [5]. Therefore, it is of interest to reveal new physical phenomena that arise due to spatial dispersion. In the present work, we address two types of metamaterials operating in such regime that the nonlocal effects are essential: the three-dimensional structure consisting of the uniaxial dipoles in the frequency range corresponding to the transition from elliptic to the hyperbolic dispersion regime (Fig. 1(a)) and the structure composed of isotropic particles (Fig. 1(b)) where spatial-dispersion-induced birefringence can be observed. In our study, we employ the discrete dipole model that provides a self-consistent scheme for the description of the nonlocal effects in discrete metamaterials [6]. Note that we do not employ perturbative expansions of the effective permittivity dyadic with respect to wave vector in this scheme.

2. TOPOLOGICAL TRANSITION IN THE STRUCTURE CONSISTING OF THE UNIAXIAL ELECTRIC SCATTERERS

We consider the structure consisting of the uniaxial electric scatterers located in the sites of a cubic lattice with the period a (Fig. 1(a)). Such scatterers can be realized as short dielectric rods in

(a)   (b)
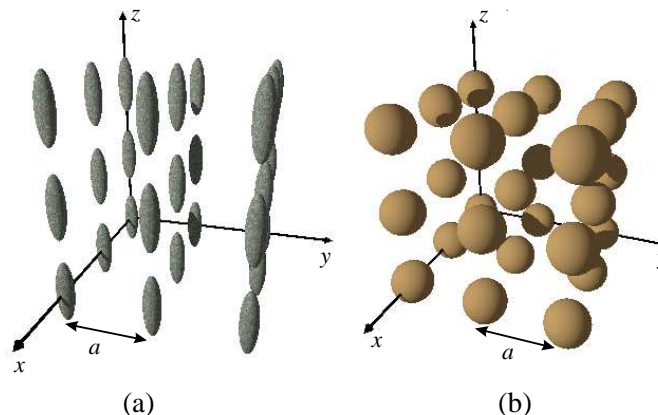
Figure 1: Discrete metamaterials under study. (a) Structure composed of the uniaxial electric scatterers in the sites of a cubic lattice. (b) Structure composed of isotropic particles in the sites of a cubic lattice.

optical metamaterials or short wires with some load, inductive or capacitive, in metamaterials for microwave range. In the further study, we do not concretize the structure of the scatterers, because in this approach their properties are fully described in terms of polarizability tensor $\hat{\alpha} = \alpha_{zz} \vec{e}_z \otimes \vec{e}_z$, where $\vec{e}_z$ is a unit vector directed along the anisotropy axis.

Within the frame of discrete dipole model the effective nonlocal permittivity tensor of the composite is given by

$$\varepsilon_{zz}\left(\omega, \bar{k}\right) = 1 + \frac{4\pi}{a^3}\left[\alpha_{zz}^{-1} - C_{\bar{k}}^{zz}\left(\omega, \bar{k}\right)\right]^{-1}, \tag{1}$$

where $C_{\bar{k}}^{zz}(\omega, \bar{k}) = G_{\bar{k}}^{zz}(\omega, \bar{k}) + 4\pi/a^3(q^2 - k_z^2)/(q^2 - k^2)$, $G_{\bar{k}}^{zz} \equiv \sum\limits_{(m,n,l) \neq (0,0,0)} G^{zz}(\omega; \bar{r}_{mnl})e^{-i\bar{k}\cdot\bar{r}_{mnl}}$, and $G^{zz}(\omega; \bar{r})$ is a matrix element of the dyadic Green's function that determines the electric field created by the point dipole. $\alpha_{zz}^{-1} = \alpha_{0zz}^{-1} - 2i\omega^3/(3c^3)$, the latter imaginary term takes into account the radiation loss contribution, and α_{0zz} is a bare polarizability of the scatterer. In the limit $ka \ll 1$, $wa/c \ll 1$, one can derive Clausius-Mossotti formula that does not contain spatial dispersion corrections:

$$\varepsilon_{zz}^{\text{loc}}(\omega) = \frac{1 + 2\varkappa/3}{1 - \varkappa/3}, \tag{2}$$

where $\varkappa = 4\pi\alpha_{0zz}/(3\,a^3)$. From Eqs. (1), (2), it follows that spatial dispersion corrections to local permittivity Eq. (2) are the most essential when the numerator or the denominator of the fraction Eq. (2) tends to zero. But this situation corresponds to the topological transition in metamaterial when ε_{zz} changes its sign and the topology of isofrequency contours changes from a closed quasi-ellipsoid to an open quasi-hyperboloid, i.e., the dispersion regime changes from elliptic to the hyperbolic one. Using the expression for the effective permittivity Eq. (1) we derive the dispersion equation

$$\alpha_{zz}^{-1}(\omega) - G_{\bar{k}zz}\left(\omega, \bar{k}\right) = 0. \tag{3}$$

Solving Eq. (3) numerically one can plot the system of isofrequency contours for different frequencies. The analysis of isofrequency contours system suggests that the transition from elliptic dispersion regime (that corresponds to the quasi-elliptic closed isofrequency contours) to the hyperbolic one (corresponding to the quasi-hyperbolic opened isofrequency contours) is not instantaneous. Namely, there exists a transition dispersion regime that combines elliptic and hyperbolic isofrequency contours. Further, we refer this regime as mixed dispersion regime. The conditions of observation of the mixed dispersion regime are shown in the "frequency-polarizability" diagram Fig. 2; the typical isofrequency contours are also sketched in Fig. 2. The detailed investigation of the mixed dispersion regime properties is provided in our recent work [7]. It is interesting that the complicated structure of isofrequency contours in the mixed dispersion regime gives rise to the threerefringence of the wave incident from air at the boundary of the discrete structure with a special orientation of the anisotropy axis. Note also, that the discrete dipole model allows one to describe low- and high-ε mixed regime within a single framework (i.e., by the single formula for the effective permittivity) whereas in the perturbative description of spatial dispersion effects one
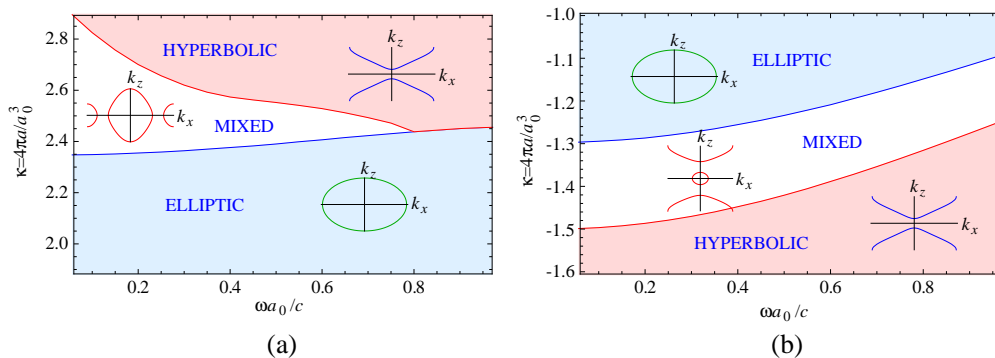
Figure 2: Different dispersion regimes in the discrete dipole structure composed of the uniaxial electric scatterers shown on "frequency-polarizability" diagram. The isofrequency contours typical for the given regime are sketched. (a) The vicinity of high-ε mixed regime. (b) The vicinity of low-ε mixed regime.

deals with the expansions of $\varepsilon_{zz}(\omega, \bar{k})$ or $\varepsilon_{zz}^{-1}(\omega, \bar{k})$ with respect to wave vector in low- and high-ε mixed regimes, respectively.

3. SPATIAL-DISPERSION-INDUCED BIREFRINGENCE IN THE STRUCTURE COMPOSED OF ISOTROPIC PARTICLES

In the similar manner we analyse spatial dispersion effects in the structure consisting of isotropic particles (for example, plasmonic spheres) located in the sites of a cubic lattice with the period a (Fig. 1(b)). Homogenization of the structure within the frame of the discrete dipole model yields [8]:

$$\hat{\varepsilon}\left(\omega, \bar{k}\right) = 1 + \frac{4\pi}{a^3}\left[\hat{I}\alpha^{-1}(\omega) - \hat{C}_{\bar{k}}\left(\omega, \bar{k}\right)\right]^{-1},\qquad(4)$$

where α is a polarizability of isotropic particle. Note, that the tensor $\hat{C}_{\bar{k}}(\omega, \bar{k})$ representing the lattice interaction constant is not proportional to the identity matrix in the general case. Therefore, Eq. (4) suggests that the effective permittivity tensor of the structure consisting of isotropic particles is not proportional to the identity matrix and, consequently, the structure exhibits anisotropy at least in a certain spectral range. The intrinsic reason for this anisotropy is spatial dispersion, because the direction of the wave vector with respect to the lattice axes provides a selected direction in space. One can also envision the frequency range where spatial-dispersion-induced birefringence can be notable. Indeed, as the anisotropy of the structure is determined by anisotropic tensor $\hat{C}_{\bar{k}}$, the anisotropy would be the strongest if the isotropic term $\hat{I}\alpha^{-1}$ vanishes. This situation corresponds to the resonance of the individual particle. The described phenomenon of spatial-dispersion-induced birefringence was discussed in the theoretical works [3, 9] employing the perturbative expansions of the effective permittivity tensor and some symmetry considerations. The effect was also observed experimentally for such natural materials as Cu_2O [10], CaF_2 and BaF_2 [11], but expectedly was sufficiently weak. For that reason, the study of spatial-dispersion-induced birefringence in the field of metamaterials with strong nonlocal response is promising.

To provide a quantitative demonstration of the effect, we plot the dispersion diagram Fig. 3 for metamaterial consisting of spherical isotropic particles with the radius $R = a/2.1$, permittivity of material $\varepsilon_p = 1 - 3\frac{\omega_0^2}{\omega^2}$, where the resonance frequency of a single particle is $\omega_0 a/c = 0.132$. The inverse particle polarizability is set to $\alpha^{-1} = \frac{\varepsilon_p+2}{\varepsilon_p-1}R^3 - \frac{2iq^3}{3}$ with the latter term describing the radiation loss contribution. The dispersion diagram Fig. 3 shows that the degeneracy of the two transverse eigenmodes inherent to anisotropic media is removed for the direction of propagation ΓK. One can also see that the anisotropy of the structure is the most essential in the frequency interval in the vicinity of a single particle resonance as it was discussed above. The phenomenon of spatial-dispersion-induced birefringence in metamaterials can be detected experimentally by measuring the reflection coefficients for two polarizations of the wave incident from air at the boundary of the
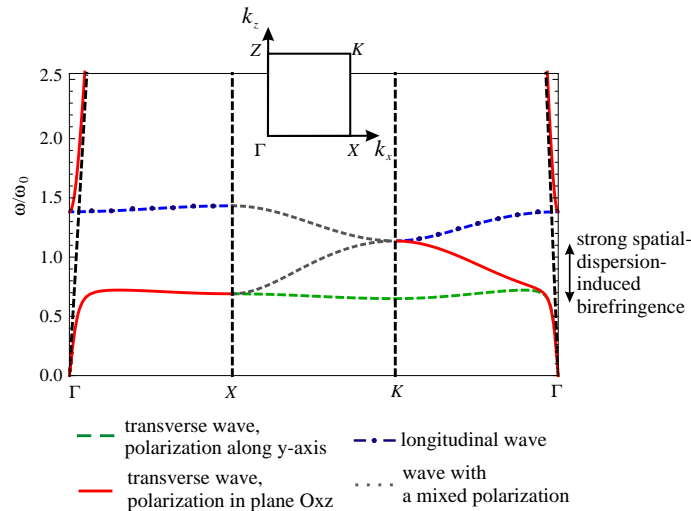
Figure 3: The dispersion diagram for the structure composed of isotropic particles with electric polarizability. Propagation in the plane $k_y = 0$ is studied.

discrete structure with the wave vector aligned along ΓK direction of the cubic crystal. Further details regarding the observation of spatial-dispersion-induced birefringence in metamaterials and the corresponding calculations are expounded in our work [12].

4. CONCLUSION

Metamaterials with the pronounced nonlocal effects constitute an important class of materials. The possibility to tailor their spatially dispersive response provides a novel degree of freedom in material science and challenges metamaterial engineers. In the present work, we apply the discrete dipole model to describe nonlocal effects in discrete three-dimensional metamaterials. We demonstrate the existence of the mixed dispersion regime accompanying topological transition in discrete metamaterials composed of the uniaxial electric scatterers. We also consider the phenomenon of spatial-dispersion-induced birefringence in metamaterials based on three-dimensional cubic arrays of isotropic particles.

REFERENCES

1. Capolino, F., *Theory and Phenomena of Metamaterials*, CRC Press, New York, 2009.
2. Milton, G. W., *The Theory of Composites*, Cambridge University Press, Cambridge, 2002.
3. Agranovich, V. M. and V. L. Ginzburg, *Spatial Dispersion in Crystal Optics and the Theory of Excitons*, Wiley-Interscience, New York, 1966.
4. Landau, L. D. and E. M. Lifshitz, *Electrodynamics of Continuous Media*, Pergamon Press, New York, 1984.
5. Belov, P. A. and R. Marques, "Strong spatial dispersion in wire media in the very large wavelength limit," *Phys. Rev. B*, Vol. 67, 113103, 2003.
6. Belov, P. A. and C. R. Simovski, "Homogenization of electromagnetic crystals formed by uniaxial resonant scatterers," *Phys. Rev. E*, Vol. 72, 036615, 2005.
7. Gorlach, M. A. and P. A. Belov, "Effect of spatial dispersion on the topological transition in metamaterials," *Phys. Rev. B*, Vol. 90, 115136, 2014.
8. Silveirinha, M. G., "Generalized Lorentz-Lorenz formulas for microstructured materials," *Phys. Rev. B*, Vol. 76, 245117, 2007.
9. Ginzburg, V. L., "Ob elektromagnitnyh volnah v izotropnyh sredah pri ychete yavleniya prostranstvennoi dispersii dielectricheskoi pronicaemosti," *Journal of Experimental and Theoretical Physics*, Vol. 34, No. 6, 1593–1604, 1958 (in Russian).
10. Gross, E. F. and A. A. Kaplianskiy, "Opticheskaya anizotropiya cubicheskih cristallov, vyzvannaya yavleniyem prostranstvennoi dispersii," *Reports of the USSR Academy of Sciences*, Vol. 132, No. 1, 98–101, 1960 (in Russian).
11. Burnett, J. N., Z. H. Levine, and E. L. Shirley, "Intrinsic birefringence in calcium fluoride and barium fluoride," *Phys. Rev. B*, Vol. 64, 241102, 2001.
12. Chebykin, A. V., M. A. Gorlach, and P. A. Belov, "Spatial-dispersion-induced birefringence in metamaterials with cubic symmetry," in Preparation.

Pure Electric and Magnetic Hotspots by Dielectric Cylindrical Dimers

Ali Mirzaei and Andrey Miroshnichenko

Nonlinear Physics Centre, Research School of Physics and Engineering
Australian National University, 59 Mills road, Acton, ACT 2601, Australia

Abstract— We analyze the near-field enhancement in dielectric nanowire dimers, using mode expansion analytical method and a genetic algorithm. We study the electric and magnetic hotspots and how they form in both TE and TM polarizations and compare them with plasmonic dimers, considering experimental data to describethe materials. We show that in dielectric dimers, two pure magnetic and electric hotspots can be achievable simultaneously in two sides of the dimer gap and with strength comparable to plasmonic dimers. We show that in plasmonic dimers these pure hotspots are closer and less distinguishable and in the opposite directions compared to dielectric dimers.

1. INTRODUCTION

Various structures have been reported to control the near-field behavior of light [1–3]. Near-field enhancement by localized plasmon polaritons is attracting more attentions to nanoplasmonics [4–8]. However, plasmonic structures suffer from strong dissipative losses in metallic components, even far from plasmonic resonances [9]. Recently, dielectric materials are investigated as competitive alternatives to plasmonic counterpart to reduce the dissipative losses [1]. At the same time, the ability to achieve such level of the near-field enhancement comparable with plasmonic nanostructures, is still a challenge [11–14]. To address this, we analyze and design optimal dimers configurations to achieve the strongest near-field enhancement in the visible regimes by using realistic experimental data of the materials [15, 16]. We demonstrate that by using dielectric materials, it is possible to create both electric and magnetic hotspots comparable with plasmonic structures in TE polarization (magnetic field parallel to the axis of nanowires). We also show the possibility to achieve near-field-enhancement in TM polarization with dielectrics nanowires, which is not possible by using metallic materials. Finally we introduce pure magnetic and electric hotspots both together simultaneously by using dielectric cylindrical dimers. In this work, despite of our previously done study [17], we will concentrate only on near field studies and add more in depth interpretations of hotspots forming.

2. METHODOLOGY
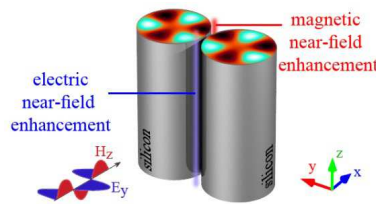
Figure 1: Schematic of a cylindrical dimer, incident planewave and the hotspots.

To simplify our analysis we focus on a symmetric dimer configuration as is shown in Fig. 1 and assume that the nanowires are made of the same material, with same diameter and also placed symmetrically around the origin [18]. Two-dimensional general arrangement of dimer's elements (nanowires) is shown in Fig. 2. The incident planewave is illuminating in the x direction with either TE or TM polarization. In TE polarization, the incident planewave can be written as $H^{inc} = H_0 e^{-i\omega t + i2\frac{\pi}{\lambda} r \cos(\varphi)}$, in which φ is the polar angle in cylindrical coordinate. We use the multipole expansion method to describe the interaction of light with nanowires [19, 20]. The total field of an individual nanowire can then be presented as [21]:

$$H_{total}^l = H_0 e^{-i\omega t} \sum_{n=-\infty}^{+\infty} e^{in(\varphi+\frac{\pi}{2})} \left[\tau_n^l J_n\left(\beta_l r\right) + \rho_n^l H_n^{(1)}(\beta_l r) \right], \tag{1}$$

where $\beta_l = \frac{2\pi}{\lambda}\sqrt{\varepsilon_l(\lambda)}$, H_0 is the incident planewave amplitude, J_n and $H_n^{(1)}$ are the n'th order Bessel and Hankel functions of the first kind, respectively; n is the mode number, l is the number of layer which is 1 for the nanowires material and 2 for the surrounding material which is air, $\varepsilon_l(\lambda)$ is the dielectric constant of the l'th layer at wavelength λ and r is the radius. For TM polarization, an expression similar to Eq. (1) can be written for E_{total}^l. Also the size-dependent effect of plasmonic layers has been taken into account [22, 23].

By solving the boundary condition equations in $r = R$ and for individual wires separately, first we obtain the expansion coefficients, τ_n^l and ρ_n^l [20, 21]. Then we employ multiple scattering problem solution, to consider the interaction between the nanowires [19, 24, 25]. Using the translation additional theorem [26]. In this case, the scattered field from one cylinder becomes an incident wave on another in addition to the incident planewave. This procedure leads the modified expansion coefficients ρ_n^{air} and consequently τ_n^l of each nanowire.

Then, we search for the optimized parameters to maximize the fields amplitude in the middle of the dimer's gap to form enhanced hotspots using a genetic algorithm (GA) [27] we have developed for electromagnetic optimization [28, 29]. We define a fitness function in the middle of the gap as is described in [17].

3. RESULTS AND DISCUSSION

Silicon and silver as two commonly used dielectric and plasmonic materials have been chosen here to provide a competitive analysis of dimer structures. We analyze two different directions of the dimer's axis, parallel and perpendicular to the direction of the incident plane wave propagation. The last row of Table 1 illustrates the optimization results by using the optimized radius, gap size, and the wavelength which are shown in the previous rows for electric and magnetic hotspots in both orientations. The summary of the optimization results and the position of the electric and magnetic hotspots is also demonstrated schematically in Fig. 2. The results reveal that for TE polarization, electric and magnetic hotspots are achievable with almost lossless dielectric dimers, comparable with plasmonic ones. The results also show that for TM polarization, it is possible to obtain strong hotspots by dielectric dimers, which is not possible using plasmonic materials. Our study shows that the hotspots are not exactly in the middle of the gap in perpendicular arrangement. In particular, Fig. 2(a) shows that in dielectric dimers, the location of the magnetic hotspot is shifted toward $+x$ direction, in respect to the middle of the gap (the same as Fig. 2(e)). The electric hotspot in this dimer is shifted in the opposite direction. It is interesting to note, that the shifts of the location of the hotspots in plasmonic dimers are reversed, as can be seen from Fig. 2(c). However, the amount of these shifts in plasmonic dimers are smaller and the two hotspots have overlapped fields in the middle.
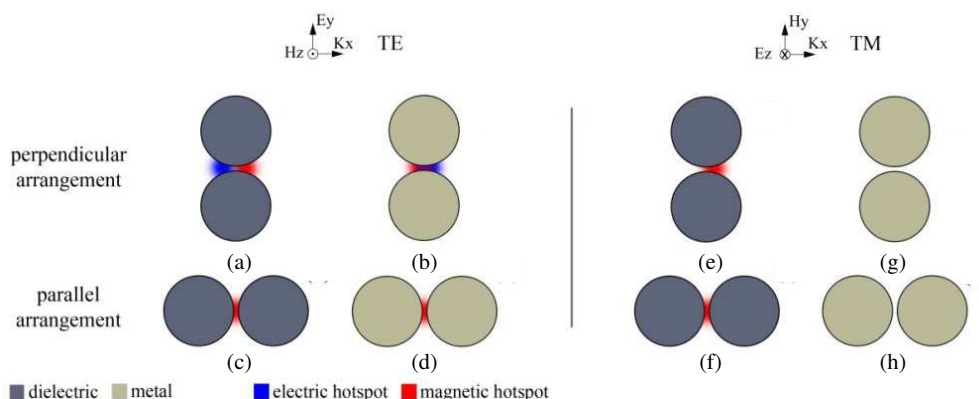
Figure 2: Schematic near-field hotspots excitation in dielectric and metallic dimers. Panel (a) demonstrates that for dielectric nanowires, it is possible to separate magnetic and electric hotspots. The small shift of hotspots' location from the centre of the gap is demonstrated in panels (a), (e). The shift becomes smaller with almost overlapped magnetic and electric hotspots in the plasmonic case, as demonstrated in panel (c). Panels (a), (c), (e) show that the direction of the locational displacements of magnetic and electric hotspots are opposite in dielectric and plasmonic dimers. Note here, that such hotspots do not exist for TM polarization in metallic nanowires.

Table 1: Optimization results for the electric and magnetic hotspots in the middle of the gap in dimers with their axis perpendicular/parallel to the direction of the incident planewave. The optimized field values are normalized to the corresponding H_0 or E_0 values. In all our calculations the first 30 modes have been taken into account.

	perpendicular								parallel							
Mat.	Si				Ag				Si				Ag			
Pol.	TE		TM		TE		TM		TE		TM		TE		TM	
Param.	$\|Hz\|$	$\|Et\|$	$\|Ez\|$	$\|Ht\|$	$\|Hz\|$	$\|Et\|$	$\|Ez\|$	$\|Ht\|$	$\|Hz\|$	$\|Et\|$	$\|Ez\|$	$\|Ht\|$	$\|Hz\|$	$\|Et\|$	$\|Ez\|$	$\|Ht\|$
λ	626	613	579	615	806	432	318	306	634	650	634	554	477	330	324	310
R	121	151	51	89	200	57	10	16	84	133	93	28	55	20	20	20
Gap	3	3	3	3	3	3	20	17	3	3	3	3.1	3	7.8	40	3.1
Optm. value	8.1	17.9	2.2	9.6	9.3	20.4	0.9	1	6.2	2	2.6	8.5	7.7	1.6	0.9	1
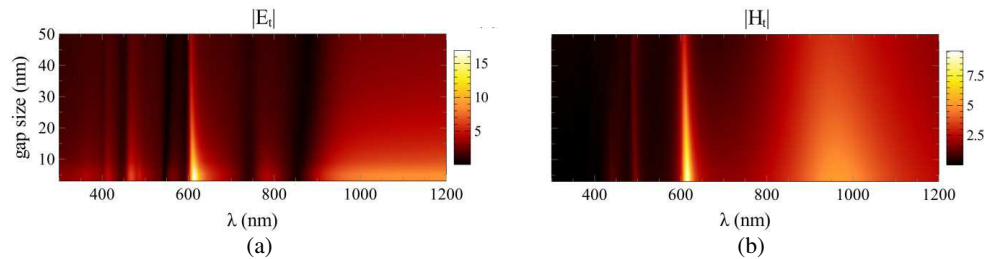
Figure 3: Spectral variation of absolute value of the fields in the middle of the gap by changing the gap size in twodifferentsilicondimersbased on (a) column 2 and (b) column 4 of Table 1.

To have a better understanding of the hotspots behaviour, the dependancy of the hotspots to the gap size has been plotted in a wide spectral range in Fig. 3. Both dimers show considerable field enhancement around 614 nm which stay almost enhanced by increasing the gap size. Here we noe that the dimers can be optimized to creat hotspots at any wavelength but the results in Table 1, demonstrate the best parameters value we could obtain. Dark and bright areas in Fig. 3. Reveal that changing the gap size does not considerably affect the spectral behaviour of the hotspots.

Now we analyse the local shifts of hotspotsin both dielectric and plasmonic dimers, presented in Figs. 2(a), (c), (e). All three figures indicate that the local shift of magnetic and electric hotspots are opposite for dielectric and plasmonic dimers independent of the polarization. Here we plot the field profile of two different dimers with optimized electric and magnetic hotspots with TE and TM polarizations in Fig. 4. The parameters for dielectric and plasmonic dimers can be found in the Table 1 in the second and fourth columns, respectively. In spite of plasmonic dimers, in dielectric structures the magnetic field intends to remain mainly inside the nanowires. Fig. 4 demonstrates that the maximum of the absolute value of the fields is more than the optimized results in the Table 1 which presents values in the middle of the gap. Figs. 4(a) and (b) show the electric and magnetic hotspots for two different silicon dimers, based on the results in columns two and four of Table 1, respectively. Similarly, Figs. 4(d) and (e) show the electric and magnetic hotspots for two different silver dimers, based on the results in columns six and five of the Table, respectively. In Figs. 4(c) and (f) we show the exact location of the hotspots and the field distribution around it, along the line perpendicular to the dimer's axis passing through the centre of the gap. Comparison between Figs. 4(c) and (f) reveals that the amounts of the local shifts of the hotspots from the centre of the gap are much less in plasmonic dimers compare to dielectric ones.

The results shown in Figs. 4(c) and (f) reveal another interesting fact that the electric field becomes near zero in a region close to the electric hotspot, making two maximized and minimized electric field strength points close to each other. This becomes more interesting in the case of dielectric dimers, where this zero electric field point, overlaps the magnetic hotspot. This means that the magnetic hotspot in dielectric cylindrical dimers, is pure magnetic. Fig. 5 compares the electric and magnetic field profiles in the dimer shown in Fig. 4(a) which also demonstrates a similar pure electric hotspot with near zero magnetic field.

To have a dipper insight to the origin of how these hotspots are formed, we present modes decomposition of the dimer and analyse the dominant mode contribution to the formation of the
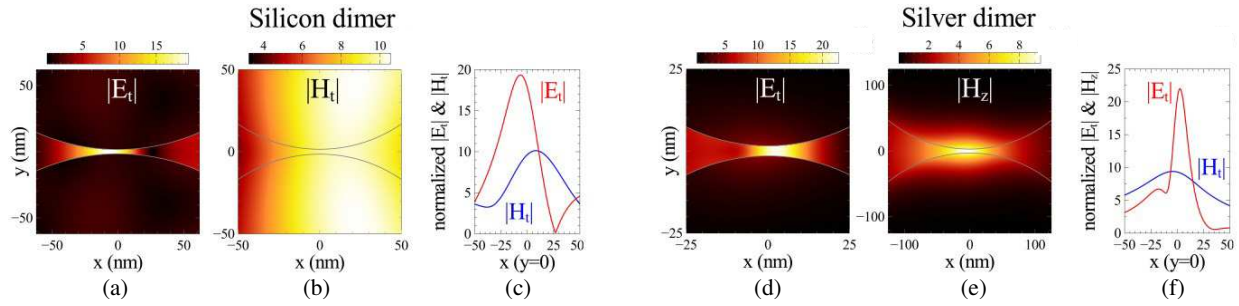
Figure 4: The field profile of two different silicon dimers optimized for their (a) electric and (b) magnetic hotspots, based on the results in the second and fourth columns of Table 1 respectively. Fig. 4(c) shows the fields distribution along the x axis, and the location of the hotspots in the structures of Figs. 4(a) and (b). The incident planewave is illuminating in x direction and the fields value are normalized with respect to the absolute value of the incident fields. Similar results are shown for two different silver dimers in Fig. 4(d) to (f).

corresponding hotspots, which are created by interference of different overlapping harmonics. In Fig. 5 we show the real part of the magnetic field profile of the first four harmonics in the same silicon dimer, with perpendicular propagation. As a result of the symmetrical incidence, the expansion coefficients ρ_n^l of one cylinder are equal to ρ_{-n}^l of the other one, which confirms the theory that the cylinders are practically indistinguishable in broadside illumination. Fig. 5 demonstrates how the superposition of the different modes forms the total field profile with no symmetry with respect to the centre of the gap in x direction, resulting magnetic bright and dark spots shifted from the centre of the gap. In other words, destructive and constructive effects of different harmonics of the scattered and incident fields, make it possible to engineer the magnetic hot and cold spots in two sides of the gap. The map of the electric filed modes' distribution also shows the similar results but in the opposite direction. Consequently, by overlapping the electric and magnetic hotspots on the other field's dark area, both pure magnetic and pure electric hotspots are formed as is demonstrated in Fig. 5. Here we note that the above investigated silicon dimer is optimized for the electric near field enhancement, based on the descriptions in column two of Table 1, which indicates that the behaviour of the resulting magnetic hotspot is not necessarily optimal.
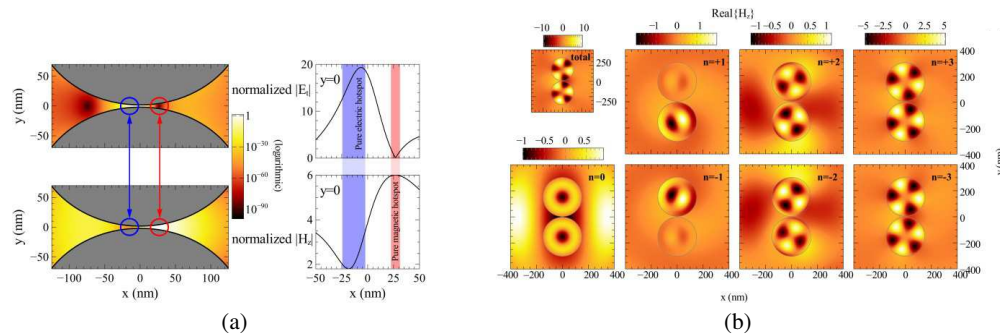
Figure 5: The hotspots in the silicon dimer shown in Fig. 4(a) based on column two of Table 1, with plane wave illuminating from left. (a) Compares the locations of the hotspots and demonstrates their electric and magnetic purity (The fields' amplitude values are normalized to those of the incident wave). (b) The real part of magnetic field profile of the dimer. The field amplitude for modes $n>3$ becomes negligible. The expansion coefficient ρ_n^l of one cylinder is equal to ρ_{-n}^l of the other one. The dimer is optimized for its electric hotspot but the magnetic field is plotted instead of the electric one which is much weaker than magnetic field inside the structure.

4. CONCLUSION

We studied dielectric/plasmonic nanowire dimers, with two parallel/perpendicular dimer configurations with respect to the direction of the incident wave propagation. We analysed both electric/magnetic hotspots and their different harmonics in both TE/TM polarizations. The displacement of the hotspots from the centre of the gap is also analysed in details. We showed that for

electric/magnetic hotspots in dielectric dimers, there is a point on the other side of the gap with zero amplitude of the same field (electric/magnetic), which overlaps the hotspot of the other field (magnetic/electric). This leads to formation of both pure magnetic and electric hotspots in opposite sides of the gap. All the results are achieved analytically by multipole expansion method using the first 30 harmonics. The optimized designs have been also presented for all the cases separately using a genetic algorithm. These results offer new approaches for near-field engineering of variety of applications.

REFERENCES

1. Rahmani, M., E. Yoxall, B. Hopkins, Y. Sonnefraud, Y. Kivshar, M. Hong, C. Phillips, S. A. Maier, and A. E. Miroshnichenko, "Plasmonic nanoclusters with rotational symmetry: Polarization-invariant far-field response vs changing near-field distribution," *ACS Nano*, Vol. 7, No. 12, 11138–11146, 2013.

2. Miroshnichenko, A. and Y. Kivshar, "Fano resonances in all-dielectric oligomers," *Nano Lett.*, Vol. 12, No. 12, 6459–6463, 2012.

3. Filonov, D., A. Slobozhanyuk, A. Krasnok, P. Belov, E. Nenasheva, B. Hopkins, A. Miroshnichenko, and Y. Kivshar, "Near-fieldmapping of Fano resonances in all-dielectricoligomers," *Appl. Phys. Lett.*, Vol. 104, 021104, 2014.

4. Siegfried, T., Y. Ekinci, O. Martin, and H. Sigg, "Gap plasmons and near-field enhancement in closely packed sub-10 nm gap resonators," *Nano Lett.*, Vol. 13, No. 11, 5449–5453, 2013.

5. Dodson, S., M. Haggui, R. Bachelot, J. Plain, S. Li, and Q. Xiong, "Optimizing electromagnetic hotspots in plasmonic bowtie nanoantennae," *J. Phys. Chem. Lett.*, Vol. 4, No. 3, 496–501, 2013.

6. Aouani, H., M. Rahmani, H. Sipova, V. Torres, K. Hegnerova, M. Beruete, J. Homola, M. Hong, M. Navarro-Cía, and S. Maier, "Plasmonic nanoantennas for multispectral surface-enhanced spectroscopies," *J. Phys. Chem. C*, Vol. 117, No. 36, 18620–18626, 2013.

7. Rahmani, M., A. Miroshnichenko, D. Lei, B. Luk'yanchuk, M. Tribelsky, A. Kuznetsov, Y. Kivshar, Y. Francescato, V. Giannini, M. Hong, and S. Maier, "Beyond the hybridization-effects in plasmonic nanoclusters: Diffraction-induced enhanced absorption and scattering," *Small*, Vol. 10, No. 3, 576–583, 2013.

8. Yang, J., M. Rahmani, J. Teng, and M. Hong, "Magnetic-electricinterference in metal-dielectric-metaloligomers: Generation of magneto-electric Fano resonance," *Opt. Mat. Express*, Vol. 2, No. 10, 1407–1415, 2012.

9. Maier, S., *Plasmonics: Fundamentals and Applications*, Springer, 2007.

10. Bakker, R., D. Permyakov, Y. Yu, D. Markovich, R. Dominguez, L. Gonzaga, A. Samusev, Y. Kivshar, B. Luk'yanchuk, and A. Kuznetsov, "Magnetic and electric hotspots with silicon nanodimers," *Nano Lett.*, Vol. 15, No. 3, 2137–2142, 2015.

11. Sigalas, M., D. Fattal, R. Williams, S. Wang, and R. Beausoleil, "Electric field enhancement between two Si microdisks," *Opt. Express*, Vol. 15, No. 22, 14711–14716, 2007.

12. Laroche, M., S. Albaladejo, R. Carminati, and J. Saenz, "Optical resonances in one-dimensional dielectric nanorod arrays: Field-induced fluorescence enhancement," *Opt. Lett.*, Vol. 32, No. 18, 2762–2764, 2007.

13. Albella, P., M. Poyli, M. Schmidt, S. Maier, F. Moreno, J. Saenz, and J. Aizpurua, "Low-loss electric and magnetic field-enhanced spectroscopy with subwavelength silicon dimers," *J. Phys. Chem. C*, Vol. 117, No. 26, 13573–13584, 2013.

14. Boudarham, G., R. Abdeddaim, and N. Bonod, "Enhancing the magnetic field intensity with a dielectric gap antenna," *App. Phys. Lett.*, Vol. 104, 021117, 2014.

15. Palik, E., *Handbook of Optical Constants of Solids*, Academic Press, 1998.

16. Aspnes, D. and A. Studna, "Dielectric functions and opticalparameters of Si, Ge, GaP, GaAs, GaSb, InP, InAs, and InSb from 1.5 to 6.0 eV," *Phys. Rev. B*, Vol. 27, No. 2, 985–1009, 1983.

17. Mirzaei, A. and A. Miroshnichenko, "Electric and magnetichotspots in dielectricnanowiredimers," *Nanoscale*, Vol. 7, 5963–5968, 2015.

18. Tsuei, T. and P. Barber, "Multiple scattering by twoparalleldielectriccylinders," *App. Optics*, Vol. 27, No. 16, 3375–3381, 1988.

19. Balanis, C., *Advanced Engineering Electromagnetics*, Wiley, 1998.

20. Schachter, L., *Beam-Wave Interaction in Periodic and Quasi-Periodic Structures*, Springer, 2011.

21. Mirzaei, A., A. Miroshnichenko, N. Zharova, and I. Shadrivov, "Light scattering by nonlinear cylindrical multilayer structures," *J. Opt. Soc. Am. B*, Vol. 31, No. 7, 1595–1599, 2014.

22. Kreibig, U., "Electronicproperties of smallsilverparticles: The optical constants and their temperature dependence," *J. Phys. F: Metal. Phys.*, Vol. 4, No. 7, 999–1014, 1974.

23. Mirzaei, A., I. Shadrivov, A. Miroshnichenko, and Y. Kivshar, "Cloaking and enhancedscattering of core-shell plasmonic nanowires," *Opt. Express*, Vol. 21, No. 9, 10454–10459, 2013.

24. Olaofe, G., "Scattering by two cylinders," *Radio Sci.*, Vol. 5, No. 11, 1351–1360, 1970.

25. Quinten, M., *Optical Properties of Nanoparticle Systems: Mie and Beyond*, J. Wiley, 2010.

26. Watson, G., *A Treatise on the Theory of Bessel Functions*, University Press, 1966.

27. Mitchell, M., *An Introduction to Genetic Algorithms*, MIT Press, 1966.

28. Mirzaei, A., A. Miroshnichenko, I. Shadrivov, and Y. Kivshar, "Superscattering of light optimized by a geneticalgorithm," *Appl. Phys. Lett.*, Vol. 105, 011109, 2014.

29. Mirzaei, A., A. Miroshnichenko, I. Shadrivov, and Y. Kivshar, "All-dielectric multilayer cylindrical structures for invisibility cloaking," *Sci. Reports*, Vol. 5, 9574, 2015.

30. Zhu, W. and K. Crozier, "Quantum mechanicallimit to plasmonic enhancement as observed by surface-enhanced Raman scattering," *Nat. Comm.*, Vol. 5, 5228, 2014.

Controlled Photonic Surface Modes in 'Cholesteric Liquid Crystal — Phase Plate — Metal' Structure

M. V. Pyatnov[1], S. Ya. Vetrov[1, 2], and I. V. Timofeev[1, 2]

[1]Siberian Federal University, Krasnoyarsk 660074, Russia
[2]Kirensky Institute of Physics, Siberian Branch of the Russian Academy of Sciences
Krasnoyarsk 660036, Russia

Abstract— Light transmission spectrum has been calculated for a 'cholesteric liquid crystal-phase plate-metal' structure. It is shown that the system can have an isolated waveguide surface mode with characteristics efficiently controllable by external fields acting on the cholesteric. This mode is similar to optical Tamm state. We observed anisotropy of transmission of the structure under consideration in the propagation of light of a certain polarization in forward and backward directions. This property is inherent in optically chiral media, such as the cholesteric liquid crystal.

1. INTRODUCTION

Surface electromagnetic waves in photonic crystals have long attracted the attention of researchers [1]. Optical Tamm state (OTS) is especially promising surface phenomenon. This state is electromagnetic analogue of the Tamm electronic state in solid state physics. OTS can be excited between two different photonic crystals having overlapping band gaps [2] or between a photonic crystal and a medium with negative dielectric constant [3, 4]. This state can be observed when incident waves are normal to the PC layers. Experimentally, OTS appears in the form of a narrow resonance in the spectra of reflection and transmission [5].

In recent years the series of devices based on OTS was proposed and carried out: optical switches [6], multichannel filters [7], organic solar cells [8], absorbents [9] and others. Recently the OTS laser structure was proposed and experimentally realized. It consists of quantum wells embedded in a Bragg reflector whose surface is covered with a layer of silver [10].

Most of the proposed devices have the disadvantage that they are not tunable. Correcting of this deficiency is possible using materials with spectral properties controlled by external fields. One such promising photonic material is a cholesteric liquid crystal (CLC). Applying external fields (electric, magnetic, ultraviolet radiation) can change the position of the Bragg reflection band of this material [11, 12]. A characteristic feature of the CLC is the strong dependence of its properties on the polarization of light. In CLC there is a photonic band gap for light propagating along the CLC helix with a circular polarization coinciding with the twist of the CLC helix. Light of opposite circular polarization does not undergo diffractive reflection and passes through the CLC medium almost unaffected., The light wave of such polarization does not change the sign of its polarization when reflected from CLC.

2. RESULTS AND DISCUSSION

In this Paper, we show a possibility to realize optical surface states, similar to optical Tamm states, in a structure with CLC [13] and study their characteristics unique to chiral media. Unlike the case with OTS observed at a PC — metal interface, we could not to obtain a surface state at a CLC — metal interface under normal incidence of light. The one difficulty is to change wave polarization reflected from the metallic surface. The other difficulty is that Bragg reflection exists not for every arbitrary polarization. For light localization between CLC and metal to occur, we need to change the phase of the wave. To this end, between CLC and metal we introduce an anisotropic quarter-wave plate cut parallel to the optical axis and shifting the wave phase by $\pi/2$. Cholesteric molecules at the CLC — phase plate interface align along the optical axis. The proposed structure is shown in Fig. 1. The system consists of a CLC layer of thickness L, phase plate of thickness d and refractive coefficients n'_e, n'_o, such that $2\pi(n'_e - n'_o)d/\lambda = \pi/2$, and metal.

Optical properties and field distribution in the structure were numerically analyzed on the basis of Berreman's 4×4 transfer matrix for normal incidence [14]. Light propagating along z axis with frequency ω is given by

$$\frac{d\Psi}{dz} = \frac{i\omega}{c}\Delta(z)\Psi(z), \tag{1}$$
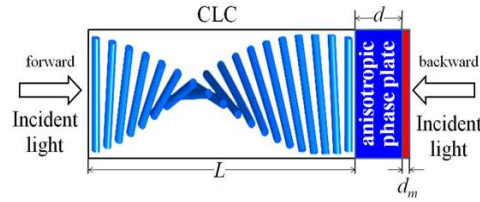
Figure 1: Schematic of the 'CLC – phase plate — metal' structure.
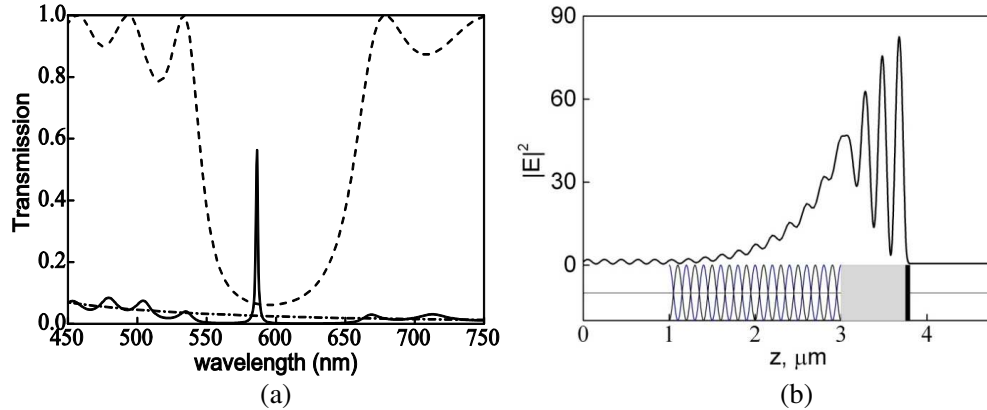
Figure 2: (a) Transmission versus wavelength with light incidence normal to CLC (dashed line), to the silver film (dash-dotted line) and to the 'CLC — phase plate — metal' structure (solid line). (b) Distribution of the squared modulus of the electric field intensity $|E(z)|^2$ in the 'CLC — phase plate — metal' structure for $\lambda = 586.5$ nm. Field is normalized to the input field equal to unity.

where $\Psi(z) = (E_x, H_y, E_y, -H_x)^T$ and $\Delta(z)$ is the Berreman matrix dependent on the dielectric function and incident wave vector.

The parameters used in this study are as follows: ordinary and extraordinary refractive indices of the phase plate and CLC were taken to be $n_o = 1.4$ and $n_e = 1.6$, respectively. The CLC layer helix is right handed and there is a photonic band gap for light with right-hand, diffracting polarization. The pitch is $p = 0.4\,\mu$m, thickness of the CLC layer is $L = 2\,\mu$m, thickness of the phase plate is $d = 0.75\,\mu$m. The phase plate is coupled with a silver film having the thickness $d_m = 50$ nm. The permittivity of silver can be expressed as the Drude model:

$$\varepsilon(\omega) = \varepsilon_0 - \frac{\omega p^2}{\omega(\omega + i\gamma)}, \qquad (2)$$

where $\varepsilon_0 = 5$ is the background dielectric constant, $\hbar\omega_p = 9$ eV is the plasma frequency, and $\hbar\gamma = 0.02$ eV is the plasma collision rate.

Figure 2(a) shows individual transmission spectra of the CLC, silver film and the structure under consideration. The CLC transmission spectrum clearly exhibits a band gap for right-hand circular polarization of light. The figure shows that a peak of the waveguide surface mode in the transmission spectrum (solid line) occurs when an anisotropic quarter-wave plate controlling the phase of light waves is introduced between CLC and metal. Fig. 2(b) shows distribution of the electric field for the wavelength corresponding to maximum transmission in the 'CLC — phase plate — metal' structure shown in Fig. 2(a). Attenuation of the field of the localized mode inside metal is associated with negative permittivity of the metal film whereas inside CLC it is associated with Bragg reflection at the CLC — phase plate interface.

By varying parameters of the system we can control position of the transmission peak via an isolated surface waveguide mode. Strong dependence of the helical pitch, e.g., on temperature, as compared to other structural elements, can be used to effectively control frequency of the transmission peak associated with tunneling of light through the surface state.

Figure 3 shows the reflection spectrum versus the period of the CLC. It can be seen that the peak shift to longer wavelengths is almost directly proportional to the increase of the period.

Now consider the propagation of light through the sample in the backward direction when the

light is incident normally on the metal layer at the right side in Fig. 1. When light propagates in the forward direction transmittance for light diffracting right polarization is equal to 0.57, in the opposite direction the transmittance is equal to 0.34. Thus, we observe the anisotropy of the transmission (Fig. 4). It should be noted that this effect is essentially impossible in scalar structures.

To understand the mechanism of occurrence of this effect, consider the evolution of the polarization of light falling on the CLC and metal. Both cases are shown in Fig. 5.
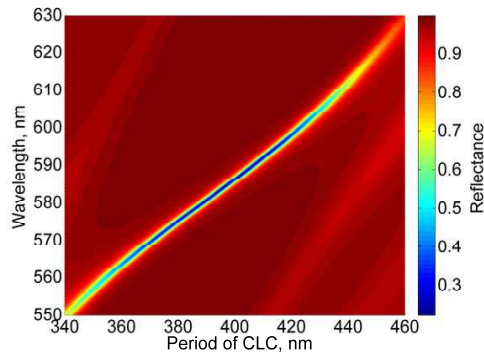
Figure 3: The reflection spectrum of structures for different periods of the cholesteric helix.
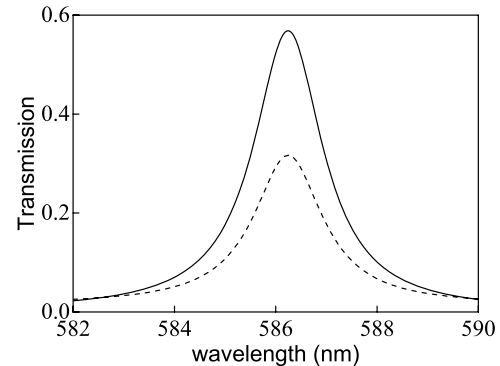
Figure 4: The transmission spectrum of the structure for the right circular polarization: solid line — for light incident on the CLC; dashed line — for light incident on the metal.

(a)   (b)
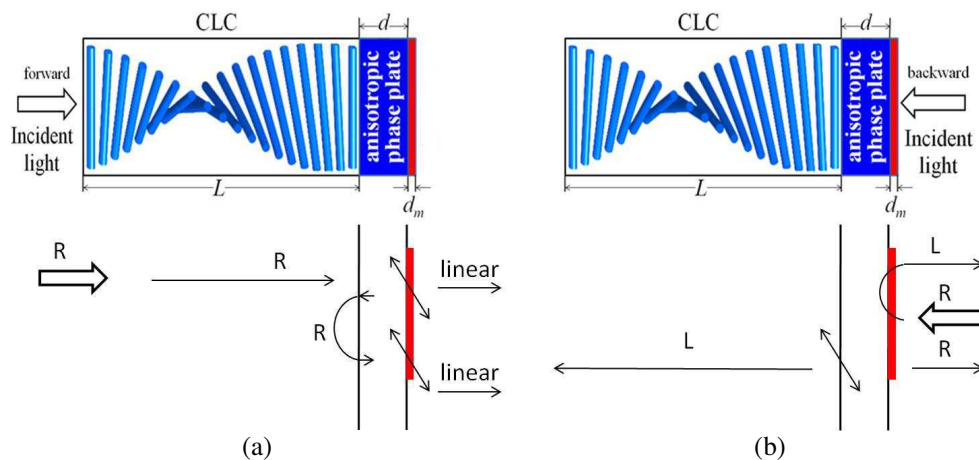
Figure 5: The evolution of polarization for light incident on the (a) CLC and (b) metal, R — right-hand circular polarization, L — left-hand circular polarization, linear — linear polarization.

If at the thin layer of CLC the diffracting right-handed polarized light falls down, it keeps its polarization at the output of the CLC. After passing through the quarter-wave plate, the light becomes linearly polarized. The unabsorbed part of the light comes out of metal layer. Upon reflection from the metal the linear polarization is concerved. After have passed through the plate in the opposite direction, the light gets the right-handed circular polarization. When reflected from CLC the light retains the right-handed circular polarization. Again the light of linear polarization comes out of the metal layer (Fig. 5(a)).

When light is incident on the metal (Fig. 5(b)), the situation is qualitatively different. In this case, the half of the light, unabsorbed and unreflected from the metal layer, is reflected from the cholesteric layer because it is linearly polarized.

For this reason, the structure considered in this paper may be used as a polarizing optical diode. The advantage of this optical diode is its tunability and ease of manufacture, as it consists of just three elements.

3. CONCLUSION

In summary, we have demonstrated existence of surface electromagnetic states localized in the system containing CLC as a structural element. Spectral properties of such a system can be efficiently controlled due to high sensitivity of CLC structural parameters to external factors. Because of changes in polarization of the wave reflected from metal and because of special polarization properties of CLC we have to use a phase plate between CLC and the metal layer. A possibility to control the passband position by varying the thickness of the CLC pitch by external fields has been demonstrated. We also note that the resultant surface mode is essentially an eigenmode of the microcavity where CLC layer and the metal film act as mirrors. Consequently, it is possible to realize lasing in a microcavity using optically active material as a phase plate.

It was established that the transmission spectra of the propagation of light in the forward and backward direction are different. This property is inherent in optically chiral media, which include CLCs. On this basis, we proposed the construction of the polarization of the optical diode based on surface photon modes.

Note also that it is hard to create direct contact between CLC and metal. This requires the use of orientant which is a layer of anisotropic material. Therefore orientant can simultaneously be a quarter phase plate, picking up the thickness correspondent to the localized state.

ACKNOWLEDGMENT

REFERENCES

1. Vinogradov, A. P., A. V. Dorofeenko, A. M. Merzlikin, and A. A. Lisyansky, "Surface states in photonic crystals," *Phys. Usp.*, Vol. 53, 243–256, 2010.
2. Kavokin, A. V., I. A. Shelykh, and G. Malpuech, "Lossless interface modes at the boundary between two periodic dielectric structures," *Phys. Rev. B*, Vol. 72, 233102, 2005.
3. Kaliteevski, M., I. Iorsh, S. Brand, R. A. Abram, J. M. Chamberlain, A. V. Kavokin, and I. A. Shelykh, "Tamm plasmon-polaritons: Possible electromagnetic states at the interface of a metal and a dielectric Bragg mirror," *Phys. Rev. B*, Vol. 76, 165415, 2007.
4. Vetrov, S. Ya., R. G. Bikbaev, and I. V. Timofeev, "Optical Tamm states at the interface between a photonic crystal and a nanocomposite with resonance dispersion," *JETP*, Vol. 117, 988–998, 2013.
5. Sasin, M. E., R. P. Seisyan, M. A. Kalitteevski, S. Brand, R. A. Abram, J. M. Chamberlain, A. Yu. Egorov, A. P. Vasil'ev, V. S. Mikhrin, and A. V. Kavokin, "Tamm plasmon polaritons: Slow and spatially compact light," *Appl. Phys. Lett.*, Vol. 92, 251112, 2008.
6. Zhang, W. L. and S. F. Yu, "Bistable switching using an optical Tamm cavity with a Kerr medium," *Opt. Commun.*, Vol. 283, 2622–2626, 2010.
7. Zhou, H., G. Yang, K. Wang, H. Long, and P. Lu, "Multiple optical Tamm states at a metal-dielectric mirror interface," *Opt. Lett.*, Vol. 35, 4112, 2010.
8. Zhang, X.-L., J.-F. Song, X.-B. Li, J. Feng, and H.-B. Sun, "Optical Tamm states enhanced broad-band absorption of organic solar cells," *Appl. Phys. Lett.*, Vol. 101, 243901, 2012.
9. Gong, Y., X. Liu, H. Lu, L. Wang, and G. Wang, "Perfect absorber supported by optical Tamm states in plasmonic waveguide," *Opt. Exp.*, Vol. 19, 18393, 2011.
10. Symonds, C., G. Lheureux, J. P. Hugonin, J. J. Greffet, J. Laverdant, G. Brucoli, A. Lemaitre, P. Senellart, and J. Bellessa, "Confined Tamm plasmon lasers," *Nano Lett.*, Vol. 13, 3179, 2013.
11. Belyakov, V. A., *Diffraction Optics of Complex Structured Periodic Media*, Springer Verlag, New York, 1992.
12. Hsiao, Y., H. Wang, and W. Lee, "Thermodielectric generation of defect modes in a photonic liquid crystal," *Opt. Express*, Vol. 22, 3593, 2014.
13. Vetrov, S. Ya., M. V. Pyatnov, and I. V. Timofeev, "Surface modes in 'photonic cholesteric liquid crystal — phase plate — metal' structure," *Opt. Lett.*, Vol. 39, 2743, 2014.
14. Berreman, D. W., "Optics in stratified and anisotropic media: 4×4-matrix formulation," *J. Opt. Soc. Am.*, Vol. 62, 502–510, 1972.

An Efficient and Innovative Modelisation for Nanolasers

T. Wang[1, 2], **G. P. Puccioni**[3], **and G. L. Lippi**[1, 2]

[1]Institut Non Linéaire de Nice, Université de Nice-Sophia Antipolis, France
[2]UMR 7335 CNRS, France
[3]Istituto dei Sistemi Complessi, CNR, Italy

Abstract— Nanolaser modelling still presents difficulties stemming from the complexity of the physical problem and lacking a simple and efficient way of predicting the temporal evolution of the laser field. The application of a Stochastic Simulator to the case of a large-β laser shows how this new approach can deliver precious information on the relative fraction of stimulated (and spontaneous) photons in the output, together with the fluctuations intrinsic to the stochasticity of the physical processes (emission by *atoms* and transmission by the cavity). A brief discussion of the open problems in nanolaser modelling and characterization is offered.

1. INTRODUCTION

Progress in laser miniaturisation has been steady and successful since the proposal of the Vertical Cavity Surface Emitting Semiconductor Laser (VCSEL) [1] in 1988. The idea of *turning around* the cavity axis by placing the plane of the active medium (e.g., a quantum well) ortogonally to the direction of propagation of the electromagnetic (e.m.) field and using very high mirror reflectivities has allowed for the realization of the first microcavities. Their length is now limited to half a wavelength (in the material of refractive index n) and their steadily decreasing diameter, to ensure a high-quality transverse mode and very low thresholds of operation (i.e., minimal electric currents), has permitted the reduction of the active volume to a few tens of cubic micrometers.

Modelling efforts, parallel with technological developments, showed that the miniaturisation smoothed out the *kink* normally observed in the laser response (cf. Figure 1), thus leading to difficulties in a clear identification of the transition towards field coherence. In the limit of a cavity consisting of a single e.m. field mode — i.e., one and only mode both for the spontaneous as well as for the stimulated emission ($\beta = 1$, where β represents the fraction of spontaneous emission coupled into the lasing mode) — the kink may entirely disappear, producing what has been called the *thresholdless laser*. In reality, a transition towards field coherence persists, but its identification remains very difficult to achieve [2], even in today's nanolasers [3].
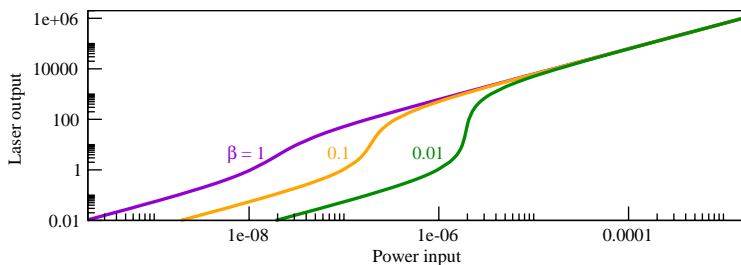
Figure 1: Laser output vs. injected power (arbitrary units) from Eq. (25) in [4] with parameter values: $\gamma = 1 \times 10^{10}\,\text{s}^{-1}$, $\xi = 0.1$, $\tau_{sp} = 1 \times 10^{-9}\,\text{s}$, $\tau_{nr} = 1 \times 10^{-10}\,\text{s}$.

In nanolasers, the problem is further complicated by the extremely low level of optical power which can be recovered from the device and by the technical restriction (still current in most devices) of pulsed operation. Thus, the experimental tools available for testing the degree of coherence of the output field remain quite limited and most investigations offer a characterisation of the laser emission in terms of second (or, at times, higher) order (auto-)correlation functions. Since their interpretation amounts to solving a mathematical inverse problem, good modelling guidance is indispensable. In this paper, we briefly discuss the physical peculiarities of the nanolaser and show how a new modelling approach can contribute to shed new light into the physics of coherence buildup.

2. THE PHYSICAL PECULIARITY OF THE NANOLASER

The principal advantage of the nanolaser is its extremely small cavity size, allowing for: a. integration into nano-optical circuits for on-chip information transmission and processing; and b. extremely low power consumption. Good optical coupling, due to the on-chip integration, reduces spurious losses and improves optical efficiency, while the extremely small cavity volume minimizes the radiative losses through spontaneous emission in the "unwanted" e.m. cavity modes.

However, since the traditional, sharp *threshold* is a direct consequence of the large cavity volume in a standard laser [5, 6], the difficulties arising in the large-β [7] limit are not surprising. In a nanolaser possessing a unique e.m. cavity mode **all** photons end up into this mode, whether they are spontaneous or stimulated, and collectively contribute to the photon output. Thus, experimental measurements must either detect the statistical properties of the different photon (cf. below) or measure directly the phase noise [8]. Models must therefore be able to either account for the phase of the total e.m. field, or describe self-consistently the fraction of spontaneous and stimulated photons and their fluctuations, without ressorting to hypotheses on their statistics (as is done, for instance, when adding Langevin noise to rate equations). This is where the SS provides itself as a very useful tool, since it preserves the simplicity and versatility of population-based models (i.e., rate equations [5]) which can be rigorously proven to be consistent with more sophisticated Maxwell-Bloch techniques [9], while keeping track of all spontaneous photon populations and self-consistently including the stochasticity of the emission and cavity transmission.

One point which remains unclear for the moment is the true nature of the photon statistics in the extended transition (or threshold) *region*. Class A-based [10] photon statistics predicts the existence of a *statistical mixture* of spontaneous and stimulated photons [11], postulated also in a microcavity device [12]. However, cross-correlation measurements performed in a nanolaser prove the existence of strong correlations (i.e., predominantly stimulated photons) but over short times [13] (compatible results are obtained in a microcavity [14]). Since the statistical distributions do not give access to time-resolved information, the modelling requires efficient stochastic predictions on temporal sequences of events to compare to experiments.

3. FLUCTUATIONS, CORRELATIONS AND PHOTON STATISTICS

The coherence of laser output is characterized by a spectrum of fluctuations which crucially differ from that of thermal radiation [15]. Photon statistics, developed in Class A lasers as a tool to answer this question [11], has been very successfully used on a wide gamut of laser devices. However, most lasers currently in use belong to the Class B [10], due to their much higher efficiency in storing energy in the internal (quantum) states with almost negligible losses (which instead dominate in Class A devices).

Semiconductor micro- and nanocavities belong to the Class B: their temporal dynamics is predicted to be more complex [16, 17] and experimental results suggest that their statistical features present a more complex evolution across the threshold region [14]. This may be the basis for the difficulties in interpreting the observed convergence (or lack thereof) in the (auto)correlation functions [18, 19], it could explain the inconsistencies observed in the convergence of higher-order correlations [20], it would match the observation of coherent oscillations [21, 22] and may also be in agreement with the short correlation times observed in cross-correlation analysis [13]. For all these reasons, fast access to predictions relying fluctuation-related information, even in the temporal domain [17], becomes crucial. The advantage of the SS is that using a minimal amount of assumptions (usual in semiclassical modeling of lasers) it is possible to have access to the intrinsic stochastical features of the physics of laser emission.

4. LASER MODELLING WITH THE STOCHASTIC SIMULATOR

The Stochastic Simulator (SS), detailed elsewhere [16], offers predictions based on the estimate of the probability of occurrence of the competing physical processes which take place when *atoms* (where the term here denotes any kind of physical element storing energy in its internal state) relax from an excited state with emission of a photon. Only the discrete physical processes and their probabilities are included, thus excluding all hypotheses necessary for writing differential models. The scheme is illustrated in Figure 2.

The introduction of photon classes (three colors in the figure) is the crucial tool for the success of this modelling approach based on dynamically following the photon evolution from the entirely uncorrelated (spontaneous) to the predominantly correlated (stimulated) regime *across* the thresh-
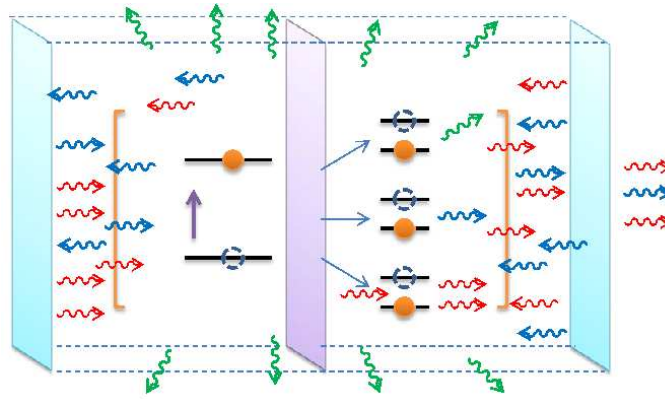
Figure 2: Illustration of the Stochastic Simulator principle. Each *atom* (represented by the two quantum levels) is externally pumped and may decay radiatively in one of the three channels — 1. the *off-axis spontaneous "mode"*, grouping all modes other than the lasing one (green photons); 2. the *on-axis spontaneous mode* (blue photons); 3. the (on-axis) *stimulated mode* (red photons). On-axis photons are recycled by the cavity (light turquoise-green planes) and are transmitted by the coupling mirror (right); the off-axis (green) photons exit the interaction volume laterally. The full pumping process is represented by the upward magenta arrow. The large bracket collects all interactions occurring, e.g., in the grey plane. Absorption and nonradiative relaxations are neglected, their effect being limited to raising the laser threshold.
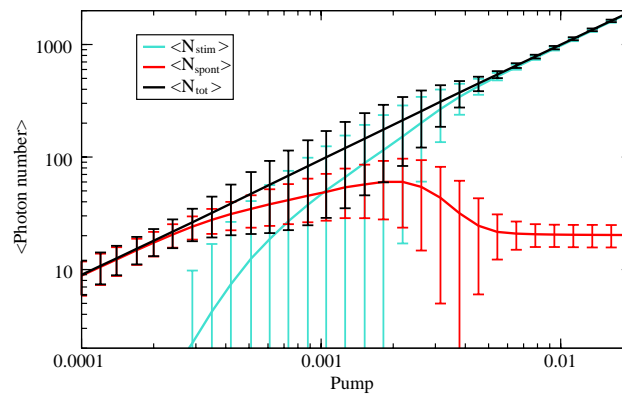
Figure 3: Average photon number as a function of pump for a laser with $\beta = 0.9$. Red line: spontaneous photon fraction emitted on-axis; blue line: stimulated fraction of photons. The black line represents the total number of photons transmitted by the output coupler. The error bars represent the fluctuations and are computed, for the black curve, on the sum of the two photon populations.

old region. This way, it is possible to see how the "phase transition" takes place for different values of β [16], since its value reflects the presence of off-axis spontaneous modes. A clear threshold can be identified in macroscopic (low β) devices [16] and a progressively smoother transition naturally appears as the cavity volume is reduced. Of course, this representation is a semi-classical approximation of the actual quantum-mechanical description and cannot reproduce interference effects and the collapse of the phase of the e.m. field. The strong computational efficiency of the scheme [16], however, offers the possibility of easily repeating the calculations for averaging and for statistical information.

Figure 3 shows the computed average photon numbers, together with their fluctuations (error bars), when varying the pump strength. The blue curve reproduces the growth of the stimulated fraction of photons, whose contribution in the left part of the graph is entirely negligible (notice the logarithmic scale). The spontaneous photons (red) entirely dominate the low pump interval and slow their growth until they drop to a saturated value as the pump grows sufficiently, while the stimulated fraction eventually takes a linear growth. The average total number of photons emitted on-axis — i.e., the combination of spontaneous and stimulated which cannot be discerned when measuring the output power with a detector — show a practically linear response (black curve). The fluctuations of the total output, however, display a marked increase in the central region of

the figure to decrease to a level almost indistiguishable from the line in the upper pumping range. This is the signature of the transition to lasing, and we can reasonable consider that the laser output is coherent starting from pump values approaching 0.01. No clear threshold, however, can be assigned, contrary to the low-β situation [16]. Notice that the asymmetry (top-bottom) in the error bars in the graph is due to the representation in logarithmic scale, rather than to a true asymmetry in the fluctuations.

The information obtained from the SS goes well beyond what rate equations can provide. While on the one hand, the latter can easily predict the shape of the *input-output* curve (average photon number vs. pump — cf., e.g., Figure 1), the rate-equation-approach is entirely incapable of providing any meaningful information about the minimum value of pump above which the laser output can be considered coherent. Indeed, even when introducing noise (e.g., in Langevin form) to the model, the rate equations for a very small system will at best reflect the noise characteristics of the noise scheme which has been chosen, rather than those of the stochastic processes which lead to *atomic* relaxation and then – under suitable conditions — lasing.

The predictions of the SS instead, given their intrinsic stochastic nature, provide meaningful information about the fluctuations around the average and, given the explicit inclusion of the three photon classes, can be used to follow the transition between the spontaneous and the coherent regime (within the approximations of the model). This information can be used to follow the relative fluctuations, compute the Fano factor, etc., thus allowing for a more complete characterization of the predicted laser response. External fluctuations can be added, e.g., to the pump, to further investigate their influence on the device's operation. Here we have exclusively focussed on the internal noise.

5. CONCLUSION

In conclusion, we have given a quick overview of the features of nanolasers which still pose problems and of some of the techniques which have and can be used for their characterization. Since numerous problems remain open in the description of these nanosources and modelling presents difficulties, either related to the inadequacy of simplified approaches, or the complexity of advanced techniques, we have presented the advantages offered by the Stochastic Simulator and shown how its use can efficiently provide useful information about the operation of very small lasers.

REFERENCES

1. Iga, K., F. Koyama, and S. Kinoshita, "Surface emitting semiconductor lasers," *IEEE J. Quantum Electron.*, Vol. 4, No. 9, 1845–1855, 1988.
2. Chow, W. W., F. Jahnke, and C. Gies, "Emission properties of nanolasers during the transition to lasing," *Light: Science & Applications*, Vol. 3, No. 8, e201(1–8), 2014.
3. Strauf, S. and F. Jahnke, "Single quantum dot nanolaser," *Laser Photonics Rev.*, Vol. 5, No. 5, 607–633, 2011.
4. Björk, G. and Y. Yamamoto, "Analysis of semiconductor microcavity lasers using rate equations," *IEEE J. Quantum Electron.*, Vol. 27, No. 11, 2386–2396, 1991.
5. Siegman, A. E., *Lasers*, University Science Books, Mill Valley, CA, 1986.
6. Dohm, V., "Nonequilibrium phase transition in laser-active media," *Solid State Commun.*, Vol. 11, No. 9, 1273–1276, 1972.
7. Björk, G., A. Karlsson, and Y. Yamamoto, "Definition of a laser threshold," *Phys. Rev. A*, Vol. 50, No. 2, 1675–1680, 1994.
8. Piels, M., W. Xue, C. Schäffer, Y. Yu, E. Semenova, L. Ottaviano, K. Yvind, I. Tafur Monroy, J. Mørk, and D. Zibar, "Highly sensitive photonic crystal cavity laser noise measurements using Bayesian filtering," *Optical Fiber Communication Conference*, W2A-28(1–3), Anaheim, CA, USA, Mar. 2015.
9. Narducci, L. M. and N. B. Abraham, *Laser Physics and Laser Instabilities*, World Scientific, Singapore, 1988.
10. Tredicce, J. R., F. T. Arecchi, G. L. Lippi, and G. P. Puccioni, "Instabilities in lasers with an injected signal," *J. Opt. Soc. Am. B*, Vol. 2, No. 1, 173–183, 1985.

11. Arecchi, F. T. and V. Degiorgio, "Statistical properties of laser radiation during a transient buildup," *Phys. Rev. A*, Vol. 3, No. 3, 1108–1124, 1971.
12. Aßmann, M., F. Veit, M. Bayer, C. Gies, F. Jahnke, S. Reitzenstein, S. Höfling, L. Worschech, and A. Forchel, "Ultrafast tracking of second-order photon correlations in the emission of quantum-dot microresonator lasers," *Phys. Rev. B*, Vol. 81, No. 16, 165314(1–5), 2010.
13. Lebreton, A., I. Abram, R. Braive, I. Sagnes, I. Robert-Philip, and A. Beveratos, "Unequivocal differentiation of coherent and chaotic light through interferometric photon correlation measurements," *Phys. Rev. Lett.*, Vol. 110, No. 16, 163603(1–5), 2013.
14. Wang, T., G. P. Puccioni, and G. L. Lippi, in Preparation.
15. Mandel, L. and E. Wolf, *Optical Coherence and Quantum Optics*, Cambridge University Press, Cambridge, 1995.
16. Puccioni, G. P. and G. L. Lippi, "Stochastic simulator for modeling the transition to lasing," *Opt. Express*, Vol. 23, No. 3, 2369–2374, 2015.
17. Wang, T., G. P. Puccioni, and G. L. Lippi, "An efficient and innovative modelisation for nanolasers," *PIERS Proceedings*, Paper 150204094555, Prague, Czech Republic, Jul. 2015, in Preparation.
18. Ulrich, S. M., C. Gies, S. Ates, J. Wiersig, S. Reitzenstein, C. Hofmann, A. Löffler, A. Forchel, F. Jahnke, and P. Michler, "Photon statistics of semiconductor microcavity lasers," *Phys. Rev. Lett.*, Vol. 98, No. 4, 043906(1–4), 2007.
19. Wiersig, J., C. Gies, F. Jahnke, M. Aßmann, T. Berstermann, M. Bayer, C. Kistner, S. Reitzenstein, C. Schneider, S. Höfling, A. Forchel, C. Kruse, J. Kalden, and D. Hommel, "Direct observation of correlations between individual photon emission events of a microcavity laser," *Nature*, Vol. 460, No. 7252, 245–249, 2009.
20. Elvira, D., X. Hachair, V. B. Verma, R. Braive, G. Beaudoin, I. Robert-Philip, I. Sagnes, B. Baek, S. W. Nam, E. A. Dauler, I. Abram, M. J. Stevens, and A. Beveratos, "Higher-order photon correlations in pulsed photonic crystal nanolasers," *Phys. Rev. A*, Vol. 84, No. 6, 061802(R)(1–4), 2011.
21. Lebreton, A., I. Abram, N. Takemura, M. Kuwata-Gonokami, I. Robert-Philip, and A. Beveratos "Stochastically sustained population oscillations in high-β nanolasers," *New J. Phys.*, Vol. 15, No. 3, 033039(1–11), 2013.
22. Takemura, N., J. Omachi, and M. Kuwata-Gonokami, "Fast periodic modulations in the photon correlation of single-mode vertical-cavity surface-emitting lasers," *Phys. Rev. A*, Vol. 85, No. 5, 053811(1–5), 2012.

THz Twist Polarizer Based on Supramolecular Fermat's Spiral Chiral Metamaterial

N. Yogesh, **Quanqiang Yu**, and **Zhengbiao Ouyang**

Solid State Photonics Laboratory, THz Technical Research Center
Shenzhen Key Laboratory of Micro-nano Photonic Information Technology
Key Laboratory of Optoelectronic Device and Systems of Ministry of Education and Guangdong Province
College of Electronic Science and Technology, Shenzhen University, Shenzhen 518060, China

Abstract— A THz twist polarizer formed by supramolecular Fermat's spiral chiral metamaterial (SFSCMM) is reported. Twist polarizers (TPs) are the 90° polarization rotators, in which transverse magnetic linear polarization is converted into transverse electric linear polarization and vice versa. The proposed SFSCMM consists of twisted bilayered supramolecular Fermat's spiral patterns, in which each layer is chiral in nature. The design is implemented in polyimide substrate using silver as a metal. Full-wave simulations demonstrated its function of TP, where the SFSCMM shows the zero-point ellipticity with the polarization rotation angle of 89.49° at 7.765 THz. The proposed SFSCMM has a dimension of $\lambda/1.38 \times \lambda/1.38 \times \lambda/10.3$ at the operating wavelength and can be fabricated through standard layer-by-layer method for the realization of optical logic gates and THz switches.

1. INTRODUCTION

Terahertz (THz) radiation (300 GHz to 20 THz) is an inevitable tool in communication, imaging and industrial sectors due to its unique spatial and temporal characteristics [1]. For example, THz radiation can give higher contrast ratio and greater penetration depth in certain low contrast and optically opaque materials than X rays and infrared waves. At the same time, the vast range of THz spectrum is available for high-speed data transfer in communication sector. In industrial applications, THz radiation can serve as a main component in non-destructive evaluation for quality control and defect inspection. Owing to these potential applications, the development of sources, detectors and other optical components has gained greater attention over these decades. Especially, the manipulation of THz polarization state is vital for all applications. However, the realization of linear and circular polarizers using natural materials is limited for THz radiation, as many of the conventional materials do not exhibit optical activity at THz wavebands.

The advent of chiral metamaterials can overcome this limitation that one can effectively manipulate the THz radiation in the form of various polarization elements. Chiral metamaterials (CMMs) are the artificial sub-wavelength structures that lack mirror symmetry along the direction of propagation of light and they could entail giant optical activity and larger circular dichroism [2, 3]. In literature, giant optical activity of more than $2700°/\lambda$ is demonstrated using various enantiomeric chiral geometries at the microwave length scales based on the strong coupling nature of CMMs [4, 5].

In principle, one can scale any CMM geometry at any of the electromagnetic length scales. Nevertheless, the inherent metallic and dielectric losses impose constraints on the design of THz polarizing elements based on the birefringence response. For example, linear polarization rotators require pure optical activity, in which the ellipticity should be zero at the operating frequency. However, the challenging part is the requirement of zero ellipticity response of the chiral medium. For a dispersive optical medium, the linear birefringent characteristics would result in a non-zero elliptical response. So in birefringent based systems, linear polarization-rotator realization is suffering from low optical isolation values.

However, it is possible to eliminate the linear birefringence response of CMMs and one can enhance the pure optical activity based on the coupling mechanism [5]. Importantly, it is interesting to note that besides the dispersive nature of the CMMs, pure optical activity is possible with the zero-ellipticity response. For example, Kenanakis group investigated pure optical activity of CMMs at THz range with five different bilayered CMMs structures such as Z-type Gammadion structure, U-shaped split ring resonators, rotated-squares and so on [6]. However, the condition for twist polarization (i.e., 90° polarization rotation) is not met in these systems.

Twist polarizers are 90° polarization rotators, in which transverse electric (TE) polarized light is converted into transverse magnetic (TM) polarized light and vice versa. The degree of twist polarization (i.e., the optical isolation between TE and TM waves at the input and output ports)
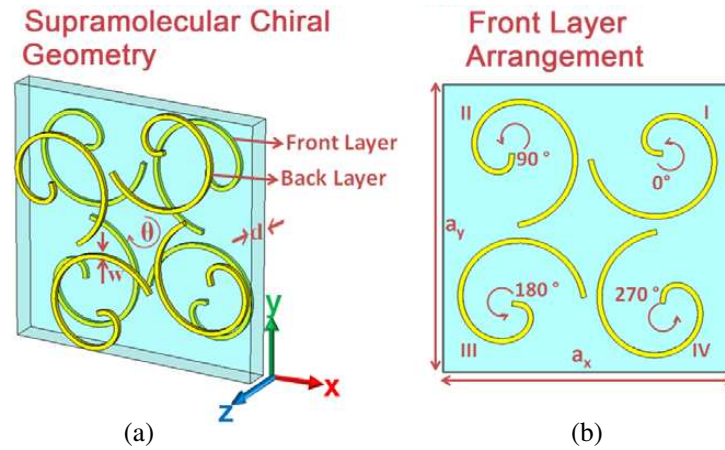
Figure 1: (a) Geometry of the single unit cell of the proposed SFSCMM. (b) Front layer arrangement of the proposed SFSCMM. The positions of the four rings are I $(-s/l, s/l)$, II $(-s/l, -s/l)$, III $(s/l, -s/l)$, IV $(s/l, s/l)$, where s and l are taken as $20\,\mu m$ and $2.75\,\mu m$, respectively. The position parameters are chosen based on the parameter studies for maximum coupling.

represents the quality of the twist polarizer. At THz regime, various wire grid polarizers are currently employed for the realization of linear polarization rotators in the frequency range of $0.1\,THz$ to $3\,THz$ [7]. Suppose, one could design a twist polarizer directly from a chiral metamaterial response with the 100% polarization purity, then ultrafast THz optical switches and polarization logic gates can be developed and such components are highly warranted for integrated photonic devices.

It is observed that several reports have successfully synthesized CMMs for twist polarizer applications at microwave frequencies [4, 8, 9]. Nevertheless, scaling such structures to THz length scale drastically reduces the amplitude of the twist polarized light. In general, the cross polarized light amplitude for any CMMs is low at zero-ellipticity point. Unless the amplitude is high-enough at microwave frequencies, scaling procedure of CMMs may not be meaningful. For example, the C_4 symmetry cut-wire pair structure shows 90% transmission at microwave frequencies [4], whereas the same structure scaled at THz frequencies shows a transmission less than 30% [10]. Similarly, the combination of Gammadion and cut-wire pair structure [9] shows higher transmission at microwave frequencies, but the infrared scaling of Gammadion structure provides transmission only around 30% [11]. Even though, transmission is a constraint in CMM based twist polarizer, the purity of twist polarization is nearly 100%. In line of these aspects, we propose the bilayered supramolecular chiral metamaterial formed by Fermat's spirals and study its twist polarization properties at the far-infrared spectrum.

2. DESIGN AND OPTICAL ACTIVITY OF THE PROPOSED CHIRAL METAMATERIAL

Figure 1 shows the geometry of proposed supramolecular Fermat's spiral chiral metamaterial (SF-SCMM). The proposed SFSCMM structure consists of twisted bilayered supramolecular patterns. Supramolecular patterns are themselves chiral in nature [12]. For example, the front layer geometry indicated in Fig. 1(b) shows four segments of Fermat's spirals, where each segment is rotated in such a way that adjacent rings maintain an angular difference of $90°$. This operation enhances the additional coupling between the adjacent neighbors and the layer lacks both x- and y-in-plane mirror symmetries. The Fermat's spiral present in the design has a functional dependence of $r = A\sqrt{\theta}$, where A is the spiraling constant taken to be $2.8\,\mu m/\sqrt{rad}$. Each Spiral is traced out of a metal with the thickness and width of $0.5\,\mu m$, respectively. The metal is modeled as Silver with the conductivity of $\sigma = 6.3012 \times 10^7\,S/m$. The back metal layer of the proposed SFSCMM is a mirror structure of the front layer. Moreover, the back layer is rotated by $22.5°$ for enhanced coupling. The front and back layers are separated by a dielectric spacer of thickness $d = 2.75\,\mu m$. The dielectric is modeled as polyimide substrate with the dielectric permittivity $\varepsilon_r = 2.9$ and $\tan\delta = 0.03$. The lattice constants of the proposed SFSCMM are taken as $a_x = a_y = 28\,\mu m$. Total thickness of the free standing SFSCMM unit cell is $3.75\,\mu m$.
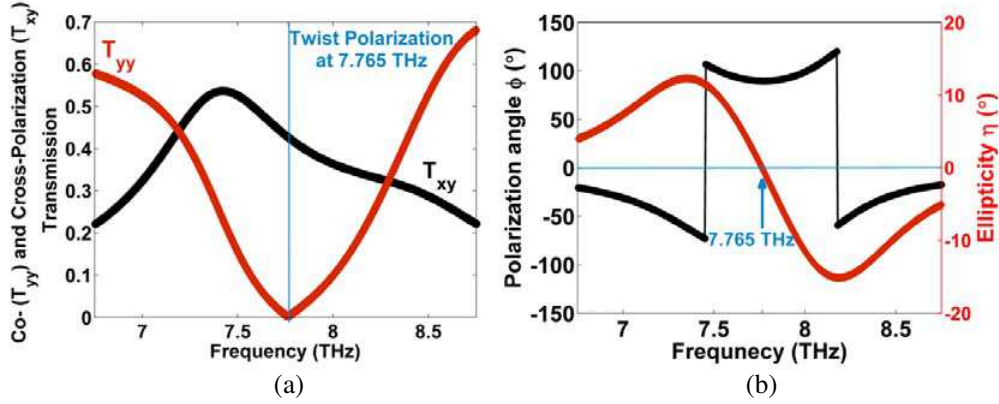
Figure 2: (a) Co- and cross-polarization transmission spectra of SFSCMM. (b) Polarization angle (φ) and ellipticity (η) responses of the proposed SFSCMM.

The optical activity of the proposed SFSCMM is studied through full-wave electromagnetic simulations using commercial solver CST Microwave Studio with frequency domain calculations. Unit cell boundaries are applied along the x- and y-directions of the proposed SFSCMM and Floquet ports are applied along the propagation direction. The co- ($T_{yy} = E_y^t/E_y^i$) and cross-polarization ($T_{xy} = E_x^t/E_y^i$) transmissions are computed by exciting the first two cut-off modes of the Floquet port, which are TE and TM polarizations respectively. Here E_x^t and E_y^t are the x and y components of the transmitted electric field respectively and E_y^i is the input electric field of the y-polarized incident wave. The polarization rotation angle (ϕ) and ellipticity (η) of the transmitted wave are computed as follows;

$$\phi = \frac{1}{2}\left[\arg\left(T_{++}\right) - \arg\left(T_{--}\right)\right],$$
$$\eta = \frac{1}{2}\tan^{-1}\left(\frac{|T_{++}|^2 - |T_{--}|^2}{|T_{++}|^2 + |T_{--}|^2}\right), \tag{1}$$

where $T_{++} = T_{yy} + iT_{xy}$ and $T_{--} = T_{yy} - iT_{xy}$ are the transmission coefficients of RCP and LCP waves, respectively.

From Fig. 2(a), we can observe that at 7.765 THz, the computed co- and cross polarized transmissions are $T_{yy} = 0.003$ and $T_{xy} = 0.427$, respectively. This corresponds to the cross over point on the ellipticity spectrum given in Fig. 2(b), where the computed polarization rotation angle is 89.49° at 7.765 THz. The optical isolation between the co- and cross-polarized transmissions is found around 43 dB at 7.765 THz. This represents a high degree of spectral purity around 99% at 7.765 THz, which is the desired criterion for the realization of ultrafast THz optical switches despite its higher transmission loss. The overall dimension of the proposed SFSCMM is $\lambda/1.38 \times \lambda/1.38 \times \lambda/10.3$ at the operating wavelength.

3. MECHANISM OF TWIST POLARIZATION

To probe the mechanism behind the twist polarization function of the proposed SFSCMM, surface current distribution is plotted at 7.765 THz in Fig. 3. The dashed and solid arrows represent surface current directions at the front and back layers of the SFSCMM, respectively. It is clear that at twist polarization frequency, both layers are oscillating anti-symmetrically. It is also observed that smaller arrows indicate the presence of symmetric current distribution at some parts of the structure. However, the anti-symmetric current distribution is dominant in the structure (For example, one can refer segments I to IV in Fig. 3). The surface current in each ring induces a magnetic dipole for the E-polarized incident wave and such dipoles present in the adjacent neighbors are interacting transversely [13]. Moreover, the magnetic dipole distribution at the front and back layers are interacting longitudinally. Similarly, one can analyze various interactions of electric dipoles but it is noticed that their contribution is weaker compared to the magnetic dipole interaction as the 90° rotational arrangement of the segments cancelled out mostly the electric dipole contribution since their inner product is zero [13]. Hence for a given anti-symmetric current
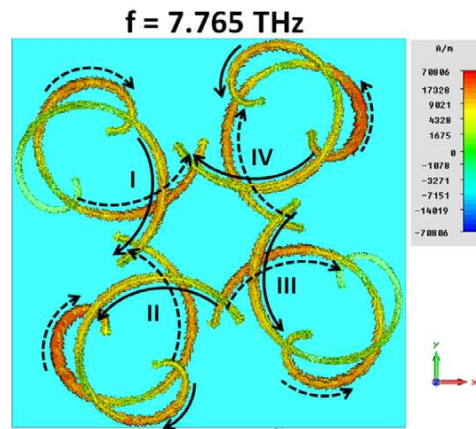
Figure 3: The surface current distribution of the proposed SFSCMM at 7.765 THz. The oscillating currents in this figure correspond to a phase of 90°. The solid and dashed arrows represent the current directions at the front and back layers, respectively.
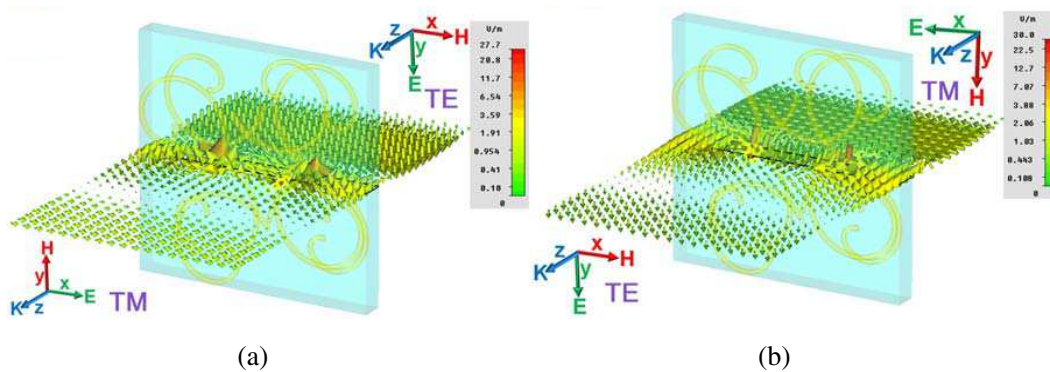
Figure 4: (a), (b) show TE to TM and TM to TE conversion functionalities of the proposed SFSCMM at 7.64 THz, respectively. In both cases, the arrow plots show a 90° rotation of the electric fields.

distribution, the induced magnetic dipoles aligned along the direction of the applied electric field of the input wave will couple strongly and will result in a twist polarized field at the output port.

4. TE TO TM CONVERSION: PLANE WAVE EXCITATION RESULTS

To visualize the twist polarization functionality of the proposed SFSCMM, additional simulations are carried out. Plane waves with TE and TM polarizations are excited and their field distributions are solved through transient electromagnetic computations. Figs. 4(a) and 4(b) present the electric field map at 7.64 THz, in which the proposed FSCMM structure clearly demonstrates TE to TM (Fig. 4(a)) and TM to TE (Fig. 4(b)) conversion function. Since the field computations are done with transient solver using different mesh settings, the twist polarization frequency is slightly shifted with respect to that in frequency domain calculations.

5. PERSPECTIVES AND CONCLUSIONS

There are three directions, in which the current research needs to be further carried out: 1) On the requirement of zero ellipticity response, the proposed SFSCMM is an ample candidate for the realization of twist polarizer. However, the intensity aspect of the proposed SFSCMM needs to be further improved. At the same time, this is a universal problem, where all CMMs at zero-point ellipticity witness lower amplitude. To overcome this problem, one may counter to balance the impedance mismatch by electromagnetic tunneling (EMT) concept [8, 14]. For example, EMT is reported at microwave frequencies but its extension to higher frequencies must balance all loss factors [15]. Some group also suggests the use of gain media to enhance the intensity of cross polarizers [16]. 2) Twist polarizers in the form of metasurfaces are well known in reflective configurations [15]. The transmission type exhibits high loss but metasurface approach may be useful for bandwidth enhancement. 3) Combining the first two perspectives, unit transmittance accom-

panied with the zero-ellipticity is an ideal target for the THz twist polarizers. This can be fulfilled by introducing newer analytical approaches and optimization methods. For example, the current analytical approach in the literature [17] based on the coupling picture gives excellent physical intuition but still it needs numerical simulations and rigorous optimizations. Conclusively, our present investigations on the THz twist polarizer formed by the supramolecular Fermat's spiral chiral metamaterial will find applications in the development of ultrafast THz switches, polarization logics and spectroscopic elements with the aforementioned perspectives.

ACKNOWLEDGMENT

REFERENCES

1. Tonouchi, M., "Cutting-edge terahertz technology," *Nat. Photon.*, Vol. 1, No. 2, 97–105, 2007.
2. Svirko, Y., N. Zheludev, and M. Osipov, "Layered chiral metallic microstructures with inductive coupling," *Appl. Phys. Lett.*, Vol. 78, No. 4, 498–500, 2001.
3. Papakostas, A., A. Potts, D. M. Bagnall, S. L. Prosvirnin, H. J. Coles, and N. I. Zheludev, "Optical manifestations of planar chirality," *Phys. Rev. Lett.*, Vol. 90, No. 10, 107404, 2003.
4. Ye, Y. amd S. He, "90° polarization rotator using a bilayered chiral metamaterial with giant optical activity," *Appl. Phys. Lett.*, Vol. 96, 203501, 2010.
5. Decker, M., R. Zhao, C. M. Soukoulis, S. Linden, and M. Wegener, "Twisted split-ring-resonator photonic metamaterial with huge optical activity," *Opt. Lett.*, Vol. 35, 1593–1595, 2010.
6. Kenanakis, G., R. Zhao, A. Stavrinidis, G. Konstantinidis, N. Katsarakis, M. Kafesaki, C. M. Soukoulis, and E. N. Economou, "Flexible chiral metamaterials in the terahertz regime: A comparative study of various designs," *Opt. Mat. Exp.*, Vol. 2, No. 12, 1702–1712, 2012.
7. Yan, F., C. Yu, H. Park, E. P. J. Parrott, and E. P. MacPherson, "Advances in polarizer technology for terahertz frequency applications," *J. Infrared Milli. Terahz Waves*, Vol. 34, No. 9, 489–499, 2013.
8. Mutlu, M. and E. Ozbay, "A transparent 90° polarization rotator by combining chirality and electromagnetic wave tunneling," *Appl. Phys. Lett.*, Vol. 100, 051909, 2012.
9. Song, K., Y. Liu, Q. Fu, X. Zhao, C. Luo, and W. Zhu, "90° polarization rotator with rotation angle independent of substrate permittivity and incident angles using a composite chiral metamaterial," *Opt. Exp.*, Vol. 21, 7439–7446, 2013.
10. Xi, C., "Terahertz angle-insensitive 90° polarization rotator using chiral metamaterial," *Physica B*, Vol. 422, 83–86, 2013.
11. Kwon, D.-H., P. L. Werner, and D. H. Werner, "Optical planar chiral metamaterial designs for strong circular dichroism and polarization rotation," *Opt. Exp.*, Vol. 16, 11802–11807, 2008.
12. Valev, V. K., J. J. Baumberg, C. Sibilia, and T. Verbiest, "Chirality and chiroptical effects in plasmonic nanostructures: Fundamentals, recent progress, and outlook," *Adv. Mater.*, Vol. 25, 2517–2534, 2013.
13. Liu, N. and H. Giessen, "Coupling effects in optical metamaterials," *Angew. Chem. Int. Ed.*, Vol. 49, 9838–9852, 2010.
14. Zhou, L., W. Wen, C. T. Chan, and P. Sheng, "Electromagnetic-wave tunneling through negative permittivity media with high magnetic fields," *Phys. Rev. Lett.*, Vol. 94, 243905, 2005.
15. Grady, N. K., J. E. Heyes, D. R. Chowdhury, Y. Zeng, M. T. Reiten, A. K. Azad, A. J. Taylor, D. A. R. Dalvit, and H.-T. Chen, "Terahertz metamaterial for linear polarization conversion and anomalous refraction," *Science*, Vol. 340, 1304–1307, 2013.
16. Zhu, W., I. D. Rukhlenko, F. Xiao, and M. Premaratne, "Polarization conversion in U-shaped chiral metamaterial with four-fold symmetry breaking," *J. Appl. Phys.*, Vol. 115, 143101, 2014.
17. Niemi, T., A. O. Karilainen, and S. A. Tretyakov, "Synthesis of polarization transformers," *IEEE Trans. Anten. Propag.*, Vol. 61, 3102–3111, 2013.

The Lidar Sounding of the Atmosphere in St. Petersburg

Dmitry Samulenkov[1], **Maxim Sapunov**[1], **Irina Melnikova**[1],
Vladislav Donchenko[1], **and Anatoly Kuznetsov**[2]

[1]Resource Center "Observatory for Ecological safety", Reasearch Park
St. Petersburg State University, Universitetskaya nab., 7/9, St. Petersburg 199034, Russia
[2]Russian State Hydrometeorological University, Malookhtinsky, 98, St. Petersburg 196195, Russia

Abstract— Measurements of the vertical profile of aerosols parameters, wind velocity and direction in the Observatory of ecological safety, Research Park, St. Petersburg University in the center of St. Petersburg was held from the beginning of 2014, the height of laser sounding of wind characteristics of up to 12 km and of aerosols properties is up to 25 km. The results of vertical profiling aerosol particles and wind parameters above the central part of St. Petersburg in day and night obtained from observations 5 March 2015 time are presented. Results include profiling the extinction and backscattering coefficients, particle size distribution, depolarization rate, particle concentration and real and imagine parts of refractive index. The wind characteristics are presented in the nearest time and the same date. It is shown that the meteorological parameters of the atmosphere and time of day affect the dynamics of changes "pollution cap" over the city.

1. INTRODUCTION

The Observatory of ecological safety in ranges of the Resource Centre (RC) of the St. Petersburg state University (SPbSU) is located in the center of St. Petersburg on Vasilievsky Island, 10th Line, 33/35 at the height 35 m, geographical coordinates Lat 59.943N, Lon 30.273E. The main objectives of the Observatory of environmental safety of RC St. Petersburg state University are [1]:

1. Formation of models of the influence on the environment of potentially hazardous industries and large-scale construction works.
2. Estimation of transboundary pollutant transport in the atmosphere.
3. The creating forecast models of the development of the unfavorable situation in the Environment and methods for the assessment of possible economic damage.
4. Preparation of the situational synthesized maps of suspected areas and sites of occurrence of environmental safety threats with the assessment of the state of environmental safety of the areas and sites of high ecological risk.

The SPbSU lidar RC is included in the frames of the European lidar network station (EARLINET) that enables the use of data of lidar monitoring stations for modelling transboundary pollutant transport over Europe. Stationary multi-wave lidar complexes provides information on the concentration and the physical nature of atmospheric aerosol at a distance of 20 km in the vertical direction and the wind and turbulence at a distance 10 km. Lidar complex includes components and state of the art technology, both Russian and foreign manufacturers and allows remote sensing in a wide spectral wavelength range. Klett and Raman methods are used for retrieving aerosol optical parameters [2].

Values of polluting components concentrations in the atmosphere obtained with the laser complex in the Observatory of environmental safety allow directly, comparing the obtained results with the threshold values of concentrations, determine the occurrence of dangerous situations for ecosystems and population (Melnikova et al., 2010). Lidar sounding is successful only in the clear sky. Heavy clouds are not suitable for the lidar remote sensing because of prevalent multiple scattering and very low values of the backscattering part of cloud phase function.

2. OBSERVATIONAL AND INVERSION RESULTS

Here we demonstrate results of observation accomplished in St. Petersburg center 5 March 2015.

Figure 1 shows an example of a vertical profile of the volume extinction coefficient $\alpha(z)$ in the coordinates height (m) — time (hour) obtained from observation to the zenith direction in the channel 355 nm, accomplished 05 March 2015 during 12 hours. The figures clearly traced a "pollution cap" above the city up to the height of 1.8 km. One can see that extinction coefficient reach maximal values from 15:30 till 17:30, and remains high values till 20 hours. After 22 hours extinction coefficient is 4 times less than in day time and significantly dissipates and elevates.
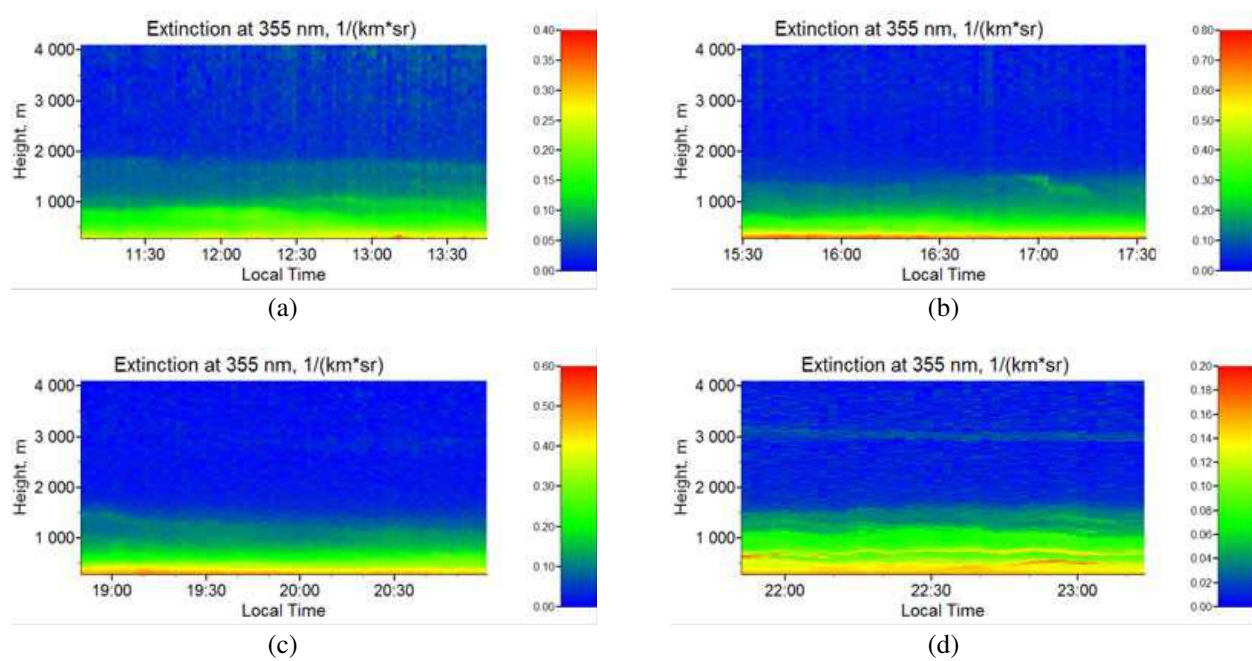
Figure 1: Dynamics of the aerosol extinction vertical profile variations during 12 hours from observations 5 March 2015 in 532 nm channel.
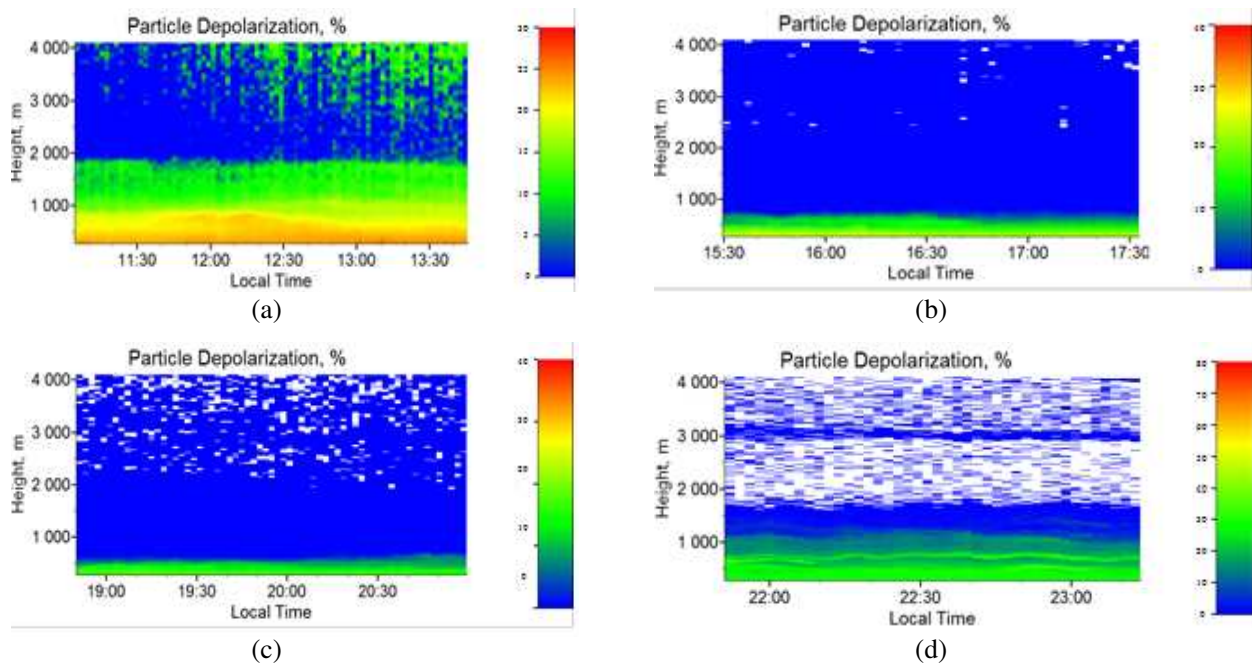
Figure 2: Dynamics of the linear depolarization vertical profile variations during 12 hours from observations 5 March 2015 in 532 nm channel.

Another characteristic of aerosol particles is their form. Usually one differs particles of spherical (or close to spherical) and not spherical (crystals, chains and other). The shape of the particles is determined by their origin and may indicate the source of aerosols.

Figures 2(a) and 2(b) show the linear depolarization factor of atmospheric aerosols. One can see that in the near surface layer < 1 km the "pollution cap" where dust particles with a shape close to spherical (but not absolutely spherical) are dominated in the night time (after 19:00 h). It might be soot. Linear depolarization of the backscatter light points to dust (kind of crystal particle) in the first half of day time till 13 hours. It is seen noisy errors in heights upper 2 km.

In the Fig. 3 the particle size distributions is presented at two heights: 315 and 1140 m. It is demonstrated for four mentioned time periods: 1 — 11:00–14:00, 2 — 15:30–17:30, 3 — 18:45–21:00 and 4 — 21:45–23:30 hours of the local time that pointed in the figure.

(a)

(b)
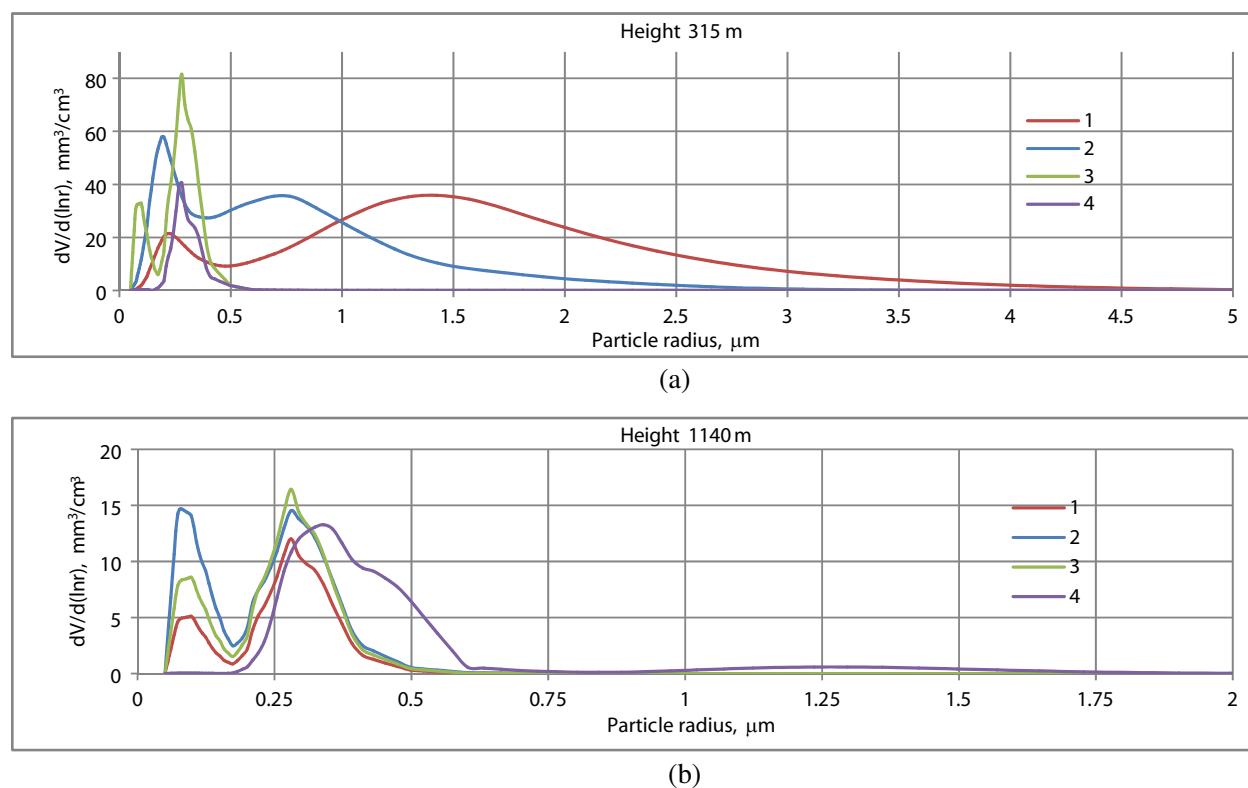
Figure 3: Particle size distribution at two heights (a) 315 and (b) 1140 m in four time intervals: 1 — 11:00–14:00, 2 — 15:30–17:30, 3 — 18:45–21:00 and 4 — 21:45–23:30 of local times.

(a)

(b)
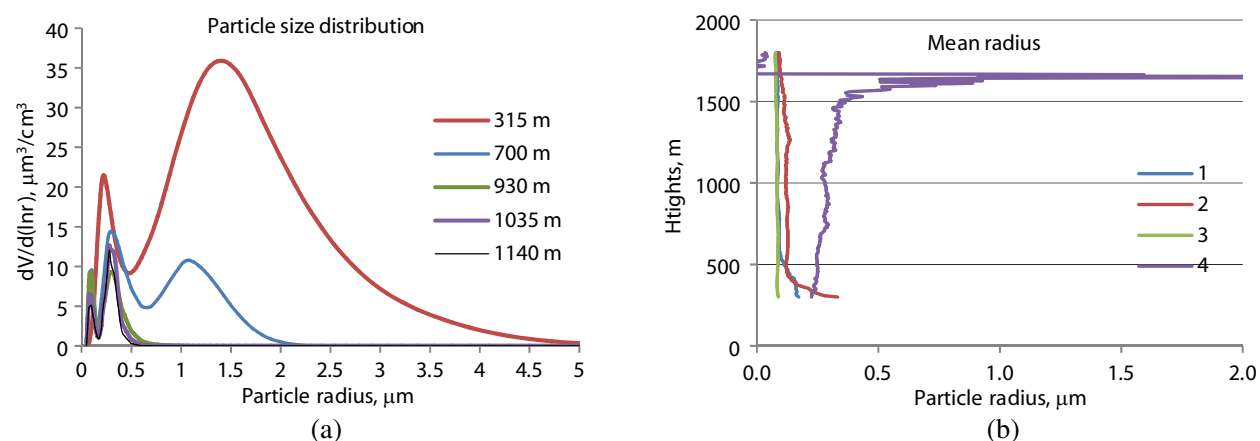
Figure 4: (a) Particle size distribution at 5 altitudes pointed in legend averaged over the time period 2; (b) altitudinal dependence of the mean radius in four time periods pointed in legend.

It is seen that larger particle (more 0.75 μm) are only in lower heights and in the period from 11:00 till 17:30 h. In the night time (purple line) the part of larger particle is increased at higher level (a) that differs from the lower level (b).

The transformation of particle size distribution with altitude in the time period 2 (15:30–17:30 h) is shown in the Fig. 4(a). It is clear a coarse mode of particles at 315 and 700 m levels with radius larger 1–2 μm. One can see the stable during pointed four time period distribution of particles with the mean radius less than 0.5 mm at upper levels higher 900 m. The Fig. 4(b) demonstrates the particle mean radius in the atmosphere from 300 till 1600 m — in the pollution cap. It is seen the increasing of larger particles in the night time (purple line). It might be a growth of small soot particles in the atmosphere with increased moisture [4].

The Fig. 5(a) shows vertical profiles of the volume particle concentrations in considered time periods. One can see how decreasing particle numbers in the pollution cap (layer till 1000 m) during the day. Real part of the refraction index varies in the lowers and highest of the considered levels and remain constant in the middle heights (800–1400 m). In the morning time it points to the
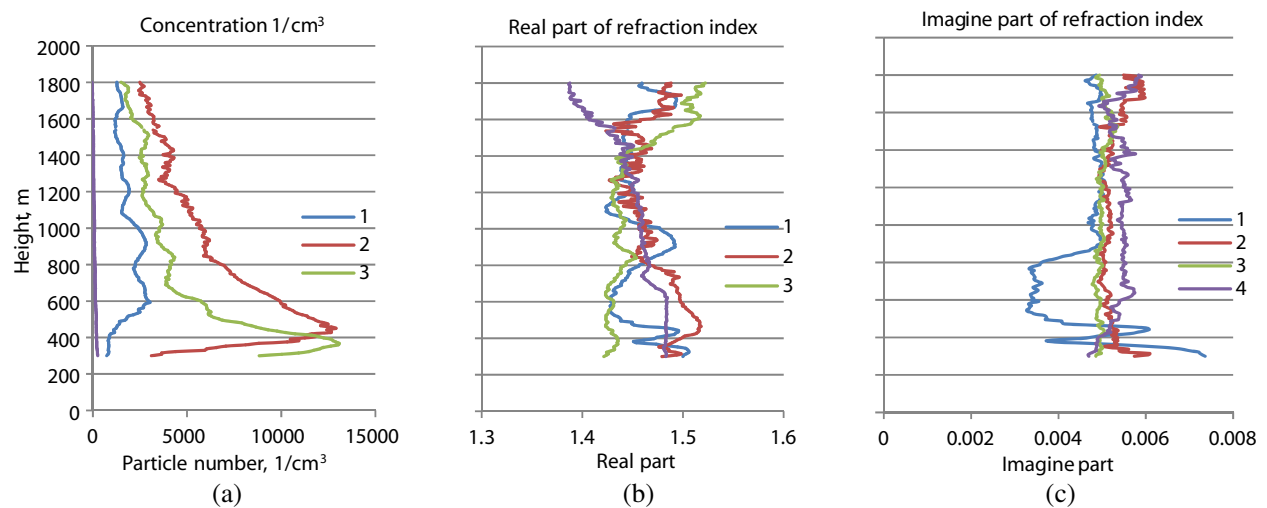
Figure 5: Vertical profiles of: (a) aerosol particles concentration; (b) real and (c) imagine parts of the refractive index for four time periods.
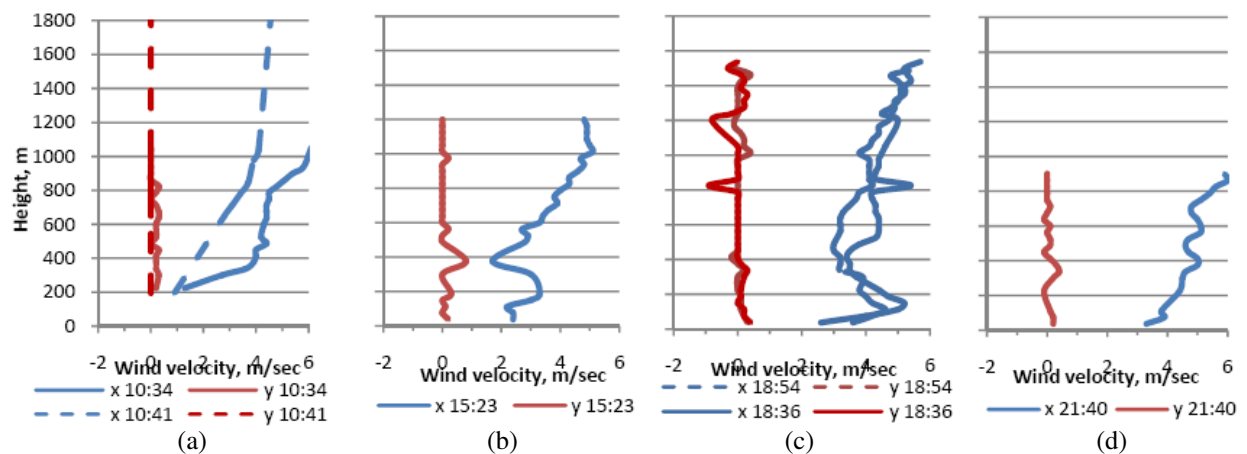
Figure 6: Vertical profiles of wind horizontal (blue lines) and vertical (red lines) in different time moments pointed in legend.
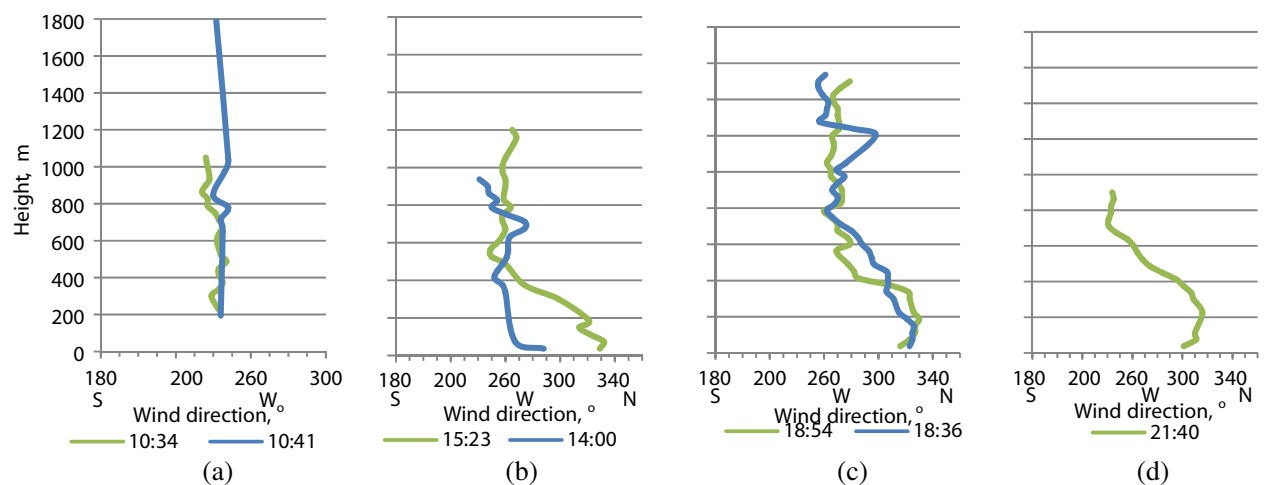
Figure 7: Vertical profile of the wind direction. Local time of observations pointed in the legend.

aerosols stratification. The layer 600–800 m is expressed in these three parameters.

The horizontal and vertical wind components are in the Fig. 6. Wind observations were made between aerosols observations. Time is pointed in the figure. The wind profiles characterize a
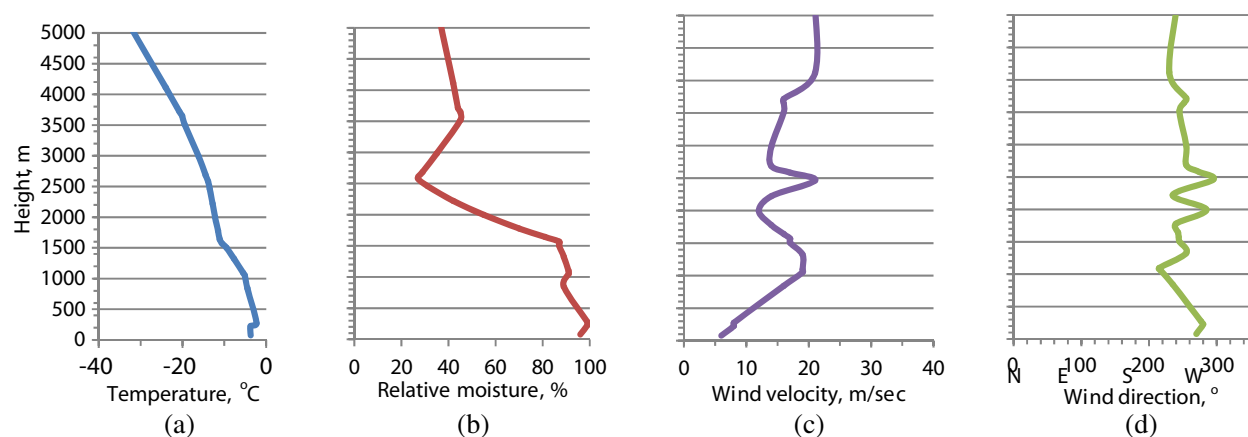
Figure 8: Vertical profiles of (a) the temperature, (b) moisture, (c) wind velocity and (d) wind direction from radio-sounding at 03:00 a.m. in Voeikovo station.

ground atmospheric layer and show increasing in at 200 m in the day time from 15 till 19 hours. The vertical wind component characterizes upward motion at the 400 m that has a maximum 1 m/sec in 15 h. In the evening after 18:00 h the detectable downward motions appears at heights 800, 1200 and 1500 m.

Wind observations have been accomplished in different cone angle that provides different maximal heights of sounding and different resolution. The Fig. 7 demonstrates the wind direction obtained in the same times. The significant wind shift is appears in 15 h.

The results of radiosounding in the nearest station Voeikovo that is in 25 km from lidar sounding is available only in night time (03:00 a.m.) hence the direct comparison is impossible. However the tendency of meteoparameters variation is seen. In Fig. 8 the vertical profiles of temperature, relative moisture and wind parameters are presented.

The analysis of the complicated links between wind characteristics and formation of the pollution cap above the city need in more statistics and it is out this consideration. We are only presenting here the information obtained from one experiment accomplished 5 March 2015 in the city center.

ACKNOWLEDGMENT

REFERENCES

1. Donchenko, V., A. Boreisho, A. Chugreev, I. Melnikova, and D. Samulenkov, "Laser systems of the resources center SPsU. possibilities, problem statement and first results," *Current Problems in Remote Sensing of the Earth from Space*, Vol. 10, No. 3, 122–132, Moscow, 2013.
2. Veselovskii, I., D. N. Whiteman, A. Kolgotin, E. Andrews, and M. Korenskii, "Demonstration of aerosol property profiling by multi-wavelength lidar under varying relative humidity conditions," *J. of Atmosphericand Oceanic Tech.*, Vol. 26, 1543–1557, 2009.
3. Melnikova, I., V. Donchenko, A. Boreisho, and A. Morozov, "Laser complexes for the solution of the inverse problem of ecological monitoring," *Proceedings of the 25th International Laser Radar Conference*, 131–133, St.-Petersburg, Russia, Jul. 5–9, 2010.
4. Mikhailov, E. F. and S. S. Vlasenko, "Structure and optical properties of soot aerosols in a humid atmosphere: 2. The influence of the hydrophilic properties of particles on the extinction, scattering and absorption coefficients," *Izvestiya RAS, Atmospheric and Oceanic Physics*, Vol. 43, No. 2, 221–233, 2007.
5. Ivlev, L. S., A. V. Vasilyev, B. D. Belan, M. V. Panchenko, and S. A. Terpugova, "Optics-microphysical models of urban aerosols," *Proceedings 3rd International Conference Natural and Anthropogenic Aerosols*, St. Petersburg, Sep. 9–Sep. 27, 2001; Edd L. Ivlev. NIICh SPSU, 161–170, 2003.

A 16-Element Wideband Microwave Applicator for Breast Cancer Detection Using Thermoacoustic Imaging

Hao Nan[1], Shiyu Liu[2], Nemat Dolatsha[1], and Amin Arbabian[1]

[1]Department of Electrical Engineering, Stanford University, USA
[2]Department of Electronic Engineering, Tsinghua University, China

Abstract— Microwave-induced thermoacoustic (TA) imaging is a hybrid technique that combines the high dielectric contrast of microwave imaging with the high resolution of ultrasound detection. This technique can achieve a penetration depth in excess of 5 cm, even in dispersive tissue. With all these capabilities, TA imaging is a suitable method for breast cancer screening, which requires a high contrast between cancer and benign tissues, and millimeter-level resolution. The most popular way to excite the imaging target is to employ a waveguide, which is limited in bandwidth and usually not well matched to the target for TA imaging. In this paper, a wideband and compact microwave applicator, which can efficiently excite the tissue in the near and quasi-near field range, is designed. A 16-element conformal phased array based on the proposed applicator focuses the microwave energy and controls the location of high specific absorption rate (SAR) region by tuning the phase of array elements. This architecture increases local SAR of the focus area and directly results in a higher signal-to-noise ratio (SNR) of the target region in the reconstructed image compared to uniform excitation. Full-wave electromagnetic simulations demonstrate the ability to localize and control the high SAR region across the target in the entire bandwidth.

1. INTRODUCTION

Microwave-induced thermoacousic (TA) imaging [1–3] is a hybrid technique that combines the high dielectric contrast in the microwave range and the high resolution of ultrasound imaging. It can be used for frequent breast screenings [3] without posing ionizing radiation. In TA imaging, a short microwave pulse excites the tissue to generate a small differential temperature rise in the range of a millikelvin. The resultant thermal expansion generates pressure waves, which can be detected by the ultrasound transducer to reconstruct the image [4].

One challenge in TA imaging is the weak level of the generated pressure. A higher pressure level requires a higher local SAR which results from a higher microwave energy absorption. The majority of TA experiments utilize a waveguide as the RF excitation device [1–3, 5], but this method is not efficient in generating the desired SAR pattern in tissue. For breast cancer detection, for example, a high local SAR at the tumor site is desired to increase the generated pressure and SNR of the reconstructed image. To address this challenge, we propose to use a conformal phased array of applicators around the breast to increase local SAR at the target site. Using this method in the near and quasi-near field, we are able to move the focal point of the applicator array across the entire target by sequential beamforming. This sectionalized approach provides a high local SAR at
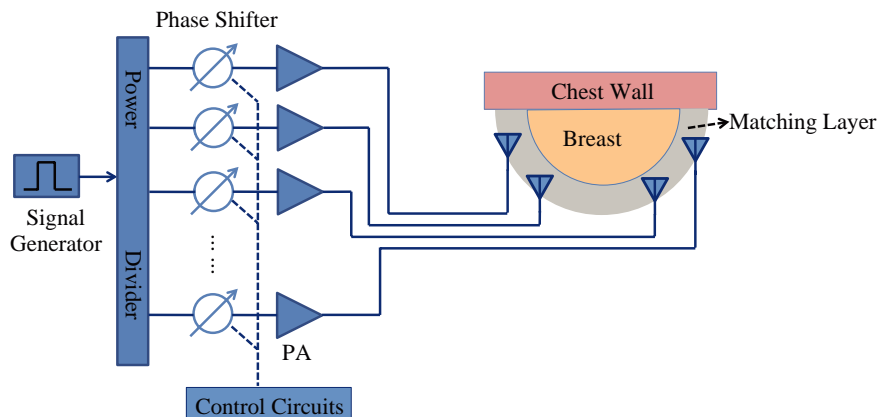
Figure 1: Block diagram of phased array TA system for breast cancer detection. The power amplifier (PA) boosts the microwave energy to the desired level.

the focus area and increases the generated pressure level. In addition, a relatively large frequency bandwidth is required to enable frequency spectroscopy [6] in TA imaging. This technique helps to characterize tissue properties in a wide frequency range and leads to better tumor classification. In this paper, we design a wideband dipole antenna as the microwave applicator in the phased array system.

A conceptual schematic of the proposed conformal phased array system is shown in Figure 1. The microwave pulse is divided into multiple channels for phase shift adjustments and power amplification. Then, the proposed applicator couples the microwave energy into the breast tissue. To improve coupling efficiency, we introduce a matching layer with appropriate dielectric property between the breast tissue and the applicator array.

2. APPLICATOR DESIGN

Figure 2(a) shows the bowtie dipole antenna [7] printed on Rogers 4350 dielectric. It is modified to obtain a large bandwidth and high efficiency required for the microwave applicator. As shown in Figure 2(b) (bottom side), the dipole is fed by a differential balun through via holes. Eventually, a coplanar waveguide (CPW) transition connects the balun to an SMA connector. Due to the trade-off between penetration depth and microwave absorption, the operating frequency between 1.5 GHz and 3.5 GHz is chosen.

The wavelength in the matching layer ($\varepsilon_r \approx 6$) and the breast ($\varepsilon_r \approx 5.1$) is about 5 cm at the center frequency of the bandwidth. Therefore the sample is in the mid-field of the dipole element. The dipole structure provides a desired microwave energy distribution in the mid-field, helping to concentrate energy in the target. Meanwhile, the applicator is able to maintain a low profile (4.5 cm in length and 2.9 cm in width) and fits a compact surface area.

The dielectric properties of involved tissues are obtained from the literature [8]. The simulated return loss of the antenna installed on the matching layer is shown in Figure 3(a). A 69% bandwidth from 1.6 GHz to 3.3 GHz is achieved for the return loss of better than -10 dB. The input impedance is shown in Figure 3(b).
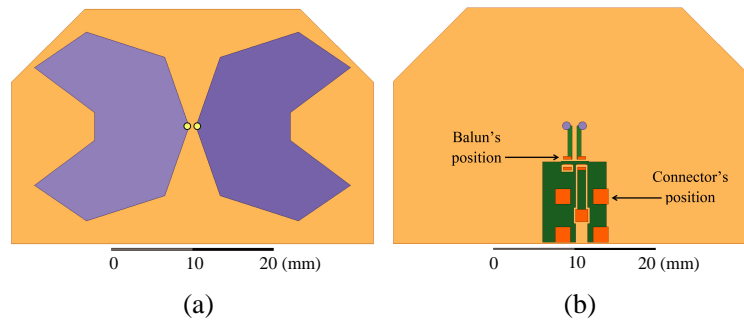
Figure 2: Geometry of the designed applicator. (a) Top side. (b) Bottom side.
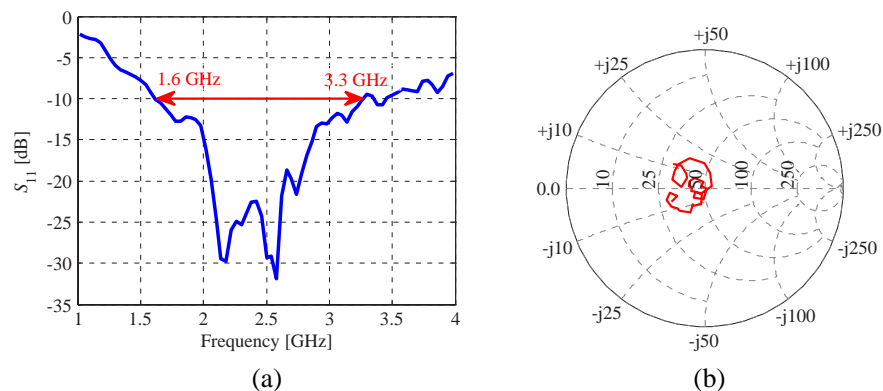
Figure 3: The simulated applicator S_{11} and input impedance. (a) S_{11}. (b) Simulated input impedance of the designed applicator in Smith chart, frequency range 1.6 GHz~3.3 GHz.

3. RESULTS AND DISCUSSION

For the phased array, we employ 16 applicators in a conformal architecture as shown in Figure 4. The array elements are arranged in two rows to enable movement of high-SAR region in both horizontal and vertical directions. All the elements are directed toward the center of the breast. Adjacent elements in the same row have 45 degree difference in the orientation. They are fed by synthetic short microwave pulses with specific delays controlled by the phase shifters. The pulse applied to each applicator has a peak power of 25 W and a pulse width of 1 µs. The duty cycle is set to 1/1000. We use a matching layer between the applicator array and the breast tissue to improve the energy coupling efficiency. The breast is modeled as a half sphere with 5 cm radius. The chest wall is modeled as a thin layer of fat and a thick layer of muscle, as shown in Figure 4.

Figure 5 shows the SAR distribution when the focal point is at the center of the breast. It demonstrates the energy concentration capability of our proposed system at 2.5 GHz. As shown in Figure 5, the microwave power absorption in the matching layer is negligible. The breast tissue shows a high-SAR region in the center (shown as red color) which results from energy concentration from the applicator array. Most of the energy is absorbed by the breast region. The chest wall shows a very small absorption as desired. The tissue in the high-SAR region has an instantaneous local SAR higher than 1500 W/kg during the microsecond pulse, which contributes to an enhanced pressure generation in TA imaging. The average SAR is still limited to below 1.5 W/kg for safety concerns.

By adjusting the phase of each applicator, we can control the high-SAR region location. This capability enables spatial scan of the target, section by section. Figure 6 shows the simulation results at 2.0 GHz, 2.5 GHz, and 3.0 GHz, demonstrating that the designed system has the ability to control the high-SAR region within the bandwidth. The high-SAR region can move in the horizontal direction as shown in the figures of the same row, and in the vertical direction as shown in the figures of the same column. In some cases, a secondary high SAR region is generated due to the limited number of applicators in the array. At higher microwave frequencies, the high-SAR region is smaller in size because of smaller wavelength. However, the SAR value is also smaller due to larger attenuation.
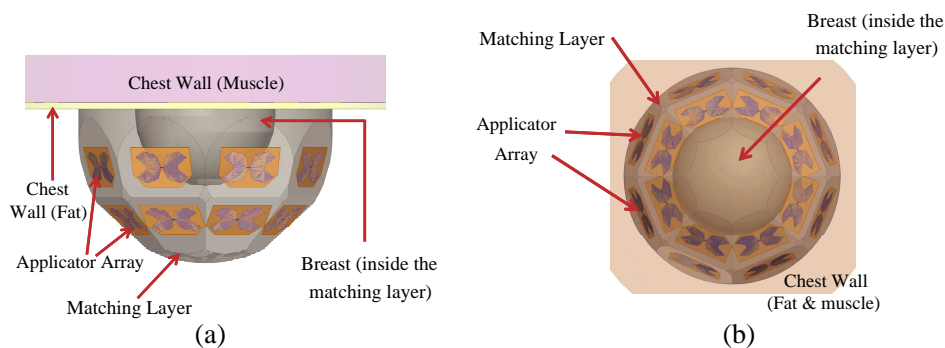
Figure 4: Setup of 16-element applicator array. For clarity, the matching layer is set to be transparent. (a) Front view. (b) Bottom view. Part of chest wall is outside this figure.
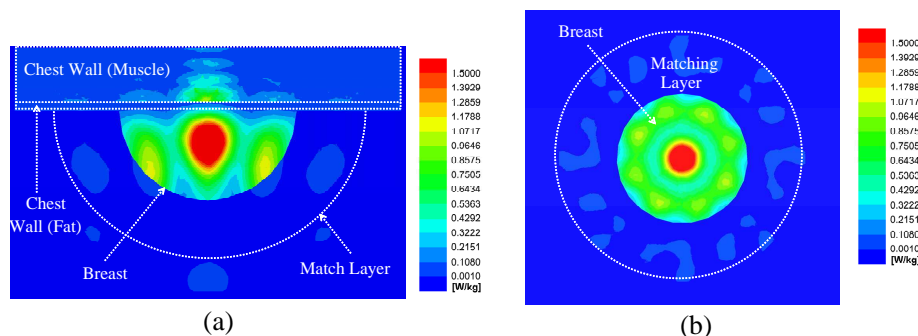
Figure 5: SAR (average value) distribution in the imaging target at 2.5 GHz. (a) Vertical cross section view. (b) Horizontal cross section view (2 cm from the surface of chest wall).

(a)

(b)

(c)
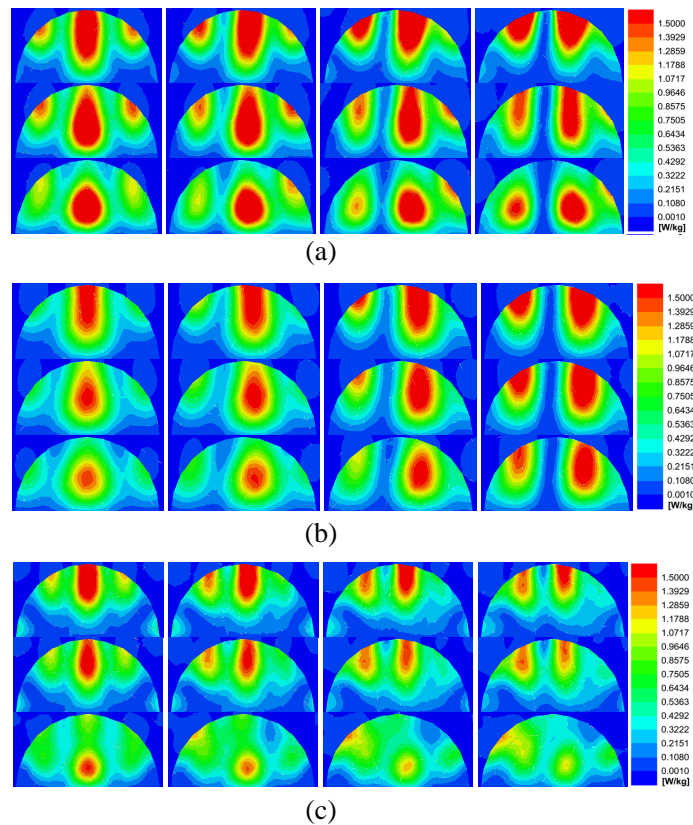
Figure 6: SAR (average value) in the breast tissue with different focal point locations by adjusting phase of each applicator. Vertical cross section view. (a) Microwave frequency: 2.0 GHz. (b) Microwave frequency: 2.5 GHz. (c) Microwave frequency: 3.0 GHz.

(a)   (b)
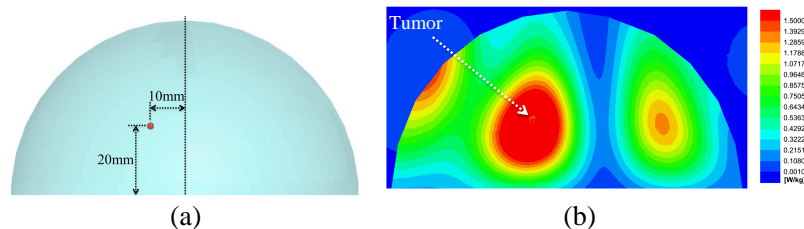
Figure 7: Microwave energy concentration at an example tumor location with 2.5 GHz microwave frequency. Vertical cross section view. (a) An example tumor in breast tissue. (b) SAR (average value) when high SAR region covers tumor.

Figure 7(a) shows an example tumor with 2 mm diameter in the breast tissue. By using 2.5 GHz microwave and adjusting phases of the applicators, we can concentrate the microwave energy on the tumor. Figure 7(b) shows the SAR distribution in the cross section of the breast tissue. We can see that the high-SAR region covers the target tumor. This increases the pressure generation of the target region and consequently improves the quality of the reconstructed TA image.

4. CONCLUSION

In this paper, we design a microwave applicator for localizing microwave energy on the tissue sample for TA imaging. The designed applicator has a high bandwidth and a high energy coupling efficiency. Using the designed applicator, we propose to use a 16-element phased array applicator system to excite the target for breast cancer detection. The proposed system can help concentrate the microwave energy on a small region that can be controlled in both the horizontal and vertical directions by tuning the phase of each channel. Full 3D EM simulations demonstrate this ability across the target and over the operation bandwidth.

ACKNOWLEDGMENT

REFERENCES

1. Ku, G. and L. V. Wang, "Scanning microwave-induced thermoacoustic tomography: Signal, resolution, and contrast," *Med. Phys.*, Vol. 28, No. 1, 4–10, 2001.
2. Xu, M., G. Ku, and L. V. Wang, "Microwave-induced thermoacoustic tomography using multi-sector scanning," *Med. Phys.*, Vol. 28, No. 9, 1958–1963, 2001.
3. Nie, L., D. Xing, Q. Zhou, D. Yang, and H. Guo, "Microwave-induced thermoacoustic scanning CT for high-contrast and noninvasive breast cancer imaging," *Med. Phys.*, Vol. 35, No. 9, 4026–4032, 2008.
4. Xu, M., Y. Xu, and L. V. Wang, "Time-domain reconstruction algorithms and numerical simulations for thermoacoustic tomography in various geometries," *IEEE Trans. Biomed. Eng.*, Vol. 50, No. 9, 1086–1099, 2003.
5. Wang, X., D. R. Bauer, R. Witte, and H. Xin, "Microwave-induced thermoacoustic imaging model for potential breast cancer detection," *IEEE Trans. Biomed. Eng.*, Vol. 59, No. 10, 2782–2791, 2012.
6. Bauer, D. R., X. Wang, J. Volllin, H. Xin, and R. S. Witte, "Spectroscopic thermoacoustic imaging of water and fat composition," *Appl. Phys. Lett.*, Vol. 11, No. 3, 033705, 2012.
7. Raut, S. and A. Petosa, "A compact printed bowtie antenna for ultra-wideband applications," *Proceedings of European Microwave Conference*, 081–084, Rome, Italy, Sep./Oct. 2009.
8. Andreuccetti, S., R. Fossi, and C. Petrucci, "An internet resource for the calculation of the dielectric properties of body tissues in the frequency range 10 Hz–100 GHz," Website at http://niremf.ifac.cnr.it/tissprop/, IFAC-CNR, Florence, Italy, 1997, Based on data published by C. Gabriel, et al., in 1996.

High Resolution Range Imaging via Model-based Compressed Sensing

V. Adler[1], J. Moll[2], M. Kuhnt[2], B. Hils[2], V. Krozer[2], and K. Hoffmann[1]

[1]Department of Electromagnetic Field, Faculty of Electrical Engineering, CTU in Prague, Czech Republic
[2]Department of Physics, Goethe University Frankfurt am Main, Frankfurt am Main, Germany

Abstract— The paper proposes a method for high resolution range imaging at millimeter wave frequencies (85 GHz to 100 GHz) based on model-based compressed sensing (CS). A detailed description of the underlying CS-theory, the experimental setup and radar sensor are presented along with experimental results for one-dimensional range imaging. The proposed method is based on motorized reference measurements, which form the dictionary matrix for subsequent CS-processing. These reference measurements are tested against measurements from a glass fiber reinforced polymer (GFRP) component. A comparison of the CS-processed data to a classical Fourier-domain analysis revealed superior ranging performance of the CS-approach at the expense of a higher signal processing load.

1. INTRODUCTION

Compressed Sensing (CS) is an exciting radar based signal processing which reduces data rates by solving an underdetermined system of linear equations and has the potential to increase the range resolution of the radar range profiles which may be conducive to improved object detection and localization capabilities. Recent advances of compressed sensing applied to radar can be found, for example, in [1, 2].

This paper presents a case study of the CS-formulation in [3] for complex-valued signals where experiments are to be performed using a radar-transceiver in the mm-wave frequency range. The paper is organized in the following way: Section 2 presents the theoretical background of the CS-formulation and the experimental setup and the signal processing results are presented in Sections 3 and 4, respectively.

2. THEORETICAL BACKGROUND

2.1. Basics of Compressed Sensing

Herewithin is a short overview concerning current CS-based strategies for complex-valued signals. Consider the complex scene $\mathbf{b} \in \mathbb{C}^n$. To obtain information about the scene, m measurements are recorded. The measurement process is described as

$$\mathbf{y} = \mathbf{\Phi b} + \mathbf{e}, \tag{1}$$

in which $\mathbf{y} \in \mathbb{C}^m$ denotes the measurements, $\mathbf{\Phi} \in \mathbb{C}^{m \times n}$ models the linear measurement process and $\mathbf{e}$ is the measurement noise. Assuming that the number of measurements m is much smaller than the dimension of the signal n, Equation (1) becomes underdetermined. Nevertheless, in the CS-theory scene $\mathbf{b}$ can still be recovered if there is an orthonormal basis $\mathbf{\Psi} \in \mathbb{C}^{n \times n}$, so that $\mathbf{b} = \mathbf{\Psi x}$, in which $\mathbf{x} \in \mathbb{C}^n$ denotes a sparse vector.

One of the most prominent reconstruction techniques is Basis Pursuit Denoising (BPDN) [4]. The principle of BPDN is the solution of the following problem:

$$\min_x \frac{1}{2} \|\mathbf{y} - \mathbf{Ax}\|_2 + \lambda \|\mathbf{x}\|_1, \tag{2}$$

where $\mathbf{A}$ is the dictionary matrix $\mathbf{A} = \mathbf{\Phi \Psi}$ and λ represents a regularization parameter enforcing the sparsity of $\mathbf{x}$.

Most contemporary algorithms solving this problem can only be applied to real-valued signals. Thus, the complex signals have to be decoupled as follows:

$$\tilde{A} = \begin{pmatrix} \Re\{\mathbf{A}\} & -\Im\{\mathbf{A}\} \\ \Im\{\mathbf{A}\} & \Re\{\mathbf{A}\} \end{pmatrix}, \tag{3}$$

$$\tilde{\mathbf{y}} = \begin{pmatrix} \Re\{\mathbf{y}\} \\ \Im\{\mathbf{y}\} \end{pmatrix}, \tag{4}$$

and

$$\tilde{\mathbf{x}} = \begin{pmatrix} \Re\{\mathbf{x}\} \\ \Im\{\mathbf{x}\} \end{pmatrix}, \tag{5}$$

where $\Re\{\cdot\}$ and $\Im\{\cdot\}$ are the real and imaginary parts, respectively. These decomposed signals can then be treated with common CS-solvers like SPGL1 and TFOCS (see [5–7]).

2.2. Compressed Sensing Applied to IQ-modulated Signals

Consider a multistatic radar setup with N_{Tx} transmitters and N_{Rx} receivers using inphase and quadrature (IQ) demodulation. To obtain information on the radar scene $\mathbf{b} \in \mathbb{C}^n$ m measurements are recorded. Assuming that the number of scatterers N_S is small, the measurement process is represented as

$$\mathbf{y} = \mathbf{A}\mathbf{x} + \mathbf{e}, \tag{6}$$

where x is the image vector containing only N_S non-zero entries and $\mathbf{A}$ is the dictionary matrix. The additive noise term is again denoted as $\mathbf{e}$. Consider measurements from a single transmitter-receiver pair m; then the IQ-signal $\mathbf{y_m} = I_m(t) + jQ_m(t)$ can be represented as

$$\mathbf{y_m} = \mathbf{A_m}\mathbf{x_m} + \eta \tag{7}$$

where non-zero entries correspond to scatterers and $\mathbf{A_m} = [\mathbf{y}_{1m}^{model}, \mathbf{y}_{2m}^{model}, \cdots, \mathbf{y}_{Nm}^{model}]$ is the dictionary comprising the scattered signals, with $\mathbf{y}_{nm}^{model}$ corresponding to the expected signal for a scatterer located at distance x_n for the transmitter-receiver pair m.

As there are a total number of $p = N_{Tx} \times N_{Rx}$ pairs of transducers, we obtain the following system of equations

$$\mathbf{y_1} = \mathbf{A_1}\mathbf{x_1} + \eta, \tag{8}$$
$$\mathbf{y_2} = \mathbf{A_2}\mathbf{x_2} + \eta, \tag{9}$$
$$\vdots \tag{10}$$
$$\mathbf{y_m} = \mathbf{A_m}\mathbf{x_m} + \eta. \tag{11}$$

By concatenating these vectors and solving this equation using a common CS-solver, we can then determine the distance between the target and each transmitter-receiver pair.

3. EXPERIMENTAL SETUP

The measurement setup consists of a fully coherent stepped frequency continuous wave (SFCW) radar sensor, where the schematic of the sensor is shown in Fig. 1(a). To have a more flexible and rearrangeable measurement system working in the W frequency band the waveguide implementation of all main components, as depicted in Fig. 1(b), was chosen. A frequency multiplication (x6) of the output signal with a maximum frequency of 18 GHz was used and to ensure a high dynamic range of the measurement system power levels were optimized so the receiver in the TEST channel always worked in linear mode. Moreover, both receivers in the REF. and TEST path had significant reflections on its input ports so that a strong frequency dependence was observed in the path from directional coupler outputs to the receivers inputs. Consequently, a lock-in amplifier was used as the IQ demodulator because of its high dynamic range capabilities. The only disadvantage of using the proposed lock-in amplifier was the relatively long time of 0.5 s to lock on to the IF of 10 MHz at each new frequency point of the frequency sweep. To avoid time instabilities and excessively high phase noise in the IF signal, both RF and LO synthesizers were coupled with a single 10 MHz frequency standard. The employed antennas were a custom-made horn antenna with a gain of approx. 14 dB.

To exploit the dynamic range of the measurement setup maximally the device under test (DUT) had to be sufficiently large with respect to the antenna beamwidth and the distance from the antenna to achieve the aim of receiving most of the reflected wave from the DUT. The CS technique requires round-trip calibration measurements that form the dictionary matrix. To study the performance of the CS technique the reference positions of the DUT had to be very dense. Hence, manual positioning of the DUT was unacceptable, so a motorized linear stage which provided positioning

Figure 1: (a) Schematic of the radar sensor, (b) photo of the experimental setup.

precision better than $1\,\mu$m was used. The whole measurement setup was connected via GPIB and RS-232 databus and controlled from a computer using custom-made application programmed in Matlab resulting in completely automated measurement setup.

The dictionary was then designed using experimentally determined IQ-signals incorporating the complex envelope $y = I + jQ$. The SPGL1 method, considered to be one of the best available solvers [8] was used for signal reconstruction, and these results were compared with the TFOCS solver using Lan, Lu and Monteiro's accelerated method which restarts every 200 iterations [5, 9].

4. RESULTS

A total of 3,501 measurements covering an interval of 10 mm were recorded. In these measurements a flat aluminum plate was used as a reference reflector that had been translated linearly using a motorized stage. The spacing between two adjacent measurements was, hence, approximately $3\,\mu$m. To ensure the stable operation of the two synthesizers and the Lock-In amplifier the total time for data acquisition in this case study was around 1.5 days. The frequency range of the measurements was 85 GHz to 100 GHz using 51 frequency points. In total 500 measurements per frequency point were recorded and averaged to increase the signal-to-noise ratio. Moreover, an open-measurement was measured by placing an attenuator before the DUT to eliminate the reflections inside the antenna by simple subtraction. In the subsequent step, eleven test measurements from a glass-fiber-reinforced structure were recorded as shown in Fig. 1(b).

Figure 2: (a) Reconstructed high resolution range profiles using the proposed CS-approach, (b) conventional Fourier transform to create the range profiles, (c) close-up of the range profiles shown in (middle), where the spike train indicates the maximum values.

Figure 2 compares the range profile from conventional Fourier-domain radar signal processing with the range profiles obtained by the proposed CS-method. Fig. 2(a) shows that the CS-processed range profiles exhibit a very high resolution (spike train) for each considered measurement position in the interval $[-2,\ 2]$. In contrast, the conventional FFT-based range profiles strongly overlap and the localization error, represented by the position of the maximum, changes non-uniformly as shown in Figs. 2(b), 2(c). This result proves that the CS-framework enables very precise range imaging with excellent accuracy determined by the spacing of the reference measurements that constitute the dictionary. At the same time the proposed CS-approach demonstrates robustness against additional random measurement noise.

Figure 3 shows the effect when the dictionary does not cover the actual position of the current measurement. This directly leads to the off-grid case which aims to reconstruct the target at a position that is not covered by the dictionary measurements. Therefore, Fig. 3(a), firstly, shows the basis pursuit solution implemented in TFOCS. It can be observed that a single target can

(a)   (b)

Figure 3: Analysis of the off-grid effect: Reconstruction errors occur when increasing the distance offset to the target in the dictionary for (a) the basis pursuit (implemented in TFOCS) and (b) basis pursuit denoise problem (implemented in the SPGL1 software package). The actual target position in this example is $x = 1$ mm.

(a)   (b)

Figure 4: Effect of non-equidistant sampling based on uniform distribution for random dictionary selection and basis pursuit denoise problem: (a) three random experiments using $N = 100$ measurement positions (from a total of 3,501 measurements), (b) three random experiments using a subset of $N = 30$ measurement positions..

be accurately reconstructed when the dictionary offset tends to zero. When the dictionary offset increases the corresponding signal energy is split to the adjacent measurements points. Due to a large dictionary offset several spurious peaks occurred leading to erroneous results. Slightly different results have been obtained by the solution of the basis pursuit denoising problem implemented in the SPGL1 software package. Although the same scenario has been considered, the erroneous peaks had a lower amplitude, but the energy of the intended peak has been separated to the adjacent measurement points.

The conventional Fourier-domain signal processing produces range profiles by multiplying the time-domain signal with the speed of light. This results in an equidistant sampling of the signal which is not necessarily required in the proposed CS-approach as shown in Fig. 4. Here, two scenarios with a different number of sampling points are considered, i.e., $N = 100$ and $N = 30$. In each case three random experiments have been conducted to take the respective number of sampling points from a uniform distribution. It can be concluded that the position of the target which is located in this example at $x = 1$ mm can be correctly reconstructed for 100 sampling points. On the other hand, when the number of sampling points is further reduced, it is then likely that spurious

peaks occur at incorrect positions. However, this result demonstrated the possibility of having a reduction of sampling points which is beneficial for various applications.

5. CONCLUSION

In this paper it was demonstrated that Compressed Sensing can be used to perform accurate Time-of-flight measurements taking into account complex valued measurement data as the dictionary. The limitations of the proposed approach were demonstrated in terms of the varied number of non-equidistant sampling points as well as the off-grid effects. Concerning the off-grid effect, it was found that solving the basis pursuit and the basis pursuit denoising problem leads to spurious signal components that degrade the ranging result.

ACKNOWLEDGMENT

REFERENCES

1. Ender, J. H., "On compressive sensing applied to radar," *Signal Processing, Special Section on Statistical Signal & Array Processing*, Vol. 90, No. 5, 1402–1414, 2010.
2. Cetin, M., I. Stojanovic, N. Nhon, K. Varshney, S. Samadi, W. Karl, and A. Willsky, "Sparsity-driven synthetic aperture radar imaging: Reconstruction, autofocusing, moving targets, and compressed sensing," *Signal Processing Magazine, IEEE*, Vol. 31, No. 4, 27–40, Jul. 2014.
3. Kuhnt, M., J. Moll, and V. Krozer, "A compressed sensing formulation based on i/qdictionary: experimental case study at millimeter-wave frequencies," *9th German Microwave Conference (GeMiC 2015)*, 229–232, 2015.
4. Chen, S. S., D. L. Donoho, and M. A. Saunders, "Atomic decomposition by basis pursuit," *SIAM Review*, Vol. 43, No. 1, 129–159, 2001, [Online] Available: http://dx.doi.org/10.1137/S003614450037906X.
5. Becker, S., E. Candés, and M. Grant, "Templates for convex cone problems with applications to sparse signal recovery," *Mathematical Programming Computation*, Vol. 3, No. 3, 165–218, 2011.
6. Van den Berg, E. and M. P. Friedlander, "Probing the pareto frontier for basis pursuit solutions," *SIAM Journal on Scientific Computing*, Vol. 31, No. 2, 890–912, 2008, Available: http://link.aip.org/link/?SCE/31/890.
7. Van den Berg, E. and M. P. Friedlander, "SPGL1: A solver for large-scale sparse reconstruction," June 2007, http://www.cs.ubc.ca/labs/scl/spgl1.
8. Van den Berg, E. and M. P. Friedlander, "Probing the pareto frontier for basis pursuit solutions," *SIAM Journal on Scientific Computing*, Vol. 31, No. 2, 890–912, 2009, [Online] Available: http://dx.doi.org/10.1137/080714488.
9. Becker, S., E. Candés, and M. Grant, "Templates for first-order conic solvers user guide," [Online] Available: http://cvxr.com/tfocs/doc/.

Fast Level Set Based Method for High Contrast Microwave Imaging

Pratik Shah and Mahta Moghaddam

Department of Electrical Engineering, University of Southern California, California, USA

Abstract— Microwave imaging is a non-ionizing modality and has applicability in many areas. Many numerical and experimental studies on microwave imaging have been performed in the past several years, with common impediments being the inability to recover high dielectric contrasts and slow speed of computation. We propose a method based on level set formulation to recover the shape of imaged targets even for the high-contrast case, when prior information on permittivity of the object is known. Our method significantly differs from the previous work as we evaluate the inverse problem without solving the adjoint field and consider the variational level set for regularizing the level set evolution. Hence, the proposed method is very fast. The applicability of the method is demonstrated on synthetically generated data for a two-dimensional (2D) scenario. The reconstructed images indicate that the method can produce accurate object localization and shape identification even for high contrast objects.

1. INTRODUCTION

In Microwave imaging, electromagnetic waves are transmitted, scattered and received in an investigation domain and the electrical properties such as permittivity and conductivity are estimated at each discretized element in the domain. Microwave imaging has applications in through-the-wall imaging, non destructive testing, and medical imaging. The imaging problem is usually performed by formulating it using the volume integral equation. The integral equation represents the relationship between complex permittivitty and the electric field inside and outside of the inhomogeneous imaged domain. It is non-linear in general since the electric field inside the object, which appears inside the integral, is a function of medium's properties. Common practice to solve for the unknown object properties is to linearize the integral equation by iteratively solving for the unknown complex permittivity and the field. This linearizing approach performs well when the object is not too large compared to the wavelength or the contrast (complex permittivity of the object with reference to that of the background) is not too high. However, its performance on contrast recovery degrades rapidly as the contrast goes higher. The primary reasons are non linearity of the problem and presence of multiple solutions (that is, nonuniqueness).

To overcome the limitation of the linearized approach, many approaches using global optimization methods are proposed. They are usually very slow and their applicability to 3-dimensional problems is particularly implausible. Approaches also have been suggested where prior information about the unknowns can be leveraged. Having accurate priors about dielectric properties, the microwave imaging problem essentially becomes locating the object and estimating the shape of the object. In other words, it can be thought of as a shape segmentation problem. Although it is understood that the prior knowledge about contrasts in the imaged domain may not be very accurate or easily available, we will make the assumption that the contrast is known to within some uncertainty. This is so that we can decouple the contrast and the shape retrieval problems, address the latter, and defer the accurate solution of the former to a separate solution step. We also note that even if the contrast values are known, conventional microwave imaging techniques such as the Born/Distorted Born Iterative Methods, or the Contrast Source Inversion method, still do not converge.

The level set method, one of the best shape estimation techniques in image processing, is a candidate that we wish to consider for this work. Although level set based shape recovery approaches for microwave imaging have been proposed before [4], they are very slow in general. For example, the approach used in [7] takes around 4–7 hrs on a single 64-bit AMD Opteron 246 processor running at 2 GHz to recover a 2D shape profile of 10 cm radius. The main computational burden is to estimate the field for given parameters at each iteration. The field computation has to be performed at every iteration, when the adjoint field based approach is used. We propose a method which is not based on the adjoint field evaluation.

2. THEORETICAL BACKGROUND

Microwave imaging is an electromagnetic inverse scattering problem. We assume a z-independent two dimensional (2D) scatterer, and the electric field polarized along the z-direction, corresponding

to a transverse magnetic (TM) polarization. For a 2D scattering problem, the scalar electric field volume integral equation for a heterogeneous, isotropic, non-magnetic medium, enclosed in a region D is given by [1]

$$E(r) = E_i(r) + k_b^2 \int_D G(r, r')\chi(r')E(r')dv',$$ (1)

where $E(r)$ and $E_i(r)$ are total and incident fields, respectively, k_b is the wavenumber of the background medium with lossless permittivity, $G(r, r') = \frac{i}{4}H_0^{(2)}(k\|r - r'\|)$ is the Green's function, $\chi(r) = [\epsilon_r(r')/\epsilon_b - 1] + i[(\sigma(r') - \sigma_b)/(\epsilon_b\epsilon_0\omega)]$ is the dielectric contrast in terms of the permittivity and conductivity contrast, where the subscript r denotes the relative permittivity, and b denotes the background. Equation (1) represents the solution of the wave equation and it is used to determine the fields given the complex dielectric contrast. It is also called the forward solution.

Defining the scattered field as $E_s(r) = E(r) - E_i(r)$, with measurement points r on a surface S that encloses D in (1), we get

$$E_s(r) = k_0^2 \int_D G(r, r')\chi(r')E(r')dv' \quad r \in S, r' \in D.$$ (2)

Equation (2) can be used to estimate the dielectric contrast of an unknown medium, given some observations of the scattered field. Let L define the linear operator represented by $L\{\cdot\} = k_0^2 \int_D G(r, r') \cdot dv'$, then Eq. (2) is written using short-hand notation as $E_s = L\{\chi, E\}$. It is also sometimes called the data equation.

3. APPROACH

3.1. Level Set Formulation

Equation (2) is a non-linear problem in general, since the electric field, $E(r')$, is itself a function of the dielectric contrast. The idea is to use (1) or (2) to estimate the contrast and the field such that the error $\|E_s - L\{\chi, E\}\|$ is minimized. Permittivity and conductivity are well documented for many materials. Utilizing this information as a prior in the estimation problem, the image reconstruction becomes as a shape and location estimation problem. Once again we note that this is an intermediate and convenient assumption, and that ultimately we need to solve for the contrast as well. But we will assume the contrast is known as a stepping stone towards solving the high-contrast shape function inverse problem. Level set methods are widely used in the image processing field especially for segmentation, registration and denoising. Here, we exploit the level set method for image reconstruction. For image reconstruction, the cost function $J(\chi)$ can be defined without using any regularization as,

$$J(\chi) = \|E_s - L\{\chi, E\}\|.$$ (3)

The unknowns χ can be parameterized using a level set function ϕ as follows:

$$\chi(r) = \chi_i U(\phi(r)) + \chi_e(1 - U(\phi(r))).$$ (4)

where χ_i and χ_e are prior information on the object and background contrast respectively and $U(r)$ is the standard Heaviside function. We note that $\phi > 0$ ($\phi < 0$) represents the region occupied by the object (background) so $\phi = 0$ traces the boundary of the object. The object can also be non-connected.

The minimization of the cost function on the premise of the gradient flow can be written in the form of the evolution equation of the level set function using Euler-Lagrange equation as

$$\frac{\partial \phi}{\partial t} + \frac{\partial J}{\partial \phi} = 0.$$ (5)

Formally differentiating J and the first order Taylor series approximation yields the Gateaux derivate of functional $J(\phi)$ as

$$\frac{\partial J}{\partial \phi} = \text{Re}\left\{[R'(\chi)]^+ R(\chi)\right\}(\chi_i - \chi_e)\delta(\phi).$$ (6)

Here, Re indicates real part of the argument, R is the residue ($R = E_s - L\{\chi, E\}$) for the given estimation of E using ϕ, $^+$ indicates adjoint operation and R' denotes the derivative operation. From

now on we use the notation A for the operator L, when the field E is known or estimated. Generally in Electromagnetics, the adjoint operations have been performed by defining the adjoint fields and solving the electromagnetic scattering problem. Solving the adjoint problem is computationally as intense as solving a forward problem and it has to be solved at every iteration. Though the adjoint and the forward problem can be solved together, they account for the majority of the computation time in the inverse problem. Having the prior information about the contrast, the computational time can drastically be reduced by applying linearized operations. Linearized operations have two key features. The adjoint operation for a linear system is the combination of the transpose operation and the complex conjugate operation, and estimation of the best reconstruction for the given field is similar to iterating the level set evolution until it converges. Hence,

$$\frac{\partial J}{\partial \phi} = \mathrm{Re} \left\{ A^+ R(\chi) \right\} (\chi_i - \chi_e) \delta(\phi). \tag{7}$$

Level set evolution typically develops irregularities during its evolution, which eventually destroys the stability of the level set evolution. One of the remedies is re-initialization, which has been extensively used to avoid irregularities and has ensured desirable results [2]. However, we consider the variational level set formulation [6], which does not require re-initialization, but instead the signed distance function is used as a regularization.

We propose a cost function for image reconstruction, which minimizes the residue energy and non uniform distance energy. The new defined cost function or equivalently an energy function $\mathcal{E}(\phi)$ is written as

$$\mathcal{E}(\phi) = \mu R_p(\phi) + J(\phi), \tag{8}$$

where $R_p(\phi)$ is the regularization term, $\mu > 0$ is a constant, $J(\phi)$ is the external energy function similar to (3). The regularization is called the internal energy of the function ϕ since it is function of ϕ only. The external energy is the residue rather than the edge indicator function as in [6]. The evolutionary approach balances between these two energies. The regularization term is defined similarly to [6] by

$$R_p(\phi) = \int p(|\nabla \phi|) dx, \tag{9}$$

where p is a potential energy defined by

$$p(s) = \begin{cases} \frac{1}{(2\pi)^2}(1 - \cos(2\pi s)) & \text{if} \quad s < 1 \\ \frac{1}{2}(s-1)^2 & \text{if} \quad s \geq 1. \end{cases} \tag{10}$$

The potential energy has to be minimum at $s = 1$ to maintain the signed distance uniform and at $s = 0$ to keep the derivative of $R_p(\phi)$ away from $-\infty$. For details, refer to [6].

The Gateaux derivative of the functional $R_p(\phi)$ is

$$\frac{\partial R_p}{\partial \phi} = -\mathrm{div} \left(\frac{p'(|\nabla \phi|)}{|\nabla \phi|} \nabla \phi \right). \tag{11}$$

Linearity of the Gateaux derivative and, from (11), the level set evolution equation can be expressed as

$$\frac{\partial \phi}{\partial t} = \mu \mathrm{div} \left(\frac{p'(|\nabla \phi|)}{|\nabla \phi|} \nabla \phi \right) - \mathrm{Re} \left\{ A^+ R(\chi) \right\} (\chi_i - \chi_e) \delta(\phi). \tag{12}$$

3.2. Numerical Implementation

For solving the forward electromagnetic scattering problem, we use a two-dimensional, vector element based finite element method (FEM) [5]. In this implementation of the FEM, we employ first-order Whitney edge elements as basis functions for the total electric field, and a first-order absorbing boundary condition to terminate the computational domain.

For solving the evolution of the level set function, we use the central difference scheme to approximate all of the spatial partial derivatives, whereas we use the forward difference scheme to approximate the temporal partial derivative. The approximation of Eq. (12) by the above difference scheme can be simply written as

$$\frac{\phi_{i+1} - \phi_i}{\Delta t} = L(\phi_i), \tag{13}$$

where $L(\phi_i)$ is the approximation of the right hand side of Eq. (12). Δt is artificial time, and it represents the evolution iterations. We choose μ and Δt such that the Courant-Friedrichs-Lewy(CFL) condition $\mu \Delta t < 1/4$ is satisfied.

4. RESULTS

We performed several experiments to validate the proposed method. In the reported numerical results, the scattered field data have been obtained by using a numerical simulator based on FEM. The simulation has been performed using the following configuration. The T/R antennas are located $20°$ apart from each other on the circumference of the circular domain of radius 1.5λ. The operating freespace wavelength is $14.28\,\mathrm{cm}$ and the domain is meshed at $\lambda/100$ to maintain error in field calculation within a nominal bound. The total number of measurement is 324. In the image reconstruction process, the domain D was meshed at $\lambda_g/50$ for the forward solver (FEM), where λ_g is the wavelength in the object medium. The domain D used for estimating the complex permittivity (for (2)) was a circular domain of radius 1λ (free space wavelength). The domain was meshed at $\lambda/21$. The discretization gives image size of 41×41 pixels.

The results shown here are generated by calling the forward solver only 12 times, and 80 level set iterations for each call of the forward solver. Comparing with the existing methods [3, 7] where the forward solver has to be called on the order of 1000 times, it reduces the number of the call to forward solver by a factor of 100. In terms of the computation time, the average runtime for each forward solver is 25 seconds and the average runtime for each call of level set is 35 seconds on a Linux desktop with a Xeon processor and 24 GB RAM so the reconstructed image is generated on an average in 12 mins.

The background medium is considered to be as air/vacuum. The starting point for vector χ is the minimum energy solution $(A^T y)$. The level set evolution equation parameters are set as $\Delta t = 0.15$ and $\mu = 0.12/\Delta t$. The reported values are by means of preliminary trial and error evaluations.

The first experiment is on objects with high contrast. We considered a circular cylinder having radius 0.4λ, located at the center of simulation domain. We performed two simulations. In the first simulation, the permittivity of cylinder is 6 and in the second simulation, it is complex and is $2 - 1.5i$. The respective reconstruction images are shown in Fig. 1. The reconstruction domain is
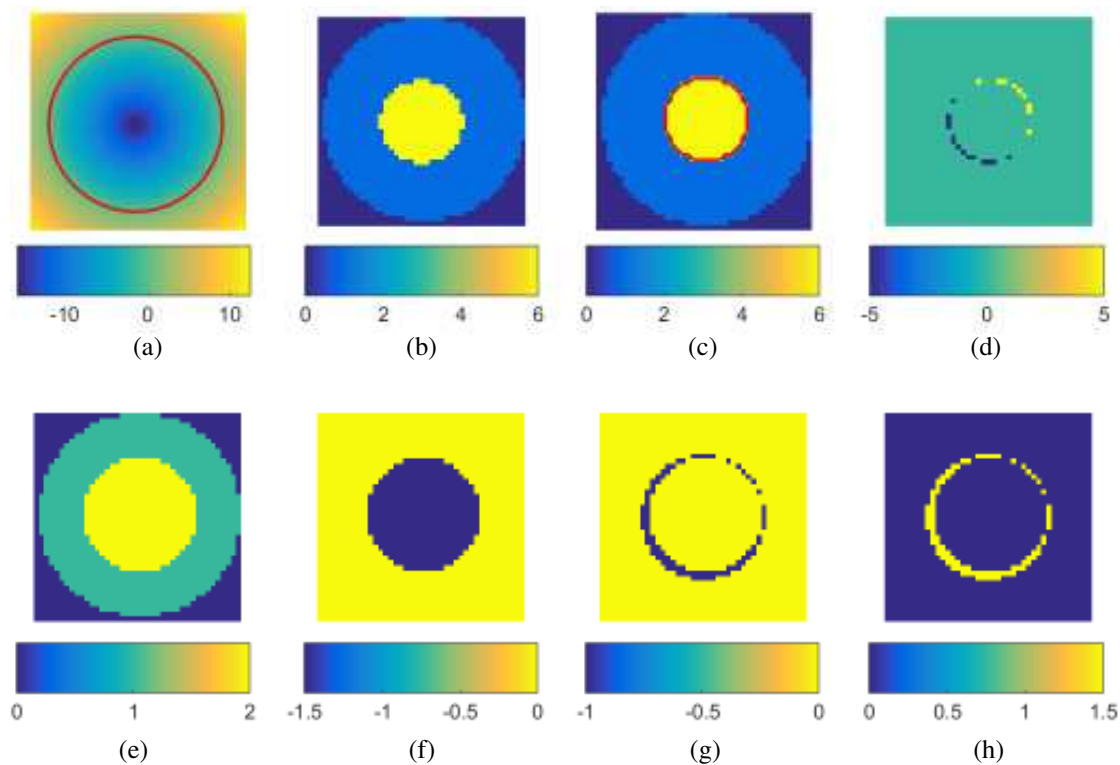
Figure 1: (a) Initialization for a level set function. The red contour illustrates the zeroth level, i.e., object boundary. (b) Actual configuration and lossless object. (c) Reconstructed image using the converged level set (depicted by red contour). (d) Error in reconstruction. (e), (f), (g), (h) Actual configuration of the object with loss; (e) real part and (f) imaginary part. (g), (h) Error in reconstruction. Colorbar at bottom represents permittivity.

circular so that outside of the largest circle, the region is void. The method estimates the shape correctly within the accuracy of the numerical error.

To evaluate the efficiency of different shapes, we considered different cases, which consist of non-connected objects and sharp boundary. The geometry of the problem and various cases are shown in Fig. 2. We started the minimization with the initialization of the level set function the same as for objects in Fig. 1. The reconstructed results are shown in Fig. 2, where the red contours depict the object boundary and they are in good match with the true objects.
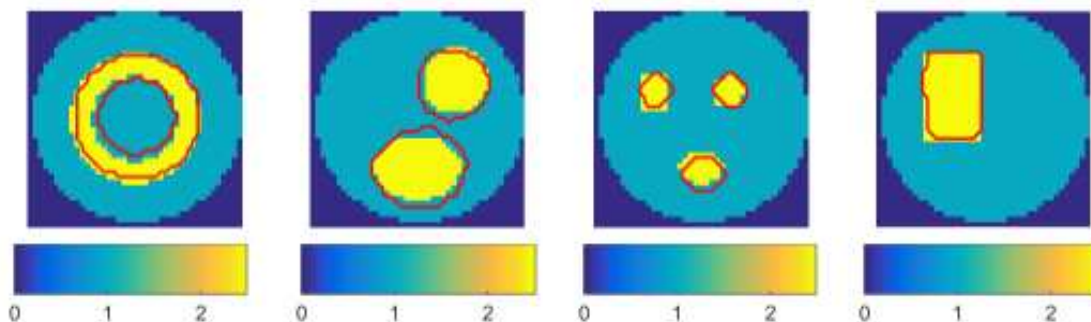
Figure 2: Testing set: images of different objects. True objects are shown in yellow. The converged level sets(boundary of the reconstructed objects) are overlaid as a red contour. Colorbar at bottom represents permittivity.

5. CONCLUSION

We presented the fast level set method without solving the adjoint field for microwave imaging. The prior information on permittivity allows us to recover high contrast using the level set shape based method. Our approach is computationally less intense than other approaches because it reduces the number of forward solver calls by about two orders of magnitude. The reconstructed images for various shapes and high contrast had an excellent shape recovery, localization and error to within a single pixel. Future work includes evaluating the performance of the method on actual data, incorporating objects with discrete permittivity in the level set framework and extending it to 3-dimensional framework.

REFERENCES

1. Balanis, C. A., *Advanced Engineering Electromagnetics*, Wiley, New York, 1989.
2. Fedkiw, S. O. R., *Level Set Methods and Dynamic Implicit Surfaces*, Springer, 2003.
3. Hajihashemi, M. R. and M. El-Shenawee, "Shape reconstruction using the level set method for microwave applications," *IEEE Antennas Wireless Propag. Lett.*, Vol. 7, No. 4, 92–96, 2008.
4. Hassan, A. M., T. C. Bowman, and M. El-Shenawee, "Efficient microwave imaging algorithm based on hybridization of the linear sampling and level set methods," *IEEE Trans. Antennas Propag.*, Vol. 61, No. 7, 3765–3773, 2013.
5. Khankhoje, U., J. van Zyl, and T. Cwik, "Computation of radar scattering from hetero-geneous rough soil using the finite-element method," *IEEE Trans. Geosci. Remote Sens.*, Vol. 51, No. 6, 3461–3469, 2013.
6. Li, C., C. Xu, C. Gui, and M. D. Fox, "Distance regularized level set evolution and its application to image segmentation," *IEEE Trans. Imag. Proc.*, Vol. 19, No. 12, 3243–3254, 2010.
7. Woten, D. A., M. R. Hajihashemi, A. M. Hassan, and M. El-Shenawee, "Experimental microwave validation of level set reconstruction algorithm," *IEEE Trans. Antennas Propag.*, Vol. 58, No. 1, 230–233, 2010.

On the Connection between Jones Matrix and Sinclair Matrix

T. Dallmann and D. Heberling

Institute of High Frequency Technology, RWTH Aachen University, Germany

Abstract— The Sinclair matrix and the Jones matrix describe the scattering behavior of radar targets using different coordinate systems. To analyze the physical scattering mechanisms occuring at a target, the Sinclair matrix can be decomposed with a coneigenvalue decomposition. This decomposition is mathematically challenging and still not fully understood. In contrast the Jones matrix can be decomposed with an eigenvalue decomposition, which can be easily implemented. In the literature a simple connection between Jones and Sinclair matrices was derived which gives rise to the question if the coneigenvalue decomposition of the Sinclair matrix can be replaced by an eigenvalue decomposition of a suitable Jones matrix by exploiting this connection. Within this paper it will be proven that, depending on the type of connection, this is either not possible or requires high mathematical effort. Therefore the coneigenvalue decomposition remains the method of choice for the aforementioned analysis of scattering mechanisms.

1. INTRODUCTION

The polarimetric scattering behavior of radar targets can be described with two different 2×2 matrices: The Sinclair matrix $\underline{\mathbf{S}}$ which specifies the backscattering of a target and which is commonly used by polarimetric monostatic radar systems, and the Jones matrix $\underline{\mathbf{J}}$ which characterizes the forward scattering of a target and originates from optics [1, 2]. Both matrices are suitable for the description of radar targets in the monostatic case, but rely on different coordinate systems. The Sinclair matrix is based on the backward scattering alignment (BSA) convention, where the wave vector of the incident wave is parallel to the wave vector of the scattered wave. In this convention the polarization of incident and scattered wave are described by the antenna polarization, which is defined as the polarization of a wave radiated by an antenna [3]. Therefore the BSA convention is also termed to be *antenna-oriented*. The Jones matrix is based on the forward scattering alignment (FSA) convention, where the wave vector of the incident wave is antiparallel to the wave vector of the scattered wave. Since the wave vectors are oriented along the propagation direction of the waves, the FSA convention is termed to be *wave-oriented*.

The decomposition of the Sinclair matrix into so-called Huynen-Euler parameters [4] has gained some attention in recent publications [5, 6]. This decomposition is based on a diagonalization of the Sinclair matrix [7, 8]

$$\underline{\mathbf{\Sigma}} = \underline{\mathbf{U}}^T \, \underline{\mathbf{S}} \, \underline{\mathbf{U}} \tag{1}$$

where $\underline{\mathbf{U}}$ is a unitary matrix describing a change of the polarization basis of the incident and scattered electromagnetic wave. This allows to characterize the target by fundamental scattering mechanisms independent from the polarization of the incident and scattered wave. To these mechanisms belong single and double reflections as well as circularly polarizing and linearly polarizing structures. Since all scatterers influence in which directions and at which frequencies the scattering occurs they give a physical interpretation to the radar-cross section signatures of radar targets. This interpretation is made possible by the Huynen-Euler parameters, which are used to differentiate between the mechanisms. As can be seen from (**??**) the approach requires a coneigenvalue decomposition [9]. Up to now, little research has been conducted in the field of consimilarity transformations and coneigenvalues. Some of the implications of these decompositions are therefore still unknown [7, 8]. Moreover, there exist only few decompositions of $\underline{\mathbf{S}}$ into coneigenvalues which are either mathematically cumbersome [5] or miss out some of the Huynen-Euler parameters [9, 10].

In contrast the Jones matrix can be decomposed into [7, 8]

$$\underline{\mathbf{\Lambda}} = \underline{\mathbf{U}}^H \, \underline{\mathbf{J}} \, \underline{\mathbf{U}}. \tag{2}$$

Since $\underline{\mathbf{U}}$ is a unitary matrix this equation describes an eigenvalue decomposition. The mathematics of eigenvalues and similarity transformations are known and well understood [9]. Moreover, there are various methods available for eigenvalue decomposition which are both numerically stable and computationally efficient [11].

In [12] a misleading, but simple connection between the Jones matrix $\underline{\mathbf{J}}$ and the Sinclair matrix $\underline{\mathbf{S}}$ was established:

$$\underline{\mathbf{J}} = \underline{\mathbf{T}}\,\underline{\mathbf{S}} = \begin{bmatrix} 1 & 0 \\ 0 & -1 \end{bmatrix} \underline{\mathbf{S}} \tag{3}$$

This equation was derived for linear polarizations only. Unfortunately in most publications it is not emphasized that this connection is limited to linear polarizations [1, 2], leading the reader to the wrong assumption that (3) is generally valid. If this would be the case, the decomposition of Sinclair matrices could be extremely simplified by transforming them to Jones matrices and performing an eigenvalue decomposition afterwards:

$$\underline{\mathbf{\Lambda}} = \underline{\mathbf{U}}^H \underline{\mathbf{J}}\,\underline{\mathbf{U}} = \underline{\mathbf{U}}^H \underline{\mathbf{T}}\,\underline{\mathbf{S}}\,\underline{\mathbf{U}}. \tag{4}$$

For clarity, this decomposition will be called *simplified decomposition* in the following. Within this paper it will be shown that the simplified decomposition will not deliver valid results if the transformation matrix $\underline{\mathbf{T}}$ in (3) is used. Moreover, it will be shown that this is also the case for any other transformation matrix $\underline{\mathbf{T}}$ which does not change with $\underline{\mathbf{S}}$. Due to this it will become clear that coneigenvalue decompositions are still the only possibility to extract Huynen-Euler parameters from a Sinclair matrix and that additional research in the field of consimilarity transformations and coneigenvalues is indespensable.

2. TARGET-INDEPENDENT TRANSFORMATION MATRICES

As described by J. R. Huynen in [4], a coneigenvalue decomposition of the Sinclair matrix $\underline{\mathbf{S}}$ allows to characterize the scattering mechanism occuring at the target independent from the polarization of the incoming and scattered wave. Thus the coneigenvalues of two targets $\underline{\mathbf{S}}_1$, $\underline{\mathbf{S}}_2$ will be identical if the response of both targets is caused by the same scattering mechanism. It should be noted that despite his groundbreaking work in the field of radar polarimetry Huynen did not realize the fundamental difference between coneigenvalues and eigenvalues — a pitfall which was discussed in detail by Lüneburg in [7, 8].

If the simplified decomposition described in Section 1 would be valid, then the eigenvalues of two targets $\underline{\mathbf{J}}_1$, $\underline{\mathbf{J}}_2$ must be identical if the response of both targets is caused by the same scattering mechanism. Since two matrices with the same (con)eigenvalues are (con)similar to each other [9], it follows that the Jones matrices $\underline{\mathbf{J}}_1$, $\underline{\mathbf{J}}_2$ of two targets must be similar if the Sinclair matrices $\underline{\mathbf{S}}_1$, $\underline{\mathbf{S}}_2$ of two targets are consimilar. If the simplified decomposition can be applied depends strongly on the transformation matrix $\underline{\mathbf{T}}$: If $\underline{\mathbf{T}}$ is target-independent, which means that $\underline{\mathbf{T}}$ does not change with $\underline{\mathbf{S}}$ and therefore always has the same entries $\underline{t}_{mn}$, then the simplified decomposition is not applicable. This will be shown with the following proof:

Theorem 1. *Let M_2 be the set of all 2×2-matrices. It does not exist a single full-rank matrix $\underline{\mathbf{T}}$ for arbitrary $\underline{\mathbf{S}}_1, \underline{\mathbf{S}}_2 \in M_2$ for which the following property holds: If $\underline{\mathbf{S}}_1$ is consimilar to $\underline{\mathbf{S}}_2$, then $\underline{\mathbf{J}}_1 = \underline{\mathbf{T}}\,\underline{\mathbf{S}}_1$ is similar to $\underline{\mathbf{J}}_2 = \underline{\mathbf{T}}\,\underline{\mathbf{S}}_2$.*

Proof. Assume that there exists a full-rank $\underline{\mathbf{T}}$ which fulfills the stated property. Then one should be able to derive the entries $\underline{t}_{mn}$ of $\underline{\mathbf{T}}$. Therefore the following matrices are used:

$$\underline{\mathbf{S}}_{1,A} = \begin{bmatrix} +1 & 0 \\ 0 & +1 \end{bmatrix} \qquad \underline{\mathbf{S}}_{2,A} = \begin{bmatrix} -1 & 0 \\ 0 & -1 \end{bmatrix} \qquad \underline{\mathbf{U}}_A = \begin{bmatrix} +j & 0 \\ 0 & -j \end{bmatrix}$$

$$\underline{\mathbf{S}}_{1,B} = \begin{bmatrix} +1 & 0 \\ 0 & -1 \end{bmatrix} \qquad \underline{\mathbf{S}}_{2,B} = \begin{bmatrix} -1 & 0 \\ 0 & +1 \end{bmatrix} \qquad \underline{\mathbf{U}}_B = \begin{bmatrix} 0 & -1 \\ +1 & 0 \end{bmatrix}$$

$$\underline{\mathbf{S}}_{1,C} = \begin{bmatrix} 0 & +1 \\ +1 & 0 \end{bmatrix} \qquad \underline{\mathbf{S}}_{2,C} = \begin{bmatrix} 0 & -1 \\ -1 & 0 \end{bmatrix} \qquad \underline{\mathbf{U}}_C = \begin{bmatrix} 0 & +j \\ +j & 0 \end{bmatrix}$$

$$\underline{\mathbf{S}}_{1,D} = \begin{bmatrix} 0 & +1 \\ +1 & 0 \end{bmatrix} \qquad \underline{\mathbf{S}}_{2,D} = \begin{bmatrix} 0 & +j \\ +j & 0 \end{bmatrix} \qquad \underline{\mathbf{U}}_D = \begin{bmatrix} +1 & 0 \\ 0 & +1 \end{bmatrix} e^{+j\frac{\pi}{4}}$$

$\underline{\mathbf{S}}_{1,i}$ is consimilar to $\underline{\mathbf{S}}_{2,i}$ over the unitary matrix $\underline{\mathbf{U}}_i$ for all $i \in \{A, B, C, D\}$.

- $\mathbf{\underline{J}}_{1,A} = \mathbf{\underline{T}}\,\mathbf{\underline{S}}_{1,A}$ and $\mathbf{\underline{J}}_{2,A} = \mathbf{\underline{T}}\,\mathbf{\underline{S}}_{2,A}$ yields

$$\mathbf{\underline{J}}_{1,A} = \begin{bmatrix} \underline{t}_{11} & \underline{t}_{12} \\ \underline{t}_{21} & \underline{t}_{22} \end{bmatrix} \qquad \mathbf{\underline{J}}_{2,A} = \begin{bmatrix} -\underline{t}_{11} & -\underline{t}_{12} \\ -\underline{t}_{21} & -\underline{t}_{22} \end{bmatrix}$$

  If $\mathbf{\underline{S}}_{1,A}$ is consimilar to $\mathbf{\underline{S}}_{2,A}$ then $\mathbf{\underline{J}}_{1,A}$ must be similar to $\mathbf{\underline{J}}_{2,A}$. Thus $\mathrm{tr}(\mathbf{\underline{J}}_{1,A}) = \mathrm{tr}(\mathbf{\underline{J}}_{2,A})$. From this follows $\underline{t}_{11} = -\underline{t}_{22}$.

- $\mathbf{\underline{J}}_{1,B} = \mathbf{\underline{T}}\,\mathbf{\underline{S}}_{1,B}$ and $\mathbf{\underline{J}}_{2,B} = \mathbf{\underline{T}}\,\mathbf{\underline{S}}_{2,B}$ yields

$$\mathbf{\underline{J}}_{1,B} = \begin{bmatrix} \underline{t}_{11} & -\underline{t}_{12} \\ \underline{t}_{21} & -\underline{t}_{22} \end{bmatrix} \qquad \mathbf{\underline{J}}_{2,B} = \begin{bmatrix} -\underline{t}_{11} & \underline{t}_{12} \\ -\underline{t}_{21} & \underline{t}_{22} \end{bmatrix}$$

  If $\mathbf{\underline{S}}_{1,B}$ is consimilar to $\mathbf{\underline{S}}_{2,B}$ then $\mathbf{\underline{J}}_{1,B}$ must be similar to $\mathbf{\underline{J}}_{2,B}$. Thus $\mathrm{tr}(\mathbf{\underline{J}}_{1,B}) = \mathrm{tr}(\mathbf{\underline{J}}_{2,B})$. From this follows $\underline{t}_{11} = \underline{t}_{22}$. Together with $\underline{t}_{11} = -\underline{t}_{22}$ this results in $\underline{t}_{11} = \underline{t}_{22} = 0$.

- $\mathbf{\underline{J}}_{1,C} = \mathbf{\underline{T}}\,\mathbf{\underline{S}}_{1,C}$ and $\mathbf{\underline{J}}_{2,C} = \mathbf{\underline{T}}\,\mathbf{\underline{S}}_{2,C}$ yields

$$\mathbf{\underline{J}}_{1,C} = \begin{bmatrix} \underline{t}_{12} & 0 \\ 0 & \underline{t}_{21} \end{bmatrix} \qquad \mathbf{\underline{J}}_{2,C} = \begin{bmatrix} -\underline{t}_{12} & 0 \\ 0 & -\underline{t}_{21} \end{bmatrix}$$

  If $\mathbf{\underline{S}}_{1,C}$ is consimilar to $\mathbf{\underline{S}}_{2,C}$ then $\mathbf{\underline{J}}_{1,C}$ must be similar to $\mathbf{\underline{J}}_{2,C}$. Since $\mathbf{\underline{J}}_{1,C}$, $\mathbf{\underline{J}}_{2,C}$ are diagonal matrices, the diagonal entries are eigenvectors. Since both matrices must have the same eigenvectors, it holds either $\underline{t}_{12} = \underline{t}_{21} = 0$ or $\underline{t}_{12} = -\underline{t}_{21}$, depending on the order of the eigenvectors.

- If $\underline{t}_{12} = -\underline{t}_{21}$, then $\mathbf{\underline{J}}_{1,D} = \mathbf{\underline{T}}\,\mathbf{\underline{S}}_{1,D}$ and $\mathbf{\underline{J}}_{2,D} = \mathbf{\underline{T}}\,\mathbf{\underline{S}}_{2,D}$ yields

$$\mathbf{\underline{J}}_{1,D} = \begin{bmatrix} \underline{t}_{12} & 0 \\ 0 & -\underline{t}_{12} \end{bmatrix} \qquad \mathbf{\underline{J}}_{2,D} = \begin{bmatrix} j\underline{t}_{12} & 0 \\ 0 & -j\underline{t}_{21} \end{bmatrix}$$

  If $\mathbf{\underline{S}}_{1,D}$ is consimilar to $\mathbf{\underline{S}}_{2,D}$ then $\mathbf{\underline{J}}_{1,D}$ must be similar to $\mathbf{\underline{J}}_{2,D}$. The diagonal entries of $\mathbf{\underline{J}}_{1,D}$ and $\mathbf{\underline{J}}_{2,D}$ must be the same eigenvectors again. Therefore $\underline{t}_{12} = \underline{t}_{21} = 0$.

From $\underline{t}_{11} = \underline{t}_{12} = \underline{t}_{21} = \underline{t}_{22} = 0$ follows $\mathrm{rank}(\mathbf{\underline{T}}) = 0$, which contradicts the initial assumption.   □

It was shown that the simplified decomposition will not succeed if $\mathbf{\underline{T}}$ is full-rank and target-independent. For completeness it should be mentioned that this is also true if $\mathrm{rank}(\mathbf{\underline{T}}) = 1$. This can be shown by describing $\mathbf{\underline{T}}$ with two linearly dependent row vectors $\mathbf{t}_1 = \underline{c}_1[\underline{t}_1 \quad \underline{t}_2]$ and $\mathbf{t}_2 = \underline{c}_2[\underline{t}_1 \quad \underline{t}_2]$ so that $\mathbf{\underline{T}} = [\mathbf{t}_1 \quad \mathbf{t}_2]^T$. The proof follows from the matrices $\mathbf{\underline{S}}_{1,A}$, $\mathbf{\underline{S}}_{2,A}$, $\mathbf{\underline{S}}_{1,B}$ and $\mathbf{\underline{S}}_{2,B}$ by reasoning similar to Theorem 1. For the trivial case $\mathrm{rank}(\mathbf{\underline{T}}) = 0$ the eigenvalues of $\mathbf{\underline{J}}$ are always zero and different targets are therefore indistinguishable. Thus the simplified decomposition will not succeed for any target-independent $\mathbf{\underline{T}}$. This also includes the transformation matrix in (2) which was derived in [12].

3. TARGET-DEPENDENT TRANSFORMATION MATRICES

It is possible to give a physical explanation of the results of Section 2. The coneigenvalue decomposition in (1) changes the polarization basis of $\mathbf{\underline{S}}$ in a way which leads to a diagonalization of $\mathbf{\Sigma}$ [7, 8]. Since the transformation matrix in (2) was derived for a linear polarization base only [12], this matrix is susceptible to fail for nonlinear polarization bases.

However, if $\mathbf{\underline{T}}$ changes with $\mathbf{\underline{S}}$ and thus depends on the target's properties, the simplified decomposition can be applied. This is shown in the following proof:

Theorem 2. *Let M_2 be the set of all 2×2-matrices. For arbitrary $\mathbf{\underline{S}}_1, \mathbf{\underline{S}}_2 \in M_2$ distinct full-rank matrices $\mathbf{\underline{T}}_1$, $\mathbf{\underline{T}}_2$ can be constructed for which the following property holds: $\mathbf{\underline{J}}_1 = \mathbf{\underline{T}}_1\,\mathbf{\underline{S}}_1$ is similar to $\mathbf{\underline{J}}_2 = \mathbf{\underline{T}}_2\,\mathbf{\underline{S}}_2$ iff $\mathbf{\underline{S}}_1$ is consimilar to $\mathbf{\underline{S}}_2$.*

Proof. In the following all matrices will be denoted using the index $i \in \{1, 2\}$. This results in the six matrices $\underline{\mathbf{S}}_i$, $\underline{\mathbf{T}}_i$ and $\underline{\mathbf{J}}_i$.

- Let there be $\underline{\mathbf{J}}_0 \in M_2$ which is similar to both $\underline{\mathbf{J}}_i$. In this case $\underline{\mathbf{J}}_0 = \underline{\mathbf{U}}_i^H \underline{\mathbf{J}}_i \underline{\mathbf{U}}_i$ for unitary $\underline{\mathbf{U}}_i$. Due to the transitivity of matrix similarity also both $\underline{\mathbf{J}}_i$ are similar to each other. The matrices $\underline{\mathbf{T}}_i$ can now be defined to $\underline{\mathbf{T}}_i = \underline{\mathbf{U}}_i \underline{\mathbf{U}}_i^T$. This yields

$$
\begin{aligned}
\underline{\mathbf{J}}_0 &= \underline{\mathbf{U}}_i^H \underline{\mathbf{J}}_i \underline{\mathbf{U}}_i \\
&= \underline{\mathbf{U}}_i^H \underline{\mathbf{T}}_i \underline{\mathbf{S}}_i \underline{\mathbf{U}}_i \\
&= \underline{\mathbf{U}}_i^H \underline{\mathbf{U}}_i \underline{\mathbf{U}}_i^T \underline{\mathbf{S}}_i \underline{\mathbf{U}}_i \\
&= \underline{\mathbf{U}}_i^T \underline{\mathbf{S}}_i \underline{\mathbf{U}}_i
\end{aligned}
$$

  Since this is a consimilarity transformation, both $\underline{\mathbf{S}}_i$ are similar to $\underline{\mathbf{J}}_0$. Therefore also both $\underline{\mathbf{S}}_i$ are consimilar to each other.

- Conversely, let there be $\underline{\mathbf{S}}_0 \in M_2$ which is consimilar to both $\underline{\mathbf{S}}_i$. In this case $\underline{\mathbf{S}}_0 = \underline{\mathbf{U}}_i^T \underline{\mathbf{S}}_i \underline{\mathbf{U}}_i$ for unitary $\underline{\mathbf{U}}_i$. Due to the transitivity of matrix consimilarity also both $\underline{\mathbf{S}}_i$ are consimilar to each other. Moreover, $\underline{\mathbf{S}}_i = \underline{\mathbf{T}}_i^{-1} \underline{\mathbf{J}}_i$ since both $\underline{\mathbf{T}}_i$ have full rank. The matrices $\underline{\mathbf{T}}_i$ can now be defined to $\underline{\mathbf{T}}_i^{-1} = \underline{\mathbf{U}}_i^* \underline{\mathbf{U}}_i^H$. This yields

$$
\begin{aligned}
\underline{\mathbf{S}}_0 &= \underline{\mathbf{U}}_i^T \underline{\mathbf{S}}_i \underline{\mathbf{U}}_i \\
&= \underline{\mathbf{U}}_i^T \underline{\mathbf{T}}_i^{-1} \underline{\mathbf{J}}_i \underline{\mathbf{U}}_i \\
&= \underline{\mathbf{U}}_i^T \underline{\mathbf{U}}_i^* \underline{\mathbf{U}}_i^H \underline{\mathbf{J}}_i \underline{\mathbf{U}}_i \\
&= \underline{\mathbf{U}}_i^H \underline{\mathbf{J}}_i \underline{\mathbf{U}}_i
\end{aligned}
$$

  Since this is a similarity transformation, both $\underline{\mathbf{J}}_i$ are similar to $\underline{\mathbf{S}}_0$. Therefore also both $\underline{\mathbf{J}}_i$ are similar to each other.

Therefore $\underline{\mathbf{J}}_1$ is similar to $\underline{\mathbf{J}}_2$ iff $\underline{\mathbf{S}}_1$ is consimilar to $\underline{\mathbf{S}}_2$. $\qquad \square$

Although this approach seems to enable the simplified decomposition in an easy way, the transformation matrices $\underline{\mathbf{T}}_i$ in the proof of Theorem 2 require the knowledge of the matrices $\underline{\mathbf{U}}_i$. These matrices are connected to $\underline{\mathbf{S}}_i$ via a consimilarity transformation to the unknown matrix $\underline{\mathbf{S}}_0$. Therefore the construction of the transformation matrices $\underline{\mathbf{T}}_i$ is again based on consimilarity. Since the simplified decomposition was analyzed to prevent the application of methods from this field, this decomposition does not allow to retrieve the Huynen-Euler parameters in the desired manner.

4. CONCLUSION

Within this paper it was shown that the matrix $\underline{\mathbf{T}}$ constructed in [12] cannot be used for a simplification of the coneigenvalue decomposition of $\underline{\mathbf{S}}$ by eigenvalue decomposition of $\underline{\mathbf{J}} = \underline{\mathbf{T}} \underline{\mathbf{S}}$. This is also true for any other matrix $\underline{\mathbf{T}}$ which does not depend on $\underline{\mathbf{S}}$. If $\underline{\mathbf{T}}$ depends on $\underline{\mathbf{S}}$, then the eigenvalue decomposition of $\underline{\mathbf{T}} \underline{\mathbf{S}}$ will deliver valid results. However, the proof of Theorem 2 implies that $\underline{\mathbf{T}}$ can only be acquired using consimilarity transformations. Therefore a simplification of the coneigenvalue decomposition is not possible without shifting the underlying mathematical problem to other parts of the decomposition process. Due to this coneigenvalue decompositions still require extensive research to solve the problems related to the decomposition of the Sinclair matrix into Huynen-Euler parameters.

REFERENCES

1. *Single vs Multi-Polarisation SAR Data*, PolSARpro documentation, European Space Agency, 2005.
2. Lee, J. and E. Pottier, *Polarimetric Radar Imaging: From Basics to Applications*, CRC Press, Boca Raton, 2009.
3. *IEEE Standard for Definitions of Terms for Antennas*, IEEE Standard 145, 2013.
4. Huynen, J. R., *Phenomenological Theory of Radar Targets*, Ph.D. dissertation, TU Delft, 1970.
5. Baird, C. S., *Design and Analysis of an Euler Transformation Algorithm Applied to Full-polarimetric ISAR Imagery*, Ph.D. dissertation, University of Massachusetts Lowell, Massachusetts, 2007.

6. Dallmann, T. and D. Heberling, "Discrimination of scattering mechanisms via polarimetric rcs imaging [measurements corner]," *IEEE Antennas and Propagation Magazine*, Vol. 56, No. 3, 154–165, 2014.

7. Serbest, A. H. and S. Cloude, *Direct and Inverse Electromagnetic Scattering*, CRC Press, Boca Raton, 1996.

8. Lüneburg, E., "Aspects of radar polarimetry," *Turk J. Elec. Engin.*, Vol. 10, No. 2, 219-243, 2002.

9. Horn, R. A. and C. R. Johnson, *Matrix Analysis*, Cambridge University Press, Cambridge, 2013.

10. Jiang, T. and M. Wei, "On the reduction of a complex matrix to triangular or diagonal by consimilarity," *Numerical Mathematics: A Journal of Chinese Universities (English Series)*, Vol. 15, No. 2, 107-112, 2006.

11. Golub, G. H. and C. F. Van Loan, *Matrix Computations*, John Hopkins University Press, Baltimore, 2009.

12. Ulaby, F. T. and C. Elachi, *Radar Polarimetry for Geoscience Applications*, Artech House, Norwood, 1990.

Detection of Breast Tumors by Applying FDTD Modelling of Holographic Radar

I. L. Alborova and L. N. Anishchenko

Biomedical Engineering Department, Bauman Moscow State Technical University
5, 2d Baumanskaya str., Moscow 105005, Russia

Abstract— This paper presents the results of mathematical simulation carried out to confirm the ability of holographic radar to detect breast tumors. The simulation software used the Finite-Difference Time-Domain Method. The simulations were performed for three different scenarios: in the first model the inclusion depth under the surface was varied; for the second model two inclusions were used; while the dielectric properties of malignant tissue were modified in the third model. The model is a 3D block with dimensions $200 \times 200 \times 100$ mm, which mimicked normal breast tissue, with one or two spherical inclusion — malignant neoplasm of breast tissue. Frequency dispersion of normal and malignant tissues dielectric properties (conductivity and permittivity) was taken into account.

The results showed that differences in the dielectric properties allow to use of the radiolocation method for detecting inclusion (diameter 4 mm) on a depth up to 5 mm. The results proved that the greatest impact on the detection of inclusion has a ratio of conductivity values of normal and malignant tissues. Also the proposed method makes possible to distinguish two different objects at the distance between them of 16 mm or more, otherwise they will be identified as one inclusion.

1. INTRODUCTION

Nowadays one of the most topical problems in medical diagnostics is early breast cancer detection. In some countries this pathology is the leading cause of death among the women. Every 9th female in the USA is under the risk of this highly dangerous disease. As a rule, the routine diagnostic procedure consists of individual examination by doctors and mammography or ultrasound screening. Screening for early detection of breast cancer is conducted by these methods at 12–24 month intervals, which cannot guarantee identification of aggressive tumors [1].

In addition, however rarely, such methods as computed tomography, positron-emission tomography, magnetic resonance imaging, all kinds of biopsy are applied. They allow to purposefully look for certain changes in the mammary glands and specify their cause, nature and prevalence [2]. However, none of them is applicable for routine scanning because of high cost, prolonged time of a diagnostic procedure and invasiveness (for biopsy). Therefore, it is advisable to complete a routine diagnostic procedure using a different noninvasive screening method, which could detect tumors at the earliest possible stage [3].

In this paper we describe the results of the mathematical simulation carried out to confirm the possibility of using holographic radar for the detection of breast tumors. It is known that the dielectric properties of normal and malignant breast tissues differ even at the earliest stage of tumor genesis. Thus, frequent scans with a holographic radar could be used for safe early stage breast tumor detection. Although at present there is a growing interest in literature in the usage of ultra-wideband radars for breast malignant tumors detection, these devices have not yet achieved the necessary accuracy and specificity when applied on realistic breast phantoms. During the experiments the software designed for the numerical solution of electromagnetic problems using the Finite-Difference Time-Domain Method was applied, which description are given in paragraph 2. Paragraph 3 presents the results of mathematical simulation for three scenarios: for the first model inclusion's depth under the surface was varied; for the second model two inclusions were placed into a tissue; for the third, dielectric properties of malignant tissue were modified.

2. METHODS

In the work the software XFdtd [4] was used, which is designed for the numerical solution of electromagnetic problems using the Finite-Difference Time-Domain Method, which solves Maxwell's equations for the electric and magnetic fields.

In the experiments is realistic phantoms of a mammary gland, which are planned to be carried put in future, we suppose to use a multi-frequency holographic radar RASCAN-5/7000 designed at Bauman Moscow State Technical University with the frequency range 6.6–7.0 GHz [5]. Therefore

simulation, which is described in this article, was carried out at a frequency of 7 GHz for estimating theoretically achievable values of resolution and penetration depth.

3. FDTD MODELLING OF HOLOGRAPHIC RADAR

In the used simulation environment the objects can be created in the graphical editor window using the built-figures, or imported from other systems of automated programming. The fragment of a breast was modeled as a 3D block with dimensions $200 \times 200 \times 100$ mm. It is mimicking the normal tissue of the breast, with a spherical inclusion — malignant neoplasm of breast tissue.
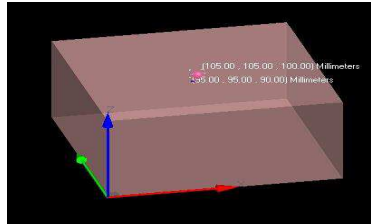
Figure 1: The model geometry.

The dielectric properties depend on the probing frequency. The conductivity and relative permittivity values for the model are listed below [6] (Table 1).

Table 1: Dielectric properties of normal and malignant tissues [6].

Frequency	Normal tissue		Malignant tissue	
	Conductivity [Sm/m]	Relative permittivity	Conductivity [Sm/m]	Relative permittivity
7 GHz	0.26	4.4	8.1	50.8

Outer-boundaries were set to be absorbing. The model was divided into 5 segments. In the area $[90; 110]$ the cell size was 1 mm; in the area $[80; 90]$ and $[110; 120]$-2 mm, in the area $[0; 80]$ and $[120; 200]$-4 mm (Fig. 2).
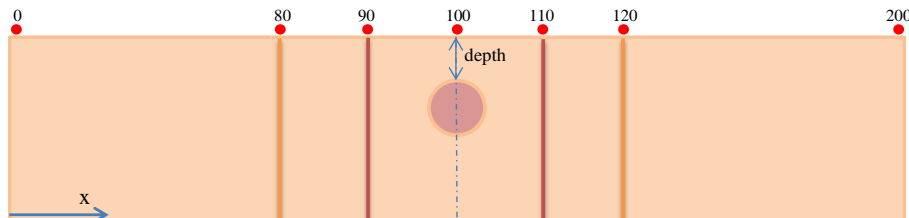
Figure 2: Scheme of the model.

Outer-boundaries were set to be absorbing. For each receiver we calculated y-component of electric field $|\dot{E}_y|$. Results of an absolute values $|\dot{E}_y|$ calculation are presented in Fig. 3.

The peak of $|\dot{E}_y|$ amplitude is located directly over tumor. Side peaks are cased by the edge effects For the further simulation we used only selected points in the central zone from 80 mm till 120 mm.

Three different imaging scenarios were analyzed.

In the first imaging experiment (Fig. 4), $|\dot{E}_y|$ was calculated for the model with the inclusion of 4 mm and its depth of 2, 4, 6 mm.

The results of the simulation (Fig. 4) proved that it is possible to detect a tumor with size of 4 mm at a depth up to 4–5 mm by using a probing frequency of 7 GHz.

In the second imaging experiment, two spherical inclusions were placed inside the block simulating the normal tissue. The distance between inclusions was varied.

As can be seen from Fig. 5 the proposed method do not allow to distinguish two inclusions as separate ones if they are placed closer than 15 mm.
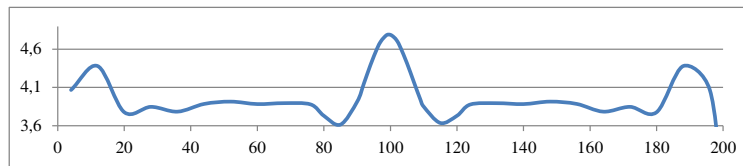
Figure 3: Scattered $|\dot{E}_y|$ values at $7\,\mathrm{GHz}$, inclusion size is $4\,\mathrm{mm}$, depth $= 2\,\mathrm{mm}$.
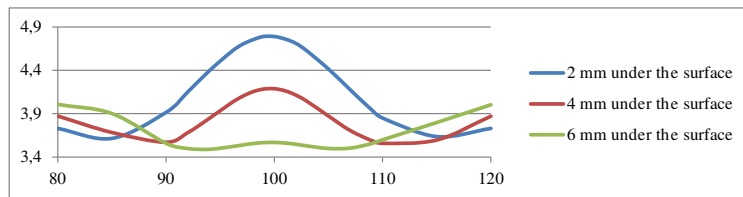
Figure 4: Scattered $|\dot{E}_y|$ values at $7\,\mathrm{GHz}$, inclusion's size is $4\,\mathrm{mm}$.
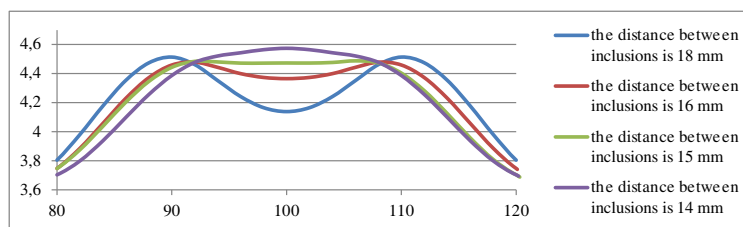
Figure 5: Scattered $|\dot{E}_y|$ values at $7\,\mathrm{GHz}$ probing frequency, inclusions' size are $4\,\mathrm{mm}$.

Table 2: Dielectric properties of malignant tissues.

Malignant tissue			
Conductivity [Sm/m]		Relative permittivity	
Scale factor	Value	Scale factor	Value
1.0	8.10	1.0	50.80
0.7	5.67	0.9	45.72
0.5	4.05	0.7	35.56
0.4	3.24	0.5	25.40
0.3	2.43	0.3	15.24
0.1	0.81	0.1	5.08
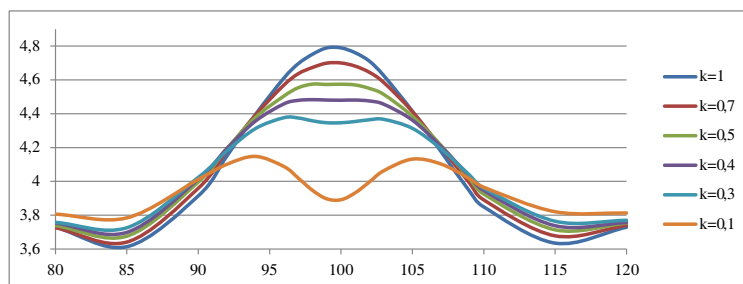
Figure 6: Scattered $|\dot{E}_y|$ values at $7\,\mathrm{GHz}$, inclusion's size is $4\,\mathrm{mm}$ (the conductivity of malignant tissue is varied).

In the scientific literature there are no data on the effect depending on a fat/fibrous tissue ratio in the breast, which changes with age synd depends on the physiological state of each woman. In this work mathematical modeling of a situation in which the ratio in the structure of breast increases was carried out. Table 2 shows the values of the dielectric properties of malignant tissue of the

breast, which we used in simulation. Table 2 uses data from a large-scale study of the ultrawideband microwave dielectric properties of normal, benign and malignant breast tissues obtained from cancer surgeries conducted by Lazebnik, et al. [6].

Results of the simulation revealed that it is impossible to detect the tumor if the conductivity value for the malignant tissue decreases for more than 50%. However even if the relative permittivity of malignant and normal tissue are equal, it is still possible to detect the tumor (Figs. 6, 7).
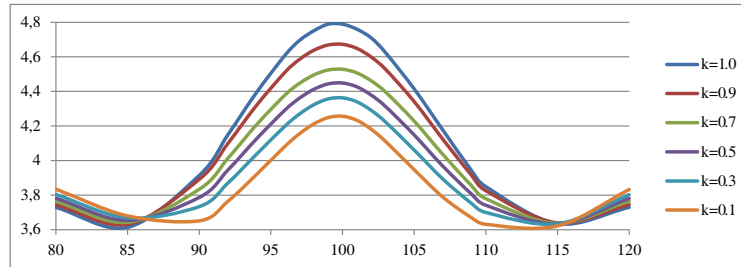
Figure 7: Scattered $|\dot{E}_y|$ values at 7 GHz, inclusion's size is 4 mm (the relative permittivity of malignant tissue is varied).

4. CONCLUSION

Experimental results showed that the maximum depth of the inclusion (diameter 4 mm) detection by the proposed method does not exceed 5 mm, it is due to the strong attenuation of electromagnetic radiation in the medium. This depth limit can be increased by using lower frequencies at the expense of resolution and by using matched antennas. The proposed method allows to distinguish two different inclusions at the distance of 16 mm or more, otherwise they will be identified as one. Variation of biological tissue conductivity in physiological adequate limits has stronger influence on the possibility of an inclusion detection compared to the same parameter for relative permittivity.

ACKNOWLEDGMENT

REFERENCES

1. Vershinina, S. and E. Potyavina, "Breast disease. Modern methods of treatment," *Krylov*, 2009.
2. Kulikov, E. P. and B. M. Warren, "Breast cancer," *Ryazan*, 75 pages, 2002.
3. Ivashov, S. I., V. V. Razevig, I. A. Vasiliev, A. V. Zhuravlev, T. D. Bechtel, and L. Capineri, "Holographic Subsurface Radar of RASCAN type: Development and applications," *IEEE Journal of Selected Topics in Earth Observations and Remote Sensing*, Vol. 4, No. 4, 2011.
4. REMCOM, "XFdtd® EM simulation software," URL: http://www.remcom.com/xf7, 2013.
5. Anishchenko, L. N., A. A. Demendeev, S. I. Ivashov, V. V. Razevig, I. A. Vasiliev, and T. D. Bechtel, "Holographic radar in breast cancer imaging," *RADARCON*, 1004–1007, Atlanta, USA, 2012.
6. Lazebnik, M., L. McCartney, D. Popovic, C. B. Watkins, M. J. Lindstrom, J. Harter, S. Sewall, A. Magliocco, J. H. Booske, M. Okoniewski, and S. C. Hagness, "A large-scale study of the ultrawideband microwave dielectric properties of normal breast tissue obtained from reduction surgeries," *Physics in Medicine and Biology*, Vol. 52, 2637–2656, 2007.

Characterization of the Electromagnetic Propagation through Building Rubble by Means of Numerical Random Models

I. Lucresi, **E. Di Giampaolo**, and **P. Tognolatti**

Department of Industrial and Information Engineering and Economics, University of L'Aquila, Italy

Abstract— In this work we propose random models representing collapsed building rubble to evaluate phenomena of attenuation and propagation of radio signal through this kind of transmission medium. The aim of the work is to offer a valid propagation channel model to facilitate, in case of emergency, rescue operations using modern technologies employing RF signals. The models involves different materials and the propagation is examined for several conditions of the rubble (degree of compression, graininess etc.). The study permits to estimate the Path Loss by calculating mean, standard deviation and minimum value for a large number of scenarios to provide a statistical analysis of the collected data.

1. INTRODUCTION

The rescue of victims buried in building rubble because of earthquakes, landslides, explosions in industrial plants or terrorist attacks, can take advantage from real-time measurements employing wireless communications devices.

Rising technologies like rescue robots, allow rubble exploration and victims localization exploiting radio signal transmissions [1, 2]. Moreover, radio detection of vital signs or detection of radio signals emitted by personal RF devices (e.g., cell-phone, radios, RFID, etc.) that may be close to the owner (especially in case of rescuers involved in subsequent collapses) can be very useful in post emergency operations since immediacy of action may lead to a considerable reduction in the number of victims [4–8]. For these reasons communications plays a big role in this kind of systems. These operations efficacy however, is strictly related to the characteristics of propagation channel in the disaster scenario. Attenuation, multipath and noise make the radio-link weak and untrustworthy, in spite of this adequate systems can be designed if a sufficiently accurate knowledge of the features of the propagation channel is available.

This work has been developed after the earthquakes which stroked the Italian territory in the last years. The considered scenarios are then composed by rubble and debris of collapsed buildings, that is a very complex environment because of different materials, morphologies of urban fabric involved and physical characteristics of rubble and debris (i.e., shape, dimensions, humidity and level of compression), for which no general channel model exists [9–11]. The characterization of electromagnetic propagation in complex medium consisting of different materials arranged in random and variable manner as building rubble is very difficult and there are few studies on this topic in the literature. Some models are based on artificial scenarios while other are specialized to specific models as the layered model of rubble [10] which unfortunately seems too ordered and simplified when compared to real cases.

In this work, in a completely new way compared to the literature, we simulate different models of rubble to evaluate phenomena of attenuation and propagation of radio signal through an extremely heterogeneous transmission medium structured in a not predictable manner.

The aim of the work is the development of a random model of the rubble that would reflect a wide range of environments, for this reason random rubble scenarios were generated and simulated through an electromagnetic tool where the transmission source is represented by a dipole antenna buried into rubble. The model involves typical materials, in established and plausible proportions, of both modern buildings (concrete, bricks and iron) and ancient ones (stones and bricks). A number of parameters characterize the model of the rubble: the degree of compression (defined as the ratio between the empty and filled spaces), the graininess (i.e., the size of the blocks of homogeneous material), the number of different materials, the dielectric properties of each material, the moisture, the thickness of the layers (one or more layers are considered). A large number of simulations have been performed for different frequencies: at 13 MHz, 432 MHz and 900 MHz. These frequencies have been chosen because they mainly concern rescue devices and are near the frequency bands of many communication services in Italy and European Countries. The study is focused on the analysis of Path Loss at different heights from the ground and for various angles of incidence of

the electromagnetic wave. A statistical analysis of data are also carried out by calculating mean, standard deviation and minimum value of Path Loss for a large number of simulations.

The proposed model takes cue from a measurement campaign carried out in a number of buildings collapsed or partially destroyed in L'Aquila territory that was stroked by a severe earthquake in 2009 [12, 13].

Comparison between model results and measurement data allow us the tuning of the model parameters and is under development.

In the following sections the developed models and the simulation results are shown.

2. PROPOSED MODEL

We propose a realistic numerical model made up of cubes of various materials and sizes arranged in a random way to represent the scenario of a collapsed building with good approximation. It plies blocks of different materials to form a heap having the shape of a big prism with square basis. Each block has the dielectric properties of a material randomly selected from a predefined list. Also blocks of air are included in the model to take into account the void spaces present in a real heap of rubble. The heap of rubble is resting on a layer of moist soil having dielectric characteristics to absorb the electromagnetic radiation completely, so that it permits to simulate the behavior of the real soil conditions with a layer of reduced thickness. A transmitter is placed in the heap of rubble at a point near to the soil. It is modeled as an ideal voltage generator connected to the terminals of a dipole antenna. The propagation through the rubble and out of the heap of rubble is studied by means of a full-wave analysis based on FDTD (or similar Time-Domain approaches, e.g., FIT — Finite Integration Technique) method. Because FDTD is computational cumbersome the geometrical size of the model is limited to $5\,\text{m} \times 5\,\text{m}$ corresponding to a medium/large room in order to have a manageable computational charge. Numerical analysis has been performed on a personal computer having 48 GB RAM and twelve 2Core Intel processors.

The model involves typical materials, in established and plausible proportions, of both modern buildings (concrete, bricks and iron) and ancient ones (stones, mortar and bricks). A number of parameters characterize the model of the rubble: the degree of compression (defined as the ratio between the empty and filled spaces), the graininess (i.e., the size of the blocks of homogeneous material), the number of different materials, the dielectric properties of each material, the moisture, the thickness of the layers (one or more layers are considered).

2.1. Materials

Modern buildings made of concrete and ancient ones in stone and sand are considered. In Table 1 the list of used materials and the corresponding dielectric parameters are reported [14–18], iron is also included but it is modeled as PEC material. For the ground a relative dielectric constant of $\varepsilon_r = 10$ and a conductivity of $\sigma = 0.1\,\text{S/m}$ are assumed [13].

These parameters are constant for all simulation frequencies.

Table 1: List of materials.

Material	ε_r	σ [S/m]
Concrete	6	0.005
brick	4.45	0.031
stone	4	0.02
sand	3	0.01

2.2. Degree of Compression

A significant parameter, typical of each real condition, is the level of compression of the rubble. Here, it is defined as the ratio between full and empty space for the scenarios.

Naming V_{solid} the volume occupied by walls and ceiling (i.e., $V_{\text{solid}} = V_{\text{walls}} + V_{\text{ceiling}}$), V_{air} the volume of the empty spaces inside rubble and V_{tot} the total volume occupied after the collapse, the degree of compression is

$$\text{DoC}(\%) = \frac{V_{\text{solid}}}{V_{\text{air}}} \cdot 100 = \frac{V_{\text{walls}} + V_{\text{lofts}}}{V_{\text{tot}}} \cdot 100 \tag{1}$$

As an example, assuming that a room of $25\,\text{m}^2$, $3\,\text{m}$ height and thickness of walls and ceiling of $25\,\text{cm}$ and $30\,\text{cm}$ respectively collapses into a pile of rubble of height $1.5\,\text{m}$ the degree of compression is about 40%, i.e., 40% of the space is occupied by rubble after the collapse.

2.3. Percentage of Materials

The quantity of each material, i.e., the volume of a given material with respect to V_{solid} depends on the building typolgy. In case of concrete buildings, the percentage has been determined according to the Italian rules for building construction it has been set to: 57% brick, 40% concrete, 3% reinforcement iron. For scenarios concerning antique stone buildings the materials considered are, instead, stone, construction sand and brick in respective percentages of 60%, 30% and 10%.

2.4. Graininess

The size of the blocks of homogeneous material is variable and uncertain. In case of old building, it corresponds to the size of stones used in the construction and it depends on building typology. Typically, in historic center of Italian and European towns, roughly squared stone blocks mixed with bricks and dressed stone blocks are used. Large squared stone blocks are used for quoins in both common buildings and mansions. In case of concrete buildings, the uncertainty of the size of homogeneous blocks are greater than that of old building because some structural parts of the building (e.g., reinforced concrete beam) may be collapsed intact while other parts (e.g., bricks) are crushed.

For these reasons the size of the single block is considered a variable of the model, similar scenarios having all the model parameters identical except for the size of the blocks are analyzed. Two different sizes are considered in order to analyze the effects that debris dimension has on the propagation of the electric field. In particular, cube blocks with side of $20\,\text{cm}$ and $50\,\text{cm}$ are considered.

2.5. Model Generation

Because of the extreme variety of scenarios in an actual collapse, a statistical analysis based on the generation of a large number of random models is required to characterize the propagation channel. A large amount of numerical data is necessary to obtain statistical significant results. A computer code able to generate automatically different random scenarios and to perform the electromagnetic analysis is developed. It is based on two simulation tools: CST Microwave Studio and Matlab.

The FIT (Finite Integration Technique) solver of CST is used to perform the analysis of each random scenario. CST generates a file.mod (Model.mod) which contains all the simulation settings of a scenario, i.e., geometrical description of the scenario, materials properties, measurement unit, frequency range, field monitors, transmitted electric field intensity etc.. Instead of using the software graphical interface to generate that file, the template file is written as a text file using Matlab after generating the single random scenario.

A scenario consists of cubic blocks randomly arranged in an area of $25\,\text{m}^2$ to form a heap $1.5\,\text{m}$ high, the developed Matlab code uses a 3D matrix (A) of random elements (of dimensions $25\times25\times8$ for cubes with side $20\,\text{cm}$ and $10\times10\times3$ in the case of cubes with side $50\,\text{cm}$) in which each element represents a cube of material. The type of material of each cube is determined taking into account the percentage of each material and the degree of compression of the rubble. In Table 2 an example of allocation of materials for representative scenarios of concrete building is shown. A variable q is considered, it can randomly assume values between 0 and 1 with uniform distribution. For each cube having indices (i, j, k) the value of q is randomly extracted, if $q \leq 0.012 = 3\%$ of 40% the PEC material is assigned to that cube, if $0.012 \leq q \leq 0.242 = 57\%$ of 40% brick properties are assigned, if $0.242 \leq q \leq 0.4 = 40\%$ of 40% the cube has the property of concrete otherwise it is made of air. At the boundary PML absorbing conditions are imposed, any cube made of PEC and located at the sides of the scenario are removed and replaced by air. Also the buried dipole is surrounded by air assuming it is placed in a void space inside the rubble. Once the matrix is generated, Matlab calculates the coordinates of each cube in the scenario and write the mod-file inserting in the header the absorbing boundary conditions, the calculation domain and the parameters of the mesh to be adopted and all other simulation parameters, then it continues with the description of the other structures involved (soil, cubes and dipole antenna). Fig. 1 shows two examples of scenarios obtained with the described method while Fig. 3 shows a layered scenario with interspaces randomly filled.

Finally, the Matlab code starts the running of a batch file, which launches the CST solver with the current generation of the mod-file. Once the electromagnetic simulation terminates the results

Table 2: Material allocation.

Matrix element value	Assigned material
$A(i,j,k) <= 0.012$	PEC
$0.012 < A(i,j,k) <= 0.242$	brick
$0.242 < A(i,j,k) <= 0.4$	concrete
$0.4 < A(i,j,k) <= 1$	air

(a)   (b)
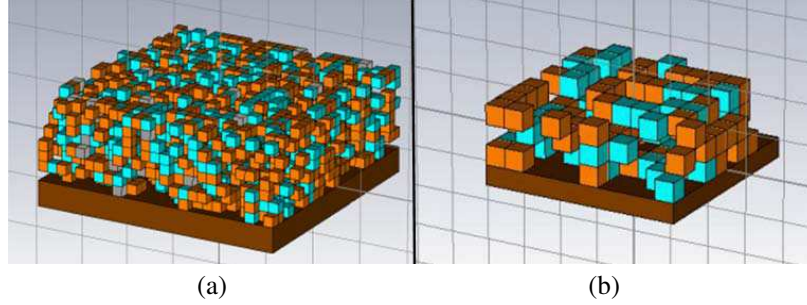
Figure 1: Random scenarios. Cubes with side of (a) 20 cm and (b) 50 cm. Colour: orange for brick, blue for concrete, gray for iron, brown for soil.
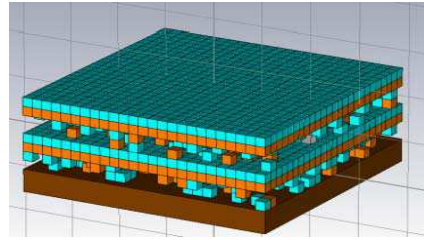
Figure 2: Layered model.

are saved, a new environment is made and a new simulation starts again with automatic process.

Three different frequencies are considered: 13 MHz 432 MHz and 900 MHz, buried dipole antenna is a short dipole at the frequency of 13 MHz and in a $\lambda/2$ dipole at the frequencies of 432 MHz and 900 MHz.

3. SIMULATION RESULTS

Aim of the work is the investigation of the possibility to localize a buried antenna starting from the analysis of the electric field on a plane located 0.5 m above the pile of rubble. The path loss and the phase of the received signal are evaluated at the points of that plane.

A virtual antenna is used at any receiving point. At 13 MHz ($\lambda = 23$ m) a short dipole of length 23 cm is used. It is characterized by a radiation resistance of

$$R_r = 80\pi^2 \left(\frac{l}{\lambda}\right)^2 = 0.08\Omega \tag{2}$$

and effective height

$$\underline{h}(\vartheta) = \frac{l}{2} sen(\vartheta) \, \hat{\underline{\vartheta}} \tag{3}$$

being ϑ the angle of the observation point with respect to the dipole axis.

The received power is therefore

$$P_R = \frac{1}{8} \frac{|V_a|^2}{R_r} \quad \text{with} \quad V_a = \underline{h}(\vartheta) \cdot \underline{E} \tag{4}$$

Being the power transmitted (P_T) by the buried dipole known, the path loss (PL) is calculated

exploiting (4), i.e.,

$$PL = -10 \log \left(\frac{P_R}{P_T} \right). \tag{5}$$

At 432 MHz ($\lambda = 69$ cm) or 900 MHz ($\lambda = 33$ cm), instead, a virtual half wavelength ($\lambda/2$) dipole is considered, for which the radiation resistance is $Rr = 73.13\,\Omega$ and the effective height is calculated as

$$\underline{h}(\vartheta) = \frac{\lambda}{\pi} \frac{\cos\left(\frac{\pi}{2}\cos(\vartheta)\right)}{sen(\vartheta)} \hat{\underline{\vartheta}} \tag{6}$$

For a given realization of the scenario we obtain numerical data of the electromagnetic field inside and outside the rubble. In Fig. 3 it is shown, as an example, the obtained electric field at points of a plane placed 0.5 m above the rubble. It is obtained for rubble having DoC = 40%, size of the cube 20 cm and frequency 423 MHz. Both amplitude and phase are calculated in order to evaluate the possibility to detect the buried transmitting dipole by means amplitude and phase measurements. In the reported case, amplitude is stronger in the nearness of the vertical projection of the buried dipole while phase shows a characteristic behaviour made of concentric equi-phase lines (like wavefronts) centered in the nearness of the vertical to the transmitter.

(a)　　　　　　　　　　　　　　　　(b)
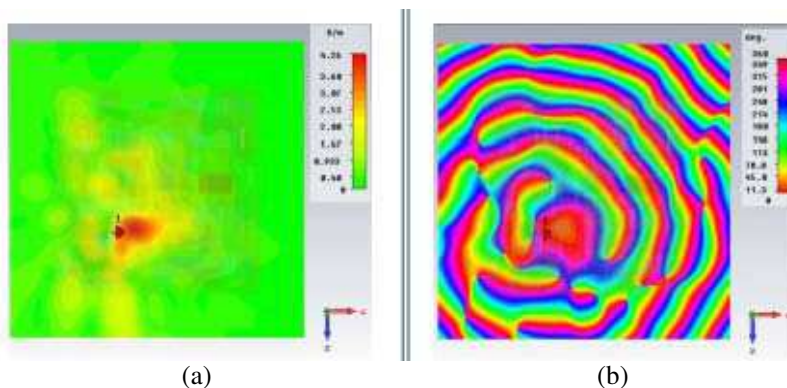
Figure 3: (a) Amplitude and (b) phase of electric field on a plane 0.5 m above rubble at 432 MHz, DoC = 40%, cube side = 20 cm.

The analysis of numerical data for different parameters of the scenario, in particular the frequency and the size of the cubes, allows us to have an in depth knowledge of the propagation inside that model of rubble. At lower frequency (i.e., 13 MHz) the map of field amplitude on a plane above the rubble shows a spot of strong field amplitude (like that of Fig. 2) but the phase has a coarse map because of the large length of the wavelength. Therefore amplitude measurements are more suited to be used for localization than phase measurements. At higher frequency (i.e., 900 MHz) instead the amplitude map shows different peaks of the maximum field spread all over the considered area. On the other hand the phase map preserves the almost circular equi-phase lines so that, at higher frequency, phase measurements appear more adequate for localization than amplitude measurements.

Considering the analysis by varying the size of the rubble, i.e., the size of the cube, it appears that larger is the size of the rubble lower are the spread of peaks of the maximum of the emerging field while the phase map is better represented by concentric equi-phase lines.

Here, we show results for four scenarios having different model parameters, in particular at the frequency of 432 MHz.

The first and second scenarios have DoC = 40% and rubble size 20 cm and 50 cm, the third scenario concerns DoC = 30% and rubble size 20 cm while the fourth scenario is a stratified model made up of four layers of homogeneous thickness (20 cm). Each layer consists alternately of concrete and bricks interspersed with layers where the ratio between materials and air is 20% (Fig. 2). This whole scenario has a ratio between full volume and total volume of 60%, is therefore characteristic of a situation in which the rubble are more compressed than in the other cases. For each type of scenario 30 realizations (i.e., simulations) are considered.

To have a quantitative analysis of the possibility to localize a buried transmitter using an amplitude map, the distance between the maximum of the electric field module or the maximum of

Table 3: Localization uncertainty.

scenario	variable	$e_{\min}$ (cm)	e_{avg} (cm)	$e_{\max}$ (cm)
1: DoC = 40% cube size 20 cm	Elettric field module	11	51	88
	Power flow module	12	52	106
2: DoC = 40% cube size 50 cm	Elettric field module	13	49	145
	Power flow module	11	49	115
3: DoC = 30% cube size 20 cm	Elettric field module	29	80	190
	Power flow module	24	73	188
4: DoC = 60% layered	Elettric field module	9	67	90
	Power flow module	14	67	139

the power flow module and the projection of the transmitting dipole position onto the observation plane, is determined. Table 3 shows the values of maximum, minimum (i.e., $e_{\max}$ and $e_{\min}$) and average value of the localization uncertainty. Note that there is not a simple relationship between the changing of the DoC of the scenario and the uncertainty of localization instead it seems to exist for the size of the rubble. In fact, smaller are the rubble larger is the uncertainty, probably because small debris entails a greater diffraction which gives and the occurrence of many local maxima that make the amplitude analysis less clear than in other cases.

Data relating to path loss are analyzed, the minimum of path loss is calculated on a plane 0.5 m above the rubble for each realization. Two different calculations are carried out (case 1 and case 2) which distinguish for evaluating the average and standard deviation of the path loss values. In case 1, the average is evaluated as the minimum value of the average matrix calculated over the entire observation plane for all simulations/realizations, in case 2 instead it is the average of the minimum values of path loss recognized in each matrix relative to a single simulation/realization. For the two average values the respective standard deviations are calculated.

The standard deviation is calculated as

$$\sigma = \sqrt{\frac{\sum (x_i - \bar{x})^2}{n}} \tag{7}$$

where x_i is the minimum path loss value for the current simulation/realization, $\bar{x}$ is the average (calculated in the two exposed ways), n is the total number of simulations considered for each scenario. In Table 4 the results obtained are shown. Similarly to the calculation of the uncertainty of localization the path loss is larger for smaller size of the cube rubble, evidently a stronger interaction of the electromagnetic wave with the rubble occurs.

In comparison to the measurements taken in real scenarios and published in [12, 13] the obtained results of path loss shown in Table 4 are greater. The discrepancy can be ascribed to the particular choice of the parameters of the considered scenarios (i.e., DoC, rubble size dielectric properties of materials as well as the percentage of the materials). Evidently, a tuning of the parameters to obtain numerical results aligned to measured data is possible but a lot of carefulness is necessary in pursuing that objective for not specializing the tuned scenario to a specific measurement site. An additional measurement campaign is therefore necessary to collect experimental data from a large number of different sites.

Table 4: Path loss calculation.

scenario		avg (dB)	σ (dB)
1: DoC = 40% cube size 20 cm	Case 1	63.04	7.88
	Case 2	58.79	2.83
2: DoC = 40% cube size 50 cm	Case 1	48.65	7.63
	Case 2	44.85	3.84
3: DoC = 30% cube size 20 cm	Case 1	59.08	8.06
	Case 2	54.81	3.22
DoC = 60% layered	Case 1	61.56	7.71
	Case 2	57.32	2.35

4. CONCLUSION

This work has focused attention on a transmission medium particularly complex and difficult to characterize as building rubble. In order to analyze a large number of scenarios, and then consider many of the possible real situations, random models are developed. The model are automatically generated allowing to obtain a large number of data for a significant statistical analysis. The electromagnetic simulation are performed in the time domain in order to determine the attenuation properties of the transmission medium and its effects on the electric field characteristics.

The study highlights the fundamental importance of the rubble dimension rather than the specific materials involved. Furthermore it shows that it is possible to determine the position of a buried transmitting antenna analyzing the amplitude and the phase of the electric field and the power flow module.

REFERENCES

1. Doroodgar, B., M. Ficocelli, B. Mobedi, and G. Nejat, "The search for survivors: Cooperative human-robot interaction in search and rescue environments using semi-autonomous robots," *2010 IEEE International Conference on Robotics and Automation Anchorange Convention District*, Anchorage, Alaska, USA, May 3–8, 2010.

2. Yokokohji, Y., M. Kurisu, S. Takao, Y. Kudo, K. Hayashi, and T. Yoshikaww, "Constructing a 3-D map of rubble by teleoperated mobile robots with a motion canceling camera system," *Proceedings of the 2003 IEEE/RSJ Intl. Conference on Intelligent Robots and Systems*, Las Vegas, Nevada, Oct. 2003.

3. Wiesner, A., "CW radar based vital signs detection," *Proceedings of the 39th European Microwave Conference*, 2009.

4. Ivashov, S. I., V. V. Razevig, A. P. Sheyko, and I. A. Vasilyev, "Detection of human breathing and heartbeat by remote radar," *PIERS Proceedings*, Pisa, Italy, Mar. 28–31, 2004.

5. Bimpas, M., K. Nikellis, N. Paraskevopoulos, D. Economou, and N. Uzunoglu, "Development and testing of detector system for trapped humans in building ruins," *33rd European Microwave Conference*, Munich, 2003.

6. Yarovoy, A. G., L. P. Ligthart, J. Matuzas, and B. Levitas Geo Zondas, "UWB radar for human being detection," *IEEE A&E System Magazine*, Mar. 2006.

7. Zaikov, E., J. Sachs, M. Aftanas, and J. Rovnakova, "Detection of trapped people by UWB radar," 2008.

8. Filali, B., F. Boone, J. Rhazi, and G. Ballivy, "Design and calibration of a large open-ended coaxial probe for the measurement of dielectric properties of concrete," *IEEE Transactions on Microwave Theory and Techniques*, Vol. 56, No. 10, Ottobre, 2008.

9. Pana, F., "Measurement and modeling of propagation losses in brick and concrete walls for 900-MHz band," *IEEE Transactions on Antennas and Propagation*, Vol. 51, No. 1, Gennaio, 2003.

10. Oestges, C., B. Montenegro-Villacieros, and D. Vanhoenacker-Janvier, "Modeling propagation into collapsed buildings for radio-localization-based rescue search mission," *IEEE*, 978-4244-3647-7/09/$25.00 ©, 2009.

11. Di Carlofelice, A., E. Di Giampaolo, M. Elaiopoulos, M. Feliziani, M. Roselli, and P. Tognolatti, "Localization of radio emitters into collapsed buildings after earthquake: Measurements of path loss and direction of arrival," *2012 International Symposium on Electromagnetic Compatibility (EMC EUROPE)*, 1–6, Sep. 17–21, 2012.

12. Di Carlofelice, A., E. Di Giampaolo, M. Feliziani, and P. Tognolatti, "Experimental characterization of electromagnetic propagation under rubble of a historic town after disaster," *IEEE Transactions on Vehicular Technology*, 2014, DOI: 10.1109/TVT.2014.2346580.

13. Teggi, S. and T. di Laurea, "Metodi geofisici," Facoltà di Ingegneria-Università degli studi di Modena e Reggio Emilia, A.A., 2007/2008.

14. Martinez, B., "Modeling dielectric-costant values of geologic materials: An aid to ground-penetrating radar data collection and interpretation," *Current Researc in Earth Sciences*, 247, Part I, Bulletin, 2001.

15. Del Conte, A., "Il radar penetrante (GPR)," *Artemis Diagnostica Edilizia*, 22, Ancona, Gennaio, 2004.

16. Philippakis, C. Martel, and D. Kemp, "Application of FSS structures to selectively control the propagation of signals into and out of buildings," *ERA Technology*, 1–54, Febbraio, 2004.

Combined Breast Microwave Imaging and Diagnosis System

B. L. Oliveira[1], A. Shahzad[1], M. O'Halloran[1],
R. C. Conceicao[2, 3], M. Glavin[1], and E. Jones[1]

[1]Electrical and Electronic Engineering, National University of Ireland Galway, Ireland
[2]Institute of Biomedical Engineering, University Oxford, United Kingdom
[3]Instituto de Biofsica e Engenharia Biomdica, FCUL, Portugal

Abstract— This paper presents results from the development and evaluation of a dedicated Computer-Aided Detection and Diagnosis (CAD) system for Microwave Imaging (MWI) of the breast. CAD systems play a very important role in aiding breast cancer detection, since they help minimising the number of false positives usually associated with most breast imaging techniques. Both imaging and diagnosis of the breast are integrated in the proposed system, by using state of the art Microwave Tomography techniques and refined tumour-grading algorithms. With the proposed system, microwave images allow for the isolation of the tumour response in the recorded signals which ultimately leads to improved performances when diagnosing tumours based on their level of malignancy.

1. INTRODUCTION

Several Computer-Aided Detection and Diagnosis (CAD) systems have been proposed in recent years for various breast imaging modalities, such as X-Ray Mammography, which generally involve pre-processing and segmentation of images followed by diagnosis [1]. In the context of breast Microwave Imaging (MWI), the development of a dedicated CAD system combining features both from microwave images and radar return signals with richer information would greatly contribute to the performance of the technique in terms of specificity. In this paper, the authors focus on an improved method for automated diagnosis of breast cancer based on recorded backscattered signals.

MWI is based on the contrast between the dielectric properties of different types of breast tissue at microwave frequencies. The majority of existing studies which considered MWI of the breast have focused primarily on tumour detection, with automated tumour diagnosis usually seen as a secondary concern. Some studies have investigated the use of Radar Target Signatures (RTS) for the classification of tumours [2–5]. The shape, size and, most importantly, the degree of spiculation at the border of a tumour can significantly influence its RTS, thus allowing for the identification of tumours based on their level of malignancy. However, it is unclear whether the performance of these algorithms can provide sufficient information in anatomical and dielectrical heterogeneous scenarios. More recently, different studies have proposed the use of contrast agents to account for dielectric heterogeneity [6, 7]; nevertheless, doubts still remain about the available dielectric contrast from contrast agents and the targeted delivery of these agents to cancerous tissues. Despite all of these challenges, there is a growing demand for dedicated tumour diagnosis algorithms within the MWI community, given their very significant clinical potential. In fact, recent studies have already analysed classification techniques for pre-clinical microwave imaging prototypes, e.g., [8, 9].

In this paper, a new approach for the grading of tumours is proposed, which integrates microwave imaging and diagnosis of breast cancer in a single system. By using well-documented Microwave Tomography (MT) algorithms to reconstruct the dielectric profile of the breast, tumours can be detected and their location within the breast identified with precision. This information can then be used to process the backscattered signals, by accurately extracting the RTS of any tumour detected in the microwave images, while eliminating most of the unwanted existing clutter sources in the signals. The tumour-grading algorithm can then be more efficiently applied to the tumour responses, and provide a more accurate diagnosis of the tumours level of malignancy. The proposed combined breast microwave imaging and diagnosis system is benchmarked against previous studies which examined standard unprocessed microwave signals, by simulating anatomically-accurate Finite Difference Time Domain (FDTD) breast and tumour models.

The remainder of this paper is organised as follows: Section 2 describes the numerical models, simulation setup, the microwave tomography approach, the windowing technique and the tumour diagnosis approach. Evaluation and results obtained with the proposed system are discussed in Section 3. Finally, some concluding remarks are made in Section 4.

2. COMBINED BREAST MICROWAVE IMAGING AND DIAGNOSIS SYSTEM

The framework of the system proposed in this paper is summarised in Figure 1. To summarise the operation of the system, by way of example, a Class 1 breast model from the UWCEM repository [10] containing a tumour labelled as malignant in the upper-outer quadrant is shown. The model is simulated with FDTD, and the resultant signals are used as input to the MT algorithm to reconstruct an image of the breast. This image is then used to identify the location and extent of the tumour, which further allows windowing the tumour response from the original backscattered signals (the tumour response highlighted in red). Finally, the tumour response is diagnosed according to its level of malignancy. The proposed system is benchmarked against previous studies which analysed standard unprocessed backscattered signals for the diagnosis of breast malignancies. Each element of the system will be described in greater detail in the following subsections.
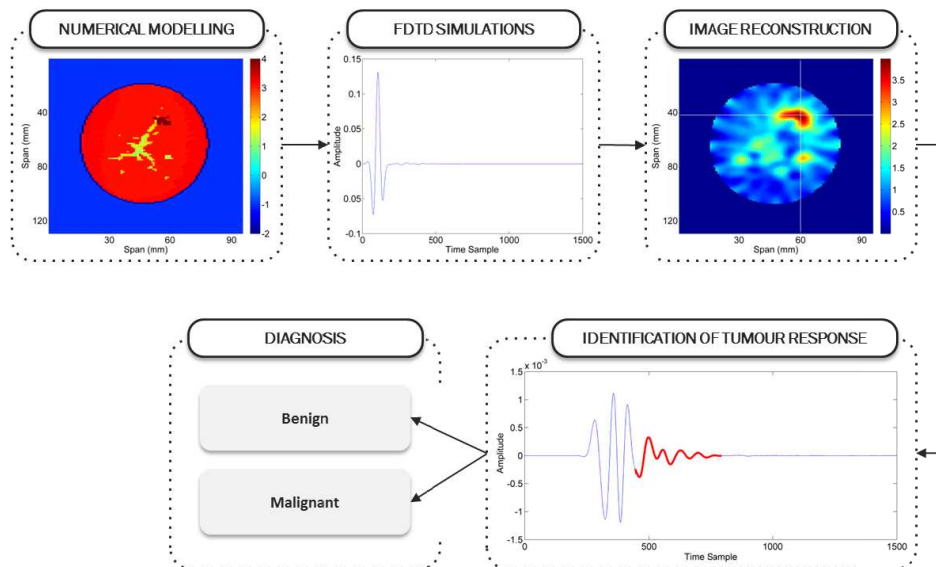
Figure 1: Flowchart of the proposed combined breast microwave imaging and diagnosis system.

2.1. Numerical Modelling and Electromagnetic Simulation

In order to verify the proposed system for the imaging and diagnosis of breast cancer, homogeneous and class 1 numerical breast phantoms adapted from the UWCEM repository [10] were used, where the dielectric properties of different tissue types in the numerical models were derived from the study of Lazebnik et al. [11]. Tumour models of varying sizes and degrees of spiculation were created using the clinically-informed tumour modelling algorithm described in [12]. The tumours were generated with (x, y) diameters of $(6, 8)$, $(6, 12)$, $(10, 12)$, $(15, 16)$ and $(18, 10)$ mm. A degree of spiculation of 0.08 was chosen to generate tumour models with circumscribed margins, which were labelled as benign. For malignant tumours with spiculated and irregular margins, a larger value for of 0.8 was chosen for the degree of spiculation.

The electromagnetic (EM) measurements system was modelled using two concentric rings of Hertzian dipole antennas (each containing 16 antennas) positioned around the breast. The antennas were immersed in a matching medium with dielectric properties equivalent to the fatty tissue, and a differentiated Gaussian pulse with centre frequency of 6 GHz and a -3 dB bandwidth of 6 GHz was used to illuminate the breast model.

2.2. Image Reconstruction and Tumour Windowing

A gradient based time-domain MT algorithm [13] was used to reconstruct the dielectric properties of the breast. In this MT algorithm, the error between measured EM signals from the target object and the computed EM signals from an estimated numerical model of the target is minimized. The least square solution to the minimization problem can be expanded as:

$$F(\epsilon_r, \sigma) = \int_0^T \sum_{m=1}^M \sum_{n=1}^N W(t) \left| E_{m,n}^{meas}(t) - E_{m,n}^{est}(\epsilon_r, \sigma, t) \right|^2 dt \tag{1}$$

where $E_{m,n}^{meas}(t)$ and $E_{m,n}^{est}(\epsilon_r, \sigma, t)$ are the measured and estimated electrical signals at receiving antenna n corresponding to a transmitted pulse from transmitting antenna m. The weighting factor $W(t)$ is a non-negative weighting function that dictates the behaviour of error functional, and T is the measurement time; M and N are the numbers of the transmitting and receiving points, respectively. The Frchet derivative of the functional $F(\epsilon_r, \sigma)$ is used to derive gradients with respect to relative permittivity, ϵ_r, and conductivity, σ, at each spatial position, $r = (x, y)$ in the reconstruction region.

$$G_{e_r}(r) = 2w_{e_r} \int_0^T \sum_{m=1}^M E_{m,r}^{adj}(\epsilon_r, \sigma, t) . \frac{d}{dt} E_{m,r}^{est}(\epsilon_r, \sigma, t) dt \tag{2}$$

$$G_{\sigma(r)} = 2w_\sigma \int_0^T \sum_{m=1}^M E_{m,r}^{adj}(\epsilon_r, \sigma, t) E_{m,r}^{est}(\epsilon_r, \sigma, t) dt \tag{3}$$

where $E_{m,r}^{est}(\epsilon_r, \sigma, t)$ is the computed EM field at position r in the reconstruction space due to transmitter m on an estimated model with relative permittivity ϵr, and conductivity σ. The signal $E_{m,r}^{adj}(\epsilon_r, \sigma, t)$ is the solution to Maxwell's adjoint field equations, numerically calculated by reverse time propagation of the difference of measured and estimated EM signals. Additional scaling factors, w_{e_r} and w_σ are used to compensate for the variations in sensitivity of the dielectric parameters. The gradients $G_{e_r}(r)$ and $G_{\sigma(r)}$ are in the conjugate gradient method to find the conjugate direction, and the optimal step size α is determined by a line search in the conjugate direction. The dielectric parameters in the kth iteration are updated at each spatial position r in the estimated model according to Equations (4) and (5):

$$\epsilon_r^{k+1} = \epsilon_r^k + \alpha^k d_\epsilon^k(r) \tag{4}$$

$$\sigma_r^{k+1} = \sigma_r^k + \alpha^k d_\sigma^k(r) \tag{5}$$

where the conjugate directions $d_\epsilon^k(r)$ and d_σ^k are determined using the Polak-Ribire (PR) method. It is assumed that the skin information is *a priori* known, which is used as an initial estimate in the reconstruction algorithm for realistic class 1 numerical phantoms. Considering the known dielectric properties of tumours, the reconstructed permittivity and conductivity maps are then thresholded to identify the tumour extent and location. Assuming that the average dielectric properties of the breast tissues are available, a time-gating technique is applied to extract the RTS of the tumour based on the round-trip distance between each antenna and the detected tumour. The estimated tumour signature is windowed from the backscattered signal, where the approximate window length is decided empirically by evaluating different window lengths over a dataset of numerical breast phantoms. It is found that a window length of twice the pulse width is appropriate to extract the tumour response from the radar signals. The windowed signals are further used for classification of benign and malignant tumours.

2.3. Tumour Diagnosis

The final step in the proposed system is diagnosing tumours found in the breast according to their level of malignancy. Previous studies have shown promising results by combining feature extraction techniques, namely Principal Component Analysis (PCA), with Support Vector Machines for the classification of tumours in simplified anatomical and dielectric scenarios [4, 5].

PCA is a useful tool which aids in reducing the dimensionality of a dataset. PCA transforms the basis of the original dataset into a new orthonormal basis, allowing the principal components, i.e., the features of the new dataset, to express maximised variance. Here, the variance along each principal component provides a measurement of the relative importance of each dimension. Further details on PCA can be found in [14].

Once the dimensionality of the recorded radar signals is reduced, SVM classifiers can then more efficiently be applied. SVM classifiers use a method to handle nonlinear relations between the input vectors and their corresponding labels by transforming linearly inseparable data to a higher-dimensional space in which they can be more readily separated into the two pre-defined classes of this study: benign or malignant. The system proposed in this paper uses the Radial Basis Function (RBF) kernel to map the tumour data. The kernel parameters are optimised via 10-fold cross-validation, so the best classifier performance can be achieved [15].

(a) (b) (c)
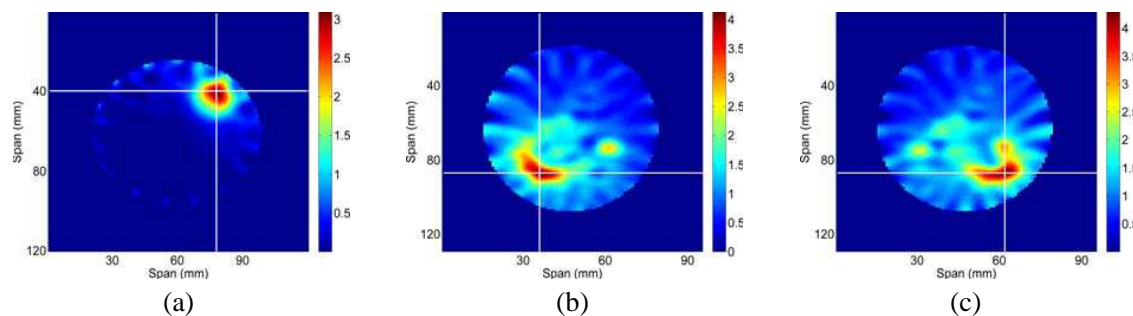
Figure 2: Reconstructed conductivity maps after one iteration of the MT algorithm. (a) Refers to a homogeneous breast with a benign tumour in the upper-inner quadrant; (b) and (c) feature a class 1 breast with a malignant tumour located in the lower-outer quadrant and lower-inner quadrant, respectively.

Table 1: Results of the tumour diagnosis process. Accuracy, sensitivty and specificity are detailed for the homogeneous and class 1 breast types used in this study, for standard unwindowed signals and signals processed with the proposed system.

		Accuracy (%)	Sensitivity (%)	Specificity (%)
Homogeneous Breast	No post-processing	71.6	81.2	61.9
	Proposed system	83.4	95.9	70.9
Class I Breast	No post-processing	63.6	75.3	51.9
	Proposed system	69.5	73.7	65.3

3. RESULTS OF TUMOUR DIAGNOSIS

In Figure 2, results of the MT reconstruction process are shown for the simulated homogeneous and class 1 breast types. For the current implementation of the MT algorithm described in Section 2.2, the authors found that the reconstructed conductivity map yielded a better detection of the extent and location of the tumour, which can be identified by the cross-section of the white lines in Figure 2. For the sake of computational complexity, the tumour extent and location can be identified after a single iteration of the MT algorithm, which is sufficient for the purpose of this study.

As previously mentioned, the diagnosis was performed separately for the homogeneous and class 1 breast types, and included tumours of different sizes and levels of malignancy, placed in different locations within the breast; this diversity in the dataset adds to the complexity of the classification problem. Table 1 details the results of this diagnosis process. For the homogeneous breast type, an improvement of 11.8% in the accuracy of the diagnosis is observed when the proposed windowing of signals is performed; the sensitivity and specificity also improve, by 14.7% and 9%, respectively. For the class 1 breast type, the diagnosis improves by a lower margin of 5.9% when the proposed system is applied. Interestingly, the sensitivity of the diagnosis decreases marginally, but the specificity improves 13.4%. The improvement of the specificity when diagnosing breast tumours is very significant as it ultimately contributes to minimising the false positive rate of MWI as a breast cancer detection technique.

4. CONCLUSIONS AND FUTURE WORK

In this paper, a novel combined breast microwave imaging and diagnosis system has been presented. With this system, images of the breast are generated with MT, and the information obtained from these images is used to produce an automated diagnosis of any tumours found in the breast. The tumour responses are identified and windowed from the recorded signals, and further diagnosed with a refined tumour-grading algorithm. The proposed system was compared to a benchmark system based on standard approaches, where no windowing of tumour responses is performed.

When the system proposed in this paper is applied, the authors observed an improvement in the accuracy of the diagnosis of 11.8% and 5.9% for the homogeneous and class 1 breast types, respectively. Importantly, the specificity of the diagnosis process also improved by 9% and 13.4% for both breast types, which results in less false positive cancers being diagnosed. These results are very significant as they demonstrate the potential of the proposed method to more accurately classify breast tumours according to their level of malignancy in high-clutter scenarios. The clinical applications of a dedicated CAD system for MWI are vast, as there is great interest in finding new

methods that can help minimise the number of false positives usually associated with current breast cancer screening techniques. Future work in this project includes a more detailed analysis of the relationship between the number of PCA components and the accuracy of the SVM classifier. In addition, a study into which pairs of antennas carry more information about the tumour response can impact the performance of the diagnosis process.

REFERENCES

1. Tang, J., R. M. Rangayyan, J. Xu, T. El Naqa, and Y. Yang, "Computer-aided detection and diagnosis of breast cancer with mammography: Recent advances," *IEEE Trans. Inf. Technol. Biomed.*, Vol. 13, No. 2, 236–251, 2009.
2. Davis, S. K., B. D. Van Veen, S. C. Hagness, and F. Kelcz, "Breast tumor characterization based on ultrawideband microwave backscatter," *IEEE Trans. Biomed. Eng.*, Vol. 55, No. 1, 23–46, 2008.
3. Chen, Y., E. Gunawan, K. S. Low, S.-C. Wang, C.-B. Soh, and T. C. Putti, "Effect of lesion morphology on microwave signature in 2-D ultra-wideband breast imaging," *IEEE Trans. Biomed. Eng.*, Vol. 55, No. 8, 2011–2021, 2008.
4. Conceicao, R. C., M. O'Halloran, E. Jones, and M. Glavin, "Investigation of classifiers for early-stage breast cancer based on radar target signatures," *Progress In Electromagnetics Research* Vol. 105, 295–311, 2010.
5. O'Halloran, M., B. McGinley, R. C. Conceicao, F. Morgan, E. Jones, and M. Glavin, "Spiking neural networks for breast cancer classification in a dielectrically heterogeneous breast," *Progress In Electromagnetics Research*, Vol. 113, 413–428, 2011.
6. Chen, Y., I. J. Craddock, and P. Kosmas, "Feasibility study of lesion classification via contrast-agent-aided UWB breast imaging," *IEEE Trans. Biomed. Eng.*, Vol. 57, No. 5, 1003–1007, 2010.
7. Chen, Y. and P. Kosmas, "Detection and localization of tissue malignancy using contrast-enhanced microwave imaging: Exploring information theoretic criteria," *IEEE Trans. Biomed. Eng.*, Vol. 59, No. 3, 766–776, Mar. 2012.
8. Santorelli, A., E. Porter, E. Kirshin, Y. J. Liu, and M. Popovic, "Investigation of classifiers for tumor detection with an experimental time-domain breast screening system," *Progress In Electromagnetics Research*, Vol. 144, 45–57, 2014.
9. Conceicao, R. C., H. Medeiros, M. O'Halloran, D. Rodriguez-Herrera, D. Flores-Tapia, and S. Pistorius, "SVM-based classification of breast tumour phantoms using a UWB radar prototype system," *2014 XXXIth URSI General Assembly and Scientific Symposium (URSI GASS)*, 1–4, 2014.
10. Zastrow, E., S. K. Davis, M. Lazebnik, F. Kelcz, B. D. Van Veen, and S. C. Hagness, "Database of 3D grid-based numerical breast phantoms for use in computational electromagnetics simulations," Online Available: http://uwcem.ece.wisc.edu/MRIdatabase/.
11. Lazebnik, M., M. Okoniewski, J. H. Booske, and S. C. Hagness, "Highly accurate debye models for normal and malignant breast tissue dielectric properties at microwave frequencies," *IEEE Microw. Wirel. Compon. Lett.*, Vol. 17, No. 12, 822–824, 2007.
12. Oliveira, B., M. Glavin, E. Jones, M. O'Halloran, and R. Conceicao, "Avoiding unnecessary breast biopsies: Clinically-informed 3D breast tumour models for microwave imaging applications," *2014 IEEE APSURSI*, 1143–1144, 2014.
13. Shahzad, A., M. O'Halloran, M. Glavin, and E. Jones, "A novel optimized parallelization strategy to accelerate microwave tomography for breast cancer screening," *2014 36th Annual International Conference of the IEEE Engineering in Medicine and Biology Society (EMBC)*, 2456–2459, 2014.
14. Shlens, J., "A tutorial on principal component analysis," ArXiv Prepr. ArXiv14041100, 2014.
15. Hsu, C. W., C. C. Chang, and C. J. Lin, "A practical guide to support vector classification," 1–16, SeerX, 2003.

Internal Photoeffect under the Action of Ultrashort Electromagnetic Pulses: Dependence of Pulse Duration

Valery A. Astapenko and Sergey V. Sakhno

Moscow Institute of Physics and Technology (State University)
9 Institutskii lane, Dolgoprudniy, Moscow Region 141700, Russia

Abstract— The paper is devoted to theoretical analysis of internal photoeffect induced by ultrashort electromagnetic pulses (USP). The total probability (during all time of USP action) of photo-excitation of impurity state into the energy band in a semiconductor matrix was calculated. We also calculated the spectral probability of total photo-excitation for various pulse durations and analyzed the obtained spectra.

It has been found that internal photoeffect induced by USP has specific features which differ from characteristics of this phenomenon under the action of long electromagnetic pulses.

1. INTRODUCTION

Development of techniques for generating ultrashort electromagnetic pulses (USP) of different shapes and durations makes relevant theoretical studies of the interaction of such pulses with matter.

In particular, the investigation of interaction of such pulses with semiconductors is of big practical importance, that may lead to new effects and opportunities of their applications. In our work all results were obtained for gallium arsenide (GaAs) doped with manganese (Mn) impurity. In general case all these results can be extended to other types of semiconductors.

2. CALCULATIONS

The calculations are based on the expression for probability of photo-induced processes derived in paper [1] in the frame of perturbation theory:

$$W = \frac{c}{(2\,\pi)^2} \int\limits_0^\infty \sigma\left(\omega'\right) \frac{\left|F\left(\omega'\right)\right|^2}{\hbar\,\omega'}\,d\omega'. \tag{1}$$

Here $\sigma(\omega')$ is the cross-section of the impurity-band photo-excitation, $F(\omega')$ is Fourier transform of the electric field strength in the pulse, c is light velocity.

In the contrast to the paper [2] where only carrier distribution function in the valence band was considered, in the present work main attention is given to the dependence of excitation probability (W) on the pulse duration τ for various values of carrier frequency (ω) of the pulse.

We consider the absorption of several types of USP:

$$E_{cor}\left(t\right) = \mathrm{Re}\left[-i\,E_0\, \frac{\left(1 + i\,t\big/\omega\,\tau^2\right)^2 + 1\big/\left(\omega\,\tau\right)^2}{1 + 1\big/\left(\omega\,\tau\right)^2}\, \exp\left(-t^2\big/2\,\tau^2\right)\exp\left(i\,\omega\,t + i\varphi\right)\right] \tag{2}$$

$$E_{\sin}(t,\tau) = \frac{\sqrt{2}E_0}{\sqrt[4]{\pi}}\frac{t}{\tau}\exp\left(\frac{-t^2}{2\tau^2}\right) \tag{3}$$

$$E_{\cos}(t,\tau) = \frac{2E_0}{\sqrt{3}\sqrt[4]{\pi}}\left(1 - \left[\frac{t}{\tau}\right]^2\right)\exp\left(\frac{-t^2}{2\tau^2}\right) \tag{4}$$

It is so called corrected Gaussian pulse (CGP) (2) [3], sine- (3) and cosine (4) wavelet pulses. Such pulses have no constant component in their spectrum in contrast with traditional Gaussian pulse. It should be noted that the presence of a constant component for ultrashort pulse durations leads to unphysical results.

Let us calculate the spectral probability of photo-excitation. In accordance to the law of energy conservation we can write the following expression:

$$\hbar\omega' = I_{th} + \varepsilon \tag{5}$$

where ω' — frequency of monochromatic component of CGP, I_{th} — excitation threshold approximately equal to 0.1 eV [4], ε — is hole energy in the valence band.

So, with the use of (5) we can obtain from the expression (1):

$$\frac{dW}{d\varepsilon} = \frac{c}{(2\pi)^2} \int_0^\infty \sigma\left(\omega'\right) \frac{|E(\omega')|^2}{\hbar\omega'} \delta\left(\hbar\omega' - I_{th} - \varepsilon\right) d\omega' \tag{6}$$

Due to the presence of δ-function in the integral (6), the expression for spectral probability of photo-excitation can be rewritten as:

$$\frac{dW}{d\varepsilon} = \frac{c}{(2\pi)^2 \hbar} \sigma\left(\frac{I_{th}+\varepsilon}{\hbar}\right) \frac{\left|E\left(\frac{I_{th}+\varepsilon}{\hbar}\right)\right|^2}{I_{th}+\varepsilon} \tag{7}$$

In all calculations used cross-section $\sigma(\omega')$ calculated from experimental data taken from [6]. Electric field strength E_0 for all types of pulses equals to $5 \cdot 10^{-3}$ at.u.

3. RESULTS

In Figure 1 the dependencies of total probability of photo-excitation are shown as a function of pulse duration at different carrier frequencies ω of corrected Gaussian pulse. It is shown that for
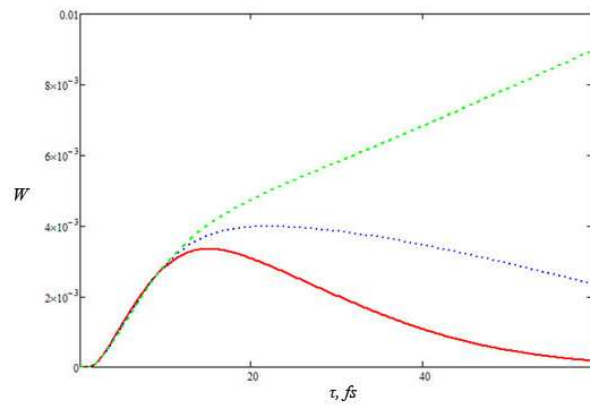
Figure 1: Total probability of photo-excitation as a function of pulse duration at different carrier frequencies of incident CGP. The solid line: $\omega = 0.08$ eV; dotted line: $\omega = 0.09$ eV; dashed line: $\omega = 0.1$ eV.
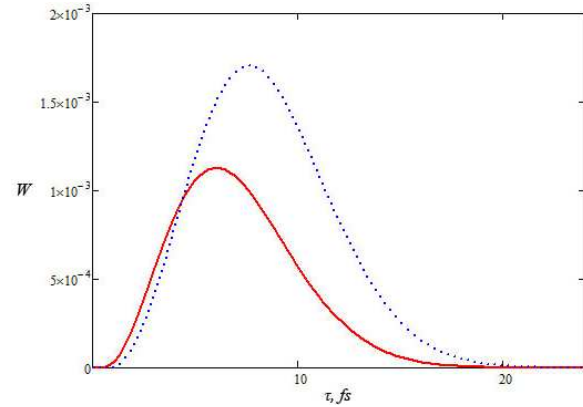
Figure 2: Total probability of photo-excitation for wavelet pulses. The solid line: sine wavelet; dotted line: cosine wavelet.
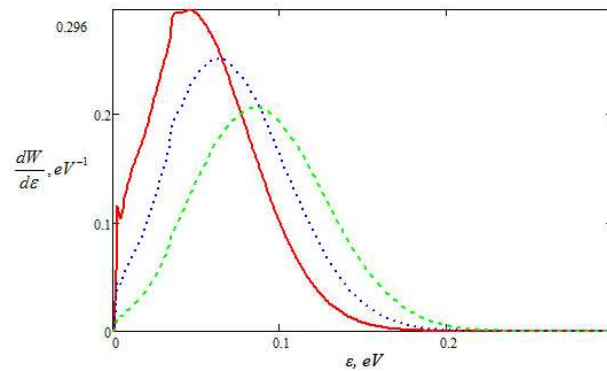
Figure 3: Spectral probability of total photo-excitation as a function of hole energy at different carrier frequencies of CGP and pulse duration 10 fs. The solid line: $\omega = 0.09$ eV; dotted line: $\omega = 0.12$ eV; dashed line: $\omega = 0.15$ eV.
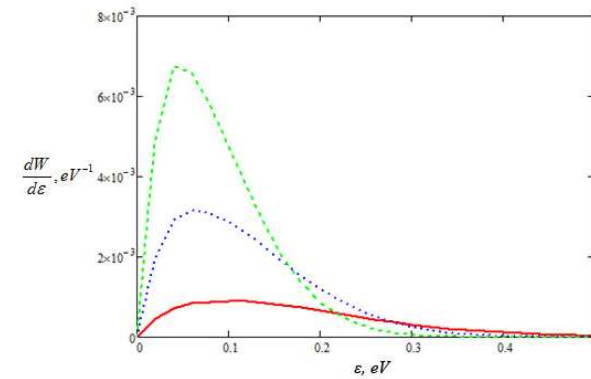
Figure 4: Spectral probability of total photo-excitation as a function of hole energy for sine wavelet at different pulse durations. The solid line: $\tau = 2$ fs; dotted line: $\tau = 3$ fs; dashed line: $\tau = 4$ fs.

frequency ω smaller than the excitation threshold (I_{th}), the dependence $W(\tau)$ looks as a curve with a maximum $W(\tau \to \infty) \to 0$. On the contrary for $\hbar\omega' > I_{th}$, excitation probability rises with the increase of pulse duration and transforms to the linear dependence at sufficiently large values of parameter τ.

In the case of sine- and cosine wavelet pulses, the results are shown on Figure 2. Qualitatively the dependencies for both pulses are similar, but the curve corresponding to the cosine wavelet has a maximum shifted to longer pulses durations and has larger probability.

In Figure 3 spectral probability of total photo-excitation is shown as a function of the hole energy at different carrier frequencies of CGP and pulse duration 10 fs. We can see that the grater central frequency of CGP the less amplitude at maximum of all dependencies and they are shifting to the higher hole energy.

Figure 4 presents the spectral probability of total photo-excitation as a function of the hole energy for sine wavelet at different pulse durations. We can see that the increasing of pulse duration lead to increasing of amplitude of spectral probability.

4. CONCLUSIONS

We have calculated and analyzed the total and spectral probability of photo-excitation of Mn impurity state in GaAs matrix under the action of various USP as a function of pulse duration — $W(\tau)$ and $dW/d\varepsilon$. Particular attention was given to near threshold range of carrier frequency of the pulse. It was shown that the character of $W(\tau)$ in the case of corrected Gaussian pulse is strongly dependent on carrier frequency ω. So for $\hbar\omega' < I_{th}$ the function $W(\tau)$ is the curve with a maximum which goes to zero with the increase of τ. The position of maximum shifts into long-pulse region as $\eta\omega$ approaches to the threshold. When $\hbar\omega' > I_{th}$, the total probability of photo-excitation monotonically increases and for sufficiently long CGP it transforms into linear function of τ as in the case of monochromatic excitation. Another situation takes place for wavelet pulses without carrier frequency. Namely, the total probability $W(\tau)$ has maximum at $\tau = 5$–7 fs and always approaches to zero for large values of pulse duration.

Spectral probability as a function of the hole energy in the valence band has maximum which position shifts to a higher energy with the increase of CGP carrier frequency and the decrease of duration of wavelet pulses. The maximum value of spectral probability is higher for CGP in comparison with wavelet pulse case.

REFERENCES

1. Astapenko, V. A., *Physics Letters A*, Vol. 374, 1585–1590, 2010.
2. Astapenko, V. A. and M. I. Mutafyan, *Russian Physics Journal*, Vol. 55, No. 1, Jun. 2012.
3. Lin, Q., J. Zheng, and W. Becker, *Phys. Rev. Lett.*, Vol. 97, 253902, 2006.
4. Chapman, R. A. and W. G. Hutchinson, *Phys. Rev. Lett.*, Vol. 18, 443, Published, Mar. 20, 1967.

High Definition Multimedia Interface in the Process of Electromagnetic Infiltration

Rafal Przesmycki

Faculty of Electronics, Military University of Technology
Gen. S. Kaliskiego 2 str., Warsaw 00-908, Poland

Abstract— The article concerns problems of electromagnetic compatibility and compromising emission that is the information security. The article describes the electromagnetic channels of penetration information, and then focuses on High Definition Multimedia Interface for which shows signals of extortion used during of disclosing emission measurements. The article presents the results of compromising emissions measurements derived from High Definition Multimedia Interface. In addition, the article discusses the laboratory stand for measuring disclosing emissions.

1. INTRODUCTION

Information security against electromagnetic permeability of devices and electromagnetic systems (IT) is of great importance. This problem increases with a higher and higher use of ICT devices for processing and transmitting information which should not fall into the wrong hands. It results from the fact that each electronic device is the source of undesirable (secondary) emission of electromagnetic energy induced in surrounding space and in all close conductors and metal structures. When signals of undesirable emission are correlated with unclassified information, they can be used for reconstructing that information by intelligence services. The phenomenon of such undesirable emission is called compromising emission and its use by intelligence-penetration or electromagnetic infiltration. Undertakings which aim is to hinder system recognition on the basis of compromising emission are called information protection against electromagnetic penetration or emission safety. Electromagnetic emissions with the feature of compromising emission can arise at any stage of processing of encoded information in the form of electric current courses. There is also no possibility to conduct tests of the source itself and the channel of information permeability. However such tests can be conducted in laboratory conditions in which examined devices are introduced into operation mode allowing to learn their infiltration susceptibility. In this article an example of such experiments has been presented. It seems that most suitable for illustrating the issue of electromagnetic information permeability are devices or their components which process information in serial way and the rule of encoding is uncomplicated and well-known.

2. HIGH DEFINITION MULTIMEDIA INTERFACE

High Definition Multimedia Interface (HDMI) is an extension of Digital Visual Interface (DVI). HDMI standard developed by the Silicon Image company, which also developed a standard DVI. HDMI uses the same protocol TMDS (ang. Transition Minimized Differential Signaling)developed by Sillicon Image. TMDS protocol was used which was used first in the DVI interface. The difference between DVI and HDMI interface is the ability to transmit audio in digital form. Standard specification of digital image transmission between the graphics card and the monitor was set by the organization DDWG (ang. Digital Display Working Group) in 1999. The main aim of the TMDS protocol is to eliminate data transmission interference, through appropriate coding of transmitted data. The physical layer TMDS signal is a differential signal with a minimized number of logic changes. This property has been achieved by means of suitable coding algorithms, converting the data in 8-bit format to a 10-bit TMDS data. All signals are sent by three TMDS lines. Additional signals, other than the video is transmitted when it takes blanking the screen on TMDS1 and TMDS2 lines. In HDMI version 1.2 color transfer was held on 24 bits. Since version 1.3 introduced Deep Color mode which gives the possibility to send the color in the words of 30, 36 and 48 bit systems. In HDMI version 1.3 image is transmitted with a clock frequency of 25 to 340 MHz in Single-link (TMDS protocol). In the Dual-link is the maximum clock frequency are 2×340 MHz. At frequency 340 MHz bandwidth is 10.2 Gb/s.

3. THE LABORATORY STAND FOR MEASURING COMPROMISING EMISSION

In order to determine sources of compromising emission deriving from HDMI interface it is necessary to estimate a contents degree of test signal intentionally generated by HDMI interface (HDMI cable) in the signal received by measuring position as radiated or conducted compromising emission.The laboratory stand for conducting tests of determining sources of compromising emission should make reception of generated test signal propagating as radiated or conducted compromising emission possible. In this article attention has been paid to radiated compromising emission. HDMI interface as enforcing compromising emission used the selected imaged is play on the LED monitor screen.With the use of receiving antennas [7–14] signal received by antenna gets through commutator which switches antennas to FSET 22 broadband receiver. In the receiver those signals are filtered and their conversion into lower frequency range takes place. Signal after detection is passed to VIDEO output in the receiver and then it is passed to input of external channel of oscilloscope on which there is a possibility of displaying received information in time domain [1–6].

4. MEASUREMENT RESULTS

Common observation of spectrum obtained during HDMI interface operation display random images or movies can't give you an answer as to the possibility of occurrence of compromising emission. In order to determine the distinctive features of HDMI interface (on data lines) during operation reflected in components of frequency spectrum or in time domain test patterns used during tests conducted with HDMI interface working have been chosen. Measurements were made for Full HD resolution (1980 × 1080) [15, 16].

The following images have been chosen as test signals generated to the process of displaying the selected image on the monitor screen: white image on the monitor screen, two black and white horizontal stripes evenly spaced on the monitor screen, two black and white vertical stripes evenly spaced on the monitor screen, the black letter Hon a white background dealing with full screen. The look of test images generated during operation of the HDMI interface has been shown in Figure 1.

(a) (b) (c) (d)

Figure 1: Test images used during the test of the compromising emissions derived from HDMI.
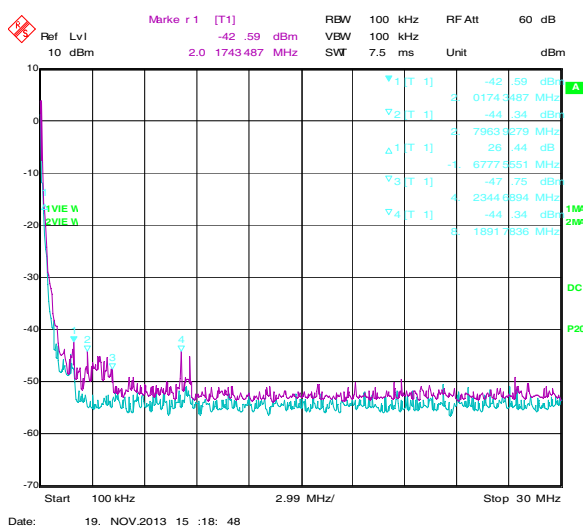
Figure 2: Radiated emission deriving from HDMI interface while displaying the white image on the monitor screen (blue colour) and test pattern (violet colour) within frequency range 100 kHz–30 MHz.
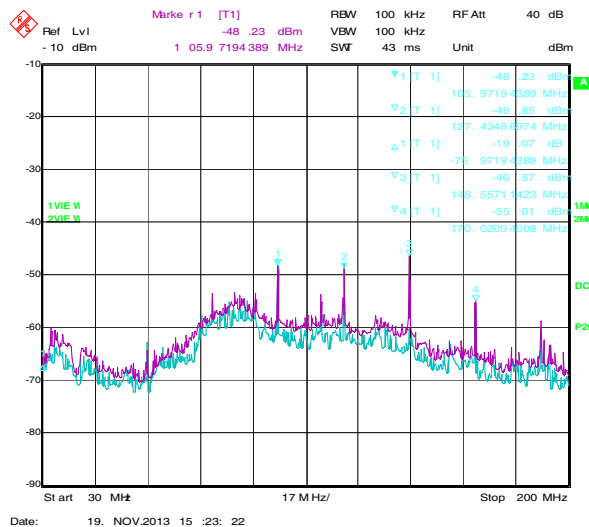
Figure 3: Radiated emission deriving from HDMI interface while displaying the white image on the monitor screen (blue colour) and test pattern (violet colour) within frequency range 30 MHz–200 MHz.

Measurement results for the two mentioned test patterns (white image on the monitor screen and the black letter H on a white background dealing with full screen) have been presented in Figure 2, Figure 3, Figure 4 and Figure 5.

Very often evaluation of spectrum itself is insufficient due to difficulties resulting from rating of appearing signals at particular frequencies. Because of that it is necessary to use other methods consisting in the use of more advanced measuring devices. Anyway in most cases qualification of emissions occurs with the use of visual method. It should be remembered though that in doubtful cases or in such ones where visual assessment is impossible evaluation methods based on digital methods of processing of recorded signals are used [17–19].
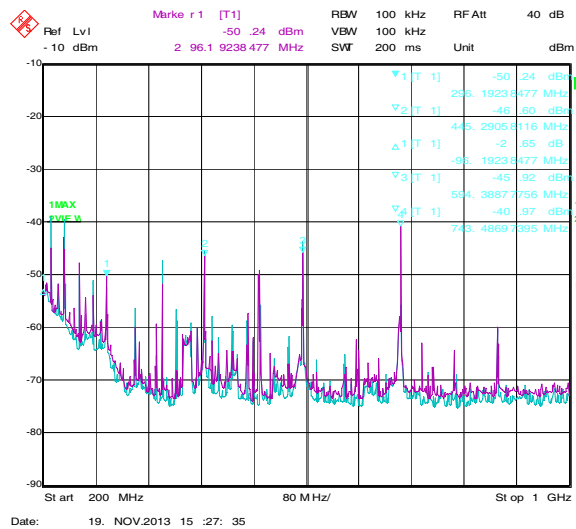
Figure 4: Radiated emission deriving from HDMI interface while displaying the white image on the monitor screen (blue colour) and test pattern (violet colour) within frequency range 200 MHz–1000 MHz.
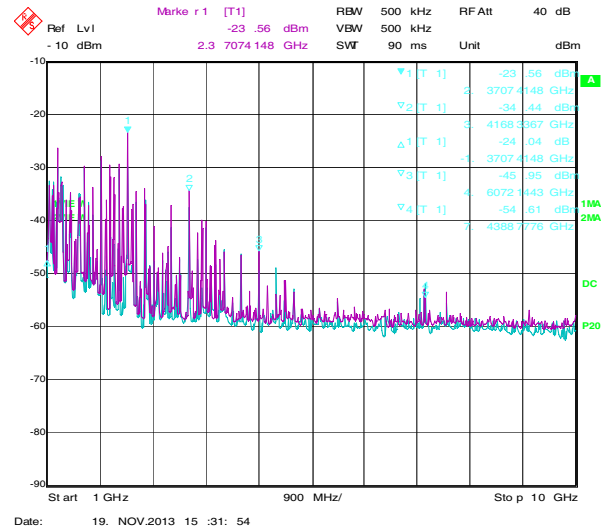
Figure 5: Radiated emission deriving from HDMI interface while displaying the white image on the monitor screen (blue colour) and test pattern (violet colour) within frequency range 1000 MHz–10000 MHz.
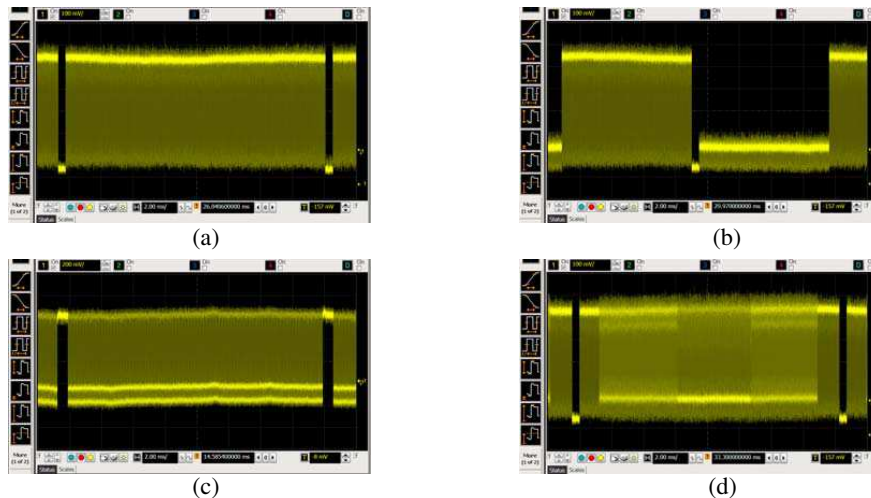
Figure 6: Oscillogram for HDMI interface while displaying on the monitor screen: (a) a test pattern a; (b) a test pattern b; (c) a test pattern c; (d) a test pattern d. The signal received by antenna for $f = 743,48$ MHz given from VIDEO output of FSET22 receiver.

Identification is a process or a result of processes of identifying a particular object with other object. It may include distinguishing common features, capturing similarities between a tested object and other objects of the same category, estimating values of observed parameters of a particular object. Using any methods of signal identification of compromising emission requires

determination of distinctive features characteristic for model information signals and determination of a similarity degree of those features for analogous parameters of tested signals. On the basis of an analysis of radiated emission levels by HDMI interface probable signal reception frequencies of compromising emission have been determined. To test whether radiated signals within that frequency range actually have the character of compromising emission, a series of recordings of those signals has been made with the use of digital oscilloscope and analyzed. The measurements have been made while displaying on the monitor screenthe images defined in Figure 1. The sample results have been placed in Figure 6 [20, 21].

5. CONCLUSION

The presented above time courses of radiated emission signals by HDMI interface show clearly that those signals have an evident connection with contents of displayed images and thus they have the character of compromising emission signals. Time courses directly identify the contents form of displayed images. On the basis of the measurements obtained from the oscilloscope waveforms appearing on the interface transmission lines and their spectrograms received using a spectrum analyzer and oscilloscope can be concluded that: by selecting the pattern image is generated on the computing device,the test form can be formed on the time course of signal transmission lines HDMI interface in such a way that it can be easily identified on the oscillogram, the test image should be black and white because the color of black and white are represented by extreme values in the signal voltage at the HDMI interface (This structure facilitates the identification signals on the oscillogram. This allows notice any change in the oscillogram for changing color in horizontal line son the screen), the test image should be static (stationary elements of the image), the test image should have aperiodic structure (repetitive components of image are easier to identification signals on the oscillogram).

ACKNOWLEDGMENT

REFERENCES

1. Kubacki, R., M. Wnuk, and J. Modelski, "From nanoelectronics to the advanced microwave applications," *IEEE Microwave Magazine*, Vol. 13, No. 7, 94–96, 2012

2. Kubacki, R., M. Wnuk, W. Kolosowski, and J. Sobiech, "New approach to electromagnetic field calculations in the near-field of microwave antennas," *Computational Methods and experimental Measurements, XI Book Series: Computational Engineering*, Vol. 4, 413–422, 2003.

3. Kubacki, R., E. Cwalina, M. Kuchta, and A. Dukata, "Specyfika rozkładu pola elektromagnetycznego wewnątrz pomieszczeń i obudów komputerowych od wysokomocowych impulsów elektromagnetycznych," *Przegląd Elektrotechniczny (Electrical Review)*, No. 12b, 209–212, 2012.

4. Kubacki, R. and S. Lamari, "The UWB microstrip antenna with metamaterial and periodic structure," *PIERS Proceedings*, 2651–2655, Guangzhou, August 25–28, 2014.

5. Kubacki, R., "New attempt to building materials permittivity measurements," *PIERS 2014 Conference Proceedings*, 2676–2680, Guangzhou, August 25–28, 2014.

6. Lamari, S., R. Kubacki, and M. Czyżewski, "Frequency range widening of the microstrip antenna with the sierpinski fractal patterned metamaterial structure," *MIKON2014 Conference Proceedings*, 773–775, 2014

7. Bugaj, M. and M. Wnuk, "Influence of parameters of dielectric in aperture-coupled stacked patch antenna on bandwidth," *Przeglad Elektrotechniczny*, 50–53, Sep. 2009.

8. Wnuk, M. and M. Bugaj, "Analysis of radiating structures placed on multilayer dielectric," *WIT Transactions on Modelling and Simulation*, Vol. 46, 747–755, 2007.

9. Bugaj, M., "Measurements of wall attenuation in closed spaces inside a building," *PIERS 2014 Conference Proceedings*, 2681–2686, Guangzhou, August 25–28, 2014.

10. Bugaj, M. and M. Wnuk, "Optimization parameters of dielectric in aperture-coupled stacked patch antenna on bandwidth," *4th Microwave and Radar Week, MRW-2010 — 18th International Conference on Microwaves, Radar and Wireless Communications, MIKON 2010 — Conference Proceedings*, 2010.

11. Bugaj, J. and M. Wnuk, "Analysis of the impact of surface on parameters of cylindrical microstrip antennas," *Przeglad Elektrotechniczny*, 48–51, Mar. 2015.

12. Bugaj, J. and M. Wnuk, "Analysis of conformal multilayer antenna working in X band," *Przeglad Elektrotechniczny*, 46–49, Sep. 2009.

13. Wnuk, M. and J. Bugaj, "Analysis of surface waves in microstrip array," *16th International Conference on Microwaves, Radar and Wireless Communications, MIKON 2006*, 2006.

14. Bugaj, M., "Attenuation measurements of materials used in construction of buildings," *PIERS Proceedings*, 2671–2675, Guangzhou, August 25–28, 2014.

15. Gajewski, P., J. Lopatka, L. Nowosielski, B. Uljasz, and Z. Piotrowski, "Multimedia transmission over HF links," *Proceedings — IEEE Military Communications Conference MILCOM*, Vol. 1, 45–47, 2000.

16. Nowosielski, L., M. Wnuk, and C. Ziółkowski, "Interlaboratory tests in scope of measurement of radio disturbance," *Conference Proceedings — 39th European Microwave Conference, EuMC 2009*, Article number 5296286, 288–291, 2009.

17. Nowosielski, L., J. Łopatka, and M. Siłaczuk, "Modelling of electromagnetic wave propagation with the use of the ray-tracing method," *PIERS Proceedings*, 2701–2705, Guangzhou, August 25–28, 2014.

18. Nowosielski, L. and C. Piotrowski, "Honeycomb ventilation grill shielding effectiveness measuring methodology," *PIERS Proceedings*, 2692–2696, Guangzhou, August 25–28, 2014.

19. Nowosielski, L. and M. Wnuk, "Compromising emanations from USB 2 interface," *PIERS Proceedings*, 2666–2670, Guangzhou, August 25–28, 2014.

20. Kaszuba, A., R. Checinski, M. Kryk, J. Lopatka, and L. Nowosielski, "Electromagnetically shielded real-time MANET testbed," *PIERS Proceedings*, 2706–2710, Guangzhou, August 25–28, 2014.

21. Nowosielski, L. and J. Lopatka, "Measurement of shielding effectiveness with the method using high power electromagnetic pulse generator," *PIERS Proceedings*, 2687–2691, Guangzhou, August 25–28, 2014.

Analze the Impact of Discretization on the Structure of the Simulation Result

Marek Bugaj and Jarosław Bugaj

Faculty of Electronics, Military University of Technology
Gen. S. Kaliskiego 2 str., Warsaw 00-908, Poland

Abstract— This paper presents an analysis of the impact of digitization of the antenna structure on obtained simulation results for the two most popular methods of calculation MoM and FDTD. Simulations were performed for linear and microstrip antennas.

1. INTRODUCTION

The demands for modern radio systems forced to look for new solutions in constructions of antennas [11, 15, 17, 18, 25]. Antennas are an essential element of the plurality of measurement [5–8, 10, 19–21]. This requires conduct many tests and measurements

Research of antennas are a complex, lengthy and relatively expensive [3, 4]. In the laboratory, often we don't have possible to investigate the effect of the relationship between physical parameters of the antenna and its electrical parameters and characteristics of the radiation. This is due to the fact that almost always we must change the antenna physical parameters (dimensions) leads to irreversible structural changes of the antenna, which is extremely expensive. In microstrip antennas are important parameters of the dielectric, which can be explored to measure in accordance with the methods described in the [1, 2, 9, 12, 16]. Radiations pattern of the antenna can also be determined from measurements of the near field [13, 14].

With using a variety of simulation environments, we can study the antenna of any size and shap. This article uses the software Numerical Electromagnetics Code (Nec2d) and CST STUDIO SUITE for analyzing the electromagnetic response of the antenna structure at any distance from the Earth, or without taking into account its impact 4Nec2 program based on the method of moments MoM and CST STUDIO SUITE program based on the finite difference time domain FDTD

2. DISCRETIZATION OF STRUCTURE IN MOM AND FDTD METHODS

The main condition for obtaining correct results of simulations using the method of moments MoM or FDTD is discretization of antenna structure. In the case of using the MoM method structure is mapped using thin wires. Conditions to be met by the dimensions of wires must meet the conditions shown in Figure 2. When using the FDTD method for analyzing the structure of the analyzed antenna is mostly mapped using cubes (Figure 1) The value limit is the size of the cell (length guide), which should not exceed 0.1 wave length because it is the limit of error generation.

3. ANALYSIS OF THE INFLUENCE OF ANTENNA STRUCTURE DISCRETIZATION ON THE SIMULATION RESULT FOR MOM

The simulation was carried out for 12-element Yagi Uda-antenna. This antenna operates at the frequency $f_0 = 435\,\text{MHz}$. Parameter that has been changed in the process of simulation is the
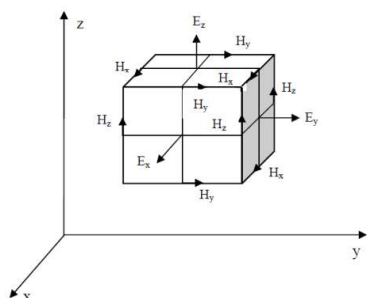
Figure 1: Distribution vectors electric and magnetic field in a cubic cell of the grid Yee'a.
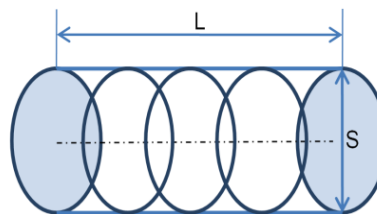
Figure 2: Terms of correct discretization cable in order to get the correct results using MoM (Method of Moments).
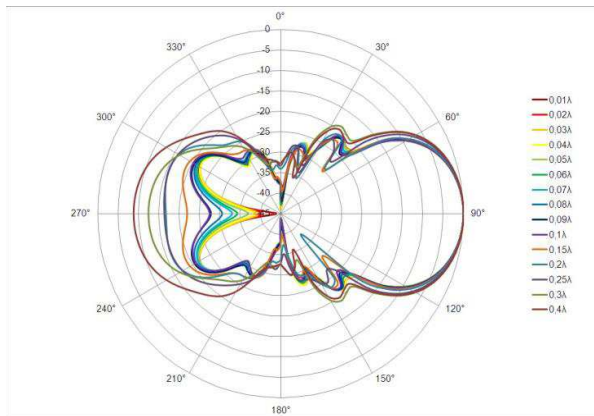
Figure 3: Radiation pattern of Uda-Yagi antenna — vertical polarization (V).
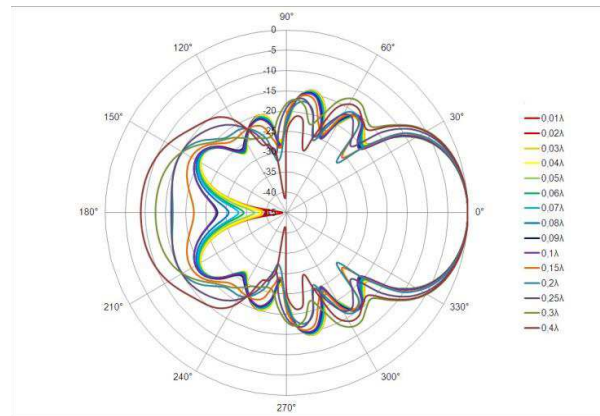
Figure 4: Radiation pattern of Uda-Yagi antenna — horizontal polarization (H).
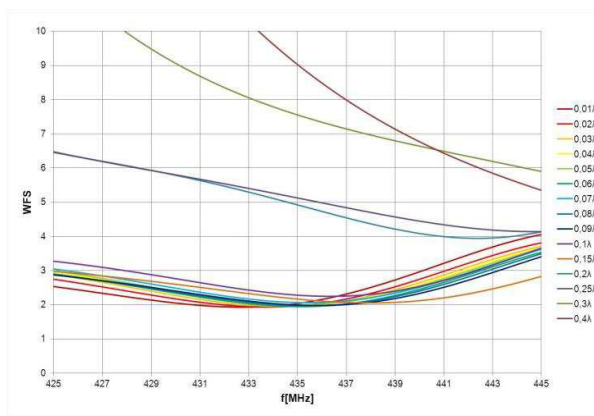
Figure 5: VSWR of Uda-Yagi antenna as a function of dis-cretization of the structure.
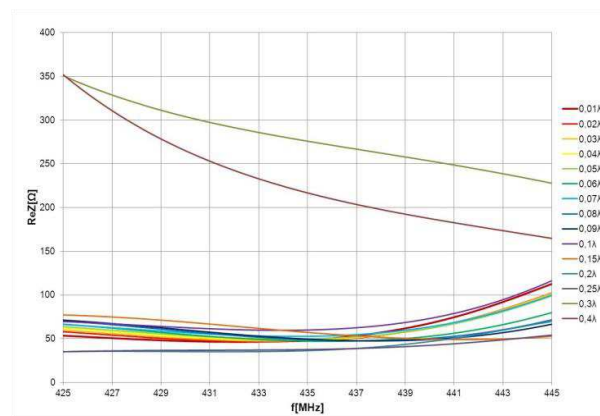
Figure 6: Resistance of Uda-Yagi antenna as a function of discretization of the structure.

degree of discretization of the structure (changing cell size). Cell Size test points varied in the range of 0.01λ to 0.4λ. As a result of the simulation were calculated radiation pattern of the test antanna with vertical polarization (V), horizontal polarization (H) and f the most important parameters such as the WFS real and imaginary impedance, width of main lobe$(-3\,\mathrm{dB})$, frequency and duration of work simulation.

Of the two above-described characteristics of the radiation pattern in the vertical polarization (V) (Figures 3 and 4), we can see that the cell size has no significant effect on the radiation of the main lobe. In the case of the radiation lobe reverse impact is significant. To the distribution 0.1λ the radiation of reverse lobe slightly changes its shape. On the other hand above 0.1λ it can be seen significant increase radiation of reverse lobe. For division of structure 0.4λ we have increase value of reverse lobe equal to $11\,\mathrm{dBi}$.

As can be seen simulation shows that the characteristics of the standing wave ratio (Figures 5 and 6) to a value 0.08λ shows a normal waveform characteristics, since the minimum value of VSWR fall on the $435\,\mathrm{MHz}$ frequency which coincides with the resonant frequency of the antenna test. In contrast, above the misrepresentation occurs 0.08λ results. Next characteristic (Figure 8) shows the dependence the input resistance of the antenna from the frequency.

The input resistance of the antenna to the 0.25λ value has the correct shape. For discretization below 0.25λ for the $435\,\mathrm{MHz}$ resonance frequency the input resistance falls within the range $50\,\Omega$. When the value is above 0.25λ we can see significant errors.

4. ANALYSIS OF THE INFLUENCE OF ANTENNA STRUCTURE DISCRETIZATION ON THE SIMULATION RESULT FOR FDTD

To analyze the impact of digitization on the structure of the simulation results using the FDTD method, we made the simulation of a rectangular microstrip antenna radiator shown in (Figures 7 and 8). This antenna operates at the resonance frequency $f = 1.79\,\mathrm{GHz}$. Parameter that has been

changed in the process of simulation is the size of a cubic grid Yee'a.

As can be seen simulation shows that the characteristics of the standing wave ratio (Figure 9) to the size of a cell below 0.1λ shows a correct value. The measurement results confirm the results of the simulation. In both cases, the WFS reaches the minimum value for $f = 1.79$ GHz. With the increase in cell size above 1.1 simulation results are burdened with more and bigger mistake.

The resistance of the antenna (Figure 10) for the Yee cell sizes below 0.1. takes the correct value.
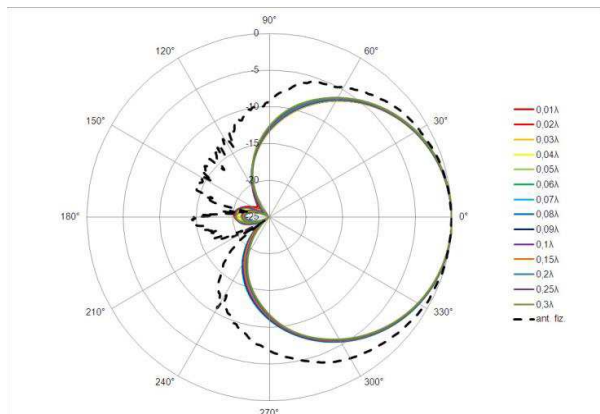
Figure 7: Section of building with the marked first measuring position. Measurement of attenuation between room 1.12 and corridor through closed door.
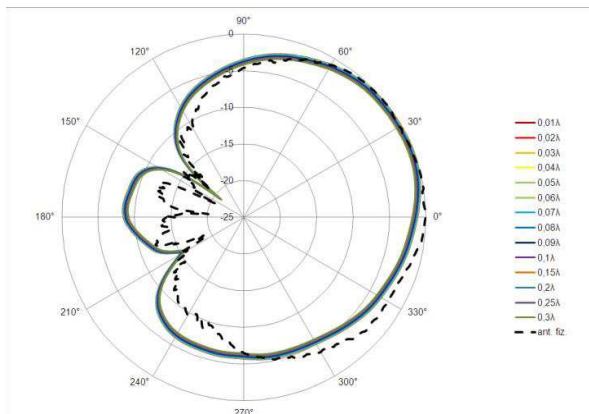
Figure 8: Attenuation received as a result of measurement through gypsum-cardboard wall between room 1.12 and corridor.
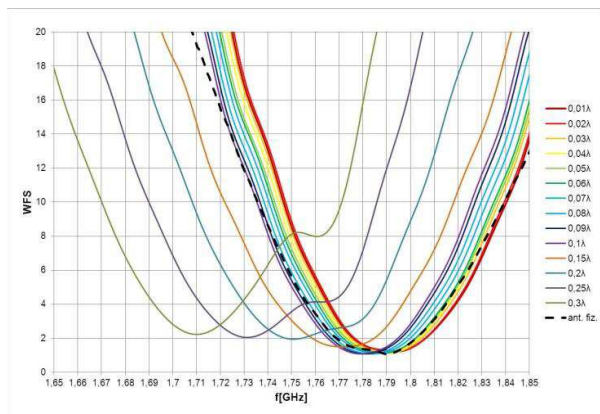
Figure 9: VSWR of microstrip antenna with rectangular patch as a function of discretization of the structure.
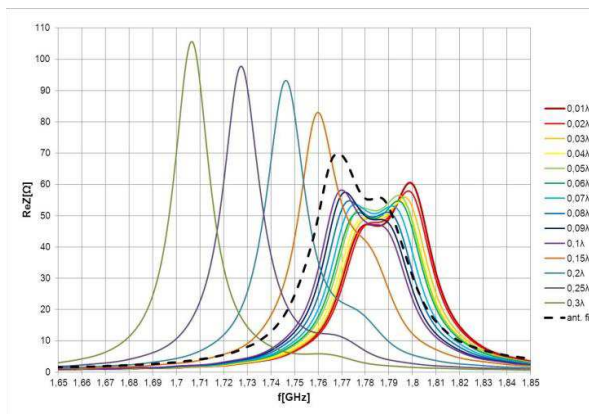
Figure 10: Resistance of microstrip antenna with rectangular patch as a function of discretization of the structure.
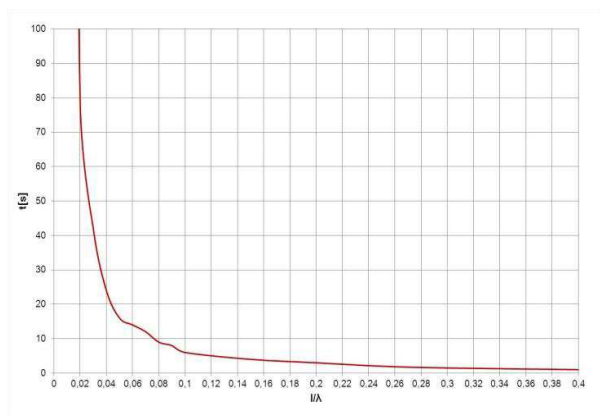
Figure 11: Charakterystyka czasu trwania symulacji anteny Yagi-Uda w zależności od stopnia dyskretyzacji struktury.
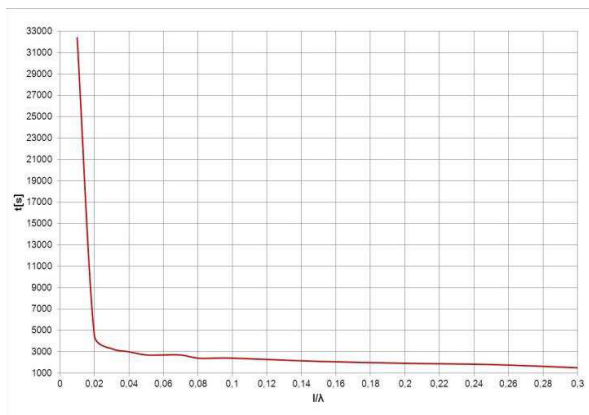
Figure 12: Charakterystyka czasu trwania symulacji anteny mikropaskowej z prostokątnym promiennikiem.

Wskazuje to na dobre dopasowanie impedancji wejściowej do impedancji przewodu równej $50\,\Omega$. When the value is above 0.1λ obtained results differ significantly from the results of measurements and the simulation results.

For Yee cell size smaller than 0.04λ duration of the simulation begins to grow exponentially.

5. CONCLUSIONS

Analyzing the structure of the antenna using MoM moments can be concluded that the size of the cells in the simulation has a very large impact on the results achieved. The size of the cells has a very large impact on the parameters of the tested antennas and less on the characteristics of the radiation. The radiation characteristics of the biggest changes can be seen in the back-lobe level. For antennas with simple structure simulation duration is not too long. It does not pay to increase the size of the cells to simulate as soon as possible reducing the duration of the simulation reduce the accuracy of the calculation, resulting in the generation of errors and inaccuracies. The optimal distribution of antenna structures to simulate 0.05λ value. This is the result of a compromise between the duration of the simulation and the accuracy of the results.

Tested antenna structure with the using finite difference time domain FDTD show that the size of the cubic cell has less impact on the simulation process than is the case method of moments MoM. Simulation durations are very long, e.g., for microstrip antenna with a rectangular radiator for a cubic grid size 0.01λ imulation lasted more than nine hours. In contrast, for comparison, the same antenna simulated for the cubic grid size 0.1λ lasted 30 minutes.

The time difference is enormous, but this difference can be seen in the results of the simulation. For values 0.1λ and 0.01λ the results were not different from each other in significant ways. As you can see the duration plays a very important role. The optimal size of a cubic grid for the analyzed antenna is 0.08λ value. For the 0.08λ simulation takes about $35\,\text{min}$ with very small errors. You may also note that the antenna measurements carried out in an anechoic chamber are similar with the results of the simulation carried out in the CST Studio Suite.

REFERENCES

1. Kubacki, R., R. Przesmycki, and J. Ferenc, "Wlasności elektromagnetyczne nanokrystalicznego proszku stopu Fe-Si-B-Cu-Nb w zakresie mikrofalowym," *Przeglad Elektrotechniczny (Electrical Review)*, NR 12b/2011, 92–95, 2011, ISSN: 0033-2097.
2. Kubacki, R., J. Ferenc, R. Przesmycki, and M. Wnuk, "The nanocrystalline FeSiBCuNb finemet absorption properties at microwaves," *IEEE Transactions on Electromagnetic Compatibility*, Vol. 54, No. 1, 93–100, Feb. 2012, ISSN: 0018-9375.
3. Przesmycki, R., L. Nowosielski, and R. Kubacki, "The improved technique of electric and magnetic parameters measurements of powdered materials," *Advances in Engineering Software*, Vol. 42, No. 11, Nov. 2011, ISSN: 0965-9978.
4. Kubacki, R., L. Nowosielski, and R. Przesmycki, "Technique for the electric and magnetic parameter measurement of powdered materials," *Computotional Methods and Experimental Measurements XIV 2009, WIT Transactions on Modelling and Simulation*, Vol. 48, 241–250, 2009, ISSN: 1743-355X.
5. Piwowarczyk, K., R. Przesmycki, L. Nowosielski, and M. Wnuk, "Pomiar odporności urządzeń informatycznych na promieniowane pole elektryczne o częstotliwości radiowej w zakresie (80–1000) MHz," *Przeglad Elektrotechniczny (Electrical Review)*, R.86 NR 3/2010, 165–167, 2010, ISSN: 0033-2097.
6. Nowosielski, L., R. Przesmycki, and M. Wnuk, "The laboratory stand for conducted emissions measurement in accordance with the military standard," *IEEE International Symposioum on Electromagnetic Comatibility*, 275–278, 2010.
7. Przesmycki, R., M. Wnuk, L. Nowosielski, and K. Piwowarczyk, "Small chambers shielding efficiency measurements," *PIERS Online*, Vol. 7, No. 3, 256–260, 2011.
8. Nowosielski, L., R. Przesmycki, M. Wnuk, and J. Rychlica, "The methods of measuring attenuation of thin absorbent materials used for electromagnetic shielding," *PIERS Online*, Vol. 7, No. 3, 261–265, 2011.

9. Kubacki, R., L. Nowosielski, R. Przesmycki, and R. Frender, "Metoda pomiarów przenikalności elektrycznej i magnetycznej materiałów proszkowych," *Przeglad Elektrotechniczny (Electrical Review)*, R.85 NR 12/2009, 83–87, 2009, ISSN: 0033-2097.

10. Przesmycki, R., "Measurement and analysis of compromising emanation for laser printer," *PIERS Proceedings*, 2661–2665, Guangzhou, China, Aug. 25–28, 2014.

11. Przesmycki, R. and P. Skokowski, "Dual band microstrip antenna," *PIERS Proceedings*, 2641–2645, Guangzhou, China, Aug. 25–28, 2014.

12. Kubacki, R., M. Wnuk, and J. Modelski, "From nanoelectronics to the advanced microwave applications," *IEEE Microwave Magazine*, Vol. 13, No. 7, 94–96, 2012.

13. Kubacki, R., M. Wnuk, W. Kolosowski, and J. Sobiech,, "New approach to electromagnetic field calculations in the near-field of microwave antennas," *Computational Methods and Experimental Measurements, XI Book Series: Computational Engineering*, Vol. 4, 413–422, 2003.

14. Kubacki, R., E. Cwalina, M. Kuchta, and A. Dukata, "Specyfika rozkładu pola elektromagnetycznego wewnatrz pomieszczeń i obudów komputerowych od wysokomocowych impulsów elektromagnetycznych," *Przeglad Elektrotechniczny (Electrical Review)*, No. 12b, 209–212, 2012.

15. Kubacki, R. and S. Lamari, "The UWB microstrip antenna with metamaterial and periodic structure," *PIERS Proceedings*, 2651–2655, Guangzhou, China, Aug. 25–28, 2014.

16. Kubacki, R., "New attempt to building materials permittivity measurements," *PIERS Proceedings*, 2676–2680, Guangzhou, China, Aug. 25–28, 2014.

17. Lamari, S., R. Kubacki, and M. Czyzewski,, "Frequency range widening of the microstrip antenna with the Sierpinski fractal patterned metamaterial structure," *MIKON-2014 Conference Proceedings*, 773–775, 2014.

18. Gajewski, P., J. Lopatka, L. Nowosielski, B. Uljasz, and Z. Piotrowski, "Multimedia transmission over HF links," *Proceedings — IEEE Military Communications Conference MILCOM*, Vol. 1, 45–47, 2000.

19. Nowosielski, L., M. Wnuk, and C. Ziólkowski, "Interlaboratory tests in scope of measurement of radio disturbance," *European Microwave Week 2009, EuMW 2009: Science, Progress and Quality at Radiofrequencies, Conference Proceedings — 39th European Microwave Conference, EuMC 2009*, Article No. 5296286, 288–291, 2009.

20. Nowosielski, L., J. Lopatka, and M. Silaczuk, "Modelling of electromagnetic wave propagation with the use of the ray-tracing method," *PIERS Proceedings*, 2701–2705, Guangzhou, China, Aug. 25–28, 2014.

21. Nowosielski, L. and C. Piotrowski, "Honeycomb ventilation grill shielding effectiveness measuring methodology," *PIERS Proceedings*, 2692–2696, Guangzhou, China, Aug. 25–28, 2014.

22. Nowosielski, L. and M. Wnuk, "Compromising emanations from USB 2 interface," *PIERS Proceedings*, 2666–2670, Guangzhou, China, Aug. 25–28, 2014.

23. Kaszuba, A., R. Checinski, M. Kryk, J. Lopatka, and L. Nowosielski, "Electromagnetically shielded real-time MANET testbed," *PIERS Proceedings*, 2706–2710, Guangzhou, China, Aug. 25–28, 2014.

24. Nowosielski, L. and J. Lopatka, "Measurement of shielding effectiveness with the method using high power electromagnetic pulse generator," *PIERS Proceedings*, 2687–2691, Guangzhou, China, Aug. 25–28, 2014.

25. Gruszczynski, M., M. Wnuk, and L. Nowosielski, "Multisystem microstrip antenna for mobile communications," *IEEE Antennas and Propagation Society, AP-S International Symposium (Digest) 2012*, Article No. 6349179, 2012.

Directed Energy Applications to the Destruction of Informatic Devices

Rafal Przesmycki

Faculty of Electronics, Military University of Technology
Gen. S. Kaliskiego 2 str., Warsaw 00-908, Poland

Abstract— The article concerns the problems of high energy electromagnetic environment. The article describes an high power electromagnetic pulse and discusses the laboratory stand for generate HPEM pulses. In addition, the paper presents an analysis of possibilities of shaping the pulses spectrum generated for the destruction of IT devices, and presents the results of measurements.

1. INTRODUCTION

The IT infrastructure and personal computers (especially PC) are an integral part of our business and everyday life. If you use the IT equipment in critical infrastructure or use for the preservation IT security is not acceptable appearance of any disturbances in the electromagnetic environment. In an environment of high power electromagnetic microwave source is a relatively new kind of risks, both for military systems, and civilian systems. Operation using this type of source is generally referred to as intentional electromagnetic disturbance. HPEM radiated environment, which is naturally harmful, can also occur at frequencies up to several tens MHz. Generate a high-power electromagnetic pulse in the direction of the electronic system makes that on the electronic circuits accumulates very high voltage. This phenomenon causes damage to the circuit elements which makes the device unfit for further operation. In the case of a purposeful interaction an impulse is very important in terms of its effectiveness to generate sufficiently strong impulse at the required frequency.

2. HIGH POWER ELECTROMAGNETIC PULSE

High-power electromagnetic pulse called HPEM is a very short duration pulse (of the order of nanoseconds) and high power (order of tens of gigawatts). HPEM pulse is also often called a E bomb, due to its potential to cause irreversible damage to all electronic equipment located within destruction range an impulse. Also, it should be noted that as yet there were no adverse effects of such a pulse on living organisms by which electromagnetic pulses were known as a humanitarian weapon. HPEM pulses for the first time were observed as a side effect in outbreaks of atomic bombs, it was also found that the extent of such radiation greatly exceeds the means of destruction yet. Currently, several generation methods of HPEM pulse were developed through dedicated generators of electromagnetic radiation. Destructive action of E bombs depends on the destruction of all electronic equipment based on semiconductor technology, and in particular cases of destroying whole infrastructure of communications and power transmission. Figure 1 shows an appearance of HPEM pulse in the time domain, while Figure 2 shows the frequency spectrum of the pulse.
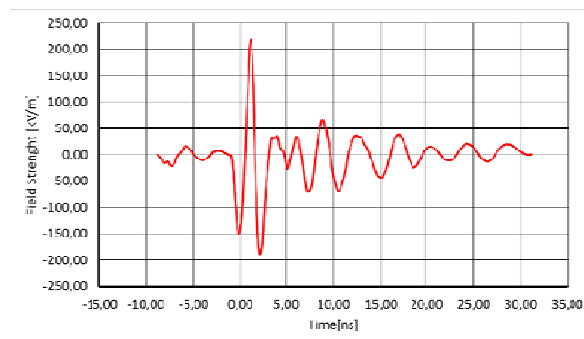
Figure 1: An example of a graphical representation of the HPEM pulse in the time domain.
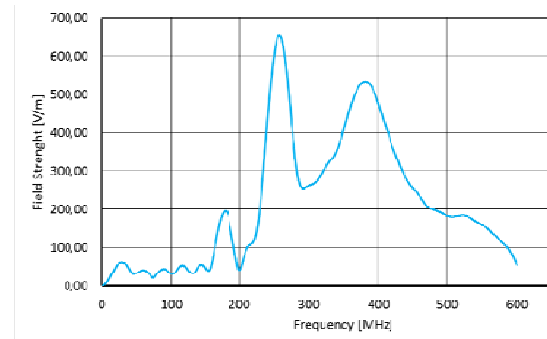
Figure 2: An example of frequency spectrum for sample HPEM pulse.

3. THE LABORATORY STAND OF THE GENERATION AND MEASUREMENT OF HPEM PULSE

The main element responsible for the generation of a HPEM pulse is a generator Diehl DS 110, which is shown in Figure 3. It is compact enclosed equipment, looks like a suitcase. Components of the generator are high-voltage power supply, 300 kV Marx generator and a resonant antenna. High voltage power supply system supplies the Marx generator by 50 kV voltage (symmetrical voltage ± 25 kV), he is charged until the threshold set by the switch that sets pressure gas N_2 in the generator. When changing the position of the switch, antenna is fed a 300 kV voltage, the sparker contained in the air is isolated by the pressure gas N_2 [15–18].
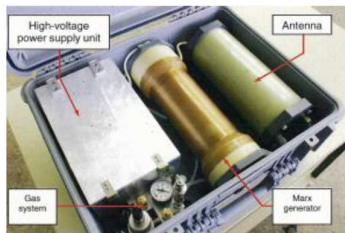
Figure 3: View from inside the generator Diehl DS 110.

Figure 4: Remote control switch generator Diehl DS 110.

Figure 5: The measuring probe D-dot probe Prodyn AD-70 with matching system Prodyn BIB-170F.

Trigger pulse generator can be done by direct actuation by means of a button on the device, or by using the remote control switch (Figure 4) connected to the generator by optical fiber. The main elements of the receiving side of HPEM pulse is D-dot probe AD-70 shown in Figure 5 and Tektronix oscilloscope DPO70404C. The D-dot probe is a detector of electromagnetic induction, it serves as an antenna in a changing electromagnetic pulse electrical signal [7–14]. This is a passive element, and the output signal is derived from the electric field changes over time. The effective electric surface probe is 10^{-3} [m^2].

Oscilloscope receives a signal from the probe and using the Ethernet interface to transmits to the computer a measurement samples, where using a dedicated software is integrated signal so we get the form of a time signal from the generator actually generated. In order to prevent damage to the oscilloscope input signal should be suppressed using the faders of adequate (selected experimental) values. Tektronix oscilloscope characterized by high bandwidth (4 GHz) and a sampling time of 25 GS/s.

The Figure 8 has been presented a block diagram of the laboratory stand of the generation and measurement HPEM pulse. The main elements of this laboratory stand are the generator and receiving antenna, which they are placed in an anechoic chamber so that the probability of damage other electronic devices located near the generator is very small. In addition, they have been placed on the metal floor thus ensuring that a common reference mass. Devices in the measurement room allow their safe operation by authorized persons.

Also in this case a common reference mass of the measuring devices is ensured by a protective metal casing [4–6]. Components of the laboratory stand located in the anechoic chamber arranged in accordance with block diagram of Figure 6 is shown in Figure 7. In this case, the generator is enclosed by reflector for greater concentration of radiation in a one direction (this is optional).
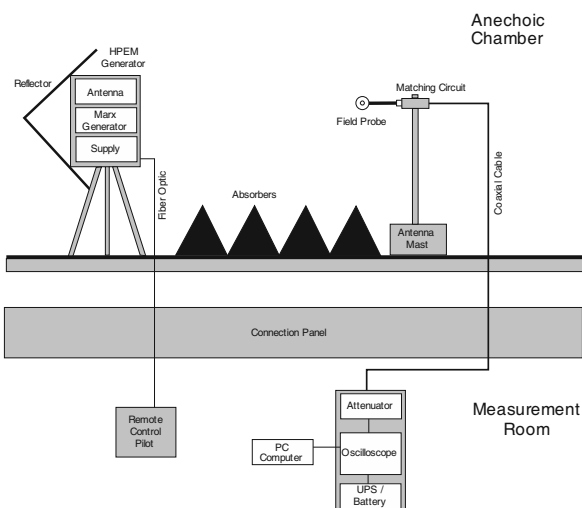
Figure 6: The block diagram of laboratory stand for measurement of HPEM pulse.

Figure 7: The view of laboratory stand for measurement of HPEM pulse in anechoic chamber.

4. ESTIMATION OF SUSCEPTIBILITY THRESHOLDS FOR INFORMATICS DEVICE

Estimating the susceptibility thresholds for the information device is to determine the threshold of susceptibility to the impact of this device by pulsed electromagnetic field. Estimation of susceptibility thresholds will be presented on the example of the PC unit. Before proceeding to determining the threshold of susceptibility, we must refer to the properties of the device. When we more data collect about the components and construction of the device we can more precisely specify the thresholds for immunity [1–3]. Knowing all of elements which can affect the thresholds of susceptibility/immunity PC to the impact of pulsed electromagnetic field we can presented by points on the frequency graph. In this case, have been measured at a distance of 3 m radiated emissions for the PC, and then these values have been converted into radiated emission values derived from the PC test inside the machine. The values of the above-mentioned radiated emissions is shown in Figure 8.
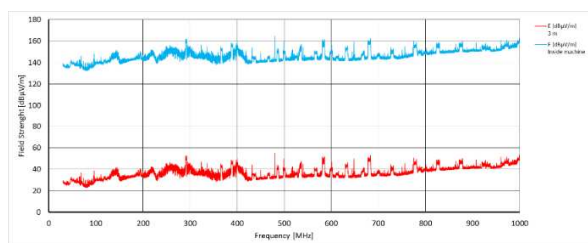
Figure 8: Radiated emission values for PC.
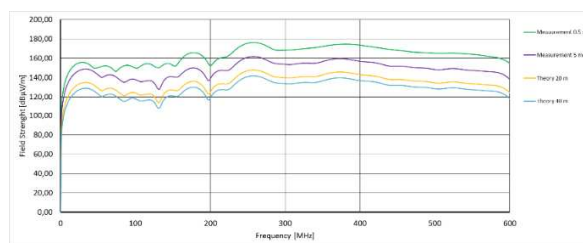
Figure 9: The amplitude-frequency values of HPEM generator for distance: 0.5 m, 5 m, 20 m, 40 m.

5. ANALYSIS OF IMPACT HPEM PULSE ON THE COMPUTER UNIT

The laboratory tests consisted of checking the behavior of the device in pulse high power electromagnetic field. The test object (information device) was placed in an anechoic chamber at a height of 80 cm above the ground and moves away from the HPEM generator to compensate different distances. The laboratory test was performed for the distance of 0.5 m and 5 m, while for longer distances (due to the size of an anechoic chamber), only we estimated values of pulsed electromagnetic field. For a distance of 0.5 m and 5 m, the values of electric field strength respectively: 220 kV/m and 35 kV/m. And for distance 40 m and 20 m we calculated the expected value of the electric field and was obtained, respectively: 7.5 kV/m and 3.6 kV/m. In Figure 9 shown the amplitude-frequency graph in dB for the HPEM generator in the above-mentioned distances [19–21].

PC operation as tested with BurnInTest program in which we can make the choice of tests used for testing software and hardware. Each test is designed to test the different components of the

computer system. These tests can be performed simultaneously. At a distance of 0.5 m the PC crashed and was necessary reset the device by switching off and on the power again after a few minutes. At a distance of 5 m work PC has been disrupted. PC reset the central unit after stopping of exposure, and the basic functions of the PC operation returned to normal. On the basis of the estimated value of the generated pulse electromagnetic field, this phenomenon will be present to the distance from the HEMP source of the device approx. 20–40 meters. However, for a distance of over 40 m the PC should run without interruption during exposing pulse electromagnetic field. For this distance the susceptibility thresholds of computer are above the value of the intensity of the electromagnetic field from a HPEM source. The amplitude-frequency characteristics of the HPEM generator in dB for distances of 0.5 m, 5 m, 20 m, 40 m with plotted susceptibility thresholds of PC computer shown in Figure 10.
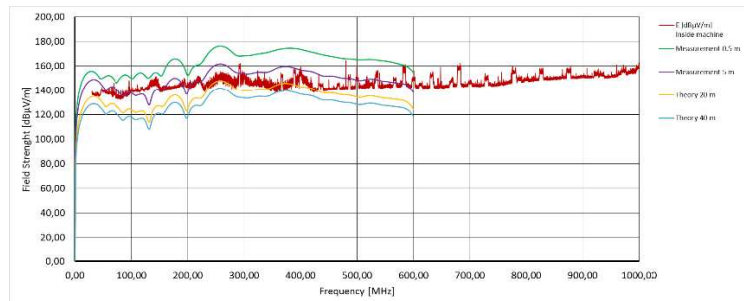
Figure 10: The amplitude-frequency values field strength of HPEM generator with susceptibility thresholds of PC computer.

6. CONCLUSIONS

The possibility of an attack on information technology equipment which work only on a specific frequency significantly restricts the use of this equipment in critical infrastructure. Generate an electromagnetic pulse located in the working range of PC computer can result burnout internal circuits which will make it will be completely unsuitable for further work. Remember to adequately protect the device information. The article presents the intensity of pulsed electromagnetic field for which the PC computer is not susceptible to exposure HEMP pulses. These values are valid for electromagnetic pulse characterized as a high power. When setting these values were used thresholds of susceptibility of computer designated for a single PC computer.

REFERENCES

1. Kubacki, R., M. Wnuk, and J. Modelski, "From nanoelectronics to the advanced microwave applications," *IEEE Microwave Magazine*, Vol. 13, No. 7, 94–96, 2012.
2. Kubacki, R., M. Wnuk, W. Kolosowski, and J. Sobiech, "New approach to electromagnetic field calculations in the near-field of microwave antennas," *Computational Methods and experimental Measurements, XI Book Series: Computational Engineering*, Vol. 4, 413–422, 2003.
3. Kubacki, R., E. Cwalina, M. Kuchta, and A. Dukata, "Specyfika rozkładu pola elektromagnetycznego wewnątrz pomieszczeń i obudów komputerowych od wysokomocowych impulsów elektromagnetycznych," *Przegląd Elektrotechniczny (Electrical Review)*, No. 12b, 209–212, 2012.
4. Kubacki, R. and S. Lamari, "The UWB microstrip antenna with metamaterial and periodic structure," *PIERS Proceedings*, 2651–2655, Guangzhou, August 25–28, 2014.
5. Kubacki, R., "New attempt to building materials permittivity measurements," *PIERS Proceedings*, 2676–2680, Guangzhou, August 25–28, 2014.
6. Lamari, S., R. Kubacki, and M. Czyżewski, "Frequency range widening of the microstrip antenna with the Sierpinski fractal patterned metamaterial structure," *MIKON2014 Conference Proceedings*, 773–775, 2014.
7. Bugaj, M. and M. Wnuk, "Influence of parameters of dielectric in aperture-coupled stacked patch antenna on bandwidth," *Przeglad Elektrotechniczny*, 50–53, September 2009.

8. Wnuk, M. and M. Bugaj, "Analysis of radiating structures placed on multilayer dielectric," *WIT Transactions on Modelling and Simulation*, Vol. 46, 747–755, 2007.

9. Bugaj, M., "Measurements of wall attenuation in closed spaces inside a building," *PIERS Proceedings*, 2681–2686, Guangzhou, August 25–28, 2014.

10. Bugaj, M. and M. Wnuk, "Optimization parameters of dielectric in aperture-coupled stacked patch antenna on bandwidth," *4th Microwave and Radar Week, MRW-2010 — 18th International Conference on Microwaves, Radar and Wireless Communications, MIKON 2010 — Conference Proceedings*, 2010.

11. Bugaj, J. and M. Wnuk, "Analysis of the impact of surface on parameters of cylindrical microstrip antennas," *Przeglad Elektrotechniczny*, 48–51, March 2015.

12. Bugaj, J. and M. Wnuk, "Analysis of conformal multilayer antenna working in X band," *Przeglad Elektrotechniczny*, 46–49, Sep. 2009.

13. Wnuk, M. and J. Bugaj, "Analysis of surface waves in microstrip array," *16th International Conference on Microwaves, Radar and Wireless Communications, MIKON 2006*, 2006.

14. Bugaj, M., "Attenuation measurements of materials used in construction of buildings," *PIERS Proceedings*, 2671–2675, Guangzhou, August 25–28, 2014.

15. Gajewski, P., J. Lopatka, L. Nowosielski, B. Uljasz, and Z. Piotrowski, "Multimedia transmission over HF links," *Proceedings — IEEE Military Communications Conference MILCOM*, Vol. 1, 45–47, 2000.

16. Nowosielski, L., M. Wnuk, and C. Ziółkowski, "Interlaboratory tests in scope of measurement of radio disturbance," *Conference Proceedings — 39th European Microwave Conference, EuMC 2009*, Article number 5296286, 288–291, 2009.

17. Nowosielski, L., J. Łopatka, and M. Siłaczuk, "Modelling of electromagnetic wave propagation with the use of the ray-tracing method," *PIERS Proceedings*, 2701–2705, Guangzhou, August 25–28, 2014.

18. Nowosielski, L. and C. Piotrowski, "Honeycomb ventilation grill shielding effectiveness measuring methodology," *PIERS Proceedings*, 2692–2696, Guangzhou, August 25–28, 2014.

19. Nowosielski, L. and M. Wnuk, "Compromising emanations from USB 2 interface," *PIERS Proceedings*, 2666–2670, Guangzhou, August 25–28, 2014.

20. Kaszuba, A., R. Checinski, M. Kryk, J. Lopatka, and L. Nowosielski, "Electromagnetically shielded real-time MANET testbed," *PIERS Proceedings*, 2706–2710, Guangzhou, August 25–28, 2014.

21. Nowosielski, L. and J. Lopatka, "Measurement of shielding effectiveness with the method using high power electromagnetic pulse generator," *PIERS Proceedings*, 2687–2691, Guangzhou, August 25–28, 2014.

Measurement of the Pulses Generated by the High Power Electromagnetic Pulse Generator

Leszek Nowosielski

Faculty of Electronics, Military University of Technology, Gen. S. Kaliskiego 2 str., Warsaw 00-908, Poland

Abstract— In the article the pulses parameters generated by the high power electromagnetic pulse generator HPEM-RF are described. In the article the structure of the meter of electromagnetic field strength and the measurement methodology of the pulses parameters generated by the high power electromagnetic pulse generator HPEM DS110 is presented too. The block diagram of the meter of the pulses generated by the high power electromagnetic pulse generator is presented too. The meter of the pulses consists of: operating computer, oscilloscope with RF attenuators and sensor (AD-70D or AD-80D) with matching block. Display of data collected from sensor in the time domain occurs in the oscilloscope. Installed software of the operating computer allows, on the basis of high power pulse recorded in the time domain, to determine the frequency spectrum with the use of FFT. In order to conduct validation of the meter of the pulses equipped with electric field sensor AD-70D the measuring results acquired with the use AD-70D and AD-80D are compared.

1. INTRODUCTION

The method of measuring of the pulses parameters generated by the high power electromagnetic pulse generator HPEM DS110 is described here. The method is based on using operating computer, oscilloscope with RF attenuators and sensor (AD-70D or AD-80D) with matching block. Described in the article measuring procedure comes down to conduct of measurement of the signal level in the function of time at the input of sensor being a part of meter of the high power pulse level. Spectrum of recorded probing pulses is next calculated with the use of Fast Fourier Transform (FFT). In the article the measurement results of the high power electromagnetic pulse generated by the HPEM DS110 generator obtained with the use of the described method were presented. The measuring results acquired with the use AD-70D and AD-80D sensor are compared. The article is connected with the references [1–3, 8, 9, 11, 15].

2. THE PULSES PARAMETERS GENERATED BY HPEM GENERATOR

As the HPEM generator can be used the Marx generator. The shape of test signal generated by the above generator in the time function and its spectrum are presented in Fig. 1.
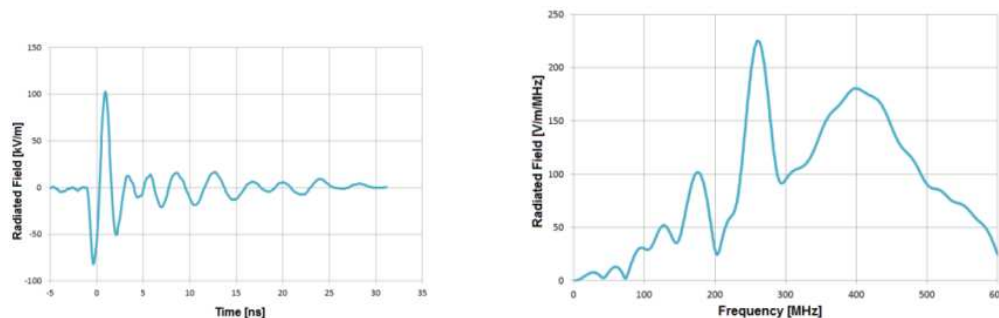
Figure 1: Representation of high power pulse generated by HPEM DS110 generator in time and frequency domain.

The shape of test signal generated by the above generator in the time function can be described by the Equation (1).

$$E(t) = E_0 \cdot \sin(\varphi + 2 \cdot \pi \cdot f \cdot t) \cdot \left(e^{\frac{-a \cdot t}{\tau}} - e^{\frac{-b \cdot t}{\tau}} \right) \tag{1}$$

where: E_0 — the initial value of electric field source function, a — the discharging coefficient, b — the charging coefficient, τ — the time constant of the charging source function.

The above equation has physical meaning in that a source of radiant energy charges the medium at the point under consideration, while the energy radiating away from the point under consideration simultaneously discharges the medium.

Due to significant levels of spectrum components of test pulse and its coverage in the frequency range it can be used as probing signal in many applications [6, 7, 20] where the electromagnetic field strength distribution is needed. The transmitter of the probing signal consists of high power pulse generator HPEM DS110 along with transmitting antenna. The set is placed in a portable case of external dimensions not exceeding $550 \times 450 \times 250$ mm. The task of the generator is to supply pulses with minimum value of electric field strength 90 kV/m with maximum duration of a single pulse not exceeding 5 ns. The effect of its action is obtaining high power pulse at the input of transmitting antenna of the order of several hundred thousand volts for a very short period of time. The structure of signal transmitter is shown in Fig. 2.
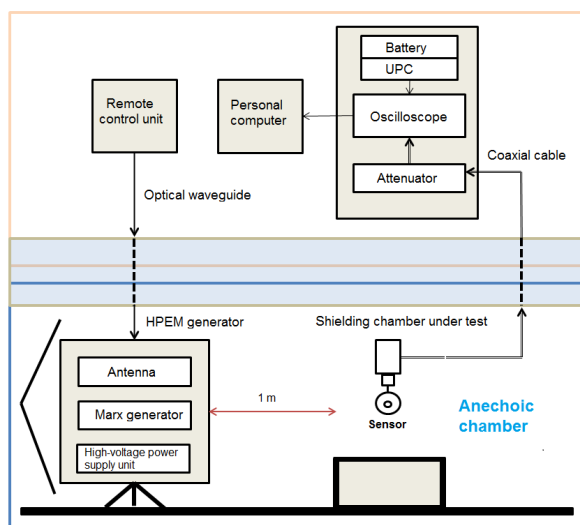
Figure 2: The structure of the meter of electromagnetic field strength.

3. THE MEASUREMENT METHODOLOGY

The structure of the meter of electric field strength is presented in Fig. 2. The meter of electric field strength consists of: operating PC computer, oscilloscope with RF attenuator and sensor with matching block. Sensor with matching unit connected through RF attenuator to oscilloscope with the use of coaxial cable is used for monitoring generated electric field strength. Display of data collected from sensor in the time domain occurs in the oscilloscope. In order to guarantee correct measurement the oscilloscope must be placed in a special shielding casing protecting it from the high generated electric field strength level. Installed software of the operating computer allows, on the basis of high power pulse recorded in the time domain, to determine the frequency spectrum with the use of FFT.

The sensors which can be used during signal level measurements are presented in Fig. 3. The parameters of the sensors are presented in Table 1. The references describing different sensors (antennas) are [4, 5, 10, 12–14, 16–19, 21–24].

Table 1: The parameters of the sensors AD 70 and AD-80.

No	Parameter	Sensor AD-70	Sensor AD-80
1.	Equivalent area	1×10^{-3} m^2	1×10^{-4} m^2
2.	Freq. resp.	> 3.5 GHz	> 5.5 GHz
3.	Rise time	< 0.11 ns	< 0.064 ns
4.	Maximum output	± 1.5 kV	± 1 kV
5.	Output connector	SMA (Female)	SMA (Female)

(a)   (b)

Figure 3: The sensors (a) AD-80 and (b) AD-70.
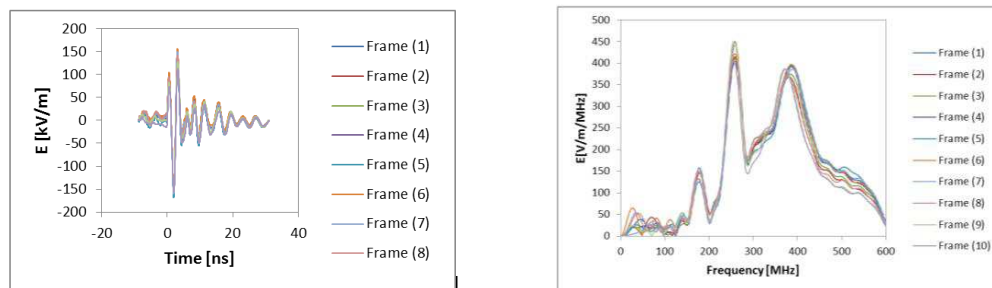
Figure 4: The representation of high power pulse measured with the use AD-70D sensor.
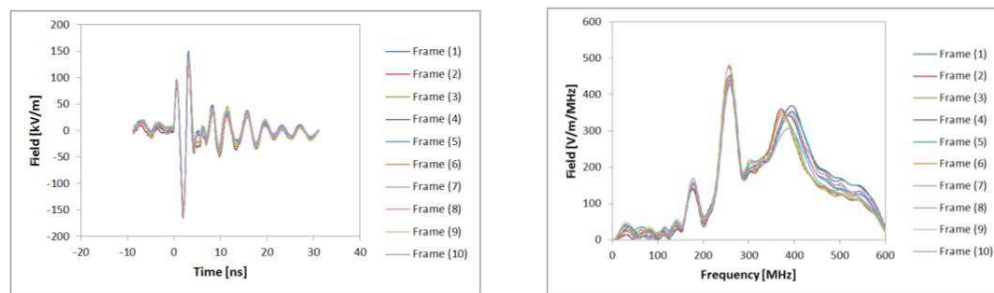
Figure 5: The representation of high power pulse measured with the use AD-80D sensor.

4. THE MEASUREMENT RESULTS

In order to conduct validation of the designed measuring methodology levels of HPEM pulses obtained as a result of measurements carried out with the method described above with the use electric field sensor AD-70D and AD-80D are compared.

In Fig. 4 the measured signal level in time and frequency domain of probing signal with the use of electric field sensor AD-70D are presented. In Fig. 5 the measured signal level in time and frequency domain of probing signal with the use of electric field sensor AD-80D are presented. The signal levels measured with the use of electric field strength sensors AD-70D and AD-80D in time domain and in frequency domain are comparable.

5. CONCLUSIONS

The signal levels measured with the use of electric field strength sensors AD-70D and AD-80D in time domain and in frequency domain are comparable. The described measuring method has many advantages and disadvantages such as:

1. Advantages: large dynamics range of signal level, large measurement rate.
2. Disadvantages: in order to guarantee correct measurement the oscilloscope must be placed in a special shielding casing protecting it from the high generated electric field strength level, in order to protect the input circuit of the oscilloscope the RF attenuators have to be used.

The measuring methodology can be used in many applications where the electromagnetic field strength distribution is needed.

REFERENCES

1. Przesmycki, R., M. T. Wnuk, M. Bugaj, and K. Piwowarczyk, "Analiza metod pomiarowych tlumiennosci torów w.cz.," *Przeglad Elektrotechniczny (Electrical Review)*, No. 2, 17–19, ISSN 0033-2097, 2012.

2. Przesmycki, R., "Measurement and analysis of compromising emanation for laser printer," *PPIERS Proceedings*, 2661–2665, Guangzhou, August 25–28, 2014.

3. Przesmycki, R., M. T. Wnuk, P. Skokowski, and M. Bugaj, "Identification of interface in the complex systems based on radiated emission of mobile computer," *PIERS Proceedings*, 2656–2660, Guangzhou, August 25–28, 2014.

4. Przesmycki, R., M. Bugaj, and M. T. Wnuk, "Wideband microstrip antenna," *PIERS Proceedings*, 2646–2650, Guangzhou, August 25-28, 2014.

5. Przesmycki, R. and P. Skokowski, "Dual band microstrip antenna," *PIERS Proceedings*, 2641–2645, Guangzhou, August 25–28, 2014.

6. Kubacki, R., M. T. Wnuk, and J. Modelski, "From nanoelectronics to the advanced microwave applications," *IEEE Microwave Magazine*, Vol. 13, No. 7, 94–96, 2012.

7. Kubacki, R., J. Ferenc, R. Przesmycki, and M. T. Wnuk, "The nanocrystalline fesibcunb finemet absorption properties at microwaves," *IEEE Transactions on Electromagnetic Compatibility*, Vol. 54, No. 1, 93–100, 2012.

8. Kubacki, R., M. T. Wnuk, W. Kolosowski, and J. Sobiech, "New approach to electromagnetic field calculations in the near-field of microwave antennas," *Computational Methods and experimental Measurements, XI Book Series: Computational Engineering*, Vol. 4, 413–422, 2003.

9. Kubacki, R., E. Cwalina, M. Kuchta, and A. Dukata, "Specyfika rozkładu pola elektromagnetycznego wewnątrz pomieszczeń i obudów komputerowych od wysokomocowych impulsów elektromagnetycznych," *Przegląd Elektrotechniczny (Electrical Review)*, No. 12b, 209–212, 2012.

10. Kubacki, R., S. Lamari, and M. Czyzewski, "Ultra-wideband antenna with metamaterial and periodic structure," *PIERS Proceedings*, 2651–2655, Guangzhou, August 25–28, 2014.

11. Kubacki, R., "New attempt to building materials permittivity measurements," *PIERS Proceedings*, 2676–2680, Guangzhou, August 25–28, 2014.

12. Lamari, S., R. Kubacki, and M. Czyżewski, "Frequency range widening of the microstrip antenna with the sierpinski fractal patterned metamaterial structure," *MIKON-2014 Conference Proceedings*, 773–775, 2014.

13. Bugaj M. and M. T. Wnuk, "Influence of parameters of dielectric in aperture-coupled stacked patch antenna on bandwidth," *Przeglad Elektrotechniczny*, No. 9, 50–53, 2009.

14. Wnuk, M. and M. Bugaj, "Analysis of radiating structures placed on multilayer dielectric," *WIT Transactions on Modelling and Simulation*, Vol. 46, 747–755, 2007.

15. Bugaj, M., R. Przesmycki, M. T. Wnuk, and K. Piwowarczyk, "Analysis of methods measuring attenuation of RF line," *Przeglad Elektrotechniczny*, No. 2, 17–19, 2012.

16. Bugaj, M., "Measurements of wall attenuation in closed spaces inside a building," *PIERS Proceedings*, 2681–2686, Guangzhou, August 25–28, 2014.

17. Bugaj, M. and M. T. Wnuk, "Optimization parameters of dielectric in aperture-coupled stacked patch antenna on bandwidth," *4th Microwave and Radar Week, MRW-2010 — 18th International Conference on Microwaves, Radar and Wireless Communications, MIKON*, 2010.

18. Bugaj, J. and M. T. Wnuk, "Analysis of conformal multilayer antenna working in X band," *Przeglad Elektrotechniczny*, No. 85, No. 9, 46–49, 2009.

19. Wnuk, M. and J. Bugaj, "Analysis of surface waves in microstrip array," *16th International Conference on Microwaves, Radar and Wireless Communications, MIKON*, 2006.

20. Bugaj, M., "Attenuation measurements of materials used in construction of buildings," *PIERS Proceedings*, 2671–2675, Guangzhou, August 25–28, 2014.

21. Bugaj, M. and M. T. Wnuk, "Optimization parameters of dielectric in aperture-coupled stacked patch antenna on bandwidth," *4th Microwave and Radar Week, MRW-2010 — 18th International Conference on Microwaves, Radar and Wireless Communications, MIKON*, 2010.

22. Ziólkowski, C. and J. M. Kelner, "Geometry-based statistical model for the temporal, spectral, and spatial characteristics of the land mobile channel," *Wireless Personal Communications*, doi: 10.1007/s11277-015-2413-3, article in press, 2015.

23. Gajewski, P., J. M. Kelner, and C. Ziólkowski, "Dynamic location of the emission sources based on Doppler effect," *Przeglad Elektrotechniczny*, Vol. 89, No. 7, 223–226, 2013.

24. Gajewski, P., J. M. Kelner, and C. Ziólkowski, "Using SDF method for simultaneous location of multiple radio transmitters," *19th International Conference on Microwaves, Radar and Wireless Communications, MIKON-2012*, Vol. 2, 634–637, Warsaw, Poland, May 21–23, 2013.

Theoretical and Experimental Analysis of the Impact of Conformal Surface on Parameters of Microstrip Antennas

Jarosław Bugaj and Marek Bugaj

Faculty of Electronics, Military University of Technology
Gen. S. Kaliskiego 2 str., Warsaw 00-908, Poland

Abstract— The article presents analysis of the impact of conformal antennas radius of curvature on their basic parameters and characteristics of radiation. In order to verify the numerical results there were built models of practically analyzed conformal antennas, their measurements were taken in anechoic chamber and compared to those of planar antennas. Numerical analysis has been carried out (for basic shapes: cylinder, sphere, toroid) using CST Studio Suite software. Analysed antenna worked within frequency range between 2200–2300 MHz (aviation, in telemetry systems).

1. INTRODUCTION

The main reason for intensive development of conformal microstrip antennas is the fact that it is relatively easy to integrate them with the shape of the surface on which they are installed [11, 15, 16, 24]. Mainly this applies to aircraft, spacecraft, high-speed trains, rockets and missiles in which each projecting element affects adversely aerodynamics, fuel consumption, etc., while conformal antenna can be in a simple way mounted on the aircraft wings or on the outer surface of the hull. This is particularly important as on the surfaces of modern aircraft there are often more than 30 different antenna systems installed.

Another reason for rapid development of conformal microstrip antennas is their easy incorporation into existing elements of urban architecture. Antennas are an essential element of the plurality of measurement [5–8, 10, 19–21]. In microstrip antennas are important parameters of the dielectric, which can be explored to measure in accordance with the methods described in the [1, 2, 9, 12, 16].

2. ANALYZED MODELS OF ANTENNAS

To analyze the impact of conformal antennas radius of curvature on their basic parameters and characteristics of radiation there was selected frequency ranges: 2200–2300 MHz. This range is used in aviation, in telemetry systems.

For selected frequency was designed planar coaxially fed microstrip antenna. Then each antenna was placed sequentially on conformal surfaces: cylinder, sphere, torus, where for each of them full-wave analysis of antennas numerical parameters was carried out in CST Studio Suite.

Figure 1 shows analyzed conformal antenna placed on the side surface of the cylinder. Radiating element has a rectangular shape with dimensions $2L = 38.0 \, \text{mm}$ and $2b\Phi = 39.4 \, \text{mm}$ (width of radiating element as seen from inside of the cylinder). This element is placed on a dielectric of thickness $h = R - b = 3.048 \, \text{mm}$, dielectric permittivity $\varepsilon = 2.55$. The antenna is fed by a $50 \, \Omega$ coaxial probe ($\Phi_p = 5.54 \, \text{mm}$; $Z_p = 5.84 \, \text{mm}$). Around the cylinder of R radius there is vacuum of parameters: $\varepsilon_0 \, i \, \mu_0$.

For each conformal surface radius length was varied in the range 30–10000 mm. It took on average about 1 hour to perform antenna analysis for selected single radius length by applying distribution of analysed antenna's structure in the programme CST Studio Suite at about 6 million meshcells and using PC with processor Intel Core Duo (E4500, 2.2 GHz, 2 GB RAM). Each antenna was analysed for 30 different radius length of conformal surface. Results of conformal antenna analysis for subsequent changes of the radius of curvature R are presented on consecutive figures. Obtained results of the analysis are plotted on graphs as red "×" (for each R change) and connected with each other by B-spline curves (Basis spline function). Dashed line marks value of the parameter for corresponding planar antenna.

3. CONFORMAL ANTENNA ON THE SIDE SURFACE OF THE CYLINDER

The chapter presents analysis of conformal coaxially fed antenna (shown on Figure 1) working in the frequency range between 2200–2300 MHz and placed on the side surface of the cylinder with radius R, which value was changed within the range $30 \, \text{mm}–10000 \, \text{mm}$ ($0.227\lambda_0–75.717\lambda_0$). The

aim of this analysis is to examine impact of curvature of the side surface of the cylinder on antenna's basic parameters.

The graph in Figure 2 shows dependence of antenna resonance frequency f_0 on cylinder radius R. Almost for all changes of radius length the value of antenna resonance frequency is maintained at the level of planar antenna resonance frequency $f_0 = 2.27\,\text{MHz}$ (dashed line). Only in the range of low values of radius $R < \lambda_0$ we can observe increase in resonance frequency.

Next Figure 3 shows dependence of reflection coefficient S_{11} for conformal antenna resonance frequency placed on cylinder side surface depending on cylinder radius R. On the graph we can see that value of reflection coefficient S_{11} for $R > 12\lambda_0$ is almost constant and equals $S_{11} = -19.74\,\text{dB}$. For radius value $R < \lambda_0$ this coefficient decreases its value even to the level of $S_{11} = -43.5\,\text{dB}$.

Dependence of reflection coefficient S_{11} of low values of cylinder radius $r < 1.5\lambda_0$ of conformal antenna placed on the cylinder side surface is shown in Figure 4.

Figure 5 presents bandwidth of cylindrical conformal antenna Δf depending on cylinder radius R.

4. CONFORMAL ANTENNA OF THE SPHERE SURFACE

Antenna shown in Figure 1 was next placed on the sphere surface with radius R. Analysis results for antenna working in the frequency range 2200–2300 MHz placed on the surface of the sphere are shown in Figures 6–9.

The graph in Figure 6 shows dependence of antenna resonance frequency f_0 of the sphere radius R. Almost for all changes of radius R resonance frequency of the antenna is maintained at the level of planar antenna resonance frequency $f_0 = 2.27\,\text{MHz}$. Only in the range $R < \lambda_0$ we can observe
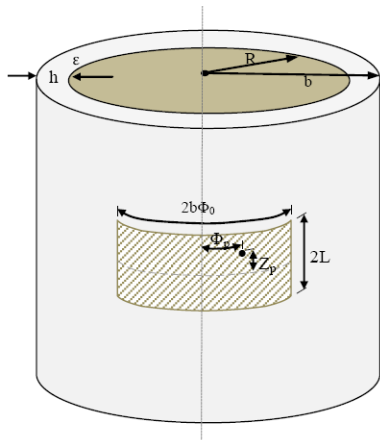
Figure 1: Analyzed conformal antenna on the side surface of the cylinder.
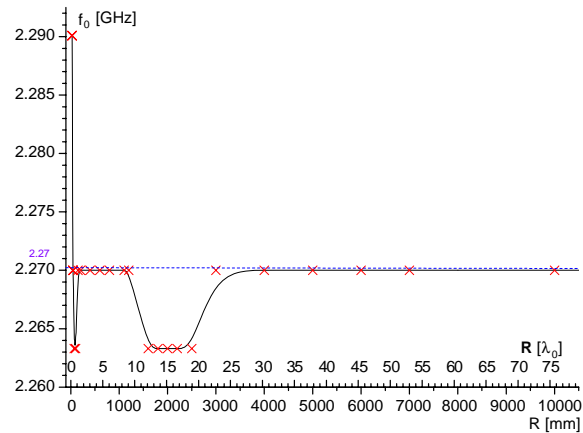
Figure 2: Resonance frequencies of conformal cylindrical antenna depending on length of cylinder radius R.
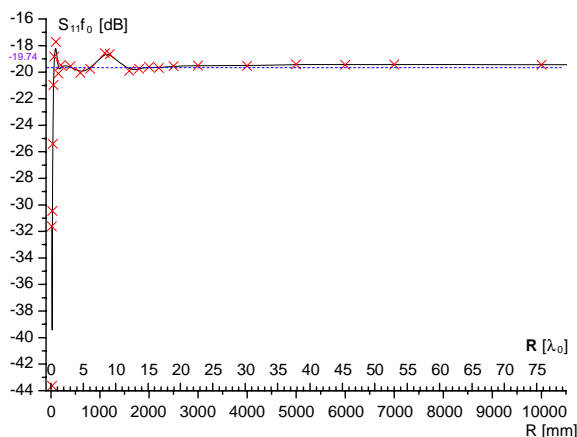
Figure 3: Reflection coefficient S_{11} of cylindrical conformal antenna depending on length of cylinder radius R.
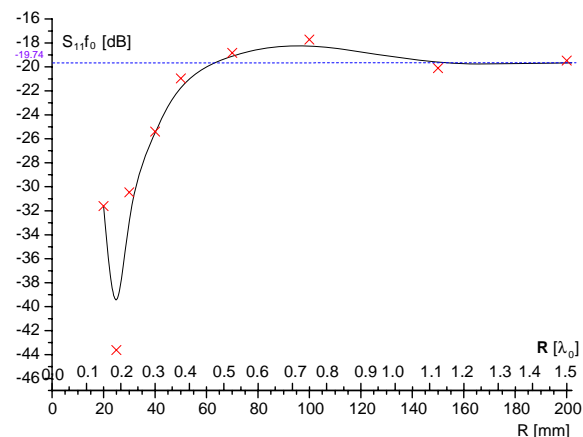
Figure 4: Reflection coefficient S_{11} of cylindrical conformal antenna depending on length of cylinder radius ($R < 1.5\lambda_0$).
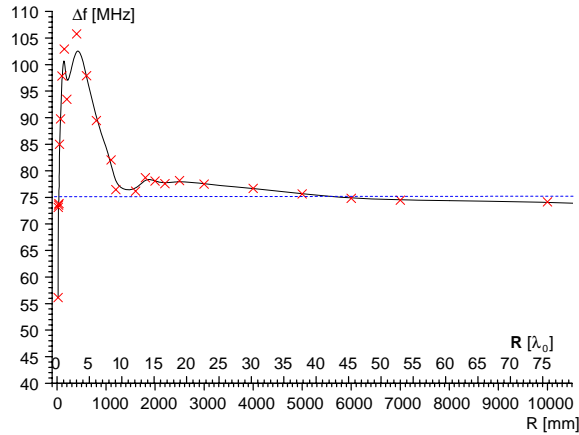
Figure 5: Bandwidth depending on length of cylinder radius R.
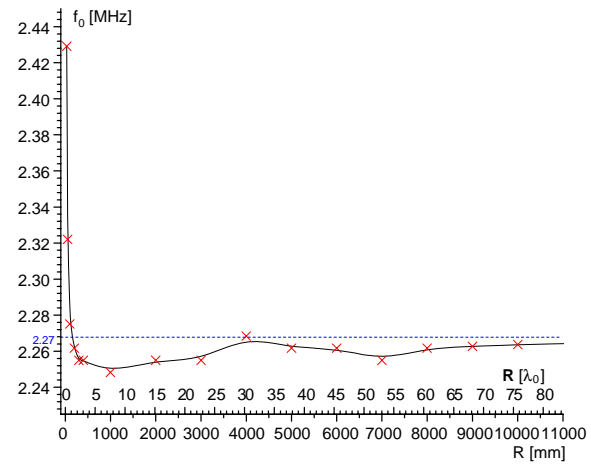
Figure 6: Resonance frequencies of conformal antenna depending on length of sphere radius R.
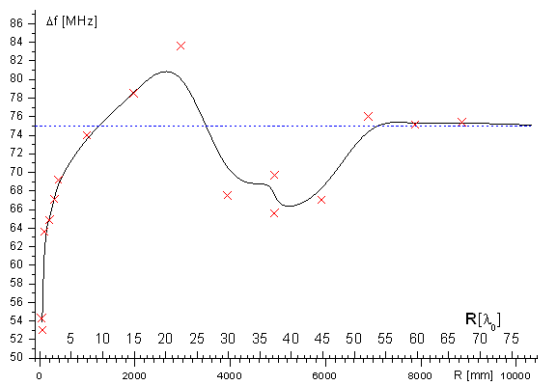
Figure 7: Bandwidth depending on length of sphere radius R.
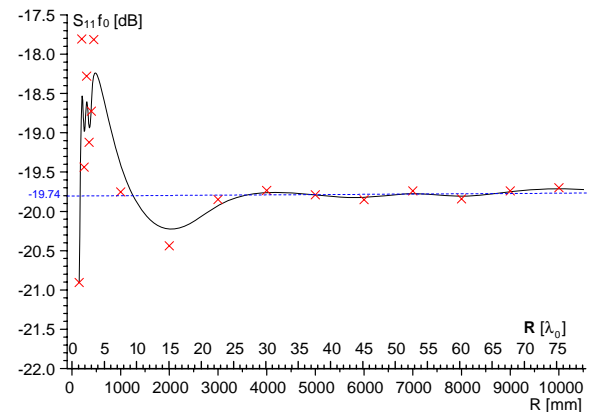
Figure 8: Reflection coefficient S_{11} of conformal antenna depending on length of of torus radius R.

dramatic increase in resonance frequency.

Figure 7 shows bandwidth of antenna Δf depending on radius R of the sphere on which the antenna is placed.

5. CONFORMAL ANTENNA ON THE TORUS SURFACE

Antenna shown in Figure 1 was next placed on the torus surface with internal radius $r = 0.379\lambda_0$ (50 mm) and external radius R which was changed in the range 30 mm–10000 mm ($0.227\lambda_0$–$75.717\lambda_0$).

Figure 8 shows dependence of reflection coefficient S_{11} of torus radius R for antenna resonance frequency f_0. We can observe in the graph that value of reflection coefficient for resonance frequency is practically constant for $R > 23\lambda_0$. For radius length range $R = 3$–$7\lambda_0$ value of reflection coefficient for resonance coefficient is set at the highest values, approx. -18.0 dB.

6. CONCLUSIONS

In order to verify if numerical analysis carried out in previous chapters are correct some models of antennas were built practically and their basic parameters were measured. As part of research the following antennas were built: planar and three cylindrical antennas with radius of curvature $R = \lambda, 2\lambda, 4\lambda$.

Practically built antennas have very similar conditions to results obtained during computer-aided numerical simulation in CST Studio. Discrepancies between resonance frequencies of built antennas and simulation results stay at the level of a single percent.

The research presents analysis results of impact of conformal antenna radius of curvature antennas (for shapes: cylinder, sphere, torus) on their basic parameters. In order to verify obtained

numerical results some models of conformal antennas were built and tested.

As results from presented analysis the radius of curvature of the surface on which microstrip antenna was placed clearly affects the performance of this antenna for low values of $R < \lambda_0$. For large values of the radius of surface curvature the impact is negligibly low, for the transition areas it stays at several or ten-odd percent.

REFERENCES

1. Kubacki, R., R. Przesmycki, and J. Ferenc, "Wlasności elektromagnetyczne nanokrystalicznego proszku stopu Fe-Si-B-Cu-Nb w zakresie mikrofalowym," *Przegląd Elektrotechniczny (Electrical Review)*, NR 12b/2011, 92–95, 2011, ISSN: 0033-2097.

2. Kubacki, R., J. Ferenc, R. Przesmycki, and M. Wnuk, "The nanocrystalline FeSiBCuNb finemet absorption properties at microwaves," *IEEE Transactions on Electromagnetic Compatibility*, Vol. 54, No. 1, 93–100, Feb. 2012, ISSN: 0018-9375.

3. Przesmycki, R., L. Nowosielski, and R. Kubacki, "The improved technique of electric and magnetic parameters measurements of powdered materials," *Advances in Engineering Software*, Vol. 42, No. 11, Nov. 2011, ISSN: 0965-9978.

4. Kubacki, R., L. Nowosielski, and R. Przesmycki, "Technique for the electric and magnetic parameter measurement of powdered materials," *Computotional Methods and Experimental Measurements XIV 2009, WIT Transactions on Modelling and Simulation*, Vol. 48, 241–250, 2009, ISSN: 1743-355X.

5. Piwowarczyk, K., R. Przesmycki, L. Nowosielski, and M. Wnuk, "Pomiar odporności urządzeń informatycznych na promieniowane pole elektryczne o częstotliwości radiowej w zakresie (80–1000) MHz," *Przegląd Elektrotechniczny (Electrical Review)*, R.86 NR 3/2010, 165–167, 2010, ISSN: 0033-2097.

6. Nowosielski, L., R. Przesmycki, and M. Wnuk, "The laboratory stand for conducted emissions measurement in accordance with the military standard," *IEEE International Symposioum on Electromagnetic Comatibility*, 275–278, 2010.

7. Przesmycki, R., M. Wnuk, L. Nowosielski, and K. Piwowarczyk, "Small chambers shielding efficiency measurements," *PIERS Online*, Vol. 7, No. 3, 256–260, 2011.

8. Nowosielski, L., R. Przesmycki, M. Wnuk, and J. Rychlica, "The methods of measuring attenuation of thin absorbent materials used for electromagnetic shielding," *PIERS Online*, Vol. 7, No. 3, 261–265, 2011.

9. Kubacki, R., L. Nowosielski, R. Przesmycki, and R. Frender, "Metoda pomiarów przenikalności elektrycznej i magnetycznej materiałów proszkowych," *Przegląd Elektrotechniczny (Electrical Review)*, R.85 NR 12/2009, 83–87, 2009, ISSN: 0033-2097.

10. Przesmycki, R., "Measurement and analysis of compromising emanation for laser printer," *PIERS Proceedings*, 2661–2665, Guangzhou, China, Aug. 25–28, 2014.

11. Przesmycki, R. and P. Skokowski, "Dual band microstrip antenna," *PIERS Proceedings*, 2641–2645, Guangzhou, China, Aug. 25–28, 2014.

12. Kubacki, R., M. Wnuk, and J. Modelski, "From nanoelectronics to the advanced microwave applications," *IEEE Microwave Magazine*, Vol. 13, No. 7, 94–96, 2012.

13. Kubacki, R., M. Wnuk, W. Kolosowski, and J. Sobiech,, "New approach to electromagnetic field calculations in the near-field of microwave antennas," *Computational Methods and Experimental Measurements, XI Book Series: Computational Engineering*, Vol. 4, 413–422, 2003.

14. Kubacki, R., E. Cwalina, M. Kuchta, and A. Dukata, "Specyfika rozkładu pola elektromagnetycznego wewnatrz pomieszczeń i obudów komputerowych od wysokomocowych impulsów elektromagnetycznych," *Przegląd Elektrotechniczny (Electrical Review)*, No. 12b, 209–212, 2012.

15. Kubacki, R. and S. Lamari, "The UWB microstrip antenna with metamaterial and periodic structure," *PIERS Proceedings*, 2651–2655, Guangzhou, China, Aug. 25–28, 2014.

16. Lamari, S., R. Kubacki, and M. Czyzewski,, "Frequency range widening of the microstrip antenna with the Sierpinski fractal patterned metamaterial structure," *MIKON-2014 Conference Proceedings*, 773–775, 2014.

17. Gajewski, P., J. Lopatka, L. Nowosielski, B. Uljasz, and Z. Piotrowski, "Multimedia transmission over HF links," *Proceedings — IEEE Military Communications Conference MILCOM*, Vol. 1, 45–47, 2000.

18. Nowosielski, L., M. Wnuk, and C. Ziólkowski, "Interlaboratory tests in scope of measurement of radio disturbance," *European Microwave Week 2009, EuMW 2009: Science, Progress and Quality at Radiofrequencies, Conference Proceedings — 39th European Microwave Conference, EuMC 2009*, Article No. 5296286, 288–291, 2009.

19. Nowosielski, L., J. Lopatka, and M. Silaczuk, "Modelling of electromagnetic wave propagation with the use of the ray-tracing method," *PIERS Proceedings*, 2701–2705, Guangzhou, China, Aug. 25–28, 2014.

20. Nowosielski, L. and C. Piotrowski, "Honeycomb ventilation grill shielding effectiveness measuring methodology," *PIERS Proceedings*, 2692–2696, Guangzhou, China, Aug. 25–28, 2014.

21. Nowosielski, L. and M. Wnuk, "Compromising emanations from USB 2 interface," *PIERS Proceedings*, 2666–2670, Guangzhou, China, Aug. 25–28, 2014.

22. Kaszuba, A., R. Checinski, M. Kryk, J. Lopatka, and L. Nowosielski, "Electromagnetically shielded real-time MANET testbed," *PIERS Proceedings*, 2706–2710, Guangzhou, China, Aug. 25–28, 2014.

23. Nowosielski, L. and J. Lopatka, "Measurement of shielding effectiveness with the method using high power electromagnetic pulse generator," *PIERS Proceedings*, 2687–2691, Guangzhou, China, Aug. 25–28, 2014.

24. Gruszczynski, M., M. Wnuk, and L. Nowosielski, "Multisystem microstrip antenna for mobile communications," *IEEE Antennas and Propagation Society, AP-S International Symposium (Digest) 2012*, Article No. 6349179, 2012.

Analysis of Distinctive Features and Database Conception for Hardware Interface of It Devices in the Process of Their Identification Based on Radiated Emission

Rafal Przesmycki and Marian Wnuk

Faculty of Electronics, Military University of Technology
Gen. S. Kaliskiego 2 str., Warsaw 00-908, Poland

Abstract— In the article distinctive feature for modern IT equipment present on the European Union market have been presented. The collected measurement results of radiated emission generated by particular components of IT devices allowed it to build data base which could be used for identification of components characterized by too high level of radiated emission.

This paper describes the concept of building a database for IT devices in the process of identification based on radiated emissions. In addition, the article presents a similarity measure radiated emissions for each hardware interfaces of PC computer.

1. INTRODUCTION

Generally, energy emitted by any source can depend on frequency (f), time (t) and direction (Φ). Quantity ε can be found as operator describing conversion of energy released in source (which depends only on frequency and time) into space-time-frequency distribution of energy in medium surrounding source. If direction, frequency and time features of source are independent of each other, then its emissivity ε can be presented in the form of product of three functions representing separate characteristics describing frequency, direction and time selectivity of source. With large amount of emission sources working simultaneously the resultant process contains prevailing discrete components with particularly large intensity and electromagnetic background close to noise. Basically intensity of intentional emission can be estimated on the basis of space-time-frequency distribution of sources, radiated power and other nominal parameters of related devices. Whereas unintentional emission is much more difficult for quantity assessment. Such an example is collocated system in which there are a few sources of electromagnetic emission at the same time.

Based on there search and obtained measuring results it can be concluded that it is possible to identify the hardware interfaces of information device giving rise an increase in emission. Distinctive feature of the work of the individual interfaces is therefore the working frequency and the level of emission allowing the identification of the hardware interface. Given the above,it is possible to build a database that will help an easy way identify individual interfaces of computer devices.

2. IDENTIFICATION PROCESS OF HARDWARE INTERFACES IN IT DEVICES

In general,the process of identifying the hardware interfaces in IT device can be divided into two stages. The first step it is the measurement process, used for the assembly of distinctive features the work of individual hardware interfaces, which can include working frequency and the level of emission. The second stage is the main process of identifying the hardware interface in IT device based on a database created and defined similarity measures radiated emissions coming from the IT device.

2.1. The Measurement Process

The measurement process consists in making very large amount measurements of radiated emission derived from different information devices in order to obtain empirical data used to build a database containing the distinctive features of individual hardware interfaces. The first step in the measurement process is to measure the radiated emission of the device when,the work of all hardware interfaces is turned off.Thenweextortionworkone of the hardware interfaces (e.g., USB, Parallel, RS-232, DVI, VGA, LAN, etc.) and make measurement of radiated emission of information device for this configuration. After completion of the measurement we were writing the measurement results and check to see if we have to run another hardware interface into IT device. If yes then we go back to start point of the next hardware interface (remember to work individually hardware interfaces) and make measurements of radiated emission. After completing all measurements the measurement process for a single device coming to an end. It should be noted that in

order to build a database of measurements must be taken for a specified number of samples (several dozen) and perform averaging the results [3, 6–10]. Algorithm of the measurement process is shown in Figure 1.
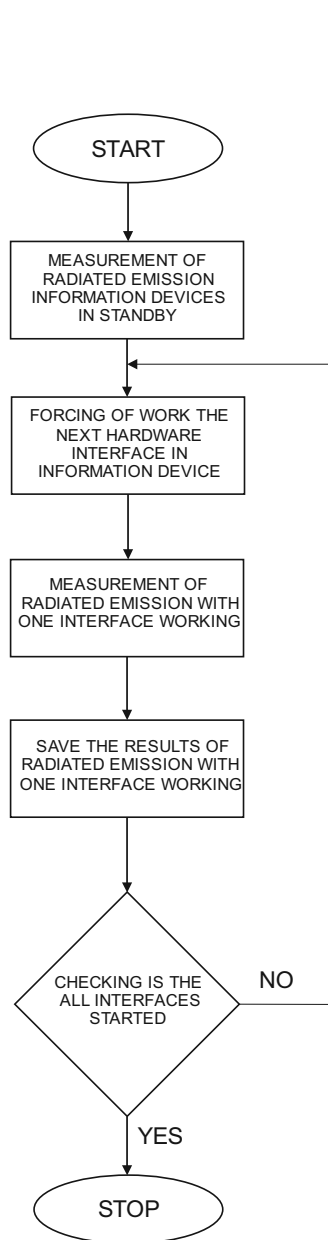
Figure 1: Algorithm of the measurement process for one IT device.
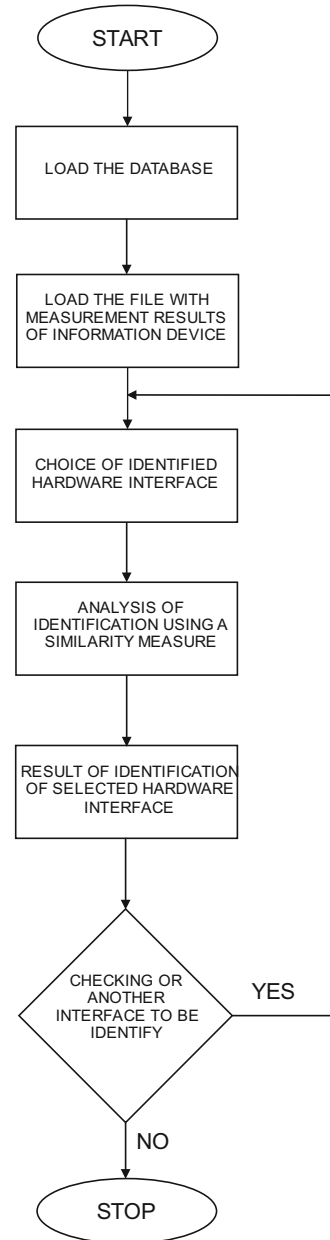
Figure 2: Algorithm of the main hardware interface identification process in IT device.

2.2. The Main Hardware Interface Identification Process

The basic hardware interface identification process is based on identifying work of the individual hardware interfaces during normal operation of IT device. The first step in the identification process is to load the database containing the distinctive features of each hardware interfaces into computer. Then we load the measurement results of the radiated emission for tested IT device. We choose one of the hardware interfaces (e.g., USB, Parallel, RS-232, DVI, VGA, LAN, etc.) which we want to identify and make identification analysis using measure probability of radiated emissions. After identification, we have information on whether it is specified interface, and then check to see if we have to identify another interface hardware in the device. If yes then we go back to point of select the next hardware interface and make an analysis of radiated emissions again. After all the tests of identification hardware interfaces for device identification process comes to an end. Algorithm

for the main hardware interface identification process is shown in Figure 2.

3. THE LEVELS OF RADIATED EMISSION

On the basis of there search and obtained measurement results one can state that there is a possibility to identify hardware interfaces of IT device which cause the increase of emission level. So, a distinctive feature of operation of specific interfaces is its work frequency and emission level allowing to identify a given hardware interface [4, 5]. The results of hardware interface identification have been collected in Table 1.

Table 1: Levels of EM field from hardware interfaces into PC unit.

Device/kind of interface	f [MHz]	Emission level within the distance 3 m from PC [dBµV/m]		Device/kind of interface	f [MHz] Przy pracy Interfejsu	Emission level within the distance 3 m from PC [dBµV/m]	
		With work of Interface	Without work of interface			With work of Interface	Without work of interface
LAN	30–34	33,91	27,30	USB	240,00	40,71	32,47
USB	62,00	31,11	25,72	USB	247,00	44,68	35,60
USB	62–70	33,67	24,50	LAN	250,00	40,63	35,33
USB	92,00	31,30	26,68	USB	260–290	31,05	24,30
RS-232	92,20	31,43	26,72	RS-232	287,90	41,98	33,84
USB	119,00	35,45	31,06	VGA	288,00	41,98	34,55
USB	120,00	35,50	32,18	USB	305,00	44,14	33,20
USB	124,00	35,69	28,82	USB	330–350	33,01	24,70
USB	140–160	33,18	28,79	USB	336,00	44,66	41,44
LPT	144,00	39,73	34,14	RS-232	370,30	33,20	28,50
VGA	153,00	37,22	28,92	HDD	374,00	31,56	28,01
LPT	203,00	36,11	34,40	VGA	382,00	43,46	35,10
RS-232	403,60	34,67	28,17	LAN	600,00	46,55	38,94
RS-232	415,70	32,40	29,02	LAN	618,00	37,40	32,90
VGA	417–421	43,08	28,67	LAN	619,00	37,38	32,91
USB	450,00	36,48	32,72	VGA	650,00	40,58	34,74
HDD	450,00	37,31	32,37	CPU, RAM	663–666	36,89	33,04
USB	480,00	54,44	35,79	USB	743,00	37,87	34,94
VGA	511–514	38,42	32,61	USB	749,00	39,87	34,37
USB	587,00	40,57	35,26	HDD	801,80	46,92	44,70
HDD	600,00	46,91	40,02	RS-232	820,00	50,25	39,04
VGA	600,00	48,65	37,34	VGA	820,00	46,71	38,84
HDD	868,90	46,50	42,09	USB	975,00	53,94	48,87
USB	960,00	54,87	45,92	USB	983,00	48,14	43,96

4. SIMILARITY MEASURE OF RADIATED EMISSIONS

Measurement radiated emissions methodology of internal components in IT device refers to measuring the strength of electromagnetic field level emitted by such devices for certain frequencies [11, 12]. In order to determine the similarity between the measured radiated emission with a specific reference spectrum of radiated emissions for each hardware interfaces, you can use the following similarity measure of radiated emissions on different frequencies:

- the average value,
- the correlation function,
- the relative value of the error signal level,
- the maximum value of the relative error signal level,

- the indicator z,
- the numer En.

The above-mentioned similarity measure of radiated emissions were considered by the author and are discussed in detail in the publications [1, 2, 8, 9].

5. THE CONCEPT OF DATABASE FOR HARDWARE INTERFACE OF INFORMATION DEVICES

The database is one of the basic cells of the effective functioning identify system of hardware interfaces into the IT device. It is an essential part of supporting the process of recognizing the individual hardware interfaces based on of radiated emissions, which the aim is to increase the probability of correct identification. The concept of a database must include the largest possible number of factors affecting the foreseeable possibilities for its use, and should include distinctive features for each hardware interfaces of IT device empirically determined. Figure 3 shows the appearance of the concept of a database created for identification of hardware interfaces.
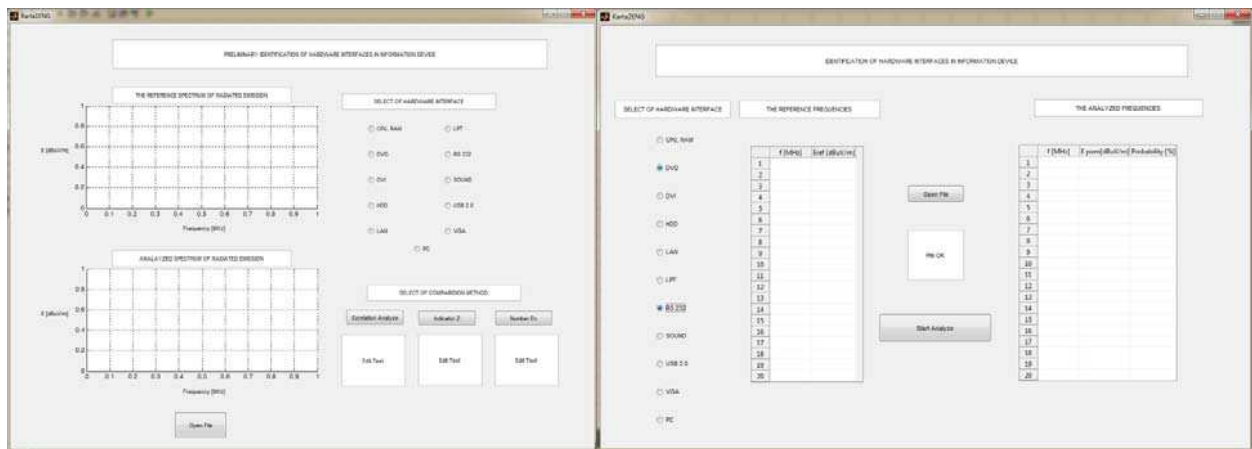
Figure 3: The appearance of database concepts created for the identification of hardware interfaces.

Presented in this chapter, the concept of database provides an accuracy and uniformity of the designated of distinctive features for individual hardware interfaces in information device. The database is stored sets of parameters and analysis functions allowing identification of the hardware interface. The proposed structure of the database contains two tabs for initial identification the hardware interface and the precise identification of the interface on different frequencies during information device normal working.

6. CONCLUSION

Collected as part of research conducted by the author test results of radiated emissions generated by different hardware interfaces of information devices allowed it to build a database, which can then be used to identify the components which are characterized by very high levels of radiated emissions. Identification is based on measures of the probability of radiated emissions of modern information devices. The designated distinctive features of hardware interfaces can be the basis in the early stages during design process of electromagnetic security of modern information device aiming to provide compliance with relevant standards in force in the European Union. In addition by identifying the hardware interfaces of information device resulting in increased emissions, there is an opportunity to significantly speed up the process of preparing device to sale where the emission level is incompatible with the standard.

REFERENCES

1. Nowosielski, L., M. Wnuk, and C. Ziółkowski, "Interlaboratorytests in scope of measurement of radio disturbance," *Conference Proceedings — 39th European Microwave Conference, EuMC 2009*, 288–291, Article number 5296286, 2009.
2. Przesmycki, R., L. Nowosielski, M. Bugaj, and K. Piwowarczyk, "Stability analysis of emissivity levels of the mobile computers," *MIKON 2012, 19th International Conference on Microwaves, Radar and Wireless Communications, IEEE Xplore*, 555–558, May 21–23, 2012.

3. Kubacki, R., E. Cwalina, M. Kuchta, and A. Dukata, "Specyfika rozkładu pola elektromagne-tycznego wewnatrz pomieszczen i obudów komputerowych od wysokomocowych impulsów elek-tromagnetycznych," *Przeglad Elektrotechniczny (Electrical Review)*, No. 12b, 209–212, 2012.

4. Kubacki, R. and S. Lamari, "The UWB microstrip antenna with metamaterial and periodic structure," *PIERS Proceedings*, 2651–2655, Guangzhou, Aug. 25–28, 2014.

5. Lamari, S., R. Kubacki, and M. Czyzewski, "Frequency range widening of the microstrip an-tenna with the sierpinski fractal patterned metamaterial structure," *MIKON 2014 Conference Proceedings*, 773–775, 2014.

6. Bugaj, M., "Measurements of wall attenuation in closed spaces inside a building," *PIERS Proceedings*, 2681–2686, Guangzhou, Aug. 25–28, 2014.

7. Bugaj, M., "Attenuation measurements of materials used in construction of buildings," *PIERS Proceedings*, 2671–2675, Guangzhou, Aug. 25–28, 2014.

8. Gajewski, P., J. Lopatka, L. Nowosielski, UB. ljasz, and Z. Piotrowski, "Multimedia transmis-sion over HF links," *Proceedings — IEEE Military Communications Conference, MILCOM*, Vol. 1, 45–47, 2000.

9. Nowosielski, L., J. Łopatka, and M. Siłaczuk, "Modelling of electromagnetic wave propagation with the use of the ray-tracing method," *PIERS Proceedings*, 2701–2705, Guangzhou, Aug. 25–28, 2014.

10. Nowosielski, L. and C. Piotrowski, "Honeycomb ventilation grill shielding effectiveness mea-suring methodology," *PIERS Proceedings*, 2692–2696, Guangzhou, Aug. 25–28, 2014.

11. Kaszuba, A., R. Checinski, M. Kryk, J. Lopatka, and L. Nowosielski, "Electromagnetically shielded real-time MANET testbed," *PIERS Proceedings*, 2706–2710, Guangzhou, Aug. 25–28, 2014.

12. Nowosielski, L. and J. Lopatka, "Measurement of shielding effectiveness with the method us-ing high power electromagnetic pulse generator," *PIERS Proceedings*, 2687–2691, Guangzhou, Aug. 25–28, 2014.

The Analysis of the Radius Impact on the Properties of Cylindrical Antenna with Coaxial Feed

Jarosław Bugaj and Marek Bugaj

Faculty of Electronics, Military University of Technology
Gen. S. Kaliskiego 2 str., Warsaw 00-908, Poland

Abstract— The article presents analysis of conformal multilayer antenna and array antenna with coaxial feed. The antenna has the shape of the cylinder with a radius R. It was examined an effect of change radius R on the basic operating parameters of the antenna.

For the selected frequency range (5031–5090.6 MHz) there was designed planar and cylindrical microstrip antenna and antenna array with coaxial feed. For conformal surface radius length was varied in the range 0.2–160λ. The full-wave analysis of antennas numerical parameters was carried out in CST Studio Suite.

The analysis of the tested antenna has been focused on the determination of the impact of the R-radius of the side surface of the cylinder, on which the conformal antenna have been installed, on the basic operating parameters of the antenna.

1. INTRODUCTION

Themicrostrip antennas constitute one of the most innovative areas of aerial technology for a number of years. An interest in such types of antennas dates back to 1953, when G. A. Deschamps developed a concept of printed antenna [11, 15, 17, 18, 25].

Despite many years, there are still few studies in the literature that describe microstrip antennas on conformal surfaces. Most authors limit themselves only to the analysis of structures made on flat surfaces, which in many cases are not sufficient. Increased interest in this subject matter can be seen in journals and at international conferences only since 1997. During the same period, first review articles about conformal antennas were published and their first practical applications were presented. It was certainly affected by one of the most important research problems in the field of aerial technology which has emerged in the last decade — a problem of conformality of the shape of the surface on which the radiating elements of antennas are installed, as well as the conformality of elements alone.

A conformal antenna is an antenna that conforms to something. In our case, it conforms to a prescribed shape. The shape can be some part of an airplane, high-speed train, or other vehicle. The purpose is to build the antenna so that it becomes integrated with the structure and does not cause extra drag. The purpose can also be that the antenna integration makes the antenna less disturbing, less visible to the human eye, for instance, in an urban environment. A typical additional requirement in modern defense systems is that the antenna not backscatter microwave radiation when illuminated by, for example, an enemy radar transmitter (i.e., it has stealth properties). In microstrip antennas are important parameters of the dielectric, which can be explored to measurein accordance with the methods described in the [1, 2, 9, 12, 16]. Antennas are an essential element of the plurality of measurement [5–8, 10, 19–21].

2. ANALYZED MODELS OF ANTENNAS

To analyze the impact of conformal antennas radius of curvature on their basic parameters and characteristics of radiation there was selected frequency ranges: 5031–5090.6 MHz. This range is used in aviation,in Microwave Landing System (MLS).

For selected frequency was designed planar coaxially fed microstrip antenna and array antenna. Then each antenna was placed sequentially on conformal surfaces: cylinder, sphere, torus, where for each of them full-wave analysis of antennas numerical parameters was carried out in CST Studio Suite.

Figure 1 shows analyzed conformal antenna placed on the side surface of the cylinder. Radiating element has a rectangular shape with dimensions $2L = 14.4$ mm and $2b\Phi = 19.0$ mm (width of radiating element as seen from inside of the cylinder). This element is placed on a dielectric of thickness $h = R - b = 1.52$ mm, dielectric permittivity $\varepsilon = 3.5$ (ROGERS RO3035™). The antenna is fed by a $50\,\Omega$ coaxial probe ($\Phi_p = 0$ mm; $Z_p = 4, 45$ mm). Around the cylinder of R radius there is vacuum of parameters: ε_0i μ_0. Fig. 2 shows analyzed array antenna.
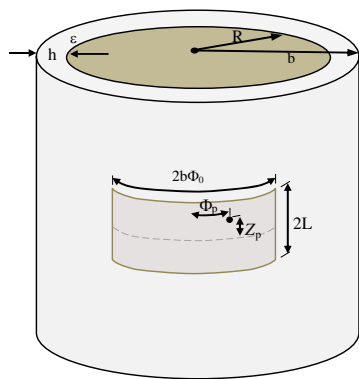
Figure 1: Analyzed conformal antenna on the side surface of the cylinder.
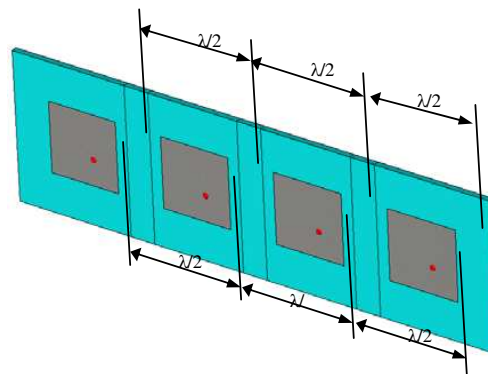
Figure 2: Analyzed array antenna (4×1).

3. CYLINDRICAL MICROSTRIP ANTENNA

The chapter presents analysis of conformal coaxially fed antenna (shown on Fig. 1) working in the frequency range between 5031–5090.6 MHz and placed on the side surface of the cylinder with radius R, which value was changed within the range 0.507–$168.95\lambda_0$ (30–10000 mm). The aim of this analysis is to examine impact of curvature of the side surface of the cylinder on antenna's basic parameters.
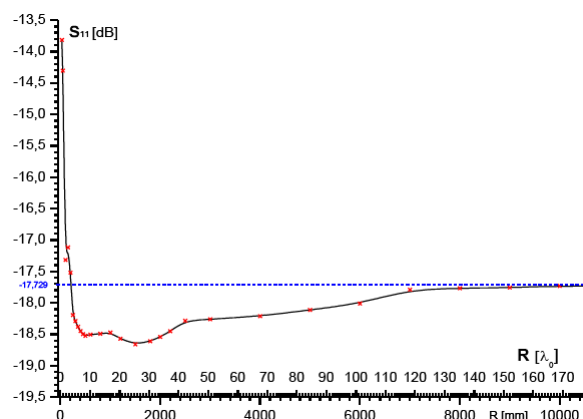
Figure 3: Reflection coefficient S11 of cylindrical conformal antenna depending on length of cylinder radius R.
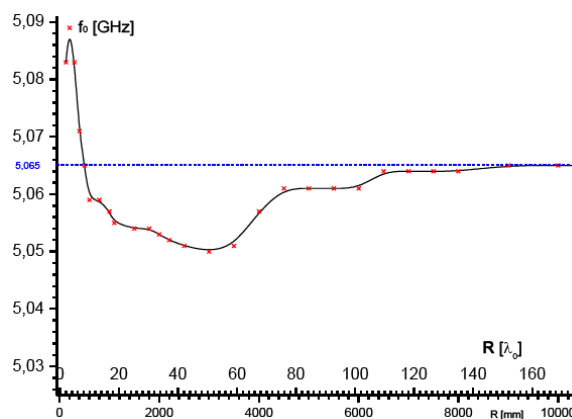
Figure 4: Resonance frequencies of conformal antenna depending on length of sphere radius R.

The graph in Fig. 3 shows dependence of reflection coefficient S_{11} for conformal antenna resonance frequency placed on cylinder side surface depending on cylinder radius R.

Next Fig. 4 shows dependence of antenna resonance frequency f_0 on cylinder radius R. Almost for all changes of radius length the value of antenna resonance frequency is maintained at the level of planar antenna resonance frequency $f_0 = 5.065$ MHz (dashed line). Only in the range of low values of radius $R < \lambda_0$ we can observe increase in resonance frequency.

Figure 5 and Fig. 6 presents bandwidth of cylindrical conformal antenna Δf depending on cylinder radius R.

Figure 7 and Fig. 8 shows normalized E-plane and H-plane patterns for different radii R.

4. CYLINDRICAL MICROSTRIP ARRAY ANTENNA

Antenna array shown in Fig. 2 was next placed on the and placed on the side surface of the cylinder R surface with radius R. Analysis results for array antenna working in the frequency range 5031–5090.6 MHz placed on the surface of the sphere are shown in Figs. 10–12. Radiations pattern of the antenna can also be determined from measurements of the near field [13, 14].
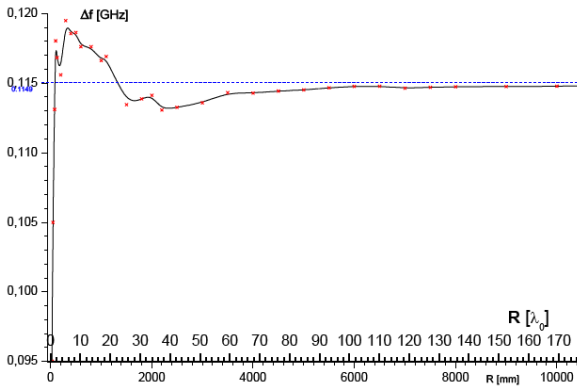
Figure 5: Bandwidth depending on length of cylinder radius R.
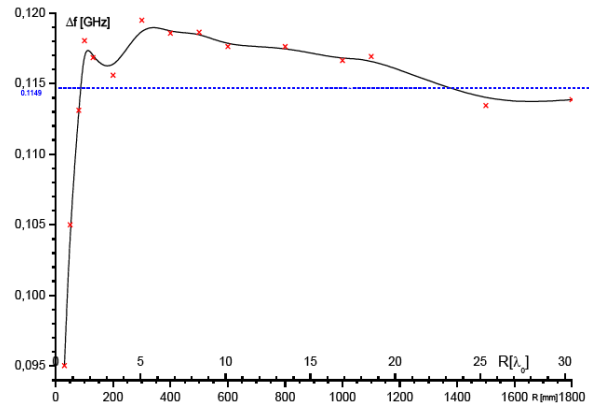
Figure 6: Bandwidth depending on length of cylinder radius $R < 25\lambda_0$.
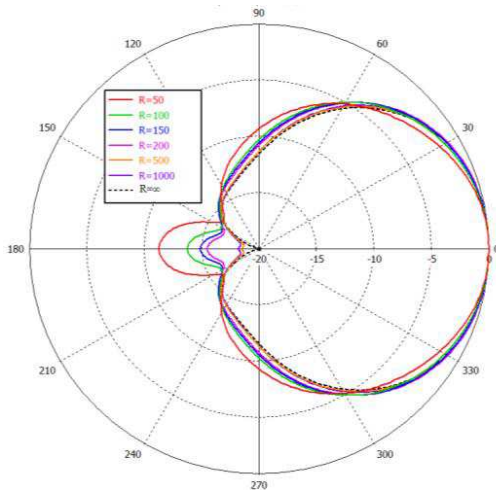
Figure 7: Normalized E-plane patterns for different radii R.
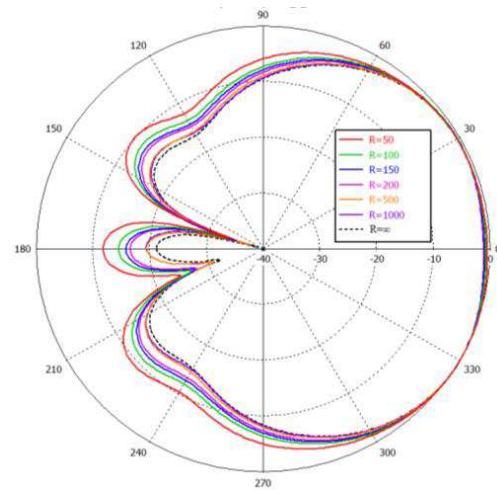
Figure 8: Normalized H-plane patterns for different radii R.
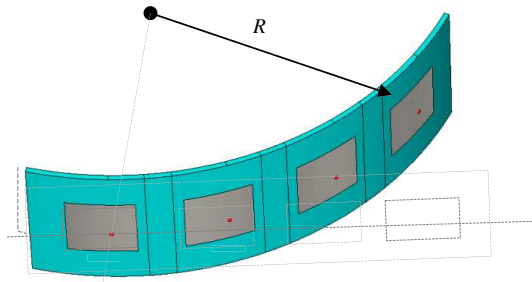
Figure 9: Analyzed cylindrical microstrip array antenna (4×1).
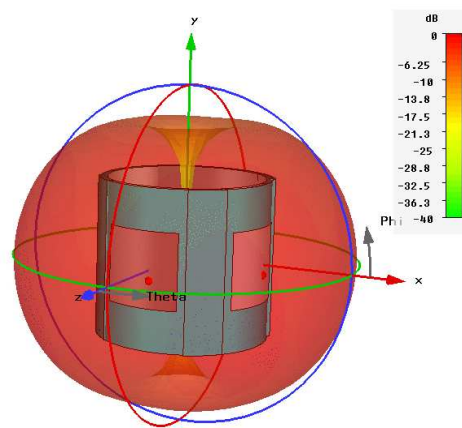
Figure 10: Characteristics of the radiation in the full angular range conformal array antenna.

Calculated characteristics of the radiation in the full angular range have been presented in Fig. 10.

Figure 7 and Fig. 8 shows normalized E-plane and H-plane patterns for different radii R.
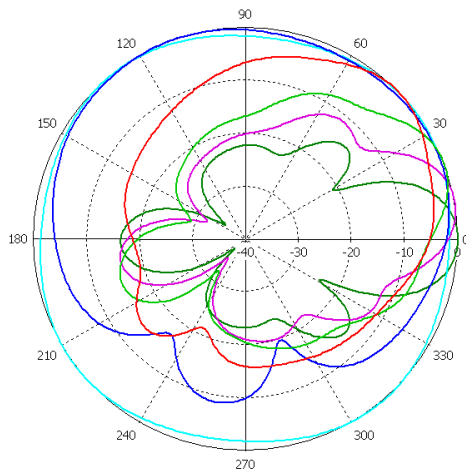
Figure 11: Normalized E-plane patterns for different radii.
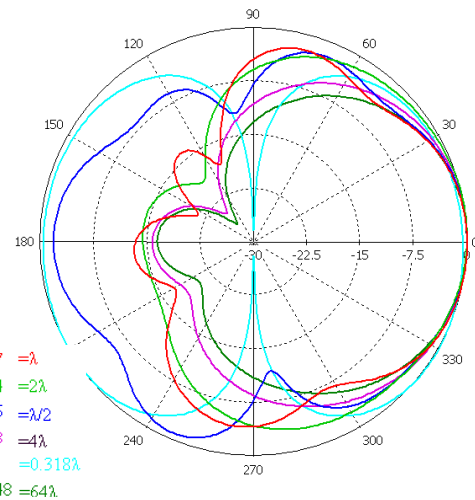
Figure 12: Normalized H-plane patterns for different radii.

5. CONCLUSIONS

The analysis of structures of conformal antennas is a complex and complicated process. Presented analysis shows how many factors affect the final result. In order to obtain the conformal multi-layered structure which would be optimal at desired angle, one shall be prepared for a series of calculations and simulations. Nevertheless, the necessity of concentrating and focusing propagated radio waves increases the demand for integrated antennas systems of cylindrical, spherical or conical shape, thanks to which both the desired properties of spatial radio channels, as well as significant reduction in the number of aerial system components can be obtained. Due to the aforementioned reasons, a considerable widespread of conformal antennas is expected in the future.

Characteristics of radiation, as well as of the working bandwidth, are closely related to the value of R-radius measured on the side surface of the cylinder on which the analyzed antenna is installed. Along with the increase in curvature of the antenna radiator (reduction in the R-radius), the radiation beam is widened, and the working bandwidth of the antenna narrows.

REFERENCES

1. Kubacki, R., R. Przesmycki, and J. Ferenc, "Własności elektromagnetyczne nanokrystalicznego proszku stopu Fe-Si-B-Cu-Nb w zakresie mikrofalowym," *Przegląd Elektrotechniczny (Electrical Review)*, 92–95, ISSN 0033-2097, NR 12b, 2011.

2. Kubacki, R., L. Nowosielski, and R. Przesmycki, "Technique for the electric and magnetic parameter measurement of powdered materials," *Computotional methods and experimental measurements XIV 2009, WIT Transactions on Modelling and Simulation*, 241–250, Vol. 48, ISSN 1743-355X, 2009.

3. Piwowarczyk, K., R. Przesmycki, L. Nowosielski, and M. Wnuk, "Pomiar odporności urządzeń informatycznych na promieniowane pole elektryczne o częstotliwości radiowej w zakresie (80–1000) MHz," *Przegląd Elektrotechniczny (Electrical Review)*, 165–167, R. 86 NR 3, 2010.

4. Przesmycki, R., L. Nowosielski, and M. Wnuk, "The laboratory stand for conducted emissions measurement in accordance with the military standard," *IEEE International Symposioum on Electromagnetic Comatibility*, 978-1-4244-6306-0/10/$26.00©2010, Article number 5711284, IEEE str 275–278, Florida, USA, 25–30 July 2010.

5. Nowosielski, L., R. Przesmycki, M. Wnuk, and K. Piwowarczyk, "Small chambers shielding efficiency measurements," *PIERS Proceedings*, 875–879, Marrakesh, Morocco, March 20–23, 2011.

6. Nowosielski, L., R. Przesmycki, M. Wnuk, and J. Rychlica, "The methods of measuring attenuation of thin absorbent materials used for electromagnetic shielding," *PIERS Proceedings*, 870–874, Marrakesh, Morocco, March 20–23, 2011.

7. Kubacki, R., L. Nowosielski, R. Przesmycki, and R. Frender, "Metoda pomiarów przenikalności elektrycznej i magnetycznej materiałów proszkowych," *Przegląd Elektrotechniczny (Electrical-Review)*, 83–87, ISSN 0033-2097, R. 85 NR, December 2009.

8. Przesmycki R., "Measurement and analysis of compromising emanation for laser printer," *PIERS Proceedings*, 2661–2665, Guangzhou, China, August 25–28, 2014.

9. Przesmycki, R. and P. Skokowski, "Dual band microstrip antenna," *PIERS Proceedings*, 2641–2645, Guangzhou, China, August 25–28, 2014.

10. Kubacki, R., M. Wnuk, and J. Modelski, "From nanoelectronics to the advanced microwave applications," *IEEE Microwave Magazine*, Vol. 13, No. 7, 94–96, 2012.

11. Kubacki, R., J. Ferenc, R. Przesmycki, and M. Wnuk, "The nanocrystallinefesibcunbfinemet absorption properties at microwaves," *IEEE Transactions on Electromagnetic Compatibility*, Vol. 54, No. 1, 93–100, 2012.

12. Kubacki, R., L. Nowosielski, and R. Przesmycki, "The improved technique of electric and magnetic parameters measurements of powdered materials," *Advances in Engineering Software*, Vol. 42, No. 11, 911–916, 2011.

13. Kubacki, R., M. Wnuk, W. Kolosowski, and J. Sobiech, "New approach to electromagnetic field calculations in the near-field of microwave antennas," *Computational Methods and experimental Measurements, XI Book Series: Computational Engineering*, Vol. 4, 413–422, 2003.

14. Kubacki, R., E. Cwalina, M. Kuchta, and A. Dukata, "Specyfika rozkładu pola elektromagnetycznego wewnątrz pomieszczeń i obudów komputerowych od wysokomocowych impulsów elektromagnetycznych," *Przegląd Elektrotechniczny (Electrical Review)*, No. 12b, 209–212, 2012.

15. Kubacki, R. and S. Lamari, "The UWB microstrip antenna with metamaterial and periodic structure," *PIERS Proceedings*, 2651–2655, Guangzhou, China, August 25–28, 2014.

16. Kubacki, R., "New attempt to building materials permittivity measurements," *PIERS Proceedings*, 2676–2680, Guangzhou, China, August 25–28, 2014.

17. Lamari, S., R. Kubacki, and M. Czyżewski, "Frequency range widening of the microstrip antenna with the sierpinski fractal patterned metamaterial structure," *MIKON-2014 Conference Proceedings*, 773–775, 2014.

18. Gajewski, P., J. Lopatka, L. Nowosielski, B. Uljasz, and Z. Piotrowski, "Multimedia transmission over HF links," *Proceedings — IEEE Military Communications Conference MILCOM*, Vol. 1, 45–47, 2000.

19. Nowosielski, L., M. Wnuk, C. Ziółkowski, "Interlaboratory tests in scope of measurement of radio disturbance," *European Microwave Week 2009, EuMW 2009: Science, Progress and Quality at Radiofrequencies, Conference Proceedings — 39th European Microwave Conference, EuMC 2009*, Article number 5296286, 288–291, 2009.

20. Nowosielski, L., J. Łopatka, and M. Siłaczuk, "Modelling of electromagnetic wave propagation with the use of the ray-tracing method," *PIERS Proceedings*, 2701–2705, Guangzhou, China, August 25–28, 2014.

21. Nowosielski, L. and C. Piotrowski, "Honeycomb ventilation grill shielding effectiveness measuring methodology," *PIERS Proceedings*, 2692–2696, Guangzhou, China, August 25–28, 2014.

22. Nowosielski, L. and M. Wnuk, "Compromising emanations from USB 2 interface," *PIERS Proceedings*, 2666–2670, Guangzhou, China, August 25–28, 2014.

23. Kaszuba, A., R. Checinski, M. Kryk, J. Lopatka, and L. Nowosielski, "Electromagnetically shielded real-time MANET testbed," *PIERS Proceedings*, 2706–2710, Guangzhou, China, August 25–28, 2014.

24. Nowosielski, L. and J. Lopatka, "Measurement of shielding effectiveness with the method using high power electromagnetic pulse generator," *PIERS Proceedings*, 2687–2691, Guangzhou, China, August 25–28, 2014.

25. Gruszczynski, M., M. Wnuk, and L. Nowosielski, "Multisystem microstrip antenna for mobile communications," *EEE Antennas and Propagation Society, AP-S International Symposium (Digest)*, Article number 6349179, 2012.

Implementation of Universal RF-shielded Enclosure for IT Equipment Protection

Leszek Nowosielski and Marain Wnuk

Faculty of Electronics, Military University of Technology
Gen. S. Kaliskiego 2 str., Warsaw 00-908, Poland

Abstract— In order to decrease the level of radiated emissions from information technology (IT) equipment and in order to protect the IT equipment in high level of electric field strength environment the RF shielded enclosures are needed. In the paper the implementation of universal RF shielded enclosure is presented. The description and the block diagram of the RF-shielded enclosure is presented. In the article the shielding efficiency (SE) of real RF-shielded enclosure is presented. Furthermore the paper presents the methodology and block diagram of laboratory stand for SE measurements conducted in anechoic chamber.

1. THE DESCRIPTION OF THE RF-SHIELDED ENCLOSURE

In order to decrease the level of radiated emissions from information technology (IT) equipment and in order to protect the IT equipment in high level of electric field strength environment the RF-shielded enclosure are needed. Moreover, even pervasive equipment (e.g., smartphones, handsets) with build-in software should be taken into consideration in terms of radiated emission [14, 15]. Below the implementation of universal RF shielded enclosure is presented. The references connected with the topic of this article are [1–3, 6, 8, 10, 12, 13].

The RF-shielded enclosure has dimensions: $0.440\,\text{m} \times 0.300\,\text{m} \times 0.550\,\text{m}$ and is made of galvanized steel sheet. The view of the RF-shielded enclosure along with the terminal panels is shown in Fig. 1. Interface panel has a special hole which allows to insert light pipe inside a shielded cubicle. The shielded enclosure is equipped with the power supply and signal filters which increase the system immunity for conducted interferences. On the panel there are interfaces for connection of auxiliary equipment: N-connectors (female), VGA filter and D-Sub filter (9-pin). The interfaces of RF-shielded enclosure ensure the proper communication with external devices via the cable and fiber-optical connections. The block diagram of the elaborated RF-shielded enclosure is presented in Fig. 2. Enclosure also provide of shielding effectiveness. In order to ensure the proper air exchange the special honeycomb filters were used.
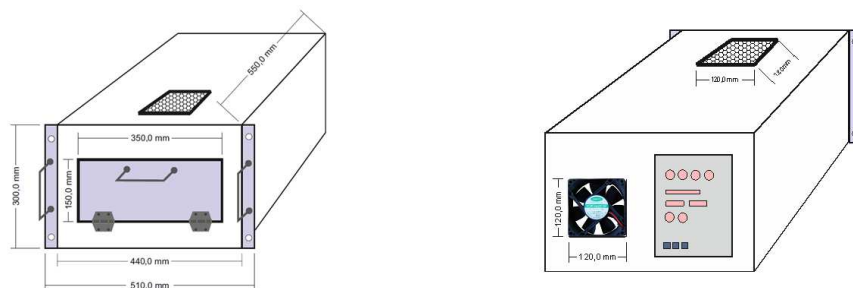
Figure 1: The view of the studied RF-shielded enclosure.

2. THE METHODOLOGY AND BLOCK DIAGRAM OF LABORATORY STAND

In order to measure the shielding efficiency (SE) of RF-shielded enclosure the measuring set is required which includes the measuring signal transmitter and the meter of electromagnetic field strength. Particular parts of the measuring set also consist of software, which activated on an operating computer makes automation of the SE measuring process possible.

The measurement of SE contributed by the RF-shielded enclosure comes down to make two measurements of the level of electromagnetic field strength for particular probing frequencies. The first measurement is carried out as so called standardization measurement. With determined value of the signal level generated by the probing signal transmitter, the level of electromagnetic field
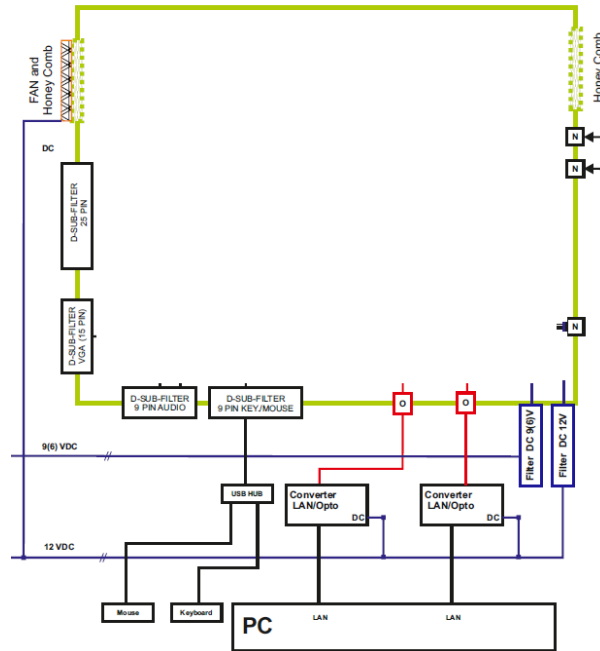
Figure 2: The block diagram of the elaborated RF-shielded enclosure.

strength is measured in the place of installation of receiving antenna connected to the measuring receiver, which functions as a meter of electromagnetic field strength. During standardization measurement the transmitting antenna of the probing signal transmitter and the receiving antenna are located opposite each other (without the RF-shielded enclosure under test) within the distance equal to a required distance, due to structural reasons of the tested RF-shielded enclosure, when the receiving antenna is situated inside the tested RF-shielded enclosure. The measurements can be made on discrete frequencies or in a given band with determined step. The measured values of electromagnetic field strength corresponding with particular measuring frequencies should be remembered.

After performing standardization measurement it is necessary to conduct basic measurement during which the transmitting antenna of the probing signal transmitter is placed outside the tested RF-shielded enclosure whereas the receiving antenna is situated inside the RF-shielded enclosure. With determined value of the signal level generated by the probing signal transmitter, the level of electromagnetic field strength is measured in the place of installation of receiving antenna. The measurements ought to be made in the same way as during standardization measurement on discrete frequencies or in a given frequency band with determined step. The measured values of electromagnetic field strength corresponding with particular measuring frequencies should be remembered. After subtracting the recorded levels of electromagnetic field strength levels corresponding with particular frequencies of the probing signal, during standardization $(E(f)_{stand})$ and basic $(E(f)_{basic})$ measurement we will receive the difference of levels of received signals in [dB], which makes the value of SE contributed by the tested RF-shielded enclosure. In this way we can obtain characteristics of shielding effectiveness in the frequency function.

$$\mathrm{SE} = 20 \log_{10} \left(E(f)_{stand}/E(f)_{basic} \right) \text{ [dB]}. \tag{1}$$

Measurements of shielding effectiveness should be conducted for each of the four sides of the RF-shielded enclosure. As the final result of SE results measurements with the SE lowest value should be chosen from the set of four values corresponding with each side of the RF-shielded enclosure, for each frequency of test signal. The SE depends on the parameters of the material used for tested enclosure. The parameters of materials can be obtained by using measurement methodology described in literature items.

A simplified block diagram of the measuring position for SE of RF-shielded enclosure measurement is shown in Fig. 3. The position consists of the measuring signal transmitter and the meter of electromagnetic field strength. The measuring signal transmitter and the meter of electromagnetic
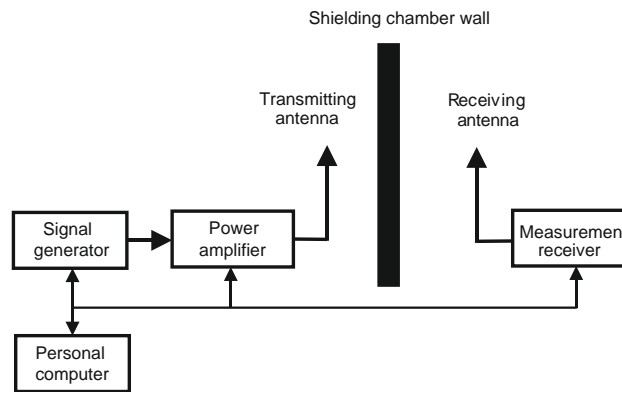
Figure 3: Simplified block diagram of the SE measuring position.
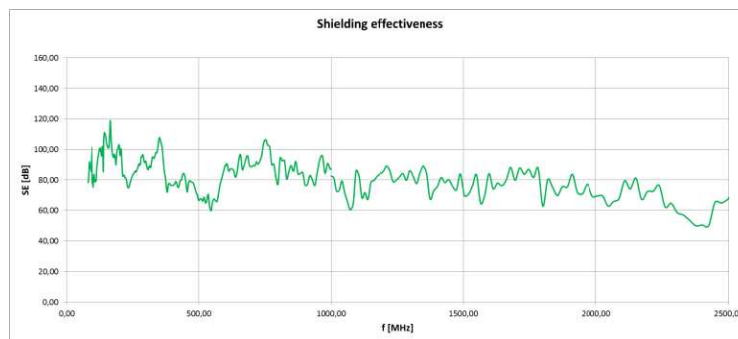
Figure 4: Shielding effectiveness in the range of 80 MHz to 2500 MHz.

field strength have to be equipped with the measurement antennas [4, 5, 7, 9, 11].

3. MEASUREMENT RESULTS

In order to present measuring possibilities described in Chapter 2 measurements of SE the RF-shielded enclosure described above have been conducted. The measurements show that the level of SE for the RF-shielded enclosure does not exceed 50 dB for radiated disturbances in the frequency range from 80 MHz to 2,5 GHz. Characteristic of SE made in anechoic chamber are shown in Fig. 4.

4. CONCLUSIONS

In order to decrease the level of radiated emissions from information technology (IT) equipment and in order to protect the IT equipment in high level of electric field strength environment the RF shielded enclosures are needed. In the paper the implementation of universal RF shielded enclosure is presented. The description and the block diagram of the RF-shielded enclosure are presented. The shielding efficiency (SE) of elaborated RF shielded enclosure does not exceed 50 dB for radiated disturbances in the frequency range from 80 MHz to 2,5 GHz. The elaborated universal RF shielded enclosures can be used for decrease the level of radiated emissions from information technology (IT) equipment.

ACKNOWLEDGMENT

REFERENCES

1. Kubacki, R., R. Przesmycki, and J. Ferenc, "Wlasności elektromagnetyczne nanokrystalicznego proszku stopu Fe-Si-B-Cu-Nb w zakresie mikrofalowym," *Przegląd Elektrotechniczny (Electrical Review)*, NR 12b/2011, 92–95, 2011, ISSN: 0033-2097.

2. Przesmycki, R., "Measurement and analysis of compromising emanation for laser printer," *PIERS Proceedings*, 2661–2665, Guangzhou, China, Aug. 25–28, 2014.

3. Przesmycki, R., M. Wnuk, P. Skokowski, and M. Bugaj, "Identification of interface in the complex systems based on radiated emission of mobile computer," *PIERS Proceedings*, 2656–2660, Guangzhou, China, Aug. 25–28, 2014.

4. Przesmycki, R., M. Bugaj, and M. Wnuk, "Wideband microstrip antenna," *PIERS Proceedings*, 2646–2650, Guangzhou, China, Aug. 25–28, 2014.

5. Przesmycki, R. and P. Skokowski, "Dual band microstrip antenna," *PIERS Proceedings*, 2641–2645, Guangzhou, China, Aug. 25–28, 2014.

6. Kubacki, R., J. Ferenc, R. Przesmycki, and M. Wnuk,, "The nanocrystalline fesibcunb finemet absorption properties at microwaves," *IEEE Transactions on Electromagnetic Compatibility*, Vol. 54, No. 1, 93–100, 2012.

7. Kubacki, R., M. Wnuk, W. Kolosowski, and J. Sobiech,, "New approach to electromagnetic field calculations in the near-field of microwave antennas," *Computational Methods and Experimental Measurements, XI Book Series: Computational Engineering*, Vol. 4, 413–422, 2003.

8. Kubacki, R., E. Cwalina, M. Kuchta, and A. Dukata, "Specyfika rozkładu pola elektromagnetycznego wewnatrz pomieszczeń i obudów komputerowych od wysokomocowych impulsów elektromagnetycznych," *Przegląd Elektrotechniczny (Electrical Review)*,, No. 12b, 209–212, 2012.

9. Kubacki, R. and S. Lamari, "The UWB microstrip antenna with metamaterial and periodic structure," *PIERS Proceedings*, 2651–2655, Guangzhou, China, Aug. 25–28, 2014.

10. Kubacki, R., "New attempt to building materials permittivity measurements," *PIERS Proceedings*, 2676–2680, Guangzhou, China, Aug. 25–28, 2014.

11. Lamari, S., R. Kubacki, and M. Czyzewski,, "Frequency range widening of the microstrip antenna with the Sierpinski fractal patterned metamaterial structure," *MIKON-2014 Conference Proceedings*, 773–775, 2014.

12. Bugaj, M., "Measurements of wall attenuation in closed spaces inside a building," *PIERS Proceedings*, 2681–2686, Guangzhou, China, Aug. 25–28, 2014.

13. Bugaj, M., "Attenuation measurements of materials used in construction of buildings," *PIERS Proceedings*, 2671–2675, Guangzhou, China, Aug. 25–28, 2014.

14. Piotrowski, Z. and M. Ciolek, "Changing the voice of a subscriber on the example of an implementation of the PSOLA algorithm for the iOS and Android mobile platforms," *Multimedia Communications Services and Security, MCSS 2013, Book Series: Communications in Computer and Information Science*, Vol. 368, 181–193, 2013.

15. Rózanowski, K., Z. Piotrowski, and M. Ciolek, "Mobile application for driver's health status remote monitoring," *2013 9th International Wirless Communications and Mobile Computing Conference (IWCMC)*, 1738–1743, 2013.

16. Bajda, A., M. Wrazen, and D. Laskowski, "Diagnostics the quality of data transfer in the management of crisis situation," *Electrical Review*, Vol. 87, No. 9A, 72–78, 2011.

17. Laskowski, D., P. Lubkowski, E. Pawlak, and P. Stanczyk, "Anthropo-technical systems reliability, safety and reliability: Methodology and applications," *Proceedings of the European Safety and Reliability Conference, ESREL 2014*, 399–407, 2014.

18. Ziólkowski, C. and J. M. Kelner, "Geometry-based statistical model for the temporal, spectral, and spatial characteristics of the land mobile channel," *Wireless Personal Communications*, 2015, Article in Press, Doi: 10.1007/s11277-015-2413-3.

19. Gajewski, P., J. M. Kelner, and C. Ziólkowski, "Dynamic location of the emission sources based on Doppler effect," *Przegląd Elektrotechniczny (Electrical Review)*, Vol. 89, No. 7, 223–226, 2013.

20. Gajewski, P., J. M. Kelner, and C. Ziólkowski, "Using SDF method for simultaneous location of multiple radio transmitters," *19th International Conference on Microwaves, Radar and Wireless Communications, MIKON-2012*, Vol. 2, 634–637, Warsaw, Poland, May 21–23, 2013.

The Exposure Level of High Power Microwave Pulses

Roman Kubacki and Salim Lamari

Faculty of Electronics, Military University of Technology, Warsaw, Poland

Abstract— In the paper the investigation of dosimetry of exposure to high power microwave (HPM) pulses has been discussed. The dosimetry was based on recommendations of the International Commission of Nonionizing Radiation Protection and by the Institute of Electrical and Electronics Engineers. Taking into account the high values of amplitude of HPM pulses and their very short durations the modification of assessing technique was presented. Two parameters considered as basic restriction parameters, i.e., specific absorption rate (SAR) and specific absorption (SA) have been analyzed.

1. INTRODUCTION

Currently more and more institutions and EMC laboratories investigate the high power microwave (HPM) pulsed radiation [1,–6, 10, 11, 15, 17]. Such radiation has unique electrical parameters, i.e., extreme power in peak (hundreds kV/m) and very short duration of pulses (nanoseconds) and it is obvious that such radiation should be investigated taking into account the electromagnetic compatibility as well as the biological damages in exposed tissues [8, 9, 12–14, 18, 19]. From this point of view the dosimetry assessment is necessary to investigate potential health hazard and to compare with established guidelines where the permissive exposure levels (PEL) have been predicted. The important difficulty is that the literature does not provide sufficient information about human health hazard when exposed to HPM pulses and because of this guidelines propose only conservative attempt taking into account the thermal effect, deeply recognize for exposure to long-term radiation.

To protect against electromagnetic radiation in the human exposure the permissive exposure limits have been recommended by the International Commission of Nonionizing Radiation Protection (ICNIRP) and by the Institute of Electrical and Electronics Engineers (IEEE) and also by national regulations. The maximum permissible limitations have been based on the highest peak of electric or magnetic field strengths or the plane-wave equivalent to power densities. The most authoritative exposure guidelines recommend also specific absorption rate (SAR) as a basic restriction. The SAR is the time derivative of the incremental energy absorbed by an incremental mass contained in a volume element of given density. Additionally, for pulsed exposures in the frequency range 0.3 to 10 GHz in order to limit or avoid auditory effects caused by thermoelastic expansion, the threshold level of specific absorption (SA) is also recommended.

Electromagnetic pulse-radiation emitted from HPM generators can also be treated as ultra-wideband (UWB) signals. The UWB signals have different forms of interaction with biological structures compared with continuous signals because the frequency spectrum of harmonics of such radiation sometimes exceeds 500 MHz.

Taking into account that the electrical properties (complex permittivity) of biological tissues change its values in function of frequency the attempt of dosimetry should be redefined. Values of the real and imaginary part of permittivity of blood in the frequency from 100 MHz to 600 MHz have been presented in Figure 1.
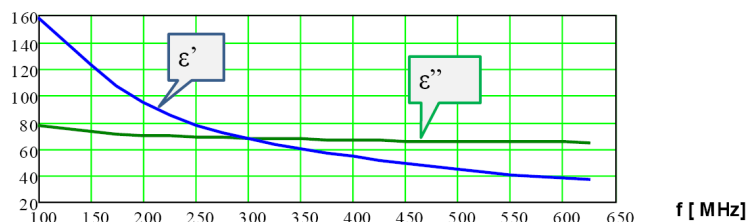
Figure 1: Permittivity of blood in function of frequency.

2. PEMISSIVE EXPOSURE LEVEL

At microwaves, for long-term exposure the exposure limitations are described by the electric field strength expressed in V/m, the power density in W/m^2 or additionally by the SAR in W/kg and SA in J/kg. Established values are derived with consideration of adverse effects thresholds and are considered protective for all human exposure. They were established after the thorough review and consideration of the literature. When the exposure is a short-term or pulsed radiation regime the specific absorption (SA) expressed in J/kg is especially recommended. In case of pulsed exposure, e.g., radar exposure the maximum peak in time should not exceed values of long-term exposure multiplied by a factor of 32. For radar pulsed exposure the SA should not exceed 10 mJ/kg averaged over 10 g of tissue in order to limit and avoid auditory effects caused by thermo-elastic expansion.

In the guidelines the general limitations of pulsed exposure are done in the following way — for exposures to pulsed RF fields, in the range of 100 kHz to 300 GHz, the peak (temporal) electric field strength or power density are limited only by the use of time averaging and the limit on peak E field value of the electric field strength is 100 kV/m.

Nevertheless, there exists an exception to this limitation allowing exposure to higher strength pulsed field but additional investigation of SAR or SA must be derived basing on the following regulation — the total incident energy density during any one-tenth second period within the averaging time shall not exceed one-fifth of the total energy density permitted during the entire averaging time for a continuous field, i.e.,

$$\sum\nolimits_0^{0.1\,\text{s}}(\text{SAR}_{pk} \times \tau) \le 28.8\,\text{J/kg} \tag{1}$$

where τ is the pulse width, SAR_{pk} — SAR in peak.

Additional conditioning to this exception states that a maximum of five pulses with pulse durations less than 0.1 s is permitted during any period equal to the averaging time. If there are more than five pulses during the averaging time, or if the pulse duration is more than 0.1 s, normal averaging time calculations apply and the limitation is SA = 144 J/kg.

The assessment of dosimetry of the exposure to HPM pulses will be presented for pulses emitted by commercially available Marx generator type DS110 (DIEHL, Germany). Pulses emitted by such generator have the pulse widths from 4 to 100 ns and frequency pulse repetition depending on the demand but typically it is 10 Hz. The value of 200 kV/m of the electric strength in peak can be obtained. During the experiments it is possible to emit few pulses (less than 5 pulses) as well as more than 5 pulses. For such emissions two cases of exposure assessments will be analyzed:

- dosimetry of 1 pulse,
- dosimetry of a series of pulses.

According to IEEE recommendations the investigation of SAR and SA should be derived in a volume called planar slab model. This model is a parallelepiped with a frontal surface area of 0.9 m^2 and depth of 7.8 cm, which is representative for a man of 70 kg weight. In the work a modification of dimensions of the model is proposed. The proposed planar slab model is also a parallelepiped but with a frontal surface area of $L1 \times L2 = 0.47\,\text{m}^2$ and a depth of $L3 = 15$ cm, as shown in Figure 2(a). The new model has a smaller frontal surface area, but on the other hand dimension $L3$ is bigger and it is four times bigger than the skin depth in the investigated tissue in the range of MHz frequencies. The dimension $L3 = 15$ cm allows to reduce the rays reflected from the back side of the model and simplifies the calculation of the dosimetry.

Electromagnetic field incident to the planar slab model surface is reflected according to the boundary condition. The remaining part propagates inside the material and is attenuated due to imaginary part of permittivity. Electric field strength decreases in function of z, thus SAR is also a function of z as follows.

$$\text{SAR}(z) = \frac{\sigma}{\rho}|Ein(z)|^2 \tag{2}$$

where: σ — conductivity, ρ — density of tissue, Ein — electric field inside the tissue.

When determining compliance with the guidelines the specific absorption rate (SAR) should be averaged over the averaging volume. In this case the maximum local SAR should be averaged over any ten-grams of tissue in the shape of a cube (SARav). Taking into account the density of tissue of 1 g/cm^3 the side of averaging cube is $Lav = 2.14$ cm (Figure 2(b)). The averaged value of SAR
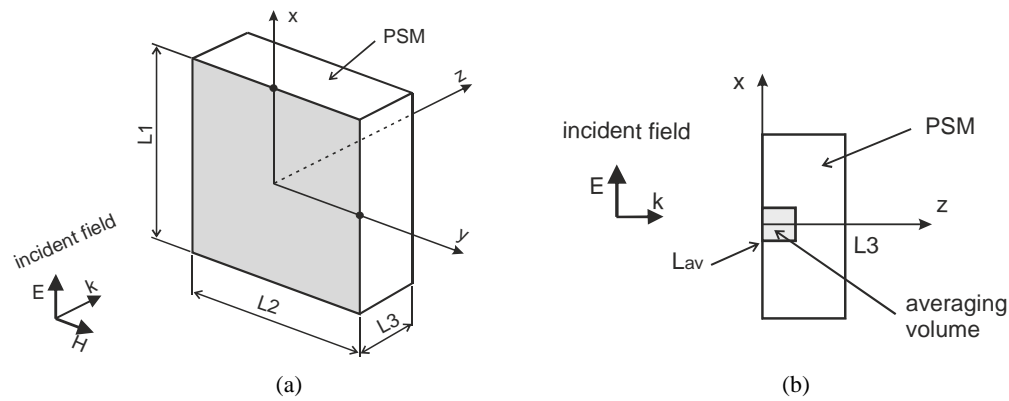
Figure 2: Planar slab model (PSM): (a) general view, (b) cross section in plane xz, where: $Lav = 2.14$ cm.

can be determined using the following formula:

$$\text{SARav} = \frac{1}{Lav} \int_0^{Lav} \text{SAR}(z)dz \tag{3}$$

In this attempt the assumption that SARav does not change its value inside the averaging volume in function of x and y is taken into account.

3. DOSIMETRY ASSESMENT

The method proposed for assessing the dosimetry of HPM exposure was realized in the following way.

- Analyzed HPM pulse (Figure 3(a)) has been expanded in to Fourier series. Fourier transform allows to determine the amplitudes of harmonics in the frequency domain.
- Calculation of SAR(z) and SARav was realized for each harmonic treated as a plane wave for suitable frequency. Permittivity values of blood have been also taken for the frequency of harmonics.
- Calculation of SA.

In Figure 3(b), the values of specific absorption rate averaged over 10 g (SARav) have been presented for all harmonics. The total SAR$_{tot}$ of signal presented in Figure 3(a) can be obtained by summing all values of SARav for all harmonics. In the analyzed case of HPM pulses the SAR$_{tot}$ is of 110 kW/kg. This value is extremely high but it should be underlined that investigated pulse widths are very short in time and from this point of view rather specyfic absorption (SA) should be analyzed. For a single pulse the SA has value of 0.5 mJ/kg. Such value of SA is much lower than permissive exposure level which is of 28.8 J/kg. On the other hand, for series of pulses in averaging time, the SA is of 1.9 J/kg. The obtained value is also lower than the limitation which has been recommended as 144 J/kg.
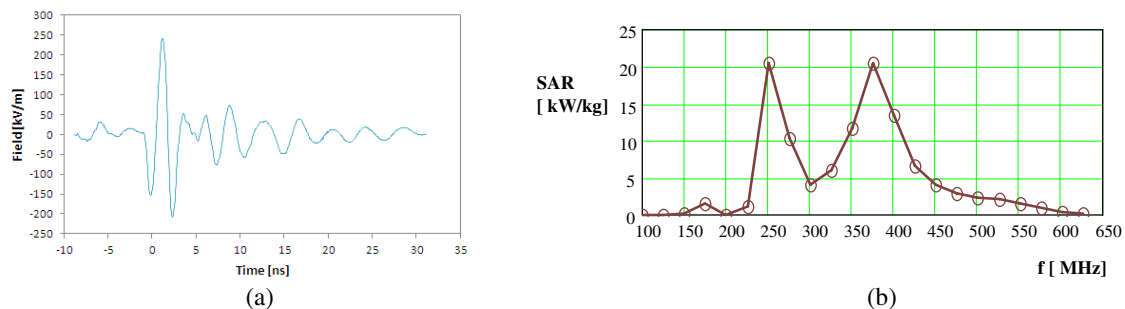
Figure 3: (a) HPM pulse in the time domain, (b) averaged values of SARav for all harmonics in function of frequency.

4. CONCLUSIONS

In the paper the investigation of dosimetry of exposure to high power microwave (HPM) pulses has been discussed. The dosimetry was based on recommendations of the International Commission of Nonionizing Radiation Protection and by Institute of Electrical and Electronics Engineers. Taking into account the high values of amplitude of HPM pulses and their very short durations in time the modification of assessing technique was presented. Two parameters as basic restriction parameters, i.e., specific absorption rate (SAR) and specific absorption (SA) have been analyzed.

ACKNOWLEDGMENT

REFERENCES

1. Bugaj, M., "Attenuation measurements of materials used in construction of buildings," *PIERS Proceedings*, 2671–2675, Guangzhou, August 25–28, 2014.
2. Bugaj, J. and M. T. Wnuk, "Analysis of the impact of surface on parameters of cylindrical microstrip antennas [Analiza wielowarstwowej anteny cylindrycznej ze względu na promień krzywizny]," *Przegląd Elektrotechniczny (Electrical Review)*, No. 3, 48–51, 2015.
3. Bugaj, J. and M. T. Wnuk, "Analysis of conformal multilayer antenna working in X band [Analiza wielowarstwowej anteny konformalnej pracujaej w pasmie X]," *Przegląd Elektrotechniczny (Electrical Review)*, No. 9, 46–49, 2009.
4. Bugaj, M., "Measurements of wall attenuation in closed spaces inside a building," *PIERS Proceedings*, 2681–2686, Guangzhou, August 25–28, 2014.
5. Bugaj, M. and M. T. Wnuk, "Optimization parameters of dielectric in aperture-coupled stacked patch antenna on bandwidth," *18th International Conference on Microwaves, Radar and Wireless Communications, MIKON*, 2010.
6. Nowosielski, L. and J. Lopatka, "Measurement of shielding effectiveness with the method using high power electromagnetic pulse generator," *PIERS Proceedings*, 2687–2691, Guangzhou, August 25–28, 2014.
7. Nowosielski, L. and Z. Piotrowski, "Honeycomb ventilation grill shielding effectiveness measuring methodology," *PIERS Proceedings*, 2692–2696, Guangzhou, August 25–28, 2014.
8. Przesmycki, R., M. T. Wnuk, L. Nowosielski, and K. Piwowarczyk, "Small chambers shielding efficiency measurements," *PIERS Proceedings*, 875–879, Marrakesh, Morocco, March 20–23, 2011.
9. Nowosielski, L., R. Przesmycki, M. T. Wnuk, and J. Rychlica, "The methods of measuring attenuation of thin absorbent materials used for electromagnetic shielding," *PIERS Proceedings*, 870–874, Marrakesh, Morocco, March 20–23, 2011.
10. Nowosielski, L. and M. T. Wnuk, "Compromising emanations from USB 2 interface," *PIERS Proceedings*, Guangzhou, 2666–2670, August 25–28, 2014.
11. Piwowarczyk, K., R. Przesmycki, L. Nowosielski, and M. T. Wnuk, "Pomiar odporności urządzeń informatycznych na promieniowane pole elektryczne o częstotliwości radiowej w zakresie (80–1000) MHz," *Przegląd Elektrotechniczny (Electrical Review)*, No. 86, 165–167, 2010.
12. Przesmycki, R., "Measurement and analysis of compromising emanation for laser printer," *PPIERS Proceedings*, 2661–2665, Guangzhou, August 25–28, 2014.
13. Przesmycki, R., L. Nowosielski, M. Bugaj, and K. Piwowarczyk, "Analiza emisji promieniowanej współczesnych urządzeń informatycznych," *Przegląd Elektrotechniczny (Electrical Review)*, No. 2, 4–6, 2012.
14. Przesmycki, R., L. Nowosielski, M. Bugaj, and K. Piwowarczyk, "Pomiar absorpcji materiałów pochłaniających fale elektromagnetyczne," *Przegląd Elektrotechniczny (Electrical Review)*, No. 2, 33–35, 2012.
15. Przesmycki, R., L. Nowosielski, and M. T. Wnuk, "The laboratory stand for conducted emissions measurement in accordance with the military standard," *IEEE International Symposioum on EMC, Florida*, 275–278, 2010.
16. Przesmycki, R. and P. Skokowski, "Dual band microstrip antenna," *PIERS Proceedings*, 2641–2645, Guangzhou, August 25–28, 2014.
17. Przesmycki, R., M. T. Wnuk, L. Nowosielski, K. Piwowarczyk, and M. Bugaj, "Analysis of the radiated emissions of IT equipment," *PIERS Proceedings*, 1419–1423, Moscow, Russia, August 19–23, 2012.

18. Przesmycki, R., M. T. Wnuk, L. Nowosielski, K. Piwowarczyk, and M. Bugaj, "The conducted and radiated emission levels from IT devices," *PIERS Proceedings*, 77–81, Kuala Lumpur, Malaysia, March 27–30, 2012.

19. Przesmycki, R., M. T. Wnuk, M. Bugaj, and K. Piwowarczyk, "Analiza metod pomiarowych tłumienności torów w.cz," *Przegląd Elektrotechniczny (Electrical Review)*, No. 2, 17–19, 2012.

20. Wnuk, M. T. and J. Bugaj, "Analysis of surface waves in microstrip array," *16th International Conference on Microwaves, Radar and Wireless Communications, MIKON*, 2006.

21. Wnuk, M. T., M. Bugaj, R. Przesmycki, L. Nowosielski, and K. Piwowarczyk, "Wearable antenna constructed in microstrip technology," *PIERS Proceedings*, 67–71, Kuala Lumpur, Malaysia, March 27–30, 2012.

Electromagnetic Compatibility Studies of Selected Components for Present Day Cars

Leszek Nowosielski and Marian Wnuk

Faculty of Electronics, Military University of Technology
Gen. S. Kaliskiego 2 str., Warsaw 00-908, Poland

Abstract— A present car includes more and more electronics. Today each car is stuffed with integrated circuits. Some of them are responsible for correct operation of the engine, others watches over the security, and next ones else control equipment correcting comfort. However, from one hand the electronics in the cars brings the enormous advantage, from the other hand it is the cause of problems. These statements were the base to carry out measurements of emissivity for one of the elements fittings of a modern car. The systems and measurement stands as well as the results of radiated and conducted disturbance emissions have been shown in the article as the function of frequency for motors of car window wipers.

1. STRUCTURE OF THE WINDOW WIPER MOTOR

DC electric motors are very often used execution elements within regulation systems. The primary advantages of these motors are: high torque, good efficiency as well as small dimensions whereas the disadvantages are: sparking (industrial interferences) and wearing and tearing of commutator brushes. For last ten years a series of motors with a special design having very good dynamic characteristics have been introduced into the market. The primary disadvantage from EMC point of view is that sparking on the commutator generates plenty of electromagnetic interferences. A measurement methodology of conducted and radiated disturbances generated by the DC motor is presented later on in the article. The references connected with the topic of this article are [4, 6, 8, 10–17].

2. MEASUREMENT STAND FOR RADIATED AND CONDUCTED DISTURBANCES LEVELS AS WELL AS MEASUREMENT RESULTS

Two electric motors Mitsuba PP-T40 from the car Subaru Forester II and Subaru Forester I used to drive the windscreen wipers are the equipment tested. The measurements of electromagnetic interferences radiated emission levels of the tested motors No. 1 and No. 2 were done within the frequency range from 2 MHz to 1 GHz.

Before making the radiated disturbances measurement, the legalisation of the measurement path between the antenna and measurement data registration equipment has been done [2]. In order to do so, the program application EMC 32 has been used. The EMC 32 application is used to control the measurement process as well as in order to calculate the electric field strength according to the dependence:

$$E = U_{wej} - T + K, \tag{1}$$

where:
E — the electric field strength in the installation site of the measurement antenna [dB(μV/m)],
U_{wej} — signal level at the input of the measurement receiver [dBμV],
T — attenuation of the HF path connecting the measurement antenna with the measurement receiver input [dB],

Figure 1: Motors of windscreen wipers of Subaru Forester II and I.
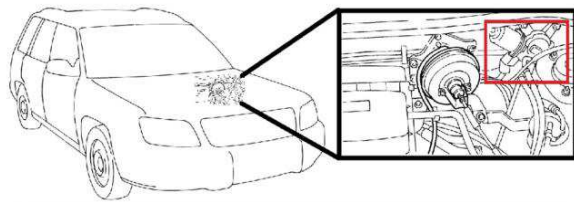
Figure 2: Location of the equipment tested in the Subaru Forester car.
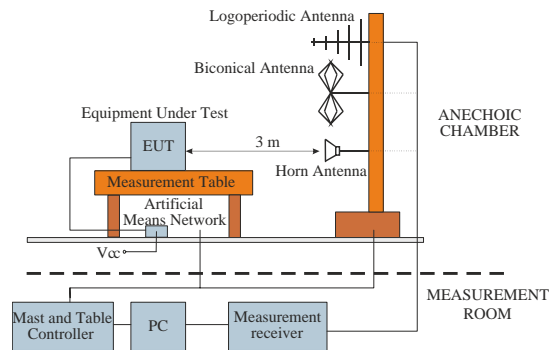
Figure 3: Block diagram of laboratory stand for radiated disturbances measurement.
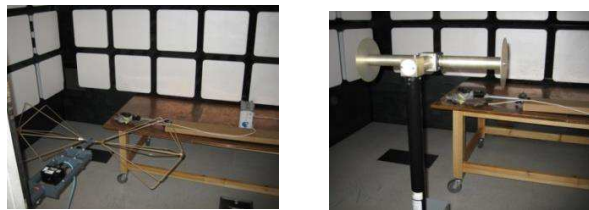
Figure 4: Laboratory stand for radiated disturbances measurement.
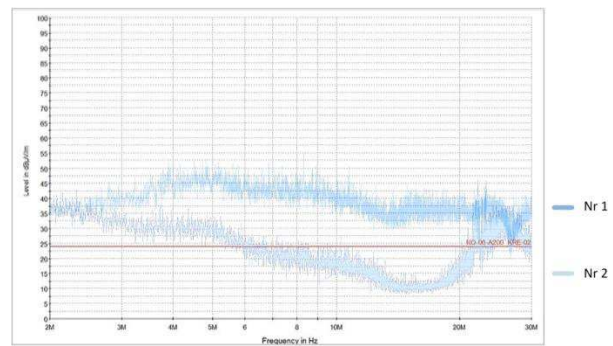
Figure 5: Amplitude diagram of radiated disturbances vs. frequency for windscreen wipers No. 1 and 2.
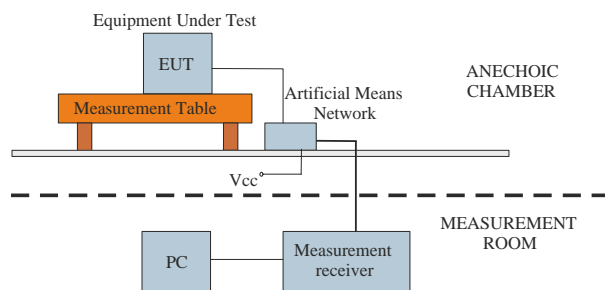
Figure 6: Block diagram of laboratory stand for conducted disturbances measurement.
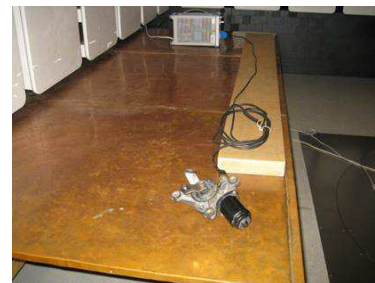
Figure 7: Laboratory stand for conducted disturbances measurement.

K — correction coefficient of the measurement antenna used, which takes the effective surface of the antenna into account [dB/m].

The appearance of the motors tested as well as their location inside the vehicle is shown in the Figs. 1 and 2 respectively.

The electrical motor of the windscreen wipers is placed in the higher right corner under the bonnet of the Subaru Forester car.

Measurements of the radiated disturbances and conducted levels generated by the tested windscreen wipers motors have been done inside the anechoic chamber. The block diagram of the measuring stand for radiated disturbances as well as its external view is presented in the Figs. 3 and 4. During the measurement the antennas have ti be used [3, 5, 7]. The measurement results of radiated emission of the windscreen wipers motors No. 1 and No. 2 within the frequency range of 2 MHz–30 MHz is presented in the Fig. 5.

The block diagram as well as external view of the measurement stand for conducted disturbances within the power supplying circuit are presented in the Figs. 6 and 7 respectively. The measurement results of the conducted emissions for the motors of the windscreen wipers No. 1 and No. 2 for the

| + line | Neutral line |
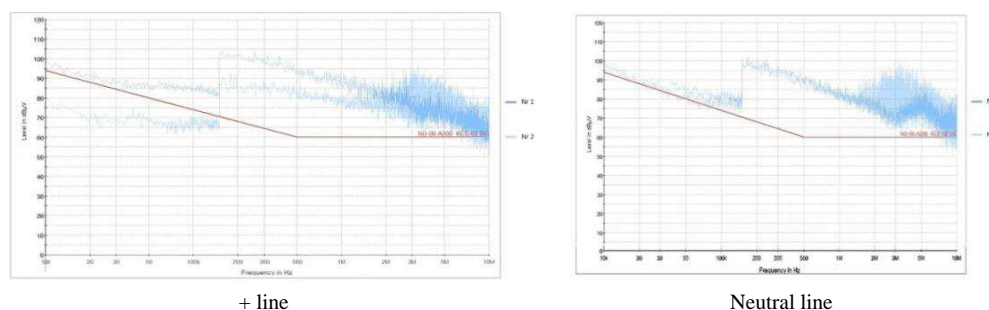
Figure 8: Amplitude diagram of conducted disturbances vs. frequency.

phase as well as neutral conductors within the frequency range of 10 kHz–10 MHz are presented in
the Fig. 8.

3. CONCLUSIONS

A lot of various subassemblies and components are installed in cars. They are stressed to elec-
tromagnetic interferences, and also they can generate interferences themselves. Standards of the
International Electrical Engineering Committee describe selected processes taking place inside the
cars. Manufacturers of the motorisation branch have their own methods for testing electromagnetic
emissions as well as own requirements related to the electromagnetic compatibility of radiated and
conducted interferences. The requirements related to defence equipment, including vehicles, are
given in the standard MIL-STD-461F.

After measurements of radiated and conducted emissions of disturbances for two motors of
windscreen wipers used in the Subaru Forester I and II cars done in the anechoic chamber the above
amplitude vs. frequency diagrams have been achieved. It can be inferred from these diagrams
that the motor No. 2 produced in earlier years (1997–2002) emits higher disturbances than the
motor No. 1 from the Subaru Forester II (2002–2008). It can be stated that together with passing
years the progress of technology makes that equipment manufactured emit less of electromagnetic
disturbances. Both motors do not satisfy requirements related to the disturbances levels forced by
the defence standard. In destination, in order to reduce disturbances in the moment of installation
of the motors within the cars the suitable technical measures should be used. One of the ways
of limiting interferences generated is to use protecting diodes that are to be installed in order
to eliminate voltage pins. The diodes should be mounted near the interfering equipment in the
way eliminating electromagnetic interferences in the place of their generation. A next way to
level interferences that are mainly generated within the DC brush motors is to use capacitors and
impedance coils. In order to reduce the radiated emissions from electronic equipment the dedicated
materials have to be used [1, 8, 9] for their enclosures.

ACKNOWLEDGMENT

REFERENCES

1. Kubacki, R., R. Przesmycki, and J. Ferenc, "Wlasnosci elektromagnetyczne nanokrystalicznego
   proszku stopu Fe-Si-B-Cu-Nb w zakresie mikrofalowym", *Przeglad Elektrotechniczny (Electrical
   Review)*, NR 12b/2011, 92–95, 2012, ISSN 0033-2097.
2. Przesmycki, R., "Measurement and analysis of compromising emanation for laser printer,"
   Progress In Electromagnetics Research Symposium Abstracts, 2066, Guangzhou, China,
   Aug. 25–28, 2014.
3. Przesmycki, R. and P. Skokowski, "Dual band microstrip antenna," *PIERS Proceedings*, 2641–
   2645, Guangzhou, China, Aug. 25–28, 2014.
4. Kubacki, R., E. Cwalina, M. Kuchta, and A. Dukata, "Specyfika rozkladu pola elektromagne-
   tycznego wewnatrz pomieszczen i obudów komputerowych od wysokomocowych impulsów elek-
   tromagnetycznych," *Przeglad Elektrotechniczny (Electrical Review)*, No. 12b, 209–212, 2012.
5. Kubacki, R. and S. Lamari, "The UWB microstrip antenna with metamaterial and periodic
   structure," *PIERS Proceedings*, 2651–2655, Guangzhou, China, Aug. 25–28, 2014.

6. Kubacki, R., "New attempt to building materials permittivity measurements," *PIERS Proceedings*, 2676–2680, Guangzhou, China, Aug. 25–28, 2014.

7. Lamari, S., R. Kubacki, and M. Czyzewski, "Frequency range widening of the microstrip antenna with the Sierpinski fractal patterned metamaterial structure," *MIKON-2014 Conference Proceedings*, 773–775, 2014.

8. Bugaj, M., "Measurements of wall attenuation in closed spaces inside a building," *PIERS Proceedings*, 2681–2686, Guangzhou, China, Aug. 25–28, 2014.

9. Bugaj, M., "Attenuation measurements of materials used in construction of buildings," *PIERS Proceedings*, 2671–2675, Guangzhou, China, Aug. 25–28, 2014.

10. Rozanowski, K., Z. Piotrowski, and M. Ciolek, "Mobile application for driver's health status remote monitoring," *9th International Wireless Communications and Mobile Computing Confwerence (IWCMC)*, 1738–1743, 2013.

11. Rozanowski, K., T. Sondej, Z. Piotrowski, and K. Sawicki, "Architecture of car measurement system for driver monitoring," *Communication Technologies for Vehicles, Lecture Notes in Computer Science*, Vol. 7266, 68–79, 2012.

12. Rozanowski, K., Z. Piotrowski, T. Sondej, K. Sawicki, and M. Glowacki, "Wireless driver and vehicle surveillance system based on IEEE 802.11 networks," *Communication Technologies for Vehicles, Lecture Notes in Computer Science*, Vol. 7266, 57–67, 2012.

13. Bajda, A., M. Wrazen, and D. Laskowski, "Diagnostics the quality of data transfer in the management of crisis situation," *Przeglad Elektrotechniczny (Electrical Review)*, Vol. 87, No. 9A, 72–78, 2011.

14. Laskowski, D., P. Lubkowski, E. Pawlak, and P. Stanczyk, "Anthropo-technical systems reliability, safety and reliability: Methodology and applications," *Proceedings of the European Safety and Reliability Conference, ESREL 2014*, 399–407, 2014.

15. Ziólkowski, C. and J. M. Kelner, "Geometry-based statistical model for the temporal, spectral, and spatial characteristics of the land mobile channel," *Wireless Personal Communications*, 2015, Article in Press, Doi: 10.1007/s11277-015-2413-3.

16. Ziólkowski, C. and J. M. Kelner, "Influence of the propagation environment on statistical properties of bearing," *Przeglad Elektrotechniczny (Electrical Review)*, Vol. 91, No. 3, 96–99, 2015.

17. Gajewski, P., J. M. Kelner, and C. Ziólkowski, "Dynamic location of the emission sources based on Doppler effect," *Przeglad Elektrotechniczny (Electrical Review)*, Vol. 89, No. 7, 223–226, 2013.

Bandwidth Enhancement of a Microstrip Patch Antenna Using the Metamaterial Planar Periodic Structure

Salim Lamari, **Roman Kubacki**, **and Miroslaw Czyżewski**

Faculty of Electronics, Military University of Technology, Warsaw, Poland

Abstract— In this paper we present a compact microstrip antenna with an ultra-wide frequency bandwidth. The ultra-wideband characteristic is obtained by applying the metamaterial concept to an ordinary rectangular microstrip patch antenna with a limited bandwidth of 0.225 GHz. This concept consists of embedding the metallic parts of the antenna, patch and ground plane, by repeating the patterns of a unit cell. The unit cell, designed with different pattern shapes on its upper and lower layers, verifies the metamaterials criterion by means of the dispersion diagram, showing the phase velocity and the group velocity oppositely directed. The new antenna, resulting from this operation was designed and simulated by means of CST Microwave Studio. To attest this approach, the design of the new antenna was experimentally verified after fabricating it on the Rogers RT5880 substrate ($\varepsilon_r = 2.2$ and $h = 0.787$ mm) and measuring its characteristics.

1. INTRODUCTION

Nowadays, light weight compact and low cost devices seem to be much preferred by wireless communication users. Printed antenna technology can meet these needs for the radiating element equipping these devices [1, 2, 5, 10, 16, 18, 19, 23, 24]. But, the same users are more and more eager to be continuously connected. To meet this requirement, these devices should comply with all systems like cellular systems, Wi-Fi, Bluetooth, GPS, NFC, etc. [3, 4, 6, 7, 8, 9, 11–14, 19]. Consequently the printed antenna such as the microstrip antenna, which enjoys its low profile, conformality, low cost, has a narrow bandwidth and hence cannot work with all those systems. Many efforts have been achieved to address this issue which remains the main drawback of the microstrip antenna. Since its inception, the microstrip antenna experienced many methods and techniques in order to enhance its bandwidth. A direct technique to widen the bandwidth can be done by achieving a good impedance matching between the feeding line and the radiating element [20]. Another technique consists of adding parasitic patches electromagnetically gap coupled with the main patch, hence the resonances staggering will yield wider bandwidth. Electromagnetic gap coupling can be used differently to enhance the bandwidth by stacking two or three patches. To keep the low profile of the microstrip patch antenna and at the same time enhance the bandwidth, a U shaped slot was cut on the patch. Cutting 2 slits on the patch, giving hence a patch with the shape of the E letter also widens the bandwidth [23, 24]. But unfortunately, these techniques couldn't exceed the level of 40% fractional bandwidth, and then another approach is needed to tackle this issue.

The appearance of new materials, human engineered, called metamaterials because of their properties not found in natural materials, like both negative permittivity and permeability or double negative materials (DNM), negative refractive index (NRI), and left-handedness (LHM), gave some possibilities [22]. Metamaterials are divided into categories, resonant and non-resonant. The first category is based on cells consisting of split ring resonators and wires [21]. However, this type is less interesting because of its high loss and narrow bandwidth. On the other hand, the second type can be realized directly on a planar transmission line, and showed hence possible realization of microwave devices and antennas in the microwaves range. Thus, the non-resonant type is LHM is better from an application point of view. This type can be easily manufactured in a planar structure, with distinct pattern, by means of lithographic technique. The patterns are usually formed by repeating periodically a unit cell in such way to make an array.

Following a similar approach, we propose in this paper a different metamaterial patterned structure to be applied on a microstrip patch antenna, in order to enhance further the bandwidth. The planar patterns of the patch consist of an array of 3×4 cells, and those of the ground of an array of 7×6 cells. The arrangement of both upper and lower patterns, formed by the repetition of the unit cell, produced a periodic structure.

2. THE METAMATERIAL STRUCTURE

The unit cell, which is the basis of the periodic structure, is square and consists for the lower layer, of etched slots along the four edges and radially in the four angles, and for the upper layer of four cross-ordered L-shaped slots, as shown in Figure 1.
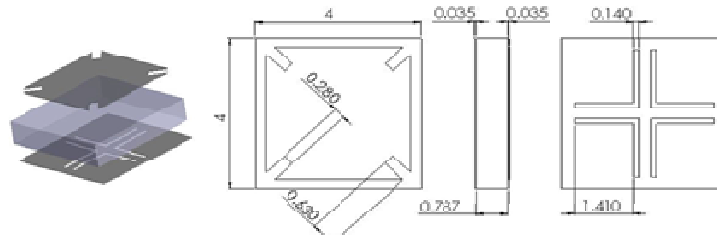
Figure 1: The metamaterial unit cell with dimensions.

A dispersion diagram was simulated under the CST Microwave Studio environment after applying periodic boundary conditions in the x and y directions. Figure 2 shows the dispersion characteristics of the unit cell along the paths between the high symmetry points Γ, X and M in the Brillouin zone, and are represented by and a ω-β curve.
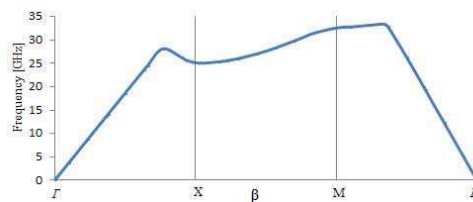
Figure 2: The dispersion diagram.

The slope of the straight line connecting the origin and a certain point on the ω-β curve represents the phase velocity V_p, and the that the slope of the line tangential to the curve at that point represents the group velocity V_G. We notice from Figure 2 that the slope representing V_G is negative, hence the group velocity and phase velocity are in opposite directions, which leads to the conclusion that the structure supports backward (LH) waves.

3. THE ANTENNA DESIGN

A conventional microstrip patch antenna with $28 \times 32 \times 0.787\,\mathrm{mm}^3$, was designed and simulated for comparison. Its patch is $12 \times 16\,\mathrm{mm}^2$, and its feeding line is $2.46 \times 8\,\mathrm{mm}^2$. Our antenna has the following dimensions: $28 \times 32 \times 0.787\,\mathrm{mm}^3$, the feeding line is $2.4 \times 8\,\mathrm{mm}^2$, we notice that the feeding line is less wider here. The geometry of the proposed antenna is shown in Figure 3. The substrate of the antenna is Rogers RT 5880, with dielectric permittivity of 2.2. The metamaterial structure consists for the patch of four cross ordered L shaped slots cells, and the ground plane of star gaps connected by slots on the corners of the cells. The left handed property is driven by the whole structure comprising the patch, the ground plane and the coupling between them, enabling thus much wider impedance bandwidth. The designs and the simulations were carried out under CST Microwave Studio environment.
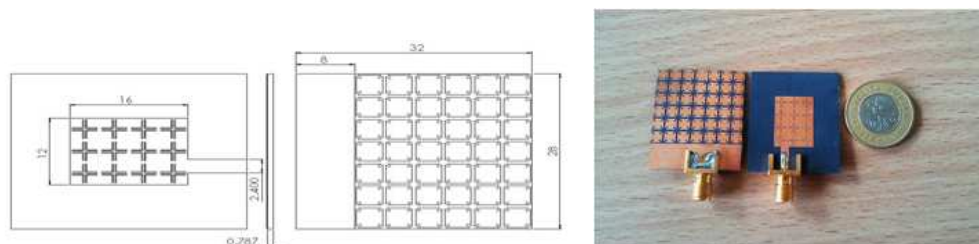
Figure 3: The antenna configuration and picture of its fabrication.

4. RESULTS AND DISCUSSION

During the simulation, all the dimensions of the antenna, comprising its length and width, the width and offset of the feeding line and the size of every edge composing the planar pattern were

submitted to parameter study for optimization.

The conventional microstrip patch antenna and the proposed antenna with planar patterned metamaterial, after being designed and simulated, were physically fabricated in order to compare them, the proposed one is depicted in Figure 2. Once this done, we carried out measurements of the S_{11} by means of the HP network analyzer. As we can notice from the Figure 4, where respectively results of the conventional and the proposed antenna are depicted, that there is a good agreement between the simulation and measurement.
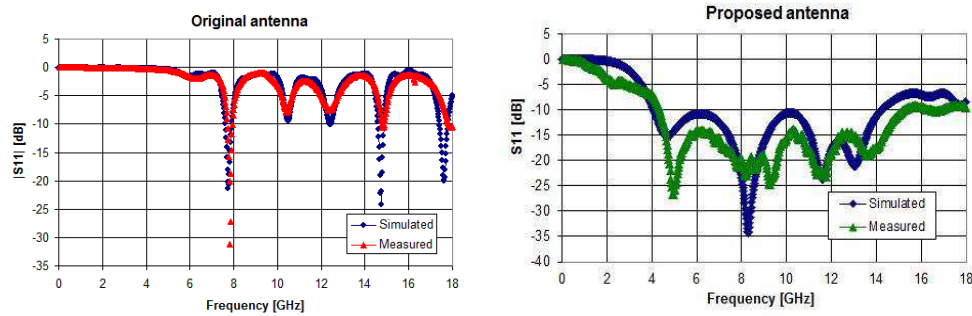
Figure 4: The simulated and measured S_{11} of the original and the proposed antennas.

The proposed antenna achieved a -10 dB frequency band ranging from 4.314 to 15.237 GHz, which represents 10.923 GHz bandwidth, realizing 111.77% fractional bandwidth, whereas the conventional one realized 0.220 GHz. The bandwidth enhancement is almost by fifty times. The results of the radiation pattern are also carried out and plotted in Figure 5 for the following frequencies 8.05 GHz and 11.608 GHz in the x-z and x-y planes respectively. The radiation is mainly directed around the 120° for both planes and frequencies.

(a)   (b)
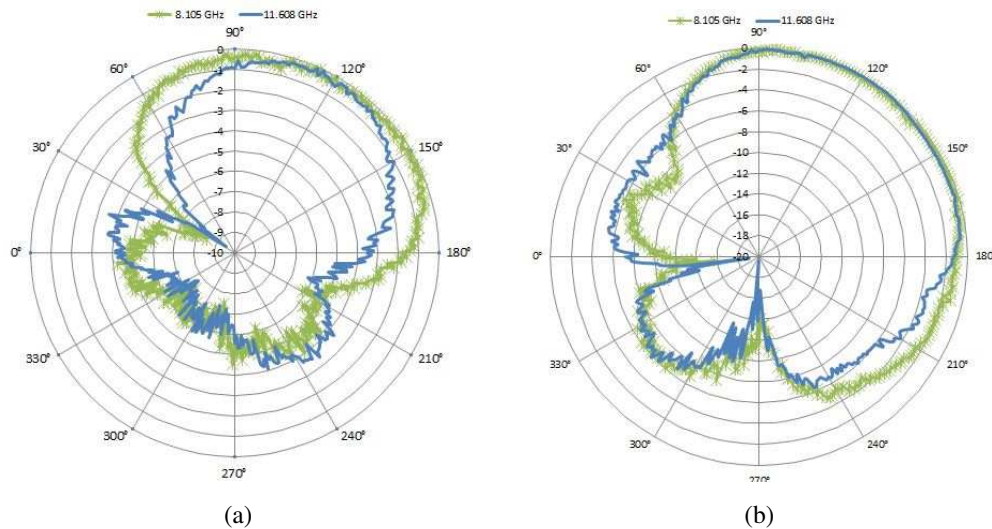
Figure 5: The radiation pattern for the (a) x-z and (b) x-y planes at 8.105 and 11.608 GHz.

5. CONCLUSION

A compact ultra wideband antenna is proposed in this paper basing on the principle of planar patterned metamaterial. This structure allowed a much wider frequency bandwidth of about 10.923 GHz, which represents 111.7% fractional bandwidth. The radiation pattern of the antenna was also measured and showed the same direction in two planes at two distinct frequencies.

REFERENCES

1. Bugaj, J. and M. T. Wnuk, "Analysis of the impact of surface on parameters of cylindrical microstrip antennas [Analiza wielowarstwowej anteny cylindrycznej ze względu na promień krzywizny]," *Przegląd Elektrotechniczny (Electrical Review)*, No. 3, 48–51, 2015.

2. Bugaj, J. and M. T. Wnuk, "Analysis of conformal multilayer antenna working in X band [Analiza wielowarstwowej anteny konformalnej pracujacej w pasmie X]" *PrzeglądElektrotechniczny (Electrical Review)*, No. 9, 46–49, 2009.

3. Bugaj, M., "Measurements of wall attenuation in closed spaces inside a building," *PIERS Proceedings*, 2681–2686, Guangzhou, August 25–28, 2014.

4. Bugaj, M., "Attenuation measurements of materials used in construction of buildings," *PIERS Proceedings*, 2671–2675, Guangzhou, August 25–28, 2014.

5. Bugaj, M. and M. T. Wnuk, "Optimization parameters of dielectric in aperture-coupled stacked patch antenna on bandwidth," *18th International Conference on Microwaves, Radar and Wireless Communications, MIKON*, 2010.

6. Nowosielski, L. and J. Lopatka, "Measurement of shielding effectiveness with the method using high power electromagnetic pulse generator," *PIERS Proceedings*, 2687–2691, Guangzhou, August 25–28, 2014.

7. Nowosielski, L. and Z. Piotrowski, "Honeycomb ventilation grill shielding effectiveness measuring methodology," *PIERS Proceedings*, 2692–2696, Guangzhou, August 25–28, 2014.

8. Nowosielski, L., R. Przesmycki, M. T. Wnuk, and J. Rychlica, "The methods of measuring attenuation of thin absorbent materials used for electromagnetic shielding," *PIERS Proceedings*, 870–874, Marrakesh, Morocco, March 20–23, 2011.

9. Przesmycki, R., M. T. Wnuk, L. Nowosielski, and K. Piwowarczyk, "Small chambers shielding efficiency measurements," *PIERS Proceedings*, 875–879, Marrakesh, Morocco, March 20–23, 2011.

10. Nowosielski, L. and M. T. Wnuk, "Compromising emanations from USB 2 interface," *PIERS Proceedings*, Guangzhou, 2666–2670, August 25–28, 2014.

11. Piwowarczyk, K., R. Przesmycki, L. Nowosielski, and M. T. Wnuk, "Pomiar odporności urządzeń informatycznych na promieniowane pole elektryczne o częstotliwości radiowej w zakresie (80–1000) MHz," *Przegląd Elektrotechniczny (Electrical Review)*, No. 86, 165–167, 2010.

12. Przesmycki, R., "Measurement and analysis of compromising emanation for laser printer," *PPIERS Proceedings*, 2661–2665, Guangzhou, August 25–28, 2014.

13. Przesmycki, R., L. Nowosielski, M. Bugaj, and K. Piwowarczyk, "Analiza emisji promieniowanej współczesnych urządzeń informatycznych," *Przegląd Elektrotechniczny (Electrical Review)*, No. 2, 4–6, 2012.

14. Przesmycki, R., L. Nowosielski, M. Bugaj, and K. Piwowarczyk, "Pomiar absorpcji materiałów pochłaniających fale elektromagnetyczne," *Przegląd Elektrotechniczny (Electrical Review)*, No. 2, 33–35, 2012.

15. Przesmycki, R., L. Nowosielski, and M. T. Wnuk, "The laboratory stand for conducted emissions measurement in accordance with the military standard," *IEEE International Symposioum on EMC, Florida*, 275–278, 2010.

16. Przesmycki, R. and P. Skokowski, "Dual band microstrip antenna," *PIERS Proceedings*, 2641–2645, Guangzhou, August 25–28, 2014.

17. Przesmycki, R., M. T. Wnuk, M. Bugaj, and K. Piwowarczyk, "Analiza metod pomiarowych tłumienności torów w.cz.," *Przegląd Elektrotechniczny (Electrical Review)*, No. 2, 17–19, 2012.

18. Przesmycki, R., M. T. Wnuk, L. Nowosielski, K. Piwowarczyk, and M. Bugaj, "The conducted and radiated emission levels from IT devices," *PIERS Proceedings*, 77–81, Kuala Lumpur, Malaysia, March 27–30, 2012.

19. Przesmycki, R., M. T. Wnuk, L. Nowosielski, K. Piwowarczyk, and M. Bugaj, "Analysis of the radiated emissions of IT equipment," *PIERS Proceedings*, 1419–1423, Moscow, Russia, August 19–23, 2012.

20. Pues, H. F. and A. Van de Capelle, "An impedance matching technique for increasing the bandwidth of microstrip antennas," *IEEE Transactions on Antennas and Propagation*, Vol. 37, No. 11, Nov. 1989.

21. Simovski, R., P. A. Belov, and H. Sailing, "Backward wave region and negative material parameters of structure formed by lattices of wires and split-ring resonators," *IEEE Trans. Ant. Propag.*, Vol. 51, 2582–2591, 2003.

22. Veselago, V. V., "The electrodynamics of substances with simultaneously negative values of ε and μ," *Sov. Phys. Uspekhi*, Vol. 10, No. 4, 509–514, 1968.

23. Wnuk, M. T. and J. Bugaj, "Analysis of surface waves in microstrip array," *16th International Conference on Microwaves, Radar and Wireless Communications, MIKON*, 2006.

24. Wnuk, M. T., M. Bugaj, R. Przesmycki, L. Nowosielski, and K. Piwowarczyk, "Wearable antenna constructed in microstrip technology," *PIERS Proceedings*, 67–71, Kuala Lumpur, Malaysia, March 27–30, 2012.

25. Zilkowski, R. W., "Design, fabrication and testing of double negative metamaterials," *IEEE Trans. Anten. Propag.*, Vol. 51, No. 7, 1516–1529, 2003.

Computing the Electric and Magnetic Green's Functions in General Gyrotropic Media

V. G. Yakhno[1] and B. Çiçek[2]

[1]Electrical and Electronics Engineering Department, Dokuz Eylul University, Turkey
[2]Graduate School of Natural and Applied Sciences, Dokuz Eylul University, Turkey

Abstract— A method for an approximate computation of the electric and magnetic Green's functions for the time-harmonic Maxwell's equations in the general gyrotropic media is proposed in this paper. The method is based on the Fourier transform with respect to space variables, matrix transformations and numerical computation of the inverse Fourier transform. The approximate computation of the inverse Fourier transform has been implemented by MATLAB tools. The computational experiments confirm the robustness of the method.

1. INTRODUCTION

The study of the electromagnetic fields in gyrotropic media is an important issue of the recent electromagnetic theory [1, 2, 6]. The electric and magnetic fluxes $\mathbf{D}$ and $\mathbf{B}$ in general gyrotropic media have the following form

$$\mathbf{D} = \varepsilon_0 \bar{\bar{\varepsilon}} \cdot \mathbf{E}, \quad \mathbf{B} = \mu_0 \bar{\bar{\mu}} \cdot \mathbf{H},$$

where $\mathbf{E}$ and $\mathbf{H}$ are electric and magnetic fields, respectively; positive constants ε_0 and μ_0 are defined as the permittivity and permeability of free space; the relative permittivity and permeability matrices $\bar{\bar{\varepsilon}}$ and $\bar{\bar{\mu}}$ have the following form (see, for example, [1–4]):

$$\bar{\bar{\varepsilon}} = \begin{pmatrix} \epsilon_{11} & \epsilon_{12} + ig_3 & \epsilon_{13} - ig_2 \\ \epsilon_{12} - ig_3 & \epsilon_{22} & \epsilon_{23} + ig_1 \\ \epsilon_{13} + ig_2 & \epsilon_{23} - ig_1 & \epsilon_{33} \end{pmatrix}, \quad \bar{\bar{\mu}} = \begin{pmatrix} \mu_{11} & \mu_{12} + ih_3 & \mu_{13} - ih_2 \\ \mu_{12} - ih_3 & \mu_{22} & \mu_{23} + ih_1 \\ \mu_{13} + ih_2 & \mu_{23} - ih_1 & \mu_{33} \end{pmatrix}, \quad i^2 = -1. \quad (1)$$

The main objects of our paper are the electric and magnetic Green's functions for Maxwell's partial differential equations in the general gyrotropic media. We suggest a method of an approximate (regularized) computation of the infinite-body Green's functions for the time-harmonic Maxwell's equations in the general gyrotropic media.

2. ELECTRIC AND MAGNETIC MATRIX GREEN'S FUNCTIONS

The electric and magnetic Green's functions are matrix functions

$$\begin{pmatrix} E_1^1(x) & E_1^2(x) & E_1^3(x) \\ E_2^1(x) & E_2^2(x) & E_2^3(x) \\ E_3^1(x) & E_3^2(x) & E_3^3(x) \end{pmatrix}, \quad \begin{pmatrix} H_1^1(x) & H_1^2(x) & H_1^3(x) \\ H_2^1(x) & H_2^2(x) & H_2^3(x) \\ H_3^1(x) & H_3^2(x) & H_3^3(x) \end{pmatrix}, \quad (2)$$

whose columns $\mathbf{E^k} = (E_1^k, E_2^k, E_3^k)^T$, $\mathbf{H^k} = (H_1^k, H_2^k, H_3^k)^T$ satisfy equations

$$-\left(\frac{\omega}{c}\right)^2 \bar{\bar{\varepsilon}} \mathbf{E^k}(x) + \nabla \times \left(\bar{\bar{\mu}}^{-1} \nabla \times \mathbf{E^k}(x)\right) = i\omega\mu_0 \mathbf{e^k} \delta(x), \quad (3)$$

$$-\left(\frac{\omega}{c}\right)^2 \bar{\bar{\mu}} \mathbf{H^k}(x) + \nabla \times \left(\bar{\bar{\varepsilon}}^{-1} \nabla \times \mathbf{H^k}(x)\right) = \nabla \times \left(\bar{\bar{\varepsilon}}^{-1} \mathbf{e^k} \delta(x)\right). \quad (4)$$

Here $x = (x_1, x_2, x_3) \in \mathbb{R}^3$ is the $3D$ space variable; ω is a fixed parameter (frequency); $\mathbf{e}^1 = (1, 0, 0)^T$, $\mathbf{e}^2 = (0, 1, 0)^T$, $\mathbf{e}^3 = (0, 0, 1)^T$ are basis vectors of $\mathbb{R}^3$; i is the imaginary unit $i^2 = -1$; $\delta(x) = \delta(x_1)\delta(x_2)\delta(x_3)$, $\delta(x_j)$ is the Dirac delta function concentrated at $x_j = 0$ for $j = 1, 2, 3$.

2.1. Computing the Electric Green's Function

Let $\mathcal{F}_x$ be the operator of the Fourier transform with respect to $x = (x_1, x_2, x_3)$, i.e.,

$$\mathcal{F}_x[E(x)](\nu) = \int_{-\infty}^{\infty} \int_{-\infty}^{\infty} \int_{-\infty}^{\infty} E(x)e^{i\nu \cdot x} dx_1 dx_2 dx_3,$$

for the scalar integrable function $E(x)$, where $\nu = (\nu_1, \nu_2, \nu_3)$ is a $3D$ parameter of the Fourier transform; $\nu \cdot x = \nu_1 x_1 + \nu_2 x_2 + \nu_3 x_3$. The operator of the Fourier transform is defined in [8] for any generalized function (tempered distribution).

Let $\widetilde{\mathbf{E}}^{\mathbf{k}}(\nu) = (\widetilde{E}_1^k, \widetilde{E}_2^k, \widetilde{E}_3^k)$, where $\widetilde{E}_j^k = \mathcal{F}_x[E_j^k(x)](\nu)$, $j, k = 1, 2, 3$. Applying the operator of the Fourier transform $\mathcal{F}_x$ to (3) and using equality (see, [9], page 415)

$$\mathcal{F}_x \left[\nabla \times \left(\bar{\bar{\mu}}^{-1} \nabla \times \mathbf{E}^{\mathbf{k}}(x) \right) \right] = S(\nu) \bar{\bar{\mu}}^{-1} S(\nu) \widetilde{\mathbf{E}}^{\mathbf{k}}(\nu),$$

we find

$$- \left(\frac{\omega}{c} \right)^2 \bar{\bar{\varepsilon}} \widetilde{\mathbf{E}}^{\mathbf{k}}(\nu) + S(\nu) \bar{\bar{\mu}}^{-1} S(\nu) \widetilde{\mathbf{E}}^{\mathbf{k}}(\nu) = i\omega\mu_0 \mathbf{e}^{\mathbf{k}}, \tag{5}$$

where

$$S(\nu) = \begin{pmatrix} 0 & -\nu_3 & \nu_2 \\ \nu_3 & 0 & -\nu_1 \\ -\nu_2 & \nu_1 & 0 \end{pmatrix}. \tag{6}$$

Let ϵ be a symmetric real 3×3 matrix and g be an antisymmetric real 3×3 matrix defined by

$$\epsilon = \begin{pmatrix} \epsilon_{11} & \epsilon_{12} & \epsilon_{13} \\ \epsilon_{12} & \epsilon_{22} & \epsilon_{23} \\ \epsilon_{13} & \epsilon_{23} & \epsilon_{33} \end{pmatrix}, \quad g = \begin{pmatrix} 0 & g_3 & -g_2 \\ -g_3 & 0 & g_1 \\ g_2 & -g_1 & 0 \end{pmatrix}, \tag{7}$$

and let us assume that $\bar{\bar{\mu}}$ has an inverse matrix $\bar{\bar{\mu}}^{-1} = \bar{\mu} + i\bar{h}$.

The matrix $\bar{\bar{\varepsilon}}$ defined by (1) can be written as $\bar{\bar{\varepsilon}} = \epsilon + ig$. Further, let B and $C(\nu)$ be symmetric 6×6 matrices defined by

$$B = \begin{pmatrix} \epsilon & -g \\ g & \epsilon \end{pmatrix}, \quad C(\nu) = \begin{pmatrix} S(\nu)\bar{\mu}S(\nu) & -S(\nu)\bar{h}S(\nu) \\ S(\nu)\bar{h}S(\nu) & S(\nu)\bar{\mu}S(\nu) \end{pmatrix}. \tag{8}$$

In the paper, we suppose that B is positive definite.

Remark 1. *Positive definiteness of B is natural for a wide class of gyrotropic media because the matrix ϵ is always positive definite and the elements of matrix g essentially smaller then elements of ϵ (see, for example, [7]).*

Let us denote V_j^k as the real part of j component of $\widetilde{\mathbf{E}}^{\mathbf{k}}(\nu)$ and V_{j+3}^k as the imaginary part of j component of $\widetilde{\mathbf{E}}^{\mathbf{k}}(\nu)$, i.e., $V_j^k = \text{Re}(\widetilde{E}_j^k(\nu))$ and $V_{j+3}^k = \text{Im}(\widetilde{E}_j^k(\nu))$, $j = 1, 2, 3$. Then equality (5) can be written as the vector equation

$$- \left(\frac{\omega}{c} \right)^2 B\mathbf{V}^{\mathbf{k}}(\nu) + C(\nu)\mathbf{V}^{\mathbf{k}}(\nu) = \mathbf{F}^{\mathbf{k}}, \tag{9}$$

where $\mathbf{F^1} = \omega\mu_0(0, 0, 0, 1, 0, 0)^T$, $\mathbf{F^2} = \omega\mu_0(0, 0, 0, 0, 1, 0)^T$, $\mathbf{F^3} = \omega\mu_0(0, 0, 0, 0, 0, 1)^T$.

Applying technique and computational tools of [9], it is possible to compute a non-singular matrix $T(\nu)$ and diagonal matrix $D(\nu) = \text{diag}(d_1(\nu), d_2(\nu), \ldots, d_6(\nu))$, such that

$$T^T(\nu)C(\nu)T(\nu) = D(\nu), \quad T^T(\nu)BT(\nu) = I.$$

The solution of (9) is determined by $\mathbf{V}^{\mathbf{k}}(\nu) = T(\nu)\mathbf{Y}^{\mathbf{k}}$, where $\mathbf{Y}^{\mathbf{k}}(\nu) = (Y_1^k(\nu), Y_2^k(\nu), \ldots, Y_6^k(\nu))$ is the vector whose components for $\left(\frac{w}{c} \right)^2 - d_l(\nu) \neq 0$ can ve written as

$$Y_l^k(\nu) = \frac{(T^T\mathbf{F}^{\mathbf{k}})_l}{-(\omega/c)^2 + d_l(\nu)}.$$

The components of $\widetilde{\mathbf{E}}^{\mathbf{k}}(\nu, \omega)$ are found by

$$\widetilde{E}_j^k = V_j^k(\nu) + iV_{j+3}^k(\nu), \quad j = 1, 2, 3; \; k = 1, 2, 3. \tag{10}$$

Finally, applying the inverse Fourier transform to (10), we find the k-column of the electric Green's function as a tempered distribution, i.e.,

$$\mathbf{E}^{\mathbf{k}}(x) = \mathcal{F}_\nu^{-1}\left[\widetilde{\mathbf{E}}^{\mathbf{k}}(\nu)\right](x), \tag{11}$$

where $\mathcal{F}_\nu^{-1}$ is the operator of the inverse Fourier transform in the space of distribution $S'(\mathbb{R}^3)$ [8]. The right hand side of (11) can be regularized by

$$\frac{1}{(2\pi)^3} \int_{-A}^{A} \int_{-A}^{A} \int_{-A}^{A} \widetilde{\mathbf{E}}^{\mathbf{k}}(\nu)\, e^{-i\nu\cdot x} d\nu_1 d\nu_2 d\nu_3, \tag{12}$$

where A is the parameter of regularization.

We take $A = N\Delta$ and approximate the integral (12) by the integral sum

$$\frac{1}{(2\pi)^3} \sum_{n=-N}^{N} \sum_{m=-N}^{N} \sum_{l=-N}^{N} \widetilde{\mathbf{E}}^{\mathbf{k}}(n\Delta, m\Delta, l\Delta)\, e^{-i\Delta(nx_1 + mx_2 + lx_3)} (\Delta\nu)^3,$$

for the numerical computation. The parameters N and Δ have been chosen by empirical observations, as the best parameters for the case of isotropic media for which there exists explicit formulas for the Green's functions and their Fourier images.

2.2. Computing the Magnetic Matrix Green's Function

Applying the Fourier transform with respect to x to the Equation (4) and using equalities

$$\mathcal{F}_x\left[\nabla \times \left(\bar{\bar{\varepsilon}}^{-1}\nabla \times \mathbf{H}^{\mathbf{k}}(x)\right)\right] = S(\nu)\bar{\bar{\varepsilon}}^{-1}S(\nu)\widetilde{\mathbf{H}}^{\mathbf{k}}(\nu), \;\; \mathcal{F}_x\left[\nabla \times \left(\bar{\bar{\varepsilon}}^{-1}\mathbf{e}^{\mathbf{k}}\right)\right] = S(\nu)\bar{\bar{\varepsilon}}^{-1}\mathbf{e}^{\mathbf{k}},$$

we find

$$-\left(\frac{\omega}{c}\right)^2 \bar{\bar{\mu}}\widetilde{\mathbf{H}}^{\mathbf{k}}(\nu) + S(\nu)\bar{\bar{\varepsilon}}^{-1}S(\nu)\widetilde{\mathbf{H}}^{\mathbf{k}}(\nu) = S(\nu)\bar{\bar{\varepsilon}}^{-1}\mathbf{e}^{\mathbf{k}}, \tag{13}$$

where $\widetilde{\mathbf{H}}^{\mathbf{k}}(\nu) = (\widetilde{H}_1^k, \widetilde{H}_2^k, \widetilde{H}_3^k)$, $\widetilde{H}_n^k(\nu) = \mathcal{F}_x[H_n^k(x)](\nu)$, $n = 1, 2, 3;$, $S(\nu)$ is defined by (6) and let μ be a symmetric real 3×3 matrix and h be an antisymmetric real 3×3 matrix defined by

$$\mu = \begin{pmatrix} \mu_{11} & \mu_{12} & \mu_{13} \\ \mu_{12} & \mu_{22} & \mu_{23} \\ \mu_{13} & \mu_{23} & \mu_{33} \end{pmatrix}, \quad h = \begin{pmatrix} 0 & h_3 & -h_2 \\ -h_3 & 0 & h_1 \\ h_2 & -h_1 & 0 \end{pmatrix},$$

and let us assume that $\bar{\bar{\varepsilon}}$ has an inverse matrix $\bar{\bar{\varepsilon}}^{-1}$.

Let $X_n^k(\nu)$, $G_n^k(\nu)$, $R_r(\nu)$ be the real parts of $\widetilde{H}_n^k(\nu)$, $(S(\nu)\bar{\bar{\varepsilon}}^{-1}\mathbf{e}^{\mathbf{k}})$, $(S(\nu)\bar{\bar{\varepsilon}}^{-1}S(\nu))$ and $X_{n+3}^k(\nu)$, $G_{n+3}^k(\nu)$, $R_i(\nu)$ be the imaginary parts of $\widetilde{H}_n^k(\nu)$, $(S(\nu)\bar{\bar{\varepsilon}}^{-1}\mathbf{e}^{\mathbf{k}})$, $(S(\nu)\varepsilon^{-1}S(\nu))$, respectively.

Denoting $\mathbf{X}^{\mathbf{k}}(\nu) = (X_1^k(\nu), X_2^k(\nu), \ldots, X_6^k(\nu))$ and $\mathbf{G}^{\mathbf{k}}(\nu) = (G_1^k(\nu), G_2^k(\nu), \ldots, G_6^k(\nu))$ the equation (13) can be written in the form

$$-\left(\frac{\omega}{c}\right)^2 K\mathbf{X}^{\mathbf{k}}(\nu) + P(\nu)\mathbf{X}^{\mathbf{k}}(\nu) = \mathbf{G}^{\mathbf{k}}(\nu), \tag{14}$$

where $P(\nu)$ and K are 6×6 symmetric matrix defined by

$$K = \begin{pmatrix} \mu & -h \\ h & \mu \end{pmatrix}, \quad P(\nu) = \begin{pmatrix} R_r(\nu) & -R_i(\nu) \\ R_i(\nu) & R_r(\nu) \end{pmatrix}. \tag{15}$$

In the paper we suppose that K is positive definite.

We note that $(S(\nu)\bar{\bar{\varepsilon}}^{-1}S(\nu)) = R_r(\nu) + iR_i(\nu)$, where

$$R_i(\nu) = \frac{1}{\xi_4}\begin{pmatrix} 0 & -a_{12} & a_{13} \\ a_{12} & 0 & -a_{23} \\ -a_{13} & a_{23} & 0 \end{pmatrix}, \quad R_r(\nu) = \frac{1}{\xi_4}\begin{pmatrix} b_{11} & b_{12} & b_{13} \\ b_{12} & b_{22} & b_{23} \\ b_{13} & b_{23} & b_{33} \end{pmatrix},$$

$a_{12} = \nu_2\nu_3\xi_1 + \nu_3^2\xi_2 + \nu_1\nu_3\xi_3, \; a_{13} = \nu_2^2\xi_1 + \nu_2\nu_3\xi_2 + \nu_1\nu_2\xi_3, \; a_{23} = \nu_1\nu_3\xi_2 + \nu_1^2\xi_3 + \nu_1\nu_2\xi_1,$
$b_{11} = -\nu_2^2\xi_5 + 2\nu_2\nu_3\xi_6 - \nu_3^2\xi_7, \; b_{12} = \nu_1\nu_2\xi_5 - \nu_1\nu_3\xi_6 - \nu_2\nu_3\xi_8 + \nu_3^2\xi_9,$
$b_{13} = \nu_1\nu_3\xi_7 - \nu_1\nu_2\xi_6 - \nu_2^2\xi_8 - \nu_2\nu_3\xi_9, \; b_{22} = -\nu_1^2\xi_5 + 2\nu_1\nu_3\xi_8 - \nu_3^2\xi_{10},$
$b_{23} = \nu_2\nu_3\xi_{10} - \nu_1\nu_2\xi_8 - \nu_1^2\xi_6 + \nu_1\nu_3\xi_9, \; b_{33} = -\nu_1^2\xi_7 + 2\nu_1\nu_2\xi_8 - \nu_2^2\xi_{10},$
$\xi_1 = \epsilon_{12}g_1 + \epsilon_{22}g_2 + \epsilon_{23}g_3, \; \xi_2 = \epsilon_{13}g_1 + \epsilon_{23}g_2 + \epsilon_{33}g_3, \; \xi_3 = \epsilon_{11}g_1 + \epsilon_{12}g_2 + \epsilon_{13}g_3,$
$\xi_4 = \epsilon_{33}\epsilon_{12}^2 - 2\epsilon_{12}\epsilon_{13}\epsilon_{23} + 2\epsilon_{12}g_1g_2 + \epsilon_{22}\epsilon_{13}^2 + 2\epsilon_{13}g_1g_3 + \epsilon_{11}\epsilon_{23}^2 + 2\epsilon_{23}g_2g_3 +$
$+\epsilon_{11}g_1^2 + \epsilon_{22}g_2^2 + \epsilon_{33}g_3^2 - \epsilon_{11}\epsilon_{22}\epsilon_{33}, \xi_5 = \epsilon_{12}^2 + g_3^2 - \epsilon_{11}\epsilon_{22}, \; \xi_6 = g_2g_3 - \epsilon_{12}\epsilon_{13} + \epsilon_{11}\epsilon_{23},$
$\xi_7 = \epsilon_{13}^2 + g_3^2 - \epsilon_{11}\epsilon_{33}, \; \xi_8 = g_1g_3 - \epsilon_{12}\epsilon_{23} + \epsilon_{13}\epsilon_{22}, \; \xi_9 = g_1g_2 - \epsilon_{13}\epsilon_{23} + \epsilon_{12}\epsilon_{33},$
$\xi_{10} = \epsilon_{23}^2 + g_1^2 - \epsilon_{22}\epsilon_{33}.$

Using the technique, from [5] we can compute an invertible matrix $Q(\nu)$ and $M(\nu)$ such that

$$Q^T(\nu)KQ(\nu) = I, \quad Q^T(\nu)P(\nu)Q(\nu) = M(\nu),$$

where $M(\nu) = \text{diag}(m_n(\nu), \; n = 1, 2, 3, 4, 5, 6)$.

Let $\mathbf{Z^k}(\nu) = Q^T(\nu)\mathbf{X^k}(\nu)$, then (14) can be written in the form

$$-\left(\frac{\omega}{c}\right)^2\mathbf{Z^k}(\nu) + M(\nu)\mathbf{Z^k} = Q^T(\nu)\mathbf{G^k}. \tag{16}$$

For $(\omega/c)^2 - m_n(\nu) \neq 0$ the solution of (16) can be found in a component form as follows

$$Z_n^k(\nu) = \frac{(Q^T(\nu)\mathbf{G^k})_n}{-(\omega/c)^2 + m_n(\nu)}, \quad n = 1, 2, \ldots, 6, \tag{17}$$

where $\mathbf{Z^k}(\nu) = (Z_1^k(\nu), Z_2^k(\nu), \ldots, Z_6^k(\nu))$. As a result of it the solution of (13) is found by

$$\mathbf{H^k}(\nu) = \left(H_1^k(\nu), H_2^k(\nu), \ldots, H_6^k(\nu)\right), \; \widetilde{H}_n^k = X_n^k(\nu) + iX_{n+3}^k(\nu), \; k = 1, 2, 3; \; n = 1, 2, 3. \tag{18}$$

Applying the inverse Fourier transform to (18), we find the k-column of the magnetic Green's function as a tempered distribution, i.e.,

$$\mathbf{H^k}(x) = \mathcal{F}_\nu^{-1}\left[\widetilde{\mathbf{H}}^{\mathbf{k}}(\nu)\right](x). \tag{19}$$

The right hand side of (19) can be regularized by

$$\frac{1}{(2\pi)^3}\int_{-A}^A\int_{-A}^A\int_{-A}^A\widetilde{\mathbf{H}}^{\mathbf{k}}(\nu)\,e^{-i\nu\cdot x}d\nu_1d\nu_2d\nu_3, \tag{20}$$

where A is the parameter of regularization.

We take $A = N\Delta$ and approximate the integral (20) by the integral sum

$$\frac{1}{(2\pi)^3}\sum_{n=-N}^N\sum_{m=-N}^N\sum_{l=-N}^N\widetilde{\mathbf{H}}^{\mathbf{k}}(\Delta\,n, \Delta\,m, \Delta\,l)\,e^{-i\Delta(nx_1+mx_2+lx_3)}(\Delta\nu)^3.$$

for the numerical computation. The parameters N and Δ are determined by the procedure described in Section 2.1.

3. THE APPROXIMATE COMPUTATION OF THE ELECTRIC AND MAGNETIC GREEN'S FUNCTIONS

For the computational experiment we take $\bar{\bar{\varepsilon}}$ and $\bar{\bar{\mu}}$ as follows

$$\begin{pmatrix} 30.79 & -12.73+i0.05 & -14.34-i0.04 \\ -12.73-i0.05 & 5.52 & 5.87+i0.02 \\ -14.34+i0.04 & 5.87-i0.02 & 6.75 \end{pmatrix}, \begin{pmatrix} 3 & 1+i0.01 & 2-i0.03 \\ 1-i0.01 & 5 & 4+i0.04 \\ 2+i0.03 & 4-i0.04 & 9 \end{pmatrix}.$$

The computation of electric and magnetic Green's functions have been done in MATLAB by the method of Sections 2.1 and 2.2. Some results of these computations are presented as $3D$ graphs of $\mathrm{Re}(E_3^1(x_1,x_2,0))$ and $\mathrm{Im}(H_3^1(x_1,x_2,0))$ for $\omega=2c$ in Fig. 1(a) and Fig. 1(b) respectively. Here the horizontal axes are x_1 and x_2, respectively. The vertical axis is the magnitude of $\mathrm{Re}(E_3^1(x_1,x_2,0))$ and $\mathrm{Im}(H_3^1(x_1,x_2,0))$, respectively.
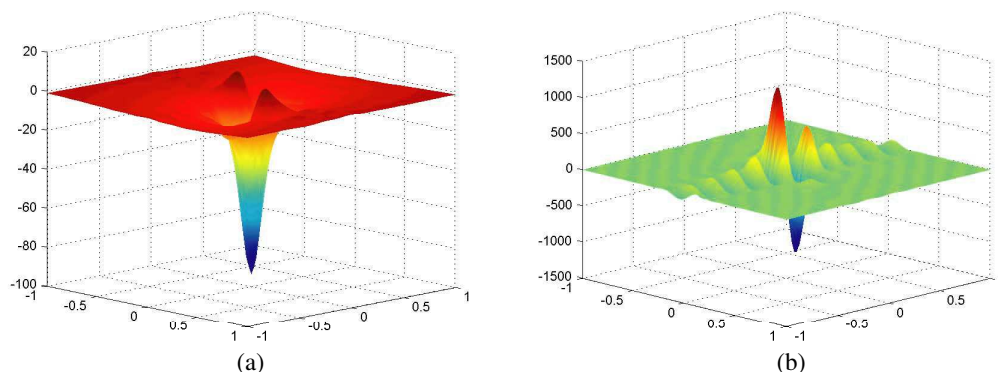
Figure 1: $\omega=2c$, (a) $3D$ plot of $\mathrm{Re}(E_1^3(x_1,x_2,0))$; (b) $3D$ plot of $\mathrm{Im}(H_1^3(x_1,x_2,0))$.

4. CONCLUSION

The method for the approximate computation of the electric and magnetic Green's functions for the time-harmonic Maxwell's equations in general gyro-electric media has been developed in the paper. The method is based on the Fourier transform meta-approach where the Fourier image of the Green's function is computed by some matrix transformations and symbolic computations in MATLAB. After that the inverse Fourier transform is computed in a regularized (approximate) form. The parameters of the regularization have been chosen by the comparison of the regularized Green's function with Green's function obtained by the explicit formula for the isotropic case. The approximate computation of the inverse Fourier transform has been implemented by MATLAB tools. The computational experiments confirm the robustness of the method.

REFERENCES

1. Eroglu, A., *Wave Propagation and Radiation in Gyrotropic and Anisotropic Media*, Springer, 2010.
2. Eroglu, A. and J. K. Lee, "Dyadic Green's function for a gyro-electric medium," *IEEE International*, Vol. 2, 1100–1103, 2006.
3. Eroglu, A. and J. K. Lee, "Dyadic Green's function for an electrically gyrotropic medium," *Progress In Electromagnetics Research*, Vol. 58, 223–241, 2006.
4. Eroglu, A. and J. K. Lee, " Wave propagation and dispersion characteristics for a nonreciprocal electrically gyrotropic medium," *Progress In Electromagnetics Research*, Vol. 62, 237–260, 2006.
5. Kong, J. A., *Electromagnetic Wave Theory*, John Wiley and Sons, 1984.
6. Lee, J. K. and S. Y. Rhee, "Reflection and transmission of plane waves at the planar interface of a magnetically gyrotropic medium," *IEEE, Geoscience and Remote Sensing Symposium*, 2005.
7. Pershan, P. S., "Magnetooptical effects," *Journal of Applied Physics*, Vol. 38, 1482, 1967.
8. Vladimirov, V. S., *Generalized Functions in Mathematical Physics*, MIR, Moscow, 1979.
9. Yakhno, V. G.,"Computing and simulation of time-dependent electromagnetic fields in homogeneous anisotropic materials," *International Journal of Engineering Science*, Vol. 46, 411–426, 2008.

On the Theory of Transition Radiation in the Anisotropic Magneto Dielectric Plate in a Waveguide

Eduard A. Gevorkyan

Moscow State University of Economics, Statistics and Informatics
7, Nezhinskaya Str., Moscow 119501, Russia

Abstract— The transition radiation of charged particle in a regular waveguide of arbitrary cross section filled with anisotropic magneto dielectric plate of finite length is considered. It is assumed that the charged particle crosses the plate perpendicular to the waveguide axis. The wave equations and the analytical expressions for the transverse-electric (TE) field in various regions in the waveguide are obtained. Taking into account the obtained analytical expressions for TE field and using the Poynting vector the energy of transition radiation of moving particle is calculated. The case of rectangular waveguide is considered and the energy of transition radiation is analyzed in this case. The analytical expression of the transition radiation of charged particle for the case of thin plate in the waveguide (the wavelength in the plate is much grater than the length of the plate) is found. The possibility of appearance of Vavilov-Cerenkov radiation is analyzed. The conditions under which occurs the Cerenkov radiation are found. The frequency of Cerenkov radiation is determined too.

1. INTRODUCTION

The study of transition radiation of charged particle in the anisotropic magneto dielectric plate in the waveguide presents the great interest both from point of view of development of the theory and possibilities of wide application of the effect of transition radiation in practice [1]. In [2, 3] the transition radiation of charged particle moving perpendicular to the waveguide axis with anisotropic magneto dielectric filling was considered. In this article the transition radiation of charged particle in the anisotropic magneto dielectric plate in the waveguide is considered, when the particle crosses the plate perpendicular to the waveguide axis.

2. STATEMENT OF THE PROBLEM AND ITS SOLUTION

Consider the regular waveguide of arbitrary cross-section which axis coincides with oz axis of some rectangular coordinate system. Let in the waveguide placed the anisotropic magneto dielectric plate which occupies the region $-d \leq z \leq d$. Suppose that the permittivity and permeability of the plate have the form

$$\widehat{\varepsilon} = \begin{pmatrix} \varepsilon_1 & 0 & 0 \\ 0 & \varepsilon_1 & 0 \\ 0 & 0 & \varepsilon_2 \end{pmatrix}, \quad \mu = \begin{pmatrix} \mu_1 & 0 & 0 \\ 0 & \mu_1 & 0 \\ 0 & 0 & \mu_2 \end{pmatrix}, \tag{1}$$

where $\varepsilon_1 = const$, $\varepsilon_2 = const$, $\mu_1 = const$, $\mu_2 = const$.

Let the particle with charge q moves with constant velocity $\vec{v} = \{v, 0, 0\}$ in the direction perpendicular to the axis of the waveguide and crosses the surface of the plate in the points $A_1(x_1, y_0, 0)$ and $A_2(x_2, y_0, 0)$. In this case the charged density the current density of the particle are described with help of Dirac's δ function in he form [4, 5]

$$\rho = q \cdot \delta(x - vt) \cdot \delta(y - y_0) \cdot \delta(y), \quad j = j_x = q \cdot v \cdot \delta(x - vt) \cdot \delta(y - y_0) \cdot \delta(y). \tag{2}$$

Transverse-electric (TE) filed, as in our early articles (see [6, 7]), we shall describe by longitudinal component of magnetic vector $H_z(x, y, z, t)$. The wave equation for H_z is received from Maxwell equations

$$rot\vec{E} = -\frac{\partial \vec{B}}{\partial t}, \quad rot\vec{H} = j + \frac{\partial \vec{D}}{\partial t}, \quad div\vec{D} = \rho, \quad div\vec{B} = 0, \quad D = \varepsilon_0 \widehat{\varepsilon} \vec{E}, \quad \vec{B} = \mu_0 \mu \vec{H}, \tag{3}$$

where $\varepsilon_0 = (36\pi \cdot 10^3)^{-1} F/m$ is dielectric constant, $\mu_0 = 4\pi \cdot 10^{-7} H/m$ is magnetic constant. In Fourier representation in different regions of the waveguide its has a form:

I and III regions ($z \geq d$ and $z \leq -d$)

$$\Delta_\perp H_{\omega z} + \frac{\partial^2 H_{\omega z}}{\partial z^2} + \varepsilon_0^2 \mu_0^2 \omega^2 H_{\omega z} = 0, \tag{4}$$

II region ($-d \leq z \leq d$)

$$\Delta_\perp H_{\omega z} + \frac{\mu_2}{\mu_1} \cdot \frac{\partial^2 H_{\omega z}}{\partial z^2} + \varepsilon_0 \mu_0 \varepsilon_1 \mu_2 \omega^2 H_{\omega z} = \frac{\partial j_\omega}{\partial y}, \tag{5}$$

where

$$j_\omega = \frac{1}{\sqrt{2\pi}} \cdot q \cdot e^{-i\omega \frac{x}{v}} \cdot \delta(z) \cdot \delta(y - y_0), \tag{6}$$

$\Delta_\perp = \partial^2/\partial x^2 + \partial^2/\partial y^2$ is a two-dimensional Laplace operator.

The solutions of the Equations (4) and (5) we shall look in the form

$$H_{\omega z} = \sum_{n=0}^{\infty} H_n(z) \cdot \widehat{\psi}_n(x, y), \tag{7}$$

where the orthonormal eigenfunctions $\widehat{\psi}_n(x, y)$ of the second boundary-value problem for the cross-section of the waveguide (the Neumann problem) satisfy the Helmholtz's equation with corresponding boundary condition

$$\Delta_\perp \widehat{\psi}_n(x, y) + \widehat{\lambda}_n^2 \widehat{\psi}_n(x, y) = 0, \quad \left. \frac{\partial \widehat{\psi}_n(x, y)}{\partial \vec{n}} \right|_\Sigma = 0. \tag{8}$$

Note that in (8) Σ is the counter of the cross-section of the waveguide, $\vec{n}$ is the normal to Σ, $\widehat{\lambda}_n$ are the eigenvalues of the Neumann problem. The transverse components of the TE filed are obtained from Maxwell's equations and have a form:

I and III regions ($z \geq d$ and $z \leq -d$)

$$\vec{H}_{\omega\tau} = \sum_{n=0}^{\infty} \widehat{\lambda}_n^{-2} \frac{dH_n(z)}{dz} \nabla \widehat{\psi}_n(x, y), \quad \vec{E}_{\omega\tau} = -i\mu_0^2 \omega \sum_{n=0}^{\infty} \widehat{\lambda}_n^{-2} H_n(z) \left[\vec{z}_0 \nabla \widehat{\psi}_n(x, y) \right], \tag{9}$$

where τ refers to the transverse components, $\nabla = \vec{i}(\partial/\partial x) + \vec{j}(\partial/\partial y)$ is the operator nabla, $\vec{z}_0$ is the unit vector of the oz axis.

II region ($-d \leq z \leq d$)

$$\vec{H}_{\omega\tau} = \frac{\mu_2}{\mu_1} \sum_{n=0}^{\infty} \widehat{\lambda}_n^{-2} \frac{dH_n(z)}{dz} \nabla \widehat{\psi}_n(x, y), \quad \vec{E}_{\omega\tau} = -i\mu_0 \mu_2 \omega \sum_{n=0}^{\infty} \widehat{\lambda}_n^{-2} H_n(z) \left[\vec{z}_0 \nabla \widehat{\psi}_n(x, y) \right], \tag{10}$$

Substituting (7) in (4) and (5) in view of (8) and making integration over the cross-section of the waveguide for $H_n(z)$ in different regions of the waveguide we obtain the following equations:

I and II regions ($z \geq d$ and $z \leq -d$)

$$\frac{d^2 H_n(z)}{dz^2} + \widehat{\gamma}_n^2 H_n(z) = 0, \tag{11}$$

where

$$\widehat{\gamma}_n^2 = \varepsilon_0^2 \mu_0^2 \omega^2 - \widehat{\lambda}_n^2. \tag{12}$$

II region ($-d \leq z \leq d$)

$$\frac{d^2 H_n(z)}{dz^2} + \widehat{\Gamma}_n^2 H_n(z) = -\frac{\mu_1}{\mu_2} \cdot \frac{q\delta(z)}{\sqrt{2\pi}} \cdot \widehat{B}_n, \tag{13}$$

where

$$\widehat{\Gamma}_n^2 = \frac{\mu_1}{\mu_2}\left(\varepsilon_0\mu_0\varepsilon_1\mu_2\omega^2 - \widehat{\lambda}_n^2\right), \quad \widehat{B}_n = \int\limits_{x_1}^{x_2} \frac{\partial\widehat{\psi}_n(x,y)}{\partial y}\bigg|_{y=y_0} \cdot e^{-i\omega\frac{x}{v}}dx. \tag{14}$$

The solution of differential Equations (11) and (13) in view of a condition of radiation (there are no waves running to the plate from infinity) and the fact, that the directions $z \geq d$ and $z \leq -d$ are equivalent, results to the following expressions:

$$H_{n1}(z) = \widehat{a}_n \cdot e^{-i\widehat{\gamma}_n z}, \quad H_{n3}(z) = \widehat{b}_n \cdot e^{i\widehat{\gamma}_n z},$$

$$H_{n2}(z) = \widehat{c}_n \cdot e^{i\widehat{\Gamma}_n z} + \widehat{d}_n \cdot e^{-i\widehat{\Gamma}_n z} - \frac{iq\mu_1}{2\mu_2} \cdot \frac{e^{i\widehat{\Gamma}_n|z|}}{\widehat{\Gamma}_n} \cdot \widehat{B}_n. \tag{15}$$

The unknown coefficients $\widehat{a}_n$, $\widehat{b}_n$, $\widehat{c}_n$ and $\widehat{d}_n$ we shall obtain from the boundary conditions at the $z = \pm d$. They have a form

$$\begin{aligned} z = -d \quad & \mu_0 H_{n3}(z) = \mu_2 H_{n2}(z), \quad \frac{dH_{n3}(z)}{dz} = \frac{\mu_2}{\mu_1} \cdot \frac{dH_{n2}(z)}{dz}, \\ z = d \quad & \mu_2 H_{n2}(z) = \mu_0 H_{n1}(z), \quad \frac{\mu_2}{\mu_1} \cdot \frac{dH_{n2}(z)}{dz} = \frac{dH_{n1}(z)}{dz}, \end{aligned} \tag{16}$$

Substituting (15) in (16) and solving the resulting system of equations for the unknown coefficients we find

$$\widehat{c}_n = \widehat{d}_n = \frac{\widehat{\beta}_n}{\widehat{\beta}_n^+ \cdot e^{i\widehat{\Gamma}_n d} + \widehat{\beta}_n^- \cdot e^{-i\widehat{\Gamma}_n d}}, \tag{17}$$

$$\widehat{a}_n = \widehat{b}_n = \frac{\mu_2}{\mu_0} \cdot \frac{\widehat{\beta}_n}{\widehat{\beta}_n^+ \cdot e^{i\widehat{\Gamma}_n d} + \widehat{\beta}_n^- \cdot e^{i\widehat{\Gamma}_n d}} \cdot \left[e^{i\left(\widehat{\Gamma}_n + \widehat{\gamma}_n\right)d} + e^{-i\left(\widehat{\Gamma}_n - \widehat{\gamma}_n\right)d}\right] - i\frac{q\mu_1}{2\mu_0} \cdot \frac{\widehat{B}_n}{\widehat{\Gamma}_n} \cdot e^{i\left(\widehat{\Gamma}_n + \widehat{\gamma}_n\right)d}, \tag{18}$$

where

$$\widehat{\beta}_n = i\frac{q\mu_1}{2\mu_2} \cdot \widehat{B}_n \cdot \left(\frac{\mu_1\widehat{\gamma}_n}{\widehat{\Gamma}_n} + \mu_0\right) \cdot e^{i\widehat{\Gamma}_n d}, \quad \widehat{\beta}_n^\pm = \mu_1\widehat{\gamma}_n \pm \mu_0\widehat{\Gamma}_n. \tag{19}$$

The energy of transition radiation for $z > d$ can be calculated using the Poynting vector according to the formula

$$S_{zn}^{(1)} = \frac{1}{2}\text{Re}\int\limits_{-\infty}^{\infty}\iint\limits_{s}\left(E_{n1x} \cdot H_{n1y}^* - H_{n1x}^* \cdot E_{n1y}\right)dsdt, \tag{20}$$

where s is a cross-sectional area of the waveguide, H_{n1y}^* and H_{n1x}^* are the complex conjugate quantities of H_{n1y} and H_{n1x}. Then from (20) with help of (9) and having lead integration on s we shall receive

$$S_{zn}^{(1)} = \frac{\mu_0^2}{\sqrt{2\pi}\widehat{\lambda}_n^2}\text{Re}\int\limits_{0}^{\infty}\widehat{\gamma}_n \cdot |H_{n1}(z)|^2\,\omega d\omega. \tag{21}$$

If we now take into account the expressions for $H_{n1}(z)$ (see (15)) and $\widehat{a}_n$ (see (18)) then (21) can be converted to the form

$$S_{zn}^{(1)} = \frac{q^2\mu_0^2\mu_1^2}{16\sqrt{2\pi}\widehat{\lambda}_n^2}\text{Re}\int\limits_{0}^{\infty}\frac{\widehat{\gamma}_n\left|\widehat{B}_n\right|^2\omega}{\mu_1^2\widehat{\gamma}_n^2\cos^2\widehat{\Gamma}_n d + \mu_0^2\widehat{\Gamma}_n^2\sin^2\widehat{\Gamma}_n d}\cdot d\omega. \tag{22}$$

The total energy of transition radiation for $z > d$ has the form $S^{(1)} = \sum\limits_{n} S_{zn}^{(1)}$, where the summation is carried out by propagating in the waveguide modes.

Let us consider the case of rectangular waveguide, assuming that the charged particle in its motion crosses the surface of the waveguide at the points $A_1(0; a)$ and $A_2(0; b)$. Caring out the integration on x from 0 to a in expression for $\widehat{B}_n$ (see (14)) taking into account, that $\widehat{\psi}_n(x, y)$ expressed by the formula

$$\widehat{\psi}_n(x, y) = \widehat{\psi}_{n,m}(x, y) = \sqrt{\frac{\delta_n \delta_m}{ab}} \cdot \cos \frac{\pi m}{a} x \cdot \cos \frac{\pi n}{b} y,$$

$$\delta_p = 2, \quad p \neq 0, \quad \delta_0 = 1, \quad \widehat{\lambda}_n = \widehat{\lambda}_{n,m} = \pi \sqrt{\frac{m^2}{a^2} + \frac{n^2}{b^2}} \tag{23}$$

and substituting in (22), for $S_{zn,m}^{(1)}$ we shall receive

$$S_{zn,m}^{(1)} = \frac{q^2 \mu_0^2 \mu_1^2 \sqrt{\pi^3} n^2 \delta_n \delta_m \sin^2 \frac{\pi n}{b} y_0}{4\sqrt{2} \, \widehat{\lambda}_{n,m}^2 ab^3 v^2} \cdot \int_{\omega_1}^{\infty} \frac{\widehat{\gamma}_{n,m} \omega^3}{\mu_1^2 \widehat{\gamma}_{n,m}^2 \cos^2 \widehat{\Gamma}_{n,m} d + \mu_0^2 \widehat{\Gamma}_{n,m}^2 \sin^2 \widehat{\Gamma}_{n,m} d} \cdot \frac{\sin^2 \left(\frac{\pi m}{a} - \frac{\omega}{v}\right) \frac{a}{2}}{\left[\left(\frac{\pi m}{a}\right)^2 - \frac{\omega^2}{v^2}\right]^2} \, d\omega, \tag{24}$$

where $\omega_1 = \widehat{\lambda}_{n,m} / \varepsilon_0 \mu_0$ is the solution of the equation $\widehat{\gamma}_{n,m} = 0$.

From the received expression (24) follows that at performance of conditions

$$\frac{\pi n y_0}{b} = k\pi, \quad k = 1, 2, 3, \ldots, \quad \left(\frac{\pi m}{a} - \frac{\omega}{v}\right) \frac{a}{2} = l\pi, \quad l = 1, 2, 3, \ldots \tag{25}$$

in the transition radiation will be no corresponding modes and corresponding frequencies.

As shown in [2–5] under the realization of the condition $\varepsilon_0 \mu_0 \varepsilon_2 \mu_1 v^2 > 1$ at the frequency $\omega_m = \pi m v / a$, which is determined from the equation $(\pi m/a) - (\omega/v) = 0$, in the spectrum of the transition radiation appears the sharp peak of the Vavilov-Cerenkov radiation. The width of Cerenkov radiation is determined by the formula $\Delta \omega_{n,m,cer.} = 4\pi v/a$. Note that the Cerenkov radiation of the charged particle is locked in the plate and is not propagated in the waveguide.

3. CONCLUSION

The received expression of the energy of transition radiation of the charged particle shows that firstly, under the certain conditions in the radiation will be absent some modes and some frequencies, secondly, under the condition of the appearance of Cerenkov radiation around a certain frequency occurs the Cerenkov radiation, which is not coming out of the plate.

REFERENCES

1. Bolotovskiy, B. M., "Vavilov-Cerenkov radiation: Discovery and application," *Uspekhi Fizicheskikh Nauk*, Vol. 179, No. 11, 1161–1173, Nov. 2009.
2. Gevorkyan, E. A., "On the radiation of charged particle moving in a waveguide with anisotropic magneto dielectric filling," *Proceedings of International Seminar/Workshop on DIPED*, 69–71, Lviv, Ukraine, Sep. 2013.
3. Gevorkyan, E. A., "On the radiation of charged particle in a waveguide filled with anisotropic magneto dielectric medium," *Proceedings of International Seminar/Workshop on DIPED*, 33–35, Tbilisi, Georgia, Sep. 2014.
4. Barsukov, K. A., E. D. Gazazyan, and E. M. Laziev, "To the theory of transition radiation in a waveguide," *Izvestiya Visshikh Uchebnikh Zavedeniy, Radiofizika*, Vol. 15, No. 2, 191–195, Feb. 1972.
5. Barsukov, K. A., E. A. Begloyan, E. D. Gazazyan, E. A. Gevorkyan, and E. M. Laziev, "On the transition radiation in dielectric plate in waveguide at passing of a charged particle perpendicular to waveguide axis," *Izvestiya AN Armyanskoy SSR, Fizika*, No. 7, 397–405, Jul. 1972.
6. Gevorkyan, E. A., "On the electrodynamics of space-time periodic mediums in the waveguide of arbitrary cross-section," *Uspekhi Sovremennoy Radioelektroniki*, No. 1, 3–29, Jan. 2006.
7. Gevorkyan, E. A., "On the electrodynamics of space-time periodic mediums in a waveguide of arbitrary cross-section," *Wave Propagation*, Chapter 13, 267–284, INTECH Open Access Publisher, Croatia, 2011.

Scattering of an Obliquely Incident Electromagnetic Plane Wave by an Array of Magnetized Plasma Cylinders

V. A. Es'kin, **A. V. Ivoninsky**, and **A. V. Kudrin**

University of Nizhny Novgorod, Russia

Abstract— Scattering of a linearly polarized electromagnetic plane wave by an array of magnetized parallel plasma cylinders is studied in the case of oblique incidence. It is shown that the interaction of individual and collective mechanisms of scattering can lead to either reduction or enhancement of the scattered field compared with the case of scattering by a single cylinder. In the case of incidence of an H-polarized wave with a zero longitudinal electric-field component, conditions have been found under which the scattered field is characterized by a pronounced layered spatial structure of this component and a chessboard-type 2D-periodic structure of the longitudinal magnetic-field component.

1. INTRODUCTION

In recent years, the issues of scattering of the electromagnetic radiation by two-dimensional arrays, photonic crystals, and other periodic structures formed by identical elements have attracted increased interest. Such an interest is stimulated by numerous applications of the corresponding structures in, e.g., lithography, near-field microscopy, wave diagnostics of media, information processing and transmission, etc. [1–3]. Despite significant progress in studies of electromagnetic wave scattering by arrays of nongyrotropic elements [1], the results recently obtained for arrays of gyrotropic scatterers have revealed a variety of new interesting features [2, 3]. In particular, it has been found that the presence of gyrotropy in photonic crystals can significantly influence the reflection and transmission of electromagnetic waves [2]. For example, nonreciprocal properties of such crystals can be used for creating materials with one-path transmission of electromagnetic energy, as well as slow-wave systems and wideband isolators in the optical band. Moreover, it can be expected that the joint contribution of the individual and collective resonance-scattering mechanisms to the diffracted field of an array containing frequency-dependent resonance elements can lead to some interesting phenomena, which are yet to be determined.

In this work, we study the scattering of an obliquely incident electromagnetic plane wave by an equidistant array of axially magnetized parallel plasma cylinders.

2. BASIC FORMULATION

Consider an equidistant array consisting of identical, infinitely long, circular cylinders of radius a, which are filled with a magnetoplasma and located in free space (see Figure 1). The cylinders are aligned with the z axis of a Cartesian coordinate system (x, y, z). The axes of the cylinders lie in the xz plane and are separated by distance L, so that the coordinates of axes are specified by the relations $x = jL$ and $y = 0$, where $j = 0, \pm 1, \pm 2, \ldots$. An external static magnetic field $\mathbf{B}_0$ is parallel to the axes of the cylinders. The cold collisionless magnetoplasma is described by the permittivity tensor $\vec{\varepsilon}$ with the nonzero elements $\varepsilon_{\rho\rho} = \varepsilon_{\phi\phi} = \varepsilon$, $\varepsilon_{\rho\phi} = -\varepsilon_{\phi\rho} = -ig$, and $\varepsilon_{zz} = \eta$ in a cylindrical coordinate system (ρ, ϕ, z). Here, $\varepsilon = 1 - \omega_p^2/(\omega^2 - \omega_H^2)$, $g = \omega_p^2 \omega_H/[(\omega^2 - \omega_H^2)\omega]$, and $\eta = 1 - \omega_p^2/\omega^2$, where ω_p and ω_H are the plasma frequency and the gyrofrequency of electrons, respectively, and ω is the angular frequency. When writing the tensor elements, we neglected the contribution of ions. This is possible under the condition $\omega \gg \omega_{\mathrm{LH}}$, which is assumed throughout
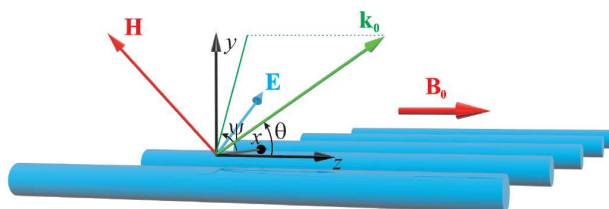
Figure 1: Geometry of the problem.

this work (here, ω_{LH} is the lower hybrid resonance frequency). Note that Gaussian units are used in this paper.

Let a plane monochromatic wave with frequency ω (the time factor $\sim e^{i\omega t}$ is assumed) be incident on the array at an angle θ to the z axis such that the wave vector projection onto the xy plane makes an angle ψ with the x axis. It is assumed that the wavelength $\lambda = 2\pi c/\omega$, where c is the speed of light in free space, is much longer than the cylinder radius a. The field in the incident wave can be written as

$$\mathbf{E}^{(i)} = \mathbf{E}_0 \exp\left[-ik_0\left(qx\cos\psi + qy\sin\psi + pz\right)\right], \quad \mathbf{H}^{(i)} = \mathbf{H}_0 \exp\left[-ik_0\left(qx\cos\psi + qy\sin\psi + pz\right)\right]. \quad (1)$$

Hereafter, $k_0 = \omega/c$ is the wave number in free space, $p = \cos\theta$ and $q = \sin\theta$ are the normalized (to k_0) longitudinal and transverse components of the wave vector $\mathbf{k}_0$ in the incident wave, respectively, and the superscript (i) denotes the incident wave.

In the cylindrical coordinate system (ρ_j, ϕ_j, z) related to the jth cylinder, the total field can be represented in terms of the azimuthal harmonics with the indices $m = 0, \pm 1, \pm 2, \ldots$ as follows:

$$\mathbf{E} = \sum_{m=-\infty}^{\infty} \mathbf{E}_m(\rho_j)\exp\left[-i(m\phi_j + k_0 pz)\right], \quad \mathbf{H} = \sum_{m=-\infty}^{\infty} \mathbf{H}_m(\rho_j)\exp\left[-i(m\phi_j + k_0 pz)\right]. \quad (2)$$

In turn, the vector quantities $\mathbf{E}_m(\rho_j)$ and $\mathbf{H}_m(\rho_j)$ can be expressed via their longitudinal components $E_{z;j,m}$ and $H_{z;j,m}$, which satisfy the following equations in the plasma medium [4]:

$$\hat{L}_m E_{z;j,m} - k_0^2 \frac{\eta}{\varepsilon}\left(p^2 - \varepsilon\right)E_{z;j,m} = -ik_0^2 \frac{g}{\varepsilon}pH_{z;j,m}, \quad \hat{L}_m H_{z;j,m} - k_0^2\left(p^2 + \frac{g^2}{\varepsilon} - \varepsilon\right)H_{z;j,m} = ik_0^2 \frac{g}{\varepsilon}\eta p E_{z;j,m}, \quad (3)$$

where $\hat{L}_m = \frac{d^2}{d\rho_j^2} + \frac{1}{\rho_j}\frac{d}{d\rho_j} - \frac{m^2}{\rho_j^2}$. The transverse field components $E_{\rho;j,m}$, $E_{\phi;j,m}$, $H_{\rho;j,m}$, and $H_{\phi;j,m}$ are expressed via the longitudinal components $E_{z;j,m}$ and $H_{z;j,m}$ as

$$E_{\rho;j,m} = A\left\{ipg\frac{m}{\rho_j}E_{z;j,m} + ip\left(\varepsilon - p^2\right)\frac{dE_{z;j,m}}{d\rho_j} + \left(\varepsilon - p^2\right)\frac{m}{\rho_j}H_{z;j,m} + g\frac{dH_{z;j,m}}{d\rho_j}\right\}, \quad (4)$$

$$E_{\phi;j,m} = A\left\{p\left(\varepsilon - p^2\right)\frac{m}{\rho_j}E_{z;j,m} + pg\frac{dE_{z;j,m}}{d\rho_j} - ig\frac{m}{\rho_j}H_{z;j,m} - i\left(\varepsilon - p^2\right)\frac{dH_{z;j,m}}{d\rho_j}\right\}, \quad (5)$$

$$H_{\rho;j,m} = A\left\{\left[g^2 - \varepsilon\left(\varepsilon - p^2\right)\right]\frac{m}{\rho_j}E_{z;j,m} - p^2 g\frac{dE_{z;j,m}}{d\rho_j} + ipg\frac{m}{\rho_j}H_{z;j,m} + ip\left(\varepsilon - p^2\right)\frac{dH_{z;j,m}}{d\rho_j}\right\}, \quad (6)$$

$$H_{\phi;j,m} = A\left\{ip^2 g\frac{m}{\rho_j}E_{z;j,m} - i\left[g^2 - \varepsilon\left(\varepsilon - p^2\right)\right]\frac{dE_{z;j,m}}{d\rho_j} + p\left(\varepsilon - p^2\right)\frac{m}{\rho_j}H_{z;j,m} + pg\frac{dH_{z;j,m}}{d\rho_j}\right\}, \quad (7)$$

where $A = k_0^{-1}[g^2 - (p^2 - \varepsilon)^2]^{-1}$.

To obtain equations for the longitudinal field components and expressions for the corresponding transverse components outside the cylinder, one should put $\varepsilon = 1$, $g = 0$, and $\eta = 1$ in Eqs. (3)–(7).

The azimuthal harmonics of the longitudinal field components inside the jth cylinder are represented in the form [4]

$$E_{z;j,m}^{(t)} = \frac{i}{\eta}\sum_{k=1}^{2}B_{j,m}^{(k)}n_k J_m(k_0 q_k \rho_j), \quad H_{z;j,m}^{(t)} = -\sum_{k=1}^{2}B_{j,m}^{(k)}J_m(k_0 q_k \rho_j). \quad (8)$$

Here, the superscript (t) denotes the field transmitting to the cylinder, J_m is a Bessel function of the first kind of order m, $B_{j,m}^{(1)}$ and $B_{j,m}^{(2)}$ are the amplitude coefficients corresponding to the azimuthal index m for the field inside the jth cylinder, and

$$q_k^2(p) = \frac{1}{2\varepsilon}\left\{\varepsilon^2 - g^2 + \varepsilon\eta - (\varepsilon+\eta)p^2 + (-1)^k\left[(\varepsilon-\eta)^2 p^4 + 2\left(g^2(\varepsilon+\eta) - \varepsilon(\varepsilon-\eta)^2\right)p^2 + \left(\varepsilon^2 - g^2 - \varepsilon\eta\right)^2\right]^{1/2}\right\},$$

$$n_k = -\frac{\varepsilon}{pg}\left(p^2 + q_k^2 + \frac{g^2}{\varepsilon} - \varepsilon\right), \quad k = 1, 2. \quad (9)$$

The presence of two transverse wave numbers q_1 and q_2 in the magnetized plasma medium, which correspond to the same longitudinal wave number p, is related to anisotropic properties of a magnetoplasma, in which two normal waves, ordinary and extraordinary, are excited by an obliquely incident plane electromagnetic wave. This circumstance represents an essential difference of the problem discussed herein from that in [5], where an H-polarized plane wave incident normally on the array of gyrotropic cylinders was considered and only the extraordinary wave could be excited inside the cylinders.

The azimuthal harmonics of the longitudinal field components in the incident plane wave are written as

$$E_{z;j,m}^{(i)} = E_{0z}(-i)^m J_m(k_0 q \rho_j) e^{i(m\psi - k_0 q L j \cos\psi)}, \quad H_{z;j,m}^{(i)} = H_{0z}(-i)^m J_m(k_0 q \rho_j) e^{i(m\psi - k_0 q L j \cos\psi)}, \quad (10)$$

where E_{0z} and H_{0z} are constants.

The total scattered field, denoted by the superscript (s), is also written in terms of the cylindrical functions and has the following longitudinal components (with the $\exp(-ik_0 pz)$ factor dropped):

$$E_z^{(s)} = \sum_{j=-\infty}^{\infty} \sum_{m=-\infty}^{\infty} D_{j,m}^{(E)} H_m^{(2)}(k_0 q \rho_j) e^{-im\phi_j}, \quad H_z^{(s)} = \sum_{j=-\infty}^{\infty} \sum_{m=-\infty}^{\infty} D_{j,m}^{(H)} H_m^{(2)}(k_0 q \rho_j) e^{-im\phi_j}, \quad (11)$$

where $H_m^{(2)}$ is a Hankel function of the second kind of order m, and $D_{j,m}^{(E)}$ and $D_{j,m}^{(H)}$ are the scattering coefficients of jth cylinder, which correspond to the azimuthal index m.

Satisfying the boundary conditions for the tangential field components on the surface of the jth cylinder and using the technique based on the scattering matrix method [6], we can exclude coefficients $B_{j,m}^{(1,2)}$ and obtain a system of equations for the scattering coefficients $D_{j,m}^{(E)}$ and $D_{j,m}^{(H)}$ in the form

$$\tilde{S}_m^{HE} D_{j,m}^{(E)} + \tilde{S}_m^{HH} D_{j,m}^{(H)} = \sum_{n=-\infty}^{\infty} \left[\sum_{l<j} (-1)^{m-n} D_{l,n}^{(H)} H_{m-n}^{(2)}(k_0 q L |j-l|) + \sum_{l>j} D_{l,n}^{(H)} H_{m-n}^{(2)}(k_0 q L |j-l|) \right]$$
$$+ H_{0z}(-i)^m \exp\left[i(m\psi - k_0 q L j \cos\psi)\right],$$
$$(12)$$
$$\tilde{S}_m^{EE} D_{j,m}^{(E)} + \tilde{S}_m^{EH} D_{j,m}^{(H)} = \sum_{n=-\infty}^{\infty} \left[\sum_{l<j} (-1)^{m-n} D_{l,n}^{(E)} H_{m-n}^{(2)}(k_0 q L |j-l|) + \sum_{l>j} D_{l,n}^{(E)} H_{m-n}^{(2)}(k_0 q L |j-l|) \right]$$
$$+ E_{0z}(-i)^m \exp\left[i(m\psi - k_0 q L j \cos\psi)\right],$$

where $\tilde{S}_m^{HH}$, $\tilde{S}_m^{HE}$, $\tilde{S}_m^{EH}$, and $\tilde{S}_m^{EE}$ are the elements of the matrix that is inverse of the single-cylinder scattering matrix. To find these elements, we consider the system of equations

$$\begin{pmatrix} \dfrac{in_1}{\eta} J_m^{(1)} & \dfrac{in_2}{\eta} J_m^{(2)} & -H_m^{(2)} & 0 \\ i\hat{J}_m^{(1)} & i\hat{J}_m^{(2)} & \dfrac{pm}{Q^2} H_m^{(2)} & -\dfrac{i}{Q} H_m^{(2)\prime} \\ -J_m^{(1)} & -J_m^{(2)} & 0 & -H_m^{(2)} \\ -n_1 \tilde{J}_m^{(1)} & -n_2 \tilde{J}_m^{(2)} & \dfrac{i}{Q} H_m^{(2)\prime} & \dfrac{pm}{Q^2} H_m^{(2)} \end{pmatrix} \begin{pmatrix} R_m^{(1)} \\ R_m^{(2)} \\ S_m^{(1)} \\ S_m^{(2)} \end{pmatrix} = \begin{pmatrix} J_m \\ -\dfrac{pm}{Q^2} J_m \\ 0 \\ -\dfrac{i}{Q} J_m' \end{pmatrix} C_m^{(E)} + \begin{pmatrix} 0 \\ \dfrac{i}{Q} J_m' \\ J_m \\ -\dfrac{pm}{Q^2} J_m \end{pmatrix} C_m^{(H)}, \quad (13)$$

where

$$J_m^{(k)} = J_m(Q_k), \quad \hat{J}_m^{(k)} = \dfrac{J_{m+1}^{(k)}}{Q_k} + \alpha_k m \dfrac{J_m^{(k)}}{Q_k^2}, \quad \tilde{J}_m^{(k)} = \dfrac{J_{m+1}^{(k)}}{Q_k} - \beta_k m \dfrac{J_m^{(k)}}{Q_k^2},$$

$$Q_k = k_0 q_k a, \quad Q = k_0 q a, \quad \alpha_k = -1 + \dfrac{p^2 + q_k^2 - \varepsilon}{g}, \quad \beta_k = 1 + \dfrac{p}{n_k}.$$

In system (13), the prime indicates the derivative with respect to the argument, and the arguments of the functions $J_m(Q)$ and $H_m^{(2)}(Q)$ are omitted for brevity. Upon finding the solutions $R_m^{(1,2)}$ and $S_m^{(1,2)}$ of system (13), the desired quantities $\tilde{S}_m^{HH}$, $\tilde{S}_m^{HE}$, $\tilde{S}_m^{EH}$, and $\tilde{S}_m^{EE}$ are represented as

$$\tilde{S}_m^{HH} = S_{11}/\Delta, \quad \tilde{S}_m^{HE} = -S_{12}/\Delta, \quad \tilde{S}_m^{EH} = -S_{21}/\Delta, \quad \tilde{S}_m^{EE} = S_{22}/\Delta, \quad \Delta = S_{11}S_{22} - S_{12}S_{21}, \quad (14)$$

where $S_{11} = S_m^{(1)}$ and $S_{12} = S_m^{(2)}$ under the conditions $C_m^{(H)} = 0$ and $C_m^{(E)} = 1$, while $S_{21} = S_m^{(1)}$ and $S_{22} = S_m^{(2)}$ under the conditions $C_m^{(H)} = 1$ and $C_m^{(E)} = 0$.

Using the translational symmetry of the problem, i.e., the identity $\mathbf{H}^{(s)}(x+L, y, z) = \mathbf{H}^{(s)}(x, y, z)$ $\times e^{-ik_0qL\cos\psi}$, we can establish the relation between the terms $D_{j+1,m}^{(E,H)}$ and $D_{j,m}^{(E,H)}$ in the form $D_{j+1,m}^{(E,H)} = D_{j,m}^{(E,H)}e^{-ik_0qL\cos\psi}$. Hence, we may put $D_{j,m}^{(E,H)} = \hat{D}_m^{(E,H)}e^{-ik_0qLj\cos\psi}$, where $\hat{D}_m^{(E,H)} \equiv D_{0,m}^{(E,H)}$. As a result, we arrive at the following system of equations for $\hat{D}_m^{(E,H)}$:

$$\tilde{S}_m^{HE}\hat{D}_m^{(E)} + \tilde{S}_m^{HH}\hat{D}_m^{(H)} = H_{0z}(-i)^m e^{im\psi} + \sum_{n=-\infty}^{\infty} \hat{D}_n^{(H)}G_{n-m},$$

$$\tilde{S}_m^{EE}\hat{D}_m^{(E)} + \tilde{S}_m^{EH}\hat{D}_m^{(H)} = E_{0z}(-i)^m e^{im\psi} + \sum_{n=-\infty}^{\infty} \hat{D}_n^{(E)}G_{n-m},$$

(15)

where

$$G_m = \sum_{l=1}^{\infty} H_m^{(2)}(k_0qLl) \left[e^{ik_0qLl\cos\psi} + (-1)^m e^{-ik_0qLl\cos\psi} \right].$$

(16)

The above expressions allow us to proceed to numerical calculations of the scattered field, the results of which are discussed in what follows.

3. NUMERICAL RESULTS

We now consider the scattering of a monochromatic H-polarized plane wave whose magnetic field has a nonzero H_z component, but a zero E_z component. All field components are normalized to the magnetic-field amplitude in the incident wave.

Numerical calculations were performed for the following values of parameters: $\omega_p/\omega_H = 8$, $\omega_p a/c = 0.188$, and $\psi = \pi/2$. Figures 2(a) and 2(b) show the absolute values of the scattered and total magnetic fields at the resonant frequency $\omega = 6.043\omega_H$ for normal incidence on the array when $\theta = \pi/2$. In this case, the scattered field has a layered structure [Figure 2(a)] and is almost periodic along the x axis. Note that the maximum value of the scattered field at the indicated frequency, which is reached near the array plane, exceeds the magnetic-field amplitude in the incident wave. Because of this, the total field [Figure 2(b)], which is formed due to interference of the incident and scattered waves, has a cell-like spatial structure with quasi-periodically alternating maxima and minima in the direction of the y axis. In this case, the magnetic-field structure is almost symmetric with respect to the array plane $y = 0$.

In the case of oblique incidence where $\theta \neq \pi/2$, the scattered field is hybrid, i.e., the longitudinal components of both the electric and magnetic fields are nonzero. Let us dwell on the case where the H wave is incident on the array at the angle $\theta = \pi/4$ to the axes of the cylinders. Analysis of the frequency dependences of the scattering coefficients of the electric- and magnetic-field components shows that near the resonant frequencies of the array, frequency ranges exist in which the absolute values of these coefficients are much smaller than the field amplitude in the incident wave.
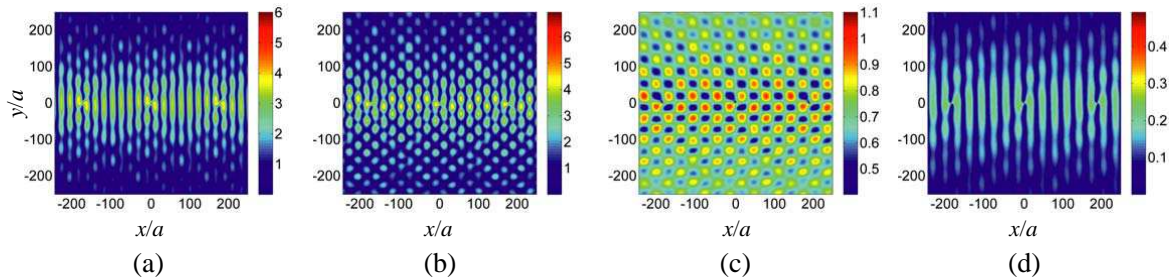
Figure 2: Absolute values of the longitudinal component of (a) the scattered and (b) total magnetic fields for normal incidence of the H wave on the array at the resonant frequency $\omega = 6.043\omega_H$ for $k_0L/2\pi = 3.9909$, $L/a = 177$, and $\theta = \pi/2$, and the absolute values of the longitudinal component of (c) the total magnetic and (d) electric fields for oblique incidence of the H wave on the array at the angle $\theta = \pi/4$ to the axes of the cylinders for $\omega = 6.023\omega_H$, $k_0qL/2\pi = 4.2465$, and $L/a = 189$.

Moreover, at the resonant frequencies of the array, these coefficients vanish. Thus, the interaction of the individual and collective scattering mechanisms can lead to a significant weakening and even suppression of the scattered field.

Note that in the case of oblique incidence of the H wave, the longitudinal component of the total magnetic field comprises the corresponding components of the incident and scattered waves, whereas the longitudinal component of the total electric field is determined only by the corresponding component of the scattered field. This feature is illustrated by Figures 2(c) and 2(d), which show the spatial structures of the magnitudes of the longitudinal magnetic- and electric-field components at the frequency $\omega = 6.023\omega_H$, which is slightly higher than the nearest resonant frequency of the array. In this case, the electric field has the layered structure and its amplitude is comparable with the amplitude in the incident wave. The corresponding component of the magnetic field has the 2D-periodic chessboard-type structure.

4. CONCLUSION

In this work, we have studied the scattering of an H-polarized electromagnetic plane wave by an array of equidistant parallel cylinders filled with a cold collisionless magnetoplasma. The solution for the field in the case of incidence at an arbitrary angle to the axes of the cylinders has been obtained. It is shown that the interaction of the individual and collective scattering mechanisms can lead to either enhancement or weakening of scattering compared with the case of a single cylinder. Conditions have been determined under which this or that scattering mechanisms gives a dominant contribution to the scattering by the array. It is shown that in the case of oblique incidence of the H wave on the array, the longitudinal component of the electric field can have, under certain conditions, a layered structure elongated in the direction perpendicular to the array, whereas the longitudinal component of the magnetic field can have a 2D-periodic chessboard-type structure.

ACKNOWLEDGMENT

REFERENCES

1. Decoopman, T., G. Tayeb, S. Enoch, D. Maystre, and B. Gralak, "Photonic crystal lens: From negative refraction and negative index to negative permittivity and permeability," *Phys. Rev. Lett.*, Vol. 97, No. 7, 073905, 2006.
2. Liu, S., W. Chen, J. Du, Z. Lin, S. T. Chui, and C. T. Chan, "Manipulating negative-refractive behavior with a magnetic field," *Phys. Rev. Lett.*, Vol. 101, No. 15, 157407, 2008.
3. He, C., M.-H. Lu, X. Heng, L. Feng, and Y.-F. Chen, "Parity-time electromagnetic diodes in a two-dimensional nonreciprocal photonic crystal," *Phys. Rev. B*, Vol. 83, No. 7, 75117, 2011.
4. Kondrat'ev, I. G., A. V. Kudrin, and T. M. Zaboronkova, *Electrodynamics of Density Ducts in Magnetized Plasmas*, Gordon and Breach, Amsterdam, 1999.
5. Kudrin, A. V., V. A. Eskin, and T. M. Zaboronkova, "Electromagnetic wave scattering by an array of parallel gyrotropic cylinders," *Proceedings of the XXXIst URSI General Assembly and Scientific Symposium (URSI GASS)*, BP1.34, Beijing, China, Aug. 2014.
6. Yasumoto, K., *Electromagnetic Theory and Applications for Photonic Crystals*, Taylor and Francis, Boca Raton, 2006.

Theorem for the $G_1(c, n)$ Numbers

Georgi Nikolov Georgiev[1] and Mariana Nikolova Georgieva-Grosse[2]

[1]Faculty of Mathematics and Informatics
University of Veliko Tirnovo "St. St. Cyril and Methodius", Veliko Tirnovo BGC5000, Bulgaria
[2]Consulting and Researcher in Physics and Computer Sciences, Gerlingen D-70839, Germany

Abstract— The theorem for existence of the $G_1(c, n)$ numbers (finite real positive numbers, coherent with the zeros $\kappa_{z,n}^{(c)}$ in the imaginary part κ of the complex first parameter a of the complex Kummer confluent hypergeometric function $\Phi(a, c; x)$ with $a = c/2 + j\kappa$ — complex, $c = 2\mathrm{Re}a$ — restricted positive integer ($c = 1, 2, 3, \ldots$), κ — real (positive, negative or zero, $-\infty < \kappa < +\infty$), $x = jz$ — positive purely imaginary, z — real, positive and $n = 1, 2, 3, \ldots$) is formulated and proved numerically. It serves as a definition of quantities in question and determines them as the limit of the infinite sequence of real numbers $\{D_1(c, n, z)\}$ ($D_1(c, n, z) = \kappa_{z,n}^{(c)} z$) for $z \to 0$. Supposedly this assumption holds, the theorem states that the sequence of the zeros $\{\kappa_{z,n}^{(c)}\}$ is divergent and its terms become infinitely large positive. Moreover, if $z \to +\infty$ both $\{\kappa_{z,n}^{(c)}\}$ and $\{D_1(c, n, z)\}$ are divergent and tend to $-\infty$. Tables and graphs illustrate the influence of parameters c and n on $G_1(c, n)$. The benefit of numbers is manifested in the theory of azimuthally magnetized circular ferrite waveguides, propagating normal TE_{0n} modes.

1. INTRODUCTION

The zeros of Kummer confluent hypergeometric function $\Phi(a, c; x)$ [1] with $a = c/2 - jk$ — complex, c — real, ($c \neq l$, $l = 0, -1, -2, -3, \ldots$), k — real, $x = jz$, z — real, positive and $n = 1, 2, 3, \ldots$ are of special interest in the theory of circular anisotropic waveguides of azimuthal magnetization [2–6]. Until now the attention has been the focused mainly on the positive purely imaginary zeros $\zeta_{k,n}^{(c)}$ of $\Phi(a, c; x)$ with respect to its independent variable z [2–6]. It has been established that for them it holds: $\lim_{k_+ \to +\infty} \zeta_{k_+,n}^{(c)} = +\infty$ and $\lim_{k_- \to -\infty} \zeta_{k_-,n}^{(c)} = 0$, where the subscripts "+" ("−") label quantities, corresponding to positive (negative) sign of k ($k_+ > 0$ and $k_- < 0$) [2]. The numerical analysis has shown that if $c \neq l$ the sequences $\{K_-(c, n, k_-)\}$ and $\{M_-(c, n, k_-)\}$ ($K_-(c, n, k_-) = |k_-|\zeta_{k_-,n}^{(c)}$ and $M_-(c, n, k_-) = |a_-|\zeta_{k_-,n}^{(c)}$) are convergent provided $k_- \to -\infty$, though the multiples in the products $|k_-|\zeta_{k_-,n}^{(c)}$ and $|a_-|\zeta_{k_-,n}^{(c)}$ become unrestricted, resp. infinitesimal. They tend to finite real positive limits, called $L_1(c, n)$ numbers (denoted by $L(c, n)$, too) [2, 4, 5, 7–9]. The definition of the latter has been extended for $c = l$, as well [7–9]. Later on a similar property of the positive purely imaginary zeros in z of certain special functions, incorporating several complex confluent and possibly also a few real cylindrical ones of specially selected parameters has been found out [8–11]. The discussion has been extended to the real case, too [11].

Recently, an investigation of the zeros $\kappa_{z,n}^{(c)}$ in κ of the complex Kummer function $\Phi(a, c; x)$ of $a = c/2 + j\kappa$ — complex, $c = 2\mathrm{Re}a$ — restricted positive integer ($c = 1, 2$ and 3), κ — real, $x = jz$ — positive purely imaginary, z — real, positive and $n = 1, 2, 3, \ldots$ has been made, assuming z as parameter. It has been established that when z diminishes, tending to zero, $\kappa_{z,n}^{(c)}$ grow monotonously and become very large, going to $+\infty$ [12]. This hinted that the latter might possess features, resembling those of the zeros $\zeta_{k,n}^{(c)}$ (new families of real numbers might be advanced, linked with $\kappa_{z,n}^{(c)}$).

Following the above approach, here new auxiliary numbers $D_1(c, n, z)$ are introduced through the relation: $D_1(c, n, z) = \kappa_{z,n}^{(c)} z$. The sequences $\{\kappa_{z,n}^{(c)}\}$ and $\{D_1(c, n, z)\}$ are constructed and the dependence of their terms on variable z is studied in a wide interval of variation of this parameter. It is found out that the first is divergent both for $z \to 0$ and $z \to +\infty$. In the first case it holds $\lim_{z \to 0} \kappa_{z,n}^{(c)} = +\infty$ and in the second one $\lim_{z \to +\infty} \kappa_{z,n}^{(c)} = -\infty$. As for the second set of sequences when the parameter mentioned acquires large positive values, they are divergent and tend to $-\infty$, obviously faster than $\{\kappa_{z,n}^{(c)}\}$. If $z \to 0$, however, $\{D_1(c, n, z)\}$ is convergent and possesses a finite positive

real limit, depending on the numerical equivalents of c and n. The set of these limits is regarded as a family of new finite positive real numbers, called $G_1(c,n)$ ones. This is the basic results of the investigation, stated as a Theorem for existence of $G_1(c,n)$ numbers. The latter is proved numerically for positive integer c and natural n. Examples for the substantiation of assertion are given for suitably picked up (without lost of generality) and arbitrarily changing z. The work is richly illustrated by detailed tables and graphs, revealing the influence of parameters on quantities examined. The application of the new numbers in the theory of azimuthally magnetized circular ferrite waveguides, propagating normal TE_{0n} modes is demonstrated.

2. THEOREM FOR EXISTENCE OF THE $G_1(C, N)$ NUMBERS

Theorem 1: *If $\kappa_{z,n}^{(c)}$ is the nth zero $(n = 1, 2, 3 \ldots)$ in the imaginary part κ of the complex first parameter a of the complex Kummer confluent hypergeometric function $\Phi(a,c;x)$ with $a = c/2 + j\kappa$ — complex, $c = 2\mathrm{Re}a$ — restricted positive integer $(c = 1, 2, 3 \ldots)$, κ — real (positive, negative or zero, $-\infty < \kappa < +\infty$), $x = jz$ — positive purely imaginary, z — real, positive and if $D_1(c,n,z) = \kappa_{z,n}^{(c)} z$, then the infinite sequence of real numbers $\{\kappa_{z,n}^{(c)}\}$ is divergent and grows unlimitedly (tends to $+\infty$) in case $z \to 0$, whereas on the same condition the sequence $\{D_1(c,n,z)\}$ is convergent $(c, n$ — fixed). Its limit equals the finite real positive number G_1 where $G_1 = G_1(c,n)$. It holds:*

$$G_1(c,n) = \lim_{z \to 0} D_1(c,n,z). \tag{1}$$

Stipulating that $z \to +\infty$ both $\{\kappa_{z,n}^{(c)}\}$ and $\{D_1(c,n,z)\}$ are divergent and go to $-\infty$.

Numerical proof: The proof of Theorem 1 is illustrated in Table 1 for $c = 1$ and $n = 1$ (1) 4, and in Tables 2–4 for $c = 2$ (1) 7 and $n = 1$ (cf. the digits marked by bold face type). Tables 1 and 2 contain results for $z = 1 \cdot 10^{-s}$, $s = -1$ (1) 8, Table 3 — for z varying from $1 \cdot 10^{-4}$ to $1 \cdot 10^{-7}$, and Table 4 — for z taking in values from $1.0916527843 \cdot 10^1$ to $1.4738592601 \cdot 10^{-8}$. The numerical equivalents of z in Table 3 are specially chosen and in Table 4 are arbitrary. The dependence of $D_1(c,n,z) = \kappa_{z,n}^{(c)} z$ on z is portrayed with blue solid lines in Figures 1–4 for selected values of

Table 1: Numbers $\kappa_{z,n}^{(c)}$ and $D_1(c,n,z)$ for $c = 1$ and $n = 1$, 2, 3 and 4 in case of small $z = 1 \cdot 10^{-s}$, $s = -1$ (1) 8.

z	$\kappa_{z,n}^{(c)}$	$D_1(c,n,z)$	$\kappa_{z,n}^{(c)}$	$D_1(c,n,z)$
	$n = 1$		$n = 2$	
$1 \cdot 10^1$	$(-1)\ -7.648271756996514$	-7.648271756996514	$(-1)\ 1.22948\ 32177\ 89881$	$1.22948\ 32177\ 89881$
$1 \cdot 10^0$	$(0)\ 1.39096\ 86145\ 43394$	**1.**39096 86145 43394	$(0)\ 7.54004\ 45591\ 61164$	**7.**54004 45591 61164
$1 \cdot 10^{-1}$	$(1)\ 1.44525\ 13179\ 65011$	**1.44**525 13179 65011	$(1)\ 7.61703\ 69580\ 49011$	**7.61**703 69580 49011
$1 \cdot 10^{-2}$	$(2)\ 1.44579\ 10393\ 18058$	**1.44579** 10393 18058	$(2)\ 7.61780\ 77995\ 46547$	**7.61780** 77995 46547
$1 \cdot 10^{-3}$	$(3)\ 1.44579\ 64362\ 22541$	**1.44579 64**362 22541	$(3)\ 7.61781\ 55080\ 51823$	**7.61781 55**080 51823
$1 \cdot 10^{-4}$	$(4)\ 1.44579\ 64901\ 91555$	**1.44579 64901** 91555	$(4)\ 7.61781\ 55851\ 36884$	**7.61781 55851** 36884
$1 \cdot 10^{-5}$	$(5)\ 1.44579\ 64907\ 31245$	**1.44579 64907** 31245	$(5)\ 7.61781\ 55859\ 07735$	**7.61781 55859** 07735
$1 \cdot 10^{-6}$	$(6)\ 1.44579\ 64907\ 36642$	**1.44579 64907 366**42	$(6)\ 7.61781\ 55859\ 15444$	**7.61781 55859 15**444
$1 \cdot 10^{-7}$	$(7)\ 1.44579\ 64907\ 36696$	**1.44579 64907 36696**	$(7)\ 7.61781\ 55859\ 15521$	**7.61781 55859 15521**
$1 \cdot 10^{-8}$	$(8)\ 1.44579\ 64907\ 36696$	**1.44579 64907 36696**	$(8)\ 7.61781\ 55859\ 15521$	**7.61781 55859 15521**
	$n = 3$		$n = 4$	
$1 \cdot 10^1$	$(-1)\ 11.23870\ 61195\ 42211$	$11.23870\ 61195\ 42211$	$(-1)\ 26.89746\ 05255\ 44971$	$26.89746\ 05255\ 44971$
$1 \cdot 10^0$	$(0)\ 18.64070\ 20791\ 32000$	**18.**64070 20791 32000	$(0)\ 34.67797\ 16513\ 50657$	**34.**67797 16513 50657
$1 \cdot 10^{-1}$	$(1)\ 18.72094\ 06258\ 98684$	**18.72**094 06258 98684	$(1)\ 34.75924\ 97637\ 33569$	**34.75**924 97637 33569
$1 \cdot 10^{-2}$	$(2)\ 18.72174\ 35868\ 98565$	**18.72174** 35868 98565	$(2)\ 34.76006\ 28931\ 51317$	**34.76006** 28931 51317
$1 \cdot 10^{-3}$	$(3)\ 18.72175\ 16165\ 66037$	**18.72175 16**165 66037	$(3)\ 34.76007\ 10244\ 80322$	**34.76007** 10244 80322
$1 \cdot 10^{-4}$	$(4)\ 18.72175\ 16968\ 62717$	**18.72175 169**68 62717	$(4)\ 34.76007\ 11057\ 93614$	**34.76007 11**057 93614
$1 \cdot 10^{-5}$	$(5)\ 18.72175\ 16976\ 65684$	**18.72175 16976** 65684	$(5)\ 34.76007\ 11066\ 06746$	**34.76007 11066** 06746
$1 \cdot 10^{-6}$	$(6)\ 18.72175\ 16976\ 73716$	**18.72175 16976 73**716	$(6)\ 34.76007\ 11066\ 14882$	**34.76007 11066 14**882
$1 \cdot 10^{-7}$	$(7)\ 18.72175\ 16976\ 73795$	**18.72175 16976 73795**	$(7)\ 34.76007\ 11066\ 14963$	**34.76007 11066 14963**
$1 \cdot 10^{-8}$	$(8)\ 18.72175\ 16976\ 73795$	**18.72175 16976 73795**	$(8)\ 34.76007\ 11066\ 14962$	**34.76007 11066 14963**

Table 2: Numbers $\kappa_{z,n}^{(c)}$ and $D_1(c,n,z)$ for $c = 2$ and 3, and $n = 1$ in case of small $z = 1\cdot 10^{-s}$, $s = -1$ (1) 8.

z	$\kappa_{z,n}^{(c)}$	$D_1(c,n,z)$	$\kappa_{z,n}^{(c)}$	$D_1(c,n,z)$
	$c = 2$		$c = 3$	
$1\cdot 10^1$	(−1) −6.985596396425155	−6.985596396425155	(−1) 5.26046 84863 74887	5.26046 84863 74887
$1\cdot 10^0$	(0) 3.58691 89372 16388	**3.**58691 89372 16388	(0) 6.49118 71834 61350	**6.**49118 71834 61350
$1\cdot 10^{-1}$	(1) 3.66965 93031 82381	**3.66**965 93031 82381	(1) 6.59263 11796 40417	**6.59**263 11796 40417
$1\cdot 10^{-2}$	(2) 3.67048 43271 95238	**3.670**48 43271 95238	(2) 6.59364 38776 93587	**6.5936**4 38776 93587
$1\cdot 10^{-3}$	(3) 3.67049 25771 97640	**3.67049 2**5771 97640	(3) 6.59365 40044 99892	**6.59365 **40044 99892
$1\cdot 10^{-4}$	(4) 3.67049 26596 97640	**3.67049 26**596 97640	(4) 6.59365 41057 67938	**6.59365 41**057 67938
$1\cdot 10^{-5}$	(5) 3.67049 26605 22640	**3.67049 26605 **22640	(5) 6.59365 41067 80618	**6.59365 41067 **80618
$1\cdot 10^{-6}$	(6) 3.67049 26605 30890	**3.67049 26605 30**890	(6) 6.59365 41067 90746	**6.59365 41067 90**746
$1\cdot 10^{-7}$	(7) 3.67049 26605 30973	**3.67049 26605 30973**	(7) 6.59365 41067 90847	**6.59365 41067 90847**
$1\cdot 10^{-8}$	(8) 3.67049 26605 30973	**3.67049 26605 30973**	(8) 6.59365 41067 90848	**6.59365 41067 90848**

Table 3: Numbers $\kappa_{z,n}^{(c)}$ and $D_1(c,n,z)$ for $c = 4$ and 5, and $n = 1$ in case of small specially chosen $z = \langle 1\cdot 10^{-4} \div 1\cdot 10^{-7}\rangle$.

z	$\kappa_{z,n}^{(c)}$	$D_1(c,n,z)$	$\kappa_{z,n}^{(c)}$	$D_1(c,n,z)$
	$c = 4$		$c = 5$	
1.10^{-4}	(4) 10.17661 64533 89198	**10.17661 64533 89198**	(4) 14.39573 52245 55291	**14.39573 522**45 55291
8.10^{-5}	(5) 1.27207 70567 25889	**10.17661 64538 **07115	(5) 1.79946 69031 26448	**14.39573 52250 **11587
6.10^{-5}	(5) 1.69610 27423 55360	**10.17661 64541 **32162	(5) 2.39928 92042 27747	**14.39573 52253 **66485
4.10^{-5}	(5) 2.54415 41135 91085	**10.17661 64543 **64338	(5) 3.59893 38064 04995	**14.39573 52256 **19982
2.10^{-5}	(5) 5.08830 82272 51822	**10.17661 64545 **03644	(5) 7.19786 76128 86040	**14.39573 52257 **72080
1.10^{-5}	(5) 10.17661 64545 38470	**10.17661 64545 **38470	(5) 14.39573 52258 10105	**14.39573 52258 **10105
8.10^{-6}	(6) 1.27207 70568 17831	**10.17661 64545 **42651	(6) 1.79946 69032 26834	**14.39573 52258 **14670
6.10^{-6}	(6) 1.69610 27424 24317	**10.17661 64545 **45901	(6) 2.39928 92043 03036	**14.39573 52258 **18218
4.10^{-6}	(6) 2.54415 41136 37056	**10.17661 64545 **48223	(6) 3.59893 38064 55188	**14.39573 52258 2**0754
2.10^{-6}	(6) 5.08830 82272 74808	**10.17661 64545 **49616	(6) 7.19786 76129 11137	**14.39573 52258 22**275
1.10^{-6}	(6) 10.17661 64545 49964	**10.17661 64545 **49964	(6) 14.39573 52258 22655	**14.39573 52258 22**655
8.10^{-7}	(7) 1.27207 70568 18751	**10.17661 64545 50**006	(7) 1.79946 69032 27838	**14.39573 52258 227**01
6.10^{-7}	(7) 1.69610 27424 25006	**10.17661 64545 50**039	(7) 2.39928 92043 03789	**14.39573 52258 227**36
4.10^{-7}	(7) 2.54415 41136 37515	**10.17661 64545 50**062	(7) 3.59893 38064 55690	**14.39573 52258 227**62
2.10^{-7}	(7) 5.08830 82272 75038	**10.17661 64545 5007**6	(7) 7.19786 76129 11388	**14.39573 52258 227**77
1.10^{-7}	(7) 10.17661 64545 50079	**10.17661 64545 50079**	(7) 14.39573 52258 22781	**14.39573 52258 2278**1

Table 4: Numbers $\kappa_{z,n}^{(c)}$ and $D_1(c,n,z)$ for $c = 6$ and 7, and $n = 1$ in case of small arbitrary $z = \langle 1.0916527843\cdot 10^1 \div 1.4738592601\cdot 10^{-8}\rangle$.

z	$\kappa_{z,n}^{(c)}$	$D_1(c,n,z)$	$\kappa_{z,n}^{(c)}$	$D_1(c,n,z)$
	$c = 6$		$c = 7$	
$1.0916527843\cdot 10^1$	(−1) 1.91110 05127 17661	2.0862581957 85393	(−1) 6.30276 35571 41752	6.880429 38593 83663
$6.4579803216\cdot 10^0$	(0) 2.08374 96909 78616	13.45681 44994 79985	(0) 2.88536 95948 94069	18.63366 00643 68859
$5.4698720315\cdot 10^{-1}$	(1) 3.50908 33885 10577	19.19423 70830 15252	(1) 4.50448 40337 16057	**24.63**895 12323 61765
$4.9675802134\cdot 10^{-2}$	(2) 3.87198 54180 50890	19.23439 81492 82930	(2) 4.96845 86081 62088	**24.681**21 66730 02891
$9.7685401239\cdot 10^{-3}$	(3) 1.96904 74652 68049	**19.23471** 91703 34529	(3) 2.52663 69606 91400	**24.68155** 45290 42686
$8.7964502138\cdot 10^{-4}$	(4) 2.18664 70577 55958	**19.23473** 19787 02541	(4) 2.80585 54768 36671	**24.68156 8**0091 11842
$3.7946508213\cdot 10^{-5}$	(5) 5.06890 69927 72371	**19.23473 20832** 16992	(5) 6.50430 54766 89861	**24.68156 81191** 07269
$7.3495602817\cdot 10^{-6}$	(6) 2.61712 69227 21889	**19.23473 20834** 04539	(6) 3.35823 73874 47573	**24.68156 81193** 04654
$2.1743590628\cdot 10^{-7}$	(7) 8.84616 18011 89630	**19.23473 20834 11843**	(7) 11.35119 24233 56703	**24.68156 81193 1234**1
$1.4738592601\cdot 10^{-8}$	(8) 13.05058 94315 21979	**19.23473 20834 11849**	(8) 16.74621 77614 14835	**24.68156 81193 12347**

parameters c and n. The limiting $G_1(c,n)$ numbers to which the $D_1(c,n,z)$ ones (the curves) tend provided z gets infinitesimal, are depicted in by red circles at the left vertical (zero) axes of the figures mentioned. The effect of c and n on $G_1(c,n)$ is presented in Table 5 and Figure 5. In the latter the quantities studied for the specific n are pictured by the same and for different c — by

distinct symbols. The statement of Theorem 1 concerning the impact z on zeros $\kappa_{z,n}^{(c)}$ of $\Phi(a,c;x)$

Table 5: Dependence of the $G_1(c,n)$ numbers on $c = 1\ (1)\ 10$ and $n = 1\ (1)\ 5$.

$c\backslash n$	1	2	3	4	5
1	1.44579 64907 36696	7.61781 55859 15521	18.72175 16976 73795	34.76007 11066 14962	55.73307 59044 08538
2	3.67049 26605 30973	12.30461 40804 23651	25.87486 34737 84145	44.38019 17034 51162	67.82041 35682 18332
3	6.59365 41067 90848	17.71249 97297 73964	33.75517 72164 92605	54.73004 72864 15859	80.63877 90731 36191
4	10.17661 64545 50079	23.81939 31360 09286	42.34886 24565 24859	65.80021 35637 52044	94.18134 98580 41812
5	14.39573 52258 22781	30.60694 90162 32036	51.64245 25942 48102	77.58056 49669 69119	108.44028 40984 51510
6	19.23473 20834 11849	38.06028 83854 37220	61.62386 65333 12550	90.06137 04799 38087	123.40765 80609 09464
7	24.68156 81193 12347	46.16720 18347 92032	72.28247 08239 01675	103.23361 85655 50203	139.07584 47505 93669
8	30.72690 00509 04058	54.91750 16695 84654	83.60892 14637 20086	117.08907 44284 45232	155.43765 71908 63442
9	37.36322 02158 56614	64.30255 02494 75972	95.59497 37577 97756	131.62024 25129 25234	172.48638 78484 82913
10	44.58433 53104 07377	74.31492 00693 89638	108.23330 94261 80086	146.82029 86714 54876	190.21580 17213 53713
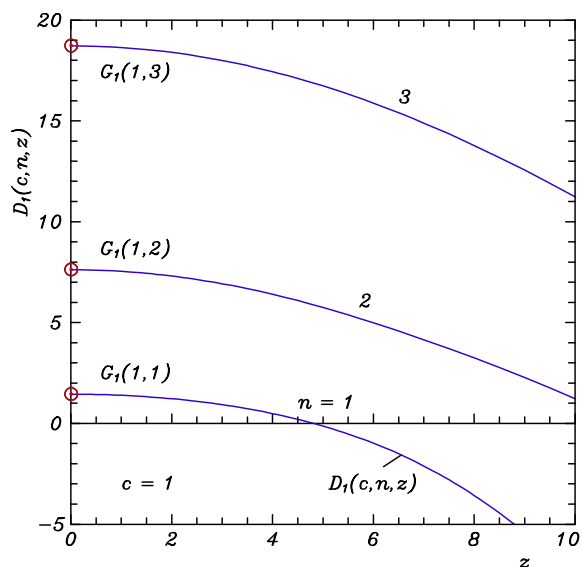
Figure 1: Graphical representation of the $D_1(c,n,z) = \kappa_{z,n}^{(c)} z$ numbers vs. z and of the $G_1(c,n)$ numbers for $c = 1$ and $n = 1\ (1)\ 3$.
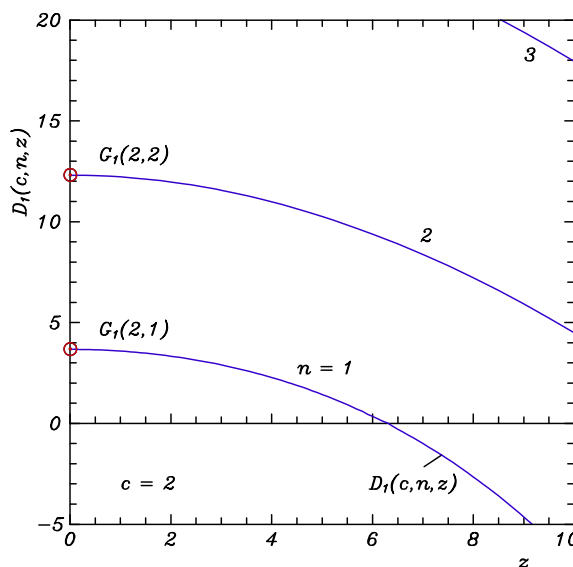
Figure 2: Graphical representation of the $D_1(c,n,z) = \kappa_{z,n}^{(c)} z$ numbers vs. z and of the $G_1(c,n)$ numbers for $c = 2$ and $n = 1, 2$.
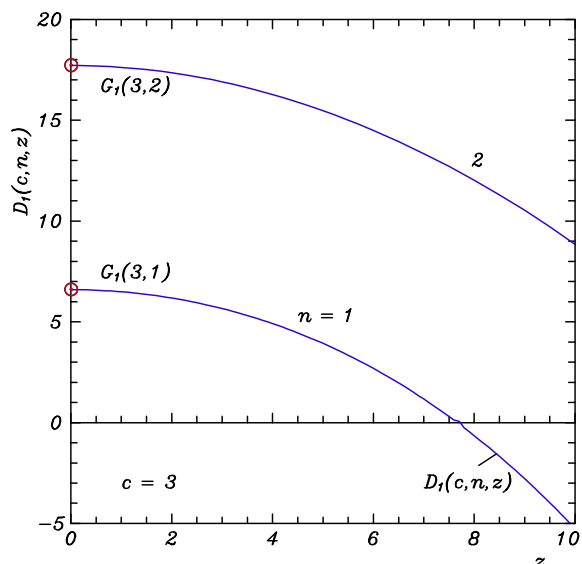
Figure 3: Graphical representation of the $D_1(c,n,z) = \kappa_{z,n}^{(c)} z$ numbers vs. z and of the $G_1(c,n)$ numbers for $c = 3$ and $n = 1\ (1)\ 3$.
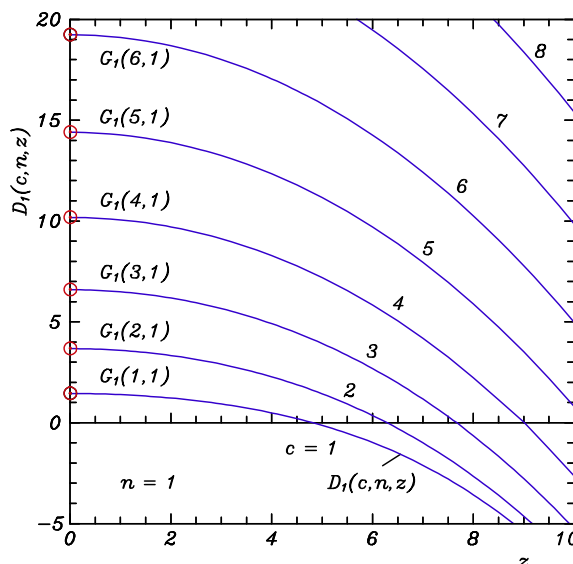
Figure 4: Graphical representation of the $D_1(c,n,z) = \kappa_{z,n}^{(c)} z$ numbers vs. z and of the $G_1(c,n)$ numbers for $c = 1\ (1)\ 8$ and $n = 1$.
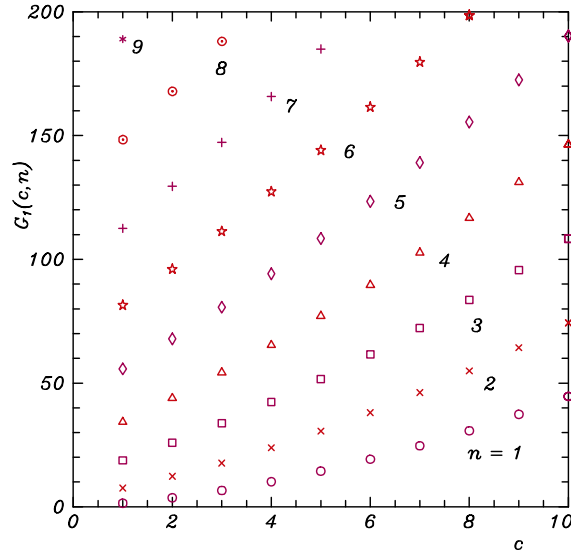
Figure 5: Dependence of the $G_1(c, n)$ numbers on $c = 1$ (2) 10 and $n = 1$ (1) 9.

is supported by the data in the first columns of Tables 1–4, presented here and in Tables 1(a), 1(b) and Figures 1–4 in Ref. [12]. The variation of $D_1(c, n, z)$ with z is demonstrated in Tables 1–4 and in Figures 1–4.

3. APPLICATION

3.1. Propagation Problem for Normal TE_{0n} Modes in the Azimuthally Magnetized Circular Ferrite Waveguide

The transmission of normal TE_{0n} modes of phase constant β in the circular waveguide of radius r_0, uniformly filled with azimuthally magnetized lossless remanent ferrite, described by a scalar permittivity $\varepsilon = \varepsilon_0 \varepsilon_r$ and a Polder permeability tensor of off-diagonal element $\alpha = \gamma M_r / \omega$, $0 < |\alpha| < 1$, (γ — gyromagnetic ratio, M_r — remanent magnetization, ω — angular frequency of the wave), is governed by the equation [2, 3]:

$$\Phi(a, c; x_0) = 0, \tag{2}$$

in which $a = c/2 - jk$, $c = 3$, $x_0 = jz_0$, $k = \alpha \bar{\beta}/(2\bar{\beta}_2)$, $z_0 = 2\bar{\beta}_2 \bar{r}_0$, $\bar{\beta} = \beta/(\beta_0 \sqrt{\varepsilon_r})$, $\bar{\beta}_2 = \beta_2/(\beta_0 \sqrt{\varepsilon_r})$, $\bar{r}_0 = \beta_0 r_0 \sqrt{\varepsilon_r}$, $\beta_0 = \omega \sqrt{\varepsilon_0 \mu_0}$, $\beta_2 = [\omega^2 \varepsilon_0 \mu_0 \varepsilon_r (1 - \alpha^2) - \beta^2]^{1/2}$ — radial wavenumber, i.e., $\bar{\beta}_2 = [(1 - \alpha^2) - \bar{\beta}^2]^{1/2}$, ($k$, z_0 — real, $-\infty < k < +\infty$, $z_0 > 0$).

3.2. Traditional Solution in Terms of the Zeros $\zeta_{k,n}^{(c)}$ of $\Phi(a, c; x)$ and the $L_1(c, n)$ Numbers

The approach for finding the phase portrait of the structure which historically first has been developed, uses the roots (zeros) $\zeta_{k,n}^{(c)}$ ($n = 1, 2, 3$) in z_0 of Eq. (2) (of the Kummer function) with the values of its parameters, given in Subsection 3.1 [2, 3, 5]. In particular, the eigenvalue spectrum is determined from the term [2, 3, 5]:

$$\bar{\beta}_2 = \zeta_{k,n}^{(c)} / (2\bar{r}_0) \tag{3}$$

and the $\bar{\beta}(\bar{r}_0)$ — phase characteristics are computed by means of the expressions [2, 3, 5]:

$$\bar{r}_0 = \left(k \zeta_{k,n}^{(c)} / \alpha\right) \left\{ \left[1 + (\alpha/(2k))^2\right] / \left(1 - \alpha^2\right) \right\}^{1/2}, \tag{4}$$

$$\bar{\beta} = \left\{ \left(1 - \alpha^2\right) / \left[1 + (\alpha/(2k))^2\right] \right\}^{1/2}, \tag{5}$$

in that α is a discrete and k — a varying parameter. For the purpose a special iterative technique has been elaborated [2, 5]. A peculiarity of the configuration considered is the appearance of cut-off for higher frequencies in case of negative (clockwise) ferrite magnetization in addition to the

conventional ones. They lie on a special En_{1-} — envelope line of equation $\bar{\beta}_{en-} = \bar{\beta}_{en-}(\bar{r}_{0en-})$, presented in parametric form as [2,5]:

$$\bar{r}_{0en-} = L_1(c,n) / \left[|\alpha_{en-}| \left(1 - \alpha_{en-}^2 \right)^{1/2} \right], \tag{6}$$

$$\bar{\beta}_{en-} = \left(1 - \alpha_{en-}^2 \right)^{1/2} \tag{7}$$

with α_{en-} is a parameter. (The subscript "$en-$" distinguishes the quantities, relevant to the envelope.)

3.3. New Solution in Terms of the Zeros $\kappa_{z,n}^{(c)}$ of $\Phi(a,c;x)$ and the $G_1(c,n)$ Numbers

Quite recently a novel line of attack to the task in question has been advanced, employing It is suggested to expresses the roots $\kappa_{z,n}^{(c)}$ ($n = 1,\ 2,\ 3$) in κ of Eq. (2) (of the Kummer function) in which its first parameter is rewritten in the form $a = c/2 + j\kappa$ ($\kappa = -k$) [12]. Accordingly, Formulae (3)–(5) are modified as follows [12]:

$$\bar{\beta}_2 = \left\{ \left(1 - \alpha^2 \right) / \left[1 + \left(2\kappa_{z,n}^{(c)}/\alpha \right)^2 \right] \right\}^{1/2}. \tag{8}$$

$$\bar{r}_0 = \left(\kappa_{z,n}^{(c)} z/\alpha \right) \left\{ \left[1 + \left(\alpha / \left(2\kappa_{z,n}^{(c)} \right) \right)^2 \right] / \left(1 - \alpha^2 \right) \right\}^{1/2}, \tag{9}$$

$$\bar{\beta} = \left\{ \left(1 - \alpha^2 \right) / \left[1 + \left(\alpha / \left(2\kappa_{z,n}^{(c)} \right) \right)^2 \right] \right\}^{1/2}, \tag{10}$$

where α is a discrete and z — a varying parameter.

Applying the statement of Theorem 1 for $z \to 0$ ($\kappa_{z,n}^{(c)} z \to G_1(c,n)$ and $\kappa_{z,n}^{(c)} \to +\infty$) a new representation of the En_{1-} — line is obtained:

$$\bar{r}_{0en-} = G_1(c,n) / \left[|\alpha_{en-}| \left(1 - \alpha_{en-}^2 \right)^{1/2} \right], \tag{11}$$

$$\bar{\beta}_{en-} = \left(1 - \alpha_{en-}^2 \right)^{1/2}. \tag{12}$$

4. CONCLUSION

The finite real positive numbers $G_1(c,n)$ are advanced for c — positive integer and n — bounded natural number as limits of special sequences of real numbers. The terms of the latter are devised as products of the zeros $\kappa_{z,n}^{(c)}$ of the complex Kummer function $\Phi(a,c;x)$ in the imaginary part κ of its complex first parameter $a = c/2 + j\kappa$ by the imaginary part z of its positive purely imaginary variable $x = jz$ ($n = 1, 2, 3, \ldots$ — numbers of the zeros). The limits in question are attained for infinitesimal z. This constitutes the essence of the formulated and numerically proved here Theorem for existence of $G_1(c,n)$ numbers being the core of the study. The usage of some of their representatives is also considered.

REFERENCES

1. Tricomi, F. G., *Funzioni Ipergeometriche Confluenti*, Edizioni Cremonese, Rome, Italy, 1954.
2. Georgiev, G. N. and M. N. Georgieva-Grosse, "A new property of the complex Kummer function and its application to waveguide propagation," *IEEE Antennas Wireless Propagation Lett.*, Vol. 2, 306–309, Dec. 2003.
3. Georgiev, G. N. and M. N. Georgieva-Grosse, "Iterative method for differential phase shift computation in the azimuthally magnetized circular ferrite waveguide," *PIERS Online*, Vol. 6, No. 4, 365–369, 2010.

4. Georgieva-Grosse, M. N. and G. N. Georgiev, "Numerical modeling of the area of phase shifter operation of the azimuthally magnetized circular ferrite waveguide," *Proc. 6th Europ. Conf. Antennas Propagat. EuCAP 2012*, Article ID P-23, 5 Pages, Prague, Czech Republic, Mar. 26–30, 2012.

5. Georgiev, G. N. and M. N. Georgieva-Grosse, "Advanced computational methods for analysis of the circular waveguide completely filled with azimuthally magnetized ferrite: Review of recent results," *Proc. Fourteenth Int. Conf. Electromagn. Adv. Applicat. ICEAA'12*, 62–65, Cape Town, South Africa, Sep. 2–7, 2012, (*Invited Paper* in the Special Session "Modern problems of mathematical and computational electromagnetics and their advanced applications," organized by M. N. Georgieva-Grosse and G. N. Georgiev).

6. Georgiev, G. N. and M. N. Georgieva-Grosse, "Theory of the circular waveguide completely filled with azimuthally magnetized ferrite: Review of recent results," (*Invited Paper*), *The Seventh Int. Conf. " Inverse problems: Modeling & Simulation"*, 67, Ölüdeniz, Fethiye, Turkey, May 26–31, 2014.

7. Georgiev, G. N. and M. N. Georgieva-Grosse, "Theory of the L numbers: Definition, computational modeling, properties and application," *Proc. Thirteenth Int. Conf. Electromagn. Adv. Applicat. ICEAA'11*, 544–547, Turin, Italy, Sep. 12–16, 2011, (*Invited Paper* in the Special Session "Future challenges in mathematical and computational electromagnetics and its applications," organized by G. N. Georgiev and M. N. Georgieva-Grosse).

8. Georgiev, G. N. and M. N. Georgieva-Grosse, "Theorem for the relation between the $L_1(c, n)$ and $L_2(c, \rho, n)$ numbers," *Proc. 2014 XXXI URSI GASS General Assembly and Scientific Symposium*, Vol. 2, 826–829, Beijing, China, Aug. 16–23, 2014.

9. Georgiev, G. N. and M. N. Georgieva-Grosse, "Theory of the L numbers and its application to electromagnetism," (*Invited Paper*), *Proc. 1st URSI Atlantic Radio Sci. Conf. URSI AT-RASC 2015*, Paper ID 1192(B20-4), Gran Canaria, Canary Islands, Spain, May 18–22, 2015.

10. Georgiev, G. N. and M. N. Georgieva-Grosse, "Theory of the $\tilde{L}_4$ numbers: Existence theorem and physical interpretation," *Proc. XXX URSI General Assembly*, Article ID DP1.7, 4 Pages, Istanbul, Turkey, Aug. 13–20, 2011.

11. Georgiev, G. N. and M. N. Georgieva-Grosse, "Hypothesis for the identity of the $L_2(c, \rho, n)$ and $\hat{L}_2(\hat{c}, \hat{\rho}, \hat{n})$ numbers and its application in the theory of waveguides," *Progress In Electromagnetics Research Symposium Abstracts*, 805–806, Stockholm, Sweden, Aug. 12–15, 2013; *PIERS Proceedings*, 940–945, Stockholm, Sweden, Aug. 12–15, 2013.

12. Georgieva-Grosse, M. N. and G. N. Georgiev, "Contribution to the theory of the complex Kummer function," *Proc. Sixteenth Int. Conf. Electromagn. Adv. Applicat. ICEAA'14*, 387–390, Palm Beach, Aruba, Aug. 3–8, 2014, (*Invited Paper* in the Special Session, Challenges in mathematical and computational electromagnetics and its applications," organized by G. N. Georgiev, and M. N. Georgieva-Grosse).

Inverse Spectral Theory and Kramers-Kronig Relations

G. F. Crosta

University of Milan Bicocca, Milan, Lombardy, Italy

Abstract— Inverse problems aimed at locating cracks and voids inside a dielectric medium by means of electromagnetic waves involve knowledge of transmission eigenvalues. The subject has been actively investigated by many Authors for some years and results have been presented in articles and books. Unfortunately, the frequency dependence of dielectric permittivity and magnetic permeability of the material has not been taken into account. A theorem which provides existence and asymptotic properties of real transmission eigenvalues is shown to be physically inconsistent, because it ignores the Kramers-Kronig relations.

1. INTRODUCTION

Inverse problems, which consist of determining voids or cracks inside a dielectric from knowledge of one or more incident plane waves and the corresponding (complex valued) scattered waves in the far zone, involve the so-called transmission eigenvalues. In a scalar setting, which makes sense if the dielectric body has size, shape and physical properties which are translation-invariant, e.g., along the x_3 axis and either the $\vec{E}$ or the $\vec{H}$ fields of the incident waves are polarised accordingly, then one can state the following.

Pbm. (*interior, scalar transmission eigenvalue problem.*) Let the dielectric medium be enclosed inside a right cylinder of axis x_3 and cross section D with sufficiently smooth boundary, ∂D, and be surrounded by empty space. Find a non trivial pair, $\{w_1, w_2\}$, of transmission eigenfunctions and the corresponding free space, real wavenumber, k, complying with

$$w_2 - w_1 \in H_0^2(D) \tag{1}$$

and

$$\left(\Delta + \chi^2\right) w_2 = 0 \text{ in } D, \quad \left(\Delta + k^2\right) w_1 = 0 \text{ in } D, \quad w_2 = w_1 \text{ and } \partial_n w_2 = \partial_n w_1 \text{ on } \partial D. \tag{2}$$

Here the complex valued function $\chi[\cdot]$ describes the electric and magnetic properties of the medium, as well as their spatial dependence. Knowledge of transmission eigenvalues is relevant to two classes of inverse problems. If the so-called sampling methods are applied to reconstruct the support of the scatterer [1], incident waves shall have frequencies which do not correspond to transmission eigenvalues. In particular, the latter shall at most form a countable set. More recently, transmission eigenvalues have been said to play a role in the reconstruction of the scatterer from far zone measurements [2–4].

2. TYPICAL EXISTENCE RESULT FOR TRANSMISSION EIGENVALUES

A result believed to play a key role in the spectral theory of interior transmission problems involving inhomogeneous, isotropic dielectric media [5] has been stated for a function $\chi[\cdot]$ which factorises according to

$$\chi^2 := k^2 n^2[\vec{x}], \tag{3}$$

where the refractive index, $n[\cdot]$, is real valued and depends at most on $\vec{x} \in D$. In particular [5, Thm. 2.5], if either

$$\inf_D n^2[\vec{x}] > 1 + \alpha, \ \forall \vec{x} \in D, \tag{4}$$

with some $\alpha > 0$, fixed, or

$$\sup_D n^2[\vec{x}] < 1 - \beta, \ \forall \vec{x} \in D, \tag{5}$$

with some $\beta > 0$, fixed, then there exists an infinite, countable set of real transmission eigenvalues with $+\infty$ as the only accumulation point.

The need to impose Ineqs. (4) or (5) arises, because the pair of Helmholtz equations (with obvious notation) $\{\mathcal{K}_2 w_2 = 0; \mathcal{K}_1 w_1 = 0\}$, appearing in the transmission problem of Eq. (2) is transformed into

$$-\left(\mathcal{K}_2 \left(\mathcal{K}_2 - \mathcal{K}_1\right)^{-1} \mathcal{K}_1\right) [w_2 - w_1] = 0 \text{ in } D. \tag{6}$$

The operator $(\mathcal{K}_2 - \mathcal{K}_1)^{-1}$ is no longer differential. Instead, it acts as multiplication by $(n^2[\vec{x}] - 1)^{-1}$, which stays bounded, provided in Eqs. (4) or (5) hold. In the variational form of Eq. (6) the term $(n^2[\vec{x}] - 1)^{-1}$ appears in an integral over D.

The boundedness of $|n^2[\vec{x}] - 1|$ away from zero $\forall \vec{x} \in D$ is a recurrent requirement in other articles which address transmission eigenvalue problems [6].

3. ASYMPTOTIC INCONSISTENCY OF THE THEORY

Claim (*physical inconsistency of the hypothesis under which existence of transmission eigenvalues is derived.*) The above results, which pertain to existence and asymptotic properties of transmission eigenvalues, have been derived under hypotheses which do not take the physical properties of materials into account. Moreover, if ω stands for the angular frequency of the incident wave, the determination of transmission eigenvalues is asymptotically ill-posed for $\omega \to \infty$.

Proof. The control variable is angular frequency, ω. Transmission eigenvalues relate to wavenumbers. In order to attain $k \to \infty$, the dispersion relation of empty space, $\omega = ck$, implies $\omega \to \infty$. Even if, in many applications, magnetic permeability, μ, of the medium can be regarded as independent of frequency and equal to the permeability of vacuum, μ_0, the ω-dependence of relative dielectric permittivity, ϵ_r, cannot be ignored. In fact, it <u>must</u> be taken into account if asymptotic properties are to be investigated. Let a model of the Lorentz class be chosen for the dependence of ε_r on ω [7, p. 284 ff.], and let the material medium in D be uniformly distributed, resulting in N_{mol} molecules per unit volume, each of them with Z electrons. If there are Z_j electrons per molecule with binding frequency ω_j and damping constant γ_j, $1 \le j \le J$, then

$$\varepsilon_r[\omega] = 1 + 4\pi \frac{e^2}{m} N_{\mathrm{mol}} \sum_{j=i}^{J} \frac{Z_j}{\omega_j^2 - \omega^2 - \mathrm{i}\omega\gamma_j}, \tag{7}$$

subject to

$$\sum_{j=i}^{J} Z_j = Z. \tag{8}$$

In the limit, $\omega \to \infty$, neither in Eq. (4) nor in Eq. (5) are met by the $\varepsilon_r[\omega]$ of Eq. (7), hence $\lim_{\omega \to \infty}(\mathcal{K}_2 - \mathcal{K}_1) = 0$ and the existence proof of Sect. II collapses.

Rem. The same conclusion would be attained if the Lorentz model of Eq. (7) were replaced by any other **causal** relation between the displacement, $\vec{D}$, and the electric, $\vec{E}$, fields, as formalised by Kramers and Kronig [8, 9; 7, §7.10].

Rem. Absorbing media with frequency dependent dielectric permittivity have been recently addressed [10]. The type of wavenumber-dependence introduced into $\varepsilon_r[\cdot]$ is however the result of a low frequency approximation and, as such, still affected by asymptotic inconsistency.

REFERENCES

1. Cakoni, F. and D. Colton, *Qualitative Methods in Inverse Scattering Theory*, Springer, Berlin, 2006.
2. Cakoni, F., D. Colton, and P. Monk, "On the use of transmission eigenvalues to estimate the index of refraction from far field data," *Inverse Problems*, Vol. 23, 507–522, 2007.
3. Cakoni, F., M. Cayoren, and D. Colton, "Transmission eigenvalues and the non destructive testing of dielectrics," *Inverse Problems*, Vol. 26, 065016, 2008.
4. Cakoni, F., D. Colton, and H. Haddar, "The computation of the lower bounds for the norm of the index of refraction in an anisotropic medium," *J. Integr. Equat. Appl.*, Vol. 21, 443–456, 2009.
5. Cakoni, F., D. Gintides, and H. Haddar, "The existence of an infinite set of transmission eigenvalues," *SIAM J. Mathem. Analysis*, Vol. 42, 237–255, 2010.

6. Cakoni, F., D. Colton, and H. Haddar, "On the determination of Dirichlet or transmission eigenvalues from far field data," *C. R. Acad. Sc. Paris — Ser. I*, Vol. 348, 379–383, 2010.

7. Jackson, J. D., *Classical Electrodynamics*, John Wiley & Sons, New York, NY, 1975.

8. Fourès, Y. and I. E. Segal, "Causality and analyticity," *Trans. Amer. Mathemat. Society*, Vol. 78, 385–405, 1955.

9. Toll, J. S., "Causality and the dispersion relation: Logical foundations," *Physical Review*, Vol. 104, 1760–1770, 1956.

10. Cakoni, F., D. Colton, and H. Haddar, "The interior transmission eigenvalue problem for absorbing media," *Inverse Problems*, Vol. 28, 045005, 2012.

Algebraic Regularization of Universal Functions in EM via Self-induced Hadamard Finite Parts

A. R. Baghai-Wadji

University of Cape Town, South Africa

Abstract— In boundary element method applications there are contradicting requirements which need to be accommodated skillfully in order to achieve high accuracy and high speed at the same time. Regarding acceleration of computations, it is desirable, besides parallelization and other conventional measures, to extract costly "universal" features from the computations which are common to a certain class of problems. If successful the resulting Universal Functions (UFs) can be pre-calculated and stored and referred to whenever necessary. As can be shown the introduction of UFs, however, requires additive factorization of terms, leading to high-order algebraic singularity in infrared region in spectral domain (zero and small values of the wavenumbers). Thereby, the algebraic order of the additional singularity depends on the degree of smoothness of the basis- and testing functions employed — the smoother the basis and testing functions the higher the order of singularity at the origin of the coordinate system in the spectral domain. On the other hand smooth basis- and weighting functions improve the convergence of the involved Fourier-type integrals algebraically in ultraviolet region (large values of the wavenumber in spectral domain). The main result in this contribution is the fact that all the aforementioned seemingly contradicting requirements can be reconciled naturally. The magic is done by recognizing that Hadamard Finite Parts appear in the introduced Universal Functions automatically, with one additional pleasant surprise: Ordinarily Hadamard Finite Parts technique, as the name implies, considers finite parts of infinite integrals, thus throwing away the infinities in the calculations. In the proposed procedure the infinities add up to zero exactly. Finally it should be pointed out that the Hadamard Finite Parts in the UFs are exclusively induced by the chosen basis- and testing functions, thus, justifying the using of the "self-induced" property in the title.

1. INTRODUCTION

In an accompanying paper a second renormalization technique has been proposed which ensures exponential decay of dyadic Green's functions in ultraviolet region in spectral domain. The exponential regularization has its genesis in the construction of problem-specific Dirac delta functions; it tempers the slowly-decaying divergent behavior of Green's functions. In contrast the algebraic regularization, proposed in this contribution, has its origin in the smoothness properties of the chosen basis- and weighting functions. Consequently, the next logical question is whether or not the two regularization techniques, exponential and algebraic, can be combined to even further enhance the quality of our computations. The answer is unconditionally affirmative. Thus the combined exponential- and algebraic regularization techniques promise ultra-precise calculations of the near-fields in EM simulations, while permitting the construction of Universal Functions. Furthermore, it is worth emphasizing that both regularization techniques apply to closed-form Green's functions as well Green's functions which can only be calculated numerically. The latter property is crucially important: it enables the simulation of nanoscale devices involving complex media.

2. PREPARATORY CONSIDERATIONS

Consider the following convolution type integral in spectral domain:

$$\varphi(x,y) = \int\limits_{-\infty}^{\infty} \int\limits_{-\infty}^{\infty} \frac{dk_1}{2\pi} \frac{dk_2}{2\pi} \bar{\varphi}(k_1,k_2) e^{jk_1x} e^{jk_2y} = \int\limits_{-\infty}^{\infty} \int\limits_{-\infty}^{\infty} \frac{dk_1}{2\pi} \frac{dk_2}{2\pi} \bar{G}(k_1,k_2)\bar{\rho}(k_1,k_2) e^{jk_1x} e^{jk_2y} \tag{1}$$

A bar indicates quantities in (k_1, k_2)-spectral domain. Furthermore, $\bar{G}(k_1, k_2)$ stands for a generic Green's function. It has been assumed that $G(x,y)$ is translationally invariant; i.e., G $(x\text{-}x', y\text{-}y')$, where (x, y) and (x', y'), respectively, refer to the observation- and source point. In addition we shall assume the following source distribution with *a priori* unknown coefficients ρ_n:

$$\rho(x,y) = \sum_{n=1}^{N} \rho_n b_n(x,y) \quad \text{with} \quad b_n(x,y) = \begin{cases} 1 & x_n^b < x < x_n^e \text{ and } y_n^b < y < y_n^e \\ 0 & \text{elsewhere} \end{cases} \tag{2}$$

The Fourier transform of $\rho(x, y)$ denoted by $\bar{\rho}(k_1, k_2)$ is:

$$\bar{\rho}(k_1, k_2) = \sum_{n=1}^{N} \rho_n \underbrace{\frac{e^{-jk_1 x_n^e} - e^{-jk_1 x_n^b}}{-jk_1}}_{2\triangle x_n \text{ for } k_1 \to 0} \underbrace{\frac{e^{-jk_2 y_n^e} - e^{-jk_2 y_n^b}}{-jk_2}}_{2\triangle y_n \text{ for } k_2 \to 0} \tag{3}$$

where $2\triangle x_n (= x_n^e - x_n^b)$ and $2\triangle y_n (= y_n^e - y_n^b)$, respectively, denote linear dimensions in the x- and y-direction of the nth sub-square. Denoting the integral of the source on the nth sub-square by Q_n we have $Q_n = \rho_n (2\triangle x_n)(2\triangle y_n)$. Using Q_n and rearranging (3) reads:

$$\bar{\rho}(k_1, k_2) = \sum_{n=1}^{N} \frac{Q_n}{-4\triangle x_n \triangle y_n k_1 k_2} \left(e^{-jk_1 x_n^e} - e^{-jk_1 x_n^b} \right) \left(e^{-jk_2 y_n^e} - e^{-jk_2 y_n^b} \right) \tag{4}$$

Testing $\varphi(x, y)$ by the weighting functions $b_m(x, y)$, $m = 1, \ldots, M$, and denoting the average of $\varphi(x, y)$ on the mth sub-sqaure by φ_m we have:

$$\varphi_m = \frac{1}{(x_m^e - x_m^b)(y_m^e - y_m^b)} \int_{x_m^b}^{x_m^e} \int_{y_m^b}^{y_m^e} dx dy \varphi(x, y) \tag{5}$$

Substituting the far-most term in (1) into (5) and rearranging the order of integrals we obtain

$$\varphi_m = \int_{-\infty}^{\infty} \int_{-\infty}^{\infty} \frac{dk_1}{2\pi} \frac{dk_2}{2\pi} \bar{G}(k_1, k_2) \bar{\rho}(k_1, k_2) \underbrace{\frac{1}{4\triangle x_m \triangle y_m} \int_{x_m^b}^{x_m^e} dx e^{jk_1 x} \int_{y_m^b}^{y_m^e} dy e^{jk_2 y}}_{\bar{w}_m(k_1, k_2)} \tag{6}$$

where we have introduced $\bar{w}_m(k_1, k_2)$ with

$$\bar{w}_m(k_1, k_2) = \frac{1}{4\triangle x_m \triangle y_m} \underbrace{\frac{e^{jk_1 x_m^e} - e^{jk_1 x_n^b}}{jk_1}}_{2\triangle x_m \text{ for } k_1 \to 0} \underbrace{\frac{e^{jk_2 y_m^e} - e^{jk_1 y_n^b}}{jk_2}}_{2\triangle y_m \text{ for } k_2 \to 0} \tag{7}$$

and $\lim_{(k_1, k_2) \to (0,0)} \bar{w}_m(k_1, k_2) = 1$. In the following we shall use the form:

$$\bar{w}_m(k_1, k_2) = \frac{1}{-4\triangle x_m \triangle y_m k_1 k_2} \left[e^{jk_1 x_m^e} - e^{jk_1 x_n^b} \right] \left[e^{jk_2 y_m^e} - e^{jk_1 y_n^b} \right]; \quad (m = 1, \ldots, M) \tag{8}$$

Considering (6) and introducing $\bar{R}_m(k_1, k_2)$ we have:

$$\varphi_m = \int_{\infty}^{\infty} \int_{-\infty}^{\infty} \frac{dk_1}{2\pi} \frac{dk_2}{2\pi} \bar{G}(k_1, k_2) \underbrace{\bar{w}_m(k_1, k_2) \bar{\rho}(k_1, k_2)}_{\bar{R}_m(k_1, k_2)}; \quad (m = 1, \ldots, M) \tag{9}$$

The solvability condition requires $M = N$: choosing the same number of basis- and testing functions. Furthermore, note that the following properties are valid, as established above:

$$\lim_{(k_1, k_2) \to (0,0)} \bar{\rho}(k_1, k_2) = \sum_{n=1}^{N} Q_n, \quad \text{and} \quad \lim_{(k_1, k_2) \to (0,0)} \bar{w}_m(k_1, k_2) = 1 \tag{10}$$

3. AUTOMATIC EMERGENCE OF HADAMARD FINITE PARTS

Consider $\bar{R}_m(k_1, k_2)$ as introduced in (9). It is evident that $\bar{R}_m(k_1, k_2)$ only depends on the selected basis- and testing functions, implying that the Green's function plays no role in the structure of $\bar{R}_m(k_1, k_2)$. On the other hand $\bar{R}_m(k_1, k_2)$ shall play a significant role in the algebraic regularization of the field integrals, to any degree desirable. Furthermore, $\bar{R}_m(k_1, k_2)$ will automatically

give rise to the emergence of Hadamard Finite Parts ([1, Ref. 3]). In order to establish these results we substitute for $\bar{\rho}(k_1, k_2)$ and $\bar{w}_m(k_1, k_2)$, respectively, from (4) and (8), and rearrange to obtain:

$$
\bar{R}_m(k_1, k_2) = \sum_{n=1}^{N} Q_n \frac{1}{16 \triangle x_m \triangle y_m \triangle x_n \triangle y_n k_1^2 k_2^2}
$$
$$
\times \left[e^{j(k_1 x_m^e + k_2 y_m^e)} - e^{j(k_1 x_m^e + k_2 y_m^b)} - e^{j(k_1 x_m^b + k_2 y_m^e)} + e^{j(k_1 x_m^b + k_2 y_m^b)} \right]
$$
$$
\times \left[e^{-j(k_1 x_n^e + k_2 y_n^e)} - e^{-j(k_1 x_n^e + k_2 y_n^b)} - e^{-j(k_1 x_n^b + k_2 y_n^e)} + e^{-j(k_1 x_n^b + k_2 y_n^b)} \right] \quad (11)
$$

Lemma 1 The following relationship holds true:

$$
\bar{\mathcal{R}}_m(k_1, k_2) = \sum_{n=1}^{N} Q_n \frac{1}{16 \triangle x_m \triangle y_m \triangle x_n \triangle y_n k_1^2 k_2^2}
$$
$$
\times \Big[+ \left\{ 1 + [j(k_1 x_m^e + k_2 y_m^e)] + \frac{1}{2}[j(k_1 x_m^e + k_2 y_m^e)]^2 \right\}
$$
$$
- \left\{ 1 + [j(k_1 x_m^e + k_2 y_m^b)] + \frac{1}{2}[j(k_1 x_m^e + k_2 y_m^b)]^2 \right\}
$$
$$
- \left\{ 1 + [j(k_1 x_m^b + k_2 y_m^e)] + \frac{1}{2}[j(k_1 x_m^b + k_2 y_m^e)]^2 \right\}
$$
$$
+ \left\{ 1 + [j(k_1 x_m^b + k_2 y_m^b)] + \frac{1}{2}[j(k_1 x_m^b + k_2 y_m^b)]^2 \right\} \Big]
$$
$$
\times \Big[+ \left\{ 1 + [-j(k_1 x_n^e + k_2 y_n^e)] + \frac{1}{2}[-j(k_1 x_n^e + k_2 y_n^e)]^2 \right\}
$$
$$
- \left\{ 1 + [-j(k_1 x_n^e + k_2 y_n^b)] + \frac{1}{2}[-j(k_1 x_n^e + k_2 y_n^b)]^2 \right\}
$$
$$
- \left\{ 1 + [-j(k_1 x_n^b + k_2 y_n^e)] + \frac{1}{2}[-j(k_1 x_n^b + k_2 y_n^e)]^2 \right\}
$$
$$
+ \left\{ 1 + [-j(k_1 x_n^b + k_2 y_n^b)] + \frac{1}{2}[-j(k_1 x_n^b + k_2 y_n^b)]^2 \right\} \Big] = \sum_{n=1}^{N} Q_n \quad (12)
$$

Proof: A comparison between (11) and (12) reveals that the expression for $\bar{\mathcal{R}}_m(k_1, k_2)$ has been derived $\bar{R}_m(k_1, k_2)$ by replacing the exponential functions with their corresponding Taylor series expansions, and retaining the first three dominant terms only. Thus, we can expect that properties of $\bar{\mathcal{R}}_m(k_1, k_2)$ reveals the properties of $\bar{R}_m(k_1, k_2)$ in the limit $(k_1, k_2) \to (0, 0)$. The first pair of square brackets involve m-dependent x- and y coordinates of the mth testing function, while the second pair of square brackets involve n-dependent x- and y coordinates of the nth basis function. Focusing on the first m-dependent square brackets it is easily seen that the four ones cancel out. Furthermore, the four first-order terms taken collectively vanish. However, the quadratic terms result in $-k_1 k_2 (2\triangle x_m)(2\triangle y_m)$: *The quadratic terms do not cancel out.* Considering the second n-dependent square brackets analogous statements can be made *mutatis mutandis*: in particular the fact that quadratic terms sum up to $-k_1 k_2 (2\triangle x_n)(2\triangle y_n)$. Thus, multiplying the two square brackets gives $16 \triangle x_m \triangle y_m \triangle x_n \triangle y_n k_1^2 k_2^2$ which exactly equals the denominator of the fraction standing after Q_n in the first line of (12); the latter fact establishes the proof.

Note that for systems with certain structural symmetry we may have $\sum_{n=1}^{N} Q_n = 0$; thus leading to $\bar{R}_m(k_1, k_2) = 0$. The above result suggests the following Lemma.

Lemma 2: The expression at the right-hand side of (11) is equivalent to the expression at the right-hand side of (13) given below, for arbitrary finite value of the constant α. (The cases $\alpha = 0, 1$ will be of particular interest for the purposes in this paper.)

$$
\bar{R}_m(k_1, k_2) = \sum_{n=1}^{N} Q_n \frac{1}{16 \triangle x_m \triangle y_m \triangle x_n \triangle y_n k_1^2 k_2^2}
$$

$$\times \left\{ +\exp\left\{ j\left[k_1(x_m^e - x_n^e) + k_2(y_m^e - y_n^e) \right] \right\} - \alpha \sum_{l=0}^{3} \frac{1}{l!} \left(j\left[k_1(x_m^e - x_n^e) + k_2(y_m^e - y_n^e) \right] \right)^l \right.$$

$$-\exp\left\{ j\left[k_1(x_m^e - x_n^e) + k_2\left(y_m^e - y_n^b \right) \right] \right\} + \alpha \sum_{l=0}^{3} \frac{1}{l!} \left(j\left[k_1(x_m^e - x_n^e) + k_2\left(y_m^e - y_n^b \right) \right] \right)^l$$

$$-\exp\left\{ j\left[k_1\left(x_m^e - x_n^b \right) + k_2(y_m^e - y_n^e) \right] \right\} + \alpha \sum_{l=0}^{3} \frac{1}{l!} \left(j\left[k_1\left(x_m^e - x_n^b \right) + k_2(y_m^e - y_n^e) \right] \right)^l$$

$$+\exp\left\{ j\left[k_1\left(x_m^e - x_n^b \right) + k_2\left(y_m^e - y_n^b \right) \right] \right\} - \alpha \sum_{l=0}^{3} \frac{1}{l!} \left(j\left[k_1\left(x_m^e - x_n^b \right) + k_2\left(y_m^e - y_n^b \right) \right] \right)^l$$

$$-\exp\left\{ j\left[k_1(x_m^e - x_n^e) + k_2\left(y_m^b - y_n^e \right) \right] \right\} + \alpha \sum_{l=0}^{3} \frac{1}{l!} \left(j\left[k_1(x_m^e - x_n^e) + k_2\left(y_m^b - y_n^e \right) \right] \right)^l$$

$$+\exp\left\{ j\left[k_1(x_m^e - x_n^e) + k_2\left(y_m^b - y_n^b \right) \right] \right\} - \alpha \sum_{l=0}^{3} \frac{1}{l!} \left(j\left[k_1(x_m^e - x_n^e) + k_2\left(y_m^b - y_n^b \right) \right] \right)^l$$

$$+\exp\left\{ j\left[k_1\left(x_m^e - x_n^b \right) + k_2\left(y_m^b - y_n^e \right) \right] \right\} - \alpha \sum_{l=0}^{3} \frac{1}{l!} \left(j\left[k_1\left(x_m^e - x_n^b \right) + k_2\left(y_m^b - y_n^e \right) \right] \right)^l$$

$$-\exp\left\{ j\left[k_1\left(x_m^e - x_n^b \right) + k_2\left(y_m^b - y_n^b \right) \right] \right\} + \alpha \sum_{l=0}^{3} \frac{1}{l!} \left(j\left[k_1\left(x_m^e - x_n^b \right) + k_2\left(y_m^b - y_n^b \right) \right] \right)^l$$

$$-\exp\left\{ j\left[k_1\left(x_m^b - x_n^e \right) + k_2(y_m^e - y_n^e) \right] \right\} + \alpha \sum_{l=0}^{3} \frac{1}{l!} \left(j\left[k_1\left(x_m^b - x_n^e \right) + k_2(y_m^e - y_n^e) \right] \right)^l$$

$$+\exp\left\{ j\left[k_1\left(x_m^b - x_n^e \right) + k_2\left(y_m^e - y_n^b \right) \right] \right\} - \alpha \sum_{l=0}^{3} \frac{1}{l!} \left\{ j\left[k_1\left(x_m^b - x_n^e \right) + k_2\left(y_m^e - y_n^b \right) \right] \right\}^l$$

$$+\exp\left\{ j\left[k_1\left(x_m^b - x_n^b \right) + k_2(y_m^e - y_n^e) \right] \right\} - \alpha \sum_{l=0}^{3} \frac{1}{l!} \left\{ j\left[k_1\left(x_m^b - x_n^b \right) + k_2(y_m^e - y_n^e) \right] \right\}^l$$

$$-\exp\left\{ j\left[k_1\left(x_m^b - x_n^b \right) + k_2\left(y_m^e - y_n^b \right) \right] \right\} + \alpha \sum_{l=0}^{3} \frac{1}{l!} \left\{ j\left[k_1\left(x_m^b - x_n^b \right) + k_2\left(y_m^e - y_n^b \right) \right] \right\}^l$$

$$+\exp\left\{ j\left[k_1\left(x_m^b - x_n^e \right) + k_2\left(y_m^b - y_n^e \right) \right] \right\} - \alpha \sum_{l=0}^{3} \frac{1}{l!} \left(j\left[k_1\left(x_m^b - x_n^e \right) + k_2\left(y_m^b - y_n^e \right) \right] \right)^l$$

$$-\exp\left\{ j\left[k_1\left(x_m^b - x_n^e \right) + k_2\left(y_m^b - y_n^b \right) \right] \right\} + \alpha \sum_{l=0}^{3} \frac{1}{l!} \left(j\left[k_1\left(x_m^b - x_n^e \right) + k_2\left(y_m^b - y_n^b \right) \right] \right)^l$$

$$-\exp\left\{ j\left[k_1\left(x_m^b - x_n^b \right) + k_2\left(y_m^b - y_n^e \right) \right] \right\} + \alpha \sum_{l=0}^{3} \frac{1}{l!} \left(j\left[k_1\left(x_m^b - x_n^b \right) + k_2\left(y_m^b - y_n^e \right) \right] \right)^l$$

$$\left. +\exp\left\{ j\left[k_1\left(x_m^b - x_n^b \right) + k_2\left(y_m^b - y_n^b \right) \right] \right\} - \alpha \sum_{l=0}^{3} \frac{1}{l!} \left(j\left[k_1\left(x_m^b - x_n^b \right) + k_2\left(y_m^b - y_n^b \right) \right] \right)^l \right\} \qquad (13)$$

Proof: It is advantageous to introduce the following abbreviations: $x_{mn}^{ee} = x_m^e - x_n^e$, $x_{mn}^{eb} = x_m^e - x_n^b$, $x_{mn}^{be} = x_m^b - x_n^e$, and $x_{mn}^{bb} = x_m^b - x_n^b$. Similarly, introduce $y_{mn}^{ee} = y_m^e - y_n^e$, $y_{mn}^{eb} = y_m^e - y_n^b$, $y_{mn}^{be} = y_m^b - y_n^e$, and $y_{mn}^{bb} = y_m^b - y_n^b$. Next consider $\bar{\mathcal{R}}_m^{(3)}(k_1, k_2)$ involving the first three Taylor series expansion terms of the exponential functions in (13). Show that $\bar{\mathcal{R}}_m^{(3)}(k_1, k_2) = 0$.

$$\bar{\mathcal{R}}_m^{(3)}(k_1, k_2) = \sum_{n=1}^{N} Q_n \frac{1}{16 \triangle x_m \triangle y_m \triangle x_n \triangle y_n k_1^2 k_2^2}$$

$$\times \Bigg(+ \left\{ 1 + j\left[k_1 x_{mn}^{ee} + k_2 y_{mn}^{ee}\right] - \frac{1}{2}\left[k_1 x_{mn}^{ee} + k_2 y_{mn}^{ee}\right]^2 - \frac{j}{6}\left[k_1 x_{mn}^{ee} + k_2 y_{mn}^{ee}\right]^3 \right\}$$

$$- \left\{ 1 + j\left[k_1 x_{mn}^{ee} + k_2 y_{mn}^{eb}\right] - \frac{1}{2}\left[k_1 x_{mn}^{ee} + k_2 y_{mn}^{eb}\right]^2 - \frac{j}{6}\left[k_1 x_{mn}^{ee} + k_2 y_{mn}^{eb}\right]^3 \right\}$$

$$- \left\{ 1 + j\left[k_1 x_{mn}^{eb} + k_2 y_{mn}^{ee}\right] - \frac{1}{2}\left[k_1 x_{mn}^{eb} + k_2 y_{mn}^{ee}\right]^2 - \frac{j}{6}\left[k_1 x_{mn}^{eb} + k_2 y_{mn}^{ee}\right]^3 \right\}$$

$$+ \left\{ 1 + j\left[k_1 x_{mn}^{eb} + k_2 y_{mn}^{eb}\right] - \frac{1}{2}\left[k_1 x_{mn}^{eb} + k_2 y_{mn}^{eb}\right]^2 - \frac{j}{6}\left[k_1 x_{mn}^{eb} + k_2 y_{mn}^{eb}\right]^3 \right\}$$

$$- \left\{ 1 + j\left[k_1 x_{mn}^{ee} + k_2 y_{mn}^{be}\right] - \frac{1}{2}\left[k_1 x_{mn}^{ee} + k_2 y_{mn}^{be}\right]^2 - \frac{j}{6}\left[k_1 x_{mn}^{ee} + k_2 y_{mn}^{be}\right]^3 \right\}$$

$$+ \left\{ 1 + j\left[k_1 x_{mn}^{ee} + k_2 y_{mn}^{bb}\right] - \frac{1}{2}\left[k_1 x_{mn}^{ee} + k_2 y_{mn}^{bb}\right]^2 - \frac{j}{6}\left[k_1 x_{mn}^{ee} + k_2 y_{mn}^{bb}\right]^3 \right\}$$

$$+ \left\{ 1 + j\left[k_1 x_{mn}^{eb} + k_2 y_{mn}^{be}\right] - \frac{1}{2}\left[k_1 x_{mn}^{eb} + k_2 y_{mn}^{be}\right]^2 - \frac{j}{6}\left[k_1 x_{mn}^{eb} + k_2 y_{mn}^{be}\right]^4 \right\}$$

$$- \left\{ 1 + j\left[k_1 x_{mn}^{eb} + k_2 y_{mn}^{bb}\right] - \frac{1}{2}\left[k_1 x_{mn}^{eb} + k_2 y_{mn}^{bb}\right]^2 - \frac{j}{6}\left[k_1 x_{mn}^{eb} + k_2 y_{mn}^{bb}\right]^3 \right\}$$

$$- \left\{ 1 + j\left[k_1 x_{mn}^{be} + k_2 y_{mn}^{ee}\right] - \frac{1}{2}\left[k_1 x_{mn}^{be} + k_2 y_{mn}^{ee}\right]^2 - \frac{j}{6}\left[k_1 x_{mn}^{be} + k_2 y_{mn}^{ee}\right]^3 \right\}$$

$$+ \left\{ 1 + j\left[k_1 x_{mn}^{be} + k_2 y_{mn}^{eb}\right] - \frac{1}{2}\left[k_1 x_{mn}^{be} + k_2 y_{mn}^{eb}\right]^2 - \frac{j}{6}\left[k_1 x_{mn}^{be} + k_2 y_{mn}^{eb}\right]^3 \right\}$$

$$+ \left\{ 1 + j\left[k_1 x_{mn}^{bb} + k_2 y_{mn}^{ee}\right] - \frac{1}{2}\left[k_1 x_{mn}^{bb} + k_2 y_{mn}^{ee}\right]^2 - \frac{j}{6}\left[k_1 x_{mn}^{bb} + k_2 y_{mn}^{ee}\right]^3 \right\}$$

$$- \left\{ 1 + j\left[k_1 x_{mn}^{bb} + k_2 y_{mn}^{eb}\right] - \frac{1}{2}\left[k_1 x_{mn}^{bb} + k_2 y_{mn}^{eb}\right]^2 - \frac{j}{6}\left[k_1 x_{mn}^{bb} + k_2 y_{mn}^{eb}\right]^3 \right\}$$

$$+ \left\{ 1 + j\left[k_1 x_{mn}^{be} + k_2 y_{mn}^{be}\right] - \frac{1}{2}\left[k_1 x_{mn}^{be} + k_2 y_{mn}^{be}\right]^2 - \frac{j}{6}\left[k_1 x_{mn}^{be} + k_2 y_{mn}^{be}\right]^3 \right\}$$

$$- \left\{ 1 + j\left[k_1 x_{mn}^{be} + k_2 y_{mn}^{bb}\right] - \frac{1}{2}\left[k_1 x_{mn}^{be} + k_2 y_{mn}^{bb}\right]^2 - \frac{j}{6}\left[k_1 x_{mn}^{be} + k_2 y_{mn}^{bb}\right]^3 \right\}$$

$$- \left\{ 1 + j\left[k_1 x_{mn}^{bb} + k_2 y_{mn}^{be}\right] - \frac{1}{2}\left[k_1 x_{mn}^{bb} + k_2 y_{mn}^{be}\right]^2 - \frac{j}{6}\left[k_1 x_{mn}^{bb} + k_2 y_{mn}^{be}\right]^3 \right\}$$

$$+ \left\{ 1 + j\left[k_1 x_{mn}^{bb} + k_2 y_{mn}^{bb}\right] - \frac{1}{2}\left[k_1 x_{mn}^{bb} + k_2 y_{mn}^{bb}\right]^2 - \frac{j}{6}\left[k_1 x_{mn}^{bb} + k_2 y_{mn}^{bb}\right]^3 \right\} \Bigg) = 0 \qquad (14)$$

In the 1st "column" the ± 1 terms cancel out pair-wisely. In the 2nd "column" the linear terms of the generic form $\pm j[k_1 x_{mn}^{rs} + k_2 y_{mn}^{pq}]$ add up to zero. In the 3rd "column" the quadratic terms cancel out collectively. In the 4th "column" the cubic terms add up to zero, completing the proof.

Had we included the quartic terms as well, they would have resulted in $\bar{\mathcal{R}}_m^{(4)}(k_1, k_2) = \sum_{n=1}^{N} Q_n$. Thus for systems with certain structural symmetry where $\sum_{n=1}^{N} Q_n = 0$, even the 4th order terms would have canceled out. There is however, a fundamental difference between the terms up to and including the 3rd order terms, and terms higher than 3rd order: the columns corresponding to the 0th, 1st, 2nd, and 3rd order terms add up to zero column-wise and without involving any constraints upon the value of $\sum_{n=1}^{N} Q_n$, a fact which is not true for higher order terms. This distinction is the guiding principle for determining the number of terms in Taylor series expansions in Lemma 2.

Next consider the first "row" in (13). Adopt polar coordinates ($\bar{G}(k_1, k_2) = \bar{\mathcal{G}}(k, \theta)$) and subdivide the range of k into two sections $[0, k_c]$ and $[k_c, \infty)$. Here, k_c maybe any conveniently chosen or "critical" wavenumber. Furthermore, choose $\alpha = 1$ when k varies in infrared region $[0, k_c]$ and $\alpha = 0$ when k varies in ultraviolet domain $[k_c, \infty)$ leading to the following "Universal Function."

4. UNIVERSAL FUNCTIONS

Inspired by the aforementioned properties and Lemma 2 we define the geometry-independent "Universal Function," which can be pre-computed and stored for future numerical calculation:

$$U(X, Y) = \int\limits_{0}^{2\pi} d\theta \frac{1}{\sin^2\theta \cos^2\theta} \left\{ \int\limits_{0}^{k_c} dk\, k\, \bar{\mathcal{G}}(k, \theta) \frac{1}{k^4} \left(e^{jk(\sin\theta X + \cos Y)} - \sum_{l=0}^{3} \frac{1}{l!}\left[jk(\sin\theta X + \cos Y)\right]^l \right) \right.$$

$$+ \int\limits_{k_c}^{\infty} dk \, k \bar{\mathcal{G}}(k, \theta) \frac{1}{k^4} e^{jk(\sin\theta X + \cos\theta Y)} \Bigg\} \tag{15}$$

The $\int_0^{k_c} dk$-integral in (15) resembles Hadamard Finite Part ([1, Ref. 3]). Note that for $k \ll 1$ the first dominant term in this integral is $o(k^4)$, which cancels the $1/k^4$-term perfectly. An important question is how to proceed if $\bar{\mathcal{G}}(k, \theta) \propto 1/|k|$ for $k \ll 1$. Then the total source in the universe must add up to zero ($\sum_{n=1}^{N} Q_n = 0$) (regularizing condition in the infrared region). In such a case we can include in (15) the 4th-order terms as well by letting l run from 0 to 4. On the other hand, note that the $\int_{k_c}^{\infty} dk$-integral in (15) decays sufficiently strongly for $k \to \infty$, thus ensuring convergence of the integral. Consequently, $U(X, Y)$ is regular in the infrared- as well as ultraviolet regions. In electrodynamics certain dyadic Green's functions are proportional to k for $k \to \infty$, implying that $k \bar{\mathcal{G}}(k, \theta)/k^4$ behaves according to $1/k^2$. Considering the $\int_{k_c}^{\infty} dk$-integral it can be concluded that the integrability in ultraviolet region is safely guaranteed even in such cases.

Upon construction it is immediate that the interaction elements in the Method of Moments applications, A_{mn}, can be written in terms of the Universal Function $U(X, Y)$ as follows:

$$\begin{aligned}
A_{mn} = \frac{1}{64\pi^2 \triangle x_m \triangle y_m \triangle x_n \triangle y_n} \Big\{ & +U\left(x_{mn}^{ee}, y_{mn}^{ee}\right) - U\left(x_{mn}^{ee}, y_{mn}^{eb}\right) - U\left(x_{mn}^{eb}, y_{mn}^{ee}\right) + U\left(x_{mn}^{eb}, y_{mn}^{eb}\right) \\
& -U\left(x_{mn}^{ee}, y_{mn}^{be}\right) + U\left(x_{mn}^{ee}, y_{mn}^{bb}\right) + U\left(x_{mn}^{eb}, y_{mn}^{be}\right) - U\left(x_{mn}^{eb}, y_{mn}^{bb}\right) \\
& -U\left(x_{mn}^{be}, y_{mn}^{ee}\right) + U\left(x_{mn}^{be}, y_{mn}^{eb}\right) + U\left(x_{mn}^{bb}, y_{mn}^{ee}\right) - U\left(x_{mn}^{bb}, y_{mn}^{eb}\right) \\
& +U\left(x_{mn}^{be}, y_{mn}^{be}\right) - U\left(x_{mn}^{be}, y_{mn}^{bb}\right) - U\left(x_{mn}^{bb}, y_{mn}^{be}\right) + U\left(x_{mn}^{bb}, y_{mn}^{bb}\right) \Big\}
\end{aligned} \tag{16}$$

It is worth noting that replacing $e^{jk(\sin\theta X + \cos\theta Y)}$ with $e^{jk(\sin\theta X + \cos\theta)Y} - 1$ in the $\int_{k_c}^{\infty} dk$-integral, (15), does not alter the value of A_{mn}. Therefore, denoting the corresponding Universal Function by $V(X, Y)$, it can been shown that $V(0, 0) = 0$, a result which is of theoretical and computational significance. For completeness it should be mentioned that MoM leads to $\sum_{n=1}^{N} A_{mn} Q_n = \varphi_m$.

5. CONCLUSION

A method has been proposed for algebraic regularization of slowly-decaying Fourier-type integrals arising in computational electromagnetics, when employing the Method of Moments (MoMs). It is shown that Hadamard Finite Part regularization scheme arises in the formulation automatically. The concept of Universal Functions for the calculation of the system matrix (self-action and mutual interaction) elements in MoMs applications, introduced previously, has been refined fundamentally. The results widen the scope of formulations proposed in [1] and the works cited therein significantly. The main result in this paper is that the proposed method does not impose any symmetry constraints on the dyadic Green's functions involved. A second important result is that the formalism permits o- and O-calculations by design; a property of theoretical and computational importance.

ACKNOWLEDGMENT

REFERENCES

1. Baghai-Wadji, A. R., "3D electrostatic charge distribution on finitely-thick bus-bars in micro-acoustic devices: Combined regularization in the near- and far-field," *IEEE Transactions on Ultrasonics, Ferroelectrics, and Frequency Control*, Special Issue, 2015.

On the Accuracy of Method of Moments for Solution of Full 3D Vectorial Electromagnetic Forward Scattering Problem

O. Güren[1], M. N. Akıncı[2], and M. Çayören[2]

[1]Electromagnetic Research Lab., Istanbul Technical University, Turkey
[2]Department of Electronics and Communication Engineering, Istanbul Technical University, Turkey

Abstract— In this communication, an analysis on the accuracy of the method of moments solution of full 3D vectorial electromagnetic forward scattering problem is presented. Although different mathematical techniques are developed for determination of the error rate of method of moments [1–6], this paper presents a numerical approach to this problem. In contrast to weak formulations of method of moments as in [7], we use a dyadic Green function based approach. We adopted the pulse functions as basis functions and obtained equations are weighted by the dirac-delta functions. In fact such a choice obliges us to calculate the hypersingular integrals of the components of the well known dyadic Green function. We utilize from [8] for the Cauchy principal value of these singular integrals. To be able to decrease memory requirement and computational complexity, bi-conjugate gradient method is applied togather with the fast fourier transform (FFT) algorithm for the matrix multiplication. An accuracy analysis is made by comparing the simulated fields with the analytical expressions of the scattering field from a dielectric sphere. The results show that such an dyadic Green function based implementation of the method of moments works sufficiently well for a wide range of various parameters.

1. INTRODUCTION

Microwave technologies has become an important ingredient of today's science. Researches regarding microwaves can range from inverse problems [9–14] to different applications in electronics [15, 16]. Although each of these areas require different approaches, their common point is perhaps that: all of them depends on solving Maxwell equations.

Figure 1: Error defined in (1) for (a) $0.50\,\mathrm{GHz}$, (b) $0.75\,\mathrm{GHz}$, (c) $1.00\,\mathrm{GHz}$, (d) $1.25\,\mathrm{GHz}$, (e) $1.50\,\mathrm{GHz}$ when the field is measured on the cylinder having radius of $R = 7\,\mathrm{cm}$. (ϵ_r stands for the dielectric permittivity of the corresponding medium.).

One of the effective forward electromagnetic solution technique is the Method of Moments (MoM) [7, 17, 18]. The accuracy rate of MoM procedure is a significant issue, since this method is extensively used in different applications of electromagnetics. There are a few papers that present some analytical approaches for the accuracy of the MoM [1–6].

In this paper, we analyze the accuracy of MoM numerically. Our implementation is based on evaluation of hypersingular integrals, which are coming from dyadic Green function [8]. To be able to reduce the computational burden bi-conjugate gradient fast fourier transform (BiCG-FFT) method is employed [19]. For the discretization purposes the investigation region is divided into cubes with an edge length of one tenth of the minimum wavelength. The accuracy analysis is based on comparing the scattering from a dielectric sphere. For this aim, the root of the mean square error between the evaluated scattered electric fields and the analytical solution is computed for different cases. In particular, the accuracy analysis includes the following parts:

- Accuracy rate vs. the dielectric contrast between sphere and medium (Here the frequency of illumination and the size of the sphere are constant).
- Accuracy rate vs. the frequency of illumination (Here the dielectric contrast between sphere and medium and the size of the sphere are constant).
- Accuracy rate vs. the size of the sphere (Here the dielectric contrast between sphere and medium, the frequency of illumination are constant).

Obtained results show that MoM procedure is feasible for various scattering problems.

2. RESULTS AND DISCUSSION

As explained above the comparisons are made for an plane wave incidence on a dielectric sphere. Here two distinct case is considered. In the first case the radius of the sphere is 5 cm. For this case, the measurements are taken on three different horizontal circles, which belong to a cylinder Γ having a radius of $R = 7$ cm. The heights of the circles are chosen as -5 cm, 0 cm, 5 cm respectively.
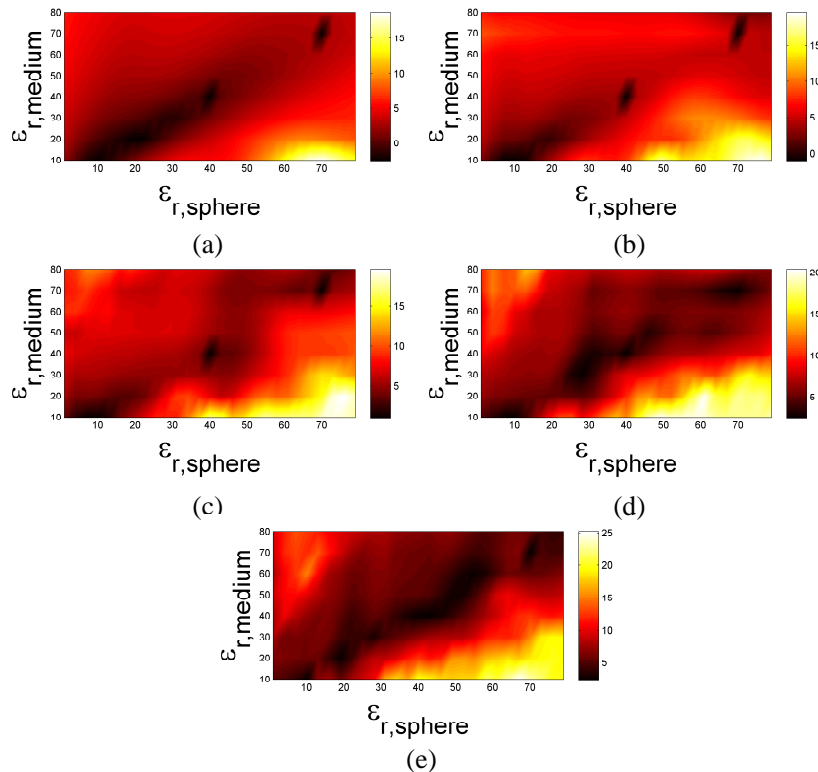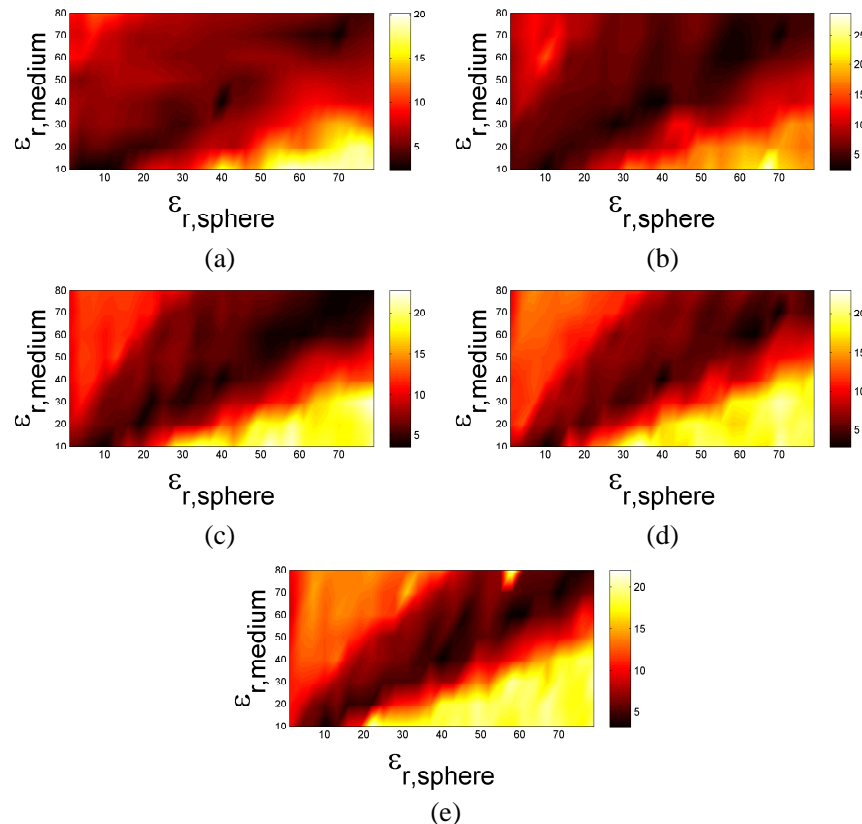

Figure 2: Error defined in (1) for (a) 0.50 GHz, (b) 0.75 GHz, (c) 1.00 GHz, (d) 1.25 GHz, (e) 1.50 GHz when the field is measured on the cylinder having radius of $R = 12$ cm. (ϵ_r stands for the dielectric permittivity of the corresponding medium.).

On each circle, all three components of the electric fields are sampled at 12 uniformly distributed points, which results in 36×3 measurements in total. The accuracy rate of the simulated field is assessed as:

$$\text{Log-RMS} = 10 \log_{10} \left(\frac{100}{3} \times \left(\sum_{j \in \{x,y,z\}} \frac{||E_{anal,j} - E_{MoM,j}||_{\Gamma}}{||E_{anal,j}||_{\Gamma}} \right) \right) \text{ [dB]} \tag{1}$$

where $||\cdot||_{\Gamma}$ denotes the Euclidean norm defined over surface Γ and $E_{\text{anal},j}, j \in \{x, y, z\}$, $E_{\text{MoM},j}, j \in \{x, y, z\}$ stand for the Cartesian components of the analytical, simulated fields, respectively. As can be seen from these result in Figure 1 as the frequency gets larger the accuracy rate of the solutions decreases. Furthermore, it can also be stated that the solution becomes more accurate when the dielectric permittivities of the medium and the sphere is close to each other.

Finally, the same setup is repeated when the radius of the sphere is $10 \, \text{cm}$ and the radius of the measurement cylinder Γ is $R = 12 \, \text{cm}$. The logarithmic errors are given in Figure 2 for this case. By comparing Figure 1 with Figure 2, one can conclude that the errors gets higher when the radius of the scatterer gets larger.

ACKNOWLEDGMENT

REFERENCES

1. Warnick, K. F. and W. C. Chew, "Accuracy of the method of moments for scattering by a cylinder," *IEEE Transactions on Microwave Theory and Techniques*, Vol. 48, No. 10 1652–1660, 2000.
2. Warnick, K. F. and W. C. Chew, "Error analysis of scattering amplitudes and RCS," *IEEE Antennas and Propagation Society International Symposium*, Vol. 4. IEEE, 2002.
3. Warnick, K. F. and W. C. Chew, "Error analysis of the moment method," *IEEE Antennas and Propagation Magazine*, Vol. 46, No. 6, 38–53, 2004.
4. Warnick, K. F., "An intuitive error analysis for FDTD and comparison to MoM," *IEEE Antennas and Propagation Magazine*, Vol. 47, No. 6, 111–115, 2005.
5. Hamlett, N. A. and W. Wasylkiwskyj, "A performance baseline for the convergence of electromagnetic integral-equation calculations using pulse functions," *IEEE Transactions on Antennas and Propagation*, Vol. 54, No. 5, 1523–1537, 2006.
6. Tyzhnenko, A. G. and Y. V. Ryeznik, "Estimates of accuracy and efficiency of a MoM algorithm in for 2-D screens," *Progress In Electromagnetics Research*, Vol. 71, 295–316, 2007.
7. Zwamborn, P. and P. M. Van den Berg, "The three dimensional weak form of the conjugate gradient FFT method for solving scattering problems," *IEEE Transactions on Microwave Theory and Techniques*, Vol. 40, No. 9, 1757–1766, 1992.
8. Gao, G., C. Torres-Verdin, and T. M. Habashy, "Analytical techniques to evaluate the integrals of 3D and 2D spatial dyadic Green's functions," *Progress In Electromagnetics Research*, Vol. 52, 47–80, 2005.
9. Chew, W. C. and Y. M. Wang, "Reconstruction of two-dimensional permittivity distribution using the distorted Born iterative method," *IEEE Transactions on Medical Imaging*, Vol. 9, No. 2, 218–225, 1990.
10. Van Den Berg, P. M. and R. E. Kleinman, "A contrast source inversion method," *Inverse Problems*, Vol. 13, No. 6, 1607, 1997.
11. Colton, D., H. Haddar, and M. Piana, "The linear sampling method in inverse electromagnetic scattering theory," *Inverse Problems*, Vol. 19, No. 6, S105, 2003.
12. Kirsch, A. and N. Grinberg, *The Factorization Method for Inverse Problems*, Vol. 36, Oxford University Press, Oxford, 2008.
13. Akinci, M. N. and M. Cayoren, "Microwave subsurface imaging of buried objects under a rough airsoil interface," *Remote Sensing Letters*, Vol. 5, No. 8, 703–712, 2014.
14. Guren, O., et al., "Surface impedance based microwave imaging method for breast cancer screening: Contrast-enhanced scenario," *Physics in Medicine and Biology*, Vol. 59, No. 19, 5725, 2014.

15. Chang, D. C. and J.-X. Zheng, "Electromagnetic modeling of passive circuit elements in MMIC," *IEEE Transactions on Microwave Theory and Techniques*, Vol. 40, No. 9, 1741–1747, 1992.

16. Aksun, M. I., "A robust approach for the derivation of closed-form Green's functions," *IEEE Transactions on Microwave Theory and Techniques*, Vol. 44, No. 5, 651–658, 1996.

17. Richmond, J., "Scattering by a dielectric cylinder of arbitrary cross section shape," *IEEE Transactions on Antennas and Propagation*, Vol. 13, No. 3, 334–341, 1965.

18. Harrington, R. F., and J. L. Harrington, *Field Computation by Moment Methods*, Oxford University Press, 1996.

19. Gan, H. and W. C. Chew, "A discrete BCG-FFT algorithm for solving 3D inhomogeneous scatterer problems," *Journal of Electromagnetic Waves and Applications*, Vol. 9, No. 10, 1339–1357, 1995.

Fast Model Order Reduction Approach to Uncertainty Quantification in Electrokinetics

Lorenzo Codecasa and Luca Di Rienzo

Politecnico di Milano, Milan, Italy

Abstract— A novel approach based on Model Order Reduction and Polynomial Chaos Expansion is proposed for uncertainty quantification in electrokinetics due to randomness in material parameters. Such approach is validated by considering a simplified geometry of a typical system for resistance welding. In this situation the Model Order Reduction approach allows to reduce the computational time by about two orders of magnitude with respect to the most efficient approaches based on sparse-grids.

1. INTRODUCTION

The perfect knowledge of material parameters is required in electromagnetic computations. However in many cases some uncertainty must be associated with that knowledge in the modeling process. In order to quantify the uncertainty of the output quantities of interest coming from the lack of knowledge of the input material parameters, the spectral stochastic finite element method, based on Polynomial Chaos Expansion (PCE), can be applied. This method, in both the intrusive and non-intrusive forms [1], allows to dramatically reduce computational time with respect to Monte Carlo (MC) methods. Nevertheless, in many applications computational complexity can still be prohibitively large.

In this paper, uncertainty quantification (UQ) in electrokinetic problems due to randomness in material parameters is considered. For such problems a novel approach based on Model Order Reduction (MOR) is here proposed. MOR was first introduced for accelerating UQ in [2]. Our starting point is a non-intrusive PCE method, in which the PCEs of the variables are estimated from the solutions of the deterministic electrokinetic problems for all values of the random material parameters in a sparse grid. The main idea of the proposed algorithm is that of reducing the number of solutions of such deterministic electrokinetic problems by constructing a parametric reduced order model, which is used to approximate the solution to the deterministic electrokinetic problems. Such parametric reduced order model is tailored to approximate with a chosen accuracy the deterministic elecrokinetic problems for the values of the random material parameters in the chosen sparse grid. The parametric reduced order model is generated in an efficient way by solving a reduced number of deterministic elecrokinetic problems with respect to that in a non-intrusive PCE approach. Moreover the computational cost for the solutions to the deterministic elecrokinetic problems required to construct the parametric reduced order model is optimized by exploiting the relatedness among the solutions to the deterministic electrokinetic problems for different values of the random material parameters.

The proposed MOR approach is then validated by modeling a simplified geometry of a typical system for resistance welding [3]. In this situation the MOR approach allows to reduce the computational time by about two orders of magnitude with respect to that of a standard non-intrusive PCE approach, maintaining the same level of accuracy. The storage requirement of the novel approach is comparable to that of a single deterministic electrokinetic problem. The proposed approach thus seems a novel promising candidate for uncertainty quantification analysis in electrokinetics. The extension of the approach to more general electromagnetic problems seems feasible and is currently under investigation.

2. DETERMINISTIC ELECTROKINETIC FORMULATION

A deterministic electrokinetic problem in the spatial domain Ω is ruled by the equation

$$\nabla \cdot (-\sigma(\mathbf{r}, \mathbf{p})\nabla\varphi(\mathbf{r}, \mathbf{p})) = 0, \tag{1}$$

in which $\sigma(\mathbf{r}, \mathbf{p})$ is the electric conductivity, function of the position vector $\mathbf{r}$ and of J parameters p_j, with $j = 1, \ldots, J$, forming a vector $\mathbf{p}$. The unknown $\varphi(\mathbf{r}, \mathbf{p})$ is the electric potential, which is a function of both the position vector $\mathbf{r}$ and the parameters vector $\mathbf{p}$. Such electric conductivity

distribution is assumed to be a linear combination of the J parameters p_j, with $j = 1, \ldots, J$, forming vector $\mathbf{p}$, in the form

$$\sigma(\mathbf{r}, \mathbf{p}) = \sigma_0(\mathbf{r}) + \sum_{j=1}^{J} \sigma_j(\mathbf{r}) \, p_j. \tag{2}$$

Conditions on the boundary $\partial\Omega$, of outward unit vector $\mathbf{n}(\mathbf{r})$, are assumed of mixed Dirichlet's and Neumann's type. Thus, in the part Σ_φ of the boundary $\partial\Omega$, the electric potential is assigned, so that

$$\varphi(\mathbf{r}, \mathbf{p}) = \varphi_s(\mathbf{r}), \tag{3}$$

while in the remaining part Σ_j of the boundary $\partial\Omega$, the normal component of current density is assigned

$$- \sigma(\mathbf{r}, \mathbf{p}) \frac{\partial\varphi}{\partial n}(\mathbf{r}, \mathbf{p}) = j_s(\mathbf{r}).$$

As it is well known a Finite Element Model (FEM) can be constructed by rewriting the electrokineticks problem in the weak form

$$\int_\Omega \nabla u'(\mathbf{r}) \cdot \sigma(\mathbf{r}, \mathbf{p}) \nabla(u(\mathbf{r}, \mathbf{p}) + \varphi_s(\mathbf{r})) \, d\mathbf{r} + \int_{\Sigma_\varphi} u'(\mathbf{r}) j_s(\mathbf{r}) \, d\mathbf{r} = 0. \tag{4}$$

for all functions $u'(\mathbf{r})$, in which $u'(\mathbf{r})$ and $\varphi(\mathbf{r}, \mathbf{p}) = u(\mathbf{r}, \mathbf{p}) + \varphi_s(\mathbf{r})$ belong to the same chosen FEM space X of dimension $|X| = N$. Besides $\varphi_s(\mathbf{r})$ is constructed in X starting from its trace on Σ_φ given by (3); $u(\mathbf{r}, \mathbf{p})$ and $u'(\mathbf{r}, \mathbf{p})$ are assumed to belong to X and to be zero over Σ_φ.

3. STOCHASTIC ELECTROKINETIC FORMULATION

The electric conductivities are now modeled as random variables. Thus in a stochastic analysis the parameters forming vector $\mathbf{p}$ are assumed to be random variables. Applying PCE, $u(\mathbf{r}, \mathbf{p})$ is approximated in the form

$$u(\mathbf{r}, \mathbf{p}) = \sum_{|\boldsymbol{\beta}| \leq M} u_{\boldsymbol{\beta}}(\mathbf{r}) \psi_{\boldsymbol{\beta}}(\mathbf{p}), \tag{5}$$

in which $\boldsymbol{\beta}$ are multi-indices of J elements and $\psi_{\boldsymbol{\beta}}(\mathbf{p})$ are polynomials of degrees less than a chosen value M, constituting an orthonormal basis of $Q = \binom{M+J}{J}$ elements, in the probability space of random variables forming vector $\mathbf{p}$. Both intrusive and non-intrusive PCE approaches can be approached to determine (4). In non-intrusive PCE approaches, commonly adopted as the most efficient alternative to Monte Carlo techniques, functions $u_{\boldsymbol{\beta}}(\mathbf{r})$ are reconstructed from the solutions $\varphi(\mathbf{r}, \mathbf{p})$ of the deterministic problems (4) for all values of $\mathbf{p}$ in a proper set $\mathcal{G}$. However, even using sparse-grids [1], the set $\mathcal{G}$ becomes very large when the number J of parameters or the polynomial degree M increases. Thus the number of deterministic problems to be solved also becomes very large.

4. THE MODEL ORDER REDUCTION APPROACH

Hereinafter the alternative Algorithm 1 is proposed which constructs a reduced order model tailored to PCE analysis solving a much smaller number of deterministic problems with respect to the non-intrusive approaches. Moreover the computational cost of the solution to these deterministic problems is much smaller with respect to the non-intrusive approaches, since accurate estimations of the solution to these deterministic problems are derived from the reduced order model solutions taken as starting points in the adopted iterative methods for solving linear systems. The PCE expansion of the solution to the original problem is then obtained from such reduced order model. In the algorithm, at step 1, the FEM discretization of the electrokinetics deterministic problem (4) is numerically approximated, for each selected value of $\mathbf{p}$. A preconditioned conjugate gradient method is used and the number of iterations is reduced by assuming as initial point the $\hat{\varphi}(\mathbf{r}, \mathbf{p})$ estimation provided by the previously computed compact model. At step 2 an orthonormal basis of

---

Algorithm 1: MOR-based algorithm

Set $k := 0$ (dimension of the reduced model);
Set $\vartheta := 0$ (norm of the residual);
Set linear space $\mathcal{S}_0 := \emptyset$;
Choose vector $\mathbf{p}$ in $\mathcal{G}$;
Set $\hat{\varphi}(\mathbf{r}, \mathbf{p}) := 0$;
repeat

    Set $k := k + 1$;

1   Solve problem (4) for $\varphi(\mathbf{r}, \mathbf{p})$ using $\hat{\varphi}(\mathbf{r}, \mathbf{p})$ as initial estimation in the iterative technique;

2   Generate an orthonormal basis of the linear space $\mathcal{S}_k$ spanned by $\mathcal{S}_{k-1}$ and $\varphi(\mathbf{r}, \mathbf{p})$;

3   Generate reduced order model $\mathcal{R}_k(\mathbf{p})$, projecting problem $\mathcal{D}$ onto space $\mathcal{S}_k$;

    for all $\mathbf{q} \in \mathcal{G}$ **do**

4   Solve the reduced order model $\mathcal{R}_k(\mathbf{q})$ obtaining $\hat{\varphi}(\mathbf{r}, \mathbf{q})$ as an approximation for $\varphi(\mathbf{r}, \mathbf{q})$;

5   Estimate the approximation residual η;

        if $\eta > \vartheta$ **then**

            Set $\vartheta := \eta$;

6   Set $\mathbf{p} := \mathbf{q}$;

until $\vartheta > \varepsilon$;

7 Determine the PCE expansion of the solution to the reduced order model $\mathcal{R}_k(\mathbf{p})$ and reconstruct the PCE expansion of $\varphi(\mathbf{r}, \mathbf{p})$;

---

space $\mathcal{S}_k$ is generated, computing a set of functions $v_h(\mathbf{r})$, with $h = 1, \ldots, k$, spanning all functions $u(\mathbf{r}, \mathbf{p})$ computed at step 1 and forming a column vector

$$\boldsymbol{v}(\mathbf{r}) = [v_h(\mathbf{r})].$$

At step 3 the reduced order model $\mathcal{R}_k(\mathbf{p})$ is constructed. This model is obtained from (4) assuming that the X space is substituted by its subspace $\mathcal{S}_k$, spanned by functions $v_h(\mathbf{r})$, with $h = 1, \ldots, k$. In this way the compact model takes the form

$$\left(\hat{\mathbf{S}}_0 + \sum_{j=1}^{J} p_j \hat{\mathbf{S}}_j\right) \hat{\mathbf{x}}(\mathbf{p}) = \left(\hat{\mathbf{R}}_0 + \sum_{j=1}^{n} p_j \hat{\mathbf{R}}_j\right) \tag{6}$$

in which $\hat{\mathbf{S}}_j$, with $j = 1, \ldots, J$, are square matrices of dimension k given by

$$\hat{\mathbf{S}}_j = \left[\int_\Omega \nabla v_h(\mathbf{r}) \cdot \sigma_j(\mathbf{r}) \nabla v_l(\mathbf{r}) \, d\mathbf{r}\right], \quad j = 1, \ldots, J,$$

and $\hat{\mathbf{R}}_j$, with $j = 1, \ldots, J$, are column vectors of k rows

$$\hat{\mathbf{R}}_0 = \left[-\int_{\partial\Omega} v_h(\mathbf{r}) j_s(\mathbf{r}) - \int_\Omega \nabla v_h(\mathbf{r}) \cdot \sigma_0(\mathbf{r}) \nabla \varphi_s(\mathbf{r}) \, d\mathbf{r}\right],$$

$$\hat{\mathbf{R}}_j = \left[-\int_\Omega \nabla v_h(\mathbf{r}) \cdot \sigma_j(\mathbf{r}) \nabla \varphi_s(\mathbf{r}) \, d\mathbf{r}\right], \quad j = 1, \ldots, J.$$

Vector $\hat{\mathbf{x}}(\mathbf{p})$ allows to approximate the solution $u(\mathbf{r}, \mathbf{p})$ to (4) as (step 4)

$$\hat{u}(\mathbf{r}, \mathbf{p}) = \sum_{h=1}^{k} v_h(\mathbf{r}) \hat{x}_h(\mathbf{p}) = \boldsymbol{v}^T(\mathbf{r}) \hat{\mathbf{x}}. \tag{7}$$

At step 5, η represents the residual when $\varphi(\mathbf{r}, \mathbf{q})$ is substituted by $\hat{\varphi}(\mathbf{r}, \mathbf{q}) = \hat{u}(\mathbf{r}, \mathbf{p}) + \varphi_s(\mathbf{r})$ in (4). At step 6, the value of $\mathbf{q}$ in $\mathcal{G}$ maximizing the value of η becomes the candidate $\mathbf{p}$ for solving the deterministic problem (4) at next step 1. At step 7, an intrusive PCE approach is applied to the reduced order model $\mathcal{R}_k$. Thus $\hat{\mathbf{x}}(\mathbf{p})$ is approximated by its PCE

$$\hat{\mathbf{x}}(\mathbf{p}) = \sum_{|\boldsymbol{\beta}| \leq M} \hat{\mathbf{x}}_{\boldsymbol{\beta}} \psi_{\boldsymbol{\beta}}(\mathbf{p}). \tag{8}$$

Substituting this expansion into (6), multiplying then (6) by $\psi_{\boldsymbol{\alpha}}(\mathbf{p})$, with $|\boldsymbol{\alpha}| \leq M$, and applying the expected value operator $\mathbf{E}[\cdot]$, it results in

$$\left(\mathbf{I}_N \otimes \hat{\mathbf{S}}_0 + \sum_{j=1}^{J} \mathbf{P}_j \otimes \hat{\mathbf{S}}_j\right) \hat{\mathbf{X}} = \left(\mathbf{I}_N \otimes \hat{\mathbf{R}}_0 + \sum_{j=1}^{N} \mathbf{P}_j \otimes \hat{\mathbf{R}}_j\right),$$

in which $\hat{\mathbf{X}} = [\hat{\mathbf{x}}_{\boldsymbol{\alpha}}]$ is a column vector with kQ columns and

$$\mathbf{P}_j = [\mathbf{E}[p_j \psi_{\boldsymbol{\alpha}}(\mathbf{p}) \psi_{\boldsymbol{\beta}}(\mathbf{p})]]$$

are square matrices of order Q. This linear system of equations has reduced dimensions with respect to an intrusive PCE approach, so that it can be solved at negligible cost. From the PCE expansion of $\hat{\mathbf{x}}(\mathbf{p})$, the PCE expansion of $\hat{u}(\mathbf{r}, \mathbf{p})$ approximating the PCE of $u(\mathbf{r}, \mathbf{p})$ is straightforwardly obtained as

$$\hat{u}_{\boldsymbol{\alpha}}(\mathbf{r}, \mathbf{p}) = \sum_{|\boldsymbol{\beta}| \leq M} \boldsymbol{v}^T(\mathbf{r}) \hat{\mathbf{x}}_{\boldsymbol{\beta}} \psi_{\boldsymbol{\beta}}(\mathbf{p}). \tag{9}$$

5. NUMERICAL RESULTS

The 3D problem shown in Fig. 1 is considered [3]. The geometry describes three aluminum electrodes over a conductive aluminum substrate. Three contact resistances are modeled by three statistically independent conductivities σ_1, σ_2, σ_3, with uniformly distributed probability density functions in the range $1.41\,\mathrm{MS/m}$–$11.3\,\mathrm{MS/m}$.

The conductive region without the surrounding air region is discretized. Homogeneous Neumann's boundary conditions are used everywhere, with the exception of the three electrodes at which Dirichlet's boundary conditions are used, as indicated in Fig. 1. A set of primal tetrahedral grids is generated. Among these a tetrahedral mesh with about $N = 16,000$ nodes is chosen whose
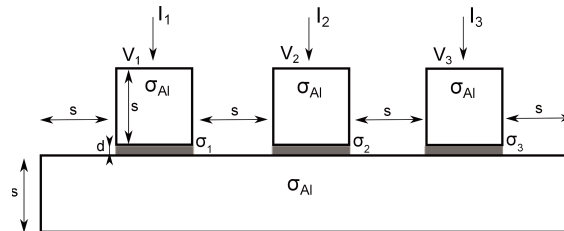
Figure 1: 2D section of the considered example, the depth being equal to s, with $s = 10\,\mathrm{mm}$ and $d = 1\,\mathrm{mm}$.
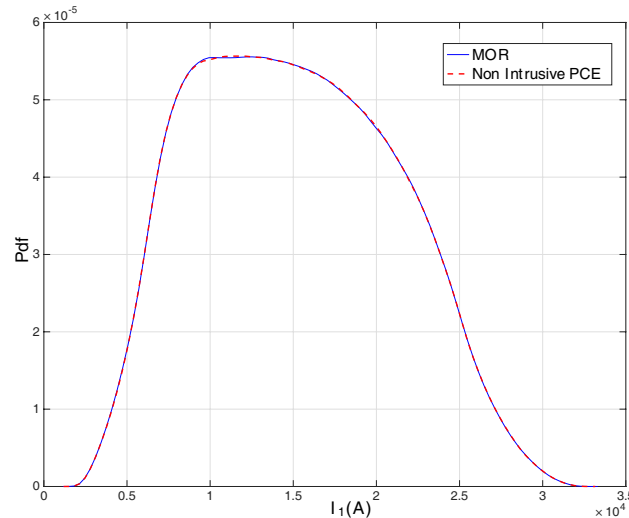
Figure 2: Probability density function of the current I_1.

further refining introduces variations in the potential distribution lesser that 1% in the energy norm. A first order FEM disretization is performed over such mesh.

The PCE of the electric current I_1 is estimated in the situation in which $V_1 = V_3 = 1$ and $V_2 = 0$. A PCE order $M = 7$ is assumed and a Gauss-Legendre sparse grid $\mathcal{G}$ of dimension $|\mathcal{G}| = 681$ is used. With these choices the non-intrusive PCE approach requires the solution of 681 sistems of equations. By applying a preconditioned conjugate gradient algorithm this requires about 167.7 s on a 2.3 Ghz Intel Core i7. Instead the application of Algorithm 1 allows to approximate the solution of the problem with a 0.01% accuracy in $k = 5$ steps and in about 1.5 s, with about two orders of magnitude improvement in computational time.

In Fig. 2, the probability density function (Pdf) of the current I_1 computed by Algorithm 1 is compared to the solution computed by the non-intrusive PCE approach, showing excellent agreement. The tiny difference visible in the two pdfs of Fig. 2 is not due to the difference in the MOR and non intrusive PCE solutions but to the approach used to estimate the probability density function starting from the PCE of I_1. In Fig. 3, the error in the approximation of the PCE of the spatial distribution of the electric potential is shown as a function of the step number k in Algorithm 1, showing a practically exponential decay with respect to k.
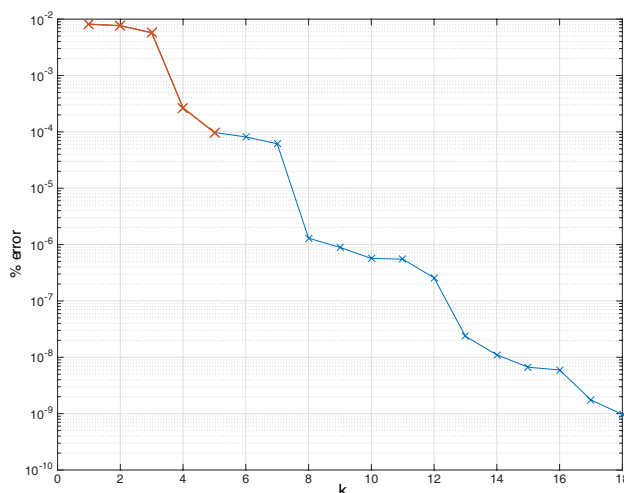
Figure 3: Relative error in the energy norm of the PCE of the electric potential as a function of the step number k of Algorithm 1. The red line shows the iteration steps performed for getting a 0.01% accuracy.

6. CONCLUSION

In this paper a novel approach based on MOR has been proposed for uncertainty quantification problems due to random material parameters in electrokinetics. The proposed MOR approach has been validated by considering a simplified geometry of a typical system for resistance welding. In this situation the novel approach allowed to reduce the computational time by about two orders of magnitutude with respect to that of standard non-intrusive PCE approach, maintaining the same level of accuracy.

REFERENCES

1. Xiu, D., *Numerical Methods for Stochastic Computations: A Spectral Method Approach*, Princeton University Press, 2010.
2. Boyaval, S., C. L. Bris, T. Lelievre, Y. Maday, N. Nguyen, and A. Patera, "Reduced basis techniques for stochastic problems," *Arch. Comput. Methods Engrg.*, Vol. 17, 1–20, 2010.
3. Codecasa, L. and L. Di Rienzo, "Stochastic finite integration technique formulation for electrokinetics," *IEEE Transactions on Magnetics*, Vol. 50, No. 2, Article 7014104, 2014.

Uncertainty Quantification for Complex RF-structures Using the State-space Concatenation Approach

J. Heller, **T. Flisgen**, **C. Schmidt**, **and U. van Rienen**

Institute of General Electrical Engineering, University of Rostock
Albert-Einstein-Strasse 2, Rostock 18059, Germany

Abstract— In various applications of computational engineering and accelerator physics, the computation of the electromagnetic behavior of a structure is of crucial importance for the design and operation. The electromagnetic properties of the structure depend on its geometry, which, for real-life radio-frequency (RF) structures, generally deviates from their design values due to fabrication tolerances and operation. To make assessments about the effects of such deviations as well as to employ robust optimizations, a so-called uncertainty quantification (UQ) is applied. For large and complex structures such computations are heavily demanding and cannot be carried out using standard brute-force approaches. In this paper, we propose a combination of established techniques to perform UQ for long and complex structures, where the uncertainty is located only in parts of the structure. As exemplary structure, we investigate the third-harmonic cavity, which is being used at the FLASH accelerator at DESY, assuming an uncertain geometry of the left higher order mode coupler. The investigation is carried out using the so-called polynomial chaos expansion (gPC). For that, the repeated numerical solution of Maxwell's equations is necessary. Usually, such investigations are carried out on supercomputers or small computer clusters with heavily parallelized code. Due to the fact that maximum-performance computational infrastructure is scarce and expensive, the electromagnetic properties are being computed on standard workstation computers using a newly proposed non-overlapping domain decomposition scheme named State-Space Concatenation (SSC) which is based on model-order reduction of the decomposed segments. Using the SSC scheme has the most important advantage that only the uncertain part of the structure, in our case the left coupler, needs to be recomputed when using a non-intrusive scheme like gPC. In comparison to the huge computational demand of a straightforward simulation, the combination of uncertainty quantification and model-order reduction allows for a reasonable improvement of the computational efficiency. Both schemes can be separately applied to structures related to accelerator physics. Yet, just their combination will enable the investigation of long and complex structures beyond the scope of standard approaches.

1. INTRODUCTION

The design of RF-structures usually does not take fabrication tolerances into account. These tolerances make the operated design uncertain. For a thorough design, the effects of the uncertain geometry regarding the RF-properties of the structure need to be assessed which is of growing interest in RF-design [1–4]. This is employed using uncertainty quantification (UQ) [5]. Usually this requires the repeated solution of Maxwell's equations [6] for the entire structure under consideration in order to compute the eigenmodes. Since in general no closed, analytical solutions can be found, numerical techniques are employed. Due to the fact that the investigated structures are large and complex, standard discretisation techniques might lead to extreme computational demands which make the investigations only feasible using supercomputers [7]. In this paper, we propose a new approach that will decrease the needed computational time for UQ by using a newly proposed non-overlapping decomposition scheme named State-Space concatenations (SSC) [8] for the repeated solution of Maxwell's equations in combination with the generalised polynomial chaos (gPC) technique.

2. UNCERTAINTY QUANTIFICATION

For design considerations, assessments about the influence of uncertainties of design values need to be made. In the literature, the influence of uncertain design parameters on output parameters is regarded as uncertainty propagation. Usually the probability density functions (PDF) of physical parameters of the designed structures (further referred to as output parameters) are quantities of interest. These ought to be computed using the estimated PDFs of the design parameters (further referred to as input parameters). UQ techniques are usually computationally demanding. Furthermore, standard approaches like Monte Carlo (MC) only converge with the square-root of the number of samples used. To overcome the poor convergence and lower the computational

demand, a different approach was proposed in [9]. The main idea is to approximate the multi-dimensional, stochastical space by a set of orthogonal polynomials. The expansion coefficients for these polynomials are obtained by computing the solution of a deterministic problem for several collocation points in the stochastical space. This approach is generally referred to as polynomial chaos [10]. For a low dimensional stochastical space, hence few uncertain input parameters, the gPC might be faster than other techniques. However, for many uncertain input parameters, the method becomes more demanding than comparable, straight-forward approaches. A detailed description is beyond the scope of this article. For a complete description please refer to [10] and references therein. A more detailed comparison of the applicable techniques for UQ in RF-design, is given in [11]. For the design of accelerating structures usually the fabrication tolerances of the structure have the highest influence [16]. Important output quantities of interest are for example the resonant frequencies of certain higher order modes (HOMs) [13].

3. STATE-SPACE CONCATENATIONS

The SSC scheme employs a non-overlapping, domain-decomposition method to the investigated structure in order to compute the eigenmodes for closed structures. In a first step, the structure is decomposed into several, non-overlapping domains. For these domains a second order state space model (SSM) is computed using a model-order reduction (MOR). The SSM are then concatenated to a larger SSM which contains all the RF-parameters of the full structure in the given frequency interval. Since the concatenation of the models is relatively fast (several seconds for this application), the computational demand of the UQ is mainly governed by the recomputation of the uncertain part. Thus, compared to standard approaches, a significant decrease in the computational demand can be observed. The accuracy and suitability of the SSC scheme was proven in several publications [8, 14, 15].

4. APPLICATION EXAMPLE

As application example, a part of the third-harmonic cavity of the FLASH accelerator in Hamburg is chosen as depicted in Fig. 1. The structure consists of a superconducting 9-cell cavity, a superconducting HOM coupler (attached to the left iris of the cavity) and a HOM coupler including an input coupler (attached to the right iris of the cavity). For the application of SSC, a suitable decomposition needs to be selected. In this example, the decomposition is chosen as depicted in Fig. 2.

As a practical example, we try to investigate the effect of a geometrical uncertainty in the left HOM coupler (depicted in blue in Fig. 2). For this purpose, the depth of the antenna, as well as the distance between the coupler and the cavity are chosen to be uncertain as depicted in Fig. 3. It should be noted, that even though the uncertainty is located in the coupler, it still can influence all the eigenmodes, even when they are not solely located in the uncertain part of the structure. Both uncertain parameters are assumed to be symmetrically uniformly distributed with a
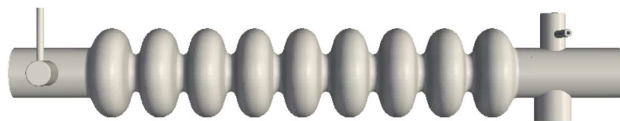
Figure 1: Qualitative plot of the third-harmonic cavity with HOM couplers and input coupler. This structure is being used in the FLASH accelerator in Hamburg at DESY [16].
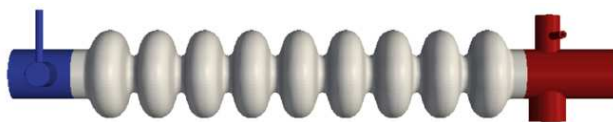
Figure 2: Decomposition of the computed structure into three parts. The blue part depicts the left HOM coupler whose geometry is considered uncertain. The white color depicts the 9-cell cavity (it should be noted that for the computation of the cavity symmetry boundary conditions can be applied since the structure is rotationally symmetric). The red color indicates the right HOM coupler which also contains the input coupler that is used to excite the accelerating mode inside the cavity. In the application example, some geometrical parameters of the blue part are assumed to be uncertain.
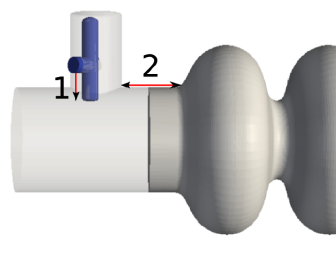
Figure 3: Segment of the full structure including the uncertain geometry parameters. The depth of the coupler antenna (depicted in blue with number 1) and the distance between the coupler and the cavity (depicted with number 2) are assumed to be uncertain.
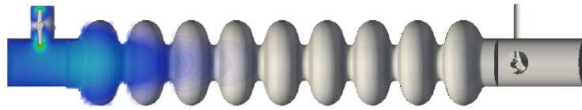
Figure 4: Qualitative plot of the magnitude of the electric field of an investigated mode at roughly 4.11 GHz. This mode is mainly located at the coupler and thus it is highly sensitive with respect to uncertainties in the said coupler in question.
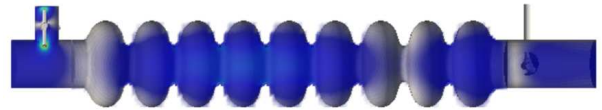
Figure 5: Qualitative plot of the magnitude of the electric field of an investigated mode at roughly 4.30 GHz. This mode is able to traverse through the entire structure but it is mainly located at the coupler. Thus it is highly sensitive to uncertainties in the coupler.

maximum deviation of 0.125 mm. Since the practical knowledge about deviations of HOM couplers is scarce, these values are assumptions based on deviations expected in the cavity and might not reflect the real-life behaviour. As result we compute the PDFs of several resonant frequencies inside the structure. In order to show the scope of the presented methods, this example is beyond the capabilities of direct approaches on standard workstation computers and by this can not be verified using standard brute force approaches. However, both methods were validated separately, in several other applications as described, e.g., in [17].

5. RESULTS

As results of the UQ, the probability density functions (PDF) of the resonant frequencies of two eigenmodes were computed using gPC using an expansion degree of up to 4. As first example the resonant frequency of some mode at roughly 4.11 GHz located inside the left HOM coupler was investigated. The field pattern computed for the certain design is depicted in Fig. 4. Due to its good coupling to the HOM coupler this mode is expected to have a strong dependence on the uncertainty of the coupler. The PDF computed using gPC is shown in Fig. 6(a). It can be seen that the difference between the computation using a polynomial degree of $p = 3$ and $p = 4$ is relatively small, hence the solution of the gPC converges. It should be noted, that this convergence only refers to the gPC. The convergence of the mesh of the deterministic problem needs to be examined beforehand. Which polynomial degree is necessary depends on the application and the finally desired accuracy. When the goal is only a rough assessment, hence only lowest-order stochastical moments, even a polynomial degree of $p = 2$ might be sufficient. For higher accuracy a polynomial degree of $p = 3$ might be needed. It should be noted, that this assessment needs to be made separately for every mode and does not need to hold for the other modes as well.

Further, the PDF of the resonant frequency of a mode at roughly 4.30 GHz was investigated. A qualitative plot of the electric field can be seen in Fig. 5. This mode has its maximum amplitude in the uncertain coupler but is able to traverse through the entire structure. In Fig. 6(b), the PDF of this mode is computed using gPC with different polynomial orders p. It can be seen that an order of $p = 3$ is sufficient in order to make assessments about the stochastical moments. As a third example the resonant frequencies of the first monopole band of the cavity were investigated which are located approximately between 3.75 GHz and 3.9 GHz. For these modes, the UQ can not be performed properly since the changes in the frequencies caused by the uncertain design, were below the actual numerical accuracy of the model (several 100 kHz). However, one can still claim that, since the changes in the frequency are below the models numerical accuracy, these modes
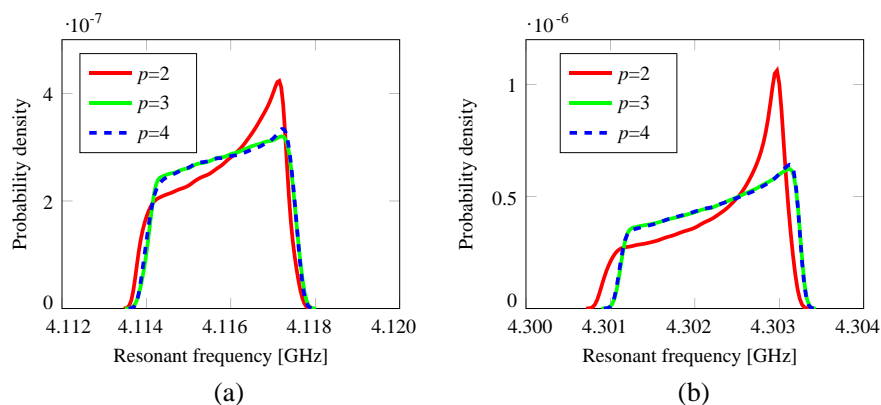
Figure 6: PDFs of resonant frequency (a) of the mode shown in Fig. 4 at roughly 4.11 GHz and (b) of the mode shown in Fig. 5 at roughly 4.30 GHz computed using gPC with different polynomial degrees.

are barely sensitive regarding uncertainties in the coupler. The full computation of the structure using SSC takes approximately 90 minutes. However, for any collocation point of gPC, only the uncertain coupler needs to be recomputed. Hence, the recomputation of the solution for any gPC sample takes approximately 10 minutes and 30 seconds each. This results in a time for full UQ for a polynomial degree of $p = 3$ of approximately 4.5 hours for the full spectrum.

6. CONCLUSION

In this investigation, we could show the successful combination of gPC and SSC in order to employ UQ for large and complex RF-structures. Therefore, an example from accelerator physics was picked, the Third-Harmonic cavity of the FLASH accelerator. In this application, parts of the upstream HOM coupler were assumed to be uncertain regarding their geometry. Using the proposed approach, we were able to compute the PDFs of several eigenmodes as well as their low-order stochastical moments. It could be shown, that modes from the first monopole band of the cavity, are hardly influenced by the uncertainty of the coupler. However, it should be noted that for a real assessment of the PDFs of these modes, the accuracy of the model needs to be several orders of magnitude higher.

As expected, modes that have a strong coupling to the uncertain coupler are heavily influenced. In both cases a polynomial degree of $p = 3$ was necessary to quantify the standard deviation with a relative accuracy below 10^{-6}. The combination of the two techniques allows for investigations on workstation computers instead of brute force approaches on high performance computers. Nevertheless, it should be mentioned that in this investigation, only parts of the structure were assumed to be uncertain, which, in real-life applications might not hold.

A reasonable claim against a full eigenmode analysis might be, that the investigation of the frequency can also be carried out using scattering parameters. However, for the tracking of a mode through the uncertain spectrum this might not be possible, because a specific mode is characterized and thus recognized by its specific field pattern while the frequency information might not be sufficient. In future investigations we will focus on the investigation of fully uncertain, large and complex structures. Further, in future investigations, the full spectrum will be investigated. For this, a decent mode recognition needs to be implemented as in, e.g., [18].

REFERENCES

1. Valles, N. and M. Liepe, "Seven-cell cavity optimization for cornells energy recovery linac," *Proceedings of SRF 2009*, Berlin, Germany, 2009.

2. Deryckere, J., et al., "Stochastic response surface method for studying microphoning and lorentz detuning of accelerator cavities," *Proceedings of ICAP 2012*, 158–160, Rostock Warnemünde, Germany, 2012.

3. Müller, W. F. O., W. Koch, and T. Weiland, "Numerical calculation of trapped modes in TESLA cavities considering production tolerances," *Proceedings of EPAC 2002*, Paris, France, 2002.

4. Sukhanov, A., et al., "Higher order modes in project-X linac," *Nuclear Instruments and Methods in Physics Research Section A: Accelerators, Spectrometers, Detectors and Associated Equipment*, Vol. 734, 9–22, 2014.

5. Saltelli, A., K. Chan, and E. M. Scott, *Sensitivity Analysis*, Vol. 134, Wiley, New York, 2000.

6. Maxwell, J. C., "A treatise on electricity and magnetism," *Nature*, Vol. 7, No. 182, 478–480, 1873.

7. Akcelik, V., et al., "SRF cavity imperfection studies using advanced shape uncertainty Quantification Tools," *LINAC*, 2008.

8. Flisgen, T., H.-W. Glock, and U. van Rienen, "Compact time-domain models of complex RF structures based on the real eigenmodes of segments," *IEEE Transactions on Microwave Theory and Techniques*, Vol. 61, No. 6, Jun. 2013.

9. Ghanem, R. G. and P. D. Spanos, *Stochastic Finite Elements: A Spectral Approach*, Springer-Verlag, New-York, 1991.

10. Xiu, D., *Numerical Methods for Stochastic Computations: A Spectral Method Approach*, Princeton University Press, Princeton, 2010.

11. Schmidt, C., T. Flisgen, J. Heller, and U. van Rienen, "Comparison of techniques for uncertainty quantification of superconducting radio frequency cavities," *International Conference on Electromagnetics in Advanced Applications 2014 (ICEAA 2014)*, 117–120, Palm Beach, Aruba, 2014.

12. Aune, B., et al., "Superconducting TESLA cavities," *Physical Review Special Topics — Accelerators and Beams*, Vol. 3, No. 9, 092001, 2000.

13. Padamsee, H., J. Knobloch, and T. Hays, *RF Superconductivity for Accelerators*, John Wiley and Sons, 2008.

14. Flisgen, T., J. Heller, and U. van Rienen, "Lumped equivalent models of complex RF structures," *Proceedings of ICAP 2012*, 245–249, Warnemünde, Germany, 2012.

15. Heller, J., T. Flisgen, and U. van Rienen, "Computation of wakefields and HOM port signals by means of reduced order models," *Proceedings of SRF 2013*, 361–363, Paris, France, 2013.

16. Sekutowicz, J., R. Wanzenberg, W. F. O. M`uller, and T. Weiland, "A design of a 3rd harmonic cavity for the TTF 2 photoinjector," DESY-TESLA-FEL-2002-05, 2002.

17. Heller, J., T. Flisgen, C. Schmidt and U. van Rienen, "Quantification of geometric uncertainties in single cell cavities for BESSY VSR using polynomial chaos," *Proceedings of 5th IPAC*, 415–417, Dresden, Germany, 2014.

18. Brackebusch, K., T. Galek, and U. van Rienen, "Automated mode recognition algorithm for accelerating cavities," *Proceedings of 5th IPAC*, Dresden, Germany, Jun. 15–20, 2014.

Application of Krylov-type Parametric Model Order Reduction in Efficient Uncertainty Quantification of Electro-thermal Circuit Models

Y. Yue[1], L. Feng[1], P. Meuris[2], W. Schoenmaker[2], and P. Benner[1]

[1]Max Planck Institute for Dynamics of Complex Technical Systems
Sandtorstr. 1, Magdeburg 39106, Germany
[2]MAGWEL NV, Martelarenplein 13, Leuven B-3000, Belgium

Abstract— As CMOS devices scale down to the nanoscale regime, it becomes increasingly more desired to design systems robust to device variations due to the fabrication process. In robust system design, uncertainty quantification plays an indispensable role. This paper considers uncertainty quantification of power-MOS devices used in energy harvesting. Uncertainty quantification of such a system is usually computationally demanding because it requires either simulating the high-order system at many sampling points, or simulating an even larger system. This paper uses parametric model order reduction techniques to accelerate uncertainty quantification of electro-thermal systems. We embed the reduced model into two uncertainty quantification methods, namely a Latin hypercube sampling method and a stochastic collocation method. Numerical results show that for both methods, uncertainty quantification based on a reduced model not only yields accurate results, but also achieves a significant speedup.

1. INTRODUCTION

In the nanoscale era, we have to consider uncertainty in circuit design because uncertainty is unignorable and unavoidable. Therefore, uncertainty quantification (UQ), which quantifies the uncertainties of the system outputs propagated from the process variations, serves as a useful tool for robust design [11]. This paper studies efficient UQ of power-MOS devices. These devices are commonly used in energy harvesting, where energy from external sources like light and environmental heat are collected in order to power small devices such as implanted biosensors [10]. A major problem in UQ of power-MOS devices is the high computational cost. A finite element model of a power-MOS device, which is derived from a fine 3D mesh of a multi-layered structure consisting of dielectric, vias, contacts, and metal interconnection, is normally of an extremely high order. Therefore, simulation analysis of electro-thermal systems is already computationally demanding. The computational cost of its UQ is even higher since it requires simulating the model at many parameter samples, or simulating a coupled system with a much higher dimension.

The goal of this paper is to use parametric model order reduction (pMOR) techniques [4], which prove to be efficient in many application fields such as circuit simulation, acoustics, and structural vibrations, to reduce the high computational cost in UQ of electro-thermal systems. A pMOR method builds a parametric reduced order model (pROM) that can capture the system dynamics regardless of parameter changes within a certain range. In this work, we use a Krylov-type pMOR method [3], whose goal is to match the (cross-)moments of the state vector, because of its modest requirements on system properties and low computational complexity. To reduce the computational cost of non-intrusive UQ methods, we employ pROM-based methods, which replace the full-order model (FOM) with the pROM in non-intrusive UQ methods. In this paper, we use pROM-based methods to accelerate two UQ methods, namely a Latin hypercube sampling (LHS) method [7] and a stochastic collocation (SC) method [9]. In our numerical test, the system of interest is a nonlinear electro-thermal system with one-way coupling from the electrical part to the thermal part. Numerical results show that a pROM of a low order exhibits high accuracy over a very large parameter range in approximating the original high-order model, and for both UQ methods, pROM-based UQ not only computes accurate results, but also achieves a significant speedup.

2. MATHEMATICAL FORMULATION

The model of interest in this paper is a Power-MOS device shown in Figure 1(a). The device has three contacts: the drain, the source, and the back contact. Here we study the system behavior within the time interval $t \in [0\,\mathrm{s}, 10^{-6}\,\mathrm{s}]$, where $10^{-6}\,\mathrm{s}$ is the rise time of the source voltage. The
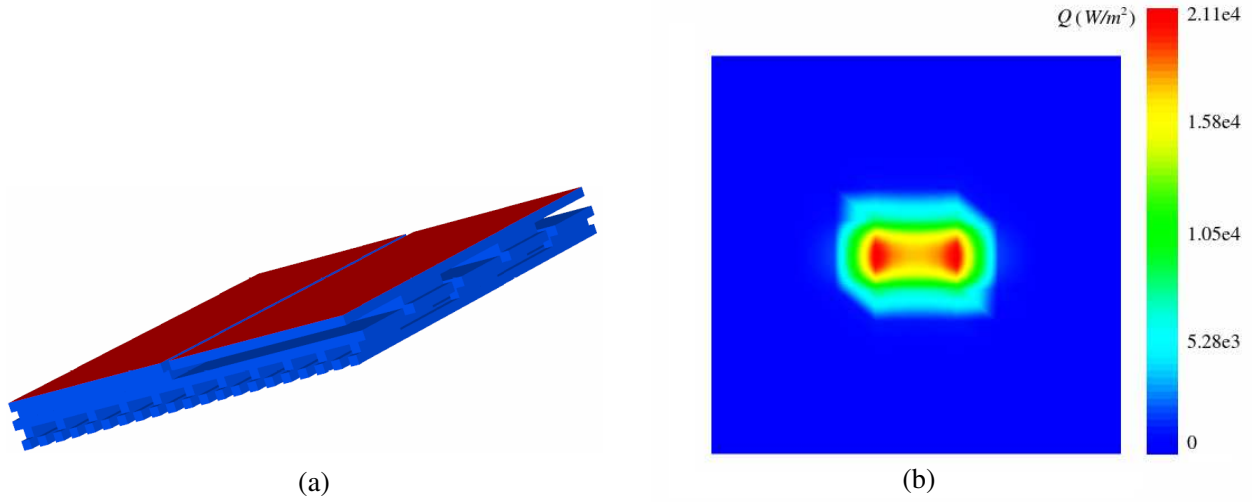
Figure 1: The Power-MOS device and its heat flux density on the back contact at $t = 10^{-6}$ s. (a) Power-MOS device (the back contact is not shown). (b) Heat flux density on the back contact at $t = 10^{-6}$ s.

inputs of the system include the voltages (V) and temperatures (T) of the three contacts, namely:

$$V_{\text{drain}}(t) = V_{\text{back}}(t) = 0\,(V), \quad V_{\text{source}}(t) = 10^7 t\,(V), \quad (t \in [0\,\text{s}, \, 10^{-6}\,\text{s}])$$
$$T_{\text{drain}}(t) = T_{\text{source}}(t) = T_{\text{back}}(t) = 300\,(K).$$

As the voltage on the source rises, the chip is heated up as is shown in Figure 1(b). The outputs we consider here include the currents (I) and thermal fluxes (ϕ) of the three contacts. The electro-thermal model of the power-MOS device that we consider in this paper is

$$A_E(p)x_E(p,t) = -B_E(p)u(t), \quad \text{(Electrical Part)}, \tag{1a}$$
$$E_T(p)\dot{x}_T(p,t) = A_T(p)x_T(p,t) + B_T(p)u(t) + F(p) \times_2 x_E(p) \times_3 x_E(p), \quad \text{(Thermal Part)}, \tag{1b}$$
$$x_T(p,0) = x_T^0, \quad x_E(p,0) = x_E^0, \quad \text{(Initial Conditions)}, \tag{1c}$$
$$y(p,t) = C_E(p)x_E(p,t) + C_T(p)x_T(p,t) + D(p)u, \quad \text{(Output)}. \tag{1d}$$

For the whole system, p represents parameter(s), $u(t) \in \mathcal{R}^l$ is the input vector and $y(p) \in \mathcal{R}^m$ is the output vector. In the electrical part governed by algebraic Equation (1a), $A_E(p) \in \mathcal{R}^{n_E \times n_E}$ is the system matrix, $B_E(p) \in \mathcal{R}^{n_E \times l}$ is the input matrix and $x_E \in \mathcal{R}^{n_E}$ is the state vector. In the thermal part governed by ordinary differential Equation (1b), which is a set of ordinary differential equations, $B_T(p) \in \mathcal{R}^{n_T \times l}$ is the input matrix, $x_T(p) \in \mathcal{R}^{n_T}$ is the state vector, $A_T(p), E_T(p) \in \mathcal{R}^{n_T \times n_T}$ are system matrices. The tensor $F(p) \in \mathcal{R}^{n_T \times n_E \times n_E}$, which can be considered as n_T slices of n_E by n_E matrices $F_i(p) \in \mathcal{R}^{n_E \times n_E}$, $i = 1, \ldots, n_T$, represents the nonlinear coupling from the electrical part to the thermal part. Denoting the i-mode tensor-matrix product by $\times_i$ [2, 8], the product $F(p) \times_2 x_E(p) \times_3 x_E(p)$ is a vector of length n_T, whose i-th component is the standard vector-matrix-vector product $x_E(p)^T F_i(p) x_E(p)$. In the output part (1d), $D \in \mathcal{R}^{m \times l}$ represents the feed through, and $C_E(p) \in \mathcal{R}^{m \times n_E}$ and $C_T(p) \in \mathcal{R}^{m \times n_T}$ represent the output matrices corresponding to the electrical part and the thermal part, respectively. In this formulation, some weak factors are ignored, e.g., the Joule heating related to the input variables and the coupling from the thermal part to the electrical part. System (1b) shows that the system has a one-way coupling from the electrical part to the thermal part through the tensor $F(p)$, and the coupling the other way round is ignored. All parametric matrices in system (1) are of the form

$$Y(p) = Y_c + pY_v, \quad Y \in \{A_E, A_T, B_E, B_T, C_E, C_T, D, E_T, F\}. \tag{2}$$

In our numerical tests, p represents a single parameter σ, the conductivity of the third metal layer.

3. KRYLOV-TYPE PMOR METHODS

Krylov-type pMOR methods belong to projection-type pMOR methods. To reduce a general parametric linear system of order n:

$$\left(G_0 + p_1 G_1 + p_2 G_2 + \ldots + p_q G_q\right) X = Pu, \tag{3}$$

where $G_i \in \mathcal{R}^{n \times n}$ $(0 \leq i \leq q)$, $P \in \mathcal{R}^{n \times l}$ and $u \in \mathcal{R}^l$, a projection-type pMOR method generates a basis $V \in \mathcal{R}^{n \times k}$ for an order-n system, with which we can build an order-k pROM of the form

$$\left(\hat{G}_0 + p_1 \hat{G}_1 + p_2 \hat{G}_2 + \ldots + p_l \hat{G}_q\right) \hat{X} = \hat{P}u, \tag{4}$$

where $\hat{G}_i = V^T G_i V$ and $\hat{P} = V^T P$ [4]. Different projection-type pMOR methods vary in the way of constructing V. In this paper, we use the Krylov-type method proposed in [3], which matches the dominant multi-moments to a certain order implicitly in a numerically stable manner.

To reduce the electro-thermal system (1), we need to conduct pMOR on both (1a) and (1b). Since system (1a) can easily be rearranged into form (3), Krylov-type pMOR methods can be directly applied to compute a basis V_E and the corresponding pROM. To reduce system (1b), however, we have to conduct the Laplace transform first to obtain a frequency domain representation. Following the approach presented in [6], we first ignore the nonlinear part in system (1b) and conduct the Laplace transform to obtain its frequency domain representation

$$\left(A_1 + \sigma A_2 - s E_1 - (\sigma s) E_2\right) X = \begin{bmatrix} B_1 & B_2 & A_1 x_T^0 & A_2 x_T^0 \end{bmatrix} \begin{bmatrix} -U^T & -\sigma U^T & \dfrac{-1}{s} & \dfrac{-\sigma}{s} \end{bmatrix}^T, \tag{5}$$

where X and U represent the Laplace transforms of the state vector $x_T(p, t)$ and the input vector u, respectively, and s and σ denote the radial frequency and the conductivity, respectively. System (5) can be reduced by the pMOR method in [3] with $G_0 \leftarrow A_1$, $G_1 \leftarrow A_2$, $G_3 \leftarrow -E_1$, $G_4 \leftarrow -E_2$, $p_1 \leftarrow \sigma$, $p_2 \leftarrow s$, $p_3 \leftarrow \sigma s$, and $P = [B_1\ B_2\ A_1 x_T^0\ A_2 x_T^0]$. Denote the basis built for (5) by V_T. To obtain a pROM for (1b), we approximate x_E by $V_E \hat{x}_E$ and x_T by $V_T \hat{x}_T$, and then force the approximation error to be orthogonal to the range of V_T. The resulting pROM is

$$\hat{E}_T(p) \dot{\hat{x}}_T(p, t) = \hat{A}_T(p) \hat{x}_T(p, t) + \hat{B}_T(p) u + \hat{F}(p) \times_2 \hat{x}_E(p) \times_3 \hat{x}_E(p), \tag{6}$$

where $\hat{E}_T(p) = V_T^T E_T(p) V_T$, $\hat{A}_T(p) = V_T^T A_T(p) V_T$, $\hat{B}_T(p) = V_T^T B_T(p)$, $\hat{F}(p) = F(p) \times_1 V_T \times_2 V_E \times_3 V_E$. To obtain the reduced tensor $\hat{F}(p)$, we first approximate $x_E(p)$ in the range of V_E, and then project the approximation onto the test subspace V_T, i.e., the tensor product $\hat{F}(p) \times_2 \hat{x}_E(p) \times_3 \hat{x}_E(p)$ equals $V_T^T [F(p) \times_2 (V_E \hat{x}_E(p)) \times_3 (V_E \hat{x}_E(p))]$. The advantage of the tensor formulation for the ROM is that using the reduced tensor, evaluating the ROM does not require computations with quantities of the order of the FOM. In our actual computations, the parametric matrices in the ROM are computed by

$$\hat{Y}(p) = \hat{Y}_c + p \hat{Y}_v, \quad \hat{Y} \in \left\{ \hat{A}_T, \hat{B}_T, \hat{C}_T, \hat{E}_T, \hat{F} \right\}, \tag{7}$$

where $\hat{Y}_c$ and $\hat{Y}_v$ are pre-computed at the construction of the pROM.

4. PROM-BASED UQ

UQ methods can be categorized into non-intrusive methods and intrusive methods [9]. Non-intrusive methods conduct UQ by solving the original deterministic system, e.g., system (1), at various parameter points. Intrusive methods, however, require building a large-scale coupled system, which is often of a much higher order than the original deterministic system. In this paper, we focus on non-intrusive methods since the pROM of the original deterministic model (FOM) can be directly used to replace the FOM in UQ. We embed our pROMs into two UQ methods, namely the Latin hypercube sampling (LHS) method and the stochastic collocation (SC) method.

- LHS [7]. To obtain n samples, LHS divides the input distribution into n intervals of equal probability, and selects one sample randomly in each interval. The mean and standard deviation of the samples are used to approximate those of the original continuous model. Compared to the standard Monte-Carlo sampling, LHS ensures a set of evenly distributed samples.

- SC [9]. Since the mean and the standard deviation can be computed via numerical integration, SC uses a quadrature rule to present the relevant integrals as a weighted sum of the corresponding function values at the collocation points. As we conduct UQ on a single normally-distributed random variable, we use the Gauss-Hermite quadrature rule.

The computationally dominant part of both LHS and SC is the simulation of the high-order FOM at all sampled points p_i. Since our pROMs are highly accurate for these simulations as we will show in §5, pROM-based UQ replaces the FOM (1) with pROMs for these simulations to achieve a significant speedup.

5. NUMERICAL TESTS

In this section, we test the effectiveness and efficiency of pROM-based UQ. All codes are implemented in MATLAB®. For the SC method, we use the SGMGA library [5] to compute the quadrature rule. For tensor computations, we use the Tensor Toolbox [1, 2].

First, we check the quality of the pROMs in a simulation analysis. For (1), we build an order-2 pROM for the order-1660 FOM of the electrical part (1a), and an order-50 pROM for the order-11556 FOM of the thermal part (1b). Both pROMs are built at the interpolation point $\sigma = 3 \times 10^7$ S/m with the radial frequency shifts $s_i = \frac{(i-1) \times 10^8}{9}$ rad/s ($i = 1, 2, \ldots, 10$). Figure 2 shows the relative error for thermal fluxes for $\sigma = 10$ S/m and $\sigma = 10^{11}$ S/m, which are extreme points far away from the interpolation point $\sigma = 3 \times 10^7$ S/m. When the system starts, the relative errors are high because: 1) the thermal fluxes are close to zero since the system is hardly heated up; 2) the thermal outputs are dominated by modeling error and numerical error at the starting stage:
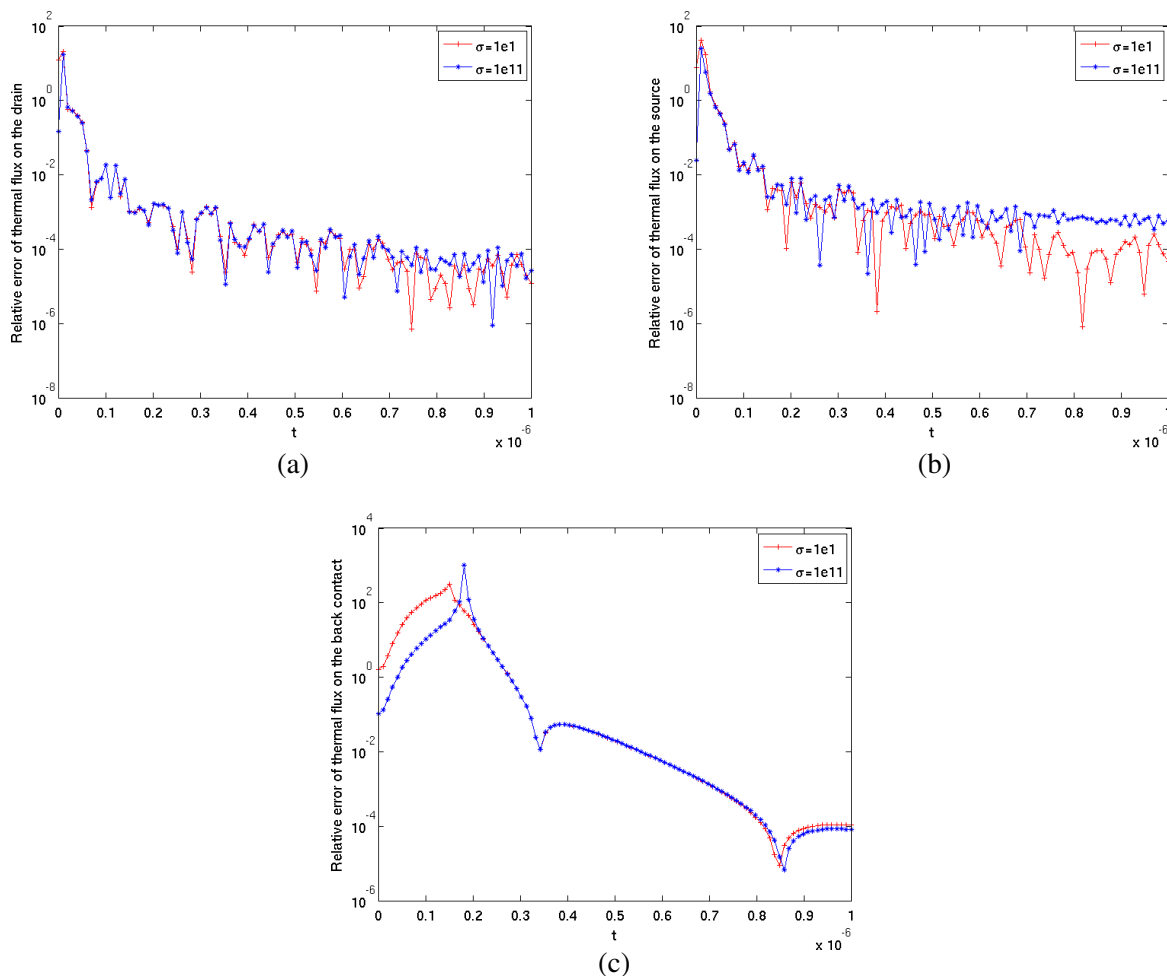

Figure 2: The evolution of the relative errors of the thermal outputs for extreme σ's at $t = 10^{-6}$ s. (a) Relative error of the thermal flux on the drain. (b) Relative error of the thermal flux on the source. (c) Relative error of the thermal flux on the back contact.

the outputs of the FOM also oscillate slightly around zero even when the temperature is the same everywhere and no voltage excitation is imposed. However, as time elapses, the relative errors decrease to the order of 10^{-4} and therefore, the dominant dynamics are accurately captured over a large parameter range.

Now we apply the pROMs to UQ analysis of the electro-thermal system (1). Here we conduct UQ on the outputs at $t = 10^{-6}$ s. We assume that the conductivity obeys the normal distribution $\mathcal{N}(3 \times 10^7, (10^7)^2)$. The numerical results in Table 1 show that for both UQ methods, pROM-based UQ computes highly accurate means ($E(\cdot)$). For the nontrivial electrical outputs I_{drain} and I_{source}, which are sensitive to the change in the conductivity with the same coefficient of variation (CV) of 33.23%, the standard deviations ($\sigma(\cdot)$) are also computed with high accuracy. The thermal outputs ϕ_{drain}, ϕ_{source} and ϕ_{back}, however, are insensitive to the change in the conductivity with CV's of 3.77e-07, 4.4138e-07 and 2.3483e-08, respectively. Although the standard deviations to these insensitive thermal outputs are not of so high accuracy, the relative orders are correct.

Table 1: UQ results for the outputs at $t = 10^{-6}$ s.

	LHS using FOM	LHS using ROM	SC using FOM	SC using ROM
$E(I_{\text{drain}})$	7.4621e-04	7.4621e-04	7.4602e-04	7.4602e-04
$\sigma(I_{\text{drain}})$	2.4794e-04	2.4794e-04	2.4867e-04	2.4867e-04
$E(I_{\text{source}})$	-7.4621e-04	-7.4621e-04	-7.4602e-04	-7.4602e-04
$\sigma(I_{\text{source}})$	2.4794e-04	2.4794e-04	2.4867e-04	2.4867e-04
$E(I_{\text{back}})$	0	0	0	0
$\sigma(I_{\text{back}})$	0	0	0	0
$E(\phi_{\text{drain}})$	5.8479e-04	5.8478e-04	5.8479e-04	5.8479e-04
$\sigma(\phi_{\text{drain}})$	1.5838e-10	1.5677e-10	1.5985e-10	1.5719e-10
$E(\phi_{\text{source}})$	4.1977e-04	4.1975e-04	4.1977e-04	4.1977e-04
$\sigma(\phi_{\text{source}})$	1.8528e-10	9.1986e-11	4.6370e-11	9.2124e-11
$E(\phi_{\text{back}})$	6.6781e-07	6.6773e-07	6.6781e-07	6.6781e-07
$\sigma(\phi_{\text{back}})$	1.5682e-14	1.7778e-14	1.1199e-14	1.6189e-14
Number of sampled points	100	100	11	11
CPU time	6001.14 s	94.19 s	733.64 s	30.51 s

REFERENCES

1. Bader, B. W. and T. G. Kolda, "Efficient MATLAB computations with sparse and factored tensors," *SIAM Journal on Scientific Computing*, Vol. 30, 205–231, 2007.

2. Bader, B. W., T. G. Kolda, et al., "Matlab tensor toolbox version 2.6," available online, Feb. 2015.

3. Benner, P. and L. Feng, "A robust algorithm for parametric model order reduction based on implicit moment matching," *Reduced Order Methods for Modeling and Computational Reduction*, A. Quarteroni and G. Rozza, eds., Vol. 9 of *MS&A — Modeling, Simulation and Applications*, 159–185, Springer International Publishing, 2014.

4. Benner, P., S. Gugercin, and K. Willcox, "A survey of model reduction methods for parametric systems," Max Planck Institute Magdeburg, Preprint MPIMD/13-14, MPI-Magdeburg, Aug. 2013, available from http://www.mpi-magdeburg.mpg.de/preprints/.

5. Burkardt, J., "SGMGA: Sparse grid mixed growth anisotropic rules," http://people.sc.fsu.edu/~jburkardt/m_src/sgmga/sgmga.html.

6. Chen, Y., "Model order reduction for nonlinear systems," Master's Thesis, Massachusetts Institute of Technology, 1999.

7. Helton, J. and F. Davis, "Latin hypercube sampling and the propagation of uncertainty in analyses of complex systems," *Reliability Engineering & System Safety*, Vol. 81, 23–69, 2003.

8. Kolda, T. G. and B. W. Bader, "Tensor decompositions and applications," *SIAM Review*, Vol. 51, 455–500, 2009.

9. Le Maître, O. and O. Knio, *Spectral Methods for Uncertainty Quantification: With Applications to Computational Fluid Dynamics, Scientific Computation*, Springer, Netherlands, 2010.

10. Spirito, P., G. Breglio, V. d'Alessandro, and N. Rinaldi, "Thermal instabilities in high current power MOS devices: Experimental evidence, electro-thermal simulations and analytical modeling," *23rd International Conference on Microelectronics, MIEL*, Vol. 1, 23–30, 2002.

11. Zhang, Z., I. Elfadel, and L. Daniel, "Uncertainty quantification for integrated circuits: Stochastic spectral methods," *IEEE/ACM International Conference on Computer-Aided Design (ICCAD)*, 803–810, 2013.

Broadband Analysis Including Beam Steering of Phased Array Antennas by Order Reduction

O. Floch, **A. Sommer**, **O. Farle**, and **R. Dyczij-Edlinger**

Chair for Electromagnetic Theory, Saarland University, Saarbrücken D-66123, Germany

Abstract— This paper combines projection-based model-order reduction and the empirical interpolation method to generate an efficient numerical procedure for analyzing electrically large antenna arrays at the fields level. The method handles arbitrary aperture illuminations over wide frequency bands and yields both circuit parameters and farfield patterns. A numerical example demonstrates the benefits of the suggested approach.

1. INTRODUCTION

Phased antenna arrays are capable of producing a variety of beam forms over a wide range of scan angles, over wide frequency bands. Ideally, their farfield patterns are obtained as the product of element and array factors. In practice, however, parasitic coupling of antenna elements causes deviations in the farfield patterns, or even to scan blindness. Moreover, resonant radiators get detuned, and input impedances vary across the array.

Numerical fields simulation methods, such as the finite-element (FE) method, include such parasitic effects but tend to be very time-consuming: The large electric size and number of radiators of typical antenna arrays lead to FE matrices of large dimension and large numbers of right-hand sides (RHS). When iterative solvers are employed, the availability of efficient preconditioners is of utmost importance. For electrically large structures, domain decomposition (DD) methods have proven to be highly effective. Still, solving the large-scale FE system remains expensive, particularly when broad frequency bands are to be covered.

To reduce computational efforts, we propose a two-step model order reduction (MOR) approach similarly to [1, 2], but with the focus on electrically large structures: We first construct a reduced-order model (ROM) for the frequency-dependent nearfields and circuit parameters. For this purpose, a multi-point MOR method with self-adaptive expansion point selection [3] is employed. The second step utilizes the empirical interpolation method (EIM) [4] to construct an affine approximation to the nearfield to farfield (NF-FF) operator as a function of frequency f and look angles (θ, ϕ). The resulting model has a small memory footprint, and typical ROM solution times are fractions of a second on a low-cost PC. The proposed method does not only produce circuit parameters (S matrices) but also farfield patterns for arbitrary excitations. It is therefore well-suited for advanced applications such as broadband antenna pattern synthesis. A numerical example is presented to demonstrate the characteristic features of the suggested approach.

2. TIME-HARMONIC BOUNDARY VALUE PROBLEM

In the following, a bounded domain $\Omega \subset \mathbb{R}^3$ with boundary $\partial\Omega$ and outward-unit normal $\hat{\mathbf{n}}$ is considered. The boundary consists of electric walls Γ_E, absorbing boundaries Γ_{ABC}, and T ports $\Gamma_{P_1}, \ldots, \Gamma_{P_T}$. The electric field is denoted by $\mathbf{E}$, the magnetic field by $\mathbf{H}$, the relative magnetic permeability by μ_r, the relative electric permittivity by ϵ_r, and the electric conductivity by σ. The abbreviations k_0 and η_0 stand for the free-space wave number and characteristic impedance, respectively. The excitation of port m is given by the surface current density $\mathbf{K}^m$.

We consider the time-harmonic boundary value problem (BVP)

$$\nabla \times \mu_r^{-1} \nabla \times \mathbf{E} + jk_0\eta_0\sigma\mathbf{E} - k_0^2\epsilon_r\mathbf{E} = \mathbf{0} \qquad \text{in } \Omega, \tag{1a}$$

$$\pi_t(\mathbf{E}) = \mathbf{0} \qquad \text{on } \Gamma_E, \tag{1b}$$

$$\left[\mu_r^{-1}\nabla \times \mathbf{E}\right] = -jk_0\eta_0\mathbf{K}^m \qquad \text{on } \Gamma_{P_m}, \tag{1c}$$

$$\gamma_t\left(\mu_r^{-1}\nabla \times \mathbf{E}\right) - jk_0\sqrt{\tfrac{\epsilon_r}{\mu_r}}\pi_t(\mathbf{E}) = \mathbf{0} \qquad \text{on } \Gamma_{ABC}. \tag{1d}$$

Here, $\gamma_t(\mathbf{E}) := \hat{\mathbf{n}} \times \mathbf{E}$ denotes the tangential trace and $\pi_t(\mathbf{E}) := \hat{\mathbf{n}} \times (\mathbf{E} \times \hat{\mathbf{n}})$ the tangential component trace mapping [5]. The jump operator $[\mathbf{E}]$ is defined by $[\mathbf{E}] : [\mathbf{E}]_{ij} := \gamma_t(\mathbf{E}_i) + \gamma_t(\mathbf{E}_j)$.

3. NUMERICAL APPROXIMATION OF THE BOUNDARY VALUE PROBLEM

Discretizing the BVP (1) by a FE-DD method results in an affinely parametrized linear system of equations [6, 7] of the general form

$$\left(\sum_{i=1}^{I} f_i(k_0)\mathbf{A}_i\right)\mathbf{X}(k_0) = g(k_0)\mathbf{B}, \tag{2}$$

where $\mathbf{X} \in \mathbb{C}^{N \times T}$ denotes the solution matrix. Both the functions $f_i(k_0) : \mathbb{R} \to \mathbb{C}$ and $g(k_0) : \mathbb{R} \to \mathbb{C}$ and the matrices $\mathbf{A}_i \in \mathbb{C}^{N \times N}$ and $\mathbf{B} \in \mathbb{C}^{N \times T}$ are independent of the wavenumber. The matrix $\mathbf{B}$ contains excitation vectors $\mathbf{b}_m$ according to single port excitations, i.e.,

$$\mathbf{B} = [\mathbf{b}_1 \mathbf{b}_2 \dots \mathbf{b}_T] \in \mathbb{C}^{N \times T}. \tag{3}$$

4. MODEL ORDER REDUCTION

Since the block FE-DD system (2) exhibits affine wavenumber-dependence, it is well-suited for projection-based MOR [3]. Let $\mathbf{x}_m(k_0) \in \mathbb{C}^N$ be the solution of the linear system

$$\left(\sum_{i=1}^{I} f_i(k_0)\mathbf{A}_i\right)\mathbf{x}_m(k_0) = g(k_0)\mathbf{b}_m. \tag{4}$$

A multi-point ROM is built from the FE solutions $\mathbf{x}_m(k_0^i)$ of (4) at M expansion points $k_0^1, \dots, k_0^M$, with $M \ll N$. The expansion points k_0^i as well as the excitation vector $\mathbf{b}_m$, for which (4) is solved, are selected adaptively; see Section 4.1. Next, a unitary projection matrix $\mathbf{V} \in \mathbb{C}^{N \times M}$ is computed such that

$$\mathbf{X} \approx \mathbf{V}\tilde{\mathbf{X}} \quad \text{with range}\,(\mathbf{V}) = \text{span}\left\{\mathbf{x}(k_0^i)\right\}, \quad i = 1 \dots M. \tag{5}$$

Then, Galerkin projection leads to a ROM of the form

$$\left(\sum_{i=1}^{I} f_i(k_0)\tilde{\mathbf{A}}_i\right)\tilde{\mathbf{X}}(k_0) = g(k_0)\tilde{\mathbf{B}}, \tag{6}$$

wherein the reduced matrices and vectors are defined as

$$\tilde{\mathbf{A}}_i = \mathbf{V}^*\mathbf{A}_i\mathbf{V} \in \mathbb{C}^{M \times M} \quad \text{with } i = 1 \dots I, \tag{7}$$
$$\tilde{\mathbf{B}} = \mathbf{V}^*\mathbf{B} \in \mathbb{C}^{M \times T}. \tag{8}$$

4.1. Adaptivity

As demonstrated in [8], the 2-norm of the residual $\mathbf{r}_m(k_0)$ of (2) of the ROM solution $\tilde{\mathbf{x}}_m(k_0)$,

$$\mathbf{r}_m(k_0) = g(k_0)\mathbf{b}_m - \left(\sum_{i=1}^{I} f_i(k_0)\mathbf{A}_i\right)\mathbf{V}\tilde{\mathbf{x}}_m(k_0), \tag{9}$$

can be evaluated very efficiently, using reduced-order quantities only. It was suggested in [9] to employ the relative residual norm ρ,

$$\rho(k_0) = \max_{m=1\dots T}\frac{\|\mathbf{r}_m(k_0)\|_2}{\|g(k_0)\mathbf{b}_m\|_2} \quad \text{with } m = 1 \dots T, \tag{10}$$

as an inexpensive error indicator for guiding the placement of the expansion points k_0^i: At a given stage of ROM generation, ρ is evaluated for a dense sampling $\{k_0^s\}$ of the wavenumber interval. The following expansion point is chosen where the relative residual (10) is the largest. ROM generation terminates when ρ has fallen below a user-defined threshold ρ_0 for all k_0^s.

In practice we have $M \ll N$, thus having formed the ROM, the nearfields of the antenna array are computed much more rapidly by solving (6) than the original FE system (2).

5. FARFIELD COMPUTATION

By the vector Huygens principle in the frequency domain [10], the radiation vector $\mathbf{F}$ of an arbitrary antenna array enclosed by a surface S is given by

$$\mathbf{F}(k_0, \hat{\mathbf{r}}) = \hat{\mathbf{r}} \times \oint_S e^{jk_0\hat{\mathbf{r}}\cdot\mathbf{r}'}\mathbf{J}_s(\mathbf{r}', k_0) \, \mathrm{d}S' \times \hat{\mathbf{r}} + \frac{1}{\eta_0} \oint_S e^{jk_0\hat{\mathbf{r}}\cdot\mathbf{r}'}\mathbf{M}_s(\mathbf{r}', k_0) \, \mathrm{d}S' \times \hat{\mathbf{r}}. \quad (11)$$

The unit vector $\hat{\mathbf{r}}$ represents the direction to the observer. The equivalent electric and magnetic surface current densities, $\mathbf{J}_s$ and $\mathbf{M}_s$, are given by

$$\mathbf{J}_s(\mathbf{r}', k_0) = \hat{\mathbf{n}}_s \times \mathbf{H}(\mathbf{r}', k_0) \quad \text{and} \quad \mathbf{M}_s(\mathbf{r}', k_0) = -\hat{\mathbf{n}}_s \times \mathbf{E}(\mathbf{r}', k_0) \quad \text{with } \mathbf{r}' \in S. \quad (12)$$

Herein, $\hat{\mathbf{n}}_s$ denotes the outward-pointing unit normal vector on the Huygens surface S. The farfields $\mathbf{E}_F$ and $\mathbf{H}_F$ are determined from (11) by

$$\mathbf{E}_F(k_0, \mathbf{r}) = -j\eta_0 k_0 \frac{e^{-jk_0 r}}{4\pi r}\mathbf{F}(k_0, \hat{\mathbf{r}}) \quad \text{and} \quad \mathbf{H}_F(k_0, \mathbf{r}) = -jk_0 \frac{e^{-jk_0 r}}{4\pi r}\hat{\mathbf{r}} \times \mathbf{F}(k_0, \hat{\mathbf{r}}). \quad (13)$$

The numerical treatment in terms of ROM quantities by means of the EIM is presented in detail in the companion paper [12].

6. NUMERICAL EXAMPLE

We consider a linear array of $T = 32$ equally spaced, perfectly conducting dipoles in the frequency range $f \in [3, 5]$ GHz. The array is suitable for arbitrary scan angles, including the endfire direction. Since analytic solutions for the element patterns are available, reference results for the ideal array, without mutual coupling, are readily constructed.

The geometry of the FE domain is shown in Fig. 1. On the outer surface absorbing boundary conditions are applied. The dipoles are excited at their centers by lumped ports of impedance $Z_P = 73\,\Omega$. We construct the ROM by the adaptive multi-point-MOR method described in Section 4. The FE-DD system (2) is solved by the restarted GMRES(30) iterative method with stopping criteria $\delta = 10^{-3}$; see [11]. Computational data are listed in Table 1. It can be seen that once the ROM is available, the $\mathbf{S}$ matrix (ROM evaluation for 32 RHS) at any frequency is obtained within half a second; computing the farfields at 40000 look angles takes another 13 s.
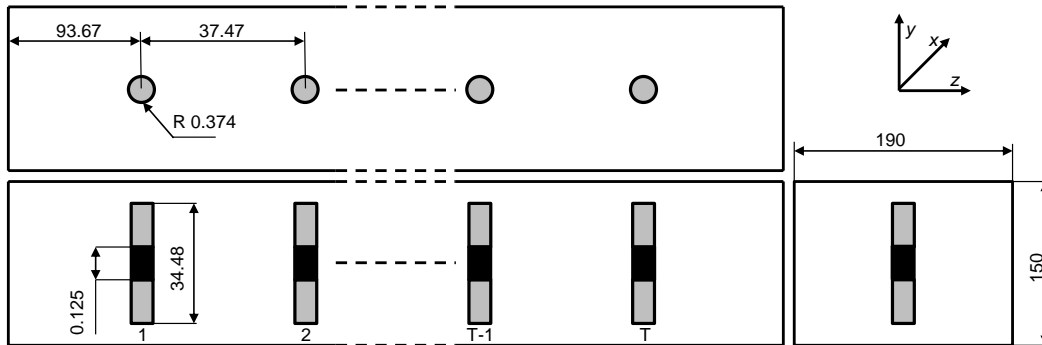
Figure 1: Linear array of dipoles. Black rectangles indicate lumped ports. Dimensions are in mm.

Table 1: Computational data*.

Model	ROM	FE-DD	Stopping criteria
Dimension	300	$4 \cdot 10^6$	-
FE-DD solution for 1 RHS (s)	-	412	-
ROM construction (h)	48	-	10^{-3}
EIM construction (h)	56	-	10^{-3}
ROM evaluation for 32 RHS (s)	$5 \cdot 10^{-1}$	-	-
Farfield evaluation at 40000 look angles (s)	13	300	-

* Matlab prototype code on Intel Core i5-4570 CPU @ 3.2 GHz.

To demonstrate the capabilities of the proposed approach, we consider three types of aperture illuminations: uniform, Dolph-Tschebycheff, and Taylor-n-bar distribution. In the latter cases, the desired side lobe level is set to be $D_s = -20$ dB. Fig. 2–Fig. 4 compare the radiation patterns of the proposed method and analytic pattern multiplication, for broadside ($\theta_s = \frac{\pi}{2}, \phi_s = 0$), intermediate ($\theta_s = \frac{\pi}{4}, \phi_s = 0$), and endfire ($\theta_s = 0, \phi_s = 0$) configurations at $f = 3.8$ GHz. Mutual coupling leads to markable differences in the side lobes and, in the endfire case, even the beamwidth of the main lobe is significantly affected. Fig. 5(a) presents the frequency response of the reflection coefficient for a central and an outer antenna element. Position-dependent detuning is clearly visible. The transmission coefficients between one radiator and its three closest neighbors are shown in Fig. 5(b). As expected, mutual coupling between immediate neighbors is strong and more pronounced at the center of the array than at its edges.
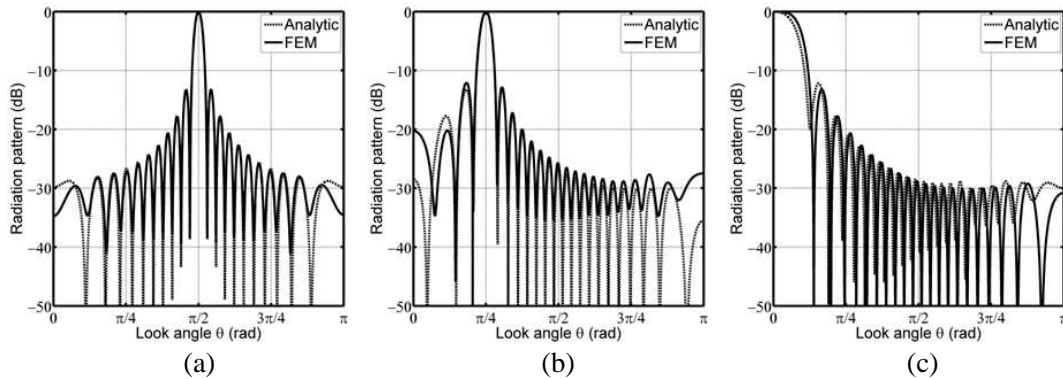
Figure 2: Uniform distribution: farfields plane $\phi = 0$ rad, $f = 3.8$ GHz. (a) Steering angle $\theta_s = \frac{\pi}{2}$ rad. (b) Steering angle $\theta_s = \frac{\pi}{4}$ rad. (c) Steering angle $\theta_s = 0$ rad.
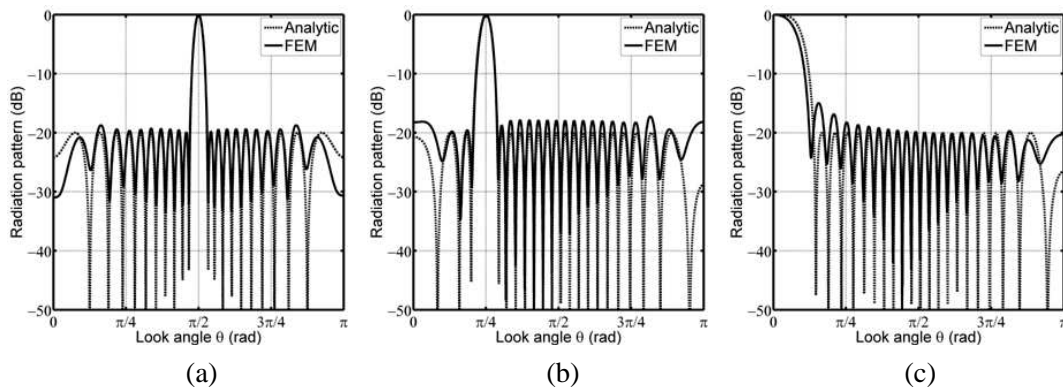
Figure 3: Dolph-Tschebycheff distribution: side lobe level $= -20$ dB, farfields plane $\phi = 0$ rad, $f = 3.8$ GHz. (a) Steering angle $\theta_s = \frac{\pi}{2}$ rad. (b) Steering angle $\theta_s = \frac{\pi}{4}$ rad. (c) Steering angle $\theta_s = 0$ rad.
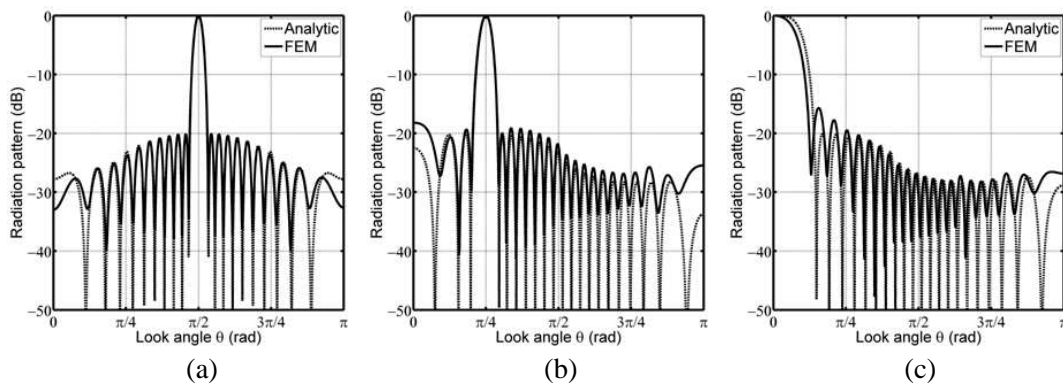
Figure 4: Taylor distribution: $n = 5$, side lobe level $= -20$ dB, farfields plane $\phi = 0$ rad, $f = 3.8$ GHz. (a) Steering angle $\theta_s = \frac{\pi}{2}$ rad. (b) Steering angle $\theta_s = \frac{\pi}{4}$ rad. (c) Steering angle $\theta_s = 0$ rad.
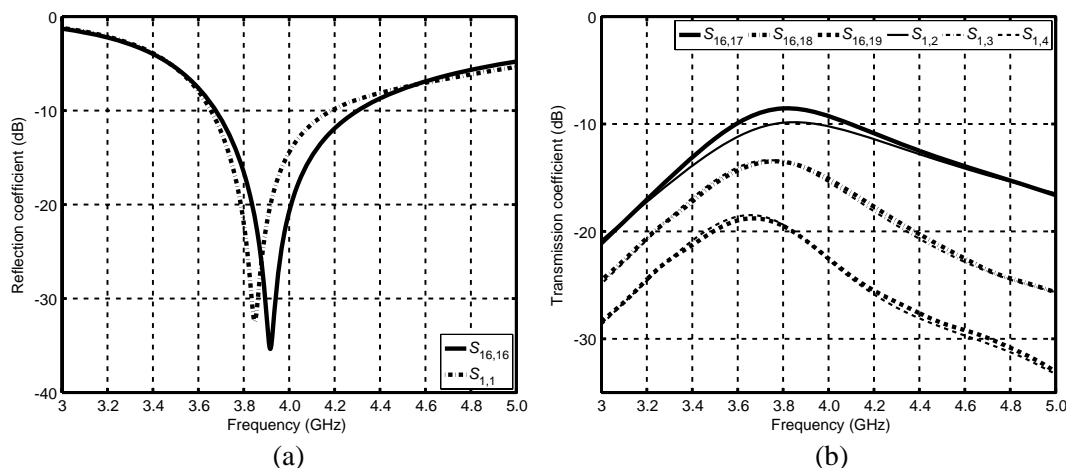
Figure 5: Frequency response of selected scattering parameters. (a) Magnitude of reflection coefficient. (b) Magnitude of transmission coefficient.

7. CONCLUSION AND OUTLOOK

A MOR-based numerical method for characterizing antenna arrays at the fields level has been proposed. It is well-suited for broad frequency bands and allows for arbitrary excitations. Numerical experiments demonstrate the accuracy and efficiency of the suggested approach. Future work will include antenna pattern synthesis, including mutual coupling of antenna elements.

REFERENCES

1. Fares, M., J. S. Hesthaven, Y. Maday, and B. Stamm, "The reduced basis method for the electric field integral equation," *J. Comput. Phys.*, Vol. 230, No. 14, 5532–5555, 2011.
2. Sommer, A., O. Farle, and R. Dyczij-Edlinger, "Efficient finite-element computation of farfields of phased arrays by order reduction," *COMPEL*, Vol. 32, No. 5, 1721–1734, 2013.
3. Rozza, G., D. B. P. Huynh, and A. T. Patera, "Reduced basis approximation and a posteriori error estimation for affinely parametrized elliptic coercive partial differential equations," *Arch. Comput. Methods Eng.*, Vol. 15, No. 3, 229–275, 2008.
4. Barrault, M., Y. Maday, N. C. Nguyen, and A. T. Patera, "An empirical interpolation method: Application to efficient reduced-basis discretization of partial differential equations," *C. R. Math. Acad. Sci. Paris*, Vol. 339, No. 9, 1721–1734, 2013.
5. Buffa, A. and P. Ciarlet, "On traces for functional spaces related to Maxwell's equations. Part I: An integration by parts formula in Lipschitz polyhedra," *Math. Meth. Appl. Sci.*, Vol. 21, 9–30, 2001.
6. Rawat, V. and J.-F. Lee, "Non-overlapping domain decomposition with second order transmission condition for time-harmonic Maxwell's equations," *SIAM J. Sci. Comput.*, Vol. 32, No. 6, 3584–3603, 2010.
7. Floch. O., A. Sommer, O. Farle, and R. Dyczij-Edlinger, "Is model-order reduction viable for the broadband finite-element analysis of electrically large antenna arrays?," Accepted for Publication in *Advances in Radio Science*.
8. Patera, A. T. and G. Rozza, "Reduced basis approximation and a posteriori error estimation for parametrized partial differential equations," *MIT Pappalardo Graduate Monographs in Mechanical Engineering*, Vol. 1, 2006–2007, 2008.
9. De la Rubia, V., U. Razafison, and Y. Maday, "Reliable fast frequency sweep for microwave devices via the reduced-basis method," *IEEE Transactions on Microwave Theory and Techniques*, Vol. 57, No. 12, 2923–2937, 2009.
10. Rothwell, E. and M. Cloud, *Electromagnetics*, 2nd Edition, CRC Press, 2008.
11. Saad, Y. and M. H. Schultz, "GMRES: A generalized minimal residual algorithm for solving nonsymmetric linear systems," *SIAM J. Sci. Stat. Comput.*, Vol. 7, No. 3, 856–869, 1986.
12. Sommer, A., O. Floch, O. Farle, and R. Dyczij-Edlinger, "Parametric near-field-to-far-field transformation by precomputed empirical-interpolation patches," to Appear in *PIERS Proceedings*, 2015.

Parametric Near-field-to-far-field Transformation by Precomputed Empirical-interpolation Patches

A. Sommer, **O. Floch**, **O. Farle**, and **R. Dyczij-Edlinger**

Chair for Electromagnetic Theory, Saarland University, Saarbrücken D-66123, Germany

Abstract— This paper presents an efficient parametric near-field-to-far-field transformation technique for electrically large antenna arrays. The suggested approach combines a sub-domain strategy on the Huygens surface with precomputed empirical-interpolation patches. A real-world example is provided to demonstrate the efficiency and accuracy of the proposed method.

1. INTRODUCTION

Using conventional finite-element (FE) methods, the broadband analysis of antenna arrays and the resulting far-fields tends to be computationally demanding, because the FE systems are of large size and need to be solved at a high number of frequency points. Methods of order-reduction provide an attractive alternative. They need some extra time to construct a reduced-order model (ROM), but the ROM itself is so cheap to solve that evaluation time is usually dominated by the costs of the near-field-to-far-field (NF-FF) transformation. To improve runtimes even further, it was suggested in [1, 2] to replace the steps of field reconstruction on the Huygens surface and subsequent NF-FF transformation by a procedure that computes the far-fields directly from the ROM. For this purpose, an affine approximation to the NF-FF operator is constructed by the empirical interpolation method (EIM) [3]. The suggested approach greatly accelerates the *online* computation of far-fields, at the price of increased *offline* time for constructing the model.

In a previous paper [4], the authors proposed a sub-domain approach on the Huygens surface that allows to restrict the EIM domain to a small number of reference surfaces. Since the sub-face areas are much smaller than that of the entire Huygens surface, the offline part of the EIM is performed much more efficiently. Still, the EIM offline step is not cheap and needs to be done for every antenna structure anew. The present work shows that the offline part of the EIM may be computed upfront, without reference to a specific FE model. The resulting data structures are stored as templates which may be incorporated into ROMs later on, by cheap scaling and compression steps. The proposed method computes an affine approximation to the NF-FF operator for the Huygens surface similarly to [4] and supports fast online computation of far-fields as a function of frequency and observation angles. Section 5 presents a real-world example that demonstrates the efficiency and accuracy of the suggested approach.

2. FAR-FIELD COMPUTATION

2.1. Vector Huygens Principle

By the vector Huygens principle in the frequency domain [5], the radiation vector $\boldsymbol{F}$ of an arbitrary antenna array enclosed by a surface S is given by

$$\boldsymbol{F}\left(k_0, \hat{\boldsymbol{r}}\right) = \hat{\boldsymbol{r}} \times \oint_S e^{jk_0 \hat{\boldsymbol{r}} \cdot \boldsymbol{r}'} \boldsymbol{J}_s\left(\boldsymbol{r}', k_0\right) \mathrm{d}S' \times \hat{\boldsymbol{r}} + \frac{1}{\eta_0} \oint_S e^{jk_0 \hat{\boldsymbol{r}} \cdot \boldsymbol{r}'} \boldsymbol{M}_s\left(\boldsymbol{r}', k_0\right) \mathrm{d}S' \times \hat{\boldsymbol{r}}. \qquad (1)$$

Here η_0 denotes the characteristic impedance of vacuum, the unit vector $\hat{\boldsymbol{r}}$ represents the direction to the observer, and k_0 stands for the vacuum wavenumber, which is related to the vacuum wavelength λ_0 by $k_0 = \frac{2\pi}{\lambda_0}$. The equivalent electric and magnetic surface current densities, $\boldsymbol{J}_s$ and $\boldsymbol{M}_s$, are given in terms of the electric and magnetic near-fields $\boldsymbol{E}$ and $\boldsymbol{H}$ by

$$\boldsymbol{J}_s\left(\boldsymbol{r}', k_0\right) = \hat{\boldsymbol{n}} \times \boldsymbol{H}\left(\boldsymbol{r}', k_0\right) \quad \text{and} \quad \boldsymbol{M}_s\left(\boldsymbol{r}', k_0\right) = -\hat{\boldsymbol{n}} \times \boldsymbol{E}\left(\boldsymbol{r}', k_0\right) \quad \text{with} \quad \boldsymbol{r}' \in S. \qquad (2)$$

Herein, $\hat{\boldsymbol{n}}$ denotes the outward-pointing unit normal vector on the Huygens surface S. The far-fields $\boldsymbol{E}_F$ and $\boldsymbol{H}_F$ are determined from (1) by

$$\boldsymbol{E}_F\left(k_0, \boldsymbol{r}\right) = -j\eta_0 k_0 \frac{e^{-jk_0 r}}{4\pi r} \boldsymbol{F}\left(k_0, \hat{\boldsymbol{r}}\right) \quad \text{and} \quad \boldsymbol{H}_F\left(k_0, \boldsymbol{r}\right) = -jk_0 \frac{e^{-jk_0 r}}{4\pi r} \hat{\boldsymbol{r}} \times \boldsymbol{F}\left(k_0, \hat{\boldsymbol{r}}\right). \qquad (3)$$

2.2. Numerical Near-Field Computation

FE discretization of an array of T antennas results in a linear system of the form

$$\left(\mathbf{A}_0 + k_0\mathbf{A}_1 + k_0^2\,\mathbf{A}_2\right)\mathbf{x}\left(k_0\right) = k_0\sum_{p=1}^{T}\mathbf{b}_p, \tag{4a}$$

$$\mathbf{y}_0\left(k_0\right) = k_0^{-1}\mathbf{C}\,\mathbf{x}\left(k_0\right), \tag{4b}$$

$$\mathbf{y}_1\left(k_0\right) = \mathbf{D}\,\mathbf{x}\left(k_0\right), \tag{4c}$$

where $\mathbf{A}_0, \mathbf{A}_1, \mathbf{A}_2 \in \mathbb{C}^{N\times N}$ denote the stiffness, damping, and mass matrices, respectively, $\mathbf{x}$ is the solution vector in terms of $\boldsymbol{E}$, and N the dimension of the FE system. The output vectors $\mathbf{y}_0 \in \mathbb{C}^{3H}$ and $\mathbf{y}_1 \in \mathbb{C}^{3H}$ hold the values of the equivalent electric and magnetic surface current densities $\boldsymbol{J}_s$ and $\boldsymbol{M}_s$, respectively, sampled at H points on the Huygens surface S. The matrices $\mathbf{C} \in \mathbb{C}^{3H\times N}$ and $\mathbf{D} \in \mathbb{C}^{3H\times N}$ carry out the sampling process. The RHS of (4a) is constructed by a superposition of T linearly independent vectors $\mathbf{b}_p \in \mathbb{C}^N$.

2.3. Numerical Near-Field-to-Far-Field Transformation

Once the equivalent surface current densities on the Huygens surface S have been computed, a post-processing step is necessary to determine the far-fields of the antenna array. Without loss of generality, we just consider the x component of the second integral in (1). Applying a midpoint quadrature rule with H patches of area ΔS_h leads to

$$I_x\left(k_0, \hat{\boldsymbol{r}}\right) = \oint_S e\left(\boldsymbol{r}', k_0, \hat{\boldsymbol{r}}\right) M_{s,x}\left(\boldsymbol{r}', k_0\right)\,\mathrm{d}S' \approx \sum_{h=1}^{H} e\left(\boldsymbol{r}_h', k_0, \hat{\boldsymbol{r}}\right) M_{s,x}\left(\boldsymbol{r}_h', k_0\right)\Delta S_h' \tag{5}$$

with

$$e\left(\boldsymbol{r}', k_0, \hat{\boldsymbol{r}}\right) = e^{jk_0\hat{\boldsymbol{r}}\cdot\boldsymbol{r}'}. \tag{6}$$

We express the direction $\hat{\boldsymbol{r}}$ in terms of the look angles (θ, ϕ) and introduce the parameter vector $\mathbf{p} = (k_0, \theta, \phi) \in \mathcal{D} \subset \mathbb{R}^3$, where $\mathcal{D}$ stands for the considered parameter domain. Given a sampling point $\boldsymbol{r}_h' \in S$, we denote by $\mathbf{D}(\boldsymbol{r}_h') \in \mathbb{C}^{3\times N}$ the corresponding rows of $\mathbf{D}$. By expressing the surface current densities $\boldsymbol{M}(\boldsymbol{r}_h')$ by means of the FE solution $\mathbf{x}(k_0)$ according to (4c) we arrive at

$$I_x\left(\mathbf{p}\right) = \sum_{h=1}^{H} e\left(\boldsymbol{r}_h', \mathbf{p}\right)\mathbf{Q}\left(\boldsymbol{r}_h'\right)\mathbf{x}\left(k_0\right) \qquad \text{with} \quad \mathbf{Q}\left(\boldsymbol{r}_h'\right) = \Delta S_h'\,\mathbf{D}_x\left(\boldsymbol{r}_h'\right),\, \mathbf{Q} \in \mathbb{C}^{H\times N}. \tag{7}$$

3. FAR-FIELD COMPUTATION BY ORDER REDUCTION

3.1. Near-Field Computation by Model Order Reduction

To obtain the equivalent electric and magnetic surface current densities, the large-scale system (4) has to be solved at each operating point k_0 of interest. Our aim now is to bypass this time-consuming procedure by employing a model order reduction (MOR) method: We denote the wavenumber interval under consideration by $\mathcal{D}_k \subset \mathbb{R}$, such that $k_0 \in \mathcal{D}_k$. Thanks to affine parameter-dependence [6] on k_0, the underlying FE model is well-suited for projection-based MOR. The idea of this method is to approximate the FE solution $\mathbf{x}(k_0)$ in a low-dimensional subspace according to

$$\mathbf{x}\left(k_0\right) \approx \hat{\mathbf{x}}\left(k_0\right) = \mathbf{V}\tilde{\mathbf{x}}\left(k_0\right) \qquad\qquad \forall k_0 \in \mathcal{D}_k \tag{8}$$

with $\hat{\mathbf{x}} \in \mathbb{C}^N, \tilde{\mathbf{x}} \in \mathbb{C}^n, \mathbf{V} \in \mathbb{C}^{N\times n}$ and $n \ll N$. For numerical robustness, the columns of the trial matrix $\mathbf{V}$ are chosen to be orthogonal. Substituting the approximation (8) for the FE solution $\mathbf{x}(k_0)$ in (4a) and subsequent testing with $\mathbf{V}^*$ leads to a reduced order model (ROM) of the form

$$\sum_{q=0}^{2} k_0^q\tilde{\mathbf{A}}_q\tilde{\mathbf{x}}\left(k_0\right) = k_0\sum_{i=1}^{T}\tilde{\mathbf{b}}_i, \tag{9a}$$

$$\hat{\mathbf{y}}_0\left(k_0\right) = \tilde{\mathbf{C}}\,\tilde{\mathbf{x}}\left(k_0\right), \tag{9b}$$

$$\hat{\mathbf{y}}_1\left(k_0\right) = k_0^{-1}\tilde{\mathbf{D}}\,\tilde{\mathbf{x}}\left(k_0\right), \tag{9c}$$

wherein the reduced matrices and vectors are given by

$$\tilde{\mathbf{A}}_q = \mathbf{V}^* \mathbf{A}_q \mathbf{V} \qquad \text{with} \quad \tilde{\mathbf{A}}_q \in \mathbb{C}^{n \times n}, \tag{10a}$$

$$\tilde{\mathbf{b}}_i = \mathbf{V}^* \mathbf{b}_i \qquad \text{with} \quad \tilde{\mathbf{b}}_i \in \mathbb{C}^n, \tag{10b}$$

$$\tilde{\mathbf{C}} = \mathbf{C} \mathbf{V} \qquad \text{with} \quad \tilde{\mathbf{C}} \in \mathbb{C}^{3H \times n}, \tag{10c}$$

$$\tilde{\mathbf{D}} = \mathbf{D} \mathbf{V} \qquad \text{with} \quad \tilde{\mathbf{D}} \in \mathbb{C}^{3H \times n}. \tag{10d}$$

Using a multi-point (MP) MOR method, the trial matrix $\mathbf{V}$ is constructed from the FE solutions on a discrete set $\mathcal{D}_{k,e} \subset \mathcal{D}_k$ of expansion points $k_{0,i} \in \mathcal{D}_{k,e}$ such that

$$\text{range}\mathbf{V} = \text{span}\left\{ \mathbf{x}\left(k_{0,1}\right), \ldots, \mathbf{x}\left(k_{0,n}\right) \right\}. \tag{11}$$

To obtain appropriate expansion points, we apply a greedy method with self-adaptive expansion point selection [1]. Since, in practice, $n \ll N$, the ROM (9) is solved much more efficiently than the original FE model (4). Hence, the computational efforts for determining the equivalent surface current densities are greatly reduced.

3.2. NF-FF Transformation by Empirical Interpolation

Substituting the ROM approximation (8) for $\mathbf{x}(k_0)$ in (7) leads to

$$I_x\left(\tilde{\mathbf{x}}\left(k_0\right), \mathbf{p}\right) = \sum_{h=1}^{H} e\left(\mathbf{r}_h', \mathbf{p}\right) \tilde{\mathbf{Q}}\left(\mathbf{r}_h'\right) \tilde{\mathbf{x}}\left(k_0\right) \qquad \text{with} \quad \tilde{\mathbf{Q}} = \mathbf{Q} \mathbf{V}, \tilde{\mathbf{Q}} \in \mathbb{C}^{H \times n}. \tag{12}$$

It can be seen that, even though the solution $\tilde{\mathbf{x}}(k_0)$ of the ROM (9) is used, still $O(H + Hn)$ online operations are required to evaluate (12) for a given parameter point $\mathbf{p} \in \mathcal{D}$. Thus, the complexity of the far-field computation depends on the dimension H of the original FE model (4).

To reduce computational costs, we adopt an approach from [1] and construct an affine approximation to the exponential function (6) by the EIM [3]. In the offline part of this method, a greedy algorithm is applied to determine a set of M basis functions $\{q_m\}_{m=1}^{M}$, interpolation points $\{\mathbf{r}_m'\}_{m=1}^{M}$, and parameter values $\{\mathbf{p}_m\}_{m=1}^{M}$ such that the interpolant defined by

$$\hat{e}\left(\mathbf{r}', \mathbf{p}\right) = \sum_{m=1}^{M} \alpha_m\left(\mathbf{p}\right) q_m\left(\mathbf{r}'\right) \tag{13}$$

approximates (6) for all $(\mathbf{r}', \mathbf{p}) \in S \times \mathcal{D}$. The parameter-dependent coefficients $\{\alpha_m(\mathbf{p})\}_{m=1}^{M}$ are determined online, by solving the lower triangular system

$$[\mathbf{B}_M] \begin{bmatrix} \alpha_1\left(\mathbf{p}\right) \\ \vdots \\ \alpha_M\left(\mathbf{p}\right) \end{bmatrix} = \begin{bmatrix} e\left(\mathbf{r}_1', \mathbf{p}\right) \\ \vdots \\ e\left(\mathbf{r}_M', \mathbf{p}\right) \end{bmatrix} \qquad \text{with} \qquad \mathbf{B}_M = \begin{bmatrix} q_1\left(\mathbf{r}_1'\right) & & \\ \vdots & \ddots & \\ q_1\left(\mathbf{r}_M'\right) & \cdots & q_M\left(\mathbf{r}_M'\right) \end{bmatrix}, \tag{14}$$

which is of complexity $O\left(M^2\right)$. Expressing the interpolant (13) by means of $\mathbf{B}_M{}^{-1}$ leads to

$$\hat{e}\left(\mathbf{r}', \mathbf{p}\right) = \left[q_1\left(\mathbf{r}'\right), \ldots, q_M\left(\mathbf{r}'\right)\right] [\mathbf{B}_M]^{-1} \left[e\left(\mathbf{r}_1', \mathbf{p}\right), \ldots, e\left(\mathbf{r}_M', \mathbf{p}\right)\right]^T = \sum_{m=1}^{M} e\left(\mathbf{r}_m', \mathbf{p}\right) v_m\left(\mathbf{r}'\right). \tag{15}$$

Since we wish to compute the expression (6) on a fixed finite set of sampling points $\{\mathbf{r}_h'\}_{h=1}^{H}$, the determination of the basis functions $\{v_m\}_{m=1}^{M}$ can be performed offline. Thus, in the online part of the EI method, we just need to evaluate (15), which is of complexity $O(M)$. Substituting the approximation (15) for $e(\mathbf{r}', \mathbf{p})$ in (7) results in

$$I_x\left(\tilde{\mathbf{x}}\left(k_0\right), \mathbf{p}\right) = \sum_{m=1}^{M} e\left(\mathbf{r}_m', \mathbf{p}\right) \mathbf{w}_m \tilde{\mathbf{x}}\left(k_0\right) \quad \text{with} \quad \mathbf{w}_m = \sum_{h=1}^{H} v_m\left(\mathbf{r}_h'\right) \tilde{\mathbf{Q}}\left(\mathbf{r}_h'\right), \mathbf{w}_m \in \mathbb{C}^{1 \times n}. \tag{16}$$

Hence, the computational costs of the post-processing step, i.e., the evaluation of (16) for a given parameter point $\mathbf{p} \in \mathcal{D}$, are just of order $O(M + Mn)$. Since in practice we always have $M \ll H$, the far-fields of the antenna array are computed efficiently.
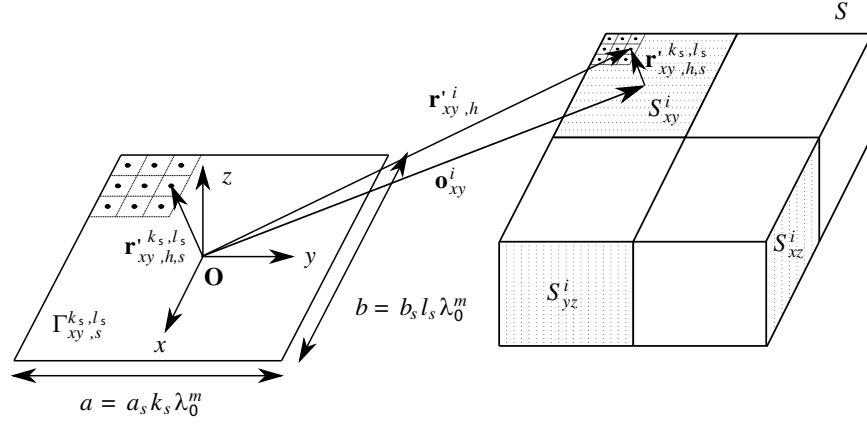
Figure 1: Sub-domain strategy on the Huygens surface S using precomputed EIM patches.

4. NF-FF TRANSFORMATION BY PRECOMPUTED EIM PATCHES

While the online strategy of Section 3.2 for EIM-based far-field computation is of low complexity, the offline part of the method tends to be rather time-consuming, especially when the considered structures become electrically large. As a remedy, we propose to employ precomputed EIM patches rather than to perform the offline part of the EIM for every antenna array anew. For this purpose, the Huygens surface S is taken to be a box, whose surfaces are partitioned into a number of equal sub-faces S_{xy}^i, S_{xz}^i and S_{yz}^i, according to Figure 1:

$$
S = \left(\bigcup_{i=1}^{L_{xy}} S_{xy}^i \right) \cup \left(\bigcup_{i=1}^{L_{xz}} S_{xz}^i \right) \cup \left(\bigcup_{i=1}^{L_{yz}} S_{yz}^i \right). \tag{17}
$$

Without loss of generality, we consider the sub-faces $\{S_{xy}^i\}_{i=1}^{L_{xy}}$ in the xy plane.

4.1. Computation of EIM Patches

We introduce the parameter vector $\mathbf{d} = (\theta, \phi) \in \mathcal{B}$, where $\mathcal{B} = [0, \pi] \times [0, 2\pi)\,\mathrm{rad}^2 \subset \mathbb{R}^2$ denotes the domain of all possible look angles (θ, ϕ), and the normalized vector $\mathbf{r}'_\lambda$, defined by $\mathbf{r}'_\lambda = \frac{1}{\lambda_0}\mathbf{r}'$. With the help of $\mathbf{r}'_\lambda$ and $\mathbf{d}$, the exponential function (6) is rewritten as

$$
e\left(\mathbf{r}'_\lambda, \mathbf{d}\right) = e^{j2\pi\hat{\mathbf{r}}(\mathbf{d})\cdot\mathbf{r}'_\lambda}. \tag{18}
$$

Next, we define two sets of K^2 reference sub-faces $\{\{\Gamma_{xy}^{k,l}\}_{k=1}^K\}_{l=1}^K$ and $\{\{\Gamma_{xy}^{k,l,\lambda}\}_{k=1}^K\}_{l=1}^K$ by

$$
\Gamma_{xy}^{k,l} := \left\{ (x,y,z) \in \mathbb{R}^3 \ \middle| \ -k\frac{\lambda_0}{2} \le x \le k\frac{\lambda_0}{2}, \quad -l\frac{\lambda_0}{2} \le y \le l\frac{\lambda_0}{2}, \quad z = 0 \right\}, \tag{19}
$$

$$
\Gamma_{xy}^{k,l,\lambda} := \left\{ (x,y,z) \in \mathbb{R}^3 \ \middle| \ -\frac{k}{2} \le x \le \frac{k}{2}, \quad -\frac{l}{2} \le y \le \frac{l}{2}, \quad z = 0 \right\}. \tag{20}
$$

Then, we construct the empirical interpolants $\{\{\hat{e}_{xy}^{k,l}\}_{k=1}^K\}_{l=1}^K$ of the exponential function (18) for all $(\mathbf{r}'_\lambda, \mathbf{d}) \in \Gamma_{xy}^{k,l,\lambda} \times \mathcal{B}$ according to

$$
\hat{e}_{xy}^{k,l}\left(\mathbf{r}'_\lambda, \mathbf{d}\right) = \sum_{m=1}^{M_{xy}^{k,l}} e\left(\mathbf{r}'^{k,l,\lambda}_{xy,m}, \mathbf{d}\right) v_{xy,m}^{k,l}\left(\mathbf{r}'_\lambda\right). \tag{21}
$$

Finally, we determine for each $(k,l) \in \{1,\cdots,K\} \times \{1,\cdots,K\}$ two sets of equidistantly sampled points $\Gamma_{d,xy}^{k,l} \subset \Gamma_{xy}^{k,l}$ and $\Gamma_{d,xy}^{k,l,\lambda} \subset \Gamma_{xy}^{k,l,\lambda}$ using an appropriate sampling rate r_s,

$$
\Gamma_{d,xy}^{k,l} = \left\{\mathbf{r}'^{k,l}_{xy,h}\right\}_{h=1}^{H_{xy}^{k,l}} \quad \text{and} \quad \Gamma_{d,xy}^{k,l,\lambda} = \left\{\mathbf{r}'^{k,l,\lambda}_{xy,h}\right\}_{h=1}^{H_{xy}^{k,l}} \quad \text{with} \quad H_{xy}^{k,l} = kl\left(r_s\right)^2, \tag{22}
$$

and compute the basis functions $\left\{v_{xy,m}^{k,l}\right\}_{m=1}^{M_{xy}^{k,l}}$ for all $\mathbf{r}'_\lambda \in \Gamma_{d,xy}^{k,l,\lambda}$ offline.

4.2. Application of Precomputed EIM Patches

Let $a \times b$ be the size of the sub-faces $\{S_{xy}^i\}_{i=1}^{L_{xy}}$, and let the following condition hold for the maximum wavenumber $k_0^m \in \mathcal{D}_k$ and the corresponding wavelength λ_0^m:

$$\max\{a, b\} \leq K\lambda_0^m. \tag{23}$$

We select the reference sub-face $\Gamma_{xy}^{k_s, l_s} \in \{\{\Gamma_{xy}^{k,l}\}_{k=1}^K\}_{l=1}^K$ according to

$$k_s = \left\{ k \in \{1, \cdots, K\} \;\middle|\; \min_k (a \leq k\lambda_0^m) \right\} \quad \text{and} \quad l_s = \left\{ l \in \{1, \cdots, K\} \;\middle|\; \min_l (b \leq l\lambda_0^m) \right\} \tag{24}$$

and determine the scaling factors $a_s = \frac{a}{k_s\lambda_0^m}$ and $b_s = \frac{b}{l_s\lambda_0^m}$. Furthermore, we scale the x and y dimension of the reference sub-face $\Gamma_{xy}^{k_s, l_s}(\lambda_0^m)$ such that

$$\Gamma_{xy,s}^{k_s, l_s} = \left\{ (x, y, z) \in \mathbb{R}^3 \;\middle|\; -a_s k_s \frac{\lambda_0^m}{2} \leq x \leq a_s k_s \frac{\lambda_0^m}{2}, -b_s l_s \frac{\lambda_0^m}{2} \leq y \leq b_s l_s \frac{\lambda_0^m}{2}, z = 0 \right\} \tag{25}$$

fits in the sub-faces $\{S_{xy}^i\}_{i=1}^{L_{xy}}$. Similarly, we determine the scaled sampling points $\Gamma_{d,xy,s}^{k_s, l_s} = \left\{ r_{xy,h,s}^{\prime k_s, l_s} \right\}_{h=1}^{H_{xy}^{k_s, l_s}}$ and interpolation points $\left\{ r_{xy,m,s}^{\prime k_s, l_s} \right\}_{m=1}^{M_{xy}^{k_s, l_s}}$ by

$$r_{xy,h,s}^{\prime k_s, l_s} = \operatorname{diag}(a_s, b_s, 1) \lambda_0^m r_{xy,h}^{\prime k_s, l_s, \lambda} \quad \text{and} \quad r_{xy,m,s}^{\prime k_s, l_s} = \operatorname{diag}(a_s, b_s, 1) \lambda_0^m r_{xy,m}^{\prime k_s, l_s, \lambda}. \tag{26}$$

Given a point $r_{xy,s}^{\prime k_s, l_s}$ on the reference sub-face $\Gamma_{xy,s}^{k_s, l_s}$, the corresponding sampling point $r_{xy}^{\prime i} \in S_{xy}^i$ is obtained by adding a constant translation vector o_{xy}^i according to Figure 1: $r_{xy}^{\prime i} = o_{xy}^i + r_{xy,s}^{\prime k_s, l_s}$. Hence, the exponential function (6) is represented as

$$e\left(r_{xy}^{\prime i}, \mathbf{p} \right) = e\left(o_{xy}^i, \mathbf{p} \right) e\left(r_{xy,s}^{\prime k_s, l_s}, \mathbf{p} \right). \tag{27}$$

Proposition 1. *The empirical interpolant* $\hat{e}_{xy}^{k_s, l_s}\left(r_{xy,s}^{\prime k_s, l_s}, \mathbf{p} \right)$ *defined by*

$$\hat{e}_{xy}^{k_s, l_s}\left(r_{xy,s}^{\prime k_s, l_s}, \mathbf{p} \right) = \sum_{m=1}^{M_{xy}^{k_s, l_s}} e\left(r_{xy,m,s}^{\prime k_s, l_s}, \mathbf{p} \right) v_{xy,m}^{k_s, l_s}\left(r_{xy}^{\prime k_s, l_s, \lambda} \right) \tag{28}$$

with $r_{xy,s}^{\prime k_s, l_s} = \operatorname{diag}(a_s, b_s, 1) \lambda_0^m r_{xy}^{\prime k_s, l_s, \lambda}$ *approximates* (6) *for all* $\left(r_{xy,s}^{\prime k_s, l_s}, \mathbf{p} \right) \in \Gamma_{xy,s}^{k_s, l_s} \times \mathcal{D}$.

Proof. Using the basis functions $\left\{ v_{xy,m}^{k_s, l_s} \right\}_{m=1}^{M_{xy}^{k_s, l_s}}$ and the interpolation points $\left\{ r_{xy,m}^{\prime k_s, l_s, \lambda} \right\}_{m=1}^{M_{xy}^{k_s, l_s}}$ of Section 4.1, the exponential function (18) is approximated by

$$\hat{e}_{xy}^{k_s, l_s}\left(r_\lambda^\prime, \mathbf{d} \right) = \sum_{m=1}^{M_{xy}^{k_s, l_s}} e\left(r_{xy,m}^{\prime k_s, l_s, \lambda}, \mathbf{d} \right) v_{xy,m}^{k_s, l_s}\left(r_\lambda^\prime \right) \tag{29}$$

for all $\left(r_\lambda^\prime, \mathbf{d} \right) \in \Gamma_{xy}^{k_s, l_s, \lambda} \times \mathcal{B}$. The representation

$$e^{j 2\pi \hat{r}(\mathbf{d}) \cdot r_\lambda^\prime} = e^{j 2\pi \hat{r}(\mathbf{d}) \cdot \frac{\lambda_0^m}{\lambda_0^m} r_\lambda^\prime} = e^{j \frac{2\pi}{\lambda_0^m} \hat{r}(\mathbf{d}) \cdot \lambda_0^m r_\lambda^\prime} = e^{j k_0^m \hat{r}(\mathbf{d}) \cdot r^\prime} \tag{30}$$

shows that the empirical interpolant $\hat{e}_{xy}^{k_s, l_s}$ also approximates the exponential function (6) for all $(\mathbf{r}^\prime, \mathbf{p}) \in \Gamma_{xy}^{k_s, l_s}(\lambda_0^m) \times (\{k_0^m\} \times \mathcal{B})$:

$$\hat{e}_{xy}^{k_s, l_s}\left(r^\prime, \mathbf{p} \right) = \sum_{m=1}^{M_{xy}^{k_s, l_s}} e\left(r_{xy,m}^{\prime k_s, l_s}, \mathbf{p} \right) v_{xy,m}^{k_s, l_s}\left(r_\lambda^\prime \right) \quad \text{with} \quad r_{xy,m}^{\prime k_s, l_s} = \lambda_0^m r_{xy,m}^{\prime k_s, l_s, \lambda}, \quad r^\prime = \lambda_0^m r_\lambda^\prime. \tag{31}$$

Using the representations

$$\boldsymbol{r}' = [x, y, z], \tag{32}$$
$$\hat{\boldsymbol{r}} = [\sin(\theta)\cos(\phi), \sin(\theta)\sin(\phi), \cos(\theta)], \tag{33}$$
$$a_x = k_0^m \sin(\theta)\cos(\phi), \tag{34}$$
$$a_y = k_0^m \sin(\theta)\sin(\phi), \tag{35}$$
$$a_z = k_0^m \cos(\theta), \tag{36}$$

the exponential function (30) is rewritten as

$$e^{jk_0^m \hat{\boldsymbol{r}}(\mathbf{d})\cdot\boldsymbol{r}'} = e^{j(k_0^m \sin(\theta)\cos(\phi)x + k_0^m \sin(\theta)\sin(\phi)y + k_0^m \cos(\theta)z)} = e^{j(a_x x + a_y y + a_z z)}. \tag{37}$$

Furthermore, we exploit the fact that the reference sub-face $\Gamma_{xy}^{k_s,l_s}(\lambda_0^m)$ is located in the xy plane: Substituting $\boldsymbol{r}' = (x, y, 0)$ in (37) results in

$$e^{jk_0^m \hat{\boldsymbol{r}}(\mathbf{d})\cdot\boldsymbol{r}'} = e^{j(k_0^m \sin(\theta)\cos(\phi)x + k_0^m \sin(\theta)\sin(\phi)y)} = e^{j(a_x x + a_y y)}. \tag{38}$$

By introducing the parameter domain $\mathcal{M}_{xy}$ defined by

$$\mathcal{M}_{xy} = \left\{ (a_x, a_y, a_z) \in \mathbb{R}^3 \;\middle|\; \sqrt{a_x^2 + a_y^2} \le k_0^m, \quad a_z = 0 \right\} \tag{39}$$

and the vector $\mathbf{a}_{xy} = (a_x, a_y, 0) \in \mathcal{M}_{xy}$, we obtain the EIM approximation to (38):

$$\hat{e}_{xy}^{k_s,l_s}(\boldsymbol{r}', \mathbf{a}_{xy}) = \sum_{m=1}^{M_{xy}^{k_s,l_s}} e\left(\boldsymbol{r}_{xy,m}'^{k_s,l_s}, \mathbf{a}_{xy}\right) v_{xy,m}^{k_s,l_s}(\boldsymbol{r}_\lambda') \qquad \forall (\boldsymbol{r}', \mathbf{a}_{xy}) \in \Gamma_{xy}^{k_s,l_s}(\lambda_0^m) \times \mathcal{M}_{xy}. \tag{40}$$

Finally, we consider (6) for an arbitrary $\mathbf{p} = (k_0, \theta, \phi) \in \mathcal{D}$ with $k_0 = s_k k_0^m$ and $s_k \in [0, 1]$, and the scaled vector $\boldsymbol{r}_s' = \mathrm{diag}(a_s, b_s, 1)\boldsymbol{r}' \in \Gamma_{xy,s}^{k_s,l_s}$ with $a_s \in [0, 1]$ and $b_s \in [0, 1]$:

$$e^{jk_0 \hat{\boldsymbol{r}}(\mathbf{d})\cdot\boldsymbol{r}_s'} = e^{js_k k_0^m \hat{\boldsymbol{r}}(\mathbf{d})\cdot\mathrm{diag}(a_s,b_s,1)\boldsymbol{r}'} = e^{j(s_k a_s a_x x + s_k b_s a_y y)} = e^{js_k \mathrm{diag}(a_s,b_s,1)\mathbf{a}_{xy}\cdot\boldsymbol{r}'}. \tag{41}$$

Since $s_k \mathrm{diag}(a_s, b_s, 1)\mathbf{a}_{xy}$ is included in $\mathcal{M}_{xy}$ and $e(\boldsymbol{r}_s', \mathbf{p}) = e(\boldsymbol{r}', s_k \mathrm{diag}(a_s, b_s, 1)\mathbf{a}_{xy})$, we arrive at the EIM approximation (28):

$$\hat{e}_{xy}^{k_s,l_s}(\boldsymbol{r}_s', \mathbf{p}) = \sum_{m=1}^{M_{xy}^{k_s,l_s}} e\left(\boldsymbol{r}_{xy,m,s}'^{k_s,l_s}, \mathbf{p}\right) v_{xy,m}^{k_s,l_s}(\boldsymbol{r}_\lambda') \quad \forall (\boldsymbol{r}_s', \mathbf{p}) \in \Gamma_{xy,s}^{k_s,l_s} \times \mathcal{D} \tag{42}$$

with $\boldsymbol{r}_s' = \mathrm{diag}(a_s, b_s, 1)\lambda_0^m \boldsymbol{r}_\lambda'$ and $\boldsymbol{r}_{xy,m,s}'^{k_s,l_s} = \mathrm{diag}(a_s, b_s, 1)\lambda_0^m \boldsymbol{r}_{xy,m}'^{k_s,l_s,\lambda}$. $\qquad\square$

Thus it is permissible to use the precomputed basis functions of Section 4.1 and the scaled interpolation points $\left\{\boldsymbol{r}_{xy,m,s}'^{k_s,l_s}\right\}_{m=1}^{M_{xy}^{k_s,l_s}}$ to approximate $e\left(\boldsymbol{r}_{xy,h,s}'^{k_s,l_s}, \mathbf{p}\right)$ for all $\left(\boldsymbol{r}_{xy,h,s}'^{k_s,l_s}, \mathbf{p}\right) \in \Gamma_{d,xy,s}^{k_s,l_s} \times \mathcal{D}$:

$$\hat{e}_{xy}^{k_s,l_s}\left(\boldsymbol{r}_{xy,h,s}'^{k_s,l_s}, \mathbf{p}\right) = \sum_{m=1}^{M_{xy}^{k_s,l_s}} e\left(\boldsymbol{r}_{xy,m,s}'^{k_s,l_s}, \mathbf{p}\right) v_{xy,m}^{k_s,l_s}\left(\boldsymbol{r}_{xy,h}'^{k_s,l_s,\lambda}\right). \tag{43}$$

Substituting (43) in (27), we arrive at the final approximation $\hat{e}_{xy}^i$,

$$\hat{e}_{xy}^i\left(\boldsymbol{r}_{xy,h}'^i, \mathbf{p}\right) = e\left(\boldsymbol{o}_{xy}^i, \mathbf{p}\right) \sum_{m=1}^{M_{xy}^{k_s,l_s}} e\left(\boldsymbol{r}_{xy,m,s}'^{k_s,l_s}, \mathbf{p}\right) v_{xy,m}^{k_s,l_s}\left(\boldsymbol{r}_{xy,h}'^{k_s,l_s,\lambda}\right) \quad \forall \left(\boldsymbol{r}_{xy,h}'^i, \mathbf{p}\right) \in S_{d,xy}^i \times \mathcal{D}, \tag{44}$$

where the set $S_{d,xy}^i = \left\{\boldsymbol{r}_{xy,h}'^i\right\}_{h=1}^{H_{xy}^{k_s,l_s}}$ contains the sampling points on the sub-face S_{xy}^i, which are related to $\boldsymbol{r}_{xy,h,s}'^{k_s,l_s}$ by $\boldsymbol{r}_{xy,h}'^i = \boldsymbol{o}_{xy}^i + \boldsymbol{r}_{xy,h,s}'^{k_s,l_s}$.

Table 1: Computational data for radiation pattern at $f = 10.3\,\text{GHz}$.

General parameters	Frequency range	[9, 11] GHz
	Dimension of Huygens box $a_S \times b_S \times c_S$	$0.2 \times 0.0316 \times 0.2\,\text{m}^3$
	Number of look angles P	57,121
	Sampling rate r_s (per λ_0^m)	20
Conventional method	FE dimension N	2,088,966
	Number of sampling points H	57,330
	Time[1,2] for solving FE system (4a)	58.14 s
	Time[1] for NF-FF transformation for a given $\mathbf{p} \in \mathcal{D}$	$3.062 \cdot 10^{-2}$ s
Proposed method	ROM dimension n	9
	Number of precomputed EIM-patches K^2	100
	Number of sub-faces L_{xy}, L_{xz}, L_{yz}	4, 2, 4
	Selected reference sub-faces $\Gamma_{xy}^{k_s,l_s}, \Gamma_{xz}^{k_s,l_s}, \Gamma_{yz}^{k_s,l_s}$	$\Gamma_{xy}^{8,1}, \Gamma_{xz}^{8,8}, \Gamma_{yz}^{1,8}$
	Scaling factors (a_s, b_s) for xy plane	$(0.9173, 0.5794)$
	Scaling factors (a_s, c_s) for xz plane	$(0.9173, 0.9173)$
	Scaling factors (b_s, c_s) for yz plane	$(0.5794, 0.9173)$
	Number of EIM interpolation points M_t	2,760
	Time[1] for solving ROM (9a)	$4.566 \cdot 10^{-5}$ s
	Time[1] for NF-FF transformation for a given $\mathbf{p} \in \mathcal{D}$	$1.73 \cdot 10^{-3}$ s
	Average error e_D	$1.306 \cdot 10^{-4}$

[1]MATLAB R2012a on Intel® Core™ i7-2600K CPU @ 3,40 GHz.
[2]Intel® MKL 10.2.1 PARDISO for solving sparse linear systems of equations.

4.3. Far-Field Computation by Precomputed EIM Patches

Using the solution (8) and the sampling points $\left\{ S_{d,xy}^i \right\}_{i=1}^{L_{xy}}$ on the sub-faces $\left\{ S_{xy}^i \right\}_{i=1}^{L_x y}$, we obtain

$$I_{x,xy}\left(\tilde{\mathbf{x}}\left(k_0\right), \mathbf{p}\right) = \sum_{i=1}^{L_{xy}} \sum_{h=1}^{H_{xy}^{k_s,l_s}} e\left(\boldsymbol{r}_{xy,h}^{\prime i}, \mathbf{p}\right) \tilde{\mathbf{Q}}\left(\boldsymbol{r}_{xy,h}^{\prime i}\right) \tilde{\mathbf{x}}\left(k_0\right). \tag{45}$$

Substituting (44) for $e\left(\boldsymbol{r}_{xy,h}^{\prime i}, \mathbf{p}\right)$ in (45) leads to the final approximation $\hat{I}_{x,xy}$:

$$\hat{I}_{x,xy}\left(\mathbf{p}\right) = \sum_{i=1}^{L_{xy}} e\left(\boldsymbol{o}_{xy}^i, \mathbf{p}\right) \sum_{m=1}^{M_{xy}^{k_s,l_s}} e\left(\boldsymbol{r}_{xy,m,s}^{\prime k_s,l_s}, \mathbf{p}\right) \left(\sum_{h=1}^{H_{xy}^{k_s,l_s}} v_{xy,m}^{k_s,l_s}\left(\boldsymbol{r}_{xy,h}^{\prime k_s,l_s,\lambda}\right) \tilde{\mathbf{Q}}\left(\boldsymbol{r}_{xy,h}^{\prime i}\right) \right) \tilde{\mathbf{x}}\left(k_0\right). \tag{46}$$

The contributions $\hat{I}_{x,xz}$ and $\hat{I}_{x,yz}$ of the surfaces parallel to the xz and yz planes are obtained in analogous fashion. Hence the approximation $\hat{I}_x$ due to the equivalent surface current densities $M_{s,x}$ on the Huygens surface S is given by

$$\hat{I}_x\left(\mathbf{p}\right) = \hat{I}_{x,xy}\left(\mathbf{p}\right) + \hat{I}_{x,xz}\left(\mathbf{p}\right) + \hat{I}_{x,yz}\left(\mathbf{p}\right). \tag{47}$$

Let $M_t = L_{xy} M_{xy}^{k_s,l_s} + L_{xz} M_{xz}^{k_s,l_s} + L_{yz} M_{yz}^{k_s,l_s}$ denote the total number of EIM interpolation points. Then the online costs for computing the far-field for a given parameter point $\mathbf{p} \in \mathcal{D}$ by (47) are of order $O\left(M_t + M_t n\right)$. If $M_t < H$ holds, which is to be expected in practice, this compares favorably to $O\left(H + Hn\right)$ for the conventional NF-FF transformation.

5. NUMERICAL RESULTS

We consider the FE model of a 10×10 patch antenna array (PAA). The considered frequency band is given by $f \in [9, 11]$ GHz, and the look angles of interest are in the range of $(\theta, \phi) \in [0, \pi] \times [0, \pi]$ rad^2. We construct the ROM (9) of the PAA for $\mathcal{D}_k$ by the MP-MOR method of Section 3.1. According to Section 4, the Huygens surface S is partitioned into $L = L_{xy} + L_{xz} + L_{yz}$ sub-faces, and appropriate empirical interpolants $\hat{e}_{xy}^{k_s,l_s}, \hat{e}_{xz}^{k_s,l_s}, \hat{e}_{yz}^{k_s,l_s}$ are selected by (24). To investigate the accuracy of the proposed method, we consider the average relative error in directive gain $D(k_0, \theta, \phi)$ [7]:

$$e_D\left(k_0\right) = \frac{1}{P} \sum_{p=1}^{P} \left| \frac{D\left(k_0, \theta_p, \phi_p\right) - \hat{D}\left(k_0, \theta_p, \phi_p\right)}{D\left(k_0, \theta_p, \phi_p\right)} \right|. \tag{48}$$

Herein, P denotes the number of considered look angles (θ_p, ϕ_p). Figure 2 shows the radiation pattern of the 10×10 PAA, determined by the combined use of the ROM (9) and the suggested NF-FF transformation technique of Section 4. Computational data are listed in Table 5. It can be seen that the far-field computation time for a given parameter vector $\mathbf{p} \in \mathcal{D}$ is reduced from $58.17\,\mathrm{s}$ to $1.776 \cdot 10^{-3}$, which corresponds to a speed-up factor of more than $3.27 \cdot 10^4$. In addition, the proposed method achieves high accuracy: The average error in directive gain is just $1.306 \cdot 10^{-4}$.
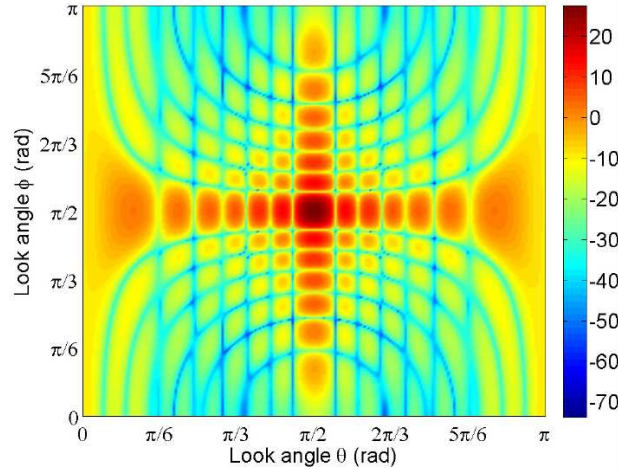

Figure 2: Radiation pattern of the 10×10 PAA at $f = 10.3\,\mathrm{GHz}$, using $P = 57,121$ look angles.

6. CONCLUSION

The proposed MOR approach provides an efficient and accurate method for computing the far-fields of antenna arrays as a function of frequency and observation direction. Since the NF-FF transformation is based on precomputed EIM patches, it is no longer necessary to perform the time-consuming offline part of the EIM for every antenna array anew. The efficiency and accuracy of the suggested method have been demonstrated by a numerical example.

REFERENCES

1. Fares, M., J. S. Hesthaven, Y. Maday, and B. Stamm, "The reduced basis method for the electric field integral equation," *J. Comput. Phys.* , Vol. 230, No. 14, 5532–5555, 2011.
2. Sommer, A., O. Farle, and R. Dyczij-Edlinger, "Efficient finite-element computation of far-fields of phased arrays by order reduction," *COMPEL* , Vol. 32, No. 5, 1721–1734, 2013.
3. Barrault, M., Y. Maday, N. C. Nguyen, and A. T. Patera, "An 'empirical interpolation' method: Application to efficient reduced-basis discretization of partial differential equations," *C. R. Math. Acad. Sci. Paris* , Vol. 339, No. 9, 1721–1734, 2013.
4. Sommer, A., O. Floch, O. Farle, R. Baltes, and R. Dyczij-Edlinger, "An efficient parametric near-field-to-far-field transformation technique," *Proceedings of the 2013 International Conference on Electromagnetics in Advanced Applications*, 332–335, Torino, Italy, September 2013.
5. Rothwell, E. and M. Cloud, *Electromagnetics*, 2nd Edition, CRC Press, 2008.
6. Rozza, G., D. B. P. Huynh, and A. T. Patera, "Reduced basis approximation and a posteriori error estimation for affinely parametrized elliptic coercive partial differential equations," *Arch. Comput. Methods Eng.*, Vol. 15, No. 3, 229–275, 2008.
7. Orfanidis, S., *Electromagnetic waves and antennas*, www.ece.rutgers.edu/~orfanidi/ewa.

Electromagnetic Scattering-matrix Theories Based on Plane Waves and Complex-source Beams

T. B. Hansen

Seknion Inc., Boxford, Massachusetts, USA

Abstract— Two scattering-matrix theories for time-harmonic fields in three dimensions are presented: (i) a plane-wave theory with a directional spectrum that is obtained through a complex-source point substitution procedure, and (ii) a complex-source beam theory based on a beam expansion of spherical multipole fields. Scattering matrices for plane-wave expansions, which determine the plane-wave spectrum of the scattered field of an object due to an incoming plane wave, are readily available. The analogous scattering matrices based on complex-source beams will be derived from Waterman's T matrices. These scattering matrices determine the beam weights for the scattered field in terms of the output of elementary beam receivers, which sample the incident field at complex points in space. The two scattering-matrix formulations will also be compared with Kerns plane-wave theory.

1. INTRODUCTION

Plane waves and complex-source beams constitute complete sets of basis functions for electromagnetic fields in homogeneous source-free regions. From the completeness of these basis functions, we derive exact scattering-matrix theories, which can lead to efficient computation schemes for electromagnetic field transformations in both near and far-field regions. The plane-wave basis functions have sources of infinite extent whereas the complex-source beams have sources of finite extent. Hence, the two types of expansions are distinctly different in many ways.

Figure 1 shows the electromagnetic scattering problem under consideration. The primary source generates the electric field $\mathbf{E}_p(\mathbf{r})$ that interacts with the scatterer to produce the scattered electric field $\mathbf{E}_s(\mathbf{r})$. Multiple interactions between the primary source and the scatterer are neglected. The minimum sphere of radius R_s centered at the origin encloses the scatterer, and the primary source region and the observation region are assumed to be outside this sphere. The global (x, y, z) coordinate system has origin near the scatterer. Further, $\mathbf{r}_p$ is a point in the source region that generates the primary field, and $\mathbf{r}_o$ is a point in the observation region.

The standard rectangular coordinates are denoted by (x, y, z) with unit vectors $\hat{\mathbf{x}}$, $\hat{\mathbf{y}}$, and $\hat{\mathbf{z}}$, so that a general point in space can be expressed as $\mathbf{r} = x\hat{\mathbf{x}} + y\hat{\mathbf{y}} + z\hat{\mathbf{z}}$. The spherical coordinates (r, θ, ϕ) are related to the rectangular coordinates through $x = r\sin\theta\cos\phi$, $y = r\sin\theta\sin\phi$, and $z = r\cos\theta$. The three spherical unit vectors are $\hat{\mathbf{r}} = \sin\theta\cos\phi\hat{\mathbf{x}} + \sin\theta\sin\phi\hat{\mathbf{y}} + \cos\theta\hat{\mathbf{z}}$, $\hat{\boldsymbol{\theta}} =$
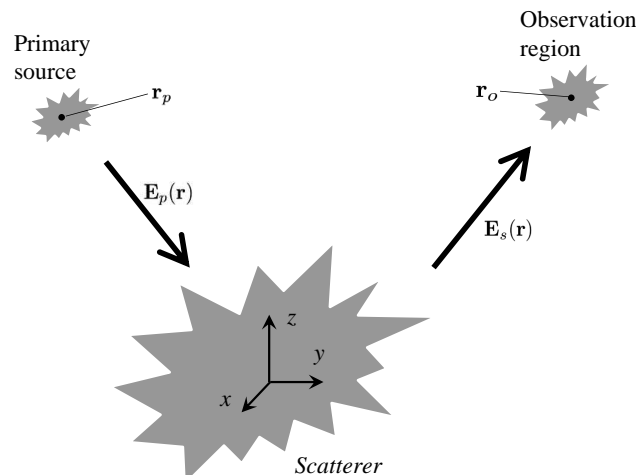

Figure 1: The scattering configuration. The field $\mathbf{E}_p(\mathbf{r})$ of the primary source encounters the scatterer. The scattered field $\mathbf{E}_s(\mathbf{r})$ is observed in the observation region. $\mathbf{r}_p$ is a point in the source region and $\mathbf{r}_o$ is a point in the observation region.

$\cos\theta\cos\phi\hat{\mathbf{x}} + \cos\theta\sin\phi\hat{\mathbf{y}} - \sin\theta\hat{\mathbf{z}}$, and $\hat{\boldsymbol{\phi}} = -\sin\phi\hat{\mathbf{x}} + \cos\phi\hat{\mathbf{y}}$. Throughout, $e^{-i\omega t}$ time dependence with $\omega > 0$ is assumed and suppressed. The wave number is $k = 2\pi/\lambda = \omega/c$, with c being the wave speed and λ the wave length.

2. EXPANSION BASED ON COMPLEX-SOURCE BEAMS

The complex-source beam of the present paper (also referred to as a Gaussian beam) was first obtained by Deschamps [1] by inserting a complex source point $\mathbf{r}' = ia\hat{\mathbf{r}}'$ with $a > 0$ into the scalar free-space Green's function to get

$$G\left(\mathbf{r}, ia\hat{\mathbf{r}}'\right) = \frac{e^{ik\sqrt{(\mathbf{r}-ia\hat{\mathbf{r}}')^2}}}{4\pi\sqrt{(\mathbf{r}-ia\hat{\mathbf{r}}')^2}} \tag{1}$$

where the distance $\sqrt{(\mathbf{r} - ia\hat{\mathbf{r}}')^2}$ is complex with the square root defined to have a non-negative real part and its branch cut placed along the negative real axis [2]. For fixed $\hat{\mathbf{r}}'$ and varying $\mathbf{r}$ the branch cut manifests itself in real 3D space by a branch-cut disk of radius a, centered at the origin with normal $\hat{\mathbf{r}}'$. Hence, the field $G(\mathbf{r}, ia\hat{\mathbf{r}}')$ satisfies the homogeneous Helmholtz equation everywhere except on this branch-cut disk where the sources reside.

The far-field formula (valid for large r)

$$G\left(\mathbf{r}, ia\hat{\mathbf{r}}'\right) \sim \frac{e^{ikr}}{4\pi r} e^{ka\hat{\mathbf{r}}\cdot\hat{\mathbf{r}}'} \tag{2}$$

shows that for $k > 0$ and $a > 0$ the beam radiates most strongly in the direction $\hat{\mathbf{r}}'$ and most weakly in the direction $-\hat{\mathbf{r}}'$. The name "Gaussian beam" is sometimes used because $G(\mathbf{r}, ia\hat{\mathbf{r}}')$ exhibits Gaussian behavior near the direction $\hat{\mathbf{r}}'$: let $\cos\Theta = \hat{\mathbf{r}}\cdot\hat{\mathbf{r}}'$ in (2) to get $G(\mathbf{r}, ia\hat{\mathbf{r}}') \sim [e^{ikr}/(4\pi r)]\, e^{ka(1-\Theta^2/2)}$ when Θ is small.

2.1. The Scattered Field

According to [3, Eq. (38)], the scattered field can be expressed in terms of complex-source beams with beam parameter a_s as ($\int d\Omega'$ denotes the integral over the unit sphere with respect to $\hat{\mathbf{r}}'$)

$$\mathbf{E}_s(\mathbf{r}) = \int d\Omega'\, G(\mathbf{r}, ia_s\hat{\mathbf{r}}')\left[\mathbf{F}_M(\mathbf{r}, ia_s\hat{\mathbf{r}}')W_A\left(\theta',\phi'\right) + \mathbf{F}_N(\mathbf{r}, ia_s\hat{\mathbf{r}}')W_B(\theta',\phi')\right] \tag{3}$$

with

$$\mathbf{F}_M(\mathbf{r}, \mathbf{r}') = \left(\frac{1}{R^2} - \frac{ik}{R}\right)\mathbf{r}' \times \mathbf{r}, \quad R = \sqrt{(\mathbf{r}-\mathbf{r}')^2}, \tag{4}$$

$$\mathbf{F}_N(\mathbf{r}, \mathbf{r}') = \frac{2}{k}\left(\frac{1}{R^2} - \frac{ik}{R}\right)\mathbf{r}' + \left(\frac{3}{R^2} - \frac{3ik}{R} - k^2\right)\frac{\mathbf{r}R\cdot\mathbf{r}' - \mathbf{r}'R\cdot\mathbf{r}}{kR^2}, \quad \mathbf{R} = \mathbf{r} - \mathbf{r}' \tag{5}$$

and

$$W_A(\theta,\phi) = \sum_{\ell=1}^{L}\sum_{m=-\ell}^{\ell} \frac{A_{\ell m}\, Y_{\ell m}(\theta,\phi)}{\sqrt{\ell(\ell+1)}\, ik\, j_\ell(ika_s)}, \quad W_B(\theta,\phi) = \sum_{\ell=1}^{L}\sum_{m=-\ell}^{\ell} \frac{B_{\ell m}\, Y_{\ell m}(\theta,\phi)}{\sqrt{\ell(\ell+1)}\, ik\, j_\ell(ika_s)} \tag{6}$$

where $Y_{\ell m}(\theta,\phi)$ is the spherical harmonic function and $j_\ell(Z)$ is the spherical Bessel function. Also, $A_{\ell m}$ and $B_{\ell m}$ are the spherical expansion coefficients of the scattered field to be determined below. Moreover, for non-resonant scatterers the truncation number is

$$L = \text{int}\left(kR_s + \gamma(kR_s)^{1/3}\right), \quad \gamma = \frac{(-3\ln\mathcal{E})^{2/3}}{2} \tag{7}$$

with $\mathcal{E}$ being the desired relative accuracy, and "ln" and "int" denoting the natural logarithm and integer part, respectively.

2.2. The Primary Field

The spherical expansion coefficients for the standing spherical-wave representation of the primary field can be expressed in terms of the output of elementary complex-point receivers as [3, Eqs. (52)–(53)]

$$C_{\ell m} = \frac{1}{j_\ell(ika_p)} \int d\Omega \mathbf{E}_p(ia_p\hat{\mathbf{r}}) \cdot \mathbf{M}^*_{\ell m}(\theta, \phi), D_{\ell m} = \frac{1}{v_\ell^{(1)}(ika_p)} \int d\Omega \mathbf{E}_p(ia_p\hat{\mathbf{r}}) \cdot \mathbf{N}^*_{\ell m}(\theta, \phi) \quad (8)$$

where $a_p > 0$ is a beam parameter, $*$ denotes complex conjugation, $v_\ell^{(1)}(Z) = \frac{1}{Z}\frac{\partial}{\partial Z}[Zj_\ell(Z)]$, and

$$\mathbf{M}_{\ell m}(\theta, \phi) = \hat{\boldsymbol{\theta}} \frac{im\, Y_{\ell m}(\theta, \phi)}{\sqrt{\ell(\ell+1)}\sin\theta} - \hat{\boldsymbol{\phi}} \frac{\frac{\partial}{\partial\theta}Y_{\ell m}(\theta, \phi)}{\sqrt{\ell(\ell+1)}}, \quad \mathbf{N}_{\ell m}(\theta, \phi) = \hat{\mathbf{r}} \times \mathbf{M}_{\ell m}(\theta, \phi) \quad (9)$$

are the transverse vector-wave functions. The quantity $\mathbf{E}_p(ia_p\hat{\mathbf{r}})$ is the output of a complex-point receiver as explained in [3]; see also Section 2.3 below.

2.3. The Scattering Matrix

The spherical-wave scattering matrix $\bar{\mathbf{\Lambda}}$ (also referred to as Waterman's T-matrix) for a particular scatterer determines the spherical expansion coefficients $A_{\ell m}$ and $B_{\ell m}$ for the scattered field in terms of the spherical expansion coefficients $C_{\ell m}$ and $D_{\ell m}$ for the primary field as [4, 5] (note that [5] defines the scattering matrix in terms of "incoming" and "outgoing" spherical waves rather than the "standing" and "outgoing" spherical waves used here; see [5, Page 46])

$$A_{\ell m} = \sum_{\ell'=0}^{L} \sum_{m'=-\ell'}^{\ell'} \left[\Lambda_{\ell\ell'mm'}^{(AC)} C_{\ell'm'} + \Lambda_{\ell\ell'mm'}^{(AD)} D_{\ell'm'} \right], \quad B_{\ell m} = \sum_{\ell'=0}^{L} \sum_{m'=-\ell'}^{\ell'} \left[\Lambda_{\ell\ell'mm'}^{(BC)} C_{\ell'm'} + \Lambda_{\ell\ell'mm'}^{(BD)} D_{\ell'm'} \right]. \quad (10)$$

Hence, the scattered field can be expressed in terms of the output of elementary complex-point receivers as

$$\mathbf{E}_s(\mathbf{r}) = \int d\Omega'\, G\left(\mathbf{r}, ia_s\hat{\mathbf{r}}'\right) \left[\mathbf{F}_M\left(\mathbf{r}, ia_s\hat{\mathbf{r}}'\right) \int d\Omega''\, \mathbf{Q}_A\left(\hat{\mathbf{r}}', \hat{\mathbf{r}}''\right) \cdot \mathbf{E}_p\left(ia_p\hat{\mathbf{r}}''\right) \right.$$

$$\left. + \mathbf{F}_N(\mathbf{r}, ia_s\hat{\mathbf{r}}') \int d\Omega''\, \mathbf{Q}_B(\hat{\mathbf{r}}', \hat{\mathbf{r}}'') \cdot \mathbf{E}_p(ia_p\hat{\mathbf{r}}'') \right] \quad (11)$$

where the complex-source scattering matrices are given by

$$\mathbf{Q}_A\left(\hat{\mathbf{r}}', \hat{\mathbf{r}}''\right) = \sum_{\ell=1}^{L} \sum_{m=-\ell}^{\ell} \frac{(ik)^{-1}Y_{\ell m}(\theta', \phi')}{\sqrt{\ell(\ell+1)}\, j_\ell(ika_s)} \sum_{\ell'=0}^{L} \sum_{m'=-\ell'}^{\ell'} \left[\Lambda_{\ell\ell'mm'}^{(AC)} \frac{\mathbf{M}^*_{\ell'm'}(\theta'', \phi'')}{j_{\ell'}(ika_p)} + \Lambda_{\ell\ell'mm'}^{(AD)} \frac{\mathbf{N}^*_{\ell'm'}(\theta'', \phi'')}{v_{\ell'}^{(1)}(ika_p)} \right] \quad (12)$$

and $\mathbf{Q}_B(\hat{\mathbf{r}}', \hat{\mathbf{r}}'')$ is given by (12) with $\Lambda_{\ell\ell'mm'}^{(AC)}$ replaced by $\Lambda_{\ell\ell'mm'}^{(BC)}$ and $\Lambda_{\ell\ell'mm'}^{(AD)}$ replaced by $\Lambda_{\ell\ell'mm'}^{(BD)}$. One can derive integral equations from which the complex-source scattering matrices can be computed numerically for a given scatterer without using Waterman's T-matrix.

The Formula (11) expresses the scattered field directly in terms of the output $\mathbf{E}_p(ia_p\hat{\mathbf{r}}'')$ of an elementary complex-point receiver pointing in all directions (in other words, in terms of the incident electric field evaluated at imaginary points of the form $ia_p\hat{\mathbf{r}}''$, where $\hat{\mathbf{r}}''$ covers the unit sphere). The directivity of these receivers ensure that one can neglect directions $\hat{\mathbf{r}}''$ that do not point towards the primary source region. Similarly, the directivity of the transmitting beams in the $\hat{\mathbf{r}}'$ integral ensure that one can neglect directions $\hat{\mathbf{r}}'$ that do not point towards the observation region. Also, note that the scattering matrix contains two free parameters (the disk radii a_p and a_s) that can be used to optimize the efficiency of the scattering calculation. Numerical examples that demonstrate the directional nature of the scalar analog of this scattering-matrix formulation can be found in [6].

Let us briefly discuss how $\mathbf{E}_p(ia_p\hat{\mathbf{r}}'')$ can be obtained through simulations or measurements. If the software used to perform simulations defines the square root to have non-negative real part and its branch cut along the negative real axis (Matlab's square root is defined this way), one simply sets the observation point equal to the imaginary point $ia_p\hat{\mathbf{r}}''$. No further work is needed. If the software defines the square root differently, one must write a new square-root function defined as described above. If the primary field is measured on a sphere centered on the primary source, outgoing spherical expansion coefficients are known. One can then compute $\mathbf{E}_p(ia_p\hat{\mathbf{r}}'')$ directly from the spherical vector-wave function expansion.

3. EXPANSION BASED ON PLANE WAVES

We next derive a scattering-matrix formulation that is based on the directional plane-wave expansion from [7].

3.1. The Scattered Field

We begin by introducing the far-field pattern of the scattered field through the equation

$$\boldsymbol{\mathcal{F}}_s(\hat{\mathbf{r}}) = \lim_{r \to \infty} r \, e^{-ikr} \mathbf{E}_s(r\hat{\mathbf{r}}) \tag{13}$$

and find from [7, Eq. (52)] that

$$\mathbf{E}_s(\mathbf{r}) = \frac{ik}{4\pi} \int d\Omega_k \, \boldsymbol{\mathcal{F}}_s(\hat{\mathbf{k}}) \, e^{i\mathbf{k} \cdot (\mathbf{r} - \mathbf{r}_o)} \, T_{N_o}\left(\hat{\mathbf{k}}, \mathbf{r}_o, \Delta_s\right) \tag{14}$$

where $\int d\Omega_k$ is the integral over the $\mathbf{k}$ unit sphere and

$$T_{N_o}\left(\hat{\mathbf{k}}, \mathbf{r}_o, \Delta_s\right) = e^{k\Delta(\hat{\mathbf{k}} \cdot \hat{\mathbf{r}}_o - 1)} \sum_{n=0}^{N_o} i^n (2n+1) \tilde{h}_n^{(1)}(k\{r_o + i\Delta_s\}) P_n\left(\hat{\mathbf{k}} \cdot \hat{\mathbf{r}}_o\right) \tag{15}$$

is the Gaussian translation operator that results in directional plane-wave spectra; see [7] for details. Further,

$$\tilde{h}_n^{(1)}(Z) = h_n^{(1)}(Z) \, e^{\texttt{Im}(Z)} \tag{16}$$

is a normalized spherical Hankel function and $P_n(Z)$ is the Legendre polynomial. The truncation number N_o, which depends on the beam parameter Δ_s as well as on the size of the scatterer and observation region, can be found from the procedure in [7, Sec. VI] to achieve any desired accuracy. Note that the Gaussian translation operator (15) equals the standard translation operator when the beam parameter Δ_s equals zero.

3.2. The Primary Field

With the far-field pattern of the primary source (with respect to the origin $\mathbf{r}_p$) defined as

$$\boldsymbol{\mathcal{F}}_p(\hat{\mathbf{r}}) = \lim_{r \to \infty} r \, e^{-ikr} \mathbf{E}_p\left(r\hat{\mathbf{r}} - \mathbf{r}_p\right) \tag{17}$$

we find that

$$\mathbf{E}_p(\mathbf{r}) = \frac{ik}{4\pi} \int d\Omega_k \, \boldsymbol{\mathcal{F}}_p(\hat{\mathbf{k}}) \, e^{i\mathbf{k} \cdot \mathbf{r}} \, T_{N_p}\left(\hat{\mathbf{k}}, -\mathbf{r}_p, \Delta_p\right) \tag{18}$$

where the truncation number N_p, which depends on the beam parameter Δ_p as well as on the size of the scatterer and primary source region, can be found from the procedure in [7, Sec. VI]. According to (18), the plane-wave spectrum for the incoming primary field is $[(ik)/(4\pi)]\boldsymbol{\mathcal{F}}_p(\hat{\mathbf{k}}) \, T_{N_p}(\hat{\mathbf{k}}, -\mathbf{r}_p, \Delta_p)$.

3.3. The Scattering Matrix

The far-field plane-wave scattering matrix $\bar{\mathbf{F}}(\hat{\mathbf{k}}', \hat{\mathbf{k}}'')$ determines the scattered far-field pattern in the direction $\hat{\mathbf{k}}'$ when the incident field is a single plane wave $\mathbf{E}_0 \, e^{i\mathbf{k}'' \cdot \mathbf{r}}$ (with the constant vector $\mathbf{E}_0$ satisfying $\mathbf{E}_0 \cdot \mathbf{k}'' = 0$) as

$$\boldsymbol{\mathcal{F}}_s(\hat{\mathbf{k}}') = \bar{\mathbf{F}}(\hat{\mathbf{k}}', \hat{\mathbf{k}}'') \cdot \mathbf{E}_0 \tag{19}$$

which in turn gives the final expression for the scattered field

$$\mathbf{E}_s(\mathbf{r}) = -\frac{k^2}{16\pi^2} \int d\Omega'_k \, e^{i\mathbf{k}' \cdot (\mathbf{r} - \mathbf{r}_o)} \, T_{N_o}(\hat{\mathbf{k}}', \mathbf{r}_o, \Delta_s) \int d\Omega''_k \, T_{N_p}(\hat{\mathbf{k}}'', -\mathbf{r}_p, \Delta_p) \, \bar{\mathbf{F}}(\hat{\mathbf{k}}', \hat{\mathbf{k}}'') \cdot \boldsymbol{\mathcal{F}}_p(\hat{\mathbf{r}}''). \tag{20}$$

In general, a scatterer that is illuminated by a single plane wave will produce plane waves propagating in all directions. Hence, the scattering matrix Formula (20) contains an integral over both incoming plane-wave directions of propagation $\hat{\mathbf{k}}''$ and scattered plane-wave directions of propagation $\hat{\mathbf{k}}'$. The directionality of the Gaussian translation operators ensures that large portions of the $\hat{\mathbf{k}}'$ and $\hat{\mathbf{k}}''$ integration regions can be neglected.

The important special scattering geometry involving a half space was investigated in [8] using the standard translation operator ($\Delta_s = \Delta_p = 0$). The plane-wave scattering matrix for the half space is degenerate in the sense that a single incident plane wave will produce only one scattered plane wave. Therefore, for the half-space scatterer, the Formula (20) simplifies so that it involves only the integral over incoming (or outgoing) plane-wave directions of propagation.

4. CONCLUSIONS

The two scattering-matrix formulations in (11) and (20) will now be compared to Kerns' plane-wave scattering-matrix formulation (one-sided) in which the scattered field is written as [9, Pages 57–61]

$$\mathbf{E}_s(\mathbf{r}) = \int d\mathbf{K}' \, e^{i\mathbf{k}'\cdot\mathbf{r}} \int d\mathbf{K}'' \bar{\mathbf{S}} \left(\mathbf{K}', \mathbf{K}''\right) \cdot \mathbf{T}_p \left(\mathbf{K}''\right) \tag{21}$$

where $\bar{\mathbf{S}}(\mathbf{K}', \mathbf{K}'')$ is Kerns' plane-wave scattering matrix, and $\mathbf{T}_p(\mathbf{K}'')$ is the plane-wave spectrum of the primary field. Moreover, $\mathbf{K}'$ is the transverse part of the plane-wave propagation vector $\mathbf{k}'$ for the scattered field. Similarly, $\mathbf{K}''$ is the transverse part of the plane-wave propagation vector $\mathbf{k}''$ for the primary field. The plane-wave spectrum of the primary field $\mathbf{T}_p(\mathbf{K}'')$ can be thought of as the output of a plane-wave receiver that picks out a single plane-wave component of the primary field.

It is challenging to use the plane-wave expansion (21) in numerical computations that require a preselected accuracy. First, the integrand of the $\mathbf{K}'$ integral has an integrable singularity at $|\mathbf{K}'| = k$ that in many situations necessitates a change of variables [10, Chapter 3]. Second, in general the integrands do not decay until the evanescent regions $|\mathbf{K}'| > k$ and $|\mathbf{K}''| > k$ are reached. In some situations one must integrate all the way into the evanescent regions to avoid strong end-point contributions [7]. Nevertheless, there are some favorable situations where the integrals in (21) can be truncated to include only small regions in the propagating domains without introducing significant errors.

The expansions (11) and (20) have the same structure as (21). However, there are important differences. For example, the regions of integrations in both (11) and (20) are unit spheres whereas it is an infinite planar $\mathbf{K}$ surface in (21). Also, the integrands in (11) and (20) are well-behaved functions on the unit spheres that are directional at high frequencies, so that only parts of the unit spheres need to be included to achieve high accuracy. Hence, from a numerical point of view, the expansions (11) and (20) appear to have distinct advantages.

ACKNOWLEDGMENT

REFERENCES

1. Deschamps, G. A., "Gaussian beam as a bundle of complex rays," *Electron. Lett.*, Vol. 7, 684–685, 1971.
2. Felsen, L. B., "Complex source point solution of the field equations and their relation to the propagation and scattering of Gaussian beams," *Symposia Mathematica*, Vol. 18, 39–56, 1976.
3. Hansen, T. B., "Exact Gaussian-beam theory for outgoing and standing spherical waves: Application to transmitting and receiving antennas," *IEEE Trans. Antennas Propagat.*, Vol. 60, 1291–1302, Mar. 2012.
4. Waterman, P. C., "Matrix formulation of electromagnetic scattering," *Proceedings of the IEEE*, Vol. 53, 805–812, Aug. 1965.
5. Hansen, J. E., J. Hald, F. Jensen, and F. H. Larsen, Eds., *Spherical Near-field Antenna Measurements,* Peter Peregrinus, 1988.
6. Hansen, T. B., "Exact scattering-matrix theory based on Gaussian beams," *J. Acoust. Soc. Am.*, in Review.
7. Hansen, T. B., "Exact plane-wave expansion with directional spectrum: Application to transmitting and receiving antennas," *IEEE Trans. Antennas Propagat.*, Vol. 62, 4187–4198, Aug. 2014.
8. Schmidt, C. H. and T. F. Eibert, "Multilevel plane wave based near-field far-field transformation for electrically large antennas in free-space or above material halfspace," *IEEE Trans. Antennas Propagat.*, Vol. 57, 1382–1390, May 2009.
9. Kerns, D. M., *Plane-wave Scattering-matrix Theory of Antennas and Antenna-antenna Interactions,* NBS Monograph 162, US Government Printing Office, Washington, DC, 1981.
10. Hansen, T. B. and A. D. Yaghjian, *Plane-wave Theory of Time-domain Fields,* IEEE Press, 1999.

Flow Aggregation and Migration Scheme Based on Real-time Monitoring for Time-varying Traffic in Optical Networks

Yuan Wen, Wei Guo, and Weisheng Hu

State Key Laboratory of Advanced Optical Communication Systems and Networks
Shanghai Jiao Tong University, China

Abstract— We propose a flow aggregation and migration (AM) scheme for circuit switched optical networks. In our proposed AM scheme, flows could be aggregated into a lightpath to improve bandwidth utilization and be migrated from heavily loaded lightpath to avoid packet loss. The benefits of improved bandwidth utilization and reduced blocking rate are illustrated through simulation results.

1. INTRODUCTION

Nowadays, the transport network is experiencing a challenge of bulky data transfer for large-scale applications, such as E-science computing, data center data back-ups and cloud services [1]. When these applications require high transmission rate (e.g., 10 GE or more), a lightpath with guaranteed bandwidth provided by optical circuit-switched networks becomes an effective solution to meet application performance requirements, such as bit rate, packet loss and latency. However, the bandwidth of a lightpath is often underutilized. A major reason is that flows generated by applications may have a time-varying bandwidth demands, typically, higher traffic volume during daytime and lower traffic volume at night. If a lightpath is dedicatedly used by a flow, this may lead to bandwidth resource waste when flow rate becomes low.

In order to make better utilization of bandwidth resources, we proposed a flow aggregation method implemented by an extended SDN controller [2]. This method is to aggregate multiple fine-granularity flows into a lightpath, whose bandwidth resources have not been fully utilized. In this way, these flows can share the same lightpath and lightpath bandwidth utilization increases. However, the transmission rates of flows vary frequently over time. If the total transmission rate of the flows exceeds the bandwidth of the lightpath, packet loss will occur and transmission quality of flows will degrade.

In this paper, we propose a flow aggregation and migration scheme (AM) based on real-time monitoring to improve bandwidth utilization while guaranteeing transmission performance of the entire network. Our method is to aggregate some fine-granularity flows (with low-priority) into a lightpath with spare bandwidth resources. To guarantee transmission performance, the low-priority flows will be migrated into another lightpath when bandwidth resources of the original lightpath are used up. Since flow migration needs time, we set a threshold to control the maximal load in the lightpath. Once the overall flow rate exceeds the threshold (but still less than the bandwidth of the flightpath), flow migration will be executed to reduce packet loss. Due to the flexible programmability of SDN controller to flow, we can easily complete the flow aggregation and flow migration. We have tested the performance of our extended controller on our testbed. Experimental results show that our extended controller can migrate a flow from one lightpath into another in 2 seconds, with no influence on data transmission delay and packet loss of the original flow (with high-priority). In addition, we can reduce the packet loss of low-priority flows by reducing the threshold. We also conduct simulations, which illustrate that our AM scheme improves the lightpath bandwidth utilization and reduces the blocking rate.

2. SDN BASED IP OVER OPTICAL NETWORKS ARCHITECTURE

As shown in Figure 1, we proposed an SDN based IP over optical networks architecture, where packets are transmitted by SDN switches, and SDN switches are connected by circuit-switched optical connections. Our extended SDN controller controls the SDN switches via OpenFlow [3]. The management plane of the optical network set up a lightpath based on network resource state and application demands. The extended SDN controller can acquire the information of lightpaths in the form of network abstraction by management plane.

In Figure 1, we assume that a high-priority flow (the red line) is transmitted by a 10 Gbps lightpath between two end-systems with guaranteed bandwidth and packet loss rate. The rate
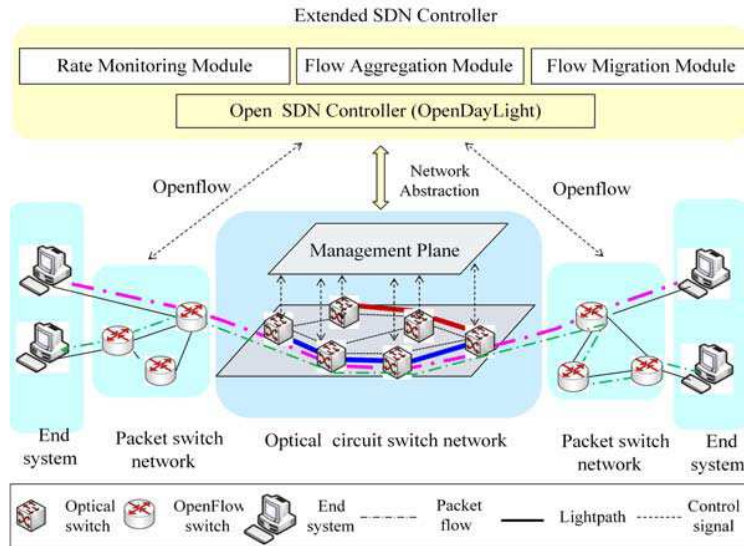
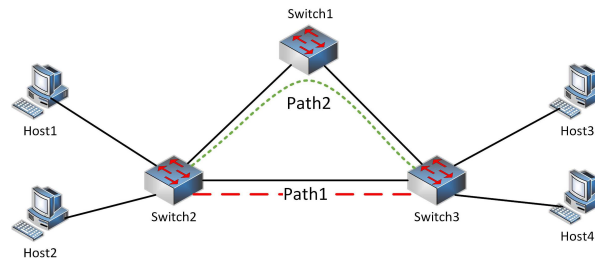Figure 1: SDN based IP over optical networks architecture.

Figure 2: Experiment network topology.

monitoring module will always monitor the transmission rate of all flows, with the assistance of which, the controller could acquire the usage of all lightpaths. When a new low-priority flow (e.g., the green line in Figure 1) arrives, if the lightpath has enough unused bandwidth capacity to transmit the low-priority flow, the controller will use the flow aggregation module to aggregate the low-priority flow into the lightpath in the IP network by configuring flow entry in SDN switch. When the transmission rate of flows increases and finally exceeds the lightpath bandwidth, the rate monitoring module will perceive this event and notify the controller. In order to guarantee transmission performance of the flows, the controller will migrate the low-priority flow from the lightpath into another lightpath which has enough unused bandwidth. If no lightpath could transmit the flow, the management plane of the optical network will set up a new lightpath for the flow.

3. EXPERIMENT ON FLOW MIGRATION TIME

Our extended controller will migrate flow(s) from lightpath when the bandwidth resources are used up to avoid transmission performance decline. However the packet loss will still occur if the transmission rate increases too fast that the controller could not complete the migration of flow in time. Figure 3(b) Illustrates the reason of packet loss, the shaded part represents the lost packets. We define flow migration time as the duration from transmission rate exceeding the lightpath bandwidth to controller accomplishing the migration of flows.

We extend the feature module on the SDN open source controller OpenDayLight [4] and choose Open vSwitch [5] as SDN switch considering its advantages of flexible configuration, low cost, and easy extension. Our experimental network topology is shown in Figure 2, including 4 hosts connected to 3 Open vSwitch through 1 GE interface. High-priority Flow 1 is between Host 1 and Host 3, and low-priority Flow 2 is between Host 2 and Host 4. We use Iperf to transfer UDP flows. In order to guarantee the transmission quality of high-priority Flow 1, we can set priority queue in SDN switch ports, insert the Flow 1 into high-priority queue and insert the Flow 2 into low-priority queue. In this way, the packet loss of Flow 1 will not appear. As shown in Figure 3(a), in Step 1,
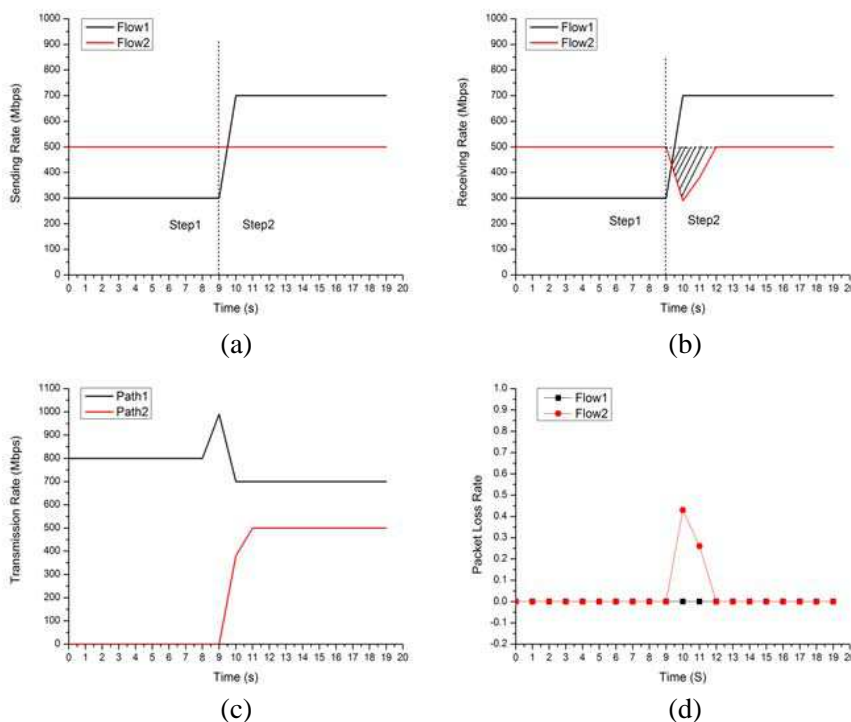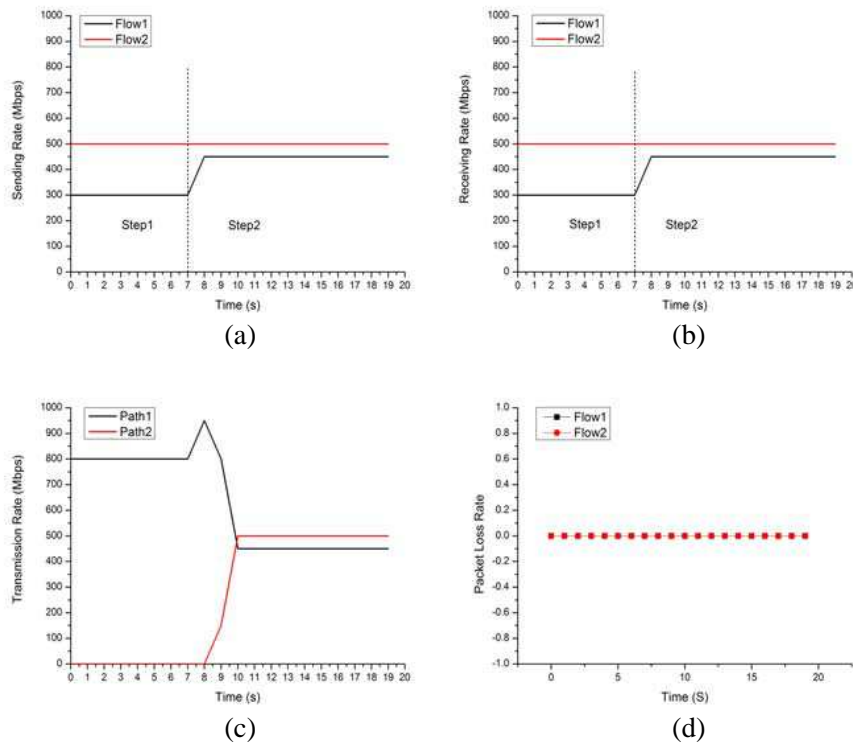
Figure 3: (a) Sending rate of Flow 1 and Flow 2. (b) Receiving rate of Flow 1 and Flow 2. (c) Transmission rate in Path 1 and Path 2. (d) Packet loss rate of Flow 1 and Flow 2.

the send rate of Flow 1 and Flow 2 are 300 Mbps and 500 Mbps respectively, and they share the bandwidth of Path 1 (red line). In Step 2, we increase the send rate of Flow 1 to 700 Mbps, and the total send rate in Path 1 exceeds the bandwidth of Path 1. As we can see in Figure 3(d), Flow 2 has packet loss for two seconds, then it returns to normal because the controller migrates Flow 2 into the Path 2 (green line). This indicates that the extended controller needs about 2 seconds to migrate a flow from one lightpath to another. During the migration, the low-priority flow will have packet loss while the transmission performance of high-priority flow will be guaranteed.

4. AGGREGATION AND MIGRATION SCHEME

Actually, the dynamism of IP convergence flows is smooth, which means that flows rates seldom change rapidly in an instant. To reduce packet loss of low-priority flows, we propose a flow Aggregation and Migration Scheme in the IP-over Optical network. In our scheme, we set a threshold for lightpath, which is a constant used to control the maximal load in the lightpath. When the transfer rate exceeds the threshold, the controller could migrate the flow into another lightpath. As long as the transfer rate does not exceed the bandwidth of lightpath during flow migration (about 2 seconds according to our experiment result), packet loss of low-priority flow could be avoided. We assume that many lightpaths with large bandwidth capacity have already existed for high-priority flow usage, and the transfer rate of the high-priority flows are time-varying. Low-priority request flows arrive dynamically. The workflow is shown as follows.

Step 1: Controller collects information about lightpath.

Step 2: When a new request flow arrives, search the lightpath database to find the lightpaths which have the same source and destination address. Aggregate the flow into one of these lightpaths whose total transmission rate after aggregation does not exceed the threshold. Add the flow into transmission queue and jump to Step 4. If no lightpath is found to aggregate the flow, jump to Step 3.

Step 3: Set up a new lightpath for the request flow and jump to Step 1. If there is no resource available to set up a new lightpath, block the request and jump to Step 2.

Step 4: Acquire the transfer rate of the flows in the transmission queue and update the usage of lightpaths. If the load of a light exceeds the threshold, choose a low-priority flow to migrate. We treat it as a new request flow and jump to Step 2.

5. DEMONSTRATION AND SIMULATION

We deploy an experiment to demonstrate our scheme. The experimental environment is the same as in Section 3. In this experiment, we set the threshold as 90% of path bandwidth capacity. As shown in Figure 4(a), in Step 1, send rates of Flow 1 and Flow 2 are 300 Mbps and 500 Mbps respectively, and they are transmitted normally. In Step 2 we increase the send rate of Flow 1 to 450 Mbps. As shown in Figure 4(d), both flows are also transmitted normally without any packet loss. However,

Figure 4: (a) Sending rate of Flow 1 and Flow 2. (b) Receiving rate of Flow 1 and Flow 2. (c) Transmission rate in Path 1 and Path 2. (d) Packet loss rate of Flow 1 and Flow 2.
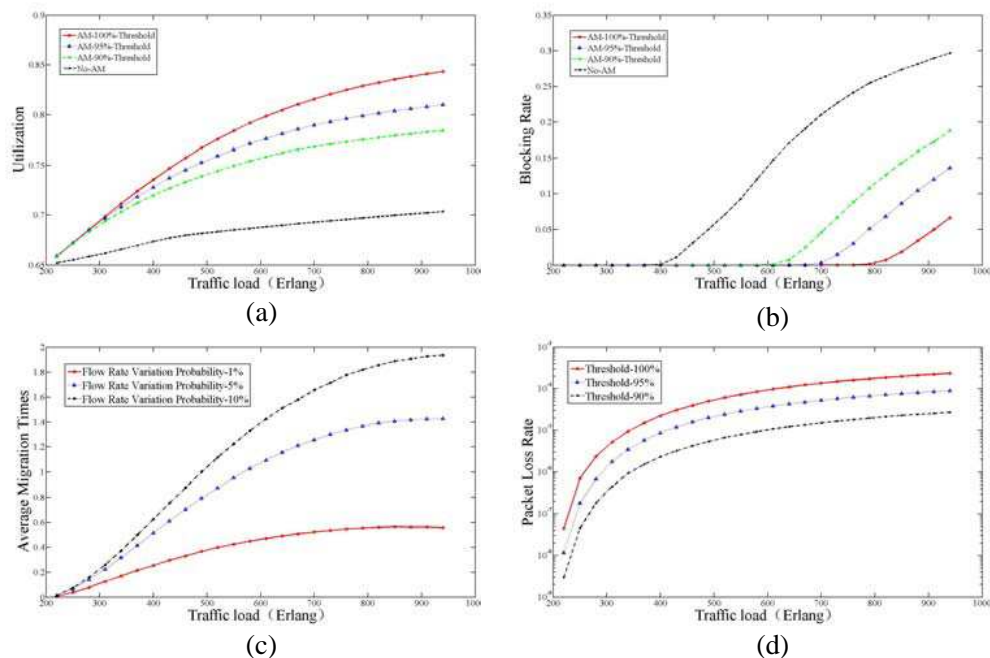

Figure 5: (a) Utlization vs. traffic load. (b) Blocking rate vs. traffic load. (c) Average migration times vs. traffic load. (d) Packet loss rate vs. traffic load.

from Figure 4(c) we can see that Flow 2 has been migrated into Path 2. This experiment results suggests that as long as the total transmission rate does not exceed the lightpath bandwidth, we can migrate a flow from a lightpath into another without any packet loss with the assistance of a pre-specified threshold value.

In order to evaluate our proposed scheme, we conducted simulations over 14-node NSFNET. We assumed that initially each link has a bandwidth of 320 Gbps. 200 lightpaths with 10 Gbps bandwidth has already existed in the network and each lightpath has a high-priority flow. The arrival of requests follows the Poisson distribution with rate λ. Source node and destination node are randomly generated among the 14 nodes. The bandwidth of request low-priority flows is 1 Gbps, and the duration time of the request chosen from an exponential distribution with a mean value of 1000 s. We assume that transmission rate of both high and low priority flow will fluctuate between 50% and 80% of the request bandwidth. If a request cannot be delivered successfully, we consider it to be blocked. We analyze our scheme in terms of lightpath utilization and blocking rate.

Figure 5(a) shows the lightpath utilization rate performance of our AM scheme and traditional bandwidth allocation policy which allocates a single lightpath for every flow under various traffic loads. We observe that our AM scheme increases the lightpath utilization compared to traditional policy. This is because the flow aggregation makes use of unused bandwidth resources of lightpath. and the lightpath utilization increases as the threshold increases. Figure 5(b) shows the blocking rate performance of our AM Scheme and tranditional bandwidth allocation policy under various traffic loads. We can observe that our scheme has lower blocking rate than traditional bandwidth allocation policy. That is because many flow can share same lightpath using our scheme, the network can transmit more request flow. Figure 5(c) shows the average times of migration. We can observe that every flow in the network will be migrated 1.5 times in average. This will not degrade the performance of controller. Figure 5(d) shows the packet loss rate of our scheme. We can observe that the packet loss rate will decrease as the threshold reduces. As a result we can reduce the packet loss rate by reducing the threshold when packet loss rate is high.

6. CONCLUSION

In this paper, we proposed a flow aggregation and migration (AM) scheme for optical networks. Flows could be aggregated into lightpath with spare bandwidth resources and be migrated from heavily loaded lightpath. Experimental results show that we can guarantee the transmission quality of high-priority flows and reduce packet loss of migrated low-priority flow under our scheme. Simulation result shows that our AM scheme improves lightpath bandwidth utilization and reduces blocking rate. We can also reduce the packet loss rate of low-priority flows by reducing the threshold.

REFERENCES

1. Smarr, L., "The OptIPuter and its applications," *LEOSST*, 151–152, 2009.
2. Guo, W., B. Wang, Y. Jin, et al., "Joint optimization of transmission performance and bandwidth utilization based on software defined networks," *Optical Fiber Communications Conference and Exhibition (OFC)*, 1–3, 2014.
3. McKeown, N., T. Anderson, H. Balakrishnan, et al., "OpenFlow: Enabling innovation in campus networks," *ACM SIGCOMM Computer Communication Review*, Vol. 38, No. 2, 69–74, 2008.
4. http://www.opendaylight.org.
5. http://openvswitch.org.

Impact of Protection to Converged Access Networks Planning in Rural Areas

Carmen Mas Machuca[1] and Ana Muñoz Díaz[1, 2]

[1]Technical University of Munich, Germany
[2]Technical University of Madrid, Spain

Abstract— Network operators are reluctant to offer broadband access in rural areas due to the high investments and limited revenues. Protection in those areas is even more unfeasible and hence, it has not been considered by operators yet. One alternative to decrease costs when offering high bitrates in rural areas is the use of new architectures such as Hybrid Passive Optical Network (HPON). These architectures offer several advantages not only from the longer reach and higher client count, but for the possibility of offering different bandwidth per end point. The recently proposed HPON architecture could be used to offer higher bandwidth to the connected Base Stations (BS) (e.g., 10 Gbps) than the bandwidth delivered to residential users (300–500 Mbps). Recent work has presented a detailed framework using real building and street data distibution provided by OpenStreetMap, which allows computing a practical fiber layout for different access architectures and splitting ratios. This approach aims at minimizing the duct length, since costs associated to ducts and trenching have been shown to be cost drivers in access deployment. This framework has been now applied in rural areas to compare the infrastructure required for a disjoint versus a joint planning. Savings depend on the building density, area size and the inter BS distance. The contribution of this paper is focused on the analysis of the cost impact of BS protection. The required availability is obtained when protection of feeder fiber and distribution fiber is guaranteed. The investment and extra fiber and duct infrastructure required for two protection schemes are compared with the unprotected scenario. The cost increase is shown to be relatively low compared with the unprotected solution.

1. INTRODUCTION

Over the years, technology has significantly changed and steered the way people communicate. Originally, the telephone replaced previous ways of communications and, nowadays mobile devices are leading the bandwidth increase of telecommunication networks. However, users are not only expecting higher bandwidth but also high reliability while avoiding increasing their monthly fee. This fact, together with the fast and huge technological progress, is forcing operators to continuously upgrade their networks. Furthermore, the number of users is significantly increasig, not only in fixed networks, but also in mobile networks, being estimated to reach 2.3 billion globally by end 2014 [1]. Due to this increasing dependency on broadband networks, redundancy and protection in the access network has started to play an important role for FTTH providers in the recent years, even for applications that were not categorized as reliability-critical, and several analysis have already been performed [2].

Nevertheless, operators have always been reticent to offer broadband access in rural areas, due to the fact that they compose the access scenarios where deployment of optical networks becomes less profitable [3]. This, however, has changed during the last years as new solutions are being proposed, becoming the Hybrid Passive Optical Access network one of the most promising alternatives. Regarding this converged solution, in which fixed users and mobile backhaul share a single access network, recent work has already shown the great savings obtained, both in urban and rural areas, with the implementation of this architecture [4]. The impact in costs that protection of HPON involves has mainly been studied for urban areas [5]. In addition, this paper contains a costs analysis of two different protection scenarios for HPON in rural areas, where several constraints such as street network topology or large distances are found.

Going even further regarding availability issues, it has to be noted that not all users connected to the access network can afford to pay a high extra cost for protection, reason why resilience has to be provided in a cost-efficient way. Due to this fact, different degrees of offering reliability to the network have already been proposed and analyzed; having concluded that the benefits of providing protection up to the first remote node (feeder fibre) are very high and low extra investment is needed [6]. In this study, feeder fiber protection in HPON is analyzed in a rural scenario, meanwhile protection of base stations is also considered in the second protection scheme for the same rural scenario.

2. OPTICAL ACCESS NETWORK ARCHITECTURES AND PROTECTION SCHEMES

This section introduces the considered architecture as well as the protection schemes.

2.1. Hybrid Passive Optical Network (HPON)

A new architecture referred to as Hybrid Passive Optical Network (HPON) has been recently proposed and studied in the OASE project [7] just for residential users. This architecture has been slightly modified so that base stations can also be connected to the same access network but getting higher bandwith than residential users and hence, obtaining a converged access network architecture.

A HPON consists of an Optical Line Terminal (OLT) at the operator's central office (CO) that is connected to several Optical Network Units (ONUs) at the end users. These end users can be either residential users or Base Stations (BS). HPON is a point-to-multipoint architecture with two splitting points. The first one, which is closest to the OLT, is an Arrayed Wavelength Grating (AWG) $1 : N$, which splits the incoming WDM signal into N single wavelength signals. Each of these signals is distributed either to a BS or to a power splitter $1 : M$ (also referred to as second splitting point). The power splitter uses TDMA in order to share the capacity between M residential users. The HPON architecture is depicted in Figure 1, where dedicated wavelengths are directly assigned to the BS, providing them with 10Gbps peak data rates; whereas guaranteed downlink data rates for residential users after applying TDMA schemes are 300–500 Mbps (depending on whether the power splitting ratio M is 32 or 16).

In this study, four different architectures have been considered:

- **HPON(40,16)** considers a HPON with an AWG $1 : 40\lambda$ and a power splitter $1 : 16$ (hence providing to each residential user with 500 Mbps).

- **HPON(80,16)** considers a HPON with an AWG $1 : 80\lambda$ and a power splitter $1 : 16$ (hence providing to each residential user with 500 Mbps).

- **HPON(40,32)** considers a HPON with an AWG $1 : 40\lambda$ and a power splitter $1 : 32$ (hence providing to each residential user with 300 Mbps).

- **HPON(80,32)** considers a HPON with an AWG $1 : 80\lambda$ and a power splitter $1 : 32$ (hence providing to each residential user with 300 Mbps).
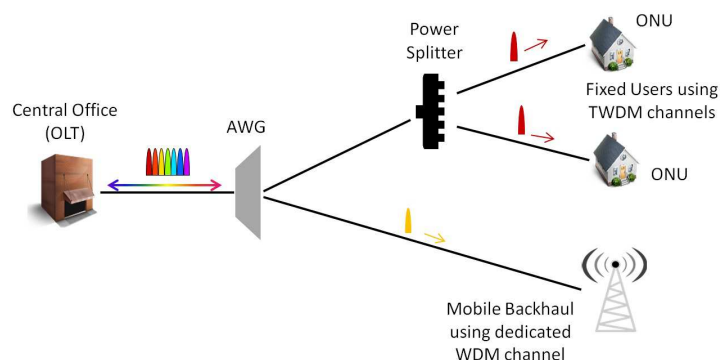

Figure 1: HPON architecture connecting fixed users and base stations.

2.2. Protection Schemes

The protection schemes addressed in this study aim at protecting the fiber infrastructure, which has been shown to be more vulnerable than equipment (due to its location, specially in rural areas).

It has been shown [5] that protection costs are directly related to the planning time and the protection approach. Let us consider in this study a greenfield scenario where both working and protection fibres are designed at the same time in such a way that the cost is minimized. As explained earlier, the infrastructure cost is driven by trenching and hence, duct sharing is encouraged. This approach is also followed for the protection fibre so that it shares as much disjoint duct as possible achieving protection while minimizing costs (as depicted in Figure 2).
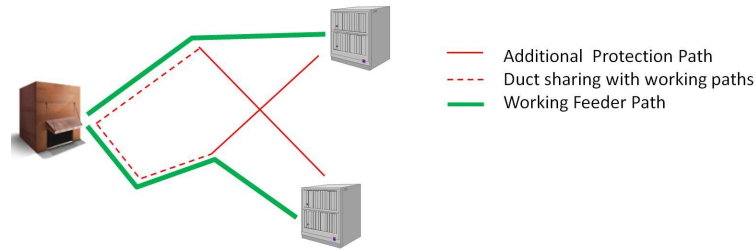
Figure 2: Greenfield-shared protection scheme.

3. METHODOLOGY

The method used in this study has as input a certain area and the splitting ratios of the power splitters and the AWGs. The methodology for the unprotected architecture shown in Figure 1 is as follows:

1. Get area database: From OpenStreetMap, an area can be selected. The relevant information for the planning such as streets, ways, buildings, etc. is extracted.

2. BS distribution: BS are distributed using an hexagonal grid, given an interBS distance. Since the obtained locations may not be realistic (e.g., in a river or in the middle of a forest), the BS are relocated to the closest street, which is consistent with the operator approach to have BS accesible for maintenance and power.

3. Clustering: Residential users are clustered based on the power splitting ratio. For this purpose, an 80% of port utilization has been considered, so that some ports are left for future use. The centroid of each cluster is considered as ideal location of the power splitter but it is realocated to the closest street (for practical reasons). Power splitters and BS are also clustered based on the AWG splitting ratio. The centroid of each cluster is considered as ideal location of the AWG but it is realocated to the closest street (for practical reasons).

4. Once the locations of power splitters and AWGs are identified, the fibre layout is computed using Dijkstra. In order to encourage duct sharing, the streets that have already been considered for routing have a lower weight.

5. Since rural areas present longer distances than urban areas, Reach Extenders (RE) may be required for ONUs exceeding the maximum reach of each network architecture. The maximum reach depends on the power splitter and AWG splitting ratios. In case RE are needed, they are indetified and the best location is found in order to minimize the cost.

The output of this methodology gives the dimensioning of the access network (i.e., the number and location of the power splitters and the AWG required) as well as the fibre layout (i.e., the number and length of the required fibres and ducts).

4. SCENARIOS AND CASE STUDY

Two protected scenarios are evaluated and compared in this paper with respect the unprotected HPON previously shown in Figure 1.

4.1. Disjoint FF

In any point-to-multipoint architecture, the Feeder Fibre (FF) is the component with the highest failure impact factor [6]. Hence, FF is the first component to be protected. In this protected scenario, a disjoint feeder fibre protection path is offered in order to protect any AWGs of the HPON architecture. This protected scenario is depicted in Figure 3(a).

4.2. Disjoint FF and DF for BS

As base stations require higher availability than fixed users, additional protection for base stations should be considered when including BS in the HPON planning. In order to offer protection to the base stations, a disjoint protection fibre is deployed from the BS to its associated AWG. This disjoint protection path is established aiming at performing duct sharing by reusing sections that were already selected for working paths. One of the major advantages of this scheme is that no extra wavelengths need to be reserved for protection at the AWG as the same one can be reused for protection. The scheme can be seen in Figure 3(b).
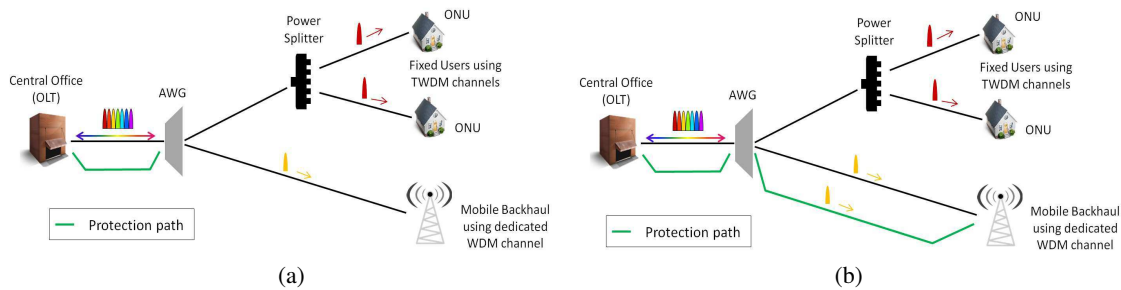
Figure 3: Proposed protected scenarios. (a) Disjoint FF protection for AWGs. (b) Disjoint FF protection for AWGs and Disjoint DF protec- tion for BS.

4.3. Case Study: Impact of Protection on Total Costs

Let us compare the two protection schemes with respect to the unprotected HPON in rural areas. For that purpose, a rural area in Germany close to Miesbach has been considered: the selected surface covers approximately $17\,km^2$ and has a building density of around $160\,buildings/km^2$.

First of all, let us compare the cost per offered Gbps for the disjoint scenario (GPON 1 : 32 to fixed users and P2P to BS) versus the HPON, as shown in Figure 4. It can be observed that for an inter BS distance of 0.5 km, the cost per Gbps decreases more than 87% when the splitting ratio of the power splitter is 16, and almost 75% when the splitting ratio of the power splitter is 32, which is the one limiting the delivered bandwitdth to the fixed users using TDM.

Focusing on the protection, let us first compare the required infrastructure of the unprotected and the protected scenarios. The infrastructure is compared in terms of fiber and duct length as
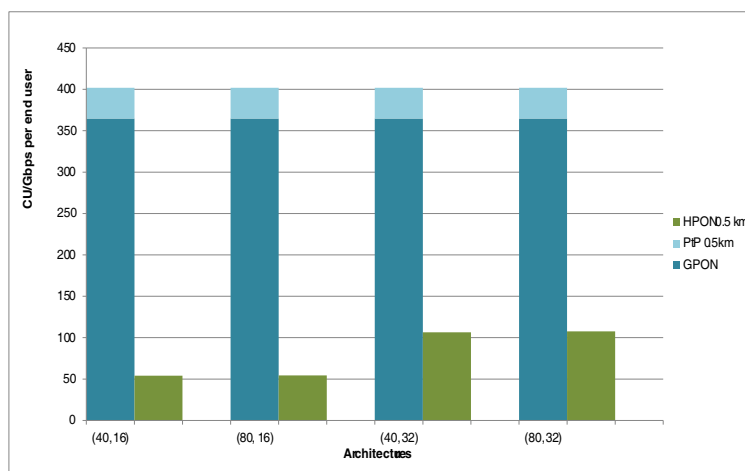

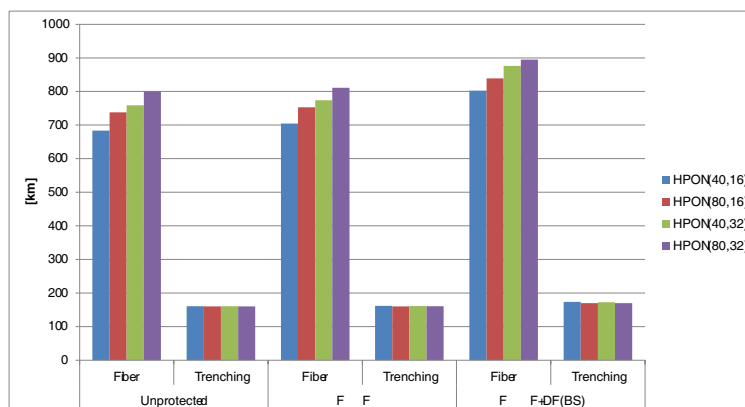Figure 4: Disjoint versus joint planning cost per Gpbs.
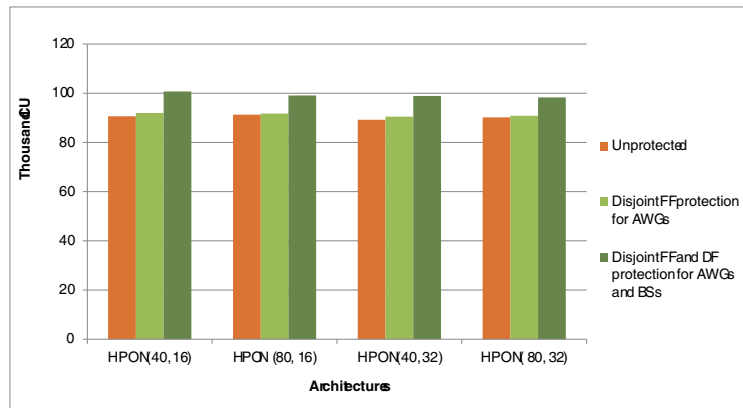

Figure 5: Infrastructure required.

Figure 6: Costs comparison between unprotected HPON and the two considered protected scenarios.

shown in Figure 5. It can be observed that for the FF protection, only 1–3% more fiber and .1–.6% more trenching is required. Hence, the operator can protect the FF with limited extra investment. In order to protect also the DF of BS, an increase of 10–13% fiber and 5–7% trenching is needed.

Figure 6 compares the total costs of the unprotected versus the protected scenarios. It can be observed that there are not significant differences among the architectures. It has been shown that duplicating fibre only for protecting the FF paths does not require high extra investment, only about 0.5–1.5% of the total costs of unprotected HPON. This solution increases availability in a great degree and the additional costs are so low that should not become a huge restriction for operators. On the other hand, if the BSs included in the access network need to be protected too, higher total costs have been registered. Increases of approximately 8.5–11% for protecting FF and DF have been obtained respect to total costs of the unprotected solution.

5. CONCLUSION

This paper has evaluated the impact that protection of FF or FF and DF for BS schemes have on the total costs. It has been shown that in a greenfield scenario offering broadband access to users (300–500 Mbps/residential users and 10 Gbps/BS), FF protection does not require significant extra costs (less than 2%). In case operators aim at protecting the BS, an extra cost of 10% may be required.

REFERENCES

1. ITU, "ICT facts and figures," *The World in 2014*, 2014.
2. Wosinska, L., J. Chen, C. Mas Machuca, and M. Kantor "Impact of protection mechanisms on cost in PONs," *Proceedings of 11th International Conference on Transparent Optical Networks (ICTON)*, Ponta Delgada, Portugal, June–July 2009.
3. Reyes, R. R., R. Zhao, and C. M. Machuca, "Advanced dynamic migration planning toward FTTH," *IEEE Communications Magazine*, 2014.
4. Díaz, A. M. and C. M. Machuca, "Are converged access networks suitable in rural areas?," *Proceedings of 17th International Conference on Transparent Optical Networks (ICTON)*, 2015.
5. Machuca, C. M. and B. Topalogu, "Impact of protection strategies on the cost of Next Generation Hybrid PON access networks," *Proceedings of 9th International Conference on the Design of Reliable Communication Networks (DRCN)*, Budapest, Hungary, March 2013.
6. Mahloo, M., J. Chen, L. Wosinska, A. Dixit, B. Lannoo, D. Colle, and C. M. Machuca, "Toward reliable hybrid WDM/TDM passive optical networks," *IEEE Communications Magazine*, 2014.
7. OASE Project.

Programmable Photonics in Data Centers: Architectures and Algorithms

Carla Raffaelli

DEI, University of Bologna, Italy

Abstract— Flexible networking is a challenge to design future Internet scenarios and service convergence. The main aspects related to data center interconnection based on emerging software defined photonics and networking concepts are here introduced and discussed. The programmable optical backplane is described and applied as a mean to provide enhanced network functionalities in a scalable and reconfigurable perspective.

1. INTRODUCTION

The recent evolution of the Internet is characterized by the need to dynamically share physical resources like storage, computing capacity and even networks themselves, thus enabling modern applications, like social networking, cloud computing, video streaming and others to efficiently perform their services.

Data centers are emerging as aggregates of increasingly powerful physical facilities which generate high amount of traffic and consume high power, accordingly. In spite of the continue increase of peak performance, the allowable power consumption is required to increase at a much slower rate [1]. As a consequence, data center interconnection design will result one of the most challenging networking problem in the next future which can be solved in a massive adoption of new technological solutions, possibly based on photonic solutions.

On the network service side, the evolving characteristics of content providers call for enhanced dynamic network reconfiguration capability. Emerging photonic technology can provide interconnection at extremely high rates with enhanced flexibility in spectrum sharing [2]. At the same time network control and management technologies should be able to exploit this flexibility in relation to cloud-based application dynamics.

Solutions based on combinations of Network Function Virtualization (NFV) and Software Defined Networking (SDN) can achieve the extreme flexibility required to support current and future development of cloud computing paradigms. Programmable features of emerging photonic technology can be fruitfully exploited in this context thus defining new roles and chances for optical interconnection both in capacity exploitation and energy efficiency perspective [3]. In any case the joint deployment of photonics and SDN to fulfill future dynamic network requirements, needs algorithms and architectures to harmonize and optimize several functionalities [4], which are addressed in this presentation.

The application of standard protocols like Open Flow [5] must be studied to map network management functionalities on programmable photonics. Different approaches can be adopted based on protocol extensions or on protocol compliance. Architectures and algorithms to support the management of flexible grid channels are here considered through possible virtualization of photonic network elements based on emerging SDN protocols. Solutions to optimize the usage of wavelength channels while supporting quality of service will be also discussed in terms of procedures and performance.

The reference data center architecture consists of several servers organized in racks. Traffic generated by servers is aggregated by top of the rack switches (ToRs) which possibly implement quality of service mechanisms. They are called hybrid switches because they implement both circuit and packet services and interface to server with elecrical interfaces and to the optical core switch with optical WDM interfaces. Example of such ToR switches are described in [6].

The paper is organized as follows. In Section 2 the concept of SDN and its evolution are presented. The introduction of optical programmable backplane in design of flexible interconnection in data center is discussed in Section 3. An example of application of the programmable architecture to support quality of service is described in Section 4. Concluding remarks are given in Section 5.

2. THE ROLE OF SDN

The SDN concept can be considered as firstly introduced in [5] with the definition of the Open Flow protocol, even though it is a quite broader concept. Since then it has evolved through many

important steps while gaining increasing attention of the major players in the Internet world, like Google, Cisco, Juniper, Hewlett'Packerdand VMWare, just to cite a few. The basic concept behind SDN is not completely new, being it characterized by the separation of control and data planes [7], but what's more is the notion that the network is a programmable system. This property is achieved by the introduction of the network operating system as an analogous of the operating system of a standalone computer, distributed instead throughout the network to jointly work with software abstractions, i.e., virtualization, of available network hardware and infrastructure.

This appealing scenario requires a deep change in conceiving and designing network components and functionalities. In the SDN perspective the network intelligence is implemented in controlling entities set outside from the forwarding engines which results in simpler boxes with respect to today network nodes. Controlling entities become parts of the network operating system through which network services are configured and operated. Network elements instead provide forwarding services and standard interfaces to the network operating system.

As explained in [8] the reference SDN architecture includes control, management and data plane functionalities. The control plane, also called the network operating system, interfaces with the network application layer through a northbound interface which offer an open API (Application Programming Interface) to configure and define any kind of feasible network service with the desired characteristics. At the same time it interfaces with the forwarding plane through standard protocols, like Open Flow, at the southband interface to configure and exploit physical resources. A significant part of the SDN architecture is represented by network management that operates at all the abstraction layers which contribute to SDN implementation. Basically, the management plane supports network programmability in terms of infrastructure configuration and monitoring, while the control plane is in charge of dynamically configuring communication services on demand, typically based on flow-oriented operations. The management plane operations take place on longer time scale with respect to logical connections.

The elements in the forwarding plane are called 'network elements' and their internal organization aims at layering hardware specific functionalities and logical flow oriented operations [3].

3. PROGRAMMABLE OPTICAL ARCHITECTURES

Programmable optical architectures can play a key role in future data center networking. The concept of programmable architecture has been recently introduced and demonstrated in practical experiments [9]. Basically, a programmable architecture consists of a switching matrix that can be reconfigured via management software. Reconfiguration times depend on optical switching technology, typical values being in the order of tens of milliseconds for most popular implementations [10]. Several applications of programmable architecture can be foreseen, ranging from reconfigurable interconnections of physical devices to programmable architectures of networks devices [9]. Key network elements such as Reconfigurable Optical Add Drop multiplexers (ROADM) have been shown to improve scalability and power efficiency aspects with costs comparable with traditional architectures when adopting programmable interconnections [11].

Programmable architectures can be efficiently applied in the interconnection of software defined photonics elements for evolution of data center interconnection and related functionalites. In Figure 1 a general scheme which represents the programmable architecture functionalities is reported. The programmable optical backplane provides the interconnection paths among network elements, which can be reconfigured on a wider time scale with respect to connection operation. They are typically configured by operation on the management plane. When referring to SDN context, connection operation, instead, are typically flow-based and the mostly deployed protocol to control their configuration is represented by Open Flow [5].

The above architecture can be applied also to introduce new network functionalities, such quality of service support, which will be considered in the next section.

4. TRAFFIC MANAGEMENT AND QUALITY OF SERVICE SUPPORT

The introduction of optical WDM links in data center aims at meeting both high capacity and limited power consumption requirements [12]. Flexible grid WDM attracts particular interest for its flexibility in supporting optical channels with different capacity. This property, if suitably exploited by programmable hardware, can sensibly enhance variable capacity requirements of cloud computing and big data applications. In any case WDM offers communication capacity in the Gbit/s range that can accomodate aggregate Ethernet traffic coming from top of the rack switch for intra and inter data center data transfer. Traffic generated in data centers is typically classified
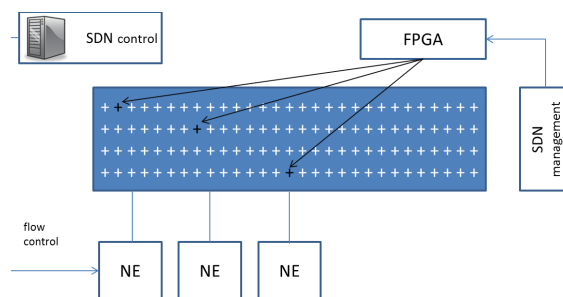
Figure 1: Programmable optical backplane in SDN context with software defined network elements.

in elephant and mice flows and mapped onto optical channel accordingly. Huge elephant flows are typically assigned circuit switched connections while light elephant flow or mice flows are switched on a lower time scale by fast packet switching [6]. A wavelength channel is able to provide very high transmission capacity up to the range of 100 Gbit/s or even beyond. Circuit and packet switched information are carried in most proposals by separate wavelength [13]. Efficient usage of this resource is highly important because even small unused intervals lead to huge waste of transport capacity.

In [14] a scheme to support three different levels of service has been proposed and in [15, 16] performance of the aggregation stage and of a core switch have been evaluated. Basically the proposed approach consists of a delayed guaranteed service traffic (GST) that experience no loss and no variable delay when traversing the WDM interface. Each GST flow is assigned to one wavelength and GTS traffic engineering is performed on a call blocking basis [17]. The delay applied to the GST traffic is represeted by the maximum acceptable duration of real time packets, which is typically very low, in the range of tens of microseconds. Real time traffic (RT) has no variable delay, being it dropped when no WDM resources are available. RT traffic engineering is performed with reference to blocking probability at a statistical multiplexer without queuing [15]. RT blocking takes place in case a GST burst is already waiting for transmisison in the system or no wavelength channels are available upon RT packet arrival. Finally best effort traffic (BE) is admitted to the free WDM channels of an interface. A pre-emptive policy is applied, meaning that a BE packet is interrupted upon arrival of GST or RT traffic.

The above quality of service mechanism can be implemented on a programmable architecture, which allow flexibility in scalability, implementation and possible upgrade of the algorithm. The proposed scheme, thought as an optical core switch for a data center, is represented in Figure 2. Basically, the scheme includes the functional blocks described in [14] which are interconnected by a prograbble backplane instead than wired interconnections, with consequent enhanced flexibility.
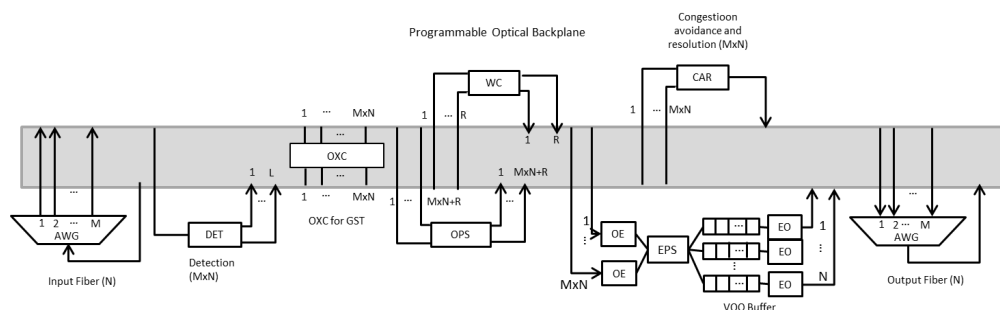

Figure 2: Programmable implementation of the optical core switch with 3-level quality of service support.

Let us assume to have N top of the rack (ToR) switches, with M WDM output channels, each. The optical core switch is configured with N input de-multiplexers with M output channels and N output demultiplexers with M channels to provide inter-rack interconnections. Additional interfaces should be provided for inter-data center interconnections that are not considered here.

Each de-multiplexed wavelength channel is sent to a detect packet type block (DET), which applies physical layer decoding to select the different kinds of traffic (GST, RT, BE). Each output of this block is connected to the corresponding required switch functionality. In case of packet switching, wavelength conversion can be applied to shift a packet from one channel to another

one of the same output interface. OPS (Optical Packet Switching) switch size is increased with R interfaces in relation to the wavelength conversion approach and packet loss performance [18].

After switching, collecting blocks are introduced with the contention avoidance and resolution mechanisms (CAR). These blocks are $L : 1$ devices, being L the number of QoS levels, M for each output interface. These blocks provide GST delay for guaranteed service and internal signaling capability. The status of these devices is properly set by the SDN controller. Each output is connected by the programmable backplane to the proper output multiplexer.

The programmable backplane introduces additional comlexity represented by the number of optical switches needed to implement the architecture. Let us introduce the following notation:

Table 1: Model parameters.

N	number of input and output fibre interfaces
M	number of wavelengths per interface
R	number of wavelength converters
L	number of QoS levels
C_{IO}	number of MEMS related to input and output interfaces
C_D	number of MEMS related to detection
C_D	number of MEMS related to switching modes
C_W	number of MEMS related to wavelength conversion
C_C	number of MEMS related to contention avoidance and resolution
C_I	total cost in MEMS of programmable interconnection

The following expressions can be obtained:

$$C_I = C_{IO} + C_D + C_S + C_W + C_C = LMN + 4MN + 2R + 3N \tag{1}$$

As shown in Equation (1), the total complexity function C_I results dominated by the product MN. At the same time the solution provides the flexibility to introduce additional level of functionality by increasing the detection module and possibly adding ne switching blocks.

In Figure 3 some numerical values are reported regarding programmable switch complexity, where the number of wavelength converters R is defined to obtain packet loss probability less then 10^{-4} with a shared per node saring scheme [18]. The figure shows the effect of the product MN which dominates the behaviour of the interconnection complexity function C_I.
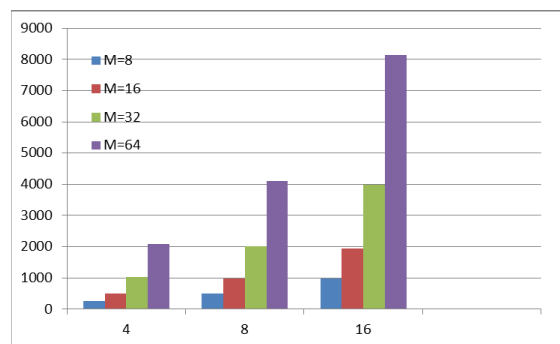

Figure 3: Number of MEMS switch in the programmable optical backplane as a function of the number of input and output interfaces, varying the number of wavelengths as a parameter, correponding to packet loss probability 10^{-4} with fully tuneable wavelength converters.

5. CONCLUDING REMARKS

In this paper the main aspects in designing future dynamic SDN based networks are presented. The concept of software defined photonic network element has been introduced and the possibility of its interfacing with SDN framework is presented. The availability of commodity optics to

implement optical programmable backplane is outline to achieve high flexibility, scalability and reconfigurability both for data center interconnections and advanced quality of service features.

REFERENCES

1. Gringeri, S., et al., "Technologies and protocols for data center and cloud networking," *IEEE Comunications Magazine*, Vol. 51, No. 9, 24–31, 2013.
2. Orlandi, P., et al., "Reconfigurable silicon filter with continuous bandwidth tunability," *Journal Optics Letters*, Vol. 37, No. 17, 3669–3671, 2012.
3. Channegowda, M., et al., "Software-defined optical networks technology and infrastructure: Enabling software-defined optical network operations," *J. Opt. Commun. Netw.*, Vol. 5, No. 10, A274–A282, 2013.
4. Raffaelli, C., et al., "SDN-controlled flexible-grid optical switch," *Proceedings EUCNC 2014*, Bologna, Italy, 2014.
5. McKeon, N., et al., "Open flow: Enabling innovation in campus networks," *ACM Sigcomm Computer Communications Review*, Vol. 38, No. 2, 69–84, April 2008.
6. Veisllari, R., et al., "Field-trial demonstration of cost efficient sub-wavelength service through integrated packet/circuit hybrid network," *IEEE/OSA Journal on Optical Communications and Networking*, March 2015.
7. Gude, N., et al., "NOX: Towards an operating system for networks," *ACM Sigcomm Computer Communication Review*, Vol. 38, No. 3,, 105–110 July 2008.
8. Araujo Wickboldt, J., W. Palm de Jesus, P. H. Isolani, C. Bonato Both, J. Rochol, and L. Zam-Benedetti Granville, "Software-defined networking: Managment requirements and challenges," *IEEE Communications Magazine*, 278–285, January 2015.
9. Peters, A., E. Hugues-Salas, G. Zervas, and D. Simeonidou, "Mesuring flexibility and design trade- offs of N×M SSS-based ROADMs and BVTs," *Proceedings of OFC*, paper W3J.5, 2015.
10. http://www.polatis.com/.
11. Garrich, M., N. Amaya, G. S. Zervas, J. R. F. Oliverira, P. Giaccone, A. Bianco, D. Simeonidou, and J. C. Oliveira, "Architecture on demand design for high-capacity optical SDM/TDM/FDM switching," *IEEE/OSA Journal of Optical Communications and Networks (JOCN)*, Vol. 7, No. 1, 21–35, January 2015.
12. "A survey on optical interconnects for data centers," *IEEE Communications Surveys & Tutorials*, Vol. 14, No. 4, 1021–1035, Fourth quarter 2012.
13. Guo, B., S. Peng, C. Jackson, Y. Yan, Y. Shu, W. Miao, H. Dorren, N. Calabretta, F. Agraz, S. Spadaro, J. Perell, G. Bernini, R. Monno, N. Ciulli, R. Nejabati, G. Zervas, and D. Simeonidou, "SDN-enabled programmable optical packet/circuit switched intra data centre network," *OFC 2015*, Los Angeles, CA, US, March 22–26, 2015.
14. Stol, N., C. Raffaelli, and M. Savi, "3-Level Integrated Hybrid Optical Network (3LIHON) to meet future QoS requirements," *IEEE Globecom 2011*, Houston, Texas, USA, ISSN: 1930-529X, 2011.
15. Cerroni, W. and C. Raffaelli, "Analytical model of quality of service scheduling for optical aggregation in data centers," *Photonic Network Communications*, Vol. 27 , No. 3, 1–12, June 2014.
16. Raffaelli, C. and G. Leli, "Performance of 3-level scheduling in optical core switch for data center interconnection," *Proc. NOC 2014*, Milan, Italy, June 2014.
17. Veisllari, R., N. Stol, S. Bjornstad, and C. Raffaelli, "Scalability analysis of SDN-controlled optical ring MAN with hybrid traffic," *ICC 2014*, Sidney, Australia, Giugno, 2014.
18. Savi, M., H. verby, Norvald Stol, and C. Raffaelli, "Cost evolution model to design optical switching fabrics with wavelength converters," *Elsevier Computer Networks*, Volu. 72, 99–112, October 29, 2014.

Dissipation-induced Super Scattering from $\mathcal{PT}$-synthetic Plasmonic Metafilms

Simin Feng

Naval Surface Warfare Center Dahlgren Division, Virginia, USA

Abstract— We found that the extraordinary transmission and reflection of a finite bandwidth can occur at the same wavelength when the electromagnetic wave is incident on a periodic array of $\mathcal{PT}$-symmetric dimers embedded in a metallic film. Remarkably, this phenomenon vanishes if the metallic substrate is lossless while keeping other parameters unchanged. When the metafilm is adjusted to the vicinity of a spectral singularity, tuning the substrate dissipation to a critical value can lead to supper scattering in stark contrast to what would be expected in conventional systems. This phenomenon implies that strong coherent radiation may be able to generate from a cavity having gain elements by tuning cavity dissipation to a critical value.

1. INTRODUCTION

In a pioneering work, Bender and colleagues proved that non-Hermitian Hamiltonian with parity-time $(\mathcal{PT})$ symmetry may exhibit entirely real spectrum below a phase transition (symmetry breaking) point [1]. Inspired by this emerging concept, in the past decade there has been a growing interest in studying $\mathcal{PT}$-symmetric Hamiltonian in the framework of optics [2–19] where the $\mathcal{PT}$ complex potential in quantum mechanics is translated into a complex permittivity profile satisfying $\epsilon(r) = \epsilon^*(-r)$ in optical systems. In optics, most of the $\mathcal{PT}$-symmetric structures are realized by parallel waveguides or media with alternating gain and loss either along or across the propagation direction. The $\mathcal{PT}$-symmetric systems are a subset of open quantum systems for which Hamiltonian is non-Hermitian and the eigenvalues are complex in general [20]. The unique properties associated with non-Hermitian Hamiltonian are exceptional points and spectral singularities. An exceptional point is associated with level repulsion [21] and symmetry breaking [14, 19, 22]. Spectral singularity is related to scattering resonance of non-Hermitian Hamiltonian and manifest itself as giant transmission and reflection with vanishing bandwidth [23, 24].

Parity-time synthetic materials represent a new class of metamaterials with novel electromagnetic properties arising from a delicate balance between loss and gain elements. Global $\mathcal{PT}$ symmetry is a demanding condition. Systems with local $\mathcal{PT}$-symmetry are easier to implement. Array of $\mathcal{PT}$-symmetric dimers where each gain-loss pair in itself possesses local $\mathcal{PT}$-symmetry with respect to its own center allows for the real spectrum in the right parameter region [2]. Except for compensating loss with gain, active plasmonic materials offer an ideal platform for studying non-Hermitian Hamiltonian in the electromagnetic domain at the subwavelength scale. Most studies on $\mathcal{PT}$-symmetric structures use analytical models based on either one dimensional scalar Helmholtz equation or two dimensional scalar paraxial wave equation. For plasmonic metamaterials having subwavelength "meta-atom" as resonators, above analytical descriptions are not applicable. In this paper, we investigate electromagnetic properties of $\mathcal{PT}$-synthetic plasmonic metafilm which is composed of a planar array of coupled $\mathcal{PT}$-symmetric dimers. We have found that this structure can display super scattering by control of plasmonic substrate dissipation. When the metafilm is steered to the vicinity of a singular region of the system, tuning the substrate dissipation to a critical value can lead to substantially amplified waves radiated from both sides of the metafilm.

2. THEORETICAL APPROACH

Figure 1 schematically depicts a unit cell in a planar subwavelength square array of gain-loss elements embedded in a ultra-thin metallic film. The gain-loss dimer repeats in the x-y plane. The plasmonic metafilm satisfies the local $\mathcal{PT}$ symmetry with respect to the x directions, i.e., $\epsilon(x, y, z) = \epsilon^*(-x, y, z)$ for $\Delta x/2 < |x| < b + \Delta x/2$. This structure cannot be described by the paraxial wave equation due to the abrupt change of electromagnetic (EM) field at the metal-dielectric interfaces. We numerically solve Maxwell's equations based on rigorous coupled-wave analysis [25]. Numerical approaches can handle more complicated structures and guide engineering designs to search for the right parameter combination. This is important for practical implementation of the extraordinary properties predicted by analytical theory.
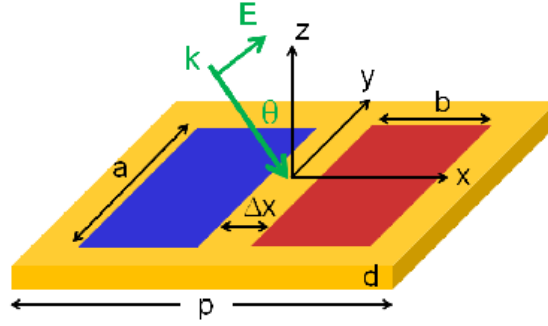
Figure 1: (Color online) A schematic showing a $\mathcal{PT}$-symmetric unit cell composed of loss (blue) and gain (red) subwavelength elements embedded within an aluminum thin-film. The dimers and the aluminum film have the same thickness, i.e., the metallic mesh is filled with gain-loss elements. The unit cell repeats in the x-y plane with the same period in both directions. The real part of the relative permittivity of the loss and gain elements is fixed at 3.6 through out this work. The imaginary part varies, but satisfies $\epsilon''_{gain} = -\epsilon''_{loss}$ to ensure the local $\mathcal{PT}$ symmetry. The permeability is unit for all the materials. The period $p = 3.5\,\mu\text{m}$, the dimer length $a = 2.5\,\mu\text{m}$ and width $b = 1.0\,\mu\text{m}$ are fixed throughout the paper. The incidence wave is p-polarized with the electric field parallel to the x-z plane.

For the infrared $\mathcal{PT}$-synthetic materials, the dispersion of metal, which is aluminum (Al) in our case, cannot be neglected. Assume a harmonic time dependence $\exp(-i\omega t)$ for electromagnetic field, the permittivity of Al was obtained by curve-fitting experimental data [26] with a Drude model,

$$\epsilon_m = 1 - \frac{\omega_p^2}{\omega^2 + i\gamma\omega}, \tag{1}$$

where the "plasma frequency" $\omega_p = 9.38\,\mu\text{m}^{-1}$ and the damping constant $\gamma = 0.048\,\mu\text{m}^{-1}$. Maxwell's equations can be recast in a Schrödinger-type form:

$$i\frac{\partial}{\partial z}\begin{pmatrix} E_t \\ \hat{\mathbf{z}} \times H_t \end{pmatrix} = \widetilde{H} \cdot \begin{pmatrix} E_t \\ \hat{\mathbf{z}} \times H_t \end{pmatrix}, \tag{2}$$

where the subscript 't' refers to the transverse (x, y) components of the EM field on the meta-surface; and $\hat{\mathbf{z}}$ is the unit vector along the z direction. The Hamiltonian is given by

$$\widetilde{H} = \begin{pmatrix} 0 & k_0\mu_t\hat{\mathbf{I}}_t + \dfrac{1}{k_0}\nabla_t\dfrac{1}{\epsilon_z}\nabla_t \\ k_0\epsilon_t\hat{\mathbf{I}}_t + \dfrac{1}{k_0}\hat{\mathbf{z}}\times\nabla_t\dfrac{1}{\mu_z}\hat{\mathbf{z}}\times\nabla_t & 0 \end{pmatrix}, \tag{3}$$

where $k_0 = \omega/c$, and the c is the speed of light in vacuum. The subscript 'z' refers to the component in the z direction. $\hat{\mathbf{I}}_t = \hat{\mathbf{I}} - \hat{\mathbf{z}}\hat{\mathbf{z}}$ is the two-dimensional unit dyadic; and

$$\nabla_t \equiv \hat{\mathbf{x}}\frac{\partial}{\partial x} + \hat{\mathbf{y}}\frac{\partial}{\partial y}. \tag{4}$$

The form of Eq. (3) can handle uniaxial anisotropic materials with the optical axis along the z direction. The Hamiltonian given by Eq. (3) is non-Hermitian. The scattering and transfer matrices, as well as the transmittance and the reflectance are calculated numerically. The transfer matrix which connects the field at the output and the input surfaces is defined as

$$|\Psi_i\rangle = \begin{pmatrix} M_{11} & M_{12} \\ M_{21} & M_{22} \end{pmatrix}|\Psi_o\rangle, \quad |\Psi\rangle \equiv \begin{pmatrix} E_t \\ \hat{\mathbf{z}} \times H_t \end{pmatrix}. \tag{5}$$

where the subscripts 'o' and 'i' refer to the EM field at the output and input surfaces, respectively. The relationship between the transfer and scattering matrices in our case is given by

$$\begin{aligned} S_{11} &= M_{21}M_{11}^{-1}, \quad S_{21} = M_{11}^{-1}, \\ S_{22} &= -M_{11}^{-1}M_{12}, \quad S_{12} = M_{22} - M_{21}M_{11}^{-1}M_{12}, \end{aligned} \tag{6}$$

where the S_{11} and S_{21} are, respectively, the reflection and transmission coefficients of the electric field. In general, the transfer and scattering matrices are multidimensional due to multiple scattering channels. We have conducted extensive numerical studies and confirmed that for our geometry the magnitudes of the higher order and cross-polarization scatterings are much smaller than that of the first order event due to the subwavelength nature of the films. Therefore, the transfer and scattering matrices can be reduced to 2×2 matrices. The problem can be effectively described in a two-dimensional space.

3. SUPER SCATTERING

In the geometry of Fig. 1, many parameters can be changed. In this work, the period ($p = 3.5\,\mu m$) of the square array, the size ($a \times b = 2.5 \times 1.0\,\mu m^2$) of the dimers, and the real part of the relative permittivity ($\epsilon'_r = 3.6$) of the dimers are fixed throughout the paper. For a comparison we show in Fig. 2 the transmittance (T) and reflectance (R) of a normal incident electromagnetic wave onto a lossless metafilm with lossless dimers. The frequency dependent permittivity of aluminum was taken from the real part of Drude model given by Eq. (1). In the lossless case we have $T + R = 1$ (energy conservation) which is clearly demonstrated in Fig. 2. An increase of the transmission is accompanied by a decrease of the reflection and vice versa. The peaks and valleys of the transmittance and the reflectance repeat periodically with the variation of the thickness of the film. The metafilm behaves like a low-Q Fabry-Pérot cavity below $9\,\mu m$. Above $12\,\mu m$, the metafilm behaves towards a perfect electric conductor (PEC).
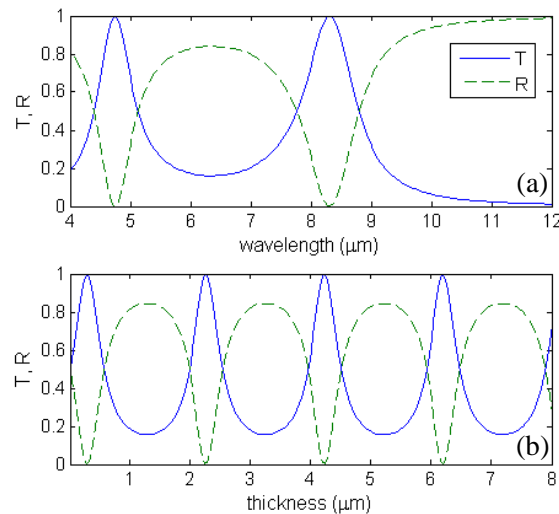

Figure 2: (Color online) Transmittance (blue solid) and reflectance (green dashed) of the normal incidence wave on a lossless metafilm versus (a) wavelength and (b) thickness with the electric field parallel to the shorter edge of the dimers. The separation of the two dimers $\Delta x = 0.5\,\mu m$ for both cases. The thickness of the metafilm $d = 1.5\,\mu m$ for the upper panel and the wavelength $\lambda = 6\,\mu m$ for the lower panel. The relative permittivity of the dimers is real and given by $\epsilon_r = 3.6$.

Now we proceed to investigate the EM scattering from a plasmonic thin-film having balanced gain-loss elements. The $\mathcal{PT}$-synthetic plasmonic metafilm no longer behaves as a Fabry-Pérot cavity. To demonstrate the effect of the substrate dissipation, we investigate the transmittance and reflectance of the metafilm with and without plasmonic dissipation in the presence of the balanced gain-loss dimers. The Fig. 3(a) shows the transmittance and reflectance of the EM wave normally incident on the $\mathcal{PT}$-synthetic lossless plasmonic metafilm of which the dispersion is given by the real part of Drude model in Eq. (1). The relative permittivity of the dimers is given by $\epsilon = 3.6(1 \pm 0.06i)$. Clearly, the sum of the transmittance and reflectance is close to unit, i.e., $T + R = 1$. Overall the metafilm performs as a conventional lossless medium where the maximum transmission is accompanied by the minimum reflection, and vice versa. This behavior can be understood as the subwavelength dimers have balanced gain-loss profile and are embedded in the lossless substrate. The situation changes dramatically when the plasmonic substrate dissipation is taken into account as shown in the Fig. 3(b) where the giant transmittance and reflectance occur at the same wavelength, unlike conventional media where the increase of one at the expense
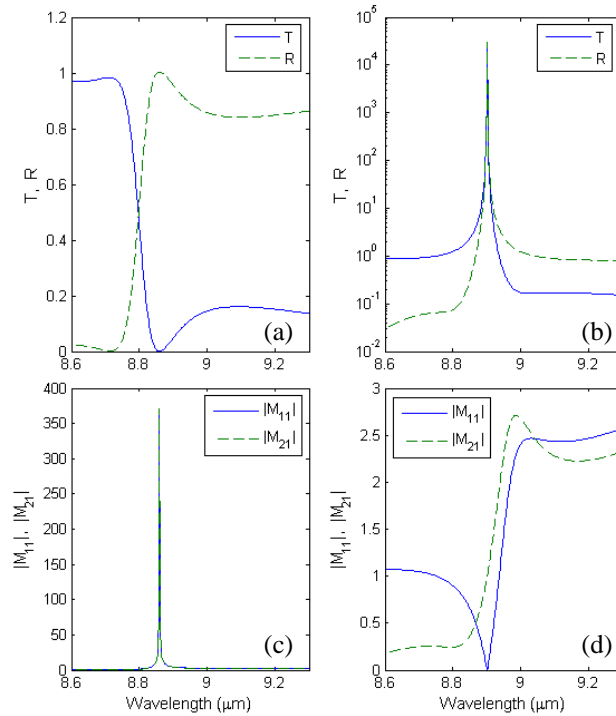
Figure 3: (Color online) Simulation (a), (c) without and (b), (d) with metallic substrate dissipation. (a), (b) Transmittance (blue solid) and reflectance (green dashed) for the normal incidence with the electric field parallel to the shorter edge of the dimers. (c), (d) The magnitude of M_{11} (blue solid) and M_{21} (green dashed). The separation of the two dimers $\Delta x = 0.5\,\mu\mathrm{m}$; and the thickness of the mesh $d = 1.5\,\mu\mathrm{m}$. The relative permittivity of the gain/loss elements $\epsilon = 3.6\ (1 \pm 0.06i)$.

of the other. This peculiar property can be analyzed through the scattering parameters S_{11} and S_{21} that have a common denominator M_{11} as shown by Eq. (6). When the denominator of S_{11} and S_{21} vanishes, both transmittance and reflectance approach infinity as long as M_{21} is finite. Figs. 3(c) and 3(d) show the magnitude of M_{11} and M_{21} with and without the substrate dissipation described by the Drude model in Eq. (1). Without the substrate dissipation (Fig. 3(c)), both magnitude of M_{11} and M_{21} are large at the wavelength about $8.88\,\mu\mathrm{m}$ which explains the null in the transmittance and the peak in the reflectance (see Fig. 3(a)). When turn on the substrate dissipation (Figs. 3(d)), the $|M_{11}|$ vanishes at the wavelength about $8.92\,\mu\mathrm{m}$ whereas the $|M_{21}|$ is finite. Thus, both transmission and reflection approach infinity. Here the spectral singularities are manifested as the dissipation-induced super scattering.

4. CONCLUSION

We have numerically demonstrated the dissipation-induced super scattering phenomenon when the system parameters are steered to the vicinity of the spectral singularity. This phenomenon implies that tuning cavity dissipation can lead to a super radiation. Our numerical experiment with the dispersive material parameters is one step further toward practical applications of $\mathcal{PT}$-synthetic materials. The existence of the narrow-band giant scattering phenomenon reveals a new type of resonant effect with potential applications in many areas, such as scattering cross sections, notch filters, and directional couplers for highly sensitive target identifications of biological and chemical agents.

ACKNOWLEDGMENT

REFERENCES

1. Bender, C. M. and S. Boettcher, "Real spectra in non-hermitian hamiltonians having PT symmetry," *Physical Review Lett.*, Vol. 80, 5243–5246, 1998.

2. Bendix, O., R. Fleischmann, T. Kottos, and B. Shapiro, "Exponentially fragile PT symmetry in lattices with localized eigenmodes," *Physical Review Lett.*, Vol. 103, 030402, 2009.

3. Makris, K. G., R. El-Ganainy, D. N. Christodoulides, and Z. H. Musslimani, "PT-symmetric optical lattices," *Physical Review A*, Vol. 81, 063807, 2010.

4. Alaeian, H. and J. A. Dionne, "Non-Hermitian nanophotonic and plasmonic waveguides," *Physical Review B*, Vol. 89, 075136, 2014.

5. Jones, H. F., "Analytic results for a PT-symmetric optical structure," *J. Phys. A*, Vol. 45, 135306, 2012.

6. Feng, L., Y. L. Xu, W. S. Fegadolli, M. H. Lu, J. E. B. Oliveira, V. R. Almeida, Y. F. Chen, and A. Scherer, "Experimental demonstration of a unidirectional reflectionless parity-time metamaterial at optical frequencies," *Nature Materials*, Vol. 12, 108–113, 2013.

7. Longhi, S., "Invisibility in PT-symmetric complex crystals," *J. Phys. A*, Vol. 44, 485302, 2011.

8. Kang, M., H. X. Cui, T. F. Li, J. Chen, W. Zhu, and M. Premaratne, "Unidirectional phase singularity in ultrathin metamaterials at exceptional points," *Physical Review A*, Vol. 89, 065801, 2014.

9. Lin, Z., H. Ramezani, T. Eichelkraut, T. Kottos, H. Cao, and D. N. Christodoulides, "Unidirectional invisibility induced by PT-symmetric periodic structures," *Physical Review Lett.*, Vol. 106, 213901, 2011.

10. Rüter, C. E., K. G. Makris, R. El-Ganainy, D. N. Christodoulides, M. Segev, and D. Kip, "Observation of parity-time symmetry in optics," *Nature Physics*, Vol. 6, 192–195, 2010.

11. Regensburger, A., C. Bersch, M.-A. Miri, G. Onishchukov, D. N. Christodoulides, and U. Peschel, "Parity-time synthetic photonic lattices," *Nature*, Vol. 488, 167–171, 2012.

12. Feng, S. and K. Halterman, "Coherent perfect absorption in epsilon-near-zero metamaterials," *Physical Review B*, Vol. 86, 165103, 2012.

13. Sun, Y., W. Tan, H. Q. Li, J. Li, and H. Chen, "Experimental demonstration of a coherent perfect absorber with PT phase transition," *Physical Review Lett.*, Vol. 112, 143903, 2014.

14. Guo, A., G. J. Salamo, D. Duchesne, R. Morandotti, M. Volatier-Ravat, V. Aimez, G. A. Siviloglou, and D. N. Christodoulides, "Observation of PT-symmetry breaking in complex optical potentials," *Physical Review Lett.*, Vol. 103, 093902, 2009.

15. Savoia, S., G. Castaldi, and V. Galdi, A. Alú, and N. Engheta, "Tunneling of obliquely incident waves through PT-symmetric epsilon-near-zero bilayers," *Physical Review B*, Vol. 89, 085105, 2014.

16. Fleury, R., D. L. Sounas, and A. Alú, "Negative refraction and planar focusing based on parity-time symmetric metasurfaces," *Physical Review Lett.*, Vol. 113, 023903, 2014.

17. Longhi, S., "PT-symmetric laser absorber," *Physical Review A*, Vol. 82, 031801(R), 2010.

18. Brandstetter, M., M. Liertzer, C. Deutsch, P. Klang, J. Schöberl, H. E. Türeci, G. Strasser, K. Unterrainer, and S. Rotter, "Reversing the pump dependence of a laser at an exceptional point," *Nature Commun.*, Vol. 5, 4034, 2014.

19. Chong, Y. D., L. Ge, and A. D. Stone, "PT-symmetry breaking and laser-absorber modes in optical scattering systems," *Physical Review Lett.*, Vol. 106, 093902, 2011.

20. Rotter, I., "A non-Hermitian Hamilton operator and the physics of open quantum systems," *J. Phys. A*, Vol. 42, 153001, 2009.

21. Heiss, W. D., "Repulsion of resonance states and exceptional points," *Physical Review E*, Vol. 61, 929–932, 2000.

22. Kang, M., F. Liu, and J. Li, "Effective spontaneous PT-symmetry breaking in hybridized metamaterials," *Physical Review A*, Vol. 87, 053824, 2013.

23. Mostafazadeh, A., "Resonance phenomenon related to spectral singularities, complex barrier potential, and resonating waveguides," *Physical Review A*, Vol. 80, 032711, 2009.

24. Aalipour, R., "Optical spectral singularities as zero-width resonance frequencies of a Fabry-Perot resonator," *Physical Review A*, Vol. 90, 013820, 2014.

25. Moharam, M. G. and T. K. Gaylord, "Rigorous coupled-wave analysis of planar-grating diffraction," *J. Opt. Soc. Am.*, Vol. 71, 811–818, 1981.

26. Palik, E. D., *Handbook of Optical Constants of Solids*, Academic Press, San Diego, 1998.

Statistical Models of Noise Distribution in Broadband PLC Networks

A. M. Nyete, **T. J. O. Afullo**, **and I. E. Davidson**

HVDC/Smart Grid Research Centre, Discipline of Electrical, Electronic and Computer Engineering
University of KwaZulu-Natal, Durban, South Africa

Abstract— The recent advancements in digital communication techniques have seen renewed interest in the possible utilization of the traditional power grid for the provision of broadband data and voice services. However, the power line communication (PLC) channel (the power network), presents a very challenging environment for communication purposes. This is due to the fact that severe noise and distortion effects are inherent in the medium. But, if these noise and distortion effects can be effectively analyzed and modeled, then the resulting models can be utilized in the optimal or sub-optimal design of a digital communication system for PLC applications. In this paper, frequency domain noise measurements done in broadband indoor PLC networks are presented. The measurement results obtained are then modeled using the alpha stable distribution, motivated by the flexibility of the distribution as a modeling tool and the fact that the measured noise distribution is heavily tailed and skewed.

1. INTRODUCTION

The traditional power grid, which was designed to deliver one way electric power, has seen tremendous evolution in the recent past. This has led to the emergence of an even more efficient, self-monitoring and controlled power system; the smart grid. The smart grid extends the traditional goal of using the power grid to deliver electric energy to include functionalities that enable real time load monitoring and control, automated meter reading, pre-paid billing as well as delivery of data services, among a plethora of other services. Traditionally, the target data rates in PLC technologies were low and the main application was in monitoring and data acquisition from different network elements. This constitutes what is referred to as narrowband power line communications (NB-PLC). However, recently, there has been a shift in PLC research, with most of the research activities focused on the use of the power grid to deliver higher data rate services. This has led to the development of new PLC technologies that seek to provide broadband services through the power grid; what is known as broadband power line communication (BB-PLC) [1–3].

Power line network systems are the most widely deployed in the world, and therefore the network provides a readily available infrastructure for the roll out of PLC technologies. PLC technologies are widely applied in smart grid applications, as mentioned earlier, networking of home equipment, monitoring and control of traffic lights in airport runways, monitoring and control of street lights, among a myriad of other applications. The fact that power network is ubiquitous renders it very attractive for exploitation as a communications medium. However, since the power grid was originally optimized for power delivery, it represents a very challenging environment for the delivery of communication services. This is due to the fact that almost all equipment connected to the power grid and even the power grid itself are possible sources of channel distortion and noise. These channel distortions manifest themselves in the form of frequency selective fading and attenuation. Moreover, the channel characteristics are highly dynamic in terms of frequency, time as well as location. Hence, different distortion effects will be experienced at different times of the day, varying mainly between peak and off peak hours, with more distortion expected during peak hours when there are a lot of activities going on in the power grid; that is, connection and disconnection of electrical equipment to/from the network. Also, the channel distortion varies across the frequency band of operation with more attenuation experienced at higher frequencies. Additionally, the attenuation tends to be highest in the low voltage (LV) networks and least in high voltage (HV) networks. However, the distortion effects will also highly depend on the weather conditions, networking loading as well as cable type and diameter [2–5].

Noise, the other biggest impairment in PLC networks, is responsible for degraded channel performance if not properly taken care of in design. The noise in PLC networks emanates from silicon controlled-rectifiers, dimmer switches, switching power supplies, brush motors and virtually all other equipment connected to the power network, for example, computers, printers, photocopiers, electric kettles, iron boxes, washing machines, et cetera. The noise in PLC network is

categorized into generalized background noise, synchronous impulsive noise and sporadic (random) impulsive noise. Given the degradation that PLC noise causes in the channel performance, it is essential that the noise measurements be done and, characterized properly; parametrically or non-parametrically [6–8]. Different authors have treated the subject on PLC noise measurements, modeling and characterization in both time and frequency domains. Recently, Nyete et al. [5], proposed a multipath model of the channel frequency response based on a Rayleigh approximation. Also, Mulangu et al. [4] have also developed a framework for the estimation of the specific attenuation in broadband channels due to scattering points. On the other hand, Zimmerman and Dostert [7] have reported on the time domain and spectral analysis of impulsive noise, with particular focus on the pulse amplitude, interarrival time and impulse width distributions in typical power lines. Additionally, they have also examined the disturbance ratio and the impulsive rate in their work. In [9], Chan and Donaldson have also reported on the interarrival time, impulse width and amplitude probability distributions of noise impulses based on measurements carried out in both residential and industrial buildings. Their measurements are carried out with or without specific electrical loads on a 120 V network. Also, in [10], a similar approach to that adopted in [7, 9] above is also employed in the classification and characterization of impulsive noise in indoor power lines. In [11], Cortes et al. combine both time and frequency domain techniques to model the PLC noise measured in different buildings. Some other noise measurements, characterization and modelling efforts are those of Katayama et al. [12] and Vines et al. [13].

In this paper, we present results of an intensive PLC frequency domain noise measurement campaign carried out in different offices, laboratories and workshops in the Department of Electrical, Electronic and Computer Engineering building at the University of KwaZulu-Natal, Howard Campus, Durban, South Africa. The results of the measured noise power spectra probability distribution are then modelled using stable distribution. The choice of this statistical tool is informed by the fact that the noise spectrum probability distribution is seen to be heavily tailed and skewed, a property that the stable laws can perfectly model. Alpha stable distribution is a very attractive modeling tool especially in cases where impulsive characteristics are recorded; which means that the resulting distribution deviates from the traditional and widely used Gaussian distribution. Stable distributions have very attractive properties, some of which are highlighted below.

2. STABLE DISTRIBUTIONS

The stable family of distributions is a special class of distributions with heavier tails than the normal distribution; which means they give better and more robust estimates of the occurrence probability of extreme events. Noise occurrence in a PLC network is one such extreme event, considering its impulsive characteristics. Furthermore, the noise distribution in PLC networks is non-Gaussian and non-white. This distribution belongs to a class of distributions that are invariant under linear combinations; with three special cases, namely the Gaussian, Cauchy and Levy distributions. However the probability density function of this distribution does not exist in closed form. Only closed form expressions of the probability density function of the Gaussian, Cauchy and Levy distributions exist. Thus, the distribution is parameterized in terms of its characteristic function [14, 15]. The characteristic function is defined as [14, 15]:

$$
\phi(t) = \begin{cases} \exp\left\{i\delta t - \gamma^{\alpha}|t|^{\alpha}\left[1 - i\beta\mathrm{sgn}(t)\tan\frac{\pi\alpha}{2}\right]\right\}, & \alpha \neq 1 \\ \exp\left\{i\delta t - \gamma|t|\left[1 + i\beta\frac{2}{\pi}\mathrm{sgn}(t)\ln|t|\right]\right\}, & \alpha = 1 \end{cases}
\tag{1}
$$

Where

$$
\mathrm{sgn}(t) = \begin{cases} 1 & \text{for } t > 0 \\ 0 & \text{for } t = 0 \\ -1 & \text{for } t < 0 \end{cases}
$$

And; $-\infty < \delta < \infty$, $\gamma > 0$, $0 < \alpha \leq 2$, $-1 \leq \beta \leq 1$.

From (1), we see that the stable distribution is defined by four parameters: the characteristic exponent, α, the skewness parameter β, the location parameter, δ, and the scale or dispersion parameter, γ. Additionally, we see that the stable distribution is a modelling tool that is very flexible, with the characteristic exponent controlling the heaviness of the distribution tails. A large value of α indicates less impulsiveness and vice versa. Again, as α approaches 2, the distribution tends to exhibit Gaussian tendencies. In fact, when $\alpha = 2$, the distribution is Gaussian. A

theoretical justification of the stable distribution as a modelling tool comes from the Central Limit Theorem, which states that a physical phenomenon is Gaussian if there is an infinite number of independent and identically distributed (i.i.d) contributing sources (factors) with finite variance. Moreover, the Generalized Central Limit Theorem for an infinite number of i.i.d random variables states that if these variables converge with or without variance to a distribution by increasing their number, the limit distribution must be stable [14, 16].

3. NOISE MEASUREMENTS AND ANALYSIS

Indoor PLC noise measurements were carried out in different rooms at the Electrical, Electronic and Computer Engineering Department building at Howard College, University of KwaZulu-Natal, Durban, South Africa. The noise measurements were done in the frequency domain using a Rhode and Schwarz FS300 spectrum analyzer and a simple coupler designed for the task. The noise was measured in the frequency range 0–30 MHz. The indoor supply voltage in South Africa is 230 V 50 Hz. Some of the results obtained are shown in Figures 1 and 2 below. We observe from Figure 1 that the noise captured in room 501 is less impulsive than that captured in the other two rooms (Figure 2). Actually, much of the noise in this room can be simply classified as background noise, whose average level is approximately −49 dBm. Room 501 is laboratory that was not in use at the time of the measurements. It only had one active PC and several florescent bulbs. All other equipment housed in the room were dormant during the measurement period. On the contrary, we see that the noise captured in the electronic workshop is the most impulsive. This is due to the fact that this room has a lot of activities going on including drilling operations and fabrication of PCBs. The room also houses several computers and soldering equipment. In all the noise measured, we see, for example in Figures 1 and 2 that the noise level between 0–10 MHz is the highest and this can be attributed to the fact that most of radio broadcast interference is prevalent in this band.

Figure 3 shows the probability density function (pdf) of the measured noise spectra. From this figure, we see that the much of the noise captured has a low power spectral density (PSD), and therefore can be classified as background noise; noise that is always present in the system either due to narrowband disturbances or colored background noise (thermal noise), which emanates from sources with low power but cannot be easily traced to their specific origin.

Additionally, we see that strong impulses are also captured, and despite the fact that their probability of occurrence is low, they are very intense when they occur. These impulses are sources
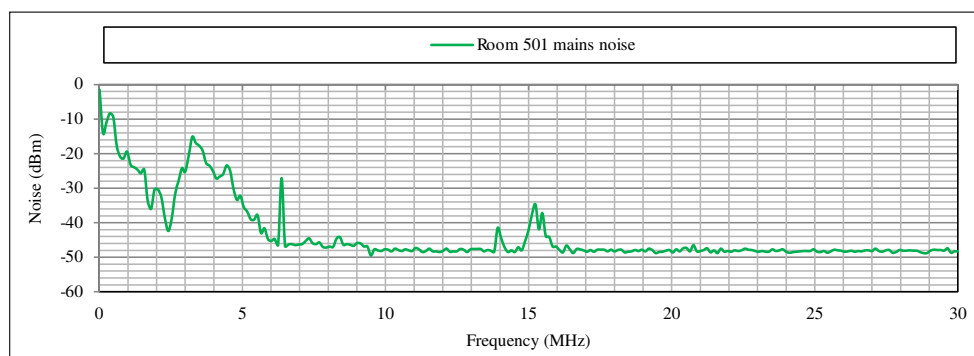

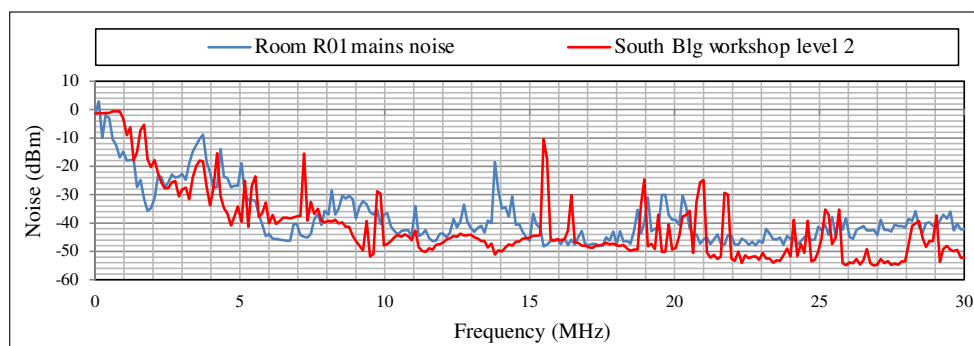Figure 1: Noise spectrum captured in a room 501.

Figure 2: Noise captured in an electronic workshop and a microwave lab (R01).

of high noise power, and when they occur, they can wipe out data streams resulting in deteriorated system performance. The difference between the lowest and highest noise values recorded is about 60 dB. This result closely ties with observations in [7, 8], where we see that the impulsive noise can be as high as 50 dB above the background noise. A simple classification of the strength of the noise captured has been derived and is shown in Table 1.
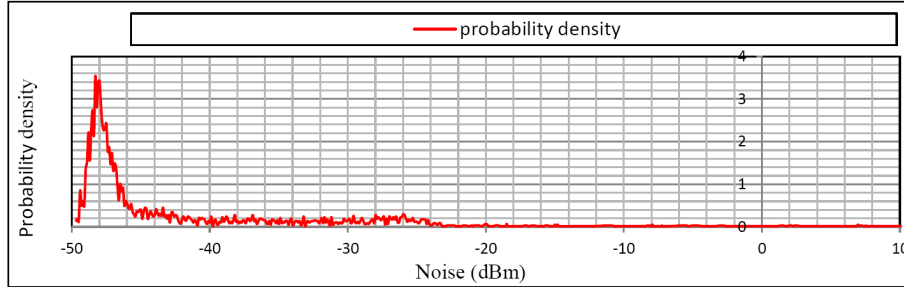

Figure 3: Probability density function of the measured noise characteristics.

Table 1: Measured noise classification.

Strength, n, dBm	Noise category
$-50 \leq n \leq -45$	Background noise
$-45 < n \leq -25$	Weak impulses
$n < -25$	Strong impulses

4. NOISE MODELING

From Figures 1, 2, and 3, we observe that the measured noise distribution is non-white, non-Gaussian, and more importantly, it is heavily tailed and skewed. The stable family of distributions is best suited to model the measured pdf shown in Figure 3 since they possess a heavy tailed characteristic (controlled by the characteristic exponent) and are also able to model any case of symmetry or asymmetry, which is controlled by the symmetry parameter. However, since the pdf of the stable distribution does not exist in closed form, we have to estimate the four parameters that define its characteristic function. Several methods exist in literature that can be used to estimate the parameters; for example, the Koutrouvelis' method [17], Dumouchel method [18] and Paulson et al. technique [19]. However, only Koutrouvelis' method is adopted in this paper due to its superior performance compared to earlier techniques, like those in [18, 19].

Koutrouvelis' method is a Fourier based method that estimates the stable distribution parameters by regressing the empirical characteristic function (ECF) onto the parameterized characteristic function. The ECF estimation interval is stored in a look-up table, and is chosen based on the initial parameter estimates and the size of the sample. Then, the regression procedure is repeated with an interval on the ECF based on the new estimates of the parameters. The entire process is repeatedly carried out until a predefined criterion of convergence is satisfied, typically a set number of iterations. This procedure is quite tasking in terms of the computational intensity but with the current supercomputing capabilities, it is not much of a problem. The method proposed by Koutrouvelis is easier to implement and faster than earlier methods; for example those proposed in [18, 19]. This regression type estimation method is based on an observation concerning the characteristic function. First, the following is implied from (1), [17]:

$$\log\left(-\log|\phi(t)|^2\right) = \log\left(c^\alpha\right) + \alpha \log|t| \tag{2}$$

where $c^\alpha = \gamma$, the scale parameter, and the real and imaginary parts of $\phi(t)$, $\text{Re}\phi(t)$ and $\text{Im}\phi(t)$, respectively, for $\alpha \neq 1$, are:

$$\text{Re}\phi(t) = \exp\left(-|ct|^\alpha\right) \cdot \cos\left[\delta t - |ct|^\alpha \beta \text{sgn}(t) \tan\left(\frac{\pi\alpha}{2}\right)\right] \tag{3}$$

$$\text{Im}\phi(t) = \exp\left(-|ct|^\alpha\right) \cdot \sin\left[\delta t - |ct|^\alpha \beta \text{sgn}(t) \tan\left(\frac{\pi\alpha}{2}\right)\right] \tag{4}$$

Apart from principal values, from Equations (3) and (4), we deduce the following:

$$\arctan\left(\mathrm{Im}\phi(t)/\mathrm{Re}\phi(t)\right) = \delta t - \beta c^{\alpha} \tan\left(\frac{\pi\alpha}{2}\right) \mathrm{sgn}(t)|t|^{\alpha} \tag{5}$$

Parameters c and α, which control Equation (2), are obtained by regressing $y = \log(-\log|\phi_n(t)|^2)$ on $\omega = \log|t|$ in the model given below:

$$y_k = \mu + \alpha\omega_k + \varepsilon_k, \quad k = 1, 2\ldots, K, \tag{6}$$

where $(t_k; k = 1, 2\ldots, K)$ is an appropriate set of real numbers, $\mu = \log(2c^{\alpha})$, and ε_k denotes an error term. After determining the fixed values of c and α, β and δ are obtained from (5), by regressing $z = g_n(u) + \pi k_n(u)$ on u and $\mathrm{sgn}(u)|u|^{\alpha}$ in the model:

$$z_l = \delta u_1 - \beta c^{\alpha} \tan\left(\frac{\pi\alpha}{2}\right) \mathrm{sgn}(u_l)|u_l|^{\alpha} + \eta_l, \quad l = 1, 2, \ldots, L \tag{7}$$

where η_l denotes the error term and $(\mu_l; l = 1, 2\ldots, L)$ is an appropriate set of real numbers, integer $k_n(u)$ is introduced to take care of any possible nonprincipal branches of the arctan function, and $g_n(u) = \arctan(\mathrm{Im}\phi(t)/\mathrm{Re}\phi(t))$. The reader is referred to [17] for more details on this method. The estimates obtained for the four parameters of the measured noise spectrum distribution are shown in Table 2.

Table 2: Noise stable distribution parameters.

	Characteristic exponent (α)	Symmetry Index (β)	Scale parameter (γ)	Location parameter (δ)
Parameter values	1.72	1	4.29	-45.69

From the estimated parameters, a stable distribution noise model was fitted. This model is shown in Figure 4 below. From this figure, we see that the fitted Alpha stable model approximates the measured statistics satisfactorily. The model approximates the location of the measured maximum density ($\delta = 45.69\,\mathrm{dBm}$) very well as well as the left skewness of the measured statistics (which is maximum as per the value of the symmetry parameter obtained, that is, $\beta = 1$).
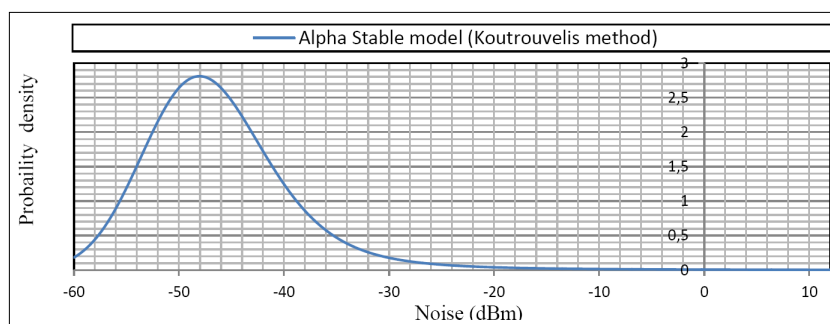

Figure 4: Alpha stable PLC noise model.

Also, we see that the heavy tailed (long tailed) characteristic of the measured data is very well captured by the fitted model. Thus the model is a good approximation of the measured noise data. However, the sharp peaked/sloped nature of the measured noise statistics, as seen in Figure 3, makes it very difficult to fit the data parametrically. This is an aspect of the noise data distribution that needs further investigation. More noise measurements are required to validate the results obtained and the approach used.

5. CONCLUSION AND FUTURE WORK

Noise in communication networks is undoubtedly the most severe source of performance degradation in virtually all wired and wireless systems. In this paper, a framework for modeling the noise

characteristics in indoor power lines using alpha stable models has been introduced. The measured statistics are seen to conform to most of the observations in other studies carried out by previous authors in the same area. We see that strong impulsive noise has a much lower probability of occurrence but is characterized by high power as compared to the background noise, and vice versa. The impulsive noise can be as high as one million times above the average background noise as seen from our results, although other studies have found it to go as high as one hundred thousand times. The results obtained here form a basis for an alternative approach in the modeling and characterization of noise in indoor broadband PLC networks. Possible avenues for future research would be to carry out more noise measurements to ascertain the validity of the results obtained here, and even employ alternative methods to model similar noise in PLC networks.

REFERENCES

1. Ferreira, H. C., H. M. Grove, O. Hooijen, and A. J. Han Vinck, "Power line communications: An overview," *IEEE Africon*, 558–563, Stellenbosch, South Africa, September 24–27, 1996.

2. Zwane, F. and T. J. O. Afullo, "An alternative approach in power line communication channel modelling," *Progress In Electromagnetics Research C*, Vol. 47, 85–93, 2014.

3. Lazaropoulos, A. G., "Broadband transmission characteristics of overhead high-voltage power line communication channels," *Progress In Electromagnetics Research B*, Vol. 36, 373–398, 2012.

4. Mulangu, C. T., T. J. Afullo, and N. M. Ijumba, "Estimation of specific attenuation due to scattering points for broadband PLC channels," *PIERS Proceedings*, 92–96, Kuala Lumpur, Malaysia, March 27–30, 2012.

5. Nyete, A. M., T. J. O. Afullo, and I. Davidson, "On rayleigh approximation of the multipath PLC channel: Broadband through the PLC channel," *2014 SATNAC Proceedings*, Port Elizabeth, South Africa, August 31–September 3, 2014.

6. Voglgsang, A., T. Lannguth, G. Korner, H. Steckenbiller, and R. Knorr, "Meausurement, characterization and simulation of noise on powerline channels," *ISPLC proceedings*, 139–146, 2000.

7. Zimmermann, M. and K. Dostert, "Analysis and modeling of impulsive noise in broad-band powerline communications," *IEEE Transactions on Electromagnetic Compatibility*, Vol. 44, No. 1, 249–258, November 2002.

8. Nyete, A. M., T. J. O. Afullo, and I. Davidson, "Performance evaluation of an OFDM-based BPSK PLC system in an impulsive noise environment," *PIERS Proceedings*, 2510–2513, Guangzhou, China, August 25–28, 2014.

9. Chan, M. H. L. and R. W. Donaldson, "Amplitude, width, and interarrival distributions for noise impulses on intrabuilding power line communication networks," *IEEE Transactions on Electromagnetic Compatibility*, Vol. 31, No. 3, 320–323, August 1989.

10. Degardin, V., M. Lienard, A. Zeddam, F. Gauthier, and P. Degauque, "Classification and characterization of impulsive noise on indoor power line used for data communications," *IEEE Transactions on Consumer Electronics*, Vol. 48, No. 4, 913–918, November 2002.

11. Cortes, J. A., L. Diez, F. J. Canete, and J. J. Sanchez-Martinez, "Analysis of the indoor broadband power-line noise scenario," *IEEE Transactions on Electromagnetic Compatibility*, Vol. 52, No. 4, 849–858, November 2010.

12. Katayama, M., T. Yamazato, and H. Okada, "A mathematical model of noise in narrowband power line communication systems," *IEEE Journal on Selected Areas in Communications*, Vol. 24, No. 7, 1267–1276, July 2006.

13. Vines, R. M., H. J. Trussell, L. Gale, and J. B. O'Neal, "Noise on residential power distribution circuits," *IEEE Transactions on Electromagnetic Compatibility*, Vol. 26, 161–168, November 1984.

14. Shao, M. and C. L. Nikias, "Signal processing with fractional lower order moments: Stable processes and their applications," *Proceedings of the IEEE*, Vol. 81, 986–1010, 1993.

15. Lombardi, M. J., "Bayesian interference for α-stable distributions: A random MCMC approach," *Computational Statistics and Data Analysis*, Vol. 51, 2688–2700, 2007.

16. Feller, W., *An Introduction to Probability Theory and Its Applications*, Vol. I, John Wiley and Sons, New York, 1967.

17. Koutrouvelis, I. A., "Regression-type estimation of the parameters of stable laws," *Journal of the American Statistical Association*, Vol. 75, No. 372, 918–928, December 1980.

18. Dumouchel, W. H., "Stable distributions in statistical inference: Information from stably distributed samples," *Journal of the American Statistical Association*, Vol. 70, 386–393, 1975.
19. Paulson, A. S., E. W. Holcomb, and R. A. Leitch, "The estimation of parameters of the stable laws," *Biometrika*, Vol. 62, 163–170, 1975.

High Quality InAlAs on InP for High Sensitivity Photodiodes

D. V. Dmitriev, A. M. Gilinsky, A. I. Toropov, E. V. Fedosenko, and K. S. Zhuravlev

Rzhanov Institute of Semiconductor Physics, The Siberian Branch of the Russian Academy of Sciences
pr. Ac. Lavrentieva, 13, Novosibirsk 630090, Russia

Abstract— The technology of synthesis of InAlAs layers lattice matched to InP by the molecular beam epitaxy technique and the details of pre-epitaxial substrate treatments are considered in this work. We find that with the arsenic beam equivalent pressure of 5×10^{-5} Torr used the optimal structural parameters and luminescent properties were achieved with the substrate temperature to $520°$C.

1. INTRODUCTION

The progress in telecommunications requires advances in the technologies of synthesis and processing of multilayer semiconductor heteroepitaxial structures for light emitters and receivers operating in the 1.3–1.6 µm wavelength range. The ultimate obtainable parameters of an optical transmission line are directly dependent on the sensitivity and the frequency range of the photodetector. The technology of creation of high sensitivity avalanche photodiodes has become therefore one of the most important directions of research and development in this field.

To further improve the parameters of high-sensitivity photodetectors for fiber-based transmission lines the utilization of InAlAs/InGaAs heterostructures with an InAlAs avalanche multiplication layer grown lattice-matched on substrates of InP have been proposed [1]. An improvement in the signal-to-noise ratio and a better temperature stability of avalanche multiplication were predicted for the InAlAs-based structures [2, 3]. However, it was shown experimentally that high dark currents and dark count rates, being at least 2–3 orders of magnitude greater than those of the more mature InGaAs/InP diodes, were observed in such structures [1, 4–7]. The high dark count rates were tentatively attributed to the high tunneling currents in the InAlAs layer, possibly via deep levels in the material present due to defects and/or uncontrolled impurities. The realization of the predicted advantages of the InAlAs/InGaAs based structures requires therefore a revision and optimization of the growth technology used for synthesis of detector heterostructures and, first of all, of the aluminum-containing multiplication layer, aimed at minimization of the concentration of centers that cause the interband carrier tunneling.

In this paper we describe the technology of synthesis of layers of InAlAs on (001)InP substrates and detail the pre-epitaxial treatments of the substrates that are required to obtain high quality layers.

2. EXPERIMENTAL TECHNIQUES

The epitaxial structures used in this study were grown on semi-insulating substrates of (001) InP by the molecular beam epitaxial (MBE) technique in a Riber-32P MBE machine. The preliminary chemical preparation of InP substrates included degreasing, removal of a near-surface damaged layer and residual oxidized layer. The samples were degreased in a 1 : 1 solution of monoethanolamine and hydrogene peroxide for two minutes, rinsed in flowing deionized water for 5 min and dried with argon. The substrates were etched using a chemo-mechanical polishing with a specially designed wafer holder. For the removal of the damaged layer, a polishing etchant of 0.3 N solution of $K_2Cr_2O_7$, hydrobromic acid and deionized water in a 2 : 2 : 1 ratio was used [8]. After 5 minutes of polishing (corresponding to an etching depth of 16 µm) the sample was rinsed for 5 min in flowing deionized water and dried with argon. To remove the residual surface oxidized layer the substrates were kept for two minutes in isopropanol saturated with hydrogen chloride and then rinsed several times in pure isopropanol and dried with argon. The resulting morphology of InP substrates was monitored using the atomic force microscopy (AFM) technique in a Solver AFM setup (NT-MDT). The chemical state of the substrate surfaces was studied using the X-ray photoelectron spectroscopy.

Prior to layer growths, the molecular fluxes of constituent materials were measured using an ionization gauge. The substrate temperature was monitored by a single-wavelength infrared pyrometer. The growth process was monitored *in situ* by reflection high-energy electron diffraction (RHEED) technique.

The *ex situ* evaluation of the layer quality was performed by the AFM, X-ray diffraction (XRD), X-ray photoelectron spectroscopy (XPS), and photoluminescence (PL) techniques. The XPS spectra were acquired using an ultra-high vacuum Cameca Nanoscan-50 analytical system. The quantitative data on the surface composition of the samples were obtained from measured areas under peaks in the spectra. The corresponding relative sensitivity factors for each element were calculated from the theoretical photoionization cross-sections (Scofield cross-sections) taking into account the transmission function of the spectrometer analyzer. The PL was excited by a cw $532\,\text{nm}$ or $405\,\text{nm}$ lasers with a power density of $2\,\text{W/cm}^2$. The PL emission was dispersed by a double monochromator equipped with a cooled photomultiplier operated in the photon counting mode. The PL spectra were measured at a temperature of $T = 77\,\text{K}$.

3. EXPERIMENTAL RESULTS AND DUSCUSSION

Figure 1 shows typical AFM images of $5 \times 5\,\mu\text{m}$ regions of InP substrates (a) after the chemical treatment, and (b) after the annealing in the growth chamber in the flux of arsenic (As$_4$) with a beam equivalent pressure (BEP) of 5×10^{-5} Torr. It is seen that the etched substrate has a smooth surface with the root mean square values of the surface roughness of about $0.28\,\text{nm}$, while after the annealing the roughness increases to $1\,\text{nm}$.

The changes in the substrate surface state during the annealing process were monitored using the RHEED technique. Figure 2 displays RHEED images taken at various temperatures under the arsenic flux with the BEP of 5×10^{-5} Torr. At a substrate temperature of $350°\text{C}$ the (2×3) surface reconstruction is formed, while with temperature increased to $450°\text{C}$ the (2×6) reconstruction appears. At a further increased temperature it gradually disappears, and at $540°\text{C}$ the (4×2) reconstruction is formed. These surface reconstructions are caused by depletion of the surface region of group V elements, P and As. To the best of our knowledge, the appearance of the (2×6) structure is reported for the first time in this work, and is possibly connected with substitution of phosphorus by arsenic atoms. As it is known, under annealing under a flux of P a (2×8) surface reconstruction is observed in the same temperature range [9–11]. At a temperature of $540°\text{C}$ residual oxides are removed, which manifests itself in a change of the ratio of intensities of the peaks and background in the diffraction picture. After the removal of oxides during the cooldown the (2×4) reconstruction appears in the pictures. The subsequent growths of InAlAs layers were performed on substrates annealed at $540°\text{C}$.

Figure 3 demonstrates the XPS spectra of these substrates. It is seen from the figure that after the annealing in the flux of As$_4$ at a temperature of $540°\text{C}$ with a subsequent cooling, a large concentration of arsenic is present on the surface. During the annealing process phosphorus atoms desorb from the surface and are partly replaced with atoms of arsenic [12–14], which is accompanied with a formation of islands of InAs. This process leads to the increase in the surface toughness of the substrate. The average lateral size of the InAs islands estimated from AFM maps is about $200\,\text{nm}$.

Layers of In$_x$Al$_{1-x}$As with the InAs contents x close to the lattice-matched value of 0.52 and a thickness of $0.5\,\mu\text{m}$ were grown using the technique described above at various substrate temperatures of 480, 500, 515, 520 and $525°$ in the arsenic flux with a BEP of 5×10^{-5} Torr. According to
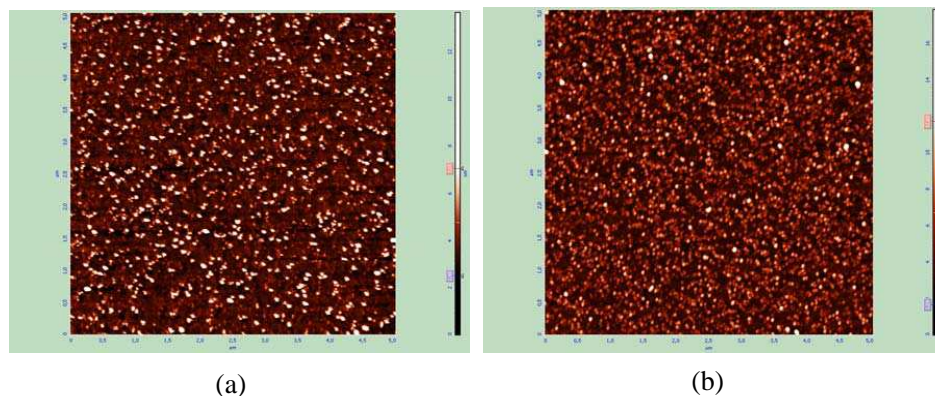

(a)   (b)

Figure 1: AFM images of 5×5 µm regions of InP substrates (a) after the chemical treatment, and (b) after the annealing in the flux of arsenic.

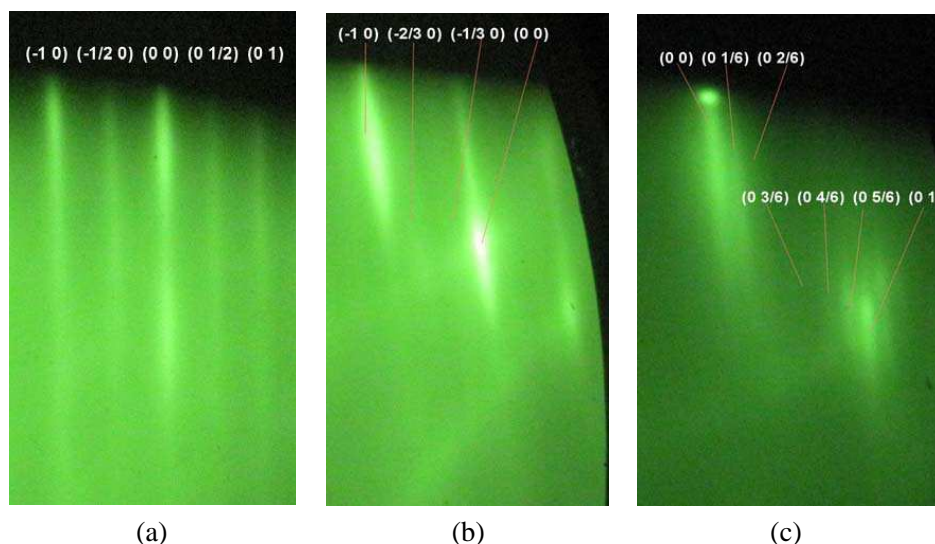(a)   (b)   (c)

Figure 2: RHEED diffraction pictures of InP substrates during annealing under the arsenic flux with the BEP of 5×10^{-5} Torr at various temperatures: (a), (b) (2×3) reconstruction at a temperature of $350°$C taken for azimuthal directions [110] and [−110], respectively,) (2×6) reconstruction at a temperature of $450°$.
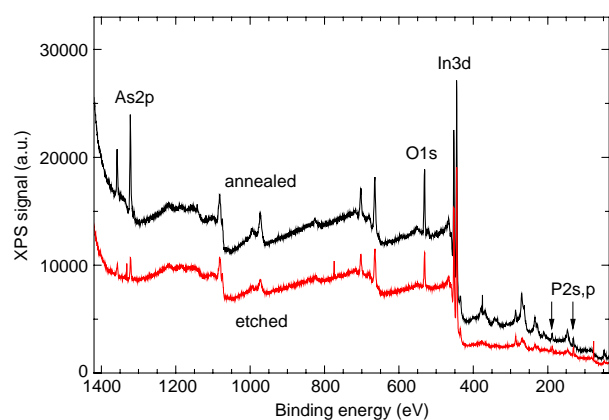

Figure 3: XPS spectra of InP substrates after the chemical treatment (lower curve) and after the annealing at $540°$C in the arsenic flux (upper curve).
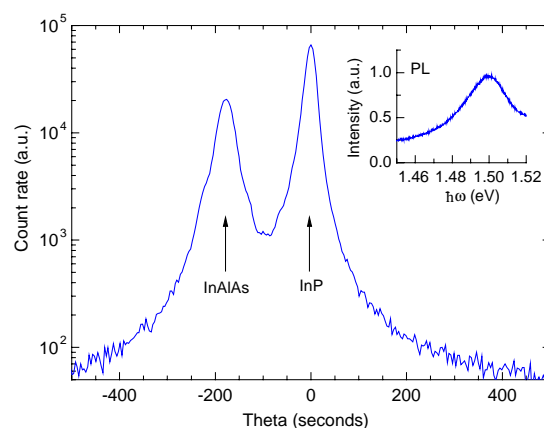
Figure 4: X-ray rocking curve (Cu Kα, 004 reflex) of an In$_{0.53}$Al$_{0.47}$As layer grown at a temperature of $520°$C. The inset shows the PL spectrum of this layer.

the X-ray diffraction data, the best structural parameters were obtained in layers grown at $520°$C. The full width at half maximum (FWHM) of double-crystal X-ray rocking curve was as low as $39''$ at this temperature, which was very close to the value of $32''$ taken on InP substrate, as illustrated in Figure 4. The inset to the figure shows the PL spectrum of the layer grown at $520°$. The spectrum consisted of a single band peaked at 1.499 eV with a FWHM of 27 meV that originated from band-to-band recombination, and in contrast to the samples grown at lower temperatures no impurity-related bands have been observed.

4. CONCLUSION

The conditions of pre-epitaxial chemical treatment and vacuum annealing of (001) InP substrates and MBE growth InAsAs layers were considered in this paper. We found that with the arsenic beam equivalent pressure of 5×10^{-5} Torr used in this work the optimal structural parameters and luminescent properties were achieved with the substrate temperature to $520°$C.

REFERENCES

1. Karve, G., X. Zheng, X. Zhang, X. Li, S. Wang, F. Ma, A. Holmes, J. C. Campbell, G. S. Kinsey, J. C. Boisvert, T. D. Isshiki, R. Sudharsanan, D. S. Bethune, and W. P. Risk, *IEEE J. Quantum Electron.*, Vol. 39, 1281, 2003.
2. Tan, L. J. J., D. S. G. Ong, J. S. Ng, C. H. Tan, S. K. Jones, Y. H. Qian, and J. P. R. David, *IEEE J. Quantum Electron.*, Vol. 46, 1153, 2010.
3. Mun, S. C. L. T., C. H. Tan, S. J. Dimler, L. J. J. Tan, J. S. Ng, Y. L. Goh, and J. P. R. David, *IEEE J. Quantum Electron.*, Vol. 45, 566, 2009.
4. Zhao, K., A. Zhang, Y. Lo, and W. Farr, *Appl. Phys. Lett.*, Vol. 91, 081107, 2007.
5. Zhao, K., S. You, J. Cheng, and Y. Lo, *Appl. Phys. Lett.*, Vol. 93, 153504, 2008.
6. Nakata, T., E. Mizuki, T. Tsukuda, S. Takahashi, H. Hatakeyama, T. Anan, K. Makita, and A. Tomita, *Proceeding of IEEE 15th OptoElectronics and Communications Conference*, 822, 2010.
7. Meng, X., C. H. Tan, S. Dimler, J. P. R. David, and J. S. Ng, *Optics Express*, Vol. 22, 22608, 2014.
8. Weyher, J. L., R. Fornari, and T. Gorog, *Mat. Sci. Engineering B*, Vol. 28, 488, 1994.
9. Esser, N., W. G. Schmidt, J. Bernholc, A. M. Frisch, P. Vogt, M. Zorn, M. Pristovsek, W. Richter, F. Bechstedt, T. Hannappel, and S. Visbeck, *J. Vac. Sci. Technol. B*, Vol. 17, 1691, 1999.
10. Ozanyan, K. B., P. J. Parbrook, M. Hopkinson, C. R. Whitehouse, Z. Sobiesierski, et al., *J. Appl. Phys.*, Vol. 82, 474, 1997.
11. LaBella, V. P., Z. Ding, D. W. Bullock, C. Emery, and P. M. Thibado, *J. Vac. Sci. Technol. A*, Vol. 18, 1492, 2000.
12. Li, C. H., L. Li, D. C. Law, S. B. Visbeck, and R. F. Hicks, *Phys. Rev. B*, Vol. 65, 205322, 2002.
13. Schmidt, W. G. and F. Bechstedt, *Surf. Sci.*, Vol. 409, 474, 1998.
14. Krzyzewski, T. J. and T. S. Jones, *Phys. Rev. B*, Vol. 78, 155307, 2008.

Finite Element Analysis of Separation Force on Non-ferrous Metals Induced by Eddy Current Separator

Ahmet Fenercioğlu and Hamit Barutcu

Department of Mechatronics Engineering, Gaziosmanpaşa University, Tokat 60250, Turkey

Abstract— Finite element method (FEM) analyses of the eddy current separator (ECS) that can separate non-ferrous metals from waste via the eddy current method have been carried out in this study. The forces induced in the non-ferrous metals to be separated by the magnetic drum determining the performance of the separator have been analyzed according to certain variables. These variables are drum speed, air gap between the material and the magnet pole, dimensions, and conductivity of the material and magnet height. The resultant force has been estimated according to these variables. The increase of drum speed and enlargement of non-ferrous metals, high conductivity and decrease of the air gap have increased the separation force. The ECS design is determined according to the analytical equalities has been verified by these analyses.

1. INTRODUCTION

Eddy current is an effective method for the separation of non-ferrous valuable metals. According to the eddy current principle, an electric charge is induced in the material in accordance with the Faraday's law when the changing magnetic flux is cut off the non-ferrous metal. Eddy currents occur in this materials and magnetic field occurs in the material due to the effect of the eddy currents in accordance with the Ampere's Law. This field is affected from the magnetic field of the magnetic drum. Thus a force is induced in the material as a result of the effect of these two fields interaction in accordance with the Biot-Savart law. The material is thrown from the product flow with the effect of this repellent force. Figure 1 shows the principle diagram [1] and actual photograph for the ECS displaying the separation of non-ferrous metals.
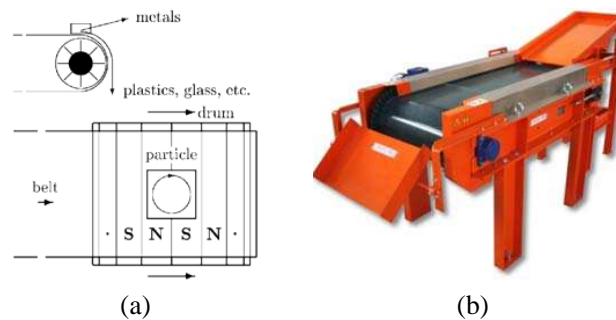

Figure 1: (a) ECS magnetic drum principle diagram [1], (b) ECS (COGELME™).

ECS is made up of a conveyor band system and a magnetic drum which is the most important part of ECS. It rotates at high speeds under the conveyor band independent of the driving gear of the band. Analyzed drum consist of 36 neodymium magnets which are placed on cylindrical iron surface as NS. Non-ferrous waste metal particles move towards the drum over the belt and fall into the container when they are interacted with the drum field. Thus, separation is completed. Literature survey has put forth that the number of studies on the magnetic analyses of ECS is not sufficient. The studies carried out aim to increase the separation performance in small particles. In Lungu study [2] the separation systems were examined for the small metal particles inside a two component non-ferrous mixture via a permanent magnet new type dynamic ECS. This ECS is also known as angular magnetic drum. This ECS contains permanent magnets and magnetic drum that is arranged as NS. Here, the effect of the angle of the drum in the horizontal position on the separation process has been examined. The experiments carried out using copper and copper aluminum have been successful [2]. Kang and Schoenung [3] have carried out studies putting forth that the main criteria for an eddy current separator are the density of the material ρ, its electrical conductivity σ and the ratio of its density to electrical conductivity σ/ρ. Materials with higher conductivity per density can be separated more easily. It is observed that the separation ratio is

higher for small particles in this separation process [3, 4]. It has been emphasized that the drum speed and the number of magnetic poles have to be increased in order to increase separation force will attain its maximum value as a result of this increase. In addition, it is also specified that separation efficiency can be increased by adjusting the material input and conveyor band speeds. Experiments have been carried out for the separation of materials from inside an aluminum and plastic mixture with different weights and a dimension of 5 mm by changing the speed of the drum between 10 Hz and 25 Hz and by changing the conveyor band rotational speed between 6 Hz and 12 Hz. It has been concluded as a result of the study that the efficiency is above 98% when the drum rotates at a speed of 25 Hz and the conveyor band rotates at a rate of 8 Hz [3, 4].

In this study; parameters that affect the separation performance for ECS design such as drum speed, air gap between the material and the magnet, type and dimensions of the materials have been examined by FEM and the results have been presented in graphs. Thus, it is a guiding study for design corrections.

2. MATERIAL AND METHOD

The most important variables that determine the separator efficiency are the amplitude and frequency of the eddy current. Increase in these variables directly affects separation efficiency since they also change the repellent force. Factors that determine the amplitude of the eddy current, its frequency and the magnitude of the repellent force depend on the material properties and separator design. The factors that depend on material properties are type, density, resistivity, conductivity, shape and dimensions. Whereas parameters that depend on separator design and drum speed, number of poles, magnetic field intensity of the drum and the air gap distance between the drum and the material. The induced current according to Faraday's law of induction in the particle subject to the variable magnetic field has been given in Eq. (1) [1, 5]. Here, the magnitude of the eddy current is determined by the rate of change of the magnetic flux with time.

$$\vec{\nabla} x \vec{J} = -\rho \frac{\partial \vec{B}}{\partial t} \tag{1}$$

where J is current density and ρ is the specific conductivity of the particle. The direction of the induction current is determined via Lenz Law. Accordingly, the direction of the induced current is opposite to the field that causes it to occur. These opposite magnetic fields generate a repellent force on the linear surface element (ds) and are represented by Eq. (2) [1, 5].

$$\vec{F}_L = I d\vec{s} x \vec{B} \tag{2}$$

Here, I is current induced on the material. F_L force provides the movement of the particle and diverts it. The force that causes separation via eddy current in the material. Wang et al. have expressed the repellent force in the eddy current separator caused by the variable magnetic field of the rotating magnetic drum in a more simplified manner with Eqs. (3) and (4) [4, 5].

$$F_r = H^2 f \times \frac{m\sigma}{\rho s} \tag{3}$$

$$f = \frac{np}{2} \tag{4}$$

where F_r represents the repellent force, H is magnetic field intensity, f is magnetic field frequency, n is speed of the magnetic drum, p is number of magnetic poles, m is mass, σ is conductivity and, ρ is density and s is shape factor. The resultant force is related with material properties for different materials. The ratio of conductivity to density (σ/ρ) determines the magnitude of the force and the difficulty of separation. Separation success is higher for materials with a higher ratio [4, 5]. The drum has been analyzed by the Ansys-Maxwell software using FEM. Drum speed, the air gap between the material and the drum magnet, the type of material and the size of the material have been examined in these analyses. The analyses carried out have put forth the effects of the axial and resultant forces that are generated on the material in accordance with the parameters given above. The design picture of the magnetic drum with 36 magnetic poles placed on a rotor and its 2 dimensional analysis model have been given in Figure 2. Transient analyses have been carried out for one pole step (from N to S) with high sampling ratio for the rotating motion since the analysis results will be the same for each pole step. To this end, the pole step duration for 2000 rpm speed

Table 1: NdFe$_{35}$ magnet specifications.

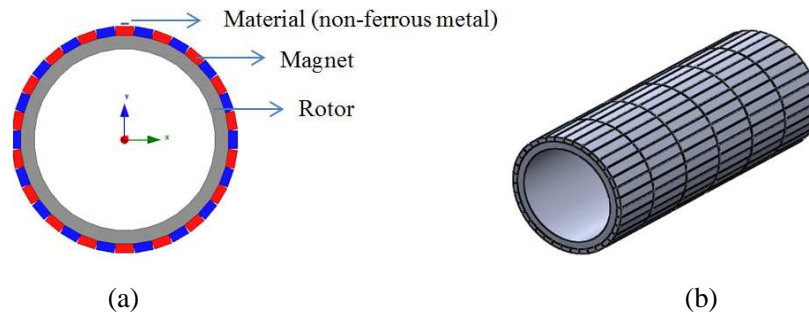| Relative permeability	1.0998	H magnitude	890000 A/m
Bulk conductivity	625000 S/m	Max. working temp.	100°C

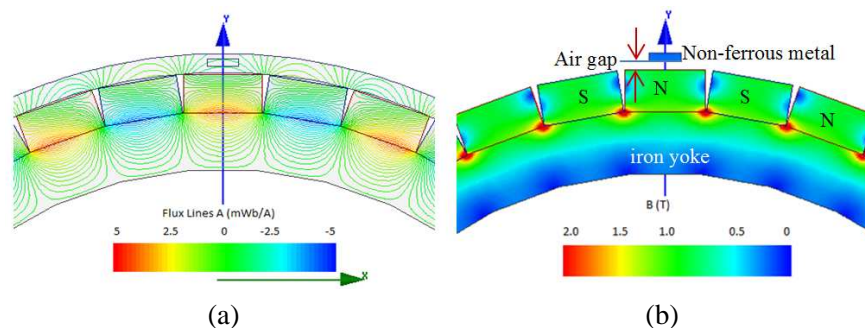Figure 2: Magnetic drum, (a) 2D analysis model, (b) 3D design model.

Figure 3: (a) Flux lines, (b) flux density.

is 833 μs. 125 solutions have been made in this time period and analysis results have been attained. Similarly, the results of the axial forces and resultant force on the material have been estimated for 2000–6000 rpm speeds with a high accuracy.

There are 36 magnet poles on the drum surface placed adjacent to each other as NS. The magnet specifications of these magnets have been given in Table 1.

3. FEM ANALYSES

Visual results that put forth the flux lines and the distribution of magnetic flux density in magnetic analyses have been given in Figure 3. It is observed that flux lines circle the material and that saturation occurs at the magnet corners.

All parameters excluding speed have been kept constant in order to examine the effect of speed on the forces that are generated on the material. During the analyses, a copper material with a height of 1 mm, width of 4 mm, and length of 10 mm has been placed on the drum. The horizontal, vertical and resultant forces on the material for drum speed values between 2000–6000 rpm have been examined. The resultant force according to speed have been given in Figure 4(a). According to the analysis results, the forces on the material verify the expressions given in Eqs. (3) and (4). It is observed that the period decreases, frequency and force increases with increasing speed.

The analyses carried out have targeted to determine the effect of the air gap on the eddy currents and thus the forces on the material. To this end, the material has been analyzed for air gap values between the material and the drum of 0.5, 1, 1.5, 2, 2.5 and 3 mm at a constant drum speed of 2000 rpm. The resultant force on the material has been given in Figure 4(b).

Magnetic reluctance increases in the air gap since magnetic flux permeability is low. Magnetic flux is inversely proportional with reluctance in a magnetic circuit. Magnetic flux that peneterate the material to be separated decreases when the air gap increases. According to the analyses results, the resultant force on the material increase when the air gap decreases. When the average value of the resultant force is considered, the force is approximately 53 mN for the case when the air gap is 3 mm and the air gap is 0.5 mm for the case when the force is 460 mN.
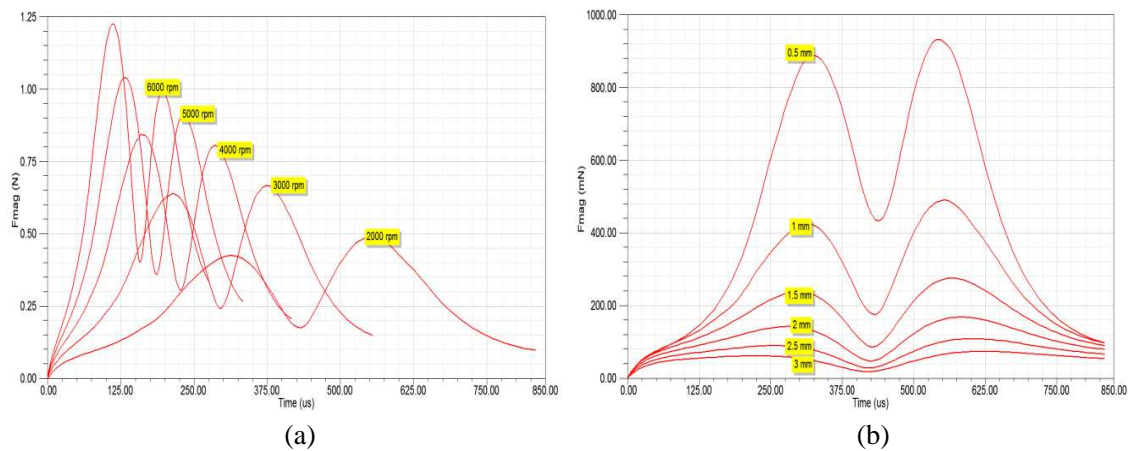
(a)   (b)

Figure 4: Resultant forces on the copper material, (a) vs. speed, (b) vs. air gap.
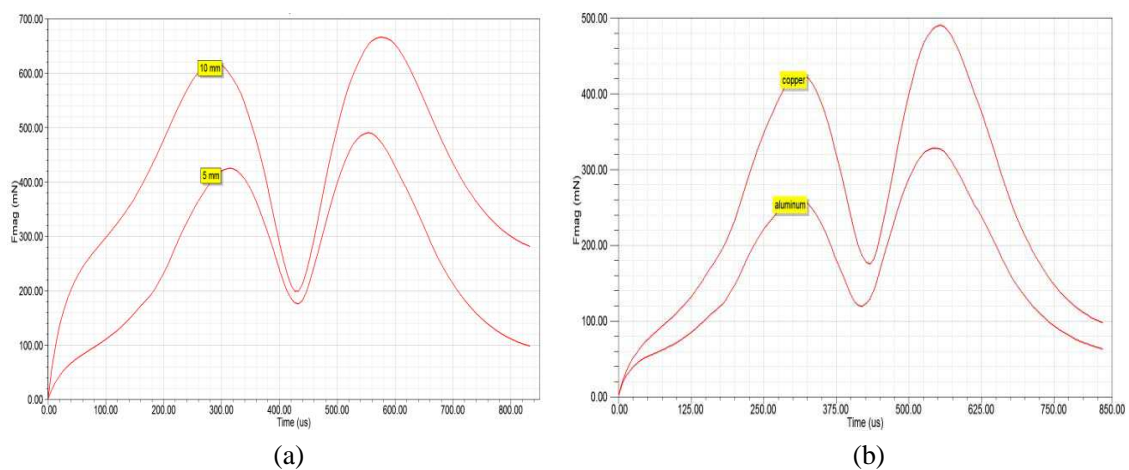

(a)   (b)

Figure 5: (a) Resultant forces acting on the copper material for different magnet dimensions, (b) resultant forces on aluminum and copper material.
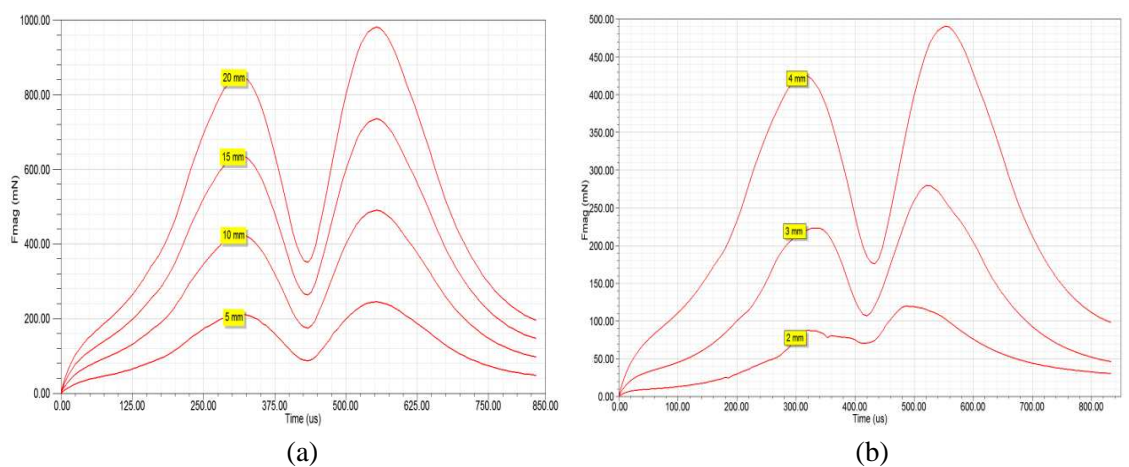

(a)   (b)

Figure 6: Resultant forces acting on the copper material, (a) vs. material length, (b) vs. material width.

Forces have been examined only for copper and aluminum during the analyses keeping all other parameters constant. The resultant force have been given in Figure 5(a). Since the specific resistance and density of the material changes according to the material type, the eddy current and force also changes. The force on materials with higher conductivity is higher.

The dimensions of the magnet have been kept constant at width of 10 mm and height of 50 mm

and height of 5 and 10 mm and analyses have been carried out. The resultant force acting on the material have been given in Figure 5(b).

The dimensions of the copper material have been kept constant at width of 4 mm and height of 1 mm and height of 5, 10, 15 and 20 mm and analyses have been carried out. The resultant force acting on the material have been given in Figure 6(a). The dimensions of the copper material have been kept constant at height of 1 mm and length of 10 mm. Variables are material width of 2, 3 and 4 mm analyses have been carried out. The resultant force acting on the material have been given in Figure 6(b). As can be seen from the graphs, the area of the material overlapping the magnetic surface increases with increasing material dimensions. Thus, eddy currents and the forces acting on the material also increase.

4. CONCLUSIONS

Non-ferrous materials are separated by ECS. According to Faraday, Ampere and Biot-Savart laws a repellent force is induced on non-ferrous material by the effect of eddy current. This force determines separation performance. The factors that affect the performance of this separation depend on the material specifications and the design of the ECS. Significant factors depend on metal conductivity, density and dimensions of the material. The variables that depend on design are drum speed, number of poles, the air gap, magnetic field intensity and magnet height. FEM analyses have been carried out for the variables are drum speed, air gap, magnet height, material type and dimensions. The increase of drum speed, material dimensions and magnet height, high conductivity of the material and decrease of air gap have increased the separation force and performance. Proposed magnetic drum design has been verified according to the obtained from these analyses.

REFERENCES

1. Rem, P. C., E. M. Beunder, and A. J. Akker, "Simulation of eddy-current separators," *IEEE Transaction on Magnetics*, Vol. 34, No. 4, 2280–2286, 1998.
2. Lungu, M., "Separation of small non-ferrous particles using an angular rotary drum eddy-current separator with permanent magnets," *International Journal of Mineral Processing*, Vol. 78, 22–30, 2005.
3. Kang, H. Y. and J. M. Schoenung, "Electronic waste recycling: A review of US infrastructure and technology options," *Resources Conversation & Recycling,* Vol. 45, 368–400, 2005.
4. Wang, Q., Y. Zhao, H. Jiao, and H. Zhang, "Effects of operation parameters of eddy current," *7th World Congress on Recovery, Recycling and Re-integration*, China, 2005.
5. Svoboda, J., *Magnetic Techniques for the Treatment of Materials*, Kluwer Academic Publishers, USA, 2004.

Numerical Estimation of Muscle Conductivity in Terms of Human Body Internal Resistance

Hiroo Tarao[1], Katsuaki Aga[1], Olenxandr Okun[2], and Leena Korpinen[3]

[1]National Institute of Technology, Kagawa College, Japan
[2]National Technical University, Ukraine
[3]Tampere University of Technology, Finland

Abstract— Internal human body resistances beween hand and foot have been calculated using a numerical human model. However, the results were about two times larger than measured ones which reported by other researchers. Focused on muscle conductivity in the present study, internal human body resistances were re-calculated and were compared with the measured ones.

1. INTRODUCTION

Numerically-anatomical human models have been often used for wide band frequency electromagnetic dosimetry [1]. For the dosimetry calculation, furthermore, typical dielectric properties such as conductivity and permittivity have been used for tissues that are assigned to each voxel of the human models. In our previous study, calculated results of human body internal resistances between hand and foot were two times larger than measured results $(500–700\,\Omega)$ [2]. One possible explanation for this is that there are few voxels assigned as blood, having relatively higher conductivity, because of the limitation that blood vessels with a diameter of less than $2\,\text{mm}$ could not be included in the model. Human body impedance is given as internal impedance combined in series with skin impedance. At low frequency, the resistive components of internal impedance are more dominant than capacitive components, and skin impedance changes greatly depending on contact area and surface wetness. Hence, we focus on internal resistances at $60\,\text{Hz}$ in the study, ignoring skin impedance and capacitive components of internal impedance. Therefore, with consideration for the fact that conductive currents in a body flow mostly through muscle, and the assumption that conductivities of blood and extracellular fluid should be mixed into the muscle conductivity, we calculate human body internal resistances between the left hand and left foot in the present paper, with changing muscle conductivity: $0.35–2.0\,\text{S/m}$. Here, $0.35\,\text{S/m}$ for muscle, $0.7\,\text{S/m}$ for blood, and $2.0\,\text{S/m}$ for extracellular fluid have been used as the typical conductivity values at $60\,\text{Hz}$ [3].

2. NUMERICAL PROCEDURES

2.1. Numerical Human Model

A realistic model of an adult male (Duke, $1.74\,\text{m}$ in height, $70\,\text{kg}$ in weight, $2\,\text{mm}$ voxel size), comprising 77 tissues and organs, was used for the numerical calculation [4]. Both conductivity and permittivity (i.e., complex conductivity) values corresponding to a given tissue can be assigned to an individual voxel. The conductivity values, except for wholly-distributed tissues such as muscle and fat, used in the calculation at $60\,\text{Hz}$ are based on the measurements of Gabriel et al. [3], which are commonly used in dosimetric calculations. In addition, the conductivity value of the skin was set to $0.1\,\text{S/m}$ in the calculation of the internal resistance to ignore skin impedance.

In the numerical human model, 1.2% of blood voxels are assigned, which is very less voxels than an actual adult male. In addition, it is found in our previous study that conductive currents in a body flow mostly through muscle. Therefore, conductivities of blood and extracellular fluid should be mixed into the muscle conductivity in the calculation. According to the Gabriel report mentioned above, the typical conductivity values for muscle, blood, and extracellular fluid are 0.35, 0.7, and $2.0\,\text{S/m}$ at $60\,\text{Hz}$, respectively. By referring to these values, muscle conductivity is set to $0.35–2.0\,\text{S/m}$ in the present calculations. As another reference, furthermore, conductivity values for blood and adipose tissue are also varied from the each typical value to $2.0\,\text{S/m}$.

2.2. Numerical Method

The numerical method used in this study is based on the scalar potential finite difference method, which has been widely used for quasi-static magnetic field induction [5]. The detailed description and the validity of our computational code were previously reported [6]. In the voxelized model, electric fields can be expressed by dividing the potential difference between the given and adjacent

voxel by the distance between their nodes. When two electrodes to which electric potentials are given in advance are attached to external surfaces of the voxelized model, current flowing between two adjacent voxels is obtained by multiplying the electric field by complex conductivity $(\sigma + i\omega\varepsilon)$ of the voxel, and further multiplying it by the cross-sectional area of the voxel. Here, σ is the electrical conductivity, and ω and ε are the angular frequency and permittivity, respectively. To determine the scalar potentials, conservation of the current that flows to a target voxel from its six adjacent voxels is applied at all nodes. Finally, the human impedance between the electrodes can be obtained by dividing the voltage across the electrodes by the total current.

2.3. Current Pathway

As typical current pathways of the human body for which resistance is measure, the study considers the pathway from the left hand to the left foot, for the numerical human model with both hands at the side. As some internal resistances have been measured in the situation [2]. As the resistances between back of left hand and top of left foot were measured in the literature [2], our calculated results for the two points would be also obtained to compare with them for validation. In the calculation, 1 V at 60 Hz is applied to the electrodes.

3. RESULTS AND DISCUSSION

Figure 1 shows the calculated human body resistance as a function of the conductivity value of each tissue. From the figure, the human body resistance does not change with higher conductivity of blood. Assuming that the blood vessels is 2 m in length and is 5 mm in diameter, the resistance can be simply calculated as 146 kΩ, which is very larger than the internal resistance between hand and foot. Therefore, change in conductivity values in the blood vessels does not influence the internal human body resistance. In contrast, it is clear from the figure that the human body resistance decreases with the higher conductivity of muscle. In addition, the internal resistance decreases gradually with the higher conductivity of adipose tissue. However, as fluid with high conductivity such as extracellular fluid is not likely to be included in the adipose tissue, the calculated result under the adipose tissue with high conductivity is clearly unrealistic.

Figure 2 shows the distribution of equipotential lines and internal electric field vector in the body. As the current flowing through the body is a fixed value, the equipotential line can be translated as the percentage of the resistance inside the human body. It is found from Figure 2 that the electric fields become higher at the joints such as wrist, elbow, knee, and ankle where the equipotential lines are short intervals. In contrast, it is clear that the electric fields in the right arm and right leg are quit small, where is not along the current path.
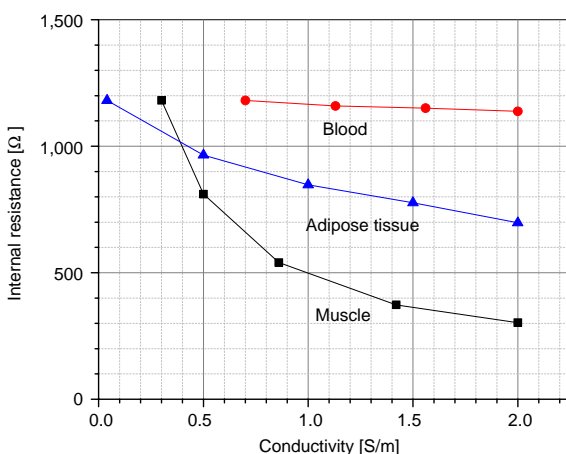

Figure 1: Calculated human body resistance as a function of the tissue conductivity.
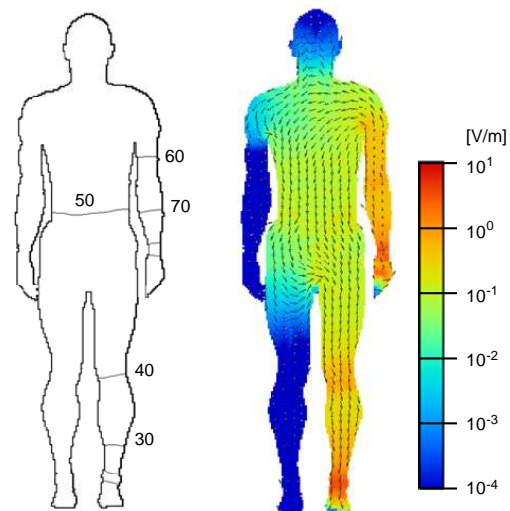
Figure 2: Distribution of equipotential lines in percentage and electric field vectors in the body.

4. CONCLUSION

It is concluded from the calculated results that the internal human resistance is reasonable compared to the measured results (500–700 Ω) when the conductivity values of muscle range from 0.7 to 1.0 S/m. More considerations including conductivity of other tissues and/or anisotropy of muscle should be further investigated.

REFERENCES

1. Xi, W., M. A. Stuchly, and O. P. Gandhi, "Induced electric currents in models of man and rodents from 60 Hz magnetics fields," *IEEE Trans. Biomed. Eng.*, Vol. 41, 1018–1023, 1994.
2. Bracken, T. D., G. G. Sias, C. Kim, R. S. Senior, and R. M. Patterson, "Survey of electrical utility worker body impedance," *IEEE Trans. on Power Delivery*, Vol. 23, 1251–1259, 2008.
3. Gabriel, S., R. W. Lau, and C. Gabriel, "The dielectric properties of biological tissues: II. Measurements in the frequency range 10 Hz to 20 GHz," *Physics in Medicine and Biology*, Vol. 41, 2251–2269, 1996.
4. Christ, A., W. Kainz, E. G. Hahn, K. Honegger, M. Zefferer, E. Neufeld, W. Rascher, R. Janka, W. Bautz, J. Chen, B. Kiefer, P. Schmitt, H. P. Hollenbach, J. Shen, M. Oberle, D. Szczerba, A. Kam, J. W. Guag, and N. Kuster, "The virtual family — Development of surface-based anatomical models of two adults and two children for dosimetric simulations," *Physics in Medicine and Biology*, Vol. 55, N23–N38, 2010.
5. Dawson, T. W. and M. A. Stuchly, "High-resolution organ dosimetry for human exposure to low-frequency magnetic fields," *IEEE Trans. Magnetics*, Vol. 34, 708–718, 1998.
6. Tarao, H., H. Kuisti, L. Korpinen, N. Hayashi, and K. Isaka, "Effects of tissue conductivity and electrode area on internal electric fields in a numerical human model for ELF contact current exposures," *Physics in Medicine and Biology*, Vol. 57, No. 10, 2981–2996, 2012.

A Necessary Condition for Application of Topological Derivative in Limited-aperture Inverse Scattering Problem

C. Y. Ahn[1], **K. Jeon**[1], **Y.-K. Ma**[2], **and W.-K. Park**[3]

[1]National Institute for Mathematical Sciences, Daejeon 305-811, Korea
[2]Department of Applied Mathematics, Kongju National University, Chungcheongnam-do 314-701, Korea
[3]Department of Mathematics, Kookmin University, Seoul 136-702, Korea

Abstract— Various studies have shown that the topological derivative-based non-iterative imaging algorithm can be employed in limited-aperture inverse scattering problems. However, this fact has been verified through the results of numerical simulations, and only a sufficient condition for its application has been theoretically discovered. In this work, we consider the topological derivative for the imaging of a thin, crack-like dielectric inhomogeneity, and explore a necessary condition for its application in a limited-aperture inverse scattering problem. This is based on a relationship between topological derivative imaging functions and infinite series of Bessel functions of integer order of the first kind. This relationship implies that the necessary condition is highly dependent on the shape of the unknown inhomogeneity. Numerical results are presented in order to support our findings.

1. INTRODUCTION

In this study, we consider an inverse scattering problem for discovering the shape of unknown thin curve-like dielectric inhomogeneities from measured boundary data. In past research, various algorithms for identifying the shape of unknown objects have been suggested. Most of these algorithms are based on Newton-type iteration schemes. However, in order to induce a good result, these schemes must start with a good initial guess, which is close to the unknown object. In order to produce a good initial guess, alternative non-iterative algorithms have been developed.

Among them, a topological derivative strategy has been applied with success. This strategy has been considered for shape optimization problems [6, 8, 9, 15], and was then successfully combined with the level-set method (see [2, 7, 12, 14]). Surprisingly, some remarkable studies [4, 5] found that topological derivatives present a non-iterative imaging algorithm. However, the majority of research has considered full-aperture problems. For more details, see [3, 11, 13]. Though it is true that various studies have confirmed that topological derivatives can be applied in limited-aperture problems, but this fact has been dependent on simulation results. Therefore, an analysis of topological derivatives in limited-aperture problems is an important requirement. Motivated by this fact, the mathematical structure of topological derivatives in limited-aperture inverse scattering problems has been established, in [1]. In this interesting research, a sufficient condition for its application has been identified theoretically, but a necessary condition remains unknown. Therefore, in this paper, we explore a necessary condition for the application of topological derivatives in limited-aperture inverse scattering problems. This is based on a relationship between topological derivatives and infinite series of Bessel functions of the first kind of the integer order.

This paper is organized as follows. In Section 2, we briefly introduce the two-dimensional direct scattering problem and the topological derivative imaging algorithm. In Section 3, we deduce a necessary condition for a successful application of topological derivatives in limited-aperture inverse scattering problems. In Section 4, several results of numerical simulations with noisy data are presented in order to support our findings. A brief conclusion is given in Section 5.

2. DIRECT SCATTERING PROBLEMS AND TOPOLOGICAL DERIVATIVES

Let $\Omega \subset \mathbb{R}^2$ be a homogeneous domain with a smooth boundary $\partial\Omega$, which contains a homogeneous thin inhomogeneity Γ with a small thickness $2h$. That is,

$$\Gamma = \{\mathbf{x} + \eta\mathbf{n}(\mathbf{x}) : \mathbf{x} \in \sigma, -h \leq \eta \leq h\},$$

where $\mathbf{n}(\mathbf{x})$ is the unit normal to σ at x, and σ denotes a simple, smooth curve in $\mathbb{R}^2$ describing the supporting curve of Γ. In this study, we assume that the applied angular frequency is of the

form $\omega = 2\pi\lambda$, where λ is a given wavelength and satisfying $h \ll \lambda$. All materials involved are non-magnetic (permeability $\mu \equiv 1$), and characterized by their dielectric permittivity at the frequency of operation ω. We define the piecewise constant permittivity $\varepsilon(\mathbf{x})$ as

$$\varepsilon(\mathbf{x}) := \begin{cases} \varepsilon_0 & \text{for } \mathbf{x} \in \Omega \backslash \bar{\Gamma} \\ \varepsilon_\star & \text{for } \mathbf{x} \in \Gamma \end{cases}$$

Let $u_{\mathrm{T}}^{(n)}(\mathbf{x}; \omega)$ be the time-harmonic total field, satisfying the boundary value problem

$$\begin{cases} \triangle u_{\mathrm{T}}^{(n)}(\mathbf{x}; \omega) + \omega^2 \varepsilon(\mathbf{x}) u_{\mathrm{T}}^{(n)}(\mathbf{x}; \omega) = 0 & \text{for } \mathbf{x} \in \Omega, \\ \dfrac{\partial u_{\mathrm{T}}^{(n)}(\mathbf{x}; \omega)}{\partial \boldsymbol{\nu}(\mathbf{x})} = \dfrac{\partial \exp(i\omega\boldsymbol{\theta}_n \cdot \mathbf{x})}{\partial \boldsymbol{\nu}(\mathbf{x})} & \text{for } \mathbf{x} \in \partial\Omega, \end{cases} \tag{1}$$

with transmission conditions on the boundary of Γ. Here, $\boldsymbol{\theta}_n = [\cos(\theta_n), \sin(\theta_n)]$ denotes a two-dimensional vector on the connected, proper subset of the unit circle $\mathbb{S}^1$, such that

$$\theta_n = \theta_1 + \frac{n-1}{N-1}(\theta_N - \theta_1), \quad 0 < \theta_N - \theta_1 < 2\pi.$$

Similarly, let $u_{\mathrm{B}}^{(n)}(\mathbf{x}; \omega) = \exp(i\omega\boldsymbol{\theta}_n \cdot \mathbf{x})$ be the background solution of (1). In this paper, we assume that $u_{\mathrm{T}}^{(n)}(\mathbf{x}; \omega)$ and $u_{\mathrm{B}}^{(n)}(\mathbf{x}; \omega)$ are measured everywhere on $\partial\Omega$. Based on this, we can define an energy functional:

$$\mathbb{E}(\Omega; \omega) := \frac{1}{2} \sum_{n=1}^{N} \int_{\partial\Omega} \left| u_{\mathrm{T}}^{(n)}(\mathbf{x}; \omega) - u_{\mathrm{B}}^{(n)}(\mathbf{x}; \omega) \right|^2 dS(\mathbf{x}). \tag{2}$$

In order to consider the topological derivative, we create a dielectric inhomogeneity, say Σ, of small diameter r at $\mathbf{z} \in \Omega \backslash \partial\Omega$, and denote corresponding domain as $\Omega | \Sigma$. Then, the topological derivative $d_T \mathbb{E}(\mathbf{z}; \omega)$ can be defined as follows (see [13])

$$d_T \mathbb{E}(\mathbf{z}; \omega) = \lim_{r \to 0+} \frac{\mathbb{E}(\Omega | \Sigma; \omega) - \mathbb{E}(\Omega; \omega)}{\varphi(r; \omega)}, \tag{3}$$

where $\varphi(r; \omega) \longrightarrow 0$ as $r \longrightarrow 0+$. From (3), we can obtain the asymptotic expansion:

$$\mathbb{E}(\Omega | \Sigma; \omega) = \mathbb{E}(\Omega; \omega) + \varphi(r; \omega) d_T \mathbb{E}(\mathbf{z}; \omega) + o(\varphi(r; \omega)). \tag{4}$$

Then, $d_T \mathbb{E}(\mathbf{z}; \omega)$ can be represented as

$$d_T \mathbb{E}(\mathbf{z}; \omega) = \mathrm{Re} \sum_{n=1}^{N} \left(u_{\mathrm{A}}^{(n)}(\mathbf{z}; \omega) \overline{u_{\mathrm{B}}^{(n)}(\mathbf{z}; \omega)} \right),$$

where $u_{\mathrm{A}}^{(n)}(\mathbf{x}; \omega)$ satisfies the following adjoint problem:

$$\begin{cases} \Delta u_{\mathrm{A}}^{(n)}(\mathbf{x}; \omega) + \omega^2 u_{\mathrm{A}}^{(n)}(\mathbf{x}; \omega) = 0 & \text{for } \mathbf{x} \in \Omega, \\ \dfrac{\partial u_{\mathrm{A}}^{(n)}(\mathbf{x}; \omega)}{\partial \boldsymbol{\nu}(\mathbf{x})} = u_{\mathrm{T}}^{(n)}(\mathbf{x}; \omega) - u_{\mathrm{B}}^{(n)}(\mathbf{x}; \omega) & \text{for } \mathbf{x} \in \partial\Omega. \end{cases} \tag{5}$$

Then, the structure of $d_T \mathbb{E}(\mathbf{z}; \omega)$ can be written as follows.

Lemma 2.1 (See [11, 13]). *Suppose that N and ω are sufficiently large, then*

$$d_T \mathbb{E}(\mathbf{z}; \omega) \approx \int_\sigma (\varepsilon_\star - \varepsilon_0) \exp(i\boldsymbol{\theta}_n \cdot (\mathbf{x} - \mathbf{z})) d\sigma(\mathbf{x}). \tag{6}$$

Note that, in limited-aperture problem, (6) can be represented as follows. This result plays an important role in establishing the necessary condition for application derived in the next section.

Lemma 2.2 (See [1]). *Let* $\boldsymbol{\theta}_n = [\cos(\theta_n), \sin(\theta_n)]$ *and* $\mathbf{x} - \mathbf{z} = \rho[\cos(\phi), \sin(\phi)]$. *If* N *and* ω *are sufficiently large, then*

$$d_T \mathbb{E}(\mathbf{z}; \omega) \approx \int_\sigma (\varepsilon_\star - \varepsilon_0) \left(J_0(\omega|\mathbf{x} - \mathbf{z}|) + \frac{\mathbb{D}(\omega|\mathbf{x} - \mathbf{z}|, \theta_1, \theta_N)}{\theta_N - \theta_1} \right) d\sigma(\mathbf{x}). \tag{7}$$

Here,

$$\mathbb{D}(\omega|\mathbf{x} - \mathbf{z}|, \theta_1, \theta_N) = 2 \sum_{m=1}^\infty \frac{(-1)^m}{m} \sin\{m(\theta_N - \theta_1)\} \cos\{m(\theta_N + \theta_1 - 2\phi)\} J_{2m}(\omega|\mathbf{x} - \mathbf{z}|).$$

3. NECESSARY CONDITION OF TOPOLOGICAL DERIVATIVES

Based on the structure of $d_T \mathbb{E}(\mathbf{z}; \omega)$ in (7), we observe that the term $J_0(\omega|\mathbf{x} - \mathbf{z}|)$ contributes to the imaging performance, while $\mathbb{D}(\omega|\mathbf{x} - \mathbf{z}|, \theta_1, \theta_N)$ is a disturbance. Therefore, eliminating the term $\mathbb{D}(\omega|\mathbf{x} - \mathbf{z}|, \theta_1, \theta_N)$ will guarantee good results, i.e., one must find some conditions such that

$$\sum_{m=1}^\infty \sin\{m(\theta_N - \theta_1)\} \cos\{m(\theta_N + \theta_1 - 2\phi)\} J_{2m}(\omega|\mathbf{x} - \mathbf{z}|) \equiv 0$$

for all $\mathbf{z} \in \Omega$. If $\omega = +\infty$, we can expect a good result, but this is an ideal condition. Therefore, let us assume that $\omega < +\infty$. Because $\mathbf{z}$ is arbitrary, we cannot control the value of the term $J_{2n}(\omega|\mathbf{x} - \mathbf{z}|)$. Therefore, we must find a condition on the range of incident directions, such that for all $m \in \mathbb{N}$,

$$\sin\{m(\theta_N - \theta_1)\} \cos\{m(\theta_N + \theta_1 - 2\phi)\} \equiv 0.$$

A simple way is to select θ_1 and θ_N such that $\theta_N - \theta_1 = \pi/2$ and $\theta_N + \theta_1 - 2\phi = \pi/2$. That is, if $\theta_1 = \phi$ and $\theta_N = \phi + \pi/2$, good results can be obtained via topological derivatives.

Based on the above observation, we also observe the following. Let $\phi(\mathbf{x})$ denote the slope of the tangential line at $\mathbf{x} \in \sigma$. Then, in order to obtain good results, θ_1 and θ_N must satisfy

$$\theta_1 = \min\{\phi(\mathbf{x}) : \mathbf{x} \in \sigma\} \quad \text{and} \quad \theta_N = \max\{\phi(\mathbf{x}) : \mathbf{x} \in \sigma\} + \frac{\pi}{2}. \tag{8}$$

This is a necessary condition for the application of topological derivatives in limited-aperture problems. Note that, based on [1], a sufficient condition for application is that $\theta_1 = 0$ and $\theta_N = \pi$. On the basis of these conditions, we conclude that the necessary condition is highly dependent on the shape of the thin inclusion, while the sufficient condition is not.

Remark 3.1. *In recent work [1, 10, 11], it has been confirmed that the application of multi-frequencies guarantees better a imaging performance than the application of a single frequency. Therefore, we consider the following normalized multi-frequency topological derivative: for several frequencies* $\{\omega_f : f = 1, 2, \ldots, F\}$, *define*

$$\mathbb{M}(\mathbf{z}; F) := \frac{1}{F} \sum_{f=1}^F \frac{d_T \mathbb{E}(\mathbf{z}; \omega_f)}{\max[d_T \mathbb{E}(\mathbf{z}; \omega_f)]}. \tag{9}$$

4. RESULTS OF NUMERICAL SIMULATION

In this section, some numerical results are presented in order to support our observation from the previous section. For this purpose, three σ_j characteristics of the thin inhomogeneity Γ_j are chosen for our illustration:

$$\sigma_1 = \{[s, 0.2] : -0.5 \le s \le 0.5\}$$
$$\sigma_2 = \{[s + 0.2, s^3 + s^2 - 0.5] : -0.5 \le s \le 0.5\}$$
$$\sigma_3 = \{[s, 0.5s^2 + 0.1 \sin(3\pi(s + 0.7))] : -0.7 \le s \le 0.7\}.$$

Throughout this section, we denote be the permittivities of Γ_j by ε_j, and their values are equal to 5. The thickness h of the Γ_j are equally set to 0.015, and ε_0 is set as 1. The applied frequency is $\omega_f = 2\pi/\lambda_f$, where $f = 1, 2, \cdots, 10$ is the given wavelength. In this paper, $N = 16$ incident

directions are to applied λ_f, and are equi-distributed within the interval $[\lambda_{10}, \lambda_1] = [0.3, 0.6]$. In order to demonstrate robustness, a white Gaussian noise with 20 dB signal-to-noise ratio (SNR) is added to the unperturbed boundary data $u_{\mathrm{T}}^{(n)}(\mathbf{x}; \omega)$ via a standard MATLAB command `awgn`.

Maps of $\mathbb{M}(\mathbf{z}; 10)$ with various ranges of directions for Γ_1 are presented in Figure 1. Note that if the range of directions is narrow, one cannot identify the shape of Γ_1, because the disturbing term $\mathbb{D}(\omega|\mathbf{x} - \mathbf{z}|, \theta_1, \theta_N)$ still exists. See Figure 1(a). Note that for Γ_1, we can easily observe that $\phi(\mathbf{x}) \equiv 0$. Therefore, based on (8), the selection of $\theta_1 = 0$ and $\theta_N = \pi/2$ will guarantee a good result. See Figure 1(b). In addition, it is true that a wider range of directions yields better results (see Figure 1(c)).

For a curve-like thin inhomogeneity Γ_2, as it is no longer straight-line shaped, $\phi(\mathbf{x})$ is no longer constant. Therefore, a selection of θ_1 and θ_N satisfying (8) will guarantee a good result. See Figure 2(b). Similar to the results in Figure 1, a result with poor resolution occurs when the range of directions is narrow, while one can obtain a good result when the range is sufficiently large. See Figures 2(a) and 2(c).

For the final example, let us consider the imaging of a thin oscillating inhomogeneity Γ_3. Based on the results of Figure 3, we observe that the necessary condition must be the same as the sufficient condition for obtaining an acceptable image of an oscillating inhomogeneity.

(a) $\theta_1 = \pi/8$ and $\theta_N = 3\pi/8$ (b) θ_1 and θ_N satisfy (8)   (c) $\theta_1 = \pi/6$ and $\theta_N = 5\pi/6$
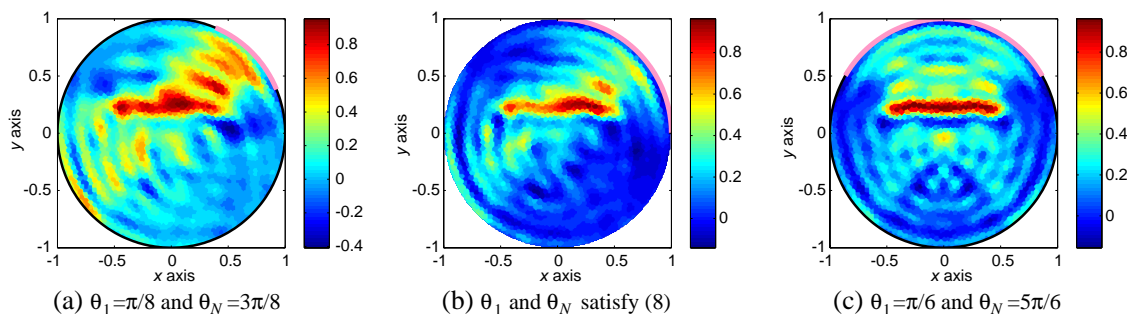
Figure 1: Maps of $\mathbb{M}(\mathbf{z}; 10)$ when the thin dielectric inhomogeneity is Γ_1.
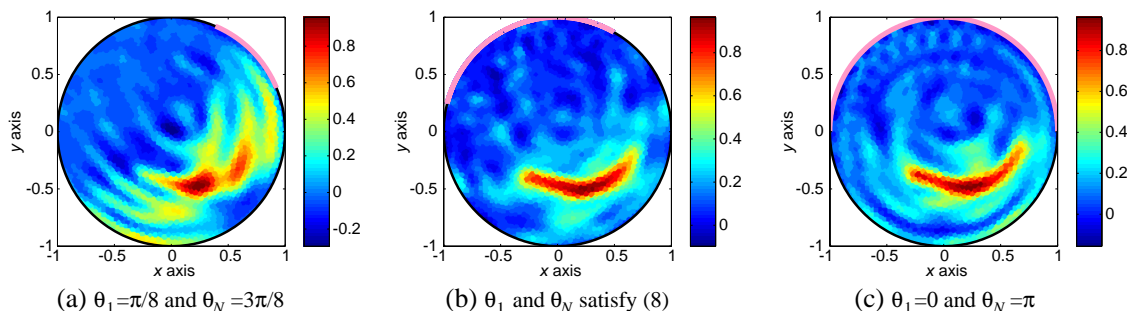
(a) $\theta_1 = \pi/8$ and $\theta_N = 3\pi/8$ (b) θ_1 and θ_N satisfy (8)   (c) $\theta_1 = 0$ and $\theta_N = \pi$

Figure 2: Similar to Figure 1, except that the inhomogeneity is Γ_2.

(a) $\theta_1 = \pi/4$ and $\theta_N = 3\pi/4$ (b) $\theta_1 = \pi/6$ and $\theta_N = 5\pi/6$ (c) $\theta_1 = 0$ and $\theta_N = \pi$
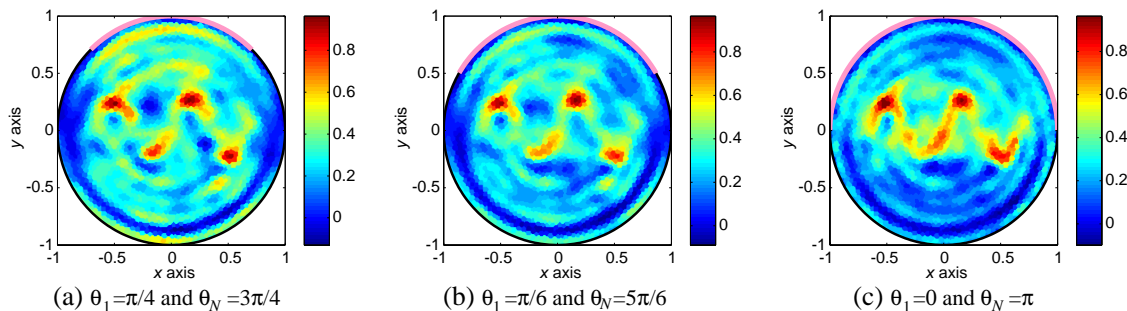
Figure 3: Similar to Figure 1, except that the inhomogeneity is Γ_3.

5. CONCLUDING REMARKS

In this contribution, we have considered the topological derivative approach to the non-iterative imaging of a thin dielectric inhomogeneity, in a limited-aperture inverse scattering problem. We reviewed a relationship with infinite series of Bessel functions of integer order of the first kind, and discovered a necessary condition for successful application to limited-aperture problems. We presented the results of some numerical simulations, which show that the discovered necessary condition is valid for the imaging of a thin inclusion, but is restricted in the imaging of an oscillating inhomogeneity. Note that the result obtained in this contribution does not guarantee the true shape of inhomogeneity. However, fortunately, they can provide a good initial guess for an iterative based algorithm or the level-set method. For more details, refer to [2, 6, 7, 12, 14].

REFERENCES

1. Ahn, C. Y., K. Jeon, Y.-K. Ma, and W.-K. Park, "A study on the topological derivative-based imaging of thin electromagnetic inhomogeneities in limited-aperture problems," *Inverse Problems*, Vol. 30, 105004, 2014.
2. Álvarez, D., O. Dorn, N. Irishina, and M. Moscoso, "Crack reconstruction using a level-set strategy," *J. Comput. Phys.*, Vol. 228, 5710–5721, 2009.
3. Ammari, H., J. Garnier, V. Jugnon, and H. Kang, "Stability and resolution analysis for a topological derivative based imaging functional," *SIAM J. Control Optim.*, Vol. 50, 48–76, 2012.
4. Ammari, H., H. Kang, H. Lee, and W.-K. Park, "Asymptotic imaging of perfectly conducting cracks," *SIAM J. Sci. Comput.*, Vol. 32, 894–922, 2010.
5. Bonnet, M., B. B. Guzina, and N. Nemitz, "Fast non-iterative methods for defect identification," *Rev. Eur. Mecan. Num.*, Vol. 17, 571–582, 2008.
6. Carpio, A. and M.-L. Rapún, "Solving inhomogeneous inverse problems by topological derivative methods," *Inverse Problems*, Vol. 24, 045014, 2008.
7. Dorn, O. and D. Lesselier, "Level set methods for inverse scattering," *Inverse Problems*, Vol. 22, R67–R131, 2006.
8. Eschenauer, A., V. V. Kobelev, and A. Schumacher, "Bubble method for topology and shape optimization of structures," *Struct. Optim.*, Vol. 8, 42–51, 1994.
9. Feijoo, G. R., "A new method in inverse scattering based on the topological derivative," *Inverse Problems*, Vol. 20, 1819–1840, 2004.
10. Park, W.-K., "Multi-frequency subspace migration for imaging of perfectly conducting, arc-like cracks in full- and limited-view inverse scattering problems," *J. Comput. Phys.*, Vol. 283, 52–80, 2015.
11. Park, W.-K., "Multi-frequency topological derivative for approximate shape acquisition of curve-like thin electromagnetic inhomogeneities," *J. Math. Anal. Appl.*, Vol. 404, 501–518, 2013.
12. Park, W.-K., "Shape reconstruction of thin electromagnetic inclusions via boundary measurements: Level-set method combined with the topological derivative," *Math. Probl. Eng.*, Vol. 2013, 125909, 2013.
13. Park, W.-K., "Topological derivative strategy for one-step iteration imaging of arbitrary shaped thin, curve-like electromagnetic inclusions," *J. Comput. Phys.*, Vol. 231, 1426–1439, 2012.
14. Park, W.-K. and D. Lesselier, "Reconstruction of thin electromagnetic inclusions by a level set method," *Inverse Problems*, Vol. 25, 085010, 2009.
15. Sokolowski, J. and A. Zochowski, "On the topological derivative in shape optimization," *SIAM J. Control Optim.*, Vol. 37, 1251–1272, 1999.

Subspace Migration for Imaging of Thin Electromagnetic Inhomogeneities without Shape Information

W.-K. Park

Department of Mathematics, Kookmin University, Seoul 136-702, Korea

Abstract— Subspace migration is a stable and effective non-iterative imaging technique for approaching the inverse scattering problem. However, for the successful imaging of thin electromagnetic inhomogeneities, *a priori* information about tangential and normal directions to unknown targets must be known. If this *a priori* information is not known, good results cannot be obtained using subspace migration. For this reason, various test vectors are applied to the imaging functional. However, this involves large computational costs, and the results may still be poor. With this as motivation, we derive the structure of single-frequency subspace migration, without any knowledge of shape information for unknown targets, and explore some properties thereof. This is based on the fact that measured far-field can be written as an asymptotic expansion formula. Some numerical results are then demonstrated, in support of our derivation.

1. INTRODUCTION

One point of view holds that the main purpose of the inverse scattering problem is to identify unknown characteristics of an object (such as its shape or material properties), using scattered field data. As a result of much research, various algorithms for reconstructing the shape of thin electromagnetic inhomogeneities or perfectly conducting cracks have been suggested, based mostly upon Newton-type iteration schemes or the level set method. Further details can be found in [1, 7, 13] and references therein. However, in order for these schemes to be successfully applied, a good initial guess is essentially required. Without that, one might encounter large computational costs, non-convergence issues, and the occurrence of local minimizer problems. Moreover, iterative schemes often require regularization terms that strongly depend on the problem at hand. Therefore, many authors have suggested the use of non-iterative reconstruction algorithms, which could at least provide good initial guesses. Further details are given in [2–4, 6, 8, 9, 11, 12].

Among such methods, subspace migration algorithm has been shown to be feasible for imaging applications. However, for the assurance of good results for the imaging of thin inhomogeneities, *a priori* information must be known about tangential and normal vectors on the boundaries (see [8, 9] for instance). As a result, many authors have applied a suitable vector to the subspace migration to consider the subspace migration without having any information about unknown targets. Motivated by this fact, we establish a relationship between single-frequency subspace migration and Bessel functions of the first kind of integer order. This is based on the fact that the far-field pattern can be represented as an asymptotic expansion formula in the presence of a thin electromagnetic inhomogeneity, refer to [5]. This relationship lets us uncover certain properties of subspace migration, and it can be applied successfully without knowing any information about a thin inhomogeneity.

This paper is organized as follows. In Section 2, we briefly introduce the two-dimensional direct scattering problem and subspace migration. In Section 3, we explore the structure of subspace migration, without consideration of the shape of thin inhomogeneities. In Section 4, we exhibit some results of numerical simulations with noisy data. A brief conclusion follows in Section 5.

2. THE DIRECT SCATTERING PROBLEM AND SUBSPACE MIGRATION

2.1. A Two-dimensional Direct Scattering Problem for a Thin Electromagnetic Inhomogeneity

Assume an extended, penetrable electromagnetic inhomogeneity Γ, with a small (with respect to the given wavelength) thickness of $2h$, is located in the two-dimensional homogeneous space $\mathbb{R}^2$. That is,

$$\Gamma = \{\mathbf{x} + \eta\mathbf{n}(\mathbf{x}) : \ \mathbf{x} \in \sigma, \ -h \leq \eta \leq h\},$$

where $\mathbf{n}(\mathbf{x})$ is the unit normal to σ at x, and σ denotes a simple, smooth curve in $\mathbb{R}^2$, describing the supporting curve of Γ. In this paper, we assume that Γ and $\mathbb{R}^2$ are characterized by their dielectric permittivities and magnetic permeabilities at a given angular frequency $\omega = 2\pi/\lambda$, where λ denotes the wavelength. Let ε_0 and $\varepsilon_\star$ be the dielectric permittivity of $\mathbb{R}^2$ and Γ, respectively; μ_0 and $\mu_\star$ are defined similarly. For the sake of simplicity, we set $\varepsilon_0 = \mu_0 \equiv 1$.

At a given ω, we denote by $u_\circ(\mathbf{x}) := \exp(i\omega\theta \cdot \mathbf{x})$ a plane-wave incident field with incident direction $\theta \in \mathbb{S}^1$, where $\mathbb{S}^1$ denotes the unit circle. Let $u(\mathbf{x})$ be the time-harmonic total field that satisfies the Helmholtz equation

$$\nabla \cdot \left(\frac{1}{\mu_\star}\chi(\Gamma) + \frac{1}{\mu_0}\chi\left(\mathbb{R}^2\backslash\overline{\Gamma}\right) \right) \nabla u(\mathbf{x}) + \omega^2 \left(\varepsilon_\star\chi(\Gamma) + \varepsilon_0\chi\left(\mathbb{R}^2\backslash\overline{\Gamma}\right) \right) u(\mathbf{x}) = 0 \quad \text{in} \quad \mathbb{R}^2, \qquad (1)$$

with a transmission condition on the boundary of Γ. Then, $u(\mathbf{x})$ can be decomposed as $u(\mathbf{x}) = u_\circ(\mathbf{x}) + u_\diamond(\mathbf{x})$, where $u_\diamond(\mathbf{x})$ is the unknown scattered field that uniformly satisfies the Sommerfeld radiation condition

$$\lim_{|\mathbf{x}|\to\infty} \sqrt{|\mathbf{x}|} \left(\frac{\partial u_\diamond(\mathbf{x})}{\partial|\mathbf{x}|} - ik_0 u_\diamond(\mathbf{x}) \right) = 0, \quad k_0 = \omega\sqrt{\varepsilon_0\mu_0} = \omega,$$

in all directions $\hat{\mathbf{x}} = \mathbf{x}/|\mathbf{x}|$.

The far-field pattern $u_\infty(\vartheta, \theta)$ of $u_\diamond(\mathbf{x})$ is defined on $\mathbb{S}^1$. Note that it is represented as

$$u_\diamond(\mathbf{x}) = \frac{\exp(i\omega|\mathbf{x}|)}{\sqrt{|\mathbf{x}|}} u_\infty(\vartheta, \theta) + o\left(\frac{1}{\sqrt{|\mathbf{x}|}} \right), \qquad (2)$$

as $|\mathbf{x}| \to \infty$ uniformly on $\vartheta = \mathbf{x}/|\mathbf{x}|$. Then, $u_\infty(\vartheta, \theta)$ can be written in the form of the following asymptotic expansion formula:

$$u_\infty(\vartheta, \theta) = h\frac{\omega^2(1+i)}{4\sqrt{\omega\pi}} \int_\sigma \left(\frac{\varepsilon_\star - \varepsilon_0}{\sqrt{\varepsilon_0\mu_0}} - \left(\sqrt{2}\vartheta \right) \cdot \mathbb{M}(\mathbf{x}) \cdot \left(\sqrt{2}\theta \right) \right) \exp\left(i\omega(\theta - \vartheta) \cdot \mathbf{x} \right) d\sigma(\mathbf{x}) + o(h), \tag{3}$$

where $o(h)$ is uniform in $\mathbf{x} \in \sigma$, and $\mathbb{M}(\mathbf{x})$ is a symmetric matrix (see [5] for instance).

2.2. Introduction to Subspace Migration

We introduce subspace migration for the imaging of Γ. For the sake of simplicity, suppose that we have a number N of different incident and observation directions, θ_l and ϑ_j respectively, for $j, l = 1, 2, \ldots, N$ and $\vartheta_j = -\theta_j$. Furthermore, suppose that the supporting curve σ is divided into M different segments, of sizes of the order of half the wavelength, $\lambda/2$. Then, considering the Rayleigh resolution limit for far-field data, any detail that is less than one half of the wavelength cannot be seen, and only one point from each segment is expected to contribute at the image space of the response matrix $\mathbb{K}$ (see [4, 9, 11, 12] for instance). Each of these points, say $\mathbf{x}_m$ for $m = 1, 2, \ldots, M$, will be imaged. With this in mind, we consider the collected MSR matrix, and perform Singular Value Decomposition (SVD) as follows:

$$\mathbb{K} = [u_\infty(\mathbf{x}_j, \theta_l)]_{j,l=1}^N = \mathbb{U}\mathbb{E}\mathbb{V}^* \approx \sum_{m=1}^{3M} \tau_m \mathbf{U}_m \mathbf{V}_m^*, \qquad (4)$$

where the superscript $*$ denotes a complex conjugate, the τ_m are non-zero singular values, and $\mathbf{U}_m$ and $\mathbf{V}_m$ are the left- and right-singular vectors of $\mathbb{K}$, respectively. Based on (4), the imaging algorithm is developed as follows. For $\mathbf{c}_n \in \mathbb{R}^{3\times1}\backslash\{\mathbf{0}\}$, $n = 1, 2, \ldots, N$, define a vector

$$\mathbf{W}(\mathbf{z}) := \frac{1}{N} \left[\mathbf{c}_1 \cdot [1, \theta_1]^T \exp(i\omega\theta_1 \cdot \mathbf{z}), \ldots, \mathbf{c}_N \cdot [1, \theta_N]^T \exp(i\omega\theta_N \cdot \mathbf{z}) \right]^T. \qquad (5)$$

Then, by virtue of results in [2, 8, 9], the following relationship holds:

$$\mathbf{W}(\mathbf{x}_m) \approx \mu_m \quad \text{and} \quad \mathbf{W}(\mathbf{x}_m) \approx \overline{\mathbf{V}}_m. \qquad (6)$$

Hence, by the orthonormal property of singular values, we can observe that

$$\begin{aligned} \mathbf{W}(\mathbf{z})^*\mathbf{U}_m \approx 1 \quad &\text{and} \quad \mathbf{W}(\mathbf{z})^*\overline{\mathbf{V}}_m \approx 1 \quad \text{if} \quad \mathbf{z} = \mathbf{x}_m, \\ \mathbf{W}(\mathbf{z})^*\mathbf{U}_m \approx 0 \quad &\text{and} \quad \mathbf{W}(\mathbf{z})^*\overline{\mathbf{V}}_m \approx 0 \quad \text{if} \quad \mathbf{z} \neq \mathbf{x}_m. \end{aligned} \qquad (7)$$

Therefore, we can introduce the subspace migration imaging functional as follows:

$$\mathcal{I}_{\mathrm{SF}}(\mathbf{z}) := \left| \sum_{m=1}^{3M} \left(\mathbf{W}(\mathbf{z})^*\mathbf{U}_m \right) \left(\mathbf{W}(\mathbf{z})^*\overline{\mathbf{V}}_m \right) \right|. \qquad (8)$$

Based on (7), $\mathcal{I}_{\mathrm{SF}}$ is expected to exhibit peaks of a magnitude of 1 at $\mathbf{z} = \mathbf{x}_m \in \sigma$, and of small magnitudes at $\mathbf{z} \in \mathbb{R}^2\backslash\Gamma$.

3. STRUCTURE OF SUBSPACE MIGRATION WITHOUT SHAPE INFORMATION

Based on the above, the definition of a vector $\mathbf{W}(\mathbf{z})$ in (5) is very important for the performance of imaging. For this purpose, one must choose suitable vectors $\mathbf{c}_n$. Note that, following from (3) and (6), each $\mathbf{c}_n$ must be a linear combination of tangential $\mathbf{t}(\mathbf{x}_m)$ and normal $\mathbf{n}(\mathbf{x}_m)$ vectors at $\mathbf{x}_m \in \sigma$. However, when we have no *a priori* information about the shape of Γ, it is impossible to select an optimal vector $\mathbf{c}_n$, and therefore also an optimal $\mathbf{W}(\mathbf{z})$. Therefore, instead of (5), we choose an alternative test vector

$$\mathbf{W}(\mathbf{z}) := \frac{1}{N} \left[\exp(i\omega\theta_1 \cdot \mathbf{z}), \exp(i\omega\theta_2 \cdot \mathbf{z}), \ldots, \exp(i\omega\theta_N \cdot \mathbf{z}) \right]^T. \tag{9}$$

Subsequently, the structure of subspace migration can be represented as follows. A detailed derivation is to appear in an extended version of this contribution.

Theorem 3.1. *For sufficiently large $N(> 3M)$ and ω, (8) can be represented as follows:*

$$\mathcal{I}(\mathbf{z}) = \left| \sum_{m=1}^{M} \left\{ J_0\left(\omega|\mathbf{z} - \mathbf{x}_m|\right) + i \left(\frac{\mathbf{z} - \mathbf{x}_m}{|\mathbf{z} - \mathbf{x}_m|} \cdot \left(\mathbf{t}(\mathbf{x}_m) + \mathbf{n}(\mathbf{x}_m)\right) \right) J_1\left(\omega|\mathbf{z} - \mathbf{x}_m|\right) \right\}^2 \right|, \tag{10}$$

where J_n denotes the Bessel function of integer order n, of the first kind.

Proof. Considering (5) and (6), $\mathcal{I}(\mathbf{z})$ can be written as

$$\mathcal{I}(\mathbf{z}) = \left| \sum_{m=1}^{3M} \left(\mathbf{W}(\mathbf{z})^*\mathbf{U}_m\right) \left(\mathbf{W}(\mathbf{z})^*\overline{\mathbf{V}}_m\right) \right| \approx \left| \sum_{m=1}^{M} \left\{ \sum_{s=1}^{3} \left(\mathbf{W}(\mathbf{z})^*\mathbf{H}_m^{(s)}\right) \right\}^2 \right|,$$

where (see [10] for instance)

$$\mathbf{H}_m^{(1)} = \frac{1}{\sqrt{N}} \left[e^{i\omega\theta_1 \cdot \mathbf{x}_m}, e^{i\omega\theta_2 \cdot \mathbf{x}_m}, \ldots, e^{i\omega\theta_N \cdot \mathbf{x}_m} \right]^T,$$

$$\mathbf{H}_m^{(2)} = \frac{1}{\sqrt{N}} \left[\theta_1 \cdot \mathbf{t}(\mathbf{x}_m)e^{i\omega\theta_1 \cdot \mathbf{x}_m}, \theta_2 \cdot \mathbf{t}(\mathbf{x}_m)e^{i\omega\theta_2 \cdot \mathbf{x}_m}, \ldots, \theta_N \cdot \mathbf{t}(\mathbf{x}_m)e^{i\omega\theta_N \cdot \mathbf{x}_m} \right]^T,$$

$$\mathbf{H}_m^{(3)} = \frac{1}{\sqrt{N}} \left[\theta_1 \cdot \mathbf{n}(\mathbf{x}_m)e^{i\omega\theta_1 \cdot \mathbf{x}_m}, \theta_2 \cdot \mathbf{n}(\mathbf{x}_m)e^{i\omega\theta_2 \cdot \mathbf{x}_m}, \ldots, \theta_N \cdot \mathbf{n}(\mathbf{x}_m)e^{i\omega\theta_N \cdot \mathbf{x}_m} \right]^T.$$

Since for $\theta, \xi \in \mathbb{S}^1$ and $\mathbf{x} \in \mathbb{R}^2$ (see [9] for instance), we have that

$$\frac{1}{N} \sum_{n=1}^{N} \exp(i\omega\theta_n \cdot \mathbf{x}) = \frac{1}{2\pi} \int_{\mathbb{S}^1} \exp(i\omega\theta \cdot \mathbf{x})d\theta = J_0(\omega|\mathbf{x}|),$$

$$\frac{1}{N} \sum_{n=1}^{N} (\theta_n \cdot \xi) \exp(i\omega\theta_n \cdot \mathbf{x}) = \frac{1}{2\pi} \int_{\mathbb{S}^1} (\theta \cdot \xi) \exp(i\omega\theta \cdot \mathbf{x})d\theta = i \left(\frac{\mathbf{x}}{|\mathbf{x}|} \cdot \xi \right) J_1(\omega|\mathbf{x}|),$$

we can perform some elementary calculus to obtain

$$\mathbf{W}(\mathbf{z})^*\mathbf{H}_m^{(1)} = J_0(\omega|\mathbf{z} - \mathbf{x}_m|),$$

$$\mathbf{W}(\mathbf{z})^*\mathbf{H}_m^{(2)} + \mathbf{W}(\mathbf{z})^*\mathbf{H}_m^{(3)} = i \left(\frac{\mathbf{z} - \mathbf{x}_m}{|\mathbf{z} - \mathbf{x}_m|} \cdot \left(\mathbf{t}(\mathbf{x}_m) + \mathbf{n}(\mathbf{x}_m)\right) \right) J_1\left(\omega|\mathbf{z} - \mathbf{x}_m|\right).$$

Hence, we can obtain (10). This completes the proof.

Based on the properties of $J_0(x)$, plots of $\mathcal{I}(\mathbf{z})$ will show peaks of magnitude 1 at $\mathbf{z} = \mathbf{x}_m \in \Gamma$, and smaller peaks at $\mathbf{z} \notin \Gamma$. It follows from the properties of $J_1(x)^2$ that two curves of large (but less than 1) magnitude, and many artifacts of smaller magnitude, will appear in the map of $\mathcal{I}(\mathbf{z})$.

4. RESULTS OF NUMERICAL SIMULATIONS

In this section, the results of some numerical simulations are exhibited in support of Theorem 3.1. For this purpose, thin inhomogeneities Γ_j and two supporting smooth curves are selected as follows:

$$\sigma_1 = \left\{ \left[s - 0.2, -0.5s^2 + 0.5 \right]^T \; : \; -0.5 \leq s \leq 0.5 \right\},$$

$$\sigma_2 = \left\{ \left[s + 0.2, s^3 + s^2 - 0.6 \right]^T \; : \; -0.5 \leq s \leq 0.5 \right\}.$$

We set the permittivities and permeabilities of Γ_j as 5, and those of $\mathbb{R}^2$ as 1. The thickness h of Γ_j is set to 0.015, and the wavelength λ is chosen as 0.5. Directions $\theta_l \in S^1$ are selected as

$$\theta_l = \left[\cos\frac{2\pi l}{N}, \sin\frac{2\pi l}{N}\right]^T \quad \text{for} \quad l = 1, 2, \ldots, N.$$

In order to show the robustness of the result, a white Gaussian noise with 20 dB signal-to-noise ratio (SNR) is added to the unperturbed data $u_\infty(\vartheta_j, \theta_l)$.

Figure 1 shows the maps of $\mathcal{I}_{SF}(\mathbf{z})$ with $\mathbf{c}_n = [1, 1, 0]^T$, $\mathbf{c}_n = [1, 0, 1]^T$, and $\mathcal{I}(\mathbf{z})$ for Γ_1. Note that since $\mathbf{n}(\mathbf{x}_m) \approx 1$ for all m, the selection of $\mathbf{c}_n = [1, 0, 1]^T$ yields good result but $\mathbf{c}_n = [1, 1, 0]^T$ is not a good choice. However, one can recognize the shape of Γ_1 via the map of $\mathcal{I}(\mathbf{z})$.
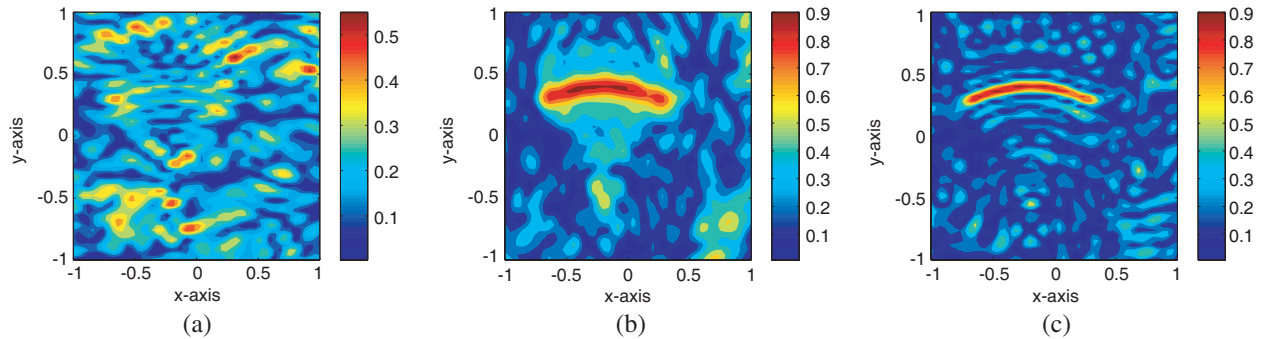
Figure 1: Maps of $\mathcal{I}_{SF}(\mathbf{z})$ with (a) $\mathbf{c}_n = [1, 1, 0]^T$, (b) $\mathbf{c}_n = [1, 0, 1]^T$, and (c) $\mathcal{I}(\mathbf{z})$ for Γ_1.

Similar to Figure 1, Figure 2 shows the maps of $\mathcal{I}_{SF}(\mathbf{z})$ and $\mathcal{I}(\mathbf{z})$, for Γ_2. In contrast to the previous result, the selection of $\mathbf{c}_n = [1, 0, 1]^T$ is no longer a good choice. Fortunately, the shape of Γ_2 is successfully reconstructed via the map of $\mathcal{I}(\mathbf{z})$.
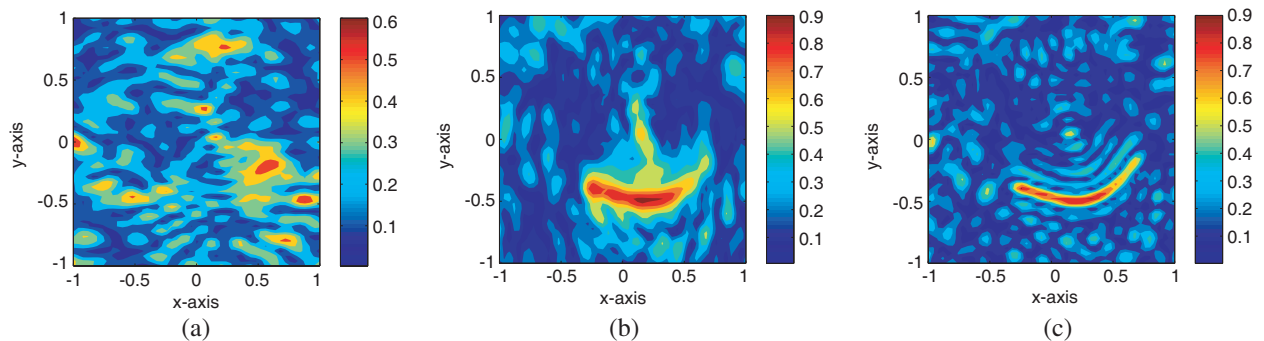
Figure 2: Similar to Figure 1, except the thin inhomogeneity, Γ_2.
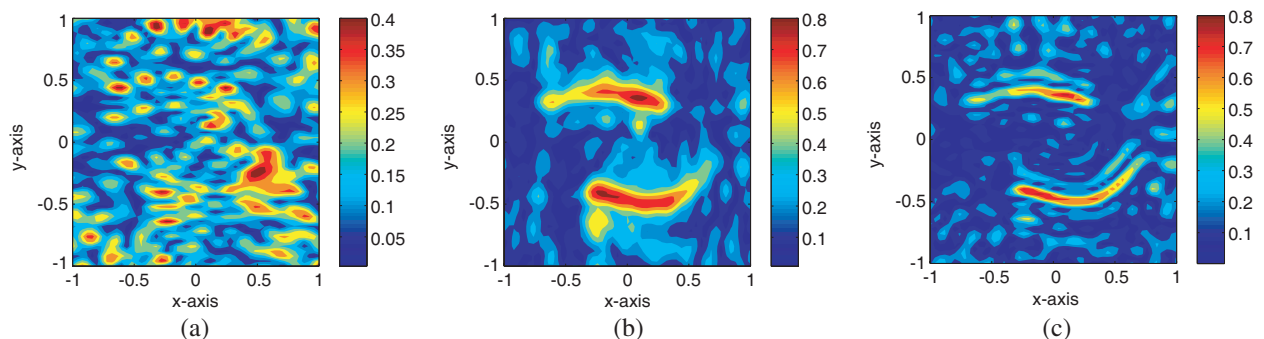
Figure 3: Similar to Figure 1, except the thin inhomogeneities, Γ_1 and Γ_2.

For the final example, let us consider the imaging results of multiple thin inhomogeneities $\Gamma_1 \cup \Gamma_2$. As with the previous results, we can observe that it is impossible to recognize the shape of $\Gamma_1 \cup \Gamma_2$

via the map of $\mathcal{I}_{\mathrm{SF}}(\mathbf{z})$ with $\mathbf{c}_n = [1, 1, 0]^T$. If one selects $\mathbf{c}_n = [1, 0, 1]^T$, the outline shape of $\Gamma_1 \cup \Gamma_2$ can be obtained, although the result is still poor. However, their shape can be successfully retrieved via the map of $\mathcal{I}(\mathbf{z})$.

5. CONCLUDING REMARKS

In this paper, we considered the subspace migration imaging functional without any information about the shape of thin inhomogeneities. We derived a relationship between the imaging functional and the Bessel functions of integer order of the first kind. The derived results indicated that although some unexpected artifacts still appear, we can obtain acceptable results using subspace migration without any consideration of the shape of unknown targets.

In the present work, we considered the imaging of thin electromagnetic inhomogeneities. Along the same lines, the analysis of subspace migration for the imaging of perfectly conducting cracks would make an interesting addition to this research.

REFERENCES

1. Álvarez, D., O. Dorn, N. Irishina, and M. Moscoso, "Crack reconstruction using a level-set strategy," *J. Comput. Phys.*, Vol. 228, 5710–5721, 2009.
2. Ammari, H., J. Garnier, H. Kang, W.-K. Park, and K. Sølna, "Imaging schemes for perfectly conducting cracks," *SIAM J. Appl. Math.*, Vol. 71, 68–91, 2011.
3. Ammari, H., E. Iakovleva, and D. Lesselier, "A MUSIC algorithm for locating small inclusions buried in a half-space from the scattering amplitude at a fixed frequency," *SIAM Multiscale Modeling Simulation*, Vol. 3, 597–628, 2005.
4. Ammari, H., H. Kang, H. Lee, and W.-K. Park, "Asymptotic imaging of perfectly conducting cracks," *SIAM J. Sci. Comput.*, Vol. 32, 894–922, 2010.
5. Beretta, E. and E. Francini, "Asymptotic formulas for perturbations of the electromagnetic fields in the presence of thin imperfections," *Contemp. Math.*, Vol. 333, 49–63, 2003.
6. Colton, D., H. Haddar, and P. Monk, "The linear sampling method for solving the electromagnetic inverse scattering problem," *SIAM J. Sci. Comput.*, Vol. 24, 719–731, 2002.
7. Dorn, O. and D. Lesselier, "Level set methods for inverse scattering," *Inverse Problems*, Vol. 22, R67–R131, 2006.
8. Park, W.-K., "Analysis of a multi-frequency electromagnetic imaging functional for thin, crack-like electromagnetic inclusions," *Appl. Numer. Math.*, Vol. 77, 31–42, 2014.
9. Park, W.-K., "Multi-frequency subspace migration for imaging of perfectly conducting, arc-like cracks in full- and limited-view inverse scattering problems," *J. Comput. Phys.*, Vol. 283, 52–80, 2015.
10. Park, W.-K., "Subspace migration for imaging of thin, curve-like electromagnetic inhomogeneities without geometric consideration," preprint.
11. Park, W.-K. and D. Lesselier, "Electromagnetic MUSIC-type imaging of perfectly conducting, arc-like cracks at single frequency," *J. Comput. Phys.*, Vol. 228, 8093–8111, 2009.
12. Park, W.-K. and D. Lesselier, "MUSIC-type imaging of a thin penetrable inclusion from its far-field multi-static response matrix," *Inverse Problems*, Vol. 25, 075002, 2009.
13. Park, W.-K. and D. Lesselier, "Reconstruction of thin electromagnetic inclusions by a level set method," *Inverse Problems*, Vol. 25, 085010, 2009.

Analysis of Matching Media Effect on Microwave Brain Stroke Imaging via a Spherically Symmetrical Head Model

E. Bilgin, **A. Aygun**, **A. Yapar**, and **I. Akduman**

Electrical and Electronics Engineering Faculty, Istanbul Technical University, Istanbul, Turkey

Abstract— The effect of using a matching medium in the brain imaging via the microwave tomography technique has been investigated using a three-dimensional multi-layered sphere as a head model. By modelling the human head as a spherically symmetrical piecewise homogeneous sphere, the related scattering problem can be transformed into a one-dimensional form. As a result, the computational complexity of the problem can be significantly reduced. This scattering problem is then solved via the discretization of the one-dimensional integral equations, and through the dyadic Green's function related to the layered spherical structures. In order to test the effect of the matching medium for the brain stroke detection, the scattered electric fields for the healthy brain model and the stroke-affected one have been compared. The results show that in the absence of a matching medium the variation in the scattered field between two cases is too small to enable a successful stroke detection mechanism based on microwave imaging. On the other hand, in the presence of the matching medium, a noticeable difference in the scattered field has been observed. However, further tests employing more realistic models must be used to evaluate the applicability of the microwave tomography in the brain stroke detection.

1. INTRODUCTION

Microwave tomography can represent an alternative to commonly used imaging techniques such as computerized tomography or magnetic resonance imaging [1]. The researches on the subject are motivated by the need to make continuous control of the patient's state possible [2]. Since non-hazardous and portable imaging systems can be designed using microwave technology, an imaging tool operating on microwave frequency would be suitable for long term monitoring [1, 2].

Microwave imaging techniques rely on the difference in the electromagnetic properties between healthy tissues and stroke areas in the brain [1]. This difference results in a variation in the scattered field when the head region is excited by an external source operating in the microwave frequencies. Therefore, it is of crucial importance to maximize the penetration of the electromagnetic field into the inner parts of the human brain where the strokes occur. To this end, a matching medium with suitable electromagnetic parameters can be used to minimize the reflection by matching the impedances, in the interface between the surrounding medium and the skin [3]. The optimal parameters for the matching medium depends on the electromagnetic properties of the healthy and malignant tissues under examination, and determining those parameters is a very important step in the design of a successful microwave imaging system [4]. The effect of the matching medium can be best assessed by using a 3-D head model, which can provide a relatively realistic structure to test both the relevancy of using a matching medium, and the effectiveness of microwave imaging techniques in general.

In this work, a four layered piecewise homogeneous sphere has been used as a head model. In order to assess the effect of the matching medium, the related three dimensional scattering problem must be solved. However, given the high contrast values of the brain tissues, the solution of the 3-D scattering problem by classical techniques, such as method of moments, is a computationally expensive procedure. Therefore, in this study the problem has been transformed into a one dimensional form by taking advantage of the spherical symmetry [5]. As an alternative method, the dyadic Green's function related to the layered spherical structures has been used to verify the results [6]. After solving the scattering problem, the effect of the matching medium on the scattered field has been analysed by comparing the results for the cases with and without a stroke-affected brain area. The comparisons show that the presence of the matching medium increases the effect of the stroke region on the scattered electric field. This effect forms the basis for a possible application of the microwave imaging techniques for brain stroke monitoring.

2. FORMULATION OF THE PROBLEM

In order to analyse the effect of matching medium two different configurations have been considered. First, as a theoretical case, the sphere of radius a, which is assumed to represent the spherically

symmetrical head model, has been assumed to be located in an open region of the matching medium, as presented in Fig. 1. The incoming electric field has been excited by an infinitesimal horizontal electric dipole with a current moment C_0 pointed in the x-direction, situated at the point $x = 0$, $y = 0$, $z = z_d$, $(z_d > a)$ on the z-axis. The region outside the sphere is characterized by a constant wave number of $k = \omega\sqrt{\epsilon_0\mu_0\epsilon_m}$, ϵ_m being the complex dielectric constant of the matching medium.

As a second configuration, a more realistic case given in Fig. 2 has been analysed. In this geometry, the layered sphere is assumed to be coated by a concentric layer of matching medium. The infinitesimal dipole is located inside the matching medium layer. The region outside this layer is considered to be free-space, characterized by the wave number $k_0 = \omega\sqrt{\epsilon_0\mu_0}$.

Different electromagnetic parameters have been used in the formulation of the head model [1, 2]. The choice of operating frequency is also an important parameter which significantly affects the outcome of the microwave imaging procedure [1]. The frequency should be chosen as an optimum value that enables the penetration of the electric field into the brain region, while ensuring the necessary resolution for the microwave imaging [1]. In this study, the operating frequency has been chosen as $f = 1$ GHz. By taking the frequency dispersion into account, the electromagnetic parameters for each layer of the head model has been presented in [2] for $f = 1$ GHz. In Table 1, the thickness and the complex dielectric constant for each layer of the head model has been given. For the brain region, in order to preserve the spherical symmetry, the mean value of the grey matter and the white matter has been chosen as the complex dielectric constant. Accordingly, the complex constant for the matching medium has been chosen as $\epsilon_m = 40 + 13i$, as given in [2].

The scattering problem related to the four layered piecewise homogeneous head model, given in Fig. 1, is a three-dimensional one. However as explained in [5], by taking advantage of the spherically symmetrical geometry, one can reduce the problem into a one-dimensional form. This transformation is achieved by expressing the interior electric field and the free space dyadic Green's function as a series expansion in terms of vector spherical harmonics, which are orthogonal over a spherical surface. Using this orthogonality, the three dimensional electric field integral equation can be transformed into a system of one-dimensional integral equations [5]. An alternative solution for the scattering problem can be formed by using the dyadic Green's function related to the layered spheres constructed in [6]. The comparison and verification of the results obtained via both methods for the scattering problem has been given in the next section.

For the geometry given in Fig. 2, the dipole is located inside the matching medium layer. The
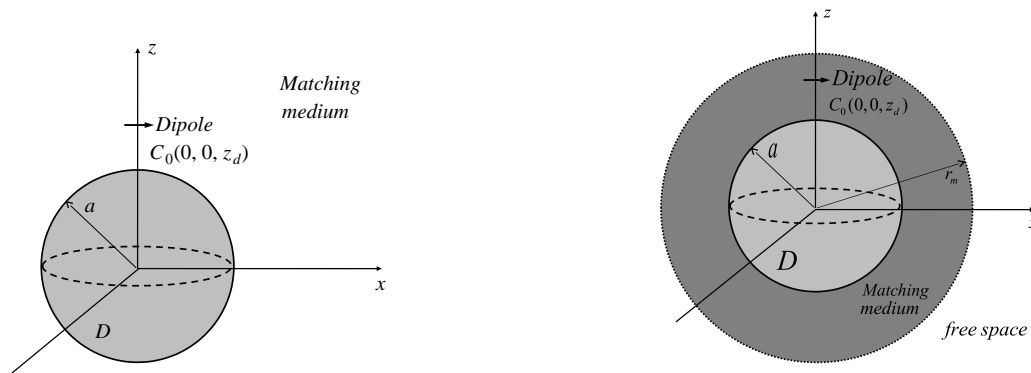

Figure 1: The geometry of the problem with an open matching medium region.

Figure 2: The geometry of the problem with a matching medium layer.

Table 1: The parameters for the layers of the head model.

Layer	Matter	ϵ_r	Thickness
1	Brain	$45 + 16.5i$	8.2 cm
2	CSF	$57 + 26i$	0.3 cm
3	Bone	$13 + 2i$	0.7 cm
4	Skin	$40 + 11i$	0.8 cm

field is also assumed to be measured within that layer. Therefore, this configuration involves a five layered sphere with an internal source. As demonstrated in [5], the presence of the internal source creates a singularity at the vicinity of the dipole, and the series for the total electric field inside the sphere fails to converge at that region. In order to avoid this problem, the thickness of the matching medium layer should be large enough to separate the source and the measurement region. The suitable values determined via numerical tests will be used in the simulations assessing the effect of the matching medium in the next section.

3. NUMERICAL RESULTS

In this section, in order to demonstrate the validity of the methods, the results obtained via both methods will be compared. First, the scattered field for the geometry given in Fig. 1 has been calculated via the one-dimensional integral equations, and the dyadic Green's function. The dipole is located at the point $z_d = 0.12\,\mathrm{m}$ on the z-axis. The scattered field is measured on a spherical surface of radius $r = 0.13\,\mathrm{m}$, in the H-plane ($\phi = \pi/2$) and in the E-plane ($\phi = 0$), for different values of θ, $\theta \in [0, \pi]$. For the method with integral equations, the integrals are discretized by 100 points to increase accuracy. The number of terms n involved in the series expansion for the field is determined as $N_{\max} = 30$ for both methods. The results presented in Fig. 3 show perfect agreement between the method with integral equations and the dyadic Green's function. In the comparison for the geometry with a matching medium layer, the thickness of the matching medium layer is chosen as 5 cm. The dipole is situated at the point $z_d = 0.11\,\mathrm{m}$, and the total electric field inside the matching medium layer is measured on the surface of the layer at $r_m = 0.15\,\mathrm{m}$. The integrals are discretized by 150 points, and the cut-off number for the series is chosen as $N_{\max} = 30$ for both methods. The agreement between the results given in Fig. 4 demonstrates that both methods are reliable in determining the total electric field inside the matching medium layer.

Since previous examples demonstrated that both method can be used in the assessment of the effect of the matching medium, the method with the integral equations will be solely used for the remaining numerical tests. The success of the microwave imaging techniques depends on the amount of variation in the electric field caused by the stroke area in the brain region. Therefore, the difference between the fields, scattered by a healthy brain and by a stroke affected one, should increase in the presence of a matching medium. In order to test this assumption, first the field scattered by a healthy brain has been compared with the field scattered by a stroke affected brain, in the absence of the matching medium. The region outside the four layered sphere is assumed to be free-space vacuum. For the stroke affected brain, the ϵ_r of the brain region is replaced by the complex dielectric constant of the stroke area given in [2] as $\epsilon_s = 36 + 13i$. Although this is not a realistic case, it is suitable for the purpose of analysing the effect of matching medium. For the measurement of the scattered field, same parameters given for Fig. 3 have been used. In all the remaining cases, the values calculated for $\theta \in [0, \pi]$ in the H-plane ($\phi = \pi/2$), and in the E-plane ($\phi = 0$) are presented in the same figure. In each figure the top half represents the values measured in the E-plane ($\phi = 0$), and the bottom half represents the values measured in the H-
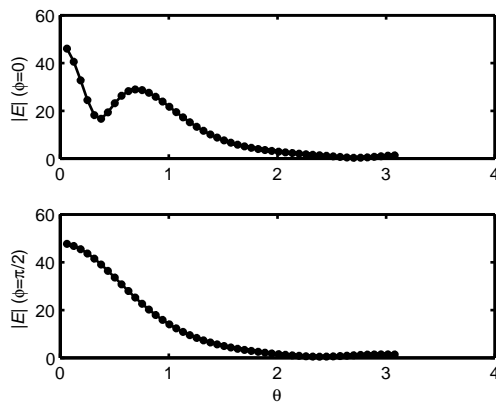

Figure 3: The magnitude of the field scattered by the four layered sphere; solid line corresponds to the solution with integral equation and dots to the dyadic Green's function.
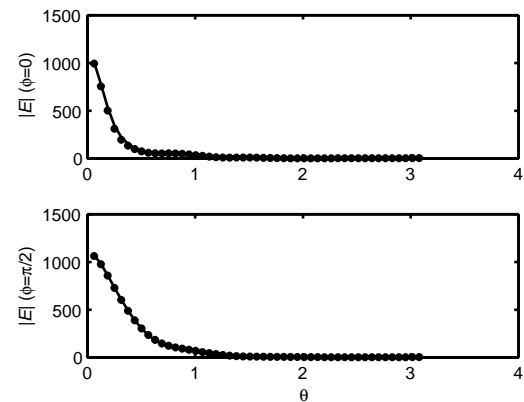
Figure 4: The magnitude of the total field inside the matching medium layer; solid line corresponds to the solution with integral equation and dots to the dyadic Green's function.
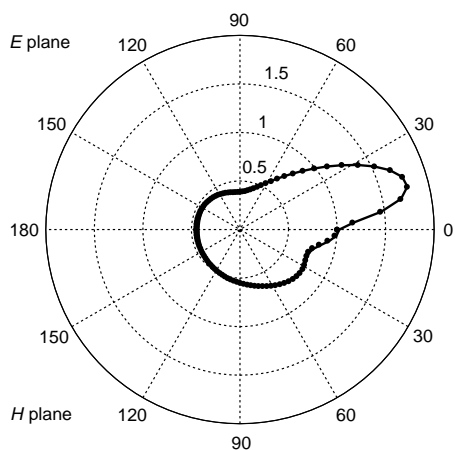
Figure 5: The magnitude of the field scattered in the absence of the matching medium; solid line corresponds to the stroke affected brain and dots to the healthy brain.
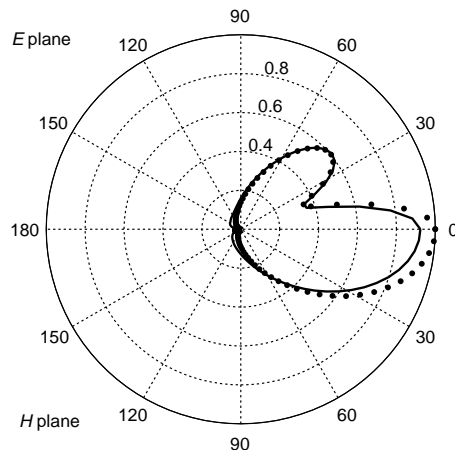

Figure 6: The magnitude of the field scattered in the presence of the matching medium; solid line corresponds to the stroke affected brain and dots to the healthy brain.
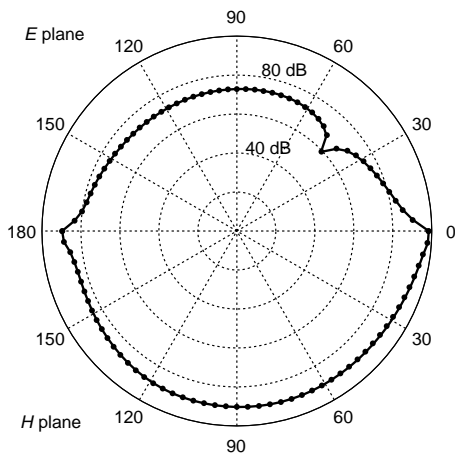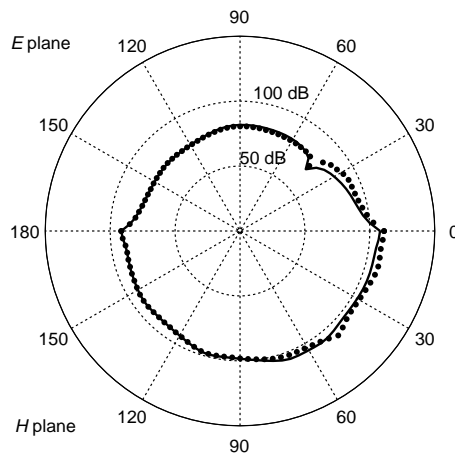

Figure 7: The ratio of $|E|/|E^i|$ in the absence of the matching medium layer; solid line corresponds the healthy brain, and dots to the stroke affected brain.

Figure 8: The ratio of $|E|/|E^i|$ in the presence of the matching medium layer; solid line corresponds the healthy brain, and dots to the stroke affected brain.

plane ($\phi = \pi/2$). The results for the normalized scattered fields, presented in Fig. 5, demonstrate that in the absence of a matching medium, no significant variation occurs in the scattered field when the brain is affected by a stroke. The results for the same case with the presence of the matching medium outside the four layered sphere is given in Fig. 6. Comparing these results with those presented in Fig. 5 shows that the matching medium causes a variation in the scattered field.

Next, the same test is performed for the geometry with a matching medium layer, previously analysed in Fig. 4. The parameters for the method and the measurement region are the same as that case. Since in this configuration the total field on the matching medium layer is calculated instead of the scattered field, the ratio of $|E|/|E^i|$, E^i being the incoming field, is plotted in the next figures. First in Fig. 7, the results in the absence of the matching medium is presented. Similar to the results in Fig. 5, there is no discernible variation in the outcome for the stroke affected case. On the other hand, in the presence of the matching medium layer, the existence of the stroke region alters the field values, as seen in Fig. 8.

4. CONCLUSION

The effect of the matching medium on the brain imaging has been tested by using a piecewise homogeneous layered sphere as a head model. Two different configurations has been used to compare the the field scattered by a healthy brain and by a brain with a stroke area. The simulations

show that without a matching medium, the presence of the stroke area do not cause a significant change in the scattered field. Therefore, it can be concluded that the presence of an appropriate matching medium layer is a prerequisite for a working microwave imaging system. However, the effect of the matching medium as observed in the numerical simulations might be inadequate for a successful implementation of the microwave tomography for the brain stroke detection.

REFERENCES

1. Scapaticci, R., L. Di Donato, I. Catapano, and L. Crocco, "A feasibility study on microwave imaging for brain stroke monitoring," *Progress In Electromagnetics Research B*, Vol. 40, 305–324, 2012.
2. Semenov, S. Y. and D. R. Corfield, "Microwave tomography for brain imaging: Feasibility assessment for stroke detection," *Intl. J. Antennas Propag.*, Vol. 2008, 1–8, 2008.
3. Fhager, A. and M. Persson, "Stroke detection and diagnosis with a microwave helmet," *Proceedings of 6th European Conf. on Antennas and Propagation, EuCAP 2012*, 1796–1798, 2012.
4. Meaney, P. M., S. A. Pendergrass, M. W. Fanning, D. Li, and K. D. Paulsen, "Importance of using a reduced contrast coupling medium in 2D microwave breast imaging," *Journal of Electromagnetic Waves and Applications*, Vol. 17, No. 2, 333–355, 2003.
5. Bilgin, E. and A. Yapar, "Electromagnetic scattering by radially inhomogeneous dielectric spheres," *IEEE Trans. Antennas Propag.*, to Appear.
6. Li, L. W., P. S. Kooi, M. S. Leong, and T. S. Yeo, "Electromagnetic dyadic Green's function in spherically multilayered media," *IEEE Trans. Microw Theory Tech.*, Vol. 42, 2302–2310, 1994.

High Resolution Ka-band Backscattering Measurement of Deciduous and Coniferous Tree

Wei-An Chuang[1], **Hsuan Ren**[1, 2], **Kuan-Liang Chen**[1], **and Jhih-Syuan Huang**[1]

[1]Institute of Space Science, National Central University, Taiwan
[2]Center for Space and Remote Sensing Research, National Central University, Taiwan

Abstract— In this paper, we present Ka-band backscattering measurement of deciduous and coniferous pine trees on National Central University (NCU) campus. The coherent radar system, designed and configured based on a vector network analyzer N5245A PNA-X (10 MHz–50 GHz) is capable of measuring the return power from 26.5 GHz to 50 GHz for VV, HH, HV polarizations at incidence angles between 30 and 80 degrees. In measuring process, the radar system has typical trace of the frequency ranges from 28 to 38 GHz of the received power for a given footprint of tree canopy. For this high resolution, the wind-induced Doppler effects can be ignored. Undesired returns from outside the antenna beam volume are conveniently rejected by gating in time domain. By this feature, the propagating depth through the tree can also be precisely determined so that the effective propagation constant and attenuation factor can be estimated. A reference measurement was taken at normal incidence using a conducting sphere as a calibration target. The calibration was conducted both in anechoic chamber and in-situ measurements. Ensemble average of 2000 samples was taken to estimate the mean return power and later by inverting the radar equation to obtain the backscattering coefficient as functions of frequencies and incident angles are then estimated. To simplify the matrix inversion, a narrow beam is realized with dish antenna. Based on the measured results, backscattering characteristics and statistical properties were analyzed for the cases of deciduous (banyan) and coniferous (pine) trees.

1. INTRODUCTION

A number of research efforts intend at characterizing propagation and backscattering in tree canopies have been reported in the past [1–4]. In Section 2, the inversion of backscattering from measured return power is presented. Those include narrow beam approximation, normalized average power for determining and the reference measurement using a spherical conducting as a target in anechoic chamber. The backscattering measurements of banyan and pine tree on National Central University (NCU) campus made at Ka band, its results at 28 GHz to 38 GHz are presented in Section 3. Based on the measured results,backscattering coefficients characteristics were analyzed for the cases of deciduous (banyan) and coniferous (pine). Finally, examples of recent experimental observations and preliminary results are discussed.

2. INVERSION OF σ° (SCATTERING COEFFICIENT) FROM RETURN POWER

It complements remote sensing in many important areas such as a geological sensing, forest biomass assessment, and so forth. After microwave remote sensing science study began to mature in the late 1970s [5], backscattering enhancement, cross polarization effects, probability density function, and radar remote sensing appeared in the 1980s [6–9]. The development of microwave scattering models appeared in the late 2010s [10]. The backscattering from measurement return power is described by backscattering coefficient (backscattering cross section per unit area). Those include narrow beam approximation, normalized average power for determining and the reference measurement using a spherical conducting as a target in anechoic chamber.

The overage power returned, P_r, is a function of several parameters. It may express as a function of the measured system, the propagation path from the transmitter antenna to the distribution target, the propagation path from the distribution target to the receiving antenna. The functional relationship between parameters and the received power have been discussed [11–13]. The overage power returned from distributed target (e.g., rough surface) that is illustrated by radar is given by:

$$P_r = \iint\limits_A \frac{P_t G^2(\theta, \phi, \theta_0)\sigma^\circ(\theta)\lambda^2}{(4\pi)^3 R^4} dA \tag{1}$$

where θ_0 is the look direction of the bore sight of the Tx/Rx antenna; R is the distance from the antenna to the illustrated area; P_t is the transmitted power; σ° is also called differential radar cross

section; G is antenna gain pattern. From Fig. 1, Radar Scattering Plane, then neglecting surface tilt, the differential unit of area on the scattering plane is given by

$$dA = R^2 \frac{\sin\theta}{\cos\theta} d\theta d\phi = R^2 \tan\theta d\theta d\phi \tag{2}$$

Let h be the radar to target distance at normal incidence, then

$$R = \frac{h}{\cos q} \tag{3}$$

Now, (1) becomes

$$P_r = \frac{P_t \lambda^2}{2(4\pi)^3 h^2} \int_0^{2\pi} \int_0^{\frac{\pi}{2}} G^2(\theta, \phi, \theta_0) sin2\theta\sigma_0(\theta) d\theta d\phi \tag{4}$$

A reference measurement may be taken at normal incidence using a spherical conducting as a target. The return power P_{rcal} from the spherical conducting is directed from (1)

$$P_{rcal} = \frac{P_{tcal}\lambda^2}{(4\pi)^3 (R_{cal})^4} G^2(\theta, \phi, \theta_0)\,\sigma_{cal} \tag{5}$$

$$P_{rcal} = \frac{P_{tcal}\lambda^2 \pi r_{cal}^2}{(4\pi)^3 (R_{cal})^4} G^2(\theta, \phi, \theta_0) \tag{6}$$

r_{cal} is the radius of spherical conducting.

Equation (4) may be normalized by division by (6), yielding the normalized average power

$$P_r = K \int_0^{2\pi} \int_0^{\frac{\pi}{2}} g^2(\theta, \phi, \theta_0)\sin 2\theta\sigma^0(\theta) d\theta d\phi \tag{7}$$

$$g^2(\theta, \phi, \theta_0) = \frac{G^2(\theta, \phi, \theta_0)}{G^2(\theta, \phi, \theta_0)} \tag{8}$$

$$g^2(0, 0, 0) = 1 \tag{9}$$

$$K = \frac{P_{rcal} P_t R_{cal}^4}{2\pi r_{cal}^2 P_{tcal} h^2} \tag{10}$$

P_{tcal} is the transmitted power, R_{cal} is the distance from the antenna to the spherical conducting.

The reference measurement in anechoic chamber is shown in Fig. 2. The coherent radar system is a wideband measurement system can be used to suppress much of the background through range gating of the return signal. This is done by using a reflection signal waveforms, the reflection signal form is shown Fig. 3.
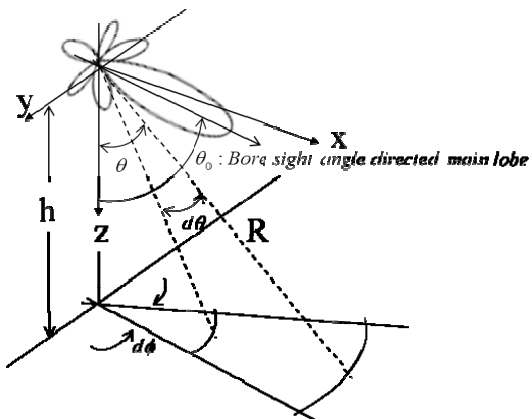
Figure 1: Radar scattering plane.

Figure 2: Reference measurements in anechoic chamber.
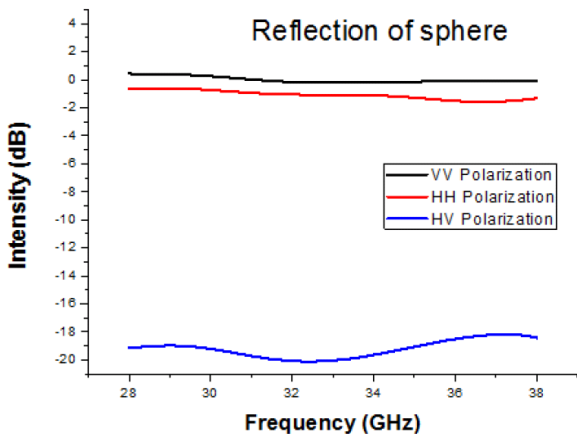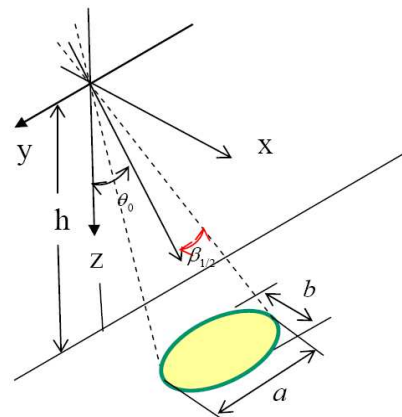
Figure 3: Recorded spectral data.

Figure 4: Narrow beam and constant gain pattern (circular beam with beam-width).

The narrow beam and constant gain pattern is shown Fig. 4.

$$a \approx \frac{2R\beta_{1/2}}{\cos\theta_0} = \frac{2\beta_{1/2}h}{\cos^2\theta_0} \tag{11}$$

$$b \approx 2R\beta_{1/2} = \frac{2h\beta_{1/2}}{\cos\theta_0} \tag{12}$$

$$A = \pi\frac{a}{2}\frac{b}{2} = \frac{\pi}{4}ab \approx \frac{\pi\beta_{1/2}^2 h^2}{\cos^3\theta_0} \tag{13}$$

$$s^0 = \frac{P_r}{P_{rcal}}\frac{P_{tcal}}{P_t}\frac{h^2 r_{cal}^2}{R_{cal}^4 b_{1/2}^2 \cos q_0} \tag{14}$$

3. MEASUREMENT SETUP

Backscattering measurements of tree canopy have been made with the coherent radar system mounted on the top of a 15 m-height roof. The platforms provide different, but complementary information about backscattering measurements statistics of tree canopy. Because of the relatively small footprint of its antenna narrow beam approximation, the platform-mounted coherent radar system is well suited for making observation of the selected tree targets, and the radar measurements can be arranged with detailed ground truth information about the tree targets.
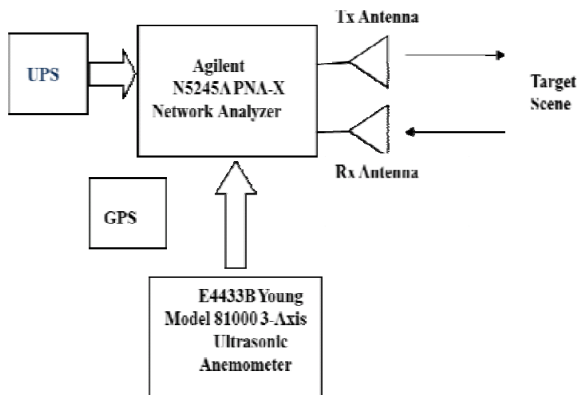
Figure 5: A simplified block diagram of the coherent radar system.

Figure 6: A agilent N5245A PNA-X network analyzer.

Figure 7: Test site as seen from the dish antenna.
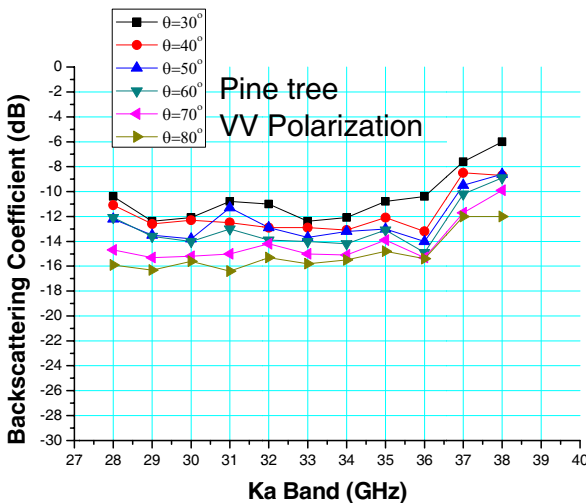
Figure 8: Backscattering coefficient of pine tree from 28 GHz to38 GHz for VV polarization.
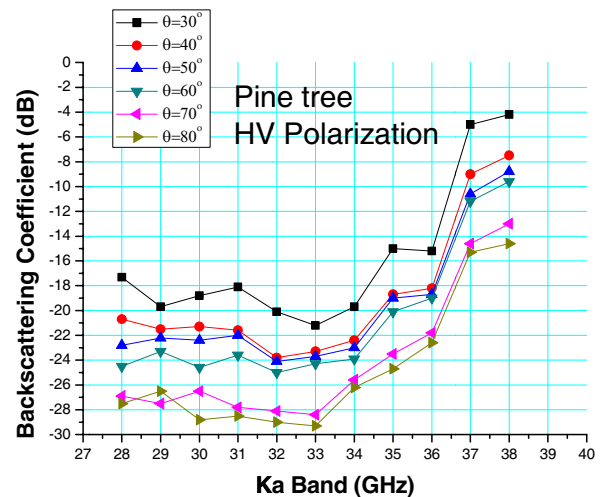
Figure 9: Backscattering coefficient of pine tree from 28 GHz to 38 GHz for HV polarization.

The coherent radar system is not very flexible, but it is discussed in some detail to illustrate calibration techniques also apply to the complex system. Fig. 5 shows a simplified block diagram of the coherent radar system, designed and configured based on a vector network analyzer N5245A PNAX (10 MHz–50 GHz), and the vector network analyzer is shown in Fig. 6.

The current backscattering measurements of tree canopy at Kaband are presented [14, 15]. The measurements show different backscattering behaviors for different tree configurations. The intention of the backscatter experiments is to research the effects of various tree components In Fig. 7 shows the test site as seen from the dish antenna, pine and banyan tree were selected for this study, the Ka band backscattering measurements were conducted on a single banyan tree and other single pine tree on National Central University (NCU) campus.

4. MEASUREMENT AND DISCUSSION

Figures 8–10 plots the backscattering coefficients of pine tree from 28 GHz to38 GHz for VV, HV and HH polarizations, respectively, with angle of incidence from 30 to 80 degrees. The other set of the plots are Figs. 11–13 for banyan tree. At Ka band, wavelength (1.1 cm $\sim$ 0.7 cm) is much smaller than most leaves and branches. For banyan tree, the leaf stems constitute a very small percentage of visible surfaces and may be reasonably ignored. In pine tree, the leaf stems constitute a large percentage of the visible surface, and contributions from multiple scattering reflections are larger than banyan trees. The interested factors that affect the properties of backscattering include frequency, polarization, incident angle, and canopy parameters. In viewing these figures, it can be seen that the cross-polarized returns generally presents higher dynamic range over the frequency and angular behavior.
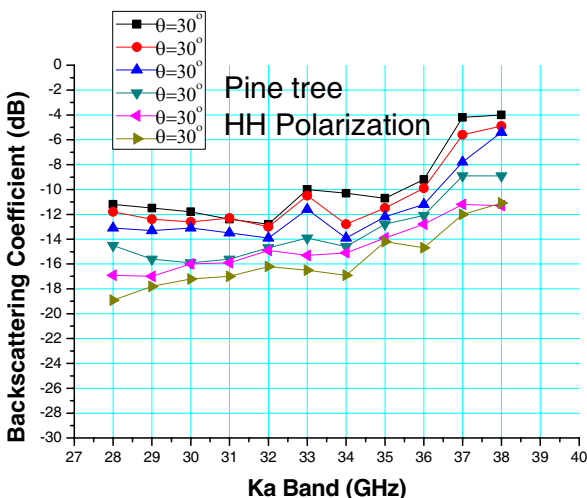
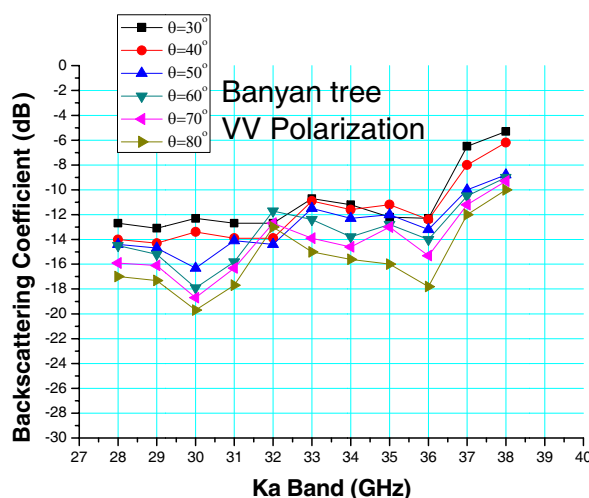Figure 10: Backscattering coefficient of pine tree from 28 GHz to 38 GHz for HH polarization.

Figure 11: Backscattering coefficient of banyan tree from 28 GHz to 38 GHz for VV polarization.
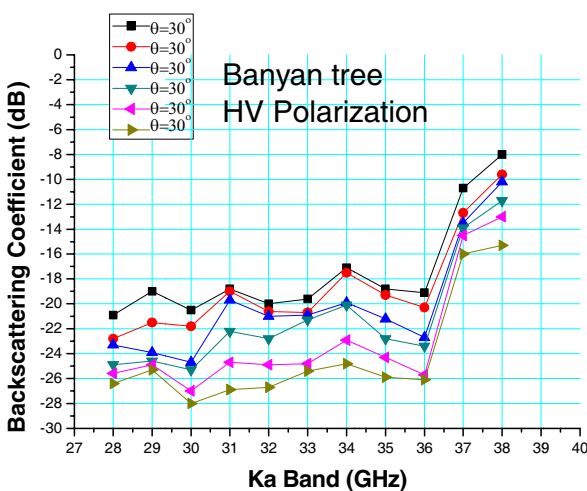

Figure 12: Backscattering coefficient of banyan tree from 28 GHz to 38 GHz for HV polarization.
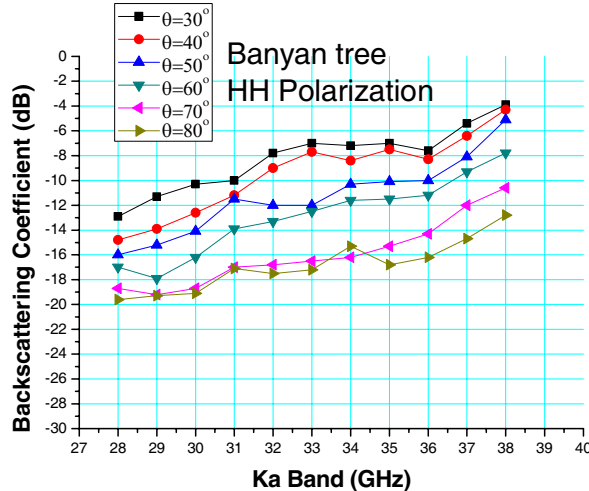

Figure 13: Backscattering coefficient of banyan tree from 28 GHz to 38 GHz for HH polarization.

5. CONCLUSION

We have measured the backscattering coefficient of trees using the coherent radar for VV, HH, HV polarizations at incidence angles between 20 and 80 degrees. The applicability of the technique to measurement of backscattering and extinction in tree canopies, we have modified and established the measured Equation (14) was verified experimentally by conducting two sets of indoor and outdoor measurements on banyan and pine tree. Ground truth measurements were made concurrently with backscatter measurements to establish a physical relationship between tree canopy parameters and the backscattering measured.

REFERENCES

1. Ulaby, F. T., R. K. Moore, and A. K. Fung, *Microwave Remote Sensing: Radar Remote Sensing*, Vol. 2, Artech House, Deham, MA, 1982.

2. Fung, A. K. and K. S. Chen, *Microwave Scattering and Emission Models for Users*, Artech House, Norwood, MA, 2010.

3. Ulaby, F. T. and M. C. Dobson, *Handbook of Radar Scattering Statistics for Terrain*, Artech House, MA, 1989.

4. Ruck, G. T., D. E. Barrick, W. D. Stuart, and C. K. Krichbaum, *Radar Cross Section Handbook*, Plenum Press, New York, 1970.

5. Ishimaru, A., *Wave Propagation and Scattering in Random Media*, Academic Press, San Francisco, CA, 1978.

6. Tsang, L., J. A. Kong, and R. T. Shin, *Theory of Microwave Remote Sensing*, John Wiley, New York, 1985.

7. Ulaby, F. T., R. K. Moore, and A. K. Fung, *Microwave Remote Sensing: Fundamentals and Radiometry*, Vol. 1, Artech House, Deham, MA, 1981.

8. Ulaby, F. T., R. K. Moore, and A. K. Fung, *Microwave Remote Sensing: From Theory to Applications*, Vol. 3, Artech House, Deham MA, 1986.

9. Ulaby, F. T., R. K. Moore, and A. K. Fung, *Microwave Remote Sensing: Radar Remote Sensing*, Vol. 2, Artech House, Deham, MA, 1982.

10. Fung, A. K. and K. S. Chen, *Microwave Scattering and Emission Models for Users*, Artech House, Norwood, MA, 2010.

11. Ulaby, F.T., and Dobson, M. Craig, *Handbook of Radar Scattering Statistics for Terrain*, Artech House, MA, 1989.

12. Ruck, G. T., D. E. Barrick, W. D. Stuart, and C. K. Krichbaum, *Radar Cross Section Handbook*, Plenum Press, New York, 1970.

13. Knott, E. F., J. F. Shaeffer, and M. T. Tuley, *Radar Cross Section*, Artech House, MA, 1993.

14. Kim, H., J. T. Johnson, and B. A. Baertlein, "Ka band backscatter measurements and modeling of tree foliage," *1998 IEEE International Geoscience and Remote Sensing Symposium Proceedings, 1998. IGARSS '98*, Vol. 4, 2086-2088, 1998.

15. Kim, H., J. T. Johnson, and B. A. Baertlein, "High resolution Ka-band images of a small tree: Measurements and models," *IEEE Transactions on Geoscience and Remote Sensing*, Vol. 38, 899–910, 2000.

Investigation of Switched Reluctance Machine for EV Propulsion Unit with Torque Smoothening Strategy

M. Ruba and D. Fodorean
Department of Electrical Machines and Drives
Technical University of Cluj-Napoca, Cluj-Napoca, Romania

Abstract— The paper deals with the investigation of a 30 kW switched reluctance machine (SRM) designed to be used in the automotive industry, as propulsion unit for electrical vehicles (EV). The paper details the most important steps when designing such an electrical machine, and validates the structure using advanced co-simulation techniques, coupling finite element analysis software (Cedrat Flux 2D) with software used to implement the controller (Matlab/Simulink). As the advantages of the SRM are known, its main drawback, the torque ripples, are reduced as much as possible using a dedicated control strategy, the torque sharing functions (TSF). The solution offered by the paper highlights the possibility of using a cheap, reliable and robust electrical machine for propulsion unit.

1. INTRODUCTION

In general, when an electrical propulsion unit is designed, permanent magnet based electrical machines are involved, having increased power density, reliability and maturity in the field of study. However, the issue of price and economical market unbalance, stock limits and political situations, forced researchers to orient their attention to machines that have passive rotors, such as the switched reluctance or the variable reluctance machines [1, 2]. Serious competitors to these machines are the induction machine (IM) or the DC machine, but the latter one has some disadvantages regarding the issue of the sliding contact on the collector. The induction, machines on the other side, are robust, reliable, but their control is not so simple due to the slip, that is quite difficult to be estimated precisely.

To be used as a propulsion unit, the electrical machine has to be reliable, low cost, hence simple design and building and able to reach high speeds of rotation. One machine that reaches all these expectations is the switched reluctance machine (SRM). One such machine is involved in the study of the present paper.

The SRM studied in this paper regards the propulsion unit of a casual small city vehicle, having a power of 30 kW. The speed of the desired SRM is 10 krpm at maximum power and the developed torque is about 28 Nm. The DC supply is ensured by a battery of 360 V. The phase current of the SRM is 150 A at rated power and rated speed.

The present paper will detail the design procedure of the SRM highlighting important aspects regarding compromises that are to be considered to reach increased reliability of the machine. Finite element analysis (FEA) will validate the theoretical studies with regards to the design and control of the SRM. Details regarding the building of the coupled simulation task between Matlab Simulink and Flux 2D are presented, followed by a stand alone Simulink program, used for simulation of the SRM based on FEA fetched results.

Taking advantage of the fast simulation of the new developed program, the linear torque sharing function control method is applied to smoothen the torque of the machine, to fulfill the requirements of the automotive industry with regards to the torque ripple of the propulsion unit.

2. THE PROPOSED SRM

Preliminary to the design of the SRM, some parameters need to be established. The main parameters (given in Table 1) that will guide the sizing process are: the rated current (I), the number of phases (m), the machine's rated power (P_{2N}), the mechanical air-gap (g) the air-gap flux density in aligned position $(B_{g\max})$, the rated speed (n_N) and the rated torque (T_N).

When sizing a SRM it is important to have a proper selection of the stator to rotor number of poles ratio. Lower number of phases, hence lower number of stator poles, will return a structure with increased torque ripples. This represents a serious disadvantage for automotive applications. However, increasing the number of phases and increasing the number of stator poles will decrease the torque ripples. The drawback here is the size of the machine that increases with the number of phases. A second drawback is the complexity and price of the power converter.

Table 1: The SRM's specifications.

Parameter	Value	Unit
Battery voltage	360	[V]
Imposed current	150	[A]
Output power	30	[kW]
Rated torque	28	[Nm]
Rated speed	10000	[r/min]
Number of stator poles	8	-
Number of rotor poles	6	-
Rated efficiency	0.8	-
Maximum airgap flux desity	1.9	[T]
Airgap length	0.4	[mm]

Hence, the compromise is taken for a 8/6 structure, a four phase SRM.

The main and maybe the most important step when designing the machine is a proper sizing for the mean diameter (D_g) that will have a direct impact on the torque development [3].

$$D_g = \sqrt[3]{\frac{P_{2N} \cdot Q_s \cdot k_\sigma}{Q_R \cdot \pi^2 \cdot k_L \cdot \frac{n_N}{60} \cdot B_{g\max} \cdot \left(1 - \frac{1}{K_{cr}}\right) \cdot A_S}} \tag{1}$$

Based on the size of the mean diameter, the rest of the stator and rotor dimensions can be easily computed, based on geometric models for the poles and the slots of the machine [3].

Each phase of the machine is compound of two coils placed on diametrically opposed stator poles. The coils are connected in series, hence the same current will pass through them. The calculations around the number of turns per coil are based on the relation of the magneto-motive force H and the geometrical details of the machine [3, 4].

$$\Theta = H_{Fe} \cdot (l_s + l_r) + H_g \cdot l_g \tag{2}$$

Hence, the number of turns per coil is computed as ratio between the magneto-motive force and the rated current of the machine. The proper cross section area has to be chosen function of the rated current. Here, about 9.37 was chosen. The height of the stator and rotor poles can be computed now, knowing the final dimensions of the coils. Table 2 contains the data regarding the dimensions of the SRM designed. Their correspondence on the machine's blueprint are depicted in Fig. 1.

The first method to validation is to analytically compute the developed torque of the newly design SRM. This can be accomplished function of the MMF and the machine's mean diameter.

$$T_v = k_{unal} \cdot (N_f \cdot I)^2 \cdot \frac{D_g}{2} \cdot \mu_0 \cdot \frac{l_a}{2 \cdot g} \tag{3}$$

Table 2: The SRM's geometry dimensions.

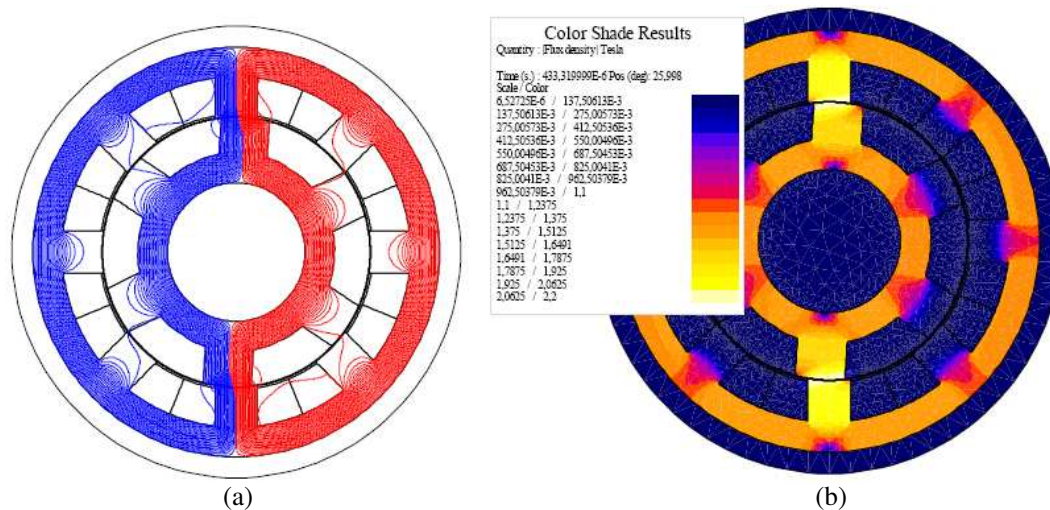| Parameter	Notation	Value	Unit
Height of stator pole	h_{pS}	18	[mm]
Height of rotor pole	h_{pR}	17	[mm]
Height of stator yoke	h_{jS}	14	[mm]
Height of rotor yoke	h_{jR}	14	[mm]
Width of stator pole	b_{pS}	20	[mm]
Width of rotor pole	b_{pR}	23	[mm]
Active stack length	l_S	100	[mm]
Air-gap length	g	0.4	[mm]

Figure 1: (a) The magnetic flux paths and (b) the flux distribution in the aproached SRM.

where k_{unal} is a constant that considers the contribution of the magnetic flux in un-aligned position. The developed torque, computed analytically with (3) is 28.2 Nm, quite close to the value imposed at the beginning of the design procedure.

3. ANALISYS BY SIMULATION METHODS OF THE SRM

3.1. The Coupled FEA Model for the SRM

Finalizing the sizing process of the SRM, the next step is to validate the results using FEA methods. For this a dedicated software was used, Flux 2D. The model is built considering the possibility to simulate the machine's operation controlled with its power converter [4].

The FEA model of the machine, designed in Flux 2D is coupled to the power converter's controlled, designed in Matlab Simulink [5]. This way, hysteresis current control can be performed in order to observe the machine's behavior and torque development capability.

As it can be seen in Fig. 1, the magnetic flux developed by the SRM closes in the correct paths, involving poles from diametrically opposite directions. However, there is flux that leaks out of the structure, but the ratio of the usable to leakage flux is about 0.9, hence, nearly all the magnetic flux is used for torque development.

Another important aspect to be verified is the flux density in the machine. As depicted in Fig. 1(b), the values of the flux density does not reach hazardous values. Peak values, such as 2 T in the edges of the poles, are acceptable and usual for SR machines. From this point of view, the machine is sized correctly.

The test via cosimulation of Matlab Simulink with Flux 2D was performed at rated speed, 10000 rpm and rated currents, 150 A. It needs to be mentioned that classical hysteresis controller was involved to maintain the currents at their rated value. In Fig. 2 the evolution of the currents and of the torque function of time is depicted.

The mean developed torque is about 28 Nm, the value desired from the design process, and at the DC voltage of 360 V, the machine is able to form the currents even at the rated speed. It is important to mention that several tests were performed in order to find the proper switching angle. For a so wide range of speeds, from 0 to 10 krpm the switching angle cannot be kept constant. Hence, in the controller, it is important to create a look up table containing the ON and OFF angles function of the speed of the machine.

However, analyzing Fig. 2, the torque characteristic has increased ripples. In this condition, the machine cannot operate as propulsion unit for domestic vehicles. Hence, a dedicated torque smoothening procedure is required to diminish as much as possible these ripples. For this, the linear torque sharing function (LTSF) is engaged in study.

3.2. The LUT Based Matlab/Simulink Model

Studying the LTSF control strategy of the SRM directly on the FEA model is quite difficult and time consuming. However, building a particular model of the machine, based on the classical equations combined with results fetched from the FEA model, proved to be the proper solution. This new
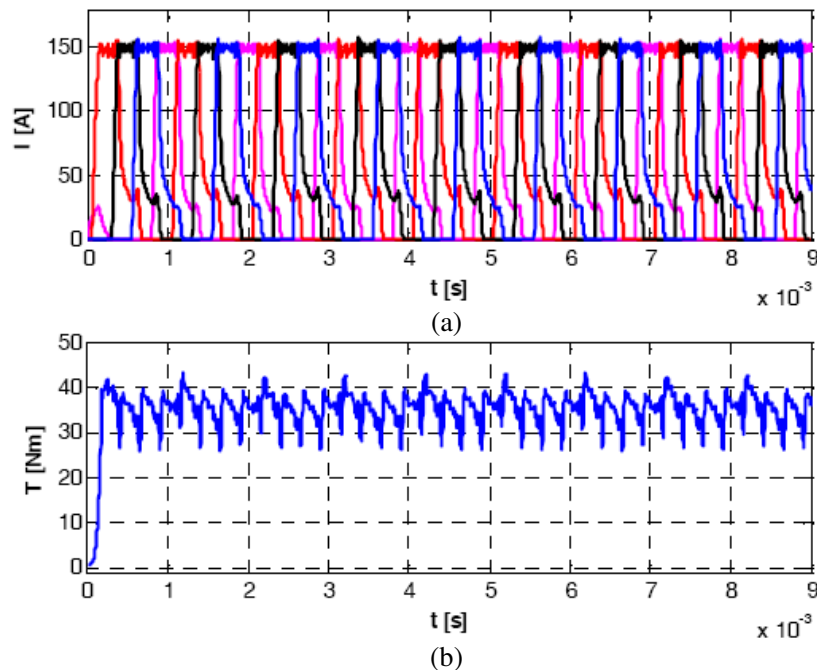
Figure 2: (a) The currents and (b) the developed torque.

model was created in Matlab Simulink based on 3D matrixes from the FEA model containing data regarding data for the magnetic flux and magnetic torque vs. currents and rotor positions [6].

These results are obtained by imposing in one phase of the machine increasing currents from 0 to a current above the rated one (200 A) and for each current moving the rotor from unaligned to aligned, and again to unaligned positions. In order to increase more the accuracy of the model, the characteristics obtained are multiplied for more currents and positions than those imposed using interpolation functions [7–9]. This way one can offer highly accurate results for any simulation scenarios.

The LUT's used in the model are depicted in Fig. 3. In order to compute the flux in the machine, as the input for the first LUT, the analytical expression of the flux function of the voltage is involved (1).

Having the flux and rotor position as input in the LUT, the actual current in the machine can be determined. This will be used then in the second LUT to define the value of the developed
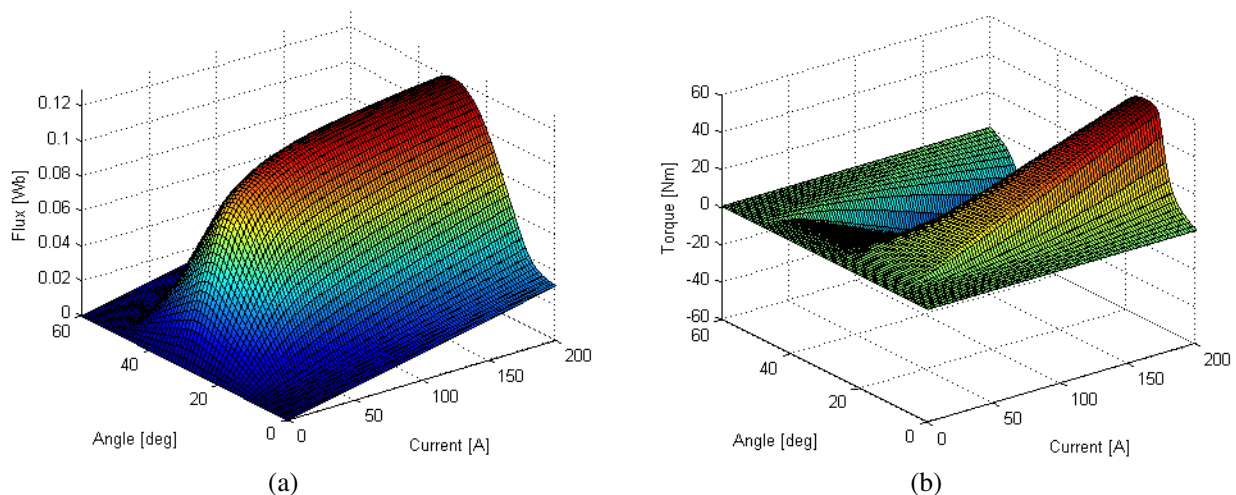
Figure 3: (a) The magnetic flux and (b) magnetic torque variations vs. current and rotor postion.

torque for the same rotor position.

$$\Psi = \int (u - R_f \cdot i) \cdot dt \qquad (4)$$

This approach has the benefit of high accuracy and very fast solving, reducing the computation time from tens of hours with the FEA model to few minutes.

4. RESULTS OF THE ANALYSIS

The LTSF used in the model is based on two different equations that compute the current shape reference function of the torque and of the rotor position. One function is with respect to the increase of the current and one is with respect to the decreasing slope of the current (2). Hence only when phase commutation occurs, the functions are engaged. When one phase conducts, the reference of the controller is the desired torque.

$$f_{inc}(\theta) = \frac{T_{ref}}{\theta_{ov}} (\theta - \theta_{on}) \quad f_{dec}(\theta) = T_{ref} - \frac{T_{ref}}{\theta_{ov}} (\theta - \theta_{off}) \qquad (5)$$

As it can be seen in Fig. 4, the LTSF performs well smoothening the torque characteristic as desired both at rated and under rated speeds. The θ_{on}, θ_{off} and θ_{ov}, the ON, OFF and overlap angles can be computed in order to reach even better performances to smoothen even more the developed torque. Also, adding other functions, such as exponential or cubic TSFs can improve the control of the torque characteristic of the machine [10, 11].
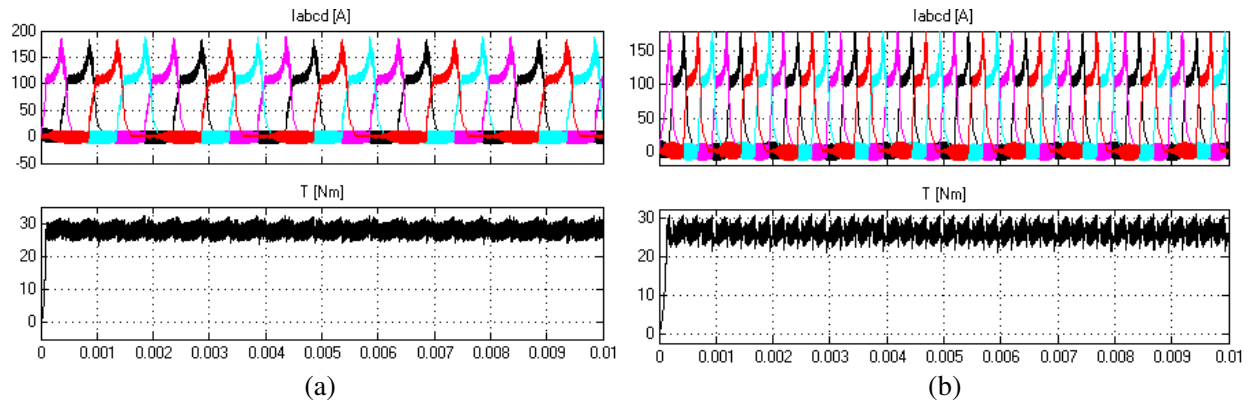

Figure 4: The developed torque and currents for (a) 5000 rpm and (b) 10000 rpm.

5. CONCLUSIONS

In the paper it was detailed the design procedure of a SRM for traction applications followed by FEA based analysis. The torque ripple issue was solved using linear torque sharing function as method of control, smoothening the torque characteristic even at rated speed of 10000 rpm. Hence it was proved that the SRM is a serious candidate to be used as propulsion unit in the automotive industry.

Future investigations regard implementation of several other control strategies combined with noise and vibration analysis.

REFERENCES

1. Vrazic, M., D. Vuljaj, A. Pavasovic, and H. Paukovic, "Study of a vehicle conversion from internal combustion engine to electric drive," *IEEE International Energy Conference*, 1544–1548, May 13–16, 2014.
2. Omekanda, A. M., "Switched reluctance machines for EV and HEV propulsion: State-of-the-art," *IEEE Workshop on Electrical Machines Design Control and Diagnosis*, 70–74, 2013.

3. Ruba, M., L. Szabo, and D. Fodorean, "Design and analysis of low voltage high current SRM for small automotive applications," *International Symposium on Power Electronics, Electrical Drives, Automation and Motion*, 341–346, Sorrento, Italy, 2012.

4. Ruba, M., I. A. Viorel, and L. Szabó, "Modular stator switched reluctance motor for fault tolerant drive systems," *IET Electric Power Applications*, Vol. 7, No. 3, 159–169, Mar. 2013, 2013, ISSN: 1751-8660.

5. Ruba, M. and D. Fodorean, "Design, analysis and torque control of low voltage high current SRM for small automotive applications," *Proceedings of EuroCon. 2013*, 1499–1503, Zagreb, Croatia, Jul. 1–4, 2013, ISBN:978-1-4673-2232-4/13.

6. Fodorean, D., D. C. Popa, F. Jurca, and M. Ruba, "Optimizing the design of radial/axial PMSM and SRM used for powered wheel-chairs," *Proceedings of the International Conference on Electrical, Computer, Electronics and Communication Engineering*, 120–125, Paris, France, Nov. 14–16, 2011.

7. Dowlatshahi, M., S. M. S. Nejad, and J. W. Ahn, "Torque ripple minimization of switched reluctance motor using modified torque sharing function," *Iranian Conference on Electrical Engineering*, 1–6, May 14–16, 2013.

8. Hwu, K. I. and C. M. Liaw, "Intelligent tuning of commutation for maximum torque capability of a switched reluctance motor," *IEEE Transactions on Energy Conversion*, Vol. 18, No. 1, 113–120, 2003.

9. Mademlis, C. and I. Kioskeridis, "Performance optimization in switched reluctance motor drives with online commutation angle control," *IEEE Transactions on Energy Conversion*, Vol. 18, No. 3, 448–457, 2003.

10. Sahoo, N. C., J. X. Xu, and S. K. Panda, "Low torque ripple control of switched reluctance motors using iterative learning," *IEEE Transactions on Energy Conversion*, Vol. 16, No. 4, 318–326, 2001.

11. Pop, A. C., V. Petrus, C. S. Martis, V. Iancu, and J. Gyselinck, "Comparative study of different torque sharing functions for losses minimization in switched reluctance motors used in electric vehicles propulsion," *13th International Conference on Optimization of Electrical and Electronic Equipment (OPTIM)*, 356–365, May 24–26, 2012.

Achieving Tunable Mode Splitter and Omnidirectional Absorber by Semiconductor Photonic Crystal

Guo-Wen Ding[1], **Shao-Bin Liu**[1], **Hai-Feng Zhang**[1, 2],
Xiang-Kun Kong[1], **Bo-Ri Bian**[1], and **Hai-Ming Li**[1]

[1]College of Electronic and Information Engineering
Nanjing University of Aeronautics and Astronautics, Nanjing 210016, China
[2]Nanjing Artillery Academy, Nanjing 211132, China

Abstract— The properties of one-dimensional (1D) photonic crystals (PCs) composed of the semiconductor (GaAs) and dielectric layers are theoretically investigated by the transfer matrix method (TMM). Due to the Voigt effect, the dielectric constant of the semiconductor could be modified in different modes and frequency ranges. If the frequency range of the incident wave is larger than the plasma frequency, TE and TM modes of the incident wave will be absorbed in a wide incident angle. TM wave will be absorbed but TE wave will be reflected while the frequency range is less than the plasma frequency. By varying the external magnetic field, the absorption of semiconductor can be tuned. The proposed PCs have a reconfigurable application to design a tunable omnidirectional absorber and mode splitter at same time.

1. INTRODUCTION

Photonic crystals (PCs) are artificial materials with a periodic arrangement of refractive index which become a new research focus recently [1, 2]. A perfect absorber utilizing the electromagnetic (EM) response-tailorable ability of metamaterial has been widely explored since it was first proposed by Landy et al. [3]. A broadband omnidirectional absorption in heterostructures with a highly absorptive metallic film and a dielectric Bragg reflector is realized [4]. A mode splitter which can separate the two orthogonal modes of light, is one of the most important components in modern optical communication systems [5]. Various mode splitters have been reported. The fabrication of the mode splitter based on an asymmetrical Y-junction structure [6] or Mach-Zehnder interferometer [7] requires complex processes such as photobleaching and poling. Recently, PCs containing the semiconductor as one of the constituents also have been the focuses of researchers' interests. It is shown that, in semiconductor-based PCs, there are two magneto-optical effects: Faraday and Voigt effects after introducing the external magnetic. Therefore, PBGs of such semiconductor-based PCs will be tuned correspondingly [8], which have important applications in the mode splitter. They found that the dielectric constant of semiconductor is modified differently in different frequency ranges. But limited work had been conducted on investigating a tunable omnidirectional absorber and TE-TM modes splitter based on the similar semiconductor PCs.

The purpose of this paper is to explore the EM wave absorption properties in a PC made of semiconductor and dielectric layers. The semiconductor will be considered to operate near the plasma frequency. The EM waves propagating through the proposed structure are simulated by the transfer matrix method (TMM) [9]. If the frequency range is larger than the plasma frequency, a tunable omnidirectional absorber is obtained. When the frequency range is less than the plasma frequency, TM wave is absorbed. Therefore, only TE wave can be reflected by PCs in wide-range. Due to the Voigt effect of semiconductor, the frequency range that TE and TM waves are splitted can be tuned by adjusting the intensity of the external magnetic field. The proposed tunable omnidirectional mode splitter has some important potential practical applications.

2. THEORETICAL MODEL

Let us consider a finite binary semiconductor-based PC denoted as $(AB)^N$ where layer A is the dielectric, layer B is the semiconductor, and N is the number of periods. The thickness of the layer $A(B)$ is $d_A(d_B)$. The refractive index of the layer $A(B)$ is $n_A(n_B)$. The relative permittivity and permeability layers A and B are ε_i and μ_i ($i = A$, B), respectively. The PC is assumed to be immersed in air. The incident angle of the incident wave is defined as θ.

The Voigt effect is a well-known magneto-optical effect of the semiconductor that should be considered, when the propagation direction of EM waves is perpendicular to the external magnetic direction. If the electric field of the incident waves is parallel to the external magnetic field, the

permittivity will be unchanged by the external magnetic field. The relative permittivity can be expressed as [10]

$$\varepsilon_{\parallel}(\omega) = \varepsilon_0 \left(1 - \frac{\omega_p^2}{\omega^2 + i\omega/\tau} \right) \tag{1}$$

where ε_0 is the static dielectric constant, where τ is the scattering time and ω_p is the screened plasma frequency. The plasma frequency depends on the densities n and effective masses m^* of the free carriers and can be written as [11]

$$\omega_P^2 = \sum_i \frac{4\pi n_i e^2}{m_i^* \varepsilon_0} \tag{2}$$

where i is the relevant conducting or valence band of free electrons and holes an e is the charge. For the electric field of the incident waves which is perpendicular to the external magnetic field, the permittivity will be changed if the external magnetic field is modified. The permittivity is given by [12]

$$\varepsilon_{\perp}(\omega) = \varepsilon_0 \left(1 - \frac{(\omega^2 + i\frac{\omega}{\tau})\omega_P^2 - \omega_P^4}{\left(\omega^2 + i\frac{\omega}{\tau}\right)\left(\omega^2 - \omega_c^2 - \omega_P^2 + i\frac{\omega}{\tau}\right)} \right) \tag{3}$$

where ω_c is the cyclotron frequency and it can be expressed as [10]

$$\omega_c = \frac{eB}{m^*c} \tag{4}$$

B denotes the external magnetic field and c is the speed of light in vacuum. For a semiconductor layer, the relative permittivity can be expressed as $\varepsilon_B(\omega) = \varepsilon_{\parallel}(\omega)$ for TE mode and $\varepsilon_B(\omega) = \varepsilon_{\perp}(\omega)$ for TM mode.

3. NUMERIAL RESULTS AND DISSUSSION

In this section, we investigate the properties of the relative permittivity of semiconductor, absorption and mode split of 1D semiconductor-based PC. Without loss of generality, we plot $\omega a/2\pi c$ with the normalization convention $\omega_0 a/2\pi c = 1$. With this definition, we choose the parameters as follows: the number of periods $N = 4$, $\varepsilon_A = 1$, $\mu_A = 1$, $d_A = 0.03a$. We consider the semiconductor as GaAs. The thickness of the layer B is $d_B = a$. We can define the plasma frequency as $\omega_p = 4.16\omega_0$ and the scattering time $\tau = 1.2\pi/\omega_0$ [12]. If the external magnetic field is $B = 1\,\mathrm{T}$, the cyclotron frequency becomes $\omega_c = 0.93\omega_0$. The static dielectric constant is taken to be $\varepsilon_0 = 12.9$ [12]. The thickness of the GaAs is $d_B = a$.

As shown in Figure 1(a), the absorption band is insensitive to the incident angle. When the incident angle increases, the absorption decreases and the pass band remains the same. As a result, it is convenient to realize an omnidirectional absorber. On the other hand, the absorption for incident wave at large incidence could not be more than 80% in our case. Therefore, we only discussed the band with absorption over 70%, which is an important criteria to evaluate an absorber. Therefore, as shown in Figure 1(a), the omnidirectional absorption band with absorption over 70% is located from $4.57\omega_0$ to $9\omega_0$.

Partial view of Figure 1(a) is shown in Figure 1(b). As is shown in Figures 1(a) and 1(c), it is obviously that when the frequency range is less than the plasma frequency and runs from $3.68\omega_0$ to $4.1\omega_0$, TE wave will be reflected but TM wave is absorbed by PCs in different angles. Thus the proposed structures can be used as omnidirectional mode splitter. As shown in Figure 1(d), if the frequency range covers from $3.68\omega_0$ to $4.1\omega_0$, we can find that the real part of ε_B for TM wave is positive, which can be tuned by the external magnetic. According to the results in Ref. [13], impedance matching for TM wave has been met. But the real part of ε_B for TE wave will not be influenced by the external magnetic and it is negative. Thus, the impedance matching for TE wave has not been met [13]. Therefore, TM wave will be absorbed and TE wave will be reflected in the region ranging from $3.68\omega_0$ to $4.1\omega_0$. These results may be provided theoretical instructions for semiconductor of future mode splitter applications.

In order to study the effect of the external magnetic field on absorption of PCs, the high and low band of absorption as a function of the external magnetic field is shown in Figure 2. It is obviously that if $\omega = 4.1\omega_0$, the real part of ε_B for TE wave will be close to zero, which is not
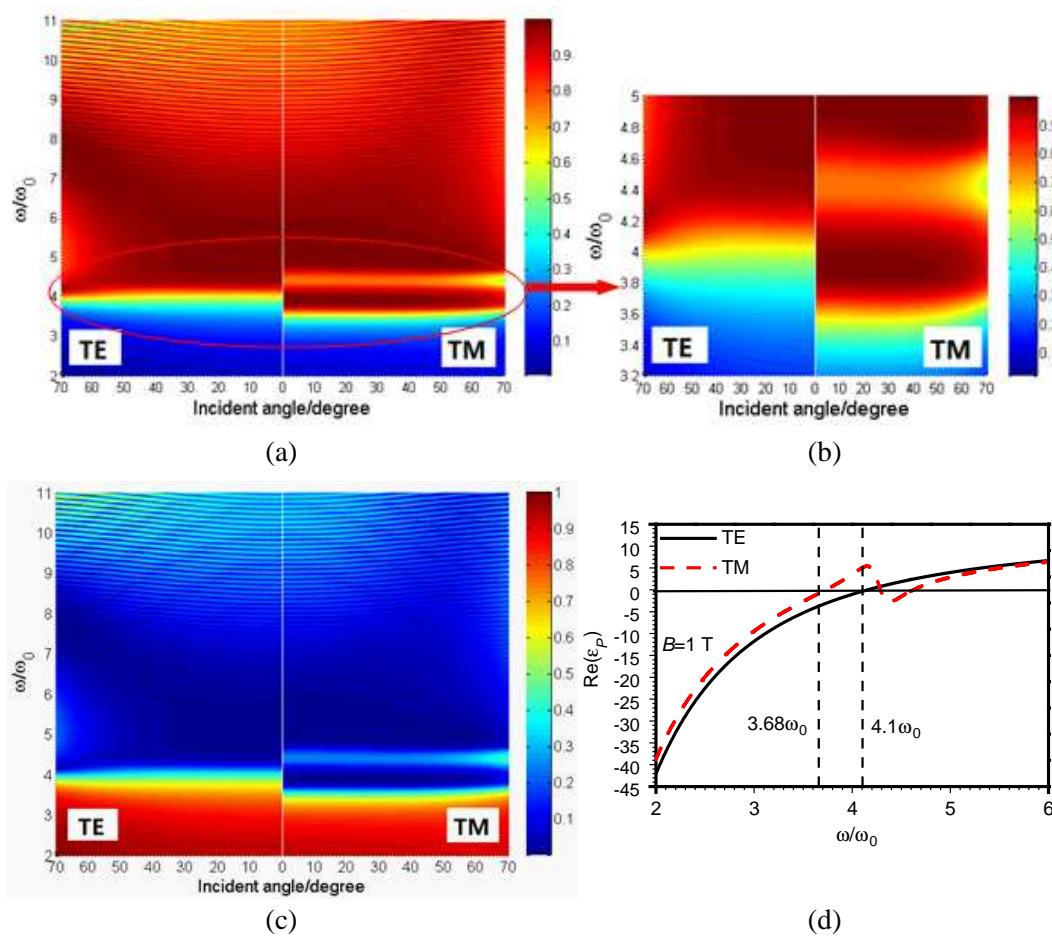
(a)

(b)

(c)

(d)

Figure 1: (a) Absorbance of PCs in terms of angular frequency and incident angle for TE wave and TM wave. (b) Partial view of Figure 1(a). (c) Reflectance of PCs in terms of angular frequency and incident angle for TE wave and TM wave. (d) The real parts of the dielectric permittivity of the GaAs as $B = 1\,\mathrm{T}$.
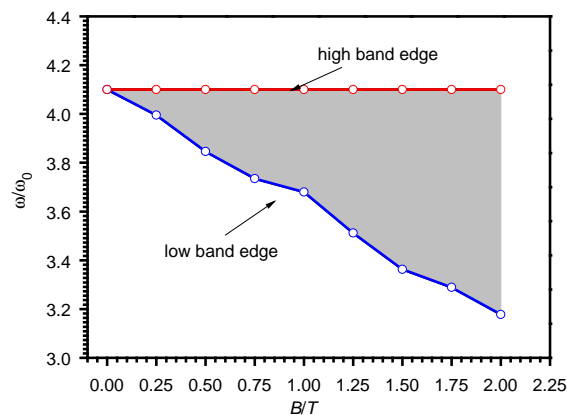

Figure 2: The high and low band edges as a function of the external magnetic field if $d_A = 0.03l$, $d_B = l$.

influenced by the external magnetic field B. Thus, the high band edge is equal to $4.1\omega_0$ which is less than the plasma frequency, and it's not changed as B increased. Meantime, the low band edge will decreased obviously with increasing B. When $B = 0\,\mathrm{T}$, the real parts of ε_B for TE and TM waves are equal. Thus the low band edge is equal to the high band edge, so the bandwidth of mode splitter is zero. If B is increased to $2\,\mathrm{T}$, the real part of ε_B for TM wave will be positive and it's negative for TE wave as the frequency ranging from $3.32\omega_0$ to $4.1\omega_0$. Thus, the impedance matching for TE wave has not been met, but the impedance matching for TM wave has been met. Therefore, the frequency range of the mode splitter will be $3.32\omega_0 \sim 4.1\omega_0$. As mentioned above, we

can get a conclusion that the bandwidth of mode splitter is broadened as B is increased.

4. CONCLUSION

In summary, a novel of PCs structure composed of conventional material and semiconductor material is proposed. If the frequency of incident EM wave is larger than the plasma frequency ω_p, due to the impedance matching, the proposed structure can be used to realize an omnidirectional absorber. Due to the Voigt effect, when the frequency range is less than the plasma frequency ω_p, TE and TM waves will be split obviously. The frequency range of the incident wave, whose modes can be split, will be expanded by increasing the external magnetic field B. Therefore, these properties could be applied in an omnidirectional absorber or a number of photonic devices controlling the polarization-dependent propagation of light.

REFERENCES

1. John, S., "Strong localization of photons in certain disordered dielectric superlattices," *Physical Review Letters*, Vol. 58, No. 23, 2486–2489, 1987.
2. Yablonovitch, E., "Inhibited spontaneous emission in solid-state physics and electronics," *Physical Review Letters*, Vol. 58, No. 20, 2059–2062, 1987.
3. Landy, N. I., S. Sajuyigbe, J. J. Mock, D. R. Smith, and W. J. Padilla, "Perfect metamaterial absorber," *Physical Review Letters*, Vol. 100, No. 20, 207402, 2008.
4. Gong, Y., X. Liu, H. Lu, L. Wang, and G. Wang, "Perfect absorber supported by optical Tamm states in plasmonic waveguide," *Optics Express*, Vol. 19, No. 19, 18393–18398, 2011.
5. Shi, Y., "A compact polarization beam splitter based on a multimode photonic crystal waveguide with an internal photonic crystal section," *Progress In Electromagnetics Research*, Vol. 103, 393–401, 2010.
6. Hu, M. H., J. Z. Huang, R. Scarmozzino, M. Levy, and R. M. Osgood, Jr., "Tunable Mach-Zehnder polarization splitter using height-tapered Y-branches," *IEEE Photonics Technology Letters*, Vol. 9, No. 6, 773–775, 1997.
7. Soldano, L. B., A. I. de Vreede, M. K. Smit, B. H. Verbeek, E. G. Metaal, and F. H. Green, "Mach-Zehnder interferometer polarization splitter in InGaAsP/InP," *IEEE Photonics Technology Letters*, Vol. 6, No. 3, 1994.
8. Xu, C., D. Han, X. Wang, X. Liu, and J. Zi, "Extrinsic photonic crystals: Photonic band structure calculations of a doped semiconductor under a magnetic field," *Applied Physics Letters*, Vol. 90, No. 6, 061112, 2007.
9. Zhang, H. F., S. B. Liu, X. K. Kong, B. R. Bian, and Y. Dai, "Omnidirectional photonic band gap enlarged by one-dimensional ternary unmagnetized plasma photonic crystals based on a new Fibonacci quasiperiodic structure," *Physics of Plasmas*, Vol. 19, No. 11, 112102, 2012.
10. Feng, L., X. P. Liu, Y. F. Tang, Y. F. Chen, J. Zi, S. N. Zhu, and Y. Y. Zhu, "Tunable negative refraction in a two-dimensional active magneto-optical photonic crystal," *Physical Review B*, Vol. 71, No. 19, 195106, 2005.
11. Kong, X. K., S. B. Liu, H. F. Zhang, S. Y. Wang, B. R. Bian, and Y. Dai, "Tunable bistability in photonic multilayers doped by unmagnetized plasma and coupled nonlinear defects," *IEEE Journal of Selected Topics in Quantum Electronics*, Vol. 19, No. 1, 8401407–8401407, 2013.
12. Xu, C., X. Hu, Y. Li, X. Liu, R. Fu, and J. Zi, "Semiconductor-based tunable photonic crystals by means of an external magnetic field," *Physical Review B*, Vol. 68, No. 19, 193201, 2003.
13. Zhou, J., L. Jin, and E. Y. B. Pun, "Tunable multichannel nonreciprocal perfect absorber based on resonant absorption," *Optics Letters*, Vol. 37, No. 13, 2613–2615, 2012.

Tunable Electromagnetically Induced Transparency Like Transmission in Graphene Metamaterials with Indirect Coupling

Guo-Wen Ding[1], Shao-Bin Liu[1], Hai-Feng Zhang[1, 2], Xiang-Kun Kong[1],
Bo-Rui Bian[1], and Hai-Ming Li[1]

[1]College of Electronic and Information Engineering
Nanjing University of Aeronautics and Astronautics, Nanjing 210016, China
[2]Nanjing Artillery Academy, Nanjing 211132, China

Abstract— An novel graphene-based metamaterial with tunable electromagnetically induced transparency (EIT)-like transmission is numerically studied in this paper. The designed structure consists of a graphene layer composed of coupled cut-wire pairs printed on a substrate. The simulation confirms that an EIT-like transparency phenomenon occurs in the metamaterial owing to indirect coupling and the proposed structure can be used in terahertz frequency range. More importantly, the transparency windows for the structures with indirect coupling can be dynamically controlled over a broad frequency range by varying the Fermi energy levels of the graphene layer (through electrostatic gating). The proposed metamaterial structure offers an additional opportunity to design novel applications such as switching and modulators.

1. INTRODUCTION

Electromagnetically induced transparency (EIT) in atomic physics is a very important phenomenon, which is the result of a quantum destructive interference between two pathways induced by another field [1]. Recently, many interests of researchers have been focused on the mimic classical EIT phenomenon by using metamaterial [2, 3]. Transparency windows of most work mentioned above have been realized at a fixed frequency. It is essential to reconstruct the geometries or modify the substrates if the resonance is tuned to different working frequency, but it is difficult to achieve once the devices are fabricated. Obviously, how to obtain a tunable EIT has been the focus of the interest of the researchers recently.

Graphene, which is a two-dimensional layer of carbon atoms arranged in a honeycomb pattern, has become a hot material in researches since it was discovered in 2004 [4, 5]. Its conductivity can be controlled by changing the Fermi energy levels. In this work, the graphene was introduced into the EIT metamaterial with indirect coupling. Therefore, the transparency windows for the structures with indirect coupling can be dynamically controlled over a broad frequency range by varying the Fermi energy levels of the graphene layer (through electrostatic gating) [6–8]. It is very convenient to tune the properties of the EIT comparing with other works. And the EIT-like phenomenon can be observed in terahertz frequency. The proposed graphene-based tunable EIT has some important potential practical applications.

2. THEORETICAL MODEL

The unit cell of the graphene-based EIT metamaterial we propose is plotted in Figure 1. The resonator is printed on a dielectric substrate. The graphene layer and the substrate are illustrated in grey and green, respectively. Two kinds of cut-wire resonators with different resonant frequencies are placed with a gap of g_2. The resonant frequencies of different cut-wire resonators are determined by the length of each graphene wire s_1, and the gap of g_1 in the cut-wire. The difference of the two resonant frequencies will be determined by the difference between w_1 and w_2. The thicknesses of graphene and substrate are d_1 and d_2. The array periodicities in both x and y directions are l. The relative permittivity of the substrate is defined as ε_d. The wave vector $\mathbf{K}(\omega)$ for incident wave is perpendicular to the xz plane.

The surface conductivity σ of graphene is the sum of the intraband σ_{intra} and the interband term σ_{inter}. Therefore, the surface conductivity of a graphene sheet $\sigma = \sigma_{intra} + \sigma_{inter}$ can be written as [9, 10]

$$\sigma(\omega) = i\frac{e^2 k_B T}{\pi \hbar^2 (\omega + i\Gamma)} \left(\frac{E_F}{k_B T} + 2\ln\left(e^{-\frac{E_F}{k_B T}} + 1\right) \right) + i\frac{e^2}{4\pi \hbar^2} \ln\left(\frac{2E_F - (\omega + i\Gamma)\hbar}{2E_F + (\omega + i\Gamma)\hbar}\right) \quad (1)$$
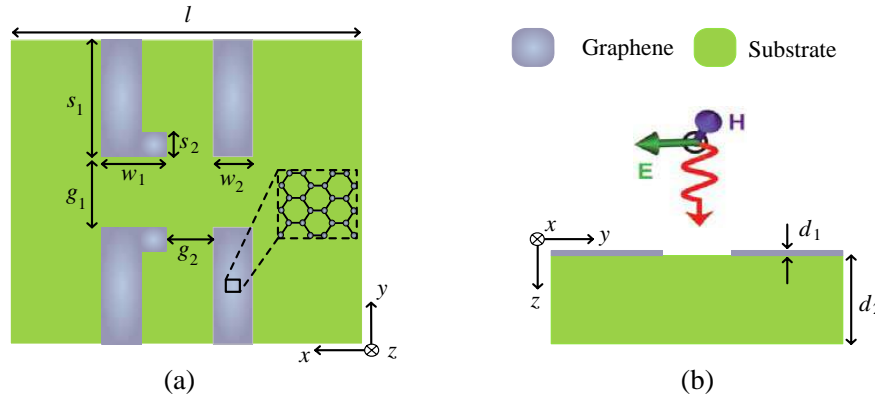
Figure 1: (a) Top view of the unit cell with dimensions. (b) Cross section view and the normally incident excitation.

where e is the charge of the electron, k_B is the Boltzmann constant, T is the temperature in K, $\hbar = h/2\pi$ is the reduced Planck constant, $\Gamma = 1/\tau$ is the carrier scattering rate with τ being the carrier relaxation time, E_F is the Fermi energy in graphene.

We assume that the electronic band structure of the graphene sheet is not affected by the neighboring, so the permittivity of graphene for different Fermi energy values can be obtained by [9, 10]

$$\varepsilon(\omega) = 1 + i\frac{\sigma}{d\omega\varepsilon_0} \qquad (2)$$

where d is the thickness of graphene sheet, and ε_0 is the permittivity in the vacuum.

3. NUMERIAL RESULTS AND DISSUSSION

In this section, we investigate the transmission property of graphene-based EIT metamaterial. We choose the geometrical parameters as follows: square lattice with period $l = 160$ nm, $s_1 = 70$ nm, $s_2 = 10$ nm, $w_1 = 50$ nm, $w_1 = 40$ nm, $g_1 = 20$ nm, $g_2 = 30$ nm. The thicknesses of graphene and substrate are $d_1 = 1$ nm and $d_2 = 20$ nm, respectively. The carrier scattering rate is taken to be $\Gamma = 2.4$ THz. The relative permittivity of the substrate is set to $\varepsilon_d = 3.3$. We can define the Fermi energy as $E_F = 0.6$ ev.

Figure 2 shows the transmission spectra of two different cut-wires serving as the bright modes under the electromagnetic field excitation. The curve in Figure 2(a) (Figure 2(b)) represents the transmission spectrum of the metamaterial composed of one kind of cut-wires shown in the left-hand side (the right-hand side) of Figure 1. The cut-wire in the left-hand side (the right-hand side) exhibits visible transmission dip at 10.98 THz (11.85 THz) owing to the electric resonance. As shown in Figure 3, when the two different kinds of cut-wires are placed along the electric field direction, an EIT-like narrow transmission window with transmission peak located between two dips is observed in the simulate transmission. The transmission peak at 11.13 THz exceeds 83% (-1.6 dB) and two transmission dips are located at 10.57 THz and 11.78 THz. Because the excited
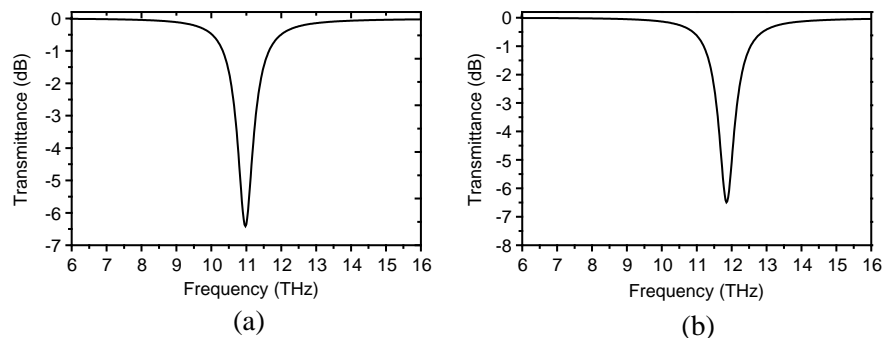

Figure 2: Transmission coefficient for (a) the cut-wire in the left-hand side and (b) the cut-wire in the right-hand side.
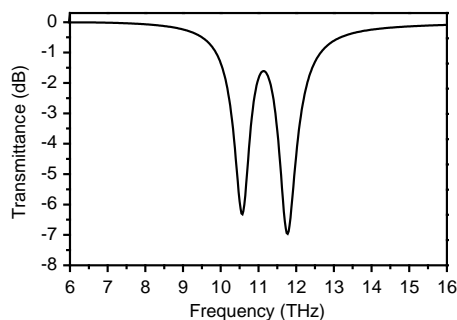
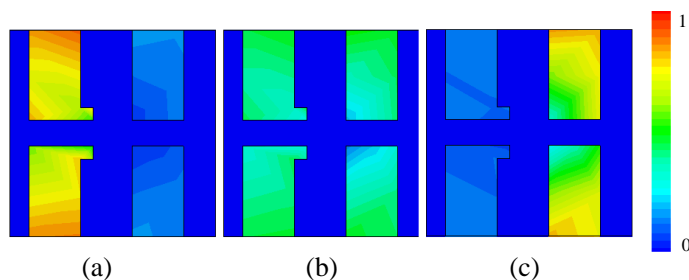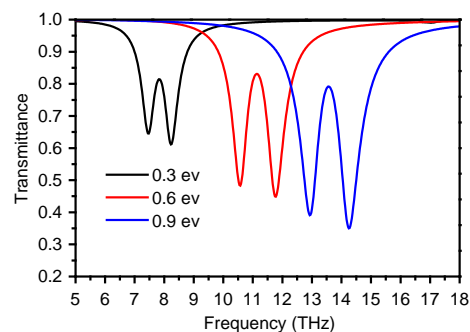Figure 3: Transmission spectra of the metamaterial EIT.

Figure 4: Current density distributions on the unit cell computed at frequencies: (a) 10.57 THz, (b) 10.98 THz, (c) 11.78 THz. The color scale is normalized between 0 and 1.

Figure 5: Transmission spectra of the metamaterial EIT for various of E_F.

two cut-wires are very weakly hybridized, the two resonance modes (10.57 THz and 11.78 THz) are close to their initial frequencies (10.98 THz and 11.85 THz) as shown in Figure 2.

To better understand the physical meaning of the EIT-like transparency phenomenon, the current density at two transmission dips and transmission peak are calculated which is shown in Figure 4. When frequency is 10.57 THz, only the left cut-wire is excited strongly by incident light, and the right cut-wire is excited very weakly, as shown in Figure 4(a). On the contrary, only the right cut-wire is excited by incident light strongly, and the left cut-wire is excited very weakly when frequency is 11.78 THz, as shown in Figure 4(c). Both cut-wires are excited simultaneously at 10.98 THz owing to the resonance detuning which is the characteristic of electromagnetically-trapped mode, as shown in Figure 4(b).

As mentioned above, the most important advantage of the proposed structure is the tuneability of the graphene, which can be tuned by chemical doping and electrostatic gating. The transmission properties of the proposed metamaterial structure can be tuned by applying different bias voltages. Therefore designed structure can work at different frequencies without modifying the parameter of the physical structure. This is very important and practical in the many practical applications comparing with metal-based metamaterial structure. Because it is very difficult to change the parameter of the physical structure if the structure is fabricated. As shown in Figure 5, It is obviously that the EIT-like narrow transparency window can be shifted over a broad range by merely varying the Femi energy in the investigated frequency regime. As the Femi energy is increased from 0.3 ev to 0.9 ev, the peak frequency of the transmission window can be tuned from 7.83 THz to 13.58 THz. Due to the tuneability of transparency windows, there are many important applications such as switches or modulators in the terahertz frequency band. For example, the transmission is about 35% at 14.3 THz if the Femi energy is 0.9 ev, while the transmission at 14.3 THz is tuned to be 97.6% when deceasing Femi energy to 0.6 ev. Therefore, the transmission could be switched between 35% and 97.6% by simply changing the Femi energy. As a consequence, a transmission magnitude modulation depth of 62.6% could be achieved by changing the Femi energy from 0.9 ev to 0.6 ev.

4. CONCLUSION

In summary, a tunable EIT-Like transmission in graphene-based metamaterial with indirect coupling is proposed. The coupling induced indirectly by the incident electromagnetic wave results in an EIT-like narrow transparency window in terahertz frequency range. Due to the tuneability of the graphene, when the Femi energy is changed through electrostatic gating, the EIT-like narrow transparency window can be shifted over a broad range. Increasing Femi energy red-shifts the peak frequency of the transmission window. Therefore, the proposed structure can work at different frequencies without reconstructing the physical structure. These properties could be applied in many important applications, such as switches or modulators in the terahertz frequency band.

ACKNOWLEDGMENT

REFERENCES

1. Boller, K. J., A. Imamolu, and S. E. Harris, "Observation of electromagnetically induced transparency," *Physical Review Letters*, Vol. 66, No. 20, 2593, 1991.
2. He, X. J., L. Wang, J. M. Wang, X. H. Tian, J. X. Jiang, and Z. X. Geng, "Electromagnetically induced transparency in planar complementary metamaterial for refractive index sensing applications," *Journal of Physics D: Applied Physics*, Vol. 46, No. 36, 365302, 2013.
3. Xu, H., Y. Lu, Y. Lee, and B. S. Ham, "Studies of electromagnetically induced transparency in metamaterials," *Optics Express*, Vol. 18, No. 17, 17736–17747, 2010.
4. Zhu, W., I. D. Rukhlenko, and M. Premaratne, "Graphene metamaterial for optical reflection modulation," *Applied Physics Letters*, Vol. 102, No. 24, 241914, 2013.
5. Yao, Y., M. A. Kats, P. Genevet, N. Yu, Y. Song, J. Kong, and F. Capasso, "Broad electrical tuning of graphene-loaded plasmonic antennas," *Nano Letters*, Vol. 13, No. 3, 1257–1264, 2013.
6. Vasić, B., G. Isić, and R. Gajić, "Localized surface plasmon resonances in graphene ribbon arrays for sensing of dielectric environment at infrared frequencies," *Journal of Applied Physics*, Vol. 113, No. 1, 013110, 2013.
7. Cheng, H., S. Chen, P. Yu, J. Li, B. Xie, Z. Li, and J. Tian, "Dynamically tunable broadband mid-infrared cross polarization converter based on graphene metamaterial," *Applied Physics Letters*, Vol. 103, No. 22, 223102, 2013.
8. Fallahi, A. and J. Perruisseau-Carrier, "Manipulation of giant faraday rotation in graphene metasurfaces," *Applied Physics Letters*, Vol. 101, No. 23, 231605, 2012.
9. Andryieuski, A. and A. V. Lavrinenko, "Graphene metamaterials based tunable terahertz absorber: Effective surface conductivity approach," *Optics Express*, Vol. 21, No. 7, 9144–9155, 2013.
10. Ning, R., S. Liu, H. Zhang, B. Bian, and X. Kong, "A wide-angle broadband absorber in graphene-based hyperbolic metamaterials," *The European Physical Journal Applied Physics*, Vol. 68, No. 2, 20401, 2014.

Reversal of Microwave Propagation Nonreciprocity in Metastructures by Voltage Application under Ferromagnetic Resonance Excitation near Resonance of Dipole or Chiral Elements

G. A. Kraftmakher, **V. S. Butylkin**, **and Yu. N. Kazantsev**

Kotelnikov Institute of Radioengineering & Electronics, RAS, Russia

Abstract— Ferrite plate/varactor-loaded conductive resonance elements (chains or single element) metastructures are investigated experimentally in waveguide to achieving voltage controlled inversion of sign of the nonreciprocity δ of microwave propagation. Dipoles of various shapes (butterfly, loop, snake, double split rings) with different type-varactors have been investigated. The metastructures show unique magnetically and electrically controlled nonreciprocal effects under coupled ferromagnetic resonance (FMR) in ferrite and resonance in dipoles (DR). Inversion of sign of δ occurs by the application of a bias voltage to a varactor when resonance frequency of DR passes through the FMR frequency as a result of which reversal of sense of rotating elliptically polarized h-field takes place. Usually inversion of nonreciprocal propagation of microwaves in ferrite is implemented by reversal of magnetization direction as a result of which reversal of sense of spins precession occurs.

1. INTRODUCTION

In recent years, there has been increasing interest in the study of resonance metamaterials on basis of resonant conductive elements [1, 2] as well nonreciprocal metamaterials, containing combination of ferrite and resonance elements, with tunable or switchable characteristics for development of microwave devices such as filters, nonreciprocal isolators and circulators. The emphasis is novel functionality as the fast electric control of amplitude-frequency characteristics in comparison with traditional [3] magnetic control of ferrite by external static magnetic field. In the case of magnetic control time switching is not so fast because one depends on not fast enough complex processes of magnetization and remagnetization. At the present time varactor-loaded split ring are used for electrically tunable filters at microwave frequencies [4] and for tunable nonlinear phenomena [5]. Besides, electric field tunable ferromagnetic resonance (FMR) response is investigated in ferromagnetic-ferroelectric heterostructures through the voltage controlled dielectric permittivity of the ferroelectric layer [6, 7]. Many publications are devoted to fundamental science of multiferroics, materials that simultaneously show ferromagnetism and ferroelectricity and can be controlled by both magnetic and electric field [8]. Nonreciprocity in periodic strip arrays on ferrite-dielectric substrate is discussed and calculated in [9]. At present there are ideas about artificial Faraday rotation in magnetless metamaterials without gyrotropic component [10], but strong losses complicate verification and real application.

We suggest another way by using metastructures containing ferrite plate and grating or chains of conductive resonant elements. The metastructures can show unique resonant nonreciprocal effects in the case when the FMR in ferrite is excited in the neighborhood of resonance of conductive elements [11–15]. It has been observed appearance of nonreciprocity and giant nonreciprocal FMR while there is not nonreciprocity when ferrite is placed without grating.

Recently, it has been observed that planar metastructure, formed by a transversely magnetized ferrite plate and conductive twice-split ring loaded with two varactors, can provide electrically tunable frequency bands of nonreciprocal resonant response and wide tuning range by the application of a bias voltage V_{DC} to a varactor [16, 17]. Dipoles of various shapes (butterfly, loop, snake) with different type-varactors have been investigated; the best frequency change has been reached with butterfly shape and varactor MA46H120 [18].

2. MEASUREMENTS METHODS, EXPERIMENTAL RESULTS

In this paper we demonstrate a way to achieving voltage controlled sign reversal of the nonreciprocity δ in the presence of a static magnetic field H without reversal of the magnetization direction in contrast to traditional magnetic switching magnetization direction.

A governing phenomenon of nonreciprocal microwave devices under consideration is ferromagnetic resonance. In this case circular or elliptical polarization of microwave magnetic field is necessary. Waveguide nonreciprocal devices contain transversely magnetized ferrite plate at distance of $\pm\lambda/8$ from the side wall in a rectangular waveguide, where polarization of microwave magnetic field is circular. In the case of metastructures necessary h-field is formed by the grating of resonant elements.

When a static magnetic field H, required for the FMR excitation, is applied and senses of the spins precession around H and rotating microwave magnetic field h are the same, power of the wave is absorbed by a ferrite. In the case when senses of precession and h-field rotation are opposite, absorption is absent. Senses of the h-field rotating are opposite for forward and counter-propagating waves. Senses of the spins precession are opposite for opposite directions of magnetization.

The nonreciprocity $\delta(\text{dB})$ of microwave propagation is characterized as difference between transmission coefficients for two situations. In the first situation senses of spin precession and rotating h-field are the same. In the second situation senses of spin precession and rotating h-field are opposite. The nonreciprocity δ of microwave propagation can be defined as difference between transmission coefficients for propagating modes in the opposite directions without reversal of magnetization direction, when senses of h-field rotation are opposite but senses of spin precession are the same, nonreciprocity $\delta(\text{dB}) = |S_{21}|^2 - |S_{12}|^2$. The nonreciprocity δ can be also defined without reversal of the propagation direction (single-channel measurements). In this case nonreciprocity δ (dB) is defined as the difference between transmission coefficients $T = |S_{21}|^2$ corresponding to the opposite direction of magnetization, when senses of h-field rotation are the same but senses of spin precession are opposite, $\delta(\text{dB}) = T(H_-) - T(H_+)$. $\mathbf{H}_+$ and $\mathbf{H}_-$ correspond to opposite directions of the external transverse static magnetic field H and provide opposite senses of spins precession.

Below the suggested method for reversing the sign of the nonreciprocity is confirmed by direct experimental proofs on a ferrite plate/varactor-loaded split Butterfly dipole metastructure placed along 48×24-mm rectangular waveguide axis. The metastructure under study is shown in Fig. 1. It involves a plate of iron-yttrium garnet $3Y_2O_3{\cdot}5Fe_2O_3$, near which a split Butterfly dipole, made of copper foil on polyimide film, is placed on 0.5-mm-thick hardened paper substrate at distance s. One MA46H120 (MAKOM) varactor, with a capacitance variable from 1 to 0.15 pF by supplying back bias voltage V_{DC} from 0 to 30 V, is welded into the gap in the dipole with width τ. The sizes of the dipole are chosen so that the resonance response will be observed in the given range 3–6 GHz of the voltage standing wave ratio (VSWR) panoramic measurer. Resistors with $R_L = 100\,\text{k}\Omega$ are connected to the wires from the feed source in order to eliminate possible excitation of parasitic resonances. We use single-channel method.

The metastructure shows two resonance minima of T. The first resonance minimum is due to the dipole resonance (DR). The DR is excited by microwave electric field without static magnetic field and can be tuned by application of a bias voltage V_{DC} to a varactor. In Fig. 2(a) we see that under $V_{DC} = 0\,\text{V}$ and $H = 0$ resonance response of metastructure (DR$_{0,0}$) is observed at 3.6 GHz and shifts to 4.85 GHz with V_{DC} increase to 20 V (DR$_{0,20}$). The second resonance effect is due to the FMR in ferrite, it is excited in the presence of H-field and controlled by the H-field magnitude. In the case when the FMR approaches to the DR, metastructure acquires nonreciprocal properties which can be controlled by both bias voltage V_{DC} and static magnetic field H in dependence on distance between ferrite plate and dipole. At the same time, it is observed dependence of nonreciprocity sign on the FMR-position relatively to the DR frequency. When position "FMR below DR" changes to "FMR above DR", reversal of sense of rotation of elliptically polarized h-field occurs and sign reversal of the nonreciprocity is observed. One can reverse the nonreciprocity sign by the FMR or DR positional control. To observe this effect in the given frequency range 3–6 GHz of panoramic measurer we correlate the DR frequency by application of a bias voltage V_{DC} to a varactor, the FMR frequency is correlated by application of necessary static magnetic field H (Figs. 2(b), 2(c)). Figs. 2(b), 2(c) shows measured transmission coefficients T in metastructure under different position of the FMR relatively to the DR. Dot curves correspond to the DR in the H-field absence.

Figure 2(b) shows frequency dependences of $T(H_-)$ and $T(H_+)$ at $V_{DC} = 0\,\text{V}$. In this case at $H = 0\,\text{Oe}$, we see only the DR$_{0,0}$ (dot curve) at 3.6 GHz. With application of static magnetic field $H = 850\,\text{Oe}$, the FMR is excited at about 4.25 GHz and the DR$_{0,0}$ shifts towards 3.2 GHz. Both the FMR and the DR frequency domains possess nonreciprocal properties with opposite signs of the nonreciprocity: transmission coefficients $T(H_-)$ and $T(H_+)$ are not the same. One can see that in the FMR frequency domain, the sign of δ is positive. In this case the FMR is excited above the

DR.

Figure 2(c) shows frequency dependences of $T(H_-)$ and $T(H_+)$ at $V_{DC} = 20$ V. In this case the $DR_{0,20}$ is observed at 4.77 GHz. With application of field $H = 600$ Oe the FMR is excited below the DR at about 3.55 GHz. The sign of δ is getting negative in contrast to Fig. 2(b) ("FMR above DR"). So, nonreciprocity sign depends on the FMR position relatively to the DR.
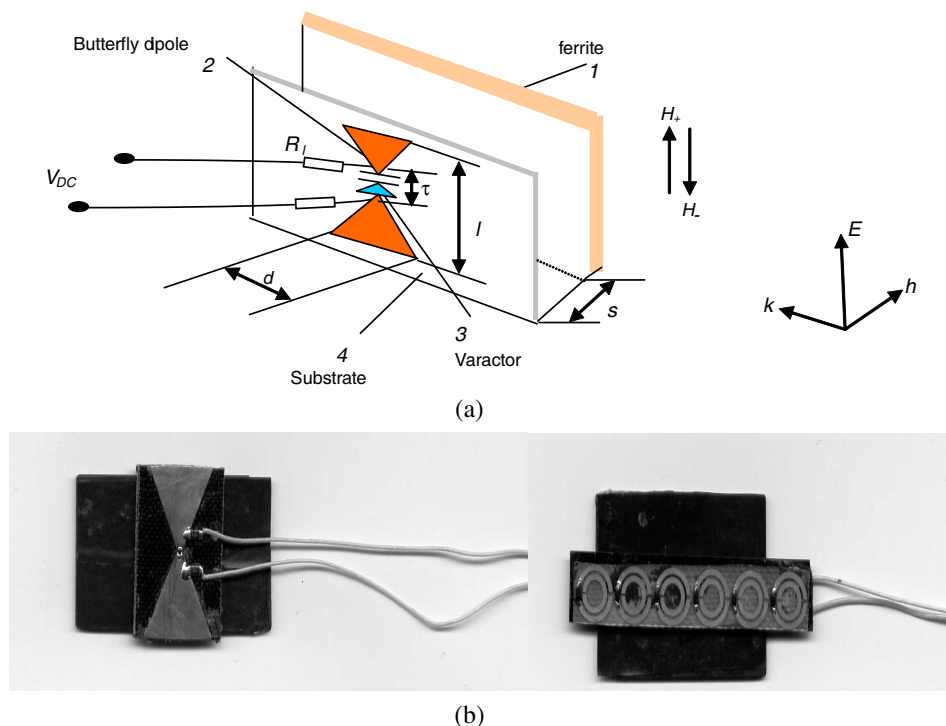

(a)

(b)

Figure 1: (a) Planar metastructure containing ferrite plate 1 ($30 \times 20 \times 1.9$ mm) of iron-yttrium garnet $3Y_2O_3 \cdot 5Fe_2O_3$ and varactor 3-loaded copper split Butterfly dipole 2; hardened paper substrate 4, resistors $R_L = 100$ kΩ, $l = 22$ mm, $\tau = 1.5$ mm, $d = 10$ mm. $s = 6.5$ mm. Area between ferrite 1 and substrate 4 has been filled with foam and (b) Photos of ferrite plate/varactor loaded split Butterfly dipole and ferrite plate/varactor loaded double split rings metastructures.
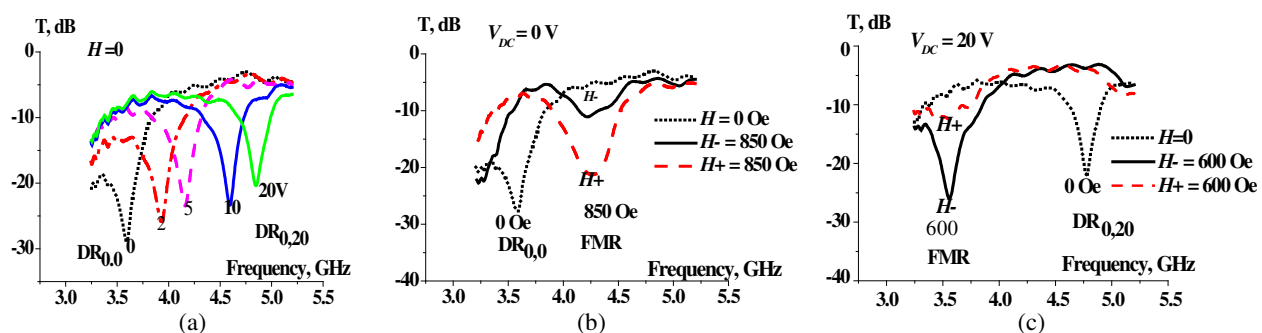

Figure 2: Measured frequency dependences of transmission coefficients T in metastructure; (a) dipole resonance (DR_0) excited by microwave electric field in the absence of external static magnetic field H at different bias voltages V_{DC}; (b) DR below the FMR at $V_{DC} = 0$ and $H = 850$ Oe; (c) DR above the FMR at $V_{DC} = 20$, and $H = 600$ Oe;.

One can observe sign reversal of δ by only electrical tuning the DR position, if the resonance frequency of a dipole passes through the FMR frequency, as shown in Figs. 3(a), 3(b). Fig. 3(a) presents the frequency dependences of nonreciprocity δ in metastructure ferrite plate/varactor loaded split Butterfly dipole under $H = 800$ Oe. In this case the FMR is excited slightly above the DR at the bias voltage $V_{DC} = 0$ and δ sign is positive at frequency domain around 4 GHz. With applying $V_{DC} = 29$ V, when the DR passes through the FMR to position "the FMR below the DR", sign of δ is getting negative. At that the FMR position remains practically unchanged.
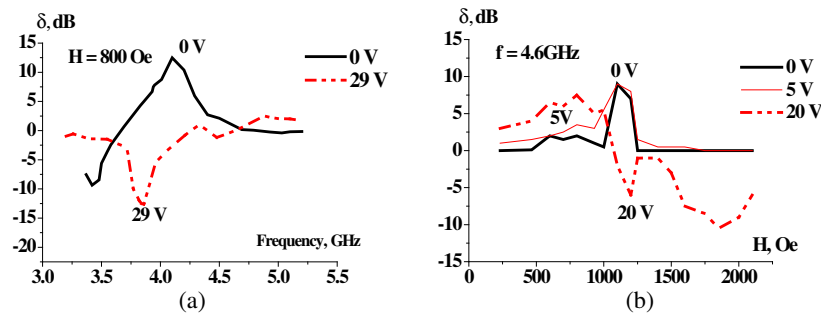
Figure 3: (a) Dependences of nonreciprocity δ, dB $= T(H_-) - T(H_+)$ on frequency in metastructure ferrite plate/varactor loaded split Butterfly dipole under $H = 800$ Oe at bias voltage $V_{DC} = 0$ (sign of δ is positive) and $V_{DC} = 29$ V (sign of δ is negative). (b) Dependences of δ on H-field value in metastructure ferrite plate/ chains of varactor loaded double split rings under $f = 4.6$ GHz at bias voltage $V_{DC} = 0, 5, 20$ V.

Fig. 3(b) demonstrates sign reversal of δ in dependence on H-field value in ferrite plate/varactor loaded double split rings metastructure under fixed frequency 4.6 GHz at different bias voltages V_{DC}. One can see that at certain values of H-field positive δ at $V_{DC} = 0$ is getting negative at $V_{DC} = 20$ V.

3. CONCLUSION

Observed nonreciprocal effects are due to the FMR, to influence of the DR as well to features of microwave magnetic field h in metastructure. Reversing the sign of the nonreciprocity δ occurs by the application of a bias voltage to a varactor when frequency of the DR passes through the FMR frequency. In this case position "DR below FMR" changes to "DR above FMR" and at the FMR-domain left-handed h-field is transformed into right-handed but sense of spin precession is not changed because direction of H-field is not reversed. Usually reversing sign of the nonreciprocity in ferrite is achieved by not so fast reversal of magnetization direction, as a result of which reversal of sense of spins precession occurs.

Thus, the metastructures ferrite plate/varactor-loaded resonant elements provide fast electrically controlled reversing sign of the nonreciprocity of microwave propagation and open up wide prospects for applications in the field of fast switchable nonreciprocal devices.

REFERENCES

1. Zheludev, N. I. and Yu. S. Kivshar, "From metamaterials to mtadevices," *Nature materials*, Vol. 11, No. 11, 917–924, 2012.
2. Thomas, H. H. and S. A. Cummer, "Controllable magnetic metamaterial using digitally addressable split-ring resonators," *IEEE Antennas and Wireless Propagation Lett.*, Vol. 8, 262–265, 2009.
3. Lax, B. and K. J. Button, *Microwave Ferrites and Ferromagnetics*, McGraw-Hill, New York, 1962.
4. Gil, I., J. Garcia-Garcia, J. Bonache, F. Martin, M. Sorolla, and R. Marques, "Varactor-loaded split ring resonators for tunable notch filters at microwave frequencies," *Electronics Letters*, Vol. 40, No. 21, 1347–1348, 2004.
5. Kapitanova, P. V., A. P. Slobozhnanyuk, I. V. Shadrivov, P. A. Belov, and Y. S. Kivshar, "Competing nonlinerities with metamaterials," *Appl. Phys. Letters*, Vol. 101, No. 23, 231904, 2012.
6. Ustinov, A. B. and G. Srinivasan, "Subterahertz excitations and magnetoelectric effects in hexaferrite-piezoelectric bilayers," *Appl. Phys. Letters*, Vol. 93, No. 14, 142503, 2008.
7. Song, Y.-Y., J. Das, P. Krivosik, N. Mo, and C. E. Patton, "Electric field tunable 60 GHz ferromagnetic resonance response in barium ferrite-barium strontium titanate multiferroic heterostructures," *Appl. Phys. Letters*, Vol. 94, No. 18, 182505, 2009.
8. Pyatakov, A. P. and A. K. Zvezdin, "Magnetoelectric and multiferroic media," *Physics $\pm$ Uspekhi*, Vol. 55, No. 6, 557–581, 2012.
9. Cochet, G., A. Vallecchi, A. G. Schuchinsky, and P. Queffelec, "Entwined spiralarrays on ferrite substrate," *6 Int. Congress on Advanced Electromagnetic Materials in Microwaves and Optics*, 215–217, Sankt-Peterburg, Russia, Sept. 17–20, 2012.

10. Kodera, T., D. L. Sounas, and C. Caloz, "Artificial Faraday rotation using a ring metamaterial structure without static magnetic field," *Appl. Phys. Letters*, Vol. 99, No. 3, 031114, 2011.
11. Butylkin, V. S. and G. A. Kraftmakher, "Giant nonreciprocal effect under conditions of mutual influence of ferromagnetic and chiral resonance," *Tech. Phys. Letters.*, Vol. 32, No. 9, 775–778, 2006.
12. Butylkin, V. S. and G. A. Kraftmakher, "Nonreciprocal microwave transmission in metastructures with transversely magnetized ferrite plate and a grating of resonant elements," *Tech. Phys. Letters.*, Vol. 33, No. 10, 856–860, 2007.
13. Butylkin, V. S. and G. A. Kraftmakher, "Nonreciprocal transmission spectrum of a ferrite plate — Resonant element grating metasandwich with split resonance," *Tech. Phys. Letters*, Vol. 35, No. 5, 397–400, 2009.
14. Kraftmakher, G. A. and V. S. Butylkin, "Nonreciprocal amplitude-frequency resonant response of metasandwiches 'ferrite plate-grating of resonant elements'," *Eur. Phys. J. Appl. Phys.* Vol. 49, 33004, 2010.
15. Butylkin, V. S., G. A. Kraftmakher, and V. P. Mal'tsev, "The nonreciprocity of microwave transmission along a bianisotropic-ferrite metastructure," *J. Commun. Technol. Electron.*, Vol. 58, No. 6, 543–550, 2013.
16. Kraftmakher, G. A., V. S. Butylkin, and Yu. N. Kazantsev, "Electrically controlled frequency bands of nonreciprocal passage of microwaves in metastructures," *Tech. Phys. Letters*, Vol. 39, No. 6, 505–508, 2013.
17. Kraftmakher, G. A., V. S. Butylkin, and Yu. N. Kazantsev, "Electrically tunable nonreciprocity of microwave transmission through 'ferrite-varactor loaded resonant element' planar metastructure," *Phys. Status Solidi C*, Vol. 11, Nos. 5–6, 1033–1038, 2014.
18. Kazantsev, Yu. N., G. A. Kraftmakher, and V. P. Mal'tsev, "Methods for resonance frequency tuning ranges of frequency-selective surfaces using varactors," *J. Commun. Technol. Electron.*, Vol. 58, No. 9, 933–939, 2013.

Millimeter-wave Metamaterial Antenna in Standard CMOS Technology

Kazuki Hiraishi, **Takehiro Kawauchi**, and **Eiichi Sano**

Research Center for Integrated Quantum Electronics, Hokkaido University, Japan

Abstract— A metamaterial-based antenna, such as a composite right/left-handed(CRLH) antenna, has reduced size, which results in reduced loss in the metal wire in the antenna. In this study, a CRLH monopole antenna was designed and fabricated in 0.18 μm CMOS with six metal layers. The CRLH unit cell was 300×420 μm. Two unit cells were used to construct the monopole antenna. The designed CRLH monopole antenna had LH and RH radiation modes at 41 and 65 GHz, respectively. The measured gains of the CRLH monopole antenna were -5.8 dBi in RH mode and -14.4 dBi in LH mode.

1. INTRODUCTION

The crowded bands of 2.4 and 5 GHz will push the operation bands of wireless communication systems to the millimeter (MM)-wave region (e.g., 60 GHz). Reduced sizes of antennas in the MM-wave region enable them to be monolithically integrated with CMOS RF and baseband circuits. Furthermore, on-chip antennas in standard CMOS processes can contribute to reducing costs. However, the length of a standard half-wavelength dipole antenna operating at 60 GHz is about 2.5 mm and low-resistivity ($\sim 10\,\Omega$-cm) Si substrates commonly used in standard CMOS technology degrade the antenna gain. The antenna gain at 60 GHz remains below -10 dBi in standard CMOS technology [1]. Thus, an ingenious development is needed to increase the gains of antennas fabricated on low-resistivity Si substrates.

In order to solve the problems of on-chip antennas, we focused on metamaterials. Metamaterials are artificial materials that show electromagnetic properties not generally found in nature. Since Pendry's claim that materials with a negative refractive index can act as perfect lenses [2], metamaterials have received an enormous amount of attention and interest from both scientific and industrial communities. In this paper, we propose a composite right/left-handed (CRLH) antenna in standard CMOS technology. While the radiation frequency of a standard dipole antenna is determined by the antenna size the radiation frequency of a CRLH antenna can be controlled by changing element values, which reduces the antenna size. A 2.4-GHz CRLH dipole antenna reached a theoretical (Harrington) limit for a gain versus size relationship [3, 4]. The reduced size can alleviate the influence of the Si substrate and increase the antenna gain.

2. ANTENNA DESIGN

The unit cell in a periodic CRLH transmission line (TL) is shown in Figure 1.
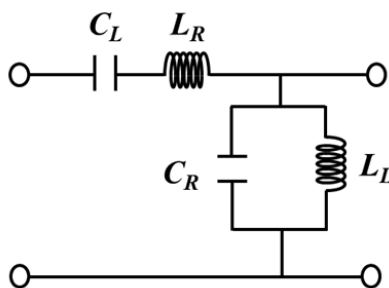

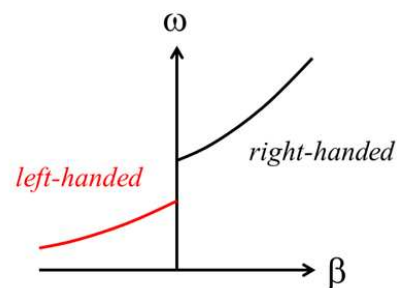Figure 1: Unit cell of CRLH TL.

Figure 2: Dispersion diagram of CRLH TL.

Shunt inductors L_L and series capacitors C_L as lefthanded elements are inserted in the right-handed transmission line. Applying the periodic boundary condition, the dispersion characteristics for the CRLH TL are described by

$$\beta p = \cos^{-1}\left[1 - \frac{1}{2}\left(\omega L_R - \frac{1}{\omega C_L}\right)\left(\omega C_R - \frac{1}{\omega L_L}\right)\right], \qquad (1)$$

where β is the phase constant and p is the length of a unit cell. A schematic dispersion diagram of the CRLH TL is shown in Figure 2.

The structure of a metamaterial dipole antenna composed of 4 CRLH cells is shown in Figure 3.
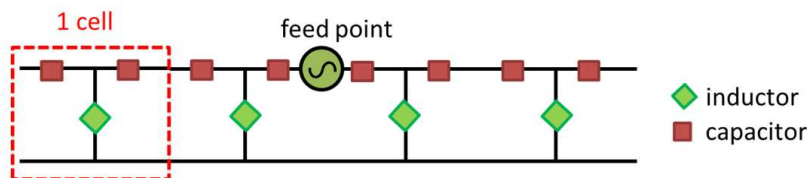

Figure 3: Structure of metamaterial antenna.

Since both ends of the lines are open, the amount of phase change between the two open ends must be π at the target frequency. This means that βp must equal $\pi/4$ in the 4-cell configuration. This structure was implemented on a printed circuit board (PCB) and a high gain of -0.01 dBi was achieved at 2.4 GHz [3, 4]. In this study, we tried to implement a CRLH monopole antenna by using this concept in $0.18\,\mu$m CMOS with six metal layers. The schematic unit cell of the proposed CRLH monopole antenna is shown in Figure 4. The thick top metal (metal6) was used as the antenna element to reduce the wire loss. Series capacitors C_L were composed of metal-insulator-metal(MIM) capacitors between metal 5 and metal 6. The parallel inductor L_L was implemented only by a straight line of metal6. The RH part of the CRLH monopole antenna was formed of a parallel line without a ground plane under the line to prevent a possible reduction in the antenna gain caused by the eddy current flowing in the ground plane.

Figure 4: Schematic (a) top and (b) cross sectional views of unit cell.

We designed a CRLH monopole antenna as follows. First, the dimensions of the RH line, C_L, and L_L were roughly determined for the antenna to operate at 60 GHz taking into account Eq. (1). The design method only using Eq. (1) is incorrect even if all the components are precisely evaluated. This is because L_L is not an ideal lumped element. Then, we analyzed the unit cell of the CRLH TL shown in Figure 5 using a finite-difference time-domain (FDTD) simulator (Keysight Tech. EMPro) to obtain a rigorous dispersion diagram. The feed points in the FDTD simulation were assumed to be ground-signal-ground (GSG) pads. Two ports are indicated by arrows in Figure 5. Finally, the whole antenna structure was evaluated by using the FDTD simulator. Figure 6 shows a die photograph of the fabricated antenna. The CRLH unit cell was $300 \times 420\,\mu$m.
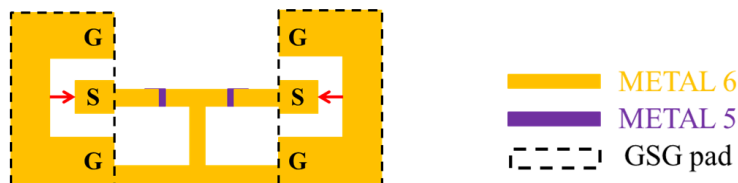

Figure 5: Analysis model for unit cell of CRLH TL.

3. MEASUREMENTS AND RESULTS

The fabricated CRLH monopole antenna on a chip was measured using a vector network analyzer (VNA) and a RF probe. A standard 1-port calibration method was used for the return loss
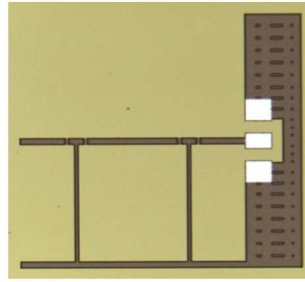
Figure 6: Die photograph of fabricated antenna.

measurement. The antenna gain was measured using the VNA and two types of horn antennas (20–40 GHz and 50–67 GHz ranges). Port 1 of the VNA was connected to one of the fabricated antennas, and port 2 of the VNA was connected to the horn antenna. The gain of the CRLH monopole antenna in each frequency range was evaluated by taking into account the transmission S_{21} between two horn antennas and the gain of the horn antenna. Figure 7(a) shows the measured and simulated return losses for the antenna. The designed impedance matching frequencies ($|S_{11}|$) of the LH and RH modes were about 28 GHz (-14.4 dB) and 62 GHz (-6.7 dB), respectively. The measured return loss was shifted about 3 to 6 GHz to a higher frequency compared with the simulated one. Figure 7(b) shows the measured and simulated antenna gains. The measured gains were -14.4 dBi at 39.3 GHz and -5.8 dBi at 66.7 GHz in LH mode and RH mode, respectively. Although the measured gain almost matched the designed gain, the measured gain was ~ 7 dB smaller than the simulation in the 50–67 GHz range. This might be caused by the different radiation pattern between the horn antenna and the fabricated antenna and/or the difference between fabricated silicon substrate resistivity and the value (10 Ω-cm)assumed in the simulations. Table 1 summarizes the performance comparison of on-chip antennas in CMOS technology. Our CRLH monopole antenna was the smallest, while the gain was almost the same as a slot antenna on an artificial magnetic conductor (AMC) plane [7].
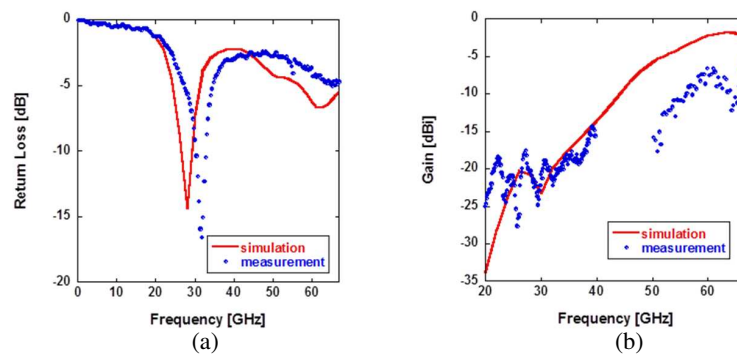

Figure 7: Measurement results of fabricated antenna.

Table 1: Performance comparison.

	Process	Gain	Size	Configuration
This work	180-nm CMOS	-5.8 dBi	600 μm × 420 μm	CRLH monopole
[5]	65-nm CMOS	-10 dBi	1000 μm × 300 μm	Dipole
[6]	180-nm CMOS	-10.6 dBi	1100 μm × 950 μm	Yagi
[7]	90-nm CMOS	-6.0 dBi	1300 μm × 1100 μm	Slot on AMC

4. CONCLUSION

On the basis of the composite right/left-handed transmission line theory, we designed and fabricated a millimeter-wave metamaterial antenna with standard CMOS technology to reduce antenna sizes. The measured return losses were -14.4 dB at 28 GHz and -6.7 dB at 62 GHz and antenna gains

were -14.4 dBi at 39.3 GHz and -5.8 dBi at 66.7 GHz in LH and RH modes, respectively. The fabricated antenna achieved a high gain and small size. Further increase in the gain can be achieved by optimizing the component values in the CRLH antenna.

ACKNOWLEDGMENT

REFERENCES

1. Chuang, H.-R., L.-K. Yeh, P.-C. Kuo, K.-H. Tsai, and H.-L. Yue, "A 60-GHz millimeter-wave CMOS integrated on-chip antenna and bandpass filter," *IEEE Trans. Electron Devices*, Vol. 58, No. 7, 1837–1845, 2011.
2. Pendry, J. B., "Negative refraction makes a perfect lens," *Phys. Rev. Lett.*, Vol. 85, No. 18, 3966–3969, 2000.
3. Takahagi, K., Y. Otsu, and E. Sano, "2.45 GHz high-gain electrically small antenna with composite right/left-handed ladder structure," *Electron. Lett.*, Vol. 48, No. 16, 971–972, 2012.
4. Hiraishi, K., T. Wada, Y. Otsu, M. Ikebe, and E. Sano, "Low-power, small-size transmitter module with metamaterial antenna," *Analog Integr. Circ. Sig. Process.*, Vol. 83, No. 1, 1–9, 2015.
5. Hirano, T., T. Yamaguchi, N. Li, K. Okada, J. Hirokawa, and M. Ando, "60 GHz on-chip dipole antenna with differential feed," *Proc. 2012 APMC*, 304–306, Dec. 4–7, 2012.
6. Hsu, S.-S., K.-C. Wei, C.-Y. Hsu, and H. R.-Chuang, "A 60-GHz millimeter-wave CPW-fed Yagi antenna fabricated by using 0.18-μm CMOS technology," *IEEE Electron Device Lett.*, Vol. 29, No. 6, 625–627, 2008.
7. Kang, K., F. Lin, D.-D. Pham, J. Brinkhoff, C.-H. Heng, Y. X. Guo, and X. Yuan, "A 60-GHz OOK receiver with an on-chip antenna in 90 nm CMOS," *IEEE J. Solid-State Circuits*, Vol. 45, No. 9, 1720–1730, 2010.

Enhanced Group Velocity Characteristics of a ENG Cladded Metamaterial Loaded Helical Guide

D. K. Sharma and S. K. Pathak

Microwave and ECE Diagnostic Division, Institute for Plasma Research, Gandhinagar, India

Abstract— In this paper, we propose an ENG Cladded Metamaterial Loaded Helical (CMLHG) waveguide structure, to achieve enhance slow wave in THz frequency spectrum. Both analytical as well as numerical computation has been done to explore the dispersion behavior of the structure. It is observed that the waveguide supports propagation of forward wave (FW) mode having parallel phase and group velocities over a wide bandwidth with an enhanced slow wave characteristic. A comparative study of slow wave behavior has been done between the ENG CMLHG waveguide and two other cases (i) when helix is in free space and (ii) when helix is cladded with DPS material and loaded with metamaterial. It is found that present structure supports slower wave as compared to those structures.

1. INTRODUCTION

There is a tremendous interest in slow down the velocity of wave. Dynamically controlled wave flow is vital for developing photonics devices. Specifically, the feature of slowing light is useful in order to regulate the data traffic at network nodes. Device like optical buffer is based on the mechanism of slow wave.

For achieving slow wave different methods are proposed such as coherent population oscillations, stimulated Brillouin scattering, quantum dot semiconductor optical amplifier etc.. Those are found unsuitable in incorporating on an optical integrated chip (IC). For rectifying this disability other methods are reported which uses dispersive behaviour of metamaterials and finds easy to accommodate on optical ICs.

Metamaterials are newly discovered composite material having negative permittivity and permeability value. It exhibits unusual characteristics such as negative refraction, backward wave, negative Goos-Hansen effect etc.. This artificial material was first investigated by Russian physicist Veslogas [1] and named this bizarre material to left-handed material. Due to presence of left-handed traied in between electric field (E), magnetic field (H) and propagation vector (k). These striking predictions were not widely accepted until their experimental verification 30 years later by Smith et al. [2]. They designed metamaterial through split ring resonators (SRR) and thin wire array.

Different research groups studied various waveguide structures which were loaded with metamaterial or itself made up of it. Metamaterial slab waveguide were studied by Bait et al. [3] and they observed that TM and TE mode propagate with slower phase velocity. Gennaro et al. [4] studied metamaterial experimentally and they found that group velocity is reduced in metamaterial medium. Savo et al. [5] studied slow wave experimentally at microwave frequency range through a planar waveguide consisting of a dielectric core cladded by single-negative metamaterial. Erfaninia et al. [6] studied multilayered metamaterial waveguide and reported reduction in group velocity as compared to conventional structures. In our recent work [7], we showed that wave velocity is greatly reduced in metamaterial loaded helical guide (MLHG) as compared to conventional cases (helix loaded with free-space and dielectric or DPS material). Helical guide is a well known slow wave structure which is widely used in travelling wave tube and travelling wave antenna etc..

In this work, we propose ENG CMLHG structure which consists of a helical guide having metamaterial core and ENG (epsilon material) cladding. For that structure, dispersion relation is derived analytically and computed numerically.

2. DISPERSION EQUATION

The structure of interest is shown in Fig. 1, here region-I (core) consists of metamaterial (permittivity and permeability ϵ_1 and μ_1 respectively) and region-II (cladding) is of ENG material (permittivity and permeability ϵ_2 and μ_2 respectively). Region outside to the cladding layer is region-III, free-space medium (permittivity ϵ_3 and μ_3 respectively).

The electric field components in different regions are:

$$E_{z,1} = -k_1^2 AI_n(k_1\rho)\, e^{jn\phi}e^{-j\beta z} \tag{1}$$

$$E_{\phi,1} = \left[\frac{n\beta}{\rho}AI_n(k_1\rho) + i\omega\mu_1 BI_n'(k_1\rho)\right]e^{jn\phi}e^{-j\beta z} \tag{2}$$

$$E_{z,2} = -k_2^2\left[CI_n(k_2\rho) + DK_n(k_2\rho)\right]e^{jn\phi} \tag{3}$$

$$E_{\phi,2} = \left[\frac{n\beta}{\rho}\left[CI_n(k_2\rho) + DK_n(k_2\rho)\right] + i\omega\mu_2\left[EI_n'(k_2\rho) + FK_n'(k_2\rho)\right]\right]e^{jn\phi}e^{-j\beta z} \tag{4}$$

$$E_{z,3} = -k_3^2 GI_n(k_3\rho)\, e^{jn\phi}e^{-j\beta z} \tag{5}$$

$$E_{\phi,1} = \left[\frac{n\beta}{\rho}GI_n(k_3\rho) + i\omega\mu_3 HI_n'(k_3\rho)\right]e^{jn\phi}e^{-j\beta z} \tag{6}$$

Here k_1, k_2 and k_3 are transverse wave vectors of different regions I, II and III respectively. For different regions I, II and III the i respectively is 1, 2 and 3. β is longitudinal propagation coefficient and related with propagation vector (k_{oi}) by wave equation $k_i = \sqrt{\beta^2 - k_{oi}^2}$. $I_n(k_i\rho)$ and $K_n(k_i\rho)$ are modified Bessel functions of first and second kind. Its derivative represent by ('). ρ is radial measure which defines core radial length by $\rho < a$, cladding by $a < \rho < b$ and region-III by $\rho > b$.

Obtained dispersion relation for HE-mode after applying boundary conditions on Equations (1) to (6) on different region interfaces:

$$V\alpha\gamma P(R - Q)(I - W) + V^2 P^2(\alpha - \gamma)^2 + V^2(\alpha T - \gamma S)(\gamma R - Q\alpha) + P^2(\gamma Y_c - j_c\alpha)$$
$$(\gamma I - \alpha W) + (\gamma Y_c R - Q j_c\alpha)(T\alpha W - s\gamma I) + VP\alpha\gamma(Y_c - j_c)(T - S) = 0 \tag{7}$$

Used coefficients in above equation are:

$$V = k_2^2 - \frac{n\beta}{a}\cot(\psi), \quad U = k_1^2 - \frac{n\beta}{a}\cot(\psi), \quad x = \omega\mu_1 k_1, \quad x_1 = \omega\epsilon_1 k_1,$$

$$y = \omega\mu_2 k_2, \quad y_1 = \omega\epsilon_2 k_2, \quad z = \omega\mu_3 k_3, \quad z_1 = \omega\epsilon_3 k_3, \quad r_1 = \frac{k_1}{k_2}, \quad r_2 = \frac{k_2}{k_3},$$

$$M = \frac{U^2 I_n(k_2 a)}{xr_1^2\cot(\psi)I_n'(k_2 a)}, \quad N = \frac{x_1\cot(\psi)I_n'(k_2 a)}{r_1^2 I_n(k_2 a)}, \quad j_c = \frac{y\cot(\psi)I_n'(k_2 a)}{I_n(k_2 a)},$$

$$Y_c = \frac{y\cot(\psi)K_n'(k_2 a)}{K_n(k_2 a)}, \quad W = M + N + \frac{y_1\cot(\psi)I_n'(k_2 a)}{I_n(k_2 a)}, \quad I = M + N + \frac{y_1\cot(\psi)K_n'(k_2 a)}{K_n(k_2 a)}, \tag{8}$$

$$P = \frac{n\beta}{b(1 - r_2^2)}, \quad R = \frac{yI_n'(k_2 b)}{I_n(k_2 b)} - \frac{zr_2^2 K_n'(k_2 b)}{K_n(k_2 b)}, \quad Q = \frac{yK_n'(k_2 b)}{K_n(k_2 b)} - \frac{zr_2^2 K_n'(k_3 b)}{K_n(k_3 b)},$$

$$S = \frac{y_1 I_n'(k_2 b)}{I_n(k_2 b)} - \frac{z_1 r_2^2 K_n'(k_3 b)}{K_n(k_3 b)}, \quad T = \frac{y_1 K_n'(k_2 b)}{K_n(k_2 b)} - \frac{z_1 r_2^2 K_n'(k_3 b)}{K_n(k_3 b)},$$

$$\alpha = I_n(k_2 a)k_n(k_2 b), \quad \gamma = I_n(k_2 b)k_n(k_2 a).$$

3. RESULT AND ANALYSIS

The Dispersion behaviour of structure is obtained by plotting longitudinal propagation coefficient (β) as function of frequency. For root finding we used Findroot method of Mathematica software package.

A comparative dispersion graph is presented in Fig. 1(b), for ENG CMLHG waveguide and two other cases: (i) when helix is in free space and (ii) when helix is cladded with DPS material and loaded with metamaterial. It is found that present structure provides almost 4 times lesser phase velocity in comparison to the helix in free space. It supports propagation of fundamental mode. Higher order modes are not observed in the guide so that most of the power is carried out by fundamental mode. Obtained slope of dispersion graph is positive that corresponds to forward wave (FW) mode which having parallel phase and group velocities.

A very large value of longitudinal propagation coefficient is observed in ENG clad MLHG structure that enhances slow wave behaviour of guide and achieved minimum normalized phase velocity
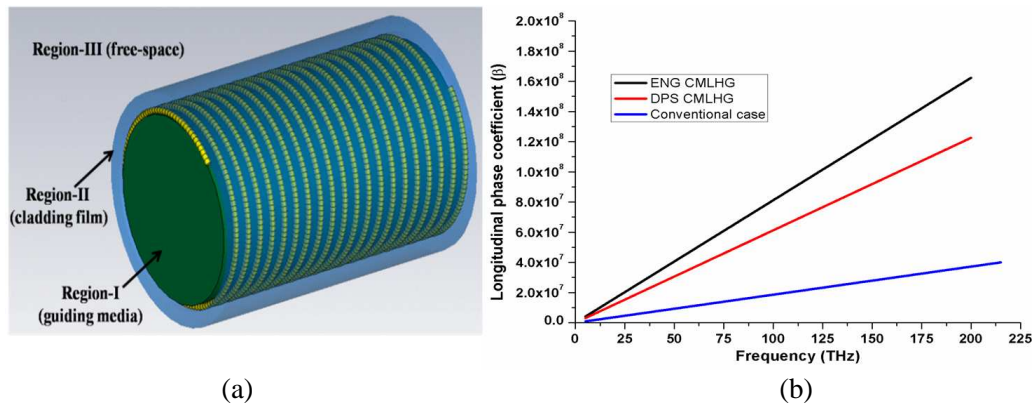
(a) (b)

Figure 1: Cladded metamaterial loaded helical guide (CMLHG) structure. Figure 1(b) Dispersion characteristic (vs frequency) is plotted for different cases (i) Conventional case, helical guide in free-space (ii) helix is cladded with DPS material and loaded with metamaterial and (iii) ENG CMLHG waveguide represents in blue, red and black colour respectively.

(v_p/c) is 0.0258. As compared to DPS clad MLHG structure reduction in slow wave behaviour is enhanced by 26.4%. In different simulations it observed that in ENG Clad MLHG structure the value of v_p/c is reached at 0.0011 by adjusting physical parameter of the guide such as radius and pitch angle and further it could reduced more.

Other advantages of ENG cladding is that it works as an insulator in order to avoid possible interaction between helix copper winding and other on-chip elements. It enhances slow wave characteristic and provides wider bandwidth as well.

4. CONCLUSION

In this work we propose cladded MLHG structure. From analytical computation it is observed that wave velocity is greatly reduced in ENG clad MLGH as compared to conventional cases. Other unique advantage of this structure is a wider bandwidth.

REFERENCES

1. Veselago, V. G., "The electrodynamics of substances with simultaneo-usly negative value of ϵ and μ," *Sov. Phys. Usp.*, Vol. 10, 509, 1968.
2. Shelby, R. A., D. R. Smith, and S. Schultz, "Experimental verification of a negative index of refraction," *Science*, Vol. 292, 77–79, 2001.
3. Bait-Suwailam, M. M. and Z. Chen, "Surface-wave along double-negative (DNG) slab waveguide," *Microwave and Optical Technology Letters*, Vol. 44, 494–498, 2003.
4. Gennaro, E. D., P. V. Parimi, W. T. Lu, and S. Sridhar, "Slow microwaves in left-handed materials," *Phy. Rev. B*, Vol. 72, 033110, 2005.
5. Savo, S., B. D. Casse, L. Wentao, and S. Sridhar, "Observation of slow-light in a metamaterials waveguide at microwave frequencies," *Applied Physics Letters*, Vol. 98, 171907, 2011.
6. Erfaninia, H. and A. Rostami, "Group velocity reduction in multilayer metamaterial waveguide," *Optik*, Vol. 124, No. 10, 1230–1233, 2013.
7. Sharma, D. K. and S. K. Pathak, "Ultra slow EM wave propagation characteristics of left-handed material loaded helical guide," *Progress In Electromagnetics Research M*, Vol. 35, 11–19, 2014.

Influence of Optical Fiber Dispersion on Mamyshev Type Regenerator Performance

Piyush Baypajee, Jurgis Porins, and Andis Supe

Institute of Telecommunications, Riga Technical University, Azenes st. 16/20, Riga, Latvia

Abstract— In this paper we present results from the study on optical signal regeneration by using Mamyshev type regenerator and its dependence on fiber dispersion. Research is performed using computer simulation software Synopsis OptSim 5.3. Setup of investigated regenerator consists of a high power erbium doped fiber amplifier, highly nonlinear fiber and an optical bandpass filter that is slightly shifted away from the signal central frequency. Signal used for regeneration was an on-off keying return-to-zero code manipulated 40 Gbit/s pulse sequence covered with white noise. The regenerator performance was evaluated by obtaining the regenerated optical signal bit error ratio for different optical filters and fiber dispersion coefficients.

1. OPTICAL SIGNAL REGENERATION

Increasing data rates in fiber optics transmission systems leads to a higher requirements to optical signal quality. This is because signal to noise ratio (SNR) requirements become more stringent for higher baud rate signals to ensure the same bit error ratio (BER) level as for lower baud rates. This statement comes from well-known Shannon's Theorem [1].

Optical signal degrades considerably during propagation in the telecommunications fiber line. It is caused by many factors: fiber attenuation, dispersion (group-velocity dispersion, material dispersion, waveguide and polarization mode dispersion) that broadens the pulses, accumulated amplified spontaneous emission that is a broadband noise source induced mostly by amplifiers and, of course, different nonlinear optical effects [2]. Distortions induced by optical fiber nonlinearity actually can be the most significant and the most difficult avoidable, especially in the high data rate multichannel transmission, used in dense wavelength division multiplexed systems.

Optical amplifiers compensate the fiber losses therefore the amplification may be considered as the first level regeneration of optical signal. But amplifiers also degrade the signal by adding ASE noise and timing jitter [3]. It is acceptable for a single stage amplification but becomes unacceptable for signal transmission over long distances with several amplification stages. Therefore there is a need for regenerators that also perform restoration of the signal shape or so called 2R regenerators (reamplifying and reshaping). Reshaping increases the SNR that in turn lowers the signal BER in such a way improving performance of transmission system.

Most commonly the regeneration of optical signals is performed in the electrical domain by performing opto-electrical conversion. Although this approach limits the maximum data transmission rate due to limitations in the electrical equipment operation speed. Therefore more perspective is the optical signal regeneration completely in the optical domain. Since it is based on some nonlinear optical effect exploitation it takes place without any significant delay because optical fiber nonlinear utterance is almost immediate [4]. From the 2R class very promising are the Mamyshev type regenerators (MTRs). The main advantage is a relatively simple design that consists of booster, highly non-linear fiber (HNLF) and optical filter. Despite of setup simplicity there are a lot of parameters that influence the MTR's working regime and therefore overall performance. All the parameters could be divided into several major groups: input signal parameters, HNLF parameters, amplifier and optical filter parameters.

The study is based on the simulations performed with computer software Synopsis OptSim 5.3. It is based on the solving the nonlinear Schrodinger equation using the split step method. Filtering influence to operation of MTR was analyzed by using three different optical filters in the simulation mock-up. Regenerator performance was evaluated by analyzing the regenerated output signal BER depending on type of filter and fiber dispersion. Fiber dispersion is a very important parameter in the regeneration process since it influences the self-phase modulation nonlinear effect. This effect in turn provides the signal quality improvement by ensuring different transfer functions for useful signal and noise. This paper consists of 3 sections. The first section describes the simulation scheme of studied regenerator setup. In the second section the results of simulations are given for three different filters used in the MTR setup. The third section gives conclusions of this research.

2. STUDIED REGENERATOR SETUP

In this section of paper the implemented Mamyshev type regenerator will be described. The simulation and experimental regenerator setup is given in the Fig. 1. Transmitter part generates the optical signal which then needs to be regenerated. Bit pattern generator generates a pseudorandom binary sequence with total number of combinations 2^{31}-1, bitrate 40 Gbps and return to zero (RZ) coding. This signal is used to modulate a continuously emitting laser output light via the Mach-Zehnder optical modulator (MZM). To make the output optical signal noisy the MZM was set to work in non-optimal regime by adjusting the operating voltage point of two Lithium Niobate crystals. Thus the output optical signal gets covered with noise.

The next stage in the setup is the regenerator part. It consists of amplifier that boosts the input signal to power level up to 24 dBm to achieve desired spectral broadening due to SPM in the HNLF. The fiber length is 1 kilometer, attenuation coefficient is 2.5 dB/km at 1550 nm and it's nonlinear coefficient is $10.7 \, W^{-1}km^{-1}$. After the HNLF follow the optical filter. Three different filters were used with the following transfer functions: Super-Gaussian, raised-cosine and measured real optical filter transfer function. Super-Gaussian and raised-cosine filter central wavelength was set to be equal to the real filter central wavelength 1550.3 nm and different filtering offsets form initial signal wavelength were achieved by using a tunable laser. All filter transfer functions are shown in the Fig. 2 and appropriate pass band widths at -3 dB and -20 dB level are summarized in the Table 1.

Receiver part consists of PIN type photodiode and optical eye pattern oscilloscope that is used to monitor the regenerator output signal BER in this way evaluating the effectiveness of the regenerator.
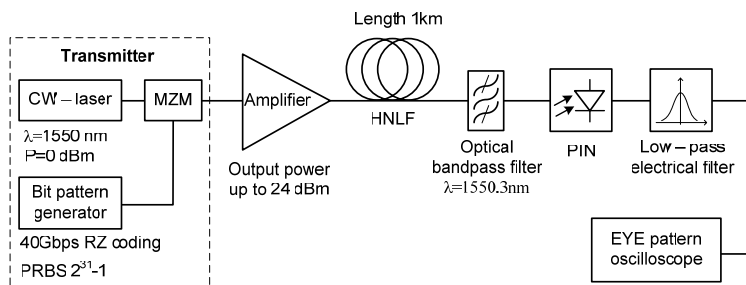

Figure 1: Simulation regenerator setup.

Table 1: Fixed and tunable filter transfer functions and corresponding pass-band widths.

	Super-Gaussian type optical filter	Raised-Cosine type optical filter	Real optical filter
-3 dB level	0.71 nm	1.21 nm	0.68 nm
-20 dB level	1.85 nm	1.82 nm	2.06 nm

3. SIMULATION RESULTS

The first of all it was found that the optimal filter central wavelength shift from signal central wavelength is 0.3 nm. Since SPM induced spectral broadening is symmetrical to both sides from central wavelength this filter shift could be made to both sides. In this research the shifting was performed to higher wavelength (lower frequency) than the initial signal wavelength.

When the filtering offset was chosen the next step was to find the necessary signal power at the input of HNLF to achieve regeneration process. This is very essential since only under certain combinations of filter central wavelength and signal power ensures signal BER improvement. In the Fig. 3 achieved results for all three filters are given. Dashed line is the distorted signal BER at the input and bars represent the regenerator output signal BER. As it can be seen the regenerated signal BER dependence on the amplified signal power shows an occasional character. Mainly this is related to accuracy at which the BER can be determined in the simulation software as well as noise from optical amplifier and receiver that is taken into account in the simulation software.

Therefore it was decided to add fitting function to these results. The second order polynomial function is used for approximation. The dashed square indicates the data area that was used to calculate the approximation function. From results it can be seen that power range that ensures signal BER improvement for Super-Gaussian type filter and real bandpass filter is approximately the same starting from 22.5 dBm up to 23.5 dBm with maximum BER improvement at 23 dBm. Slightly different results were achieved with raised-cosine type filter for which the power range that ensured signal regeneration was broader (22.25–23.8 dBm) and the lowest output signal BER was achieved at 23.4 dBm. Filter with raised-cosine type transfer function also provided an order of magnitude lower output signal BER (1×10^{-9}) compared to other two filters (1×10^{-8}).

Simulation results were also analyzed depending upon fiber dispersion to find out the MTR type regenerator operational changes. The HNLF dispersion coefficient was changed within the range 4–22 ps/nm-km. Subsequently regenerator performance was evaluated by output signal BER compared to input distorted signal BER. Results when three aforementioned filters were used in
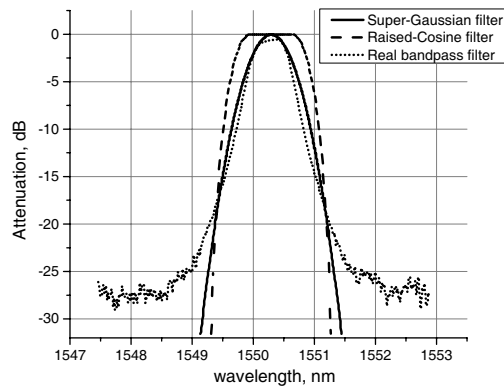

Figure 2: Transfer functions of three different filters: Super-Gaussian, Raised-Cosine and real bandpass optical filter.
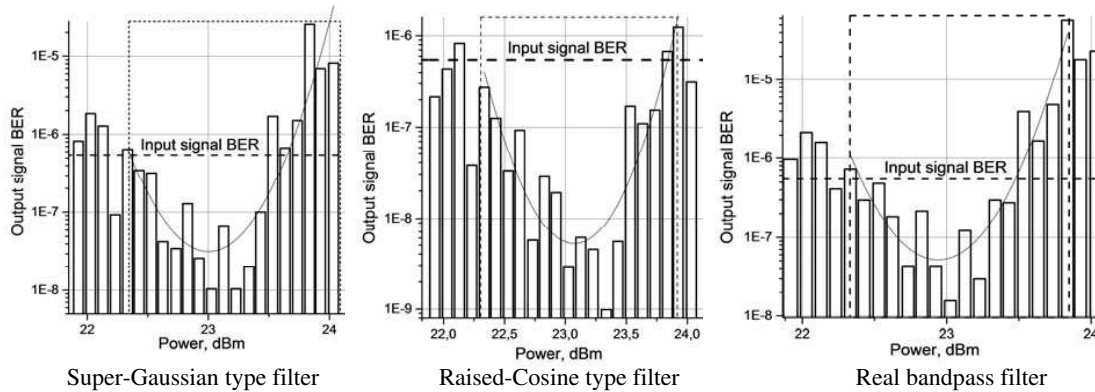

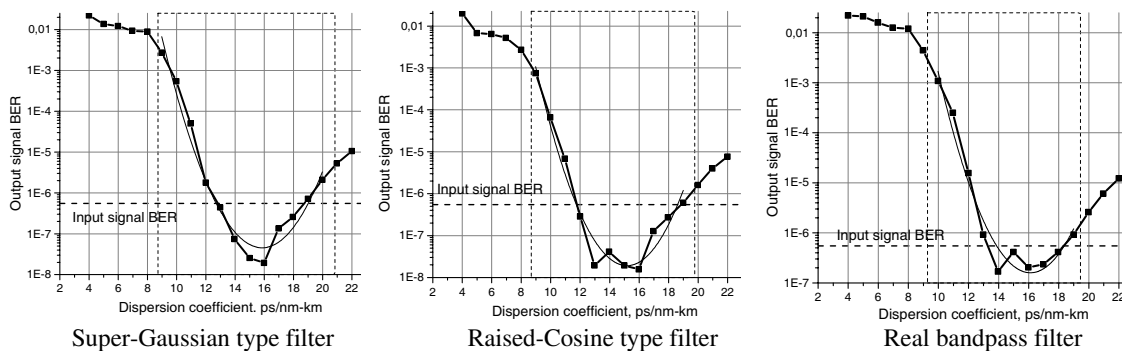Figure 3: Regenerator output signal BER depending on the amplified signal power.

Figure 4: Distorted optical signal at the regenerator input (A) and the regenerated output signal (B).

the regenerator setup are given in the Fig. 4. Similarly as in the previous results the BER values were approximated using second order polynomial function.

For all the filters the regenerator performance dependence on the dispersion turned out to be very similar. In all the cases the lowest output signal BER was when the HNLF dispersion coefficient was around 16 ps/nm-km. These results also show that MTR performance is sufficiently sensitive to dispersion since regeneration occurs only for certain range of dispersion coefficient values.

4. CONCLUSIONS

In this paper a tentative MTR setup is described and used in computer simulations to find out filter and fiber dispersion influence to regeneration process. Comparison between three different filters used in the regenerator setup were performed. Better regenerator performance considering the achieved regenerated signal BER was in the case of raised-cosine type filter. Using this filter the initial distorted signal BER (5.49×10^{-7}) was improved up to 1×10^{-9}. This can be explained by taking into account all filter transfer functions given in the Table 1. The raised-cosine filter bandwidth at -3 dB level is twice broader than other filters. It means that transfer function shape is more rectangular. This approves that filter transfer function significantly influences the regeneration process.

The study of dispersion influence to MTR operation revealed that the regenerator performance depends directly on the fiber dispersion coefficient. Only for certain range of dispersion coefficients the output signal was regenerated and its BER was lower than the input signal BER. Whereas the analyzed filter transfer functions showed quite similar performance depending on the HNLF dispersion.

REFERENCES

1. Desurvire, E., *Classical and Quantum Information Theory*, 691, Cambridge University Press, 2009.
2. Ferreira, M. F. S., *Nonlinear Effects in Optical Fibers*, 240, Wiley & Sons, 2011.
3. Becker, P. C., N. A. Olsson, and J. R. Simpson, *Erbium-Doped Fiber Amplifiers*, 481, Academic Press, 1999.
4. Provost, L., C. Finot, P. Petropoulos, K. Mukasa, and D., J. Richardson, "Design scaling rules for 2R-optical self-phase modulation-based regenerators," *Opt. Express*, Vol. 15, No. 8, 5100–5113, 2007.

Characteristics of Femtosecond Pulse in Silicon Nanowire Embedded Photonic Crystal Fiber: Variational Approach

K. Senthilnathan[1], E. Gunasundari[1], Abdosllam M. Abobaker[2], S. Sivabalan[3], K. Nakkeeran[4], and P. Ramesh Babu[1]

[1]Photonics, Nuclear and Medical Physics Division, School of Advanced Sciences
VIT University, Vellore 632 014, India
[2]Department of Communications Engineering, College of Electronic Technology, Bani Walid, Libya
[3]School of Electrical Engineering, VIT University, Vellore 632 014, India
[4]School of Engineering, University of Aberdeen, Aberdeen AB24 3UE, UK

Abstract— In this paper, we investigate the propagation characteristics of femtosecond pulses using the proposed silicon nanowire embedded photonic crystal fiber (SN-PCF). The pulse propagation in SN-PCF is governed by the well known higher order nonlinear Schrödinger (HNLS) equation. Using variational analysis, we study the propagation characteristics of an hyperbolic secant pulse, namely, pulse amplitude, width, chirp and phase.

1. INTRODUCTION

Thanks to the advancement in nanotechnology, the realization of nanowire in fiber optics called photonic nanowire (PN) has become a reality [1]. PN with core diameter less than $1\,\mu m$, which is lesser than the optical wavelength, has attracted a significant attention owing to the myriad of interesting optical properties such as tight mode optical confinement, large waveguide dispersion, high effective nonlinearity, etc. [2]. In addition, the dispersion due to this waveguide can be changed by varying the core diameter, ultimately, facilitating positive, negative and zero dispersion operations [3]. This waveguide with tailored dispersion finds applications in soliton-self compression [4], dispersion compensation, supercontinuum generation [5–7] and biosensing [8] due to its smaller core diameter.

In recent times, PNs have been fabricated from a variety of high-low index glasses such as silica glass [6, 9], chalcogenide glass [10] and silicon [11, 12]. However, of these materials, silicon is highly preferred to the rest for the reasons mentioned in what follows. First, silicon exhibits excellent transmission properties in the near infra-red wavelength range and, in particular, in the communication window. When compared to silica, silicon possesses a large nonlinearity by four order [13]. Recently, single mode operation, group velocity and waveguide dispersion have been studied experimentally using silicon nanowires [14]. Analysis of modal ellipticity and modal hybridness in a silicon nanowire has been presented [15]. Silicon waveguides find many applications in Raman lasers [16], supercontinuum generation [17, 18], all-optical regeneration [18] and pulse compression [4]. It is observed that the PN provides enhanced optical properties when embedded with a photonic crystal fiber (PCF) and the resulting waveguide is known as nanowire embedded PCF or PCF-photonic nanowire (PCF-NW) [19]. In this work, we use a silicon nanowire embedded PCF (SN-PCF) as a medium of ultrashort pulse propagation and study the dynamics of pulse parameters.

The propagation of intense light pulses in a SN-PCF can induce a host of nonlinear phenomena, such as third-order electronic (Kerr) and phonon (Raman) nonlinearities, self-steepening and the two-photon absorption (TPA) process. TPA, in turn, creates free carriers whose presence leads to additional losses through free-carrier absorption (FCA) and refractive-index changes through free-carrier dispersion (FCD). The combined effects of nonlinear phenomena and the fiber chromatic dispersion lead to many interesting dynamical processes which are difficult to understand in terms of the original pulse field, but can be easily understood by applying a collective variable (CV) approach. For example, the dynamics of the propagation of light pulses in an optical fiber can be completely described by a field, say U, which is a solution of corresponding nonlinear partial differential equation. However, for some nonlinear systems, exact solutions are not available and these systems are, in general, termed as nonintegrable systems. Hence, to study the pulse dynamics in these systems, we introduce a set of variables associated with these systems called collective variables.

In this paper, we adopt the CV approach to study the dynamics of the pulse in the proposed SN-PCF. In general, collective variables (CVs) may represent the amplitude of a pulse, its temporal

position, the pulse width, and so on. The number of CVs that can be introduced into the system is usually determined by the physics under consideration. Then one must derive a transformation which allows us to express the original field equation in terms of CVs. In other words, one must derive the equations of motion for the CVs, whose solutions will explicitly yield the complete dynamics of the nonlinear localized modes under consideration. In this paper, we consider higher-order dispersions, linear and nonlinear losses like TPA, FCA, and FCD and the nonlinear effects, namely, Kerr effect, self-steepening and Raman effect because of its resonant nature in silicon.

The paper is organized as follows. In Section 2, we model the pulse propagation in SN-PCF by modified higher-order nonlinear Schrödinger equation. We derive the propagation characteristics of an hyperbolic secant pulse, namely, pulse amplitude, temporal position, width, chirp, frequency and phase in Section 3. Finally, we summarize the findings in Section 4.

2. THEORETICAL MODEL

The propagation of an intense optical pulse (fs) through a SN-PCF is governed by the extended non-linear Schrödinger equation with self-steepening (SS) and stimulated Raman scattering (SRS) [20]

$$\frac{\partial U}{\partial z} + i\frac{\beta_2}{2}\frac{\partial^2 U}{\partial t^2} - \frac{\beta_3}{6}\frac{\partial^3 U}{\partial t^3} = i\gamma|U|^2U - \Gamma|U|^2U - \frac{\alpha}{2}U - \frac{\sigma}{2}N_cU - \gamma_s\frac{\partial}{\partial t}(|U|^2U) - i\gamma_R U\frac{\partial}{\partial t}|U|^2, \quad (1)$$

where U, β_2, β_3, γ, Γ, α, σ and N_c represent the slowly varying field amplitude, second-order dispersion, third-order dispersion, nonlinear Kerr coefficient, TPA coefficient, linear loss parameter, FCA coefficient, and free carrier density, respectively. Since the TPA-induced free-carrier density N_c has a profound effect on the pulse amplitude, the dynamic nature of N_c is included by solving the rate equation [21],

$$\frac{dN_c}{dt} = \frac{\beta_{TPA}}{2h\nu_0 A_{eff}^2}|U(z,t)|^4 - \frac{N_c}{\tau_c}, \quad (2)$$

where τ_c is the carrier life time, $h\nu_0$ is the photon energy at the incident wavelength, A_{eff} is the effective mode area, and $\beta_{TPA} = 2\Gamma A_{eff}$ is the usual TPA parameter.

For a short optical pulse ($t_0 \ll \tau_c$), one can ignore τ_c, as carriers do not have enough time to recombine over the pulse duration. In this situation, it is possible to solve Eq. (2) analytically for a given optical field. We assume that the hyperbolic secant shape of the input pulse remains unchanged during propagation but allows its parameter to evolve with the propagation distance z. In this case, a suitable form of the optical field is

$$U(z,t) = x_1(z)sech\left[\frac{t - x_2(z)}{x_3(z)}\right]\exp\left[i\frac{x_4(z)(t - x_2(z))^2}{2} - ix_5(z)(t - x_2(z)) + ix_6(z)\right], \quad (3)$$

where x_1, x_2, x_3, x_4, x_5 and x_6 represent the pulse amplitude, temporal position, width, chirp, frequency and phase, respectively and all of them vary with z. For this pulse shape, we can solve Eq. (2) analytically, and the carrier density is found to be

$$N_c = \left[\frac{\beta_{TPA}x_1^4 x_3}{2h\nu_0 a_{eff}^2}\right]\left[\frac{2}{3} + \tanh\left(\frac{t - x_2}{x_3}\right) - \frac{1}{3}\tanh^3\left(\frac{t - x_2}{x_3}\right)\right] \quad (4)$$

3. DYNAMICS OF PULSE PARAMETERS

To solve Eq. (1) with the variational technique, we first find the Lagrangian and the Rayleigh dissipation function (RDF) associated with it. They are given by

$$L = \frac{1}{2}[UU_z^* - U^*U_z] + i\frac{\beta_2}{2}|U_t|^2 - \frac{\beta_3}{6}[U_t^*U_{tt} - U_tU_{tt}^*] + i\frac{\gamma}{2}|U_t|^4 \quad (5)$$

$$R = \Gamma[UU_z^* - U^*U_z]|U|^2 + \frac{\alpha}{2}[UU_z^* - U^*U_z] + \frac{1}{2}\sigma N_c[UU_z^* - U^*U_z]$$

$$+ \gamma_s\left[U_z^*\frac{\partial|U|^2U}{\partial t} - U_z\frac{\partial|U|^2U^*}{\partial t}\right] + i\gamma_R\frac{\partial|U|^2}{\partial t}[UU_z^* + U^*U_z] \quad (6)$$

The reduced form of Lagrangian and RDF is obtained by integrating them over time [22]:

$$L_g = \int_{-\infty}^{\infty} Ldt \quad (7)$$

and

$$R_g = \int_{-\infty}^{\infty} R dt \tag{8}$$

With the help of Eqs. (3)–(7), we obtain the following explicit expressions of L_g and R_g:

$$L_g = \frac{i\beta_2 x_1^2}{3x_3}\left[1 + x_3^2\left(\frac{x_3^2 x_4^2 \pi^2}{4} + 3x_5^2\right)\right] + \frac{i\beta_3 x_1^2}{x_3 x_5}\left[\frac{1}{x_3^2} + x_5^2 + \frac{1}{4}x_3^2\pi^2\right] + $$
$$-ix_1^2\left[2x_3 x_5 \dot{x}_2 - 2x_3\dot{x}_6 - \frac{x_3^3\pi^2\dot{x}_4}{12}\right] + i\frac{2}{3}\gamma x_1^4 x_3 \tag{9}$$

Using the given ansatz (19), the reduced RDF can be obtained as

$$R_g = \left[-2ix_3x_5\dot{x}_2 - \frac{i}{12}\pi^2 x_3^3\dot{x}_4 - 2ix_3\dot{x}_6\right]\left[\frac{4}{3}\Gamma x_1^4 + \alpha x_1^2 + \frac{2}{3}\sigma\left(\frac{\beta x_1^6 x_3}{2h\nu_0 a_{eff}^2}\right)\right] + \frac{2}{3}ix_3^3\Gamma x_1^4\dot{x}_4$$
$$-2i\gamma_s x_1^3 x_3\left[\frac{2x_1 x_4\dot{x}_2}{3} + x_1\dot{x}_5 + \frac{4}{3}x_5\dot{x}_1 + \frac{x_1 x_5\dot{x}_3}{3x_3}\right] - \frac{16i\gamma_R x_1^4\dot{x}_2}{15x_3} \tag{10}$$

The Euler-Lagrange equation in the form

$$\frac{d}{dt}\left(\frac{\partial L_g}{\partial q_z}\right) - \frac{\partial L_g}{\partial q} + \frac{\partial R_g}{\partial q_z} = 0, \tag{11}$$

where $q = x_1,\ x_2,\ x_3,\ x_4,\ x_5$ and x_6 and the suffix z indicates the corresponding derivatives. Applying the generalized EulerLagrange equation, we get a set of six coupled ordinary differential equations for each q represent the dynamics of pulse parameters can be obtained as follows:

$$\dot{x}_1 = \frac{\beta_2}{2}x_1 x_4 + \frac{\beta_3}{2}x_1 x_4 x_5 - 2\Gamma x_1^3\left[\frac{1}{\pi^2} + \frac{1}{3}\right] - \frac{\alpha}{2}x_1 - \frac{\beta x_1^5 x_3\sigma}{6h\nu_0 a^2} \tag{12}$$

$$\dot{x}_2 = \beta_2 x_5 + \frac{\beta_3}{24}x_3^2 x_4^2\pi^2 + \frac{\beta_3}{2}\left[x_5^2 + \frac{1}{3x_3^2}\right] + \gamma_s x_1^2 \tag{13}$$

$$\dot{x}_3 = -\beta_2 x_3 x_4 - \beta_3 x_3 x_4 x_5 + \frac{4\Gamma x_1^2 x_3}{\pi^2} \tag{14}$$

$$\dot{x}_4 = \beta_2\left[x_4^2 - \frac{4}{x_3^4\pi^2}\right] + \beta_3 x_5\left[x_4^2 - \frac{4}{x_3^4\pi^2}\right] - \frac{4\gamma x_1^2}{\pi^2 x_3^2} - \frac{4\gamma_s x_1^2 x_5}{x_3^2\pi^2} \tag{15}$$

$$\dot{x}_5 = \frac{-2\gamma_s x_1^3 x_4}{3} - \frac{8\gamma_R x_1^3}{15x_3^2} \tag{16}$$

$$\dot{x}_6 = \beta_2\left[\frac{2}{3x_3^2} - \frac{x_5^2}{2}\right] - \frac{\beta_3 x_5}{3}\left[x_5^2 - \frac{x_3^2 x_4^2\pi^2}{24}\right] + \frac{5\gamma x_1^2}{6} - \frac{\gamma_s x_1^2 x_5}{6} \tag{17}$$

The variational Eqs. (12)–(17) show clearly how the pulse parameters change during the propagation inside a SN-PCF and how they are coupled with each other. From the above equations, it is very clear that the linear and nonlinear effects affect a particular pulse parameter. For instance, pulse width in Eq. (14) is affected directly not only by the dispersion parameter and TPA but also by the TOD. In general, dispersion may lead to pulse broadening or compression depending on the sign of β_2. On the other hand, TPA always results in pulse broadening. But, TOD creates asymmetrical pulse broadening in the pulse. This TOD affects all the parameters except frequency of the pulse which is evident from the above equations of motions. The self-steepening affects the position, chirp, frequency and phase of the pulse. The frequency of the pulse changes due to the the Raman term as is evident in Eq. (16).

4. CONCLUSION

In this work, we have successfully derived a set of equations of motions involving various pulse parameters, namely, amplitude, temporal position, width, chirp, frequency and phase, for the modified NLSE by adopting collective variable approach. From these equations, one could easily understand the influence of all the important physical effects over the pulse dynamics.

REFERENCES

1. Foster, M. A., A. C. Tuener, M. Lipson, and A. L. Gaeta, *Opt. Express*, Vol. 16, 1300–1320, 2008.
2. Afshar, S. V. and T. M. Monro, *Opt. Express*, Vol. 17, 2298–2318, 2009.
3. Mohebbi, M., *IEEE Photon. Technol. Lett.*, Vol. 20, 921–923, 2008.
4. Agrawal, G. P., *Nonlinear Fiber Optics*, 4th Edition, Academic, San Diego, CA, 2007.
5. Tong, L. M., R. R. Gattass, J. B. Ashcom, S. L. He, J. Y. Lou, M. Y. Shen, I. Maxwell, and E. Mazur, *Nature*, Vol. 426, 816–819, 2003.
6. Leon-Saval, S. G., T. A. Birks, W. J. Wadsworth, P. St. J. Russell, and M. Mason, *Opt. Express*, Vol. 12, 2864–2869, 2004.
7. Gattass, R. R., G. T. Svacha, L. M. Tong, and E. Mazur, *Opt. Express*, Vol. 14, 9408–9414, 2006.
8. Debackere, P., S. Scheerlinck, P. Bienstman, and R. Baets, *Opt. Express*, Vol. 14, 7063–7072, 2006.
9. Hu, M., C. U. Wang, Y. Li, Z. Wang, L. Chai, and A. Zheltikov, *Opt. Express*, Vol. 12, 6129–6134, 2004.
10. Grillet, C., C. Smith, D. Freeman, S. Madden, B. Luther-Davies, E. Magi, D. Moss, and B. Eggleton, *Opt. Express*, Vol. 14, 1070–1078, 2006.
11. Foresi, J. S., P. R. Villeneuve, J. Ferrere, E. R. Thoen, G. Steinmeyer, S. Fan, J. D. Joannopoulos, L. C. Kimerling, H. I. Smith, and E. P. Ippen, *Nature*, Vol. 390, 143–145, 1997.
12. Vlasov, Y. A. and S. J. McNab, *Opt. Express*, Vol. 12, 1622–1631, 2004.
13. Bogaerts, W., R. Baets, P. Dumon, V. Wiaux, S. Beckx, D. Taillaert, B. Luyssaert, J. V. Campenhout, P. Bienstman, and D. V. Thourhout, *J. Lightw. Technol.*, Vol. 23, 401–412, 2005.
14. Tong, L. M., J. Y. Lou, and E. Mazur, *Opt. Express*, Vol. 12, 1025–1035, 2004.
15. Kejalakshmy, N., A. Agrawal, Y. Aden, D. M. H. Leung, B. M. A. Rahman, and K. T. V. Grattan, *App. Opt.*, Vol. 49, 3171–3181, 2010.
16. Rong, H., A. Liu, R. Jones, O. Cohen, D. Hak, R. Nicholaescu, A. Fang, and M. Paniccia, *Nature*, Vol. 433, 292–294, 2005.
17. Tamura, K. R., H. Kubota, and M. Nagazawa, *IEEE J. Quantum. Electron.*, Vol. 36, 773–779, 2000.
18. Salem, R., M. A. Foster, A. C. Turner, D. F. Geraghty, M. Lipson, and A. L. Gaeta, *Opt. Express*, Vol. 15, 7802–7809, 2007.
19. Biancalana, F., T. X. Tran, S. Stark, M. A. Schmidt, and P. St. J. Russell, *Phys. Rev. Lett.*, Vol. 105, 093904–093907, 2010.
20. Yin, L., Q. Lin, and G. P. Agrawal, *Opt. Lett.*, Vol. 31, 1295, 2006.
21. Yin, L. and G. P., Agrawal, *Opt. Lett.*, Vol. 32, 2031, 2007.
22. Anderson, D., *Phys. Rev. A*, Vol. 27, 3135, 1983.

Optical WDM-PON Access System with Shared Light Source

Sandis Spolitis, **Lilita Gegere**, **Anita Alsevska**,
Ilja Trifonovs, **Jurgis Porins**, and **Vjaceslavs Bobrovs**
Institute of Telecommunications, Riga Technical University, Riga, Latvia

Abstract— The present paper investigates performance of next generation passive optical network (NG-PON) with effective chromatic dispersion (CD) compensation method in physical layer. We report on 16-channel spectrum sliced wavelength division multiplexed passive optical network (SS-WDM PON) with shared amplified spontaneous emission (ASE) light source as NG-PON solution, which is based on ITU-T G.694.1 DWDM frequency grid, and is capable to provide data transmission over 20 km fiber span with transmission speed at least 2.5 Gbit/s per channel. It is shown, that performance of this optical access system can be improved by using chromatic dispersion compensation module with fiber Bragg grating, in such a way providing data transmission over 20 km SMF fiber span with BER $< 10^{-10}$.

1. INTRODUCTION

The growing number of Internet users and bandwidth-driven applications, such as streaming video, online gaming, file sharing, video conferencing and others bring various challenges for network operators and force them to migrate toward new architectures and technologies [1]. Next generation passive optical networks (NG-PON) must provide higher data transmission speeds while keeping CAPEX and OPEX as low as possible [2]. There are two key factors which will influence telecommunication networks of the future. The first one is support of high bandwidth data transmission and the second one is usage of architectures which are both cost and energy efficient [3, 4]. Promising technology to fulfill the world-wide rising requirement for transmission capacity is spectrum sliced wavelength division multiplexed passive optical network named as SS-WDM PON. The strength of this technology is its ability to locate electronics and optical elements in one central office (CO) and simplify the NG-PON network architecture as well as use only one broadband light source (BLS) for all users [2, 5, 6]. SS-WDM PON optical system is energy efficient and cost effective in the way that single seed light is shared among multiple users instead of using individual light source for each of them [7].

SS-WDM PON systems benefit from the same advantages as traditional WDM-PON systems, while employing low cost incoherent light sources like amplified spontaneous emission (ASE) source or light-emitting diode (LED). The performance of the SS-WDM PON transmission systems is restricted by chromatic dispersion (CD) [6, 8]. Dispersion causes optical signal pulses to broaden and lose their shape as they travel along optical fiber. Eventually this limits the quality of transmitted signal, maximum achievable data transmission rate and transmission system reach [9, 10]. The optical bandwidth per channel of SS-WDM PON system is large compared to the bit rate and, therefore, CD significantly degrades the performance of this system more than it is observed in conventional laser-based systems like WDM-PON [7, 11]. Different CD compensation methods can be used in physical layer for NG-PON systems [8]. They can be dispersion compensation fiber (DCF) or fiber Bragg grating (FBG). In our previous researches [11] and [12] FBG provided better performance than DCF used for CD compensation, therefore FBG is used as effective CD compensation method in this research also. In this paper we investigate the performance of 16-channel SS-WDM PON system with typical access network link length of 20 km.

2. SPECTRUM SLICED WDM-PON ARCHITECTURE

Spectrum slicing technique is one of available techniques in WDM-PON systems in order to reduce cost of components and simplify the architecture of PON network [7]. This technique employs a single broadband light source (BLS) for transmission on a large number of wavelength channels. BLS like LED or ASE can be used in spectrum sliced systems for data transmission. As it is shown in Fig. 1, incoherent BLS (e.g., ASE) is sliced in equally spaced multi-wavelength channels [13]. BLS usually is sliced with arrayed-waveguide grating (AWG). Afterwards, optical slices are modulated by optical modulator, and multiplexed by second AWG for transmission over single mode (SMF) fiber span. Optical channels are demultiplexed by last AWG located after the SMF fiber span and received by direct detection optical receiver where PIN photodiode or avalanche photodiode (APD)

is implemented. It should be taken into account that a larger slice width will increase not only the total channel power but also increase the influence of dispersion on transmitter optical signal and crosstalk between channels [14].

In our SS-WDM PON system setup we use previously [14] designed ASE source as BLS for spectral slicing operation due to its high optical output power compared by other mentioned BLS. This ASE source has a nearly flat spectrum in frequency range from 192.3 THz to 194.0 THz (C-band, wavelength range from 1545.32 nm to 1558.98 nm), which was designed by manipulating parameters of two cascaded EDFAs [14]. In this way, an ASE BLS source with nearly flat spectrum (variation from average value of power level in marked area is about 0.35 dB) and total output power of cascaded EDFA system +23 dBm (200 mW) can be constructed, see Fig. 2.
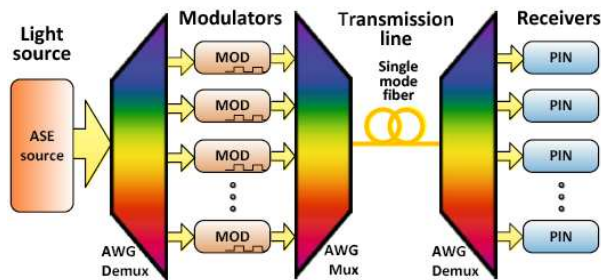

Figure 1: Operational principle of SS-WDM PON transmission system with N channels.
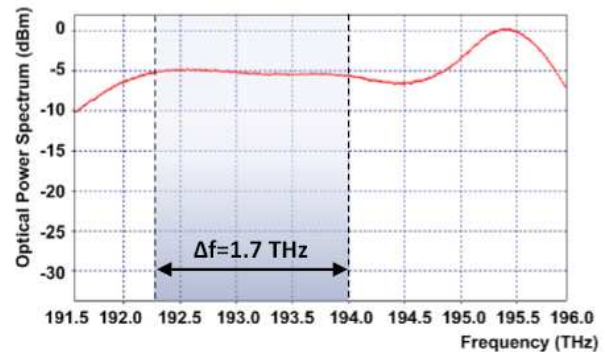

Figure 2: Output spectrum of realized noise-like ASE broadband light source.

3. EXPERIMENTAL SIMULATION MODEL OF 16 CHANNEL SS-WDM PON SYSTEM

This paper section shows realization of NG-PON 16-channel spectrum sliced WDM-PON access system in newest Synopsys RSoft simulation software which is reliable and widely used for design of high-performance optical communication systems [15]. In intensity modulated SS-WDM-PON system with NRZ line code and direct detection, transmission speed (2.5 Gbit/s) is limited due to the excess intensity noise which originates from non-coherent ASE source [11, 13]. The performance of simulated scheme was evaluated by the obtained bit error ratio (BER) value of each WDM channel in the end of the fiber optical link on each optical network terminal (ONT). BER threshold for this transmission system is set as BER $< 10^{-10}$. The SS-WDM PON system (see Fig. 3) has only one BLS light source (ASE) shared by all ONTs. Broadband ASE light source is spectrally sliced using 16-channel flattop AWG filter (AWG1) with channel spacing equal to 100 GHz. After the spectrum slicing operation, which is realized by first AWG (AWG1), optical slices are transmitted to optical
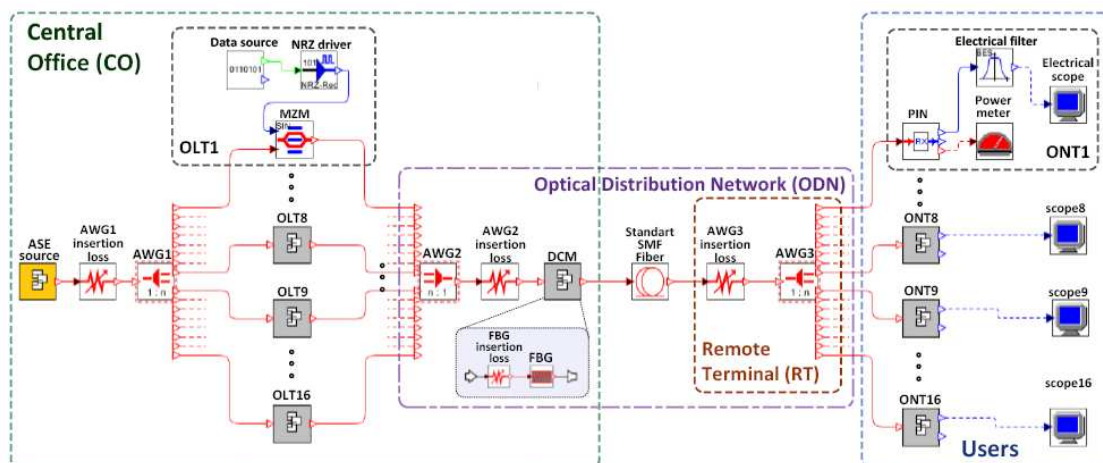

Figure 3: Simulation model of high-speed 16-channel AWG filtered and ASE seeded SS-WDM PON system with DCM module.

line terminal (OLT) transmitters located at central office (CO).

Each OLT consists of electrical data source, NRZ driver and external Mach-Zehnder modulator (MZM). Generated bit sequence from data source is sent to electrical signal driver where NRZ pulses are formed. Afterwards formed electrical NRZ pulses are send to Mach-Zehnder modulator. Each MZM has 5 dB insertion losses, 20 dB extinction ratio, modulation voltage of 5 V and maximum transmissivity offset voltage 2.5 V. Optical signals from all OLTs transmitters are coupled by optical multiplexer (AWG2) and send into standard ITU-T G.652 single mode fiber (SMF) located in optical distribution network (ODN). Insertion losses of AWG units are simulated using additional attenuation blocks. ODN includes the physical fiber and optical devices that distribute optical signals from central office (CO) to users in PON network. For CD compensation DCM with fiber Bragg grating (FBG) is used in ODN. Additional attenuator is used for simulation of FBG's insertion loss. Each ONT consists of PIN photodiode (sensitivity -25 dBm at BER $= 10^{-10}$), Bessel electrical lowpass filter (3-dB electrical bandwidth $B_E = 1.6$ GHz), optical power meter and electrical probe to evaluate the quality of received optical data signal (e.g., show eye diagram) [15]. Performance of transmission system is evaluated after 20 km transmission, because such an optical fiber span length is defined in ITU-T recommendation G.984.2 as upper limit of fiber distance between optical line terminal (OLT) and optical network terminal (ONT) in Gigabit passive optical networks (GPON) [12, 13].

4. RESULTS AND DISCUSSION

Performance results of proposed 16-channel SS-WDM PON system are shown in this section. In Fig. 4 it is shown spectrum of SS-WDM PON optical signals on the output of all OLT transmitters (OLT T $\times$ 1 to T $\times$ 16) and spectrum in the input of ONTs (ONT R $\times$ 1 to R $\times$ 16). We found that optimal 3-dB bandwidth value of AWG units for maximal quality of received signal and minimal crosstalk between channels is 90 GHz for spectrum sliced optical access system [13, 15]. The larger is width of spectral slice the higher performance we can obtain until a certain point, when arising crosstalk between channels must be taken into account [7]. Accordingly, there is a tradeoff between optical filter bandwidth and crosstalk between spectrum sliced channels, which can result in performance drop of optical access system. For spectrum sliced WDM-PON system we can see signal distortion in eye diagrams, see Fig. 5(a) and Fig. 5(b). It is seen in Fig. 5(b) that after 20 km transmission without CD compensation the performance of SS-WDM PON system is poor and data transmission with BER $< 10^{-10}$ is not possible. Therefore, for CD compensation and performance improvement of proposed 16-channel SS-WDM PON system, fiber Bragg grating dispersion compensation module was used. We found that optimal CD amount, which must be compensated by FBG DCM for 20 km SMF fiber span is 310 ps/nm at 1550 nm wavelength.

Minimal received power to obtain BER $< 10^{-10}$ must be more than -17.9 dBm for B2B configuration (without transmission line) and -16 dBm for 20 km SMF transmission line with CD compensation. Without CD compensation data transmission over 20 km fiber span with BER $< 10^{-10}$ is not possible. As one can see in Fig. 6 power penalty to receive optical signal for 16-channel SSWDM PON system with BER $< 10^{-10}$ after 20 km transmission and CD compensation with
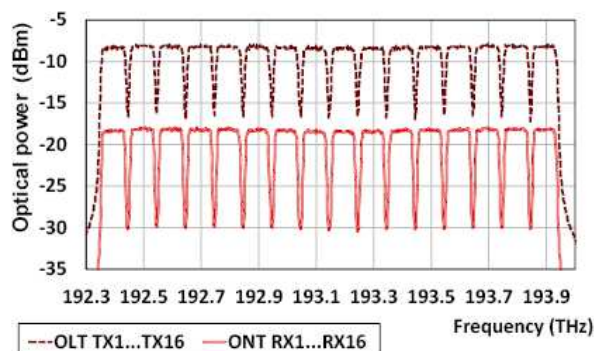

Figure 4: Optical power spectra of transmitted signals on the output of OLT transmitters and on the input of ONT receivers after 20 km transmission.
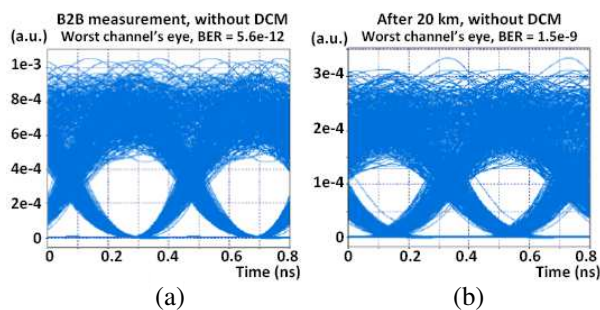
Figure 5: Eye diagrams and BER values of received signal of 16-channel SS-WDM-PON scheme without DCM module for measured, (a) B2B signal and (b) signal after 20 km transmission.
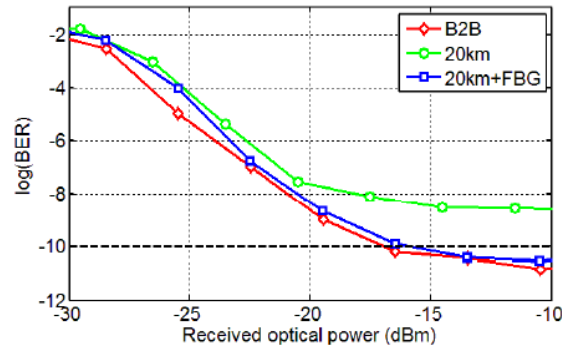
Figure 6: Measured BER versus the received average optical power for 16 channel SS-WDM PON system.

FBG DCM is 1.9 dB. This penalty is introduced by the crosstalk effects, dispersion and due to the noise-like nature of broadband ASE light source.

5. CONCLUSIONS

In this work we have realized and investigated the performance of SS-WDM PON system which is NG-PON suitable technological solution. Evaluated system is based on ITU-T DWDM frequency grid, defined in recommendation G.694.1, has 16 channels and is capable to provide data transmission over 20 km fiber span with transmission speed at least 2.5 Gbit/s. In evaluated system the fiber Bragg grating was used for accumulated chromatic dispersion compensation in DCM module to provide high system performance with BER $< 1 \cdot 10^{-10}$. It is shown that spectrum-sliced WDM PON is a good candidate for NG-PON systems, because it utilizes only one broadband light source which is shared among all users. In this research it is shown, that system performance of SS-WDM PON system can be improved by using additional CD compensation with FBG DCM. We believe that SS-WDM system architecture is potential solution for next generation passive optical networks to support high bandwidth data transmission from OLT to ONTs.

ACKNOWLEDGMENT

REFERENCES

1. Bobrovs, V., S. Spolitis, and G. Ivanovs, "Latency causes and reduction in optical metro networks," (Invited paper), *Proc. of SPIE Photonics West, Optical Metro Networks and Short-Haul Systems VI*, 1–11, 2014.
2. Mahloo, M., J. Chen, L. Wosinska, A. Dixit, B. Lannoo, D. Colle, and C. M. Machuca, "Towards reliable hybrid WDM/TDM passive optical networks," *IEEE Communications Magazine*, Vol. 52, No. 2, 14–23, 2014.
3. Machuca, M., J. Chen, L. Wosinska, M. Mahloo, and K. Grobe, "Fiber access networks: Reliability and power consumption analysis," (Invited paper), *Proc. of IEEE International Conference on Optical Network Design and Modeling*, 1–6, 2011.
4. Yuang, M. C., D. Z. Hsu, P. L. Tien, H. Y. Chen, C. C. Wei, S. H. Chen, and J. Chen, "An energy and cost efficient WDM/OFDMA PON system: Design and demonstration," *Journal of Lightwave Technology*, Vol. 31, No. 16, 2809–2816, 2013.
5. Darren, P. and E. Mitchell, "Long-reach optical access technologies," *IEEE Network*, Vol. 21, No. 5, 5–11, 2007.
6. Vukovic, A., M. Savoie, and H. Hua, "Performance characterization of PON technologies," *Proc. of International Conference on Application of Photonics Technology*, 1–10, Ottawa, 2007.
7. Choi, B. H. and S. S. Lee, "The effect of AWG-filtering on a bidirectional WDM-PON link with spectrum-sliced signals and wavelength-reused signals," *Optics Communications*, Vol. 284, No. 24, 5692–5696, 2011.
8. Spolitis, S., V. Bobrovs, and G. Ivanovs, "Reach improvement of spectrum-sliced dense WDM-PON system," *Proc. of 7th International Conference on Broadband, Wireless Computing, Communication and Applications*, 296–301, 2012.

9. Keiser, G., *Optical Communications Essentials*, McGraw-Hill, 2007.

10. Agrawal, G., *Fiber-optic Communication Systems*, John Wiley and Sons, USA, 2002.

11. Bobrovs, V., S. Spolitis, G. Ivanovs, and P. Gavars, "Performance improvement of high speed spectrum-sliced dense WDM-PON system," *Proc. of 9th International Symposium on Telecommunications*, 1–6, 2012.

12. Bobrovs, V., S. Spolitis, A. Udalcovs, and Ģ. Ivanovs, "Schemes for compensation of chromatic dispersion in combined HDWDM systems," *Latvian Journal of Physics and Technical Sciences*, Vol. 48, No. 5, 30–44, 2011.

13. Ivanovs, G., S. Spolitis, R. Parts, and V. Bobrovs, "Performance improvement of spectrum-sliced passive optical network," *PIERS Proceedings*, 308–311, Taipei, Mar. 25–28, 2013.

14. Spolitis, S., V. Bobrovs, S. Berezins, and G. Ivanovs, "Optimal design of spectrally sliced ASE seeded WDM-PON system," *Proc. of XVth International Telecommunications Network Strategy and Planning Symposium*, 1–5, 2012.

15. Bobrovs, V., S. Spolitis, and G. Ivanovs, "Comparison of chromatic dispersion compensation techniques for WDM-PON solution," *Proc. of 2nd Baltic Congress on Future Internet Communications*, 64–67, 2012.

Estimation of EDFA Performance in 40 Gbit/s 8 Channel DWDM Transmission System

Ingrida Lavrinovica, **Jurgis Porins**, **and Girts Ivanovs**

Institute of Telecommunications, Riga Technical University, Azenes st.16/20, Riga LV-1048, Latvia

Abstract— In this research, we demonstrate 8 channels wavelength division multiplexing (WDM) transmission system with in-line Erbium Doped Fiber Amplifier (EDFA) using both co-propagation (980 nm) and counter propagation (1480 nm) EDFA configuration. The performance of an EDFA in a 40 Gbit/s 8 channel dense wavelength division multiplexing (DWDM) transmission system with NRZ-OOK modulation format and 100 GHz channel spacing was investigated with an aim of finding optimal configuration. Results show that the pumping wavelength of 980 nm the usage of 15 m long doped fibers gain value is around 27 dB, thus the usage of 30 m long fiber already drives gain indicators close to 30 dB. With the increase of pump power and fiber length co-propagation EDFA configuration at pumping wavelength of 1480 nm provides noticeably high and stable gain values of more than 40 dB.

1. INTRODUCTION

Erbium Doped Fiber Amplifier (EDFA) has been considered as an attractive solution for the simultaneous amplification of all dense wavelength division multiplexing (DWDM) channels because of several major advantages — immunity to cross talk among wavelength multiplexed channels, insensitivity to light polarization state, high energy efficiency ($> 50\%$) and time constant enough to cover modulation noises. The working principle of EDFA is based on transient processes at 3-three level erbium atomic structure. Population inversion can be achieved using laser pumping at 980 nm or 1480 nm to excite electrons to the upper erbium atomic state. When excited to the upper state, electrons rapidly decay nonradioactively to the meta-stable state by emitting light within the 1525–1565 nm band. Stimulated photons are in coherence with the input signal, and that results in signal amplification [1].

If electrons in the meta-stable state are not stimulated within the electron lifetime in that state, electron transition to the lower states results in spontaneous emission (ASE). In this case, photons are emitted spontaneously in all directions, but a proportion of those will be emitted in a direction that falls within the numerical aperture of the fiber and are thus captured and guided by the fiber. Those photons captured may then interact with other dopant ions, and are thus amplified by stimulated emission [2].

Simplified transition process is shown at Fig. 1.

2. METHOD ANALYSIS

The experimental part was focused on optimization of EDFA parameters. Optimal length depends on doping level and pump power, therefore different doped fiber lengths (10 m, 15 m, 20 m, 25 m,
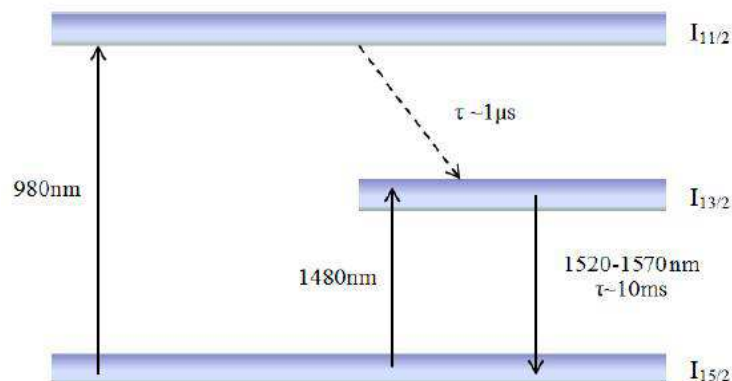

Figure 1: Simplied scheme of Er^{3+} energy levels in silica fiber [3].

and 30 m) and excitation source power (200 mW, 300 mW, 400 mW, 500 mW) were used in order to reach the highest amplification value. Simulation of an amplifier was done with the help of RSoft Design Group OptSim 5.2 software using *Sample mode* simulation core and physical model of EDFA. Physical EDFA OptSim model is based on the solution of the EDFA rate equations under the so-called "effective overlap approximation" therefore implementing a detailed model for the EDFA saturation and wavelength dependence of the gain. EDFA rate equations are used to describe absorption and emission rates. For example, in pumping at 980 nm, it is required to form a system model with three energy levels. When the excited state absorption (ESA) is considered, a forth level should also be included. If the pumping is performed at 1480 nm, a simple system model with two energy levels can be used.

This model assumes that, for each wavelength, the emission and absorption coefficients [dB/m] can be obtained by multiplying the emission and absorption cross sections [m^2] by a coefficient which depends on fiber dopant density and effective area, but does not depends on wavelength nor incident optical power. Experimental measurement scheme is shown in the Fig. 2. Simulations were done using both co-propagating (980 nm) and counter propagating (1480 nm) EDFA configuration accordingly. Gain values were measured on every WDM channel at the certain combination of doped fiber length and pump power.
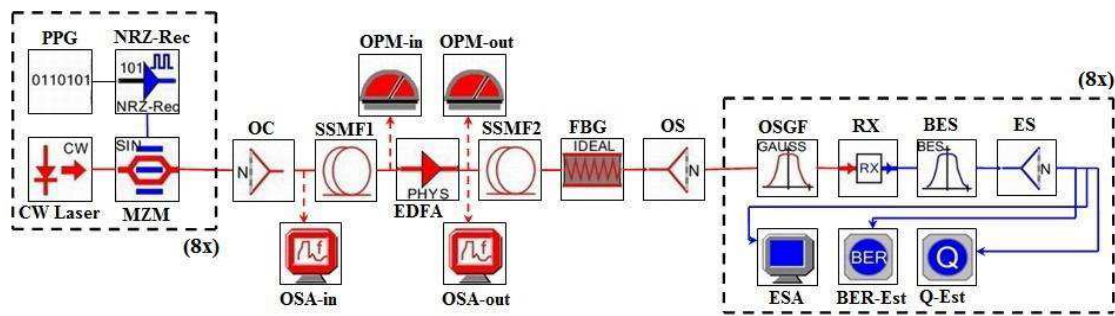

Figure 2: The experimental setup used for investigating the DWDM transmission.

3. RESULTS AND DISCUSSION

After the analysis of EDFA performance with co-propagating pumping at 980 nm wavelength the most notable results were achieved using 15 m and 30 m long fibers as it is displayed at Fig. 3. For 15 m long fiber at the pump power of 200 mW gain value is around 24 dB for all the channels and it does not change much with the increase of pump power until 300 mW — the improvement is only
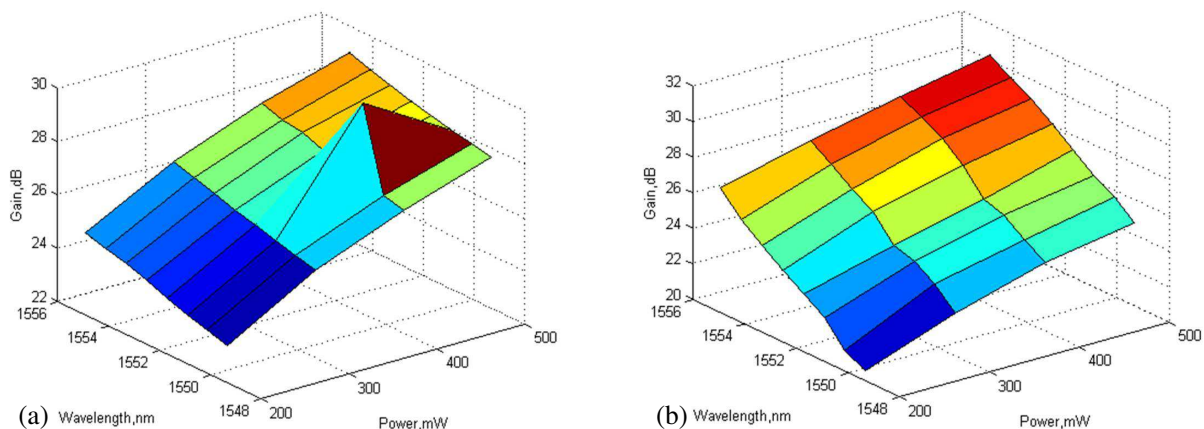

Figure 3: EDFA gain depending on the pump power for (a) 15 m and (b) 30 m long doped fibers at 980 nm pumping wavelength.
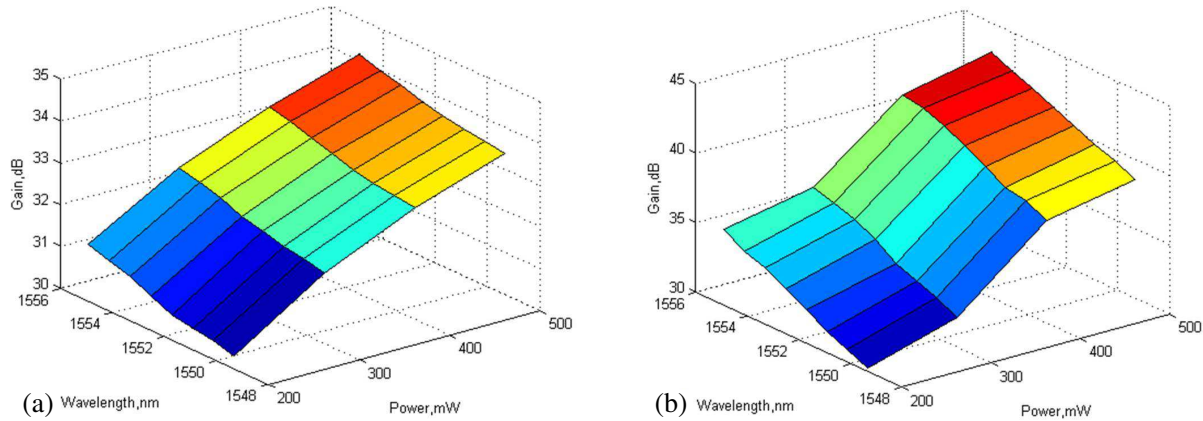
Figure 4: EDFA gain depending on the pump power for (a) 15 m and (b) 30 m doped fibers at 1480 nm pumping wavelength.

for 2 dB. The significant change is clearly visible at 400 and 500 mW where gain is already around 27–28 dB. These leaps are clearly visible at Fig. 3. In addition, the usage of higher powers gives almost constant gain at every WDM channel.

For 30 m long fiber with pump power of 200 mW notable gain value of 27 dB is observed for the first channel of WDM system and keeps slightly decreasing until 20 dB at eighth channel. With the increase of pump power to 300–400 mW gain picture is uneven — it varies around 27–29 dB for the first channels and drops to 23–24 dB in the end of WDM system. High gain values of around 29–30 dB are reached with the increase of pump power to 500 mW.

The usage of co-propagation EDFA configuration at 1480 nm (Fig. 4) gives a stable gain level on each channel, which means that with this configuration it is easier to reach EDFA saturation regime. For 15m long fiber pump power increase does not affect gain significantly — it is about 30–33 dB even if the pump power was increased for 100 mW in each case. Gain is stable throughout the whole WDM system. The situation changes dramatically in case of 30m long fiber. Gain value keeps growing with the increase of pump power: at 200 mW it is about 34–35 dB while at 400–500 mW gain value already reaches 40–43 dB.

4. CONCLUSION

In this paper 8 channels WDM transmission system with in-line EDFA was investigated using both co-propagation (980 nm) and counter propagation (1480 nm) EDFA configuration. There is always an optimum EDFA length depending on the pumping laser power. If the fiber is too short then the whole potential of the amplifier will not be realized. Some laser energy will remain unused. Whereas if the EDFA fiber is longer than the optimal value then erbium inversion level at the end of the EDF will be less than 50% and fiber will start to absorb the signal. The obtained results have shown that at the pumping wavelength of 980 nm the usage of 15 m long doped fibers gain value is around 27 dB, thus the usage of 30 m long fiber already drives gain indicators close to 30 dB. Respectively, it is more efficient to use longer fibers. With the increase of pump power and fiber length co-propagation EDFA configuration at pumping wavelength of 1480 nm provides noticeably high and stable gain values of more than 40 dB. However, in this case a large amount of ASE noise is produced as well.

REFERENCES

1. Abu-Aisheh, A. and H. Alnajjar, "Pre-amp EDFA ASE noise characterization for optical receiver transmission performance optimization," *Proceedings of The 2008 IAJC-IJME International Conference*, 2008.

2. Manoj Ramesh Rao, R., R. Johny Richards, J. Manohar, A. M. Balamurugan, and A. Sivasubramanian, "Erbium Doped Fiber Amplifiers: State of art," *International Journal of Scientific & Technology Research*, Vol. 2, No. 5, May 2013.

3. Ivanovs, G., V. Bobrovs, S. Olonkins, A. Alsevska, L. Gegere, R. Parts, P. Gavars, and G. Lauks, "Application of the Erbium-Doped Fiber Amplifier (EDFA) in Wavelength Divi-

sion Multiplexing (WDM) transmission systems," *International Journal of Physical Sciences*, Vol. 9, No. 5, 91–101, 2014.

4. Bobrovs, V., S. Berezins, and S. Olonkins, "EDFA operating parameter research and its application in WDM transmission systems," *Latvian Journal of Physics and Technical Sciences*, Vol. 6, 1, 2012.

5. Kim, H. K., S. Y. Park, D. H. Lee, and C. S. Park, "Design and control of gain flattened Erbium Doped Fiber Amplifier for WDM application," *ETRI Journal*, Vol. 20, No. 1, 28–38, 1998.

Bidirectional Radio-on-Fiber Transport Systems Using Fiber Nonlinearity and Injection Locked Technique

W. S. Tsai and G. C. Lin

Department of Electrical Engineering, Ming Chi University of Technology, Taiwan

Abstract— We propose a novel bidirectional transmission system based on stimulated Brillouin scattering (SBS) effect and injection locked distributed-feedback (DFB) laser to achieve optical single sideband (OSSB) modulation for downlink transmission. For uplink transmission, we reuse transmitting light by phase modulation (PM) to avoid signal interference each other in bidirectional transport After 25 km single mode fiber (SMF) transmission, we can observe the sideband power ratio (SBPR) > 15 dB for downlink transmission and system's power penalty is < 2.8 dB. Good performances for bit error rate (BER) analysis are observed in our proposed bidirectional transmission system.

1. INTRODUCTION

Optical carrier reuse conception is widely employed in bidirectional light transmission systems due to its economic and colorless characteristic. By replacing a light source in each subscriber premise, the optical network installation process will become easier, and the service providers can flexibly manage the network resources. Radio-onfiber (ROF) can apply to transmit microwave signal by optical fiber. The communication system with ROF technology transmits microwave signal for a long distance with high performances which makes the broad bandwidth and low transmission loss of the fiber, and solves the last mile problem to the user. In traditional intensity modulation, the optical carrier is modulated to generate an optical double sideband (DSB) format. Over a long haul fiber transmission, RF signal will cause severe power degradation due to chromatic dispersion [1]. In order to overcome RF power degradation, optical single sideband (OSSB) modulation technique must be implemented. OSSB modulation can remove a half of the optical spectrum is expected to attain a dispersion benefit [2–4]. By eliminating one of the sidebands, OSSB modulation not only immunizes to fiber dispersion but it also increases the spectral efficiency twice.

Bidirectional light wave transmission systems transmit downlink and uplink signals simultaneously which produce large crosstalk because transmit signals are disturbed each other. Phase modulation (PM) systems utilize optical phase shifting to record signal state, which provides high robustness to against crosstalk and fiber nonlinearities with high gain and low noise figure Nonlinear effects are interactions between light waves, which can cause noise and crosstalk. The nonlinear effect for Stimulated Brillouin scattering (SBS) occurs when signal power reaches a level sufficient to generate tiny acoustic vibrations in the glass. Acoustic waves change the density of a material, and thus alter its refractive index. Since the light wave being scattered itself generates the acoustic waves, it can cause input light degradation. The Brillouin frequency is about 10.8 GHz in 1550-nm region in single mode fiber.

In this letter, we propose a bidirectional transmission system with OSSB modulation scheme using stimulated Brillouin scattering (SBS) effect in fiber and injection locked distributed-feedback (DFB) laser for downlink transmission For uplink transmission, we reuse the transmission light to carry uplink data with its phase by PM to avoid transmission signals interference. The results show that good performance is achieved in this bidirectional ROF transport system.

2. EXPERIMENTAL SETUP

The bidirectional ROF transport system based on SBS effect and DFB laser injection is shown in Fig. 1. The tunable laser is used for master laser and the DFB laser is as slave laser. The wavelength of DFB laser is 1546.58 nm. The main parts of transmitter consists of a tunable laser source (TL), a microwave signal generator, a RF power amplifier, a RF power splitter, a mixer, a semiconductor optical amplifier (SOA), and a Mach-Zehnder modulator (MZM). The microwave signal is generated at 10.8 GHz by a microwave signal generator then fed into a RF power splitter to split two copies. One copy of RF signal passes through a RF power amplifier to increase signal power then couples into a mixer. The other copy supplies to another RF power amplifier to increase signal power as local oscillation (LO) signal of receiver. The 622 Mb/s non return-to-zero (NRZ) pseudorandom bit sequence (PRBS) length of $2^{31} - 1$ is mixed with a 10.8 GHz microwave carrier to generate the
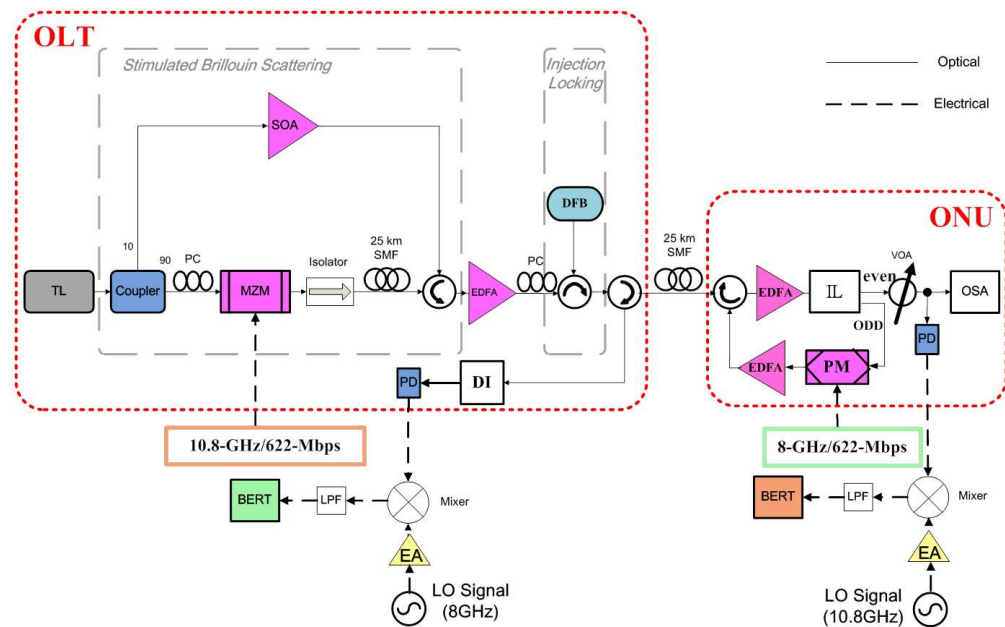
Figure 1: Experimental setup for bidirectional ROF transport system based on SBS effect and DFB laser injection.

up-conversion data signal, and the resulting microwave data signal is supplied to the MZM. TL output signal launches into a 10 : 90 coupler. The 90% light is modulated by the microwave data signal at 10.8 GHz via a MZM with insertion loss about 7 dB. The remaining 10% light is amplified by a SOA acts as feedback light for enhanced OSSB modulation. The modulated signal is launched into a 25-km SMF and interacted with the feedback light from the optical circulator (OC). After 25-km SMF transmission, output signal is using injection locked technology by a DFB laser to enhance OSSB modulation. The output OSSB signal goes into an EDFA to amplify for another 25-km SMF transmission. After fiber transmission, optical signal goes into an EDFA to amplify and then separates two parts by an optical interleaver (IL). For even part optical signal measures the optical spectrum by an optical spectrum analyzer (OSA). On the other hand, photo-detector (PD) transforms optical signal to electrical one, then performs down-conversion to base band via a mixer for bit error rate (BER) test Odd part optical signal reuses as uplink light carrier. A 622 Mb/s NRZ PRBS signal mixed with 8 GHz to generate uplink data signal is modulated by PM modulator. The modulated light signal goes into an EDFA to amplify for 25-km SMF transmission. Uplink light signal feeds into delay interferometer (DI) to transfer the phase modulated signal into intensity modulated one. Optical signal goes into receiver to perform O/E convert for BER test.

3. RESULTS AND DISCUSSIONS

Figure 2 is the optical spectrum using DFB laser injection locked. We observe the right sideband is larger 2.33 dB than left sideband because we utilize SBS effect and DFB laser injection locked to enhance the right sideband power. Because of using the SBS effect in fiber, the output spectrum for right sideband of modulated signal is amplified and left sideband is attenuated as well. The optical spectrum is likely optical SSB format. The DFB laser injection locked can double enhance the right sideband of optical spectrum and then the SBPR can be increased.

Figure 3 is the optical spectrum for downlink optical signal in even channel after optical signal passes through IL. We observe the optical signal is OSSB modulation and SBPR is > 15 dB.

Figure 4 shows the optical spectrum for uplink optical signal in odd channel after optical signal is modulated by PM modulator. The transmitting light is successfully remodulated with 622 Mbps/8 GHz RF signal for uplink transmission.

The measured BER curves as a function of the received optical power is plotted in Fig. 5 The received optical power levels at the BER of 10^{-9} are -23.3 dBm (back-to-back), -22.3 dBm (upstream) and -20.5 dBm (downstream). Power penalties about 1 dB (upstream) and 2.8 dB (downstream) for the fiber link are observed at BER test for 25-km SMF transmission.
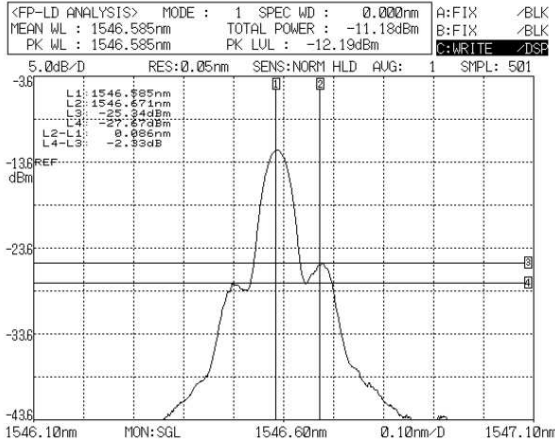
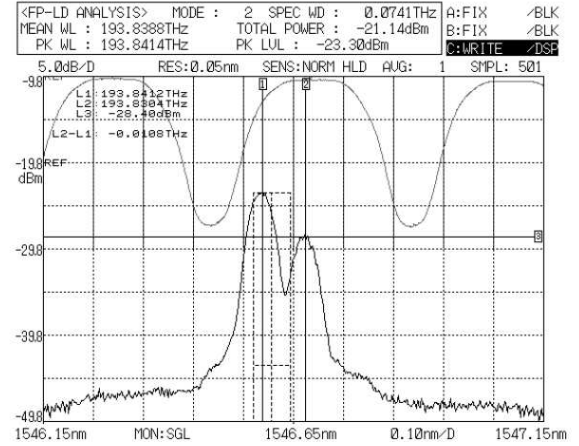Figure 2: Optical spectrum after DFB laser injection locked.

Figure 3: Optical spectrum for downlink in even channel passed through IL.
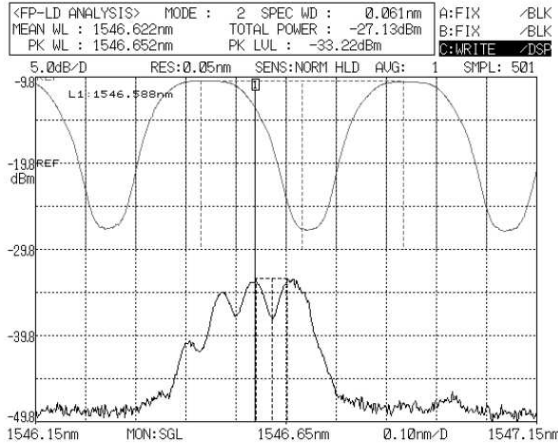

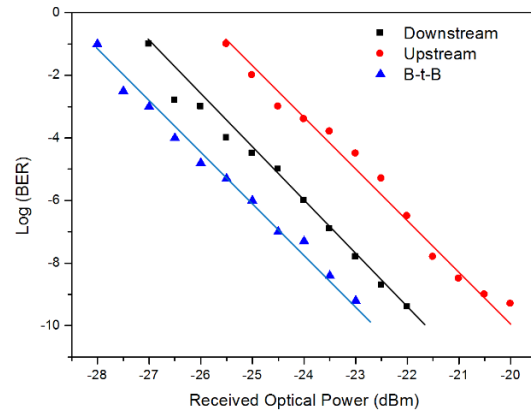Figure 4: Optical spectrum for uplink transmission in back of PM modulator.

Figure 5: Measured BER curves as a function of the received optical power.

The BER is given by

$$\text{BER} = \frac{1}{2} erfc \left(\sqrt{\frac{\text{SNR}}{2}} \right) \tag{1}$$

where SNR is systems' signal-to-noise ratio. External light injection will reduce the threshold current of DFB laser, thus increase the optical output power of DFB. Moreover, SBS effect in fiber and injection locked technology can increase the output lower sideband power and suppress the noise distortion in which leading to SNR increment. The SNR value improves will lead to better BER performances.

4. CONCLUSION

We propose a bidirectional transmission system based on SBS effect and DFB laser injection locked to achieve OSSB modulation in fiber. Two kinds of technologies fall on frequency band approximately nearby 10.8 GHz to enhance OSSB signal. First step we drive 10.8 GHz RF signal into the modulator and then used SBS effect to enhance right sideband Second step based on injection-locked DFB laser to achieve OSSB modulation for downlink transmission. For uplink transport, we reuse transmitting light to carry signal by phase modulation to avoid signals interference. Using the proposed scheme, the 622 Mbps/10.8 GHz RF signals for downlink and 622 Mbps/8 GHz RF signals for uplink are successfully transmitted over a 25-km SMF link, we can observe the sideband power ratio (SBPR) > 15 dB and system's power penalty is < 2.8 dB. The results show good performances are achieved in our purposed bidirectional ROF transport system.

REFERENCES

1. Chi, H. and J. Yao, "Frequency quadrupling and upconversion in a radio over fiber link," *Journal of Lightwave Tech.*, Vol. 26, 2706–2711, 2008.
2. Lee, U. S., H. D. Jung, and S. Kook, "Optical single sideband signal generation using phase modulation of semiconductor optical amplifier," *IEEE Photon Tech. Lett.*, Vol. 16, 1373–1375, 2004.
3. Blais, S. R. and J. Yao, "Optical single sideband modulation using an ultranarrowual-transmission-band fiber bragg grating," *IEEE Photon Tech. Lett.*, Vol. 18, 2230–2232, 2006.
4. Sung, H. K., E. K. Lau, and M. C. Wu, "Optical single sideband modulation using strong optical injection-locked semiconductor lasers," *IEEE Photon Tech. Lett.*, Vol. 19, 1005–1007, 2007.

Transponder and 3R Regenerator Impact on Energy per Bit and Optical Bandwidth Required for Data Transmission over 10-40-100 Gbps Mixed-line Rate WDM Links

Aleksjes Udalcovs and Vjaceslavs Bobrovs

Institute of Telecommunications, Riga Technical University, Riga, Latvia

Abstract— In this paper we aim at exploring the impact of transponders and 3R (re-timing, re-shaping, re-amplification) power consumption on the transmission's power efficiency for the set of link's length and on the optical bandwidth required for the allocation of the wavelength channels which number is chosen in order to minimize the overall energy consumption.

1. INTRODUCTION

Although the mixed-line rate (MLR) design of wavelength division multiplexing (WDM) optical networks has proved itself as a cost-efficient solution for dealing with the heterogeneity of continuously growing traffic demands [1], still some MLR configurations might not be the best in term of energy consumption per bit (or power efficiency in W/bps) required for the accumulation of aggregated traffic [2]. In general, power efficiency of MLR solutions depends on the number of factors, such as power consumption of transponders and 3R (re-timing, re-shaping, re-amplification) regenerators, number of the 10 Gbps, 40 Gbps, and 100 Gbps wavelengths, and the overall transmission distance. Depending on the configuration and the link length the MLR-based WDM system could outperform some of the 10 Gbps, 40 Gbps and 100 Gbps single-line rate (SLR) solutions or not. Therefore, it is important to use the proper criteria (e.g., power consumption of transponder and/or 3R regenerator; spectral efficiency which could be achieved with a particular modulation format; optical bandwidth required for the wavelength allocation in a transmission spectra) for choosing the number of different wavelengths.

Before this research, the power efficiency in WDM fiber-optical links has been studied in number of journal publications and conference papers. In [3], the power efficiency and spectral efficiency have been compared for the number of bitrates, modulation formats and fiber-optical link lengths while securing a given Quality of Transmission (QoT) at the receiving node. In [4], the impact of Mixed-Line Rate (MLR) solutions on the power efficiency and capacity that could be transmitted over the conventional band (C-band) has been compared for the different lengths of the point-to-point links. In [2], the power efficiencies for the number of 10–40–100 Gbps MLR and Single-Line Rate (SLR) solutions have been compared to each other. Such comparison is made for different link lengths in point-to-point WDM system where 3R regeneration of optical signals is made after each section of the link. Each section consists of 40 km long span of standard single mode fiber (SSMF) and inline dispersion compensation module (DCM). Regeneration is required due to the maximum tolerable spectral efficiency for each considered bitrate and modulation format. In this paper we operate with three different bitrates — 10 Gbps realized using the non-return-to-zero on-off keying (NRZ-OOK), 40 Gbps using the NRZ differential phase-shift keying (NRZ-DPSK), and 100 Gbps using the dual polarization quadrature PSK (DP-QPSK). Without 3Rs placed after each section, it would not be possible to fulfill the signal quality requirements at the receiving node. However, none of these publications explore which criterion to use if the optical bandwidth or energy consumption is a constraint when choosing the bitrate and modulation format for the transmission of aggregated traffic. Hence, in this paper we study the effect of transponder and 3R regenerator power consumption on the energy per bit and on the optical bandwidth required for the transmission of aggregated traffic with the BER $\leq 1 \cdot 10^{-9}$ defined signal quality at the receiving node of the FEC-free WDM system.

2. CONTRIBUTION OF THIS PAPER

Firstly, the comparison is given between the energy consumption in SLR and MLR systems required for data transmission over various fiber-optical link lengths. Its detailed configuration is described in [3], while the power consumption of transponder and 3R regenerator and the minimum tolerable frequency intervals were studied in [2, 4] and summarized in [5]. Then, the contribution of 3R regenerators' on overall power consumption is evaluated. This is done for the spectrally efficient

WDM links where signal quality is limited by linear crosstalk and system reach (without 3R regeneration) is fixed to one span of the transmission fiber. In this case, it is 40 km — the medium span length between two inline optical amplifiers [6]. Later on, criteria are studied that could be used when the decision is made about which bitrate and modulation format to use. In our case, the goal for such decision is to reduce the energy consumption while as criteria we used (i) power consumption of transponders and (ii) power consumption of 3R regenerators. And, finally, it is estimated how changes the optical bandwidth required for the transmission of the aggregated traffic depending on its amount and the criterion used to select one solutions (including the bitrate and modulation format) or another. This helps to explore and understand the trade-off between the spectral efficiency and energy per bit (so-called power efficiency) discovered and studied in previous publications, e.g., [2–5].

3. RESULTS AND DISCUSSIONS

This section consists of two subsections where, firstly, the energy per bit for the MLR and SLR solutions are compared and, secondly, the criteria are studied that could be used for making a decision about the use of one bitrate and modulation format or another. The impact of them on the power efficiency (energy consumption per bit) and on the optical bandwidth required for placing the wavelength in the transmission spectra are explored and compared.

3.1. Energy per Bit in WDM Links Based on the Single Line Rate and Mixed Line Rate

In this sub-section, we will analyze the difference between the energy consumption required for 1 bit transmission over MLR and SLR systems. For the SLR solutions, 10 Gbps NRZ-OOK, 40 Gbps NRZ-DPSK and 100 Gbps DP-QPSK wavelengths will be used. In studied MLR solution, number of the 10 Gbps, 40 Gbps and 100 Gbps wavelengths will be based on the realistic distribution among the 10G, 40G and 100G requests in transport optical networks. This distribution could be described using the $50:35:15$ ratio [7]. If it is assumed that for each request the individual wavelength is assigned, then this ratio could be transformed in to the widths of each sub-band: ΔF_{10G}, ΔF_{40G} and ΔF_{100G}. Using the previously discovered minimum frequency intervals between collocated wavelengths, the sub-bands widths are: $\Delta F_{10G} = 16\%$; $\Delta F_{40G} = 74\%$; $\Delta F_{100G} = 10\%$ of the entire band.

More than 2.7 Tbps of traffic could be transmitted over the conventional band (C-band) if it is sub-divided using this ratio and the 10 Gbps, 40 Gbps and 100 Gbps wavelengths are placed with the minimum acceptable frequency intervals between them. In comparison, for the 10 Gbps, 40 Gbps and 100 Gbps SLR solutions it would be 2.34 Tbps, 1.56 Tbps, and 11.70 Tbps, respectively. Figure 1 shows how the energy consumption per bit changes with the transmission distance. These values are normalized against the power efficiency in the 10 Gbps NRZ-OOK SLR solution. As it could be seen in Fig. 1, the lowest energy consumption per bit is reached with the 40 Gbps SLR solution employed the NRZ-DPSK modulation format and only for the transmission distances longer than
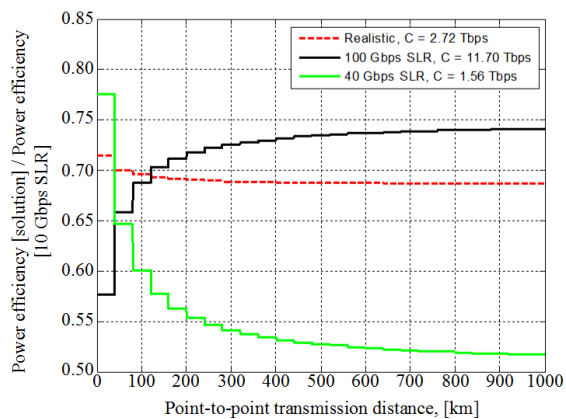

Figure 1: Energy consumption per bit required for the transmission of the aggregated traffic in cases of a spectral efficient SLR and 10–40–100 Gbps MLR solutions.
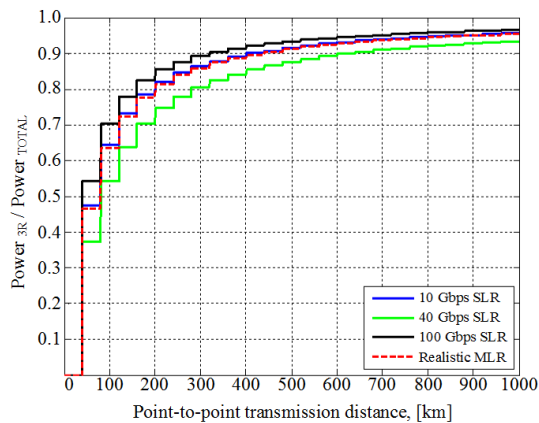
Figure 2: Ration between energy consumption due to 3Rs and the total energy consumption required for the data transmission in a spectrally efficient WDM system.

one span of the transmission fiber. If the transmission distance is more than three SSMF spans
(120 km), 100 Gbps SLR solution became worse than the realistic MLR solution. Therefore, if the
frequency band is not a constraint, then the MLR solutions provide a good compromise between
the power efficiency (energy per bit) and the traffic that could be transmitted over the frequency
band. In addition, it should be highlighted that in term of the energy consumption per bit, 10 Gbps
NRZ-OOK SLR solution is worse than any other considered (see that the values on the Y-axis are
below 1).

Since the optical signals must be regenerated after each link's section due to the maximum
tolerable spectral efficiency, then 3R regenerator power consumption will define mainly the power
efficiency in the WDM link (see Fig. 2). As one could see, the 40 Gbps curve is located below all
others. This evidences about the high energy efficiency of the 40 Gbps NRZ-DPSK regenerators.
Therefore, even if the 40 Gbps SLR solution is the worst in term of the traffic that could be
transmitted over the frequency band, it could be used in spectrally efficient WDM systems to deal
with traffic heterogeneity and to reduce the energy consumption per bit.

3.2. Power Consumption of Transponder and 3R Regenerator as a Criteria for Choosing the Bitrate and Modulation Format

Figure 3 shows the number of 10 Gbps, 40 Gbps and 100 Gbps channels that must be used to
accumulate aggregated traffic if the goal is to do it with the lowest energy consumption possible.
To make a decision about with bitrate and modulation format to use, two different criteria were used
— (i) power consumption value of each considered transponder; (ii) power consumption value of
each considered 3R regenerator. This figure shows a significant difference between these two cases.
Firstly, if the power consumption of transponders is used as a criterion for choosing the bitrate and
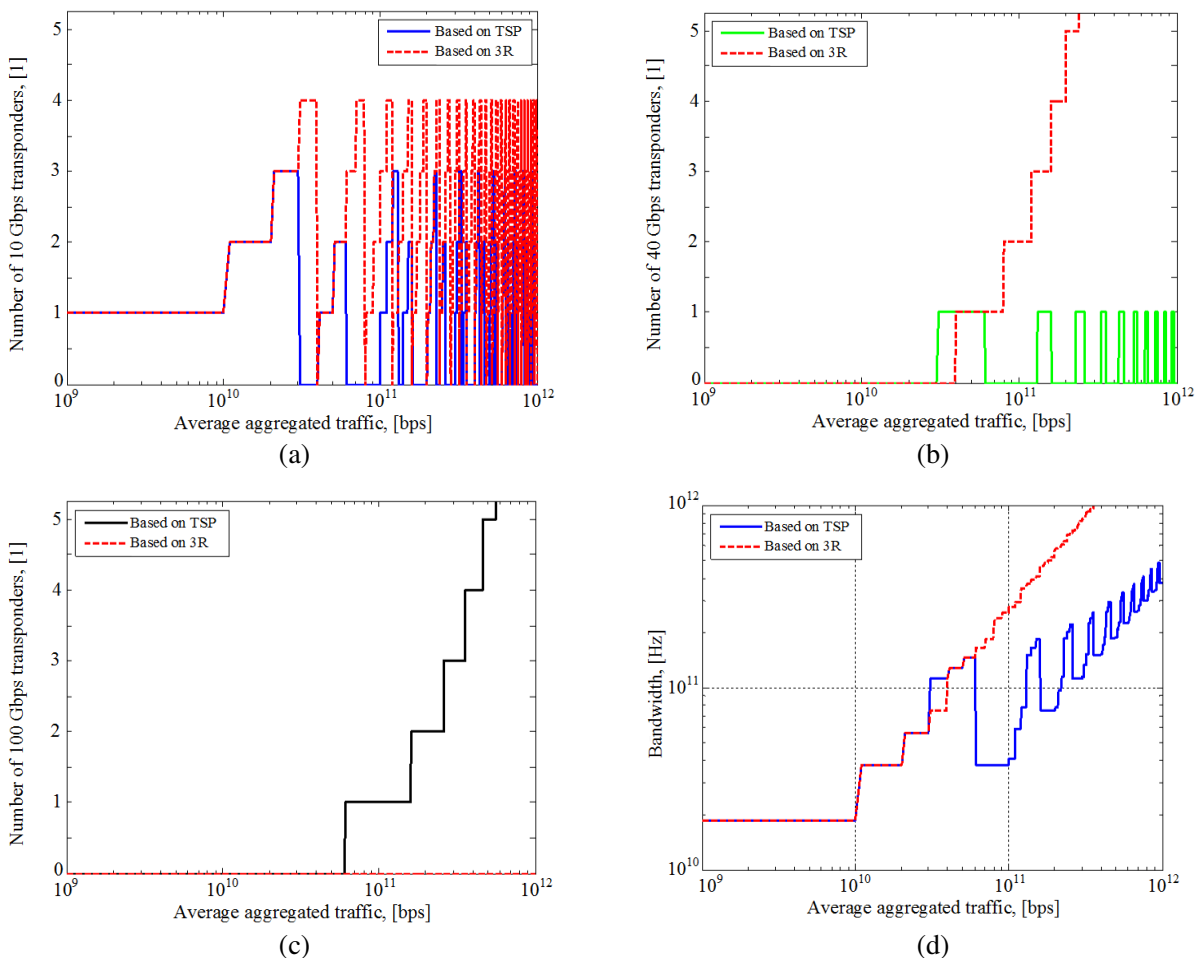

Figure 3: Number of (a) 10 Gbps, (b) 40 Gbps and (c) 100 Gbps wavelengths required for the transmission
of the aggregated traffic amounts, and (d) the optical bandwidth required for placing the wavelengths in
the transmission spectra if the transponder or 3R regenerator power consumptions are used as a criteria for
choosing the bitrate and modulation format.

modulation format, then the lowest energy consumption could be reached if not more than three 10 Gbps NRZ-OOK and not more than one 40 Gbps NRZ-DPSK are used while the number of the 100 Gbps DP-QPSK channels increases with the aggregated traffic amounts. However, situation changes if the power consumption of regenerators is used as a criterion. In this case, the lowest energy consumption could be reached if the number of the 10 Gbps NRZ-OOK channels is not more than four, 100 Gbps DP-QPSK channels are not used at all while the number of the 40 Gbps NRZ-DPSK channels growths with the traffic amount which should be transmitted.

Using the estimated number of channels and discovered previously frequency intervals, we evaluated the frequency bandwidth that must be used to place the required number of wavelengths (see Fig. 3(d)). As one could see, for the traffic amount above 60 Gbps there is a huge difference in the required bandwidths. This difference reaches almost 5 times for the traffic amount more than 300 Gbps. In addition, the decisions made based on power consumption of transponders promote the more efficient use of the frequency band available for transmission. In contrast, for the energy consumption point of view, these decisions must be made based on the power consumption of 3R regenerators.

4. CONCLUSIONS

This paper explores how the criterion used to make a decision about which bitrate and modulation format to use for the transmission of aggregated traffic effects the energy consumption per bit and the required optical bandwidth for placing the wavelength channels. Two different criteria are studied — (i) power consumption of transponders and (ii) power consumption of 3R regenerators. This research performed for the spectrally efficient WDM systems based on the MLR and SLR designs. In such fiber-optical links, system reach is limited by one span of transmission fiber. Therefore, the main power consumer is 3R regenerators in such WDM systems.

After having analyzed the presented results, it should be concluded that aggregated traffic must be transmitted mainly by the 100 Gbps DP-QPSK wavelengths if the optical bandwidth is the constraint. In contrast, the 40 Gbps NRZ-DPSK wavelengths should be used mainly, if the energy consumption is the constraint. In both case, the 10 Gbps NRZ-OOK wavelengths also should be used for both — reduction of energy consumption and accumulation of traffic heterogeneity. Hence, the mixed-line rate approach ensures a good trade-off between the power efficiency and spectral efficiency in the frequency band.

ACKNOWLEDGMENT

REFERENCES

1. Vizcaino, J. L., Y. Ye, and I. T. Monroy, "Energy efficiency analysis for flexible-grid OFDM-based optical networks," *The Int. J. of Comp. and Telecomm. Netw.*, Vol. 56, No. 10, 2400–2419, Jul. 2012.
2. Udalcovs, A., V. Bobrovs, and G. Ivanovs, "Comparison between power efficiency of mixed-line rate over single line rate in spectral efficient WDM networks with signal quality guarantee," *Latin Com.*, 1–6, 2013.
3. Udalcovs, A., P. Monti, V. Bobrovs, R. Schatz, and L. Wosinska, "Power efficiency of WDM networks using various modulation formats with spectral efficiency liminted by linear crosstalk," *Optics Communications*, No. 318, 31–36, 2014.
4. Udalcovs, A., P. Monti, V. Bobrovs, R. Schatz, L. Wosinska, and G. Ivanovs, "Spectral and energy efficiency considerations in mixed-line rate WDM networks with signal quality guarantee," *ICTON 2013*, 1–6, Tu.D1.3, 2013.
5. Bobrovs, V., P. Gavars, G. Ivanovs, I. Trifonovs, and A. Udalcovs, "Transponder impact on power and spectral efficiencies in WDM links based on 10–40–100 Gbps mixed-line rates," *PIERS Proceedings*, 1664–1668, Guangzhou, Aug. 25–28, 2014.
6. Heddeghem, W. V., F. Idzikowski, W. Vereecken, D. Colle, M. Pickavet, and P. Demeester, *Journal of Photonics Networks Communications*, No. 24, 86–112, 2012.
7. Rival, O. and A. Morea, "Resource requirements in mixed-line rate and elastic dynamic optical networks," *OFC/NFOEC 2012*, 1–3, 2012.

Diffraction Effects on a Dual External Cavity Tunable Laser ECTL Source

Ahmed Fawzy[1], Osama Elghandour[2], and Hesham F. A. Hamed[1]

[1]Electrical Engineering Department, Faculty of Engineering, Minia University, Minia, Egypt
[2]Electronics and Communications Engineering Department, Faculty of Engineering
Helwan University, Cairo, Egypt

Abstract— Diffraction and truncation effects are the important effects that appear due to miniaturization of the external cavity tunable laser source ECTL. So in this paper presents the diffraction effects on the performance of an dual external cavity tunable laser source, whose external cavities are constructed by micro electro mechanical systems (MEMS). One of the main problems in these structures is the optical diffraction as the emitting surface of the laser diode is usually quite limited in the transverse directions. The emitted beam diffracts rapidly in the air and only a small amount of light is coupled back to the source that usually limits the tuning range of the source. The simulation results have shown that dual external cavity has large tuning range than single external cavity by using new expression. It is shown that multiple reflection has significant effect in our model. To get a better engineering for the dual ECTL dimensions, diffraction and Truncation effects must be taken into account.

1. INTRODUCTION

Tunable lasers have wide applications in communication especially in wave length division multiplexing (WDM), sensing application and measurements [1–3]. There are three specifications must achieved in tunable laser to be applicable in modern applications. The specification are the wide tuning range, high tuning speed and miniaturized device dimensions [3–8]. These three specifications can be achieved using the Micro Electro Mechanical System (MEMS) technology [2, 3].

There are many features. That make MEMS technology preferred in fabrication of micromechanical structures such as self aligned, fast response in moving, high accuracy and enhanced mechanical stability [3, 9, 10]. The MEMS technology can add a lot of features like the small size, low weight as well as high tuning speed. For this purpose, MEMS based tunable laser structures have been proposed and tested in the literature using different structures [2, 3]. These structures are mainly based on one external cavity semiconductor laser in which the external cavity is formed by a moving MEMS mirror but suffer from lower tuning range. To increase the tuning range grating must be used in the structures such as Littrow or Littman but also these structures suffer from large size [2–4]. So in this paper dual external cavities is used to enhance tuning range than single external cavity and also miniaturize size than Littrow and Littman [11, 12]. The configuration consists of two cavities one reflective movable mirror element was placed close to the original cavity to form first cavity and the second mirror is transparent mirror. It was placed far from original cavity to form the second cavity. One way to fabricate this moving mirror as well as its actuator is to use the Deep Reactive Ion Etching DRIE technology on SOI wafer [2, 9, 10]. The objective of this paper is to study the diffraction in the MEMS based dual external cavity tunable laser source and to prove that the tuning range is increased in case of dual external cavity. Simulation of the optical field propagation in the structure is verified by accurate theoretical model [13]. In the model each external cavity can be represented by using effective reflection coefficient. The model is based on the plane wave expansion method. The calculation of tuning range through an effective phase perturbation technique is done by using effective reflection coefficient. In this technique phase oscillation condition for the laser oscillator is changed due to perturbation that come from external cavity phase. Based on that, the new resonance frequency (emission wavelength) is then calculated.

2. SYSTEM MODEL

MEMS dual external cavity tunable laser is shown in Fig. 1 with two external mirrors assumed to have finite dimensions limited by the technological capabilities of the DRIE technology. In our formulation we assume that L is the primary cavity's length (containing the active medium), L_{ext1} is the length of the first external cavity, L_{ext2} is the length of the second external cavity, r_1 and r_2 are the reflectivities of the facets forming the original cavity, r_{ext1} is the reflectivity of the first
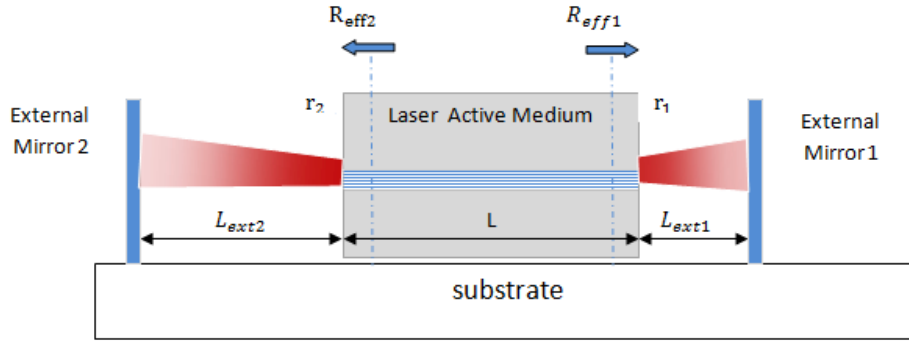
Figure 1: Schematic diagram of the studied dual ECTL source.

external mirror and r_{ext2} is the reflectivity of the second external mirror. The external reflector can be combined with the facet of the primary cavity yielding an effective reflectivity r_{eff} [12, 14] that can be expressed as:

$$r_{eff1}(\nu) = r_1 - \frac{1-R_1}{r_1}\sum_{n=1}^{\infty}\left(-r_1 r_{\text{ext1}}e^{2i\theta_{r1}}\right)^n \tag{1}$$

$$r_{eff1}(\nu) = |r_{eff1}|\exp\left(-j\emptyset r1\right) \tag{2}$$

$$r_{eff2}(\nu) = r_2 - \frac{1-R_2}{r_2}\sum_{n=1}^{\infty}\left(-r_2 r_{\text{ext2}}e^{2i\theta_{r2}}\right)^n \tag{3}$$

$$r_{eff2}(\nu) = |r_{eff2}|\exp\left(-j\emptyset r2\right) \tag{4}$$

r_{eff1}, r_{eff2}, $\emptyset r1$, $\emptyset r2$ represent the amplitude and phase of effective reflectivity of first external cavity and second external cavity respectively, R_1, R_2 is the power reflectivity of the two facets of the primary cavity and θ_r represents the phase term corresponding to each external cavity length at wavelength λ. In the dual external cavity tunable laser the external mirror of the second cavity is actually transparent so in this paper we make classification for the coupled feedback based on the first external mirror only. In case of weak feedback, $r_{\text{ext1}} \ll r_1$, so we can neglect multiple reflection and can substitute in Equation (1) by $n = 1$. In case of strong feedback, $r_{\text{ext1}} \gg r_1$, multiple reflections will affect the total amplitude and phase of effective reflectivity. From the previous work the best external cavity reflectivity is for the external cavity mirror to match the reflectivity of both internal mirror of the primary cavity [12]. As the optical frequency is mainly determined from the phase condition in the round trip of the laser cavity, we calculate the change in the round trip phase due to the existence of the external cavities. When the phase takes values of multiples of 2π, the oscillation condition can be satisfied again and a laser longitudinal mode oscillates. This change in the phase can be calculated from Equation (5) [15]:

$$\Delta\emptyset_l = 2\pi\tau_l\left(\nu - \nu_{th}\right) + \emptyset_r - \left[\alpha\left[\ln\frac{1}{|r_{eff1}|\,|r_{eff2}|} - \ln\frac{1}{|r_1|\,|r_2|}\right]\right] \tag{5}$$

where τ_l is the round trip time delay of the optical beam inside the primary laser cavity, $\emptyset_r$ represent the total phase of effective reflectivity due to two cavities, ν is the new oscillation frequency and ν_{th} is the oscillation frequency before using an external cavities and α is the linewidth enhancement factor in the semiconductor material. From this relation, we can find a new formula for the frequency shift of the laser emission that result due to using dual cavities as follows:

$$\text{Freq shift} = v - v_{th} = \frac{\left[\alpha\left[\ln\frac{1}{|r_{eff1}||r_{eff2}|} - \ln\frac{1}{|r_1|*(|r_2|)}\right] - \emptyset r\right]}{2\pi\tau_l} \tag{6}$$

This expression for the frequency shift is valid for both weak and strong feedback reflections. It can thus be used to study the effect of the diffraction on the frequency shift and hence on the resonance frequency of the laser.

To calculate this frequency shift, it is required to evaluate both the amplitude and phase of the reflected beam after travelling in the external cavity. For this purpose we use the plane wave

expansion method. In this technique, the output beam from the active medium is analyzed as a superposition of plane waves. Each plane wave has its amplitude and phase determined from the field profile using the Fast Fourier Transform FFT technique. Propagation in the external cavity is represented for each plane wave component as a multiplication by a free space transfer function [16]. The total field composed of all the plan waves is then constructed again at the surface of the external reflector using the inverse Fourier transform IFFT to return to spatial domain. When the external mirror has finite dimensions, part of beam is reflected by mirror reflectivity and another part doesn't reflect due to finite mirror size and thus we have a truncated beam. The part that reflected from mirror is modulated by the shape of mirror. The reflected beam is then transformed again to the spectral domain and propagated in the free space as before. When arriving back to the laser diode surface, the beam is returned back to the spatial domain using the IFFT and its coupling to the cavity is calculated using the overlap integral with the cavity mode [6].

For the infinite mirror, the tuning range of dual external cavity tunable laser is higher than single external cavity tunable laser as shown in Figure 2. In our calculation we assume that the laser output is an elliptical Gaussian beam with a spot size of about $3.5\,\mu\text{m}$ in the x direction and $1\,\mu\text{m}$ in the y direction [16–19]. The field distribution at the output of the laser diode can thus be expressed as

$$E(x,y) = E_m e^{\frac{-X^2}{W_{0x}^2} + \frac{-Y^2}{W_{0y}^2}} \tag{7}$$

where E_m is the field amplitude at the center of the beam, w_{ox} is the spot size in the x direction and w_{oy} is the spot size in the y direction and the beam phase front is assumed at the emitting edge of the laser diode surface. The laser source is emitting at the wavelength of 1550 nm. Because of the spot diffraction and in the absence of any focusing element, the external cavity length needs to be very short to maintain feedback efficiency acceptable. For a mirror with finite height, the power loss is more important as part of it is due to the diffraction effect and another part is due to truncation caused by the finite mirror height.

3. RESULTS

For weak feedback with $r_{\text{ext1}} \ll r_1$, in dual configuration, we assume only one round trip in the calculation. For an external mirror with high reflection coefficient, the optical beam intensity, after
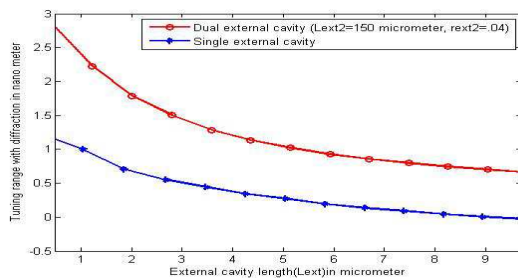

Figure 2: Tuning range of two different configurations as a function of the external mirror position.
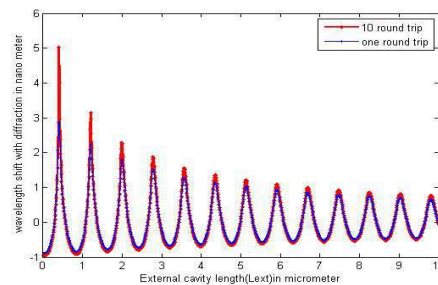

Figure 3: Wavelength shift of an dual external cavity tunable laser as a function of the external mirror position for moderate reflection coefficient first external mirror (0.32).
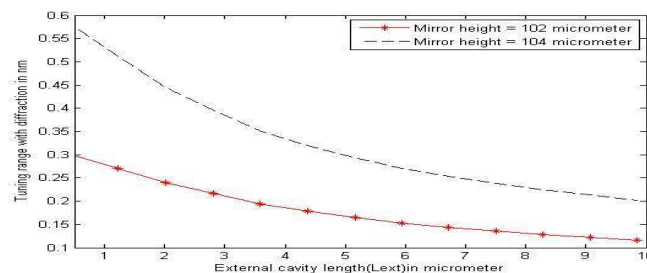

Figure 4: Tuning range of an ECTL as a function of the external mirror position for different flat mirror dimensions h_m, and optical axe height $h = 100\,\mu\text{m}$.

one round trip, may still be strong enough to perturb the operation of the laser. A model that accounts for the multiple reflections of the beam in the external cavity is thus developed. This situation is closer to the practical case as usually the mirror is coated by a metal to increase its reflection coefficient. We first examine the effect of multiple reflections on the laser performance when the external mirror reflection is moderate and the obtained results are presented in Figure 3. In case of multiple reflections the amplitude of the beam that coupled back to the laser is increased so the tuning range is increased also. Part of light that reflect from external mirrors is lost due to finite height of mirror as we see in Figure 4.

4. CONCLUSION

In this work we studied the diffraction effects on the single and dual external cavity tunable lasers and calculated the tuning range in both cases by using accurate developed model. The model accounts also multiple reflections in the external cavity tunable laser. The model shows that strong reflection can increase the tuning range. when the beam is truncated due to the finite size of the mirror, the tuning range is decreased. Based on these effects, the external cavity dimensions can be engineered for a required tuning range.

REFERENCES

1. Coldren, L. A., G. A. Fish, Y. Akulova, J. S. Barton, L. Johansson, and C. W. Coldren, "Tunable semiconductor lasers: A tutorial," *Journal of Lightwave Technology*, Vol. 22, No. 1, 193, 2004.

2. Liu, A. Q., *Photonic MEMS Devices Design, Fabrication and Control*, CRC press, 2009.

3. Liu, A. Q. and X. M. Zhang, "A review of MEMS external-cavity tunable lasers," *Journal of Micromechanics and Microengineering*, 2004.

4. Liu, A. Q., X. M. Zhang, D. Y. Tang, and C. Lu, "Tunable laser using micro machined grating with continuous wavelength tuning," 2004.

5. Zhang, X. M., A. Q. Liu, D. Y. Tang, and C. Lu, "Discrete wavelength tunable laser using microelectromechanical systems technology," 2003.

6. Solgaard, O., *Photonic Microsystems: Micro and Nanotechnology Applied to Optical Devices and Systems*, Springer, 2009.

7. Liu, A. Q., X. M. Zhang, V. M. Murukeshan, and Y. L. Lam, "A novel device level micro machined tunable laser using polysilicon 3D mirror," *IEEE Photon. Technol. Lett.*, Vol. 13, 427–429, 2001.

8. Zhu, W. M., W. Zhang, H. Cai, J. Tamil, B. Liu, T. Bourouina, and A. Q. Liu, "AMEMS digital mirror for tunable laser wavelength selection," 2009.

9. Sabry, Y. M., D. Khalil, B. Saadany, and T. Bourouina, "Multi-step etching of three-dimensional sub-millimetre curved silicon microstructures with in-plane principal axis," *Journal of Microelectronic Engineering*, 2013.

10. Sabry, Y. M., B. Saadany, D. Khalil, and T. Bourouina, "Silicon micromirrors with three-dimensional curvature enabling lens-less efficient coupling of free-space light," *Light: Science & Applications, Nature Publishing Group*, Vol. 2, e94, 2013.

11. Zhu, X. and D. T. Cassidy, "Liquid detection with InGaAsP semiconductor lasers having multiple short external cavities," *Applied Optics*, Vol. 35, No. 24, 4689–4693, 1996.

12. Abu-El-Magd, A. M., "Double tuning of a dual external cavity semi conductor laser for broad wavelength tuning with high side mode suppression," Master Thesis, McMaster University, 2005.

13. Fawzy, A. M., S. El-Sabban, I. I. Ismail, and D. Khalil, "On the modeling of an external cavity tunable laser ECTL source with finite mirror dimensions," *PIERS Proceedings*, 691–694, Stockholm, Aug. 12–15, 2013.

14. Voumard, C., R. Salathe, and H. Weber, "Resonance amplifier model describing diode lasers coupled to short external resonators," 1976.

15. Petermann, K., *Laser Diode Modulation and Noise*, Kluwer, London, 1988.

16. Saleh, B. E. A. and M. C. Teich, *Fundamentals of Photonics*, Wiley, 2007.

17. Bandres, M. A. and J. C. Gutiérrez-Vega, "Elliptical beams," *Optical Society of America*, 2008.

18. Marincic, A., "Huygens-Kirchhoff's theory in calculation of elliptical gaussian beam propagation through a lens," *Mikrotalasna Revija*, 2002.

19. Heikkinen, V., J. K. Aikio, T. Alojoki, J. Hiltunen, A.-J. Mattila, J. Ollila, and P. Karioja, "Single-mode tuning of a 1540-nm diode laser using a Fabry-Pérot interferometer," *IEEE Photon. Technol. Lett.*, Vol. 16, 1164–1166, 2004.

A Generalized Vector-potential Integral Formulation for the Paraboloidal Reflector Antenna

F. O. Okewole[1], **S. A. Adekola**[1, 2], **and A. Ike Mowete**[1]

[1]Department of Electrical and Electronics Engineering, Faculty of Engineering
University of Lagos, Lagos, Nigeria
[2]Department of Electrical and Electronics Engineering
Niger Delta University, Wilberforce Island, Yenegoa, Nigeria

Abstract— This paper develops a generalized vector magnetic potential integral formulation for the paraboloidal reflector antenna, using the elliptic paraboloid geometry as basis. First, parametric expressions informed by the problem geometry are specified for the conventional 'field' and 'source' points, and the ellipse's major and minor axes are described by a common expression, also based on the geometry. When the expressions are utilized in the integral equation for the vector magnetic potential for the problem, and following the usual 'magnitude' and 'phase' approximations, an expression for the radiation field, which may be described as a general expression for certain special cases, emerges. It is shown for example, that when the ellipse's eccentricity is set to zero to prescribe the circular paraboloid, the corresponding expression for the radiation agrees with those available in the open literature [1, 2].

1. INTRODUCTION

One of the earliest analytical treatments of the paraboloidal reflector was reported by Jones [3], whose analysis of the paraboloid reflector excited by short electric dipole, utilized the induced surface current approach to determine the reflector's aperture distribution. Thereafter, quite a few other analytical investigations have been reported over the years, and some of the more noteworthy of these, as noted by Lorenzo et al. [9], include the surface current (or aperture field) integration approach, GTD/GO [5] combination approach, the Uniform Asymptotic Theory, and the Physical Theory of Diffraction, to mention a few. In a relatively recent development, Lashab et al. [4] described a wavelet-based (basis and testing functions) moment-method solution of a physical optics formulation of the radiation field problem for a large reflector antenna. Ergül and Gürel [10] using a Magnetic-Field Integral Equation (MFIE) formulation, also described a moment-method technique, in which the MFIE is numerically discretized with the use of RWG curl-conforming expansion and testing functions defined on planar triangulations.

This paper presents an Electric Field Integral Equation (EFIE) formulation of the paraboloidal reflector antenna problem based on the 'parametric approach' described elsewhere [6, 7]. This formulation is particularly suitable for a moment-method solution, as the radiation fields of the antenna are easily determined, once an approximation to the current density is available.

2. PROBLEM FORMULATION

The coordinate system description of an elliptical parabola of revolution is given in Figure 1.

Primed quantities represent source point and unprimed for field point. $\bar{r}'$ is the distance from the focus (origin) point to the surface of the reflector (S) whilst $\bar{r}$ represents the distance from focus to the field (observation) point, P. Consequently, $\bar{R}$ is the distance between the surface of the reflector and the observation point. According to [6], the position vector $\bar{r}'$, can be written in parametric form as:

$$\bar{r}' = at\cos\varphi'\hat{x} + bt\sin\varphi'\hat{y} + ht^2\hat{z} \tag{1}$$

where

a = minor axis;
b = major axis;
h = height;
t = parameter.

The parameters 'a' and 'b' specified above can be related through eccentricity of the geometrical shape, so that a single equation will suffice to describe both of them and considerably simplify the
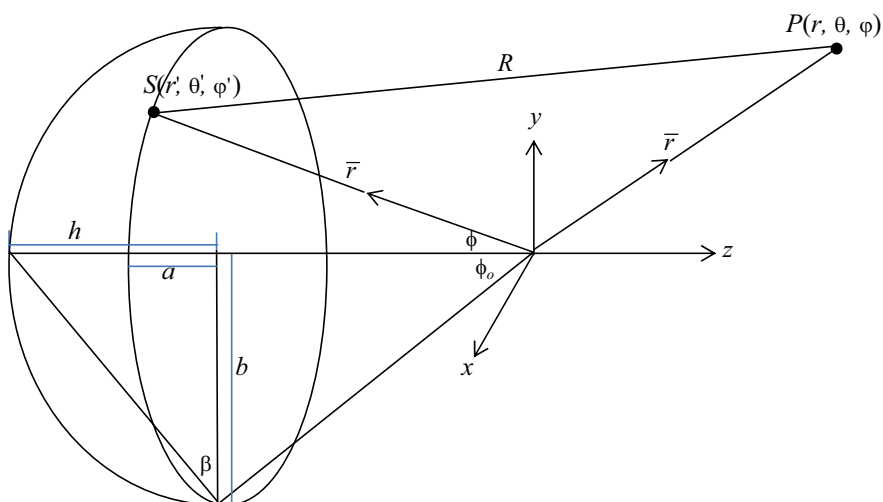
Figure 1: Coordinate geometry for an elliptic paraboloid antenna.

problem. Accordingly, if use is made of the fact established in [7], then the parameters can be represented by the same equation. Thus, the equation can be expressed as

$$r\left(\theta'\right) = \rho'\sqrt{\frac{1-e^2}{1-e^2\cos^2\theta'}} \tag{2a}$$

where

$$\rho' = \frac{2f}{1+\cos\theta'} \tag{2b}$$

$$f = \text{focal length}$$

Expression for the height of the antenna emerges from the geometry in Figure 1 and [8] as

$$dh = ds\tan\beta \tag{3a}$$

where

$$ds = \sqrt{(dx)^2+(dy)^2} = r\left(\theta'\right)t \tag{3b}$$

$$\therefore \ dh = = r\left(\theta'\right)t\tan\beta \tag{3c}$$

The integration of both sides of (3c) admits

$$h = t\tan\beta\int_0^{\pi/2} r\left(\theta'\right)d\varphi' \tag{4a}$$

Let

$$k\left(\varphi'\right) = \int_0^{\pi/2} d\varphi' \tag{4b}$$

Then,

$$h = (2/\pi)\,r\left(\theta'\right)tk\left(\varphi'\right)\tan\beta \tag{4c}$$

The substitution of (2a), (2b) & (4c) into (1) yields

$$\bar{r}' = r\left(\theta'\right)t\cos\varphi'\hat{x} + r\left(\theta'\right)t\sin\varphi'\hat{y} + (2/\pi)\,r\left(\theta'\right)t^3 k\left(\varphi'\right)\tan\beta\hat{z} \tag{5}$$

The magnetic vector potential, assuming perfect electric conductor, for the antenna is given as

$$\bar{A}(\theta,\varphi) = \frac{\mu t^2}{4\pi} \iint_S \bar{J}(\theta',\varphi') \frac{e^{-jkR}}{R} r^2(\theta') g(\theta') \sqrt{\sec^2\beta + (4/\pi^2)k^2(\varphi')t^4 \tan^2\beta} d\theta' d\varphi' \quad (6)$$

For a moment method solution of the foregoing problem, (6) can be re-written as

$$\bar{A}(\theta,\varphi) = \frac{\mu}{4\pi} \iint_S J(\theta',\varphi') \frac{e^{-jkR}}{R} r^2(\theta') g(\theta') \Big\{ (\sin\varphi' \tan\beta - (2/\pi)k(\varphi')\cos\varphi' t^2 \tan\beta)\,\hat{x}$$

$$+ (\cos\varphi' \tan\beta + (2/\pi)k(\varphi')\sin\varphi' t^2 \tan\beta)\,\hat{y} + \hat{z} \Big\} d\theta' d\varphi' \quad (7a)$$

where,

$$g(\theta') = \left[\frac{\sin\theta'}{1+\cos\theta'} + \frac{e^2 \sin 2\theta'}{(1+\cos\theta')(1-e^2\cos^2\theta')} \right] d\theta' \quad (7b)$$

To derive the expressions for far field region, the phase term reduces to

$$R = |\bar{r} - \bar{r}'| = \bar{r} - \bar{r}' \cdot \hat{a}_r \quad (8a)$$

and the amplitude term

$$R = r \quad (8b)$$

subsequently,

$$\bar{r}' \cdot \hat{a}_r = r(\theta')\, t \sin\theta \left[\cos(\varphi - \varphi') + (2/\pi)k(\varphi')\cot\theta t^2 \tan\beta \right] \quad (8c)$$

let

$$\zeta = \cos(\varphi - \varphi') + (2/\pi)k(\varphi')\cot\theta t^2 \tan\beta \quad (8d)$$

(8c) can be re-written as

$$\bar{r}' \bullet \hat{a}_r = r(\theta')\, t \sin\theta\, \zeta \quad (8e)$$

Substituting (8a), (8b), & (8e) into (7a), the equation becomes

$$\bar{A}(\theta,\varphi) = \frac{\mu e^{-jkr}}{4\pi r} \int_0^{2\pi} \int_0^{\pi} \Big\{ J(\theta',\varphi')\, e^{jkr(\theta')t \sin\theta\zeta} r^2(\theta') g(\theta')$$

$$(\sin\varphi' \tan\beta - (2/\pi)k(\varphi')\cos\varphi' t^2 \tan\beta)\,\hat{x}$$

$$+ (\cos\varphi' \tan\beta + (2/\pi)k(\varphi')\sin\varphi' t^2 \tan\beta)\,\hat{y} + \hat{z} \Big\} d\theta' d\varphi' \quad (9)$$

The generalized formulated magnetic vector potential is presented in Equation (9).

For circular paraboloid, eccentricity will be equal to zero and consequently, Equation (9) reduces to

$$\bar{A}(\theta,\varphi) = \frac{\mu e^{-jkr}}{4\pi r} \int_0^{2\pi} \int_0^{\pi} \Big\{ J(\theta',\varphi')\, e^{jkr(\theta')t \sin\theta\xi} \rho'^2 \sec\left(\frac{\theta'}{2}\right) \sin\theta'$$

$$(\sin\varphi' \tan\beta - (2/\pi)k(\varphi')\cos\varphi' t^2 \tan\beta)\,\hat{x}$$

$$+ (\cos\varphi' \tan\beta + (2/\pi)k(\varphi')\sin\varphi' t^2 \tan\beta)\,\hat{y} + \hat{z} \Big\} d\theta' d\varphi' \quad (10a)$$

$$\xi = \cos(\varphi - \varphi') + \cot\theta t^2 \tan\beta \quad (10b)$$

Equation (9) is in agreement with similar expressions reported in [2]. Equation (10a) can be re-written in terms of Cartesian coordinates as

$$\bar{A}_x(\theta, \varphi) = \frac{\mu e^{-jkr} \tan \beta}{4\pi r} \int_0^{2\pi} \int_0^{\pi} J(\theta', \varphi') \, e^{jkr(\theta')t \sin \theta \xi} \rho'^2 \sec\left(\frac{\theta'}{2}\right) \sin \theta'$$

$$\left(\sin \varphi' - (2/\pi) \, k(\varphi') \, t^2 \cos \varphi'\right) d\theta' d\varphi'$$

$$\bar{A}_y(\theta, \varphi) = \frac{\mu e^{-jkr} \tan \beta}{4\pi r} \int_0^{2\pi} \int_0^{\pi} J(\theta', \varphi') \, e^{jkr(\theta')t \sin \theta \xi} \rho'^2 \sec\left(\frac{\theta'}{2}\right) \sin \theta' \qquad (11)$$

$$\left(\cos \varphi' + (2/\pi) \, k(\varphi') \, t^2 \sin \varphi'\right) d\theta' d\varphi'$$

$$\bar{A}_z(\theta, \varphi) = \frac{\mu e^{-jkr}}{4\pi r} \int_0^{2\pi} \int_0^{\pi} \left\{ J(\theta', \varphi') \, e^{jkr(\theta')t \sin \theta \xi} \rho'^2 \sec\left(\frac{\theta'}{2}\right) \sin \theta' d\theta' d\varphi' \right.$$

So that using the identities given as

$$A_\theta = \cos \theta \cos \varphi A_x + \cos \theta \sin \varphi A_y + \sin \theta A_z$$
$$A_\varphi = -\sin \varphi A_x + \cos \varphi A_y$$

we find that the vector magnetic potentials, in both the theta and phi direction, emerge as:

$$\bar{A}_\theta = \frac{\mu e^{-jkr} \cos \theta \tan \beta}{4\pi r} \int_0^{2\pi} \int_0^{\pi} J(\theta', \varphi') \, e^{jkr(\theta')t \sin \theta \xi} \rho'^2 \sec\left(\frac{\theta'}{2}\right) \sin \theta'$$

$$\cdot \left[\sin(\varphi - \varphi') - t^2 \cos(\varphi - \varphi') - \tan \theta \cot \beta\right] d\theta' d\varphi' \qquad (12a)$$

$$\bar{A}_\varphi = \frac{\mu e^{-jkr} \tan \beta}{4\pi r} \int_0^{2\pi} \int_0^{\pi} J(\theta', \varphi') \, e^{jkr(\theta')t \sin \theta \xi} \rho'^2 \sec\left(\frac{\theta'}{2}\right)$$

$$\sin \theta' \left[t^2 \sin(\varphi - \varphi') - \cos(\varphi - \varphi')\right] d\theta' d\varphi' \qquad (12b)$$

At far field region,

$$\bar{E}_\theta = -j\omega \bar{A}_\theta \qquad (13a)$$

and

$$\bar{E}_\varphi = -j\omega \bar{A}_\varphi \qquad (13b)$$

substituting (12a) and (12b) into (13a) and (13b) respectively yields

$$\bar{E}_\theta = -\frac{j\omega\mu e^{-jkr} \cos \theta \tan \beta}{4\pi r} \int_0^{2\pi} \int_0^{\pi} J(\theta', \varphi') \, e^{jkr(\theta')t \sin \theta \xi} \rho'^2 \sec\left(\frac{\theta'}{2}\right) \sin \theta'$$

$$\cdot \left[\sin(\varphi - \varphi') - t^2 \cos(\varphi - \varphi') - \tan \theta \cot \beta\right] d\theta' d\varphi' \qquad (14a)$$

$$\bar{E}_\varphi = -\frac{j\omega\mu e^{-jkr} \tan \beta}{4\pi r} \int_0^{2\pi} \int_0^{\pi} (\theta', \varphi') \, e^{jkr(\theta')t \sin \theta \xi} \rho'^2 \sec\left(\frac{\theta'}{2}\right)$$

$$\sin \theta' \left[t^2 \sin(\varphi - \varphi') - \cos(\varphi - \varphi')\right] d\theta' d\varphi' \qquad (14b)$$

3. DISCUSSION OF RESULTS

It is apparent from the formulation that the use of Equation (2a) for the major and minor axes makes it easy to specialize to circular type. Equation (6) is a general Electromagnetic formulation that can be solved using numerical methods. In particular, a method of moment solution will provide numerical values for the unknown current density to facilitate the evaluation of the antenna's radiation fields with the use of Equations (14a) and (14b).

4. CONCLUSION

A parametric formulation of the paraboloid reflector problem, starting with the elliptical geometry, has been developed in this presentation. A check on the validity of the analytical results obtained was provided by a specialization to the circular type. Integral expressions developed in the paper, for the antenna's radiation fields are particularly suitable for a moment method solution, possibly using wavelet basis and testing functions of the type desribed in [4].

REFERENCES

1. Salman, O. I., A. S. Tahir, and A. A. Al-Hilo, "Theoretical analysis of the radiation fields of parabolic reflector antenna fed by circular shaped microstrip antennas," *Basrah Journal of Science (A)*, Vol. 30, No. 2, 30–43, 2012.
2. Maclean, T. S. M., *Principles of Antennas*, Cambridge University Press, New York, 1986.
3. Jones, E. M. T., "Paraboloid reflector and hyperboloid lens antennas," *IRE Trans. Antennas Propagat.*, Vol. 701, No. 2, 119–127, Jul. 1954.
4. Lashab, M., C. Zebiri, and F. Benabdelaziz, "Wavelet-based moment method and physical optics use on large reflector antennas," *Progress In Electromagnetics Research M*, Vol. 2, 189–200, 2008.
5. Merabtine, N., A. Boualleg, and M. Benslama, "Analysis of radiation patterns and feed illumination of the reflector antenna using the physical and geometrical optics," *Semiconductor Physics, Quantum Electronics & Optoelectronics*, Vol. 9, No. 2, 53–57, 2006.
6. Tuma, J. J., *Engineering Matthematics Handbook*, 3rd Edition, McGraw-Hill Book Company, 2006.
7. Adekola, S. A., A. Ike Mowete, and H. A. Muhammed, "A matrix-vector-potential analysis of the bi-elliptical toroidal helical antenna," *PIERS Proceedings*, 825–829, Marrakesh, Morocco, Mar. 20–23, 2011.
8. Adekola, S. A., A. I. Mowete, and A. A. Ayorinde, "Concerning a generalized formulation for the EM fields radiated by thin-wire antennas," *Proc. of Nat. Conf.*, Dept. Elec. & Elec. Eng., Univ. of Lagos, Jul. 15–17, 2006.
9. Martinez Lorenzo, J. A., A. G. Pino, I. Vega, M. Arias, and O. Rubilinos, "ICARA: Induced-current analysis of reflector antennas," *IEEE Antennas and Propagat. Magazine*, Vol. 47, No. 2, 82–100, Apr. 2005.
10. Ergül, Z. and O. Gürel, "The use of curl-conforming basis function for the magnetic-field integral equation," *IRE Trans. Antennas Propagat.*, Vol. 54, No. 7, 1917–1925, Jul. 2006.

A Compact Dual-band Balanced Slot Antenna for LTE Applications

I. T. E. Elfergani[1], **Abubakar Sadiq Hussaini**[1, 3, 4],
Jonathan Rodriguez[1, 2], **and R. A. Abd-Alhameed**[3]

[1]Instituto de Telecomunicações, Aveiro, Portugal
[2]Universidade de Aveiro, Portugal
[3]Radio Frequency, Antennas, Propagation and Computational Electromagnetics Research Group
School of Electrical Engineering and Computer Sciences, University of Bradford, Bradford, BD7 1DP, UK
[4]School of Information Technology & Communications, American University of Nigeria, Nigeria

Abstract— A low profile dual-band balanced slot antenna is presented and developed, exhibiting a dual-band operation at 700 MHz and 2600 MHz bands with a good impedance matching ($S_{11} \leq -10\,\text{dB}$) for use in Long Term Evolution (LTE) applications. The proposed antenna was implemented based on built-in planar dipoles with a folded arm structure. The antenna occupies a volume of $50 \times 12 \times 4\,\text{mm}^3$ in which mounted on top of a finite ground plane with dimensions of $100 \times 50\,\text{mm}^2$. The performance of the proposed antenna has been analysed and optimised for the two targeted frequency bands. The antenna performance is characterised in terms of the reflection coefficient, radiation pattern and surface current distribution. Owing to the compact size and simple structure, the proposed antenna can be a promising candidate for mobile handset and wireless communication applications.

1. INTRODUCTION

In recent years, the current needed on mobile phone have increased greatly in term of its shape, performances, qualities and its technology. The new technology in wireless communication has brought a lot of portable devices in the future, such as a mobile phone that will possess Long Term Evolution (LTE) function for the voices and data transmissions [1]. Conventionally, the unbalanced planar inverted F antenna (PIFA) is one of the most popular candidates for compact internalized antennas for mobile handsets due to its unique characteristic that makes it suitable for use in portable wireless device especially on mobile handsets.

However, PIFAs use the ground plane as a part of the radiator, enabling very small antennas to achieve adequate gain and bandwidth [2–4]. Therefore, radiating currents are induced on both the ground plane and the antenna element, resulting in currents flowing on the human body, which degrade the performance of the antenna's radiation characteristics and introduce losses and uncertainty in its matching [5].

To solve these problems, a balanced structure is introduced to not only to eliminate such constraints but also to avoid the degradation of antenna performance in aforementioned unbalanced antennas. In this kind of antennas, currents cancel the effect of each other, the current flows only on the antenna element and not on the ground plane. Therefore, the coupling between the antenna and the user's body will be neglected when the mobile is held by its user which leads in no effect on the performance of the antenna. In other word, the currents are mostly confined to the radiating elements, thus reducing the current flow to the ground plane [6]. It follows that a well-designed balanced antenna will reduce the specific absorption rate (SAR) to the user's body [5]. Lately, several mobile antennas with the balanced technique have proved the enhanced stability of antenna performance, compared to the unbalanced type especially when the handset is positioned in a close vicinity to the human head and/or hand [7–10]. However, all these balanced antennas in [7–10] are not capable to meet the present work target, namely 700/2600 MHz frequency bands of LTE. Thus, this work has been investigated to offer a low profile antenna for Long Term Evolution (LTE) applications at 700 MHz and 2600 MHz bands using the balanced antenna concept. The proposed antenna will be implemented based on built-in planar dipoles with two folded slot arms structure.

The layout of the paper is as follow. Section 2 presents the antenna design and concept, the results and discussions were shown and demonstrated in Section 3 and Section 4 is summarized the final conclusions of this study.

2. ANTENNA DESIGN CONCEPT

The proposed balanced antenna was achieved to generate the dual band operation of 700 and 2600 MHz LTE bands. Figure 1 shows the geometry of the balanced antenna for a mobile phone.

The antenna was designed first and then was mounted 4 mm on top of a finite ground plane with dimension of 100×50 mm^2 which acts as the mobile handset chassis or what today we would identify as the ground plane of a practical mobile phone handset, as seen in Figure 1. The dimensions of the proposed antenna geometry were found to be comparable to the practical handset size as illustrated in Table 1. The slot has a uniform width of 2 mm. The antenna was constructed from a copper sheet with thickness of 0.15 mm. One side of the folded dipole antenna, in which the cooper plate was folded up to become a folded dipole antenna as depicted in Figure 1.

Table 1: Detailed dimensions of folded arms radiators.

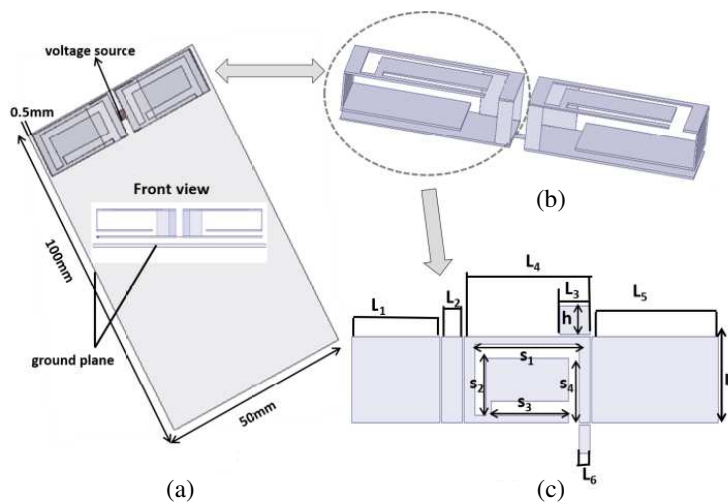| Parameter	Value (mm)	Parameter	Value (mm)
L_1	16	L_7	12
L_2	3.2	S_1	19
L_3	5	S_2	8
L_4	23	S_3	14
L_5	23	S_4	9
L_6	2	h	4

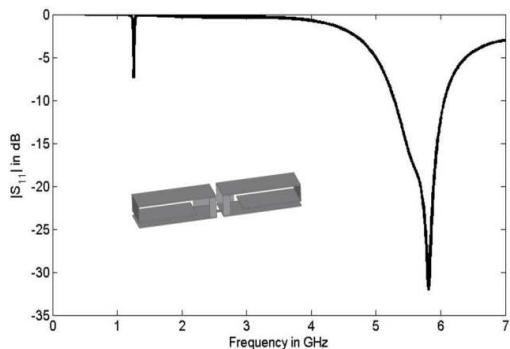Figure 1: Basic antenna structure; (a) 3D, (b) folded slotted arms, (c) unfolded slotted arm.

Figure 2: Reflection coffeicent of folded arms unslotted proposed antenna.
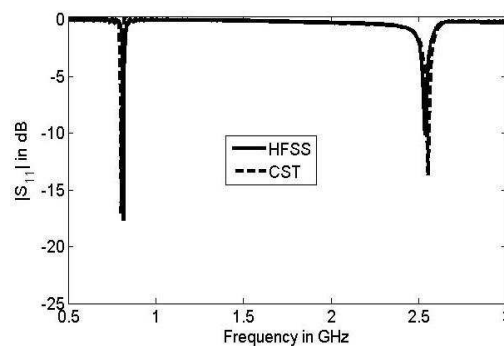

Figure 3: Reflection coffeicent of folded arms slotted proposed antenna.

3. RESULTS AND DISCUSSIONS

In order to accomplish the targeted frequency bands, two procedures were carried out. Firstly, it was started by folding the monopole arm and without slot patterned in both folded arms surface.

The proposed antenna without the inclusion of slot operates at dual band of 1200/5800 MHz as depicted in Figure 2.

However, this was not the desired goal within the proposed work. Therefore, the second step was to create/introduce slots over the surface of both folded arms as shown in Figure 1. The effectiveness of the embedded slot was seen through the simulated S_{11} in two different softwares. I.e., HFSS and CST [11, 12] for comparison and validation purposes. The slot forces the antenna to downshift both aforementioned frequencies obtained from the unslotted antenna. The loaded slot reduces the resonance frequency and thus the electrical antenna dimensions drastically. So, fundamentally, the objective of the slot was to tune the radiator structure to resonate at our targeted bands of LTE 700/2600 MHz. This was achieved through multiple simulated attempts, by conducting several modifications of the antennas in [9, 10] to move toward the desired outcome of developing highly compact and dual-band antenna for use in LTE applications. It is obvious that the S_{11} of proposed antenna generated by HFSS agrees well with the one obtained from the CST as shown in Figure 3.

The analysis of the current surface on the ground plane of the proposed antenna was studied using the EM simulator at the 700 MHz and 2600 MHz. I.e., the targeted frequencies within this work as shown in Figure 4. One can clearly note that, most of the current is induced exactly underneath the two folded slotted arms at both resonant frequencies while it is more or less vanished on the rest of the ground plane in which proves the concept of balanced antenna whereby it reduces the coupling between the handset and the user's hand.
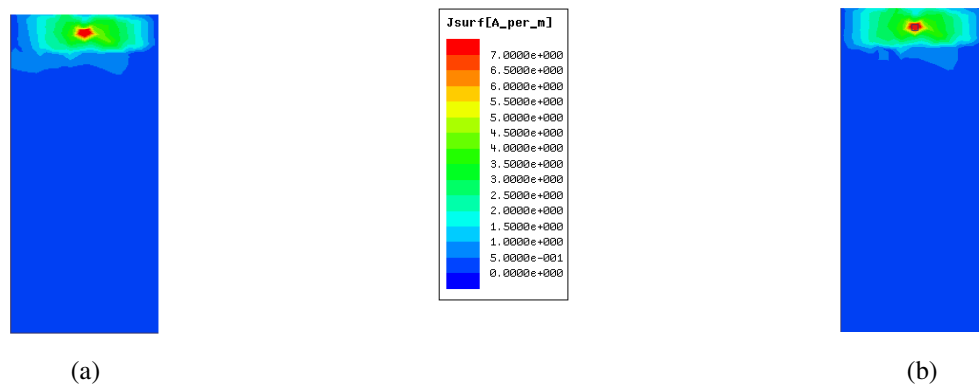

(a)   (b)

Figure 4: Surface current distributions for the proposed balanced antenna at (a) 700 MHz, (b) 2600 MHz.
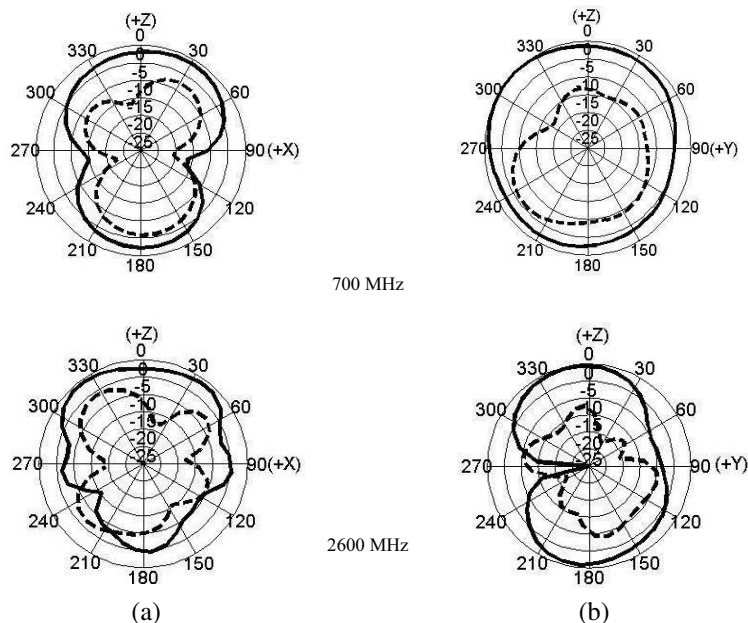

(a)   (b)

Figure 5: Normalized antenna radiation patterns for two planes ((a) xz, (b) yz) at 700 MHz, 2600 MHz, "—" co-polarization, "- - -" cross-polarization.

The radiation patterns of the proposed antenna was shown in Figure 5. Two pattern cuts were taken for both targeted operating frequencies within this study. The radiation patterns in the zx plane and zy plane for the antenna were tested at 700 and 2600 MHz as indicated in Figure 5. The patterns of the proposed antenna are seen to be quite similar to each other for both cases. Moreover, as expected the figures presented a nearly omni-directional radiation pattern in both intended two frequency components.

4. CONCLUSIONS

In this paper, a design methodology for producing miniaturized and compact dual-band balanced folded arm slot antenna suitable for LTE applications has been demonstrated. By embedding a slot over the surface of folded arms of the antenna, it has been shown that a high level of miniaturization can be achieved while covering the 700 and 2600 MHz LTE frequency bands. The results over the two frequency bands and the compact volume are important factors, which leads that the proposed design can be recommended as a promising candidate mobile-antenna solution for LTE applications.

REFERENCES

1. Kumar, N. and G. Saini, "A novel low profile planar inverted-F antenna (PIFA) for mobile handsets," *International Journal of Scientific and Research Publications*, Vol. 3, No. 3, March 2013.

2. Janapsatya, J., K. P. Esselle, and T. S. Bird, "A dual-band and wideband planar inverted-F antenna for WLAN applications," *Microwave and Optical Technology Letters*, Vol. 50, 138–141, January 2008.

3. Elfergani, I., A. S. Hussaini, J. Rodriguez, C. H. See, and R. Abd-Alhameed, "Wideband tunable PIFA antenna with loaded slot structure for mobile handset and LTE applications," *Radio Engineering*, Vol. 23, No. 1, 345–355, April 2014.

4. Elfergani, I. T. E., A. S. Hussaini, R. A. Abd-Alhameed, C. H. See, M. M. Abusitta, H. I. Hraga, A. G. Alhaddad, and J. Rodriguez, "Frequency tuned planar inverted F antenna with L shaped slit design for wide frequency range," *PIERS Proceedings*, 443–447, Marrakesh, Morocco, March 20–23, 2011.

5. Abd-Alhameed, R. A., P. S. Excell, R. A. K. Khalil, and J. Mustafa, "SAR and radiation performance of balanced and unbalanced mobile antennas using a hybrid computational electromagnetics formulation," *IEE Proceedings-Science, Measurement and Technology Special Issue on Computational Electromagnetics*, Vol. 151, 440–444, 2004.

6. Morishita, H., H. Furuuchi, and K. Fujimoto, "Performance of balance-fed antenna system for handsets in the vicinity off a human head or hand," *IEE Proceeding Microwave Antennas Propagation*, Vol. 149, 85–91, 2002.

7. Chiu, C. N. and H. R. Chen, "A new compact balance-fed T-monopole antenna for UMTS mobile applications," *Microwave and Optical Technology Letters*, Vol. 49, 1904–1907, 2007.

8. Sasaki, D., et al., "A planar folded dipole antenna for mobile handset," *IEEE International Workshop on Antenna Technology*, 133–136, March 2005.

9. Alhaddad, A. G., R. A. Abd-Alhameed, D. Zhou, I. T. E. Elfergani, C. H. See, P. S. Excell, and M. S. Bin-Melha, "Low profile balanced handset antenna with dual-arm structure for WLAN application," *IET Microwaves, Antennas and Propagation*, Vol. 5, 1045–1053, 2011.

10. Zhou, D., R. A. Abd-Alhameed, C. H. See, A. G. Alhaddad, P. S. Excell, "Compact wideband balanced antenna for mobile handsets," *IET Microwaves, Antennas and Propag.*, Vol. 4, 600–608, 2010.

11. Ansoft High Frequency Structure Simulator v10 Uses Guide, CA, USA.

12. CST v.5.0, Microwave Studio [online], http://www.cst.com.

Novel Quadrifilar Helical Antenna for RFID Applications Using Genetic Algorithms

M. O. Akinsolu[1], **A. Ali**[1], **A. Atojok**[1], **E. Ibrahim**[1, 2], **I. T. E. Elfergani**[3], **R. A. Abd-Alhameed**[1], **Abubakar Sadiq Hussaini**[1, 3, 5], **J. M. Noras**[1], and **Jonathan Rodriguez**[3, 4]

[1]University of Bradford, Bradford, West Yorkshire, BD7 1DP, UK
[2]College of Electronic Technology Bani Walid, Libya
[3]Instituto de Telecomunicacoes, Aveiro, Portugal
[4]Universidade de Aveiro, Portugal
[5]School of Information Technology & Communications, American University of Nigeria, Nigeria

Abstract— For excellent tag-read communication in RFID applications, an interrogator equipped with an antenna having a circularly polarised radiation pattern is required. The antenna must also maintain a low profile and be compact for ease of installation. A more compact QHA is developed by linearly-shifting its helical elements for minimal optimum quadrature-distance. As a result, a novel QHA design, a "linearly-shifted quadrifilar helical antenna" (LSQHA) is proposed to operate at 900 MHz RFID applications using Genetic Algorithm (GA) driver with the industry-standard NEC-2 computational analysis program. Performance of the GA-optimised antenna shows that it has a 3 dB beamwidth of 90 degrees and a total gain of 13.1 dBi at the design frequency of 900 MHz. The proposed antenna excellently meets VSWR and return loss requirements within the frequency boundary of (875–912.5) MHz. The performance also shows that the proposed LSQHA is circularly polarised.

1. INTRODUCTION

Antennas constitute a very important part of Radio Frequency Identification (RFID) systems [1]. Coming in various forms and types, they are usually designed and intended to ensure maximum effective and efficient communication links between tags or transponders and their associated readers or interrogators. One of the primary challenges in the design and development of antennas in RFID applications as it is in other wireless applications is having an antenna with optimised parametric features that are desirable and in consonance with laid down specifications and functional requirements [1, 2].

RFID systems which connote the physical interaction between a tag and a reader for automatic identification operate within the global bandwidth of (860–960) MHz as specified by the International Standards Organisation (ISO) [3]. RFID systems function by adopting a non-contact application of radio-frequency that does not require a line-of-sight channels [4]. In order to optimise an RFID system, the orientation of the tags and associated readers must be fully established through the polarisation characteristics of their corresponding antennas. RFID tags are often designed to have linearly polarised dipoles [5].

The quadrifilar helical antenna (QHA) (example see Figure 1) has been identified by previous works as a suitable antenna for omnidirectional tag reading in RFID and other wireless applications, due to its ability to give circular polarisation over a wide angular area [6, 7]. Another excellent property of QHAs in terms of the symmetry of their geometry is their ability to give a cardioid-shaped radiation pattern regardless of the axial length and diameter [8]. It has also been established that the inherent cardioid-shaped radiation patterns of QHAs can be made conical by extending the resonant fractional turns of the QHA to an integral number for improved characteristics [9].

The QHA (Figure 1) is capable of providing an excellent beamwidth pattern with desirable circular polarisation, making it a good choice in RFID applications [2]. However, optimum caution is needed in the design and development of QHAs to realise the specified axial ratio and front to back power ratio. One of the notable pitfalls in the design and development of QHAs is the overall axial length of antenna, which is often too bulky for many practical installations and applications To address this problem, a global optimisation technique was employed to constrain the geometrical parameters of the conventional QHA. The selected global optimisation technique, genetic algorithm (GA) has been exemplified as an effective and efficient tool in RF and EM engineering optimisation [10]. In addition GA has been used in previous works to achieve low profile, compact designs for QHAs in other wireless communications applications [6, 7].
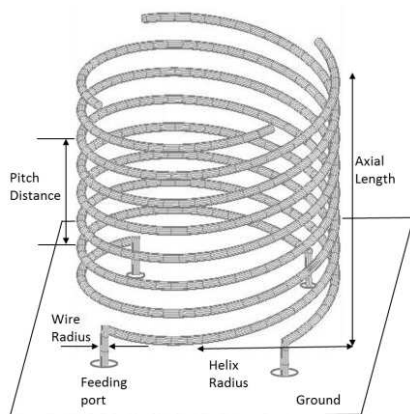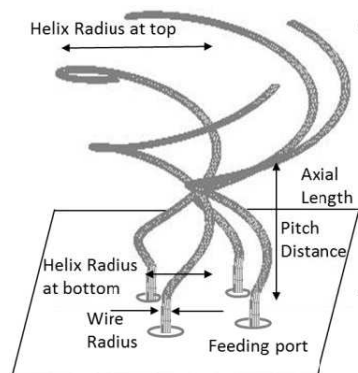
Figure 1: Basic geometry of the QHA.

Figure 2: Geometry of the linearly-shifted quadrifilar helical antenna (LSQHA).

The novel QHA antenna is named linearly-shifted quadrifilar helical antenna (LSQHA) because its elements are linearly-shifted and made compact to cover the global BW 860–960 MHz as revealed in Figure 2. With reference to its helical elements and as can be observed, the proposed LSQHA design does not take the form of the conventional QHA. Specifying a finite ground and feeding of the LSQHA via an integrated feed network is proposed, to avoid the intricacy and losses associated with multiple feed points of a centre feed. At the risk of repetition, the novel antenna structure is achieved by linearly-shifting the helical elements of the conventional QHA by 90° using a defined phase quadrature distance. This design is expected to reduce the axial length and overall volumetric equivalent of the LSQHA, while retaining good axial ratio, high power gain and wide beamwidth coverage.

2. ANTENNA DESIGN STRUCTURE

The design and optimisation of the proposed linearly-shifted quadrifilar helical antenna in RFID applications was conducted using a GA driver synchronised with the industry-standard Numerical Electromagnetic Code (NEC-2). The GA driver is initialised by a set of initial solutions or parameters defined for the proposed LSQHA. Parametric iterations are then executed with the conjunctive running of the GA driver and the NEC-2 computational analysis program. As adopted in this work, the source codes for the GA driver synchronised with the industry-standard NEC-2 were written in FORTRAN [11, 12]. The codes were intuitively modified to randomly generate and evaluate antenna samples.

To achieve optimum results, the initial geometrical and parametric solution of the proposed LSQHA was defined for optimisation with GA based on established findings in [6, 7]. In this process, real-valued GA chromosomes were defined. Antenna parameters such as the, VSWR, axial ratio (AR) and total forward gain (G_T) were optimised at an operating frequency of 900 MHz in consonance with the EPC Global RFID Tag/Reader specifications [13]. Individual antenna samples were generated using the industry-standard NEC-2 source code and corresponding results were juxtaposed with the desired fitness function.

A summary of the GA input parameters, antenna variables and best solutions for the proposed LSQHA design is detailed in Table 1. The LSQHA was designed to provide a very high forward gain and circular polarisation within the RFID global bandwidth of (860–960) MHz. As evident, the proposed design differs from the conventional QHA in Figure 1 in that its helical elements were configured to be linearly-shifted at 90° from each other using a defined phase quadrature distance. This was deemed necessary in an effort to achieve a very compact design and lower the overall profile of the proposed antenna. In the study undertaken, the LSQHA offered a better performance with its helical elements shifted.

The simulation logic and GA optimisation model were structured in such a way that an optimum linear distance between the four helical elements of the LSQHA was sought while shifting them by 90° in phase-quadrature. Optimal parametric features for the proposed LSQHA antenna, with an excellent VSWR and AR, were found within the maximum number of GA generations specified (250): the antenna's parameters for the optimum design are detailed in Table 1. The performance of the proposed LSQHA has been analysed and verified using freeware antenna modeller

Table 1: Summary of GA input parameters and antenna variables.

| GA PARAMETERS		QUADRIFILAR HELICAL ANTENNA DESIGN PARAMETERS			
	Input Values		Minimum Value (m)	Maximum Value (m)	Optimum Value (m)
Population Size	10	Pitch Distance	0.0033	0.0721	0.0558
Number of Parents	5	Axial Length	0.045	0.10	0.0885
Probability of mutation	0.02	Radius of Helix (Top)	0.01	0.035	0.035
Maximum Generation	250	Radius of Helix (Bottom)	0.01	0.035	0.0342
Probability of Crossover	0.5	Linear Quadrature Distance Between Helical Elements	0.035	0.07	0.0501
Probability of Creep	0.04	Fixed Radius of Wires	0.0005	0.0005	0.0005
Number of Possibilities	32768	Fixed Distance above ground	0.01	0.01	0.01
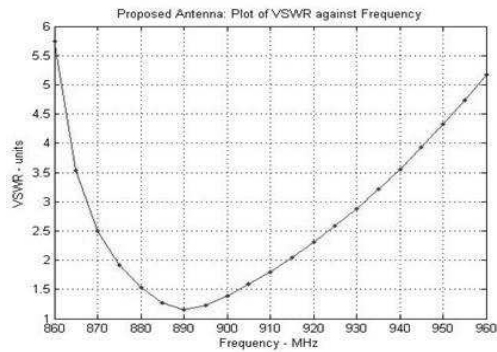
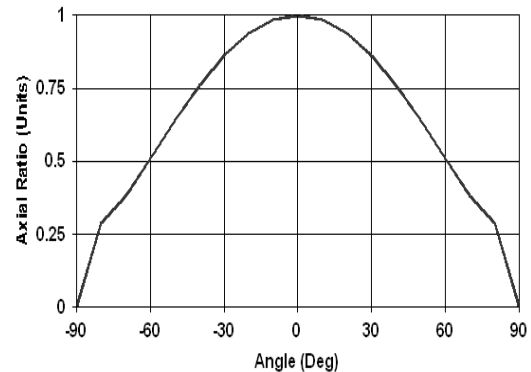Figure 3: Computed VSWR for the proposed LSQHA.

Figure 4: Axia ratio of the LSQHA.

and simulation software [14].

Evidently, the overall profile of the optimal design of LSQHA showcases the effectiveness of the compactness achieved by employing the logic and architecture illustrated in Figure 2. In contrast to the conventional QHA design (see Figure 1), the LSQHA was configured to have its helical elements more closely fitted together in volume and space. The LSQHA offers a more compact design in terms of its surface area, while retaining a good axial ratio and a very good beamwidth. Critical analysis of the performance of the optimal LSQHA was conducted to ascertain parametric features in terms of bandwidth, axial ratio coverage and antenna gain. The proposed LSQHA was found to have an optimum axial length of 8.85 cm as revealed in Figure 3.

The VSWR at the input ports of the optimised LSQHA antenna was calculated using an electromagnetic modelling software package and evaluated to be 1.39 at the EPC Global RFID Tag/Reader frequency of 900 MHz respectively as shown in Figure 3. As can be seen, the optimised antenna appears to have excellent impedance matching that covers most of the bandwidth specified for RFID communications (875–912.5) MHz.

Figure 4 confirms the excellent circularly-polarised characteristic of the proposed antenna over a good elevation angle mostly prominent in the counter-clockwise direction (left hand). Figure 5(a) and Figure 5(b) depict the measured power gain radiation patterns of the proposed LSQHA at an operating frequency of 900 MHz for two vertical cut planes at $\Phi = 0°$ and $\Phi = 90°$ respectively. The
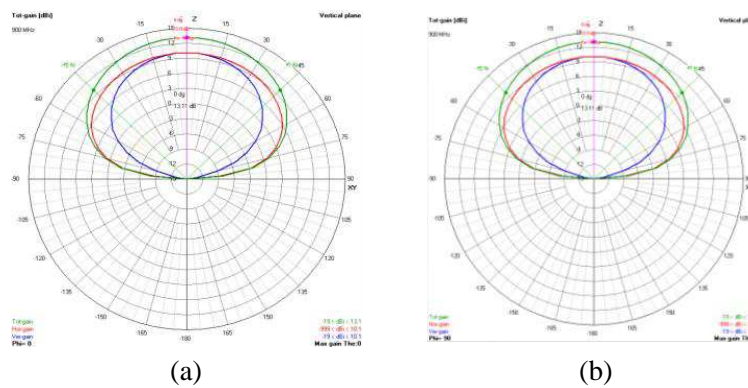
(a)   (b)

Figure 5: Computed gain radiation patterns of the proposed antenna for two vertical cut planes; (a) $\Phi = 0°$ and (b) $\Phi = 90°$.

proposed antenna shows approximately $\pm 45°$ elevation angle range for an axial ratio less than $3\,\text{dB}$ that is, a $3\,\text{dB}$ beamwidth of $90°$. Also, the proposed LQHSA revealed a total forward isotropic gain of $13.1\,\text{dBi}$.

3. CONCLUSIONS

A novel 'linearly-shifted quadrifilar helical antenna' (LSQHA) circularly polarized with a high forward isotropic gain and VSWR specifications desirable in RFID applications has been proposed. The proposed antenna is intended for deployment in RFID systems, as the reader or interrogator antenna, where the orientation and polarisation of the associated tag antennas cannot be precisely predicted. The design and optimisation of the proposed antenna using Genetic Algorithm method have been well appreciated and showcased, the specified objective being deployed for antenna design within the RFID global bandwidth of (860–960) MHz. The performance of the optimal selected antenna structure was validated using 4NEC-2. The results confirm the proposed antenna has a $3\,\text{dB}$ beamwidth of $90°$ with a resonant frequency at about $890\,\text{MHz}$ and an acceptable total forward gain of $13.1\,\text{dBi}$ at the design frequency of $900\,\text{MHz}$. The optimal design reached was found to be compact and of an excellent profile. These results tell that the proposed antenna can easily be configured to sample commercial RFID readers or interrogators. On the whole, Genetic Algorithm global optimisation method has also proved its advantage in quickly finding optimal solutions for RF and EM designs.

REFERENCES

1. Chen, Z. N. and X. Qing, "Antennas for RFID applications," *2010 International Workshop on Antenna Technology (iWAT)*, 1–4, 2010, Online Available: IEEEXplore, Doi: 10.1109/IWAT.2010.5464865.
2. Blazevic, Z. and M. Skiljio, "Helical antennas in satellite radio channel," *Advances in Satellite Communications*, M. Karimi, Ed., 2011, Online eBook Available: http://cdn.intechopen.com/pdfs/16867/InTech-Helical_antennas_in_satellite_radio_channel.pdf.
3. ISO — International Organisation for Standardisation, "ISO/IEC 18000-6:2013 information technology — RFID for item management — Part 6: Parameters for air interface communications at 860 MHz to 960 MHz general," 2013, Online Available: http://www.iso.org/iso/home/store/catalogue_tc/catalogue_detail.htm?csnumber=59644.
4. Lee, B. and P. Xiang, "Review of RFID tag antenna issues at UHF band," *Asia-Pacific Microwave Conference, APMC 2008*, 1–4, 2008, Online Available: IEEEXplore, Doi: 10.1109/APMC.2008.4958401.
5. Rimbault, N., A. Sharaiha, and S. Collardey, "Low profile high gain helix antenna over a conical ground plane for UHF RFID applications," *15th International Symposium on Antenna*

Technology and Applied Electromagnetics, ANTEM, 1–3, 2012, Online Available: IEEEXplore, Doi: 10.1109/ANTEM.2012.6262424.

6. Zhou, D., R. A. Abd-Alhameed, C. H. See, P. S. Excell, and E. A. Amushan, "Design of quadrifilar helical and spiral antennas in the presence of satellite-mobile handsets using genetic algorithms," *1st European Conference on Antennas and Propagation, EuCAP 2006*, 1–5, 2006, Online Available: IEEEXplore, Doi: 10.1109/EUCAP.2006.4584999.

7. Zhou, D., S. Gao, R. A. Abd-Alhameed, C. Zhang, M. S. Alkhambashi, and J. D. Xu, "Design and optimisation of compact hybrid quadrifilar helical-spiral antenna in GPS applications using genetic algorithm," *6th European Conference on Antennas and Propagation, EuCAP 2012*, 1–4, 2012, Online Available: IEEEXplore, Doi: 10.1109/EuCAP.2012.6206315.

8. Kilgus, C., "Resonant quadrafilar helix," *IEEE Transactions on Antennas and Propagation*, Vol. 17, No. 3, 349–351, May 1969, Online Available: IEEEXplore, Doi: 10.1109/TAP.1969.1139459.

9. Kilgus, C. C., "Shaped-conical radiation pattern performance of the backfire quadrifilar helix," *IEEE Transactions on Antennas and Propagation*, Vol. 23, No. 3, 392–397, May 1975, Online Available: IEEEXplore, Doi: 10.1109/TAP.1975.1141084.

10. Johnson, J. M. and Y. Rahmat-Samii, "Genetic algorithms in engineering electromagnetics," *IEEE Antennas and Propagation Magazine*, Vol. 38, No. 4, 7–21, Aug. 1997, Online Available: IEEEXplore, DOI: 10.1109/74.632992.

11. Carroll, D. L., FORTRAN Genetic Algorithm Driver, Version 1.7, Dec. 11, 1998, Download from: http://www.staff.uiuc.edu/~carroll/ga.html.

12. Burke, G. L. and A. J. Poggio, "Numerical electromagnetics code (NEC)-method of moments," Lawrence Livermore Laboratory, Livermore, CA, 1981.

13. GS-1 EPCglobal Inc., "Regulatory status for using RFID in the EPC Gen 2 band (860 to 960 MHz) of the UHF spectrum," May 31, 2013, Online Available: http://www.gs1.org/docs/epcglobal/UHF_Regulations.pdf.

14. Voors, A., "NEC based antenna modeler and optimizer," Mar. 2014, Online Available: http://www.qsl.net/4nec2/.

A Compact Tri-band Monopole Antenna with Multiple Meander Lines for WLAN and WiMAX Communication Applications

Xinbo Liu, Yingsong Li, and Wenhua Yu

College of Information and Communications Engineering
Harbin Engineering University, Harbin, China

Abstract— In this paper, a compact tri-band monopole antenna with three meander lines is proposed and investigated for wireless local area networks (WLANs) and worldwide interoperability for microwave access (WiMAX) applications. The designed tri-band antenna is realized by using three meander line structures that are connected to the 50-Ohm microstrip feed signal line to generate the desired triple resonance frequencies. By adjusting the dimensions of the proposed three meander lines, the expected resonant frequencies can be tuned for WLAN and WiMAX communication applications. The simulation results demonstrate that the optimized tri-band monopole antenna can give three impedance bandwidth for $S_{11} \leqslant -10\,\text{dB}$ of $156\,\text{MHz}$ (2.39–2.55 GHz), $450\,\text{MHz}$ (3.30–3.75 GHz) and $730\,\text{MHz}$ (5.14–5.87 GHz), which can be applied to cover both 2.4/5.2/5.8-GHz WLAN bands and 3.5/5.5-GHz WiMAX bands. Furthermore, omnidirectional radiation patterns can be achieved, which make the designed tri-band monopole antenna promising for integrating into modern portable devices.

1. INTRODUCTION

With the rapid progress of wireless communication, WLAN and WiMAX have been extensively studied, which result in a great demand for multiband antennas. Recently, many researchers are focused on the antenna designs with simple structure, low cost, small size and multi-bands. To achieve these performances, a great number of multiband antennas have been presented for WLAN and WiMAX applications [1–5]. However, most of these antennas are large in size. To further reduce the size of the antenna, a multi-band antenna has been developed by using parasitic elements, which can just provide dual-band [6]. In sequence, several asymmetric coplanar strip (ACS)-fed antennas with small sized have been proposed and well designed by numerical and experimental methods [7–9]. However, these proposed antennas can only operate for single or dual band applications. In [10–14], several triple band antenna have been presented for WLAN and WiMAX applications. Although these antennas can provide multiband characteristics, some of them are complex in structure or large in size.

In this paper, a simple tri-band antenna is proposed and investigated by using high-frequency structure simulator (HFSS) for WLAN and WiMAX communication applications. The designed tri-band antenna is realized by using three meander line structures that are connected to the 50-Ohm microstrip feed signal line to generate the desired triple resonance frequencies. By adjusting the dimensions of the proposed three meander lines, the expected resonant frequencies can be tuned for WLAN and WiMAX communication applications. The experimental results demonstrate that the optimized tri-band monopole antenna can give three impedance bands for $S_{11} \leqslant -10\,\text{dB}$. The proposed antenna is optimized and the results show that the antenna not only has good tri-band characteristic, but also has omnidirectional radiation patterns, which makes it suitable for both WLAN and WiMAX communication applications.

2. ANTENNA DESIGN

The configuration of the proposed tri-band WLAN and WiMAX antenna is shown in Figure 1. The proposed antenna is designed on a FR4 substrate with a relative permittivity of 4.4, loss tangent of 0.02, thickness of 0.8 mm and its total size is $30\,\text{mm} \times 20\,\text{mm}$. The proposed antenna consists of three meander lines that are connected to the feed signal line, a partial ground plane and a 50-Ohm microstrip feed signal line with a width of 1.4 mm. In this design, the meander lines are used to generate the three resonance frequency bands. All the meander lines are quarter-wavelength resonance at the desired frequencies. The desired center frequencies are tunable by adjusting the dimensions of these meander lines, which make the proposed antenna easy to fabricate. The proposed antenna is optimized and the optimal parameters are listed as follows: $W = 20$, $W_1 = 0.9$, $W_2 = 1$, $W_4 = 2$, $W_5 = 1$, $W_6 = 1.2$, $W_7 = 6$, $W_8 = 1.4$, $L = 30$, $L_1 = 2.4$, $L_2 = 5$, $L_3 = 7$, $L_4 = 20$, $L_5 = 9.5$, $L_6 = 9.5$, $L_7 = 2.5$, $L_8 = 4$, $L_9 = 7$, $L_{10} = 1$, $L_{11} = 7$ (unit: mm).
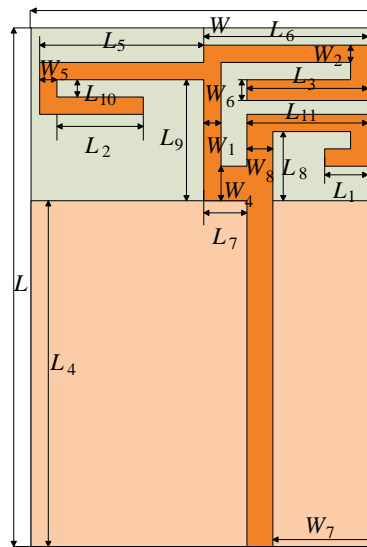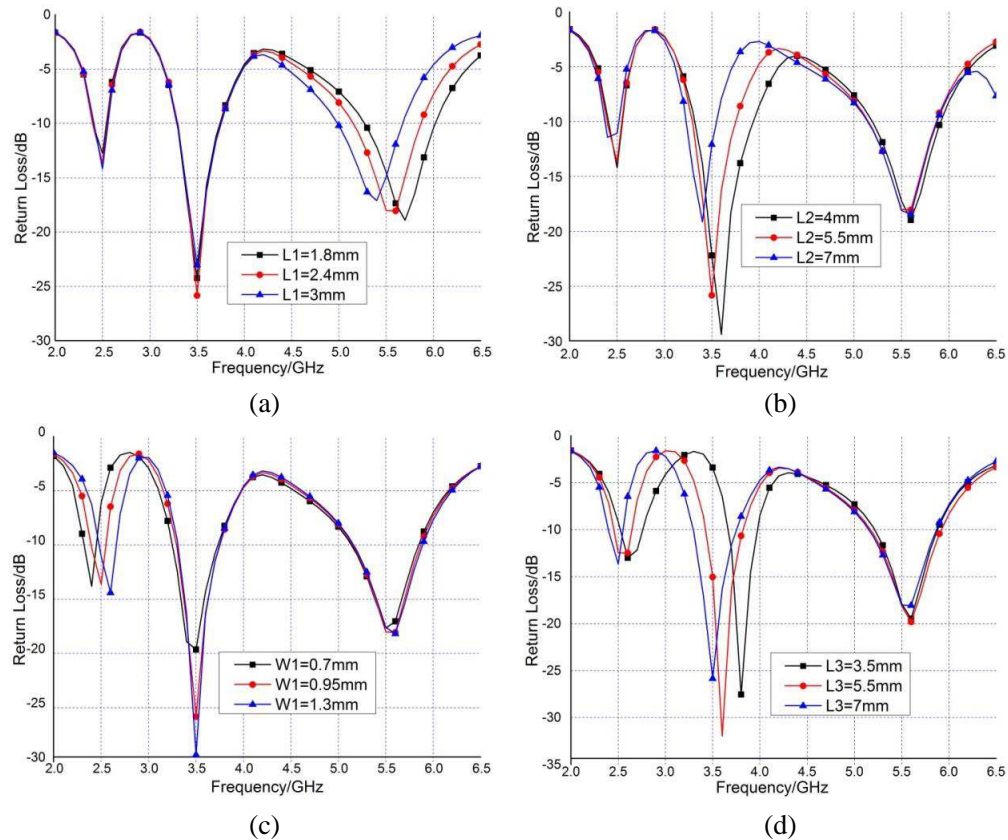
Figure 1: Geometry structure of the proposed antenna.

Figure 2: Parameter effects on the resonance characteristic of the antenna. (a) L_1. (b) L_2. (c) W_1. (d) L_3.

3. PERFORMANCE OF THE PROPOSED ANTENNA

In this section, the proposed tri-band antenna is investigated by using HFSS which is based on finite element method (FEM). The key parameters L_1, L_2, L_3 and W_1 are selected to evaluate the effects on the impedance bandwidth of the antenna. Figure 2(a) shows the effects on the impedance bandwidth of the proposed tri-band WLAN and WiMAX antenna with respect to the return loss when the parameter L_1 varies from 1.8 mm to 3 mm. With an increment of L_1, the center frequency of the highest band shifts from 5.7 GHz to 5.4 GHz. This is because the increased
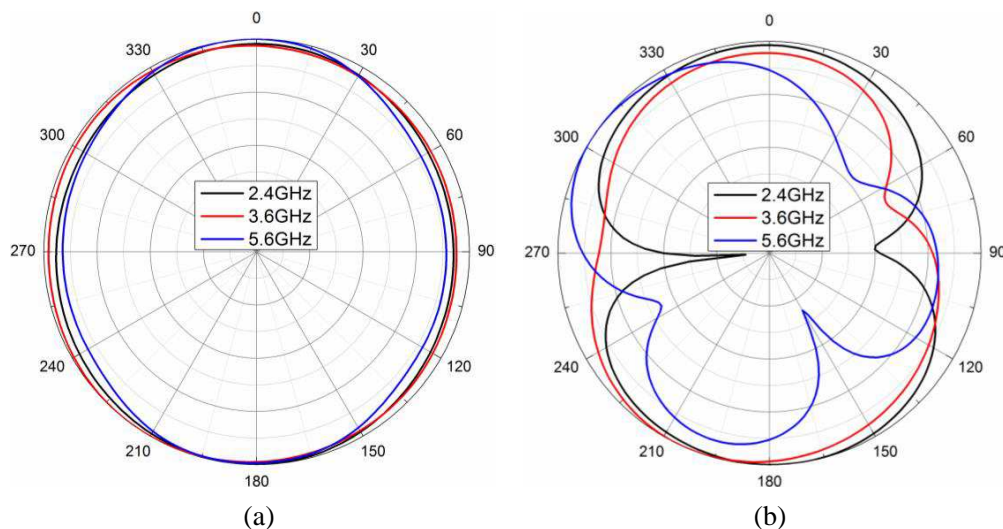
Figure 3: Radiation patterns of the proposed antenna. (a) H-plane. (b) E-plane.

L_1 increases the current path and hence the highest band moves to low frequency. The effects of L_2 are shown in Figure 2(b). When L_2 increases from 4 mm to 7 mm, the center frequency of the middle band at 3.5 GHz WiMAX moves to low frequency. We can see that the center frequency shifts from 3.6 GHz to 3.4 GHz and the bandwidth is also getting narrow because the increased L_2 not only prolong the resonance length but also enhance the coupling of the meander lines. Parameter W_1 has an important effect on the impedance bandwidth of the lowest band and the results are shown in Figure 2(c). It is observed that the center frequency of the lowest band shifts to high frequency with an increase of W_1 and the bandwidth is also slightly enhanced. In order to understand the resonance of the proposed antenna, L_3 is also investigated and the simulated results are demonstrated in Figure 2(d). It can be seen that the center frequencies of the lowest and middle bands move to low frequency. This is because the increased L_3 not only increases the resonance length and makes the lowest frequency move to low frequency, but also affect the current distribution of the left meander line and hence changes the center frequency of the middle band. Thus, we can tune the dimensions of the meander lines to control the resonance frequencies to meet the WLAN and WiMAX applications. The radiation patterns of the proposed antenna are obtained at 2.4 GHz, 3.6 GHz and 5.6 GHz and are shown in Figure 3. It is can be seen from Figure 3 that the proposed tri-band antenna has a nearly omnidirectional radiation patterns in the H-plane and the figure-of-eight-like radiation pattern in E-plane except 5.6 GHz, which indicates that the proposed tri-band WLAN and WiMAX antenna can provide desired radiation characteristics.

4. CONCLUSION

A simple tri-band antenna is proposed for WLAN and WiMAX applications by using meander lines. The key parameters of the antenna have been investigated to understand the principle of the antenna. The triple resonance frequencies can be controlled by adjusting the dimensions of the antenna structures. The results showed that the proposed antenna can achieve three operating bandwidth of 156 MHz (2.39–2.55 GHz), 450 MHz (3.30–3.75 GHz) and 730 MHz (5.14–5.87 GHz) to cover WiMAX (3.4–3.69 GHz) and WLAN (2.4–2.483 GHz, 5.15–5.825 GHz) communication systems. The proposed antenna has a small size, three resonance frequencies and omnidirectional radiation patterns, rendering it suitable for WiMAX and WLAN communication applications.

ACKNOWLEDGMENT

REFERENCES

1. Chien, H. Y., C. Sim, and C. H. Lee, "Compact size dual-band antenna printed on flexible substrate for WLAN operation," *IEEE Antennas and Propagation*, 1047–1050, 2012.
2. Chiu, C. H., C. C. Lin, C. Y. Huang, and T. K. Lin, "Compact dual-band dipole antenna with

asymmetric arms for WLAN applications," *International Journal of Antennas and Propagation*, Vol. 2014, Article ID 195749, 2014.

3. Liu, P. G., Y. L. Zou, B. R. Xie, X. L. Liu, and B. H. Sun, "Compact CPW-fed tri-band printed antenna with meandering split-ring slot for WLAN/WiMAX applications," *IEEE Antennas and Wireless Propagation Letters*, Vol. 11, 1242–1244, 2012.

4. Thomas, K. G. and M. Sreenivasan, "A novel triple band printed antenna for WLAN/WiMAX applications," *Microwave and Optical Technology Letters*, Vol. 51, No. 10, 2481–2485, 2009.

5. Zhu, J., M. A. Antoniades, and G. V. Eleftheriades, "A compact tri-band monopole antenna with single-cellmetamaterial loading," *IEEE Transactions on Antennas and Propagation*, Vol. 58, No. 4, 1031–1038, 2010.

6. Li, Y., X. Yang, Y. Bai, and T. Jiang, "Dual-band antenna handles WLAN/WiMAX," *Microwaves & RF*, Vol. 50, No. 6, 80–88, 2011.

7. Li, Y., W. Li, and R. Mittra, "A compact ACS-fed dual-band meandered monopole antenna for WLAN and WiMAX applications," *Microwave and Optical Technology Letters*, Vol. 55, No. 10, 2370–2373, 2013.

8. Deepu, V., R. K. Raj, M. Joseph, M. N. Suma, and P. Mohanan, "Compact asymmetric coplanar strip fed monopole antenna for multiband applications," *IEEE Transactions on Antennas and Propagation*, Vol. 55, 2351–2357, 2007.

9. Li, Y., W. Li, and Q. Ye, "A compact asymmetric coplanar strip-fed dual-band antenna for 2.4/5.8 GHz WLAN applications," *Microwave and Optical Technology Letters*, Vol. 55, No. 9, 2066–2070, 2013.

10. Zhang, X. Q., Y. C. Jiao, and W. H. Wang, "Compact wide tri-band slotantenna for WLAN/WiMAX applications," *Electronics Letters*, Vol. 48, No. 2, 64–65, 2012.

11. Zhao, Q., S.-X. Gong, W. Jiang, B. Yang, and J. Xie, "Compact wide-slot tri-band antenna for WLAN/WiMAX applications," *Progress In Electromagnetics Research Letters*, Vol. 18, 9–18, 2010.

12. Ren, X. S., Y. Z. Yin, W. Hu, and Y. Q. Wei, "Compact tri-band rectangular ring patch antenna with asymmetrical strips for WLAN/WiMAX applications," *Journal of Electromagnetic Waves and Applications*, Vol.24, No. 13, 1829–1838, 2010.

13. Karimian, R., I. Tehran, H. Oraizi, S. Fakhte, and M. Farahani, "Novel F-shaped quad-band printed slot antenna for WLAN and WiMAX MIMO systems," *IEEE Antennas and Wireless Propagation Letters*, Vol. 12, 405–408, 2013.

14. Wan, Y. T., D. Yu, F. S. Zhang, and F. Zhang, "Miniature multi-band monopole antenna using spiral ring resonators for radiation pattern characteristics improvement," *Electronics Letters*, Vol. 49, No. 6, 382–384, 2013.

Low-cost Implementation of a Waveguide-based Microwave Filter in Substrate Integrated Waveguide (SIW) Technology

A. Coves[1], **Á. A. San Blas**[1], **S. Marini**[2], **G. Torregrosa**[1], **E. Bronchalo**[1], **and A. Martellosio**[3]

[1]Departamento de Ingeniería de Comunicaciones, Universidad Miguel Hernández de Elche, Spain
[2]Departamento de Física, Ingeniería de Sistemas y Teoría de la Señal
I.U. Física Aplicada a las Ciencias y las Tecnologías, Universidad de Alicante, Spain.
[3]Department of Electrical, Computer and Biomedical Engineering, University of Pavia, Italy.

Abstract— This paper presents the design and practical implementation of a waveguide-based microwave filter in Substrate Integrated Waveguide (SIW) technology. The use of SIW technology for implementing waveguide filters makes the presented design specially aimed for being used in undergraduate courses related to microwave engineering and filter designing. Their low cost and easiness from the filter fabrication point of view allows their use in microwave laboratory courses where students can implement their own theoretical filter designs and measure their frequency response. The requiring mechanics in the manufacturing of microwave filters in waveguide technology (both rectangular and circular) makes its use practically unfeasible in academic laboratories because of its cost. For this reason, a practical design example of a waveguide iris filter using the impedance inverter model is proposed in this paper for academic laboratories, using SIW technology. This is a low cost and easy to manufacture technology. The overall process includes the design of the ideal band-pass prototype filter using the impedance inverter and its implementation in an inductive iris-coupled waveguide filter, by using a developed electromagnetic simulator based on the mode-matching technique. Finally, the equivalent filter in SIW technology is obtained and optimized by using HFSS simulator, including a SIW to microstrip transition. A prototype of the designed filter has been fabricated and measured, showing a good agreement between measurements and simulations.

1. INTRODUCTION

The Telecommunications Technology Engineering undergraduate program includes, in general, a great number of subjects related to the study and design of microwave filters. A common block to all subjects is usually the design of microwave filters. At low frequencies, such filters can be implemented using lumped elements. However, at higher frequencies (typically in the microwave range), due to the appearance of parasitic effects in lumped elements, such filters are designed by means of distributed parameters, i.e., by transmission line sections. A clear example of transmission line which is especially suitable for the design and practical implementation of microwave filters in a teaching laboratory is the coaxial line, which allows students, starting from a theoretical designed filter obtained in class, to desing and implement a microwave filter with transmission line sections [1]. Alternatively, microstrip technology is also attactive because it is easy to manufacture and low cost, and it allows to incorporate lumped elements of SMT (Surface Mount Technology) in the designed filters. Besides, the measurement of the resulting circuits doesn't need high cost equipment if the working frequency is not too high. For this reason, in the subject *Microwave Technology* [2] several microwave filters have been designed and implemented in microstrip technology by the students, operating in the band of 1 to 5 GHz, under individualized practical sessions. On the other hand, the mechanics required in waveguide-based microwave filter manufacture (in both rectangular and circular waveguide technology) makes it virtually impossible to use it in teaching laboratories for various reasons (cost, high operation frequency...), despite the abundant literature on waveguide-based microwave filter implementation [3]. For this reason, a practical design example of a waveguide iris filter using the impedance inverter model is proposed in this paper for academic laboratories, using SIW technology [4, 5]. In the next section it is described the design process of the ideal band-pass filter prototype using the impedance inverter model, and its implementation in an inductive iris-coupled waveguide filter, by using a developed electromagnetic simulator based on the mode-matching technique [7]. Next, the equivalent filter in SIW technology is obtained and optimized by using HFSS simulator [9], including a SIW to microstrip transition based on a microstrip taper [10] at both ends of the filter. Finally, a prototype of the designed filter has been fabricated and measured, and the measured results are compared to the simulated response.

2. DESIGN AND PRACTICAL IMPLEMENTATION OF THE FILTER IN SIW TECHNOLOGY

In this section we consider the design of a five-pole Chebyshev filter, consisting of several sections of rectangular waveguide coupled with inductive iris, as shown in Fig. 1. Although the filter design has been made in rectangular guide, the ultimate goal of this work is to implement the designed filter in SIW technology, as already mentioned in the introduction, since this technology is low cost and easy to manufacture. This guide is a low cost implementation of the traditional rectangular guide, which takes the advantages of planar lines for easy integration with other circuits, and low radiation losses of the guides. Such guide is constituted by two rows of parallel metallic posts (or via holes) separated a distance a_{SIW} made in a substrate of thickness h metallized on both sides, which delimit the area of propagation of the TE_{10} mode of the SIW guide. The via holes are characterized by a separation s_v and a diameter d_v, whose values are properly chosen to avoid radiation losses [4], so as to fulfill the following conditions:

$$d_v < \lambda_g/5, \quad s_v \leq 2d_v \tag{1}$$

where λ_g is the guided wavelength. On the other hand, the propagation constant of this guide is determined by the width a_{SIW} of the SIW and by the substrate permittivity ϵ_r. A previous study of this type of guide [6] demonstrates that a SIW can be analyzed as an equivalent rectangular waveguide of effective width a given by:

$$a = a_{SIW} - \frac{d_v^2}{0,95s_v} \tag{2}$$

Therefore the final design of the equivalent filter in SIW technology has been accomplished using Eq. (2) in each of the respective sections of rectangular waveguide.

For the design of the waveguide-based filter, the equivalent circuit model of impedance inverters of an inductive waveguide iris through a T network [3] has been employed, as it can be seen in Fig. 2(a). The filter consists of half-wave resonators separated by inductive iris. Using an electromagnetic simulator, the iris scattering matrix can be obtained and therefore its equivalent T network. The model has been combined with an electromagnetic simulator based on the mode-matching technique [7] to calculate the physical dimensions of the filter. Each iris is represented by two series reactances denoted by X_s and a shunt reactance denoted by X_p. The equivalent circuital rectangular iris filter is shown in Fig. 2(a). In order to transform it in the impedance inverters model, we use the impedance inverter circuit consisting of an inductive T network and two sections of length $\varphi/2$ on each side. The inverter is created by adding a length $\varphi/2$ and $-\varphi/2$ on each side of the discontinuity, as shown in Fig. 2(b). In this case the resonators are transmission lines of length L_n connected to two transmission lines of artificial lengths $-\varphi_n/2$ and $-\varphi_{n+1}/2$. These lengths represent the load of the resonator from the adjacent coupling inverters. The specifications of the designed filter, whose scheme is shown in Fig. 1, are the following: it is a band-pass Chebyshev filter of 5th order with a center frequency $f_0 = 4\,\text{GHz}$, a bandwidth of 600 MHz and return loss
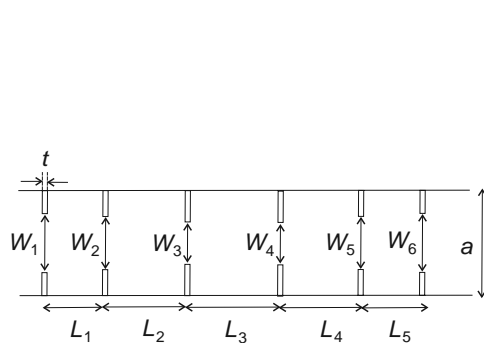

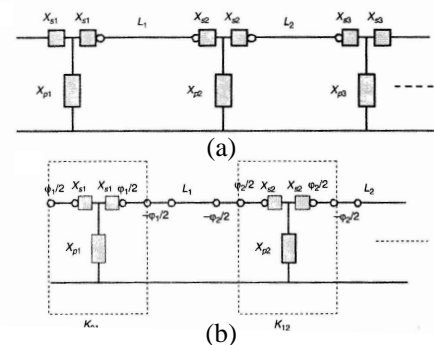Figure 1: Top view of a 5th order inductive rectangular waveguide filter.

Figure 2: (a) Equivalent circuit model of an inductive waveguide iris through a T network. (b) Equivalent impedance inverters model of an inductive waveguide iris through a T network.

of $RL = 15\,\text{dB}$ (equivalent to a $0.1\,\text{dB}$ ripple in the passband). The rectangular waveguide has a width of $a = 15.8\,\text{mm}$ and a height of $b = 0.63\,\text{mm}$, corresponding to the thickness $b = h$ of the employed substrate, which in our case is a Taconic CER-10 substrate whose $\epsilon_r = 10$ and $\tan(\delta) = 0.0035$ [8], double-sided metallized with a copper film $20\,\mu\text{m}$ thick. Iris in all cases have a thickness of $t = 3\,\text{mm}$.

The coefficients of a 5th order Chebyshev low-pass filter with $RL = 15\,\text{dB}$ are [3]: $g_0 = 1$, $g_1 = g_5 = 1.1468$, $g_2 = g_4 = 1.3712$, $g_3 = 1.9750$. The filter center frequency and band-edge frequencies are related by:

$$f_0 = \sqrt{f_1 f_2}, \quad BW = f_1 - f_2, \tag{3}$$

which give $f_1 = 3.7\,\text{GHz}$, $f_2 = 4.3\,\text{GHz}$. The filter relative bandwidth is:

$$\Delta = \frac{\lambda_{g1} - \lambda_{g2}}{\lambda_{g0}} = 0.3636 \tag{4}$$

Then, the values obtained for the impedance inverter factors are:

$$\frac{K_{01}}{Z_0} = \frac{K_{56}}{Z_0} = \sqrt{\frac{\pi\Delta}{2g_0g_1}} = 0.7051 \tag{5}$$

$$\frac{K_{12}}{Z_0} = \frac{K_{45}}{Z_0} = \frac{\pi\Delta}{2\sqrt{g_1g_2}} = 0.45546 \tag{6}$$

$$\frac{K_{23}}{Z_0} = \frac{K_{34}}{Z_0} = \frac{\pi\Delta}{2\sqrt{g_2g_3}} = 0.34706 \tag{7}$$

Using an electromagnetic simulator based on the mode matching technique [7], one can calculate the scattering parameters of a rectangular iris (referred to the discontinuity planes), which are related to the T network elements shown in Fig. 2(a), X_s and X_p by the following equations [3]:

$$j\frac{X_s}{Z_0} = \frac{1 - S_{12} + S_{11}}{1 - S_{11} + S_{12}} \tag{8}$$

$$j\frac{X_p}{Z_0} = \frac{2S_{12}}{(1 - S_{11})^2 - S_{12}^2} \tag{9}$$

where S_{11}, S_{21} and S_{12} are the scattering parameters of the TE_{10} fundamental mode of the input waveguide at the filter center frequency f_0. For the impedance inverter shown in Fig. 2(b), X_s and X_p are related to K/Z_0 and φ by:

$$\frac{K}{Z_0} = \left| \tan\left(\frac{\varphi}{2} \text{atan} \frac{X_s}{Z_0} \right) \right| \tag{10}$$

$$\varphi = -\text{atan}\left(2\frac{X_p}{Z_0} + \frac{X_s}{Z_0} \right) - \text{atan} \frac{X_s}{Z_0} \tag{11}$$

The scattering parameters of several iris of different width have been obtained, ranging from 1 to $15\,\text{mm}$, providing the curve shown in Fig. 3 in which the impedance inverter factor K/Z_0 is
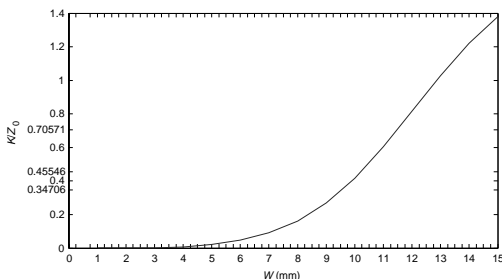

Figure 3: Impedance inverter factor $\frac{K}{Z_0}$ as a function of the width (W) of the rectangular waveguide iris.
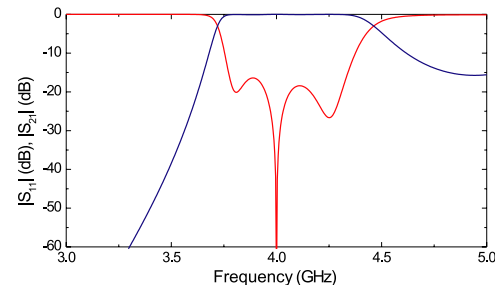

Figure 4: Electrical response of the designed rectangular waveguide filter.
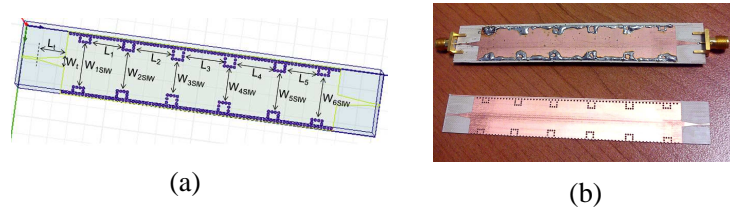
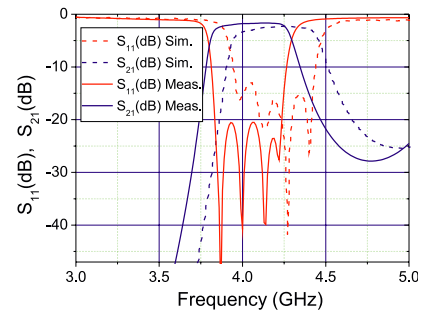Figure 5: (a) Scheme of the designed filter in SIW technology. (b) Photograph of the fabricated filter.

Figure 6: Simulated and measured response of the designed filter in SIW technology.

represented as a function of the iris width W. From the curve represented in Fig. 3, and the values of the inverter factors provided by Eqs. (5)–(7), the following values of the iris widths have been deduced for our filter: $W_1 = W_6 = 12.4\,\text{mm}$, $W_2 = W_5 = 10.65\,\text{mm}$, $W_3 = W_4 = 9.85\,\text{mm}$. For these values of iris widths, the values of the phases provided by Eq. (11) are: $\varphi_1 = \varphi_6 = -1.7\,\text{rad}$, $\varphi_2 = \varphi_5 = -1.28\,\text{rad}$, $\varphi_3 = \varphi_4 = -1.07\,\text{rad}$. Finally, the resonator lengths are given by the following equation:

$$L_n = \frac{\lambda_{g0}}{2\pi}\left[\pi + \frac{1}{2}\left(\varphi_n + \varphi_{n+1}\right)\right], \quad n = 1, \dots, N \tag{12}$$

The obtained phases yield the following values of the resonator lengths: $L_1 = L_5 = 9.4\,\text{mm}$, $L_2 = L_4 = 11.2\,\text{mm}$, $L_3 = 11.8\,\text{mm}$. In Fig. 4 it is shown the simulated response of the designed filter using the mode-matching technique. In this figure it can be seen that the designed filter meets the design specifications.

The next step in the design process is to obtain the equivalent waveguide widths in SIW technology, and de design of the microstrip to SIW transition. To this end, the following parameters for the via holes have been employed: $d_v = 0.7\,\text{mm}$, $s_v = 0.95\,\text{mm}$. With the equivalence given by Eq. (2), the widths of the different sections of SIW waveguide can be obtained. On the other hand, for the microstrip to SIW transition, the same transition presented in [10] has been implemented, consisting of a microstrip taper (see Fig. 5(a)). Such transition provides a wide bandwidth and can be designed to cover the entire operation band of the proposed filter. Finally, an optimization process of the designed filter response has been performed through HFSS simulator, providing the following final filter parameters: $W_{1SIW} = W_{6SIW} = 11.86\,\text{mm}$, $W_{2SIW} = W_{5SIW} = 10.48\,\text{mm}$, $W_{3SIW} = W_{4SIW} = 9.90\,\text{mm}$, $L_1 = L_5 = 9.4\,\text{mm}$, $L_2 = L_4 = 11.2\,\text{mm}$, $L_3 = 11.8\,\text{mm}$. The dimensions of the width and length of the taper transition are $2.60\,\text{mm}$ and $7.08\,\text{mm}$ respectively, while the microstrip line width is of $0.6\,\text{mm}$.

In Fig. 5(a) it is represented a scheme of the designed SIW filter with its final dimensions, while a photograph of the fabricated filter is shown in Fig. 5(b) (before and after metallizing the via holes). Finally, the simulated response of the designed filter in SIW technology is shown in Fig. 6 with dashed line, including the effect of conductor and dielectric losses. In this figure it is also represented with solid line the measured response of the filter with an Agilent vectorial network analyzer. The measured response shows a good impedance matching in the passband (better than $12.5\,\text{dB}$) and also a good out of band rejection performance (better than $20\,\text{dB}$). Although the measurements and simulations show the same bandwidth, a frequency shift of $100\,\text{MHz}$ is observed, which may be caused by a lower value of the relative permittivity of the employed substrate.

3. CONCLUSION

A practical design example of a waveguide iris filter using the impedance inverter model is proposed in this paper for academic laboratories, using SIW sections as a low-cost and easy to manufacture technology. An example of a band-pass filter centered at $4\,\text{GHz}$ has been designed, optimized and fabricated to show all the design and fabrication process, showing a good agreement between measurements and simulations.

ACKNOWLEDGMENT

REFERENCES

1. Coves, A., T. Martínez, G. Torregrosa, A. Rodríguez, and E. Bronchalo, "Diseño y realización práctica de filtros de microondas para laboratorios docentes," *Libro de resúmenes del XVIII Simposium Nacional de la Unión Científica Internacional de Radio,* 27–29, Sep. 2003.
2. http://www.umh.es/contenido/Estudios/:asi_g_2287_S1/datos_es.html.
3. Cameron, R. J., C. M. Kudsia, and R. R. Mansour, *Microwave Filters for Communication Systems: Fundamentals, Design, and Applications,* Wiley, 2007.
4. Deslandes, D. and K. Wu, "Design consideration and performance analysis of substrate integrated waveguide components," *32nd European Microwave Conference Proceedings*, Vol. 2, 881–884, Sep. 2002.
5. Bozzi, M., A. Georgiadis, and K. Wu, "Review of substrate integrated waveguide (SIW) circuits and antennas," *IET Microw. Antennas Propagat.*, Vol. 5, No. 8, 909–920, Jun. 2011.
6. Cassivi, Y., L. Perregrini, P. Arcioni, M. Bressan, K. Wu, and G. Conciauro, "Dispersion characteristics of substrate integrated rectangular waveguide," *IEEE Microw Wirel. Compon. Lett.*, Vol. 12, No. 9, 333–335, Sep. 2002.
7. Valero, N. C., Final Project titled "Análisis multimodal de discontinuidades en guía rectangular mediante la técnica de adaptación modal," Universidad Miguel Hernández de Elche, 2005.
8. http://www.taconic-add.com.
9. ANSYS HFSS, High Frequency Structure Simulator, Version 15.0, Ansys, Inc., Canonsburg, PA, USA.
10. Deslandes, D. and K. Wu, "Integrated microstrip and rectangular waveguide in planar form," *IEEE Microw. Wirel. Compon. Lett.*, Vol. 11, 68–70, Feb. 2001.

Band-pass Filter Based on Magnetoelectric Composite at Electromechanical Resonance

A. S. Tatarenko, **R. V. Petrov**, **V. M. Petrov**, **and M. I. Bichurin**

Novgorod State University, Russian Federation

Abstract— This paper focuses on the study of a prototype magnetoelectric filter at electrome-chanical resonance in the dual-phase structure The dual-phase structure consists of single-crystal nickel-zinc ferrite and piezoelectric lead-zirconate-titanate with dimensions of $24 \times 24 \times 2 \, \mathrm{mm}^3$ and $30 \times 20 \times 2.25 \, \mathrm{mm}^3$, correspondingly. The studied band-pass filter has the resonance frequency of $86.8 \, \mathrm{kHz}$ and bandwidth of $2 \, \mathrm{kHz}$. Magnetoelectric voltage coefficient equals $0.47 \, \mathrm{V/(cm \cdot Oe)}$ at resonance. The prototype magnetoelectric filter allows to adjust the amplitude of the gain-frequency characteristic within the limits of $10 \, \mathrm{dB}$.

1. INTRODUCTION

The present paper focuses on the study of spectrum of a prototype magnetoelectric (ME) filter at electromechanical resonance (EMR) in ferrite-piezoelectric structure. ME effect is characterized by an induced polarization in an applied magnetic field or by an induced magnetization in an applied electric field. In the EMR region, the magnetoelectric effect will allow to get a stronger ME interaction compared to the low-frequency region Theoretical estimates of ME coefficient at EMR in ME composites was reported recently [1, 2]. Experimental study of ME coupling in ferrite-piezoelectric bilayer at thickness shear mode was discussed in our earlier work [3–5]. In this work, we consider the longitudinal mode of EMR in a ferrite-piezoelectric bilayer. Longitudinal mode allows one to obtain much lower resonance frequencies than shear vibrations. This gives an opportunity to develop low-pass filtering devices. It should be noted that the characteristics of filters can be adjusted by means of dc magnetic field in a wide range of signal amplitudes Such tunable filter allows us to perform several radio engineering functions simultaneously. This filter in addition to the function of filtering can adjust the amplitude of the signal passing, also to make the power limiter either to execute a circuit of the modulator.

2. PROTOTYPE DESIGN

The design of studied filter prototype consists of solenoid coil with ME sample ME sample is a dual-phase structure consisting of a single-crystal $\mathrm{Zn_{0,2}Ni_{0,8}Fe_2O_4}$ (NZFO) and piezoelectric lead zirconate-titanate (PZT). PZT and NZFO have dimensions of $24 \times 24 \times 2 \, \mathrm{mm}^3$ and $30 \times 20 \times 2.25 \, \mathrm{mm}^3$, correspondingly. The output voltage across the piezoelectric layer is measured by using the electrodes placed on planar surfaces of piezoelectric layer. Coupling at the interface is provided by gluing. Bilayer structure is formed so that the magnetoelastic resonance frequency in ferrite layer coincides with EMR frequency in the piezoelectric material. Frequencies of both resonances are about $86 \, \mathrm{kHz}$ and primarily depend on linear dimensions. DC magnetic field H is necessary for magnetic layer to provide non-zero piezomagnetic coefficient and achieve the resonant characteristics.

3. MEASUREMENT SETUP

The measurements were carried out with used Agilent DSO-X 2002A oscilloscope. The measuring setup includes the signal generator, gaussmeter, electromagnet, and power supply as in Fig. 1. The output oscillations of signal generator are applied to the solenoid which produces the ac magnetic field of about $3 \, \mathrm{Oe}$. The ME output voltage induced by ME sample is measured by oscilloscope The electromagnet is used for bias magnetic field control. The value of bias field varies from 0 to $2000 \, \mathrm{Oe}$.

The measuring setup enabled measuring the frequency response of the filter as a function of bias magnetic field.

4. MEASUREMENT DATA

Figure 2 reveals the measuring data for prototype filter at frequencies from 70 to $100 \, \mathrm{kHz}$ for bias field of 0, 170, and $1800 \, \mathrm{Oe}$. The peak output voltage is obtained at frequency of $87 \, \mathrm{kHz}$. Induced
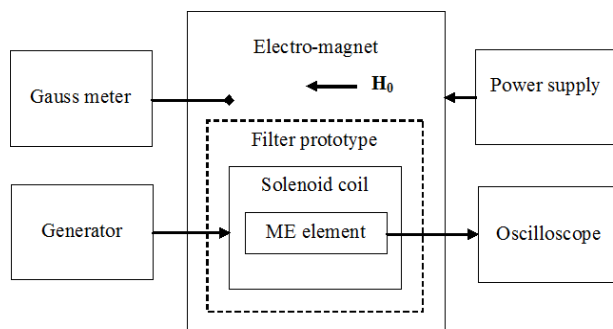
Figure 1: Measurement setup.

voltage equals 5 mV at 70 and 100 kHz and 2.46 V at 87 kHz for zero bias field. The bandwidth is about 2 kHz. Increasing bias field up to 170 Oe results in increased ME output of 12.62 V. The bandwidth remain equal to 2 kHz. It should be noted that signal amplitude variation is about 10 V. A further increase in bias field amplitude gives rise to an decrease in output voltage. Applying the bias field of 1800 Oe results in ME output of 1 V at EMR frequency. Signal amplitude variation is about 10 dB.
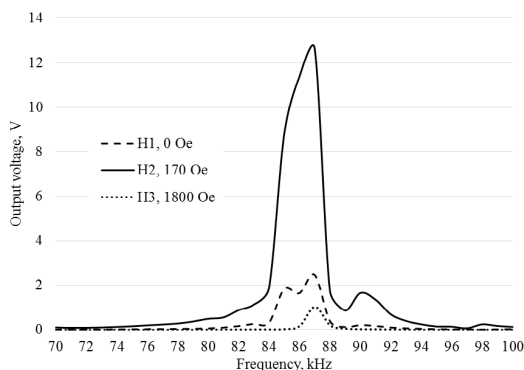

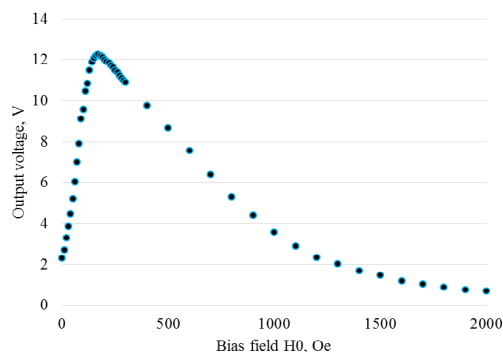Figure 2: Output voltage vs. frequency of ME filter.

Figure 3: Output voltage vs. bias field of ME filter.

Figure 3 shows the bias magnetic field dependence of output voltage. The peak output voltage of 12.62 V is obtained at bias field of 170 Oe. Then the output voltage decreases. The curve shape is similar to the bias field dependence of magnetostriction for NZFO.

Based on the obtained results, one can estimate the ME voltage coefficient. The peak ME coefficient equals 0.47 V/(cm·Oe) at EMR frequency. The bias magnetic field dependence of output voltage in Fig. 3 suggests that the filter attenuation characteristic can be adjust by applying the appropriate bias magnetic field.

5. THEORETICAL APPROACH

ME effect in composites is known to be a product property of the magnetostrictive effect in a magnetic phase and the piezoelectric effect in a piezoelectric phase. A sharp increase in ME coupling strength is obtained in the vicinity of the electromechanical resonance (EMR) frequency because the ME effect in composites is due to mechanically coupled piezoelectric and magnetostrictive subsystems. Theoretical estimates of ME coupling in the EMR region were discussed recently [1]. The main parameters that determine ME coupling strength at EMR in composites are piezoelectric and piezomagnetic coefficients. Most ferromagnetic materials show the magnetostrictive effect, however, the linear piezomagnetic effect in these materials is not observed. Linearity in such materials is provided by applying the bias magnetic field and ac magnetic field with amplitude which is assumed to be small compared to bias field. Thus the magnetoelectric effect over a short range around this bias field can be approximated as a linear effect. We consider only the Joule magnetostriction that leads to a change of shape in the direction of the applied magnetic field, while maintaining a constant volume. Taking into account the expression for magnetoelastic free

energy density for Joule magnetostriction leads to the following expression for the piezomagnetic coefficient q_{11} of a monodomain single-crystal ferrite:

$$q_{11} = 2b\mu_{11}M, \tag{1}$$

where μ_{11}, M, and b are permeability, magnetization, and magnetoelastic coefficient which only weakly depends on the external parameters. This equation can also be applicable to multidomain polycrystalline ferrite where one measures the averaged values of those quantities. Apparently, in this case one should replace magnetoelastic coefficient b with the effective coefficient b_{eff} which may vary with the change of the domain structure.

For a magnetically soft material, the value of magnetization vanishes in the absence of bias magnetic field. Eq. (1) shows that $q_{11} \approx 0$ for this case. Increasing applied magnetic field results in an increase in piezomagnetic coefficient. However, after this coefficient reaches a maximum, further increase of applied dc magnetic field leads to a decrease in piezomagnetic coefficient. As a result, the dependence of ME coefficient on bias magnetic field is a curve with one peak that is in agreement with data. Thus the transmission coefficient of the filter based on ME composite can be tuned by applying the appropriate bias magnetic field.

6. CONCLUSION

The frequency spectrum of the studied prototype of band-pass filter has the resonance pick at frequency 868 kHz, bandwidth equals 2 kHz for 0,7 level. Induced voltage equals 5 mV at 70 and 100 kHz and 2.46 V at 87 kHz for zero bias field. The bandwidth is about 2 kHz. Increasing bias field up to 170 Oe results in increased ME output of 12.62 V. The bandwidth remain equal to 2 kHz. A further increase in bias field amplitude gives rise to an decrease in output voltage. Applying the bias field of 1800 Oe results in ME output of 1 V at EMR frequency. Signal amplitude variation is about 10 dB. At the EMR frequency ME voltage coefficient reached equals 047 V/(cm·Oe). The obtained results can be further used in practical applications.

ACKNOWLEDGMENT

REFERENCES

1. Bichurin, M., V. Petrov, R. Petrov, and S. Priya, "Electromechanical resonance in magnetoelectric composites: direct and inverse effect," *Solid State Phenomena*, Vol. 189, 129–143, 2012.
2. Petrov, V. M., M. I. Bichurin, and R. V. Petrov, "Magnetoacoustic resonance in ferrite-piezoelectric film structures," *Modern Problems of Science and Education*, No. 2, 2012, URL: www.science-education.ru/102-5701.
3. Petrov, R. V., V. M. Petrov, and M. I. Bichurin, "Magnetoelectric effect in the field of magneto-acoustic resonance in the structure of YIG-PZT," *Vestnik NovSU*, No. 68, 2012.
4. Bichurin, M. I., R. V. Petrov, and V. M. Petrov, "Magnetoelectric effect at thickness shear mode in ferrite-piezoelectric bilayer," *Appl. Phys. Lett.*, Vol. 103, 092902, 2013.
5. Petrov, R. V., V. M. Petrov, A. S. Tatarenko, M. I. Bichurin, A. P. Pyatakov, and A. K. Zvezdin, "Magnetoelectric effect in magnetoacoustic resonance area in ferrite-piezoelectric structure," *Modern Problems of Science and Education*, No. 4, 2013, URL: www.science-education.ru/110-9654.

Yagi Rectenna Application to Increase the Battery Lifetime of Sensor Nodes

R. Fernández-García and I. Gil

Departmentof Electronic Engineering, Universitat Politècnica de Catalunya
08222 Colom 1, Terrassa, Spain

Abstract— In this paper a Yagi rectenna application to increase the battery lifetime of sensor nodes is presented. The proposed rectenna consists of a three pole Yagi antenna plus double voltage RF to DC converter based on a HSMS-268C Schottky diode. The rectenna has been designed by means of the commercial *SEMCAD software*. The measurement results demonstrate a maximum RF-DC efficiency of about 31% for $160\,\mu\text{W/cm}^2$.

1. INTRODUCTION

In the last years a massive increase of the use of wireless communications has been produced in industrial and domestic applications. Specifically, one of the latest applications of the wireless communication is the Wireless Sensor Networks (WSNs) [1]. The WSNs consist of small communication nodes. These nodes contain a sensing part, a microcontroller, communication components and power supply (typically a battery). Moreover, these nodes should fulfil restrictions of low-cost and low-power consumption to guarantee its usefulness. In this sense, the RF energy-harvesting technology can help to increase the battery lifetime of the sensor nodes and, in some cases, even to avoid using the battery [2]. The main RF energy harvesting element is the rectenna, which consists of an antenna plus a rectifier to convert the RF signal to DC voltage. Several rectennas have been proposed in literature. In [3] a narrowband rectenna to harvest the UHF RFID energy is presented. The achieved conversion efficiency is 54% when the incident power density is $80\,\mu\text{W/cm}^2$. In [4] a X-band rectenna is reported showing a conversion efficiency of 21% for a $245\,\mu\text{W/cm}^2$ power density. In [5] a dual band planar inverter F rectenna is proposed, and a conversion efficiency of 47.3% and 49.1% is obtained for 2.45 GHz and 5.8 GHz under 11 and 9 dBm, respectively. In [6] a 4×4 rectenna array for 35 GHz is developed. In this case a RF to DC conversion efficiency of 67% is achieved for 7 mW RF input power.

In this work, an alternative Yagi rectenna application to increase the battery lifetime of sensor nodes is proposed. The rectenna is designed at 1.8 GHz band, which is one of the main radiation bands due to GSM communications. This paper is organized as follows. In Section 2, the proposed rectenna and simulation results are detailed. The experimental results are reported and discussed in Section 3. Finally, in Section 4, the main conclusions are summarized.

2. PROPOSED RECTENNA AND SIMULATION RESULTS

2.1. Antenna

Figure 1 shows the proposed Yagi antenna implemented in a commercial FR4 substrate (dielectric constant $\varepsilon_r = 4.6$, thickness $h = 1.53\,\text{mm}$). The antenna consists of a dipole radiating element. One arm of the dipole is located in the bottom PCB layer, meanwhile the other one is located in the top layer. This layer also includes three pole directors in the front of the dipole. The reflector in located in the bottom layer. The antenna has been designed and optimized by means of the commercial *SEMCAD X 14.8 software* [7]. The optimized antenna dimensions are shown in Figure 1.

Figure 2 plots the simulated antenna performance. It can be noticed a return losses lower that $-10\,\text{dB}$ in the frequency range [1.71 GHz to 1.93 GHz], corresponding to bandwidth of 220 MHz. In this frequency range, the antenna gain increases from 8.74 dBi to 10.7 dBi.

The simulated radiation pattern of the proposed Yagi antenna is plotted in Figure 3 in 3D and polar view at the maximum gain frequency (1.93 GHz). The figure indicates a half-power beamwidth (HPBW) of 48 degrees and 60 degrees for XY and ZY plane respectively.

2.2. RF-DC Converter

The RF to DC converter consists of a voltage double converter based on HSMS-268C Schottky diodes. The lumped-element and prototype photograph is given in Figure 4. In order to consider all the printed circuit board (PCB) parasitic effects, a cosimulation using the commercial *Keysight*
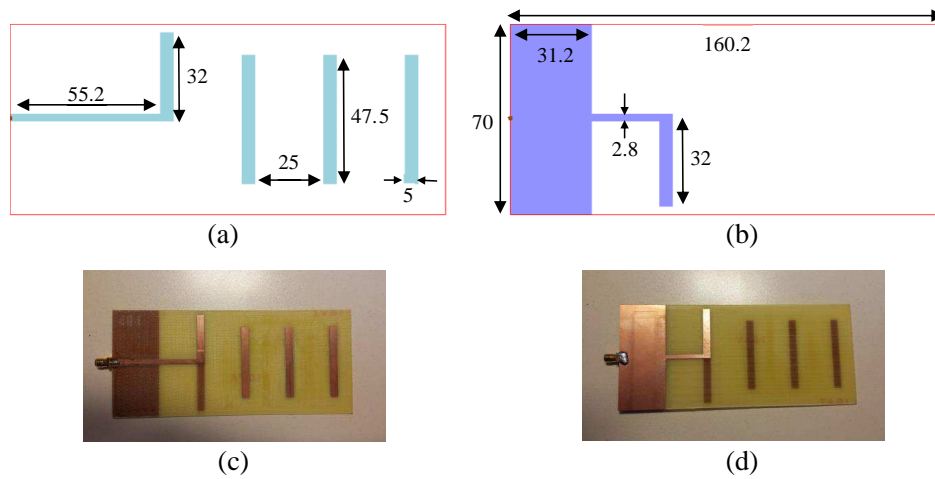
Figure 1: Geometry (in mm) and photograph of the proposed Yagi antenna. (a) Geometry top layer. (b) Geometry bottom layer. (c) Photograph top layer. (d) Photograph bottom layer.
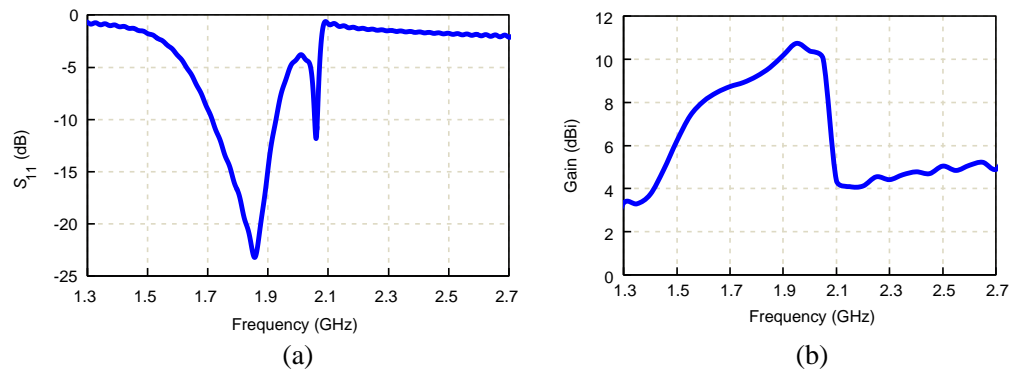

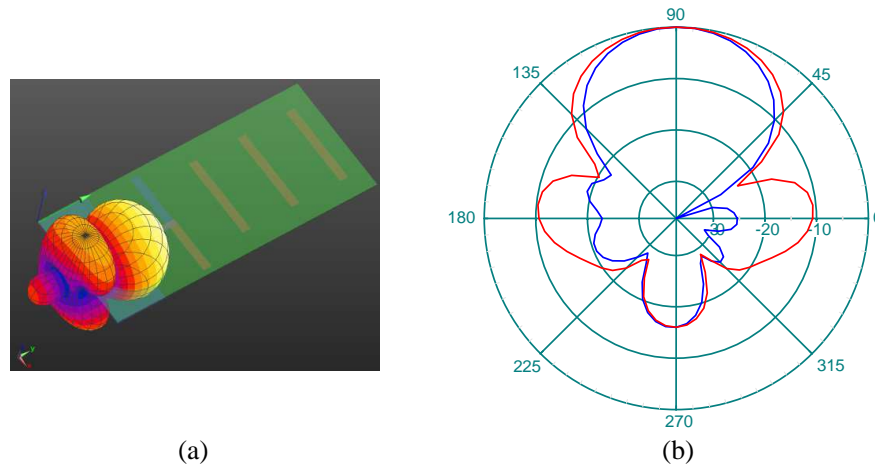Figure 2: Simulated Yagi antenna performance. (a) Return losses. (b) Gain.

Figure 3: Simulated antenna radiation diagram. (a) 3D view. (b) Normalized polar view in dB.

ADS software has been done. Moreover, the parasitic impedances of the Schottky diodes HSMS-268C packed SOT-323 have been also included. Taking into account all these effects, a LC matching network with 2.2 nH and 8.2 pF is used to match the antenna and the RF-DC converter at the operation frequency. The load impedance has been fitted in order to obtain the maximum conversion efficiency. The simulation results denote that the optimum value is 2.2 kΩ.

3. EXPERIMETAL RESULTS

The *S*-parameters of the prototype shown in Figure 1 have been measured by means of a *Keysight FieldFox N9916A Microwave Analyzer* by selecting the vector network analyser mode. The return
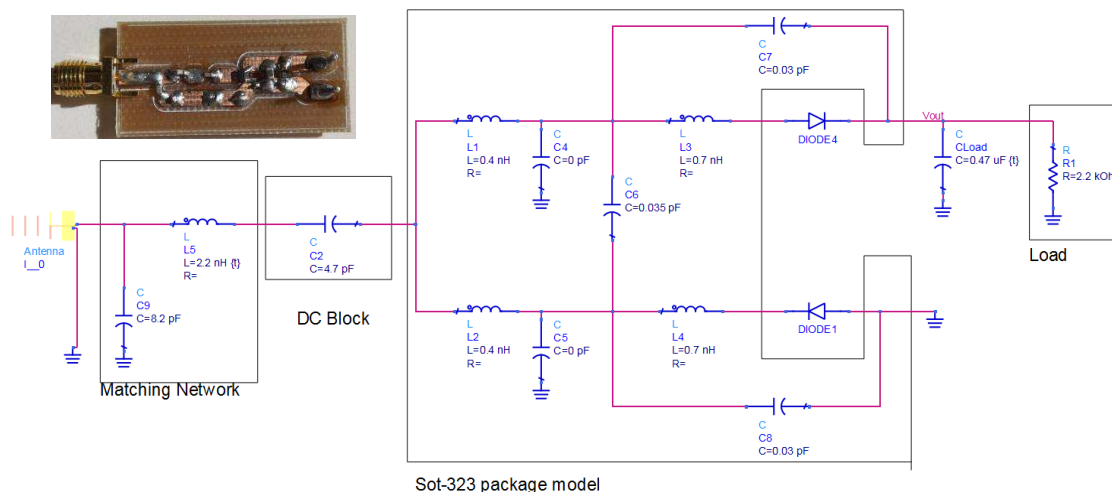
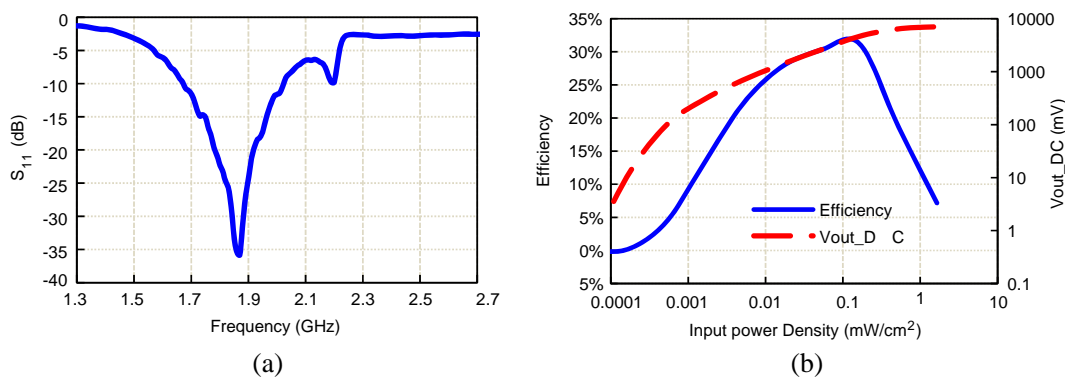Figure 4: Schematic and photograph of DC-RF converter.

Figure 5: Measured rectenna properties. (a) Return loss. (b) Efficiency and DC output voltage.

losses of the designed Yagi antenna are depicted in Figure 5(a). It can be observed a return loss coefficient lower than -10dB in the frequency range [1.68 GHz, 2.02 GHz]. It confirms a good correlation between simulation and measurement results.

In order to obtain the RF- DC conversion efficiency, the Expression (1) has been used.

$$\eta = \frac{P_{DC}}{P_{RF}} = \frac{V_{out}^2/R_L}{\wp_{in}A_{eff}}$$ (1)

where $\wp_{in}$ is the incident power density, R_L is the resistive load $(2.2\,\mathrm{k\Omega})$, V_{out}, is the DC output voltage and A_{eff} the effective area of antenna, determined by means of Expression (2).

$$A_{eff} = \left(\frac{\lambda_o^2}{4\pi}\right)G_{ant}$$ (2)

where λ_0 is the free space wavelength and G_{ant} is the antenna gain depicted in Figure 2(b). In Figure 5(b), the RF-DC efficiency and output voltage at 1.85 GHz are shown. It can be noticed a maximum efficiency of about 31% when the input power density is $160\,\mu\mathrm{W/cm}^2$. In this case, the measured DC output voltage is 4.6 V for a load impedance of $2.2\,\mathrm{k\Omega}$.

4. CONCLUSIONS

In this paper, a Yagi rectenna has been presented. The rectenna consists of three element Yagi antenna plus a voltage double RF-DC converter base on HSMSC-286C. The measurement results show a maximum efficiency of 31% and output DC voltage of 4.6 V for $160\,\mu\mathrm{W/cm}^2$ power density. These results show the feasibility of RF energy harvesting as an alternative method to increase the battery life time of the wireless sensor nodes.

REFERENCES

1. Yick, J., B. Mukherjee, and D. Ghosal, "Wireless sensor network survey," *Comput. Networks*, Vol. 52, No. 12, 2292–2330, Aug. 2008.
2. Kim, S., R. Vyas, J. Bito, K. Niotaki, A. Collado, A. Georgiadis, and M. M. Tentzeris, "Ambient RF energy-harvesting technologies for self-sustainable standalone wireless sensor platforms," *Proc. IEEE*, Vol. 102, No. 11, 1649–1666, Nov. 2014.
3. Monti, G., F. Congedo, D. De Donno, and L. Tarricone, "Monopole-based rectenna for microwave energy hardvesting of UHF RFID systems," *Progress In Electromagnetics Research C*, Vol. 31, 109–121, 2012.
4. Monti, G., L. Tarricone, and M. Spartano, "X-band planar rectenna," *IEEE Antennas and Wireless Propagation Letters*, Vol. 10, 1116–1119, 2011.
5. Lu, P., X.-S. Yang, J.-L. Li, and B.-Z. Wang, "A dual-frequency quasi-PIFA rectenna with a robust voltage doubler for 2.45- and 5.8-GHz wireless power transmission," *Microw. Opt. Technol. Lett.*, Vol. 57, No. 2, 319–322, Feb. 2015.
6. Mavaddat, A., S. Hossein, M. Armaki, and A. R. Erfanian, "Millimeter-wave energy harvesting using 4×4 microstrip patch antenna array," *Ieee Antennas Wirel. Propag. Lett.*, Vol. 14, 515–518, 2015.
7. "SEMCAD X." Schmid & Partner Engineering AG (SPEAG), www.speag.com.

A Model-free Method for Real-time High Precision Carrier Phase Observation

Tianyi Zhang, Qiao Meng, Quantao Yu, Jifei Tang, and Wei Liu

Institution of RF-&OE-ICs, Southeast University, Sipailou 2, Nanjing 210096, China

Abstract— Carrier phase observation is a high accuracy ranging method through tracking the phase of carrier signal and could be used in various applications. Carrier signal of the target in motion is a typical nonstationary signal and its model is hard to acquire. This paper describes a model-free approach of obtaining the total phase and the instantaneous frequency of the carrier signal in real-time with high resolution. The total phase is calculated and denoised using Savitzky-Golay filter to reducing measure noise. Meanwhile, the instantaneous frequency could be obtained by deriving the smoothed total phase which can also be implemented by a FIR filter like Savitzky-Golay filter. Simulation shows the performance of the proposed method.

1. INTRODUCTION

Carrier Phase Observation is a radio ranging method with high precision. It is based on measuring the difference of phase between the carrier signal received by receiver and the local reference signal [1]. Carrier phase observation could be used in various applications including radar ranging, satellite orbits determination, high precise relative GPS positioning and mobile communication location system. This method requires the full carrier cycles and the fractional cycle, which is called the total phase. Different approaches have been proposed to solve the initial integer ambiguity [2].

The total phase can be obtain by estimating frequency and phase from digitized carrier signal which has been converted to baseband signal. The problem is the carrier signal is a typical non-stationary signal and the model of carrier signal is difficult to determine due to the uncertain state of the target's motion. Since the distance is certainly a continuous smooth function of time in most situations, it can be well approximated by a polynomial within a finite duration interval, according to the Weierstrass approximation theorem. This class of signal is called the polynomial phase signal (PPS) and several approaches have been proposed for parameter estimation, such as polynomial Wigner-Ville distribution (PWVD) [3, 4], discrete polynomial-phase transform (DPT) [5], polynomial time-frequency distributions [6], etc. The computation of these algorithm increase rapidly when the required resolution of parameter estimation is high, hence the real-time observation is difficult to achieve.

This paper proposes a model-free method to obtain the total phase with high resolution in real-time. Parameters are estimated by de-chirp algorithm and chirp-Z transform in analysis window with short duration. The total phase is denoised by least squares (LS) polynomial fitting and the instantaneous frequency (IF) is got by computing the first derivative of the total phase. The rest of the correspondence is organized as follows. In Section 2, the total phase and the instantaneous frequency are introduced. The parameter estimation algorithm and smoothing filter is described and discussed in Section 3. In the Section 4, performance of the method is examined by simulation, followed by the conclusions in the Section 5.

2. TOTAL PHASE AND INSTANTANEOUS FREQUENCY

Carrier phase observation requires the estimator to keep track of the difference of phase in order to obtain the total phase including the full cycles and the fractional cycle. The average frequency is able to determine the full cycles as well, according to its definition. Therefore, the estimator can performed at intervals to relieve the pressure of computation.

Suppose the carrier signal is:

$$s(t), \qquad t \in [t_0 - T, t_0) \tag{1}$$

where T is the process interval called the integral time and t_0 is the output time. The total phase at t_0 can be expressed as:

$$\phi(t_0) = floor(\overline{f}(t_0) * T) + \varphi(t_0) \tag{2}$$

The average frequency of the signal during this time is $\overline{f}(t_0)$ and the fractional cycle at t_0 is $\varphi(t_0)$.

The velocity of target is a critical parameter for positioning and orbit determine which could be obtained by the instantaneous frequency. The instantaneous frequency of a monocomponent signal is defined as [7]:

$$f_i(t_0) = \frac{1}{2\pi}\frac{d}{dt}\phi(t)\mid_{t=t_0} \tag{3}$$

where $\phi(t)$ is the total phase. This expression indicates the instantaneous frequency is the first derivative of the phase.

3. MODEL-FREE PHASE ESTIMATION METHOD

3.1. Parameter Estimation

Windowed Fourier transform is a class of classic time-frequency analysis algorithm. A short window called observation window is used to localize spectrum in time. The critical issue of Fourier analysis is the signal in observation window is regarded as a stationary signal, which causes unpredictable errors during phase estimation. Therefore, de-chirp algorithm is performed instead. De-chirp algorithm, or called discrete polynomial transform (DPT) [8], is proposed for parameter estimation of linear frequency modulation (LFM) signal, which is a typical nonstationary signal. The advantage of De-chirp algorithm is the estimation of the frequency rate is converted to estimate the frequency of a sinusoidal signal. Discrete Fourier transform (DFT) is the classical algorithm for parameter estimation of discrete sinusoidal signal [9], while fast Fourier transform (FFT) is able to reduce the computation. The problem of DFT is that the resolution in frequency plane is limited by the length of data. Chirp-Z transform is applied to solve this problem since it can be computed rapidly with FFT as well. This estimator could be implemented in hardware conveniently as FFT can be realized through IP cores. The average frequency is calculated by frequency rate and initial frequency. Then the total phase could be got using the expression in (2).

3.2. Total Phase Smoothing

The measure noise is unacceptably large due to the length limitation of observation window. Polynomial fitting is able to reduce the measure noise since the total phase could be approximated by a polynomial. Meanwhile, the first derivative of phase is obtained conveniently by the polynomial coefficients. The polynomial fitting using the least square method is performed locally on a set of the total phase results, which is chosen by a slide window with fixed length. Data in the window is used to find the coefficients of polynomial fitting and output the polynomial value using these coefficients. As the window drops one point at the left and picks up a new point at the right, only the central result is reminded each time.

The proposed process of smoothing can be implemented by a special filter called Savitzky-Golay filter [10] or Taylor filter [11]. This kind of filter is a FIR filter, whose coefficients is readily obtained once the window length m and fitting degree p is determined. The first derivative of the phase could be got by this filter through changing the coefficients. The computation of polynomial fitting is considerably reduced and the architecture of FIR can be effectively realized in hardware.

Due to the uncertainty of signal model, the degree has to be selected cautiously. Simulation using a PPS of order 6 is performed to find the optimal value of p. Figure 1 depicts the performance
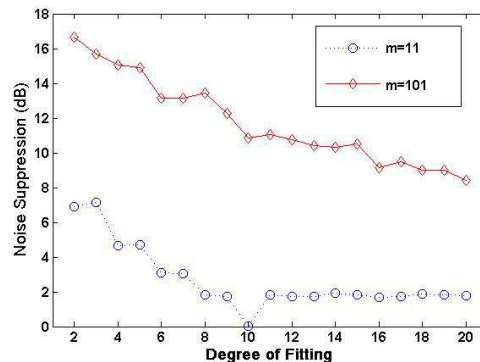

Figure 1: Performance of smoothing with different degrees.

of the smoothing when $2 \leq p \leq 20$. It also indicates that the degree of fitting should not exceed 3 though the order of PPS is higher than that.

4. SIMULATION

The performance of the method is tested by numerical simulation using PPS with additive white Gauss noise (AWGN). The precision of estimation is evaluated by root mean square error (RMSE). The simulation signal is expressed as:

$$s(n) = b_0 \sum_{i=0}^{6} \left[a_i \left(\frac{n}{f_s} \right)^i \right] + w(n), \qquad n = 0, 1, 2, \ldots, L \tag{4}$$

The parameters of the signal are $b_0 = 1$, $a_0 = 0.945975$, $a_1 = -1500.156$, $a_2 = 302.136$, $a_3 = 10068.894$, $a_4 = 60045.874$, $a_5 = 1256530.654$, $a_6 = 78413000.168$. Sample rate is $f_s = 5000\,\text{Hz}$, L is 15000 and the length of observation window is 50. The parameters of smoothing filter are $m = 11$ and $p = 3$. The signal-to-noise rate (SNR) is defined as:

$$SNR = 10 \log_{10} \frac{b_0^2}{\sigma_w^2} \tag{5}$$

where σ_w^2 is the variance of $w(n)$. Each Monte Carlo simulation is based on 100 realizations and the SNR is SNR = 8 dB. The results shows the RMSE of total phase after smoothing is $3.006°$, which means the precision of ranging is about $1\lambda/120$ (λ is the wavelength of carrier signal). Using the L1 channel of GPS signal as an example, the accuracy is about $0.159\,\text{cm}$. The RMSE of instantaneous frequency is 276.087mHz.

The RMSE of the total phase has been plotted versus SNR in Figure 2. Note that the sample rate is changed to $50\,\text{kHz}$ therefore the observation window is 500. Figure 2 shows the RMSE of the phase before and after smoothing under different SNR. The Cramér-Rao lower bound (CRLB) is displayed as well. This method exhibits a threshold at around $-4\,\text{dB}$.
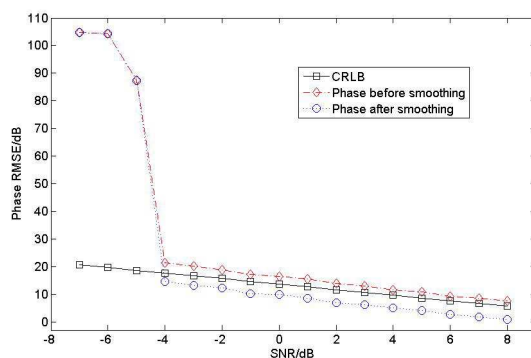
Figure 2: Errors of the total phase, relative to CRLB, as function of SNR.

5. CONCLUSIONS

This paper describes a model-free real-time method to estimating the total phase and the instantaneous frequency with high precision. Fractional phase and average frequency of the carrier signal are estimated in analysis window by de-chirp algorithm. The total phase is smoothed by Savitzky-Golay filter while the instantaneous frequency is obtained by a similar filter. The main modules of the proposed approach are FFT and FIR, which are suitable for implementing in hardware.

REFERENCES

1. Blewitt, G., "Basics of the GPS technique: Observation equations," *Geodetic Applications of GPS*, 10–54, 1997.
2. Han, S., "Carrier phase-based long-range GPS kinematic positioning," University of New South Wales, 1997.

3. Wang, P., H. Li,, and B. Himed, "Instantaneous frequency estimation of polynomial phase signals using local polynomial Wigner-Ville distribution," *2010 International Conference on Electromagnetics in Advanced Applications, ICEAA)*, 184–187, IEEE, September 2010.

4. Barkat, B. and B. Boashash, "Design of higher order polynomial Wigner-Ville distributions," 1999.

5. Peleg, S. and B. Friedlander, "The discrete polynomial-phase transform," *IEEE Transactions on Signal Processing*, Vol. 43, No. 8, 1901–1914, 1995.

6. Bi, G., Y. Ju, and X. Li, "Fast algorithms for polynomial time-frequency transforms of real-valued sequences," *IEEE Transactions on Signal Processing*, Vol. 56, No. 5, 1905–1915, 2008.

7. Boashash, B., *Time Frequency Signal Analysis and Processing: A Comprehensive Reference*, 2003.

8. Peleg, S. and B. Porat, "Linear FM signal parameter estimation from discrete-time observations," *IEEE Transactions on Aerospace and Electronic Systems*, Viol. 27, No. 4, 607–616, 1991.

9. Rife, D. C. B. P. and R. R. Boorstyn, "Single tone parameter estimation from discrete-time observations," *IEEE Transactions on Information Theory*, Vol. 20, No. 5, 591–598, 1974.

10. Savitzky, A., and M. J. E. Golay, "Smoothing and differentiation of data by simplified least squares procedures," *Analytical Chemistry*, Vol. 36, No. 8, 1627–1639, 1964.

11. Meng, Q. and J. Lu, "A filter designed based-on Talyor series model with least square method," 4, Journal of Southeast University, 1995,

Real-time Processing Technique for Panoramic Infrared Imaging System

G. Sun, G. Li, W. H. Wang, X. L. Fan, and Z. P. Chen
Science and Technology on Automatic Target Recognition Laboratory
National University of Defense Technology, Changsha 410073, China

Abstract— Panoramic infrared imaging system (PIIS) based on the long linear array long-wave detector is introduced. Due to the real-time processing and high-speed data transfer demanding, we propose a high-performance processing platform based on field programmable gate array (FPGA) + multicore digital signal processor (DSP) architecture. To reduce the platform's power consumption, dynamic power monitoring technology is used to provide variable core voltage management for DSP. Then mapping an application to the platform is illustrated, which is guided by parallel-task segmentation mechanism of multi cores system. We show that, the designed platform with the optimization strategies achieves powerful capabilities of data throughput and processing performance.

1. INTRODUCTION

Infrared imaging has abilities of passive detection, well anti-jamming and work double tides. Using infrared sensors to implement region searching and early warning, has become an important target surveillance method. To increase detection distance and accuracy of searching system for, the searching field of view (FOV) should expand as large as possible. In addition, with applications of infrared imaging in areas such as space remote sensing, multi-target surveillance and satellite-to-ground reconnaissance, the development of high-performance detector with high-resolution, large FOV and great quantities of image elements has become the urgent demand.

There are two methods to improve the detection FOV for infrared detectors at present [1]: one is to develop large area focal plane array (FPA), which is complex and high cost; another is to develop long linear array FPA (defining more than 480-elements as long linear array). Considering the factors of material, process technology and so on, obtaining long linear array through splicing short ones, is low cost and able to produce more than 1000-elements [2, 3]. In the year 2010, H. B. Fan [4] developed the 1152×6 long wave linear array, and implemented the infrared searching system for 1152×50000 high-resolution panoramic imaging.

Computing performance of image processing platform is crucial to the PIIS, which performs complex operations of $50000 \times 1152 \times 8$ bit size of raw data, such as panoramic image display, image enhancement and target detection. Thereby an efficient platform must have capabilities of high-speed data transfer and real-time processing. This paper addresses the high-speed processing platform design and performance optimization, based on Fan's imaging system engineering application.

2. PANORAMIC INFRARED IMAGING SYSTEM

The 1152×6 linear array long wave infrared detector [4] is utilized to compose the panoramic imaging system in our approach. The long linear array is achieved by the following steps: two 288×6 linear array modules are parallelly arranged in the horizontal direction, constituting one 576×6 array to increase the resolution. Then, two 576×6 array modules cascade again in the vertical direction, thereby increasing the FOV. Imaging system gets the panoramic view through the continuously scanning in horizontal direction of the long linear array detector. The whole system consists of infrared scanning head, image display and control unit, servomotor and so on, a picture of its structure shown in Fig. 1.

Installed in the servomotor, the step searching in pitching direction is through pitching control mechanism regulating the main reflector, while in azimuth direction through the linear array uniformly rotating one cycle per second to cover nearly 360 degrees searching range. The 50000 columns detection data produced in one revolution of the linear arrays are arranged column by column. The imaging system outputs up to 50000×1152 pixels per frame, which provides large enough FOV of high-resolution and high-definition panoramic image for searching. The main technical parameters of the system are as follows: 1) Detection capability: 360 degrees search per second. 2) FOV: $360° \times 4°$ panoramic view. 3) Detector: 288×6 long wave cooled detector. 4) Output image sizes: 288×50000, 576×50000, 1152×50000. 5) Frame frequency: 1 Hz.

Figure 2 shows a full frame of the real panoramic image. Because the actual size is too large to fit display, the whole image is divided into eight parts equally and compressed along the horizontal direction, with each part covering 45 degrees range.

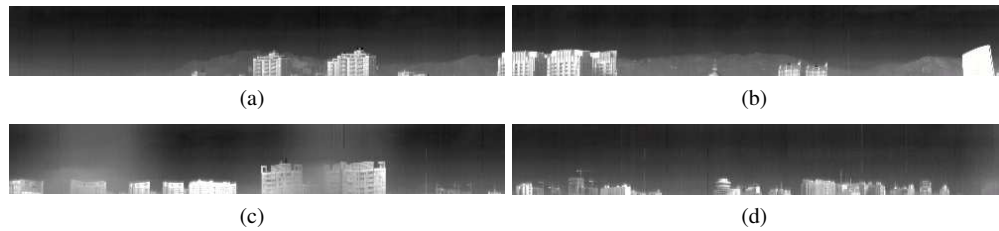Figure 1: A picture of the panoramic imaging system.

(a)   (b)

(c)   (d)

Figure 2: Total frame display of the real panoramic infrared image: part 1–4.

3. HARDWARE IMPLEMENTATION OF THE PROPOSED REAL-TIME PROCESSING PLATFORM

3.1. FPGA+DSP Architecture Design

In order to guarantee real-time, the total 54.9 MByte data acquired from the PIIS requires to be processed in one second and synchronously transferred to the display terminal. Further, the storage resources, computing speed and high-speed data transfer also should be taken into account. Texas Instruments (TI) has developed the industry's first 10 GHz multicore DSP TMS320C6678 in 2010 [5], with integrated fixed- and floating-point performance. Based on the innovative keystone architecture, the device has eight 1.25 GHz C66x cores providing 320 Giga-multiply accumulate per second (GMACs) and 160 Giga-floating point operations per second (GFLOPs) of performance. With flexible programmable ability and plenty of on-chip logic cells, FPGA devices integrate the power-efficient transceiver rocket IO with line rate up to 10 Gbps [6], which is the most suitable carrier to realize high-speed interconnection.

Based on industry's latest generation of multicore fixed- and floating-point DSP, and the high-performance FPGA, this paper designs a mix architecture of FPGA and DSP, to provides vast processing power for the PIIS, which has the following advantages: 1) Maximizing the throughput of on-board data flows and eliminating the performance bottlenecks. 2) Complex data computing by DSP, and programmable and reconfigurable resources of FPGA fully employed. 3) Hardware modules with portability and expansibility, that is ease to form more complex system and improve the performance. 4) Utilizing multi cores of single DSP to set up parallel system, yielding optimized parallelism while greatly simplifying the circuit for miniaturization and low power consumption.

Hardware block diagram of the real-time processing platform is shown in Fig. 3(a). The PCB board of the proposed platform shown in Fig. 3(b) is standard height and full-length x8 add-in card. It integrates a Virtex-6 family LX240T FPGA and a TMS320C6678 multicore DSP, that is efficient to accomplish complex algorithm for large volumes of data by parallel processing. Large-capacity DDR3 dynamic memory, the flexible depth expansion SODIMM and flash memory, yield real-time caching and high-speed fetch and load. In addition, complex system setting up and multi devices management is facile with abundant peripherals on the board.
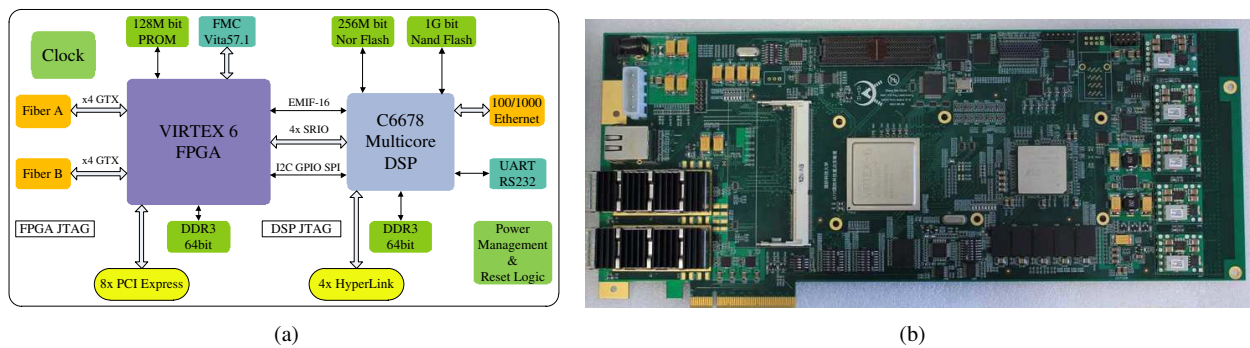
(a)   (b)

Figure 3: The proposed real-time processing platform. (a) Functional block diagram. (b) The PCB board.

3.2. Low Power Consumption: Variable Core Supply Voltage

In practical, some optimization measures can be taken to maximize the platform performance in terms of hardware design and program development. This section presents a methodology of low power consumption of DSP through the dynamic power monitoring technology. In order to decrease the power consumption while maintaining the device performance, TI developed a variable core supply solution, called SmartReflex technology [7]. It is able to dynamically monitor the power change and allows the core voltage to be optimized based on the device process corner.
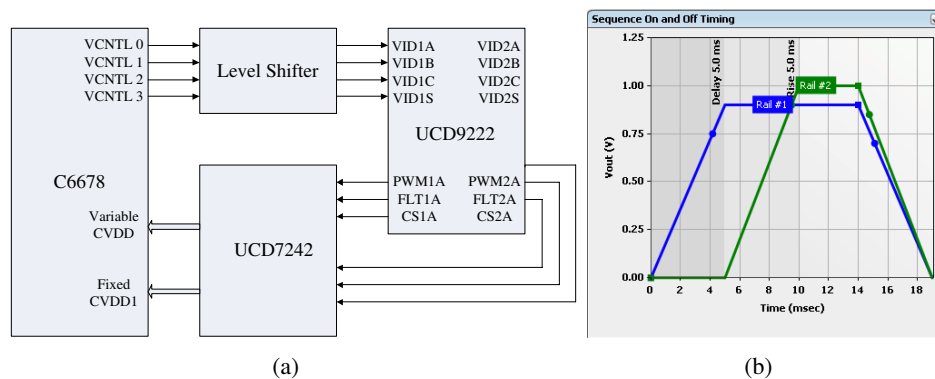

(a)   (b)

Figure 4: The variable and fixed core supply design for c6678 DSP, (a) Schematic circuit diagram. (b) On and off timing of the two power rails.

This paper uses a dual digital controller UCD9222 and a dual synchronous-buck power driver UCD7242 to regulate the DSP's core supply voltages: the variable core rail CVDD and the fixed 1.0 V core rail CVDD1. Fig. 4(a) is the schematic diagram designed for the DSP core power supply of our board, where one output of UCD9222 controller regulates the variable core rail, and the other unused output is configured as the fixed power rail. Fig. 4(b) shows the on and off timing of two core supply, where the blue curve represents the variable rail CVDD timing while the green curve represents the fixed rail CVDD1 timing.

In order to verify the validity of the hardware design and software configuration, real-time monitoring is applied to the two power rails by the UCD device design tool of fusion digital designer (Fusion GUI). Actual state on the board is read and displayed in Fig. 5. Take example for CVDD rail results shown in Fig. 5(a), the six windows on the right side are real timing of key parameters: input voltage Vin, input current Iin, output voltage Vout, output current Iout, output power Pout and the maximum temperature Temp. It can be seen clearly that, all the parameters fluctuate within the expected range, not exceeding the yellow warning curve and red error curve. This demonstrates that the hardware design in Fig. 4(a) realizes the SmartReflex technology for C6678 core supply. In addition, the two windows on the left side list the acquired information. The above one is the latest value in the "Readings group". The nether one displays the status register, where the green "OK" marks the correct state while the red "Fault" marks the wrong state.

Figure 5: Live parameters monitoring for the power rails: (a) CVDD, (b) CVDD1.

4. PLATFORM PERFORMANCE TESTS:HIGH-BANDWIDTH TRANSFER

To demonstrate the capability of high-bandwidth transfer with the designed platform, we select SRIO as an example to test. Different kinds of affairs and loads can influence the transfer speed greatly. Fig. 6 plots the curves of transfer speed for several affairs with various loads. As the load increasing, packet overhead of the SRIO protocol decreases, so the speed approximates theoretical value (1.25 GBps). When the packet load is small, affair of "Message" have the longest response time thereby the slowest rate. When the packet load is large, affair of "Nread" has the longest response time thereby the slowest rate.
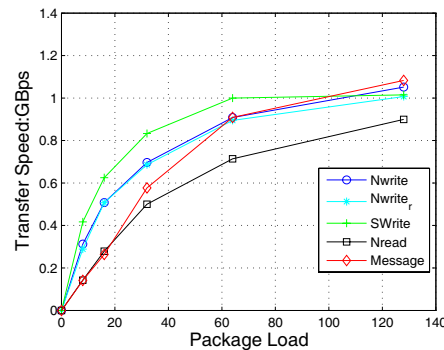

Figure 6: Transfer rate of different packages.

With maximum transfer rate set to 5 Gbps, the FPGA is used as initiator while DSP as the destination to test actual transfer rate by the SRIO protocol. Writing process is tested by sending "Swrite" packets from FPGA to DSP. On the other hand, FPGA sends "Nread" packets to DSP while DSP returns response packets to FPGA, which performs reading test. Using the ChipScope to capture continuous execution of SRIO reading and writing, the timing results are shown in Fig. 6 and Fig. 7 respectively. The average time interval by using FPGA as initiator endpoint to receive response packets (load 256 Byte) is 144 ns (36 clock cycles as the distance between the two red lines), whose transfer rate is 1.78 GBps. Similarly, the average time interval by using FPGA as destination endpoint to receive "Nread" packets (load 256 Byte) is 144 ns (35 clock cycles as the distance between the two red lines), whose transfer rate is 1.83 GBps.

Then we calculate the theoretical transfer rate and further analyze actual communication efficiency of SRIO reading and writing under the above experimental conditions. FPGA sending each "Swrite" packet will cost overhead of ten bytes, and the DSP returns a four-byte symbol to affirm reception. Therefore the theoretical transfer rate of SRIO writing data is calculated as

$$2.0\,\text{GB/s} \times \frac{256}{256 + 10 + 4} = 1.896\,\text{GB/s} \tag{1}$$

DSP returns each response packet which costs overhead of eight bytes, and also returns a four-byte symbol of affirming reception while receives the "Nread" packet. In addition, FPGA will also
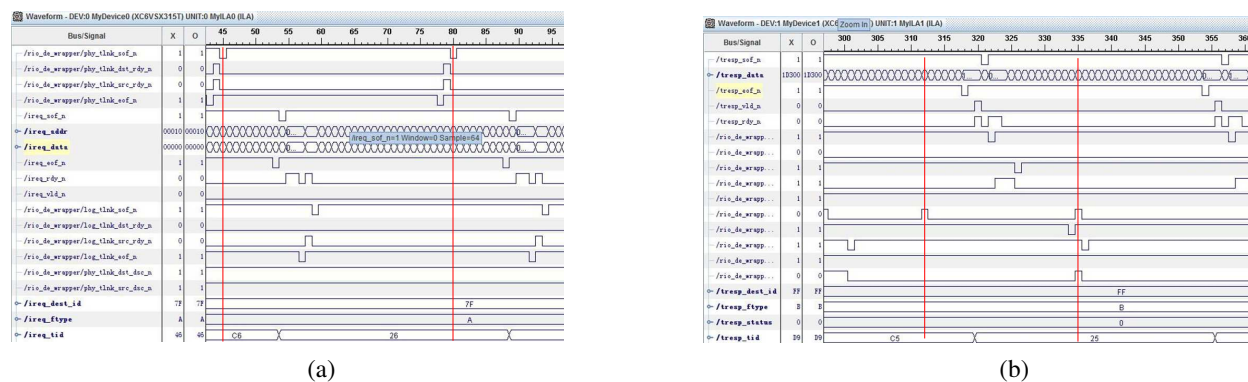
(a)   (b)

Figure 7: The real timing of SRIO rate: (a) FPGA writing data to DSP, (b) DSP writing data to FPGA.

return a four-byte symbol while receives the response packet. So the theoretical transfer rate of SRIO reading operation is given by

$$2.0\,\text{GB/s} \times \frac{256}{256 + 8 + 4 + 4} = 1.882\,\text{GB/s} \tag{2}$$

The actual communication efficiency of SRIO writing operation and SRIO reading operation are final calculated as

$$frac1.83\,\text{GB/s}1.896\,\text{GB/s} \times 100\% = 96.5\% \tag{3}$$

$$frac1.78\,\text{GB/s}1.882\,\text{GB/s} \times 100\% = 94.5\% \tag{4}$$

The testing results show that, the actual communication efficiency of SRIO approaches theoretical value. But the longer time by which DSP responses to FPGA reading request, causing a lower efficiency of reading operation.

5. CONCLUSION

The PIIS has abilities of panoramic FOV covering 360-degree airspace, high-resolution and multi-elements. This article addresses the real-time processing technique of image acquisition and panoramic display of the PIIS. It proposed a high-performance processing platform based on the FPGA + multicore DSP architecture. Using the dynamic power monitoring technology, the problem of high power consumption in circuits with high clock rate and complex device is solved effectively. The designed platform and optimization methodology make the high speed data transfer and real-time processing in PIIS possible and realizable.

REFERENCES

1. Wang, X. K., S. G. Zhu, and H. M. Gong, "The study of the micro Dewar for long linear HgCdTe IRFPA," *Laser Infrared*, Vol. 36, No. 11, 1047–1050, 2006.
2. Li, Y. J., J. R. Yang, L. He, et al., "Long-wave infrared 2048-elements linear HgCdTe focal plane array," *Journal of Infrared Millimeter Waves*, Vol. 28, No. 2, 90–92, 2009.
3. Yang, L., J. G. Yang, G. F. Che, and Z. H. Yu, "Real-time method for detecting multi-small targets in infrared large sight field," *Journal of Infrared Millimeter Waves*, Vol. 25, No. 5, 377–381, 2006.
4. Fan, H. B., "A high performance IRST system based on 1152 × 6 LWIR detectors," *Infrared Technology*, Vol. 32, No. 1, 20–24, 2010.
5. Tms320c6678 multicore fixed and floating-point digital signal processor data manual: SPRS691C datasheet, Available online: http://www.ti.com, 2012.
6. Virtex-6 Family overview: DS150 datasheet, Available online: http://www.xilinx.com, 2010.
7. Hardware design guide for keystone devices: SPRABI2A datasheet, Available online: http://www.ti.com, 2011.
8. Sam, F., *RapidIO The Embedded System Interconnect*, Publishing House of Electronics Industry, Beijing, 2006.

Monitoring for Resonant Mode of High-way System at Impulsive Impact

Shigehisa Nakamura

Kyoto University, Japan

Abstract— This note concerns on monitoring for a resonant mode of a high-way system at an impulsive impact. This work might be helpful for elementary finding of a key to show an advanced techniques at design, constructing, and maintaining of the life line systems which should be in a resonant mode for safety of public use even under any severe seismic condition on the surface of the earth.

1. INTRODUCTION

This note concerns on monitoring for a resonant mode of a high-way system at an impulsive impact. This work might be helpful for elementary finding of a key to show an advanced techniques at design, constructing, and maintaining of the life line system which should be in a resonant mode for public use even under any severe seismic condition on the surface of the earth.

2. A REVERSED PENDULUM UPSIDE DOWN

The most elementary system of the high-way system is a reversed pendulum upside down on the flat ground surface.

Now, assume a pole is set vertically on a flat surface to be horizontal in the gravity field. This pole must be stiffly fixed on the ground. Then, the pole can be an example of the reversed pendulum. If the string is made of a straight steel line, dynamics of this line can be formulated to have an simple harmonic oscillation. The frequency of the oscillation is determined by the size of the line and the essential elastic properties of the material which is consisting in the interested line.

When a weight is placed to set and fix at the top of the line. This line with the weight forms an elastic pendulum system.

In a case of a cylindrical pole made of concrete, this pole is equivalent to the steel line for a small amplitude though the concrete is not resistive to any forcing of tension, generally. Hence, a concrete pole with a buried steel skeleton is widely used in practice.

Then, the concrete pole can be equivalent under a support of a steel skeleton system to resisting external bending force which cause a tension and compression to the pole though the critical of the pole is taken in account of consideration not to breaking the pole.

Nevertheless, each of these poles made by a reinforced concrete cannot be resistive against some strong shock or an impulsive impact beyond its elastic critical.

3. A HIGH-WAY SYSTEM

A high-way system is constructed often using the space produced above an arranged linage of the multiple reinforced poles (each of poles with a top weight).

It is important to take care of the resonant mode of oscillations in practice. If not, this arrangement cannot be effective for the function of the aimed high-way system construction.

4. EXTERNAL FORCING

As for a possible external forcing to the high-way system noted above, it is essential to consider loading on the traffic above the top of the pole arrangement. In addition, some consideration should be required to consider about the local conditions of the ground surface.

Locality affects to the safety of the high-way system. Especially, the traffic in the seismic zones where some dangerous factor of accidents should be considered.

Concerning to a reinforced pole with a loading at the top, it is hard to construct the footing never yield to be in strength enough against a vertical impulsive impact as well as that for a possible horizontal forcing.

Especially, the reinforced pole structure is fragile at a vertical impulsive impact.

A specific manner of formulation for dynamics on a reinforced pole can be described as that might be seen in the field of structural mechanics for civil engineering or architectural engineering.

5. MATHEMATICAL DESCRIPTION

When a mathematical expression of dynamics of a reinforced pole with a loading at the top, could be reduced for a vertical impulsive impact, then, the vertical response $\mathbf{V}$ must be,

$$\mathbf{V}(x,y,z,t) = \int f(x,y,z,t; U(x,t), V(y,t), W(z,t)) dx dy dz dt, \tag{1}$$

where, the notation U, V, and W in a Cartesian co-ordinate $O\text{-}xyz$, and the notation f is a simplified expression for denoting a complicated mathematical solution. This can be written as follow. For the author's convenience,

$$\mathbf{V} = \int f(\mathbf{x}, \mathbf{U}, t) d\mathbf{x} d\mathbf{U} dt, \quad \text{or,} \quad V = \int f(\mathbf{x}, t) d\mathbf{x} dt, \tag{2}$$

where, $\mathbf{x} = \mathbf{x}(x,y,z,t)$, and, $\mathbf{U} = \mathbf{U}(U,V,W,t)$.

Generally, such the solution of the dynamics could be in a form of an ensemble of suffix "i" as a series of integer. Then, the above expression for $\mathbf{V}$ can be rewritten as,

$$\mathbf{V} = \int \mathbf{V}_o \exp(\mathbf{k}_i \mathbf{x} - \omega_i t) d\mathbf{x} dt. \tag{3}$$

6. IMPULSIVE IMPACT

As for a vertical impulsive impact, it can be expressed in a mathematical form by using a delta function, that is, for example,

$$\mathbf{I}_j = \mathbf{I}_j(\mathbf{x}, t) = \delta(\mathbf{I}_j; t = 0), \tag{4}$$

where, $\mathbf{I}_j = \mathbf{I}_j(\mathbf{I_x}, \mathbf{I_y}, \mathbf{I_z})$.

Then, a dynamical response $\mathbf{R}$ of the pole as a reversed pendulum with a top weight can be written as, for the vertical external impulsive impact, i.e.,

$$\mathbf{R} = \mathbf{I}_j \times \mathbf{V} = \int \mathbf{I}_j V_o \exp(\mathbf{k}_i \mathbf{x} - \omega_i t) d\mathbf{k}_i dt. \tag{5}$$

Then, the above expression can be rewritten in a more simple form, i.e.,

$$\mathbf{R} = \int \delta(\mathbf{I}_j; t = 0) V_o \exp(\mathbf{k}_j \mathbf{x} - \omega_i t) d\mathbf{k}_j dt. \tag{6}$$

Now, a resonant mode of the reinforced pole with a top weight for the given external forcing in a form of an impulsive impact can be found.

As for a set of arranged poles in a formation of a high-way net work system, the resonant mode can be found after a mathematical reduction to obtain a solution in a quite similar manner as seen above.

Figure 1: A pattern similar to "Dominoes game" found in the arranged reinforced poles under the high-way system for serving traffics and lifeline net-works in Kobe in 1995 January 17 (courtesy of Kobe City).

7. DISCUSSIONS AND CONCLUSIONS

In a case of 1995 earthquake hit Kobe, there is kept their reminding memory that a water filled in a bath tub shed out just after the impulsive impact because the bath tub landed to leave out the tap at the bath tub flat bottom.

A scientific estimation of the acceleration at the forcing of the seismic shock in a form of an impulsive impact was evaluated to produce an acceleration of more than six gal or more. Maximum must be about ten gal or more so that the bath tub must be in non-gravity forcing for a short instance.

The episode of the bath tub in a non-gravity forcing was seen just neighbor the seismic fault formation along the seismic fault at the event crossing the urban area in Kobe.

When any one of the pole supporting the high-way system is crushed in the resonant mode after yielding or creeping beyond the elastic critical, then, the arranged reinforced poles start a dominoes game to result the lifeline system's crush (cf. Figure 1).

In memory of the hazards at the Nepal earthquake on 25 April 2015.

Examples of Electromagnetic Field Sources in an Indoor Distribution Substation

Rauno Pääkkönen[1], **Marko Lundström**[2], **Jari Mustaparta**[3], **and Leena Korpinen**[1]

[1]Tampere University of Technology, Tampere, Finland
[2]Tampereen Sähköverkko Oy, Tampere, Finland
[3]Turku Energia Sähköverkot Oy, Turku, Finland

Abstract— The paper presents example measurements of electromagnetic fields in an indoor distribution substation. We measured at different places: At Place A (near the fuse panel), using (1) frequency bandwidth (FB) 40 kHz–100 kHz, fields varied 0.011–0.039 µT and using (2) FB 5 Hz–100 kHz, fields varied 67–74 µT; at Place B (the surface of the collector meter), the fields varied from 0.022 to 0.083 µT (40 kHz–100 kHz); at Place C (near the antenna of the collector meter), the maximum radio frequency field was $1.0 \, \text{W/m}^2$, and at Place D (the surface of the antenna), it was $1.8 \, \text{W/m}^{2\cdot}$. The measured values were below ICNIRP guidelines.

1. INTRODUCTION

In indoor distribution substations, there are typically extremely low frequency (ELF) electric and magnetic field sources, e.g., transformers and cables. However, nowadays there can also be smart meters or collector meters. These smart meters most often send information or communicate using either a radio frequency (800–3000 MHz) aerial signal to masts or a 50–100 kHz electromagnetic field (EF) signal via cables [3, 5]. The International Commission on Non-ionizing Radiation Protection (ICNIRP) has set different guidelines for the general public [2, 4]. For the frequency range of 5 Hz–50 kHz, the guidelines are for the magnetic flux density 27–1000 µT and 83–5000 V/m for the electric field [2]. For the 50–500 kHz, the guidelines are 83 V/m for the electric field and 27 µT for the magnetic flux density [2]. For the frequency range of 800–3000 MHz, the ICNIRP guidelines are 4–$10 \, \text{W/m}^2$ [4]. The EU has given a directive for work-related exposure [1].

The aim of this paper was to present example measurements of EF exposure to sources in an indoor distribution substation.

2. MATERIALS AND METHODS

Figure 1 shows Place A measurements, which was near the fuse panel in an indoor distribution substation. Figure 2 gives measurements for Places B, C and D.

Figure 1: Measurement Place A, near fuse panel.

We used the magnetic field meter MFM 3000 by Combinova, with a separate probe version, video recording with RMS values, and spectrum (Samsung smart phone type Samsung Galaxy S

Figure 2: Examples of measurements in different areas (Places B, C, and D).

III), the Narda EMR-300 with probe T-33C, and a Holaday 3603 VLF Survey meter. We performed measurements at three places.

Place A (Figure 1) was near the fuse panel, where we made measurements with (1) frequency bandwidth 40 kHz–100 kHz (57 measurements) and (2) 5 Hz–100 kHz (62 measurements). Place B (Figure 2) was on the surface of the collector meter (15 measurements), Place C (Figure 2) was near the antenna of the collector meter (7 measurements), and Place D (Figure 2) on the surface of the antenna (24 measurements).

3. RESULTS AND DISCUSSION

Table 1 shows the magnetic field measurement results, and Tables 2 and 3 provide the radiofrequency results. Using the bandwidth (1) in Place A, we obtained 11 values, which varied from 0.011–0.039 µT; other values were 0.0038–0.0052 µT. The source of those values can be the collector meter, which signals via cables. Utilizing the bandwidth (2), the magnetic fields were 67–74 µT.

In Place B, the magnetic fields varied from 0.022 to 0.083 µT, and the frequency bandwidth was 40 kHz–100 kHz.

Table 1: Magnetic field measurement results in different places.

Amount of measurements	Max field, µT	Average MF (all) µT (40 kHz–100 kHz)	place
57 (11 during reading)	0.04	0.01 (during reading 0.03)	A*
9 (9 during reading)	0.08	0.06 (during reading same)	B
6 (6 during reading)	0.08	0.06 (during reading same)	C
		Average MF (all) µT (5 Hz–100 kHz)	
62	73.9	70.32 (standard deviation 2.02)	A*
58	70.4	66.8 (standard deviation 1.53)	A*

*distance 50 cm, height 1.7 m

Tables 2 and 3 reveal the radiofrequency EF measurement results in Places C and D.

In Place C, the radio frequency maximum field was $1.0 \, \text{W/m}^2$, and in Place D, it was $1.8 \, \text{W/m}^2$. To evaluate the possible effects of EFs, it is possible to use guidelines of the ICNIRP, and measured values were below guidelines.

Meters and guidelines have different frequency ranges, and the comparison of measurement results to guidelines is not so easy to do. Therefore, we have used frequency analysis of magnetic flux densities to be able to do those comparisons (Figure 3).

In that figure, we can see that there is a lot of magnetic flux on frequencies of less than 3 kHz. There is only a relatively small peak at the frequency of about 80 kHz that sends the information

Table 2: Radiofrequency EF measurement results in Place C.

n	RF field, W/m^2	Place
1	0.47	C
2	0.86	C
3	1.30	C
4	0.86	C
5	0.87	C
6	1.0	C
7	0.4	C

Table 3: Radiofrequency EF measurement results in Place D.

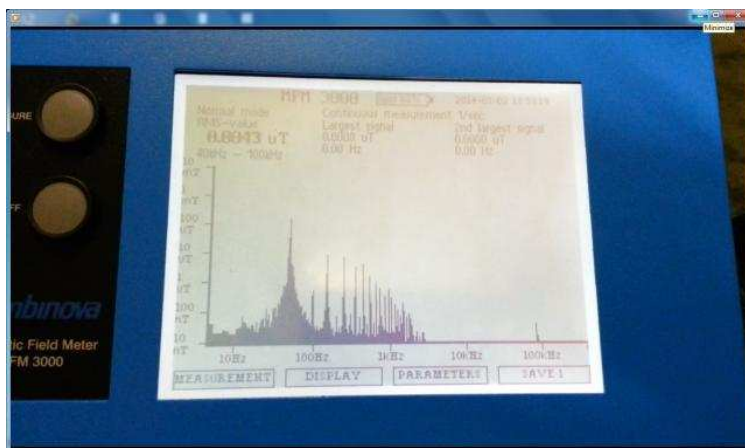| n	RF field, W/m^2	Place
1	0.47	D
2	0.47	D
3	1.76	D
4	0.86	D
5	0.51	D
6	0.99	D
7	1.0	D
8	1.3	D
9	0.43	D
10	0.84	D
11	1.06	D
12	1.28	D
13	1.48	D
14	1.23	D
15	0.62	D
16	0.64	D
17	0.65	D
18	0.65	D
19	1.31	D
20	0.68	D
21	1.3	D
22	1.80	D
23	1.64	D
24	0.53	D

Figure 3: Example measurement.

of smart meters. For the radiofrequencies, the situation is similar, and then we must know what kinds of fields exist to be able to use broadband meters reliably.

4. CONCLUSION

The measured values at the indoor distribution substation were clearly less than the ICNIRP guideline values. Therefore, no special sheltering against these fields is needed. These measurements need many meters and careful analysis of frequencies if broadband meters are to be used. Frequency analysis helps to detect if any odd fields exist in spaces.

REFERENCES

1. European Parliament and Council of the European Union, Directive 2013/35/EU of the European Parliament and of the Council on the Minimum Health and Safety Requirements regarding the Exposure of Workers to the Risks arising from Physical Agents (Electromagnetic Fields) (20th Individual Directive within the Meaning of Article 16(1) of Directive 89/391/EEC) and Repealing Directive 2004/40/EC, 21, Official Journal of the European Union, 2013.

2. "ICNIRP, guidelines for limiting exposure to time varying electric and magnetic fields (1 Hz–100 kHz)," *Health Phys.*, Vol. 99, 818–836, 2010.

3. Tell, R., R. Kavet, and G. Mezei, "Characterization of radiofrequency field emissions from smart meters," *Journal of Exposure Science and Environmental Epidemiology*, Vol. 23, 549–553, 2013.

4. "ICNIRP guidelines for limiting exposure to time-varying electric, magnetic, and electromagnetic fields (up to 300 GHz)," *Health Phys.*, Vol. 74, No. 4, 494–522, 1998.

5. "AMI meter electromagnetic field survey. Final report. Prepared for department of primary industries," Document Number: M110736, October 20, 2011, www.dpi.vic.gov.

Emission of Smart Meter Electric Fields (50–100 kHz) in Finland

Rauno Pääkkönen[1], **Marko Lundström**[2], **Jari Mustaparta**[3], **and Leena Korpinen**[1]

[1]Tampere University of Technology, Tampere, Finland
[2]Tampereen Sähköverkko Oy, Tampere, Finland
[3]Turku Energia Sähköverkot Oy, Turku, Finland

Abstract— This paper presents example measurements of electric field exposure to smart meters for cable-transmitted (50–100 kHz) signal emissions. The operator of a utility company remotely read the smart meters when we measured electric fields. Altogether, we measured 27 smart meters, which used power line communication (PLC). Meters used plan and lon protocols. We used the Holaday 3603 directional electric field meter, and the measurement distance was at the surface of the meter. The highest electric field was 5.2 V/m, which is only 6% of the recommended public exposure limit according to the ICNIRP guidelines.

1. INTRODUCTION

Discussion of the possible health effects of electromagnetic field (EMF) exposure caused by smart meters has become livelier as the use of smart meters has increased, for example, in Finland [3, 5]. Therefore, we have done measurements and also published data on the measurements of smart meters [6–10] The International Commission on Non-ionizing Radiation Protection (ICNIRP) has suggested 83 V/m as the limit for the general public at the frequency range of 3–300 kHz, which we will use to evaluate EMF exposure [2, 4]. For work-related exposure, there is also a relatively new EU directive [1].

The aim of this paper is to present example measurements of electric field exposure to smart meters for cable-transmitted (50–100 kHz) signal emissions.

2. MATERIALS AND METHODS

We used a Holaday 3603, a one-directional electric field meter (linear frequency response 2–300 kHz, 1–2000 V/m, ±2 dB). The measurement distance was at the surface of the meter because the values were so small that it was not possible to get values from other distances. The operator of a utility company remotely read the smart meters when we measured electric fields. Figures 1–3 show examples of the measurements.
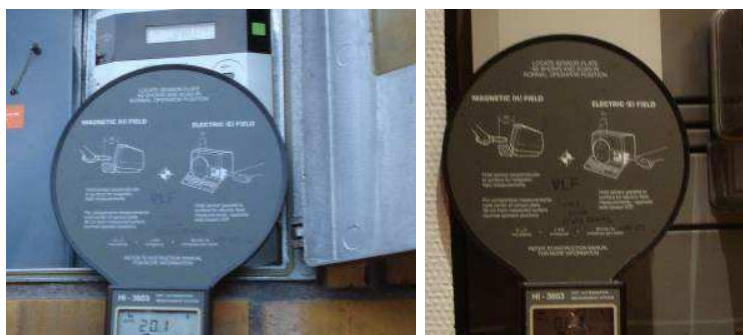

Figure 1: Examples of electric field measurements of houses with smart meter.

3. RESULTS AND DISCUSSION

Altogether, we measured 27 smart meters, which used power line communication (PLC). Meters used plan and lon protocols. Only one meter used a DLC protocol. Table 1 shows the measurement results.

The highest measured electric field was 5.2 V/m, which is only 6% of the recommended public exposure limit according to the ICNIRP guidelines. The smart meter readings were very short (about 20 s); therefore, the possible sxposure time is also very short. Secondly, the electric field is much less at a distance of 0.5 m from the smart meters. This is important to take into account when we analyze the measurement results and compare them to guidelines.

Figure 2: Example of electric field measurements of the basement.

Table 1: Electric field measurement results of the smart meters.

n	Type of the smart meter	Protocol of the meter	Electric field, V/m
1	E450-3P	plan	0.7
2	E450-3P	plan	2.2
3	E450-3P	plan	0.8
4	E450-3P	plan	2.1
5	E450-3P	plan	4.3
6	E120LiME	lon	0.2
7	ET10	lon	0.6
8	E120LiME	lon	5.2
9	E120LiME	lon	0.7
10	E450-1P	plan	2.8
11	E450-1P	plan	0.6
12	E450-1P	plan	1.2
13	E450-1P	plan	0.5
14	E450-3P	plan	2.3
15	E450-3P	plan	4.1
16	E450-3P	plan	2.3
17	E450-3P	plan	2.5
18	E450-3P	plan	1.8
19	Iskra	DLC	2.9
20	E120LiME	lon	3.5
21	E120LiME	lon	2.8
22	E120LiME	lon	4.7
23	E120LiME	lon	3.5
24	E120LiME	lon	2.6
25	E120LiME	lon	2.3
26	E120LiME	lon	3.1
27	E120LiME	lon	2.2

On the other hand, the meter was one-directional; hence, we measured only in the direction where the electric field vectors were coming from the smart meter towards the person conducting the reading. However, we also checked some sites that there did not contain more significant electric field vectors to other directions. Although, if we even multiply measured values by three (geometrical summing), the values obtained would still be far below the limit values.

4. CONCLUSION

Based on our measurements, it is possible to conclude that the electric field exposure of smart meters is significantly less than the guideline values for the general public. There is no specific need to improve the sheltering of the meters from the public. However, it is possible to more precisely measure electromagnetic field emissions from smart meters, but our preliminary results did not warrant further concern.

REFERENCES

1. European Parliament and Council of the European Union (2013) Directive 2013/35/EU of the European Parliament and of the Council on the Minimum Health and Safety Requirements regarding the Exposure of Workers to the Risks arising from Physical Agents (Electromagnetic Fields) (20th Individual Directive within the Meaning of Article 16(1) of Directive 89/391/EEC) and Repealing Directive 2004/40/EC. Official Journal of the European Union, p. 21.
2. ICNIRP, "Guidelines for limiting exposure to time varying electric and magnetic fields (1 Hz–100 kHz)," *Health Phys.*, Vol. 99, 818–836, 2010.
3. Tell, R., R. Kavet, and G. Mezei, "Characterization of radiofrequency field emissions from smart meters," *Journal of Exposure Science and Environmental Epidemiology*, Vol. 23, 549–553, 2013.
4. ICNIRP, "Guidelines for limiting exposure to time-varying electric, magnetic, and electromagnetic fields (up to 300 GHz)," *Health Phys.*, Vol. 74, No. 4, 494–522, 1998.
5. "AMI meter electromagnetic field survey," Final report, Prepared for department of primary industries, Document Number: M110736, Date: 20 October 2011, www.dpi.vic.gov.
6. Pääkkönen, R., M. Lundström, J. Mustaparta, and L. Korpinen, "Mesures préliminaires des émissions de champ électromagnétique (50-100 khz) d'un compteur intelligent en Finlande, Effetn biologiques etsanitaires des rayonnements non ionisants," Limoges, France, in press, 16 October 2014 (in French).
7. Pääkkönen, R.,, M. Lundström, J. Mustaparta, and L. Korpinen. "Examples of electromagnetic field (50–100 kHz) emissions from smart meters in Finland," *Radioprotection*, in press, 2015.
8. Pääkkönen, R., M. Lundström, J. Mustaparta, and L. Korpinen, "Preliminary measurements of smart meter electromagnetic field (50–100 kHz) emissions in Finland," *8th International Workshop on Biological Effects of Electromagnetic Fields*, Bulgaria, Varna, 2014.
9. Pääkkönen, R., M. Lundström, J. Mustaparta, and L. Korpinen, "Exposure to RF fields during the remote readings of the smart meter in Finland," *8th International Workshop on Biological Effects of Electromagnetic Fields*, Bulgaria, Varna, 2014.
10. Pääkkönen, R. and L. Korpinen, "Emission of smart meter electromagnetic field (50–100 kHz) in Finland," paper 1484 CIRED 2015 in Lyon, in press, 2015.

Smart Receiver for Multi-antenna Transmitters with Constellation Shaping

Paulo Montezuma[1,2,3], **Sara Ribeiro**[1], **Mario Marques da Silva**[2,4], **and Rui Dinis**[1,2]

[1]DEE, FCT Universidade Nova de Lisboa, Portugal
[2]IT, Instituto de Telecomunicações, Av. Rovisco Pais, Lisboa, Portugal
[3]Uninova, Instituto de Desenvolvimento de Novas Tecnologias, Quinta da Torre, Caparica, Portugal
[4]Universidade Autonoma de Lisboa, Portugal

Abstract— Spectral and power efficiency together with physical layer security can be achieved by a MISO (Multiple Input Single Output) where multilevel modulations are decomposed as a sum of BPSK (Bi Phase Shift Keying) components that are combined at channel level. The directivity is associated to the transmitted information due to the shaping of the constellation in a desired direction Θ (it is important to note that shaping means a rearrangement of the constellation symbols according to a desired direction Θ) and can be be increased by changes on phases phase shifts between antenna array or changes on the values of the coefficients that define the BPSK components. Consequently, for successful data reception it is necessary to know the configuration parameters used at transmitter. Despite the security achieved by this transmitter structure, a practical application is only possible if authorized receivers are able to decode with success the transmitted data. Here it is demonstrated the validity of the hypothesis of a smart receiver that knows these parameters based on a algorithm that can estimate the set of coefficients applied in constellation shaping and the array configuration. The cases analyzed here and the simulation results presented show that good performance is attainable by the proposed receiver, even when the directivity increases with the number of BPSK components used in the decomposition of the multilevel constellation, which validate our initial assumption.

1. INTRODUCTION

Security, power and spectral efficiencies are important requirements in wireless communication systems. The first one can be achieved by encrypted schemes from higher layers or physical layer security schemes or association of both [1–3]. On the other hand, MIMO (Multiple-input multiple-output) systems can be employed to overpass power and bandwidth constrains so common in wireless communications systems. However, the need of high spectral efficiencies apart from making scarcely recommendable physical security solutions based on codes [3], are also only attainable by multilevel constellations usually characterized by significant envelope fluctuations that compromise efficiency of power amplification. Thus, both redundancy (associated to the coded bits) and restrictions on power amplification should be avoided. These two problems can be overpassed by a transmitter structure where multilevel constellations are the sum result of several uncorrelated BPSK (Bi Phase Shift Keying) that are amplified and transmitted independently by an antenna. Obviously, this transmitter requires a separate RF (Radio frequency)-branch including a power amplifier for each antenna element [4, 5], being each RF chain associated to a BPSK sub-constellation that is combined at channel level to generate the desired multilevel constellation. Power of efficiency of amplification is improved since the constant envelope components allow the use of nonlinear (NL) amplifiers power amplification [6, 7]. Security is assured through the optimization of the transmitted constellation in the desired direction Θ, by a proper shaping of the constellation's symbols. Therefore, instead directivity on radiation pattern we have directivity at information level, i.e., at the transmitted constellation. When non compensated, this constellation shape acts as a nonlinear distortion due to phase rotations of components associated to each amplification branch (it should be noted that phase shifts between antennas also change the distances between constellation's symbols which has impact on system performance). Several factors such as the set of coefficients g_i or the distance between antennas affect directivity and the shape of the constellation. Consequently, for successful data reception it becomes crucial a robust receiver based on an algorithm that estimates the set of coefficients used at the transmitter.

Several indicators are considered to evaluate smart receiver under this security scheme such as mutual information (MI) and the bit error performance (BER) of smart receiver. It is well known that large constellations in general and non-uniform constellations in particular are very sensitive to interference, namely the residual ISI (Inter-Symbol Interference) due to frequency selective channel

effects. To cope with channel effects we consider the use of SC-FDE (Single-Carrier with Frequency-Domain Equalization) schemes, with IB-DFE (Iterative Block Decision Feedback Equalization) that can reduce substantially ISI [8, 9] levels in these constellations.

In this paper we consider how to exploit a multi-branch transmission technique with constellation shaping as a novel signal processing technique to introduce some kind of physical layer security. We admit similar channels between the source and intended receiver and between the source and the eavesdropper. We start in Section 2 by characterizing the new transmission technique. The rest of this paper is organized as follows: A brief characterization of the receiver is made in Section 4. A set of performance results is presented in Section 4.1. Section 5 resumes this paper.

2. TRANSMITTER STRUCTURE

Let us consider the transmitter whose structure is depicted in Figure 1. Contrarily to MIMO, the N_m RF branches are employed to allow an efficient amplification of the signals associated to a large constellation. Firstly, the data bits are mapped into a given constellation (e.g., a QAM (Quadrature Amplitude Modulation) constellation) characterized by the ordered set $\mathfrak{S} = \{s_0, s_1, \ldots, s_{M-1}\}$ following the rule $(\beta_n^{(\mu-1)}, \beta_n^{(\mu-2)}, \ldots, \beta_n^{(1)}, \beta_n^{(1)}) \mapsto s_n \in \mathfrak{S}$, with $(\beta_n^{(\mu-1)}, \beta_n^{(\mu-2)}, \ldots, \beta_n^{(1)}, \beta_n^{(1)})$ denoting the binary representation of n with $\mu = \log_2(M)$ bits. Next, the constellations symbols are decomposed in M_m polar components, i.e.,

$$s_n = g_0 + g_1 b_n^{(1)} + g_2 b_n^{(2)} + g_3 b_n^{(1)} b_n^{(2)} + g_4 b_n^{(3)} + \ldots = \sum_{i=0}^{M-1} g_i \prod_{m=0}^{\mu-1} \left(b_n^{(m)} \right)^{\gamma_{m,i}}, \tag{1}$$

with $(\gamma_{\mu,i}\, \gamma_{\mu-1,i} \, \cdots \, \gamma_{2,i}\, \gamma_{1,i})$ denoting the binary representation of i and $b_n^{(m)} = (-1)^{\beta_n^{(m)}}$ is the polar representation of the bit $\beta_n^{(m)}$. Thus, we have M constellation symbols in $\mathfrak{S}$ and M complex coefficients g_i, (1) is a system of M equations that can be used to obtain the coefficients g_i, $i = 0, 1, \ldots, M-1$. Let N_m denote the number of non-zero coefficients g_i coefficients, then a given constellation can be decomposed as the sum of $N_m \leq M$ polar components. Each one of the N_m polar components is modulated as a BPSK signal, that can be a serial representation of an OQPSK signal [10], with reduced envelope fluctuations and compact spectrum (e.g., a gaussian minimum shift keying (GMSK) signal). The corresponding signals are separately amplified by N_m nonlinear amplifiers before being transmitted by N_m antennas.

Since the N_m BPSK components in RF branches are uncorrelated, the N_m antenna array changes the constellation shape to optimize it in a desired direction Θ keeping at same time unchanged the radiation pattern. Consequently, security is assured through the optimization of the transmitted constellation in the desired direction Θ, by a proper shaping of the constellation's symbols. This means that when the set of coefficients g_i and the array configuration are unknown, the receiver is unable to compensate the nonlinear distortion that affects the transmitted constellation. Due to the high number of factors affecting the shape of the transmitted constellation, complexity is also assured (complexity analysis it will be analyzed in future work but now it is beyond the scope of
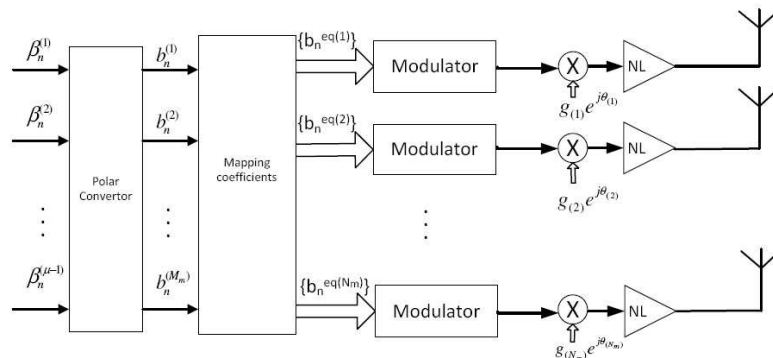

Figure 1: Structure of constellation directive transmitter.

the present paper). However, a smart receiver with knowledge about the set of coefficients g_i and array configuration is able to decode data successfully, as it will be seen in next sections.

3. MOTIVATIONS FOR A SMART RECEIVER

The motivation behind the smart receiver lies on the fact that when are known the transmitter parameters at the receiver the transmitted data can be received with success, as we shall see from the results posted in this section. Having in mind these considerations, we also present some results regarding the mutual information associated to smart receiver that sustain our initial hypothesis. It is assumed that the receiver knows the transmitter coefficients g_i as well as the array configuration. We admit that BPSK components follow a linear and uniform arrangement with antennas equal spaced by $d/\lambda = 1/4$ at the transmitter. We assume an Additive White Gaussian (AWGN) channel. Let $s(t)$ denote the nth transmitted symbol associated to a given block

$$s(t) = s_n h_T(t - nT_S), \tag{2}$$

with T_S denoting the symbol duration and $h_T(t)$ denoting the adopted pulse shape. s_n belongs to a given size-M constellation $\mathfrak{S}$. Under these conditions the received signal is

$$y(t) = f_A(s(t)) + n(t), \tag{3}$$

with $n(t)$ denoting de noise term and where f_A denotes the shaping performed by the transmitter array.

With perfect secrecy we have $I(S; Y) = 0$, with S the sent message, Y the received message and $I(\, ;)$ the mutual information. It should be noted that the mutual information (assuming equiprobable symbols) for a given signal set $\mathfrak{S}$ gives the maximum transmission rate (in bits/channel use) at which error-free transmission is possible with such constellation set [11], and can be written as

$$I(S, Y) = \log_2 M - \frac{1}{M} \sum_{s \in \mathfrak{S}} \mathbf{E}_n \left[\log_2 \left(\sum_{s'_n \in \mathfrak{S}} \exp \left(-\frac{1}{N_0} \left| \sqrt{Es}(s_n - s'_n) + n \right|^2 - |n|^2 \right) \right) \right], \tag{4}$$

where $\mathbf{E}$ denotes the expectation.

16-QAM with gray mapping is characterized by the set of non null coefficients $g_{34} = 2j$, $g_1 = 1$, $g_3 = 2$ and $g_{12} = j$, associated to the antennas $1, 2, 3$ and 4, respectively. 64-QAM is characterized by 6 coefficients with values $2j$, 1, 2, j, 4 and $4j$ associated to the antennas $1, 2, 3, 4, 5$ and 6, respectively.

Average results for MI are assured by independent trials of Monte Carlo experiments. For both constellations sizes, symbols s_n are selected with equal probability from $\mathfrak{S}$. Some MI results are expressed as function of $\frac{E_b}{N_0}$, where $N_0/2$ is the noise variance and E_b is the energy of the transmitted bits.

In Figure 2 it can be seen the MI behavior with the constellation optimization angle Θ for 16-QAM and 64-QAM, respectively. It is obvious that MI remains practically unaffected for the different values of Θ. This means that our initial hypothesis is valid since the smart receiver is able to decode the sent information independently of the direction in which the constellation is optimized. On the other hand, if coefficients g_i are only approximately known, distortion arises and MI becomes affected. To have an idea of the effects of any imprecision we also include Figures 3 and 6 with the MI results expressed as function of $\frac{E_b}{N_0}$ when errors on g_i estimates lead several Θ estimation errors (estimation errors of $4°$ and $8°$ are considered and we assume $\Theta = 75°$). As we can see from these figures, the tolerance against estimation errors decreases with constellation size. For example, in 64-QAM the tolerance is $\Delta\Theta \leq 2°$, since for higher errors the MI values are severely affected. On the other hand, in 16-QAM the MI is less affected by estimation errors, which means higher tolerance to errors on the estimate of Θ. This was expected, since the directivity and corresponding constellation shaping increases with the number of RF branches.

Let assume that a eavesdropper knows the initial set of parameters but is unable to estimate the new parameters related with the constellations optimized for $\Theta + \Delta\Theta$ with $\Delta\Theta = 0°, 4°$ and $8°$. From results of Figures 3 and 6 it is obvious the inherent security achieved by this transmitter. Obviously, if the eavesdropper do not have any information about the coefficients g_i and the array configuration the MI is always null for both constellation sizes.
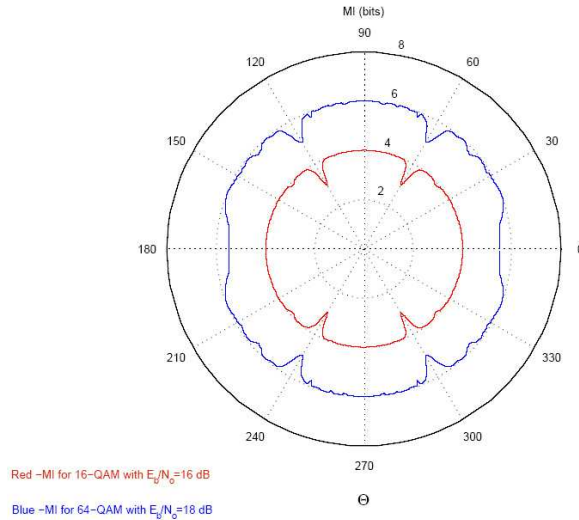
Figure 2: MI behavior with the angle Θ for 16-QAM and 64-QAM.
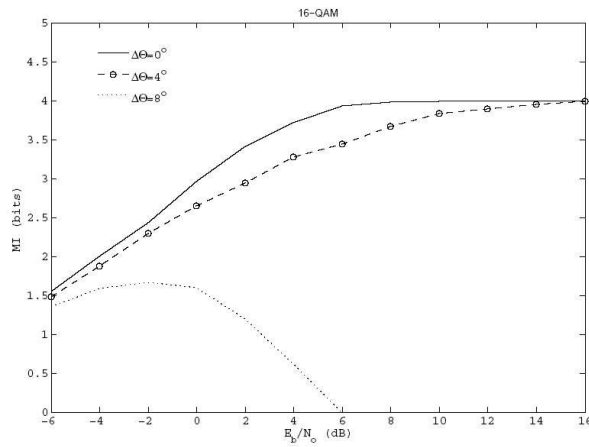
Figure 3: MI evolution for 16QAM and impact of an angle error regarding the transmission direction Θ.
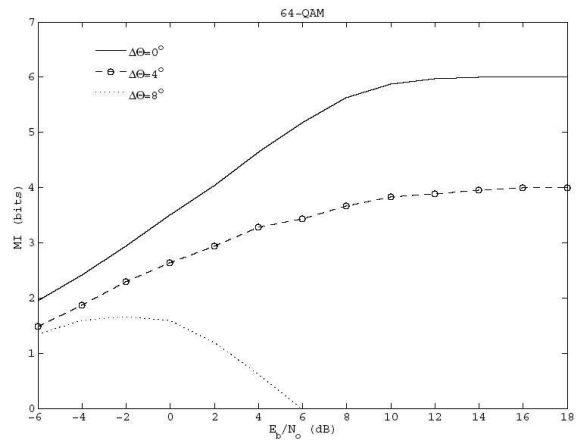
Figure 4: MI evolution for 64QAM and impact of an angle error regarding the transmission direction Θ.

4. BEHAVIOR IN FREQUENCY SELECTIVE CHANNELS

Since we admit that the smart receiver knows the channel and the set of N_m coefficients g_i, phase rotations due to channel or phase shifts associated to the array's configuration can be easily compensated. These operations must be performed before the IB-DFE receiver whose structure is depicted in Figure 5. We assume constant envelope signals in each amplification branch. Under these conditions the signal associated to a given block is

$$s(t) = \sum_{n=-N_G}^{N-1} s_n h_T(t - nT_S), \tag{5}$$

with T_S denoting the symbol duration, N_G denoting the number of samples at the cyclic prefix, N denoting the number of samples at the useful part of the block and $h_T(t)$ denoting the adopted pulse shape. The nth transmitted symbol s_n belongs to a given size-M constellation $\mathfrak{S}$. As usual, the cyclic prefix corresponds to a periodic extension of the useful part of the block, i.e., $s_{-n} = s_{N-n}$ with a length higher than the overall channel impulse response.

The samples associated to the cyclic prefix are discarded, which means null IBI (Inter Block Interference) and reduces the impact of a time-dispersive channel to a scaling factor for each frequency. Thus, the corresponding frequency-domain block is $\{Y_k; k = 0, 1, \ldots, N - 1\} = \text{DFT}$

$\{y_n; n = 0, 1, \ldots, N - 1\}$), where

$$Y_k = S_k H_k + N_k, \tag{6}$$

with H_k denoting the channel frequency response for the kth subcarrier and N_k the corresponding channel noise.

For a given iteration the output samples are given by

$$\tilde{S}_k = F_k Y_k - B_k \overline{S}_k, \tag{7}$$

where $\{F_k; k = 0, 1, \ldots, N - 1\}$ and $\{B_k; k = 0, 1, \ldots, N - 1\}$ denote the feedforward and the feedback coefficients, respectively, and $\{\overline{S}_k; k = 0, 1, \ldots, N - 1\}$ is the DFT of the block $\{\overline{s}_n; n = 0, 1, \ldots, N-1\}$, with $\overline{s}_n$ denoting the average value of s_n conditioned to the FDE output associated to the previous iteration. It can be shown that the optimum coefficients F_k, B_k and the correlation coefficient ρ are computed as described in [12, 13].

4.1. Numerical Results

To evaluate the smart receiver's performance, here we focus on the performance of the proposed system in a severely time-dispersive channel, characterized by an uniform PDP (Power Delay Profile), with 32 equal-power taps, with uncorrelated rayleigh fading on each tap. We also make the practical assumption of linear power amplification at the transmitter, perfect synchronization and channel estimation at the receiver. Results are expressed as function of $\frac{E_b}{N_0}$. It is assumed that the smart receiver can estimate the transmitter parameters with or without error. It is adopted a SC-FDE modulation with blocks of $N = 256$ useful symbols plus a cyclic prefix of 32 symbols longer than overall delay spread of the channel. We also assumed that the eavesdropper has information about the initial configuration of the transmitter under the direction Θ (for example we assume $\Theta = 75°$, but the results are similar for other values). However, is unable to estimate the small changes made in configuration parameters associated to a change of $4°$ in the direction Θ. It should be mentioned that when no information is available at eavesdropper the BER assumes a irreducible value near 0.5, for both constellations sizes.
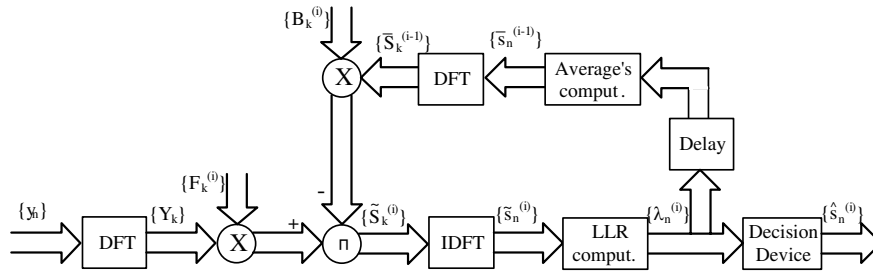

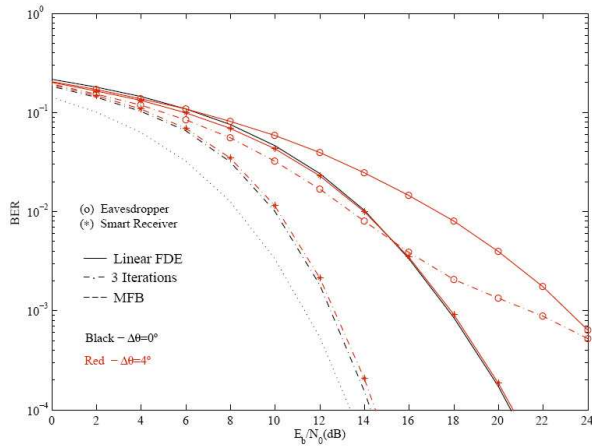
Figure 5: IB-DFE receiver with soft decisions.

Figure 6: BER performance for size-16 constellations in a frequency selective channel and an angle error regarding to the transmission direction Θ.
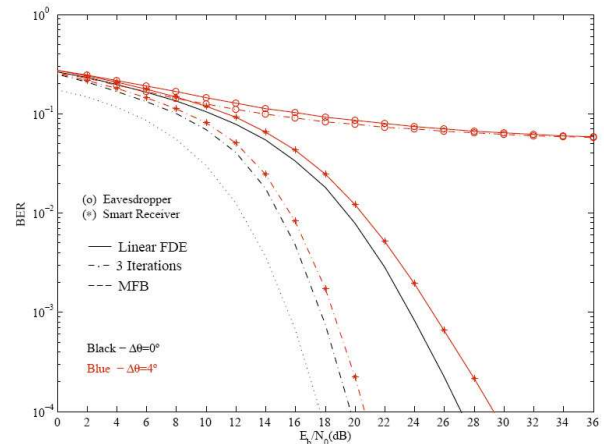
Figure 7: BER performance for size-64 constellations in a frequency selective channel and an angle error regarding to the transmission direction Θ.

In Figure 6 are shown the BER performance results for transmission schemes with 16-size constellations. Simulation results from Figure 6 lead us to conclude that the smart receiver together with the iterations of IB-DFE can cope with change in direction Θ without significant performance degradation. Figure 7 refers constellations with 64-symbols. As we can see, it is obvious the higher impact of estimation errors on BER, when compared with the transmission scheme based on 16-QAM. This was a expectable result, since the number of real components and antennas for 16-QAM is lower than the number of transmission branches in 64-QAM, the smart receiver can estimate more efficiently angle changes in the first case. Results from Figure 6 and 7 also demonstrate that despite the efficiency of smart receiver, the significant degradation associated to any estimation error means a strictly directive communication with the information only optimized in the desired direction Θ. This can be seen on the results regarding the eavesdropper for 64-QAM (for 16-QAM we have a small degradation but we assumed that the initial parameters about the configuration of the transmitter were available to the eavesdropper. So, the error on estimation of $4°$ has small impact on performance). Therefore, security is also assured since any eavesdropper is unable to decode data successfully without information about transmitter's configuration parameters.

5. CONCLUSIONS

In this paper we considered the smart receiver hypothesis for a system using multi-antenna transmission structure with constellation shaping of the transmitted information. It was shown the validity of the smart receiver hypothesis, since when the receiver is able to estimate the set of coefficients g_i used for constellation shaping at the transmitter, the MI is practically independent of the angle Θ in which the transmitted constellation is optimized. Also results demonstrated the high sensitivity of MI and system performance when estimation errors on g_i coefficients lead to angle estimate errors higher than $2°$, which imposes restrictions to any estimation algorithm to be used at receiver level. We also gave some insights about the constellation shaping potential for physical layer security and the capacity of a smart receiver. Further studies shall include the performance analysis of different algorithms for estimation of g_i parameters to be applied in smart receiver implementations for both AWGN and fading channels as well as the optimization of the constellation directivity with other array configurations.

REFERENCES

1. Bloch, M., J. Barros, M. R. D. Rodrigues, and S. W. McLaughlin, "Wireless information-theoretic security," *IEEE Trans. Inf. Theory*, Vol. 54, No. 6, 2515–2534, June 2008.

2. Massey, J. L., "An introduction to contemporary cryptology," *Proc. IEEE*, Vol. 76, No. 5, 533–549, May 1988.

3. Harrison, W. K., J. Almeida, M. R. Bloch, S. W. McLaughlin, and J. Barros, "Coding for secrecy: An overview of error-control coding techniques for physical-layer security," *IEEE Signal Process. Mag.*, Vol. 30, No. 5, 41–50, September 2013.

4. Marques da Silva, M. and F. A. Monteiro, *MIMO Processing for 4G and Beyond: Fundamentals and Evolution*, CRC Press Auerbach Publications, ISBN: 9781466598072, FL, USA, May 2014, http://www.crcpress.com/product/isbn/9781466598072.

5. Tse, D. N. C. and P. Viswanath, *Fundamentals of Wireless Communications*, Cambridge University Press, Cambridge, UK, 2005.

6. Montezuma, P. and A. Gusmão, "Design of TC-OQAM schemes using a generalised nonlinear OQPSK-type format," *IEE Elect. Letters*, Vol. 35, No. 11, 860–861, May 1999.

7. Astucia, V., P. Montezuma, R. Dinis, and M. Beko, "On the use of Multiple grossly nonlinear amplifiers for Higly Efficient Linear amplification of multilevel constellations," *Proc. IEEE VTC2013-Fall*, Las Vegas, NV, US, September 2013.

8. Benvenuto, N. and S. Tomasin, "Block iterative DFE for single carrier modulation," *IEE Elec. Let.*, Vol. 39, No. 19, 1144–1145, September 2002.

9. Dinis, R., R. Kalbasi, D. Falconer, and A. Banihashemi, "Iterative layered space-time receivers for single-carrier transmission over severe time-dispersive channels," *IEEE Comm. Letters*, Vol. 8, No. 9, 579–581, September 2004.

10. Amoroso, F. and J. Kivett, "Simplified MSK signalling technique," IEEE Trans. on Comm., Vol. 25, April 1977.

11. Caire, G., G. Taricco, and E. Biglieri, "Bit-interleaved coded modulation," *IEEE Trans. Inf. Theory*, Vol. 44, 927–947, May 1998.

12. Dinis, R., P. Montezuma, N. Souto, and J. Silva, "Iterative frequency-domain equalization for general constellations," *IEEE Sarnoff Symposium*, Princeton, USA, April 2010.

13. Gusmão, A., P. Torres, R. Dinis, and N. Esteves, "A turbo FDE technique for reduced-CP SC-based block transmission systems," *IEEE Trans. on Comm.*, Vol. 55, No. 1, 16–20, January 2007.

Impact of Aeronautical Mobile Telemetry System on MFCN SDL Operating Co-channel in Frequency Band 1452–1492 MHz

M. Zilinskas[1], E. Stankevicius[2], and S. Oberauskas[3]

[1]Vilnius University, Sauletekio al. 9, Vilnius LT-10222, Lithuania
[2]Vilnius Gediminas Technical University, Sauletekio al. 11, Vilnius LT-10223, Lithuania
[3]Communications Regulatory Authority of the Republic of Lithuania
Algirdo str. 27A, Vilnius LT-03219, Lithuania

Abstract— This paper presents the co-channel compatibility analysis between Aeronautical Mobile Telemetry system and International Mobile Telecommunications system in the frequency band 1452–1492 MHz. International Mobile Telecommunications systems (i.e., LTE) are developing at staggering rates and mobile operators always searches the new possible frequency bands to expand their networks. 1452–1492 MHz frequency band is attractive due the qualified radio propagation conditions. But this band is already operated by other technologies as radio relay, broadcasting networks and aeronautical networks. Co-channel and adjacent channel electromagnetic compatibility have to be evaluated. Electromagnetic compatibility between Aeronautical Mobile Telemetry and International Mobile Telecommunications is one of the most sensitive issues regarding the decision to designate this band to Mobile Services. This study was conducted to compare the worst case calculations based on Minimum Coupling Loss method and statistical Monte-Carlo simulations in order to obtain more realistic results.

1. INTRODUCTION

In today's world radio frequencies are being increasingly used. There is a growing mobile technology development, thus increasing demand for radio frequencies to mobile services [1, 2]. Mobile operators are often faced with the problem of spectrum scarcity. Companies have the resources to expand their networks, but it becomes increasingly difficult to avoid interference between adjacent stations due to ever growing density of wireless apparatus [3, 4].

World Radiocommunication Conference in 2012 (WRC-12) approved Resolution COM6/6 which contains the agenda for next conference in 2015 (WRC-15). For this purpose it is proposed to considered frequency bands 1429–1452 MHz, 1452–1492 MHz, 1492–1518 MHz and 1518–1525 MHz as possible candidate bands. During the preparation period for next conference sharing and compatibility studies have been launched to identify possible harmful interference to currently existing services [5]. According to frequency allocation in Section IV to Radio Regulation [6] the primary services in the frequency band 1452–1492 MHz is Mobile except aeronautical mobile service.

This paper compares two possible ways to evaluate the electromagnetic compatibility in co-channel operation between UE receivers of IMT system and airborne transmitters of Aeronautical Mobile Telemetry system based on Minimum Coupling Loss method and statistical Monte-Carlo method [7]. The results show that the compatibility is feasible in only particular configuration of networks.

2. MAIN PARAMETERS OF THE TELEMETRY SYSTEM AIRBORNE TRANSMITTER

Telemetry system could be typically used for air-to-ground information delivery or air-to-air missile [8]. For this study the technical parameters of telemetry system airborne transmitter could be taken from two possible sources:

- Assignments in the Master International Frequency Register (MIFR). These can only be in countries mentioned in RR 5.342 footnote. The entries are labelled with the class of station "MA" (this corresponds to the transmitter in aircraft);
- Recommendation ITU-R M.1459 "Protection criteria for telemetry systems in the aeronautical mobile service and mitigation techniques to facilitate sharing with geostationary broadcasting-satellite and mobile-satellite Services in the frequency bands 1452–1525 MHz and 2310–2360 MHz" [9].

The parameters of telemetry system provided in these two sources differ significant therefore both sets of characteristics provided in Table 1 below were used in compatibility study.

Table 1: Parameters of telemetry system airborne transmitter.

	ITU-R M.1459		MIFR
Central frequency	1439.65 MHz, 1460.9 MHz, 1482.15 MHz, 1503.35 MHz		
Channel bandwidth	5 MHz		21.3 MHz
Antenna pattern	Omnidirectional		Omnidirectional
Antenna gain	0 dBi	10 dBi	ITU-R M.1459
e.i.r.p.	13.98 dBW	23.98 dBW	25.15 dBW
Antenna height (maximum)	10000 m		10000 m
Transmission path length	Up to 320 km		Up to 600 km

As telemetry system is air-to-ground communication system therefore airborne transmitter antenna has to cover all radiation angles in the direction of the telemetry system receiving station hence in ideal case it should be isotropic antenna. However, in reality, there are multiple reflections and signal blocking form the fuselage of the aircraft. This can cause variations of the transmitter antenna gain (G_{TX}) pattern (i.e., from 10 dBi to -30 dBi). Such antenna gain variations (see Annex 1 of Recommendation ITU-R M.1459 [9]).

The probability that $G_{TX} \leq 0$ dBi (compared to $G_{\max} = 10$ dBi) is equal to 0.96. Nevertheless the probability does not differ greatly, but the difference of antenna gain values will have huge impact on separation distance between Interfering transmitter and Victim Receiver. Considering these variations, we will use three different cases of telemetry system airborne transmitter antenna gain in this compatibility analysis: a) $G = 0$ dBi, this case could be treated as near realistic; b) $G = 10$ dBi, this case is worst case scenario (i.e., maximum antenna gain of airborne transmitter according to the Recommendation ITU-R M.1459); c) distribution of antenna gain G_{TX}, according to Annex 1 of Recommendation ITU-R M.1459, for Monte Carlo statistical simulations only (Cumulative Distribution Function — CDF). In all cases the omnidirectional antenna type was used.

3. MFCN SDL CHARACTERISTICS

Technical characteristics of IMT UE comply with ETSI standard [10]. Parameters for IMT UE receivers for this study were taken from Report ITU-R M.2292 [11]. For protection criteria trigger based on Interference-to-Noise ratio $I/N = -6$ dB and additional 0 dB value was used. The ratio $I/N = 0$ dB represents relaxed protection requirement. The IMT UE receiver parameters used provided in Table 2.

The IMT UE reception bandwidth can varies from 1.4 MHz to 20 MHz. In this study were used only 5 MHz band regarding that this bandwidth is commonly used in others LTE frequency bands.

Two possible interference criterion were used in order to represent worst case scenario ($I/N = -6$ dB) and more realistic scenario with $I/N = 0$ dB ratio. The assumption of interference criterion

Table 2: IMT UE parameters.

Parameter	Value
Receiver bandwidth	5 MHz
Antenna height	1.5 m
Antenna pattern	Omnidirectional
Antenna gain	-3 dBi
Body loss	4 dB
Building penetration loss	15 dB (rural); 20 dB (suburban, urban)
Building blocking for UE (only urban)	10 dB
Indoor user terminal usage	50% (rural); 70% (suburban, urban)
Receiver noise figure	9 dB
Receiver Thermal Noise Level	-98 dBm
I/N target	-6 dB and 0 dB

is very sensitive, because it needs to do not over protect the system. The overprotection of victim receiver leads to non-effective spectrum use.

4. MINIMUM COUPLING LOSS (MCL) ANALYSIS

In this section the calculation results derived by Minimum Coupling Loss method (MCL) are provided. This is deterministic method and it analyses the link budget between two points. Using the MCL method the isolation is calculated which is required between victim and interferer to ensure that there is no interference.

To calculate required separation distances the co-channel interference impact from telemetry system airborne transmitter on IMT UE receiver was analysed. Using Free Space propagation model (Formula (3) of Recommendation ITU-R P.525 [12]) the calculated path loss value was converted into a physical separation distance. ITU-R P.525 propagation model is only applicable on free line of sight cases. It does not consider the refraction of radio waves, the type of earth surface. The interferer antenna height is up to 10000 m, thus ITU-R P.525 recommendation can be applied in this study.

The minimum required path loss (L) was calculated using the formula below:

$$L = P_{TX} + G_{RX} - L_{body} - C_{env} + C_{BW} - I_{\max}, \tag{1}$$

where:
P_{TX} — telemetry airborne transmitter e.i.r.p. (dBW),
G_{RX} — IMT UE receiver antenna gain (dBi),
L_{body} — human body loss (dB),
C_{env} — correction factor for building penetration loss and signal blocking in different environments (dB),
C_{BW} — correction factor for difference in bandwidth (dB),
$I_{\max}$ — the allowed maximum interference level (dBm).
There are three different types of environments, where IMT UE could experience the interference. These are: urban, suburban, and rural. In this study four different environments scenarios were analysed: a) urban indoor (taking into account building penetration loss of 20 dB and building blocking of 10 dB); b) urban outdoor (taking into account building blocking of 10 dB and assuming that IMT UE is not in line-of-sight); c) rural indoor (taking into account building penetration loss of 15 dB); d) rural outdoor. Calculation results of MCL analysis are provided below in Table 3 taking into account different I/N ratio.

From the calculation results it is seen that required protection distance varies significant depending on the protection criteria and characteristics of telemetry system used.

MCL analysis is pure link budget calculation and is worst case scenario therefore it could lead to possible overestimation of required minimum separation distances. In real situations, the telemetry system airborne transmitter will not always be able to influence IMT UE receiver because telemetry

Table 3: Separation distances according to MCL analysis between victim IMT UE receiver and interfering telemetry system airborne transmitter.

Interference criterion	Telemetry system parameters — Recommendation ITU-R M.1459, $G_{TX} = 10\,\text{dBi}$			
I/N	Urban Indoor	Urban Outdoor	Rural Indoor	Rural Outdoor
$-6\,\text{dB}$	18.5 km	185 km	104 km	412 km (limited by LoS)
$0\,\text{dB}$	9.3 km	93 km	52 km	294 km
	Telemetry system parameters from Recommendation ITU-R M.1459, $G_{TX} = 0\,\text{dBi}$			
	Urban Indoor	Urban Outdoor	Rural Indoor	Rural Outdoor
$-6\,\text{dB}$	5.9 km	59 km	33 km	185 km
$0\,\text{dB}$	2.9 km	29 km	17 km	93 km
	Telemetry system parameters from MIFR			
	Urban Indoor	Urban Outdoor	Rural Indoor	Rural Outdoor
$-6\,\text{dB}$	10.3 km	103 km	58 km	325 km
$0\,\text{dB}$	5.1 km	52 km	29 km	163 km

system airborne transmitter is always in motion (aircraft velocity is up to 1000 km/h) and the servicing the area will differ depending on the parameters of the transmitter. It could be of radius up to 320 km or up to 600 km (using characteristics from Recommendation ITU-R M.1459 and MIFR accordingly). Additionally, IMT UE is not necessarily used in areas of potential occurrence of harmful interference. As interference is not of permanent nature, it would be more naturally to use statistical methods. SEAMCAT software tool [13] based on Monte-Carlo method could give more realistic situation of possible harmful interference.

5. INTERFERENCE SCENARIO FOR SEAMCAT SIMULATION

The SEAMCAT is based on Monte-Carlo simulation method. The principle is to take samples of random variables by using their probability density functions and to generate random samples (snapshots), then to derive the probability of interference by comparing relation of wanted and unwanted signals at victim receiver in each snapshot to its interference criterion. The created interference scenario for simulations in SEAMCAT is provided below in Figure 1. Separation distance (d_{sep}) is the distance between the closest boundary of service area of telemetry system airborne transmitter and location of victim IMT UE.

1000000 snapshots were randomly generated for SEAMCAT simulations. The separations distances acquired by MCL method for rural outdoor environment were used as a starting point. The simulations were performed with relaxed interference criterion $I/N = 0$ dB. According to Report ITU-R M.2292 the proportion of 50% of IMT UE is used indoor and it was also considered in SEAMCAT simulations.

Interference probability (IP) was calculated for different required separation distances (starting from the largest required separation distance obtained by MCL analysis). In order to conduct more detailed analysis four different scenarios were modelled: a) Scenario 1 represents worst case scenario (most pessimistic) with maximum 10 dBi antenna gain. The telemetry system parameters were used according to Recommendation ITU-R M.1459; b) Scenario 2 represents near realistic scenario with 0 dBi antenna gain. The telemetry system parameters were used according to Recommendation ITU-R M.1459; c) Scenario 3 represents usual scenario because telemetry system parameters are used from MIFR where are registered the stations which are operating in real networks; d) Scenario 3 represents the realistic scenario when the gain of telemetry system antenna is reflected as probability function. The results according four modelled scenarios are presented below in Table 4.

Results by Monte-Carlo approach (using SEAMCAT simulations) show that minimum required
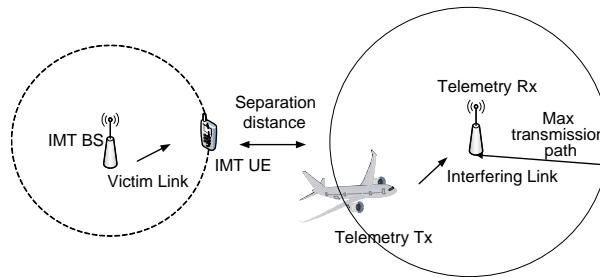

Figure 1: Interference scenario for SEAMCAT simulations.

Table 4: Simulation results using statistical Monte-Carlo approach.

	Scenario 1	Scenario 2	Scenario 4	Scenario 3
Telemetry system characteristics	ITU-R M.1459	ITU-R M.1459	MIFR	ITU-R M.1459
Telemetry system antenna gain	10 dBi	0 dBi	10 dBi	CDF from ITU-R M.1459
d_{sep} for $IP = 0\%$	294 km	93 km	163 km	71 km
d_{sep} for $IP = 0.5\%$	265 km	56 km	95 km	15 km
d_{sep} for $IP = 1.0\%$	250 km	34 km	52 km	not required
d_{sep} for $IP = 2.0\%$	225 km	not required	not required	not required
IP for $d_{sep} = 1$ km	17.4%	1.96%	1.76%	0.75%

physical separation distance between IMT UE receiver and telemetry system airborne transmitter is considerably smaller comparing it to MCL calculations considering certain acceptable interference probability for IMT UE receiver. The separation distance between telemetry interferer and MFCN victim receiver differs from 294 km to 0 km "not required". Such a high difference indicates that the results are very sensitive to the assumptions of this particular interference scenario.

6. CONCLUSIONS

The compatibility results of deterministic link budget analysis according to MCL calculation method indicate significant variations of required physical separation distance (see Table 3) for IMT UE depending on the characteristics of telemetry system airborne transmitter (according to Recommendation ITU-R M.1459 or MIFR) and different receiving environments.

Statistical Monte-Carlo approach (using SEAMCAT tool) allows take into account different proportion of IMT UE indoor and outdoor and make quantitative assessment in order to recalculate the required protection distances more realistically compared to the results obtained by MCL method. Simulations based on Monte-Carlo approach showed that physical separation distance may be reduced significantly considering certain acceptable harmful interference probability for IMT UE (see Table 4). The results of simulation using measured distribution of telemetry system airborne transmitter antenna gain (provided in Recommendation ITU-R M.1459) show that physical separation would be not required in order to protect IMT UE receiver considering that acceptable interference probability is higher than 1%.

REFERENCES

1. Zahariadis, T. and D. Kazakos, "Revolution towards 4G mobile communication systems," *IEEE Wireless Communications Magazine*, Vol. 10, No. 4, 6–7, 2003.
2. Mölleryd, B. G. and J. Markendahl, "Valuation of spectrum for mobile broadband services: Engineering value versus willingness to pay," *22nd European Regional ITS Conference*, Budapest, Hungary, Sep. 2011.
3. Himayat, N., S. Talwar, A. Rao, and R. Soni, "Interference management for 4G cellular standards," *IEEE Wireless Communications Magazine*, Vol. 48, No. 8, 86–92, 2010.
4. Boudreau, G., J. Panicker, N. Guo, R. Chang, N. Wang, and S. Vrzic, "Interference coordination and cancellation for 4G networks," *IEEE Communications Magazine*, Vol. 47, No. 4, 74–81, 2009.
5. Republic of Lithuania, "Impact of aeronautical telemetry systems on IMT UE in the frequency band 1429–1525 MHz," Document 4-5-6-7/703-E, International Telecommunication Union (ITU-R) Joint Task Group 4-5-6-7, Jul. 17, 2014.
6. ITU, "Radio regulations," 2012.
7. Sevgi, L., "Electromagnetic modeling and simulation: Challenges in validation, verification, and calibration," *IEEE Transactions on Electromagnetic Compatibility*, Vol. 56, No. 4, 750–758, 2014.
8. Muehlner, J. W., "Trends in missile and space radio telemetry," Tech. Rep., Lockheed Missiles and Space Co. Inc., Sunnyvale, Ca, USA, 1962.
9. Recommendation ITU-R M.1459, "Protection criteria for telemetry systems in the aeronautical mobile service and mitigation techniques to facilitate sharing with geostationary broadcasting-satellite and mobile-satellite services in the frequency bands 1452–1525 MHz and 2310–2360 MHz," ITU, 2000.
10. ETSI TS 136 101 V10.7.0, "Evolved universal terrestrial radio access (E-UTRA). User equipment (UE) radio transmission and reception," 3GPP TS 36.101 Version 10.7.0 Release 10, ETSI, 2012.
11. Report ITU-R M.2292, "Characteristics of terrestrial IMT — Advanced systems for frequency sharing/interference analyses," ITU, 2013.
12. Recommendation ITU-R P.525, "Calculation of free-space attenuation," ITU, 1994.
13. *SEAMCAT Handbook*, ECO, 2010.

The Influence of Atmospheric Radio Refractivity on the WiMAX Signal Level in the Areas of Weak Coverage

M. Zilinskas[1, 2]**, M. Tamosiunaite**[3]**, S. Tamosiunas**[2]**,**
M. Tamosiuniene[3]**, and E. Stankevicius**[4]

[1]Department of Radio Communication
Communications Regulatory Authority of the Republic of Lithuania, Vilnius, Lithuania
[2]Faculty of Physics, Vilnius University, Vilnius, Lithuania
[3]Center for Physical Sciences and Technology, Vilnius, Lithuania
[4]Vilnius Gediminas Technical University, Vilnius, Lithuania

Abstract— The influence of weather conditions on the signal level of the fourth generation (4G) wireless mobile network, working on the WiMAX standard, has been examined. The data of measurements are presented. The power level of the received signal was continuously measured and compared to the calculated values of atmospheric radio refractivity. The International Telecommunication Union (ITU) method for determination of radio refractivity-value has been used. In the ITU method, the measured data of air temperature, pressure, and relative humidity are used. It was examined if changes of signal level and variations of the radio refractivity-value occur at the same time. The long-term measurements were carried out at the same time and place. The experiment was carried out in an area of weak coverage. It was concluded that in the areas of weak coverage, 4G (WiMAX) signals are strongly influenced by variations of the atmospheric radio refractivity.

1. INTRODUCTION

The European Commission's Strategy [1] states that all European citizens must have access to fast internet by the year 2020. Internet connection speed must not be less than 30 Mb/s, and up to 100 Mb/s speed internet connection must be accessible to at least half of the households. To achieve these goals, fourth generation, or 4G, broadband wireless network is used. However, there are some limitations, which restrain the expansion of the 4G network. In Lithuania, there are extremely strict hygiene norms, which state that electromagnetic energy flux density limit is $10\,\mu\text{W/cm}^2$ for the radio frequency range from 300 MHz to 300 GHz. Since it leads to additional investments for the telecommunication companies and public fear of possible health effects for people living near base stations, the new base stations should be build in the most reasonable locations and set to the optimum performance.

When the new base stations are designed, all propagation losses must be taken into account. Lower frequency signals can propagate through longer distances without significant distortions. Therefore, providers are seeking to occupy the lower frequency bands. But these bands are already congested. It is known that the frequency band of 10–100 GHz is vulnerable by various meteorological factors (i.e., rain, fog, clouds) [2], but during heavy rain events some effects might show at much lower frequencies, starting from 1 GHz [3]. The developers of telecommunication links usually ignore any influence of the meteorological events at frequencies up to 3 GHz. At 3–10 GHz, the effects become visible, but still the influence is considered to be acceptable. At 10 GHz, the effects become significant. In Europe, the most popular operating frequencies of the 4G networks are 800 MHz, 1.8 GHz, and 2.6 GHz. For 4G (WiMAX), the most widespread WiMAX frequency bands are from 2.3 GHz to 3.6 GHz [4].

The mentioned frequencies are lower than 10 GHz, therefore it could seem, that there should be no noticeable influence of the meteorological events. But weather conditions are closely related to refractivity variations in the troposphere. The radio refractivity determines the curvature radius of the propagation path. Due to refractivity variations in the atmosphere various phenomena might occur in the path of the propagation: ducting, refraction, fading, range and elevation errors in radar acquisition and radio-station interference [5]. These effects might cause major losses of the signal quality and even its path. Under these circumstances, actual 4G coverage maps might differ from the ones published by the providers. Therefore it is necessary to foresee these losses and take them into account whenever new base stations are designed.

2. RADIO REFRACTIVITY

All propagating radio waves are affected by the properties of the atmosphere; they can be reflected, refracted, scattered, and absorbed by different atmospheric constituents [5]. In principle, the electromagnetic wave propagation characteristics during quiet or disturbed air conditions are straightforwardly determined by the state of atmospheric refractivity [6]. Various phenomena in the radio wave propagation such as ducting, scintillation, radar acquisition, refraction and fading of electromagnetic waves are due to refractivity variations in the troposphere [7]. In [8] and [9], the radio refractivity N (in N-units) is expressed as:

$$N = (n - 1) \times 10^6, \tag{1}$$

where n is an atmospheric refractive index.

When characterizing a radio channel, surface (ground level) and elevated refractivity data are often required; and in particular, the surface refractivity is very useful for prediction of some propagation effects [10]. As was mentioned in [9], the estimation of the refraction effect in troposphere is possible only by modelling the troposphere medium. According to [2, 5, 8] and [11], the expression (2) might well be used for all frequencies up to 100 GHz with an error less than 0.5%. It means that the value of N can be defined only by properties of the troposphere:

$$N = \frac{77.6}{T} \left(p + 4810 \frac{e}{T} \right), \tag{2}$$

where T (K) is a temperature; p (hPa) is an atmospheric pressure; e (hPa) is a partial water vapour pressure. Refractivity is dimensionless size and it is expressed in N-units.

The relationship between water vapour pressure and relative humidity is given by:

$$e = \frac{H e_s}{100}, \tag{3}$$

where H is a relative humidity (%); e_s is saturation vapour pressure (hPa) at the given temperature. The value of the e_s should be calculated using method specified in [8].

The atmospheric refractivity consists of two parts — a dry term N_{dry} and a wet term N_{wet}:

$$N = N_{\text{dry}} + N_{\text{wet}}. \tag{4}$$

The dry term is due to non-polar nitrogen and oxygen molecules; it is proportional to pressure, p, and therefore, related to the air density [5]. The wet term is proportional to vapour pressure and dominated by polar water contents in the troposphere [5]. The importance of the liquid water and water vapour in the atmosphere, when the measurements are carried in the air, are highlighted in [12].

Lithuania is situated in the intermediate zone between maritime Western Europe, continental Eastern Europe, and Asia climates. Lithuania, being in the transitional geography zone from the Baltic Sea climate to Atlantic and continentals East Europe climate, distinguishes by variable humid climate. Having in mind the variable character of Lithuanian climatic conditions, the influence of the climatic peculiarities on the radio refractivity was analysed in [13] where analysis of the seasonal and daily variations of the atmospheric radio refractivity at the ground surface in Lithuania in the year 2009 is presented.

Model for determination of territorial distribution of surface radio refractivity in the localities, where the data of air presure, temperature, and reliative humidity, are not collected and only meteorological data, measured in the surrounding localities can be used is presented in [14].

3. MEASUREMENTS

The impact of variations of the atmospheric radio refractivity on the reliability of the 4G wireless network (WiMAX technology, IEEE 802.16e-2005 Standard, working frequency 3.5 GHz) was examined. The experiment took place in an area of weak coverage. The long-term measurements were carried out at the same time and place (for measurements scheme see Figure 1).

The weather station and the router were connected to the data logging system. Due to the limitations of the equipment, the measurements from the weather station were continuously logged in 5-minute intervals. The measurements from the router were continuously logged in 1-minute
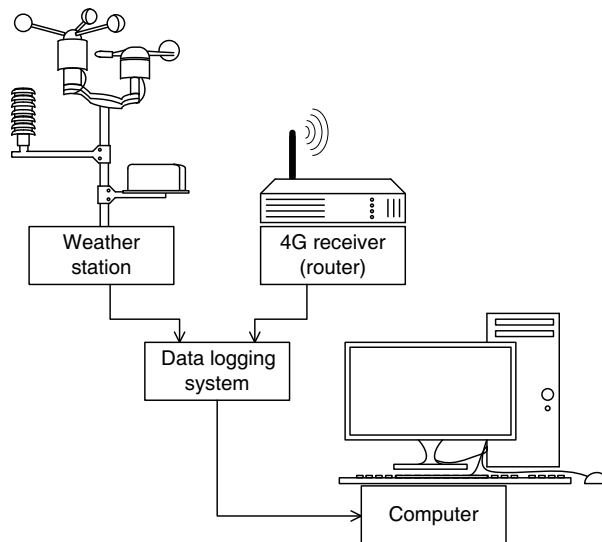
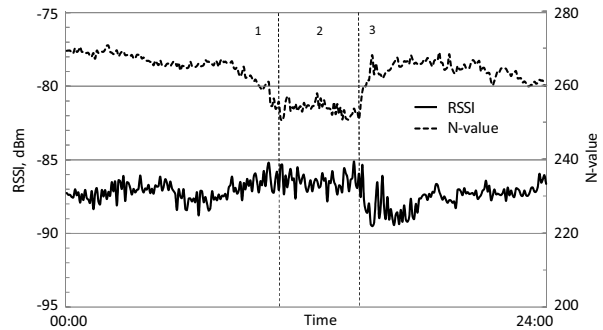Figure 1: The scheme of the measurement system.

Figure 2: The comparison of variaton of the measured *RSSI*-value and the calculated *N*-value (during twenty-four hour period).

intervals. The data collected in the logging system were processed in the computer. The measured power level strength, *RSSI* (in dBm) [15], of the received signal was compared to the calculated values of atmospheric radio refractivity. The higher the *RSSI*-value, the stronger the signal.

The values of atmospheric radio refractivity, the *N*-values, were calculated using the (2) equation and measured values of temperature, atmospheric pressure, and partial water vapor pressure.

It was examined if variations of the *N*-values and changes of signal level occur at the same time.

4. RESULTS AND DISCUSSION

In Figure 2, the measured *RSSI*-values and calculated *N*-values are compared (during twenty-four hour period). It in obvious, that variations of the *N*-value coincide with changes of the *RSSI*-value. The graph is divided into three areas, marked as 1, 2, and 3. The boundaries of these areas indicate the tendency, that the increase of the *N*-value is related to the decrease of the *RSSI*-value, and vice versa.

The comparison of the *RSSI*-value and meteorological factors, included in the (2), revealed, that there is no obvious correlation between the *RSSI*-value and atmospheric pressure. The comparison of the *RSSI*-value with the temperature and relative humidity are presented in Figure 3 and Figure 4, respectively. Although some coincides might be seen, there is no evident correlation. Therefore, it can be concluded, that the changes of the *RSSI*-value are affected by the atmospheric radio refractivity, as combination of the temperature and relative humidity (see (2)).
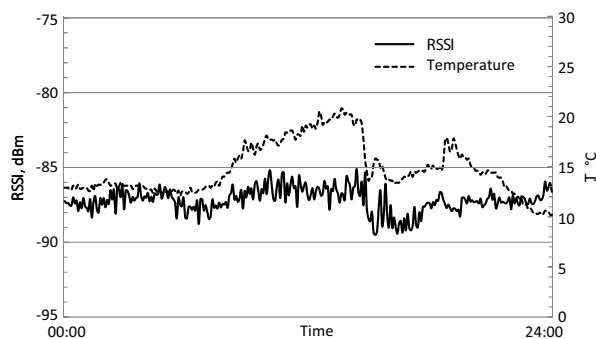

Figure 3: The comparison of variaton of the measured *RSSI*-value and the measured temperature (during twenty-four hour period).
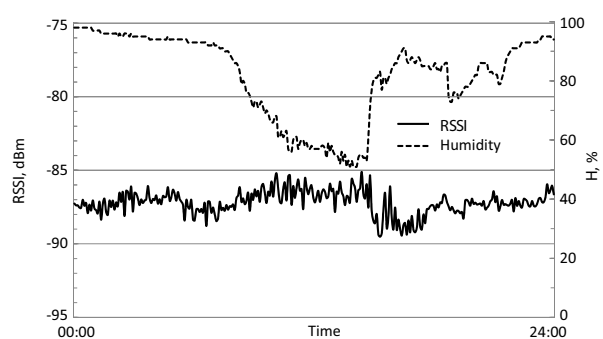

Figure 4: The comparison of variation of the measured *RSSI*-value and the measured relative humidity (during twenty-four hour period).

5. PROSPECTS IN THE THZ FREQUENCY BAND

The analysis of the data showed, that in the regions of poor coverage the level of the 4G signal (WiMAX) is influenced by the variations of the atmospheric radio refractivity, caused by the meteorological factors. Therefore, there is a need for new technological solutions. Prospects appear in the terahertz (THz) frequency band, which has not yet been allocated for specific uses, and is expected to reach up to 100 Gb/s connection speed and eliminate dependence on meteorological conditions. However, there are still unsolved problems, such as the long-distance losses, and the need for high-quality THz sources. In [16], it is suggested, that good candidates for such THz sources could be the resonant tunneling diodes. Since the problem of the long-distance losses remains unsolved, currently the THz communications are more suitable for indoor applications.

The aim of the future works is to foresee possibilities to combine the advantages of 4G technology and THz frequency band, on purpose to reduce the impact of meteorological conditions in the regions of poor coverage.

6. CONCLUSION

In the areas of weak coverage, the 4G (WiMAX technology, IEEE 802.16e-2005 Standard, working frequency 3.5 GHz) signals are strongly influenced by the variations of the atmospheric radio refractivity as a combination of the temperature and relative humidity. Therefore, actual coverage maps might differ from the ones published by the providers. There is a need for new technological solutions in the areas of weak coverage. Prospects appear in the terahertz (THz) frequency band, but there is a need for additional research.

REFERENCES

1. European Commission, "A strategy for smart, sustainable and inclusive growth EUROPE 2020," (http://ec.europa.eu/europe2020/) [retrieved Apr. 7, 2015].
2. Freeman, R. L., *Radio System Design for Telecommunications*, 3rd Edition, Wiley-Interscience, New York, 2007.
3. Maral, G. and M. Bousquet, *Satellite Communications Systems — Systems, Techniques and Technology*, 5th Edition, John Wiley & Sons Ltd., 2009.
4. Information about 4G WiMAX services in Lithuania "Mezon", http://www.mezon.lt/Apie_MEZON/Technologija/ [retrieved Apr. 7, 2015].
5. Ali, S., S. A. Malik, K. S. Alimgeer, S. A. Khan, and R. L. Ali, "Statistical estimation of tropospheric radio refractivity derived from 10 years meteorological data," *Journal of Atmospheric and Solar-Terrestrial Physics*, Vol. 77, 96–103, 2012.
6. Okoro, O. N., G. A. Agbo, J. E. Ekpe, and T. N. Obiekezie, "Comparison of hourly variations of radio refractivity for quiet and disturbed days during dry and rainy seasons at Minna," *International Journal of Basic and Applied Sciences*, Vol. 2, No. 1, 58–63, 2013.
7. Agbo, G. A., "Tropospheric refractivity dependence on atmospheric weather conditions in Jos-Nigeria," *Journal of Basic Physical Research*, Vol. 2, No. 2, 1–6, 2011.
8. "The radio refractive index: Its formula and refractivity data," Recommendation ITU-R P.453-10 (Feb. 2012).
9. Olasoji, Y. O. and M. O. Kolawole, "Seasonal effect on atmospheric refractivity in diverse terrains," *Journal of Environmental Science and Engineering*, Vol. 5, 1537–1541, 2011.
10. Adediji, A. T. and M. O. Ajewole, "Variation of radio refractivity gradient and effective Earth radius factor (k factor) over Akure, South Western Nigeria," *URSI General Assembly and Scientific Symposium of International Union Of Radio Science*, Aug. 2011.
11. Bean, B. and E. Dutton, *Radio Meteorology*, Dover Publications, 1968.
12. Li, J., L.-X. Guo, L.-K. Lin, Y. Zhao, Z. Zhao, T. Shu, and H. Han, "A dual-frequency method of eliminating liquid water radiation to remotely sense cloudy atmosphere by ground based microwave radiometer," *Progress In Electromagnetics Research*, Vol. 138, 629–645, 2013.
13. Zilinskas, M., S. Tamosiunas, M. Tamosiunaite, and M. Tamosiuniene, "Yearly, seasonal and daily variations of radio refractivity," *Acta Physica Polonica A*, Vol. 119, No. 4, 533–536, 2011.
14. Zilinskas, M., M. Tamosiunaite, S. Tamosiunas, E. Brilius, and M. Tamosiuniene, "Model for determination of territorial distribution of surface radio refractivity," *PIERS Proceedings*, 1525–1529, Stockholm, Sweden, Aug. 12–15, 2013.
15. Sauter, M., *From GSM to LTE — An Introduction to Mobile Networks and Mobile Broadband*, John Wiley & Sons, 2011.

16. Ikeda, Y., K. Okada, S. Kitagawa, S. Suzuki, and M. Asada, "Resonant-tunneling-diode oscillator with high-frequency modulation structure for high-capacity terahertz communication," *2014 39th International Conference on Infrared, Millimeter, and Terahertz waves (IRMMW-THz)*, 1–2, Tucson, AZ, Sep. 14–19, 2014.

Evaluation of LTE 700 and DVB-T Electromagnetic Compatibility in Adjacent Frequency Bands

G. Ancans[1], **E. Stankevicius**[2], **V. Bobrovs**[1], **and S. Paulikas**[2]

[1]Institute of Telecommunications, Riga Technical University, Azenes St. 12-201, Riga LV-1048, Latvia
[2]Vilnius Gediminas Technical University, Sauletekio al. 11, Vilnius LT-10223, Lithuania

Abstract— The 2012 World Radiocommunication Conference allocated the 694–790 MHz (700 MHz) band for the mobile service on a co-primary basis with other services in Region 1 (Europe, Africa, the Middle East). However, countries of Region 1 will also be able to continue the use of these frequencies for their digital terrestrial television services, if necessary. This allocation will be effective immediately after the WRC-15. The objective of this paper is to assess the electromagnetic compatibility of Digital Video Broadcasting-Terrestrial (DVB-T) operating below 694 MHz and mobile broadband (LTE) operating in 700 MHz band. The study contains an assumption of a preferred frequency division duplex (FDD) channelling arrangement which contains confined 2×30 MHz block: 703–733 MHz (uplink) and 758–788 MHz (downlink). The model consists of two elements, a LTE network and a DVB-T system. An adjacent channel scenario was analyzed in this paper: possible impact of LTE user equipment (uplink) to DVB-T receiver. The Minimum Coupling Loss method and Monte Carlo simulation within SEAMCAT software was used for interference analysis. The Minimum Coupling Loss method was chosen to calculate worst case (most conservative scenario) in order to understand most critical points of these two systems. The Monte Carlo simulations show more relaxed electromagnetic compatibility scenario. During simulations more appropriate propagation model was used (Recommendation ITU-R P.1546), which allows to analyse also non line of sight radio propagation conditions. The results obtained provide the minimum coupling distance required between LTE and DVB-T in the 700 MHz band to maintain the necessary performance level of the DVB-T system.

1. INTRODUCTION

The 2012 World Radiocommunication Conference drafted and adopted Resolution 232 (WRC-12) relating to the allocation of the frequency band 694–790 MHz (700 MHz) in Region 1 to the mobile service, except aeronautical mobile service (according to ITU Radio Regulations (RR) footnote 5.312A), on a co-primary basis with other services to which this band is allocated on a primary basis and identified it to International Mobile Telecommunications (IMT). The allocation will become effective immediately after the WRC-15. This band has already been allocated to the mobile service in Regions 2 and 3 [1]. The 700 MHz band is already being described as the *second digital dividend* following the allocation of frequencies in the 800 MHz band — the *first digital dividend* — for mobile broadband services. This part of spectrum is very valuable because it is optimum in terms of need of coverage and bandwidth. The Long Term Evolution (LTE) with 700 MHz frequency band will reduce the number of needed base stations that will further save costs of LTE network development.

Resolution 232 (WRC-12) invites ITU-R to study the compatibility between the mobile service and other services currently allocated in the frequency band 694–790 MHz [2]. This frequency range can be put into use only after all the necessary electromagnetic compatibility studies have been completed. These studies must be completed by the WRC-15. The following case study elaborates on evaluation of electromagnetic compatibility of LTE user equipment (UE) uplink operating in the 700 MHz band with TV broadcasting (DVB-T) operating below 694 MHz. The case study assesses the necessary minimum coupling distance between these systems in the 700 MHz band to maintain the necessary performance level of the DVB-T system.

Authors found that studies on evaluation of compatibility of LTE user equipment (uplink) operating above 703 MHz with DVB-T operating in digital terrestrial television (DTT) channel 48 (686–694 MHz) have been performed within the ITU-R study group JTG-4-5-6-7 [3]. According to the results of studies [3] the resulting critical separation distance between these systems is found to be around 22 meters. The Minimum Coupling Loss (MCL) method and Monte Carlo methodology was used in these studies. The studies were conducted for fixed outdoor and portable indoor DTT reception modes.

Authors found that a study [4] provides results on the coexistence requirements for the LTE deployment in the 700 MHz band and the DTT service in adjacent frequency bands. The study [4] is

based on Monte Carlo simulations to assess the potential of interference from LTE uplink operating in the lower 700 MHz frequencies into DTT frequencies below 694 MHz. Even with several worst case assumptions and parameters, simulations revealed a low interference probability.

One of main tasks of calculations in studies [3, 4] was to derive IMT (LTE) UE out-of-band (OOB) emission limit to protect the broadcasting transmission in TV channel 48 and below from interference of the mobile service (IMT) in the band 694–790 MHz, taking into account also the 700 MHz band channel arrangement, which is provided in Table 1 of this paper. In our particular study we used DVB-T and LTE UE parameters, agreed within the ITU-R study group JTG-4-5-6-7. A general LTE spectrum emission mask of 3GPP, with OOB emission limit of $-9\,\text{dBm}/8\,\text{MHz}$ (regarding the DTT channel 48) for the 10 MHz LTE channel, was used in our study. More strict OOB emission limit values were used in the studies [3, 4]. Only fixed outdoor DTT reception mode was considered in our study.

Similar study using Monte Carlo simulations was done in article [5] where obtained results show the electromagnetic compatibility situation in co-channel and adjacent channel case between interferer E-UTRA (LTE) uplink and victim DVB-T. This study concludes that both co-channel interference and adjacent channel interference from interferer E-UTRA uplink to the reception of the DVB-T downlink service would be negligible, and that in general E-UTRA uplink will not disturb DVB-T receiver performance. Therefore, geographical separation is not necessary in that case. Unlike the abovementioned study this paper presents results of using both the Minimum Coupling Loss and Monte Carlo method. Different protection ratios values, channel bandwidths, propagation models and compatibility evaluation methodologies were used in these two studies.

This paper contains an important part of evaluation of DVB-T compatibility with LTE in adjacent channels in 700 MHz band.

2. TECHNICAL CHARACTERISTICS

The study contains an assumption of a frequency division duplex (FDD) channelling arrangement which contains $2 \times 30\,\text{MHz}$ block aligned with 3GPP band 28 lower frequency: 703–733 MHz for uplink and 758–788 MHz for downlink. The 700 MHz band frequency arrangement is presented in Table 1.

Table 1: 700 MHz band channel arrangement.

Guard band	LTE Uplink	Duplex gap	LTE Downlink	Guard band
694–703 MHz	703–733 MHz	733–758 MHz	758–788 MHz	788–791 MHz
9 MHz	30 MHz	25 MHz	30 MHz	3 MHz

If the 694–790 MHz band is used for mobile service, then it corresponds to decrease of twelve DTT channels from 49 to channel 60. The first LTE uplink channel (703–713 MHz) establishes possible interference problems with the DVB-T receivers in the DTT channel 48. LTE channels with 10 MHz bandwidth were used in this study in order to evaluate a more realistic scenario.

2.1. LTE Parameters

The LTE parameters used in this study are taken from inputs to JTG 4-5-6-7 from WP5D for IMT (LTE) [6] and Report ITU-R M.2292-0 [7].

General E-UTRA spectrum emission mask was simulated according to Table 6.6.2.1.1-1 of 3GPP TS 36.101 [8]. This spectrum emission mask describes the harmful interference level in the DTT frequency band operating below 694 MHz.

2.2. DVB-T Parameters

The DVB-T parameters used in this study are taken from inputs to JTG 4-5-6-7 from WP6A for DVB-T [9]. The receiver blocking (filter) mask is the most critical parameter of the DVB-T station in this study. The receiver mask shows the selectivity level of the particular device. The DVB-T receiver blocking mask used in this study was the same like in CEPT ECC WGSE SE7 working group studies.

3. PROTECTION CRITERIA

Two methods were used in this study to assess the interference of LTE user equipment (uplink) operating above 703 MHz to DVB-T operating in DTT channel 48, namely Minimum Coupling

Loss (MCL) and Monte Carlo simulation. Two different protection criteria were used to analyse the interference from LTE user equipment (uplink) to DVB-T:

a) the protection criteria used in MCL calculations: $I/N = -10\,\mathrm{dB}$ [6];

b) the protection criteria used in Monte Carlo simulations: according to ITU-R Working Party 6A proposed protection ratios PR (Table A1.15) [9].

4. COMPATIBILITY EVALUATION METHODOLOGY

4.1. MCL Method

The Minimum Coupling Loss method calculates the isolation required between the interferer transmitter and the victim receiver to warrant that there is no harmful interference. This method is the worst case analysis and produces a boundary result for scenarios of statistical nature. This method evaluates the required path loss level according to minimum protection criteria ($I/N = -10\,\mathrm{dB}$).

4.2. Monte Carlo method

The Monte Carlo modelling is used for simulation methodology in this study in order to assess the interference from LTE UE uplink to DVB-T fixed reception receivers. Monte Carlo method is applicable to simulate mainly all possible radio communication based scenarios. This flexibility is ensured by the manner of the characterization of input parameters inside the system. The input type of each variable parameter (as horizontal and vertical antenna pattern, EIRP, propagation environment etc.) is modelled like statistical distribution function. The Monte Carlo modelling provides statistical elements of real life behaviour of mobile terminals and interference, enabling a realistic estimate of the potential interference. SEAMCAT software tool based on Monte Carlo method was used in this study [10].

5. INTERFERENCE SCENARIO

The interference scenario where LTE uplink interferes DVB-T downlink (receiver) station was evaluated in this study. SEAMCAT simulation scenario is given in Figure 1.

While there are several possible scenarios for the interference between broadcasting and mobile service, this contribution focuses only on a scenario that is mostly common as shown in figure above: outdoor mobile service UE interference into fixed outdoor DVB-T receiver.

In our simulations we addressed the case of digital broadcast receivers located randomly within the DDT cell in rural environment. For DTT network we addressed the case of fixed rooftop reception for the high power DTT transmitter for DVB-T technology.

With regard to the number of active mobile users, we chose the worst case for OOB emissions of one active mobile user per cell (3 users per base station), so that the number of subcarriers per user was equal to the total number of subcarriers. In that situation the minimum required separation distance between LTE UE and DVB-T receiver was found to DVB-T receiver would work without disruption. This situation could be difficult to control because user equipment moves randomly in area and DVB-T receivers could be placed everywhere.
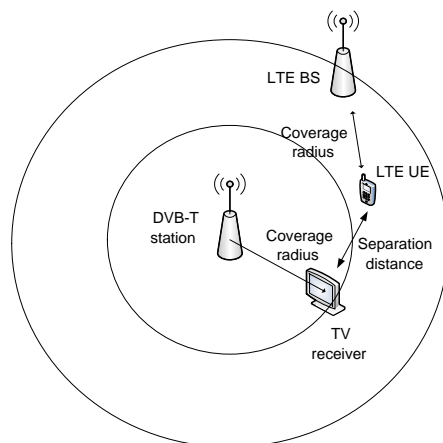

Figure 1: SEAMCAT simulation scenario.

6. COMPATIBILITY ANALYSIS AND RESULTS

6.1. MCL Calculation Results

The MCL method is useful for the initial assessment of compatibility. MCL between the interfering transmitter (I_t) and the victim receiver (V_r) is calculated further:

$$L_{Required\_path\_loss} = P_{TX} - S_{RX} + G_{RX} + BW_{Unwanted\_emissions\_BW\_conversion}, \tag{1}$$

where: $L_{Required\_path\_loss}$ — required path loss; P_{TX} — EIRP of interferer, dBm; S_{RX} — victim sensitivity level, dBm; G_{RX} — victim antenna gain, dBi; $BW_{Unwanted\_emissions\_BW\_conversion}$ — unwanted emissions bandwidth conversion or I/N value, dB.

$$L_{Required\_path\_loss_{OFDM}} = (-9\,\text{dBm}/8\,\text{MHz}) - (-98\,\text{dBm}/8\,\text{MHz}) + 9.15 + 10 = 108.15\,\text{dBm}. \tag{2}$$

The result of an MCL calculation is an isolation figure which can subsequently be converted into a physical separation choosing an appropriate path loss model [10].

The isolation is then converted into a separation distance using the *Free-Space* attenuation, $L(loss)$, between isotropic antennas by formula [11]:

$$L\,(loss) = 32.4 + 20\log_{10}(f) + 20\log_{10}(d), \tag{3}$$

where: f — frequency (MHz); d — distance (km).

The required protection distance, $d_{sep\_req\_DVB\text{-}T\text{-}BS}$, between the mobile service base station and the DTT station is 8.84 km.

6.2. Monte Carlo Simulation Results

SEAMCAT Monte Carlo simulation results show the required separation distance between the LTE UE (uplink) and DVB-T receiver, according to the protection ratios (PR) defined for DVB-T receiver. In our study the probability of interference (PoI) less than 5% was considered to be a sufficient protection level. Results of SEAMCAT simulations are given in Table 2.

Table 2: Results of SEAMCAT simulations.

Separation distance between LTE UE T_x and DVB-T R_x, km	Probability of interference (PoI), %
0.01	31.63
0.05	15.04
0.1	6.45
0.15	4.54

The simulation results show that the required separation distance must be more than approximately 0.15 km.

7. CONCLUSIONS

This study presents important results on the evaluation of coexistence requirements for the LTE deployment in the 700 MHz band and the DVB-T in adjacent frequency band below 694 MHz. This part of spectrum is very valuable because it is optimum in terms of need of coverage and bandwidth.

Electromagnetic compatibility between LTE UE uplink and DVB-T receiver was assessed with two different methods: MCL calculations for worst case scenario and Monte Carlo simulations for more realistic case. The minimum coupling distance required between LTE UE uplink and DVB-T receivers in the 700 MHz band to maintain the necessary performance level of the DVB-T system is 8.84 km according to MCL calculations. The Monte Carlo simulation results show that the required separation distance must be more than approximately 0.15 km with condition that the probability of interference (PoI) less than 5% is considered to be a sufficient protection level.

The results of this study identify that when using the selected frequency arrangement additional mitigation techniques, such as downtilting of antennas, antenna discrimination, limitation of LTE UE out-of-band emission level etc., for LTE network planning and deployment are required in order to assure the compatibility between these two services. The acquired compatibility evaluation results can be used by National Regulatory Authorities (NRAs), which are responsible for spectrum planning at the national level, mobile operators, equipment manufacturers and other interested parties when planning mobile services in the 700 MHz band and broadcasting service below 694 MHz.

REFERENCES

1. "Use of the frequency band 694–790 MHz by the mobile, except aeronautical mobile, service in Region 1 and related studies," Resolution 232 (WRC-12), Radio Regulations, Resolutions and Recommendations, International Telecommunications Union (ITU), Vol. 3, Edition of 2012, 2012.
2. Ancans, G., V. Bobrovs, and G. Ivanovs, "Spectrum usage in mobile broadband communication systems," *Latvian Journal of Physics and Technical Sciences*, Vol. 50, No. 3, 53, 2013.
3. "Preliminary draft new ITU-R report on sharing and compatibility studies under agenda item 1.2," Annex 22 to Joint Task Group 4-5-6-7 Chairman's Report, Document 4-5-6-7/715-E, Aug. 28, 2014.
4. De Sousa Chaves, F. and R. Ruismaki, "LTE 700 MHz: Evaluation of the probability of interference to digital TV," *2014 IEEE 80th Vehicular Technology Conference (VTC Fall)*, 1–7, 2014.
5. Setiawan, D., D. Gunawan, and D. Sirat, "Interference analysis of guard band and geographical separation between DVB-T and E-UTRA in digital dividend UHF band," *2009 International Conference on Instrumentation, Communications, Information Technology, and Biomedical Engineering (ICICI-BME)*, 1–6, 2009.
6. "Sharing parameters for WRC-15 agenda Item 1.2," Liaison statement to Joint Task Group 4-5-6-7, ITU Working Party 5D, Document 4-5-6-7/49-E, Oct. 16, 2012.
7. "Characteristics of terrestrial IMT — Advanced systems for frequency sharing/interference analyses," Report ITU-R M.2292-0, 13, Dec. 2013.
8. "Evolved universal terrestrial radio access (E-UTRA). User Equipment (UE) radio transmission and reception," ETSI TS 136 101 V10.7.0, (3GPP TS 36.101 V10.7.0 Release 10), ETSI, 2012.
9. "Technical characteristics and other technical issues for terrestrial television broadcasting in connection with WRC-15 Agenda Item 1.2," Liaison statement to Joint Task Group 4-5-6-7, Working Party 6A, Document 4-5-6-7/55, Nov. 5, 2012.
10. "Spectrum engineering advanced Monte Carlo analysis tool (SEAMCAT)," Developed within the Frame of European Conference of Postal and Telecommunication administrations (CEPT), Available: www.seamcat.org.

Möbius Strip with Back-to-back CPW Transmission Line: Simulation and Microwave Characterization

M. Sabrera and L. C. Kretly

Department of Communication, DECOM, University of Campinas, UNICAMP
Campinas, State of Sao Paulo, Brazil

Abstract— A Möbius Strip device composed by two CPW — coplanar Waveguide placed back-to-back was constructed simulated and characterized. This device also named B2B-CPWMÖS exhibit a behavior like an infinite transmission line with characteristics capable of retaining a large bandwidth frequencies. This work presents some insight into this behavior by EM simulations using simulators with FIT — Finite Integration Technique and measurements in microwave range from MHz to few GHz. This work also shows how to fabricate simple CPW devices and the perspectives for planarization of this 3D structure. Additional EM behavior such as infinite transmission line and retention of a large bandwidth of signal frequencies of B2B-CPWMÖS is also discussed in this paper. This last capability gives rise to real time retention, RTR behavior and originates the RTR devices. The Möbius B2B-CPW device shows a continuous phase change compared to short-circuited classical transmission line. This paper presents also a qualitative analysis of this kind of structure.

1. INTRODUCTION

1.1. Möbius Strip: Geometrical and Topological Definitions

Some Möbius strip definitions are presented. There are geometrical and topological definitions. The Mobius strip is a one-sided non-orientable surface with Euler characteristic $\chi = 0$. Topologically, the Mobius strip can be defined as the square $[0, 1] \times [0, 1]$ with its top and bottom sides identified by the relation $(x, 0) \sim (1 - x, 1)$ for $0 \leq x \leq 1$, [1] as in the diagrams shown in Fig. 1.
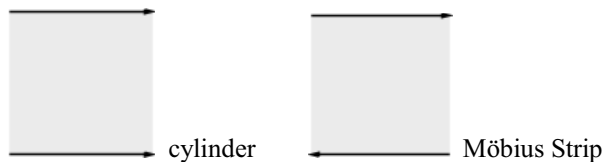
Figure 1: Topological representation of cylinder and Möbius strip.
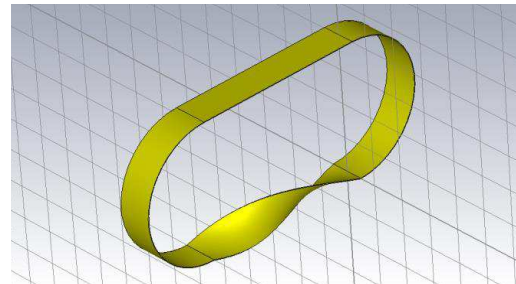
Figure 2: The classical Möbius strip in the simulator environment.

1.2. Signal Feed Considerations

One of the most critical challenges related to the Mobius strip devices is how to excite the structure by means a connection to the generator. This problem was investigated by simulation and measurements with a VNA — Vector Network Analyzer. Several Möbius strip devices were made with different length. A more sophisticated device based on Möbius strip topology is the CPW Back-to-Back Möbius Strip shown in Fig. 3. Due to this special topology, antenna with Möbius strip configuration, if properly bisected, could present approximately the double of electrical length when compared with conventional ring radiators [2]. This could improve, for example, miniaturization of RFID antennas. Several devices were simulated, fabricated and measured showing EM behavior that needs special techniques for simulation, measurement and characterization.

2. BACK-TO-BACK CPW MÖBIUS STRIP: FABRICATION PROCESS

Recent work on this type of devices was done by using special substrates such as Taconic TLY5 [3] with low dielectric constant $\varepsilon = 2.2$ [4]. Antennas and other devices are also fabricated with the above substrate [5]. Initially, in this work, the CPW line is calculated for $50\,\Omega$ impedance on a polyester PET (polyethylene terephthalate) substrate $\varepsilon = 3.4$ with $5\,\text{mils}$ ($\sim 0.125\,\text{mm}$) thickness.

(a)   (b)

Figure 3: The constructed B2B-CPWMÖS (a) copper CPW lines on the PET substrate: developed length 295 mm, (b) the complete device with one twist.

Due to the ratio between substrate and copper thicknesses adequate corrections were done. Preliminary layout of CPW lines are printed on the PET substrate. Then, cooper foils with adhesive were cut and bonded to the PET substrate. After full characterization of individual CPW lines, one directional coupler was incorporated to one of the lines. These measurements enable a more precise match between constructed CPW devices.

The dimensions of CPW lines and B2B-CPWMÖS are shown in Fig. 4.

The directional coupler was calculated by simple assumptions and dimensioned for CPW and SMA connectors. One of the CPW lines is kept with a metallic ground underneath the substrate. This additional ground works as a shield between the two CPWs. In the following step both lines are glued back-to-back. Special care must be exercised to avoid excessive adhesive layer and air bubbles between lines. Then the assembly was twisted to establish a Möbius surface and subsequently, make connections to keep electrical continuity for both lines: ground and centerline.

The directional coupler which was inserted in one of the CPW line has PORT 1 for signal feed and the PORT 2 for 50 Ω termination. After SMA connections, the B2B-CPWMÖS is read to be characterized.

3. SIMULATION ENVIRONMENT AND LIMITATION

The topological nature of Möbius strip with a non-orientable surface imposes a limitation on the meshing process in commercial software packages. The meshing procedure is essential to evaluate the response by the numerical methods. Under these constraints there is a special choice of meshing operation when it is attempted to solve the EM equations. The area with the meshes is depicted in Fig. 5.

The simulation of S_{11} parameter is carried out by CST-Studio as shown in Fig. 6.
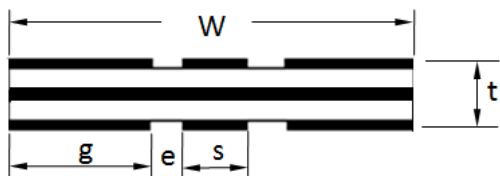

Figure 4: CPW dimensions (out of scale): $W = 10$ mm, $t = 0.445$ mm, $g = 3$ mm, $e = 1.0$ mm, $s = 2$ mm, copper foil thickness 0.065 mm, PET thickness $= 0.125$ mm.
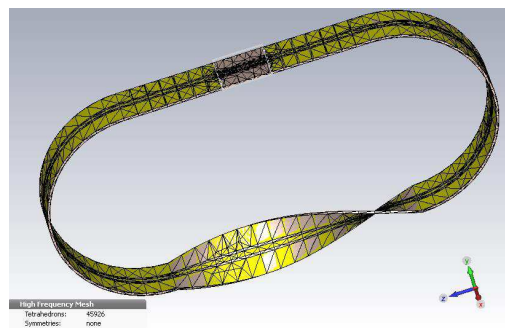

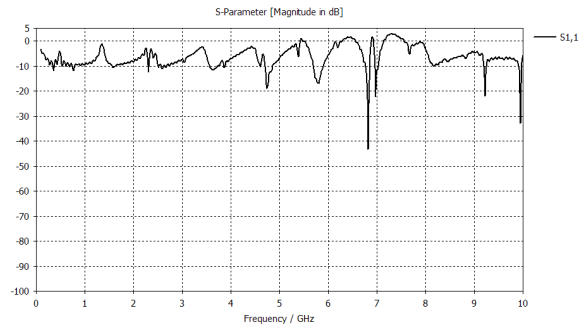Figure 5: Mesh cells on the structure of a B2B-CPWMÖS.

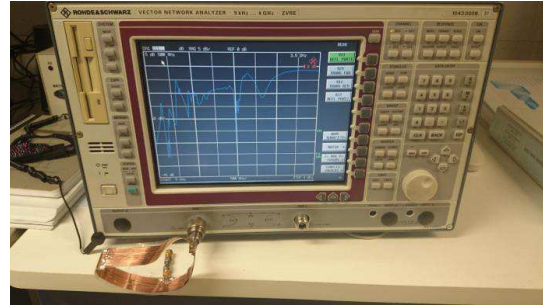Figure 6: Simulation of B2B-CPWMÖS: S_{11} up to 10 GHz.

Figure 7: Setup for measurement up to 4 GHz.

4. MEASUREMENTS, RESULTS AND DISCUSSION

The device was characterized by two VNA instruments with frequency range from 0.1 MHz to 4 GHz. The test setup is shown in Fig. 7.

The results as shown in Fig. 8, demonstrate the feasibility of B2B-CPWMÖS devices and the microwave behavior as an infinite transmission line.

Time Domain measurements, (conversion from frequency domain data with IFFT — Inverse Fast Fourier Transform) is obtained, Fig. 9.
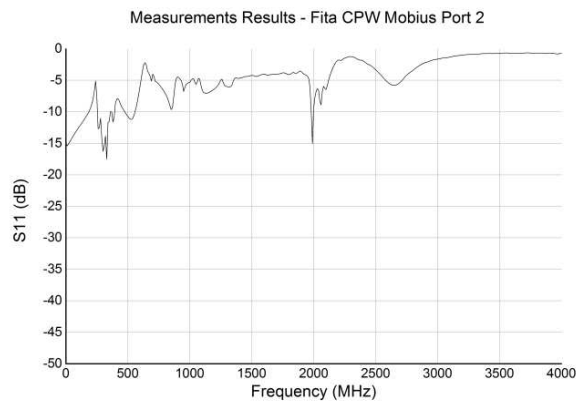
Figure 8: Return loss (S_{11}) measurement for the B2B-CPWMÖS.
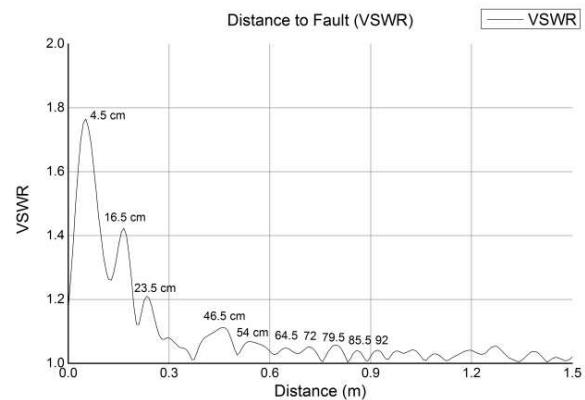
Figure 9: Time domain measurements on B2B-CPWMÖS (see text).

The multiple reflected pulses in the TDR signal (shown as cm values) indicate multiple transit of the signals around the Möbius CPW lines. The first spike at 4.5 cm indicates the reflection at PORT 2 of the directional coupler. The second spike is related the discontinuities created at the point where the two CPWs lines were welded together. The several peaks after 46.5 cm represent [4] the various transit time of the signal around the B2B-CPWMÖS device. The electrical length and guided wavelength λ_g, must be considered for this analysis.

This assumption implies that for a broadband of signal frequencies there is a retention phenomenon that could be demonstrated by real or physical TDR measurements.

There is a need for in-depth Mathematical and Electromagnetics studies to full understanding the Möbius Strip as microwave devices.

A crux of the matter to be investigated is how to planarize such devices to be integrated on planar circuits [6–8] and the combination of this structure with Metamaterials concepts [9].

REFERENCES

1. Basener, W. F., "Pure and applied mathematics: A Wiley interscience series texts, monographs and tracts," *Topology and Its Applications*, 1973.
2. Jiang, W., T. Hong, S.-X. Gong, Y.-X. Xu, and J. Ma, "An ultra-wideband monopole antenna with topological structure," *Microwave and Optical Technology Letters*, Vol. 52, No. 7, 1536–1539, Jul. 2010.
3. http://www.taconic-add.com/pdf/taconic-tlt_tlx_tly_processing.pdf.
4. Poddar, A. K., D. Sundararajan, and U. L. Rhode, "Real time signal retention device using co-planar waveguide (CPW) as Möbius strip," *IEEE MTT-S Microwave Symposium Digest 2013*, 1–4, Jun. 2013.
5. Zulkifli, F. Y., F. Narpati, and E. T. Rahardjo, "S-shaped patch antenna fed by dual offset electromagnetically coupled for 5–6 GHz high speed network," *PIERS Proceedings*, 897–900, Beijing, China, Mar. 26–30, 2007.
6. Kim, M. J., C. S. Cho, and J. Kim, "Miniaturized resonator using a planar Möbius strip bisected along the circumferential direction," *IEEE MTT-S Microwave Symposium Digest 2006*, 1385–1388, Jun. 2006.
7. Kim, M. J., C. S. Cho, and J. Kim, "Miniaturized antenna using a planar Möbius strip bisected along the circumferential direction," *Proceedings 36th European Microwave Conference*, 827–830, Oct. 2006.
8. Rhode, U. L., A. K. Poddar, and D. Sundararajan, "Printed resonators: A Möbius strip theory and applications," *Microwave Journal*, Vol. 56, No. 11, 24–54, Nov. 2013.
9. Rhode, U. L. and A. K. Poddar, "Metamaterial Möbius strip resonators for tunable oscillators," *Microwave Journal*, www.microwavejournal.com, Jan. 14, 2015.

Microwave Magnetoelectric Isolator-attenuator Based on Coplanar Line

A. S. Tatarenko, D. V. Lavrentieva, M. I. Bichurin, and D. V. Kovalenko

Novgorod State University, Veliky Novgorod 173003, Russia

Abstract— An electrically controlled magnetoelectric (ME) microwave isolator-attenuator based on layered ferrite-piezoelectric structure formed on a coplanar waveguide is considered. The simulations of different structures of coplanar devices are made for selecting of optimal waveguide and resonator characteristics.

1. INTRODUCTION

Microwave devices, such as isolators, attenuators and circulators are the devices which enabling to protect the input of the transmitter from stray electromagnetic radiation acting in the operating frequency band. They are indispensable devices for television, radar system, broadcasting radio and communications.

The task of matching the microwave power source to the load is achieved by using nonreciprocal properties of ferrites. However, the non-reciprocal ferrite devices control the parameters realized by magnetic system, so these devices have low speed of operation, high power consumption and cannot be manufactured by integrated technology.

Magnetoelectric (ME) non-reciprocal devices can reduce the disadvantages of existing ferrite devices: reduce the cost of devices; improve the speed of switching; reduce the power consumption in the control circuit; use the integral technology manufacturing [1].

The difference between the ferrite devices and proposed ME nonreciprocal devices is to replace the ferrite resonator with magnetic control system by ME resonator and system of electrodes connected to the source of the control voltage.

2. DESIGN OF MICROWAVE ISOLATOR-ATTENUATOR

Here we discuss the microwave isolator-attenuator. The basic design of ME isolator-attenuator is coplanar waveguide and ME resonator which have rectangular (or disks) composite sample based on lead zirconate titanate (PZT) — ittrium iron garnet (YIG) layered structure. The permanent magnet creates a required magnetizing field in the area of ME resonator. The control voltage is applied to the electrodes.

Figure 1 shows the design of the microwave ME coplanar isolator-attenuator. To improve the ellipticity, and hence the isolation ratio, the ceramic plate with high permittivity ($\varepsilon = 60$) with beveled edges mounted on ME resonator, as proposed in [2].

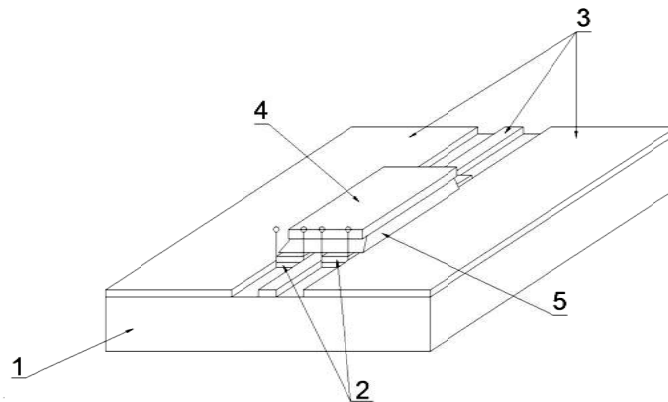Figure 2 shows the design of ME resonator.

Figure 1: Microwave ME coplanar isolator-attenuator: 1 is dielectric substrate; 2 is ME resonator; 3 is metallic conductors forming the coplanar waveguide; 4 is magnet; 5 ceramic plate with high permittivity with beveled edges.
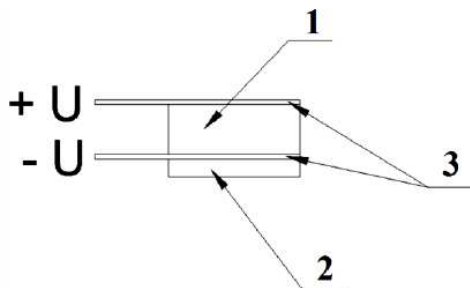
Figure 2: The structure of ME resonator: 1 is piezo-electric element; 2 is ferrite element; 3 is electrodes.
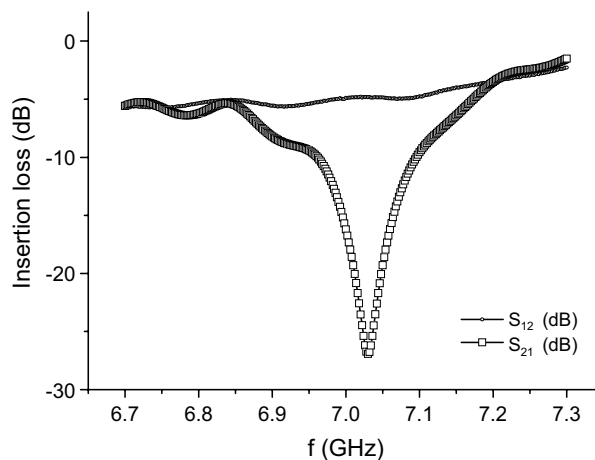

Figure 3: The experimental frequency dependence of attenuation. Constant magnetic field is $H_0 = 1780\,$Oe.

The principle of operation of the isolator-attenuator based on microwave ME effect, is to shift the ferromagnetic resonance line under the influence of an electric field. ME layered structure in this case plays the role of a resonator. Shift of magnetic resonance line at applied an electric field is defined as $\delta H_E = AE\delta H_E = AE$, where A is magnetoelectric coefficient; E is applied DC electric field.

The simulation of coplanar isolator-attenuator was made. We conducted a simulation of various types of non-reciprocal magnetoelectric devices based on slot and coplanar lines by using HFSS. It allows to get the selection of waveguide substrate parameters and the shape of ferrite and piezo-electric.

3. RESULTS AND DISCUSSION

The ME resonator based on layered structure of YIG with dimensions $13 \times 4 \times 0.9\,$mm and PZT with dimensions $15 \times 4 \times 0.5\,$mm. The coplanar waveguide has next parameters: the width of the gap $S = 3\,$mm; distance between slits $W = 2\,$mm; substrate thickness $h = 2\,$mm; dielectric permittivity of substrate $\varepsilon = 10$. The measurement of the transmission characteristics of the prototype were carried out on the measuring stand, consisting of an Agilent vector network analyzer PNA-L N5230C, electromagnet GMW5403 and DC current source Sorensen DLM 20-30.

Figure 3 shows the experimental dependence of attenuation in the forward and reverse directions for the investigated structure.

Thus, we considered the microwave ME isolator-attenuator: ME resonator based on layered magnetostrictive-piezoelectric structure with metal electrodes placed in the gap of coplanar waveguide, a ceramic plate with beveled edges with high permittivity ($\varepsilon = 60$) and a permanent magnet mounted on ME resonator.

4. CONCLUSION

The simulation and experimental study of the various structures of the microwave ME coplanar isolator-attenuator. To decrease the control voltage and the increase the isolation ratio is necessary to reduce the thicknesses of the piezoelectric, and ferrite.

Isolation ratio was about $20\,$dB. The shift of the resonance line corresponded $\pm30\,$MHz at applied an electric field $E = \pm10\,$kV/cm. Thus, the electric control allows to realize the tunable isolator or controllable isolator-attenuator. The magnitude of frequency tuning for the isolator was $60\,$MHz. The amount of attenuation change was about $20\,$dB.

The proposed model performs the functions of both the isolator and the attenuator; is controlled by an electric field; can be made by integral technology; has higher performance and lower power consumption on comparison with ferrite attenuators.

The use of ME structures in the resonant microwave devices allows electrical control of their parameters and opens promising opportunities of the designing the new devices for functional electronics.

REFERENCES

1. Tatarenko, A. S. and M. I. Bichurin, "Microwave magnetoelectric devices," *Advances in Condensed Matter Physics*, Vol. 2012, 10, 2012.
2. Wen, C. P., "Coplanar waveguide: A surface strip transmission line suitable for nonreciprocal gyromagnetic device application," *IEEE Trans. Microwave Theory Tech.*, Vol. 17, 1087–1090, 1969.

Modeling of Microwave Magnetoelectric Devices

A. S. Tatarenko and M. I. Bichurin

Novgorod State University, Veliky Novgorod 173003, Russia

Abstract— Design of integrated devices, and combine properties of several microwave non-reciprocal devices, are analyzed. The possibility for the development of a complex approach to designing and manufacturing of nonreciprocal microwave devices with improved technical characteristics is shown. Electromagnetic simulation of devices in the HFSS program is made.

1. INTRODUCTION

Computation, design and manufacturing technology of nonreciprocal microwave devices intended for application in receiving-transmitting modules of antenna array have a great interest in current time. Currently, a large development has program High Frequency System Simulator (HFSS) of company AnSoft, which is intended for the analysis of three-dimensional microwave structures, including antennas and non-reciprocal devices containing ferrites and ferroelectrics. Electromagnetic simulation in HFSS is based on the use of the finite element method (Finite Element Method, FEM).

Microstrip line, coplanar line and slot line are used in the microwave range. The microstrip lines are used most widely [1]. However, at designing the non-reciprocal devices using ferrites it requires the microwave field of circular polarization. In microstrip line this region is absent and the additional elements are needed, for example in the form of stubs to create an area of circular polarization. From this point of view, the slot and coplanar line are of interest. The structure of the microwave field in the slot line and coplanar waveguide is significantly different from the structure of the wave field in microstrip line. Coplanar waveguide (CPW) is a transmission line which consists of a center strip, two slots and a semi-infinite ground plane on either side of it [2]. This type of waveguide offers several advantages over conventional microstrip line, namely, it facilitates easy shunt as well as series mounting of active and passive devices; it eliminates the need for wraparound and the holes, and it has a low radiation loss. Another important advantage of CPW which has recently emerged is that CPW circuits render themselves to fast and inexpensive on-wafer characterization at frequencies as high as $50\,\text{GHz}$. Lastly, since the RF magnetic fields in the CPW are elliptically polarized, nonreciprocal components such as ferrite circulators and isolators can be efficiently integrated with the feed network.

These as well as other advantages make CPW useful for a monolithic microwave integrated circuit based microwave distribution network. Grounded CPW (GCPW) is a variant of CPW which incorporates an additional ground plane on the back side of the substrate. This additional ground plane can serve as a heat sink and provide mechanical strength. In addition, the ground plane serves as a shield between stacked antenna boards to improve isolation.

The use of modern simulation software allows the fast design of various types of non-reciprocal microwave devices. We conducted a simulation of various types of non-reciprocal magnetoelectric devices based on slot and coplanar lines by using the HFSS. A comparison with similar devices based on the microstrip line was made.

2. MODELING OF NON-RECIPROCAL MICROWAVE DEVICES

The simulation of ME coplanar isolator-attenuator was made. That simulation allows to get the selection of waveguide substrate parameters and the shape of ferrite and piezoelectric. The ME resonator based on layered structure of YIG and PZTwith electrodes was used.

The principle of operation of the proposed isolator-attenuator is based on microwave ME effect, which consists in a shift of the FMR line under the influence of an electric field. The design of coplanar ME isolator-attenuator is coplanar waveguide on a dielectric substrate and ME resonator, which have a rectangular shape (or in the form of disk) of layered composite of lead zirconate titanate (PZT) — yttrium iron garnet (YIG). Control voltage is applied to the ME resonator electrodes. The permanent magnet provides required magnetizing field.

Figure 1 shows the construction of the coplanar ME isolator-attenuator model with a resonator in the slot of waveguide.

Variants with two resonators in each slot of waveguide or with one resonator overlapping the both slots are also possible. All options were modeled. The layered structures of different thicknesses and configurations were investigated as resonators. Magnetizing field was directed tangentially to the plane of structures.
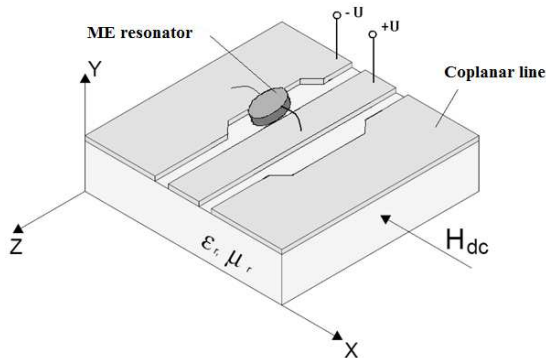

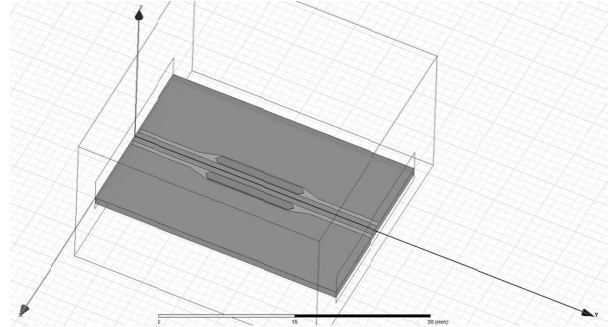Figure 1: Model of ME coplanar isolator-attenuator.

Figure 2: The model of the coplanar ME isolator-attenuator.

3. RESULTS AND DISCUSSION

Simulation of the device is made in the software environment of the HFSS program. S-parameters in the frequency range are optimized for investigated device. The phase and amplitude characteristics of inverse and direct losses were investigated.

The following simulation results are presented for the variant of the isolator-attenuator with two resonators. The magnetizing field applied to one resonator. The second resonator needs for matching of microwave signal. It allows to get symmetrical characteristics of isolator-attenuator.

Figure 2 shows the model of the coplanar ME isolator-attenuator created in the HFSS program.

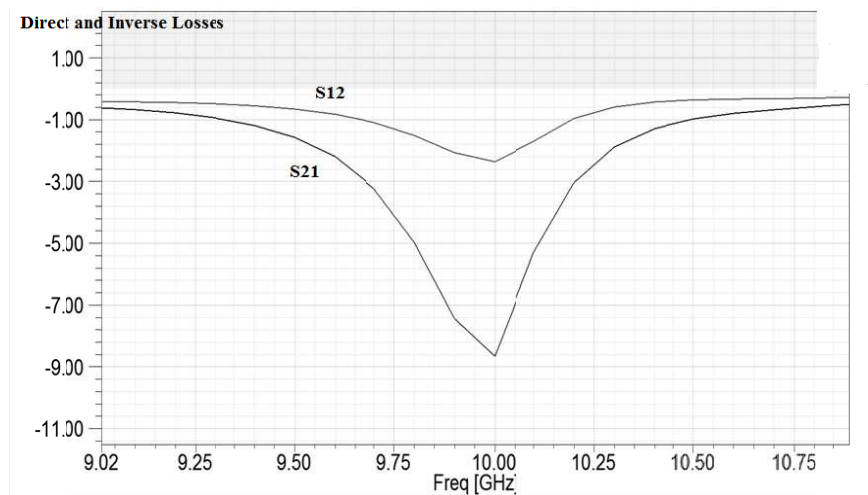Figure 3 shows the frequency dependence of inverse and direct losses.

Figure 3: The frequency dependence of inverse and direct losses.

The resulting level parameters for direct loss S_{12} is less than 1 dB, and the level of return loss S_{12} is the order of -10 dB in the frequency range of 200 MHz. The level of return loss may be varied by the component thickness ratio of the layered ME structure and may reach 25–30 dB. To decrease the control voltage and increase the isolation ratio one needs to reduce the thicknesses of the piezoelectric and the ferrite.

4. CONCLUSION

The paper presents the design and performance of CPW microwave nonreciprocal devices which have potential applications in phased arrays and in other systems.

The use of computer simulation by the HFSS program for ME structures in the non-reciprocal microwave devices opens promising opportunities for the design of new devices.

REFERENCES

1. Bichurin, M. I., V. M. Petrov, R. V. Petrov, G. N. Kapralov, F. I. Bukashev, A. Yu. Smirnov, and A. S. Tatarenko, "Magnetoelectric microwave devices," *Ferroelectrics*, Vol. 280, 213–220, 2002.
2. Wen, C. P., "Coplanar waveguide: A surface strip transmission line suitable for nonreciprocal gyromagnetic device applications," *IEEE Transactions on Microwave Theory and Techniques*, Vol. 17, No. 12, 1087–1090, Dec. 1969.

Equalization of EDFA Gain Spectrum and Increase of OSNR through Introducing a Hybrid Raman-EDFA Solution

S. Olonkins, **I. Lyashuk**, **V. Bobrovs**, and **G. Ivanovs**

Institute of Telecommunications, Riga Technical University, Azenes st. 16, Riga LV-1048, Latvia

Abstract— The main goal of this paper is to demonstrate the advantages of a hybrid Raman-EDFA optical signal amplification solution over the use of conventional EDFA amplifiers. The most promising solution of hybrid amplification is supplementing the existing discrete amplifier with a distributed Raman amplifier, as it not only can broaden and equalize the gain spectrum, but it also can increase the optical signal-to-noise ratio of the signal at the output of the amplifier and can provide higher level of amplification. The obtained results have shown, that the implementation of the hybrid solution has allowed to increase the optical single-to-noise ratio by at least 1.7 dB in all of the channels.

1. INTRODUCTION

Due to the rapid growth of the number of internet and other service users, as well as with the increasing availability of these services, a rapid increase of the amount of transferred information has been observed over the last two decades. To satisfy this constantly increasing demand for higher network capacity, fibre optical transmission systems with wavelength division multiplexing (WDM) have been intensively studied and applied [1–3]. It is possible to increase the WDM system throughput capacity either by increasing the data transmission speed in channels or the number of channels. By raising the data transmission speed, it becomes necessary to reduce the optical noise produced by optical components (light sources, modulators, amplifiers, receivers, etc.), as higher transmission speed signals have lower noise immunity. In cases where the throughput capacity of existing networks is raised by increasing the number of channels of a WDM system, the attenuation caused by the optical signal division also is being raised, especially in systems, where power splitters are used [4]. Therefore, solutions are needed for compensating the ever increasing accumulated signal attenuation in an ever broader wavelength range.

Currently, erbium doped fibre amplifiers (EDFA) are most commonly used around the globe for compensation of optical signal attenuation. The amplification bandwidth of EDFAs is strictly limited (for conventional EDFA solutions, it is only 35 nm), which restricts the wavelength range used for the transmission in existing systems [5, 6]. It is thus necessary to seek new solutions for amplifying optical signals and opportunities of expanding the amplified wavelengths range and increase the attainable amplification level for the already existing optical signal amplification solutions.

The goal of this article is to investigate the possibility of expanding and equalising the gain spectrum of a conventional EDFA and increasing the optical signal-to-noise ratio (OSNR) at the output of the amplifier by supplementing the system with a distributed Raman amplifier (DRA) and, therefore, forming a hybrid Raman-EDFA solution.

2. SIMULATION MODEL

To investigate the possibility of expanding and equalising the gain spectrum of a conventional EDFA and increasing OSNR by implementing a hybrid Raman-EDFA solution, a simulation model of a 16 channel 10 Gbps DWDM transmission system with NRZ-OOK modulation format was introduced (see Figure 1). Each of the 16 channel transmitters operates at its own frequency in range from 193.05 to 193.8 THz with 50 GHz spacing between channels, the power of each transmitter was 1 dBm. All of the 16 generated optical pulse sequences are combined using an optical power combiner and, afterwards, the obtained optical flow is sent through a 150 km long standard single-mode fibre (SMF).

At the output of this SMF fibre the attenuated signal was sent through an in-line EDFA. Two scenarios were realised to amplify the signal: 1st — when the signal was amplified only by an in-line EDFA with 25 dBm (316 mW) 980 nm co-propagating pumping radiation and 10 meters long erbium doped fibre; 2nd — when the EDFA was reconfigured and the system was supplemented with a distributed Raman amplifier, in such a way forming a hybrid amplifier. After processing through the amplifier the signal was sent through a second SMF that was 50 km long, and afterwards divided among all 16 receivers using an optical power splitter with 13.5 dB insertion loss [3]. At
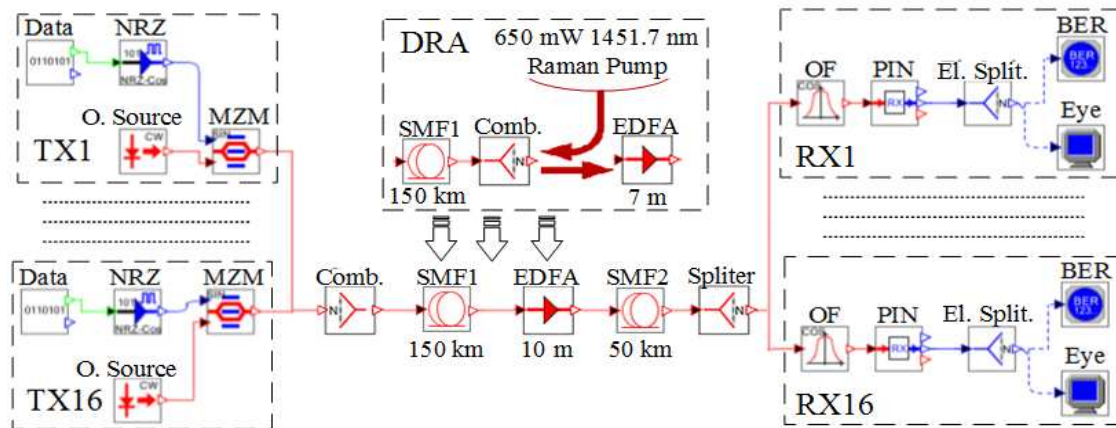
Figure 1: Simulation model of the 16 channel 10 Gbps DWDM transmission system with an EDFA inline amplifier or with a hybrid Raman-EDFA amplifier.

each receiver the signal was processed through an optical band-pass filter, leaving only the optical radiation that corresponds to the specific channel, and afterwards converted into electrical current using a PIN photodetector.

3. RESULTS AND DISCUSSIONS

When only the EDFA was used for amplification, the peak power level of each channel at the input of the amplifier has reached -37.1 ± 0.1 dBm. The in-line EDFA with 25 dBm 980 nm co-propagating pumping radiation and 10 meters long erbium doped fibre has ensured on-off gain from 38 to 39.5 dB for the 16 channels, therefore, 1.5 dB gain difference was obtained. Such gain was the minimal the minimal gain that could ensure BER values below the 10^{-12} mark in all channels. Such difference in amplification will not produce severe degradation on amplified signal quality in case in there is only one amplification span in the transmission system. The obtained Gain spectrum is shown in Figure 2(a). Our previous studies show that in systems with multiple transmission spans such amplification difference will increase with every following amplification span and as result higher pumping level will be required to ensure the required level of amplification for all channels. In such case the channels with higher level of amplification will initiate occurrence of explicit channel-channel four-wave mixing (CC-FWM) interactions, which would produce great amount of inter-channel crosstalk, thus severely degrading the quality of the signal. One more thing that degrades signal quality in such systems is the amplified spontaneous emission (ASE) noise produced by EDFAs, as each amplifier not only produced its own ASE, but also amplifies the noise that was produced by the previous amplifier. This also reduces the gain of the EDFA as significant part of the obtained population inversion is wasted on ASE amplification.

Taking into account the facts mentioned above, the Raman-EDFA hybrid solution was configured
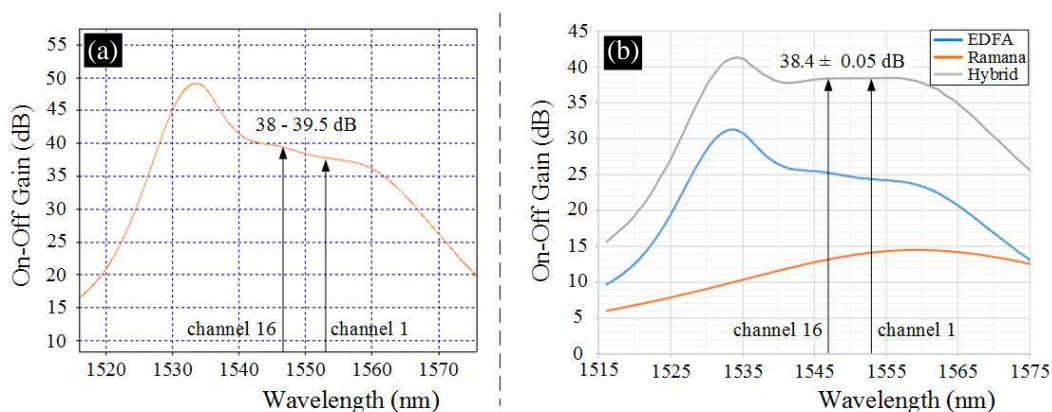

Figure 2: Gain spectra (a) of the EDFA inline amplifier and (b) of the hybrid Raman-EDFA amplifier.

with the aim to not only to equalise the gain spectrum in the wavelength band used for transmission and to ensure the required level of amplification, but also to reduce the amount of EDFA produced signal impairments. The SMF1 fibre was used as the gain medium for the DRA, where the 650 mW 1460 nm pumping radiation was launched in the counter propagating direction in respect to the signal to be amplified. Based on the obtained results it was decided to shorten the erbium doped fibre in order to reduce the amount of ASE produced by the in-line EDFA. To ensure the required level of population inversion a 23 dBm (200 mW) 980 nm co-propagating pumping radiation was used. The gain spectra that are ensured by the re-configured EDFA, by the DRA and the total gain spectrum of the hybrid solution are shown in Figure 2(b).

The results shown in Figure 2 clearly indicate that by implementing the hybrid Raman-EDFA solution much more uniform gain was obtained in the wavelength region used for transmission. The maximal difference in amplification between all 16 channels in the system with the hybrid Raman-EDFA amplifier has reached just 0.1 dB. Furthermore, the hybrid solution ensured gain difference below 1 dB over a 23 nm wavelength range (from 1538 to 1561 nm, by 17 nm more than was used for transmission of all 16 channels), which allows to significantly increase the number of channels in WDM transmission systems.

To compare the performance of the stand alone in-line EDFA and the hybrid Raman-EDFA amplifier OSNR values for all channels were obtained and compared at the output of the discrete amplifier. The obtained results are shown in Figure 3.

As can be seen in Figure 3, implementation of the hybrid solution has ensured OSNR improvement in all 16 channels from 1.7 up to 2.6 dB that in average is increase by ∼2 dB. Such OSNR improvement can be explained with the following facts:

- the usage of the distributed Raman amplifier has raised signal power at the input of the EDFA by 13.1–14.1 dB, therefore, the EDFA was functioning closer to the saturation point;
- the EDF fibre length was decreased by 3 meters, which allowed reducing the required input signal power for saturation of the EDFA;
- the coherent nature of stimulated Raman scattering (SRS) ensures that in SMF1 optical fibre, the signal was amplified more effectively than the low power optical noise, which allowed obtaining negative noise figure values (from −0.4 to −0.6 dB in the wavelength region used for transmission), and accordingly improved OSNR.
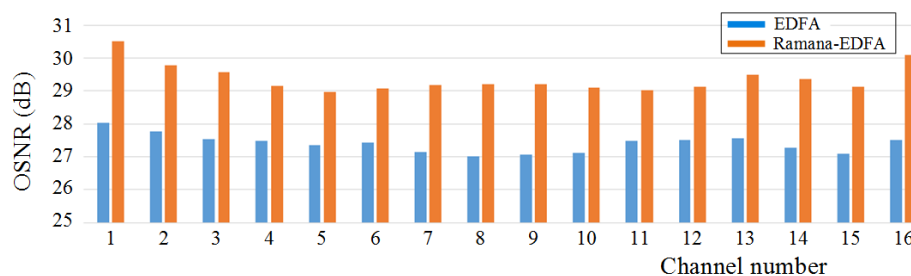

Figure 3: OSNR comparison among all 16 channels in the system with the EDFA inline amplifier and the hybrid Raman-EDFA amplifier.
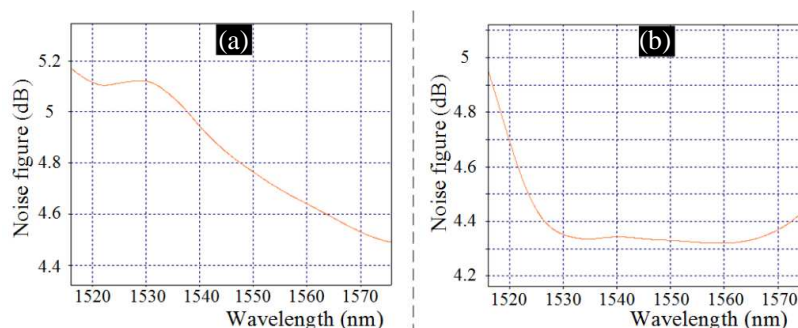

Figure 4: The EDFA Noise Figure wavelength dependence (a) in the system with the stand-alone in-line EDFA and (b) in the system with the Raman-EDFA hybrid amplifier.

    To assess the influence of implementation of the hybrid solution on the amount of ASE produced by the EDFA, noise figure (NF) wavelength dependencies were obtained for the system with the stand alone in-line EDFA, and for the system with the hybrid Raman-EDFA amplifier. The obtained results are shown in Figure 4.

    From Figure 4 it can be seen that in raising the signal power at the input of the EDFA and reducing the length of the erbium doped fibre allowed to obtain by 0.3–0.4 dB lower noise figure values for the EDFA.

4. CONCLUSIONS

In this article the authors have investigated the possibility of expanding and equalising the gain spectrum of a conventional EDFA and increasing the optical signal-to-noise ratio (OSNR) at the output of the amplifier by supplementing the system with a distributed Raman amplifier (DRA) and, therefore, forming a hybrid Raman-EDFA solution.

    After comparing the aforementioned EDFA and Raman-EDFA solutions, it was concluded that the hybrid amplifier can ensure more even amplification over a broader wavelength region and higher OSNR values. However, more powerful lasers are necessary for implementing such solutions, which increases the costs of developing this solution. For the EDFA inline amplifier 316 mW of pumping power was required to amplify the -37.1 dBm input signal by more than 38 dB. In the case of the hybrid solution, the Raman amplifier required 650 mW of pumping power to ensure that gain is high enough and that its slope can compensate the slope of the EDFA with 200 mW pump gain spectrum, but the total pumping power of the hybrid amplifier has reached 850 mW. However, the hybrid solution ensured gain difference below 1 dB over a 23 nm wavelength range (from 1538 to 1561 nm, by 17 nm more than was used for transmission of all 16 channels), which in future will allow to significantly increase the number of channels in the WDM transmission system under attention.

REFERENCES

1. Pilipetskii, A. N., "High-capacity undersea long-haul systems," *Selected Topics in IEEE Journal of Quantum Electronics*, Vol. 12, No. 4, 484–496, Jul.–Aug. 2006.
2. Sharma, P., A. Kumar, and V. K. Sharma, "Performance analysis of high speed optical network based on dense wavelength division multiplexing," *2014 International Conference on Issues and Challenges in Intelligent Computing Techniques (ICICT)*, 446–449, Feb. 7–8, 2014.
3. Olonkins, S., O. Ozolins, V. Bobrovs, J. Porins, and G. Ivanovs, "Binary PolSK to OOK modulation format conversion in single-pump FOPA for optical access networks," *4th International Workshop on Fiber Optics in Access Network (FOAN 2013)*, 15–20, Sep. 11–12, 2013.
4. 3M™ Technical Specifications, "PLC optical splitters," 1–2, USA, 2008.
5. Sharma, M. and V. R. Sharma, "Gain flattening of EDFA in C-band using RFA for WDM application," *2nd International Conference on Signal Processing and Integrated Networks (SPIN 2015)*, 346–351, Feb. 19–20, 2015.
6. Bobrovs, V., S. Olonkins, O. Ozolins, J. Porins, and G. Lauks, "Hybrid optical amplifiers for flexible development in long reach optical access system," *4th International Congress on Ultra Modern Telecommunications and Control Systems and Workshops (ICUMT 2012)*, 577–582, Oct. 3–5, 2012.

Beam-footprint Detection for Non-cooperative Spaceborne/Airborne Bistatic SAR

Feifei Yan, **Wenge Chang**, and **Xiangyang Li**

College of Electronic Science and Engineering

National University of Defense Technology, Changsha, Hunan 410073, China

Abstract— In non-cooperative spaceborne/airborne bistatic synthetic aperture radar (SAR), the position of transmitter beam footprint should be detected in real-time to realize beam synchronization. Theoretical analysis shows that signal-to-noise ratio (SNR) of the reflected echoes from the observational area is too low to use the conventional detect method. According to the cross correlation between the echoes of adjacent pulse repetition frequency (PRF) and M-out-of-N (M/N) detection, a reflected echo detect method is proposed in this paper. This method can realize the accumulation of signal energy and enormously improve the performance of LFM detection. Therefore, it can be used for transmitter beam footprint detection in real-time. Simulation results are finally presented to validate the feasibility and efficiency of the proposed method. Finally, raw data of one monostatic SAR is equivalent to verify the efficiency of the proposed algorithm.

1. INTRODUCTION

Non-cooperative bistatic SAR, which using aircraft as receiver and spaceborne radar as illuminating of opportunity, has recently been an interesting research hotspot [1]. Non-cooperative radars with low system cost can achieve additional benefits like improving feature extraction and classification of targets, increasing surveillance for applications in conflict areas. Bistatic radar use separate antennas for transmission and reception, so the observations require accurate antenna pointing for both transmitter and receiver to achieve swath overlap. For the case of non-cooperative transmitter satellite, as there has no special synchronization link between the transmitter and receiver, the accurate position of transmitter beam footprint cannot be known in real-time [2]. So the sampling signal from the anticipative observational area should be analyzed in real-time to judge whether the transmitter beam footprint is coming. Then the synchronization mechanism of the receiver is working to realize beam synchronization.

The reflected echoes from the observational area can be seen as weak linear frequency modulation (LFM) signal detection. There are some classical methods for weak signal detection [3, 4]. Traditional methods include fast Fourier transform, filtering, and lock-in amplifier, etc.. When the SNR of reflected echoes is low, the detection performance will be poor. The fractional Fourier transform (FRFT) is very suitable to detect the LFM signals because of its unique properties. However, the computation cost is very high, and then the weak signal detection cannot be realized in real-time. In conclusion, few studies are reported on beam footprint detection for non-cooperative spaceborne/airborne bistatic SAR.

Based on cross correlation and M/N detection, a beam footprint detection method is proposed in this paper. Without long time noncoherent integration in azimuth dimension, the method can enormously improve the detection efficiency. Meanwhile, the constant false alarm rate (CFAR) and M/N detection methods are used for LFM signal detection. This paper is arranged as follows: Section 2 introduces cross correlation detection method. Simulation results and experimental data results are presented in Section 3 to verify the proposed method. Finally, some conclusions are given in Section 4.

2. BACKSCATTERING ECHO DETECTION

Since the observational area between the adjacent PRF is almost the same, so the adjacent backscattering echoes have high correlation. As noises between the adjacent PRF are irrelevant, there will be a peak value in the cross correlation result, and then CFAR detection for the scene raw data can be performed. To distinguish sample signal between LFM signal and other signals, noncoherent integration and M/N detection are performed in frequency domain. The proposed detection method can realize the accumulation of signal energy and enormously improve the performance of backscattering echo detection.

2.1. Cross Correlation

The backscattering echoes of the scene between the adjacent PRF are

$$\begin{cases} x_1(\tau, \eta) = s_r(\tau, \eta) + w_1 \\ x_2(\tau, \eta) = s_r(\tau, \eta + T) + w_2 \end{cases} \tag{1}$$

where $T = 1/\text{PRF}$, $s_r(\tau, \eta)$ and $s_r(\tau, \eta + T)$ are the backscattering echoes between the adjacent PRF, respectively. w_1 and w_2 are white Gaussian noises between the adjacent PRF with zero mean and standard deviation σ^2, respectively.

The cross correlation result between the adjacent echoes is

$$R_{x_1 x_2} = R_s + R_{sw_1} + R_{sw_2} + R_{w_1 w_2} = R_s + R_w \tag{2}$$

R_w is the cross correlation result related to noise

$$R_s = R_{sw_1} + R_{sw_2} + R_{w_1 w_2} = \frac{1}{N}\left[\sum s(n) w_1^*(n) + \sum s(n) w_2^*(n) + \sum w_1(n) w_2^*(n)\right] \tag{3}$$

For N large enough, according to the central limit theorems in probability theory, R_w is nearly white Gaussian noise with zero mean and standard deviation $(2E_s\sigma^2 + \sigma^4)/N$, where E_s is the energy summation of the signal. When the sample signal is only noise, the real and imaginary part of $R_{x_1 x_2}(\tau)$ are independent, which are white Gaussian noise with zero mean and standard deviation σ^4/N. The PDFs are

$$P(x) = \begin{cases} \frac{x}{\sigma^4/N} \exp\left(-\frac{1}{2\cdot(\sigma^4/N)}x\right) & 0 \le x < \infty \\ 0 & x < 0 \end{cases} \tag{4}$$

In CFAR systems [5], the probability of false alarm is

$$P_{FA} = \int_{V_T}^{\infty} (X > TZ \,|H_0)\, f_z(z)\, dx = E_z\left(p\left(X > TZ \,|H_0\right)\right) \tag{5}$$

where Z is the mean clutter power, T is a scaling factor, $f_z(z)$ is the probability density function of Z.

Substituting $f_z(z)$ into (5), the P_{FA} is

$$P_{FA} = M_z\left(\frac{T}{2\sigma^2}\right) \tag{6}$$

where $M_z(\cdot)$ is the moment-generating function of Z. According to (6), when the false alarm probability P_{FA} is given, we can get the threshold V_T.

2.2. M/N Detection

The cross correlation result between the adjacent echoes cannot determine whether the received signal is LFM signal arisen from the spaceborne radar. As the signal bandwidth of the spaceborne radar can be getting from the direct path signal, then M/N detection is performed after noncoherent integration to distinguish the received signal between LFM signal and other signal in frequency domain.

After cross correlation, $R_s(\tau)$ is very narrow in time domain and has a symmetry distribution to the middle of $R_{x_1 x_2}(\tau)$; meanwhile, $R_{sw_1}(\tau)$, $R_{sw_2}(\tau)$, $R_{w_1 w_2}(\tau)$ distribute uniformity in time domain. When the cross correlation result $R_{x_1 x_2}(\tau)$ is cut by rectangle window in the time domain, the amplitude of noncoherent integration result in frequency domain will be smooth, and then the performance of M/N detection can be easily improved.

The M/N detection can be written

$$\sum_{i=1}^{N} u(z_i - T) \underset{H_0}{\overset{H_1}{\gtrless}} M, \quad u(z) = \begin{cases} 1 & z \ge 0 \\ 0 & z < 0 \end{cases} \tag{7}$$

where N is the sample point in range dimension.

If $P_{d,cell}$ denotes the probability that any given pulse exceeds the threshold. Now let P_d, the double threshold probability of detection, be defined as the probability that signal is detected, i.e., the threshold is crossed M times within N looks, then from (7)

$$P_d = \sum_{m=M}^{N} \frac{N!}{m!(N-M)!} \left(P_{d,cell}\right)^m \left(1 - P_{d,cell}\right)^{N-m} \qquad (8)$$

The double threshold probability of false alarm is

$$P_{fa} = \sum_{m=M}^{N} \frac{N!}{m!(N-M)!} \left(P_{f,cell}\right)^m \left(1 - P_{f,cell}\right)^{N-m} \qquad (9)$$

As can be seen from (4), after cross correlation, w' is a white Gaussian noise with zero mean and standard deviation σ^4/N. When noise only is present, the standard deviation of noise after FFT is determined by the width W of the rectangle window. Then the real and imaginary part of noise is white Gaussian noise with zero mean and standard deviation $2W\sigma_p^2$.

$$\text{real}\left(X(k)\right) \sim N\left(0, 2W\sigma_p^2\right), \quad \text{imag}\left(X(k)\right) \sim N\left(0, 2W\sigma_p^2\right) \qquad (10)$$

According to the probability theory [6], the PDFs of $z = |X(k)|^2$ are

$$P\left(z|H_0\right) = \begin{cases} \frac{z}{2W\sigma_p^2} \exp\left(-\frac{z}{2W\sigma_p^2}\right) & 0 \le z < \infty \\ 0 & z < 0 \end{cases} \qquad (11)$$

Suppose the number of noncoherent integration is N_c, then the summation of noise energy is a central chi-square distribution with degrees of $2N_c$ freedom [6]. The PDFs are

$$p\left(x\left|2N_c, \sigma^2\right.\right) = \frac{1}{\left(2W\sigma^2\right)^{N_c} \Gamma\left(N_c\right)} \left(x\right)^{N_c-1} \exp\left(-\frac{x}{2W\sigma^2}\right), \quad x \ge 0 \qquad (12)$$

Then the probability of false alarm $P_{f,cell}$ is

$$P_{f,cell} = \int_{V2}^{\infty} \frac{1}{\left(2W\sigma^2\right)^{N_c} \Gamma\left(N_c\right)} \left(x\right)^{N_c-1} \exp\left(-\frac{x}{2W\sigma^2}\right) dx \qquad (13)$$

For a given false alarm probability P_{fa}, the threshold V_2 is computed as follows:

(1) The threshold M is set by the bandwidth of LFM signal.
(2) According to (9) and M, $P_{f,cell}$ can be obtained.
(3) According to (13), we can get the threshold V_2.

The scheme of detect method is shown in Figure 1.

Figure 1: Scheme of backscattering echo detection.

3. SIMULATION AND VALIDATION

Suppose the transmitter and receiver is moving along parallel trajectories. Table 1 shows the simulation parameters.

The size of simulation scene is $2\,\text{km} \times 10\,\text{km}$, which is approaching the beam footprint width of receiver. When the beam footprint overlap between transmitter and receiver is set at 10%, the backscattering echoes of the simulation scene between the adjacent PRF are shown in Figure 2(a).
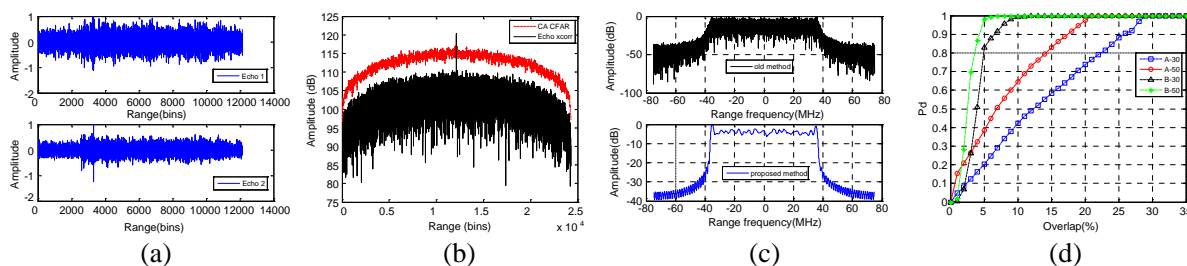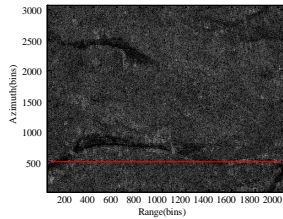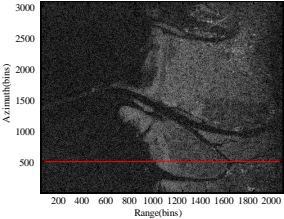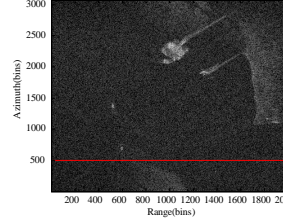
Figure 2: Detection performance, (a) adjacent echo, (b) cross correlation result, (c) power spectrum, (d) detection performance.

Table 1: Simulation parameter.

	Transmitter	Receiver
Height (km)	514	10
Velocity (m/s)	7600	100
Azimuth beam width (°)	0.33	2
Range beam width (°)	2.3	3
Incidence angle (°)	47	80
Bandwidth (MHz)	75	300
Wavelength (cm)	3.1	3.1
Antenna gain (dB)	45	28

Table 2: Detection probability of three different scenes.

Scene			
Detection probability	100%	95.77%	97.63%

The cross correlation result after CFAR detection is shown in Figure 2(b). The power spectrum is shown in Figure 2(c).

As can be seen from Figure 2(b), there is a peak value in the cross correlation result, and then the performance of CFAR detection can be enormously improved. Figure 2(c) shows the power spectrum of cross correlation result after noncoherent integration in frequency domain. The power spectrum without noncoherent integration is also presented in Figure 2(c). It is clearly seen that the power spectrum with noncoherent integration is obviously smooth than the power spectrum without noncoherent integration, which is suit for M/N detection. At the same time, the integration time is short, so the detection method can be realized in real-time.

The Monte-Carlo simulations are carried out to test the performance of the proposed detection method. The false alarm probability of M/N detection is set at 10^{-5}, the number of noncoherent integration is demonstrated using the various sizes (10 and 30). As can be seen from Figure 2(d), detection performance of the method with cross correlation (A) is superiority over the method without cross correlation (B); meanwhile, the detection performance is gradually improved with the increasing number of noncoherent integration. When the beam footprint overlap between the transmitter and receiver is over 10%, and the number of noncoherent integration exceeds 30, the backscattering echo can be stably detected by the proposed method.

Raw data of one monostatic SAR is used to test the propose detection method equivalently. From the simulation parameters in Table 1, theoretical analysis shows that the SNR of bistatic SAR is slightly higher than the monostatic SAR, then the raw data of monostatic SAR can be

equivalently seen as the beam footprint overlap of bistatic SAR is 100%. Three kinds of scene echo are chosen to test the proposed method. The number of noncoherent integration is 30. The red line is the start noncoherent integration position in azimuth dimension.

Table 2 shows the detection probability of three different scenes. It can be seen that the detection probability of homogeneous scene is slightly higher than heterogeneous scene; meanwhile, as the the raw data of monostatic SAR can be equivalently seen as the beam footprint overlap of bistatic SAR is 100%, so the probability of detection is very high.

4. CONCLUSIONS

In this paper, an efficient transmitter beam detection method for non-cooperative bistatic SAR is presented. Based on cross correlation and M/N detection, the efficiency of scene raw data detection is greatly improved. Simulation results prove that the proposed detection method is much more efficient than conventional method. When the beam footprint overlap between the transmitter and receiver and the number of noncoherent integration exceed a certain number, the proposed detection method can achieve stably detect of backscattering echo. The efficient and performance of the proposed detection method is also equivalently validated by raw data of one monostatic SAR.

REFERENCES

1. Merrill, I. and T. Skolnik, *Radar Handbook*, Publishing House of Electronics Industry, Beijing, 2010.
2. Watterscheid, I., J. Klare, and A. R. Brenner, "Challenges of bistatic spaceborne/airborne SAR experiment," *European Conference on Synthetic Aperture Radar*, 673–678, Dresden, Germany, May 2006.
3. Zhang, S. S. and T. Zeng, "Dim target detection based on keystone transform," *Proceedings of IEEE International Radar Conference*, 889–894, Washington, DC, USA, May 2005.
4. Conte, E., A. Maio, and G. Ricci, "CFAR detection of distributed targets in non-Craussian disturbance," *IEEE Trans. on Aerospace and Electronic Systems*, Vol. 38, No. 2, 612–621, 2002.
5. Bisciglie, D. and R. Mauriziodi, "CFAR detection of extended objects in high resolution SAR images," *IEEE Trans. on Geoscience and Remote Sensing*, Vol. 43, No. 4, 833–843, 2005.
6. Kay, S. M., *Fundamentals of Statistical Signal Processing Volume IIDetection Theory*, Prentice Hall, New Jersey, 1998.

Studies of the RF Energy Delivery Mechanism and Its Reformation in the Low Pressure ICP Discharge

A. F. Piskunkov and V. A. Riaby

Research Institute of Applied Mechanics and Electrodynamics of the Moscow Aviation Institute
(National Research University), Moscow, Russia

Abstract— The model of a cylindrical inductively coupled plasma (ICP) discharge based on movable current layers travelling towards the axis of discharge space from the steady-state skin sheath at the external plasma boundary has been proposed. Current layers act like magnetic electrostatic traps catching electrons with small pinch-angles that are responsible for gas atom ionization. Movement of the layers induces electric field excites currents. At the optimal driving frequency magnetic field of a definite sign fills all discharge space during current half-period in the process of convective diffusion and eventually it is replaced by the field of opposite sign. Ohmic losses in the current layers are compensated by annihilation of magnetic field. The layers are formed by the Hall Effect while their boundary areas are shaped in a forceless magnetic field. They have form of one-turn spirals and their pairs are short-circuited in the edge plasma areas.

Concentration of trapped layer particles is determined from the equation for trapped electrons entering and leaving the layer by way of single-shot Coulomb collisions at the pinch-angle.

Discharge power loss, ion energy price and electron temperature are calculated at different argon pressures for the discharge chamber of 35 cm external radius. Comparison with published experimental data showed that the proposed model satisfactorily describes the main ICP discharge characteristics.

1. INTRODUCTION

RF inductively coupled plasma (ICP) discharge has been used on a wide scale in modern ion thrusters and in plasma technologic systems [1, 2]. Different models of the RF energy delivery mechanisms and its absorption based on collision and ionization processes have been proposed in numerous theoretical and experimental studies [3–5]. For ICP discharge at moderate and low gas pressures transformer analogy of the antenna coil-plasma magnetic coupling should be corrected to find optimal discharge driving frequency influencing ionization processes. Note that formulation and solution of the self-consistent problem dealing with calculations of ICP discharge plasma parameters that depend on design and operational conditions like discharge dimension, gas flow rate, its pressure and discharge power, are still unknown. The solution of this problem should result in optimal driving frequency, electron and ion currents, plasma resistance, electron temperature and ion energy price which is necessary to optimize ICP discharge system. This is what constitutes the goal of the present work.

Novelty of the proposed ICP discharge model consists of ionization mechanism within a movable current layer travelling from the contiguous to an antenna coil discharge skin sheath towards the axis of the internal space. These current layers form circuits that are short-circuited in the end face plasma areas.

2. PHYSICO-MATHEMATICAL MODEL OF AN ICP DISCHARGE

2.1. Convectional Transfer of Magnetic Field

From the magnetic induction equation

$$\frac{\partial \vec{B}}{\partial t} + \text{rot}\frac{1}{ne}\left[\vec{J}\vec{B}\right] = -\text{rot}\left(\frac{1}{\sigma}\vec{J}\right)$$

for the curved magnetic force lines it follows that [6]

$$\frac{\partial \vec{B}}{\partial t}\frac{1}{ne\mu}\left[\vec{B}\nabla\vec{B}\right]\vec{B} = \frac{1}{\sigma\mu}\Delta\vec{B},$$

where $\vec{B}$ — magnetic field induction, $\vec{J}$ — current density, n — magnetized electron concentration, e — elementary electrical charge, σ — plasma conductivity, μ — magnetic constant.

In the framework of a one-dimensional problem the last equation can be written as

$$\frac{\partial B}{\partial t} + \left[\frac{1}{tgF} \frac{2}{r} \frac{1}{ne\mu} B \right] \frac{\partial B}{\partial r} = \frac{1}{\sigma\mu} \Delta \vec{B}, \quad B \equiv B_z,$$

where r and z are space coordinates, t is time, and F is angle between spiral curve tangent and radius vector.

Neglecting a diffuse member we have [6]

$$\frac{\partial B}{\partial t} + U \frac{\partial B}{\partial r} \cong 0.$$

Movable layer speed is equal to a convective diffuse velocity

$$U = \frac{1}{tgF} \frac{2}{r} \frac{1}{ne\mu} B.$$

For the model current layer magnetic field becomes zero in the middle of a layer at the distance l. Its Ohmic dissipation speed is equal to the Pounting's vector flow $\frac{lJ^2}{\sigma} = U\frac{B^2}{\mu}$.

Accepting average value of current density square to be equal to $J^2 = \frac{l}{2}(\frac{B}{\mu l})$ [7], we get the expression for the movable layer speed: $U = \frac{0.5}{\sigma\mu l}$.

The equality of convective diffusion and Ohmic dissipation speeds determines angle F. Note that in the present work unit system SI is used.

2.2. Plasma Density Determination

Let us suppose that electron concentration and temperature are averaged in space. Magnetized electron concentration n can be calculated using the equality of plasma magnetic moment in the volume confined by current layer and a magnetic moment of the layer current I [8]:

$$\frac{I}{h} = \frac{nkT}{B}$$

where $B \cong 0.5B_o$ [6], $B_o = \frac{\mu I_o N}{h}$, k is Boltzmann constant, T is electron temperature, I_o is antenna coil current, $N = 8$ is the number of antenna coil turns, $I \cong I_0 N$ is discharge current, and h is axial dimension of the chamber.

Integrating Maxwell electron velocity distribution limited by a spherical pinch-angle we obtain:

$$\frac{n}{n_e} = \frac{0.1(l\omega_B)^2}{2kT/m}, \quad (l\omega_B)^2 = \frac{3 \cdot 10^4 \omega_B}{\sqrt{y}},$$

where n_e is plasma electron concentration, ω_B is cyclotron frequency, $y = n_e \cdot 10^{-17}$ is non-dimensional variable.

2.3. Determination of Current Layer Parameters

Equality of magnetized electron flows from plasma to the current layer and back as a result of collisions gives:

$$nU = nv_{ef}2l; \quad U = 2v_{ef}l.$$

Effective collision frequency $v_{ef} = v_{ei} + v_a$ includes frequency of single Coulomb scattering at an angle ϑ inside pinch-angle [3]

$$v_{ei} = \left(\frac{\pi/2}{\vartheta} \right)^2 v_{cl}$$

where v_{cl} is frequency of Coulomb collisions at the angle $\pi/2$.

Average value of v_{ei} for the Maxwell electron velocity distribution function at maximal value of $\sin\vartheta = \frac{l\omega_B}{V}$ (here V is electron speed) can be written as $v_{ei} \cong \frac{2y^2}{B^2}$.

Using expression $U = \frac{0.5}{\sigma\mu l} = v_{ef}2l$ it is possible to calculate half-width of the layer $l^4 \cong \frac{3\cdot 10^4 \omega_B}{\sqrt{y}}$ and the portion of trapped electrons $\frac{n}{n_e} = \frac{3\cdot 10^3 \omega_B}{\frac{2kT}{m}\sqrt{y}}$.

Then above mentioned equality of magnetic moments for plasma and layer currents gives:

$$I_0^2 \cong 6 \cdot 10^7 \sqrt{y} \frac{h^2}{N^2} B; \quad I = I_0 N = \frac{B}{\mu} h; \quad B \cong 3 \cdot 10^{-4} \sqrt{y}.$$

Optimal driving frequency can be determined from the equation

$$U = 2r_0 f = 2v_{ef} l. \tag{1}$$

2.4. Model of collisional Mechanism within a Boundary Layer

In the forceless field electric currents flow along the magnetic lines of force [7]

$$\mathrm{rot}\vec{B} = \mu \vec{J} = (\alpha_1 + i\alpha_2) \vec{B},$$

where α_1, α_2 are constants. Faraday equation makes it possible to evaluate inducted electric field $\vec{E}$

$$\mathrm{rot}\vec{E} = -\frac{\partial \vec{B}}{\partial t}; \quad \vec{E} = \frac{\vec{J}}{\sigma};$$

Using expression for conductivity $\sigma = \frac{ne^2}{m(v_{ef} + i\omega)}$ we obtain

$$\mathrm{rot}\frac{\vec{J}}{\sigma} = \frac{(\alpha_1 + \alpha_2)^2 \vec{B}}{\mu\sigma} = -i\vec{B}\omega$$

$$\alpha_1 = \sqrt{b}\frac{1}{\sqrt{\gamma + \sqrt{\gamma^2 + 1}}}; \quad \left(\gamma = \frac{\omega}{v_{ef}}\right)$$

$$\alpha_2 = \frac{b}{\alpha_1}; \quad b = \frac{\sigma\omega\mu}{2(1 + \gamma^2)}.$$

Current in the skin sheath has two components shifted by phase. In the Cartesian coordinate system for $\vec{B} = (0, B_y, \sqrt{B^2 - B_y^2})$ it is possible to omit damping of the collisional field [9]

$$B_y = B\sin(\alpha_1 x); \quad B_z = B\cos(\alpha_1 x).$$

While electron moves along x axis across skin sheath, magnetic field vector revolves around this direction and electron is exposed to a non-uniform in space and non-periodic in time electric force. Being involved in this process it can lose phase coherency with the field resulting in stochastic scattering [3]. This mechanism was not taken into consideration in the present work. Collision frequency v_C was determined in the framework of one-dimensional problem [3]

$$v_C \cong \frac{\bar{V}}{4\delta_c}; \quad \delta_c = \left(\frac{\bar{V}}{2\omega\delta_p}\right)^{\frac{1}{3}} \delta_p; \quad 1/\delta_p = \sqrt{\frac{ne^2\mu}{m}},$$

where δ_c is the collisional skin sheath thickness and δ_p is the non-collisional skin sheath thickness.

2.5. Ionization Mechanism and Electron Temperature

Drift time for ions in the gas discharge chamber is much longer than time of current layer movement, therefore ionization processes in all discharge space can be considered as instantaneous. In the equilibrium ionization conditions $\alpha_i n_a nh = n_e \bar{V}_i (1 + \frac{h}{r_0})$, where α_i is ionization coefficient; n_a, n_e, n are concentrations of atoms, plasma electrons, and trapped particles, respectively; h and r_0 are axial and radial dimensions of the chamber, respectively, and $\bar{V}_i$ is the mean ion speed at electron temperature.

The last can be obtained from the following equation

$$\exp\left(\frac{E_i}{kT}\right) = \frac{1.6 \cdot 10^{-14} Bhn_a}{(1 + h/r_0)}, \tag{2}$$

where $E_i \approx 16\,\mathrm{eV}$ is the ionization potential for argon.

2.6. Discharge Power and Energy Price of Ions

Magnetic coupling of plasma turn with an antenna coil can be non-transformer. Time variation of plasma turn inductance gives its average resistance

$$R_L \cong \frac{\partial L}{\partial t} = \frac{\partial}{\partial t}\left[\frac{\pi\mu}{h}\left(r_0^2 - r^2\right)\right] \cong \pi\mu U \frac{r_0}{h}$$

where r is a radial coordinate. Resistance component corresponding to power loss W_i in ionization process can be written as

$$R_i = \frac{W_i}{I^2} = \frac{2I_i(16 + 2kT)(1 + h/r_0)}{I^2}$$

where I_i — ion current to a chamber face or to an emission electrode when ICP unit is used together with an ion extraction system. Resistance corresponding to current in a boundary skin sheath

$$R_c = \frac{\pi r_0}{h}\frac{1}{\sigma\delta_c}$$

Resistance of chamber face elements for current circuits was not taken into consideration. It is supposed that discharge area beside emission electrode (when it is present) is short-circuited by this electrode if it is made of electrically conducting material. Note that in the case of a half-sphere gas discharge chamber [10] radial power loss in the boundary skin sheath may be omitted.

Then total discharge power can be written as $W_\Sigma = I^2(R_L + R_i + R_c)$.

Let us denote discharge power divided by the internal surface of the discharge chamber as

$$q_\Sigma = \frac{W_\Sigma}{2\pi r_0^2(1 + h/r_0)} \tag{3}$$

and ion energy price Pr_i as

$$Pr_i = W_\Sigma/I_i \tag{4}$$

where ion current to the emission electrode can be found according to the D. Bohm's formula $I_i = 0.6\pi r_0^2 \cdot en_e(kT/m_i)^{1/2}$ where m_i is the mass of argon ion.

3. COMPARISON OF THEORETICAL RESULTS WITH EXPERIMENTAL DATA

The main ICP discharge parameters in dependence on argon plasma pressure were calculated for a cylindrical gas discharge chamber of 35 cm external diameter surrounded by a cylindrical antenna coil of the same internal diameter for two values of argon ion currents $I_i = 1$ and 5 A.

Dependence of optimal driving frequency on argon plasma pressure determined from formula (1) for both values of argon ion current is presented in Fig. 1.
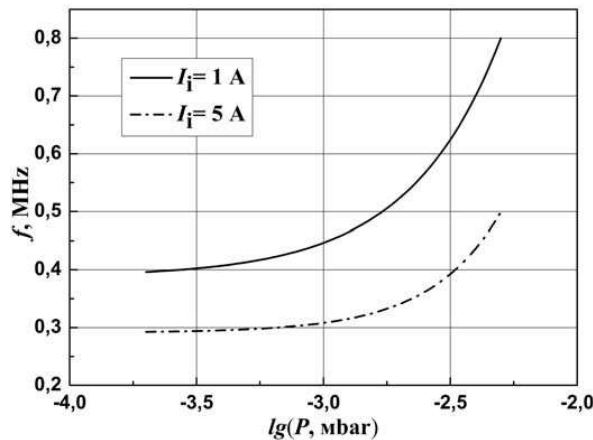

Figure 1: Calculated dependence of the ICP discharge optimal driving frequency on argon plasma pressure.
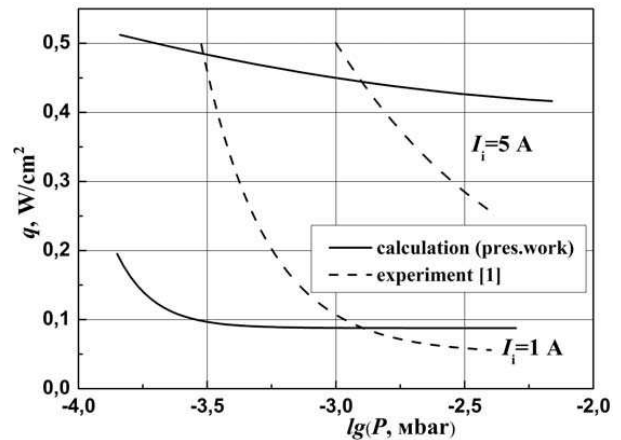
Figure 2: Calculated in the present work (solid lines) and experimental [1] (dashed lines) data on ICP discharge power vs argon plasma pressure.

It was found out that at the upper limit of the considered area of pressures optimal driving frequency for ion current $I_i = 1\,\text{A}$ came close to the experimental value $f \sim 0.75\,\text{MHz}$ [1].

ICP discharge power divided by the internal surface of the gas discharge chamber was calculated using formula (3). Results of these calculations are shown in Fig. 2.

Note that in these calculations the axial and diametral dimensions of the chamber were estimated to be both equal to $35\,\text{cm}$. Results of these calculations are compared here with experimental data [1]. General agreement of this information seems obvious. Note that the agreement can be better if experimental data [1] on plasma pressure could be considered as overvalued. Such peculiarity of the experiment [1] can be quite real because in this work plasma pressure was only estimated.

Energy price of argon ions calculated according to formula (4) is presented in Fig. 3.
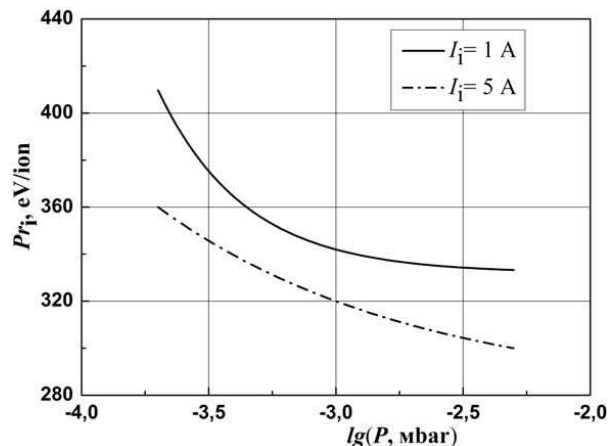
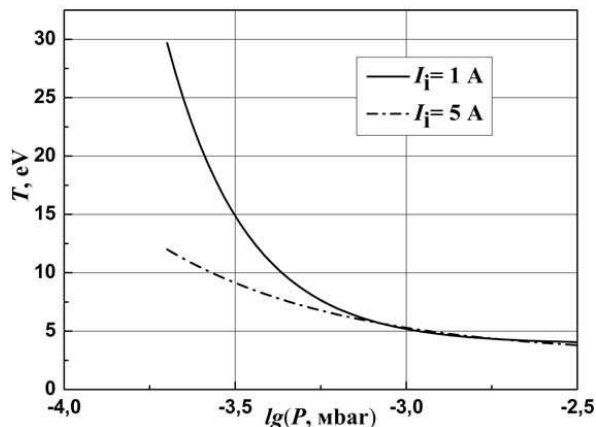Figure 3: Calculated values of energetic price of argon ions.

Figure 4: Calculation results for electron temperature of ICP discharge plasma.

Thus obtained results are close to the experimental value $Pr_i = 375\,\text{eV/ion}$ [1] for the gas discharge chamber of $35\,\text{cm}$ in external diameter.

Electron temperature calculation data obtained from the Equation (2) are shown in Fig. 4.

It can be seen here that in the case of ion current $I_i = 1\,\text{A}$ electron temperature of argon plasma reached rather high level of $T \sim 30\,\text{eV}$.

Comparison of the present theoretical results with the experiment [1] showed that the ICP discharge model proposed in the present work describes parameters of this discharge close to real life. Therefore it can be used rather confidently to predict properties of the inductive discharges.

4. CONCLUSIONS

- A new model of low pressure ICP discharge based on the concept of movable ionizing current layers has been proposed.
- It has been shown that magnetic coupling of an antenna coil with plasma turn does not always follow transformer logic.
- RF power of the ICP discharge, energy price of its argon ions, optimal driving frequency and electron temperature have been calculated for different argon pressures. Comparison with published experimental data showed that the model satisfactorily describes the main characteristics of an ICP discharge at the selected level of its operational parameters.

REFERENCES

1. Loeb, H. W., J. Freinsinger, and K. H. Groh, "Feasibility study of large-scale RF-ion thrusters," *Proc. of the 41st IAF Congress*, 231, Dresden, 1990.
2. Godyak, V. A., "Electrical and plasma parameters of ICP with high coupling efficiency," *Plasma Sources Sci. Technol.*, Vol. 20, No. 025004, 2011.
3. Liberman, M. A. and A. J. Lichtenberg, *Principles of Plasma Discharges and Materials Processing*, John Wiley & Sons, Inc., Hoboken, USA, 2005.
4. Godyak, V., R. Piejak, and B. Alexandrovich, "Electrical characteristics and electron heating mechanism of an inductively coupled argon discharge," *Plasma Sources Sci. Technol.*, Vol. 3, 169–176, 1994.
5. Charbet, P. and N. Braithwaite, *Physics of Radio-frequency Plasmas*, Cambridge University Press, 2011.
6. Gordeev, A. V., A. S. Kingsep, and L. I. Rudakov, "Electron magnetohydrodynamics," *Physics Reports*, Vol. 243, No. 5, 215–315, 1994.
7. Priest, E. R. and T. G. Forbes, *Magnetic Reconnection. MHD Theory and Applications*, Cambridge University Press, 2000.
8. Alven, H. and C. G. Falthammar, *Cosmical Electrodynamics*, Clarendon Press, Oxford, UK, 1963.
9. Priest, E. R., *Solar Magneto-hydrodynamics*, Kluwer Academic Publishers, 1982.
10. Leiter, H. J. and D. D. Feili, "RIT15S — A radio frequency ion engine for high specific impulse operation," *37th AIAA/ASME/SAE/ASEE Joint Propulsion Conference*, 2001, Doi: 10.2514/6.2001-3491.

Single Feed Dualband Miniaturized E-shaped/U-slot Patch Antenna

N. P. Yadav[1] and M. R. Tripathy[2]

[1]School of Electronic Engineering and Optoelectronic Technology
Nanjing University of Science and Technology, 210094, China
[2]Department of Electronics and Communication Engineering
Amity School of Engineering and Technology
Amity University Uttar Pradesh, Noida 201313, India

Abstract— This letter presents the design of dual band microstrip patch antenna. This antenna is with single layer E-shaped patch loaded by two U slots. The -10 dB return loss impedance bandwidths of 2.26% and 1.91% are realized at center frequencies of 10.94 GHz and 13.06 GHz with gains of 9.12 dBi and 8.54 dBi respectively. The radiation patterns are also presented. Compared with the published results of the similar scenario, in this design the size is reduced. The design guidelines are provided.

1. INTRODUCTION

During the recent years there has been rapid development in dual band microstrip antenna due to its wide applications in many communication systems. Dual band characteristics can be achieved with the same structure by exciting two different modes with suitable feed point [1], using stacked structures [2], loading reactive stub [3], slots [4], coplanar multi conductor structures [5] etc.. The broadband characteristic of a rectangular, circular and stacked U-shaped slot microstrip patch antenna has been reported [6–9], in which two different but close resonant frequencies in a single patch are combined to give a wideband operation. On the other hand, if the excited resonant frequencies are far apart, a dual-frequency operation can be achieved with the U-slot antenna [10–13]. A slot antenna has special advantage because of its simple structure, such as wider bandwidth, less conductor loss [15–17]. A probe feed microstrip antenna with an internal U-shaped slot having large impedance bandwidth with broadside radiation pattern are reported [18]. In this paper, the design of E-shaped/U-slots loaded rectangular patch antenna at single layer with co-axial feeding technique has been proposed. This antenna has improved the radiation efficiency and gain with reduced size which are the advantages over the earlier reported paper [14]. The working frequency bands are SAR (10.81 GHz–11.06 GHz), VSAT (12.92 GHz–13.17 GHz). From the simulation studies, it is found that the proposed antenna can achieve dual-band performance, high gains, reduction in the size and better band isolation. Details of the proposed antenna and its performance are given in next parts.

2. ANTENNA DESIGN AND THEORETICAL CONSIDERATION

2.1. E-shaped/U-slots Loaded Rectangular Patch Antenna

The proposed configuration of the antenna is shown in Fig. 1. In this letter a new type of two U-shaped slots loaded E-shaped, single layer rectangular patch antenna have been proposed for dualband applications. The dimensions of two U-slots and notches are chosen in such a way so that proposed antenna can exhibit dual frequency behavior with good matching condition.

The E-shaped is simpler in construction. The two parallel notches have the same length L_N and same width W_N. The separation [17, 18] of the two notches is W_S. There are thus only three parameters ($L_N W_N$, W_S) for the notches used here. Similarly the two symmetrically U-shape slots are simpler cut in same patch. The vertical slots length of first and second U-shape are L_1 and L_3, similarly horizontal slots length are L_2 and L_4 and width of both U-slots are W_1 and W_2. In this way the six parameters are included in two U-shapes, i.e., (L_1, L_2, L_3, L_4, W_1, and W_2).

A probe feed is located at the point $(-6.425, -0.475)$ for good excitation of the proposed antenna over a dualband. The current distributions of the proposed antenna in two difference frequency bands are given in Fig. 2.

Microstrip patch is considered as a parallel combination of capacitance (C_1), inductance (L_1) and resistance (R_1) as shown in Fig. 3.

The values of R_1, L_1, and C_1 can be given as [19].

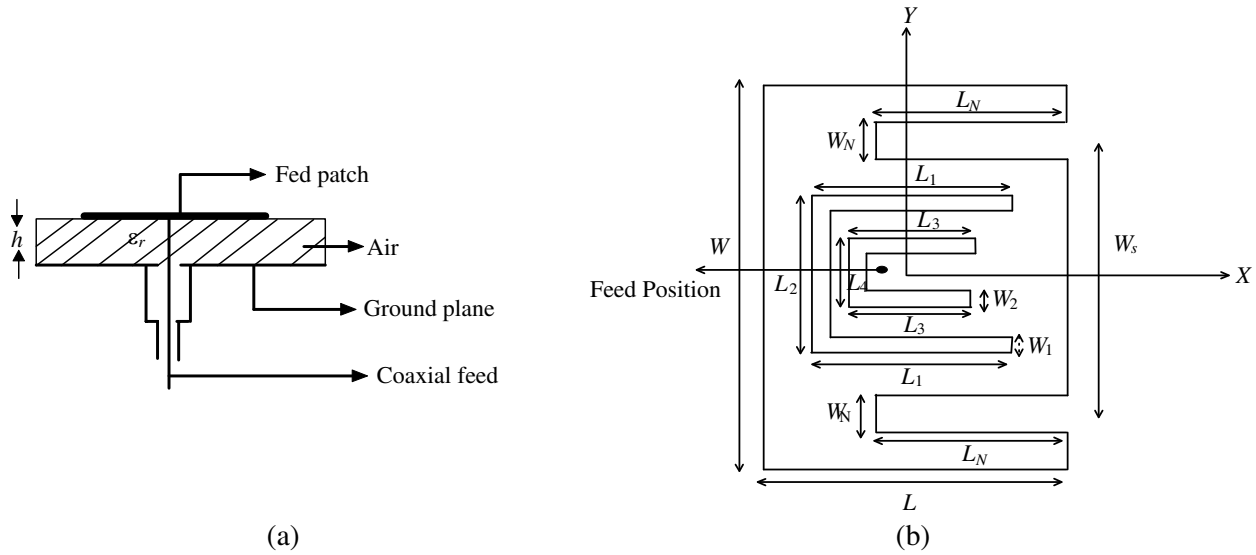$$Q_r = \frac{c\sqrt{\varepsilon_e}}{4fh}$$

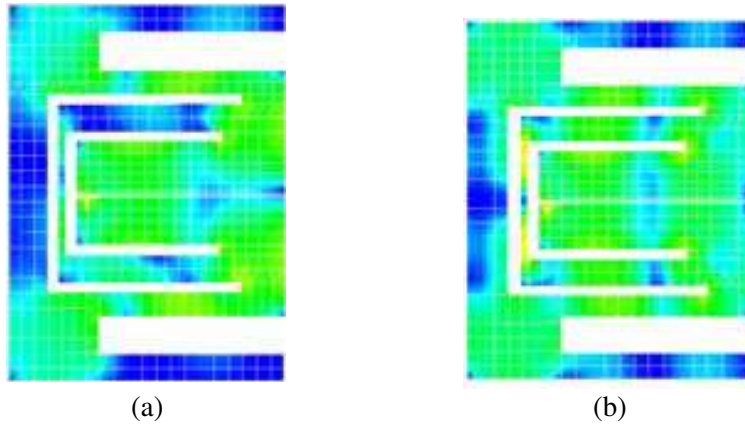Figure 1: (a) Top view and (b) side view geometry of the proposed antenna.

Figure 2: Current distribution at two difference resonance frequency. (a) Current distribution at 10.94 GHz. (b) Current distribution at 13.06 GHz.
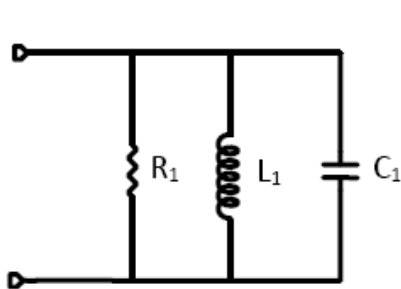

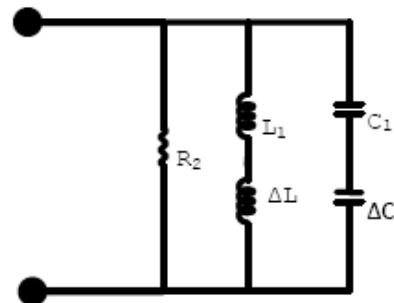Figure 3: Equivalent circuit of fed patch antenna.

Figure 4: Modified equivalent circuit due to symmetrically notch cut in fed rectangular patch.

where

c = velocity of light.

f = design frequency.

ε_e is effective permittivity of the medium which is given by [10].

$$\varepsilon_e = \frac{\varepsilon_r + 1}{2} + \frac{\varepsilon_r - 1}{2}\left(1 + \frac{10h}{W}\right)^{-1/2}$$

where, ε_r = relative permittivity of the substrate material.

Therefore, the impedance of the patch can be derived using Fig. 3.

$$Z_P = \frac{1}{\frac{1}{R_1} + \frac{1}{j\omega L_1} + j\omega C_1} \tag{1}$$

When two parallel notches are cut in the patch the current distribution are shown in Fig. 2 and the equivalent circuit of the initial patch is modified and can be given as shown in the Fig. 4.

The values of series inductance (ΔL) and series capacitance (ΔC) are calculated [20, 21]. After considering the coupling capacitance C_c the equivalent circuit of the proposed antenna is modified as shown in the Fig. 5. The value of coupling capacitance can be given as [22].

$$C_c = \frac{-(C_1 + C_T) + \sqrt{(C_1 + C_T)^2 - C_1 C_T (1 - 1/k_c^2)}}{2} \tag{2}$$

where $C_T = \frac{C_1 \Delta C}{C_1 + \Delta C}$ and $k_c = \frac{1}{\sqrt{Q_1 Q_2}}$ in which Q_1 and Q_2 are the quality factor of both the resonators.
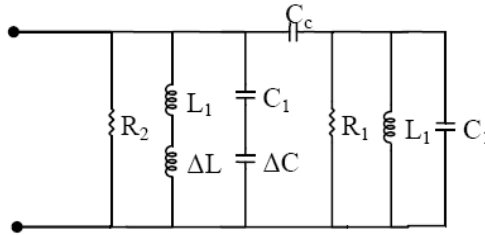

Figure 5: Equivalent circuit of symmetrically notch loaded single layer rectangular patch antenna.

The resonance resistance of the modified configuration of the rectangular patch can be calculated as [23]. Now using the equivalent circuit shown in Fig. 5 one can calculate the total input impedance of the notch loaded rectangular patch antenna as

$$Z_{NR} = \frac{Z_1 Z_2}{Z_1 + Z_2} \tag{3}$$

in which

$$Z_1 = \frac{1}{\frac{1}{R_1} + \frac{1}{j\omega L_1} + j\omega C_1} + \frac{1}{j\omega C_c}$$

and

$$Z_2 = \frac{1}{\frac{1}{R_2} + \frac{1}{j\omega L_T} + j\omega C_T}$$

in which $L_T = L_1 + \Delta L$ Slot in microstrip patch can be analyzed by using duality relationship between the dipole and the slot. In this paper the patch is fed by a coaxial feed $(50\,\Omega)$. The U-shape slot is considered as three slots, i.e., two parallel to x-axis and the third one perpendicular to the x-axis. The impedance of a single slot parallel to the x-axis is given as [20].

$$Z_s = R_r(kL_1) - j\left\{120\left(\log\left(\frac{L_1}{d}\right) - 1\right)\cot\frac{kL_1}{2} - X_A(kL_1)\right\} \tag{4}$$

where

$k = \frac{2\pi}{\lambda}$ (wave vector).

L_1 = length of the slot.

and $X_A(kL_1)$ is given as

$$X_A(kL_1) = 30 \left\{ \begin{array}{c} 2S_i(kL_1) + \cos(kL_1)[2S_i(kL_1) - S_i(2kL_1) - \sin(kL_1)] \\ \left[2C_i(kL_1) - C_i(2kL_1) - C_i\left(\frac{2kw_1^2}{L_1}\right)\right] \end{array} \right\}$$

where w_1 is the width of the slot and R_r is the radiation resistance and is given by

$$R_r = \frac{2W_T}{I_m^2} = \frac{-\eta_0}{2\pi} \int_0^{2\pi} \frac{\cos\frac{k^2\cos\theta}{2} - \cos\frac{kL_1}{2}}{\sin\theta} d\theta \tag{5}$$

here $\eta_0 = 120\pi$ (characteristic impedance of free space).

W_T = total radiated power.

I_m = maximum current in the slot.

Radiation resistance R_r is calculated as

$$R_r = 60 \left\{ \begin{array}{c} C + \ln(kL_1) - C_i(kL_1) + \frac{1}{2}\sin(kL_1)[S_i(2kL_1) - 2S_i(kL_1)] \\ +\frac{1}{2}\cos(kL_1)\left[C + \ln\left(\frac{kL_1}{2}\right) + C_i(2kL_1) - 2C_i(kL_1)\right] \end{array} \right\} \tag{6}$$

where C (Euler's constant) $= 0.5772$.

and $S_i(kL_1)$ and $C_i(kL_1)$ are the sine and cosine integral and given as

$$S_i(x) = \int_0^x \frac{\sin(x)}{x} dx$$

and $C_i(x) = -\int_x^\infty \frac{\sin(x)}{x} dx$.

Now the impedance of slot perpendicular to the x-axis is given as

$$Z_{sp} = -j\left[120\left(\ln\frac{L_3}{w_1} - 1\right)\cot\left(\frac{kL_3}{2}\right)\right]$$

L_3 = length of the slot along y-axis.

The equivalent circuit of the proposed antenna can be given as shown in Fig. 6(a) in which Z_{U1} is the impedance due to two U-slot vertical lengths and Z_{U2} is the impedance due to base length of the U-slot, Z'_{U1} and Z'_{U2} is the same for other U-slot patch antenna. And Z_{NR} is the impedance of notch loaded rectangular patch.
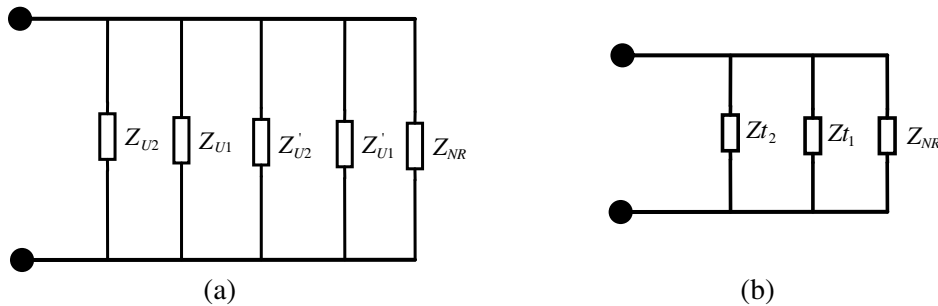

Figure 6: (a) Equivalent circuit of the proposed antenna. (b) Its modified circuit.

Now the total input impedance of double-U slot loaded parallel notch cut rectangular patch antenna can be calculated from Fig. 6(b) as

$$Z_T = \frac{Z_{t1}Z_{t2}Z_{NR}}{Z_{NR}Z_{t2} + Z_{NR}Z_{t1} + Z_{t1}Z_{t2} + Z_{NR}} \tag{7}$$

where

$$Z_{t1} = \frac{Z_{U2}Z_{U1}}{Z_{U2} + Z_{U1}}$$

$$Z_{t2} = \frac{Z'_{U2}Z'_{U1}}{Z'_{U2} + Z'_{U1}}$$

and Z_{NR} which is given by above equation Using this equation one can calculate the various antenna parameters for proposed antenna.

$$\Gamma = \frac{Z_0 - Z_T}{Z_0 + Z_T} \tag{8}$$

Table 1:

Frequency	10.0–14.0 GHz
W	40.0 mm
L	30.0 mm
L_N	20.0 mm
W_N	4.0 mm
L_1	20.0 mm
L_2	20.0 mm
L_3	16.0 mm
L_4	13.0 mm
W_1	1.0 mm
W_2	1.0 mm
Dielectric (ε_r)	22 (0.127 mm)
Thickness (h) air	1.0 mm
Feed Location (X_0, Y_0)	$(-6.425, -0.475)$

3. RESULTS AND DISCUSSION

Simulation results were carried out to demonstrate the performance of the proposed antenna.

From Fig. 7, it is seen the return loss versus frequency that, the return loss of the first band designed microstrip patch antenna is -21.98 dB at the frequency of 10.94 GHz with a frequency band 10.81 GHz to 11.06 GHz, similarly the second band is obtained at return loss -27.50 dB at the frequency of 13.06 GHz with a frequency band 12.92 GHz to 13.17 GHz. This shows that it is very useful for the radar communication.

The simulated E and H plane cross and Co-polarization radiation patterns of the proposed antenna at 10.94 GHz (lower resonance frequency) and 13.06 GHz (Upper resonance frequency) are shown in Figs. 8–9. It can be seen that, there is small deviation in maximum power in case of upper resonance frequency in comparison to lower resonance frequency. The simulated peak gains
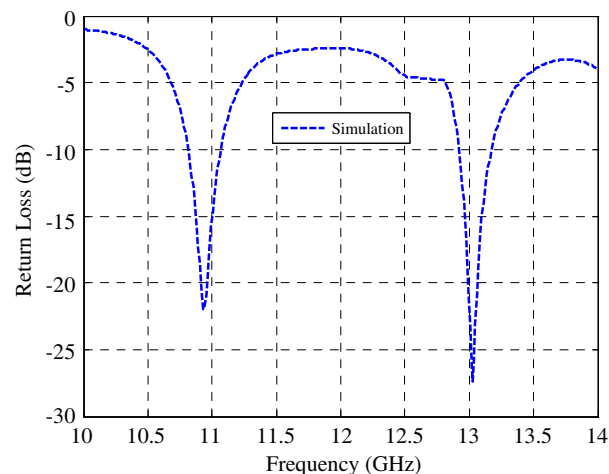

Figure 7: Comparative plot between return loss and frequency of the proposed antenna.
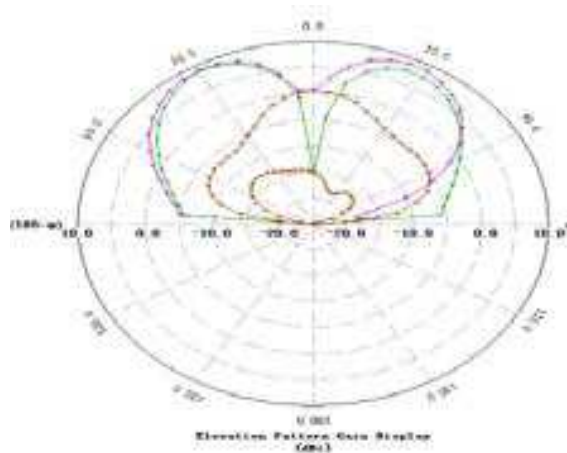

Figure 8: Simulated radiation patterns both E and H plane in cross and co-polarization of dualband antenna at 10.94 GHz resonance frequency.
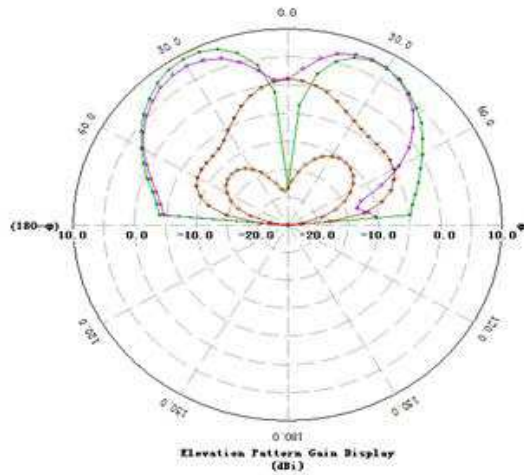
Figure 9: Simulated radiation patterns both E and H plane in cross and co-polarization of the dualband antenna at 13.06 GHz resonance frequency.
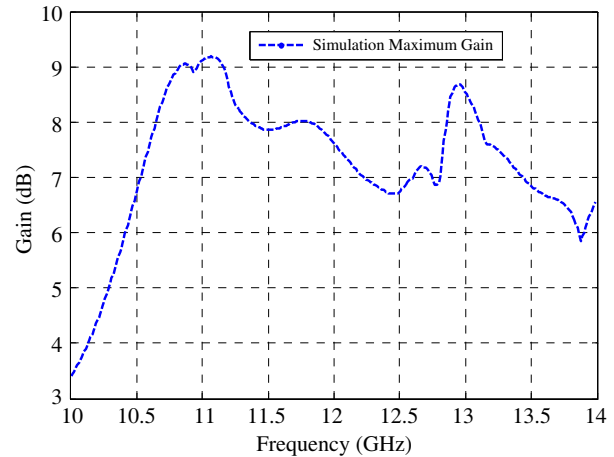
Figure 10: Gain versus frequency of the proposed antenna.

of the antenna are 9.12 dBi and 8.54 dBi shown in Fig. 10. The above study shows the influence of size and shape of notches, slots and thickness of substrate on the impedance bandwidth.

4. CONCLUSION

This proposed method for the design of dual-band patch antenna results in a structure which is simpler and easier to fabricate than the structures described before. The presented design demonstrates the use of U-slots and E-shaped patch to get the dualband operation of rectangular patch antenna. This modified rectangular patch antenna can be used for radar applications. It fulfills the demands of applications such SAR and VSAT Antenna provides impedance bandwidth of 2.26%, 1.91% at two different application bands. The peak gains are 912 dBi, and 8.54 dBi respectively.

REFERENCES

1. Richards, W. F., S. E. Davidson, and S. A. Long, "Dualband reactively loaded microstrip patch antenna," *IEEE Transaction on Antennas and Propagation*, Vol. 33, 556–561, May 1985.
2. Ansari, J. A., P. Singh, S. K. Dubey, R. U. Khan, and B. R. Vishvakarma, "H-shaped stacked patch antenna for dual band operation," *Progress In Electromagnetic Research B*, Vol. 5, 291–302, 2008.
3. Division, S. A., S. A. Long, and W. F. Richards, "Dual band microstrip antennas with monolithic reactive loading," *Electronic Lett.*, Vol. 21, 936–937, Sep. 1985.
4. Wang, E., J. Zheng, and Y. Liu, "A novel dual-band patch antenna for WLAN communication," *Progress In Electromagnetic Research C*, Vol. 6, 93–102, 2009.
5. Mishra, A., P. Singh, N. P. Yadav, J. A. Ansari, and B. R. Vishvakarama, "Compact shorted microstrip patch antenna for dual band operation," *Progress In Electromagnetic Research C*, Vol. 9, 171–182, 2009.
6. Esfahlani, S. H. S., A. Tavakoli, and P. Dehkhoda, "A compact single-layer dual-band microstrip antenna for satellite applications," *IEEE Antennas and Wireless Propagation Letters*, Vol. 10, 931–934, 2011.
7. Mok, W. C., S. H. Wong, K. M. Luk, and K. F. Lee, "Single Layer single patch dual band and triple band patch antennas," *IEEE Transaction on Antennas and Propagation*, Vol. 61, No. 8, 4341–4344, Aug. 2013.
8. Hsu, C. K. and S. J. Chung, "Compact antenna with U-shaped open-end shaped open-end slot structure for multi-band Handset application," *IEEE Transaction on Antennas and Propagation*, Vol. 62, No. 2, 929–932, Feb. 2014.
9. Osman, H. A., E. A. Abdallah, and A. A. Abdel-Rahim, "A novel broadband compact circular disk microstrip antenna for wireless application," *PIERS Online*, Vol. 4, No. 7, 761–766, 2008.

10. Ansari, J. A. and R. B. Ram, "Broadband stacked U-slot microstrip patch antenna," *Progress In Electromagnetics Research Letters*, Vol. 4, 17–24, 2008.
11. Ansari, J. A., S. K. Dubey, P. Singh, R. U. Khan, and B. R. Vishvakarama, "Analysis of U-slot loaded patch antenna for dualband operation," *Int. J. Microwave and Opt. Techno.*, Vol. 3, 80–84, 2008.
12. Bhalla, R. and L. Shafai, "Resonance behaviour of single U-slot and double U-slot antenna," *Microwave and Opt. Techno. Lett.*, Vol. 32, 332–335, 2002.
13. Guo, Y. X., K. F. Lee, and K. M. A. Luk, "Dualband patch antenna with two U-shaped slot," *Microwave and Opt. Techno. Lett.*, Vol. 26, 73–75, Jul. 2000.
14. Meng, F. and S. K. Sharma, "A single feed dual-band (2.4 GHz/5.8 GHz) miniaturized patch antenna for wireless local area network (WLAN) communications," *IEEE URSI GASS*, 978-1-4673-5225-3, 2014.
15. Ysai, S. N., H. H. Hsin, H. K. Dia, and K. T. Cheng, "Arcuate slot antenna," Assembly US Patent, No. 6373443, 2002.
16. Axelrod, A., M. Kisliuk, and J. Maoz, "Broadband microstrip fed slot radiator," *Microwave Journal*, Vol. 32, 81–84, 1989.
17. Yang, F., X.-X. Zhang, X. Ye, and Y. Rahmat-Sammi, "Wide-band E-shaped patch antennas for wireless communication," *IEEE Transactions on Antennas and Propagation*, Vol. 49, No. 7, 1094–1100, Jul. 2001.
18. Ang, B.-K. and B.-K. Chung, "A wideband E-shaped microstrip patch antennas for 5–6 GHz wireless communications," *Progress In Electromagnetic Research*, Vol. 75, 397–407, 2007.
19. Bahal, I. J. and P. Bhartia, *Microstrip Antennas*, Artech House, Boston, MA, 1985.
20. Zhang, X. X. and F. Yang, "Study of a slit cut on a microstrip antenna and its applications," *Microwave and Opt. Techno. Lett.*, Vol. 18, 297–300, 1998.
21. Bahal, I. J., *Lumped Elements for RF and Microwave Circuits*, Artech House, Boston, 2003.
22. Terman, F. E., *Electronic and Radio Engineering*, 15–73, Kogakusha, Tokyo, 1955.
23. Balanis, C. A., *Antenna Theory Analysis and Design*, 728–746, 2nd Edition, Wiely, New York, 1997.

Simulation and Study of the Effects of EM Radiations on Cantilever Beams with RF Functionality

Kshitij Chopra, **Preeti Singh**, **Kritika Nigam**, **Malay Ranjan Tripathy**, **and Sujata Pandey**

Department of Electronics and Communication, Amity School of Engineering and Technology
Amity University, Uttar Pradesh, Noida, India

Abstract— The RF functionality in wireless devices is mostly achieved through RF MEMS. These are microelectromechanical systems having resonators that employ cantilever beams to produce radio waves. Our recent work has been in the field of energy scavenging from resonators in RF MEMS through the use of piezoelectric ceramics in cantilevers. In this paper we investigate the role of radiation in functioning of piezoelectric cantilevers and feasibility of the device to produce RF functionality. Weak terahertz electromagnetic radiations are used to irradiate the piezoelectric cantilever.

1. INTRODUCTION

Wireless technology is an indispensable part of modern lifestyle. The exponential increase in the use of wireless transmission in varied forms of gadgetry has posed a grave interest in RF functionality producing circuits and systems [1]. The most prominent and promising solution the wireless transmission and microwaves technology have been through RF MEMS since it produces radio-frequency through resonating cantilevers [2–4].

RF MEMS are Microelectromechanical devices that produce radio waves for wireless transmission and other applications and are quintessential in modern circuitry for providing RF functionality. The MEMS devices are fabricated using SiO_2 and Si_3N_4 along with other insulators. The electrostatic charging in these materials poses a challenge to reliability and performance of MEMS devices [5–8]. Also, the irradiation due to Electromagnetic waves contributes significantly to this phenomenon.

The semiconductor when subjected to irradiations produces electrostatic charge that may get absorbed and hence produce a charging in the device that can alter the dynamic behavior of the device. This effect is profound when the devices are exposed to ionizing radiations.

This paper is a study of the behavior of the cantilever beams under the influence of Electromagnetic Radiation and its effect on the working and efficiency of RF MEMS especially for medical devices where RF MEMS components are used. Also, the sensitivity of RF MEMS devices towards electromagnetic irradiation is studied. Varied irradiations were studied and their effects on the materials were recorded through simulations using multiphysics simulation software. The piezoelectric materials chosen are quartz, Zinc Oxide and Aluminum Nitride. The effect of EM radiations on these structures was observed in terms of increase in leakage current.

2. STUDY DESIGN

MEMS devices that operate on electrostatic principles are sensitive to charge re-distribution in the piezoelectric layer when exposed to EM radiations.

Figure 1 shows a typically clamped resonator generally used RFICs. Figure 2 is the part of resonator which is in the shape of cantilever and was tested for the variation in charge accumulation in the dielectric layer. Different piezoelectric materials like Quartz, Zinc Oxide and Aluminum Nitride were used for testing the structure. The dimensions of the beam were taken to be $40.8\,\mu\text{m} \times 8\,\mu\text{m} \times 1\,\mu\text{m}$.

The characteristics of piezoelectric materials is characterized by the following equations and discussed elsewhere [9]. The frequency of the piezoelectric is given by:

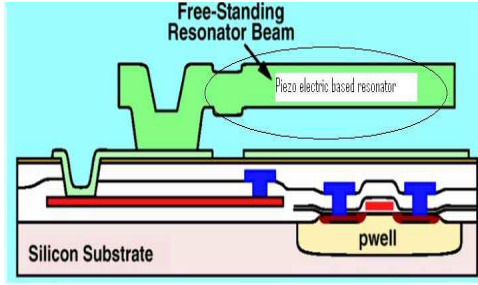$$f = \frac{v_n^2}{2\pi}\sqrt{\frac{0.236 D_{pw}}{\left(l - l_m\right)^3 \left(m_c - m_p\right)}} \tag{1}$$

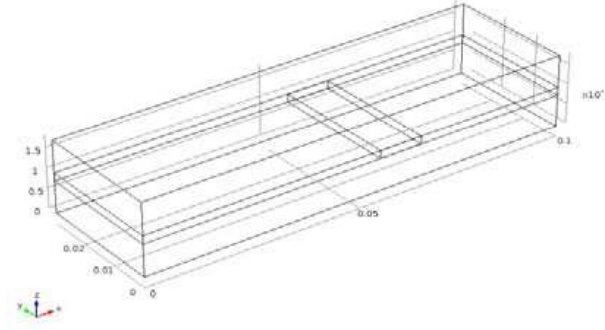Figure 1. Piezoelectric ceramic based resonator used in RFIC.

Figure 2. Test structure.

where, $v_n = 1.87$

$$m = \rho_p t_p + t_s \rho_s \tag{2}$$

$$m_c = 0.236 m w \left(l - l_m\right) + m w \frac{l_m}{2} \tag{3}$$

$$D_p = \frac{\left(E_p^2 t_p^4 + E_x^2 t_x^4 + 2 E_p E_x t_p t_x \left(2 t_p^2 + 2 t_x^2 + 3 t_p t_x\right)\right)}{12(E_p t_p + E_x t_x)} \tag{4}$$

The energy of the piezoelectric is given by:

$$q = \frac{-3 d_{31} s_s s_p t_s (t_s + t_p) l^2 F}{B} \tag{5}$$

where,

$$s_s = \frac{1}{E_s}, \quad s_p = \frac{1}{E_p}, \quad s_h = s_s t_p + s_p t_s \tag{6}$$

$$B = s_s^2 t_p^4 + 4 s_s s_p t_s t_p^3 + 6 s_s s_p t_s^2 t_p^2 + 4 s_s s_p t_p t_s^3 + s_p t_s^4 \tag{7}$$

The voltage generated by the piezoelectric is given by:

$$V = \frac{-3 d_{31} s_s s_p t_s t_p (t_s + t_p) l F}{\epsilon_{33}^T w B \left(1 + \left(\frac{3 s_p^2 s_s t_p t_s^2 (t_p + t_s)^2}{s_h B} - 1\right) K_{31}^2\right)} \tag{8}$$

where E_p Young's modulus of piezoelectric material is, E_s is Young's modulus of substrate, l_m is length of proof mass, $l = l_b$ is length of the beam, $w = w_b = w_m$ is the width of beam, t_p is the thickness of piezoelectric material, t_s is thickness of substrate, m_p is proof mass, ρ_p is the density of piezoelectric material, ρ_s is density of substrate material, ϵ_{33}^T is permittivity in the direction of the applied electric field, d_{31} is the piezoelectric constant and $K_{31} =$ coupling factor for longitudinal oscillation.

3. RESULTS AND DISCUSSIONS

Energetic particles and photons cause damage by transferring energy to the materials they penetrate. The energy loss mechanisms are complex, but the type of damage can be classified in two consequences: a) atomic displacement (i.e., moving atoms due to the collisions) and b) ionization (i.e., creating electron-hole pairs).

Figures 3(a) and (b) show voltage distribution and displacement produced across the whole test structure.

Table 1 shows the dielectric constant chosen for different piezoelectric materials in the analysis.

Figures 4(a)–(c) show the charge distribution and electric field variation in the test structure with ZnO as piezoelectric material and with radiations between 1.50–240 THz range.

(a)   (b)
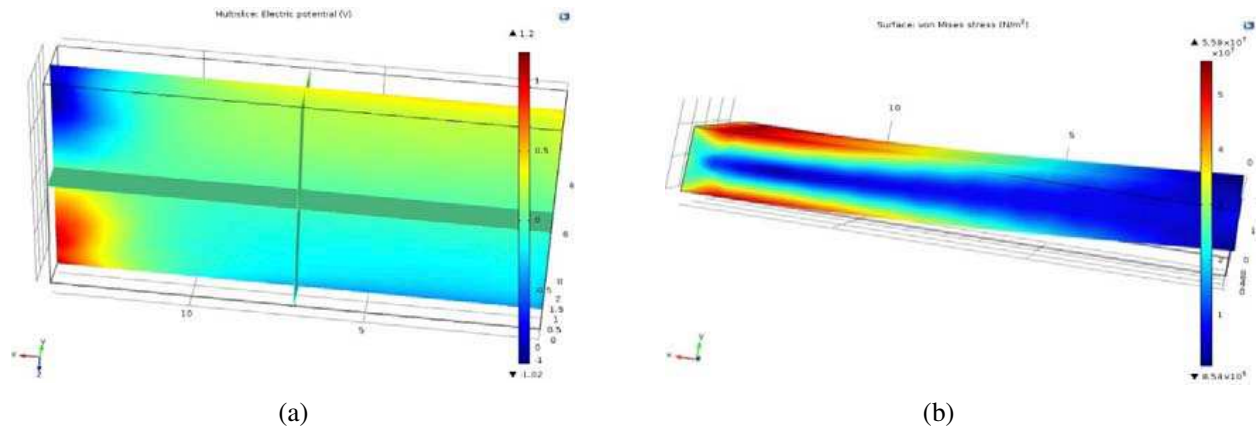
Figure 3. (a) Voltage distribution across the whole structure. (b) Displacement.

Table 1.

Piezoelectric material	Dielectric constant
Quartz	5
ZnO	10.8
AlN	9.14

(a)

(b)   (c)

Figure 4. (a) Charge distribution inside the ZnO based test structure. (b) Variation of charge concentration inside the structure. (c) Electric field variation inside the structure.

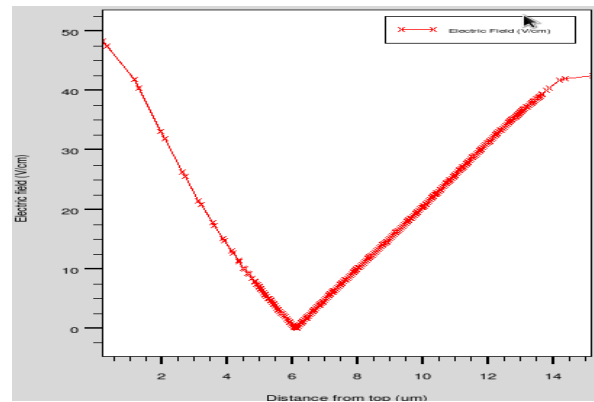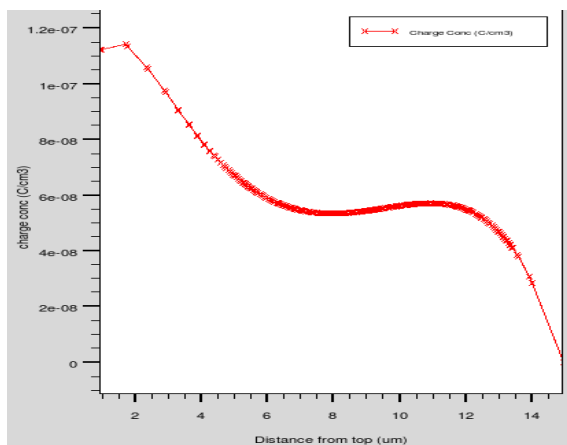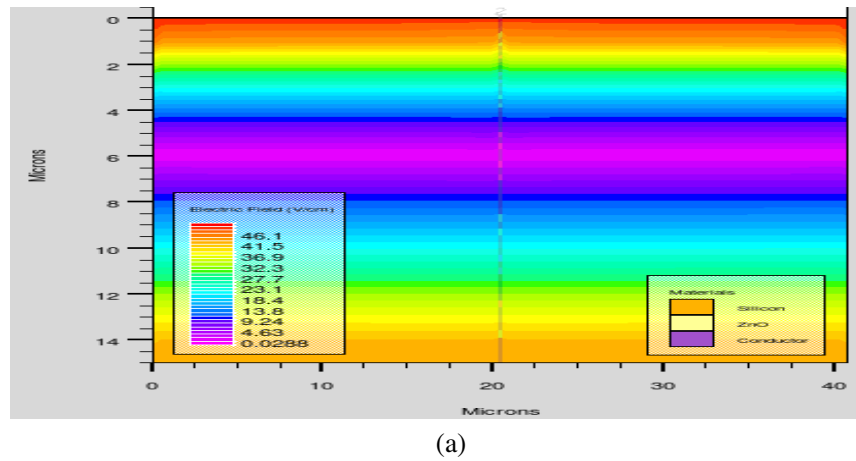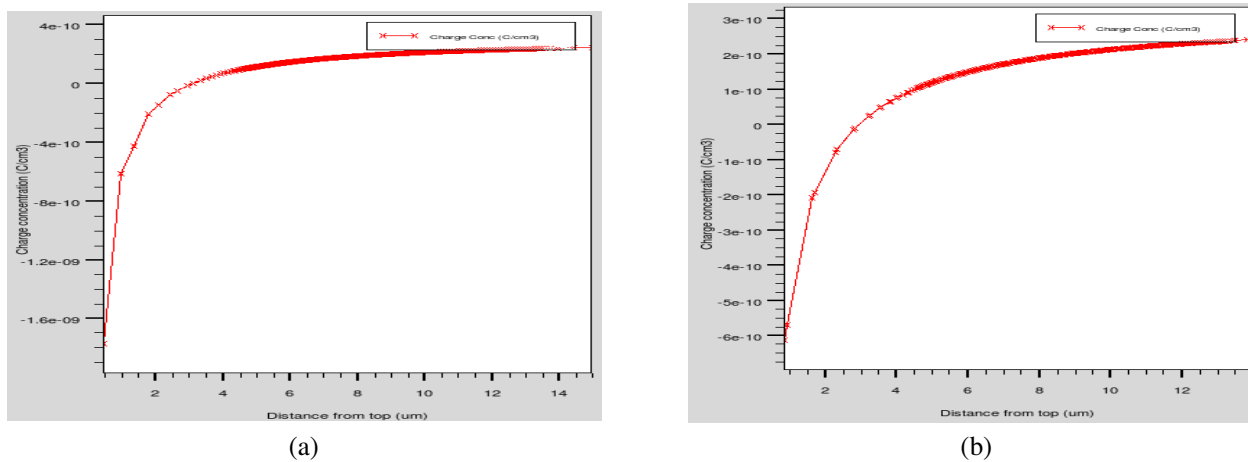Figure 5. (a) Charge concentration with strain and radiation simultaneously (ZnO). (b) Charge concentration with strain and radiation simultaneously (AlN).
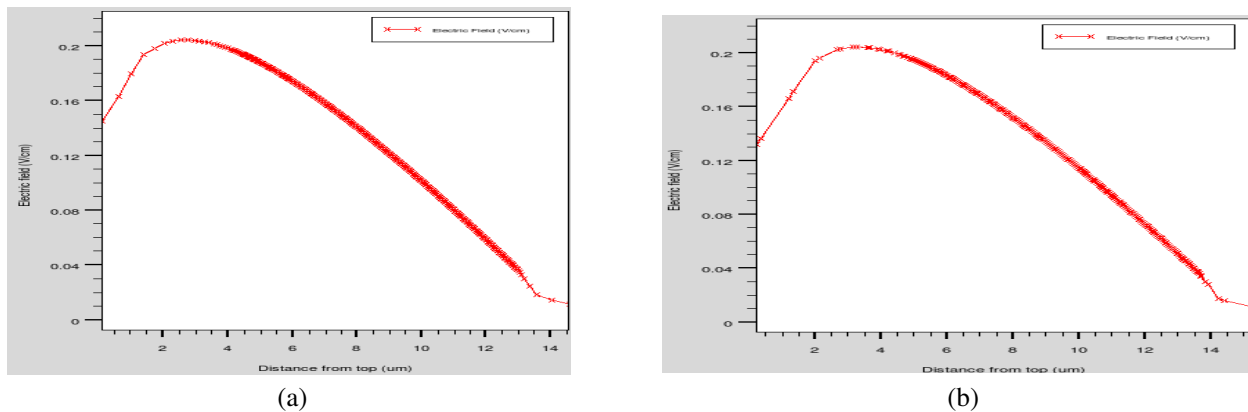

Figure 6. (a) Electric field with strain and radiation simultaneously (ZnO). (b) Electric field with strain and radiation simultaneously (AlN).

In the next simulation cycle the test structure strain as well as radiation was applied. The results obtained for charge concentration are shown in Figure 5.

Figure 6 shows the variation in electric field when strain and radiation both are applied.

Higher electric field was observed with ZnO followed by AlN and Quartz. It was observed that the behavior of the RF MEMS devices changes drastically with the change in type of different piezoelectric materials used. In the present case Zinc Oxide, Aluminum Nitride (AlN) and Quartz was used. Photon with sufficient energy can give rise to losses. It can be concluded that electric field rises because of radiation exposure. This is due to increase in charge concentration/trapping inside insulator as number of electron hole pairs are created because of non-ionizing radiation loss or displacement damage.

4. CONCLUSIONS

The paper investigates the role of radiation in functioning of piezoelectric cantilever and feasibility of the device to produce RF MEMS functionality. It was observed that behavior of piezoelectric materials changes drastically when exposed to radiations. Weak THz electromagnetic radiation is used to irradiate the piezoelectric cantilever made up of ZnO, AlN and Quartz. It was observed that electric field inside the piezoelectric material increases on radiation exposure which may affect the voltage produced when used for energy harvesting purpose.

REFERENCES

1. Santos, H. J. D. L., *RF MEMS Circuit Design for Wireless Communications*, Artech House, Micro Electro Mechanical System Library, 2002.
2. Rebeiz, G. M., *RF MEMS Theory, Design, and Technology*, Wiley, 2003.

3. Arevalo, A. and I. G. Foulds, "Parametric study of polyimide-lead zirconate titanate thin film cantilevers for transducers applications," *Proceedings of 2013 COMSOL Conference in Rotterdam*, 2013.

4. He, C., M. E. Kiziroglou, D. C. Yates, and E. M. Yeatman, "A MEMS self powered sensor and RF transmission platform for WSN nodes," *IEEE Sensors Journal*, Vol. 12, 3437–3445, 2011.

5. Jeon, Y. B., R. Sood, J.-H. Jeong, and S.-G. Kim, "MEMS poer generator with traverse mode thin film PZT," *Sensors and Actuators A*, Vol. 122, No. 1, 16–22, 2005.

6. Naduvinamani, S. N., B. G. Paramatti, and S. V. Kalalbandi, "Simulation of cantilever based RF-MEMS switch using coventware," *World Journal of Science and Technology*, Vol. 1, No. 8, 149–153, 2011.

7. Huang, Y., "Energy harvesting using RF MEMS," *2010 Proceedings 60th Electronic Components and Technology Conference (ECTC)*, 1353–1358, Jun. 1, 2010.

8. Contreras, A., et al., "A Ku-band RF MEMS frequency reconfigurable multimodal band pass filter," *International Journal of Microwave and Wireless Technology*, Vol. 6, No. 3/40, 277–285, Cambridge Press, 2014.

9. Chopra, K., K. Nigam, and S. Pandey, "A method for harvesting energy using piezoelectric transducers," *Applied Mechnics and Materials*, Vol. 727–728, 607–611, 2015.

Performances Evaluation of a Magnetic Gear with High Transmission Ratio Used for High Speed Applications

D. Fodorean[1], C. Irimia[2], and P. Minciunescu[3]

[1]Technical University of Cluj-Napoca, Romania
[2]Siemens Industry Software, Romania
[3]ICPE SA, Romania

Abstract— The paper presents a study of a magnetic gear (MG) used for high speed applications (26000 r/min); its performances are numerically evaluated. Against common mechanical gears, for which the high trasmission ratio at high power is obtained only by linking several gears, the MG offers a better power density since just one unit can be used (even for high powers), and with acceptable levels of ripples in the torque wave. The paper investigates also the use of different magnet materials, other than the very expesive rear-earth ones, to evaluate the MG's performances. It is clear that the main loss source on a MG is the iron loss component, which is affecting directly its efficiency. Thus, the use a different core meterials will be considered for a final evaluation of the MG's operation to decide on the obtained performances: power density and efficiency.

1. INTRODUCTION

The advantages of the magnetic gear (MG) are clear: there is no need for lubrication, no local heat (and losses) due to teeth contact and no risk for teeth breaking [1–3]. Moreover, a MG offers a higher range of use since for high transmission ratio there is no need to link 2, 3 or more gears together; thus, globally, the efficiency and power density are improved. Besides, with a specific configuration of the MG is possible to obtain smooth mechanical characteristics — i.e., torque and speed.

The attention of the designer, when dealing with a MG, is focused on the used materials, especially the permanent magnets and the active steel. Here, several rear-earth and non-rear-earth materials will be evaluated for the excitation of the MG, as well as different steel materials and sheets thickness. The parralle magnetization variant will be considered, since the radial one is not appropriated for the studied topoloy. To be more specific, the goal of the paper is to evaluate the performances of a high transmission-ration magnetic gear when using Nd-Fe-B, Alnico and Ferite for the magnets, M400, M330 and Vacoflux48 materials for the iron core, with different widths of the sheets (0.5 mm 0.35 mm, 0.2 mm) and parallel magnetization for the magnets. The performances will be evaluated in terms of power density and losses. Regarding this last parameter, it is clear that the main loss component is in the active iron, but for high speed applications the mechanical loss component cannot be neglected [4, 5]. All these elements will be investigated, as well as the torque wave characteristic, which should be as smooth as possible. Thus, we will have an overall picture of the efficiency and performances of the proposed high transmission ratio MG, used for high speed applications.

2. THE MAIN DATA OF THE APPLICATION AND THE TOPOLOGY OF THE MG

The popsed *high speed and high transmission ratio magnetic gear* (HS-HTR-MG) has a common topology: the inner high-speed rotor is with reduced number of pair o poles (1), equipped with inset permanent magnets — to avoid the increase of the inner air-gap, we do not considered a surface mounted solution, with retaining ring; instead, careful attention should be paid to the mechanical resistance of the steel, due to high centrifucal forces. Next, the middle part of the MG is composed by 17 fixed-teeth made of magnetic steel, alternating with empty space (air). Finally, the outer and low speed rotor, is containing 16 pair of poles and is equiped with surface mounted magnets. The cross section of the studied HS-HTR-MG is given in Figure 1.

The main data of the application under study are: 25 kW for the output power, input speed is 26'000 r/min and the output speed is 1625 r/min, meaning that the transmission ratio is 1/16.

The magnetic characteristics of the used steel material, considered for the performances comparison are given in Figure 2.
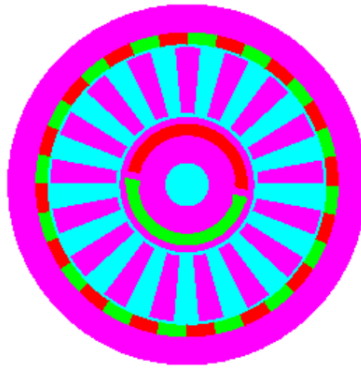
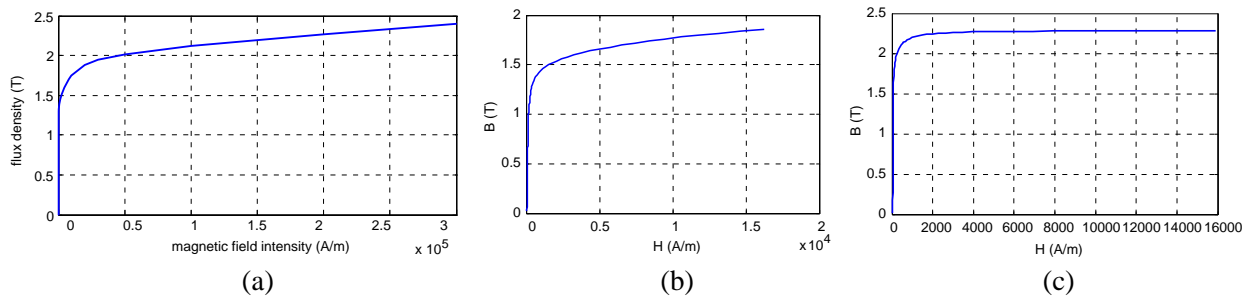Figure 1: The cross section of the studied HS-HTR-MG.

Figure 2: Magnetic characteristics of the used steel: (a) M400-50A; (b) M335-35A; (c) Vacoflux48.

3. THE NUMERICAL ANALYSIS AND THE PERFORMANCES OF THE STUDIED MG

For the simulation results, the *Flux2D* software has been used, since it permits to use two different speeds for two different rotating parts. The geometry, the materials associations and the transitory regime conditions have been considered for the studied MG. The results for when using M400-50A steel (0.5 mm sheet) and Nd-Fe-B magnet material and parallel magnetization are presented in Figure 3–6. In Figure 3, the iron saturation within the active parts of the MG is presented. It is depicted that some parts of the static and rotating parts are saturated. This iron saturation produces iron losses. While the input torque and power (and speed, at 26000 r/min) are applied at the inner-rotor, Figure 4, the MG produces the output power and torque, Figure 5. Very smooth mechanical characteristics (torque wave) is obtained for constant speed operation. The main losses component of the MG, represented by the iron losses in the static and rotating parts, is shown in Figure 6.

Similar simulation results have been obtained from the following cases: while the magnets were of Alnico material, or Ferrite, while the used iron is of M330 steel (0.35 mm sheets) or Vacoflux48 (0.2 mm sheet). The characteristics of the used materials are presented in Table 1 and the performances' comparison is given in Table 2. The simulated iron losses results, for the MG with Vacoflux48 steel, and the same Nd-Fe-B for the magnets, are presented in Figure 7 — a very
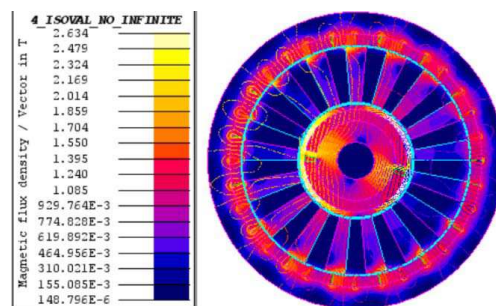
Figure 3: The field and flux density distribution in the active parts of the MG.
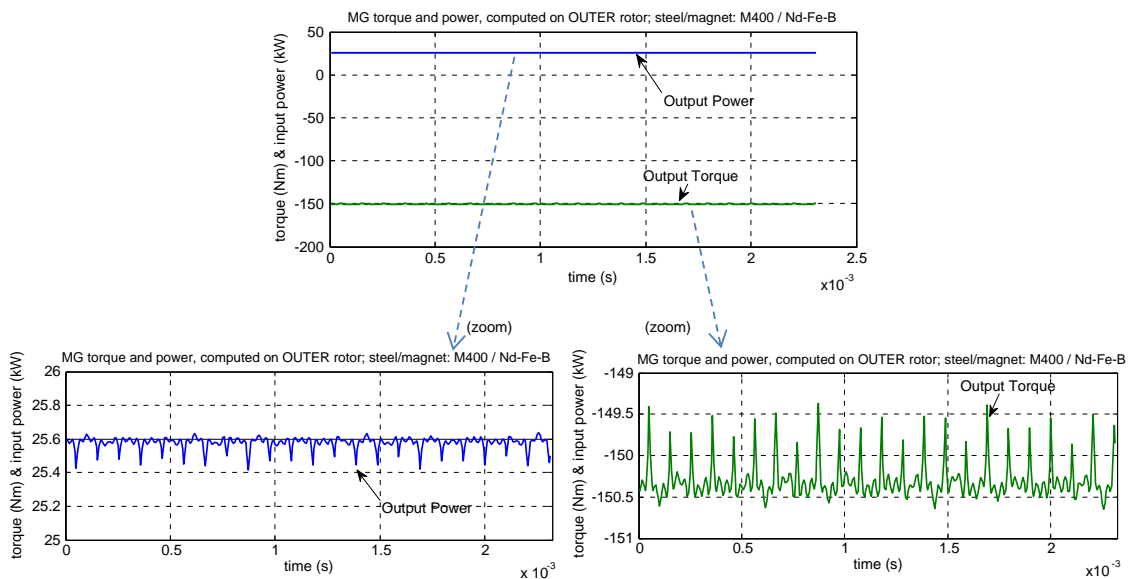
Figure 4: Simulated results for the MG with M400 steel and Nd-Fe-B magnet: input torque and power.
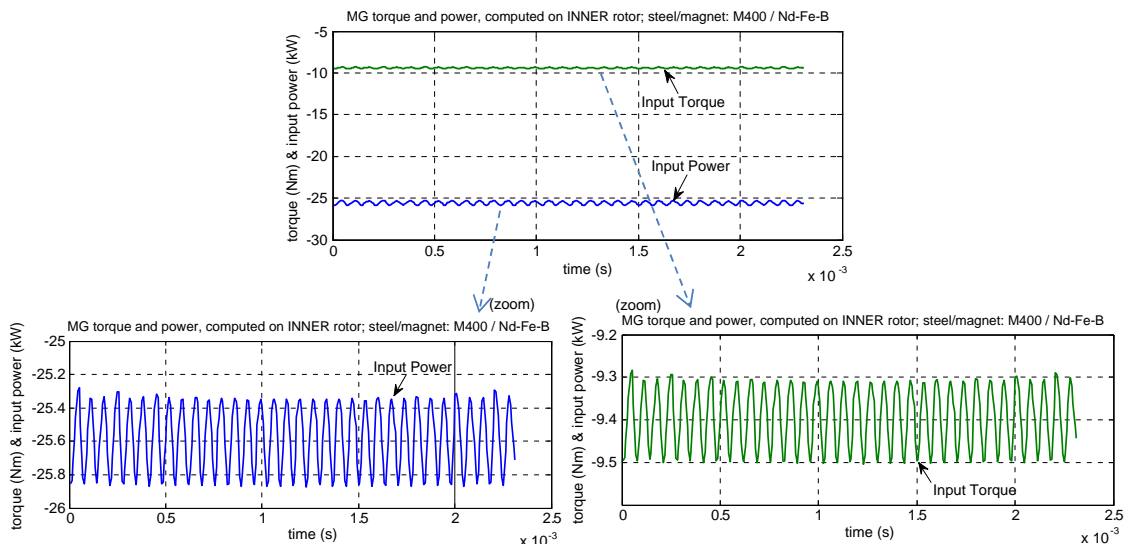
Figure 5: Simulated results for the MG with M400 steel and Nd-Fe-B magnet: output torque and power.
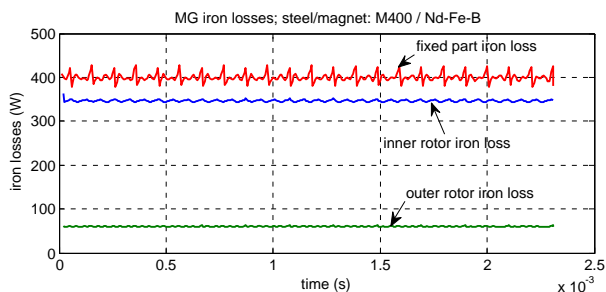
Figure 6: Simulated results for the MG with M400 steel and Nd-Fe-B magnet: iron losses in the active parts.
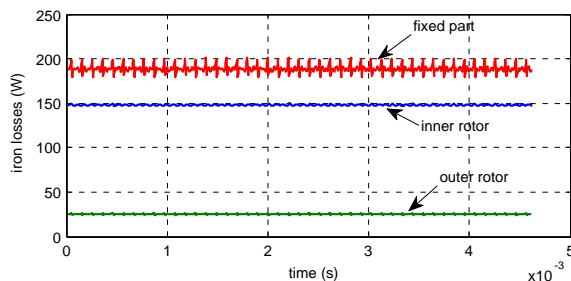
Figure 7: Simulated results for the MG with Vacoflux48 steel and Nd-Fe-B magnets: iron losses in the MG's active parts.

reduced iron loss level can be noticed.

Regarding the Ferrite and Alnico magnets case, most of the magnets flux (energy) remains at the inner rotor level. This is because of the iron bridge, considerred for the inne-rotor, necessary to

Table 1: Materials properties for the studied MG.

Material Property	Permanent magnet			Feromagnetic Steel		
	Nd-Fe-B	Alnico	Ferrite	M400 (0.5mm)	M335 (0.35mm)	Vacoflux48 (0.2mm)
Remanent flux-density	1.35 T	1.27 T	0.45 T			
Relative magnetic permeability	1.05	1	16	~4000	~4000	~4000
Magnetic field intensity (coercitivity or at saturation)	−930 kA/m	−51.5 kA/m	−300 kA/m	50 kA/m	5 kA/m	1.9 kA/m
Saturation flux-density				2 T	1.6 T	2.25 T

Table 2: Performances comparison for different used materials.

| Parameter MG' materials	Input torque (Nm)	Output torque (Nm)	Ripple of input torque (%)	Ripple of output torque (%)	Total iron losses (W)
Nd-Fe-B + M400	9.34	150.3	2.14	0.79	806.9
Alnico + M400	0.82	13.14	1.82	0.68	51.9
Ferrite + M400	0.637	10.18	3.3	0.98	229
Nd-Fe-B + M335	9.34	150.3	2.35	0.86	870
Nd-Fe-B + Vacoflux48	9.34	150.3	1.68	0.84	396.6

(a)   (b)
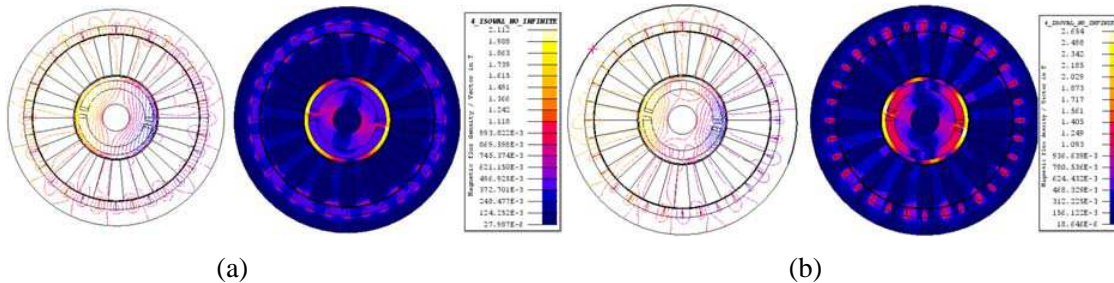
Figure 8: Field lines & flux density distribution in the MG with Vacoflux48 steel and (a) Ferrite or (b) Alnico magnet.

keep the magnets while high rotational speeds and centrifugal forces are reached. This iron bridge cannot be smaller, otherwise the rotor iron will break. A thinner iron birdge will be sufficient to force the magnets flux to pass from the inner to outer rotor, even in the case of Ferrite and Alnico magnets, but due to the high rotational speed for the inner rotor, this MG configuration is not suited for such materials, even if we have very good iron material (Vacoflux48).

The field and flux density distribution for Ferrite and Alnico materials is depicted in Figure 8. Here, one can see how the inner rotor flux remains at rotor level, because of the iron bridge. From the obtained results, it is clear that for such MG configuration (with iron bridge, needed for high rotational speed) the Ferrite and Alnico materials are not suited. Regarding the used steel, the M400 variant offers the most decreased torque ripples, — but the values are practically the same — while the Vacoflux48 is the best variant in terms of efficiency, due to very decreased iron losses. Nevertheless, the choise for one material or another should consider the cost of the steel too (the Vacoflux48 is very expensive).

4. CONCLUSIONS

This paper presents the performances comparison of a high speed magnetic gear suited for electric vehicle applications. For different steel and magnet materials (M400, M330 and Vacoflux48), with

different sheet widths, for different magnet materials (Nd-Fe-B, Alnico and Ferrite) and parallel magnetization, the output characteristics were compared in terms of torque ripples and iron loss level (efficiency). It has been found that the M400/Nd-Fe-B offers the most reduced torque ripples, while the Vacoflux48 the best efficiency.

ACKNOWLEDGMENT

REFERENCES

1. Abdel-Khalik, S. A., A. Massoud, and A. Elserougi, "Magnetic gearbox with an electric power output port and fixed speed ratio for wind energy applications," *ICEM-2012*, 702–708, Marseille, France, Sep. 2–5, 2012.
2. Davey, K., L. McDonald, and T. Hutson, "Axial flux cycloidal magnetic gears," *IEEE Transactions on Magnetics*, Vol. 50, No. 4, Article No. 8100607, Oct. 2013.
3. Fan, Y., L. Zhang, J. Huang, and X. Han, "Design, analysis and sensorless control of a self-decelerating permanent-magnet in-wheel motor," *IEEE Transactions on Industrial Electronics*, Vol. 60, No. 10, 5788–5797, Oct. 2014.
4. Fodorean, D., "Study of a high speed motorization with improved performances dedicated for an electric vehicle," *IEEE Transactions on Magnetics*, Vol. 50, No. 2, 921–924, Feb. 2014.
5. Luise, F., A. Tessarolo, S. Pieri, P. Raffin, M. Di Chiara, F. Agnolet, and M. Scalabrin, "Design and technology solutions for high-efficiency high-speed motors," *ICEM-2012*, 155–161, Marseille, France, Sep. 2–5, 2012.

An Efficient Progressive Phase Distribution Consideration of Reflectarray Antennas

M. Y. Ismail and M. Inam

Wireless and Radio Science Center (WARAS)
Universiti Tun Hussein Onn Malaysia, Batu Pahat, Johor, Malaysia

Abstract— This paper provides a novel and efficient procedure for the X-band reflectarray antenna design emphasizing on the progressive phase distribution which is required to achieve the planar wave in front of antenna aperture. Detailed theoretical procedure has been provided with mathematical modeling of the required reflection phase from each of the individual reflectarray elements. The importance of material properties in reflectarray antenna design has been highlighted and different novel design configurations has been proposed for the unit cell reflectarray elements. Scattering parameter measurements and simulated results provide a very close agreement for different slot embedded designs proposed in this work. Two different configurations of mixed rectangular and circular slots embedded patch elements have been investigated. The variation in width of slot in the case of three rectangular slot patch configuration, the measured reflection loss varied from 2.89 dB to 5.60 dB while in the case of mixed rectangular and circular slot configurations, measured reflection loss is varied from 7.90 dB to 5.60 dB by varying the radius of circular slot. Moreover a maximum frequency variation of 2.58 GHz and a dynamic phase range of 345° with the variation in slot dimensions have also been demonstrated.

1. INTRODUCTION

Reflectarray is a high gain antenna which combines the unique features of a flat reflector and an array of microstrip patch elements printed on a thin dielectric substrate. It is illuminated using a primary feed horn placed at a particular distance from the array. The reflectarray exhibits a number of significant advantages over conventional parabolic reflector and phased array antennas such as easy deployability, lower manufacturing cost, scannable beam, and surface mountability with lower mass and volume [1]. Due to these growing numbers of advantages, reflectarray has been considered as a potential alternative to the parabolic reflector and phased array antennas.

The most important aspect of reflectarray antenna design is the design of printed microstrip elements which can be used for the performance appraisal of the antenna. The individual elements of the periodic array have to be designed with progressive phase distribution so that the spherical beam from the horn antenna can be converted into a planar wavefront. The required reflection phase values from individual elements of an array also depend on the location of the feed horn. For proper phase requirements, different techniques such as, identical patches of variable-length stubs [2], square patches of variable sizes [3], identical planar elements of variable rotation [4] and identical rectangular patches with different types of slot configurations have been used [5, 6]. All these phasing techniques increase the possibility of reflectarrays to become an alternative option to the parabolic reflectors. However one of the main concerns of a reflectarray antenna is its limited bandwidth performance as compared to the parabolic reflector antennas [7–9]. Different configurations have been proposed by researchers in the past few years for the bandwidth improvement of reflectarray antennas [10, 11] but considerable efforts are still required to improve the bandwidth performance of reflectarrays.

This paper provides a detailed mathematical analysis for obtaining the required reflection phase of the array element which is used to produce a progressive phase distribution for any dielectric material using either centre or off-set feed configuration.Novel proposed individual reflectarray elements have been simulated using CST Microwave Studio and verified experimentally using waveguide scattering parameter measurements. Although the paper concentrates on the explanation of X-band reflectarray design, the same procedure can be used to design reflectarray in any frequency range.

2. REFLECTARRAY REFLECTION PHASE

2.1. Progressive Phase Distribution

In a reflectarray antenna, the incident field ($\bar{E}_i$) being illuminated by the feed horn is reflectedand scattered from the ground plane and resonating patches respectively. The reflected field ($\bar{E}_r$)

depends on the properties of the dielectric material used for the reflectarray design and scattered field $(\bar{E}_s)$ depends on the resonating element design configuration. Therefore the total electric field $(\bar{E}_t)$ in a reflectarray can be represented by:

$$\bar{E}_t = \bar{E}_i + \bar{E}_r + \bar{E}_s \tag{1}$$

This work concentrates on the analysis of reflection phase (φ_n) from the individual patch elements of a reflectarray. Fig. 1 shows the geometry of the centre feed and off-set feed reflectarrays for different planar reflector designs. The feeds F_1 and F_2 are placed at the off-set distance of $\Delta X_f = X_0 - X_1$ and $\Delta X_f = X_0 - X_2$ respectively. Different feed locations (F_0, F_1, F_2) as shown in Fig. 1 have been used to obtain the reflection phase of resonant elements which take into account the effect of material properties.
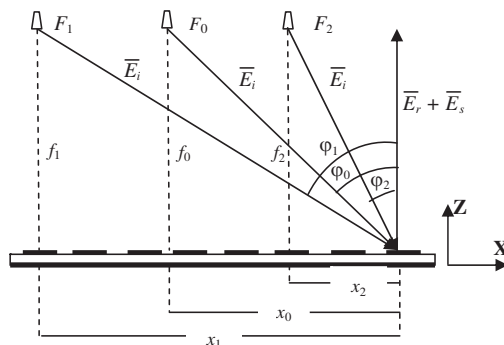

Figure 1: Reflection phase from different feed points in a reflectarray antenna.

Based on the required phase shift of reflectarray elements shown in provided in [12–14], it has been observed that the required phase shift remains constant for elements lying on circles of radius (r) in a periodic array. Hence if φ_n is calculated for the elements lying on the X-axis with radius $r = x_i$, the required phase shift of all the elements of the periodic array can be effectively approximated. In order to calculate the phase shift for the elements on X-axis, a basic formula can be derived as:

$$\varphi = -\frac{2\pi}{3}\cot^{-1}\frac{f}{x_i} \tag{2}$$

where, f is the vertical distance of feed from surface of the array and x_i is the distance between the center of ith element and the point perpendicular to the feed and φ is in degrees. Once φ, is calculated for different values of $x = x_i$, $y = 0$, the phase shift for all the array elements can be obtained. This method simplifies the calculation of the required phase shift from each of the array elements and reduces the complexity and time required for the periodic reflectarray design.

The above technique can also be used for the progressive phase distribution of off-set feed reflectarrays. In the case of off-set feed reflectarrays ΔX_f has to be introduced as the distance between the feed and the line perpendicular to the array centre. The required reflection phase can then be calculated by:

$$\varphi = -\frac{2\pi}{3}\cot^{-1}\frac{f}{x_i \pm \Delta X_f} \tag{3}$$

Figure 2 shows the progressive phase distribution obtained for the design of planar reflectors with center and off-set feed positions. X (mm) shows location of the element placed in an array with total dimensions of $120\,\text{mm} \times 120\,\text{mm}$. In the case of off-set feed, the feeds were placed at a distance of one wavelength (λ) away from the centre of the array on both sides. It can be observed from Fig. 2 that the required reflection phase curve provides a phase range of $180°$ to $-180°$ while the position of the feed clearly varies the reflection phase required from the individual element in order to produce progressive phase distribution.

2.2. Effect of Material Properties

The above analysis provides a general formulation for the design of reflectarray with progressive phase distribution for any dielectric material and either centre or off-set feed configuration. In order to obtain the progressive phase distribution of planar reflector designed with different dielectric substrates, the material properties should be incorporated in (2).
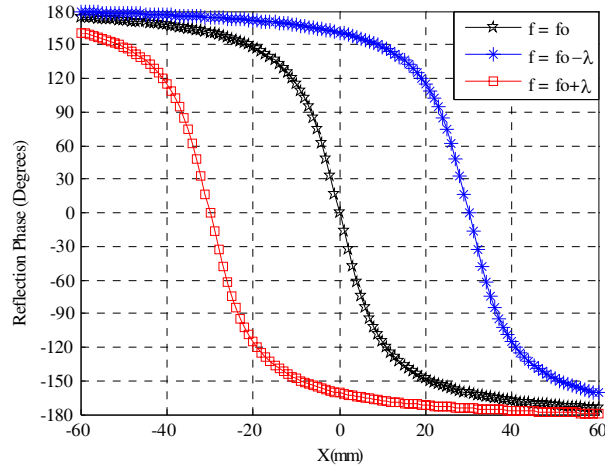
Figure 2: Reflection phase curves for progressive phase distribution of planar reflectors with different feed positions.
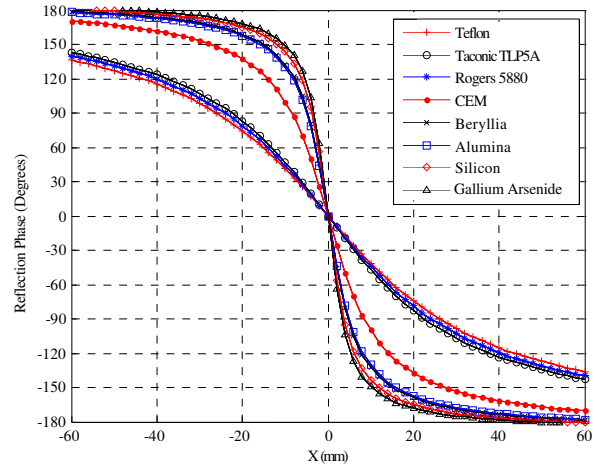

Figure 3: Reflection phase curves for planar reflectors modeled with different substrates at 10 GHz

The material properties affect the reflection coefficient (Γ) which effects the reflection phase of the reflectarray. In this case, Γ depends on the attenuation due to dielectric and conductor loss which are given by:

$$\alpha_d = \frac{\omega}{2}\sqrt{(\mu_0 \epsilon_0 \epsilon_r)} \tan \delta \tag{4}$$

$$\alpha_c = \frac{8.68}{W Z_m}\sqrt{\left(\frac{\omega \mu_0}{2 \sigma_c}\right)} \tag{5}$$

where, α_d and α_c are attenuation due to dielectric and copper loss respectively. After incorporation of effects of dielectric and copper attenuation on Γ and reflection phase of planar reflector, (2) can be written as:

$$\varphi = -\frac{2\pi}{3}\cot^{-1}\frac{f}{K(x_i \pm \Delta X_f)} \tag{6}$$

In (6), K is a variable which relates φ with Γ and depends on resonant frequency and material properties which affects the radiated and scattered fields. The value of K will be higher for the materials with higher values of dielectric permittivity and loss tangent. Therefore K is directly proportional to attenuation due to dielectric and conductor given by (4) and (5) respectively or K can be given by:

$$K \propto \alpha_d + \alpha_c \tag{7}$$
$$K = C \cdot (\alpha_d + \alpha_c) \tag{8}$$

where, C is a compensation variable and varies with different design requirements and materials used. In (8), C is dependent on the dielectric permittivity and loss tangent values of the substrate in a way that (6) can be written as:

$$\varphi = -\frac{2\pi}{3}\cot^{-1}\frac{f}{x\left(\frac{\varepsilon_r}{\tan \delta}\right)(\alpha_d + \alpha_c)(x_i \pm \Delta X_f)} \tag{9}$$

where, x is a constant that has to be derived for different materials while ε_r and $\tan \delta$ are the dielectric permittivity and loss tangent values of the substrate respectively. Mean values of x for different permittivity values have been calculated for operation at 10 GHz as:

$$x_{avg} = \begin{cases} 0.00080, & 2.08 \leq \varepsilon_r \leq 6.5 \\ 0.00040, & 6.50 < \varepsilon_r \leq 13 \end{cases} \tag{10}$$

The dependence of K on α_d and α_c depicts that as the value of K is increased, the slope of the reflection loss curve gets steeper which shows a lower bandwidth value in planar reflector

design. Moreover for lower values of K, the reflection phase range decreases much lower than $360°$ which indicates the rise of phase errors. This trade-off between bandwidth and phase errors for the periodic array follows the same trend as given in [15, 16] for the unit cell reflectarray elements designed in an infinite array environment. In order to characterize the bandwidth performance with respect to different material properties, a Figure of Merit (FoM) is defined here as the slope of reflection phase curve with respect to the dimensions of the planar reflector and is given by:

$$FoM = \frac{\Delta\emptyset}{\Delta X} °/\text{mm} \tag{11}$$

Table 1 provides the evaluated values of K and FoM for different dielectric materials. It can be observed form Table 1 that the value of K is higher for the materials with higher dielectric permittivity and loss tangent values. This shows that Gallium Arsenide will provide lowest bandwidth if used for reflectarray design. Fig. 3 shows the reflection phase curves for planar reflectors designed with different dielectric materials in X-band frequency range.

Table 1: Material properties and calculated values of x for a planar reflector design at 10 GHz.

Material	ε_r	tanδ	K	FoM ($°/$mm)
Teflon	2.08	0.0004	0.25	3.90
Taconic TLP5A	2.17	0.0004	0.29	4.40
Rogers RT/d 5880	2.20	0.0009	0.27	5.20
CEM	4.50	0.0250	0.77	10.8
Beryllia	6.50	0.0004	1.39	20.0
Alumina	9.75	0.0003	1.33	20.3
Silicon	11.9	0.0040	1.78	22.6
Gallium Arsenide	13.0	0.0060	2.05	24.0

It can be observed from Fig. 3 that for X-band planar reflector design, a minimum FoM of $3.90°/$mm for Teflon as compared to a highest FoM of $24°/$mm for Gallium arsenide has been depicted. It can be validated from Fig. 3 and Table 1 that materials with lower permittivity and low loss tangent values provide a smoother phase curve showing a higher bandwidth and lower phase range. On the other hand materials with high dielectric permittivity and loss tangent values offer a steeper phase. Hence phase range is increased but the bandwidth of the planar reflector is decreased by using higher dielectric permittivity and loss tangent materials which shows the trade-off between phase range and bandwidth performance.

3. UNIT CELL DESIGN AND MEASUREMENTS

In order to further investigate and provide elements for the reflectarray design with progressive phase distribution, mixed slot configurations embedded on the patch elements has been proposed in this work. Unit cell patch elements have been designed and fabricated in X-band frequency range using Rogers RT/d 5880 dielectric substrate. The substrate dimensions were kept same for all the design at $\lambda/2 \times \lambda/2$ and were fabricated on 0.381 mm thick sheet. It has been demonstrated earlier that the variation in the dimensions of embedded slot causes a modification in the surface current distribution and electric field intensity of the resonant element. Therefore different resonant frequencies can be obtained by varying the dimensions of one of the embedded slot configurations. This basic principle has been used in this work and a number of unit cells have been designed for each of the proposed configuration. Scattering parameter measurement has been carried out for the two patch element unit cells using vector network analyzer. The measurement procedure was followed as explained in [16]. Two different configurations proposed for this work are explained in this section.

3.1. Rectangular Slot in Centre and Along Length of Patch Elements

Two constant size vertical rectangular slots are introduced along length of patch element while one variable width horizontal rectangular slot is embedded in the centre of the patch element. In order to keep the resonant frequency within X-band, the dimensions of the rectangular patch have been adjusted to $L \times W = 7.9\,\text{mm} \times 10.0\,\text{mm}$. The dimensions of slots along length are $Ls_0 = 3\,\text{mm}$ and

$Ws_0 = 1$ mm. The length of slots in the centre of patch element is kept at $0.15L$ while the width is varied from $0.5W$ (L and W are the length and width of rectangular patch element respectively). The detailed design configuration is shown in Fig. 4.

Figure 5 shows the reflection loss and reflection phase curves for the proposed design obtained by simulations and measurements. Both the reflection loss and reflection phase curves provided a very close agreement in all the cases. It can be observed from Fig. 5 that a change in resonance frequency from 10.62 to 9.04 can be obtained by varying the slot width from $0.1W$ to $0.5W$. Moreover by this variation in width of slot, the measured reflection loss varies from 2.89 dB to 5.60 dB. The trend of increasing reflection loss with increasing width in simulated and measured results can also be observed by the slope of the reflection phase curves. The reflection phase curve provides a dynamic phase range of 323° calculated at 9.83 GHz.
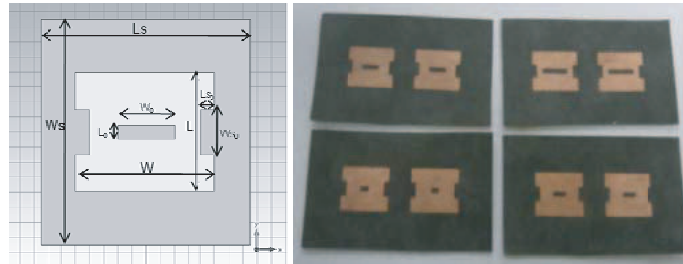

Figure 4: Proposed design and fabricated samples of rectangular slots in centre and along length of patch elements.

Figure 5: Reflection loss and reflection phase curves for rectangular slot in centre and along length of patch elements.

3.2. Rectangular Slot in Centre and Circular Slots Along Width of Patch Elements

Another mixed slot configurations has also been analyzed in this work where a rectangular slot with constant dimension is embedded in the centre of patch and two variable radius circular slots along the width of the patch element are introduced as shown in Fig. 6. This design can also be used for active reflectarray design where a lumped component can be integrated in the central rectangular slot while the slots along width can provide the progressive phase distribution. In the proposed X-band design, the dimensions of the rectangular patch are $L \times W = 8.7$ mm $\times$ 10.0 mm. The dimensions of rectangular slot in the centre are kept constant at $L_0 \times W_0 = 1.0$ mm $\times 6.0$ mm while the radius of the circular slots are varied from 0.5 mm to 3.5 mm.

Varying the radius of circular slots from 0.5 mm to 3.5 mm causes a change in resonant frequency from 8.74 GHz to 11.32 GHz depicted in Fig. 7. It can also be observed from Fig. 7 that measured and simulated results provide a very close agreement. The measured reflection loss is decreased from 7.90 dB to 5.60 dB as the radius of the slot is increased from 0.5 mm to 3.5 mm. Similarly a close agreement between the simulated and measured results can also be observed from the reflection phase curves shown in Fig. 7. In the case of rectangular slot in centre and circular slots along width of patch elements configuration, a dynamic phase range of 345° has been demonstrated at 10.03 GHz.

Figure 6: Proposed design and fabricated samples of rectangular slot in centre and circular slots along width of patch elements.
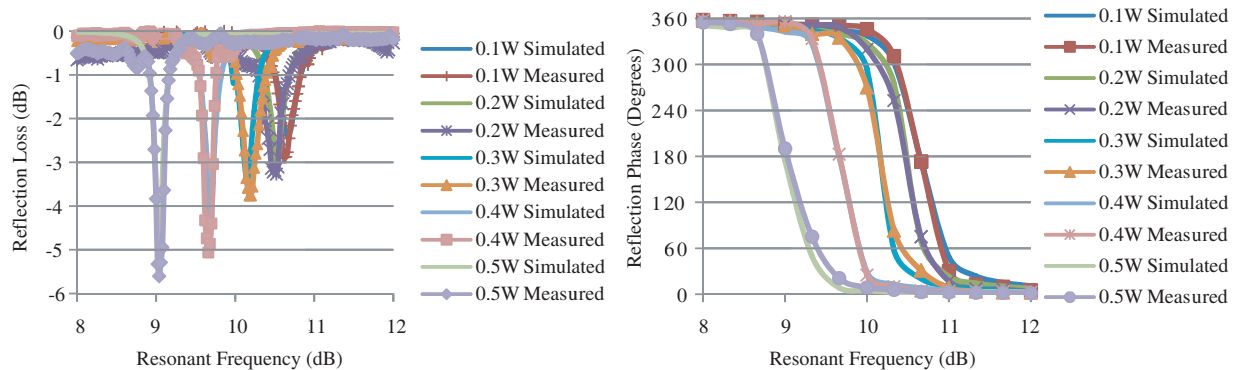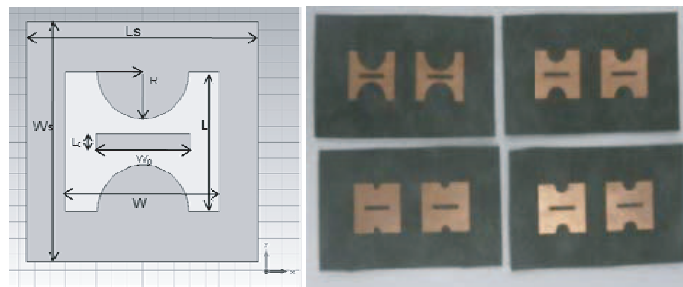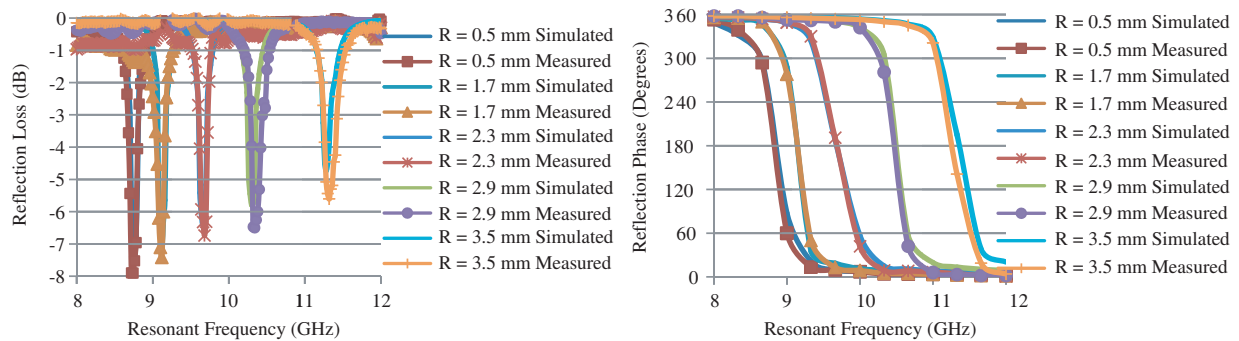

Figure 7: Reflection loss and reflection phase curves for rectangular slot in centre and circular slots along width of patch elements.

4. CONCLUSION

Mathematical modeling provided for the design of reflectarrays with progressive phase distribution can be used for different single layer configurations of unit cell patch elements. Material properties, which play an important role in the performance analysis of reflectarrays, must be included in the reflection phase analysis while designing a reflectarray antenna. Different designs, proposed in this work with validation of scattering parameter measurements, can be used for the reflectarray design with progressive phase distribution and a wide dynamic phase range.

REFERENCES

1. Huang, J., "Analysis of microstrip reflectarray antenna for microspacecraft applications," *Spacecraft Telecommunications Equipment Section*, 42–120, TDA Progress Report, Feb. 15, 1995.
2. javor, R. D., X. D. Wu, and K. Chang, "Design and performane of microstrip reflectarray antenna," *IEEE Trans. Antennas and Propagation*, Vol. 43, No. 9, 932–938, Sep. 1995.
3. Targonski, S. D. and D. M. Pozar, "Analysis and design of a microstrip reflectarrayusing patches of variable size," *IEEE AP-S/URSI Symposium*, 1820–1823, Seattle, Washington, Jun. 1994.
4. Huang, J. and R. J. Pogorzelski, "Microstrip reflectarray with elements having variable rotation angle," *IEEE AP-S Symposium Digest*, 1280–1283, Apr. 1993.
5. Ismail, M. Y. and M. Inam, "Performance improvement of reflectarrays based on embedded slots configurations," *Progress In Electromagnetics Research C*, Vol. 14, 67–78, 2010.
6. Chahmir, M. R., J. Shaker, M. Cuhai, and A. Sebak, "Reflectarray with variable slots on ground plane," *IEE Proc. — Microwaves, Antennas and Propagation*, Vol. 150, No. 6, 436–439, 2003.

7. Ismail, M. Y. and M. Inam, "Analysis of design optimization of bandwidth and loss performance of reflectarray antennas based on material properties," *Modern Applied Sci. J. CCSE*, Vol. 4, No. 1, 28–35, 2010.

8. Biallowski, M. E. and J. Encinar, "Reflectarray: Potential and challenges," *International Conference on Electromagnetics in Advanced Applications*, 1050–1053, ICEAA, 2007.

9. Pozar, D. M. and S. D. Targonski, "A shaped-beam microstrip patch reflectarray," *IEEE Transactions on Antennas Propogation*, Vol. 47, No. 7, 1167–1173, 1999.

10. Huang, J. and J. Encinar, *Reflectarray Antennas*, Wiley, Interscience, 2007.

11. Sze, K. Y. and L. Shafal, "Analysis of phase variation due to varying patch length in a microstrip reflectarray," *IEEE Trans. Antennas and Propagation*, Vol. 46, No. 7, 1134–1137, 1998.

12. Rajagoapalan, H., S. Xu, and Y. R. Samii, "Reflectarray reflection phase diagnostics," *2011 IEEE International Symposium on Antennas and Propagation (APS/URSI)*, 1636–1638, Washington, USA, 2011.

13. Tienda, C., J. A. Encinar, E. Carrasco, and M. Arrebola, "Design of dual-reflectarray antenna for beam scanning," *Journal of Wireless Networking and Communication*, Vol. 2, No. 1, 9–14, 2012.

14. Carrasco, E., J. A. Encinar, and M. Barba, "Bandwidth improvement in large reflectarrays by using true time delay," *IEEE Transactions on Antennas and Propagation*, Vol. 56, No. 8, 2498–2503, 2008.

15. Rajagopalan, H. and Y. R. Samii, "On the reflection characteristics of a reflectarray element with low-loss and high-loss substrates," *IEEE Antennas and Propagation Magazine*, Vol. 52, No. 4, 73–89, 2010.

16. Inam, M. and M. Y. Ismail, "Reflection loss and bandwidth performance of X-band infinite reflectarrays: Simulations and measurements," *Microwave and Optical Technology Letters*, Vol. 53, No. 1, 77–80, 2011.

Problems of Statistical Decisions for Remote Monitoring of the Environment

F. A. Mkrtchyan

Institute of Radioengineering and Electronics, RAS
Vvedensky sq. 1, Fryazino, Moscow Region, Russia

Abstract— The basic sense of the concept of remote monitoring consists in connection in system of means of data gathering, methods of their processing, mathematical models of natural objects, computer implementers of algorithms and models with a wide spectrum of service maintenance at visualization of results of monitoring. It is obvious that complex research of the given land and remote measurements can raise reliability of estimations of parameters of natural systems and solve a problem of planning of these measurements. Application of means of remote monitoring in many cases is connected with acceptance of the statistical decision on presence on a surveyed part of studied space of this or that phenomenon. One of features of conditions of gathering of the information for such decision is the impossibility of reception statistical samples great volumes. Therefore working out and research of optimum algorithms of distinction of the casual signals characterized by samples of the limited volume, in the conditions of parametrical aprioristic indefinite are necessary.

One of the important features for the detection and classification of phenomena on the sea surface of the sea is a "spottiness" of the sea surface. Therefore the study of the statistical characteristics of "spottiness" is important. In this paper the analysis of the statistical characteristics of "spottiness" for certain areas of the Pacific ocean. These statistical characteristics were determined for the most informative thresholds.

1. INTRODUCTION

In connection with technical progress and growth of the population of a planet the anthropogenous stress on biosphere sharply amplifies. Therefore the role of remote monitoring allowing sharply raises to receive an estimation and the forecast of anthropogenous changes, to reveal sources of influence and the reasons of these changes. Modern scientific and technical level gives sufficient means for remote monitoring [1, 2].

The basic sense of the concept of remote monitoring consists in connection in system of means of data gathering, methods of their processing, mathematical models of natural objects, computer implementers of algorithms and models with a wide spectrum of service maintenance at visualization of results of monitoring.

The organization of remote monitoring systems (RMS) is exclusively difficult, complex, multi-plane problem. In its decision the important role is played by experimental methods of research of environment. Paramount value at realization of such experiments is got by the organization of mass gathering of the information on studied object, efficiency of its processing and authentic interpretation of the given supervision on the basis of analytical and numerical mathematical models. Therefore within the limits of RMS it is possible to allocate the systems of the automated radio physical experiment intended for performance of following functions [1]:

- Gathering and trustworthy information storage about studied object.
- The preprocessing of the data including the identification, decoding and preliminary control of the given supervision with reduction of this data to some standard forms.
- The secondary data processing including various mathematical and statistical methods, intended for the decision of the identification, classification and definition of typical characteristics of investigated object.
- The forecast of a condition of studied object on the basis of interpretation of the received information with use of the developed mathematical methods.

Effective realization of these functions in modern conditions assumes wide automation (radio physical) experiment, with use of last achievements of experimental technics and methods of data processing of supervision. Automation radio physical methods of research of environment opens new possibilities before the researcher, namely:

- Considerably reduces terms of carrying out of researches.
- Raises efficiency of experiments.
- Provides complex and rational use of the expensive equipment.
- Uses qualitatively new methods of processing and interpretation.
- The experimental information.
- Releases the researcher from routine work.

Now we will short stop on principles of designing of the automated systems of gathering and processing of the information on environment. At designing of the automated systems of gathering and processing of the information within the limits of RMS it is necessary to start with following features of radio physical methods of research of environment:

- Huge volume of the information both continuous and fast increase in this volume.
- Difficult and various structure of information streams.
- Diversity of radio physical experiment.
- Evolutionary character of experiment.
- Uncertainty of experiment.
- Active participation of the person in the course of research.
- A considerable quantity of users with various inquiries.

The enormous volume of the information demands attraction difficult technical and the software providing effective processing, storage and search of the necessary information on objects. For successful carrying out of experiment often happens it is necessary to involve a considerable quantity of the aprioristic information. Hence, the organization of long storage of great volume of the data and maintenance of reference service about presence of that or other data is necessary.

The difficult and various structure of information streams in radio physical experiment is caused by following reasons: technical complexity of devices of data recording, a variety of these devices and multistage character of researches. It demands the coordination of streams of the information between various stages of processing and the analysis, and also working out of optimum methods of processing of the information, containing conditions of the operative coordination of the COMPUTER of various types and data recording devices.

Multistage radio physical experiment means that it as research process consists of many stages (steps). And, the maintenance of the next stage essentially depends on results of the previous. It defines an important place of the organization of managerial process in systems of the automated experiment. Evolutionary character of radio physical experiment is defined by constant perfection and application of methods of research, mathematical methods of data processing and development of computing means and the software. Necessity of a modularity of systems of the automated radio physical experiment that means presence of functionally independent and conveniently interfaced blocks from this follows.

2. REMOTE MONITORING SYSTEMS OF DETECTION OF ANOMALIES ON THE SEA SURFACE

One of function RMS is detection and classification of the abnormal phenomena on investigated space. Important circumstances in a considered problem is the account of presence of conditions of uncertainty in a residence and possible dynamic behavior of anomaly. Limitation of parameters of the means applied at inspection of environment, it should be considered in procedures of decision-making on presence or absence of anomaly. This many-sided nature of a problem of global detection of anomalies in biosphere demands for the decision of application of the system approach allowing from uniform positions to consider all complex of local problems and to approach to formation of monitoring system of the detection provided with reliable function of self-checking.

Limitation of means, memory size and speed of onboard computers dictates a partition of monitoring system on three subsystems (Fig. 1): a fixing block, a solving block and the selector. The last share on subsystems — the blocks which functions consist in the following: 1) periodic viewing of elements of the sea surface; 2) fixing of suspicious elements in memory; 3) formation from suspicious elements of traces of moving anomaly; 4) accumulation in time of the data about the fixed elements of a terrestrial surface for the purpose of the statistical analysis for decision-making on noise or signal character of the fixed suspicious elements; 5) multistage localization of procedure of search of anomaly.
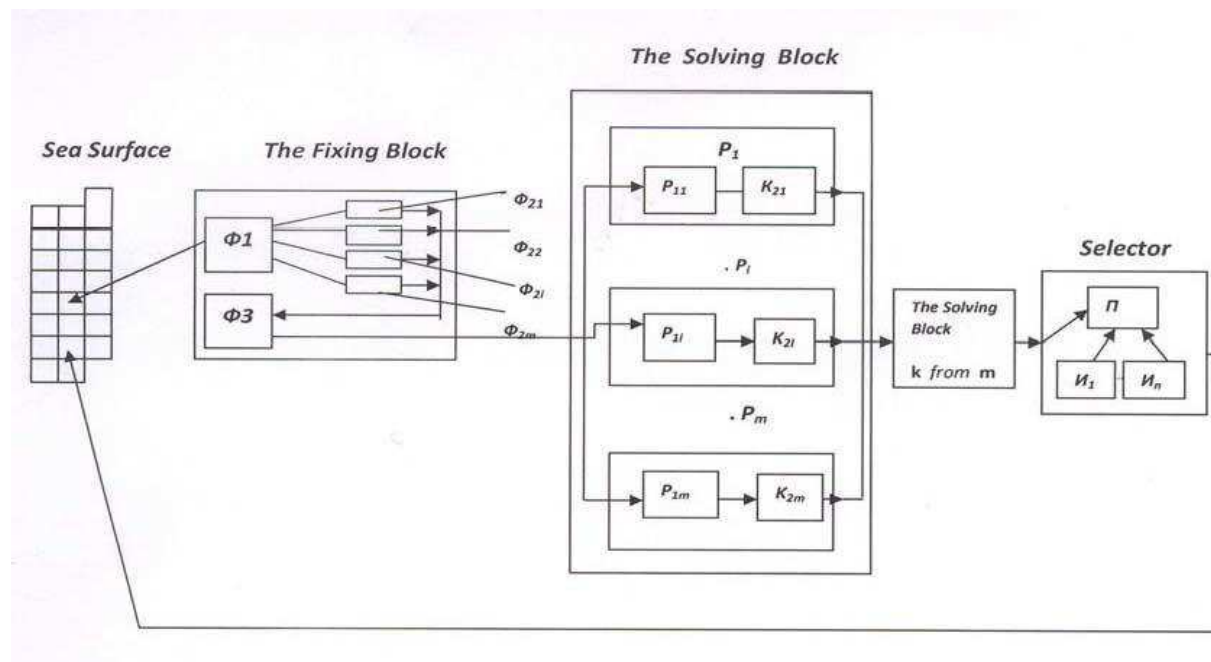
Figure 1: Block diagram RMS of search of anomalies on a sea surface.

Owing to dynamic change of anomalies the monitoring system should carry out much faster these changes scanning of elements of space and have time to process a stream of the statistical information. Therefore there is a problem of an estimation of efficiency of monitoring system as to function of its parameters.

Let the memory size of monitoring system is limited by M cells, and the information stream simultaneously proceeds from N space elements. In each element the source of the information defined by stochastic function $\xi_i(t)$. If $M \geq N$ the decision of a problem of the statistical analysis of an information stream is reduced to accumulation of the data in cells of memory and its subsequent processing by methods of mathematical statistics. In case of $M < N$ it is necessary to develop some algorithm of accumulation of statistics only about "suspicious" elements of an information stream.

Let depending on the relation a signal/noise a stochastic function $\xi_i(t)$ is defined by density of probabilities $f_a(x)$. And let the choice of "suspicious" elements in memory of monitoring system is made for storing in case of $\xi > X$, where X — the set threshold. Thus, if $a = a_0$ at noise character of stream $\xi_i(t)$ and $a = a_1$ in the presence of a signal and noise probabilities of fixing of noise and alarm elements will be equal accordingly

$$p_N = \int_X^\infty f_{a0}(x)dx, \quad p_C = \int_X^\infty f_{a1}(x)dx$$

Let's assume that shares of alarm and noise elements at the moment of time t are equal in space $1 - \gamma(t)$ and $\gamma(t)$. Then fixed during the moment t random number $\kappa(t)$ "suspicious" elements will have distribution:

$$P[\kappa(t) = k] = P_{N\gamma,pN}(k_1) \cdot P_{N[1-\gamma],pC}(k_2), \quad P_{n,p}(m) = C_n^m p^m (1 - p)^{n-m}.$$

Accepting for a time unit an interval necessary for realization of one viewing of all surveyed space, we will calculate probability of overflow during the moment t memories of monitoring system $P[\mu(t) > M]$. We will consider a case of discrete time, when the moments of occurrence and the termination of processing of a noise or signal element.

Are identified with the nearest integer. Let each arisen element is processed in a separate cell of memory up to the moment of removal of the final decision about its noise or alarm character then the memory cell is cleared and can perceive other information. Thus number $\mu(t)$ occupied during the moment t memory cells is casual integer function.

Let's enter making functions

$$g_t(x) = \sum_{k=0}^{\infty} P[\kappa(t) = k]x^k, \quad G_t(x) = \sum_{m=0}^{\infty} P[\mu(t) = m]x^m$$

Let's consider that processing time during the moment $t = s$ one element is random variable $\nu(s)$ set distribution $P[\nu(s) < t] = F_s(t)$. Then we have:

$$G_t(x) = \prod_{s=h}^{t} g_s \{1 + [1 - F_s(t - s)](x - 1)\}$$

Further we receive expressions for an average and a dispersion:

$$E\mu(t) = \sum_{s=h}^{t} E\kappa(s)[1 - F_s(t - s)]$$

$$D\mu(t) = E\mu(t) + \sum_{s=h}^{t} [D\kappa(s) - E\kappa(s)][1 - F_s(t - s)]^2$$

If $\kappa(s)$ has distribution of Puasson with parameter $\lambda(s) = E\kappa(s) = D\kappa(s)$, also it is distributed under the Puasson law with parameter $\Lambda(t) = E\mu(t)$.

All these reasonings were fair at M. If $M = \text{const} > \Lambda(t)$, $\mu(t)$ has the truncated distribution of Puasson:

$$P[\mu(t) = m; \; M = \text{const}] = P_{\Lambda(t),M}(m) = (\Lambda^m(t)/m! / \sum_{l=0}^{m} \Lambda^l(t)/l!, \quad m < M$$
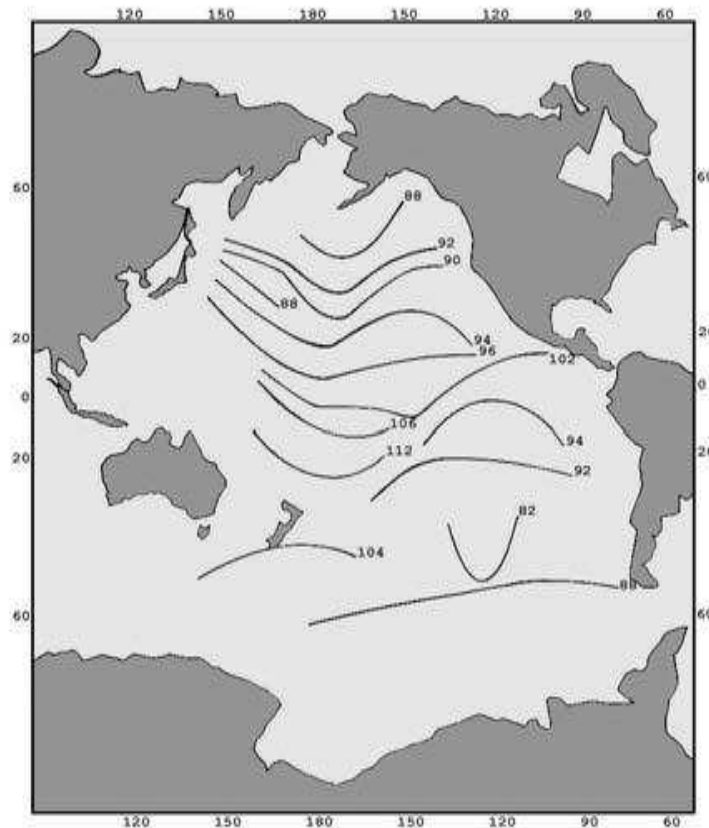

Figure 2: Map of brightness temperature of Pacific Ocean.

Hence, efficiency of monitoring system is defined by probability of overflow of its memory, i.e., probability of loss of the information. In the more general case for an estimation of efficiency of monitoring system of detection of anomalies on a terrestrial surface it is necessary to consider work of all its subsystems taking into account individual restrictions of memory available for them and speed of data processing.

3. APPLICATIONS

Criteria of an estimation of efficiency of monitoring systems finally are defined by probability of performance by them of the problems which is difficult function of parameters of systems and environment. By theoretical considerations the important role is played by environment model. One of possible this sort of models is under construction on the basis of use of concept of "spottiness" of studied space. Mobile anomaly breaks spottiness structure and as a result that its trace is formed. As stains can have the various nature the effective algorithm of detection should be multichannel, capable to analyze the hydrophysical, biological, acoustic, optical and physical and chemical information.

On Fig. 2 the example of application of RMS for monitoring of brightness temperature of a surface of Pacific Oceans on date Space Satellite (SS) "Intercosmos-21" (20–22, February 1979) is given. The system allows to receive maps of temperatures on enough rarefied grid of trajectory SS.

As can be seen from the map in the area ($-30°$ S. Lat. $-50°$ S. Lat., $110°$ W. Long., $130°$ W. Long.) is an anomalous phenomenon.

From the aforesaid follows, that statistical characteristics for "spottiness" of brightness temperatures in microwaves can be used for detection and classification of the phenomena on a surface of the ocean.

The analysis of empirical histograms for "spottiness" of "brightness temperatures in microwaves" shows, that in most cases $(l+, l-)$-characteristics will be coordinated with exponential distribution, and amplitude characteristics will be coordinated with normal distribution. Therefore for detection and classification of the phenomena on a surface of ocean it is necessary to apply optimal algorithms for the COMPUTER training to taking statistical decisions for the aforesaid distributions [2, 3].

ACKNOWLEDGMENT

REFERENCES

1. Armand, N. A., V. F. Krapivin, and F. A. Mkrtchyan, "Methods of data processing of radio-physical research of an environment," *Nauka*, Moscow, 1987 (in Russian).
2. Mkrtchyan, F. A., "The problem of statistical learning decision-making for the small sample size in geoinformation monitoring," *American Journal of Mathematics and Statistics*, Vol. 3, No. 6, 346–348, 2013.
3. Mkrtchyan, F. A., "About of statistical decisions in remote monitoring," *Procedings of the 14th International Symposium on Microwave and Optical Technology*, 99–102, Kuala-Lumpur, Malaysia, Oct. 28–31, 2013.

Simulation Evaluation of the IEEE 802.11ac ad-hoc Network for Voice Communication in Emergency Scenario

J. Jarmakiewicz, **K. Maślanka**, and **K. Parobczak**

Military University of Technology in Warsaw, Poland

Abstract— The paper presents simulation study of communication system consisting of mobile nodes during crisis situation scenario. Nodes' network interfaces support IEEE 802.11ac standard in ad-hoc mode, while devices operate under control of Google Inc. Android operating system. Overview of current Wi-Fi techniques was described, with an indication of further standard evolution. Limitations of current Wi-Fi ad-hoc mode implementation in Android were addressed, with emphasis on ongoing research projects on overcoming specific restrictions: Wi-Fi Peer-to-Peer extension and multi-hop transmission. Evaluation of network efficiency with Voice over IP service activity during an emergency scenario was performed in simulation environment. Lack of cellular connectivity, external power access and no access to special communication equipment during rescue operation were assumed. Obtained results show insignificant impact of service realization on network resources utilization, low maximum end-to-end packet delivery delay and jitter values during continuous telephone conversations. Thus, described assessment shows a high degree of IEEE 802.11ac ad-hoc network applicability in scope of basic voice communication service realization in case of absence of usually ubiquitous cellular infrastructure, with use of typical communication equipment.

1. INTRODUCTION

We face crisis situations everyday and are immediately informed on every such crisis by the mass media. These events take place in both stable and rich countries such as France and unstable, such as Ukraine. The attack on Charlie Hebdo editorial office or the racket attack on Mariupol are different examples of accidents, but they have something in common. In both the first and second case, the access to mobile telephone services was limited. In the first case, due to overload of the mobile network and its subsequent switch-off, and in the second case, due to failure of the fixed-line network. Even more severe situations occurred in 2004 in Indonesia and in 2011 in Japan, where the tsunami caused deaths of hundreds of thousands of people, and in the areas covered by the disaster, access could not be provided to telephone services which would be very useful in such a situation. Due to the damages of the power plants operating in an integrated power system over a wide area of Japan (even that not directly affected by the tsunami), a black-out occurred.

Development of the Wi-Fi standards results in their throughput similar to that of Ethernet networks. Today, it is difficult to imagine a TV, camera or smart phone without Wi-Fi — they are as common as the very telecommunications service. The range of a home-edition of Wi-Fi radio interface is limited to several dozens of meters and ensures a quick exchange of data between different devices. The unit price of manufacture of a Wi-Fi transceiver allows for using this solution even as a single-use device [1].

In the above mentioned crisis situations, the only devices that could be used for a certain time after the event included smart phones and Wi-Fi laptops, enabling Ad-Hoc cooperation. Wi-Fi devices networks are mostly used as backhauls, confronting the infrastructure of wireless routers. However, in emergency situations, where no power supply or mobile network access can be provided, the Ad-Hoc Wi-Fi operation seems the only solution to ensure telecommunications services such as IP telephony or messaging. Owing to that, people would be able to communicate [2].

Where the mobile network infrastructure is not available, Wi-Fi devices are the only generally accessible means of communication for civilians. In the case of laptops, Ad-Hoc operation can be easily forced, whereas in not all the smart phones Ad-Hoc operation is enabled on Wi-Fi interfaces. Nevertheless, in new smart phones, additional software for Ad-Hoc operation can be installed to provide, e.g., VoIP service or data exchange.

In the world-wide standardization community, the belief that radio communications means should be universal is increasingly popular. This should ensure data exchange between different network techniques and operate even without network infrastructure. The devices and systems should be able to exchange data between them and by means of relay, through intermediate points.

In the near future, the developing Wi-Fi technology, the processing power of smart phones and capacity of their batteries will enable adaptation of Wi-Fi network to Ad-Hoc operation, which

should significantly improve interoperability of the systems used, and positively in uence public safety.

In addition to the benefits, risks and losses are possible as well, which result from the unauthorized and hostile activities. The near future will determine development directions in this area. The further part of the paper presents the basic technical issues determining the Wi-Fi technology development along with its direction. As the next step, the status of Android system dominance on the telecommunications market, and its development toward implementation of the common Ad-Hoc operation was analyzed. Then, reference was made to efficiency of Wi-Fi network in relation to systems adapted to transfer telephone services in IP network.

2. TECHNICAL ISSUES DETERMINING DEVELOPMENT OF WI-FI TECHNOLOGY AND SPECIFYING ITS DEVELOPMENT DIRECTION

It is hard to believe, but today Wi-Fi technology is already adult, and its first standards were elaborated 18 years ago. At present, one can hardly imagine computer networks without Wi-Fi and laptops without this standard cards. According to one of the largest companies selling hardware, in Poland there are no no more laptops without a Wi-Fi card. It is not surprising, as this technology facilitates our life and, what is more, enables provision of services, including the Internet TV. However, to ensure such services, technical parameters must be compliant with service quality standards, and the operational mechanisms are the result of application of various patents.

In the field of mobile technology innovation, Koreans are the leading manufacturers. The global patent market share in the 3rd quarter of 2014 is shown in Fig. 1 [3]. For the Wi-Fi technology market, data from the 4th quarter of 2011 are available for 802.11ac standard — in this case the American company Qualcomm was the leader [4] Fig. 2. Selected Wi-Fi characteristics are included in Table 1. All solutions have a range of approx. 50 meters indoors and approx. 100 meters outdoors. Wi-Fi technology develops mainly toward provision of increasing transmission rates and ranges, as well as easy use.
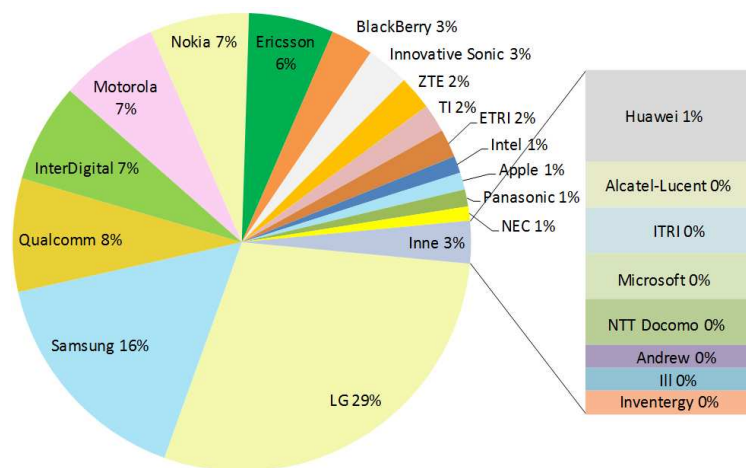
Figure 1: Innovativeness of companies in the 4th generation systems.

Wi-Fi interface was created due to the need to eliminate the Ethernet cable, whereas the transmission mechanisms remained in the same form, i.e., adapted to the computer data. This is why the performance of time-dependent services, e.g., telephony has to face efficiency constraints of radio channels sharing.

This limitation is overcome by other technologies such as WiMAX or LTE. However, WiMAX finally lost the battle for the market with Wi-Fi technology and did not find acceptance in smart phones and laptops. Standard 802.11e with the data priority-dependent access for transmission of E-DCF (Enhanced Distributed Coordination Function) or access allocated in the querying mechanism or HCF (Hybrid CF) is the solution aimed at introducing control mechanisms with access to a radio channel with priorities.

In environments, which are characterized by high density level of devices, and which can occur especially in crisis situations in heavily urbanized areas, increasing the efficiency of exchanged data streams is an issue worth an additional investigation. Proposed technique consist of optimal power

Figure 2: Innovativeness of companies in 802.11ac systems.

Table 1: Characteristics of Wi-Fi standards.

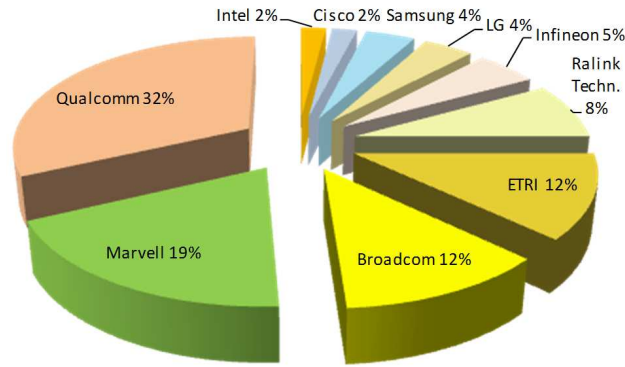| Std	Channel [MHz]	Throughput [Mb/s]	Bandwidth [GHz]	Range [m]
a	54	20	2.4	100
b	11	20	2.4	100
g	54	20	2.4	100
n	65/135	20/40	2.4/5	100
ac	86.7–780	20–160	5	100
ad	6750	2160	60	10

control procedures usage, which were developed and thoroughly discussed in [5]. The proposed mechanism allows to increase the capacity of transmission network, reducing power consumption at the same time. The latter feature is particularly important in crisis situations, where power conservation is crucial. The utilized algorithm is based on a nodes' signal to noise ratio metric, which is transmitted between networks nodes, and estimation of the optimal power for the specific data transmission path. Results of conducted simulation experiments indicate that approximately 30 percent increase in total physical capacity is possible to achieve, which noticeably improved quality of network services. At the same time, most stations work with reduced transmitter power level with respect to standard power level, even up to three-fold power level reduction.

3. GSM SPEECH CODING

Currently, a few speech codecs are used for the telephony, whose properties are shown in Table 2. Analog samples with duration of 20ms are subject to coding, and are subsequently coded by codecs. As a result, frames with different lengths (col. 2) are received and streams with different bitrate are generated (col. 3).

Table 2: Codecs used in GSM.

Codec type	Number of bits in sample	Transmission rate [kbs]
Half Rate (HR)	112	5.6
Full Rate (FR)	260	13
Enhanced FR (EFR)	244	12.2
Adaptive Multi Rate (AMR)	95/103/118/134/148/159/204/244	4.75–12.2
Adaptive Multi Rate — WideBand		6.6–12.65/14.25–23.85

4. AD-HOC COMMUNICATION IN ANDROID DEVICES

Despite the availability of Wi-Fi standard in most, if not all the devices operating under Android system, some operation modes are not natively supported by the operating system. The entry on the intention to have support for Ad-Hoc mode already appeared in January 2008, on an official bug tracking system for Android system, whereas 6 years later, on 25 December 2014, it was

granted the status of being "obsolete" [6, 7]. Meanwhile, this entry was supplemented more than 6 thousand times. In accordance with the current, official source code for Android system, the entries concerning the network in IBSS mode (Independent Basic Service Set) are ignored in the process of creating a network list when scanning the environment [8].

It should be noted that it is possible to compile the modified version of the system or substitute wpa supplicant application (on some devices it was sufficient to change ap scan parameter in wpa supplicant.conf configuration file) with a modified version ignoring IBSS ag and allowing association with Ad-Hoc network. However, this type of interference requires at least unlocking the access to system partition, which is usually connected with the loss of warranty. Modifications obtained from untrusted sources entail potential risk of device infection with malware and in many cases (if bootloader, the system kernel and the package of system and additional software are modified) partial loss of the device functionality may follow, even if the developer assures that the software is adapted to the given hardware version. The current state of development of Android system extensions (4.2.2, 4.3, 4.4, 5.0) containing support for Ad-Hoc operation (native IBSS support and Wi-Fi Direct), including source code, required improvements and technical information for developers can be found in [9].

For 4.0 and later versions of Android system (14 API level), Wi-Fi Direct Wi-Fi Peer-to-Peer (Wi-Fi P2P) extension [10] support was introduced, which, in the basic operation mode, enables peer-to-peer connection for two devices supporting this solution. The standard specification provides for the possibility of creating the so called P2P groups, where one of the clients, P2P GO (Group Owner), is functionally equivalent to the access point (AP) type node from a traditional Wi-Fi operation mode with infrastructure. Thus, frames are transmitted within the given P2P group using GO node (point-to-multipoint topology) at all times. For devices that do not support Wi-Fi Direct functionality, GO node is detected as traditional AP. Therefore, it is possible for P2P group nodes to cooperate with legacy devices. Support for Wi-Fi Direct extension in Android system was described in the official manual for developers in chapter "API Guides, Wi-Fi P2P" [11], whereas results of the experimental tests were published in [12]. Developers of Tapestry application (demonstration [13]) specify the maximum scalability of Wi-Fi Direct solution for 5–6 devices using an image, however there is no information on the Wi-Fi network mode used. The factors limiting functionality of Wi-Fi Direct solution include the necessity to provide visibility between GO nodes in the case of combining P2P groups, or the necessity to provide visibility of GO node for each of network participants, in the case of a network consisting of a single P2P group.

Considering the above, currently there are limited possibilities of using Ad-Hoc mode for multihop transmission for spontaneously compiled MANET networks (Mobile Ad-Hoc NETwork) on devices operating under Android system. Potentially, there is a possibility of using extensions of the system or additional software, developed i.a. within projects using SPAN software (Smart Phone Ad-Hoc Network), with co-financing of the not-for-profit MITRE organization [14, 15]. Although these are only "proof of concept" projects, they are implemented in some of the smart phones. The programs can be downloaded from "Google store" or directly, from the project website [16]. Using Android Manet (AM) Manager and AM Push to Talk applications, a smart phone may turn into a "walkie-talkie" and organize networks in Ad-Hoc mode. An application is also necessary to scan the network environment and deliver address data of the neighbors and "neighbors' neighbors", which will create a graphical book of neighborhood and will allow verification of nodes reachability in multi-hop relations. It is based on AM OLSRd responsible for scanning the neighborhood, whereas AM Visualizer and AM Logger are responsible for the telephone switchboard function.

The aim of another project [17], implemented under the 7th Framework Program, was to ensure multi-hop transmission in a mesh network based on Android devices. The demo version launched on Samsung Galaxy S4 phones enabled live transmission of audio and video streams between the sender and the recipient in the absence of reciprocal and direct radio visibility.

5. SCENARIO OF RESCUE OPERATION, PERFORMANCE OF WI-FI SMART PHONES AD-HOC OPERATION

Let us consider a scenario that can happen every day, e.g.: in the urban area with dense land development, gas explosion occurs in the morning. As a result of the collapse of a large part of the block of at, many residents are trapped. In the area of the disaster, rescue operations are carried out by the fire fighters, medical rescue workers and police officers (approx. 50 persons). Probably, in the building there are survivors. To find them, the rescue services are extinguishing the fire and searching for victims. As a result of the explosion, the mobile telephony radio station mounted in

the building and transformer supplying power to the housing estate are damaged, due to which mobile communications is not possible.

Until delivery of specialized communications equipment, the rescue teams use their smart phones operating in 2.4 and 5 GHz band. Ad-Hoc communication is organized by means of Wi-Fi using the available telephone application. It was managed to provide communication in 802.11ac protocol, using MU/MIMO 2×2 technology. Performance tests indicate the available bandwidth of 130 Mb/s. In a few seconds, the scanning program fills the Ad-Hoc network phone book with data concerning the rescue team. A visualization of the Ad-Hoc network appears on the screen, showing names entered by their owners. Relay connections are also possible with one intermediate point in the area with radius of 150 m (Fig. 3). For such preset conditions, we will try to answer the following questions: what is the network performance for simultaneous phone calls, what is the use of radio channel bandwidth, and how many rescuers may be supported at the same time?
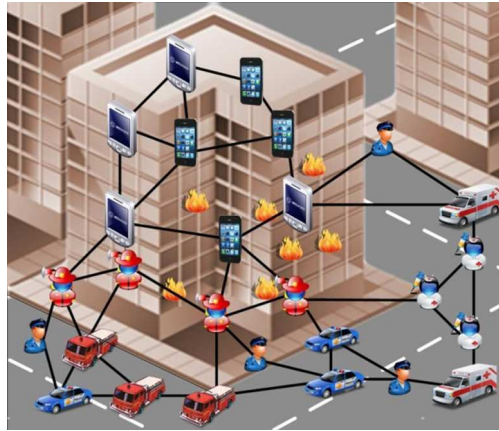

Figure 3: Scenario of rescue operation.

The test was performed using the simulation method for IEEE 802.11ac standard. The assumptions are included in Table 3. The tests did not consider the propagation properties of the radio center and outdoor propagation time was set to 1 us, which is 10 thousand times shorter than the packetization time. Safety issues were not taken into account in the tests.

Table 3: Parameters of the communications system assumed in the simulator.

Band	5 GHz
Channels for 802.11ac	1 channel 80 MHz
Channel throughput 80 MHz	130 Mb/s
Access control	DCF
Tslot, TSIFS, TDIFS, CWMIN	9 us, 16 us, 34 us, 15
Number of stations N1/N2/N3; Range	50/100/150; 300 m
AMR Coder parameters: bitrate, frame length, fps, frame delay	12.2 kb/s, 244 B, 50, 20

The results of network performance, assuming continuous telephone calls in P2P relations for scenarios N1, N2, N3, for a confidence level of 0.95 are as follows:

- Use of channel [%]:1.53; 2.76; 3.81.
- Number of collisions: 13 500; 1 581 000; 1 883 000.
- Max. frame delay [ms]: 3,2; 7,5; 16,2.

As it might have been expected, comparing the size of generated streams and available bandwidth, network usage is very low, whereas the telephony quality very high. Maximum delays (averaged for a given scenario) of 3–16 ms guarantee that the possible jitter will not have a significant impact on deterioration of the telephone call. The tests did not consider the traffic from outside the system. It can be assumed that in the crisis situation described, there will be no data exchange due to the lack of power supply in the area of disaster.

6. CONCLUSION

The use of Ad-Hoc mode has arisen great interest among owners of smart phones. According to authors of this paper, such phone service would very prospective, in particular considering the fact that its use in critical situation is the only method for provision of "any communication". However, Google — the main player on the market — is not currently interested in supporting Ad-Hoc Wi-Fi. The need to adapt 802.11ac to Ad-Hoc mode was reported by the Japanese after the disaster in 2011. The question of whether the Android users will force the support for Ad-Hoc Wi-Fi will be answered in the near future.

REFERENCES

1. Jarmakiewicz, J., "A resource management strategy based on the available bandwidth estimation to support VoIP across ad hoc IEEE 802.11 networks," *International Journal on Advances in Networks and Services*, Vol. 5, No. 1&2, 2012.
2. Sakano, T., et al., "A rapidly restorable phone service to counter catastrophic loss of telecommunications facilities," *IEEE R10-HTC2013*, NTT, 2013.
3. "4G LTE standard essential patents candidates evaluation 3Q 2014," http://techipminnovationfrontline.blogspot.com/2014/08/4g-lte-standard-essential-patents.html, 2014.
4. "802.11ac gigabit WiFi patents landscape 4Q 2011," http://techipminnovationfrontline.blogspot.com/search/label/WLAN , 2011.
5. Gajewski, P., K. Maślanka, and C. Ziółkowski, "Efektywny algorytm zarzadzania moca w sieciach Ad-hoc," *Przeglad Telekomunikacyjny i Wiadomosci Telekomunikacyjne*, June 2009 (in polish).
6. "Android open source project — Issue tracker, support Wi-Fi ad hoc networking (Issue 82)," https://code.google.com/p/android/issues/detail?id=82, 2011.
7. "Support for WiFi ad-hoc networking marked as "obsolete" in the issue tracker — Reddit," http://www.reddit.com/r/Android/comments/2qi0o7/, 2015.
8. "WifiSettings.java part of official android OS source code, line 849," https://android.googlesource.com/, 2015.
9. "Thinktube — Android IBSS, ad-hoc mode support for android 4.2.24.34.45.0," http://www.thinktube.com/android-tech/46-android-wifi-ibss, 2015.
10. "Wi-Fi alliance — Wi-Fi direct," http://www.wi-fi.org/discover-wi-fi/wi-fi-direct, 2015.
11. "Android developers — Wi-Fi P2P," http://developer.android.com/guide/topics/connectivity/wifip2p.html, 2015.
12. Camps-Mur, D., A. Garcia-Saavedra, and P. Serrano, "Device to device communications with WiFi Direct: overview and experimentation," *IEEE Wireless Communications*, 2013.
13. "Tapestry of Wi-Fi direct — Youtube," https://www.youtube.com/watch?v=6emgRvH4mTo.
14. "MITRE: Android manet manager, push to talk, manet visualizer, manet logger, manet OlSRd."
15. Thomas, J. and J. Robble, "Off-grid communications with android meshing the mobile world," *Proceedings of IEEE Conference on Technolo-gies for Homeland Security*, 2012.
16. "SPAN project," https://github.com/ProjectSPAN/.
17. "Multihop communication over android wireless mesh network," http://www.fp7-proactive.eu/article/multihop-communication-over-android-wireless-mesh-network.

Improvement of the Radiated Immunity Test Using a Broadband Signal

Hongsik Keum[1], Gunsuk Yoo[1], Jungyu Yang[2], and Heung-Gyoon Ryu[3]

[1]Electromagnetic Wave Technology Institute, RAPA, South Korea
[2]Department of Radio Environment Safety, Radio Research Agency, South Korea
[3]Department of Electronic Engineering, Chungbuk National University, South Korea

Abstract— In this paper, we have investigated improvement of the radiated immunity test using a broadband signals. We have analyzed the recent standardization activity related with radiated immunity test based on IEC 61000-4-3 and have proposed a new test method using digitally modulated broadband signals to improve the testing time and frequency step. The possibility of this new test method has been practically verified through a radiated immunity test on GTEM cell. The results show that the devices were influenced same or much more by digital modulation signal than by AM signal. It shows that we can use the broadband signal for a radiated immunity test and it is possible to improve the RS test using new method.

1. INTRODUCTION

Owing to progress of Information Communication Technology convergence, sources of electromagnetic interference have proliferated and the immunity requirements for electronic products have been strengthened to prevent the interference caused by those sources [1].

The radiated immunity test according to IEC 61000-4-3 is performed with the amplitude modulation (AM) signal source and is tested using 1% step increment to reduce the testing time on the frequency band from 80 MHz to 1 GHz [2].

The wireless communication services are being evolved to long-term evolution (LTE) technology where it transmits information through broadband signal. Research results reported that the influence caused by the digital modulation (DM) signal sources has been elevated and it is greater than that of AM, and therefore the DM signal should be incorporated into RS test sources in order to reflect these changes on wireless environment [3, 4].

In this paper, we investigate a method using the broadband signal as a signal source for RS test, to solve a problem of frequency omission caused by 1% step increment and reduce a long spent time during radiated susceptibility (RS) test.

We have performed a RS test using a giga transverse electromagnetic (GTEM) cell to verify that the AM signal for a RS testing is possible to be alternate with a broadband signal. And then we have compared and analyzed the test results obtained using with a AM and broadband LTE signal.

2. IMPROVEMENT PLAN OF RS TEST BY USING A BROADBAND SIGNAL

As mentioned in the above paragraph, the test in this study uses the broadband signal instead of the narrow band AM to solve a problem of frequency omission and to reduce extended time spent during radiated susceptibility (RS) test.

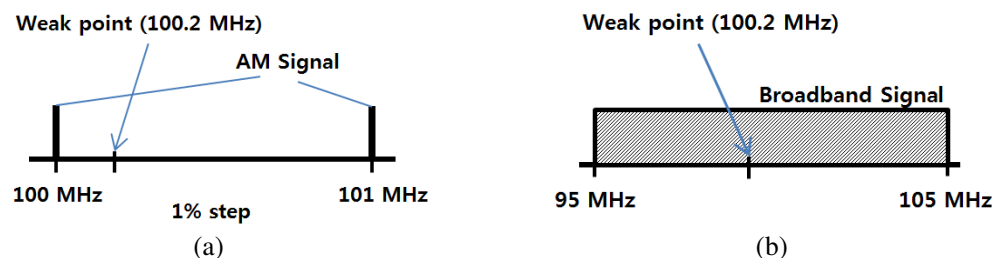First, let us suppose that a EUT has a weak point at 100.2 MHz.

Figure 1: Improvement effect of a broadband signal. (a) Frequency omission issues of AM signal. (b) Effect of whole frequency band test of a broadband signal.
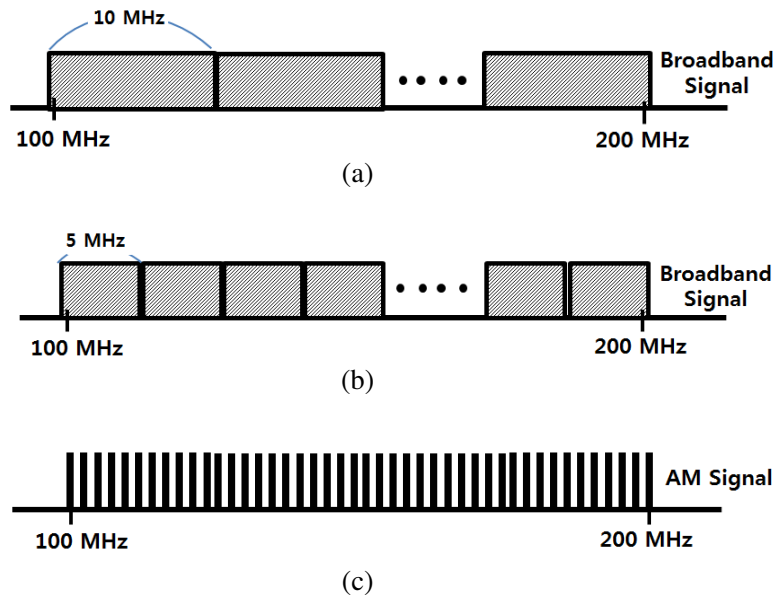
(a)

(b)

(c)

Figure 2: Effect of the test time reduction using a broadband signal. (a) Testing by 10 MHz bandwidth signal. (b) Testing by 5 MHz bandwidth signal. (c) RS test by AM signal.

In case that the weak frequency is located among frequencies to be tested during RS test, there arise a problem of skipping this frequency. It is shown in Figure 1(a). However, when the broadband signal is used, the entire frequency band as a bandwidth of broadband signal can be tested while the weak point is included within the bandwidth. It is shown in Figure 1(b).

Second, let's suppose that a EUT have causing an error between from 100 MHz to 200 MHz during RS test. If we use a broadband signal with 5 or 10 MHz bandwidth, it is achieved the effect that the test time could be shorten. It's shown at Figure 2.

3. TEST SET-UP AND CONDITIONS

To verify the effect of using a broadband signal for RS test, a RS test has been performed within a GTEM cell according to IEC 61000-4-20. To easily recognize the influence of RS, an EUT is used as a speaker with an amplifier. As a signal source the LTE signal of 10 MHz bandwidth is used with no load condition because this load condition of LTE is the worst condition reported [5].

In order to make the peak level of two signals equivalent, the signal generator is set with output level of −30 dBm at AM and −20 dBm at LTE.

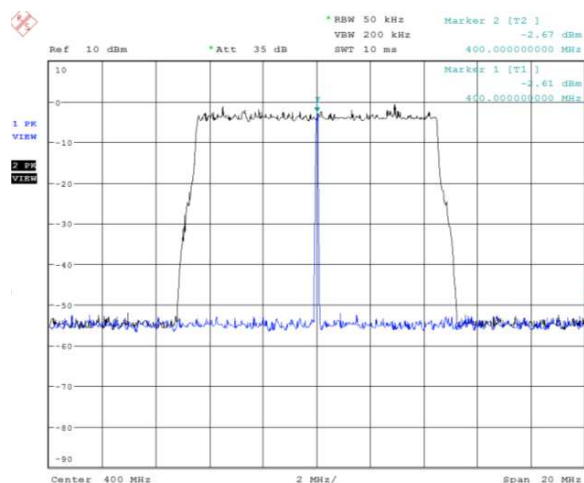The radiated signal spectra are presented in Figure 3.

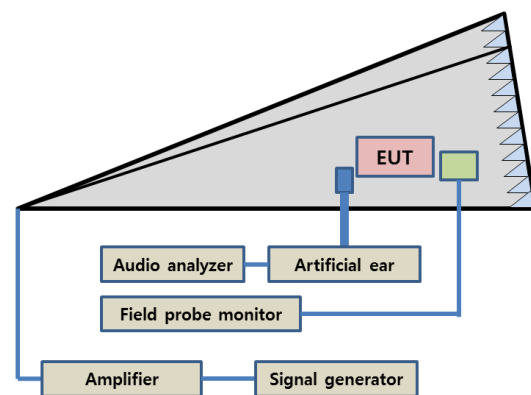Figure 3: Generated AM and LTE signal spectrums.

Figure 4: Test set-up.

The test setup is configured as shown in Figure 4.

In order to measure the output sound of the EUT, an artificial ear and an audio analyzer are utilized.

The calibration is performed to make a uniform field at the field strength of 3 V/m within the frequency range from 80 MHz to 1 GHz in accordance with IEC 61000-4-20. Test signal is generated by using a Vector Signal generator and is applied to the GTEM Cell through the amplifier. The signal level is set with the calibration level.

The RS test is performed at the frequency band between 80 MHz to 1 GHz.

Influence of RS for the EUT is measured by the value of noise level as the audio analyzer measures the noise sound generated by the speaker during RS test. Noise level is 5 mV at the absence of RS source, and that value of recognizable noise is 22 mV.

4. TEST RESULT AND ANALYSIS

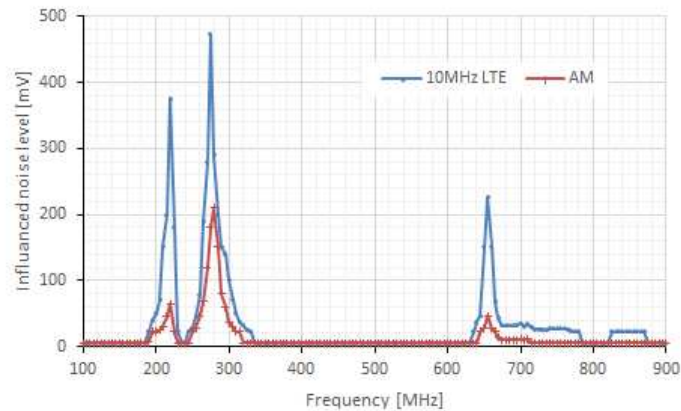The test result is shown in Figure 5.

Figure 5: Test result.

In case of radiating the AM source, the RS disturbance is caused by the frequency band from 185 MHz to 235 MHz. In case of radiating the LTE source, the RS disturbance is caused by the frequency band from 190 MHz to 229 MHz. As predicted above, the disturbance is occurred during the overlap between the weak points and the spectrum of the broadband signal. And also the broadband signal has made a disturbance on wider band than that caused by AM. The weak points may have been skipped because AM is a narrow band signal. In the contrary, since the LTE is the broadband signal, the whole frequency band can be tested without omission.

5. CONCLUSION

In these days, broadband signals such as LTE and Wi-Fi are more widely used than AM signals. And the requirements for RS testing using them are getting more strict and complex.

In this study, we have suggested a method using the broadband signal to cover current RS test problems and then verified it experimentally.

Test result demonstrates that the broadband signal generates interference in a wider frequency band than AM signal and it covers AM bandwidth range.

And therefore we conclude that the AM signal sources can be replaced by broadband signals.

By using the broadband signal, frequency omission due to 1% step scan can be effectively prevented and it leads to reduced test time due to the wide bandwidth of the broadband signal.

REFERENCES

1. Jaekel, B. W., "Electromagnetic environments — Phenomena, classification, compatibility and immunity levels," *EUROCON'09, IEEE*, 1498–1502, 2009.

2. IEC 61000-4-3, *Electromagnetic Compatibility (EMC) — Part 4-3: Testing and Measurement Techniques — Radiated, Radio-frequency, Electromagnetic Field Immunity Test*, 3rd Edition, 2nd Amendment, IEC, Mar. 2010.

3. Keum, H. S., W. S. Cho, J. G. Yang, H. G. Ryu, and S. H. Choi, "Analysis upon the effect of the immunity of electronic devices by the emitted digital modulated signals," *2012 International Symposium on IEEE Electromagnetic Compatibility (EMC EUROPE)*, 1–5, 2012.

4. Keum, H., J. Yang, and H.-G. Ryu, "Analysis of immunity by RF wireless communication signals," *PIERS Proceedings*, 64–69, Guangzhou, Aug. 25–28, 2014.

5. LTE800 Downlink/DTT Co-existence and EMC test report, *ICT Knowledge Transfer Network and Wireless Testing and Innovation Centre (Wireless TIC)*, Mar. 2013.

Study of a Wide-band Strip Line Couplers' Susceptibility Based on the Number of Transmission Lines with Non-uniform Impedances

Javad Soleiman Meiguni and Ehsan Faalpour

Faculty of Electrical and Computer Engineering, Semnan University, Semnan, Iran

Abstract— Hybrids and couplers are commonly used for the microwave applications as very important elements. These elements are made from various forms and used at the specific applications. The strip line structure is one of the cheap structures for couplers and hybrid's design due to their less radiation loss and interference on the micro strip. Presented is a wideband stripline directional coupler which is of interest in any measurement application. The susceptibility parameter of this coupler at 2–6 GHz band, have been reported based on the number of transmission line with non-uniform impedances.

1. INTRODUCTION

Directional couplers are essential components in various microwave applications for sampling from a signal or measure its power or to inject it into other parts of the system. The directivity parameter of a directional coupler is important in case of power measurement [1–5]. Accuracy of the coupling factors depends on the dimensional tolerances for the spacing of the two coupled lines. The $\lambda/4$ coupled line design is valid for coaxial and stripline implementations due to their homogeneous medium. A single 4 coupled section is good for bandwidths of less than an octave. To achieve greater bandwidth multiple $\lambda/4$ coupling sections are used. The design of such a couplers proceeds in much the same way as the design of distributed element filters.

In this paper, we present a directional coupler in 2–6 GHz band based on non-uniform transmission line design method. The sensitivity of the results due to variance of the number of sections has been reported. In order to carry out the boundary lines for this coupler, we are in need to solve an integral representing the coupling factor numerically. This integral has been solved for a 20-dB coupling factor in 2–6 GHz band.

2. COUPLER DESIGN

Figure 1 illustrates an N-section schema for an integrated non-uniform coupler. As we can see at the Fig. 1 coupler is made of the number of N transmission lines with unequal impedances. A numeric integration is performed to calculate even mode impedances namely Z_{oe}. The design procedure is carried out by means of equally ripple transmission and proper impedance bandwidth. Fig. 2, shown the steps to generate symmetrical coupler formulas with cascading ABCD matrices. The main purpose of these steps is to find out the polynomial function namely $P_N(\sin\theta)$ with equally rippled response in the frequency band of the coupler. Here, θ is the electrical length of each section. The $P_N(x)$ response has been shown in Fig. 3.

In this figure, P^+ and P represent for maximum and minimum value of $P_N(x)$ function. Details are reported in [6]. In order to find out the even mode impedances which use in boundary line
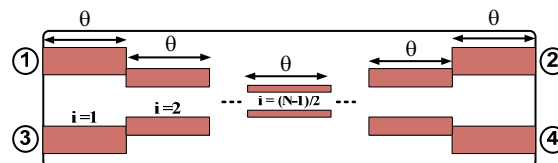
Figure 1: Internal structure of an N-section non-uniform coupler.
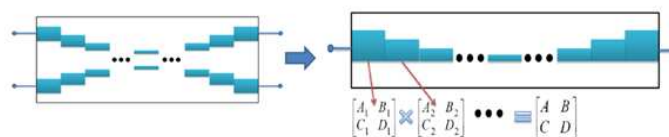
Figure 2: Steps to obtain symmetrical coupler formulas.
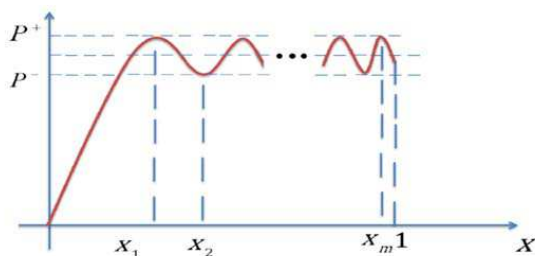
Figure 3: Ideal $P_{\mathrm{N}}(x)$ response.

calculation of the coupler, one need to solve a numeric integration reported in [7]:

$$\frac{1}{2}\ln\frac{Z_{0e}(u)}{Z_0} = \int_{\frac{-d}{2}}^{u} P(u)du = \frac{-R}{\pi}\int_{\frac{-d}{2}}^{u} wi \cdot \frac{\sin^2(\frac{u}{2})}{\frac{u}{2}}du \tag{1}$$

In which, R is the coupling coefficient and d is the length of the coupler and w_i represents the weighted parameters for i-th section.

Figure 4 illustrates the even-mode impedances versus the coupler length.
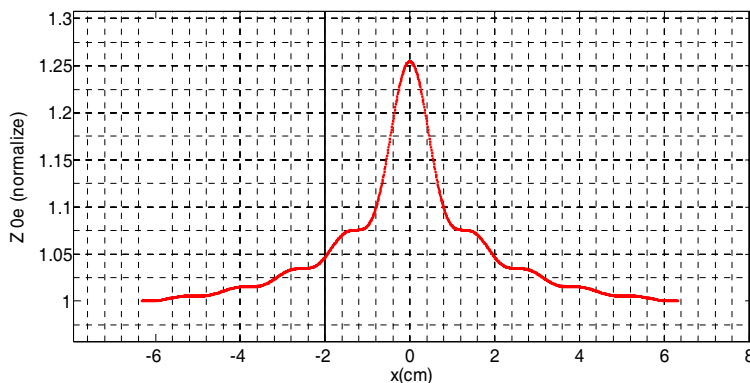
Figure 4: Even-mode impedances of nonuniform coupler.

The boundary lines of the coupler for a 20-dB coupling factor have been shown in Fig. 5
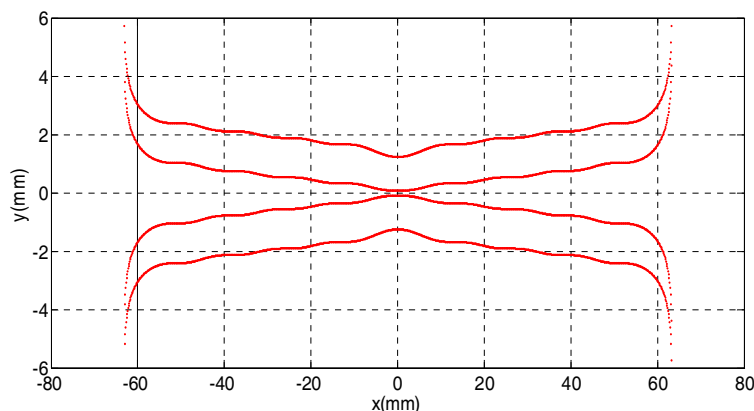
Figure 5: The boundary lines of the designed 20-dB coupler.

Presented focuses of the impact factor of this numerically integration namely L factor.

3. SIMULATION RESULTS

The aforementioned coupler has been simulated with CST microwave studio software [8]. An RT-Druid 5880 material is used for substrate with 31 mil thickness. Simulations have been done with variable $L = 40$, 50, 60 depicted in Fig. 6.
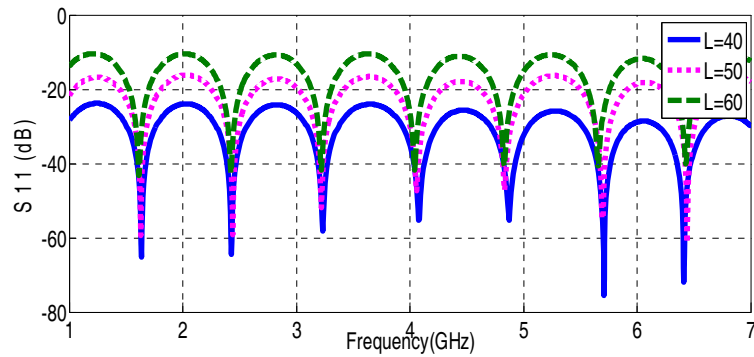
Figure 6: S_{11} parameters of the coupler with variable L parameter.

As shown in Fig. 6, choosing $L = 40$ yields to a better response of the coupler. The optimum design is shown in Fig. 7 in the CST microwave studio.
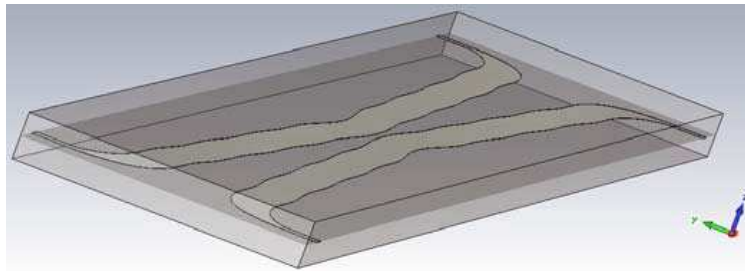
Figure 7: The coupler structure.

Coupling coefficient and return loss of the coupler are shown in Fig. 8.
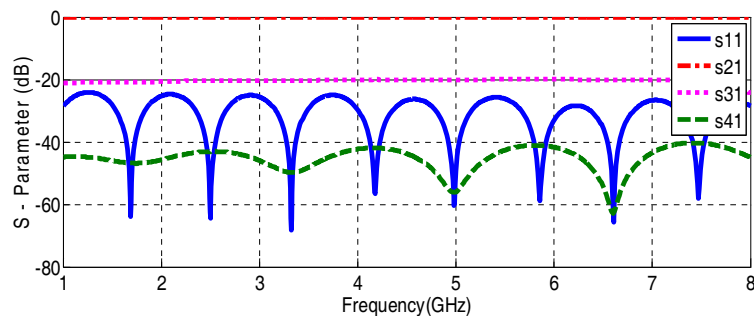
Figure 8: The scattering parameters of the designed coupler.

4. CONCLUSION

In this paper, we design a stripline coupler based on nonuniform transmission line impedances. We observe that the best value of the design can be obtained by changing the number of transmission lines. For a 20-dB coupler, $L = 40$ gives better responses rather than other parameters of L.

REFERENCES

1. Pozar, D. M., *Microwave Engineering*, John Wiley & Sons, Inc., 2005.

2. Mongia, R., I. Bahl, and P. Bhartia, *RF and Microwave Coupled-Line Circuits*, Artech House, Inc., 1999.

3. Tresselt, C. P., "The design and Construction of broadband, high-directivity, 90-degree couplers using nonuniform line technique," *IEEE Transaction of Microwave Theory and Techniques*, Vol. 14, 647–656, December 1966.

4. Seidel, H. and J. Rosen, "Multiplicity in cascade transmissoion line synthesis — Part 1," *IEEE Transaction of Microwave Theory and Techniques*, Vol. 13, 275–283, May 1965.

5. Saulich, G., "A new approach in the computation of ultrahigh degree equal-ripple polynominals for 90-Couplersynthesis," *IEEE Transaction of Microwave Theory and Techniques*, Vol. 29, No. 2, February 1981.

6. Cristal, E. G. and L. Young, "Theory and tables of optimum symmetrical TEM-mode coupled-transmission-line directional coupler," *IEEE Transaction of Microwave Theory and Techniques*, 544–558, September 1965.

7. Shelton, J. P., "Imperdances of offset parallel-coupled strip transmission lines," *IEEE Transaction of Microwave Theory and Techniques*, Vol. 14, No. 1, 7–15, January 1966.

8. *CST Reference Manual*, Computer Simulation Technology, Darmstadt, Germany, 2008.

Steady-state Analysis of Permanent Magnet Synchronous Machine for Integrated Starter-alternator Applications

Florin Jurca and Daniel Fodorean

Department of Electrical Machines and Drives, Technical University of Cluj-Napoca, Romania

Abstract— In the last decade due to their high efficiency and reliability, permanent magnet synchronous machine are widely used in automotive applications. There are two main reasons for this trend: the reduction of the fuel consumption and the increase of the travel comfort. In this study we consider the approaches of electromagnetic design of a special topology of permanent synchronous machine (radial flux machine with outer rotor) suited for automotive applications. The study design requires some analytical analysis, followed by a numerical one in order to attain the performances of the proposed machine in all three cases (starter-alternator-booster). A thermal analysis is required in order to determine the thermal requirements for the automotive applications.

1. INTRODUCTION

Current research efforts related to electric cars have problems mainly related to the accumulation of electricity. In this context (low autonomy, lack of fast charging stations) the use of this type of machine is limited to urban trails. Initially considered as a transition between conventional vehicles and the electric ones, the hybrid vehicles remain an alternative that is gaining more ground by combining the advantages of both types of vehicles. Of the two types of series and parallel hybrid vehicles, alternative series provides a simpler connection between the two engines and transmission power train. Passing to the present path of development of hybrid vehicles involves increasing the role in the operation of the electrical machines by increase its power and "responsibility" (starter-alternator-booster). The first steps were be made by using a single electric machine as a generator (alternator) and motor (starter) for starting the internal combustion engine, but for a hybrid car a second electrical machine is used for the electric propulsion. The simplification of this structure involves the use of a single electric machine incorporating three operating modes: starter-alternator-booster (ISAB). In this case ISAB will initially be able to start internal combustion engine, then when turned on will switch to a generator and will supply the electricity consumers and the electricity storage system. Due to the control strategies used, electrical machine is capable to move quickly from generator to motor (booster) and back to help the internal combustion engine for a short period of time (maximum 2 minutes), in situations where additional mechanical energy is necessary (overruns, ramps etc.) [1, 2].

The ISAB can be connected to a gasoline or diesel engine either directly through crankshaft or indirectly through belt drive, and they are accordingly called the belt-driven starter alternator (BAS) and normal ISAB, respectively. The permanent synchronous machine with outer rotor is an innovative solution of direct connection to the internal combustion engine in both cases in the context of minimal mechanical losses. Comparative whit other types of electrical machines, the permanent magnet (PM) synchronous machines have some important advantages like high power density, high efficiency and the possibility to work in high overload [3].

The present paper approaches the design and analysis of a special topology of the permanent magnet synchronous machine (radial-flux machine with outer rotor) suited for automotive application. A preliminary design procedure will be presented and the results will be implemented in a FEM based software in order to analyze the performances of the machine: magnetic field density, induced emf, torque and current. After that a thermal analysis is required because the thermal behavior can drastically influence the machine's performances. Thus a special attention should be paid on the heat transfer within the active and non-active parts of the machine.

2. PRELIMANARY DESIGN

The main problem at the electrical machine design is to find a set consisting of topological structure, materials, and geometry for a specific application. The selection of the proper machine topology for a specific application is a difficult problem to be solved during the design process.

In order to improve the electrical machines performances, several winding topologies will be analyzed. The output performances of the studied motor are: P — 6 (kW); rated voltage U_n — 72 (V); rated speed n_n — 400 rpm; pole pair number p — 15.

The output power of the electric machine, when the leakage reactance is neglected, is expressed by the number of phases of the machine, n_{ph}, the phase current, $i(t)$, the inducted electromotive force (emf), $e(t)$ [4]:

$$P_{out} = \eta \cdot \frac{n_{ph}}{T} \cdot \int_0^T e(t) \cdot i(t) dt = \eta \cdot n_{ph} \cdot k_p \cdot E_{\max} \cdot I_{\max} \tag{1}$$

In the previous equation, T is the period of one cycle of emf, $E_{\max}$, and $I_{\max}$ represent the peak value of the emf and phase current, η is the estimated efficiency, k_e — the electromotive force coefficient.

$$E_{\max} = k_E \cdot N_t \cdot B_{gap} \cdot D_{gap} \cdot L_m \cdot \frac{f_s}{p} \tag{2}$$

Using the coefficients $k_L = L_m/D_{gap}$ (geometric coefficient), $k_i = I_{\max}/I_{rms}$ (current coefficient) and the phase load ampere-turns [4],

$$A_t = \frac{2}{\pi} \cdot N_t \cdot \frac{I_{rms}}{D_{gap}} \tag{3}$$

it is possible to define the air-gap diameter of the machine:

$$D_{gap} = \sqrt[3]{\frac{2 \cdot p \cdot P_{out}}{\pi \cdot n_{ph} \cdot A_t \cdot k_e \cdot k_i \cdot k_p \cdot k_L \cdot \eta \cdot B_{gap} \cdot f_s}} \tag{4}$$

The power and the voltage coefficients are defined according to the type and current wave form, in this case the sinusoidal wave form is $k_i = \sqrt{2}$, $k_p = 0.5$ [4, 5].

By choosing the type of permanent magnet and the number of slots, and also using the expression of the air-gap diameter, the designer can determine all other geometrical parameters.

The air-gap flux density is computed based on the following formula:

$$B_{gap} = \frac{h_m \cdot B_{rm}}{\frac{D_{gap}}{2} \cdot \left(\ln \left(\frac{R_{scr} - gap}{R_{so}} \right) + \ln \left(\frac{R_{cr}}{R_{cr} - gap} \right) \right)} \tag{5}$$

For active parts of the machine, it was used good quality PMs material, of Nd-Fe-B N48 type, with 1.4 T flux density. The steel is made of M270-35A sheets.

The frequency, the number of turns, the air-gap flux per pole and a demagnetization coefficient (usually between 0.8–0.9 for rare earth PMs) make up the expression of the electromotive force:

$$E_{ph} = \sqrt{2} \cdot \pi \cdot f_s \cdot N_t \cdot k_{ws} \cdot \Psi_{gap} \cdot k_d \tag{6}$$

Next, the usual electromechanical characteristics can also be computed [5]:

$$P_{in} = n_{ph} \cdot U_{ph} \cdot (I_q \cdot \cos(\delta) - I_d \cdot \sin(\delta)) \tag{7}$$

$$P_{out} = P_{in} - \sum \text{Losses} \tag{8}$$

P_{out} — the output power, function of input power and the sum of losses (iron, copper, mechanical and supplementary losses).

$$T_m = \frac{P_{out}}{\Omega} \tag{9}$$

$$\cos(\phi) = \frac{P_{in}}{n_{ph} \cdot U_{ph} \cdot I_s}, \quad \eta = \frac{P_{in}}{P_{out}} \tag{10}$$

The obtained main dimensions and the results for the operation at rated point are shown in Table 1. The obtained structure with winding distribution is presented in Figure 1.

Stator outer diameter [m]	0.186
Rotor inner diameter [m]	0.201
Rotor outer diameter [m]	0.230
Shaft diameter [m]	0.130
Stack length [m]	0.280
Air-gap [m]	0.0015
Air-gap flux density [T]	1
Rates speed [rot/min]	400
Phase emf [V]	42
Rated current [A]	72
Power factor [%]	0.9
Efficiency [%]	0.87
Torque [N*m]	150

Table 1: The obtained results for the designed electrical machine.
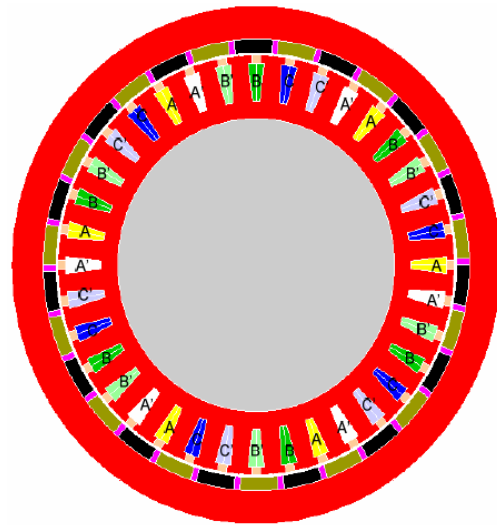
Figure 1: Studied electrical machine.

3. MAGNETIC FIELD ANALYSIS

The finite element method (FEM) is a powerful tool for the design of the electrical machines and others electromagnetic devices. FEM is a simple, robust and efficient widely used method of obtaining a numerical approximate solution for a given mathematical model of the machine. For the proposed machine FEM was used in order to observe the behavior of the machine in all operating regimes (starter-alternator-booster). Thus, we accomplished a simulation scenario in which the proposed machine is analyzed in the three considered operating regimes. In order to do this the circuit presented in Figure 2 was implemented.

The behaviour of the machine in all three regimes is presented (starter-alternator-booster) in Figure 3 (torque profile), 4 (phase voltage and current on the machine), 5 (dc voltage and current obtained on the load).
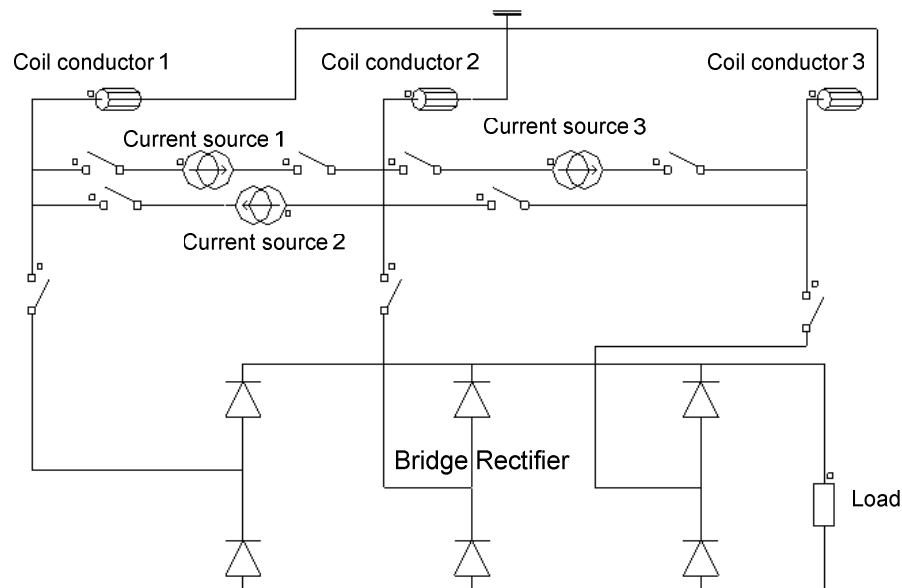
Figure 2: The circuit model of ISAB regime.
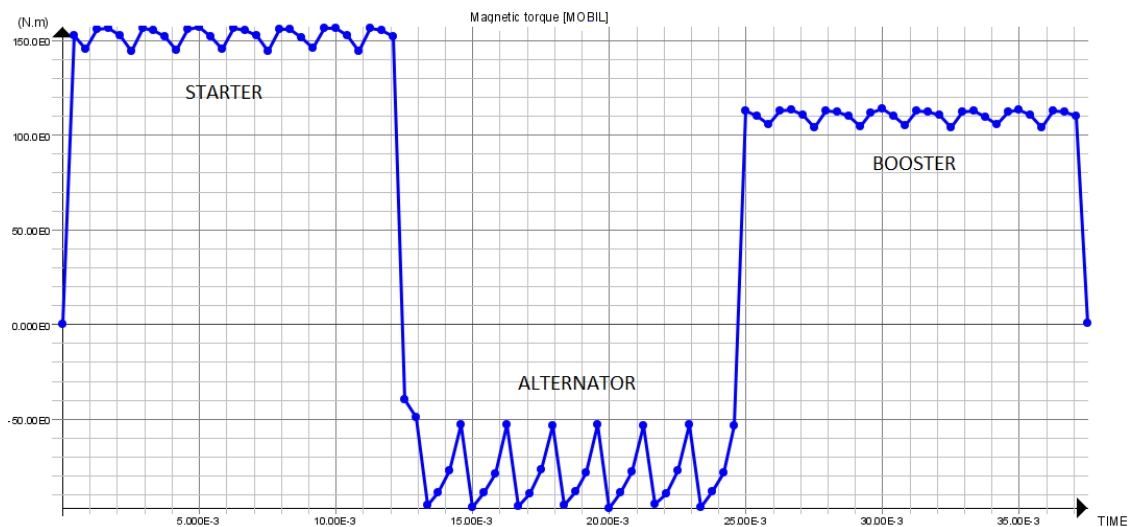
Figure 3: ISAB torque profile.
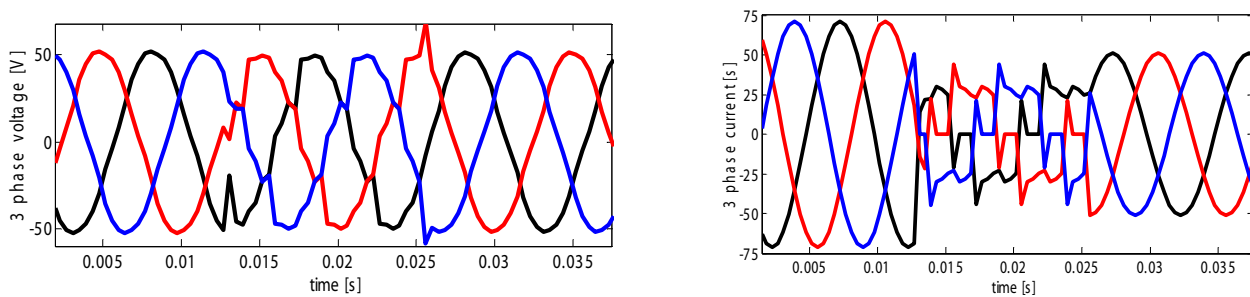
Figure 4: Three phase voltage and current obtained in ISAB regime.
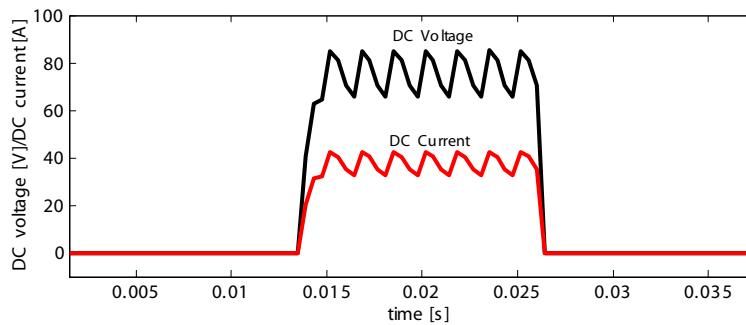
Figure 5: DC voltage and current obtained in alternator regime.

4. THERMAL ANALYSIS

In automotive applications with combustion engine, the thermal behaviour can drastically influence the machine's performances. Thus a special attention should be paid on the heat transfer within the active and non-active parts of the machine. The heat sources on the machine are: the cooper loss, the iron loss and the mechanical loss. The thermal analysis for the proposed machines was carried out using dedicated software Motor-CAD. After implementing the geometry, the winding, the materials, iron and joule losses, the cooling condition and torque profile depending on time are defined. In our case we consider the self-ventilation depending of speed for the proposed integrated starter-alternator-booster.

Usually the starter procedure lasts about 1 second, so in Motor-CAD we have set it to 10 second in order to obtain relevant results about the obtained temperature in the machine in starter mode (Figure 6). For starter mode we have considered 15 second in condition of variable load, and for
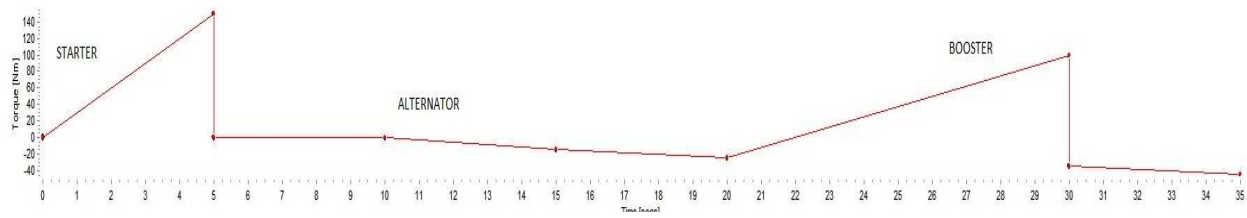
Figure 6: Duty cycle configuration.
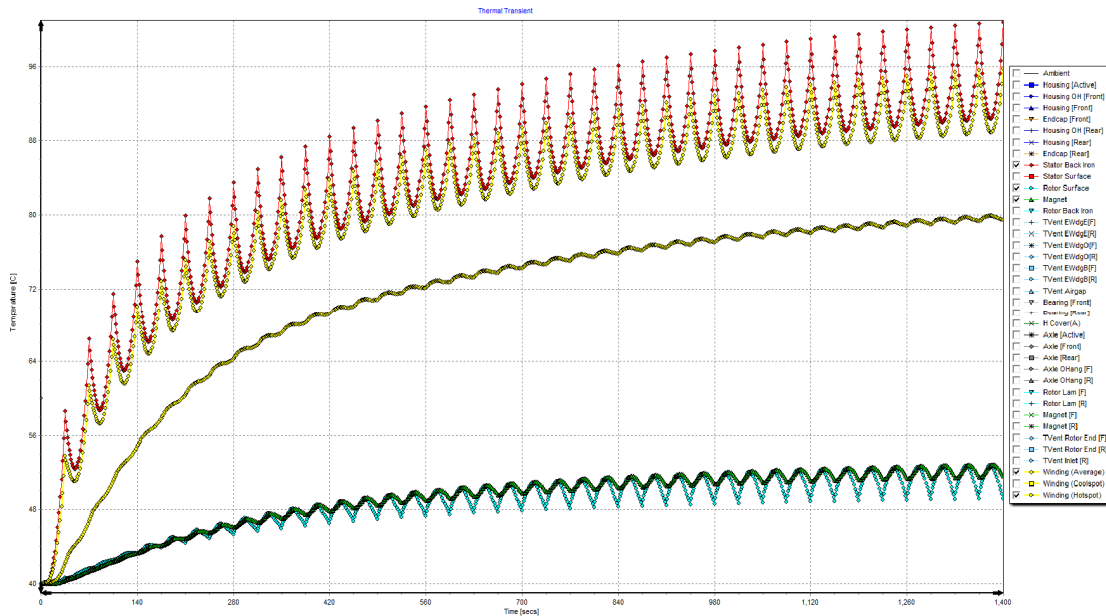
Figure 7: Thermal analysis of the proposed machine, with Motor-CAD: temperatures variation on duty cycle's.

booster we set 10 second. The analysis was made for 40 duty cycles. Highest temperatures were obtained the winding and stator back iron (96 C°), while in the permanent magnet the temperature is around 48 C°.

5. CONCLUSIONS

In this paper a structure of permanent magnet synchronous machine with outer rotor, suitable for automotive application (integrated starter-alternator-booster) is presented. The preliminary design model of the machine was developed followed by a simulation with finite element method in Flux 2D for ISAB regime. The results obtained here provide valuable information on the machine's behavior in all three operating mode. The thermal analysis for the proposed machines was carried out in order to evaluate the thermal stress of the ISAB.

ACKNOWLEDGMENT

REFERENCES

1. Cai, W., "Comparison and review of electrical machine for integrate starter-alternator applications," *IEEE Industry Applications Society Annual Meeting (IAS)*, 386–393, 2004.

2. Barcaro, M., A. Alberti, L. Faggion, M. Sgarbossa, M. Dai Pr'e, and N. Binachi, "Expereimental tests on a 12-slot 8-pole integrated starter-alternator," *Proceedings of the 2008 International Conference on Electrical Machines*, 1–6, 2008.

3. Mirahki, H. and M. Moallem, "Design improvement of interior permanent magnet synchronous machine for integrated starter alternator application," *2013 IEEE International Elec-*

tric Machines & Drives Conference (IEMDC), 382–385, IEEE Conference Publications, DOI: 10.1109/IEMDC.2013.6556279, 2013.

4. Fodorean, D., A. Djerdir, I. A. Viorel, A. Miraoui, and A. Double, "Excited synchronous machine for direct drive application — Design and prototype tests," *IEEE Transactions on Energy Conversion*, Vol. 22, No. 3, 656–665, Sep. 2007, ISSN 0885-8969.

5. Jurca, F. and D. Fodorean, "Axial flux interior permanent magnet synchronous motor for small electric traction vehicle," *International Symposium on Power Electronics, Electrical Drives, Automation and Motion, SPEEDAM*, 365–368, Sorrento, 2012, ISBN: 978-1-4673-1299-8.

Prediction of Temperature and Stress in a Multi-stage Depressed Collector under Different Enviornmental Conditions

Vishant Gahlaut[1] and Sanjay Kumar Ghosh[2]

[1]Department of Physics, Banasthali University, Banasthali, Rajasthan, India
[2]CSIR-Central Electronics Engineering Research Institute (CEERI), Pilani, Rajasthan, India

Abstract— Increasing requirement of traveling-wave tubes (TWTs) with high efficiency, high power, high gain in addition with weight and size reductiondemand proper thermal management. Specially, collectors in TWTs have to have very good heat dissipation as spent electron beam is dumped here. In high efficiency TWTs, the maximum power of the spent electron beam is recovered by collecting the electrons at different electrode potentials and remaining unrecovered power is waste as heat. The potentials of electrodes are essentially negative with respect to cathode, hence, coined as multi-stage depressed collector (MDC). With the increasing demand in size and weight reduction, complexity in thermal packaging enhances. This paper presents thermal and structural parameters, namely, temperature and stress distribution in different parts of a MDC using different software packages.

1. INTRODUCTION

With the modern innovative design concepts and with the state of the art of the technologies, high power wide band TWTs with reduced size and weight are being developed for long life and reliability applications. Efficient thermal management need proper thermal packaging, but a heavy packaging enhances the weight of the device. Thus, high efficiency, long life TWTs efficient thermal management [1–4].

MDC of a TWT is being heated up during operation due to dumping of spent electron beam and which is dissipated either through conduction and or radiation [5]. Here, source of heat is the electron beam and environment is the sink through base plate, thus, variation of environmental temperature conditions affects variation of temperature and stress in MDC. Hence, proper packaging and choice of material is very important for efficient heat dissipation at reduced size and weight of the TWT.

In this paper, authors have studied heat dissipation, expansion and stresses developed among the collector electrodes in a MDC under different environmental conditions and study has been made using COSMOS which provides one screen solution for thermal, stress, frequency and harmonic analysis. Three dimensional modeling of the complex geometry of MDC with symmetry is
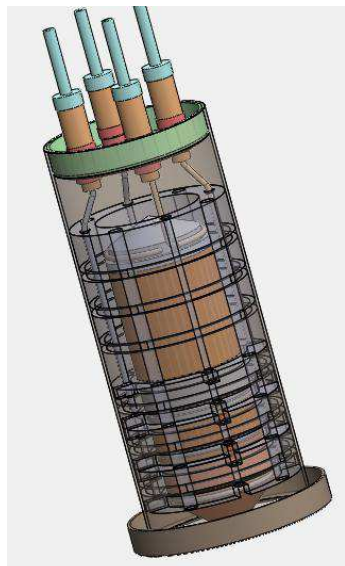
Figure 1: Thermal model of four-stage MDC.

constructed in Solid Works and imported in COSMOS finite element (FE) analysis. It has also mesh controller which enables to apply various mesh size in different zone as per requirement of level of accuracy. Range of element size can used in meshing of model with tolerance required to adjust the element size during meshing. Moreover, to validate the simulation in COSMOS, results have also been compared with different software packages, namely, ANSYS.

2. MODEL

Axially symmetric four stage MDC, under study (Figure 1), have been analyzed-using COSMOS, to predict both temperature distribution at ambient temperature ($+25°C$) as well as under different environmental conditions, typically, $-25°C$ and $+80°C$. Moreover, expansion of electrodes and stress developed at different braze joints have also been studied under RF condition, that is, when RF power is extracted. Under RF condition amount of spent beam energy recovered or amount of energy dissipated among the collectors are different and, thus, expansion, temperature and stress developed among the electrodes are different.
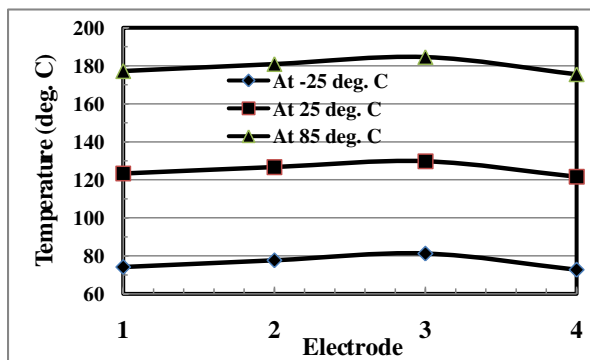
Figure 2: Electrode temperature under different temperature (environmental) conditions.
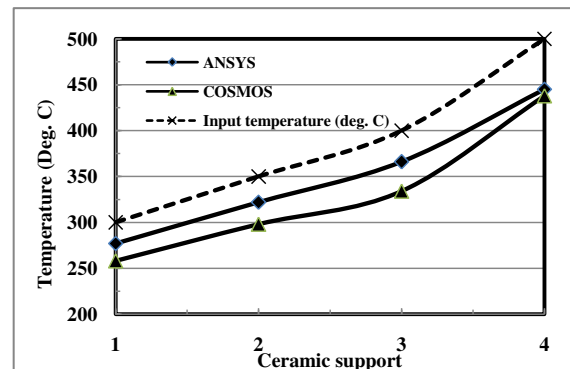
Figure 3: Comparison of temperature distribution without radiator obtained from ANSYS and COSMOS, taking temperature (broken line) as inputs.

3. RESULTS AND DISCUSSION

Boundary conditions are the Emissivity of the standard materials is given elsewhere. Thermal resistance 4.0e-5 K-m2/W at brazing joints. Figure 2 shows temperature distribution on collector electrodes under different environmental temperature conditions for same input conditions. Temperature distribution in electrodes is different when ambient temperature is different. At the extreme condition ($80°C$), the temperature in all the collector electrodes is much more compare to other two conditions.

A comparison of study has also been done using different software packages (Figure 3). To study the analysis under different software, generalized inputs have been applied in terms of temperature at the inner surface of collector. It is shown from the figure that the results obtained from different software are closely agreeing and hence further study have been made using COSMOS.

REFERENCES

1. Fong, H. H. and D. J. Hamel, "Thermal/structural analysis of travelling wave tubes using finite elements," *IEEE Trans. on Electron Devices*, CH1504-0/79/0000, 1979.
2. Han, Y., Y.-W. Liu, Y.-G. Ding, P.-K. Liuand, and C.-H. Lu, "Thermal analysis of a helix TWT slow-wave structure," *IEEE Trans. on ED*, Vol. 55, No. 5, May 2008.
3. Yao, L. M., Z. H. Yang, B. Li, L. Liao, B. Q. Zeng, and X. F. Zhu, "Thermal analysis of novel helix TWTs," *IEEE Tran. on ED*, Vol. 6, 139–140, 2006.
4. Rocci, P. J., "Thermal-structural reliability assessment of helix TWT interaction circuit using finite element analysis," *Proceeding of the Aerospace and Electronic IEEE Conference*, 1993.
5. Incropera, F. P., D. P. De Witt, et al., *Fundamentals of Heat and Mass Transfer*, 4th Edition, John Willey and Sons., 1996.

Erbium-doped Fiber Laser with Distributed Feedback from a Fiber Grating Array

Xinyong Dong[1, 2, 3], **Junwei Yuan**[3], **Lei Zhu**[3], **Perry Ping Shum**[2, 4], **and Haibin Su**[1, 2]

[1]School of Materials Science and Engineering, Nanyang Technological University, Singapore
[2]CINTRA, Research Techno Plaza, 50 Nanyang Drive, Singapore
[3]Institute of Optoelectronic Technology, China Jiliang University, Hangzhou, China
[4]School of Electrical & Electronic Engineering, Nanyang Technological University, Singapore

Abstract— An erbium-doped fiber laser with low coherence, low threshold, high efficiency and narrow linewidth is demonstrated for the first time based on distributed feedback from a fiber Bragg grating (FBG) array. The FBG array contains tens of FBGs with identical Bragg wavelength but very weak reflectivity of $\sim 5\%_0$, inscribed along a normal single-mode fiber with random separations. Low pump threshold power of 3.0 mW and high slope efficiency of 24% are achieved, which are comparable with that of normal erbium-doped fiber lasers but much better than that of conventional random fiber lasers based on distributed Rayleigh scattering.

1. INTRODUCTION

Random fiber lasers have no classical resonator, but random distributed feedback (RDFB), which make the structure very simple. In recent years, ultra-long Raman fiber lasers based on RDFB from distributed Rayleigh scattering have become a very attractive concept [1–6]. However, high pump power up to Watt level is needed because the scattering efficiency is very low [3]. Moreover, laser spectrum line-width is relatively broad (1 nm or more) [4–6]. To improve the laser performance, a number of techniques have been proposed [7–10]. By using half-opened laser cavity with fiber Bragg gratings (FBGs), one can reduce the pump threshold power roughly by half [7, 8]. By using narrow band filters or reflectors, one can reduce the line-width to ~ 0.1 nm [9, 10]. In 2009, N. Lizarraga et al. reported a random laser based on an Er/Ge co-doped single-mode fiber (SMF) with randomly spaced Bragg gratings being recorded on it [11]. The threshold of the laser is reduced to about 10 mW, and the line-width is about 0.02–0.04 nm. But Erbium-doped fiber (EDF) generates heat when it is working as gain medium, then the reflecting wavelength of the FBGs will move, making the laser output unstable. In 2014, our team reported an EDFL based on RDFB through Rayleigh scattering in a long-distance (5–30 km) SMF [12], where similar results were obtained but less thermal problem. However, the SMF is too long to make the device portable, and it introduce transmission loss.

In this work, we demonstrate a low-threshold, narrow line-width, high efficiency RDFB-based EDFL by using a randomly distributed Bragg grating array with very weak individual reflectivity of $\sim 0.5\%$. High efficiency lasing operation is realized, with low threshold pump power of only 3 mW. The slope efficiency is 24%, which is about tenfold higher than that of the previously reported conventional random fiber lasers amplified through distributed Raman scattering effect [9].

2. LASER DESIGN

Figure 1 shows the schematic diagram of the proposed EDFL based on RDFB from a grating array. It consists of a 1480 nm pump laser with a maximum output power of 400 mW, two 1480/1550 nm wavelength division multiplexers (WDMs), a FBG reflector with central wavelength of 1549.6 nm, line-width of 0.24 nm and reflectivity of 90%, a 2-m-long highly-doped EDF and a weak FBG array. The EDF has a mode field diameter of 6 μm and a high peak absorption coefficient of ~ 11 dB/m at 1480 nm. The pump laser is launched into the EDF through the WDM1. The WDM2 is used to filter out the residual pump power from the laser output. Angled polished connectors are used at the both output ends to eliminate the influence of Fresnel reflection at the fiber ends on the laser operation.

The weak FBG array including twenty identical weak Bragg gratings, was recorded on a SMF (type G.652) by using a frequency-doubled Argon laser with a conventional phase mask technique [13]. The length of each grating is about 5 mm, and the distances between two neighboring gratings are randomly distributed in the range of 4 to 5 m (the total length of the weak FBG array is ~ 100 m). The total and individual reflectivity of the FBGs are about 10% and 0.5%, respectively.
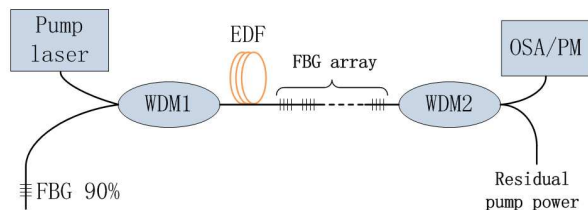
Figure 1: Schematic diagram of the proposed EDFL based on RDFB from a grating array. WDM, wavelength division multiplexer; EDF, erbium-doped fiber; FBG, fiber Bragg grating.
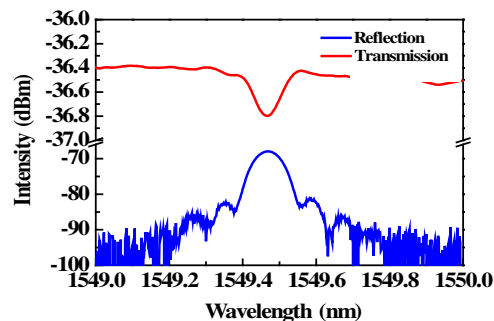
Figure 2: Measured transmission and reflection spectra of the weak FBG array.

A measured transmission and reflection spectra of the FBG array are shown in Fig. 2. The central wavelength and 3-dB bandwidth are 1549.47 nm and 0.1 nm, respectively.

3. LASER CHARACTERIZATION

The lasing operation is grounded on the EDF gain and the resonance between FBG reflection and the backward RDFB provided by the weak FBG array. When the EDF is pumped to generate population inversion of erbium, amplified spontaneous emission (ASE) is generated. Then the selected wavelength reflected by the FBG reflector and the weak FBG array. With increasing power of the pump laser, resonance happens when the gain overcomes the total cavity loss.

The laser output was measured by using an optical spectrum analyzer (OSA) with resolution of 0.02 nm and an optical power meter (OPM). Fig. 3 shows measured output spectra of the laser at different pump powers. Fig. 4 shows the output power against pump power. The threshold power of the fiber laser is about 3 mW, which is much smaller than the value, 10 mW, reported in the EDFL based on RDFB through Rayleigh scattering in a long-distance SMF [12]. The slope efficiency is 24% in our experiment, which is more than tenfold higher than that of the previously reported conventional random fiber lasers amplified through distributed Raman scattering effect [9]. The main reason for the low threshold and high slope efficiency is the RDFB provided by the weak FBG array is much stronger than that provided by Rayleigh scattering in a fiber.

Normally, the fiber lasers based on RDFB have poor stability in both output power and spectrum. For example, the emission peak wavelength and even the number of emission peaks are changing with pump power and time for the previously reported random laser based on randomly spaced FBGs written on an Er/Ge co-doped fiber [11]. Here in our case, the laser only has one emission peak and the peak wavelength is quite stable at around 1549.48 nm when the pump power is raised to over 34.1 mW. This great improvement in laser performances may mainly relate to the fact that all the twenty weak FBGs have the same central wavelength and they were not recorded
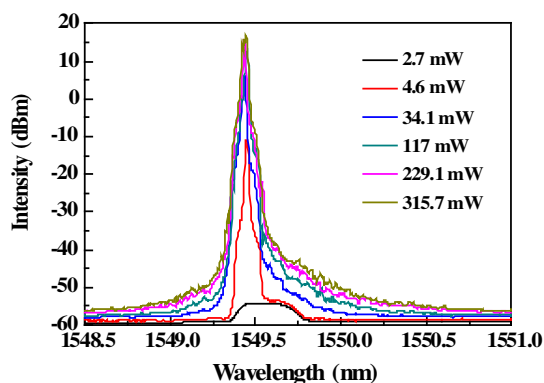
Figure 3: Measured output spectra of the RDFB-based EDFL at different pump power.
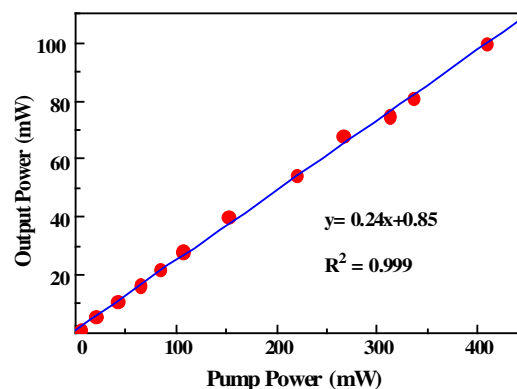
Figure 4: Output power against pump power of the proposed RDFB-based EDFL.

on the active fiber, i.e., the EDF, so their reflection wavelengths are not affected by temperature of the active fiber, which may rise with pump power. There is a small wavelength shift of 0.12 nm, from 1549.60 to 1549.48 nm, when the pump power is increased from just above the threshold to 34.1 mW. That may be caused by the little mismatch between the peak reflection wavelength of the FBG reflector (1549.60 nm) and that of the FBG array (1549.47 nm).

The laser stability with time was also tested. Fig. 5 shows the output spectra recorded every one minute when the pump power is 201 mW. The output lasers have almost same profiles at the whole measurement process, which is much better than that of the random laser based on randomly spaced FBGs written on an Er/Ge co-doped fiber [11]. This is due to the central wavelength of the weak FBG array recorded on the SMF is more stable than that of the FBG array recorded on the EDF with the work time increasing.
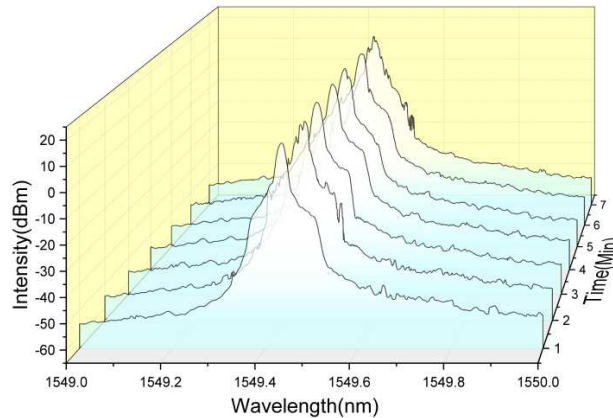
Figure 5: Laser output spectra with time at the pump power of 201 mW.

4. CONCLUSION

A low-threshold, high-efficiency and narrow line-width EDFL has been demonstrated for the first time by using a random distributed Bragg grating array feedback. The laser output spectrum was studied in different pump power. Due to the wavelength-selective feedback of the FBG reflector, the strong RDFB provided by the weak FBG array and the high-efficient gain from the pumped EDF, the threshold power of the achieved EDFL is as low as 3 mW, the slope efficiency in our experiment is up to 24%, which is comparable to that of normal EDFL. We also proved the stability of the laser is better than that of the random laser based on an Er/Ge co-doped SMF with randomly spaced Bragg gratings.

REFERENCES

1. Markushev, V. M., M. V. Ryzhkov, C. M. Briskina, H. Cao, L. A. Zadorozhnaya, E. I. Givargisov, et al., "ZnO random laser spectra under nanosecond pumping," *Laser Physics*, Vol. 17, 1109–1118, 2007.
2. Wiersma, D. S., "The physics and applications of random lasers," *Nature Physics*, Vol. 4, 359–367, 2008.
3. ID, V., C. DV, B. SA, and T. SK, "Cascaded random distributed feedback Raman fiber laser operating at 12 μm," *Optics Express*, Vol. 19, 18486, 2011.
4. Bliokh, Y., Elena I. Chaikina, N. Lizárraga, Eugenio R. Méndez, V. Freilikher, and F. Nori, "Disorder-induced cavities, resonances, and lasing in randomly layered media," *Physical Review B*, Vol. 86, 4583–4586, 2012.
5. Leonetti, M., C. Conti, and C. Lopez, "The mode-locking transition of random lasers," *Nature Photonics*, Vol. 5, 615–617, 2011.

6. Sugavanam, S., N. Tarasov, X. Shu, and D. V. Churkin, "Narrow-band generation in random distributed feedback fiber laser," *Optics Express*, Vol. 21, 16466–16472, July 15, 2013.

7. Zhang, P., T. Wang, Q. Jia, X. Liu, M. Kong, S. Tong, et al., "A novel fiber laser based on Rayleigh scattering feedback with a half-opened cavity," 890617–890617-6, 2013.

8. Zhang, W. L., Y. J. Rao, J. M. Zhu, Z. X. Y. Z. N. Wang, and X. H. Jia, "Low threshold 2nd-order random lasing of a fiber laser with a half-opened cavity," *Optics Express*, Vol. 20, 14400–14405, June 18, 2012.

9. Churkin, D. V., S. A. Babin, A. E. El-Taher, P. Harper, S. I. Kablukov, V. Karalekas, et al., "Raman fiber lasers with a random distributed feedback based on Rayleigh scattering," *Physical Review A*, Vol. 82, 033828, 2010.

10. Sebbah, P. H., C. Vanneste, and H. Cao, "Lasing with resonant feedback in weakly scattering random systems," *Photonic Metamaterials: From Random to Periodic*, WC3, Jackson Hole, WY, 2007.

11. Lizárraga, N., N. P. Puente, E. I. Chaikina, T. A. Leskova, and E. R. Méndez, "Single-mode Er-doped fiber random laser with distributed Bragg gratingfeedback," *Optics Express*, Vol. 17, 395–404, Janury 19, 2009.

12. Wang, L., X. Dong, P. P. Shum, C. Huang, and H. Su, "Erbium-doped fiber laser with distributed Rayleigh output mirror," *Laser Physics*, Vol. 24, 115101, 2014.

13. Guo, H., J. Tang, X. Li, Y. Zheng, H. Yu, and H. Yu, "On-line writing identical and weak fiber Bragg grating arrays," *Chinese Optics Letters*, Vol. 11, 030602, March 1, 2013.

Conditions for Negative Refraction and Negative Refractive Index in Lossy Media

Liming Ji and Vasundara V. Varadan

Microwave and Optics Laboratory of Imaging and Characterization, Department of Electrical Engineering
University of Arkansas, 700 W. Research Center Blvd., Fayetteville, Arkansas 72701, USA

Abstract— Negative refractive index (NRI) has been reported to be the requirement for negative refraction of electromagnetic waves in isotropic media. Such discussions have assumed that the material is lossless. Metamaterials have been used to create effective media with NRI by exciting plasmon-like resonances. In reality, there are no lossless metamaterials. In this paper, we derive the conditions for negative refraction of electromagnetic waves in isotropic and lossy media. The angles for phase refraction and energy refraction are different in lossy media. NRI is required for the negative refraction of phase but is not a requirement for achieving negative refraction of energy in lossy media. Negative permittivity or negative permeability is required for negative energy refraction at TM polarization and TE polarization, respectively. NRI is not necessary for negative energy refraction in lossy media.

1. INTRODUCTION

Negative refraction of electromagnetic waves has been studied since it was first envisaged by Veselago [1]. It was suggested that negative refraction could be employed to implement the superlensing effect, which has the potential to overcome the diffraction limit of conventional lenses [2–6]. For obliquely incident EM waves at the interface of two lossless materials, enforcing boundary conditions and using Snell's law can show that the angles of phase refraction and energy refraction are the same. Thus, if the second medium is a lossless NRI material, then NRI results in negative phase refraction and negative energy refraction [7, 8]. Experimental results have shown that man-made media with negative indices exhibit very high loss [9–11]. We may expect a different relation between NRI and negative refraction in isotropic media with loss added as a new unknown factor.

In this paper, a detailed theoretical analysis for negative refraction of waves in isotropic, lossy media was performed. This analysis can apply to media of any geometry. We demonstrate that NRI is not required for obtaining negative energy refraction in lossy isotropic media. The study follows the classic treatment of obtaining the transmitted wave for an obliquely incident TE or TM wave at a material interface where the second medium is assumed to be lossy [12]. Expressions were obtained for the angle of phase refraction and the angle of energy refraction of transmitted waves. As is well known, the two angles are different in lossy media [13]. Then, we discuss the conditions for NRI and negative refraction. We also show that TE polarization requires a negative permeability for negative energy refraction and TM polarization requires a negative permittivity for negative energy refraction. Negative phase refraction in lossy media needs NRI but negative energy refraction in lossy media does not require NRI. Three scenarios of wave refraction in a dispersive region are possible based on our theoretical study: (1) negative energy refraction occurs without negative refractive index provided either the permittivity or permeability is negative; (2) negative phase refraction (NRI) can occur without negative energy refraction; (3) both negative energy refraction and negative phase refraction can simultaneously occur in some frequency regions.

2. NEGATIVE REFRACTION FOR TM POLARIZATION IN LOSSY MEDIA

We consider the schematic as shown in Fig. 1. A plane wave is obliquely incident on a semi-infinite lossy medium (region 2) from a lossless medium (region 1). The incident angle is θ_1. ϕ and ψ are the refraction angles in region 2 for energy transmission and phase transmission, respectively. The refraction of phase and energy are treated as two different angles for a more general derivation. Starting from the positive z direction at $0°$, the refraction angle, in our convention, increases to positive values when rotating clockwise and decreases to negative values when rotating counterclockwise. Negative phase refraction occurs when $90° < \psi < 180°$ and negative energy refraction occurs when $-90° < \phi < 0°$. The wave propagation numbers in regions 1 and 2 are:

$$\text{Region 1: } \gamma_1 = j\beta_1 \tag{1}$$

$$\text{Region 2: } \gamma_2 = \alpha_2 + j\beta_2 = j\sqrt{\mu\varepsilon} \tag{2}$$

where μ and ε are the complex permeability and permittivity in region 2. Since region 1 is lossless, its propagation coefficient does not have a real part. If region 2 exhibits NRI, then $\beta_2 < 0$.
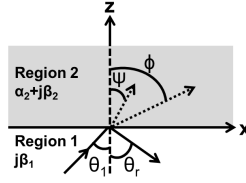
Figure 1: The schematic of a plane wave travelling through the interface of two semi-infinite media. Region 1 is lossless and region 2 is lossy. The incident angle is θ_1. The refraction angles for phase and energy, measured clockwise from the positive z-axis, are represented by ψ and ϕ, respectively. ψ can be in the first (0–90°) and fourth quadrants (−90°–0°). ϕ can be in the first and second (90–180°) quadrants.

An incident wave from region 1 reaches the boundary at $z = 0$. The wave is incident only in the x-z plane. It will be partially reflected back into region 1 and refracted into region 2. The fields in both regions can be written as follows:
Region 1:

$$\mathbf{E_i} = (\hat{\mathbf{x}}E_{0ix} - \hat{\mathbf{z}}E_{0iz})e^{-j\beta_{ix}x - j\beta_{iz}z} \tag{3}$$

$$\mathbf{H_i} = \hat{\mathbf{y}}H_{0i}e^{-j\beta_{ix}x - j\beta_{iz}z} \tag{4}$$

$$\mathbf{E_r} = (\hat{\mathbf{x}}E_{0rx} + \hat{\mathbf{z}}E_{0rz})e^{-j\beta_{rx}x - j\beta_{rz}z} \tag{5}$$

$$\mathbf{H_r} = \hat{\mathbf{y}}H_{0r}e^{-j\beta_{rx}x - j\beta_{rz}z} \tag{6}$$

Region 2:

$$\mathbf{E_t} = (\hat{\mathbf{x}}E_{0tx} - \hat{\mathbf{z}}E_{0tz})e^{-(\alpha_{tx} + j\beta_{tx})x - (\alpha_{tz} + j\beta_{tz})z} \tag{7}$$

$$\mathbf{H_t} = \hat{\mathbf{y}}H_{0t}e^{-(\alpha_{tx} + j\beta_{tx})x - (\alpha_{tz} + j\beta_{tz})z} \tag{8}$$

The subscripts "i", "r" and "t" represent incident, reflected and transmitted waves, respectively. The propagation coefficients in x and z directions in each region are related to each other:
Region 1:

$$\beta_{ix} = \beta_1 \sin\theta_1 \tag{9}$$

$$\beta_{iz} = \beta_1 \cos\theta_1 \tag{10}$$

where we have assumed that θ_1 is a real value in the range $0° < \theta_1 < 90°$.
Region 2:

$$(\alpha_{tx} + j\beta_{tx})^2 + (\alpha_{tz} + j\beta_{tz})^2 = (\alpha_2 + j\beta_2)^2 \tag{11}$$

In order to find the wave propagation coefficients in region 2, we apply boundary conditions at $z = 0$. The tangential field components on the two sides of the boundary are continuous.

$$E_{0ix}e^{-j\beta_{ix}x} + E_{0rx}e^{-j\beta_{rx}x} = E_{0tx}e^{-(\alpha_{tx} + j\beta_{tx})x} \tag{12}$$

$$H_{0i}e^{-j\beta_{ix}x} + H_{0r}e^{-j\beta_{rx}x} = H_{0t}e^{-(\alpha_{tx} + j\beta_{tx})x} \tag{13}$$

Equations (12) and (13) are valid for all values of x only when the exponential terms are the same (generalized Snell's Law):

$$j\beta_{ix} = j\beta_{rx} = \alpha_{tx} + j\beta_{tx} \tag{14}$$

Equating real and imaginary parts in Eq. (14), $\alpha_{tx} = 0$ for region 2. Hence, we can rewrite Eq. (7) and Eq. (8):

$$\mathbf{E_t} = (\hat{\mathbf{x}}E_{0tx} - \hat{\mathbf{z}}E_{0tz})e^{-\alpha_{tz}z - (j\beta_{ix}x + j\beta_{tz}z)} \tag{15}$$

$$\mathbf{H_t} = \hat{\mathbf{y}}H_{0t}e^{-\alpha_{tz}z - (j\beta_{ix}x + j\beta_{tz}z)} \tag{16}$$

The coefficients β_{tz} and α_{tz} are obtained from Eq. (11):

$$(\alpha_{tz} + j\beta_{tz})^2 = \beta_1^2 \sin^2\theta_1 + (\alpha_2 + j\beta_2)^2 \tag{17}$$

We can have the following equation by equating the imaginary parts on the two sides of Eq. (17),

$$\alpha_{tz}\beta_{tz} = \alpha_2\beta_2 \tag{18}$$

Equation (18) is valid only when region 1 is lossless and region 2 is lossy. $\alpha_{tz} > 0$ is enforced because a passive medium cannot generate energy. We find the planes of constant phase defined by

$$\beta_{ix}x + \beta_{tz}z = C \tag{19}$$

where C is a constant. The direction of phase transmission is perpendicular to the plane of constant phase. Hence, the phase refraction angle is

$$\tan\psi_{TM} = \frac{\beta_{ix}}{\beta_{tz}} = \frac{\beta_1\sin\theta_1}{\beta_{tz}} = \frac{\alpha_{tz}\beta_1\sin\theta_1}{\alpha_2\beta_2} \tag{20}$$

The direction of energy transmission in region 2 can be obtained from the Poynting vector. After deriving the transmitted electric field from Maxwell's equations, we have the Poynting vector in region 2:

$$\mathbf{P_{TM}} = \frac{1}{2}\left\{\hat{\mathbf{z}}\left[\frac{\beta_{tz}\varepsilon' + \alpha_{tz}\varepsilon''}{\omega(\varepsilon'^2 + \varepsilon''^2)}\right] + \hat{\mathbf{x}}\frac{\beta_{ix}\varepsilon'}{\omega(\varepsilon'^2 + \varepsilon''^2)}\right\}|H_{0t}|^2 e^{-2\alpha_{tz}z} \tag{21}$$

Combined with Eq. (20), the angle of energy transmission in region 2 is:

$$\tan\phi_{TM} = \frac{\varepsilon'\beta_1\sin\theta_1}{\beta_{tz}\varepsilon' + \alpha_{tz}\varepsilon''} = \frac{\varepsilon'\alpha_{tz}\beta_1\sin\theta_1}{\varepsilon'\alpha_2\beta_2 + \alpha_{tz}^2\varepsilon''} \tag{22}$$

The angles for phase refraction and energy refraction for TE polarization can be derived in a similar way:

$$\tan\psi_{TE} = \frac{\beta_1\sin\theta_1}{\beta_{tz}} = \frac{\alpha_{tz}\beta_1\sin\theta_1}{\alpha_2\beta_2} \tag{23}$$

$$\tan\phi_{TE} = \frac{\beta_1\sin\theta_1\mu'}{\beta_{tz}\mu' + \alpha_{tz}\mu''} = \frac{\mu'\alpha_{tz}\beta_1\sin\theta_1}{\mu'\alpha_2\beta_2 + \alpha_{tz}^2\mu''} \tag{24}$$

Instead of depending on the permittivity as for TM polarization, the angle of energy refraction for TE polarization is dependent on the permeability of region 2.

3. DISCUSSION

We analyze the conditions for negative refraction at TE polarization. The conditions for negative refraction at TM polarization can be obtained by simply replacing permeability with permittivity. The following parameters are always non-negative: α_{tz}, β_1, $\sin\theta_1$, α_2 and μ''. We require $\beta_2 < 0$ in region 2 for $\psi_{TE} > 90°$, which indicates negative phase refraction,. The real part of the refractive index has the same sign as β_2. Hence, NRI is necessary and is the only requirement to implement negative phase refraction. However, NRI is not necessary to implement negative energy refraction in region 2. Negative energy refraction in region 2 requires a negative numerator simultaneously with a positive denominator in Eq. (24). The conditions for negative phase and energy refraction at TE polarization in region 2 are:

$$\text{Negative Phase Refraction (TE): } \beta_2 < 0 \tag{25}$$
$$\text{Negative Energy Refraction (TE): } \mu' < 0 \tag{26}$$

$$\beta_2 < -\frac{\alpha_{tz}^2\mu''}{\mu'\alpha_2} \tag{27}$$

Similar conditions are found for TM polarization according to Eq. (20) and Eq. (24). The conditions for negative phase refraction and negative energy refraction in region 2 at TM polarization are:

$$\text{Negative Phase Refraction (TM): } \beta_2 < 0 \tag{28}$$
$$\text{Negative Energy Refraction (TM): } \varepsilon' < 0 \tag{29}$$

Table 1: The required conditions for negative phase refraction and negative energy refraction of waves travelling from a lossless medium into a lossy medium.

	Polarization	ε'	μ'	$\beta_2\ (\omega n_2')$
Negative Phase Refraction	TE		$\mu'\varepsilon'' + \varepsilon'\mu'' < 0$	$\beta_2 < 0$
	TM			
Negative Energy Refraction	TE		$\mu' < 0$	$\beta_2 < -\frac{\alpha_{tz}^2\mu''}{\mu'\alpha_2}$
	TM	$\varepsilon' < 0$		$\beta_2 < -\frac{\alpha_{tz}^2\varepsilon''}{\varepsilon'\alpha_2}$

$$\beta_2 < -\frac{\alpha_{tz}^2\varepsilon''}{\varepsilon'\alpha_2} \tag{30}$$

All the required conditions for negative refraction are summarized in Table 1.

When negative energy refraction occurs in each polarization, β_2 (same sign as the refractive index in region 2) should be less than a positive value. Hence, it can be negative or positive to realize negative energy refraction.

We listed the three possibilities for negative refraction in Fig. 2 based on the above derivations. Positive energy refraction and positive phase refraction (normal refraction) occur if their refraction vectors fall in the first quadrant. Negative energy refraction will occur if the energy refraction vector falls in the second quadrant ($-90° < \Phi < 0°$). Negative phase refraction will occur if the phase refraction vector falls in the fourth quadrant ($90° < \psi < 180°$). The energy refraction vector cannot fall into the third and the fourth quadrants to exhibit backward energy refraction. Similarly, the phase refraction vector cannot fall into the second and the third quadrants because that will violate Snell's law.
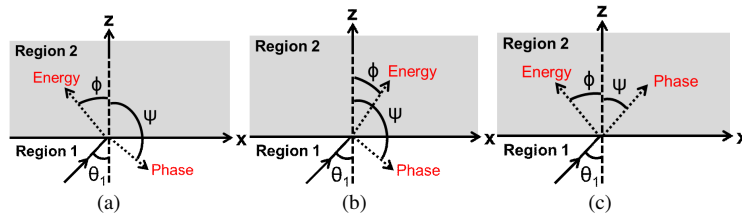
Figure 2: Schematics showing three possibilities for negative refraction. All angles are measured from the positive z-axis. If $90° < \psi < 180°$ (fourth quadrant), phase refraction is negative; if $-90° < \Phi < 0°$ (second quadrant), then energy refraction is negative. (a) Negative energy refraction and negative phase refraction; (b) Positive energy refraction and negative phase refraction; (c) Negative energy refraction and positive phase refraction.

4. CONCLUSION

We have derived the conditions for negative refraction of phase and energy in lossy media in this paper. The incident and refraction angles determined by Snell's law for lossless media do not apply in lossy media. The refraction angles of phase and energy are different in lossy media. Negative phase refraction is independent of polarization but negative energy refraction depends on the polarization of incident waves. Negative permittivity is required to realize negative energy refraction at TM polarization. Similarly, negative permeability is required to realize negative energy refraction at TE polarization. Based on our derivation, NRI is required for the negative refraction of phase in lossy media. However, it is not required for the negative refraction of energy. Hence, there are three possibilities for refraction: (a) simultaneous negative energy refraction and negative phase refraction, (b) simultaneous positive energy refraction and negative phase refraction and (c) simultaneous negative energy refraction and positive phase refraction.

REFERENCES

1. Veselago, V. G., "The electrodynamics of substances with simultaneously negative values of ε and μ," *Sov. Phys. Uspe.*, Vol. 10, No. 4, 509–514, July 1968.

2. Pendry, J. B., "Negative refraction makes a perfect lens," *Phys. Rev. Lett.*, Vol. 85, No. 18, 3966–3969, October 2000.

3. Zhang, X. and Z. Liu, "Superlens to overcome the diffraction limit," *Nature Mater.*, Vol. 7, 435–441, June 2008.

4. Aydin, K., I. Bulu and E. Ozbay, "Subwavelength resolution with a negative-index metamaterial superlens," *Appl. Phys. Lett.*, Vol. 90, No. 254102, June 2007.

5. Fang, N. and X. Zhang, "Imaging properties of a metamaterial superlens," *Appl. Phys. Lett.*, Vol. 82, No. 2, 161–163, January 2003.

6. Iyer, A. K. and G. V. Eleftheriades, "Free-space imaging beyond the diffraction limit using a veselago-pendry transmission-line metamaterial superlens," *IEEE Trans. Antennas Propag.*, Vol. 57, No. 6, 1720–1727, June 2009.

7. Smith, D. R., J. B. Pendry, and M. C. K. Wiltshire, "Metamaterials and negative refractive index," *Science*, Vol. 305, 788–792, Aug. 2004.

8. Ziolkowski, R. W. and E. Heyman, "Wave propagation in media having negative permittivity and permeability," *Phys. Rev. E*, Vol. 64, No. 056625, 1–15, October 2001.

9. Varadan, V. V. and A. R. Tellakula, "Effective properties of split-ring resonator metamaterials using measured scattering parameters: Effect of gap orientation," *J. Appl. Phys.*, Vol. 100, No. 034910, 1–8, August 2006.

10. Varadan, V. V. and L. Ji, "Temperature dependence of resonances in metamaterials," *IEEE Trans. Microw. Theory Tech.*, Vol. 58, No. 10, 2673–2681, October 2010.

11. Shelby, R. A., D. R. Smith, S. Schultz, "Experimental veripcation of a negative index of refraction," *Science*, Vol. 292, No. 6, 77–79, April 2001.

12. Varadan, V. V. and L. Ji, "Does a negative refractive index always result in negative refraction? — Effect of loss," *IEEE MTT-S International Microwave Symposium Digest*, 61–64, June 2009.

13. Holmes, J. J. and C. A. Balanis, "Refraction of a uniform plane wave incident on a plane boundary between two lossy media," *IEEE Trans. Antennas Propag.*, Vol. 26, No. 5, 738–741, September 1978.

Spatially Dispersive Inhomogeneous Dielectric Wire Media with Periodic Structure

J. Gratus[1, 3], R. Letizia[2, 3], and M. McCormack[1]

[1]Physics Department, Lancaster University, LA1 4YB, UK
[2]Engineering Department, Lancaster University, LA1 4YW, UK
[3]Cockcroft Institute of Accelerator Science, Darsbury WA4 4AD, UK

Abstract— Dielectric wire media are modelled both numerically using CST Microwave studio and analytically as media with spatially dispersion. In the latter case this leads to a differential equation that can be solved in terms of Mathieu functions. A periodic variation in the radii of the wires is considered as a method for shaping the propagating mode shape. A profile is proposed which gives a flatter shaped mode. Such a mode would increase the acceleration of particles in a particle accelerator.

1. INTRODUCTION

In this article we model the electromagnetic response to a dielectric wire grid with periodic variation in the radii of the wires (see Figure 1). Being periodic in all three dimensions, such a medium can be modelled into a standard 3D electromagnetic simulator by considering its unit cell wrapped into periodic boundary conditions. In this article we also model it as one dimensional spatially dispersive medium with a periodic inhomogeneity. Being spatially dispersive requires that the permittivity ϵ depends on k, whereas being inhomogeneous requires that the permittivity also depends on x. However k and x are Fourier conjugate variables so we need to consider what it means for a function to depends simultaneously on both k and x. In [1–3] we solve this by working in the x domain and considering the permittivity relation to be a differential equation in x, with parameters that depend on x. An alternative interpretation is in terms of a susceptibility kernel [4, 5].

Wire medium has many applications. The advantage here is that we can approximate it by a one dimensional epsilon near zero (ENZ) medium [6, 7]. As such it supports a purely electric longitudinal mode. Such modes may be used to accelerate particles. Although in general the phase velocity of such a mode is not equal to the speed of light. Therefore one may require drift tubes in order to provide positive acceleration.

By altering the shape of the wires, along the longitudinal direction, one may change the mode shape. This would enable one to flatten the shape of the mode from the usual sinusoidal shape. This would have definite advantages in that for the same power, the beam will experience enhanced acceleration. By contrast in signal transmission one may desire a higher peak for a given total energy.

In Section 2 we summarise the results of [1], when applied to longitudinal modes in a dielectric wire media. In this case the differential equation for the polarization corresponds to the Mathieu equations and therefore the modes can be written in terms of Mathieu functions. In Section 3 we compare these results to numerical simulations. We show that for a dielectric wire, the electric field is primarily in the longitudinal direction and that the average magnetic field is very low and therefore one may consider it to be modelled well by a one dimensional longitudinal wire.
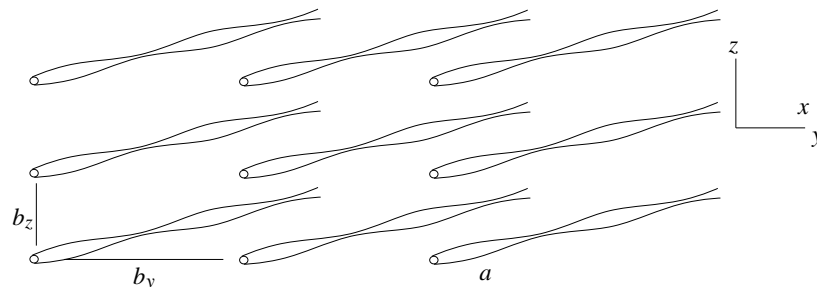
Figure 1: Wire medium with a periodic variation in the radius of the wires. The inter wire spacing are (b_y, b_z) and the period of the longitudinal variation is a.

2. WIRE MEDIA

Since the electric and polarization fields are longitudinal and the magnetic field vanishes, i.e., $\mathbf{E} = E(t,x)\mathbf{e}_1$, $\mathbf{P} = P(t,x)\mathbf{e}_1$ and $\mathbf{B} = \mathbf{0}$, then Maxwell's equations are automatically satisfied if

$$\epsilon_0 E + P = 0 \tag{1}$$

i.e., $\mathbf{D} = 0$, thus we are looking for epsilon near zero (ENZ) media. When the medium is homogeneous we will use an empirical model of the permittivity via

$$\widetilde{P}(\omega, k) = \frac{-\epsilon_0 k_{\mathrm{p}}^2}{\omega^2 - \beta^2 k^2} \, \widetilde{E}(\omega, k) \tag{2}$$

where ω is the temporal frequency, k is the wave number, β is the limiting phase velocity and k_p is the "plasma frequency". The Fourier transform of $P(t,x)$ with respect to t and x is given by

$$\widetilde{P}(\omega, k) = \int_{-\infty}^{\infty} \int_{-\infty}^{\infty} e^{-2\pi i(\omega t + kx)} P(t,x) dt\, dx \tag{3}$$

The plasma frequency will be a function of the inter wire spacing (b_y, b_z), the thickness of the wires r and the dielectric permittivity of the wires ϵ_{wire}. The denominator on the right hand side of (2) is motivated by the conducting wire medium [8, 9] and is valid when $r \ll a$.

Combining (1) and (2) we obtain the dispersion relation

$$\omega^2 - \beta^2 k^2 = k_{\mathrm{p}}^2 \tag{4}$$

By using CST Microwave Studio for a range of k with fixed a we can test the general form of the equation. In addition varying a we can get the dependence of k_{p} on a.

The simplest method to include an inhomogeneity in the permittivity is to let the plasma frequency k_{p} to depend on position x, that is $k_{\mathrm{p}} = k_{\mathrm{p}}(x)$. Since k_{p} depends on the radius r of the wires the easiest way to achieve this it to let the radius of the wires vary whilst keeping the inter wire spacing (b_y, b_z) constant. In order to extend the permittivity (2) to include inhomogeneous medium we work in the frequency-time domain. Thus (2) becomes a differential equation for $\hat{P}(\omega, x)$, which using (1) we may write as a differential equation[1] for $\hat{P}(\omega, x)$

$$\frac{\beta^2}{(2\pi)^2} \frac{\partial^2 \hat{P}}{\partial x^2} + \omega^2 \hat{P} = k_{\mathrm{p}}(x)^2 \hat{P} \tag{5}$$

where

$$\hat{P}(\omega, x) = \int_{-\infty}^{\infty} e^{-2\pi i \omega t} P(t,x) dt \tag{6}$$

The simplest modification to make the system inhomogeneous and periodic is to let the plasma frequency vary with x:

$$k_{\mathrm{p}}^2 = k_0^2 - 2\Lambda \cos(2\pi x/a) \tag{7}$$

As stated in the introduction, this can be constructed by varying $r(x)$ periodically.

From (5) this gives the Mathieu equation

$$\frac{\beta^2}{(2\pi)^2} \frac{\partial^2 \hat{P}}{\partial x^2} + \left(\omega^2 - k_0^2 + 2\Lambda \cos(2\pi x/a)\right) \hat{P} = 0 \tag{8}$$

From Floquet's theorem the solution can be written

$$\hat{P}(\omega, x) = e^{2\pi i \kappa x/a} \mathcal{P}(\omega, x) \tag{9}$$

---

[1]Note that we work with the polarization P instead of the electric field so that we can directly compare the results with [1]. Clearly one may use (1) to convert into E.

where $\mathcal{P}(\omega, x)$ is periodic in x, i.e., $\mathcal{P}(\omega, x + 1) = \mathcal{P}(\omega, x)$. For each κ in the range $0 \leq \kappa < a$ there exist an infinite number of values

$$\omega_n^2 - k_0^2 = A_n\left(\kappa, \Lambda/\beta^2\right) \tag{10}$$

such that (9) is a solution to (8) with the periodicity of $\mathcal{P}(\omega, x)$. One may therefore regard (8) as a dispersion relation. The solution to (8) is given in terms of the Mathieu Function F.

$$\hat{P}(\omega_n, x) = F\left(\frac{4a^2(\omega_n^2 - k_0^2)}{\beta^2}, \frac{4a^2\Lambda}{\beta^2}, \frac{\pi x}{a}\right) \tag{11}$$

In the case when $\Lambda = 0$ and hence $k_{\mathrm{p}} = k_0$ then (5) reduces to the simple harmonic oscillator and has solution $\hat{E}(\omega, x) = e^{2\pi k x}$. From (9) we may set $\mathcal{P}(\omega, x) = e^{2\pi i n x/a}$ where $n \in \mathbb{Z}$, so that (4) becomes the dispersion relation, for the unperturbed frequency ω_n,

$$\Omega_n = \sqrt{k_0^2 + \beta^2(\kappa + n)^2/a^2} \tag{12}$$

and hence

$$A_n(\kappa, 0) = \beta^2(\kappa + n)^2/a^2 \tag{13}$$

In [1] we look the approximation for small Λ. In order to make the translation we observe that

$$f_q(\omega) = \omega^2 - k_0^2 - \beta^2(q + \kappa)^2/a^2 \tag{14}$$

and hence $f_n(\Omega_n) = 0$. In this case

$$\mathcal{F}_q = f_q\left(\Omega_n\right) = k_0^2 - \frac{\beta^2(n + \kappa)^2}{a^2} - \left(k_0^2 - \frac{\beta^2(q + \kappa)^2}{a^2}\right) = \frac{\beta^2}{a^2}(n - q)(n + q + 2\kappa) \tag{15}$$

and $\mathcal{F}_q' = f_q'(\Omega_n) = 2\Omega_n$. In this case we see that

$$\omega_n = \Omega_n + \frac{\Lambda^2 a^2}{2\Omega_n \beta^2}\left(\frac{1}{2n + 2\kappa - 1} - \frac{1}{2n + 2\kappa + 1}\right) + O\left(\Lambda^4\right) \tag{16}$$

we then take the spatial Fourier series

$$\mathcal{P}^n(x) = \sum_{m=-\infty}^{\infty} e^{2\pi m x} P_m^n$$

and calculate the Fourier the approximate value of P_m^n, given in Equation (33) of [1]. One of the key results of [1] is the observation that this approximation scheme brakes down in the case when $\kappa = 0$ or $\kappa = \frac{1}{2}$. This can be seen in the (15) above, where $\mathcal{F}_{-n} = 0$ if $\kappa = 0$ and $\mathcal{F}_{-n-1} = 0$ if $\kappa = \frac{1}{2}$. This is because the approximate modes couple. The existence of coupled modes is a new feature of spatial dispersion. See [1] for details.

The approximation scheme described in [1] is more general since it will deal with fourth order differential equations applicable to transverse modes. Indeed it can be seen that the method is appropriate for any order differential equation in x.

3. NUMERICAL RESULTS

The eigen mode solver of CST Microwave Studio is used to perform mode analysis of the metamaterial unit cell. The unit cell has dimensions in the transverse plane $(b_y, b_z) = (22.86\,\mathrm{mm}, 10.16\,\mathrm{mm})$. Inside was a uniform dielectric rod $\epsilon_{\mathrm{wire}} = 1600\epsilon_0$, with square cross section of width between $w = 0.2\,\mathrm{mm}$ to $w = 0.5\,\mathrm{mm}$. This reproduced results in the literature [10]. This the cross section was uniform for these simulations, the result was independent of the x longitudinal period of the unit cell. However for computational reasons this was set to $10.16\,\mathrm{mm}$. By looking at at the fields, in Figure 2 it is clear that, away from the wires, the electric field is in the longitudinal direction (x) and that the magnetic field H is in the transverse plane. Not only is magnetic field concentrated

near the rod, but the magnetic field averaged over the transverse plane is zero. Therefore this dielectric wire is modelled well by looking at longitudinal electric modes in an epsilon near zero medium.

The dispersion (ω, k) curves for a variety of wire widths are given in Figure 3. It is clear that for thin wires there is a hyperbolic relation (4) whereas this relation breaks down for thicker wires at high frequency. Mapping the hyperbolic portions onto (4) we get the following values for the limiting phase velocity β and the unperturbed plasma frequency k_0^2.

$$
\begin{array}{|c|c|c|}
\hline
w & \beta & k_{\mathrm{p}}^2 = k_0^2 \\
\hline
0.2\,\mathrm{mm} & 0.157c & 257c^2\,\mathrm{m}^{-2} \\
\hline
0.3\,\mathrm{mm} & 0.155c & 157c^2\,\mathrm{m}^{-2} \\
\hline
0.4\,\mathrm{mm} & 0.154c & 101c^2\,\mathrm{m}^{-2} \\
\hline
0.5\,\mathrm{mm} & 0.155c & 97c^2\,\mathrm{m}^{-2} \\
\hline
\end{array}
\tag{17}
$$

It is clear from the Table (17) that we can use a constant phase velocity $\beta = 0.155c$. The relationship between w and k_{p}^2 may be approximated by a quadratic equation given by

$$
k_{\mathrm{p}}(w)^2 \approx c^2 \left(2420w^2 - 2230w + 607\right)
\tag{18}
$$

3.1. Proposed Model of Periodic Structure

We wish to find a function for the width $w(x)$ such that the plasma frequency given by (18) becomes (7). For this we set the unperturbed plasma frequency $k_0^2 = 100c^2\,\mathrm{s}^{-2} = (2.997\,\mathrm{GHz})^2$ and $\beta = 0.155c$. We need to choose the period a to be longer than the inter wire spacing, $22.86\,\mathrm{mm}$. A reasonable value is to set $a = 0.1\,\mathrm{m}$. The flattest mode shape can be achieved when the second

(a)   (b)
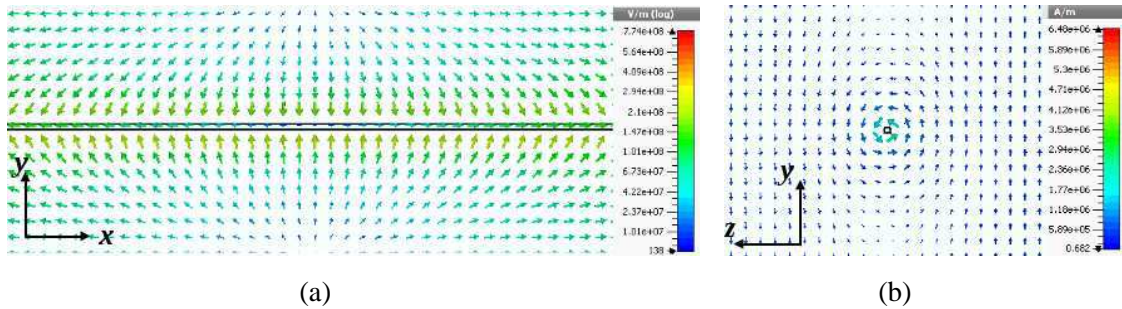
Figure 2: (a) The electric (in the (x, y) plane, and (b) magnetic field (in the (y, z) plane, for a square dielectric rod $\epsilon_{\mathrm{wire}} = 1600\epsilon_0$ (BST ceramic material) of width $0.4\,\mathrm{mm}$. The frequency was $5.39\,\mathrm{GHz}$, $k = 163.6\,\mathrm{m}^{-1}$, $a = 30\,\mathrm{mm}$, $(b_y, b_z) = (22.86\,\mathrm{mm}, 10.16\,\mathrm{mm})$.
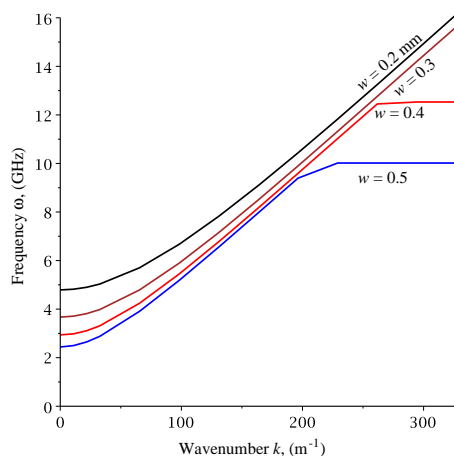
Figure 3: Dispersion relation ω versus k for a range of different widths w.
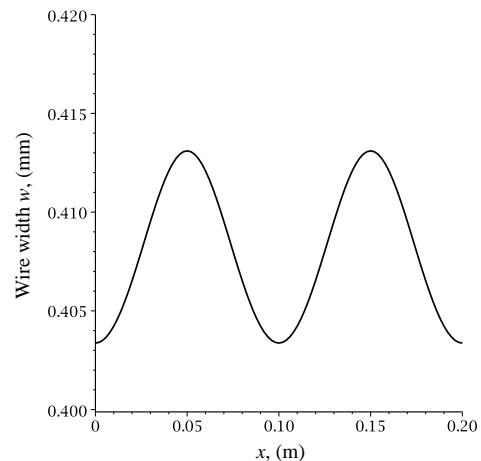
Figure 4: Proposed profile of dielectric wire to give a the periodic plasma frequency (7).
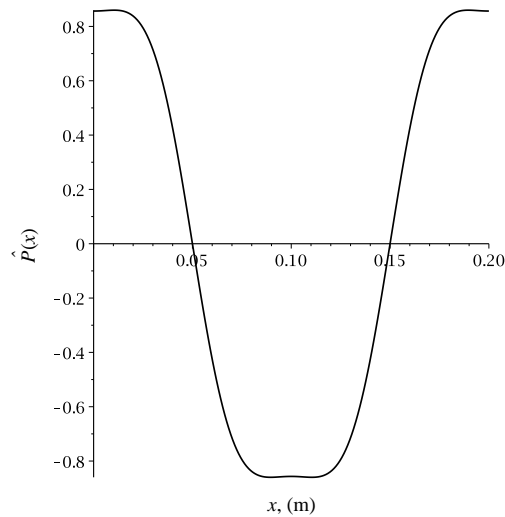
Figure 5: Mode shape of the polarization $\hat{P}(\omega, x)$ and the electric field $\hat{E}(\omega, x)$.

argument of F in (11) is equal to 1, i.e., $4a^2\Lambda/\beta^2 = 1$. This gives a value for $\Lambda = 0.618c^2\,\mathrm{m}^{-2} = (0.236\,\mathrm{GHz})^2$. Thus the with of the wires $w(x)$ varies between $0.404\,\mathrm{mm}$ and $0.413\,\mathrm{mm}$ its shape is given in Figure 4.

We also choose $\kappa = 0$. Placing these values into (10) and (11) we find that the a lowest mode has it's frequency only slightly altered $\omega_0 = 3.015\,\mathrm{GHz}$, The mode shape will then be given by Figure 5.

4. CONCLUSION

We have described how to shape the spatial modes of longitudinal mode by varying the width of a dielectric wire. We have also show how to model this in terms of a spatially dispersive media. There is clearly many exciting directions for this research. The next step will be to look at the modes numerically using CST studio or similar in order to compare the modes with the expected mode. If one wished to further shape the mode one could include a $\Lambda_1 \cos(4\pi x/a)$ in (8). The corresponding differential equation can then be solved using Heun functions. In addition, by removing one of the wires, one could create a photonic band gap structure which will maximise the fields in one region.

REFERENCES

1. Gratus, J. and M. McCormack, "Spatially dispersive inhomogeneous electromagnetic media with periodic structure," *J. Optics*, Vol. 17, No. 2, 025105, 2015.
2. Gratus, J. and M. McCormack, "Inhomogeneous spatially dispersive electromagnetic media," *Physics. Class.*, arXiv: 1309.0739v1, 2013.
3. Costa, J. and M. G. Silveirinha, "Macroscopic electromagnetic response of arbitrarily shaped spatially dispersive bodies formed by metallic wires," *Phys. Rev. B*, Vol. 86, No. 7, 075129, 2012.
4. Gratus, J. and R. W. Tucker, "Covariant constitutive relations, landau damping and non-stationary inhomogeneous plasmas," *Progress In Electromagnetics Research M*, Vol. 13, 145–156, 2010.
5. Gratus, J. and R. W. Tucker, "Covariant constitutive relations and relativistic inhomogeneous plasmas," *J. Math. Phys.*, Vol. 52, 042901, 2011.
6. Ramaccia, D., F. Scattone, F. Bilotti, and A. Toscano, "Broadband compact horn antennas by using eps-enz metamaterial lens," *IEEE Transactions on Antennas and Propagation*, Vol. 61, No. 6, 2929–2937, Jun. 2013.

7. Forati, E. and G. W. Hanson, "On the epsilon near zero condition for spatially dispersive materials," *New J. of Phys.*, Vol. 15, No. 12, 123027, 2013.

8. Belov, P. A., R. Marques, S. I. Maslovski, I. S. Nefedov, M. Silveirinha, C. R. Simovski, and S. A. Tretyakov, "Strong spatial dispersion in wire media in the very large wavelength limit," *Phys. Rev. B*, Vol. 67, No. 11, 113103, 2003.

9. Song, W., Z. Yang, X.-Q. Sheng, and Y. Hao, "Accurate modeling of high order spatial dispersion of wire medium," *Opt. Express*, Vol. 21, No. 24, 29836–29846, 2013.

10. Zhang, F., L. Chen, Y. Wang, Q. Zhao, X. He, and K. Chen, "Thermally tunable electric mie resonance of dielectric cut-wire type metamaterial." *Opt. Express*, Vol. 22, No. 21, 24908–24913, Oct. 2014.

Efficient Imaging of Dielectric Targets Based on Contrast Source Inversion Method

S. C. Yan, **C. X. Yang**, **J. Zhang**, **and M. S. Tong**

Department of Electronic Science and Technology
Tongji University, 4800 Cao'an Road, Shanghai 201804, China

Abstract— An efficient reconstruction scheme for dielectric targets is proposed based on the contrast source inversion method (CSIM). The CSIM could be preferred to the traditional Born iterative method (BIM) or its variations because it updates the contrast source and contrast simultaneously and avoids the direct solution of forward scattering integral equation (FSIE). The CSIM is similar to the modified gradient method (MGM) but it is more computationally efficient and also requires less measurement data. This is very desirable for the reconstruction when the observation is limited or measurement condition is poor. Two numerical examples with a limited observation are presented to demonstrate the approach and good images have been observed.

1. INTRODUCTION

Reconstructing targets by microwave illumination requires an efficient solution of inverse electromagnetic (EM) scattering equations. This could be very challenging because the involved governing equations are nonlinear and the solutions are inherently nonunique [1]. In particular, the problems become more difficult when measuring conditions are unfavorable and diverse scattering data are not available, which will be encountered in many applications but has been seldom considered [2]. Usually, the inverse problems are solved by linearizing governing equations and gradually minimizing the mismatch between calculated data and measured data in an iterative scheme. In the integral equation approach (IEA) for reconstructing dielectric targets, there are forward scattering integral equation (FSIE) and inverse scattering integral equation (ISIE) and traditionally we need to alternatively solve them in the context of Born iterative method (BIM) or its variations [3]. The solution of permittivity from the ISIE can reveal the profile of unknown target in the imaging domain.

In this work, we use the contrast source inversion method (CSIM) [4] to reconstruct the dielectric targets for the application in target recognition and atmosphere or space sensing. In such an application, the details of target are not important but obtaining a sufficient observation or measurement to the target may be difficult. The CSIM is motivated by and similar to the modified gradient method (MGM) [5], but it updates the contrast source and contrast simultaneously instead of the field and contrast. The CSIM can avoid the direct solution of FSIE because it defines a cost functional including mismatches or errors from both the FSIE and ISIE and update them together [6]. Compared with the MGM, the CSIM is more computationally efficient and also requires less measurement data [7]. This is particularly desirable when we consider the reconstruction with a poor measurement condition which may be encountered in many applications. Two numerical examples for reconstructing typical dielectric targets under a limited view is presented and good images can be observed.

2. GOVERNING EQUATIONS

We consider the reconstruction for a 3D dielectric target enclosed by a cubic imaging domain V in the free space which is the background medium with a wavenumber k_b). The observation surface with transmitting and receiving antennas surrounding the imaging domain is denoted with S. In the traditional BIM or its variations, we have the following forward scattering integral equation (FSIE) which is used to update the total electric field [3]

$$\mathbf{E}_j(\mathbf{r}) = \mathbf{E}_j^{inc}(\mathbf{r}) + k_b^2 \int_V \overline{\mathbf{G}}(\mathbf{r}, \mathbf{r}') \cdot \xi(\mathbf{r}')\mathbf{E}_j(\mathbf{r}')dV', \quad \mathbf{r} \in V \tag{1}$$

and inverse scattering integral equation (ISIE) which is used to update the contrast of permittivity $\xi(\mathbf{r}') = k^2(\mathbf{r}')/k_b^2 - 1$ between the imaging domain and surrounding medium

$$\mathbf{E}_j^{sca}(\mathbf{r}) = \mathbf{E}_j(\mathbf{r}) - \mathbf{E}_j^{inc}(\mathbf{r}) = k_b^2 \int_V \overline{\mathbf{G}}(\mathbf{r}, \mathbf{r}') \cdot \xi(\mathbf{r}')\mathbf{E}_j(\mathbf{r}')dV', \quad \mathbf{r} \in S. \tag{2}$$

In the above, $\mathbf{E}_j^{inc}(\mathbf{r})$ is the incident electric field from a transmitter where j represents the jth incident electric field, $\mathbf{E}_j(\mathbf{r'})$ is the jth total electric field at a source point $\mathbf{r'}$ inside the imaging domain V, and $\mathbf{E}_j^{sca}(\mathbf{r})$ denotes the jth scattered electric field obtained by measurement at an observation point $\mathbf{r}$ located at an observation or measurement surface S. Also, $\overline{\mathbf{G}}(\mathbf{r}, \mathbf{r'})$ is the dyadic Green's function defined by

$$\overline{\mathbf{G}}(\mathbf{r}, \mathbf{r'}) = \left(\overline{\mathbf{I}} + \frac{\nabla \nabla}{k_b^2}\right) g(\mathbf{r}, \mathbf{r'}) \tag{3}$$

where $\overline{\mathbf{I}}$ is an identity dyad and $g(\mathbf{r}, \mathbf{r'}) = e^{ik_b R}/(4\pi R)$ is the 3D scalar Green's function in which $R = |\mathbf{r} - \mathbf{r'}|$ is the distance between an observation point $\mathbf{r}$ and a source point $\mathbf{r'}$. In addition, $k(\mathbf{r'})$ is the wavenumber related to the contrast inside the imaging domain. In the CSIM, the equivalent contrast source is defined [4]

$$\mathbf{S}_j(\mathbf{r}) = \xi(\mathbf{r})\mathbf{E}_j(\mathbf{r}) \tag{4}$$

and the FSIE becomes an target or state equation

$$\mathbf{S}_j(\mathbf{r}) = \xi(\mathbf{r})\mathbf{E}_j^{inc}(\mathbf{r}) + \xi(\mathbf{r})\mathbf{F}_V[\mathbf{S}_j(\mathbf{r'})], \quad \mathbf{r} \in V \tag{5}$$

while the ISIE becomes a data equation

$$\mathbf{E}_j^{sca}(\mathbf{r}) = \mathbf{F}_V[\mathbf{S}_j(\mathbf{r'})], \quad \mathbf{r} \in V. \tag{6}$$

3. RECONSTRUCTION BY CONTRAST SOURCE INVERSION METHOD (CSIM)

In the CSIM, the following cost functional is defined [7]

$$C(\mathbf{S}_j, \xi) = \eta_S \sum_{j=1}^{J} ||\mathbf{E}_j^{sca}(\mathbf{r}) - \mathbf{F}_S(\mathbf{S}_j)||^2_S + \eta_V \sum_{j=1}^{J} ||\xi\mathbf{E}_j^{inc}(\mathbf{r}) + \xi\mathbf{F}_V(\mathbf{S}_j) - \mathbf{S}_j||^2_V \tag{7}$$

and it is minimized by updating the contrast source and contrast simultaneously. The contrast source is updated for the nth iteration based on the $n-1$ iteration by

$$\mathbf{S}_{j,n} = \mathbf{S}_{j,n-1} + \alpha_n^s \mathbf{v}_{j,n} \tag{8}$$

where

$$\mathbf{v}_{j,0} = 0, \quad \mathbf{v}_{j,n} = \mathbf{t}_{j,n} + \mathbf{v}_{j,n-1} \frac{\text{Re}\left\{\sum_l \langle \mathbf{t}_{l,n}, \mathbf{t}_{l,n} - \mathbf{t}_{l,n-1}\rangle\right\}_V}{\sum_l \langle \mathbf{t}_{l,n-1}, \mathbf{t}_{l,n} - \mathbf{t}_{l,n-1}\rangle_V} \tag{9}$$

and

$$\alpha_n^s = \frac{-\text{Re}\left\{\sum_{j=1}^{J} \langle \mathbf{t}_{j,n}, \mathbf{v}_{j,n}\rangle\right\}_V}{\eta_S \sum_{j=1}^{J} ||\mathbf{F}_S(\mathbf{v}_{j,n})||^2_S + \eta_{V,n} \sum_{j=1}^{J} ||\mathbf{b}||^2_V} \tag{10}$$

where $\mathbf{b} = \mathbf{v}_{j,n} - \xi_{n-1}\mathbf{F}_V(\mathbf{v}_{j,n})$. On the other hand, the contrast is updated through

$$\xi_n = \xi_{n-1} + \alpha_n^\xi d_n \tag{11}$$

where

$$\alpha_n^\xi = \frac{1}{\eta_{V,n}}, \quad d_n = \eta_{V,n} \frac{\sum_{j=1}^{J}(\mathbf{S}_{j,n} - \xi_{n-1}\mathbf{E}_{j,n}) \cdot \mathbf{E}_{j,n}^*}{\sum_{j=1}^{J}|\mathbf{S}_{j,n}|^2}. \tag{12}$$

4. NUMERICAL EXAMPLES

The reconstruction for two typical dielectric targets is considered to demonstrate the approach. It is assumed that the measurement surface is located at one side (top) of the reconstructed target so that the observation is limited and more practical. Such an observation is quite different from the standard and widely-applied experimental setup of Institut Fresnel [8]. The vertical distance between the measurement surface and the center of the imaging domain is $r = 5.0\,\mathrm{m}$ and the transmitting or receiving antennas are equally distributed on the surface in terms of its center. We choose the transmitter-receiver combination as $M_T \times M_R = 81 \times 25$. The transmitters are uniformly located at a $1.6\,\mathrm{m} \times 1.6\,\mathrm{m}$ square with a 9×9 array while the receivers are evenly located at the same square with a 5×5 array. The distance between two neighboring antennas in both x and y directions is $0.2\,\mathrm{m}$ for transmitters and $0.4\,\mathrm{m}$ for receivers. The incident wave has a single frequency $f = 3\,\mathrm{GHz}$ and is propagating toward the center of the imaging domain. For numerical simulations, the measured data for scattered electric fields are replaced with calculated data by assuming that the target to be reconstructed is known. The imaging domain is chosen as a cubic box with a dimension $L \times L \times L$ where $L = 140\,\mathrm{mm}$. In the first example, we reconstruct a dielectric sphere with a radius $a = 25\,\mathrm{mm}$ and relative permittivity $\epsilon_r = 3.5$. Fig. 1 shows the reconstructed image in a 3D view and the image can clearly reflect the real target. In the second example, we image a dielectric cylinder with a radius $a = 30\,\mathrm{mm}$ in its cross section, a height $h = 60\,\mathrm{mm}$, and a relative permittivity $\epsilon_r = 3.5$. Fig. 2 sketches its 3D-view image which is distinguishable as a cylinder.
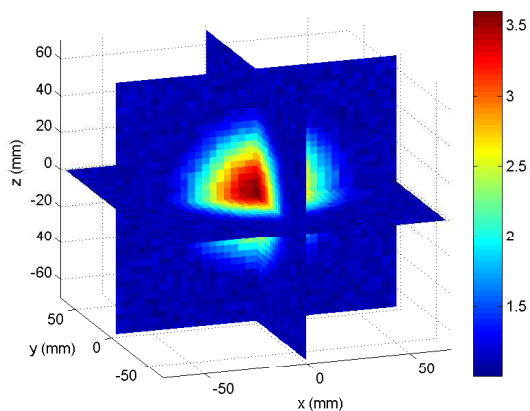
Figure 1: Reconstruction of a dielectric sphere with a radius $a = 25$ mm and a relative permittivity $\epsilon_r = 3.5$.
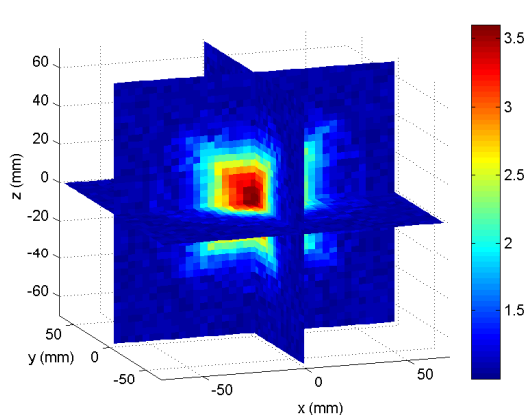
Figure 2: Reconstruction of a dielectric cylinder which has a radius $a = 30\,\mathrm{mm}$, a height $h = 60\,\mathrm{mm}$, and a relative permittivity $\epsilon_r = 3.5$.

5. CONCLUSION

In this work, we use the CSIM to reconstruct dielectric targets for target recognition and atmosphere or space sensing in which the observation to the targets may be very difficult. The CSIM updates the contrast source and contrast simultaneously in the iteration of reconstruction so that the direct solution of FSIE can be avoided, yielding much convenience in numerical implementation. Although the method is somewhat similar to the MGM, it is more computationally efficient and more importantly, it requires less density of measurement data which is particularly desirable for the applications with unfavor measurement or observation condition. We present two numerical examples with a limited observation to demonstrate the approach and good imaging results have been obtained.

REFERENCES

1. Hopcraft, K. I. and P. R. Smith, *An Introduction to Electromagnetic Inverse Scattering*, Kluwer Academic Publishers, Boston, 1992.
2. Yu, C., M. Yuan, and Q. H. Liu, "Reconstruction of 3D objects from multi-frequency experimental data with a fast DBIM-BCGS method," *Inverse Problems*, Vol. 25, No. 2, 1–24, Feb. 2009.
3. Chew, W. C., *Waves and Fields in Inhomogeneous Media*, IEEE Press, New York, 1995.
4. Van den Berg, P. M. and R. E. Kleinman, "A contrast source inversion method," *Inverse Problems*, Vol. 13, 1607–1620, 1997.
5. Kleinman, R. E. and P. M. van den Berg, "A modified gradient method for two-dimensional problems in tomography," *J. Computat. Appl. Math.*, Vol. 42, 17–35, 1992.
6. Van den Berg, P. M., A. L. van Broekhoven, and A. Abubakar, "Extended contrast source inversion," *Inverse Problems*, Vol. 15, 1325–1344, 1999.
7. Van den Berg, P. M. and A. Abubakar, "Constrast source inversion method: State of art," *Progress In Electromagnetcs Research*, Vol. 34, 189–218, 2001.
8. Geffrin, J. M. and P. Sabouroux, "Continuing with the Fresnel database: Experimental setup and improvements in 3D scattering measurements," *Inverse Problems*, Vol. 25, 1–18, 2009.

On Constructing Globally Convergent Algorithms: Applications to GPR and Marine CSEM Sounding

A. Timonov

University of South Carolina Upstate, USA

Abstract— A new approach to constructing globally convergent algorithms for the approximate solution of some coefficient inverse problems arising in electromagnetic frequency sounding is presented. Utilizing the original transformations developed for the convexification method, this approach possesses two disctinctive features: (1) Bregman iterations, and 1) the refinement with the interior data. These novelties may significantly enhance both the spatial and contrast resolutions of quantitative imaging. These algorithms can be applied to quantitative imaging in GPR and marine CSEM sounding. Some results of computational experiments are presented.

1. INTRODUCTION

Marine CSEM sounding has been in commercial use for hydrocarbon exploration since the beginning of the 21st century, though it was first proposed in the 60s last century. In the last decade, marine CSEM sounding has become significant due to the growing interest to hydrocarbon deposits on a shelf, as well as to the rapid development of the efficient inversion techniques and technologies used in marine geophysics (see, e.g., [2]). The same is true for Ground Penetrating Radar (GPR) field whose diversity of applications includes geotechnical engineering, sedimentology, glciology, landmine and UXO detection and classification, archaeology, etc, (see, e.g., [4]). Quantitative imaging needs to be performed in order to provide the high contrast and space resolution of marine CSEM or GPR sounding. In turn, quantitative imaging requires solving the Coefficient Inverse Problems (CIPs), i.e., the inverse problems for the partial differential equations where one needs to determine one or several coefficients from a given solution (or its functionals) on some manifolds (see, e.g., [6] and references cited there). Due to both the nonlinearity and ill-posedness of CIPs, providing the global convergence is very important for many, if not for all, reconstruction algorithms. Being applied to a CIP, the traditional nonlinear least squares approach normally results in a non-convex minimization problem. As a result, the traditional numerical techniques, such as the gradient or Newton-like methods, may not be applicable or they may fail to converge to the true solution or even to its estimates. On the other hand, the methods of global optimization are extremely time consuming and heuristic. The paper addresses a challenging problem of constructing computationally efficient algorithms for some CIPs arising in GPR and marine CSEM sounding.

One approach to constructing the computational algorithms for CIPs, the so-called convexification, was recently proposed in [6]. It is based on Carleman estimates allowing for constructing some strictly convex least squares functionals at each step of a layer stripping procedure with respect to the spatial variable. In [5] the layer stripping procedure with respect to the real-valued parameter of the Laplace transform combined with an iterative procedure for treatment of the so-called tails was developed and applied to solving nD ($n = 1, 2, 3$) CIPs. Unlike the numerical techniques described in [5], we do not solve an overdetermined boundary value problem when determining the initial approximations. Also, we do not use the marching scheme for performing iterates with respect to the parameter of the Laplace transform. Instead of the WKB (i.e., short wave) approximations, we use the true solution for a homogeneous medium in order to initialize the iterative procedure. The main distinctive feature of the proposed algorithm is minimizing the Tikhonov functional in the l_1-norm by Bregman iterations (see, e.g., [10]) or alternating direction method of multipliers (see, e.g., [3]) in combination with the refinement procedure, in which we search for a better approximation performing matching the interior field generated by the iterative solution by the solutions of the forward problem in the region of interest. It follows from the results of numerical experiments that these novelties are advantageous.

The paper is organized as follows. In the next section, we formulate the forward and inverse models. In the Section 3 we describe the proposed algorithm. In the Section 4 we show some results of numerical experiments with these models. We conclude the paper in Section 5.

2. THE FORWARD AND INVERSE MODELS

Without loss of generality and for the sake of clarity, consider a simple forward model of propagation and scattering of an electromagnetic pulse emitted at $z = 0$ and propagated through the

Epstein layer filled with the lossless inhomogeneous medium (see [9]). In this case, the Maxwell's equations together with the initial and boundary conditions can be reduced to the initial boundary value problem for the hyperbolic equation with respect to one of the electric components of the electromagnetic field

$$c^{-2}(z)(z)U_{tt} - U_{zz} = 0 \quad z > 0, t > 0, \tag{1}$$
$$U(z,0) = U_t(z,0) = 0, \ \ U(0,t) = \delta(t). \tag{2}$$

Here, $c(z)$ is the speed of propagation of electromagnetic waves. Note that the smallness assumption on the coefficient $c(z)$ is not imposed. This model may be suitable, for example, for quantitative imaging of the electric permittivity from the GPR data in regions with the arid climate. In conductive media, such as marine environments, the Equation (1) needs to be replaced with the parabolic equation. The inverse problem is formulated as follows. Given the function $U_z(0,t) = f(t)$, $t > 0$ and parameters $c_0 > 0, L > 0$, such that $c(z) = c_0$ for $z \geq L$, find the variable speed $c(z)$ on $(0, L)$.

Traditionally, the inverse model can be obtained by reducing the wave Equation (1) to the Helmholtz equation via the Fourier transform (see, e.g., [1]), [6, 8]). Unlike this model, we apply the Laplace transform

$$u(x,\nu) = \int_0^\infty U(z,t) \exp{(-\nu t)} dt, \ z > 0, \ \nu > \nu_0$$

to the problem (1)–(2) in accordance with [9]. Note that the Laplace transform needs to be slightly modified (e.g., by introducing $\exp{(-\nu^2 t)}$) for the parabolic problem. Introducing the dimensionless variables, we then obtain the s-parametric family of elliptic boundary value problems

$$u_{xx}(x,s) - s^2 n^2(x) u(x,s) = 0, \quad x \in (0,1), \quad s > s_0, \tag{3}$$
$$u(0,s) = 1, \tag{4}$$
$$u_x(1,s) + su(1,s) = 0. \tag{5}$$

Here, $n(x) = c_0/c(x)$ is the refraction coefficient, $s_0(s) = \nu_0 L/c_0$, and $c(x)$ and c_0 are speeds of the wave propagation in the Epstein layer and homogeneous medium. Note that for a sufficiently smooth refraction coefficient $u(x,s) > 0$ (see, e.g., [6]).

In practice, the surface admittance $Y(s) = -u_x(0,s)/u(0,s)$ (or impedance) is measured in the interval $[\underline{s}, \overline{s}], \underline{s} > s_0$. Therefore, introducing by analogy with [6] the new function

$$v(x,s) = \frac{1}{s^2} \ln u, \tag{6}$$

we obtain the family of problems

$$v_{xx} + s^2 v_x^2 = n^2(x) \ \text{ in } (0,1), \quad s \in [\underline{s}, \overline{s}], \tag{7}$$
$$v(0,s) = 0, \quad v_x(1,s) = -\frac{1}{s}. \tag{8}$$

Introducing one more function $q(x,s) = \partial_s v(x,s)$ and differentiating (7), (8) with respect to the s-variable, we obtain the family of problems that do not contain the unknown refraction coefficient $n(x)$

$$q_{xx} + 2s^2 q_x v_x = -2s v_x^2 \ \text{ in } (0,1), \ s \in [\underline{s}, \overline{s}], \tag{9}$$
$$q(0,s) = 0, \quad q_x(1,s) = \frac{1}{s^2}. \tag{10}$$

Note that for every $s \in [\underline{s}, \overline{s}]$ the Equation (9) is integro-differential because of the representation

$$v(x,s) = -\int_s^{\overline{s}} q(x,\mu) d\mu + v(x, \overline{s}). \tag{11}$$

Thus, the inverse problem of frequency sounding is reduced, basically, to estimating the interior field $q(x,s)$ given the data $q_x(0,s) = (2Y(s)/s - Y'(s))/s^2 \equiv \Psi(s)$. Once such an estimate is obtained, the functions $v(x,s)$ and $n(x)$ may also be estimated from (11) and (7).

3. THE ITERATIVE ALGORITHM

Initialization. The true solution of (7)–(8) for $n(x) \equiv 1$, i.e., the function is taken as the initial approximation

$$v^{(0)}(x, s) = -\frac{x}{s},$$

is taken as the initial approximation. Clearly, the corresponding function $q^{(0)}(x, s) = \frac{x}{s^2}$ is the true solution of the problem (9)–(10). Beginning with $v^0(x, s)$, we start the iterative process.

Step 1. Assume that the kth successive approximation $v^{(k)}(x, s)$ has been determined. Then, given $v^{(k)}(x, s)$, we determine $q^{(k)}(x, s)$ for every $s \in [\underline{s}, \overline{s}]$ as follows. We approximate the second order ODE (9) together with the boundary conditions (10) and the data $Psi(s)$ by its finite-difference analogue, i.e., the system of linear equations $Ax = y$, and minimize the Tikhonov functional

$$T_\alpha[x] = \frac{1}{2}\|Ax - y\|_2^2 + \alpha R(x), \tag{12}$$

where $\alpha > 0$ is the regularization parameter. The stabilizing term $R(x)$ is chosen as either the l_1-norm $\|x\|_1$ or the total variation norm $\|x\|_{TV}$. Because of no strict convexity and differentiability, the alternating direction method of multipliers [3] or split Bregman algorithm [10] are applied to determine the minimizing sequences converging to the approximate solution $q^{(k+1)}(x, s)$.

Step 2. We update the function $v(x, s)$ for every parameter $s \in [\underline{s}, \overline{s}]$ as follows.

$$v^{(k+1)}(x, s) = -\int_s^{\overline{s}} q^{(k+1)}(x, \nu)d\nu + v^{(k)}(x, \overline{s}), \tag{13}$$

$$v_x^{(k+1)}(x, s) = -\int_s^{\overline{s}} q_x^{(k+1)}(x, \nu)d\nu + v_x^{(k)}(x, \overline{s}), \tag{14}$$

$$v_{xx}^{(k+1)}(x, s) = -\int_s^{\overline{s}} q_{xx}^{(k+1)}(x, \nu)d\nu + v_{xx}^{(k)}(x, \overline{s}). \tag{15}$$

Step 3. Let $s^* \in [\underline{s}, \overline{s}]$ be a certain number that does not depend on k. We update the refraction coefficient as

$$n_{k+1}^2(x) = v_{xx}^{(k+1)}(x, s^*) + s^2(v_x^{(k+1)}(x, s^*))^2, \tag{16}$$

where $x \in (0, 1)$, and set $n_{k+1}(x) = 1$ for $x = 0$ and $x = 1$.

Step 4. Update the function $v(x, \overline{s})$ by first solving the problem

$$u_{xx}^{(k+1)}(x, \overline{s}) - \overline{s}^2 n_{k+1}^2(x)u(x, \overline{s}) = 0, \quad x \in (0, 1), \tag{17}$$

$$u^{(k+1)}(0, s) = 1, \quad u_x^{(k+1)}(1, s) + su^{(k+1)}(1, s) = 0. \tag{18}$$

and then determining the functions

$$v^{(k+1)}(x, \overline{s}) = \frac{\ln u^{(k+1)}(x, \overline{s})}{\overline{s}^2}, \tag{19}$$

$$v_x^{(k+1)}(x, \overline{s}) = \frac{u_x^{(k+1)}(x, \overline{s})}{\overline{s}^2 u^{(k+1)}(x, \overline{s})}, \tag{20}$$

$$v_{xx}^{(k+1)}(x, \overline{s}) = \frac{u_{xx}^{(k+1)}(x, \overline{s})}{\overline{s}^2 u^{(k+1)}(x, \overline{s})} - \left(\frac{u_x^{(k+1)}(x, \overline{s})}{\overline{s}u^{(k+1)}(x, \overline{s})}\right)^2 \tag{21}$$

for $x \in [0, 1]$.

Stopping rule. If the level of noise δ in the data $\tilde{\Psi}(s)$ is given or it can be estimated, then it is natural to stop the process at the iterate $k_{stop} = \min\left\{k : \|\partial_x u_{n_k}(0, s) - \tilde{\Psi}(s)\|_{L_2[\underline{s}, \overline{s}]} \leq \delta\right\}$, where the function $u_n(x, s)$ is determined from the solution of the original problem (1)-(2) with $n(x) = n_k(x)$ for every successive approximation $n_k(x)$.

If the approximation $n_{k_{stop}}(x)$ does not possess high spatial and contrast resolutions then one may try to refine the pair $(\tilde{n}(x), \tilde{u}(x,s))$, where $\tilde{n}(x) = n_{k_{stop}}(x) \in G$ and $\tilde{u}(x,s) = \exp\left[s^2 v^{(k_{stop})}(x,s)\right]$. Note that although for a certain $s_* \in [\underline{s}, \overline{s})$ the function $\tilde{u}(x,s_*)$ may be close to the Laplace transform of the solution of the original problem (1)–(2), it does not satisfy it. This observation motivates matching the interior field $\tilde{u}(x,s_*)$ with the Laplace transform $u(x,s_*;n(x))$ of the solution of the original problem (1)–(2). We are interested in finding a new approximation of the true refraction coefficient $n^*(x)$ whose error estimate is better than the error estimate for $\tilde{n}(x)$. To find such an approximation, we consider the injective and continuous map $F(n): n(x) \to u(x,s_*;n)$ and minimize the Tikhonov functional

$$T_\lambda[n] = \|F(n) - \tilde{u}(x,s_*;n)\|^2_{L_2(0,1)} + \lambda\|n - \tilde{n}\|_{L_1(0,1)}, \ \lambda > 0. \tag{22}$$

Let $n_\lambda(x)$ be the minimizer of the Tikhonov functional (22). By analogy with [7] one may conjecture that if the reqularization parameter is properly chosen, then

$$\left\|n_{\lambda(\gamma)} - n^*\right\| \leq \xi\|n^* - n_{k_{stop}}\|, \tag{23}$$

where $\xi \in (0,1)$. This motivates the refinement procedure.
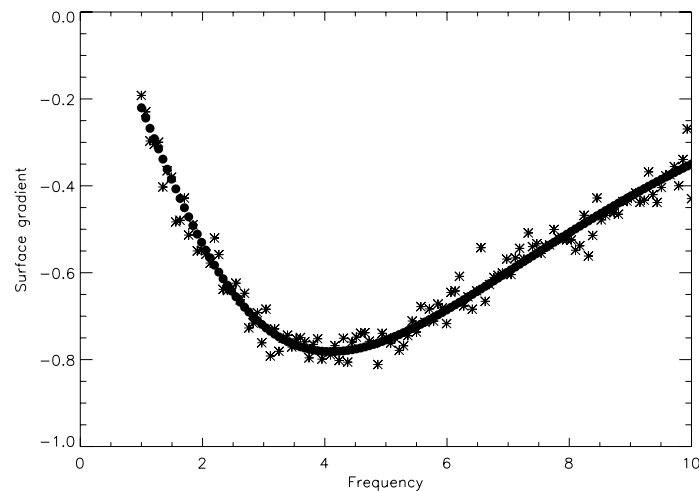
Figure 1: The simulated electromagnetic frequency data $\overline{\varphi}(s)$ in the interval $[1,10]$. The noiseless data is shown by bullets and the data corrupted by noise at the level of 5% is shown by asterisks.
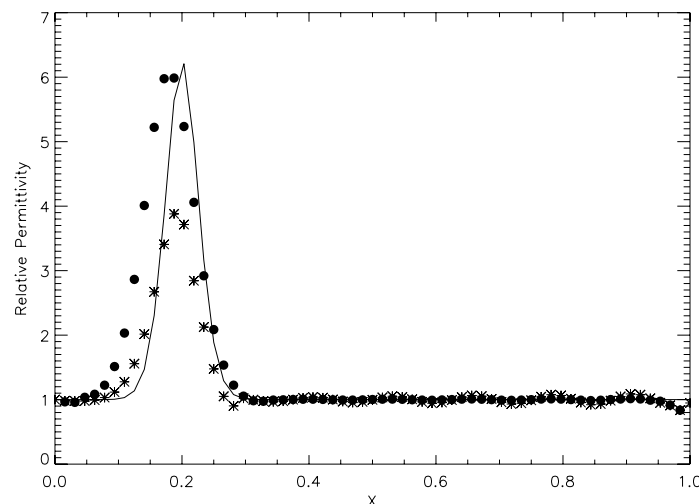
Figure 2: Recovering the relative electrical permittivity of a single mid-contrast land mine from the perturbed data (the level of noise is 5%) by the convexification method (asterisks) and proposed algorithm (bullets).

4. NUMERICAL EXPERIMENTS

To demonstrate the computational effectiveness of the proposed algorithm, we conducted several numerical experiments. As an example, we show the results reconstruction of the relative electrical permittivity of a subsurface land mine simulated by a Gaussian curve. To generate the frequency sounding data $\Psi(s)$, we solved numerically the problem (3)–(5). Figure 1 shows the typical perturbed boundary data generated by this mine embedded in the homogeneous background (air) with $\varepsilon = 1$. Figure 2 shows the mean relative electrical permittivity obtained from a sample containing twenty five realization of the pseudo-random vector.

5. CONCLUSIONS

In this paper, we briefly described the iterative algorithm for recovering the electrical permittivity or conductivity from the frequency sounding data. It was shown in numerical experiments that the proposed algorithm is capable of providing the high contrast and space resolution quantitative imaging. Future studies will be aimed at establishing the global convergence result, as well as at implementing the algorithm in high dimensions and conducting numerical experiments with the real data.

REFERENCES

1. Chen, Y. and V. Rokhlin, "On the inverse scattering problem for Helmholtz equation in one dimension," *Inverse Problem*, Vol. 8, 365–391, 1982.
2. Constable, S., "Ten years of marine CSEM for hydrocarbon exploration," *Geophysics*, Vol. 75, 75A67–75A81, 2010.
3. Eckstein, J. and D. Bertsekas, "On the Douglas-Rachford splitting method and the proximal point algorithm for maximal monotone operators," *Math. Programming*, Vol. 5, 293–381, 1992.
4. *Ground Penetrating Radar Theory and Applications*, Ed. by Jol, H. M., Elsevier, New York, 2009.
5. Kuzhuget, A. V., L. Beilina, M. V. Klibanov, et al., "Quantitative image recovery from measured blind backscattered data using a globally convergent inverse method," *IEEE Trans. Geoscience and Remote Sensing*, 1–12, 2012.
6. Klibanov, M. V. and A. Timonov, *Carleman Estimates for Coefficient Inverse Problems and Numerical Applications*, VSP, Utrecht, 2004.
7. Klibanov, M. V., A. B. Bakushinsky, and L. Beilina, "Why a minimizer of the Tikhonov functional is closer to the exact solution than the first guess," *J. Inv. Ill-Posed Problems*, Vol. 19, 83–105, 2011.
8. Sylvester, J., "Layer stripping," *Surveys on Solution Methods for Inverse Problems*, Ed. by Colton B, et al., Springer-Verlag, New York, 2000.
9. Tamasan, A. and A. Timonov, "On a new approach to frequency sounding of layered media," *Num. Func. Analysis and Optimization*, Vol. 29, 470–486, 2008.
10. Yang, Y., M. Moller, and S. Osher, "A dual split Bregman method for fast l^1 minimization," *Math. Comp.*, Vol. 82, 2061–2085, 2013.

Raw Data Generation of Maritime Scenes Using MOCEM V4 and PHYS-IQ V1

Christian Cochin[1], Jean-Christophe Louvigne[1], and Julien Houssay[2]

[1]DGA MI, French MoD, Bruz, France
[2]Corentin LE BARBU, Nicolas Pinel, Goulven Monnier Alyotech, Rennes, France

Abstract— For many years, DGA MI — expertise center of the French MoD — has developed simulation tools for SAR surveillance applications. The GPU computing has recently opened new efficient ways for raw data simulation. The tools now have the capability to generate complex EM scenes like maritime ones, and therefore can be used for other applications than their initial purpose. The simulation of realistic raw data is crucial for advanced processing, including target imagery modes (SAR/ISAR). This paper focuses on opportunities offered by this set of tools, part of the French DGA simulator named SIROS — Simulation toolset for Imagery Radar and Ocean Surveillance — for studies and for tuning processing.

1. INTRODUCTION

The DGA — Delegate for Armament of French MoD — has been for many years developing [1, 2] and improving a simulator named SIROS — Simulation toolset for Imagery Radar and Ocean Surveillance. This paper presents and illustrates the components of this simulator used for simulation of maritime applications. In maritime scenes, we have to take into account at least:

- one or several ships,
- the sea surface,
- interactions between ship(s) and the sea surface.

In a first step, we will focus on the main components of the EM modeling considering the interest and the expected use of the simulation. We focus here on the following tools: MOCEM and PHYS-IQ. These applications have been developed under DGA contracts by Alyotech technologies, a French SME.

2. SIMULATION GOALS

Even if the subject is not here to explain and detail the benefits and motivations of simulation, we must not forget that every simulation is built within a particular interest. A simulator has to render adequately a number of radar signal properties. Simulator must be driven by principles and efficient methods in order to produce "realistic enough" products required by the signal processing planned to be use. In SIROS, we focus on coherent radar processing for surveillance systems including SAR and ISAR imagery but not only. As we work in the field of military applications that include small target detection and target classification, we are highly interested in high resolution (1 m or less). We would like also be able to address radar applications in a larger field, from coastal or naval radars to airborne radars.

3. SHIP EM SIGNATURE WITH MOCEM V4

Our need is to be able to produce high resolution and multi-channel signals and images (polarimetry, interferometry). Since the very beginning, we have chosen, for target modeling, an innovative approach consisting of building directly, from an analysis of the geometry, a 3D EM scatterering model. This approach has many advantages, such as an accurate localization of points in 3D and a very fast computation time. The associated tool is MOCEM, whose original principles have been presented in several publications [3, 4]. As illustrated below, from a rough geometry (internet provider) and some improvements in CAD model in order to add common missing parts, such as barriers, we can build a 3D EM model. As we consider several types of effects, the 3D model is not made of isotropic scatterers but points associated to a level and a directivity function corresponding to the nature of the EM effect. A rectangular plate is the product of two sinc directivity function, while a dihedral is only directive across the internal edge and a trihedral is represented as a point with a smooth diagram, quite isotropic. Based on the nearest known canonic

configurations, directivity function is obviously approximated. Benefits of such modelisation are great because we get a very compact model in 3D and it is easy also to take into account surfaces less as plane as their CAD model and use a "dielectric and roughness coefficient" to reduce specular effects and enlarge visibility of contributors. We can also easily take into account a diffuse effect of surface in order to generate on complex surfaces, not detailed in CAD model, a skin level and a texture to render a spatial distribution. From this model, it is easy to localize contributors in range and Doppler according to the relative motions between ship and radar. GPU computation is fundamental to do that very efficiently. Details have been explained in [13].

Green spheres of the 3D EM model surimposed on CAD model   *range (x-axis)-doppler view and corresponding signal range profile*
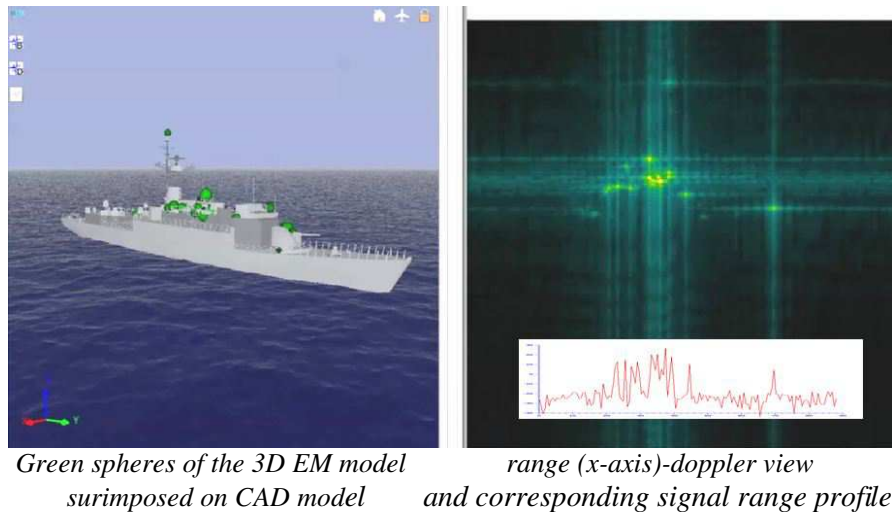
4. THE HYDRO SEA MODEL USING MERCUDA

MOCEM and PHYS-IQ share the same model of the sea surface. MERCUDA, a 3D animated model developed by Alyotech. This model is used in MOCEM and PHYS-IQ for radar purposes, but it is also used as presented in [8] for IR applications.

The hydro model is based on:

- a 2D wave power spectrum based on Jonswap formulation and its Elfouhaily [21] improved version;
- spatial frequencies computed from temporal frequencies (ergodic hypothesis) by use of the appropriate dispersion relationship;
- time sample realizations of the mean spectrum, simulated through a complex multiplicative Gaussian noise.

The EM computation requires high resolution on the surface, but another constraint is to handle large area needed for applications in order to cover the intersection of the radar beam and the sea surface.

An FFT approach is used, but using two separated grids:

- a large grid, that can support large scale phenomena such as swell and observation;
- a smaller local grid, that will be used to represent EM contribution of the gravity waves. This scale is sampled at 5λ.

In order to introduce a nonlinear sea that takes into account the dissymmetry of the waves, the model also uses the "Choppy wave Model" [10].

The hydro model is used as a support of all scene computations. It holds:

- Radar signal computation, described more thoroughly in PHYS-IQ model;
- ship motion computation in MOCEM and also in PHYS-IQ.

The first use of the hydro model is to compute ship motions which have a great impact on the Doppler properties of the signal and are used on SAR/ISAR focusing process.

The hydro model has other applications:

- Shadowing effects on the ship by the sea surface under the floating line, but also from higher waves, especially when a swell is present and in particular at low-grazing angles;
- MOCEM software computes, with some approximations, the EM coupling between the ship and the sea surface;
- influence of the ship itself on the surface with its wake (kelvin and narrow V included in MOCEM as illustrated above) but also with its stem wave (not yet included).

Wind 5 m/s   *Wind 15 m/s*   *wake behind ship*
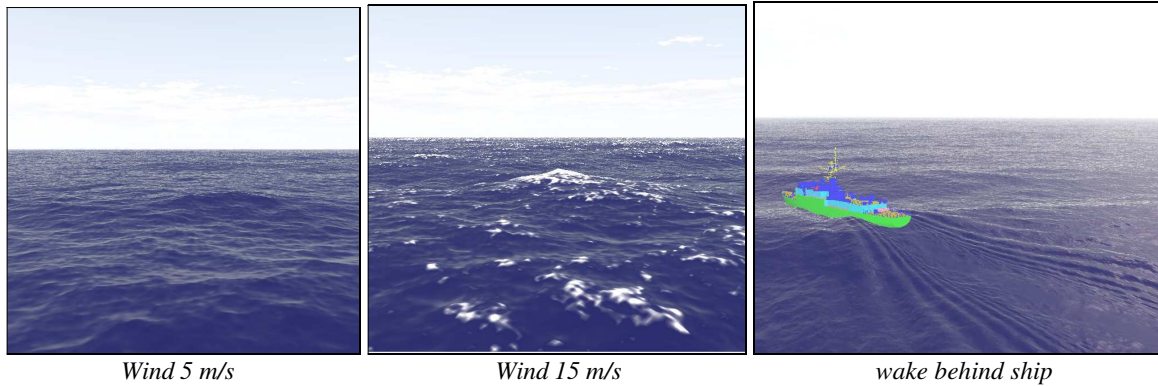
5. THE SEA CLUTTER WITH PHYS-IQ V1

PHYS-IQ [7, 10] is a specific development to compute signal from the dynamic sea model detailled above. It is a great challenge because this computation needs a large sea surface in order to cover the radar antenna beam and a sufficiently fine sampling step to correctly hold the gravity wave spectrum. For capillarity waves, we take into account the slopes, resulting of dynamic sea, to modulate the 5λ patch where Braggs effects are computed. For low sea states ($SS < 4$) and except in very grazing angles, the sigma0 variation is quite similar to GIT [9] and GOSSA model [12]. We can also observe that the Doppler spectrum of the sea clutter is well represented as well as we can observe a K distribution, similar to measurements [17, 18, 20]. We can also render the Doppler shift and its spreading [16]. It remains therefore difficult to validate these points considering the relatively scarce data available for uncertainties on the ground truth associated to available measurements.

PHYS-IQ also takes into account breaking waves that enforce the Bragg contribution and also create discrete events in the signal called "spikes" [19]. PHYS-IQ implements a sophisticated crest detector in order to locate and characterize the breaking phenomenon when it appears (a vertical acceleration is measured on the surface). Spike signatures which have been pre-computed are then added to the signal with Doppler properties associated to the local properties of the surface. Works are still under way under DGA contract with ONERA and THALES to conclude about the representativeness of sea clutter signal for sea state upper 3, and according to the wind direction form the radar.

6. VALIDATION WORKS

In [11], Alyotech and Thales have compared simulated raw data form MOCEM with some real acquisitions with ship in motion.

3D EM MOCEM MODEL   *up SAR simulated image , low Thales real*
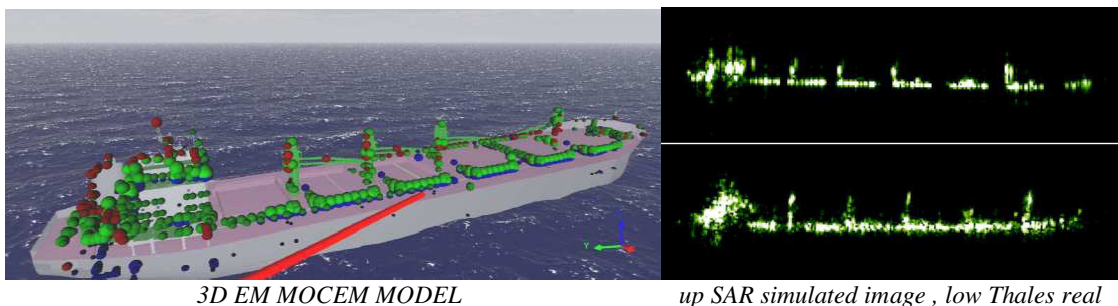
Several validation works have been conducted for each component (target, clutter) but also considering complex scenes. In [5, 6, 14], simulated image of fixed ship has been compared to

FFI (Norway MoD) acquisitions done with SELEX PicoSAR radar, not only visually, but also according to several metrics. The SSIM metric has been adapted by ONERA to radar applications. As illustrated below, its shows promising results that pave the way for target recognition using 3D models of the ships. Conducted works also show that rough EM parameters used in MOCEM are enough for image metrics. Of course a well-proportioned 3D model is needed but with nothing comparable in term of accuracy of the CAD model usually needed by RCS codes and also in terms of computation time.

FFI PicoSAR image (up) versus MOCEM (down)
On Stena Saga cruise ship

Similarity Indicator applied to compare
Crown of Scandinavia ship image with Mocem simulation

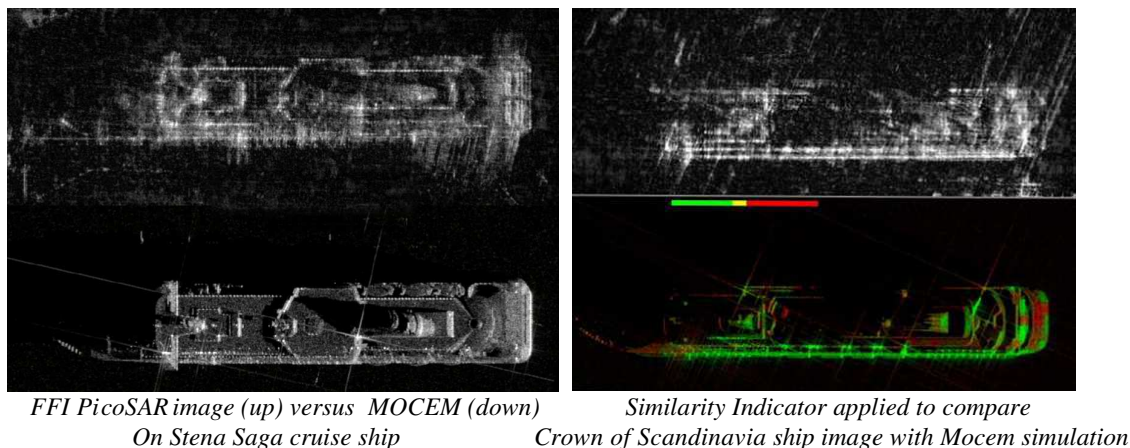In [15], DGA and FFI have simulated a real scene with a moving ship in Oslo harbor. It is interesting to note that ship motion takes into account in the simulation creates delocalization phenomena as well as seen in SAR measured image. We can also observe that coupling with the sea, create an unfocusing phenomena that is also reproduced in simulation.

Simulation view

FFI PicoSAR image of ship leaving
Oslo harbor

simulated image generated
with MOCEM

7. APPLICATIONS AND FUTURE WORKS

New applications are also currently developed. A first version of a maritime patrol simulator has been assembled. This simulation, done by ONERA under DGA contract, uses precomputed PHYS-IQ sea clutter, adds, quite in real time MOCEM target and processes detection and tracking of a target in high sea clutter in order to display result on PPI to operator.

Futures works are planned to take into account coastal effect as a multi-parameter function driving a "fetch" value in order to separate the instantaneous effect of the wind on the sea surface and its longer time effect that generates the gravity waves, scales and phenomena that have already been separated in the PHYS-IQ V1 model.

8. CONCLUSION

The presented tools appear to be very helpful for estimating radar detection performances. The signal computation, done in GPU, is a disruptive step. Signal generation opens to apply "real" processing and observe "real" performance on fully control and complex scenes. This is a great progress when considering small targets and high sea states where the signal distribution has a great impact on detection threshold driven by adaptive false alarm regulation. Moreover, the multi-point model for the target also offers a more realistic signal distribution than a Swerling law. Taking into account shadowing of the target in high sea state or swell condition is also a better approach to recreate realistic situations. We have now a toolset that can be used from the global performance prediction to most advanced processing of targets (s.a. ISAR).

REFERENCES

1. Cochin, C., "SOURSAR — Operational polarimetric scene generator," *AGARD*, 1990.
2. Cochin, C., S. Buriau, J. Saillard, and G. Delhommeau, "Simulator of ocean scenes observed by polarimetric SAR," *EUSAR*, 2000.
3. Cochin, C., P. Pouliguen, B. Delahaye, D. Le Hellard, P. Gosselin, and F. Aubineau, "MOCEM — 'all in one' tool to simulate SAR image," *EUSAR*, 2008.
4. Cochin, C., P. Pouliguen, B. Delahaye, D. Le Hellard, P. Gosselin, and F. Aubineau, "MO-CEM — Fast generator of 3D scatterers for radar simulation," *International RADAR 2009 Conference, Surveillance for a Safer World*, Brest, France, 2009.
5. Johnsen, T., "change detection and detailed analysis of stacking configuration of containers in TerraSAR-X SAR images," *RADAR 2009 Conference*, Washington, 2009.
6. Ødegaard, N., A. O. Knapskog, C. Cochin, and B. Delahaye, "Comparison of real and simulated SAR imagery of ships for use in ATR," *Proc. SPIE, Algorithms for Synthetic Aperture Radar Imagery XVII*, 7699, 2010.
7. Monnier, G., D. Le Hellard, S. Vince, T. Landeau, B. Chapron, R. Garello, G. Llort-Pujol, C. Cochin, and Y. Hurtaud, "GPU-based simulation of radar sea clutter," *OCOSS*, 2010.
8. Monnier, G., S. Vince, and J. Houssay, "Real time modelling of multispectral ocean scenes," *OCOSS*, 2010.
9. Fiche, A., C. Cochin, and Y. Hurtaud, "Combinaison of empirical/asymptotic models to characterize sea clutter at intermediate angles," *International RADAR 2013 Conference*, Adelaide, Australia, 2013.
10. Houssay, J., N. Pinel, Y.-H. Hellouvry, C. Le Barbu, and C. Cochin, "A physical radar simulation tool of the sea clutter," *Radar 2014 Conference*, Lille, 2014.
11. Le Barbu, C., J.-B. Genin, R. Fabbri, C. Cochin, and L. Boudet, "Validation of SAR/ISAR imagery radar processing using simulated raw data shozing realistic ship motions," *EUSAR 2014*, Berlin, 2014.
12. Angelliaume, S., V. Fabbro, G. Soriano, and C. A. Guerin, "The GO-SSA extended model for all incidence sea clutter modeling," *IGARSS 2014*, Quebec, 2014.
13. Cochin, C., J.-C. Louvigne, R. Fabbri, C. Le Barbu, and L. Ferro-Famil, "MOCEM V4 — Radar simulation of ship at sea for SAR and ISAR applications," *EUSAR 2014*, Berlin, 2014.
14. Knapskog, A. O., L. Vignaud, C. Cochin, and N. Ødegaard, "Target recognition of ships in harbour based on simulated SAR images produced with MOCEM software," *EUSAR 2014*, Berlin, 2014.
15. Cochin, C., J.-C. Louvigne, A. O Knapskog, and N. ØDegaard, "Radar simulation of ship at sea using MOCEM V4 and comparison to acquisitions," *RADAR 2014*, Lille, France, 2014.
16. Watts, S., L. Rosenberg, and M. Ritchie, "Characterising the Doppler spectra of high grazing angle sea clutter," *RADAR 2014*, Lille, France, 2014.
17. Rosenberg, L., S. Watts, and S. Bocquet, "Application of the K+rayleigh distribution to high grazing angle sea-clutter," *RADAR 2014*, Lille, France, 2014.
18. Fiche, A., S. Angelliaume, L. Rosenberg, and A. Khenchaf, "Statistical analysis of low grazing angle high resolution X-band SAR sea clutter," *RADAR 2014*, Lille, France, 2014.
19. Corretja, V., J. Petitjean, J.-M. Quellec, S. Kemkemian, H. Thuilliez, and S. Watts, "Sea-spike analysis in high range and doppler resolution radar data," *RADAR 2014*, Lille, France, 2014.
20. Ward, K. D., R. J. A. Tough, and S. Watts, "Sea clutter: Scattering, the K distribution and radar performance," *IET Radar, Sonar, Navigation and Avionics*, 2007.
21. Elfouhaily, T., B. Chapron, and K. Katsaros, "A unified directional spectrum for long and short wind-driven waves," *J. Geophys. Res.*, Jul. 1997.

Prediction of Signal Fadings in Air Radio Communications

Leszek Nowosielski and Marain Wnuk

Faculty of Electronics, Military University of Technology
Gen. S. Kaliskiego 2 str., Warsaw 00-908, Poland

Abstract— In the article the analysis of the fading deepness of the signal at the receiving antenna input of the aircraft flying in the air space between the repeater station and a power line were presented as well as it was determined if the level of fadings generated by signal reflections from power columns has destructive effects to the quality of radio link used. To this purpose, the analysis of the terrain between the repeater station and individual power columns was carried out. Basing on the analysis results it could be accepted that the propagation of the radio link at the sector of the ray reflected, i.e., the repeater station antenna, reflecting surface of particular power columns and receiving antenna installed on the plane, can be modeled using the free space propagation model.

1. INTRODUCTION

The algorithm of procedures during analysis of power high voltage links effects to the quality of radio communications between land repeater station and an aircraft was presented in this article. Power high voltage lines and their overhead transmission line supports — the height of which can sometime be up to 60 m, can be the factors able to change the direction of propagation. This case will take place within a radio link between a land relay station installed on a mast at h_1 height over the terrain level and aircraft being at the height of h_2. The communications of the aircraft with the flight control tower is done, among others, on the frequency from 118 MHz to 136 MHz. The rays of the electromagnetic wave reflected from metal construction elements of particular overhead transmission line supports can interfere with the direct ray generated by the relay station, and in the result of these fadings of the signal level can be formed at the aircraft's receiving antenna input. The above fadings can be the reason for periodic changes of the signal to noise ratio (S/N) at the input of the receiver, what can result in worsening the audio monitoring quality of the information transmitted. On the signal to noise ratio (S/N) has influence the used antenna type [2, 3, 5, 6].

2. POWER OF SIGNAL AT THE RECEIVER INPUT

The signal level P at the input of the receiving antenna installed on the aircraft board is dependent on the level and phase of the direct ray signal P_{ray1} as well as of the level and phase of the component being the sum of the rays P_{ray2} reflected from particular power overhead transmission line supports taken into account in a radio communication link. The signal level P can be calculated from the dependence:

$$P = P_{ray1} + P_{ray2} \tag{1}$$

In order to evaluate influences of particular power overhead transmission line supports to the quality of radio communications, the signal level P coming to the receiving antenna installed on the aircraft board was calculated taking into account the level and phase of the direct ray signal P_{ray1} as well as the level and phase of the ray signal P_{ray2} reflected from a given power overhead transmission line support.

In order to take into account influences of particular power overhead transmission line supports to the radio communication quality it should be assumed that the depth of fadings for the signal being the sum of the direct ray and reflected one at the input of the radio receiver installed on the aircraft board depends on:

1. The signal level coming to the antenna of the radio receiver installed on the aircraft board as the direct ray P_{ray1}. The signal level of the as the direct ray depends on the propagation path length between the repeater station and the receiving antenna on the aircraft as well as of electrical parameters of the repeater station.

2. The signal level coming to the antenna of the radio receiver installed on the aircraft board as the ray P_{ray2} reflected from the metal structures of particular power overhead transmission line supports. The signal level of the reflected ray depends on the:

- propagation path length that is consisted of two segments running through the points of: the repeater station, reflecting surface of particular power overhead transmission line supports as well as receiving antenna on the aircraft board,
- section of the terrain in a segment between the repeater station as well as particular power overhead transmission line supports,
- electromagnetic wave reflection coefficient from metal structures of particular power overhead transmission line supports,
- electrical parameters of the repeater station.

The diagram of affecting the signal transmitted by the repeater station to the receiving aircraft by the metal structure of the power overhead transmission line support is shown in the Fig. 1.

The depth value of the fadings at the input of receiving antenna installed on the aircraft generated by influencing the amplitude and phase of the direct ray P_{ray1} as well as reflected one P_{ray2} was determined by the simulation program written in the Matlab environment.

Arrangement parameters of the repeater station in relation to positions of particular power overhead transmission line supports located within the considered radio communication link were used as the input data for the simulation procedure. Basing on the arrangement parameters of the repeater station and power overhead transmission line supports the terrain profiles should be defined between the repeater station as well as particular power overhead transmission line supports.

The propagation of the radio link at the distance of the reflected ray: antenna of the repeater
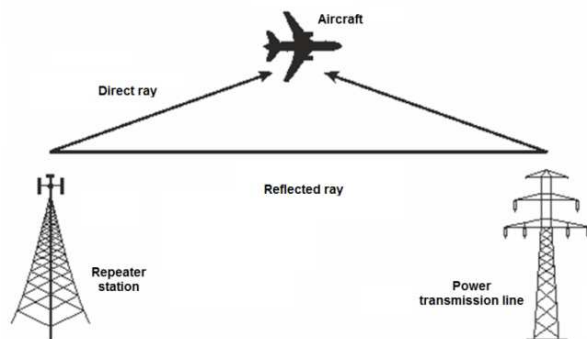

Figure 1: Radio communication link analysed.
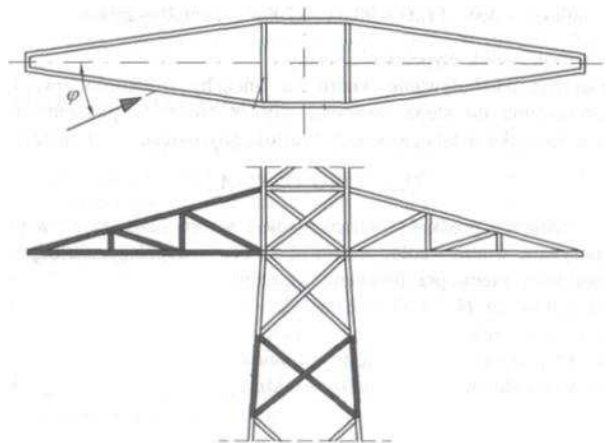
Figure 2: Example structure of power overhead transmission line support.
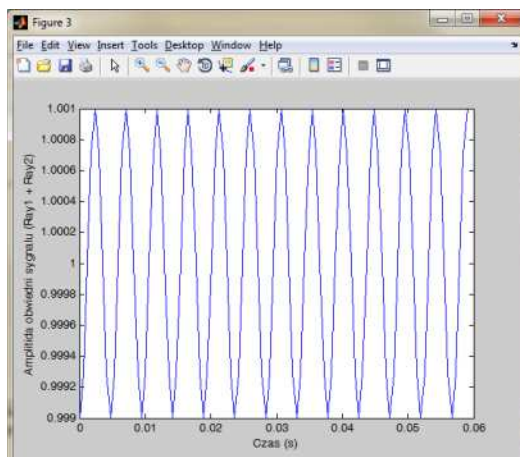
(a)
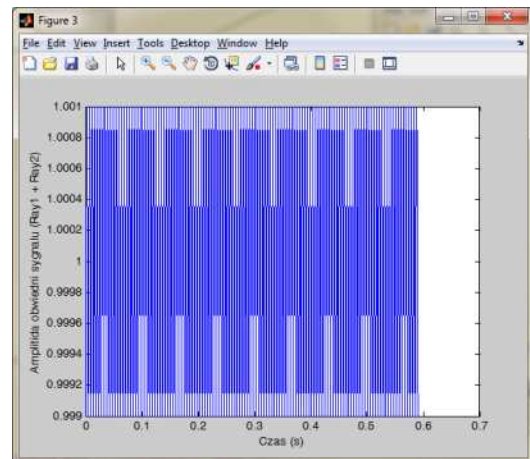
(b)

Figure 3: Amplitude of signal envelope $P_{ray1} + P_{ray2}$. (a) For a short time of observation (0.06 sek). (b) For a long time of observation (0.7 sek).

station, reflecting surface of particular power overhead transmission line supports as well as receiving antenna installed on the aircraft can be modelled using the free space (with no terrain obstacles) propagation model.

For the purpose of analysis the scenario was assumed that aircraft is moving along the straight line on a constant ceiling between the repeater station and a selected power overhead transmission line support.

The fading depth value of the signal at the input of receiving antenna is affected by the reflection coefficient of the signal from metal structures of particular power overhead transmission line supports.

Basing on the data related to metal surfaces of particular power overhead transmission line

Table 1: Values of reflection coefficients for particular segments of power lines maintained by consecutive power overhead transmission line supports.

Item	Area of metal structures of consecutive power overhead transmission line supports [m^2]	Height of the power overhead transmission line support [m]	Average value of the spacing between particular power overhead transmission line supports [m]	Reflection coefficient of a power segment line maintained by a given power overhead transmission line support
1	33.740	36.8		0.0019
2	34.200	39.1		0.0019
3	26.748	46.2		0.0015
4	33.985	55.2		0.0019
5	33.985	55.2		0.0019
6	34.453	36.8		0.0019
7	26.748	46.2	396	0.0015
8	32.214	52.2		0.0018
9	32.214	52.2		0.0018
10	34.563	39.1		0.0019
11	21.156	40.2		0.0012
12	23.097	43.2		0.0011
13	28.191	49.2		0.0016
14	33.738	36.8		0.0019

Figure 4: Signal spectrum with the component corresponding to the direct ray as well as reflected one.

supports Fig. 2, the values of reflection coefficients were evaluated for particular segments of power lines maintained by consecutive power line supports. The results of the reflection coefficients calculations are presented in the Tab. 1. Their levels oscillate around the value of 0.002. The references describing the electromagnetic factors of materials are [1, 4, 6, 7].

The results of the computer simulations for the sectors of power lines maintained by particular power overhead transmission line supports are present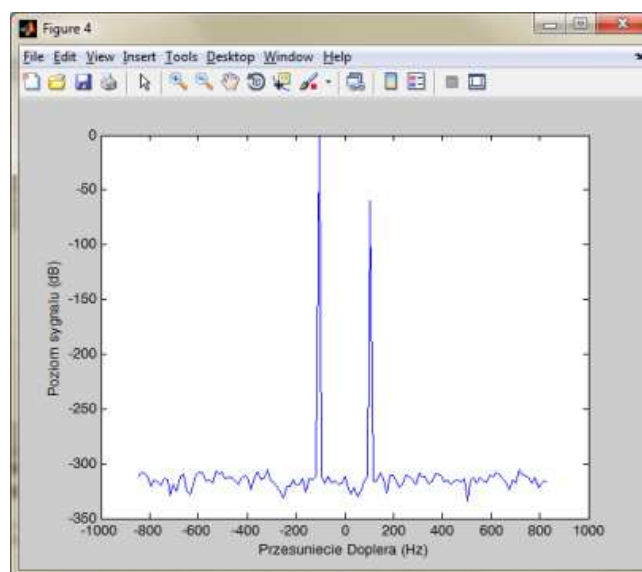ed in the consecutive figures. Fig. 3 presents amplitude of the signal envelope $P_{ray1} + P_{ray2}$. Fig. 4 presents the signal spectrum together with the component corresponding to the direct ray as well as reflected one (the difference $-70\,\mathrm{dB}$). The frequency difference of both components results from the Doppler shifting created by the motion of the aircraft.

3. CONCLUSIONS

Basing on the data presented it can be stated that the antenna of the repeater station illuminates almost as the whole of particular power supports. There is no essential terrain obstacles between the supports and transmitting antenna of the repeater station. In connection to the above it can be stated that the signal level of the reflected ray coming to the receiving antenna installed on the aircraft will be affected only by the reflection coefficient of the electromagnetic wave reflected from the metal structures of particular power overhead transmission line supports as well as by the attenuation of the path: repeater station, reflecting surface of particular power overhead transmission line supports as well as receiving antenna installed on the aircraft.

The depths of fadings corresponding to particular sectors do not exceed 2% of the carrier wave amplitude value at the input of the aircraft receiver. The depths of fadings of this order do not affect destructively onto the quality for simplex communications between the repeater station and the radio on the aircraft board.

The references connected with the topic of this article are [9–14].

REFERENCES

1. Kubacki, R., R. Przesmycki, and J. Ferenc, "Własnosci elektromagnetyczne nanokrystalicznego proszku stopu Fe-Si-B-Cu-Nb w zakresie mikrofalowym," *Przeglad Elektrotechniczny (Electrical Review)*, str: 92–95, ISSN 0033-2097, NR 12b/2011, 2011.
2. Przesmycki, R., "Measurement and analysis of compromising emanation for laser printer," *PIERS Proceedings*, 2661–2665, Guangzhou, China, Aug. 25–28, 2014.
3. Przesmycki R. and P. Skokowski, "Dual band microstrip antenna," *PIERS Proceedings*, 2641–2645, Guangzhou, China, Aug. 25–28, 2014.
4. Kubacki, R., E. Cwalina, M. Kuchta, and A. Dukata, "Specyfika rozkładu pola elektromagnetycznego wewnatrz pomieszczen i obudów komputerowych od wysokomocowych impulsów elektromagnetycznych," *Przeglad Elektrotechniczny (Electrical Review)*, No. 12b, 209–212, 2012.
5. Kubacki, R. and S. Lamari, "The UWB microstrip antenna with metamaterial and periodic structure," *PIERS Proceedings*, 2651–2655, Guangzhou, China, Aug. 25–28, 2014.
6. Lamari, S., R. Kubacki, and M. Czyzewski, "Frequency range widening of the microstrip antenna with the Sierpinski fractal patterned metamaterial structure," *MIKON, 2014 Conference Proceedings*, 773–775, 2014.
7. Bugaj, M., "Measurements of wall attenuation in closed spaces inside a building," *PIERS Proceedings*, 2681–2686, Guangzhou, China, Aug. 25–28, 2014.
8. Bugaj, M., "Attenuation measurements of materials used in construction of buildings," *PIERS Proceedings*, 2671–2675, Guangzhou, China, Aug. 25–28, 2014.
9. Piotrowski, Z., "Drift correction modulation scheme for digital signal processing," *Mathematical and Computer Modelling*, Vol. 57, No. 11–12, 2660–2670, 2013.
10. Bajda, A., M. Wrazen, and D. Laskowski, "Diagnostics the quality of data transfer in the management of crisis situation," *Electrical Review*, Vol. 87, No. 9A, 72–78, 2011.
11. Laskowski, D., P. Łubkowski, E. Pawlak, and P. Stanczyk, "Anthropo-technical systems reliability, safety and reliability: Methodology and applications," *Proceedings of the European Safety and Reliability Conference, ESREL 2014*, 399–407, 2014.

12. Ziółkowski, C. and J. M. Kelner, "Influence of the propagation environment on statistical properties of bearing," *Przeglad Elektrotechniczny*, Vol. 91, No. 3, 96–99, 2015.
13. Ziółkowski, C. and J. M. Kelner, "Geometry-based statistical model for the temporal, spectral, and spatial characteristics of the land mobile channel," *Wireless Personal Communications*, doi: 10.1007/s11277-015-2413-3, (article in press), 2015.
14. Kelner, J. M. and C. Ziółkowski, "The use of SDF technology to BPSK and QPSK emission sources' location," *Przeglad Elektrotechniczny*, Vol. 91, No. 3, 61–65, 2015.

The Reflectivity of the Ni-Zn Ferrite Tiles in the Microwave Frequency Range

Roman Kubacki

Faculty of Electronics, Military University of Technology, Warsaw, Poland

Abstract— In the paper, the investigation of the reflection coefficient of commercially available ferrite tiles at microwaves is presented. This material is typically used as an absorber in anechoic chambers but rather in low frequency range, mainly below 1 GHz where absorptive properties of sintered Ni-Zn ferrite are good enough. In the work it has been demonstrated that such ferrite absorber can also be used in higher frequencies up to 7 GHz. Proposed investigation of ferrite material allows to deeply reveal the reflection as well as the absorption properties of this material.

1. INTRODUCTION

The main advantage of testing in a chamber environment is having a clean ambient environment to work within. An anechoic chamber is the most common shield facility in use [8, 9, 11, 13, 14]. Such chamber contains ferrite tiles, carbon-filled absorber cones or mainly both of them. Generally there are two types of anechoic chambers. A full anechoic chamber is equipped with shielding material on the floor to antenna investigation while a semi-anechoic chamber has a metal ground plane on the floor [12, 16, 18–21, 23, 24].

To obtain high shielding performance for suppressing the radio frequency reflections inside the anechoic chamber the broadband absorptive materials with low level of reflection coefficient is necessary [2, 3, 6, 9]. In the frequency range below 1 GHz ferrites are the most commonly used materials as a kind of electromagnetic wave absorber. Many studies have been carried out to investigate the electromagnetic absorption properties of ferrite however, the application has been restricted by the narrow band characteristics of ferrite-absorbers [4, 5, 10, 15, 17, 21]. For the purpose of preparing a low-reflecting ferrite-absorber in the desired wide frequency range, two fundamental conditions must be satisfied, the first is that the energy of incident wave can enter the absorber (low reflectivity which can be guaranteed with suitable impedance matching characteristic of the material), and the second is that the electromagnetic wave entering into the materials can be attenuated (absorbed in the material) within the finite thickness of the material.

In this study the electromagnetic properties of commercially available Ni-Zn ferrite plates, were investigated. Typically this material is used as a metal-backed absorber. The principle of the metal-backed microwave absorber is to make use of the reflection reduction by impedance matching. According to the technical documentations the ferrite tiles can be used below 1 GHz due to their good shielding effectiveness in this frequency range. The electrical properties of commercially available Ni-Zn ferrite absorber above 1 GHz were not presented in the literature but very often such absorbers are used as the cover of the metal-floor hopefully that the reflectivity is almost low. In this work the investigation of reflection as well as absorption coefficients of commercially available Ni-Zn ferrite tiles at microwaves is studied. For this investigation the constitutive properties of material — permittivity and permeability have to be measured.

2. MEASUREMENT SYSTEM

Permittivity and permeability measurements of solid materials are commonly performed using coaxial fixtures. At microwaves, the coaxial line technique is especially recommended for broadband frequency measurements. The method of measurements of ε and μ based on determining the scattering parameters (S_{ik}) of the measured sample is the most popular [1]. In this work, the method of permittivity and permeability determination has been adopted for measurement of the slab materials in the coaxial lines. In this case, the measured material completely fills the cross section of the holder.

The single-slab plane-wave model was adapted to measure and compute the relative permittivity $\varepsilon = \varepsilon' - j\varepsilon''$ and permeability $\mu = \mu' - j\mu''$ of the measured material. The reflection and transmission S-parameters in coaxial line when the incident electromagnetic field is treated as plane wave can be interpreted as the infinite series of rays as a multiple reflections between the two surfaces of the sample. Scattering parameters of the sample S_{11} and S_{21} have been measured using the vector network analyzer (VNA) and they are the functions of unknown parameters ε and μ of the specimen.
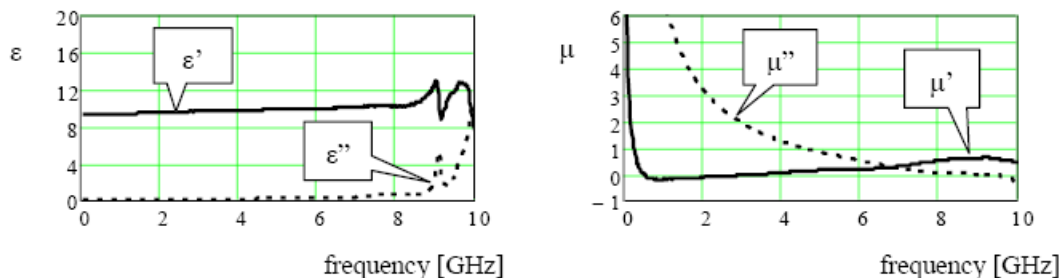
Figure 1: Real and imaginary parts of the relative permittivity and permeability of Ni-Zn sintered ferrite.

Having the scattering parameters of the sample, it is possible to calculate the permittivity and permeability using the NRW method [7, 22]. Measured values of permittivity and permeability of Ni-Zn ferrite in the frequency range from 100 MHz to 10 GHz are presented in Fig. 1.

Complex values of permittivity and permeability of Ni-Zn sintered ferrite allow to determine the reflection and absorption properties of this absorber.

3. REFLECTION COEFFICIENT

For a ferrite backed by a perfect conductor only the reflectivity can be characterized, but such information is not sufficient to recognize the absorption properties of the material. Additional analysis will be done with the S scattering parameters of a slab of the material in the free space. Two geometrical configurations of the material are taken into account:

a) the material is backed by a perfect conductor,

b) the material in the free space.

For the above geometry schematic presentations of the reflection coefficient Γ as well as reflection S_{11} and transmission S_{21} parameters of the slab of ferrite material for the case of normal incident of electromagnetic field are depicted in Fig. 2.

Figure 2(a) shows the case when analyzed ferrite absorber is backed by a perfect conductor, while Fig. 2(b) is done for investigation of such slab of material in free-space condition. The reflection coefficient Γ (Fig. 2(a)) of the slab of ferrite absorber backed by a perfect conductor can be compute using the transmission line analysis for normal incidence. For such field condition the incident electric and magnetic fields are parallel to the surface of the absorber slab. The reflection coefficient can be given as:

$$\Gamma = \frac{\sqrt{\mu}\tanh{(\gamma d)} - \sqrt{\varepsilon}}{\sqrt{\mu}\tanh{(\gamma d)} + \sqrt{\varepsilon}} \tag{1}$$

where: γ and d are the propagation constant and the thickness of the ferrite tile respectively.

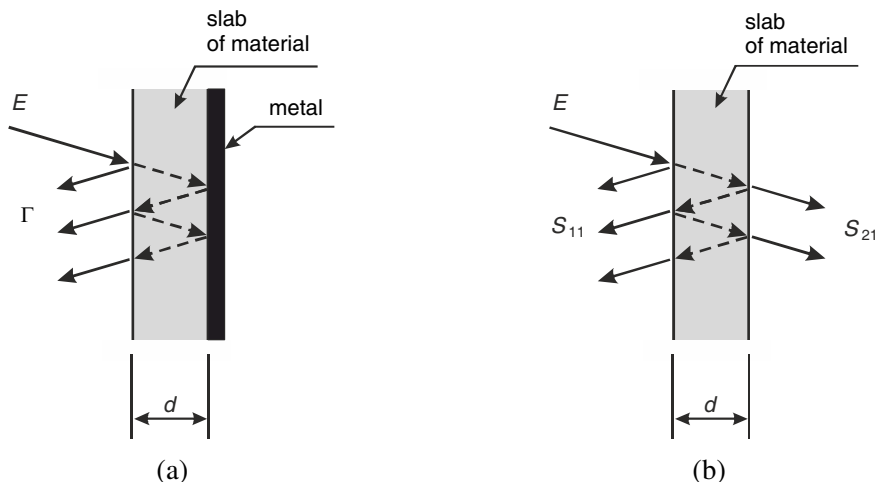(a)   (b)

Figure 2: Schematic view of the reflection and transmission of the slab of material for the case of normal incident; (a) the material is backed by a perfect conductor, (b) the material in the free space.

Alternatively, the reflection loss expressed in dB can be used and is given by:

$$LR = 20 \log(|\Gamma|) \tag{2}$$

The thickness of the ferrite tile has been taken as $d = 5.4\,\text{mm}$ and this is typical thickness of commercially available ferrite absorber. Reflection loss (LR) of this ferrite absorber backed by metal was shown in Fig. 3.
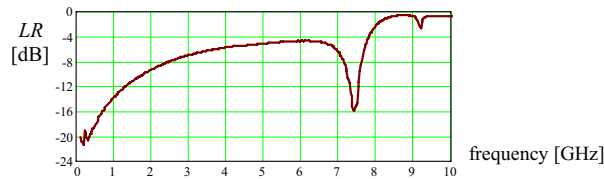

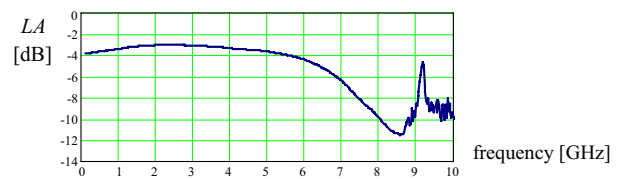Figure 3: Reflection loss of ferrite tile backed by a perfect conductor.

Figure 4: Absorption loss of ferrite tile.

As presented in Fig. 3, the reflection loss of 5.4 mm thick ferrite material backed by a metal shows good absorbing properties in the low frequency, i.e., below 1 GHz. In this case, the value of the reflection loss is low, lower than -15 dB. Thus, the reflected energy from the ferrite backed by metal can be negligible. In the frequency range from 1 to 7 GHz, the reflection loss increases with frequency and the level of reflected energy is higher, reaching value of -4 dB. At frequency 7.5 GHz, the ferrite backed by metal has good absorption properties. This good impedance matching was achieved by a quarter wavelength distance which works as a $\lambda_d/4$ transformer; where: λ_d is the wavelength in the material. For frequencies higher than 8 GHz the reflection loss is close to zero and this is why whole energy is reflected from such composite. Nevertheless, such investigation does not provide the information about the nature of such high reflection loss. To answer this question the additional investigation of absorbing properties of this material in free space condition are analyzed in the next section.

4. ABSORPTION COEFFICIENT

To obtain broader information about absorption properties of ferrite, the S-scattering parameters are necessary, Fig. 2(b). The S parameters can be acquired by the Vector Network Analyzer. According to the transmission line theory for a slab sample of material in free space, the following relationship can be formulated:

$$1 = |S_{11}|^2 + |S_{21}|^2 + |A|^2 \tag{3}$$

where: S_{11}, S_{21} — S-scattering parameters, A — absorption coefficient.

Alternatively, the absorption loss is expressed in decibels as:

$$LA = 20 \log(A)\,[\text{dB}] \tag{4}$$

The absorption loss can be used as a measure of the microwave absorption efficiency of the material. The higher the value of A is, the stronger the microwave absorbing ability of the composites would be. The value of absorption loss for Ni-Zn ferrite tile is presented in Fig. 4.

Figure 4 shows the absorption loss of ferrite tile in the free space condition. In frequencies lower than 6 GHz, the absorption loss is higher than -4 dB, which means that significant part of incident energy is absorbed by the material. In this frequency range, ferrite tiles are good absorbers and significantly reduce reflected rays. On the other hand, in frequency higher than 7 GHz the absorption loss has low value and the material does not absorb electromagnetic energy. In this case, the high value of the reflection loss mentioned in Fig. 3 is due to reflection from conducting surface on the back of ferrite because ferrite should be treated as transparent dielectric.

5. CONCLUSIONS

In this paper the investigation of the reflection coefficient of commercially available ferrite tiles used in anechoic chambers has been presented. This material is typically used as an absorber but his use in it is rather suggested for low frequency range, mainly below 1 GHz. In this work using additional investigation, it has been proved that such ferrite absorber can also be used in higher frequencies up to 7 GHz. Proposed investigation of ferrite material allows to deeply reveal the reflection as well as the absorption properties of this material.

ACKNOWLEDGMENT

REFERENCES

1. Baker-Jarvis, J., M. D. Janezic, B. F. Riddle, R. T. Johnj, P. Kabos, C. Holloway, and C. A. Grosvenor, "Measuring the permittivity and permeability of lossy materials: Solids, liquids, metals, building materials and negative-index materials," *Natl. Inst. Stand. Technol., Technical Note, NIST*, 2005.

2. Bugaj, J. and M. Wnuk, "Analysis of the impact of surface on parameters of cylindrical microstrip antennas [Analiza wielowarstwowej anteny cylindrycznej ze względu na promień krzywizny]," *Przegląd Elektrotechniczny (Electrical Review)*, No. 3, 48–51, 2015.

3. Bugaj, J. and M. Wnuk, "Analysis of conformal multilayer antenna working in X band [Analiza wielowarstwowej anteny konformalnejpracującej w pasmie X]," *Przegląd Elektrotechniczny (Electrical Review)*, No. 9, 46–49, 2009.

4. Bugaj, M., "Attenuation measurements of materials used in construction of buildings," *PIERS Proceedings*, 2671–2675, Guangzhou, Aug. 25–28, 2014.

5. Bugaj, M., "Measurements of wall attenuation in closed spaces inside a building," *PIERS Proceedings*, 2681–2686, Guangzhou, Aug. 25–28, 2014.

6. Bugaj, M. and M. Wnuk, "Optimization parameters of dielectric in aperture-coupled stacked patch antenna on bandwidth," *18th International Conference on Microwaves, Radar and Wireless Communications, MIKON*, 2010.

7. Nicolson, A. M. and G. F. Ross, "Measurement of the intrinsic properties of materials by time domain techniques," *IEEE Trans. Instrum. Meas.*, Vol. 19, 377–382, 1968.

8. Nowosielski, L. and J. Lopatka, "Measurement of shielding effectiveness with the method using high power electromagnetic pulse generator," *PIERS Proceedings*, 2687–2691, Guangzhou, Aug. 25–28, 2014.

9. Nowosielski, L. and Z. Piotrowski, "Honeycomb ventilation grill shielding effectiveness measuring methodology," *PIERS Proceedings*, 2692–2696, Guangzhou, Aug. 25–28, 2014.

10. Nowosielski, L., R. Przesmycki, M. Wnuk, and J. Rychlica, "The methods of measuring attenuation of thin absorbent materials used for electromagnetic shielding," *PIERS Proceedings*, 870–874, Marrakesh, Morocco, Mar. 20–23, 2011.

11. Nowosielski, L., R. Przesmycki, M. Wnuk, and K. Piwowarczyk, "Small chambers shielding efficiency measurements," *PIERS Proceedings*, 875–879, Marrakesh, Morocco, Mar. 20–23, 2011.

12. Nowosielski, L. and M. Wnuk, "Compromising emanations from USB 2 interface," *PIERS Proceedings*, 2666–2670, Guangzhou, Aug. 25–28, 2014.

13. Piwowarczyk, K., R. Przesmycki, L. Nowosielski, and M. Wnuk, "Pomiar odporności urządzeń informatycznych na promieniowane pole elektryczne o częstotliwości radiowej w zakresie (80–1000) MHz," *Przegląd Elektrotechniczny (Electrical Review)*, No. 86, 165–167, 2010.

14. Przesmycki, R., "Measurement and analysis of compromising emanation for laser printer," *PIERS Proceedings*, 2661–2665, Guangzhou, Aug. 25–28, 2014.

15. Przesmycki, R., L. Nowosielski, and M. Wnuk, "The laboratory stand for conducted emissions measurement in accordance with the military standard," *IEEE International Symposioum on EMC*, 275–278, Florida, 2010.

16. Przesmycki, R., L. Nowosielski, M. Bugaj, and K. Piwowarczyk, "Analiza emisji promieniowanej współczesnych urządzeń informatycznych," *Przegląd Elektrotechniczny (Electrical Review)*, No. 2, 4–6, 2012.

17. Przesmycki, R., L. Nowosielski, M. Bugaj, and K. Piwowarczyk, "Pomiar absorpcji materiałów pochłaniających fale elektromagnetyczne," *Przegląd Elektrotechniczny (Electrical Review)*, No. 2, 33–35, 2012.

18. Przesmycki, R. and P. Skokowski, "Dual band microstrip antenna," *PIERS Proceedings*, 2641–2645, Guangzhou, Aug. 25–28, 2014.

19. Przesmycki, R., M. Wnuk, L. Nowosielski, K. Piwowarczyk, and M. Bugaj, "The conducted and radiated emission levels from IT devices," *PIERS Proceedings*, 77–81, Kuala Lumpur, Malaysia, Mar. 27–30, 2012.

20. Przesmycki, R., M. Wnuk, L. Nowosielski, K. Piwowarczyk, and M. Bugaj, "Analysis of the radiated emissions of IT equipment," *PIERS Proceedings*, 1419–1423, Moscow, Russia, Aug. 19–23, 2012.

21. Przesmycki, R., M. Wnuk, M. Bugaj, and K. Piwowarczyk, "Analiza metod pomiarowych tłumienności torów w.cz.," *Przegląd Elektrotechniczny (Electrical Review)*, No. 2, 17–19, 2012.

22. Weir, W. B., "Automatic measurement of complex dielectric constant and permeability at microwave frequencies," *Proc. IEEE*, Vol. 62, 33–36, 1974.

23. Wnuk, M. and J. Bugaj, "Analysis of surface waves in microstrip array," *16th International Conference on Microwaves, Radar and Wireless Communications, MIKON*, 2006.

24. Wnuk, M., M. Bugaj, R. Przesmycki, L. Nowosielski, and K. Piwowarczyk, "Wearable antenna constructed in microstrip technology," *PIERS Proceedings*, 67–71, Kuala Lumpur, Malaysia, Mar. 27–30, 2012.

Modelling of the Angle of Arrival Scattering Using the Von Mises Function for Compatibility Analysis

Leszek Nowosielski, **Marian Wnuk**, **Jan M. Kelner**, and **Cezary Ziółkowski**

Faculty of Electronics, Military University of Technology

Gen. S. Kaliskiego 2 Str., Warsaw 00-908, Poland

Abstract— In this paper, the evaluation of the modeling capabilities of scattering angle for compatibility analysis is presented. We present an empirical power azimuth spectrum (PAS) model based on the von Mises distribution. This model allows a varied shape of AOA distribution. For different propagation scenarios, the fit of the von Mises model to empirical PAS is presented in figures. Results of measurements taken from the open literature are used as reference data. Authors present brief characteristics of measurement scenarios. Accuracy assessment of the fit of the proposed model and empirical data is shown by graphs and numerical calculations.

1. INTRODUCTION

A designing and building of sector antenna systems in the modern wireless communication systems require an analysis of a cross-sectors electromagnetic compatibility. This is due to the occurrence of the angular dispersion of the received signal. It is result of the multipath phenomena. This problem is particularly important in the urban environment.

To analyse the angle of arrival (AOA) are used two model types: the probability density function (PDF) of AOA and the power azimuth spectrum (PAS). PDF of AOA models are theoretical. In contrast, PAS models are practical, because the PAS characteristics are determined on the basis of measurements. PAS and PDF of AOA models can be divided into two main groups, i.e., theoretical geometric and empirical models. The empirical models, e.g., the Gaussian and Laplacian models, use the well-known functions (distributions) for modelling the statistical properties of AOA. For such models, physical interpretation is difficult, however, these functions fit well PAS characteristics obtained in the real environment.

This paper presents an empirical model based on the von Mises distribution. This model allows a varied shape of AOA distribution. The fit of the von Mises model to empirical PAS is presented in figures. Results of measurements taken from the open literature are used as reference data. Authors present brief characteristics of measurement scenarios. Accuracy assessment of the fit of the proposed model and empirical data is shown. The least-square error (LSE) and the rms angle spread are used as evaluation criteria.

The rms delay spread is used to classify the type of propagation environment. This parameter can be determined based on the power delay profile (PDP) or the power delay spectrum (PDS). Obtained results show that the proposed model can be applied to the channel modelling for the various scenarios and propagation conditions.

2. THE VON MISES DISTRIBUTION

The von Mises PDF for the azimuth AOA, $f(\theta)$, is given by [1]

$$f(\theta) = \frac{\exp\left(\kappa \cos\left(\theta - \theta_0\right)\right)}{2\pi I_0(\kappa)} \quad \text{for} \theta \in (-\pi, \pi\,\rangle \tag{1}$$

where $I_0(\kappa)$ is the zero-order modified Bessel function, $\theta_0 \in (-\pi, \pi\,\rangle$ accounts for the mean direction of AOA, and κ determines the width of AOA distribution. In Fig. 1, the graphs of von Mises PDF is presented for different values of κ.

As we can see, if model parameter equal to zero then this distribution is uniform that is often used for modelling of the local isotropic scattering. If the von Mises parameter tends to infinity then distribution has the high concentration and small variance like the Dirac delta. These properties are the basis for the adaptation of the model to different propagation environments. The accuracy assessment of PDF of AOA by von Mises distribution is determined on basis of measurement results for different scenarios. Since, this assessment is based on PASs comparison so von Mises distribution must be converted to PAS. Note that [2]
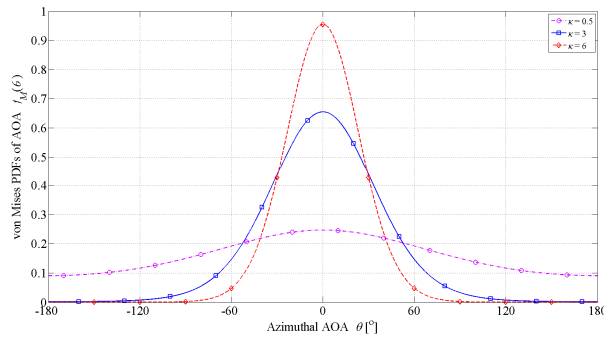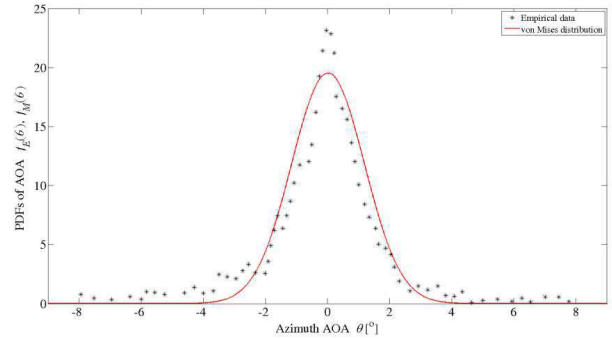
$$P(\theta) = P_0 \cdot f(\theta) \tag{2}$$

Figure 1: Von Mises PDF for different values of κ.

Figure 2: Von Mises model and empirical PAS – Bristol RA [3].

where P_0 total power of received signal.

Therefore, in logarithmic scale, we can describe PAS as

$$P_{\mathrm{dB}}(\theta) \, [\mathrm{dB}] = 10 \log_{10} \frac{P(\theta)}{\max(P(\theta))} = 10 \log_{10} \frac{f(\theta)}{\max(f(\theta))} \tag{3}$$

The error approximation assessment for empirical PAS and von Mises model is based on above expression.

3. MEASUREMENT SCENARIOS

The results of the PAS measurement that are presented in [3–6], are the basis for approximation error assessment of von Mises model for variation of propagation environments.

3.1. Scenario 1 (Sc1) [3]

The rural measurement campaign took place near Bristol in UK. This measurement place is classified as rural area (RA). The received antenna was mounted on base station (BS) tower at a height of 27 m. It ensures line-of-sight (LOS) propagation conditions. The received antenna was built with the eight-element phased antenna array. At the array output, the eight branch signals were sampled with interval equal 0.923 μs. These samples were stored on a hard disk for off-line processing. Time of recording a single measurement sequence required 4.6 ms. Transmitting antenna was an omnidirectional antenna that was mounted on the mobile station (MS). The frequency carrier and structure of the sounding signal were designed according to the DCS1800 standard. The average distance between MS and BS was 5000 m.

3.2. Scenario 2 (Sc2) [4]

The urban measurement campaign was conducted in Aarhus (Denmark). The propagation environment is characterized by an irregular street grid and buildings ranging from four to six floors. This measurement place is classified as typical urban area (TU). The measurement system was designed for uplink transmission. The BS was equipped with an eight-element uniform linear antenna array that was mounted on at a height of 32 m (12 m above average rooftop level). At the array output, the eight branch signals were sampled with interval equal 0.122 μs and recorded for further off-line processing. The signal transmitting source with an omnidirectional antenna was mounted on a car. The measurement carried out along six different routes having an average length of 2 km. The sounding signal operated at a carrier frequency of 1.8 GHz. Its bandwidth was comparable to the bandwidth used by selected wide-band Code-Division Multiple Access (CDMA) third-generation cellular system. In most cases, the propagation conditions were no line-of-sight (NLOS). The average distance between MS and BS is 1500 m.

3.3. Scenario 3 (Sc3) [4]

The measurement campaign was conducted in Stockholm (Sweden). This area is characterized as a TU with developed infrastructure. The same testbed, measurement methodology and parameters were used as in a case of the scenario 2. About difference between these two scenarios decides the height of the received antenna location. In this case, the BS antenna was mounted 21 m above ground level, which corresponds to the average rooftop level of the surrounding buildings.

3.4. Scenario 4 (Sc4) [5] and 5 (Sc5) [6]

The measurements were carried out in urban area with a high degree of urbanization. This measurement place is located in Aalborg (Denmark). The propagation environment is characterized by irregular street layout and mostly 3–5 story buildings with only a few higher buildings. It is classified as a TU area. Measurement system was designed for uplink transmission. The BS was equipped with an eight-element uniform linear antenna array that was mounted on at a height of 41 m. The signal transmitting source with an omnidirectional antenna was mounted on a car (MS). The frequency carrier (1.8 GHz) and structure of the sounding signal were designed according to the GSM standard. So, its bandwidth was comparable to the bandwidth (200 kHz) used by GSM two-generation cellular system. Measurements were carried out along four test routes, where the average distance from BS is 2.1 km. For scenario 4 and 5, the measurement campaigns were conducted in the same propagation environment. The diversity of these scenarios due to different measurement routs.

4. COMPARISON OF THE VON MISES MODEL AND EMPIRICAL RESULTS

Adaptation of von Mises model to empirical data is made possible by the parameter of the model. The selection criterion of κ value is minimize *LSE*. In Figs. 2–6, the graphical comparisons of
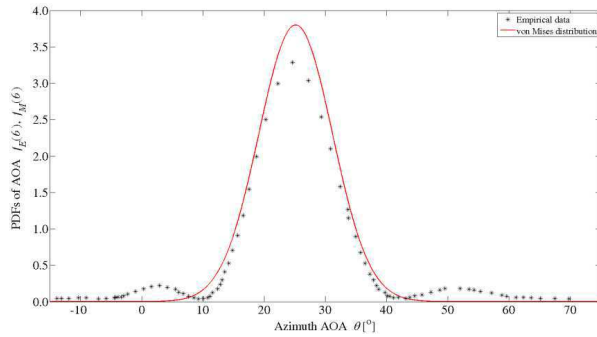
Figure 3: Von Mises model and empirical PAS — Aarhus TU [4].
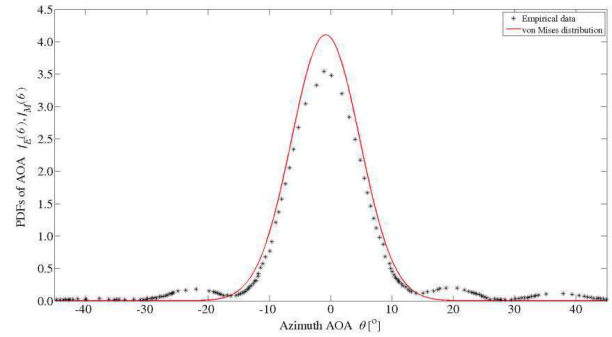
Figure 4: Von Mises model and empirical PAS — Stockholm TU [4].
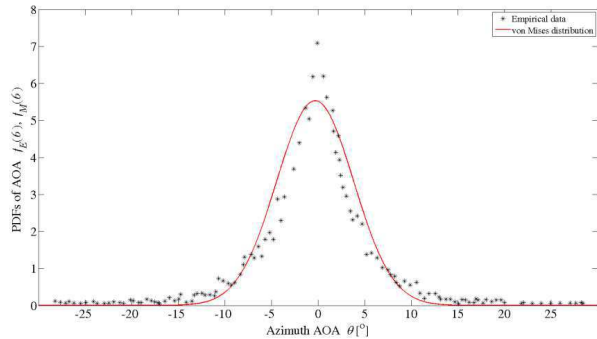
Figure 5: Von Mises model and empirical PAS — Aalborg TU [5].
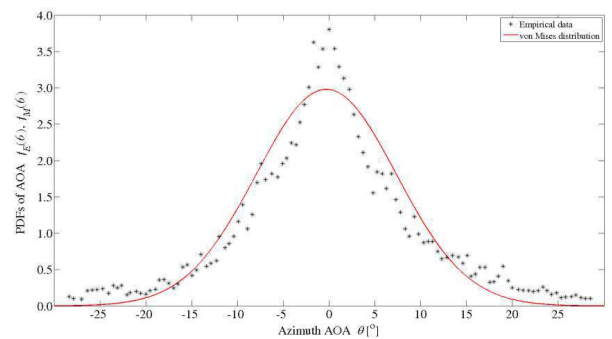
Figure 6: Von Mises model and empirical PAS — Aalborg TU [6].

Table 1: The results of numerical calculation for measurement scenarios.

	Sc1	Sc2	Sc3	Sc4	Sc5
σ_τ [µs]	0.0932	0.3221	0.6285	1.2337	1.2337
σ_θ [°]	2.089	6.428	9.445	9.782	10.169
$\sigma_{\theta M}$ [°]	1.173	4.162	7.679	5.604	6.045
LSE	3,228008	0,189050	0,083797	0,018543	0,019532
κ [1]	2398.4	192.5	56.0	106.1	90.9

where: σ_τ, σ_θ — rms delay and angle spread, respectively for measurement,
$\sigma_{\theta M}$ — rms angle spread for von Mises model,
κ — optimum value of von Mises model parameter.

empirical results and von Mises model with κ optimum value are presented.

For each measurement scenarios, the results of numerical calculations are presented in Table 1.

As we can see, von Mises model of PAS provides faithful reproduction of the scattering angle of reception signal. The approximation error of the angle spread does not exceed a few degrees. The article connected with the topic of this article are [7–11].

5. CONCLUSIONS

In this paper, the evaluation of the modeling capabilities of scattering angle for compatibility analysis is presented. Obtained results show that von Mises model of PAS reproduces probabilistic AOA properties. The choice of the model parameter value makes it possible to adopt the model to different environmental propagation conditions. This fact provides the versatility of von Mises model. It gives a basis to assess the interference level which arrives at receiver from the cells served by neighboring base stations.

REFERENCES

1. Abdi, A., J. A. Barger, and M. Kaveh, "A parametric model for the distribution of the angle of arrival and the associated correlation function and power spectrum at the mobile station," *IEEE Transactions on Vehicular Technology*, Vol. 51, No. 3, 425–434, May 2002.

2. Ziółkowski, C., "Statistical model of the angular power distribution for wireless multipath environments," *IET Microwaves, Antennas & Propagation*, Vol. 9, No. 3, 281–289, Feb. 2015.

3. Pedersen, K. I., P. E. Mogensen, and B. H. Fleury, "Power azimuth spectrum in outdoor environments," *Electronics Letters*, Vol. 33, No. 18, 1583–1584, Aug. 1997.

4. Pedersen, K. I., P. E. Mogensen, and B. H. Fleury, "A stochastic model of the temporal and azimuthal dispersion seen at the base station in outdoor propagation environments," *IEEE Transactions on Vehicular Technology*, Vol. 49, No. 2, 437–447, Mar. 2000.

5. Mogensen, P. E., K. I. Pedersen, P. Leth-Espensen, B. H. Fleury, F. Frederiksen, K. Olesen, and S. L. Larsen, "Preliminary measurement results from an adaptive antenna array testbed for GSM/UMTS," *IEEE VTC-1997 47th IEEE Vehicular Technology Conference*, Vol. 3, 1592–1596, Phoenix, AZ, USA, 1997.

6. Fleury, B. H., M. Tschudin, R. Heddergott, D. Dahlhaus, and K. I. Pedersen, "Channel parameter estimation in mobile radio environments using the SAGE algorithm," *IEEE Journal on Selected Areas in Communications*, Vol. 17, No. 3, 434–450, Mar. 1999.

7. Kubacki, R., R. Przesmycki, and J. Ferenc, "Własnosci elektromagnetyczne nanokrystalicznego proszku stopu Fe-Si-B-Cu-Nb w zakresie mikrofalowym," *Przeglad Elektrotechniczny (Electrical Review)*, 92–95, ISSN 0033-2097, NR 12b/2011.

8. Przesmycki, R., "Measurement and analysis of compromising emanation for laser printer," *PIERS Proceedings*, 2661–2665, Guangzhou, China, Aug. 25–28, 2014.

9. Przesmycki, R. and P. Skokowski, "Dual band microstrip antenna," *PIERS Proceedings*, 2641–2645, Guangzhou, China, Aug. 25–28, 2014.

10. Bugaj, M., "Measurements of wall attenuation in closed spaces inside a building," *PIERS Proceedings*, 2681–2686, Guangzhou, China, Aug. 25–28, 2014.

11. Bugaj, M., "Attenuation measurements of materials used in construction of buildings," *PIERS Proceedings*, 2671–2675, Guangzhou, China, Aug. 25–28, 2014.

Influence of the Environment on the Cross-sector Compatibility in Wireless Access System

Leszek Nowosielski, **Cezary Ziółkowski**, and **Jan M. Kelner**
Faculty of Electronics, Military University of Technology
gen. Sylwestra Kaliskiego St. No. 2, Warsaw 00-908, Poland

Abstract— This paper is devoted the evaluation of power permeation to MS from BS that is in neighbouring sector. The basis for the analysis is the power azimuth spectrum (PAS) that describes the angle distribution of the signal power at the input of receiver. The results of the numerous measurements show that with the increase of the environment urbanization degree, the angular dispersion of the received signal is increased. From among the many models, the von Mises model is used as PAS. Influence of the environment differentiation on PAS is taken into account by the adaptive selection of van Mises parameter. Obtained results provide the opportunity to evaluate of the multipath environment influence on the cross-sector compatibility in wireless system.

1. INTRODUCTION

Multipath of the wave propagation is the phenomenon that plays a dominant role in formation of internal disturbances in radio systems. This phenomenon significantly limits the possibilities of signal transmission in wireless systems. To increase the capacity of access system, the spatial sectorisation of areas that are supported by the access base station (BS), is used. The multipath phenomenon that occurs in urban area, is the cause of the signal power permeation to neighbouring sectors. It is reason the occurrence of additional disturbances in access neighbouring sectors. This phenomenon is especially important in the case of mobile object (mobile station MS) location near the border of neighbouring sectors. In wireless access systems, the effect of the phenomenon is important for the implementation handover procedure.

This paper is devoted the evaluation of power permeation to MS from BS that is in neighbouring sector. The basis for the analysis is power azimuth spectrum (PAS) that describes the angle distribution of signal power at the input of the receiver. For different types of environments, these characteristics are differentiated. The results of the numerous measurements show that with the increase of the environment urbanization degree, the angular dispersion of the received signal is increased. From among the many models, the von Mises function is used as PAS model. Influence of the environment differentiation on PAS is taken into account by the adaptive selection of van Mises parameter. The model validation is made on the basis of the results that are obtained for five measurement scenarios taken from open literature. As criterion of model validation, the least square error (LSE) minimization is used. The characteristic that shows the functional relationship of permeation power and location angle of MS with respect to BS of neighbouring sector is the analysis result presented in the paper. The obtained characteristic is the basis for the evaluation of the disturbance power level that originates from the neighbouring sectors of the wireless access system.

2. EVALUATION OF ENVIRONMENT ON POWER SCATTERING

In our paper, we analysis influence of multipath propagation on power scattering of received signal. In cellular systems, the sector antennas are used. In Fig. 1, the power patter of sector antenna is presented.

Presented pattern is a base for numerical calculation of the interference power at receiver that is located in neighbouring sector. For scattering power, von Mises model is used. In [1, 2], the description of this model is included. In our analysis, we evaluate level of the interference power for five different propagation scenarios. The differentiation degree of environments is described by different values of rms angle spread. In Figs. 2–6, the graphs of interference power for different propagation environment are presented. Details of measurement scenarios are described in [3–6].

From graphs result that with increasing scattering propagation environments increasing the level of interference power coming from the neighboring sectors. For each propagation scenarios, the results of numerical calculations are presented in Table 1. The article connected with the topic of this article are [7–21].
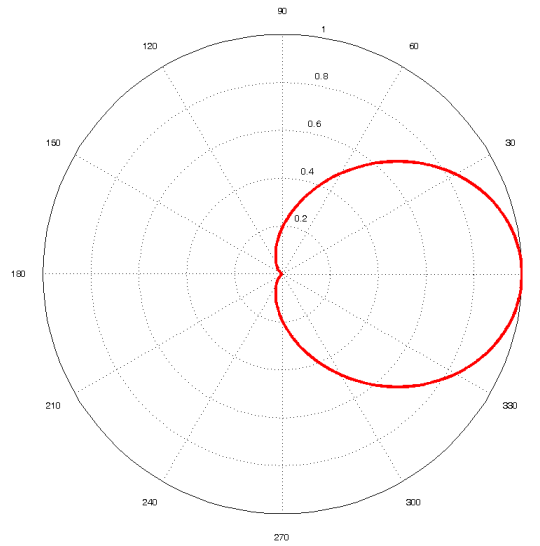
Figure 1: Power pattern of sector antenna.
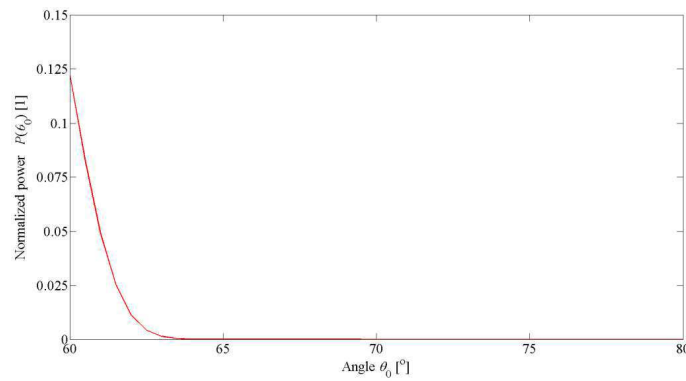
Figure 2: Interference power for Scenario 1 (RA-Bristol [3]).
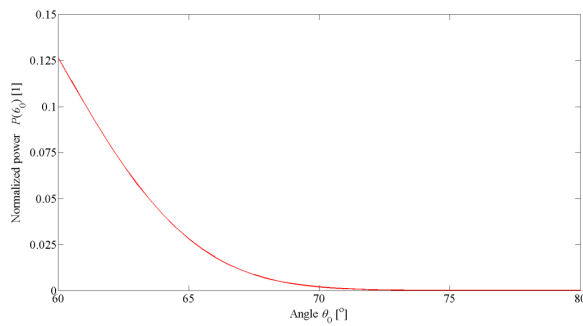
Figure 3: Interference power for Scenario 2 (TU-Aarhus [4]).
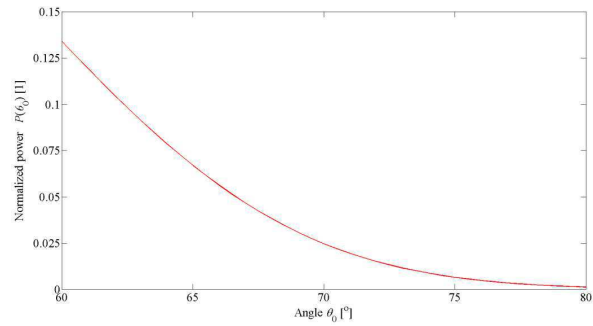
Figure 4: Interference power for Scenario 3 (TU-Stockholm [4]).

Table 1: Normalized interference power for varied propagation scenarios.

	Sc1	Sc2	Sc3	Sc4	Sc5
κ [1]	2398.4	192.5	56.0	106.1	90.9
P_Σ [°]	0.2971	0.8904	1.6718	1.1982	1.2969

where: κ — optimum value of von Mises model parameter,
P_Σ — normalized interference power.

Figure 5: Interference power for Scenario 4 (TU-Aalborg [5]).

Figure 6: Interference power for Scenario 4 (TU-Aalborg [6]).

3. CONCLUSIONS
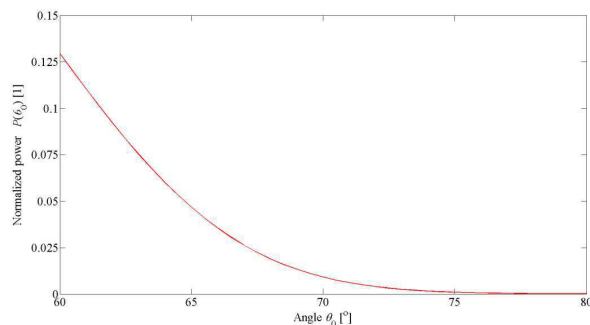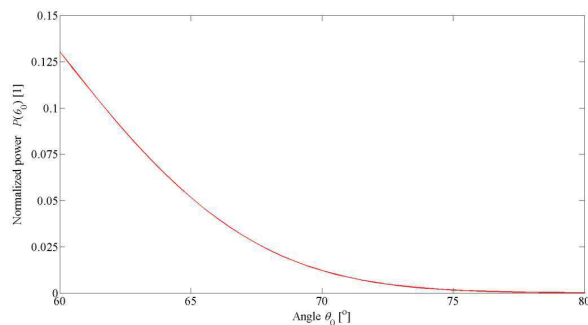
In this paper, the evaluation of the interference power from multipath propagation is presented. Obtained results show that with increasing scattering propagation environments increasing the level of interference power coming from the neighboring sectors. As PAS model the von Mises model is used. Obtained results provide the opportunity to evaluate of the multipath environment influence on the cross-sector compatibility in wireless system.

REFERENCES

1. Abdi, A. J. A. Barger, and M. Kaveh, "A parametric model for the distribution of the angle of arrival and the associated correlation function and power spectrum at the mobile station," *IEEE Transactions on Vehicular Technology*, Vol. 51, No. 3, 425-434, May 2002.
2. Nowosielski, L., M. Wnuk, J. M. Kelner, and C. Ziółkowski, "Modelling of the angle of arrival scattering usingthe von Mises function for compatibility analysis, ," *PIERS Proceedings*, Prague, Czech Republic, 6–9 July 2015.
3. Pedersen, K. I., P. E. Mogensen, and B. H. Fleury, "Power azimuth spectrum in outdoor environments," *Electronics Letters*, Vol. 33, No. 18, 1583–1584, August 1997.
4. Pedersen, K. I., P. E. Mogensen, and B. H. Fleury, "A stochastic model of the temporal and azimuthal dispersion seen at the base station in outdoor propagation environments," *IEEE Transactions on Vehicular Technology*, Vol. 49, No. 2, 437–447, March 2000.
5. Mogensen, P. E., K. I. Pedersen, P. Leth-Espensen, B. H. Fleury, F. Frederiksen, K. Olesen, and S. L. Larsen, "Preliminary measurement results from an adaptive antenna array testbed for GSM/UMTS," *47th IEEE Vehicular Technology Conference, IEEE VTC-1997*, Vol. 3, 1592–1596, Phoenix, AZ, USA, 1997.
6. Fleury, B. H., M. Tschudin, R. Heddergott, D. Dahlhaus, and K. I. Pedersen, "Channel parameter estimation in mobile radio environments using the SAGE algorithm," *IEEE Journal on Selected Areas in Communications*, Vol. 17, No. 3, 434–450, March 1999.
7. Kubacki, R., R. Przesmycki, and J. Ferenc, "Własności elektromagnetyczne nanokrystalicznego proszku stopu Fe-Si-B-Cu-Nb w zakresie mikrofalowym," *Przegląd Elektrotechniczny (Electrical Review)*, 92–95, ISSN 0033-2097, NR 12b, 2011.
8. Przesmycki, R., M. Wnuk, M. Bugaj, and K. Piwowarczyk, "Analiza metod pomiarowych tłumienności torów w.cz.," *Przegląd Elektrotechniczny (Electrical Review)*, 17–19, ISSN 0033-2097, NR 2, 2012.
9. Kubacki, R., J. Ferenc, R. Przesmycki, and M. Wnuk, "The nanocrystalline FeSiBCuNb finemet absorption properties at microwaves," *IEEE Transactions On Electromagnetic Compatibility*, Vol. 54, No. 1, 93–100, ISSN: 0018-9375, February 2012.
10. Przesmycki, R., "Measurement and analysis of compromising emanation for laser printer," *PIERS Proceedings*, 2661–2665, Guangzhou, China, August 25–28, 2014.
11. Przesmycki, R., M. T. Wnuk, P. Skokowski, and M. Bugaj, "Identification of interface in the complex systems based on radiated emission of mobile computer," *PIERS Proceedings*, 2656–2660, Guangzhou, China, August 25–28, 2014.
12. Przesmycki, R., M. Bugaj, and M. T. Wnuk, "Wideband microstrip antenna," *PIERS Proceedings*, 2646–2650, Guangzhou, China, August 25–28, 2014.

13. Przesmycki, R. and P. Skokowski, "Dual band microstrip antenna," *PIERS Proceedings*, 2641–2645, Guangzhou, China, August 25–28, 2014.

14. Bugaj, M. and M. Wnuk, "Influence of parameters of dielectric in aperture-coupledstackedpatchantenna on bandwidth [Wpływ parametrów dielektryka w wielowarstwowej antenie planarnej zasilanej szczelinowo na szerokość jej pasma pracy]," *Przeglad Elektrotechniczny*, Vol. 85, No. 9, 50–53, 2009.

15. Wnuk, M. and M. Bugaj, "Analysis of radiating structures placed on multilayer dielectric," *WIT Transactions on Modelling and Simulation*, Vol. 46, 747–755, 2007.

16. Bugaj, M., "Measurements of wall attenuation in closed spaces inside a building," *PIERS Proceedings*, 2681–2686, Guangzhou, China, August 25–28, 2014.

17. Bugaj, M. and M. Wnuk, "Optimization parameters of dielectric in aperture-coupled stacked patch antenna on bandwidth," *4th Microwave and Radar Week, MRW-2010 — 18th International Conference on Microwaves, Radar and Wireless Communications, MIKON 2010 — Conference Proceedings*, 2010.

18. Bugaj, M. and M. Wnuk, "Analysis of conformal multilayer antenna working in X band [Analiza wielowarstwowej anteny konformalnej pracujaej w pasmie X]," *PrzegladElektrotechniczny*, Vol. 85, No. 9, 46–49, 2009.

19. Wnuk, M. and J. Bugaj, "Analysis of surface waves in microstrip array," *16th International Conference on Microwaves, Radar and Wireless Communications, MIKON*, 2006.

20. Bugaj, M., "Attenuation measurements of materials used in construction of buildings," *PIERS Proceedings*, 2671–2675, Guangzhou, China, August 25–28, 2014.

21. Bugaj, M. and M. Wnuk, "Optimization parameters of dielectric in aperture-coupled stacked patch antenna on bandwidth," *4th Microwave and Radar Week, MRW-2010 — 18th International Conference on Microwaves, Radar and Wireless Communications, MIKON 2010 — Conference Proceedings*, 2010.

Mobile Recorder for Electrical Activity of the Heart

M. Bernat and Z. Piotrowski

Faculty of Electronics, Military University of Technology, Warsaw, Poland

Abstract— The presented study is dedicated to a mobile recorder designed to keep log of electric activity of the heart and incorporated into the expert system developed to detect fatigue status of a patient. The newly designed recorder has a modular structure and its enclosure houses two double-sided printed circuit boards (PCBs), separately for the analog part (BtECG) and the digital one (BtECGradio). The analog module is responsible for measurement of electric signals received from the patients' body with their further amplification, filtration and conversion to digital form. In addition, in comprises a source of stabilized voltages for both analog and digital circuits. The digital module receives binary data, extracts its useful portion, carries out formatting of the data to form of frames required for RF communication according to the Bluetooth standard and enables wireless communication with a collaborating unit. The analog subassembly is meant to record electric potentials within the range from 0.2 to 2 mV and owing to the high level of the CMRR factor it substantially eliminates the common-mode signals. Furthermore, it enables two-stage amplification, filtration of high-frequency interferences, high-pass filtration and active, five-staged low-pass filtration. The digital module of the recorder enables RF data transmission according to the Bluetooth 4.0 standard, communication with a host unit with use of the UART and SPI interfaces (reading of RF packages from the CPU module) as well as communication with a host unit with use of the Full Speed USB 2.0 (BGAPI) protocol. Its power consumption is ultra low and the communication sessions is controlled by a microprocessor of the 8051 architecture. The digital module also enables the user to embed own application and to debug them via the CC Debugger Connector link. The base chip for development of the digital module is the BLE112 Bluetooth Smart module from Bluegiga.

1. INTRODUCTION

1.1. Parameters of ECG Mobile Recorders

In the area of recording and analysis of ECG signal there are available the mobile devices with the parameters similar to the ambulatory solutions. Regardless of the necessary miniaturisation and the battery power supply they are produced in the version of one, three, seven as well as classical twelve leads.

The structures of portable [11] type can be divided into the classes: eventholters and continuous recording devices (several hours). They record the electrocardiogram onto the integrated carrier (e.g., Flash memory [11]), which is then reproduced and analysed by a cardiologist. More advanced solutions have the embedded algorithms for ECG signal processing in the real time [12]. They have the function of fast communication with the portable devices (notebooks, palmtops, smartphones), they take advantage of the computing power from the cooperating microcomputers and GPRS modules for the packet data exchange (in GSM networks) as well as they demonstrate the analysis results in the embedded displays.

From the technical point of view, the mobile devices for ECG signal recording and analysing can be described by means of the group of coherent parameters. They result directly from the structure, and indirectly from the apparatus configuration. The set of parameters which are the most essential for a design engineer as well as for a user include: number of leads, types of leads (Einthoven's: I, II, III; Goldberger's: aVR, aVL, aVF, Wilson's: V1, V2, V3, V4, V5, V6; modified [4] MCL1; 12-lead Mason-Likar variant), input impedance (10–100 MΩ), input dynamic range [1], CMRR [3, 8] (1), amplification [1], transfer bandwidth [2], converter resolution, sampling frequency, measured heart rate zone (bpm), quantum processing, transmission/interface, method for device power supply, battery capacity, data memory, certificate/approval.

$$CMRR = 20 \cdot \log \left(\frac{A_D \cdot V_{CM}}{V_{OUT}} \right) \tag{1}$$

where: A_D — differential gain, V_{CM} — common voltage applied to both differential inputs, V_{OUT} — output voltage appearing as response to the application of common voltage V_{CM}.

Additionally, it is required from the portable recorders to meet the electromagnetic compatibility prerequisite. The implementations and test results of special hood shielding for electrical equipment are well known [13–20].

Moreover, modern portable bio expert system bases on built-in advanced algorithms e.g. for drivers conditions estimation [21, 22].

1.2. Mobile System Criteria

While defining the concept of mobile system or electrocardiographic device you need specify the set of the most important features which should characterise such system. According to its purpose, we can describe it as: personal and non-ambulatory packet enabling long-term recording of ECG signal, recording on request or signal automatic analysis in the real time.

The minimum technical requirements are defined with the group of parameters such as: overall dimensions — the accepted size should not be bigger than the size of typical mobile phone, weight of ca. 100 g, L/W/H: 110/50/15 mm; number of leads — 1–12 depending on the diagnostic needs; types of leads — allowing free movement and enabling self-assembling; input impedance — 10 MΩ and more; input dynamic range — from a few to several millivolt; CMRR — 60–120 dB; transfer bandwidth — 0.05–100 Hz; converter resolution — 10 bites and more, at present reaching 24 bits; sampling frequency — 200 Hz and more, measured heart rate zone — from several bpm at the lower limit up to two hundred and more at the upper limit; transmission/interface — at least one from the cable groups: USB, RS232, PSTN and one wireless: Bluetooth [10], IrDA, GSM/GPRS, WiFi; power supply from battery or rechargeable battery with the possibility for replacement or cell recharging; safe supply voltage — a few volts; battery capacity — they allow continuous operation for the time of carrying out at least one measurement/diagnostic cycle; data memory (non-volatile memory, e.g., flash memory card) — they allow continuous recording of data or analysis results during one measurement/diagnostic cycle, certificate/approval — the device should meet the requirements of the standards PN-EN 60601 [9] (according to 93/42/EEC) and be admitted to trading on domestic/European market [7].

There is no sharp line in the classification parameters of ECG mobile devices. They result largely from the features of the newest range of products, possibilities of modern technologies and customers expectations.

1.3. Design Trends

The development of mobile devices for recording and analysing of ECG signal is stimulated with the need for miniaturisation, capacity increase, uncomplicated and interactive operation as well as the possibility for fast data exchange.

As far as the overall dimensions are concerned the standard are the devices not bigger than typical mobile phone or smartphone (less than 120/70/20 mm and not heavier than 100–150 g). The direction of capacity increase is first of all: computing power sufficient for parallel recording and analysing signals from many (even twelve) leads, algorithms realising the detection and classification of disturbances and incidents, based on the wide range of designated indicators (HR, HRV, HRT, QRS complexes, ST segments, QT, T-waves, VCG, TVCG), support for memory cards with great capacity (2 GB and more) or suitable size of the embedded memory, time of operation while using one set of the supply source from a few days up to a week.

While offering the solutions to individual customers, the producers reduce the number of leads. This way they shorten time needed for taking out the device from the box up to obtaining the first results of analysis or records of crucial segments of ECG signal. The ambulatory set of twelve skin electrodes is replaced with three basic ones or completely reduced thank to the application of the electrodes located on the device/attachment housing.

The communication with patient is provided by character or graphic displays presenting the analysis results, signal tracing (from one or a few channels simultaneously), or the values of indicators. The operation is via some key buttons on the device housing, and the advanced configuration by means of a computer and dedicated application. It is essential from the data transmission/exchange point of view to provide fast and compatible interface. The embedded USB connection (or fallen out of use RS232) is a standard. For remote observation (e.g., patient in the movement) or monitoring at a distance (under organised system of medical diagnostics/assistance) WiFi, Bluetooth and GSM/GPRS modules are used.
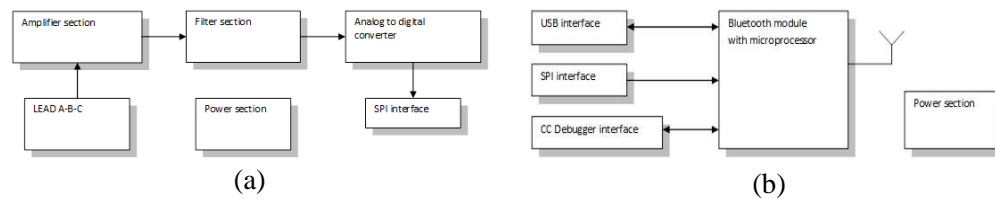
(a)   (b)

Figure 1: Mobile recorder block diagrams. (a) Block diagram of BtECG module. (b) Block diagram of BtECGradio module.
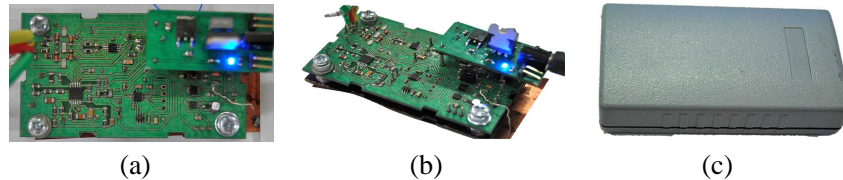

(a)   (b)   (c)

Figure 2: (a) Top and (b) side view of BtECG module with (c) device's cover.

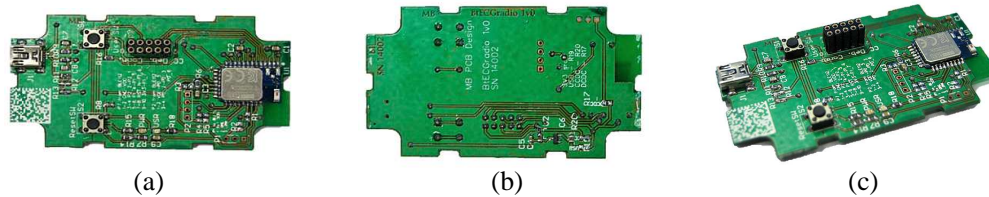(a)   (b)   (c)

Figure 3: (a) Top, (b) bottom and (c) side view of BtECGradio module device.

2. MOBILE RECORDER FOR HEART'S ACTIVITY

The designed under research work the mobile recorder for the heart's electrical activity is of modular construction. In one housing there are two bilateral printed circuits (PCB) separately for analogue part — BtECG and digital one — BtECGradio.

The analogue module (Figures 1(a) and 2) is responsible for taking/measuring the electrical signal from patient's body, its amplification, filtration and conversion to the digital form. Additionally, it provides the source of stabilised voltage (voltages) both for analogue and digital systems.

The digital module (Figures 1(b) and 3) receives binary data, separates the useful part, formats the data to the form of frames required under the radio communication of Bluetooth 4.0 standard and ensures the wireless connection with the cooperating device.

2.1. BtECG — The Analogue Module

The recorder analogue component provides: high CMRR coefficient (80–100 dB); rail-to-rail output; JFET inputs with large capacity (of 5 pF), small polarisation current and with no noise current (proper for high impedance of the source); recording of potentials from the range of 0.2–2 mV; rejection of common-mode signals (interference on the line or high frequency EMI); amplification of the useful signal ($G = 14$) as well as wide range of output dynamics enabling to obtain high amplification at the next stage; filtration of high frequency interference (natural RC filter); high pass filtration ($f_g = 0.033$ Hz) — elimination of DC offset formed between the electrodes; 50 times amplification ($G = 50$), forming the signal at the level 0–5 V; active five-stage low-pass filtration ($f_g = 157$ Hz); analogue-digital conversion; stabilised supply voltage: 3.3 V (for digital part — Bluetooth module), $+/-5$ V (for differential amplifier), 5 V (for analogue-digital converter) and 2.5 V (for operational amplifier).

The integrated circuits and binary elements used in the study carry out the functions specified above, respectively: AD8220 — Analog Devices (a, b, c, d, e, f, g), RC (g, h), AD8618 (i, j), AD7685 Analog Devices (k), OP2177 (e), ADR4350 (k), TPS61027 and TPS63031 — Texas Instruments (l).

2.2. BtECGradio — The Digital Module

The recorder digital module provides: radio data transmission in Bluetooth 4.0 standard; communication with the analogue module BtECG — interface USART 0 SPI; communication with host (RF

packets reading from CPU module) — interface USART 1 SPI; communication with host (BGAPI) — interface Full speed USB 2.0; ultra-low current consumption (transmission: 27 mA, rest: 0.4 µA); communication control based on the architecture processor 8051; establishment of own applications and debugging on CC Debugger Connector; light signalling of power supply (PWR LED) and user's signalling (USR LED); reset switch (Reset SW) and user's switch (User SW); configurable power supply modes 3.3 V from: BtECG, CC Debugger Connector or USB (stabilised from 5 V).

The basic element of the digital module is BLE112 system produced by Blue Giga. It carries out all above-mentioned functions with the power supply tolerance from 2 to 3.6 V.

3. CONCLUSION

The requirements for electronic medical devices include not only technical parameters but also reliability and user safety. They are defined by restrictive criteria: production of devices out of the highest quality components, design and assembly according to the international standards as well as application of the latest technical concept [6].

The main functionality of the heart activity monitoring device is based on the differential amplifier. It is the first rate of amplification and separation of the useful signal part from the interference (of summation signal). Despite its apparent simple construction, its production process is very demanding and obtaining of the module (in the form of integrated circuits — IC) with acceptable parameters is very expensive.

The presented design and practical realisation of the recorder meet the requirements of the mobile device for medical diagnostics. The battery power supply protects patient from accidental electrocution, the wireless interface guarantees safety communication in the range of at least 10 m, Bluetooth applied under fourth version minimises the current consumption, the selected ICs parameters are high for the mobile version, and the modular construction enables fast diagnosis and defect repair.

The practical engineering conclusions resulting from the design experience for the above-presented device are as follows:

- oscilloscope measuring probes with too low resistance and large volume are a burden of the tested system,
- tested device requires separate connection in relation to the return electrode of the earthing potential (shield) [7, 8],
- in order to avoid the negative potential tides of the oscilloscope to zero potential of the tested device, you should use the measurement differential method (negative potential of two probes are independently shorted), lack of such solution results in the saturation of amplifiers (the difference of potentials at the input of operational amplifier must not exceed 50 mV, at the differential amplifier output capacity $+/-5$ V).

REFERENCES

1. Augustyniak, P., *Przetwarzanie Sygnalow Elektrodiagnostycznych*, Wydawnictwa AGH — Uczelniane Wydawnictwa Naukowo-Dydaktyczne, Krakow, 2001, ISBN: 83-88408-37-2.
2. Izydorczyk, J., G. Plonka, and G. Tyma, *Teoria Sygnalow. Kompendium Wiedzy na Temat Sygnalow i Metod Ich Przetwarzania. Wydanie II*, Wydawnictwo Helion, Gliwice, 2006, ISBN: 83-246-0401-4.
3. Bogusz, J., "Wzmacniacze pomiarowe w medycynie," *Elektronika Praktyczna*, Vol. 2010, No. 1, 54–56, 2010.
4. "Monitorowanie elektrokardiograficzne w warunkach szpitalnych Stanowisko American Heart Association," *Medycyna Praktyczna*, Vol. 2005, No. 6, 2005.
5. Drew, B. J., R. M. Califf, M. Funk, E. S. Kaufman, M. W. Krucoff, M. M. Laks, P. W. Macfarlane, C. Sommargren, S. Swiryn, and G. F. Van Hare, "Practice standards for electrocardiographic monitoring in hospital settings. An American Heart Association scientific statement from the councils on cardiovascular nursing, clinical cardiology, and cardiovascular disease in the young," *Circulation*, Vol. 2004, No. 110, 2721–2746, 2004.
6. Dolinski, J., "Przeglad scalonych wzmacniaczy pomiarowych," *Elektronika Praktyczna*, Vol. 2010, No. 1, 57–62, 2010.
7. Crone, B., "Common-mode rejection: How it relates to ECG subsystems and the techniques used to provide superior performance," Technical Article, MS-2125, Analog Devices, Inc., Jan. 2011.

8. Acharya, V., "Improving common-mode rejection using the right-leg drive amplifier," Application Report, SBAA188, Texas Instruments Incorporated, Jul. 2011.

9. International Standard IEC 60601-2-27.

10. Tseng, S.-Y. and W.-C. Fang, "An EKG system-on-chip for portable time-frequency HRV analysis," *IEEE International Conference on Consumer Electronics*, 559–560, 2011.

11. Tseng, C.-C., S.-Y. Tseng, E. Chua, Y.-C. Lee, W.-C. Fang, and H.-C. Huang, "Advanced ECG processor with HRV analysis for real-time portable health monitoring," *IEEE International Conference on Consumer Electronics*, 172–175, Berlin, 2011.

12. Qidwai, U. and M. Shakir, "Fuzzy detection of critical cardiac abnormalities using ECG data: A ubiquitous approach," *11th International Conference on Hybrid Intelligent Systems*, 499–504, 2011.

13. Nowosielski, L., M. Wnuk, and C. Ziolkowski, "Interlaboratory tests in scope of measurement of radio disturbance," *European Microwave Week 2009, EuMW 2009: Science, Progress and Quality at Radiofrequencies, Conference Proceedings — 39th European Microwave Conference, EuMC 2009*, No. 5296286, 288–291, 2009.

14. Nowosielski, L., J. Lopatka, and M. Silaczuk, "Modelling of electromagnetic wave propagation with the use of the ray-tracing method," *PIERS Proceedings*, 2701–2705, Guangzhou, China, Aug. 25–28, 2014.

15. Nowosielski, L. and C. Piotrowski, "Honeycomb ventilation grill shielding effectiveness measuring methodology," *PIERS Proceedings*, 2692–2696, Guangzhou, China, Aug. 25–28, 2014.

16. Nowosielski, L. and M. Wnuk, "Compromising emanations from USB 2 interface," *PIERS Proceedings*, 2666–2670, Guangzhou, China, Aug. 25–28, 2014.

17. Kaszuba, A., R. Checinski, M. Kryk, J. Lopatka, and L. Nowosielski, "Electromagnetically shielded real-time MANET testbed," *PIERS Proceedings*, 2706–2710, Guangzhou, China, Aug. 25–28, 2014.

18. Nowosielski, L. and J. Lopatka, "Measurement of shielding effectiveness with the method using high power electromagnetic pulse generator," *PIERS Proceedings*, 2687–2691, Guangzhou, China, Aug. 25–28, 2014.

19. Gruszczynski, M., M. Wnuk and L. Nowosielski, "Multisystem microstrip antenna for mobile communications," *IEEE Antennas and Propagation Society, AP-S International Symposium (Digest)*, No. 6349179, 2012.

20. Nowosielski, L., M. Wnuk, and C. Ziolkowski, "Interlaboratory tests in scope of measurement of radio disturbance," *European Microwave Week 2009, EuMW 2009: Science, Progress and Quality at Radiofrequencies, Conference Proceedings — 39th European Microwave Conference, EuMC 2009*, No. 5296286, 288–291, 2009.

21. Rozanowski, K., Z. Piotrowski, and M. Bernat, "Psychophysiological determinants of drivers' condition," *Modelling in Medicine and Biology X, WIT Transactions on Biomedicine and Health*, Vol. 17, 85–96, WIT Press, 2013, ISSN: 1743-3525 Online, Doi: 10.2495/BIO130081, ISBN (print): 978-1-84564-706-3,.

22. Rozanowski, K., Z. Piotrowski, and M. Bernat, "The BIO software module for an evaluation system of drivers predispositions," *The Sustainable City IX, WIT Transactions on Ecology and the Environment*, Vol. 2, 873–883, WIT Press, 2014, ISSN: 1743-3541, Online, DOI: 10.2495/SC140742, ISBN 978-1-84564-820-6, eISBN 978-1-84564-821-3.

Implementation of a Steganographic Algorithm in an Internet VoIP Phone

Damian Bachmat and Zbigniew Piotrowski

Faculty of Electronics, Military University of Technology
Gen. S. Kaliskiego 2 Str., Warsaw 00-908, Poland

Abstract— The paper describes implementation of the steganographic method based on the least significant bits (LSB) in a program Internet phone VoIP. In the developed program Internet phone VoIP a library PJSIP has been used. Selected technology — LSB is characterized by easiness of implementation and high data rate and perceptual transparency of a signal with embedded steganographic sequence. In case of the LSB method a change in the least significant bits in a datagram takes place after quantizer of an analog-digital converter circuit. This solution enabled simple implementation of the embedding algorithm by modification of a source code of a codec G.711. The way of the method implementation protects data from errors since mechanisms of the error control and correction of the RTP protocol monitored correctness of sent data. One of the advantages of the method is the fact that for determined number of the least significant bits it does not cause an audible speech degradation and therefore, modified speech signal is perceptually transparent for a subscriber at the receiver side. The paper includes results of tests of developed steganographic phone, among others, subjective audible tests based on signal fidelity estimation standard — ITU-R BS 1116-1, tests of minimal, required time of transmission and integrity tests of steganographic sequence.

1. INTRODUCTION

Voice over IP (VoIP) or in other words Internet telephony is one of "IP world" services, which changes the picture of all telecommunication. It is a real time service enabling the user to do audio or audio-video connections within the packet network that is IP network. So-far there have been a lot of applications, also mobile ones, enabling to make use of this technology. A huge potential is in PJSIP libraries which are available as so-called open source for each user. The asset of making use from PJSIP libraries stack is the fact that it is possible to have access to the source codes of the component elements out of which the customer software VoIP is built. The access gives the possibility for modification of the library source codes so that they would be adapted to user's requirements. As the Internet telephony popularity is growing in the telecommunication, there appear new concepts for using this technology for safety data transmission, and it becomes the target for applying different marking methods and steganographic techniques. VoIP technology is also widely used in the tele-informative elements in the military connection systems. Steganography makes use of many different features of VoIP technology for the purposes of embedding secret message in the carrier which in this case are IP packets. To hide data, the network steganography uses the network protocols and the relations between them. From the steganography nature results that it should not be visible for a third party user in any way, but it should not deteriorate the quality of services offered by VoIP. Moreover, one of the most difficult requirements to be met is the data resistance to degrading impacts. The packet losses or lossy encoding, frequently occurring in VoIP technology, have a degrading impact on the hidden data. Additionally, it is required from the electronics equipment (e.g., VoIP phones) to meet the electromagnetic compatibility prerequisite [1–9]. In the article there is presented the implementation of the technique modifying the least significant bit (LSB) in the programming Internet telephone based on stack of PJSIP libraries, algorithm of embedding and extraction of message was realised by the modification of encoder source codes and standard decoder G.711 with compounding according to the encoding curve A (A-law).

2. CHARACTERISTICS OF PROJECTED SOLUTION

The accepted solution assumes the embedding of hidden message in the least significant bit of the first eight sound samples in the signal frame. The embedding process occurs just after the encoder on the samples encoded according to the standard G.711. Each 120 sound samples go to the loading space of RTP protocol, where the header details are added. So obtained packet goes to further lower layers and is sent to the addressee with whom VoIP talk is conducted. The implemented algorithm takes the data form text file byte after byte and embeds each of them in the separate

packet. The packets of RTP protocol transferring the speech samples with the length of 20 ms make the channel with the bit rate ca. 400 bps.

2.1. Embedding Process

The principle of speech samples transmission as well as all mechanisms supporting the error-free data recovery at the receiver side, indicate the favourable place for implementation of the message bit embedding algorithm in the data flow just after the encoder G.711. In the general overview this technique consists in the replacement of the least significant bit of the encoded samples of speech signal at the level of application layer, before placing the data to the loading space of RTP protocol. The encoder in its operation works on the data transcription from the input buffer — 16 bit samples, to output buffer — 8 bit encoded samples. For encoding each 16 bit sample there is called the function linear2alaw (pj_int_16_t*), which returns 8 bit samples with no mark. Algorithm of the encoder G.711 at the first step takes 16-bit samples, calls the encoding function and then transcripts the encoded values to output buffer. The implemented marking technique changes the sample value just before their transcription to output buffer, so as to leave the message bits on the least significant bit. The placing is realised by means of suitable operators of binary shifts as well as multiplication with proper mask, because the smallest data unit in C language is 1 byte. The embedding process occurs on the first 8 bits of each frame. Each byte of the message is per one frame with duration of 20 ms, which is given by the general download rate of the method equal to:

$$K_w = \frac{8\,\text{bit}}{20\,\text{ms}} = 400\,\text{b/s} \tag{1}$$

2.2. Extraction Process

At the receiver side the decoder source code was also modified properly to save the data from the last layer (LSB) bits of encoded samples just before their processing in the decoder. The values coming from the source buffer are multiplied by mask which separates the least significant bit from the whole value of the sample. This bit is then binary shifted to the right by the set number of places depending on the sample number, because n-th bit of undisclosed message is transmitted by n-th encoded sample. After writing down the least significant 8 bits from the first samples, and "locating" them in byte, it is stored to the file. The whole operation is repeated after next calling the decoder function. The decoder function uses the internal decompression function linear2alaw (pj_int_8_t*), which is called for each speech sample.

3. DESCRIPTION OF LSB METHOD AND ITS VARIATIONS

The modification of the least significant bit (LSB) is the simplest steganographic technique providing the large payload. In this technique the data is hidden in the least significant bit (bits) of the sound signal samples.

The influence of the value change of one bit in the sample on the signal quality is neglected. However, the change of the least significant bits causes the formation of some noise which is acceptable as long as its value is below the perceptive threshold. While increasing the number of changed bits we cause formation of the noise with higher power. If the noise value exceeds the threshold value, it becomes detectable by Human Auditory System. The use of bigger number of bits per sample for embedding the data increases the payload while decreasing the perceptive transparency at the same time.

4. IMPLEMENTATION OF THE PROGRAMMING VOIP INTERNET TELEPHONE

PJSIP is the stack of libraries written in C language which is characterised with small size and great capacity. This stack is distributed on GNU license of General Public License. In the packet available on the page [10] there are examples of VoIP client's scripts, by means of which after compilation it is possible to make connection within local network or by using Internet after log-in. In the application using the stack of PJSIP libraries datagrams/packets are made by means of proper modules. Hence, e.g., RTP datagram is made by the header concatenation as well as the data field in the module named RTP, and TCP packet is made by TCP module. In additional the latter is the connection-oriented protocol, so its module must provide additional functions for connecting and keeping the session. "Raw" data coming from audio stream (microphone port) is encoded according to the chosen speech encoder, and then it is introduced to the transport spaces of next protocols which add their own control information.
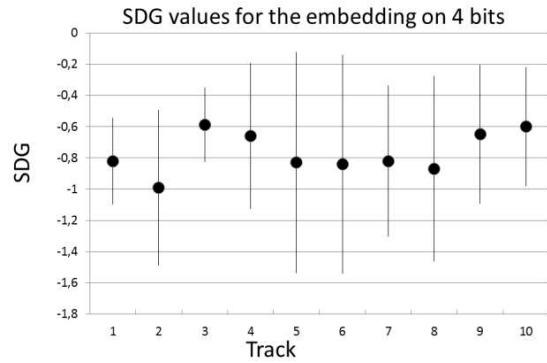
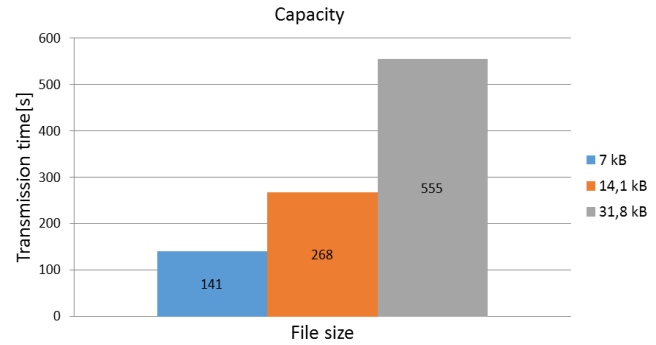Figure 1: SDG values for 4 least significant bits used for the embedding.

Figure 2: Embedding time depending on the file size.

5. RESULTS FROM EXPERIMENTS

In the first place of conducting the tests, the correctness of the algorithm operation was checked, and then some amendments were introduced. The whole test area was divided into three main areas:

- Subjective listening tests — ITU-R BS 1116-1.
- Tests of minimal required time for transmission.
- Watermark integrity tests.

Three independent tests were conducted, first of them while using the algorithm in MATLAB environment, the second and third one directly on the operating application, at the connection between two stations.

5.1. Tests of Minimal Required Time for Transmission

The capacity tests of the embedding algorithm were conducted in order to determine the minimum length of talk, which enables to send the file with set length. The algorithm theoretical download rate was defined as 400 bps. You should remember, however, about the mechanisms such as VAD, which may decrease this value during the talk. The dependence of the embedding capacity is strictly related to so-called *fill factor*. This factor defines silence duration (inactive frames) in relation to the total duration time of talk. The fill factor value equal to 0.2 during 60 seconds talk means that only in 48 seconds of talk you may embed the mark. The real rate of data hidden transmissions in the talk signal drops to the value of 320 b/s. The fill factor of typical phone call is ca. 0.4 [11].

All tests were conducted for the fill factor equal to 0.95, whereas the embedding process was realised on the least significant bit of the first eight samples encoded according to G.711.

5.2. Watermark Integrity Tests

During the conducted tests, there were no losses in the transmitted packets and therefore any falsification in the watermark structure. Information on statistical parameters of the talk conducted was presented via applications after finishing each talk.

6. CONCLUSIONS

The aim of the work was to implement the data embedding algorithm in the programming Internet telephone VoIP, operating based on the stack of PJSIP libraries. The aim was reached and the effectiveness tests of the developed algorithm were presented. The implementation of the algorithm in the programming telephone was preceded with the execution of marking program in Matlab environment, for earlier selected method. The work proves that there is possibility for changing bits of the data stream at the datagram level so that they could be used for transmitting the watermark information. The selected technique for marking is characterised with the implementation easiness, large download rate in comparison to the steganographic methods operating on the signal in bit form just after the quantizer of the analogue-digital converter system. The way of method implementation protects the data from errors occurring because the mechanisms of control and error correction of the individual layers are monitoring the data integrity. One of the method advantage is the fact that it does not cause large signal degradation of the transmitted speech, so

it is transparent. The transmission of data — mark bits takes place with no noticeable changes in the talk quality by the users.

REFERENCES

1. Piotrowski, Z., L. Zagoździński, P. Gajewski, and L. Nowosielski, "Handset with hidden authorization function," *European DSP Education & Research Symposium EDERS 2008, Proceedings*, 201–205, Published by Texas Instruments, 2008, ISBN: 978-0-9552047-3-9.

2. Nowosielski, L., M. Wnuk, and C. Ziółkowski, "Interlaboratory tests in scope of measurement of radio disturbance," *European Microwave Week 2009, EuMW 2009, Science, Progress and Quality at Radiofrequencies, Conference Proceedings — 39th European Microwave Conference, EuMC 2009*, Article No. 5296286, 288–291, 2009.

3. Nowosielski, L., J. Patka, and M. Siłaczuk, "Modelling of electromagnetic wave propagation with the use of the ray-tracing method," *PIERS Proceedings*, 2701–2705, Guangzhou, China, Aug. 25–28, 2014.

4. Nowosielski, L. and C. Piotrowski, "Honeycomb ventilation grill shielding effectiveness measuring methodology," *PIERS Proceedings*, 2692–2696, Guangzhou, China, Aug. 25–28, 2014.

5. Nowosielski, L. and M. Wnuk, "Compromising emanations from USB 2 interface," *PIERS Proceedings*, 2666–2670, Guangzhou, China, Aug. 25–28, 2014.

6. Kaszuba, A., R. Checinski, M. Kryk, J. Lopatka, and L. Nowosielski, "Electromagnetically shielded real-time MANET testbed," *PIERS Proceedings*, 2706–2710, Guangzhou, China, Aug. 25–28, 2014.

7. Nowosielski, L., and J. patka, "Measurement of shielding effectiveness with the method using high power electromagnetic pulse generator," *PIERS Proceedings*, 2687–2691, Guangzhou, China, Aug. 25–28, 2014.

8. Gruszczynski, M., M. Wnuk, and L. Nowosielski, "Multisystem microstrip antenna for mobile communications," *IEEE Antennas and Propagation Society, AP-S International Symposium (Digest)*, Article No. 6349179, 2012.

9. Nowosielski, L., M. Wnuk, and C. Ziółowski, "Interlaboratory tests in scope of measurement of radio disturbance," *European Microwave Week 2009, EuMW 2009: Science, Progress and Quality at Radiofrequencies, Conference Proceedings — 39th European Microwave Conference, EuMC 2009*, Article No. 5296286, 288–291, 2012.

10. http://www.pjsip.org/.

11. Beritelli, F., S. Casale, and G. Ruggeri, "Performance evaluation and comparison of ITU-T/ETSI voice activity detectors," *2001 IEEE International Conference on Acoustics, Speech, and Signal Processing, Proceedings, (ICASSP '01)*, 1425–1428, 2001.

Multimedia Filter for Data Hiding Counteraction

Zbigniew Piotrowski

Faculty of Electronics, Military University of Technology
Gen. S. Kaliskiego 2 str., Warsaw 00-908, Poland

Abstract— Data hiding methods are realised in the form of steganographic communication channels and in the form of digital content labelled with watermark while employing as the carrying layer among the others: speech signal, audio, video and photos. Detection of the fact of additional data hiding is hindered among the others because of constantly improved and increasingly advanced methods for embedding and extraction of hidden data. In the article there is presented the concept of the program container based on which the filtration of the above-mentioned signals is carried out in order to remove the hidden data. The purpose of multimedia filter action is to remove from the original signal (carrier) the hidden data or its significant degradation, but in such manner that the original signal itself is not degraded significantly.

1. INTRODUCTION

The methods of the hidden data removal from the multimedia content are well known. In [1] three types of attacks are described taking into account the available knowledge about the watermark structure, embedder and extractor. These attacks include: exploiting the design weakness via blind attack (I), exploring the knowledge based on embedding and extracting processes using original signal and watermarked one (II) and the last type is a combination of the two (III). The first type attack does not depend on the knowledge about the watermark embedding method. Such attacks include the basic methods for signal processing, e.g., resampling, analogue-to-digital and digital-to-analogue conversion, noise addition, lossy compression [2]. The second type attack is possible thanks to the signal analysis before and after embedding the hidden data. The signal analysis is conducted in both time and frequency fields, and considering among the others: system frequency response. The discovered differences may be the essential prerequisite for recognising the method of watermark embedding or the structure of the steganographic sequence. The attacks on the hidden data may be hindered in a defence manner described in [3] in the form of hidden data masking. The authors of the articles suggested the technique named *Data Masking* which consists in forming the Probability Density Function (PDF) of the information enciphered to PDF format similar to the audio or video signal stream. This way, the probability distribution of the enciphered data occurrence becomes similar to the statistic distribution represented by audio or video signals. As it was stated in [3] the attacks conducted by traditional stego-analysers of the hidden information on so-masked confidential data are of low effectiveness.

As it was specified in the publication [4] among the attacks on the hidden data contained in the multimedia signal there can be distinguished: removal attacks, geometric attacks, cryptographic attacks, estimation-based attacks, remodulation attacks, copy attack, synchronisation removal. The filter for removing the hidden data in the multimedia content may both remove the hidden data from the multimedia content and degrade the hidden data (represented by the watermark signal or steganographic sequence) in such way that they become impossible for extraction at the receiving side, simultaneously meeting the condition of keeping the original signal quality at the acceptable level by the user. The article proposes to apply the multimedia filter whose task is to remove the potentially occurring hidden data contained in the audio streams, video streams or in the multimedia files. It is assumed that the filter may operate also on the speech signal in the telephony systems [5]. The methods for embedding the hidden data in the video and audio signals are known [6–10]. The filter having the transmittance $H(z)$ matched depending on the selected method taken from the block of the method container DSP, makes the filtration of the signal which can potentially have the embedded hidden data. To the filter it is possible connect the digital routes from the telephone exchange PSTN/VoIP or Internet server whose task would be the filtration of the data streams or selected Internet resources. By means of testing the signal quality and fidelity before and after the filtration, it is possible to choose such processing parameters of the filter that the processed signal degradation can be minimised [11–13].

In case of the hardware realisation of the proposed multimedia filter, you should pay attention to the question of the equipment electromagnetic shielding and its electromagnetic compatibility [14–22]. The essential part of the network environment for the described multimedia filter is the

possibility of operation in the heterogenic environment with the guarantee for providing the service quality [23–25].

As the degraded signal metrics there may be used the following norms:

Maximum Difference:

$$MD = \max \left| A_n - A'_n \right|$$

Average Absolute Difference:

$$AD = \frac{1}{N} \sum_n \left| A_n - A'_n \right|$$

Normalized Average Absolute Difference:

$$NAD = \frac{\sum_n \left| A_n - A'_n \right|}{\sum_n \left| A_n \right|}$$

Mean Square Error:

$$MSE = \frac{1}{N} \sum_n \left(A_n - A'_n \right)^2$$

LP-Norm:

$$LP = \left(\frac{1}{N} \sum_n \left| A_n - A'_n \right| \right)^{1/p}$$

Signal to Noise Ratio:

$$SNR = \frac{\sum_n A_n^2}{\sum_n \left(A_n - A'_n \right)^2}$$

Audio Fidelity (AF):

$$AF = 1 - \frac{\sum_n \left(A_n - A'_n \right)^2}{\sum_n A_n^2}$$

where: A_n — original signal, A'_n — filtered signal, n — number of sample.

2. MULTIMEDIALNY FILTR SKRYTYCH DANYCH

The described concept of the multimedia filter is presented in the Figure 1.

The filter for removing the hidden data contains in its structure (Figure 1) the executive module in the block form: multimedia filter, with the transmittance $H(z)$ shaped by the method container DSP and parameters of DSP methods named DSP container. The degradation degree of the filtered signal is verified depending on the input content and the selected method of filtration in the block multimedia content quality testing and filter parameters adaptation.

In the Figure 2 there is presented an example positioning of the multimedia filter for removing the hidden data. It may work in the cascade mode, just after the module for the dedicated attack methods on the hidden data, or in the parallel mode. The filter may be installed, e.g., in the routers
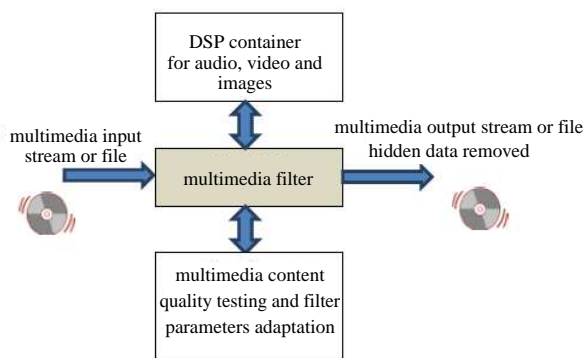

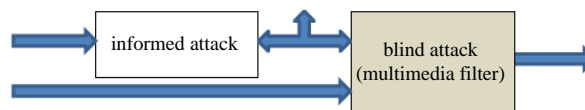Figure 1: Multimedia filter for hidden data removal.

Figure 2: Configuration of the attack methods on the hidden data.

(while using the network technique *Deep Packet Inspection*, DPI — in order to scan the datagrams containing the multimedia signal), in the telephone exchanges or in the commonly used equipment, e.g., smartphones, PSTN telephones etc., protecting against hidden steganographic transmission and against penetration of the devices and telecommunication infrastructure at the same time. The filter may also be the part of automatic scanner for computer viruses scanning the particular resources of the computer.

3. CONCLUSIONS

In the article there is presented the concept of the multimedia filter for removing the hidden data. The filter has its application in the filtration of the digital multimedia signal in order to remove or degrade significantly the hidden data represented by the watermark or steganographic sequence sent, e.g., in the speech signal in the telephonic connections.

The filter can carry out such operations on the signal as: lossy compression, re-quantization, resampling, all-pass the filtration, equalisation, noise addition etc.. The filter, depending whether the following are known: watermark structure, steganographic sequence, embedding method or extraction method for the hidden data, may work on any input signal while using the selected set of methods so-called blind attack or informed attack. The multimedia filter may be the complementation of the hidden transmission stego-analyser. In the presented concept of the system, it is necessary to model the individual parameters of the filtration depending on the quality of the digital content and assumed degree of the signal degeneration.

REFERENCES

1. Wu, M. and B. Liu, *Multimedia Data Hiding*, Springer-Verlag, 2002, ISBN: 0-387-95426-0.
2. Test Result of International Evaluation Project for Digital Watermark Technology for Music, 2000, http://www.nri.co.jp/english/news/2000/001006.html.
3. Radhakrishan, R., M. Kharrazi, and N. Memon, "Data masking: A new approach for steganography?," *Journal of VLSI Signal Processing*, Vol. 41, 293–303, 2005.
4. Voloshynovskiy, S. and T. P. Pereira, "Attacks on digital watermarks: Classification, estimation-based attacks and benchmarks," *IEEE Communications Magazine*, Vol. 39, No. 8, 118–126, 2002, ISSN: 0163-6804.
5. Piotrowski, Z. and W. Grabiec, "Voice trust in public switched telephone networks," *MCSS 2012, Communications in Computer and Information Science, CCIS 287*, 282–291, Springer, Heidelberg, 2012, ISBN: 978-3-642-30720-1.
6. Lenarczyk, P. and Z. Piotrowski, "Parallel blind digital image watermarking in spatial and frequency domains, telecommunication systems," *Telecommunication Systems*, Vol. 54, 287–303, 2013, Doi: 10.1007/s11235-013-9734-x.
7. Piotrowski, Z., "Drift correction modulation scheme for digital signal processing," *Mathematical and Computer Modelling*, Vol. 57, Nos. 11–12, 2660–2670, Elsevier, Jun. 2013, Doi: 10.1016/j.mcm. 2011.09.016.
8. Piotrowski, Z., "The national network-centric system and its components in the age of information warfare," *Safety and Security Engineering III, SAFE III*, 301–309, WIT Press, Southampton, Boston, 2009, ISBN: 978-1-84564-193-1, ISSN: 1746-4498, ISSN: 1743-3509.
9. Piotrowski, Z., "Angle phase drift correction method effectiveness," *Signal Processing Algorithms, Architectures, Arrangements, and Applications Conference Proceedings (SPA)*, 82–86, Poznan, 2009, ISBN: 978-83-62065-00-4.
10. Piotrowski, Z. and P. Gajewski, "Novel method for watermarking system operating on the HF and VHF radio links," *Computational Methods and Experimental Measurements XIII, CMEM XIII*, 791–800, WIT Press, Southampton, Boston, 2007, ISBN: 978-1-84564-084-2, ISSN: 1746-4064, ISSN: 1743-355X.
11. Piotrowski, Z. and P. Gajewski, "Fidelity estimation of watermarked audio signals according to the ITU-R BS.1116-1 standard," *Acta Physica Polonica A, Acoustic and Biomedical Engineering*, Vol. 121, No. 1-A, 82–85, 2012, ISSN: 0587-4246.
12. Piotrowski, Z., "Precise psychoacoustic correction method based on calculation of JND level," *Acta Physica Polonica A, Optical and Acoustical Methods in Science and Technology*, Vol. 116, No. 3, 375–379, 2009.
13. Piotrowski, Z. and P. Gajewski, "Acoustic watermark server effectiveness," *Computational Methods and Experimental Measurements XIV, CMEM XIV*, 251–258, WIT Press, Southampton, Boston, 2009, ISBN: 978-1-84564-187-0, ISSN: 1746-4046, ISSN: 1743-355X.

14. Nowosielski, L., M. Wnuk, and C. Ziółowski, "Interlaboratory tests in scope of measurement of radio disturbance," *European Microwave Week 2009, EuMW 2009: Science, Progress and Quality at Radiofrequencies, Conference Proceedings — 39th European Microwave Conference, EuMC 2009*, Article No. 5296286, 288–291, 2009.

15. Nowosielski, L., J. patka, and M. Siłczuk, "Modelling of electromagnetic wave propagation with the use of the ray-tracing method," *PIERS Proceedings*, 2701–2705, Guangzhou, China, Aug. 25–28, 2014.

16. Nowosielski, L. and C. Piotrowski, "Honeycomb ventilation grill shielding effectiveness measuring methodology," *PIERS Proceedings*, 2692–2696, Guangzhou, China, Aug. 25–28, 2014.

17. Nowosielski, L. and M. Wnuk, "Compromising emanations from USB 2 interface," *PIERS Proceedings*, 2666–2670, Guangzhou, China, Aug. 25–28, 2014.

18. Kaszuba, A., R. Checinski, M. Kryk, J. Lopatka, and L. Nowosielski, "Electromagnetically shielded real-time MANET testbed," *PIERS Proceedings*, 2706–2710, Guangzhou, China, Aug. 25–28, 2014.

19. Nowosielski, L. and J. Lopatka, "Measurement of shielding effectiveness with the method using high power electromagnetic pulse generator," *PIERS Proceedings*, 2687–2691, Guangzhou, China, Aug. 25–28, 2014.

20. Gruszczynski, M., M. Wnuk, and L. Nowosielski, "Multisystem microstrip antenna for mobile communications," *IEEE Antennas and Propagation Society, AP-S International Symposium (Digest)*, Article No. 6349179, 2012.

21. Nowosielski, L., M. Wnuk, and C. Ziółkowski, "Interlaboratory tests in scope of measurement of radio disturbance," *European Microwave Week 2009, EuMW 2009: Science, Progress and Quality at Radiofrequencies, Conference Proceedings — 39th European Microwave Conference, EuMC 2009*, Article No. 5296286, 288–291, 2009.

22. Piotrowski, Z., L. Nowosielski, L. Zagoździński, and P. Gajewski, "Electromagnetic compatibility of the military handset with hidden authorization function based on MIL-STD-461D results," *PIERS Online*, 566–570, 2008.

23. Lubkowski, P., M. Bednarczyk, K. Maslanka, and M. Amanowicz, "QoS-aware end-to-end connectivity provision in a heterogeneous military environment," *Military Communications and Information Systems Conference 2013*, Saint Malo, France, 2013.

24. Lubkowski, P. and D. Laskowski, "Provision of the reliable video surveillance services in heterogeneous networks," *European Safety and Reliability Conference, ESREL 2014*, Wroclaw, Poland, Accepted for Publication, 2014.

25. Hauge, M., L. Landmark, P. Lubkowski, M. Amanowicz, and K. Maslanka, "Selected issues of QoS provision in heterogenous military networks," *International Journal of Electronics and Telecommunications*, Vol. 60, No. 1, 7–13, 2014.

A Dualband Circularly Polarized Rectangular Dielectric Resonator Antenna with L-shaped Slots on the Ground

Yuxiang Sun, **Kwok Wa Leung**, and **Wei Wei Li**

Department of Electronic Engineering and State Key Laboratory of Millimeter-Waves
City University of Hong Kong, Hong Kong SAR, China

Abstract— This paper presents a dualband circularly polarized (CP) rectangular dielectric resonator (DR) antenna (DRA). Its fundamental TE_{111} mode and higher-order TE_{113} mode are excited simultaneously to obtain two working bands. The dimensions of the dual-band DRA are calculated by solving simplified formulas of the dual-mode rectangular DRA. To generate circularly polarized fields, two asymmetric diagonal L-shaped slots are etched on the ground plane to excite two degenerate orthogonal modes in each band, giving a CP dualband antenna. For demonstration, a dual-band dual-sense CP antenna working in GPS L1 band (1.575 GHz) and 2.4 GHz WLAN band are designed using ANSYS HFSS. Its reflection coefficient, axial ratio (AR), antenna gain, and radiation pattern are studied. The antenna radiates right- and left-hand circularly polarized fields in the lower and upper bands, respectively.

1. INTRODUCTION

The dielectric resonator antenna (DRA) has been studied extensively over the last three decades [1–3]. Most DRA designs generate linearly-polarized (LP) fields, but a circularly-polarized (CP) system has advantages over the LP counterpart [4]. For example, a CP antenna is relatively more flexible in its orientation. Also, it is less sensitive to multi-path propagation effects and fading problems. Today, it has been a trend to have highly-integrated systems, therefore multiband antennas are generally more desirable than single-band antennas for they can reduce the system size and cut the cost.

In this paper, a dual-band slot-coupled CP rectangular DRA working in GPS L1 band and 2.4 GHz WLAN band is introduced. The CP fields are generated by fabricating two diagonal L-shaped slots onto the ground; one for the lower band CP and the other one for the higher band. The CP polarizations in the two bands are of opposite senses due to different orientations of the slots.

2. ANTENNA DESIGN

Figure 1 shows the configuration of the proposed dual-band CP rectangular DRA. The DRA, made of material with a dielectric constant of $\varepsilon_r = 10$, has a square cross section with a side length of a, and height of h. It is located at the center of a square substrate, with a thickness of $t = 1.57$ mm, and length of $L_g = 80$ mm. The dielectric constant of the substrate is $\varepsilon_{rs} = 2.33$ and therefore the width of the 50-Ω feedline is $w_f = 4.67$ mm. A rectangular coupling slot with a length of l_s and width of w_s is cut at the center of the ground plane to excite the DRA. Two L-shaped slots of different sizes are etched along the diagonal line of the ground plane, with offsets of d_{xi}, d_{yi} ($i = 1, 2$). The total lengths of the two slots are $L_{x1} + L_{y1}$ and $L_{x2} + L_{y2}$, with the widths of w_{s1}, w_{s2}.

The proposed structure was simulated and optimized with ANSYS HFSS. To begin, the size of the DRA working in both GPS L1 band (1.575 GHz) and 2.4 GHz WLAN band was determined. By solving the equations in [5, 6] with $f_1 = 1.6$ GHz and $f_2 = 2.4$ GHz, the original dimensions of $a = 37.5$ mm and $h = 40.3$ mm were obtained. Next, the sizes of the L slots and DR were optimized with HFSS simulations to obtain a good CP antenna. The optimized parameters are obtained given by $L_g = 80$ mm, $t = 1.57$ mm, $a = 35.7$ mm, $h = 40.5$ mm, $w_f = 4.67$ mm, $l_s = 30$ mm, $w_s = 2.5$ mm, $d_{x1} = d_{y1} = 2.5$ mm, $d_{x1} = d_{y1} = 2$ mm, $L_{x1} = 16$ mm, $L_{y1} = 27.5$ mm, $L_{x2} = 16$ mm, $L_{y2} = 16$ mm, and $w_{s1} = w_{s2} = 2$ mm.

3. ANTENNA PERFORMANCE

Figure 2 shows the simulated reflection coefficient of the dualband CP rectangular DRA. With reference to the figure, wide impedance bands ($|S_{11}| < -10$ dB) are obtained at ~ 1.57 GHz and 2.4 GHz, with their fractional bandwidths given by 17.8% (1.385–1.655 GHz) and 10.3% (2.345–2.60 GHz), respectively.

(a)   (b)
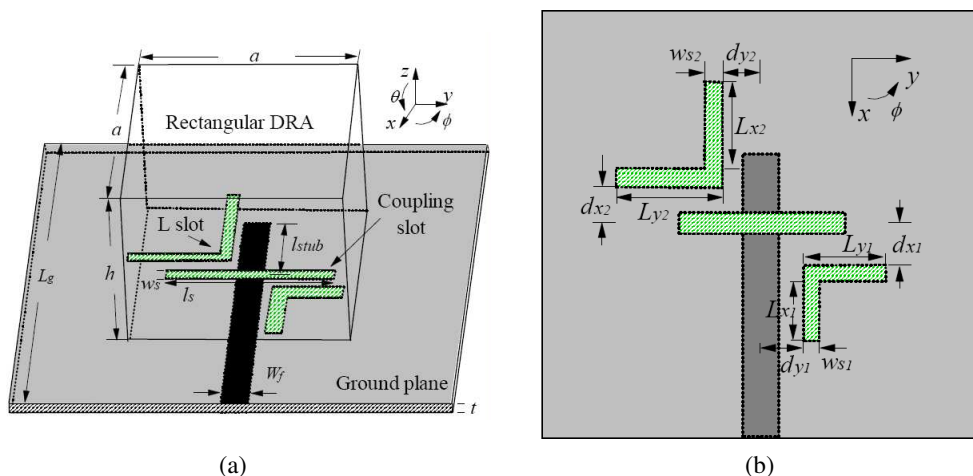
Figure 1: (a) Perspective view and (b) top view of the proposed dualband CP DRA.
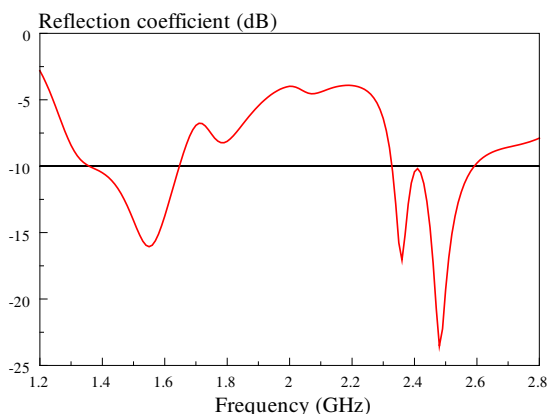

Figure 2: Simulated reflection coefficient of the proposed antenna.
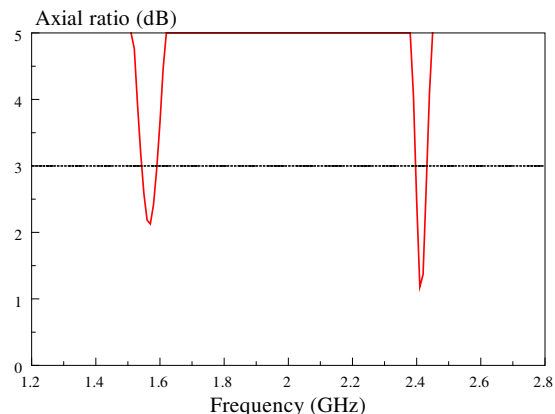
Figure 3: Simulated axial ratio (AR) of the proposed antenna in boresight direction ($\theta = 0°$).

$f = 1.575$ GHz $f = 2.42$ GHz

xoz plane ——— ··········   *yoz* plane – – – ··········
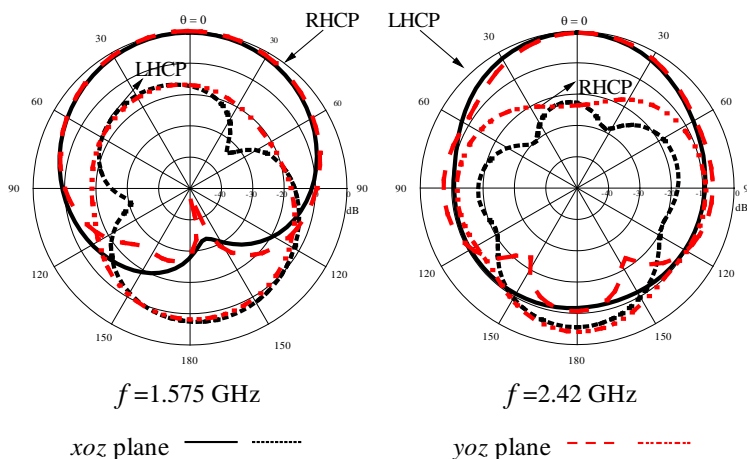
Figure 4: Simulated radiation patterns of the proposed antenna at 1.575 GHz and 2.42 GHz.

Figure 3 shows the simulated axial ratio (AR) of the proposed antenna. Two frequency bands can be observed. The 3-dB AR bandwidths of the lower and upper bands are 3.5% (1.54–1.595 GHz) and 1.65% (2.405–2.445 GHz), respectively.

Figure 4 shows the *xoz*- and *yoz*-plane simulated radiation patterns at 1.575 GHz and 2.42 GHz. As can be observed from the figure, broadside radiation patterns can be observed, as expected. At each frequency, the co-polarized fields are ∼ 20 dB stronger than their counterparts in the

boresight direction ($\theta = 0°$). It is noted from the figure that the co-polarized fields are right-hand circular polarized (RHCP) and left-hand circular polarized (LHCP) for the lower and upper bands, respectively. This is because the sense of polarization is determined by the orientations of the diagonal L-shaped slots. It can also be observed from the antenna gain given in Figure 5. With reference to the figure, the simulated peak gains are 6.33 dBic (RHCP) and 7.36 dBic (LHCP), which are quite typical for DRAs.

Figure 5: Simulated antenna gains of the proposed antenna in boresight direction ($\theta = 0°$).

4. CONCLUSION

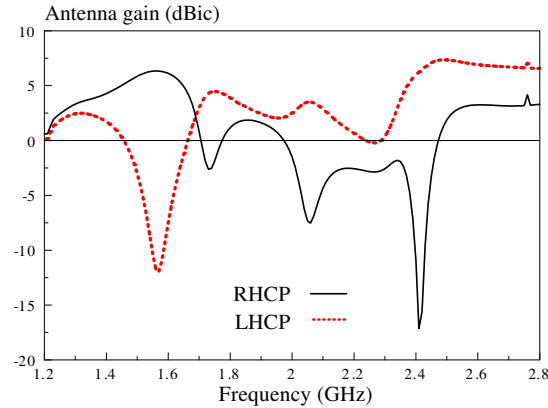In this paper, a dualband CP rectangular DRA has been studied for GPS L1 and 2.4 GHz WLAN applications. Simulated results have been obtained by using ANSYS HFSS. The proposed antenna can work in the two aforementioned bands. Broadside radiation patterns with different senses of polarization have been obtained in the lower and upper bands.

ACKNOWLEDGMENT

REFERENCES

1. Luk, K. M. and K. W. Leung, *Dielectric Resonator Antennas*, Research Studies Press, Baldock, U.K., 2003.
2. Petosa, A., *Dielectric Resonator Antenna Handbook*, Artech House, Norwood, MA, 2007.
3. Leung, K. W., E. H. Lim, and X. S. Fang, "Dielectric resonator antennas: From the basic to the aesthetic," *Proceedings of the IEEE*, Vol. 100, No. 7, 2181–2193, July 2012.
4. Li, W. W. and K. W. Leung, "Omnidirectional circularly polarized dielectric resonator antenna with top-loaded alford loop for pattern diversity design," *IEEE Trans Antennas Propag.*, Vol. 61, No. 8, 4246–4256, August 2013.
5. Fang, X. S. and K. W. Leung, "Design of single-, dual-, wide-band rectangular dielectric resonator antenna," *IEEE Trans Antennas Propag.*, Vol. 59, No. 6, 2409–2414, 2011.
6. Fang, X. S., C. K. Chow, K. W. Leung, and E. K. Lim, "New single-/dual-mode design formulas of the rectangular dielectric resonator antenna using covariance matrix adaptation evolutionary strategy," *IEEE Antennas Wireless Propag. Lett.*, Vol. 10, 734–737, 2011.

Bidirectional Dielectric Resonator Antenna Using Slotted Ground Structure

Nan Yang, Kwok Wa Leung, and Wei Wei Li

State Key Laboratory of Millimeter Waves, Department of Electronic Engineering
City University of Hong Kong, Hong Kong SAR, China

Abstract— A bidirectional cylindrical dielectric resonator antenna (DRA) is proposed in this paper. The DRA operating in its fundamental $TM_{01\delta}$ mode is fed by an axial coaxial probe protruded from a circular ground, which has the same radius of the DRA. Two slots are fabricated on the ground to obtain a bidirectional radiation pattern. It was found that the measured gain on the azimuth plane is $3.75\,dBi$ and $-10.16\,dBi$ in the mainlobe and sidelobe directions, respectively.

1. INTRODUCTION

Bidirectional antennas can be used in narrow and long spaces, such as railways, tunnels or straight roads [1]. Usually, the bidirectional antenna is long in length or large in size to increase the antenna gain. For example, two sets of stacked-microstrip dipole antenna are placed back to back to achieve bidirectional performance with a length of more than 2λ. In [2], six ring antennas are cascaded, giving a length of 2.4λ. Similar sizes are found in bidirectional leaky wave antennas [3]. Patch arrays are considered in [4] but occupied an area of more than $10\lambda^2$. In [5], a smaller bidirectional antenna is given, with the dimensions of $0.7\lambda * 0.35\lambda * 0.4\lambda$ and directivity of $4.43\,dBi$.

This paper presents a bidirectional cylindrical dielectric resonator antenna (DRA) with a radius of 0.25λ and height of 0.16λ It is excited in its fundamental $TM_{01\delta}$ mode by a coaxial probe. The DRA and ground plane have the same radius. As the $TM_{01\delta}$-mode DRA has an omnidirectional radiation pattern [6], two arc-shaped slots are introduced in the ground to obtain bidirectional radiation pattern. The two slots are symmetrically located along the x axis, stopping the surface current that flows in the $+/-x$ directions. As a result, the gain in the $+/-x$ directions are suppressed and that in $+/-y$ directions can be enhanced. To demonstrate the idea, a prototype was designed, fabricated and measured The simulated and measured gains are $4.64\,dBi$ and $3.75\,dBi$ in the main-lobe $(+/-y)$ direction, respectively, and drop to $-12.12\,dBi$ and $-10.16\,dBi$ in the sidelobe $(+/-x)$ direction, respectively.

2. ANTENNA CONFIGURATION

The configuration of the proposed antenna is shown in Figure 1, where Figure 1(a) displays the side view of the antenna while Figure 1(b) gives the top view of the slotted ground only. With reference to Figure 1(a), a cylindrical dielectric resonator with a radius of R, height of h, and dielectric constant of ε_r is mounted on a circular ground plane having a radius of R_g and thickness of t. To excite the fundamental $TM_{01\delta}$ mode, a probe with a radius of r_p and length of l_p is inserted into the DRA at its center. Two arc slots symmetrical about the center are etched on the ground to
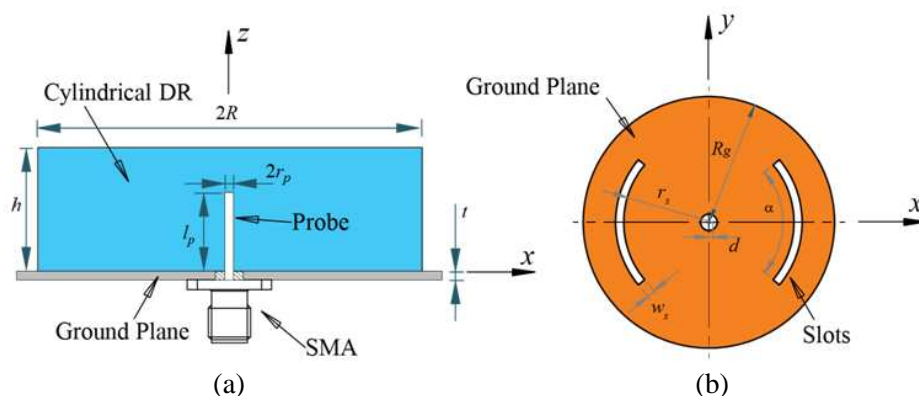

Figure 1: Configuration of proposed antenna. (a) Side view of the antenna. (b) Top view of the slotted ground.

generate bidirectional radiation. Each arc slot has an inner radius of r_s, width of w_s, subtended angle of α, and displacement of d.

3. EXPERIMENTAL RESULTS

To demonstrate the idea, a cylindrical DRA with $\varepsilon_r = 6.85$ operating at 2.4 GHz was designed, fabricated, and measured. Other design parameters are listed in Table 1.

Figure 2 compares the measured and simulated reflection coefficients of the proposed antenna. As can be seen from the figure, the 10-dB impedance bandwidth is 6.9% (2.39–2.56 GHz), entirely covering the 2.4-GHz WLAN band (2.40–2.48 GHz). The frequency shift of the measured result is due to fabrication tolerances. It was found that the effect of adding two slots on the reflection coefficient is not significant, which is desirable for the design.

Figure 3 displays the measured and simulated gains of the proposed antenna along $+y$-axis ($\theta = 90°$, $\phi = 90°$). With reference to the figure, the measured maximum gain is 3.75 dBi at 2.48 GHz, whereas the simulated one is 4.64 dBi at 2.44 GHz. It was found that the measured efficiency is higher than 85% over the entire WLAN band, which is not shown here for brevity.

The measured and simulated radiation patterns of elevation and azimuth planes are shown in Figure 4. As can be observed from Figure 4(a), the radiation pattern of the elevation y-z plane is similar to that of a conventional omnidirectional DRA. The crosspolarized field is at least 20 dB weaker than the copolarized counterpart. Figure 4(b) shows the radiation pattern on the azimuth plane. With reference to the figure, the main- and side-lobe radiations are along $+/-y$ ($\phi = 90°$, $270°$) and $+/-x$ (($\phi = 0°$, $180°$) directions, respectively. The measured copolarized

Table 1: Design parameters of the proposed antenna (unit: mm).

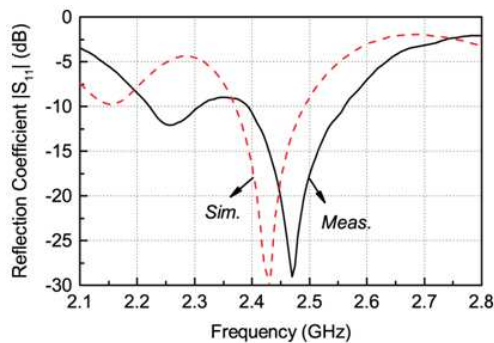| R	h	R_g	t	r_p	l_p	r_s	w_s	d	α
31	20	31	2	0.635	14	22	2	1	$80°$

Figure 2: Measured and simulated reflection coefficients of proposed antenna.
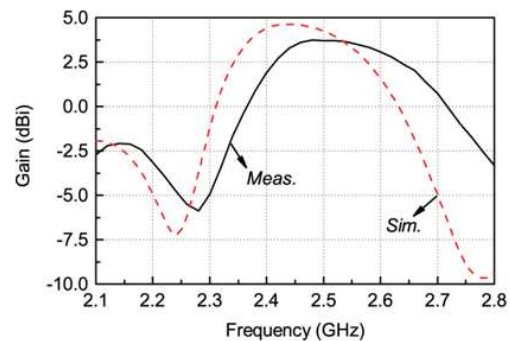
Figure 3: Measured and simulated gains of proposed antenna.
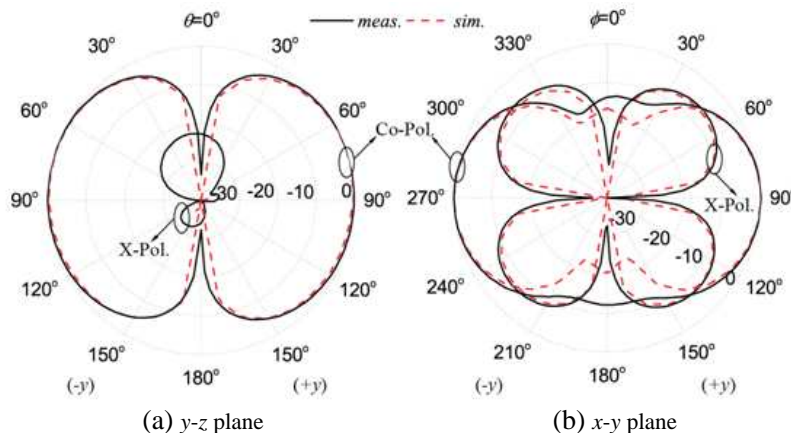

(a) y-z plane

(b) x-y plane

Figure 4: Measured (2.48 GHz) and simulated (2.44 GHz) radiation patterns of proposed antenna. (a) Elevation y-z plane. (b) Azimuth x-y plane.

field at $\phi = 90°$ is stronger than that at $\phi = 0°$ by 13.9 dB, showing satisfactory bidirectional performance.

4. CONCLUSION

The bidirectional DRA with slotted ground has been investigated in this paper. By adding two arc slots to the ground, the current distribution is perturbed, converting the conventional omnidirectional radiation pattern into a bidirectional one. The reflection coefficient is not affected by the slots significantly. Since it does not require any special-shape DRA, the design can be realized very easily.

ACKNOWLEDGMENT

REFERENCES

1. Batgerel, A., J. Choi, and S. Eom, "High-gain bidirectional mdas antenna design excited by stacked-microstrip dipole," *Journal of Electromagnetic Waves and Applications*, Vol. 26, Nos. 11–12, 1412–1422, 2012.
2. Liu, W., Z. Zhang, Z. Tian, and Z. Feng, "A bidirectional high-gain cascaded ring antenna for communication in coal mine," *IEEE Antennas Wireless Propag. Lett.*, Vol. 12, 761–764, Jun. 2013.
3. Jackson, D., C. Caloz, and T. Itoh, "Leaky-wave antennas," *Proc. IEEE*, Vol. 100, 2194–2206, Jul. 2012.
4. Chieh, J.-C. and A.-V. Pham, "A bidirectional microstrip x-band antenna array on liquid crystal polymer for beamforming applications," *IEEE Trans. Antennas Propag.*, Vol. 61, 3364–3368, Jun. 2013.
5. Lamultree, S. and C. Phongcharoenpanich, "Parametric study of a bidirectional antenna using a probe excited rectangular ring," *IEEE Antennas and Propagation Society International Symposium 2006*, 4721–4724, Jul. 2006.
6. Luk, K. M. and K. W. Leung, *Dielectric Resonator Antennas*, Research Studies Press, 2003.

Impact of Bending on the Performance of Circularly Polarized Wearable Antenna

Muhammad Rizwan, **Lauri Sydänheimo**, and **Leena Ukkonen**

Department of Electronics and Communications Engineering
Tampere University of Technology, Tampere, Finland

Abstract— Wearable electronic devices are becoming a part of human clothing for applications such as sensing, navigation and health monitoring. Textile antennas are a strong candidate for transceiver node in wearable applications due to their flexibility and low cost. In wearable systems, flat surfaces are not always available so the antenna should be able to retain its performance in bent conditions. This paper analyses the effects of bending on the performance of a circularly polarized textile antenna. The antenna under test is made on Denim substrate for Industrial, Scientific and Medical (ISM) band and Wireless Body Area Network (WBAN) applications at 2.45 GHz. Copper tape is used as the conductive material for the patch and the ground plane on 1 mm thick Denim substrate. Rectangular slot along diagonal axes at the center of the circular patch is used for achieving circular polarization at 2.45 GHz while bandwidth enhancement is done by using partial and slotted ground plane. The measured operating frequency range of antenna spans from 2.42 GHz to 2.58 GHz with gain of 2.25 dB at 2.45 GHz. Bending in both xz and yz plane is done by placing the antenna on cylinders with different radii (50 mm and 75 mm) and then analyzing the effects on return loss, bandwidth, axial ratio and radiation characteristics. Fabricated antenna shows good conformity between simulated and measured results. A set of comparative results of antenna in free space and bending conditions are compared to validate the operability of antenna with bending in different planes. In future, the performance of antenna can be analyzed on different body parts like arms and legs etc. to validate its operability for BAN applications in vicinity of human body.

1. INTRODUCTION

Wearable electronics is an emerging technology of the present time that attracts interest in many applications, ranging from health monitoring, multimedia, sports, and military. One of the most important parts of any such system is the antenna, which is required to ensure reliable communication. With the development of wearable electronics, a new type of antennas is introduced which can easily be embedded inside human clothing, called textile antennas. Textile antennas have the advantage of flexibility, lightweight and low cost, and can easily be integrated in daily used garments. Multiple techniques have been proposed for designing and improving the performance of textile antennas for use in WBAN applications [1]. However, flexibility of the textile antenna allows it to easily bend when mounted on human body; hence it becomes necessary to study the effects of bending on the performance of textile antennas [1].

In WBAN applications, single or multiple antennas are mounted as transceiver nodes on human body. The transceiver nodes may communicate with one another or some remote server for sending data depending on the application. Due to the constant motion of the body, it becomes difficult to always align the transceiver nodes for better power reception. Circular polarization (CP) operation eliminates the need to continuously align the two nodes for receiving maximum power [2, 3]. Previously reported wearable antennas are mostly non-flexible [3], thick substrate [4], linearly polarized [4, 5] or large in size [5] which makes them difficult to be used in wearable applications. Literature review shows that the bending analysis of linearly polarized textile antennas has been done to study the effect toward antenna's performance in terms of return loss, gain and radiation pattern [6–8] but it misses the details of effect on the efficiency and beam width of the antennas.

In this study, we analyzed the impact of bending on the performance of circularly polarized wearable antenna in free space. The antenna operates for ISM and WBAN applications at 2.45 GHz. The antenna uses thin substrate and has improved impedance and 3-dB Axial Ratio (AR) bandwidth, in free space measured results, than previously reported work [3, 6]. Simulated and measured results are compared in different antenna positions and bending. The test setup for bending includes two cylinders with the radii of 50 mm and 75 mm. These dimensions are typical for the human body parts, e.g., arm and leg. Antennas are bent around the cylinder along two principal planes, xz and yz planes, respectively, and results are measured for comparison purposes. Performance with respect to return loss, axial ratio and radiation characteristics have been presented, compared and

discussed briefly. Design of the antenna is explained in Section 2, while Section 3 discusses the flat antenna performance in free space. Section 4 presents the effects of bending on the performance of the antenna in free space whereas section 5 concludes the paper.

2. ANTENNA DESIGN

Figure 1 shows the fabricated antenna with dimensions. The antenna is fabricated on Denim fabric (commonly used in jeans) with the dimensions of $90 \times 90 \times 1\,\mathrm{mm}^3$, dielectric constant ($\varepsilon_r$) 1.68 and loss tangent($\delta$) 0.03. Copper tape with thickness 0.25 mm is used as conductive material (patch and ground). To achieve circular polarization a slot "s" is introduced on the patch. The position of slot "s" will excite two orthogonal modes of equal amplitude while their phase is controlled by its length. The resonant frequency of the antenna should be slightly higher than the desired resonant frequency because inserting the slot will shift the frequencies downward. Increasing the length of slot "s" till certain point (14 mm), increases the return loss and shifts the frequency to lower bands, but afterwards it splits the single frequency band into two bands and starts decreasing the return loss, which is not desirable. The designed antenna is fed by transmission line having the impedance of $50\,\Omega$ and width of 3.4 mm. The angle between the slot "s" and feed line is 45°.
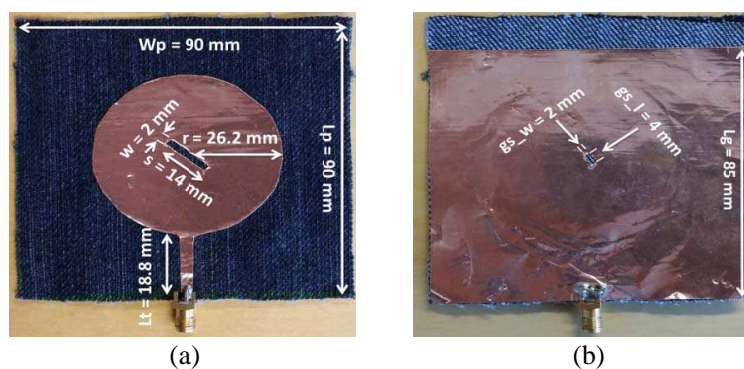

Figure 1: Fabricated antenna. (a) Patch. (b) Ground.

Micro-strip patch antennas are typically narrowband; to increase the bandwidth, partial and slotted ground plane techniques are used. The reason for the increase in bandwidth is due to the lowering of the Q factor of the antenna, which is inversely related to bandwidth [9]. Q factor of the antenna depends on the gap capacitance between the patch and the ground. Using partial ground will reduce the energy stored in capacitance between patch and ground, thus lowering the Q factor [9]. After partial grounding the bandwidth is increased to 80 MHz; starting from 2.40 GHz to 2.48 GHz. To cover the complete ISM band (2.40 GHz to 2.50 GHz), without changing the size of the radiating patch, slot "gs" was added to the ground plane which further lowers the Q factor of the antenna and increases the bandwidth. Due to the small size of the slot "gs", it will have very small effect on the resonant frequency. The increase in backward radiation due to slot "gs" is 1.4 dB, which shows that leakage radiation from slot is less. The final bandwidth of the antenna, after using slotted ground plane, increases to 120 MHz; starting from 2.39 GHz to 2.51 GHz.

3. FLAT ANTENNA PERFORMANCE

Measurements are carried out using vector network analyzer (VNA) Agilent PNA E8358A and near field measurement device Satimo Starlab. Figure 2 shows the comparison of simulated and measured results in terms of return loss and axial ratio of the antenna.

Measured return loss is similar to simulated with a shift towards higher frequencies. The reason for shifting is inaccuracies in fabrication as the antenna is fabricated by manually cutting the jeans and copper tape. The measured impedance bandwidth of the antenna is 160 MHz (2.42 GHz–2.58 GHz). The same trend is followed in the axial ratio, as it shifts toward higher frequencies with circular polarization (AR < 3 dB). The measured 3-dB AR bandwidth of the antenna is 60 MHz (2.45 GHz–2.51 GHz).

Figure 3 shows the comparison of simulated and measured results in terms of the axial ratio and gain at 2.45 GHz in xz plane. The measured 3-dB AR beam width at 2.45 GHz is approx. 218° in xz plane (from −157° to +61°). Flat antenna measurements show that antenna can efficiently operate on the desired frequency band with circular polarization in the main beam. The measured Front
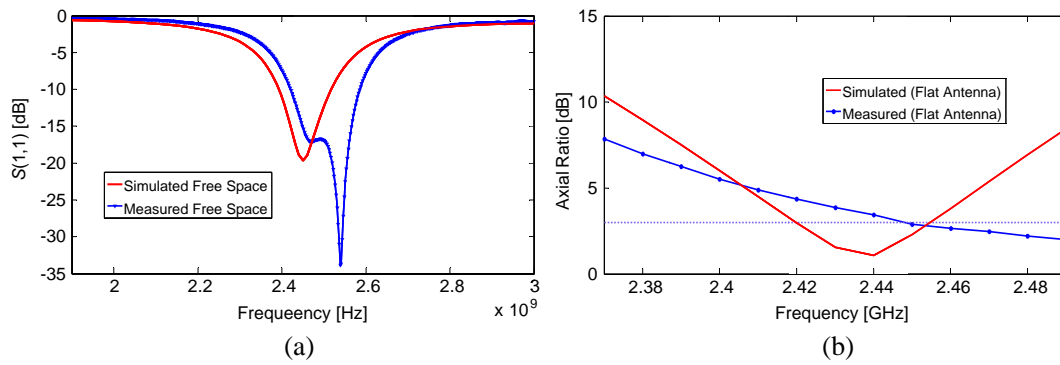
Figure 2: Simulated and measured results. (a) Return loss. (b) Axial ratio.
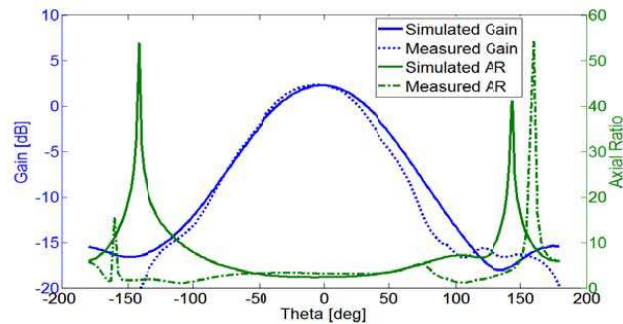

Figure 3: Simulated and measured results for gain and axial ratio at 2.45 GHz.
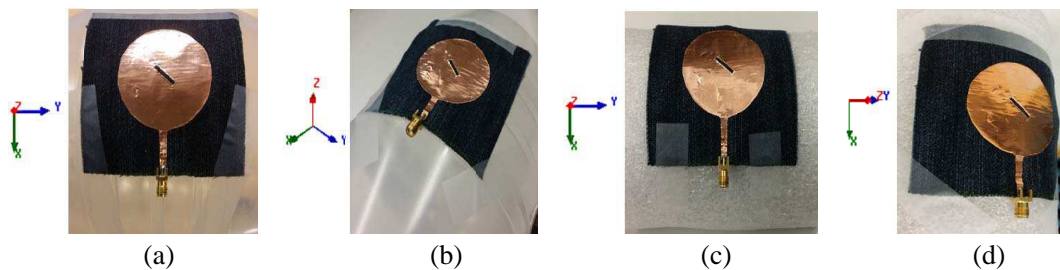
Figure 4: Bending. (a) xz 75 mm. (b) yz 75 mm. (c) xz 50 mm. (d) yz 50 mm.

to Back Ratio (FBR) is 20.09 dB which is good for wearable applications as maximum radiation is away from the antenna even with partial grounding. The antenna exhibits left hand circular polarization (LHCP).

4. ANTENNA BENDING

To demonstrate the effect of bending, two cylindrical shaped plastic bottles with radii 50 mm (small cylinder) and 75 mm (large cylinder) are used. The radius of the cylinder is inversely proportional to the bending angle. The selected radii are for typical human body parts like arms and legs etc.. The material of the cylinder does not affect the surface currents of the antenna. The antenna is bent on the cylinder in both xz and yz plane. Transparent paper tape is used to hold the antenna in proper positions during experiments. Performance of the antenna is evaluated by analyzing the effects of bending on return loss, axial ratio and radiation characteristics. Radiation characteristics include radiation patterns (xz and yz plane), peak gain, and radiation efficiency at 2.45 GHz. Figure 4 shows the bent antenna in different planes.

4.1. Effects on Return Loss and Bandwidth

Figure 5 compares the measured return loss of the antenna in flat and bent states. In general, bending an antenna changes the effective length which ultimately changes the resonant frequency. Increasing the bending, decreases the effective length, thus the resonant frequency is shifted to

Figure 5: Variation of return loss with bending.

Figure 6: Variation of axial ratio with bending.

Table 1: Change in radiation characteristics of antenna with bending.

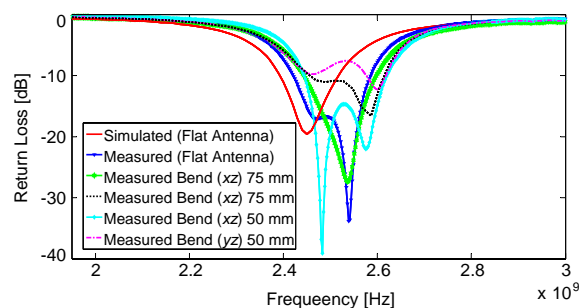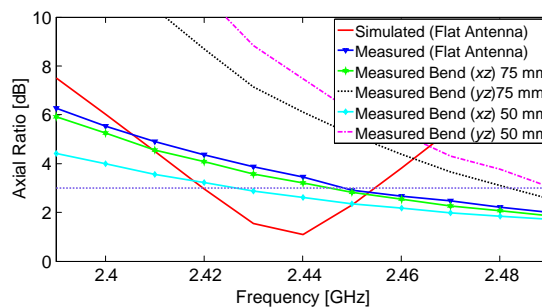| Antenna Position	Return Loss at 2.45 GHz [dB]	Bandwidth [MHz]
Simulated (Flat)	-19.620	120 (2.39 GHz–2.51 GHz)
Measured (Flat)	-15.378	160 (2.42 GHz–2.58 GHz)
Bending 50 mm xz	-11.850	180 (2.44–2.62 GHz)
Bending 50 mm yz	-9.537	50 (2.57–2.62 GHz)
Bending 75 mm xz	-11.010	150 (2.44 GHz–2.59 GHz)
Bending 75 mm yz	-9.628	160 (2.45 GHz–2.61 GHz)

higher bands. From the measured data, this is very clear in case of bending on the small cylinder. Return loss on the large cylinder is almost similar to the measured return loss of the flat antenna because of the small bending angle. The impedance band breaks into two when the antenna is bent in xz plane on the large cylinder. Effect of bending in yz plane is the worst as it shifts the resonant frequency to higher bands as well as degrades the return loss. One reason for this can be that the effective dimensions of transmission line and slot "s" are slightly modified, which detunes the input matching of the antenna. Compared with the measured results (flat antenna), yz plane bending does not have significant effect on the return loss. In all studied cases of the antenna bending, except small cylinder in yz plane, the measured impedance bandwidth is larger (25% to 50%) than the simulated impedance bandwidth of 120 MHz. Table 1 summarizes the change in return loss and bandwidth of antenna with bending.

4.2. Effects on Axial Ratio (AR)

Figure 6 compares the measured axial ratio of the antenna in flat and bent states. The measured AR follows the same trend as measured return loss in different bending scenarios. AR < 3 dB is maintained at 2.45 GHz when the antenna is bent in xz plane, while in yz plane, AR degrades at 2.45 GHz. Circular polarization changes to linear (or is highly elliptical) in yz plane bending. Improvement in AR is observed for xz plane bending. Circular polarization can easily change with bending because both length and width are in resonance with $90°$ phase shift and bending affects the effective resonating area of patch. It is always preferred to place the textile antenna on flat body parts like back and chest etc.. One solution to this problem can be designing an elliptically polarized antenna and bending it along the longer dimension to achieve circular polarization. The antenna then should be placed in specific bending for use in the wearable applications.

4.3. Effects on Radiation Characteristics

Figure 7 shows the 2D radiation patterns of antenna in xz and yz plane. Position of the antenna is shown in Figure 7 to have a better understanding of the radiation pattern around it. In xz plane bending, the beam width increases in both planes (xz and yz) on the larger cylinder, but as the bending is increased more by placing the antenna on smaller cylinder, the beam width tends to increase more in the plane of bending. The same change is observed in yz plane bending. This leads to the conclusion that antenna bending broadens the radiation pattern in the bending plane. The gain and efficiency of the antenna mainly reduces with bending. Table 2 summarizes the change in radiation characteristics of the antenna with bending. The measured results follow the theoretical relationship between gain, efficiency and directivity (calculated using beam widths) of the antenna.
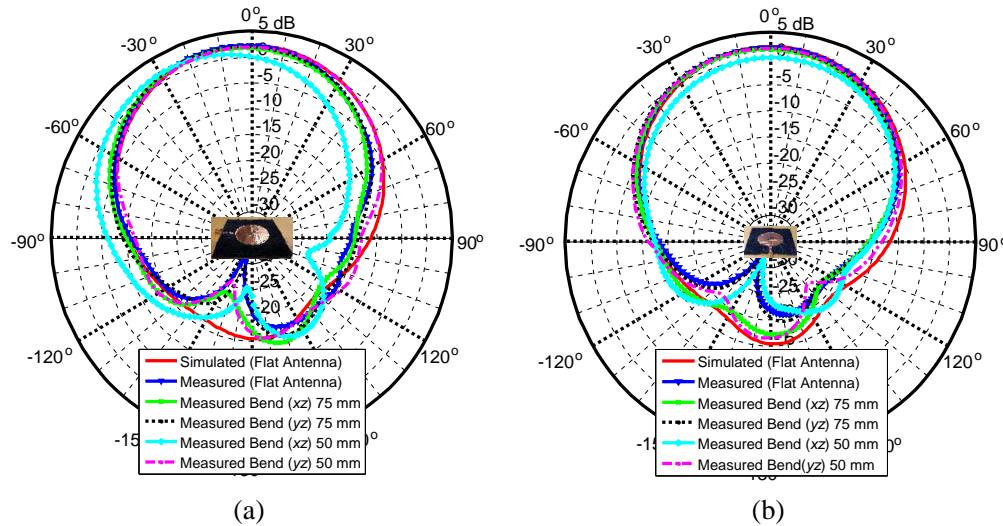
Figure 7: Radiation patterns. (a) *xz* plane. (b) *yz* plane.

Table 2: Change in radiation characteristics of antenna with bending.

Antenna Position	3 dB Beam width (xz-plane or Phi 0°)	3 dB Beam width (yz-plane or Phi 90°)	Peak Gain at 2.45 GHz [dB]	Efficiency at 2.45 GHz [%]
Simulated (Flat)	77° (+37° to −40°)	72° (+37° to −35°)	2.2612	27.505
Measured (Flat)	73° (+30° to −43°)	74° (+35° to −39°)	2.2524	25.076
Bending 50 mm *xz*	78° (+13° to −65°)	74° (+37° to −37°)	1.6579	22.387
Bending 50 mm *yz*	74° (+32° to −42°)	80° (+37° to −43°)	1.9904	26.699
Bending 75 mm *xz*	78° (+30° to −48°)	75° (+32° to −43°)	1.8872	24.582
Bending 75 mm *yz*	77° (+31° to −46°)	77° (+33° to −44°)	2.1133	26.345

5. CONCLUSION

The paper focuses on the effects of bending on the performance of the circularly polarized wearable antenna. A prototype antenna, with Denim fabric as substrate and copper tape as conductive material, is used for analysis. Two different planes, *xz* and *yz*, were selected to study the effects of bending on return loss, axial ratio and radiation characteristics of the antenna. Results show that the effect on performance is increased when the antenna is bent along the direction which determines its resonance length. In the presented work, the *yz* direction specifies the resonance length. Impedance matching is improved when the antenna is bent in *xz* plane. Beam width increases in the plane of bending which results in decreased antenna gain. Even after bending, the antenna is able to operate efficiently on the resonance frequency of 2.45 GHz. In future, the performance analysis of the antenna on different body parts like arms and legs etc. will be done to validate its operability for WBAN applications in the vicinity of human body.

REFERENCES

1. Salonen, P. and Y. Rahmat-Samii, "Wearable antenna: Advances in the design, characterization and application," *Antennas and Propagation for Body-centric Wireless Communication*, 151–188, P. Hall and Y. Hao, Eds., Artech House, Inc., MA, 2006.

2. Toh, B. Y., R. Cahill, and V. F. Fusco, "Understanding and measuring circular polarization," *IEEE Transactions on Education*, Vol. 46, No. 3, 313–318, Aug. 2003.

3. Yazdandoost, K. Y. and R. Miura, "Antenna polarization mismatch in BAN communications," *IEEE MTT-S International Microwave Workshop Series on RF and Wireless Technologies for Biomedical and Healthcare Applications (IMWS-BIO 2013)*, 1–3, Dec. 2013.

4. Alqadami, A. S. M. and M. F. Jamlos, "Design and development of a flexible and elastic UWB wearable antenna on PDMS substrate," *IEEE Asia-Pacific Conference on Applied Electromagnetics (APACE)*, 27–30, Dec. 2014.

5. Sundarsingh, E. F., et al., "Polygon-shaped slotted dual-band antenna for wearable applications," *IEEE Antennas and Wireless Propagation Letters*, Vol. 13, 611–614, 2014.

6. Ismail, M. F., et al., "Compact circularly polarized textile antenna," *IEEE Symposium on Wireless Technology and Applications (ISWTA)*, 134–136, 2014.

7. Ismail, M. F., et al., "Circularly polarized textile antenna with bending analysis," *IEEE International RF and Microwave Conference (RFM)*, 460–462, Dec. 9–11, 2013.

8. Ismail, M. F., et al., "Bending analysis on circular polarization array textile antenna," *IEEE Asia-Pacific Conference on Applied Electromagnetics (APACE)*, 139–141, Dec. 8–10, 2014.

9. Reddy, G. S., S. K. Mishra, S. Kharche, and J. Mukherjee, "High gain and low cross-polar compact printed elliptical monopole UWB antenna loaded with partial ground and parasitic patches," *Progress In Electromagnetics Research*, Vol. 43, 151–167, 2012.

Design and Optimization of Miniaturized Dual-band Implantable Antenna for MICS and ISM Bands

Muhammad Ali Babar Abbasi, Salman Arain, Photos Vryonides, and Symeon Nikolaou

Department of Electrical Engineering, Frederick University, Nicosia, Cyprus

Abstract— This work discusses the design method towards the implementation of a compact, stacked, implantable antenna for biotelemetry applications. The proposed antenna consists of three stacked layers, printed on high permittivity grounded substrate. The bottom layer of the antenna above the ground plane, contains a meandered structure with a symmetrically placed T-shaped slot. The middle layer consists of two U-shaped radiators and an M-shaped metallic segment is further added on the top layer to further enhance the radiation efficiency of the antenna. These three stacked layers, form a symmetrical closed loop structure resonating on its fundamental resonant mode, at 403 MHz, for the Medical Implant Communication Service (MICS) band. A shifted higher order mode of the same closed loop structure, along with the negative currents on ground plane enables wide band operation, at 2.45 GHz, for the industrial, scientific, and medical (ISM) band. To resolve the constraints associated with implanting an antenna in human body that usually results in detuning and impedance mismatch, the antennas most important radiating sections were thoroughly investigated. A fully parametrized solution is proposed that makes the antenna a good candidate for a device, implanted at several different areas of the human body with potentially different electrical properties with consequently different detuning effect. For further investigation, the particle swarm algorithm was implemented to optimize the antennas performance while operating inside a compact, $23 \times 23 \times 5 \, \text{mm}^3$ block of human skin, equivalent phantom. The simulated performance of the proposed prototype antenna, indicates that it can be used for either in-vitro or in-vivo operations.

1. INTRODUCTION

Biotelemetry enables full duplex wireless communication between implantable antennas with on-body receiver antennas. Designing a wearable on-body antenna is comparatively easier because of its placement in an environment where body is normally in one direction and air in the other. This, allows the designers to control the radiation pattern of the antenna towards the human body by introducing a reflector or a cavity. On the other hand, designing an implantable antenna is a more challenging task due to a number of factors. First and far most challenge is the detuning factor and impedance mismatching that occurs when the antenna is placed inside human body. This is due to high water content and high conductive human tissues. Moreover detuning and mismatching are normally unpredictable and vary from tissue to tissue because different tissues have different electrical properties. The second major problem that arises while designing implantable antenna is its size. Since, MICS band at 403 MHz is assigned for implantable devices for on-body devices communication, the antenna effective aperture area at this frequency is rather large. However, the requirement is that the antenna integrated with the implantable device, along with power unit, should be as small as possible since the device is expected to be implanted inside the human body. A significant amount of work has already been done where different antenna design topologies have been proposed by researchers. To test the performance of an antenna in in-vivo environment, simulations are generally carried out inside simple layered phantoms [1, 2] or in realistic body phantoms [3, 4]. Electrical properties of these phantoms are either modeled using Cole-Cole model [2, 5] or multi-pole Debye model [6]. Some researchers [3, 5, 7] also measured the electrical properties of human tissues (skin, fat, muscle) using dielectric probe kit or impedance analyzer and then used these properties in simulations to test the performance of their proposed solution. To achieve compactness, researchers have tried different methods and several types of antennas, including spiral [2, 8, 9], meandered patch [4, 5, 7–9], folded square IFA [10], 2D and 3D spherical [8, 11] and multilayered [12] configurations. All these methods reduce the antenna size by increasing the length of the current flow path on the same plane (meandered and spiral) or in all three dimensions (3D spiral, 3D ring and stacked). In addition, a shortening pin between ground and patch may also effectively reduce the required physical dimensions of an implantable antenna [13] and has been widely used. It has been observed that antennas designed for a specific tissue are not expected to perform equally well in any substantially different tissue surrounding. In this work, we propose a solution which not only covers MICS and ISM bands for implantable

applications, but additionally it can be customized to a random tissue environment. The behavior of the antenna is thoroughly studied and a range of geometric parameters are presented for best antenna performance.

2. PROPOSED LAYERED IMPLANTABLE ANTENNA

Figure 1 shows the geometry of the proposed layered implantable antenna. The overall dimensions of the antenna are $15 \times 18 \times 1.97\,\text{mm}^3$, and the antenna consists of three copper coated substrate layers. In this study, Roger's RO3210 as substrate was used since its electrical properties resemble with those of biocompatible substrate ceramic alumina ($\epsilon_r = 9.4$ and $\tan\delta = 0.006$). RO3210 was preferred because it can be easily available and is compatible with conventional fabrication techniques making in-house prototype fabrication possible. The proposed antenna consists of the ground layer and three stacked patch layers as shown in Figure 1. The bottom layer of the antenna, fed at the upper right corner, comprises a patch with identical slits having length and width pl_1, pl_3, pw_1 and pw_3 respectively. These slots along with the T shaped slot in the middle of the patch introduce a meandered structure used for size reduction. To further decrease the size of the antenna, a short pin is introduced on the bottom layer as shown in Figure 1. The middle layer of the antenna comprises of two U-shaped coupling resonators with a capacitive coupling gap. The right U-shaped resonator is fed at the upper right corner with extended coaxial feed whereas the left U-shaped resonator is fed by via1 connecting the bottom layer and the middle layer at the upper left corner, exactly opposite to the feed point. To further increase the resonance capacity of the antenna, an M-shaped, third layer is introduced on the top layer of the substrate. Via2 and via3 connect the middle with the top layer at lower right and lower left corners respectively. The M-shaped top layer consists of a radiating patch with two identical slits, having dimensions rl_1, rl_2, rw_1 and rw_2 respectively.

    The effective current path in this antenna comprises of a meandered patch on the bottom layer, the left U-shaped patch of the middle layer, the M-shaped patch of the top layer and the right U-shaped patch of the middle layer. This current path makes an approximately $\lambda/4$ closed loop structure, resonating at the fundamental resonant mode at 403 MHz covering the MICS band. Furthermore, a higher order harmonic of the same resonant closed loop structure, was adjusted to operate at 2.45 GHz ISM band, resulting in a dual band operation using the same structure. To further enhance the radiation efficiency of the proposed antenna at ISM band, the effective length of the meandered patch on the bottom layer, that depends upon its coupling with the ground plane was further optimized. The next step was to study the behavior of the antenna in different tissue surroundings, which is equivalent to implanting the antenna at different body parts, and to identify various antenna tuning parameters simultaneously, for MICS and ISM bands. This study resulted in a fully parametrized antenna model with a minimum and maximum defined range of geometrical parameters that may adjust the effective wavelength of the $\lambda/4$ closed loop resonator, and the
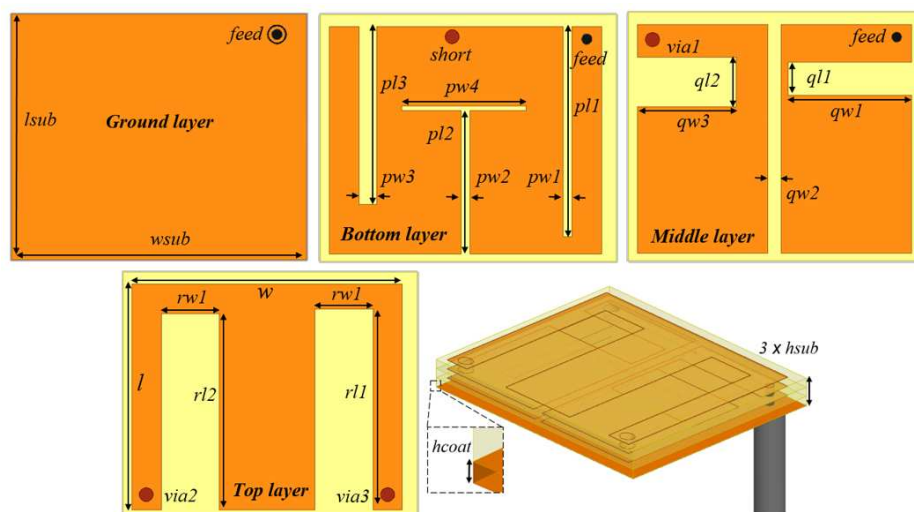

Figure 1: The geometry of proposed Implantable antenna with $l_{sub} = 15\,\text{mm}$, $h_{sub} = 0.635\,\text{mm}$, $w_{sub} = 18\,\text{mm}$, $h_{coat} = 17\,\mu\text{m}$, $l = 13.8\,\text{mm}$ and $w = 16.56\,\text{mm}$.

meandered patch of the bottom layer. One case is presented in this paper where the antenna is placed in $23 \times 23 \times 5 \,\mathrm{mm}^3$ block of human skin phantom. Note that measured electrical properties of skin tissue reported in [5], were used for this test. As predicted, significant detuning was observed both at MICS and ISM bands as shown in Figure 2.

Results shown in Figure 2(a), indicate that, when the antenna was placed in skin phantom, a resonant frequency shift of around 50 MHz towards lower frequencies, was observed for the MICS band. Significant degradation in impedance matching can also be observed in Figure 2(a). The frequency downshift was raised up to 130 MHz at the ISM band as can be seen in Figure 2(b). In order to tune the antenna dimensions on both targeted frequency bands simultaneously, particle swarm algorithm in combination with FDTD simulation was used. The resulting set of optimized values of the antenna parameters are listed in the fourth column of Table 1, where the third column shows the seed values for the particle swarm optimizer. The watch function to optimize the antenna in given tissue environment is set to be:

$$f = \max\left(|S_{11}\,(\mathrm{dB})_{403\,\mathrm{MHz}}|, |S_{11}\,(\mathrm{dB})_{2.45\,\mathrm{GHz}}|\right) \tag{1}$$

It took 20 iterations for the particle swarm algorithm to converge and tune both minima at the desired frequency bands. Impedance bandwidth of 9 MHz (from 398 MHz to 407 MHz) covering the MICS band and 72 MHz (from 2438 MHz to 2510 MHz) covering the ISM band, were achieved as a result of optimization. Note that return loss minima can be further tuned at the desired frequencies
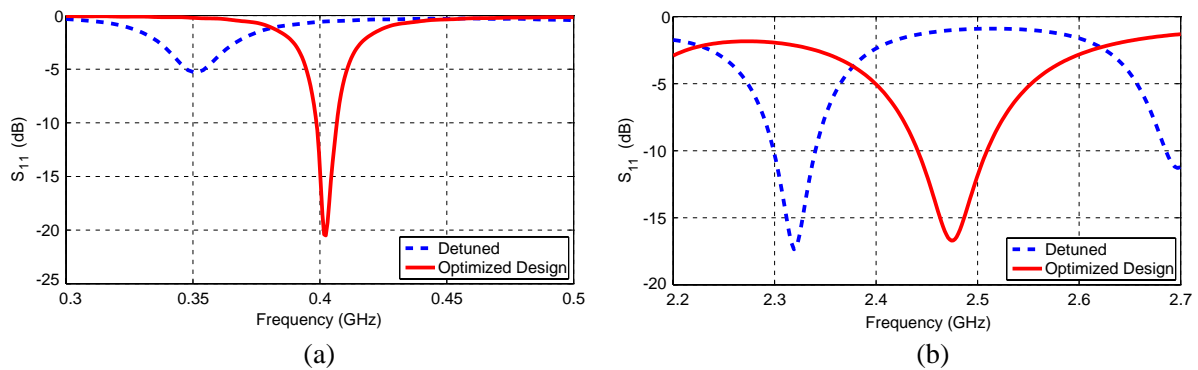
Figure 2: Detuning of antenna when placed in $23 \times 23 \times 5 \,\mathrm{mm}^3$ human skin phantom [5] and optimization using particle swarm algorithm at (a) MICS band and (b) ISM band.

Table 1: Antenna optimization parameters.

Symbol	minimum value (mm)	maximum value (mm)	seed value (mm)	optimized parameter in skin phantom
pl_1	08.60	13.60	10.60	12.75
pl_2	01.00	13.00	01.00	08.70
pl_3	08.60	13.60	10.60	10.80
pw_1	00.50	02.00	01.00	00.54
pw_2	00.50	00.70	01.00	00.50
pw_3	00.50	02.00	01.00	01.17
pw_4	04.00	08.00	06.00	07.56
ql_1	03.00	09.00	06.00	03.00
ql_2	03.00	09.00	06.00	06.00
qw_1	05.00	07.50	06.00	07.46
qw_2	00.20	00.90	00.30	00.81
qw_3	05.00	07.50	06.00	05.90
rl_1	11.00	13.00	12.00	12.30
rl_2	11.00	13.00	12.00	12.00
rw_1	03.00	06.00	04.50	03.50
rw_2	03.00	06.00	04.50	03.50

at a cost of increased iterations of the optimization algorithm. Columns 2 and 3 of Table 1 list the range of controlling geometric parameters. The particle swarm algorithm requires both a rang as well as a seed value of a geometrical parameter optimization to be initiated. Values listed in Table 1 can be used for this purpose. The expected result should be an optimized set of values for which the customized antenna operates simultaneously at both MICS and ISM bands and this should be feasible for any given random tissue surrounding environment.

3. CONCLUSION

This paper describes a miniaturized implantable antenna with a meandered and stacked structure. By varying the length and width of each parameter listed in Table 1, the antenna is excited at two resonant frequencies, at MICS and ISM bands. It was demonstrated that the proposed antenna can be tuned using the particle swarm algorithm, to operate adequately when placed inside several different human tissue models. The next phase of this work includes the antenna fabrication and in-vitro or in-vivo antenna testing, and additionally the integration of the antenna to the suitable microchip to build a complete implantable system.

REFERENCES

1. Gemio, J., J. Parron, and J. Soler, "Human body effects on implantable antennas for ISM bands applications: Models comparison and propagation losses study," *Progress In Electromagnetics Research*, Vol. 110, 437–452, 2010.
2. Permana, H., Q. Fang, and W. S. T. Rowe, "Hermetic implantable antenna inside vitreous humor simulating fluid," *Progress In Electromagnetics Research*, Vol. 133, 571–590, 2013.
3. Yilmaz, T., R. Foster, and Y. Hao, "Patch resonator for non-invasive detection of dielectric property changes in biological tissues," *IEEE Antennas and Propagation Society International Symposium (APSURSI)*, 1–2, 2012.
4. Alrawashdeh, R., Y. Huang, and P. Cao, "Flexible meandered loop antenna for implants in MedRadio and ISM bands," *Electronics Letters*, Vol. 49, No. 24, 1515–1517, 2013.
5. Karacolak, T., R. Cooper, and E. Topsakal, "Electrical properties of rat skin and design of implantable antennas for medical wireless telemetry," *IEEE Transactions on Antennas and Propagation*, Vol. 57, No. 9, 2806–2812, 2009.
6. Noroozi, Z. and F. Hojjat-Kashani, "Three-dimensional FDTD analysis of the dual-band implantable antenna for continuous glucose monitoring," *Progress In Electromagnetics Research Letters*, Vol. 28, 9–21, 2012.
7. Karacolak, T., R. Cooper, J. Butler, S. Fisher, and E. Topsakal, "In vivo verification of implantable antennas using rats as model animals," *IEEE Antennas and Wireless Propagation Letters*, Vol. 9, 334–337, 2010.
8. Merli, F., L. Bolomey, J. Zurcher, G. Corradini, E. Meurville, and A. K. Skrivervik, "Design, realization and measurements of a miniature antenna for implantable wireless communication systems," *IEEE Transactions on Antennas and Propagation*, Vol. 59, No. 10, 3544–3555, 2011.
9. Kim, J. and Y. Rahmat-Samii, "Planar inverted-F antennas on implantable medical devices: Meandered type versus spiral type," *Microwave and Optical Technology Letters*, Vol. 48, No. 3, 567–572, 2006.
10. Vidal, N., S. Curto, J. M. Lopez-Villegas, J. Sieiro, and F. M. Ramos, "Detuning study of implantable antennas inside the human body," *Progress In Electromagnetics Research*, Vol. 124, 265–283, 2012.
11. Abadia, J., F. Merli, J.-F. Zurcher, J. R. Mosig, and A. K. Skrivervik, "3D-spiral small antenna design and realization for biomedical telemetry in the MICS band," *Radioengineering*, Vol. 18, No. 4, 359–367, 2009.
12. Huang, F.-J., C.-M. Lee, C.-L. Chang, L.-K. Chen, T.-C. Yo, and C.-H. Luo, "Rectenna application of miniaturized implantable antenna design for triple-band biotelemetry communication," *IEEE Transactions on Antennas and Propagation*, Vol. 59, No. 7, 2646–2653, 2011.
13. Kiourti, A. and K. S. Nikita, "A review of implantable patch antennas for biomedical telemetry: Challenges and solutions [wireless corner]," *IEEE Antennas and Propagation Magazine*, Vol. 54, No. 3, 210–228, 2012.

A New Approach to Diffraction in Volume Gratings and Holograms

David Brotherton-Ratcliffe

Centre for Ultra-realistic Imaging, Applied Science, Computing & Engineering,
Glyndŵr University, Mold Road, Wrexham, Wales LL1 2AW, UK

Abstract— Coupled wave theory has historically been successfully used to provide various analytic theories of optical diffraction in volume phase gratings. Here we develop a different approach based on a decomposition of the permittivity profile of the grating into an infinite array of infinitesimal discontinuities or step functions. By considering the corresponding elementary Fresnel solutions from each discontinuity, a first-order set of coupled partial differential equations can be derived and then solved in a rotated frame of reference to give analytical expressions for the diffraction efficiency of the general slanted grating at arbitrary angle of incidence. The underlying differential equations derived from the approach are a rigorous representation of Maxwell's equations for the case of the unslanted grating and few assumptions are required to provide highly accurate solutions for harmonic or quasi-harmonic permittivity distributions, even at large grating slant.

1. INTRODUCTION

Historically coupled wave theory has been successfully used to provide analytic theories of optical diffraction in volume phase gratings [1–3]. Kogelnik's theory [1] has been particularly successful in this regard and indeed even today engineers frequently use his analytic expressions. Rigorous coupled wave theory [3] provides an exact estimate of the diffraction efficiency of a volume grating, but here numerical evaluation is required and in some cases such evaluations can be lengthy and subject to instability.

Here we shall describe a different approach — the PSM or Parallel Stacked Mirror model [4–11]. The PSM model is based on a decomposition of either the permittivity profile or the refractive index profile of the grating into an infinite array of infinitesimal discontinuities or step functions. By considering the corresponding elementary Fresnel solutions from each discontinuity, a first-order set of coupled partial differential equations can be derived. These equations are then solved in a rotated frame of reference to give analytical expressions for the diffraction efficiency of the general slanted grating at arbitrary angle of incidence. The underlying differential equations derived from this approach are a rigorous representation of Maxwell's equations for the case of the unslanted grating. Few assumptions are required to provide highly accurate solutions for the case of harmonic or quasi-harmonic permittivity distributions, even at large grating slant.

The method can be applied to either reflection or transmission geometry, although it is most accurate in the case of the reflection grating. It can also been extended to include finite absorption in phase gratings and to treat the cases of absorption and mixed absorption-phase gratings. It can also be used to treat multi-chromatic gratings, spatially multiplexed gratings and holograms. Finally it can be used to provide accurate analytic expressions for gratings with variable fringe contrast profiles.

Comparison with rigorous numerical computations of Maxwell's equations show that the approach works somewhat better than simple coupled wave theory for most reflection gratings, whereas the coupled wave approach appears a little better in describing the transmission geometry. The approach appears to offer a general approximate method for the analysis of electromagnetic, acoustic and other types of diffraction occurring in harmonic or quasi-harmonic structures.

2. USING FRESNEL REFLECTION TO ANALYSE DIFFRACTION

When a plane light wave propagates across the boundary of two regions of constant but differing refractive index, a portion of the light wave is reflected and a portion is transmitted. In the case of a purely real index there is no absorption and the transmitted and reflected energies add up to the incident energy. The laws describing how the amplitude of the transmitted and reflected waves depends on the indices of the two regions are known as Fresnel's laws. In the case of normal incidence they are trivially simple. If the wave passes from index n_1 to index n_2 then the ratio of the reflected to incident amplitude and the ratio of transmitted to incident amplitude are simply given by

$$r = \frac{n_2 - n_1}{n_1 + n_2}; \quad t = \frac{2n_1}{n_1 + n_2} \tag{1}$$

The PSM theory models a volume grating as many thin parallel stacked layers, each with a slightly different index. Overall the grating looks just like a normal grating except that under the microscope the index does not vary smoothly from one depth to another but rather it makes small jumps. However, by making the distance between such jumps vanishingly small, we won't know the difference.

When an illuminating wave strikes a jump between one index and the next, we can use Equation (1) to write down the amount of light transmitted and reflected. Of course these equations are only valid for the case of normal incidence but we can generalise them easily enough to incidence at any angle. Since the index layers are assumed flat and parallel in the simplest PSM model we can also use the well-known law that the angle of incidence is equal to the angle of reflection. If we then call our (monochromatic) illuminating wave, R, it is immediately obvious that at each index jump, R is slightly depleted and a new wave, which we can call S, is created by Fresnel reflection.

3. THE SIMPLEST POSSIBLE PSM THEORY — THE NORMAL-INCIDENCE VOLUME REFLECTION PHASE GRATING

We will now present the simplest possible mathematical derivation of the simplest example of PSM. This is the case of the sinusoidal unslanted lossless volume reflection phase grating under illumination at normal incidence. Fig. 1 shows a diagram of the set-up. We start by modelling the grating as a stack of parallel slices, each having a slightly differing refractive index. At this stage we don't make any assumption about the form of the index distribution other than it being composed of slices. Note that each slice will have a small but finite thickness and in the other two dimensions it will have the form of an infinite rectangular plane. We now assume that a monochromatic plane wave illuminates the grating. Mathematically we state this by the equation

$$R^{Ext} = e^{i\beta y} \tag{2}$$

where

$$\beta = \frac{2\pi n_0}{\lambda_c} \tag{3}$$

Here n_0 is the average value of index inside and outside of the grating and λ_c is the free-space wavelength. If we now label each one of the slices by the integer J and let the index of the Jth slice be n_J then we can immediately write down the following recurrence relations

$$
\begin{aligned}
R_J &= 2e^{i\beta\delta y} \left\{ \frac{n_{J-1}}{n_J + n_{J-1}} \right\} R_{J-1} + e^{i\beta\delta y} \left\{ \frac{n_{J-1} - n_J}{n_J + n_{J-1}} \right\} S_J \\
S_J &= 2e^{i\beta\delta y} \left\{ \frac{n_{J+1}}{n_{J+1} + n_J} \right\} S_{J+1} + e^{i\beta\delta y} \left\{ \frac{n_{J+1} - n_J}{n_{J+1} + n_J} \right\} R_J
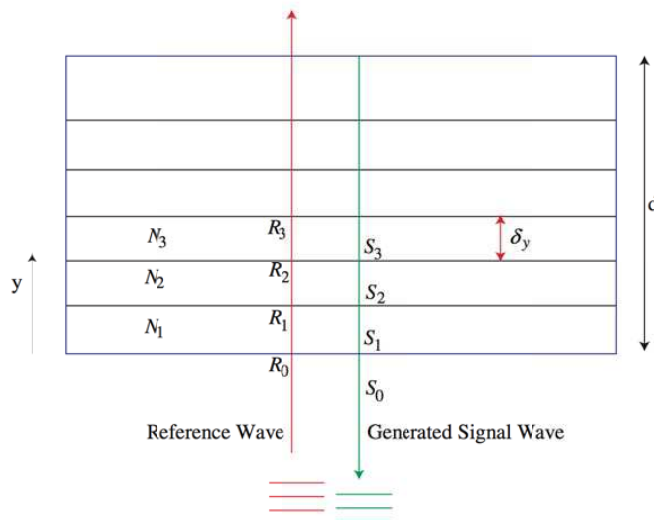\end{aligned}
\tag{4}
$$

Figure 1: Normal Incidence grating with illuminating wave R and provoked signal wave, S.

Here the terms in curly brackets are just the Fresnel amplitude reflection and transmission coefficients and the exponential is a phase propagator which advances the phase of the R and S waves as the two waves travel the distance δy between discontinuities. We now let

$$X_{J-1} = X_J - \frac{dX}{dy}\delta y - \dots \tag{5}$$

and let $\delta y \to 0$. Here X denotes R, S or n. Further expanding the exponential terms as Taylor series and ignoring quadratic terms in δy we arrive at the differential counterpart to (4)

$$\begin{aligned}
\frac{dR}{dy} &= \frac{R}{2}\left(2i\beta - \frac{1}{n}\frac{dn}{dy}\right) - \frac{1}{2n}\frac{dn}{dy}S \\
\frac{dS}{dy} &= -\frac{S}{2}\left(\frac{1}{n}\frac{dn}{dy} + 2i\beta\right) - \frac{1}{2n}\frac{dn}{dy}R
\end{aligned} \tag{6}$$

These equations, which are not surprisingly an exact representation of Maxwell's equations, can be solved to produce approximate but very accurate analytic expressions for R and S and indeed for the diffraction efficiency of the grating in the case of a sinusoidal index:

$$n = n_0 + n_1 \cos\left(\frac{4\pi n_0}{\lambda_r}y\right) = n_0 + \frac{n_1}{2}\left\{e^{\frac{4i\pi n_0}{\lambda_r}y} + e^{-\frac{4i\pi n_0}{\lambda_r}y}\right\} \tag{7}$$

Here λ_r is the free-space recording wavelength. We may write the diffraction efficiency for such a grating as

$$\eta_{PSM} = \frac{\alpha^2\kappa^2}{\beta^2(1-\alpha)^2 + \left(\alpha^2\kappa^2 - \beta^2(1-\alpha)^2\right)\coth^2\left(d\sqrt{\alpha^2\kappa^2 - \beta^2(1-\alpha)^2}\right)} \tag{8}$$

where

$$\alpha = \lambda_c/\lambda_r \quad \text{and} \quad \kappa = \frac{\pi n_1}{\lambda_c} \tag{9}$$

For comparison, Kogelnik's theory gives

$$\eta_{Kog} = \frac{\kappa^2}{\beta^2\alpha^2(1-\alpha)^2 + (\kappa^2 - \beta^2\alpha^2(1-\alpha)^2)\coth^2\left(d\sqrt{\kappa^2 - \beta^2\alpha^2(1-\alpha)^2}\right)} \tag{10}$$

Practically, the two expressions produce very similar results. However the PSM theory describes the behaviour away from Bragg resonance rather better.

4. EXTENSION TO OBLIQUE INCIDENCE AND FINITE LOSS

An unslanted lossy grating can be characterized by a harmonic refractive index

$$n = (n_0 + i\chi_0) + \frac{1}{2}(n_1 + i\chi_1)\left\{e^{i\mathbf{K}\cdot\mathbf{r}} + e^{-i\mathbf{K}\cdot\mathbf{r}}\right\} \tag{11}$$

where n_0 is the real average refractive index of the grating, n_1 is the real harmonic index modulation, χ_0 is the average imaginary index of the grating, χ_1 is the imaginary harmonic index modulation and $\mathbf{K}$ is the grating vector.

The grating is illuminated by a wave at oblique incidence

$$R = e^{ik_{cx}x + ik_{cy}y} \tag{12}$$

where

$$\mathbf{k}_c = \frac{2\pi n_0}{\lambda_c}\begin{pmatrix}\sin\theta_c \\ \cos\theta_c\end{pmatrix} = \beta\begin{pmatrix}\sin\theta_c \\ \cos\theta_c\end{pmatrix} \tag{13}$$

The grating vector, $\mathbf{K}$ can be written in terms of a recording angle θ_r and a recording free-space wavelength λ_r

$$\mathbf{K} = 2\alpha\beta\cos\theta_r\hat{\mathbf{y}} \tag{14}$$

The response of the grating to illumination is the generation of a reflected signal wave

$$S = S(y)e^{ik_{ix}x+ik_{iy}y} \tag{15}$$

with

$$\mathbf{k}_i = \beta \begin{pmatrix} \sin\theta_c \\ -\cos\theta_c \end{pmatrix} \tag{16}$$

The grating, as shown in Fig. 2, is divided into an infinite number of parallel stacked mirrors as before. At each such mirror the complex index makes a discontinuous jump and we may apply Fresnel's law to write down expressions for the amplitude transmission and reflection coefficients. Using the notation of superscripts to indicate mirror number in y and subscripts to indicate the quantised x position of a ray intersection, the transmission (t) and reflection (r) amplitude coefficients for the mirror between dielectric regions k and $k+1$ are respectively

$$\begin{pmatrix} t \\ r \end{pmatrix}_{k,k+1} = \frac{1}{\left\{ (n_{k+1}+i\chi_{k+1})\sqrt{1-\frac{n_0^2}{(n_{k+1}+i\chi_{k+1})^2}\sin^2\theta_c} + (n_k+i\chi_k)\sqrt{1-\frac{n_0^2}{(n_k+i\chi_k)^2}\sin^2\theta_c} \right\}} \begin{pmatrix} 2(n_k+i\chi_k)\sqrt{1-\frac{n_0^2}{(n_k+i\chi_k)^2}\sin^2\theta_c} \\ \left\{ (n_{k+1}+i\chi_{k+1})\sqrt{1-\frac{n_0^2}{(n_{k+1}+i\chi_{k+1})^2}\sin^2\theta_c} \\ -(n_k+i\chi_k)\sqrt{1-\frac{n_0^2}{(n_k+i\chi_k)^2}\sin^2\theta_c} \right\} \end{pmatrix} \tag{17}$$

As before coupled recurrence relations can now be derived for R and S and from these a set of coupled partial differential equations [9]. These can then be solved to define approximate but nevertheless very accurate analytic expressions for the diffraction efficiency. The coupled partial differential equations may also be solved in a rotated frame, thereby describing gratings with arbitrary slant and indeed even transmission gratings [4]. A recent study [10] has shown that the PSM model provides a generally better description of the typical reflection grating than traditional coupled wave theory, although the converse appears to be true for the transmission grating. PSM can also be extended to panchromatic gratings [4], multiplexed gratings and holograms [5] and variable contrast gratings [11]. The PSM model may additionally be utilised to **describe particle** diffraction from quantum periodic structures as the time independent Schrödinger equation for a harmonic potential is analytically identical to the corresponding Helmholtz equation describing optical diffraction from a harmonic index. Potential applications include the analysis of neutron super-mirrors that have been recorded using holographic techniques [12, 13]. Finally the results may also be useful in the study of acoustic diffraction from harmonic structures where the transfer matrix approach is well known [14].

REFERENCES

1. Kogelnik, H., "Coupled wave theory for thick hologram gratings," *Bell Syst. Tech. J.*, Vol. 48, 2909–2947, 1969.
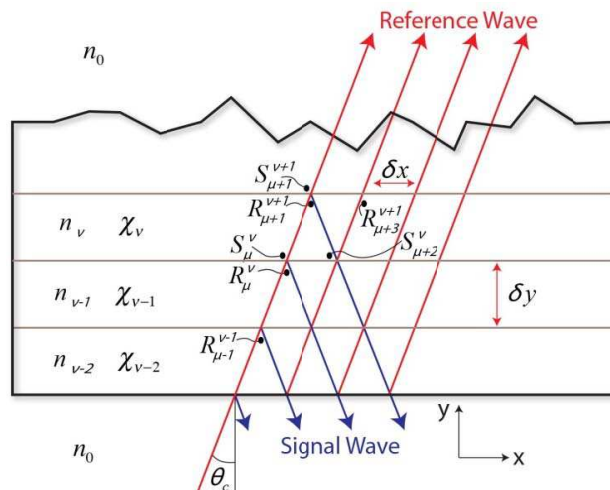
Figure 2: The Replay of an unslanted reflection grating, as treated by the PSM model, showing infinitesimally thick dielectric layers and the Signal and Reference fields present at the index discontinuities.

2. Solymar, L., *Opt. Commun.*, Vol. 23, 199–202, 1977.

3. Moharam, M. G. and T. K. Gaylord, "Rigorous coupled wave analysis of planar grating diffraction," *J. Opt. Soc. Am.*, Vol. 71, 811–818, 1981.

4. Brotherton-Ratcliffe, D., "A treatment of the general volume holographic grating as an array of parallel stacked mirrors," *J. Mod. Optics*, Vol. 59, 1113–1132, 2012.

5. Brotherton-Ratcliffe, D., "Analytical treatment of the polychromatic spatially multiplexed volume holographic grating," *Appl. Opt.*, Vol. 51, 7188–7199, 2012.

6. Brotherton-Ratcliffe, D., "A new type of coupled wave theory capable of analytically describing diffraction in polychromatic spatially multiplexed holographic gratings," *Journal of Physics, Conference Series*, Vol. 415, 012034, 2013, Doi: 10.1088/1742-6596/415/1/012034.

7. Bjelkhagen, H. and D. Brotherton-Ratcliffe, *Ultra-realistic Imaging — Advanced Techniques in Analogue and Digital Colour Holography*, CRC-Taylor and Francis, 2012.

8. Brotherton-Ratcliffe, D., "Understanding diffraction in volume gratings and holograms," *Holography — Basic Principles and Contemporary Applications*, Chapter 1, E. Mihaylova, Ed., INTECH, 2013.

9. Brotherton-Ratcliffe, D., A. Osanlou, and P. Excell, "Using the parallel-stacked mirror model to analytically describe diffraction in the planar volume reflection grating with finite absorption," *Applied Optics*, Vol. 54, 3700–3707, 2015.

10. Brotherton-Ratcliffe, D., L. Shi, A. Osanlou, and P. Excell, "A comparative study of the accuracy of the PSM and Kogelnik models of diffraction in reflection and transmission holographic gratings," *Opt. Express*, Vol. 22, No. 26, 32384–32405, 2014.

11. Brotherton-Ratcliffe, D., H. Bjelkhagen, A. Osanlou, and P. Excell, "Diffraction in volume reflection gratings with variable fringe contrast," *Applied Optics*, Vol. 54, 5057–5064, 2015.

12. Fally, M., et al., "Diffraction gratings for neutrons from polymers and holographic polymer-dispersed liquid crystals," *J. Opt. A: Pure Appl. Opt.*, Vol. 11 024019, 2009.

13. Klepp, J., et al., "Holographic gratings for slow neutron optics," *Materials*, Vol. 5, 2788–2815, 2012, Doi: 10.3390/ma5122788.

14. Abid, M., et al., "Acoustic response of a multilayer panel with viscoelastic material," *International Journal of Acoustics and Vibration*, Vol. 17, No. 2, 82—89, 2012.

Regular Coulomb Wave Function Method for Analysis of the Azimuthally Magnetized Circular Ferrite Waveguides

Mariana Nikolova Georgieva-Grosse[1] and Georgi Nikolov Georgiev[2]

[1]Consulting and Researcher in Physics and Computer Sciences, Gerlingen D-70839, Germany
[2]Faculty of Mathematics and Informatics
University of Veliko Tirnovo "St. St. Cyril and Methodius", Veliko Tirnovo BG-5000, Bulgaria

Abstract— The regular Coulomb wave function method for investigation of the circular waveguides, comprising a co-axially positioned solid ferrite cylinder of azimuthal magnetization that support normal TE_{0n} modes is regarded and put into practice to the simplest case in which the anisotropic medium fills them completely. Its main points are: i) the pertinent wave equation is a form of the Coulomb wave equation; ii) the field components are expressed by the real Coulomb wave functions $F_L(\eta, \rho)$ where $L = -0.5$ or $L = 0.5$, η and ρ — real, $\rho > 0$, $-\infty < \eta < +\infty$; iii) the solution of propagation problem needs a detailed numerical study of the functions and of their zeros in ρ. The Georgiev and Georgieva's pioneering idea is adopted and advanced to extend with new (in the case considered — with the electromagnetism and in particular with the theory of waveguides) the traditionally established field of application of the Coulomb wave functions $F_L(\eta, \rho)$ and $G_L(\eta, \rho)$ — the atomic physics and quantum mechanics. It stands on the generalized for all complex ρ, η and L Thompson and Barnett's definition of the aforesaid functions, using their relations with the confluent hypergeometric ones. It is proved numerically that the Abramowitz and Stegun's series, expressing the regular function, though initially constructed for real ρ and η ($\rho > 0$, $-\infty < \eta < \infty$) and a non-negative integer L ($L = 0, 1, 2, \ldots$): i) is applicable also for certain fractional positive and negative real L (e.g., $L = \pm 0.5$), on condition that the set of allowable values of the other two parameters is unchanged; ii) is preferable in the computations, compared to the one, harnessing the Thompson and Barnett's representation of $F_L(\eta, \rho)$ in terms of the complex Kummer function. Its advantage consists in: i) it is more rapidly convergent; ii) real parameters are used only; iii) the independent variable in it is twice smaller. In view of this, employing the expansion of functions around zero, allows practically to get outcomes for much larger values of the latter than the Thompson and Barnett's formula. The mathematical approach described is richly illustrated by graphs.

1. INTRODUCTION

The solution of the problems for normal TE_{0n} modes in the circular waveguides, containing coaxially positioned ferrite cylinder or toroid, magnetized azimuthally with respect to the direction of wave propagation faces serious obstacles of mathematical nature [1–9]. To overcome them different techniques have been proposed, allowing to reveal various aspects of microwave field-anisotropic medium interaction: i) Bolle-Heller functions [1], ii) transverse network representation [2], iii) perturbation techniques [3], iv) variational calculus [4], v) confluent hypergeometric functions [6–8], vi) Coulomb wave functions [5, 9].

The basic features of the regular Coulomb wave function method, employable to configurations in which the ferrite region is cylindrical are considered. The emphasis is placed on: i) the original idea by Georgiev and Georgieva to use in the theory of waveguides [5, 9] the generalized for all complex ρ, η and L in Thompson and Barnett's sense [10] regular and irregular (logarithmic) Coulomb wave functions $F_L(\eta, \rho)$ and $G_L(\eta, \rho)$ [11, 12], harnessed until now in the atomic physics and quantum mechanics [11]; ii) the possibility to employ the Abramowitz and tegun's representation of the latter [12] for a positive or negative factional real L, appearing in the problem under study, though the functions are defined for non-negative integer values of the parameter mentioned. In view of the geometry chosen, the discussion is confined to $F_L(\eta, \rho)$ solely. The advantages of the new approach in contrast to the one, using the complex Kummer function [10] are pointed out. Graphs are depicted, showing the variation of the generalized function $F_L(\eta, \rho)$ with ρ, provided $L = \pm 0.5$ and $\eta = 0, \pm 1, \pm 5$ and ± 10, and of its zeros $o_{\eta,n}^L$ in ρ.

The ferrite is characterized by a Polder permeability tensor $\bar{\bar{\mu}} = \mu_0[\mu_{ij}]$, i, $j = 1, 2, 3$, with non-zero components $\mu_{ii} = 1$ and $\mu_{13} = -\mu_{31} = -j\alpha$, $\alpha = \gamma M_r/\omega$, ($\gamma$ — gyromagnetic ratio, M_r — ferrite remanent magnetization, ω — angular frequency of the wave) and a scalar permittivity $\varepsilon = \varepsilon_0 \varepsilon_r$. In the particular case it is thought that it fills-in totally the waveguide. Besides, it is assumed that the latter is infinitely long, lossless and perfectly conducting and that its radius is r_0.

2. CLASSICAL ABRAMOWITZ AND STEGUN'S COULOMB WAVE EQUATION AND REGULAR COULOMB WAVE FUNCTION

The Abramowitz and Stegun's Coulomb wave equation [12]:

$$\frac{d^2 \upsilon}{d\rho^2} + \left[1 - \frac{2\eta}{\rho} - \frac{L(L+1)}{\rho^2} \right] \upsilon = 0, \tag{1}$$

is a second-order ordinary differential equation, determined for ρ and η — real, ($\rho > 0$, $-\infty < \eta < \infty$) and L — a nonnegative integer, ($L = 0, 1, 2, \ldots$). It has regular singularity with indexes $L+1$ and $-L$ at $\rho = 0$ and an irregular one at $\rho = \infty$. Its general integral [12]:

$$\upsilon(\rho) = C_1 F_L(\eta, \rho) + C_2 G_L(\eta, \rho) \tag{2}$$

is written in terms of the regular and irregular (logarithmic) Coulomb wave functions $F_L(\eta, \rho)$ and $G_L(\eta, \rho)$, resp. (C_1 and C_2 are arbitrary constants).

Abramowitz and Stegun give the following standard form of the regular Coulomb wave function [12]:

$$F_L(\eta, \rho) = C_L(\eta) \rho^{L+1} \Phi_L(\eta, \rho) \tag{3}$$

in which

$$C_L(\eta) = \frac{2^L e^{-\pi \eta / 2} |\Gamma(L+1+j\eta)|}{\Gamma(2L+2)} \tag{4}$$

and

$$\Phi_L(\eta, \rho) = \sum_{q=L+1}^{\infty} A_q^L \rho^{q-L-1}. \tag{5}$$

The coefficients A_q^L in series (5) are specified by the expressions:

$$A_{L+1}^L = 1, \tag{6}$$

$$A_{L+2}^L = \frac{\eta}{L+1} \tag{7}$$

and

$$(q+L)(q-L-1)A_q^L = 2\eta A_{q-1}^L - A_{q-2}^L, \quad (q > L+2). \tag{8}$$

3. GENERALIZED REGULAR COULOMB WAVE FUNCTION IN THE THOMPSON AND BARNETT'S SENSE

The Kummer confluent hypergeometric function is determined by the infinite power series [12, 13]:

$$\Phi(a, c; x) = \sum_{p=0}^{\infty} \frac{(a)_p}{(c)_p} \frac{x^p}{p!} \tag{9}$$

which is absolutely convergent for all real or complex values of a, c, x, except $c = l$, $l = 0, -1, -2, \ldots$, $(a)_p = a(a+1) \ldots (a+p-1)$, $(a)_0 = 1$, $(1)_p = p!$, $(p = 0, 1, 2, \ldots)$ is the Pochhammer's symbol. $\Phi(a, c; x)$ is an entire analytic function in the whole complex x-plane. It is regular at $x = 0$ and single-valued, wherever it exists. For a fixed x, $\Phi(a, c; x)$ is an entire function of a and a meromorphic one of c with simple poles at the points $c = 0, -1, -2, \ldots$.

In the partial case $a = L + 1 - j\eta$, $c = 2L + 2$ and $x = 2j\rho$ the Kummer function reduces to the regular Coulomb wave one [12]. It holds:

$$\Phi(L+1-j\eta, 2L+2; 2j\rho) = e^{j\rho} F_L(\eta, \rho) \rho^{-L-1} / C_L(\eta) \tag{10}$$

Using this relation Thompson and Barnett proposed a second more universal definition of $F_L(\eta, \rho)$, valid for all complex ρ, η and L by which they made its analytic continuation to each complex plane with cuts along the negative real ρ-axis [10]:

$$F_L(\eta, \rho) = C_L(\eta) \rho^{L+1} e^{-j\rho} \Phi(L+1-j\eta, 2L+2; 2j\rho). \tag{11}$$

4. GEORGIEV AND GEORGIEVA-GROSSE'S APPROACH

As pointed out above, $\Phi(L + 1 - j\eta, 2L + 2; 2j\rho)$ is not defined for $2L + 2 = l$. Therefore the computation of the regular Coulomb wave function is not possible directly from the Thompson and Barnett's formula (11) for $L = (l - 2)/2$ ($L = -1, -3/2, -2, -5/2, \ldots$).

Instead of $\Phi(a, c; x)$ which if c is zero or a negative integer has no sense, F. G. Tricomi suggested to utilize the modified Kummer function [3–5]:

$$\Phi^*(a, c; x) = \frac{1}{\Gamma(c)} \Phi(a, c; x) = \sum_{p=0}^{\infty} \frac{(a)(a+1)\ldots(a+p-1)}{\Gamma(c+p)} \frac{x^p}{p!} \tag{12}$$

that is finite also for $c = 1 - m$ ($m = 1, 2, 3, \ldots$). Moreover, the important relation [13]:

$$\Phi^*(a, 1 - m; x) = \lim_{c \to 1-m} \Phi^*(a, c; x) = (a)_m \frac{x^m}{m!} \Phi(a + m, m + 1; x) \tag{13}$$

reduces the discussion to a Φ function with c — a positive integer.

In view of (4), applying consecutively (12) and (13), relation (11) could be transformed to give:

$$F_L(\eta, \rho) = 2^L e^{-\pi\eta/2} |\Gamma(L + 1 + j\eta)| \rho^{L+1} e^{-j\rho} \Phi^*(L + 1 - j\eta, 2L + 2; 2j\rho) \tag{14}$$

$$F_L(\eta, \rho) = 2^{-L-1} e^{-\pi\eta/2} |\Gamma(L+1+j\eta)| \rho^{-L} e^{-j\rho} (L+1-j\eta)_{-2L-1} \frac{e^{-j\pi(2L+1)/2}}{(-2L-1)!} \Phi(-L - j\eta, -2L; 2j\rho) \tag{15}$$

Obviously $-2L = 2, 3, 4, 5, \ldots$; $-2L - 1 = 1, 2, 3, 4, \ldots$; $-L = 1, 3/2, 2, 5/2, \ldots$ $-L - 1 = 0, -1/2, -1, -3/2, \ldots$.

Accordingly, Georgiev and Georgieva-Grosse suggested to use formula (11) for finding the numerical values of $F_L(\eta, \rho)$, valid for all complex ρ, η and L, except $L = (l - 2)/2$ and (15) provided the letter holds. These authors have made a numerical experiment. The evaluation of real regular Coulomb wave function in case of fractional positive and negative L (e.g., $L = -0.5$ and $L = 0.5$) has been performed, following two approaches:

i) direct computation by means of the Abramowitz and Stegun's representation (3)–(8),

ii) calculation through the Thompson and Barnett's expansion of $F_L(\eta, \rho)$ in terms of the complex Kummer confluent hypergeometric function.

The juxtaposition of results obtained has shown perfect coincidence which is a criterion for their reliability. Hence, it could be concluded that though Abramowitz and Stegun's series $\Phi_L(\eta, \rho)$ is defined only for L — a nonnegative integer, it could be used also for fractional values of L. Moreover, the original series for $F_L(\eta, \rho)$ (3)–(8) is much more rapidly convergent in the case mentioned and is preferable in the calculations than (11). Besides, it could provide results for larger values of parameter ρ. The reason for this is the fact that the series $\Phi_L(\eta, \rho)$ which in fact is computed is real whereas the main element of (11) $\Phi(L + 1 - j\eta, 2L + 2; 2j\rho)$ is complex. Further, for fixed ρ the value of $F_L(\eta, \rho)$ from (11) is found out for the twice larger purely imaginary variable $2j\rho$.

5. REGULAR COULOMB WAVE FUNCTION METHOD

The solution of Maxwell equations in the anisotropic medium shows that the longitudinal component of the rotationally symmetric $TE(H_r, E_\theta, H_z)$ modes satisfies the following second-order ordinary differential equation [9]:

$$\left(r^{-1} D_r r D_r + \beta_f^2 - \beta^2 - \alpha\beta\, r^{-1}\right) H_z = 0 \tag{16}$$

in which $D_r = \partial/\partial r$ is a differential operator, $\beta_f^2 = \beta_0^2 \varepsilon_r \mu_{eff}$, $\beta_0^2 = \omega^2 \varepsilon_0 \mu_0$ and β are the phase constants in the unlimited space, occupied by azimuthally magnetized ferrite, and the ones in the free space and in the geometry examined, resp., and $\mu_{eff} = 1 - \alpha^2$ is the effective relative permeability of the load. If $\beta_f > \beta$ ($\hat{\beta}_f < \hat{\beta}$) it governs the propagation of normal TE_{0n} modes along the structure. Putting $\rho = \beta_2 r$, $\beta_2 = (\beta_f^2 - \beta^2)^{1/2}$ — radial wavenumber of the normal TE_{0n} modes in the anisotropic medium, $H_z(r) = \upsilon(\rho)\rho^{-1/2}$, $\eta = \alpha\beta/(2\beta_2)$ and $L = -0.5$ (ρ, β_2, η, L — real, $\rho > 0$, $\beta_2 > 0$, $L < 0$) reduces Equation (16) to the standard M. Abramowitz form of the Coulomb wave Equation (1).

Accordingly, the field components and the characteristic equation of the normal modes are given by the expressions:

$$H_r = jB \left[\frac{\left(1 - \alpha^2\right)^{1/2} \beta}{\Gamma_f} \frac{F_{L+1}(\eta, \rho)}{\rho^{L+1}} + \alpha \frac{F_L(\eta, \rho)}{\rho^{L+1}} \right], \tag{17}$$

$$E_\theta = -j \frac{B \omega \mu_0 \left(1 - \alpha^2\right)^{1/2}}{\Gamma_f} \frac{F_{L+1}(\eta, \rho)}{\rho^{L+1}}, \tag{18}$$

$$H_z = B \frac{F_L(\eta, \rho)}{\rho^{L+1}}, \tag{19}$$

$$F_{L+1}(\eta, \rho_0) = 0 \tag{20}$$

where B is an arbitrary constant, $L = -0.5$ and $\rho_0 = \beta_2 r_0$. As seen, the Equations (17)–(20) depend on the ferrite remanent magnetization (on α, resp. η). Correspondingly, it might be expected the change of the magnitude and sign of the latter will impact the field distribution and phase diagram of the $TE(H_r, E_\theta, H_z)$ waves, described by it.

It is instructive to introduce the normalized (barred) quantities: $\bar\beta = \beta/(\beta_0 \sqrt{\varepsilon_r})$, $\bar\beta_2 = \beta_2/(\beta_0 \sqrt{\varepsilon_r})$, $\bar r_0 = \beta_0 r_0 \sqrt{\varepsilon_r}$ and $\eta = \alpha \bar\beta/(2\bar\beta_2)$, and to rewrite Equations (17)–(20) in terms of them. Then, if $o_{\eta, n}^L$ stands for the nth ($n = 1, 2, 3, \ldots$) consecutive zero of $F_L(\eta, \rho)$ in ρ for given η, Equation (20) holds when $\bar\beta_2 = o_{\eta_\pm, n}^{L+1}/\bar r_0$ which specifies the eigenvalue spectrum of the transmission line.

6. NUMERICAL STUDY OF THE ZEROS OF THE REGULAR COULOMB WAVE FUNCTION

To plot the phase characteristics of the waveguide and to find the field distribution in it, requires a numerical investigation of the Coulomb function and its zeros in the real area, corresponding to the normal TE_{0n} modes for the values of parameters, given in the previous Section. In the computations the Abramowitz and Stegun's series (3)–(8) is used. The results are confronted with the ones, obtained from the Thompson and Barnett's formula (11), showing a perfect coincidence for small ρ, η and L. Figures 1 and 2 (Figures 3 and 4) visualize the change of $F_L(\eta, \rho)$ with ρ in the interval $\rho \in [0, 25]$ in case $L = -0.5$ ($L = 0.5$), assuming η as parameter. The solid (dashed) lines in the first (second) of them concur to $\eta > 0$, $\eta = 1, 5$ and 10 ($\eta < 0$, $\eta = -1, -5$ and -10). The dotted curve answers to $\eta = 0$. As seen, $F_L(\eta, \rho)$ is oscillating. When ρ gets large, it behaves like a sine function which might be expected in view of its asymptotic representation [12]. The value of independent variable at which this is exhibited, depends on the other two parameters. At
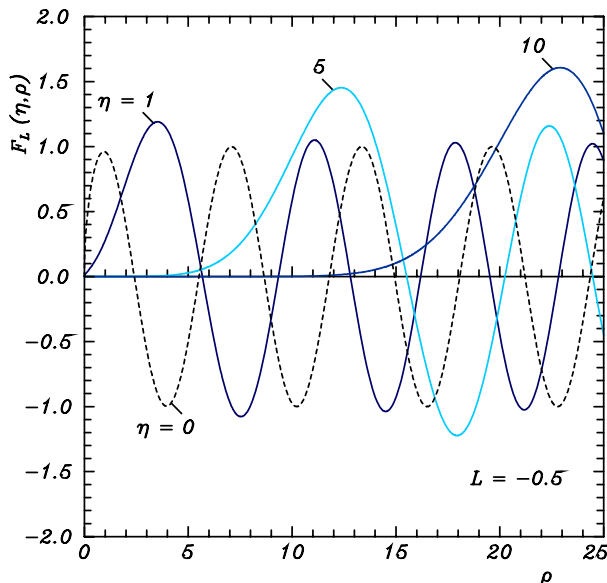

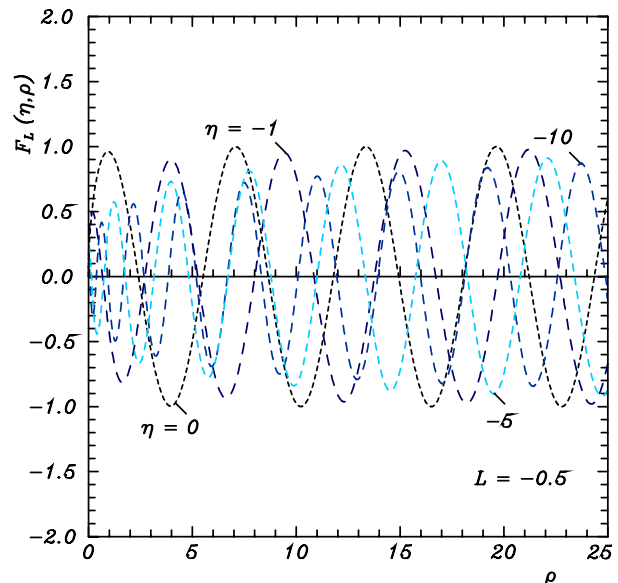Figure 1: Regular Coulomb wave function $F_L(\eta, \rho)$ vs. ρ for $L = -0.5$ and $\eta = 0, 1, 5, 10$.

Figure 2: Regular Coulomb wave function $F_L(\eta, \rho)$ vs. ρ for $L = -0.5$ and $\eta = 0, -1, -5$ and -10.
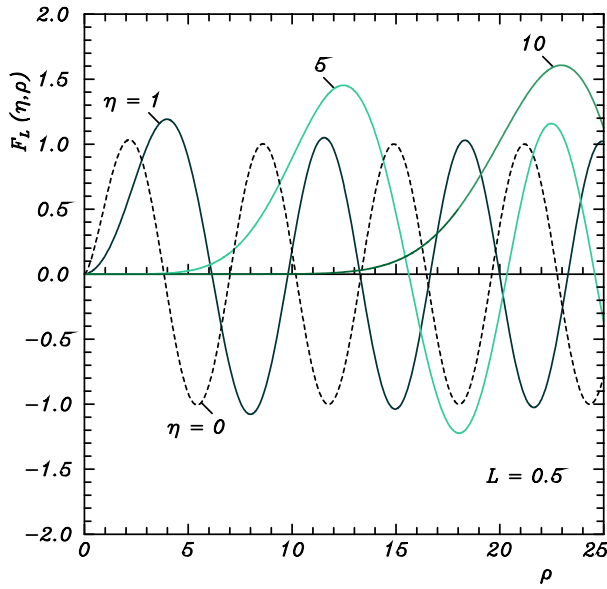
Figure 3: Regular Coulomb wave function $F_L(\eta, \rho)$ vs. ρ for $L = 0.5$ and $\eta = 0, 1, 5, 10$.

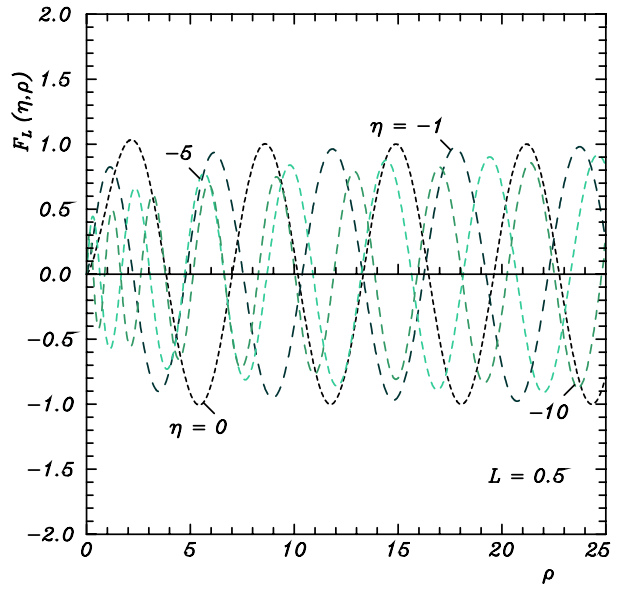Figure 4: Regular Coulomb wave function $F_L(\eta, \rho)$ vs. ρ for $L = 0.5$ and $\eta = 0, -1, -5$ and -10.
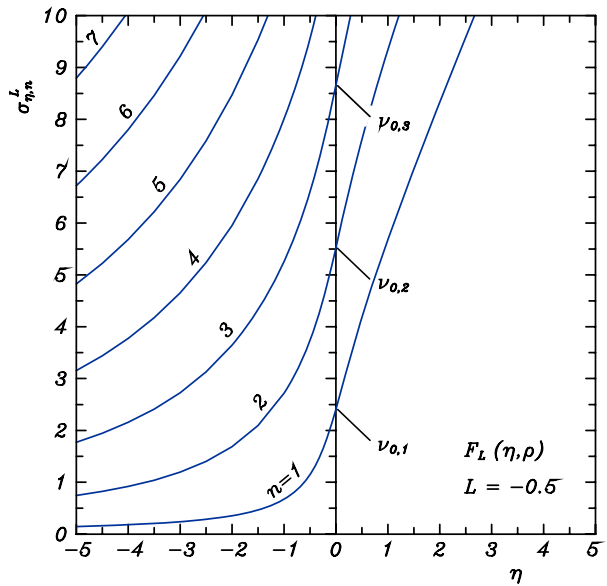

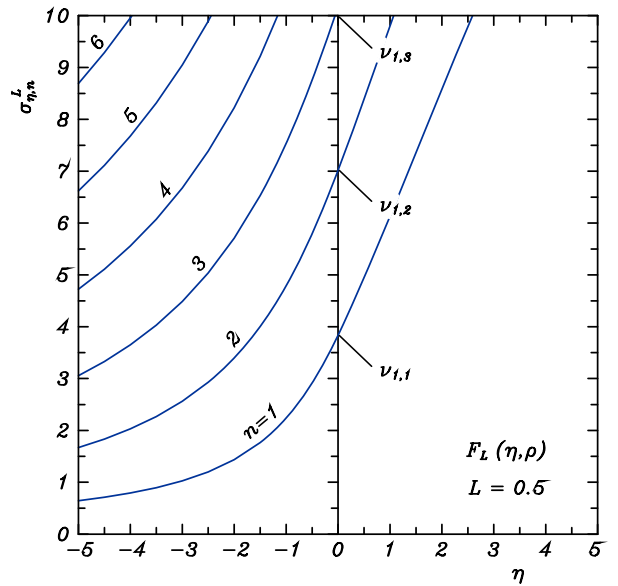Figure 5: Zeros $o_{\eta,n}^L$ of $F_L(\eta, \rho)$ in case $L = -0.5$ as a function of η for $n = 1\ (1)\ 4$.

Figure 6: Zeros $o_{\eta,n}^L$ of $F_L(\eta, \rho)$ in case $L = 0.5$ as a function of η for $n = 1\ (1)\ 4$.

given L the quasi-sine oscillations are displayed for smaller ρ, provided η diminishes. For identical η this tendency is more pronounced for larger ρ, if L increases. In addition, the maxima of the first oscillations of $F_L(\eta, \rho)$ grow with η and L. On this condition all maxima are shifted to larger ρ.

The regular Coulomb function for fractional positive and negative L has an infinite number of zeros $o_{\eta,n}^L$ in ρ, like that for a non-negative integer L. The dependence of the first several of them for $\eta \in [-5, 5]$ is portrayed in Figures 5, 6, provided $L = -0.5$ and $L = 0.5$. The symbols $\nu_{0,n}$ and $\nu_{1,n}$ in them stand for the nth zeros of the zeroth and first order Bessel functions $J_0(\rho)$ and $J_1(\rho)$, resp., (see the second Kummer theorem [12]). As seen, for fixed L and n (η), $o_{\eta,n}^L$ monotonously increase with η (grow with both L and n). Further, the numerical analysis shows that it holds:

$$\lim_{\eta_- \to -\infty} o_{\eta_-,n}^L = 0, \tag{21}$$

$$\lim_{\eta_+ \to +\infty} o_{\eta_+,n}^L = +\infty, \tag{22}$$

$$\lim_{\eta_- \to -\infty} |\eta_-| \, o^L_{\eta_-,n} = T_1(L,n), \tag{23}$$

where $T_1(L,n)$ are finite positive real numbers. Assuming $L = -0.5$ and $n = 1$, (1), 5, it is fulfilled: $T_1(L,n) = 0.72289\,82454$, $3.80890\,77930$, $9.36087\,58488$, $17.38003\,55533$, $27.86653\,79522$, resp. In case $L = 0.5$ for the same values of n, it is true: $T_1(L,n) = 3.29682\,70534$, $8.85624\,98649$, $16.87758\,86082$, $27.36502\,36432$, $40.31938\,95366$, resp.

7. PHYSICAL INTERPRETATION OF THE OUTCOMES FOR THE ZEROS

The analysis of the results presented for the zeros of $F_L(\eta, \rho)$, combined with that of the functions and with the peculiarities of the problem for the normal TE_{0n} modes examined, discloses the most important features of the phase behaviour of the circular waveguide, entirely filled with azimuthally magnetized ferrite: i) The number of modes which might get excited in the configuration is infinite, equal to the number of roots, resp. zeros $o^{L+1}_{\eta,n}$ of the concurring characteristic Equation (20), resp. wave function n in case $L+1 = 0.5$. ii) The waves might be sustained both for positive and negative magnetization of the anisotropic load; iii) The area of propagation of normal waves, observed for $-1 < \alpha < 1$, assuming negative (positive) magnetization, is bilaterally restricted (is limited from below and unbounded from the side of higher frequencies); iv) The outcomes for the zeros both at $L = -0.5$ and $L + 1 = 0.5$ are useful in the analysis of the field distribution.

8. CONCLUSIONS

The approach for examination of the circular waveguides, containing a co-axial azimuthally magnetized ferrite cylinder which support normal TE_{0n} modes, based on the real regular Coulomb wave functions of specially chosen parameters, is regarded. The discussion is focused on the structure, completely filled with the anisotropic medium mentioned. An analysis is accomplished of the methods for computation of the functional values and of certain of their zeros, necessary for the integration of the task formulated. The results are presented in graphical form and discussed. The main characteristics of wave propagation are discussed.

REFERENCES

1. Bolle, D. M. and G. S. Heller, "Theoretical considerations on the use of circularly symmetric TE modes for digital ferrite phase shifters," *IEEE Trans. Microwave Theory Tech.*, Vol. 13, No. 4, 421–426, July 1965, See also Bolle, D. M. and N. Mohsenian, Correction, *IEEE Trans. Microwave Theory Tech.*, Vol. 34, No. 4, 427, April 1986.

2. Clarricoats, P. J. B. and A. D. Olver, "Propagation in anisotropic radially stratified circular waveguides," *Electron. Lett.*, Vol. 2, No. 1, 37–38, January 1966.

3. Eaves, R. E. and D. M. Bolle, "Perturbation theoretic calculations of differential phase shifts in ferrite-loaded circularly cylindrical waveguides in the TE_{01} mode," *Electron. Lett.*, Vol. 2, No. 7, 275–277, July 1966.

4. Lindell, I. V., "Variational methods for nonstandard eigenvalue problems in waveguide and resonator analysis," *IEEE Trans. Microwave Theory Tech.*, Vol. 30, No. 8, 1194–1204, August 1982.

5. Georgiev, G. N. and M. N. Georgieva-Grosse, "On several new applications of Coulomb wave functions," *Proc. 1994 Int. Conf. Comput. Electromagn. its Appl. ICCEA '94*, 163–166, Beijing, China, December 1994.

6. Georgiev, G. N. and M. N. Georgieva-Grosse, "Analysis of the differential phase shift in the circular ferrite-dielectric waveguide with azimuthal magnetization," *Proc. 2010 IEEE AP-S Int. Symp. on Antennas Propagat. & CNC-USNC/URSI Radio Science Meeting*, Paper ID 330.9, CDROM, Toronto, ON, Canada, July 11–17, 2010.

7. Georgiev, G. N. and M. N. Georgieva-Grosse, "On the confluent hypergeometric functions and their application: Basic elements of the Tricomi theory. Case of waveguide propagation," *Telecomm. Radioeng.*, Vol. 71, No. 3, 209–216, 2012.

8. Georgieva-Grosse, M. N. and G. N. Georgiev, "Iterative method for analysis of the differential phase shift in an azimuthally magnetized circular ferrite-dielectric waveguide," *Proc. 2013 Int. Symp. Electromagn. Theory. URSI-EMTS 2013*, Article ID 23PM3E-05, 763–766, Hiroshima, Japan, May 20–24, 2013.

9. Georgiev, G. N. and M. N. Georgieva-Grosse, "Circular waveguide, completely filled with azimuthally magnetized ferrite," Chapter in *Wave Propagation*, 161–196, L. Rocha and G. Mateus, Eds., Academy Publish, Cheyenne, Wyoming, USA, 2014.

10. Thompson, I. J. and A. R. Barnett, "Coulomb and Bessel functions of complex arguments and order," *J. Comput. Phys.*, Vol. 64, 490–509, 1986.

11. Curtis, A. R., *Coulomb Wave Functions*, Computational Center of the Academy of Sciences of USSR, Moscow, USSR, 1969 (in Russian).

12. Abramowitz, M. and I. Stegun, Eds., *Handbook of Mathematical Functions with Formulas, Graphs and Mathematical Tables*, Applied Mathematics Series 55, National Bureau of Standards, Washington, DC, 1964.

13. Tricomi, F. G., *Lezioni sulle Funzioni Ipergeometriche Confluenti,* Editore Gheroni, Torino, Italy, 1952.

Undersampling to Regularize the Source Reconstruction Problem for an Electric Point Source

S. G. Sen

Electrical Electronics Engineering Department, Ataturk University, Turkey

Abstract— In this article, a source reconstruction problem is solved by sampling the tangential components of the electric field of an electric point source on the surface of a hemisphere the center of which is the location of the point source. The source reconstruction is performed by sampling the electric field at five different sampling rates. One of the sampling rate corresponds to the Nyquist rate, two of them are oversampling rates and the rest are undersampling rates. The problem is discretized into a matrix equation which is solved iteratively. For each of the solution iterate, the field components are reconstructed and the error with respect to the original fields are computed. It is shown that the error made is approximately the same for all the sampling rates. In addition, the fields are reconstructed on hemispheres outside the sampling hemisphere. The error made in this reconstruction is calculated and shown to be not too much varying among the five different sampling rates. By means of these two field reconstruction demonstrations, it is proven that the oversampling and Nyquist rate sampling do in fact provide redundant information for the source reconstruction since the oversampling and the Nyquist rate sampling do not increase the accuracy of the reconstructed fields. The current reconstruction is also made using the lowest sampling rate and it is indicated that the reconstructed current is close to the original current although the sampling rate is lowest. As a result, it is determined that undersampling regularizes the reconstruction problem by deleting the redundant information due to higher rate sampling.

1. INTRODUCTION

It is possible to determine the radiation pattern of an antenna using the antenna material properties and the antenna geometry as inputs to the electromagnetic analysis. However, the electromagnetic analysis can never produce the actual radiation properties of the manufactured antenna because the defects in the manufacturing material, distortions in the geometry of the antenna, cables and supporting accessories around the antenna cause deviations from the theoretical antenna radiation pattern. All of these real life effects can be taken into consideration by the source reconstruction method and the actual antenna radiation pattern can be determined [1].

In the source reconstruction method, the field of the actual source is sampled to obtain the necessary information for the reconstruction of the original source. The relation between the source and its fields expressed using the mixed potential integral equation is not a Fourier transform relation as indicated in [2]. Hence, it is possible to reduce the field sampling rate below the Nyquist sampling rate. In this article, the electric field components which are tangential to a hemisphere centered at the point source of the electric field ($\vec{E}$) are sampled and from these samples, the point source is reconstructed. Three sampling rates are employed: Oversampling, Nyquist rate sampling and undersampling. These sampling rates are compared according to the reconstructed field accuracy and the speed of convergence to the reconstructed source solution. The comparison shows that three different sampling schemes do not yield results very much differing from each other. Hence, it is demonstrated that undersampling regularizes the source reconstruction problem by extracting the unnecessary information from the problem.

In the Section 2, the problem and its solution are described. In the Section 3, the results are presented.

2. THE DEFINITION AND THE SOLUTION OF THE PROBLEM

The $\hat{x}$ directed point source is defined as follows:

$$\vec{J}(x, y, z) = \hat{x}\ Il\ \delta(x)\,\delta(y)\,\delta(z) \tag{1}$$

with

$$Il = 1\,\text{A} \cdot \text{m} \tag{2}$$

Assuming a time-harmonic dependence of $e^{-j\omega t}$, the θ and ϕ components of $\vec{E}$ of the point source are given in a spherical coordinate system as follows:

$$E_\theta = \frac{je^{jkr}}{4\pi\omega\epsilon} \cos(\theta) \cos(\phi) \left(-\frac{1}{r^3} + \frac{jk}{r^2} + \frac{\omega^2\mu\epsilon}{r}\right) \quad (3)$$

$$E_\phi = -\frac{je^{jkr}}{4\pi\omega\epsilon} \sin(\phi) \left(-\frac{1}{r^3} + \frac{jk}{r^2} + \frac{\omega^2\mu\epsilon}{r}\right) \quad (4)$$

In the above equations, the symbols are defined as follows: j is the imaginary unit, ω is the angular frequency. k is the wavenumber of the medium. ϵ and μ are the permittivity and permeability of the medium respectively. r is the distance variable of the spherical coordinate system. The sampling of the electric field is carried out using these formulas.

The source to be reconstructed is expressed in terms of the Rao-Wilton-Glisson (RWG) basis functions as follows:

$$\vec{J}(\vec{r}') = \sum_{n=1}^{N} I_n \vec{f}_n(\vec{r}') \quad (5)$$

In (5), $\vec{f}_n(\vec{r}')$ is the RWG basis function [3]. $\vec{r}'$ is the distance vector of a point on the reconstruction plane. N is the number of basis functions and I_n denotes the expansion coefficients. The RWG basis function $\vec{f}_n(\vec{r}')$ is defined as follows:

$$\vec{f}_n(\vec{r}') = \begin{cases} \frac{l_n}{2A_n^+} \vec{\rho}_n^+ & \text{if } \vec{r}' \text{ in } T_n^+ \\ \frac{l_n}{2A_n^-} \vec{\rho}_n^- & \text{if } \vec{r}' \text{ in } T_n^- \\ 0 & \text{if otherwise} \end{cases} \quad (6)$$

T_n^+ and T_n^- are the triangle pair belonging to the nth RWG basis function. They are shown in Fig. 1. A_n^+ and A_n^- are the areas of the triangles T_n^+ and T_n^- respectively. T_n^+ and T_n^- have one common side and two common vertices. $\vec{\rho}_n^+$ is the vector drawn from the free vertex of T_n^+ to a point in T_n^+. $\vec{\rho}_n^-$ is the vector drawn from a point in T_n^- to the free vertex of T_n^-. l_n is the length of the common edge.
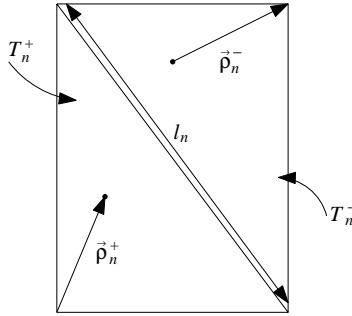

Figure 1: The triangle pair belonging to the nth RWG basis function.

Using the mixed potential integral formulation, the following integral equation is obtained for the x, y and z components of the electric field due to the nth RWG basis function:

$$E_{n_i} = \frac{j\omega\mu}{4\pi} \int_{T_n^+ + T_n^-} I_n \left[\vec{f}_n(\vec{r}')\right]_i g(\vec{r}, \vec{r}') d\vec{r}' - \frac{1}{j4\pi\omega\epsilon} \frac{\partial}{\partial i} \int_{T_n^+ + T_n^-} I_n \vec{\nabla}' \cdot \vec{f}_n(\vec{r}') g(\vec{r}, \vec{r}') d\vec{r}' \quad (i=x,y,z) \quad (7)$$

In (7), $g(\vec{r}, \vec{r}')$ is the scalar Green's function given by:

$$g(\vec{r}, \vec{r}') = \frac{e^{jk|\vec{r} - \vec{r}'|}}{|\vec{r} - \vec{r}'|} \quad (8)$$

In (8), $\vec{r}$ is the position vector of the field point. Using the integral equation in (7), the following matrix equation is obtained:

$$\begin{bmatrix} \mathbf{E_\theta} \\ \mathbf{E_\phi} \end{bmatrix} \mathbf{I} = \begin{bmatrix} \mathbf{b_\theta} \\ \mathbf{b_\phi} \end{bmatrix} \quad (9)$$

$\mathbf{E}_{\boldsymbol{\theta}}$ and $\mathbf{E}_{\boldsymbol{\phi}}$ are both $M \times N$ matrices where M is the number of sampling points on the hemisphere and N is the number of RWG basis functions. $\mathbf{E}_{\boldsymbol{\theta}}(\mathbf{p}, \mathbf{q})$ and $\mathbf{E}_{\boldsymbol{\phi}}(\mathbf{p}, \mathbf{q})$ denote the elements in the row p, column q of the matrices $\mathbf{E}_{\boldsymbol{\theta}}$ and $\mathbf{E}_{\boldsymbol{\phi}}$ respectively and are given by

$$\mathbf{E}_{\boldsymbol{\theta}}(\mathbf{p}, \mathbf{q}) = I_x^{p,q} \cos(\theta_p) \cos(\phi_p) + I_y^{p,q} \cos(\theta_p) \sin(\phi_p) - I_z^{p,q} \sin(\theta_p) \tag{10}$$

$$\mathbf{E}_{\boldsymbol{\phi}}(\mathbf{p}, \mathbf{q}) = -I_x^{p,q} \sin(\phi_p) + I_y^{p,q} \cos(\phi_p) \tag{11}$$

θ_p and ϕ_p are the θ and ϕ coordinates of the pth sampling point. The integrals I_i^{pq} ($i = x, y, z$) are defined as

$$I_i^{pq} = \frac{j\omega\mu}{4\pi} \int_{T_{n_q}^+} \frac{l_{n_q}}{2A_{n_q}^+} \left(\vec{\rho}_{n_q}^+\right)_i \frac{e^{jk|\vec{r}_p - \vec{r}_q'|}}{|\vec{r}_p - \vec{r}_q'|} ds' + \frac{j\omega\mu}{4\pi} \int_{T_{n_q}^-} \frac{l_{n_q}}{2A_{n_q}^-} \left(\vec{\rho}_{n_q}^-\right)_i \frac{e^{jk|\vec{r}_p - \vec{r}_q'|}}{|\vec{r}_p - \vec{r}_q'|} ds'$$

$$- \frac{1}{j\omega 4\pi\epsilon} \int_{T_{n_q}^+} \frac{l_{n_q}}{A_{n_q}^+} \frac{\partial}{\partial i} \left(\frac{e^{jk|\vec{r}_p - \vec{r}_q'|}}{|\vec{r}_p - \vec{r}_q'|}\right) ds' + \frac{1}{j\omega 4\pi\epsilon} \int_{T_{n_q}^-} \frac{l_{n_q}}{A_{n_q}^-} \frac{\partial}{\partial i} \left(\frac{e^{jk|\vec{r}_p - \vec{r}_q'|}}{|\vec{r}_p - \vec{r}_q'|}\right) ds' \quad (i = x, y, z) \tag{12}$$

$\vec{r}_q'$ is the position vector of a point in the triangle pair of the qth RWG basis function. $\vec{r}_p$ is the position vector of the pth sampling point. The column vector $\mathbf{I}$ in (9) is an $N \times 1$ matrix and $\mathbf{I}(q, 1)$ is the coefficient I_q used in (5). $\mathbf{b}_{\boldsymbol{\theta}}$ and $\mathbf{b}_{\boldsymbol{\phi}}$ are both $M \times 1$ matrices. $\mathbf{b}_{\boldsymbol{\theta}}(p, 1)$ and $\mathbf{b}_{\boldsymbol{\phi}}(p, 1)$ are the θ and ϕ components of the electric field respectively at the pth sampling point.

The integrals in (12) are numerically calculated using a 79 point Gaussian quadrature given in [4]. The source reconstruction problem expressed by the matrix equation is a very ill-posed problem as indicated in the first section of [5]. The matrix equation is solved by the least squares QR (LSQR) method [6]. LSQR is an effective and preferred conjugate gradient type solution method [5]. The algorithm for this method has been implemented in Fortran90 programming language by adapting the program given in [7].

If the expressions in (3) and (4) are examined, then it can be determined that the Nyquist sampling period of E_θ is $\pi° \times \pi°$ and of E_ϕ is $\pi°$. E_ϕ does not depend on θ.

3. THE SOURCE RECONSTRUCTION RESULTS

The operating frequency is $1\,\text{GHz}$. The reconstruction plane is a square of side length $0.3\,\text{m}$. The square is centered at the origin of the spherical coordinate system and it is in the x-z plane. The square is meshed into triangles using Siemens NX 9.0 software. The side lengths of the triangles are set to be $\lambda/\sqrt{300}$. The radius of the hemisphere on which the electric field sampling is made is $1\,\text{m}$. The source reconstruction problem is solved using the sampling periods of $1° \times 1°$, $2° \times 2°$, $\pi° \times \pi°$, $4° \times 4°$ and $5° \times 5°$ for E_θ and $1°$, $2°$, $\pi°$, $4°$ and $5°$ for E_ϕ. The error in the reconstructed field vector with respect to the original field vector is defined as

$$\text{error} = \sqrt{\frac{\sum_{n=1}^{M} |\text{original} - \text{reconstructed}|_n^2}{M}} \tag{13}$$

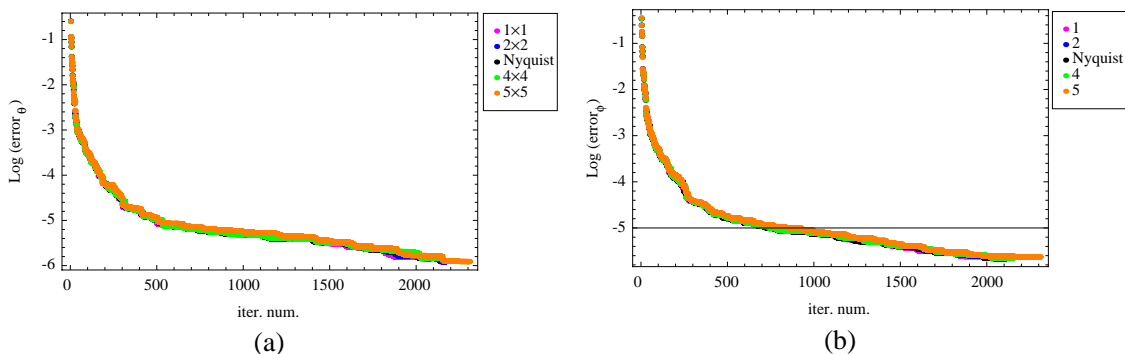M in the summation in (13) is the number of field samples or the field vector dimension.

Figure 2: The error in the reconstructed fields versus the LSQR iteration number. (a) The error in reconstructed E_θ. (b) The error in reconstructed E_ϕ.

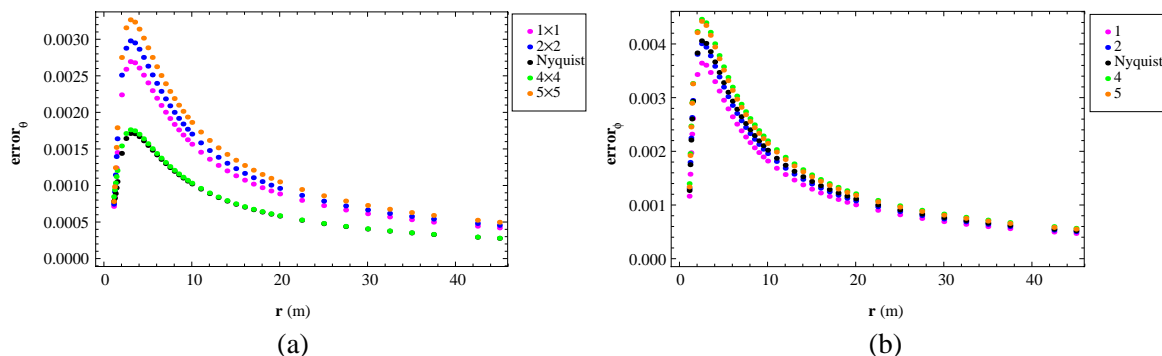(a)   (b)

Figure 3: The plots of the error in the reconstructed field components versus the radius of the reconstruction hemisphere. (a) The error in reconstructed E_θ. (b) The error in reconstructed E_ϕ.
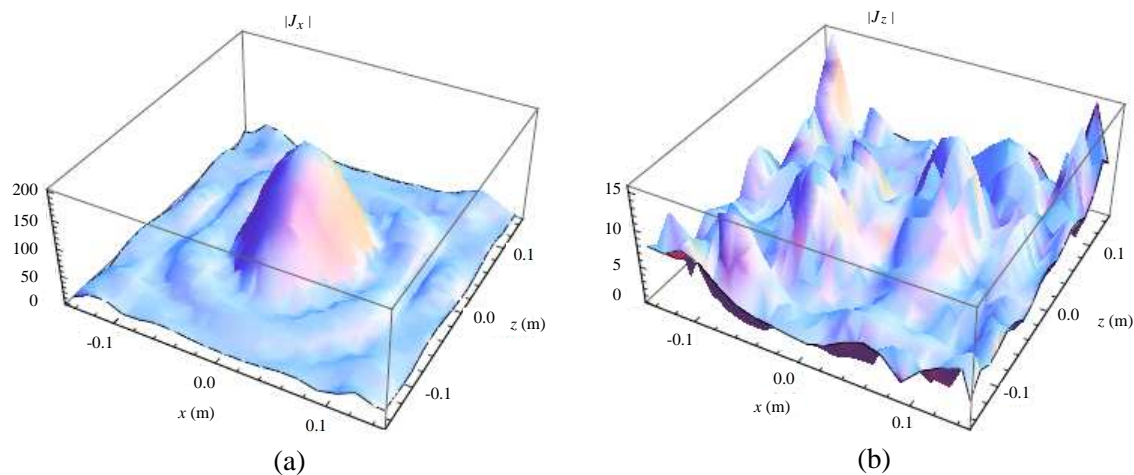

(a)   (b)

Figure 4: The magnitudes of the reconstructed electric current density components with the undersampling periods of $5° \times 5°$ and $5°$ for E_θ and E_ϕ respectively. (a) The plot of $|J_x|$. (b) The plot of $|J_z|$.

In Fig. 2, the error in the reconstructed field components are plotted versus the LSQR iteration number. As the LSQR iteration number increases, the convergence to the solution is realized. Meanwhile, the error in the reconstructed components decreases. The decrease curves are almost the same for all of the sampling rates. Hence, there is no need for oversampling or Nyquist sampling in order not to increase the computational burden in the source reconstruction problem. The oversampling and Nyquist rate sampling contains redundant information. Decreasing this redundant information by means of undersampling regularizes the problem. In Fig. 3, the reconstructed field components E_θ and E_ϕ are plotted versus the radius of the hemisphere on which the reconstruction is carried out. The error curves for various sampling rates do not differ significantly from each other. Hence, it is again proven that oversampling and Nyquist rate sampling are not necessary. Undersampling regularizes the source reconstruction problem. In Fig. 4, the spatial variations for the magnitudes of the components of the reconstructed current density are shown. This current density is reconstructed by undersampling periods of $5° \times 5°$ and $5°$ for E_θ and E_ϕ respectively. The x component can be observed to be focusing to the origin. In addition, the magnitude of the x component is at least 10 times that of the z component on the average. Hence, the reconstructed current density resembles the original x directed point source and the source reconstruction process works well.

4. CONCLUSION

A source reconstruction problem is solved for three different types of sampling schemes: Oversampling, Nyquist rate sampling and undersampling. It is demonstrated that oversampling and Nyquist rate sampling are not needed for the accurate source reconstruction. By means of undersampling, the source and field reconstruction is proven to be achieved with high accuracy. Hence, undersampling regularizes the source reconstruction problem by eliminating the redundant information due

to either oversampling or Nyquist rate sampling.

ACKNOWLEDGMENT

REFERENCES

1. Las-Heras, F., M. R. Pino, S. Loredo, Y. Alvarez, and T. K. Sarkar, "Evaluating near-field radiation patterns of commercial antennas," *IEEE Trans. Antennas Propag.*, Vol. 54, 2198–2207, 2006.
2. Petre, P. and T. K. Sarkar, "Differences between modal expansion and integral equation methods for planar near-field to far-field transformation," *Progress In Electromagnetics Research*, Vol. 12, 37–56, 1996.
3. Rao, S. M., D. R. Wilton, and A. W. Glisson, "Electromagnetic scattering by surfaces of arbitrary shape," *IEEE Trans. Antennas Propag.*, Vol. 30, 409–418, 1982.
4. Dunavant, D. A., "High degree efficient symmetrical gaussian quadrature rules for the triangle," *International Journal for Numerical Methods in Engineering*, Vol. 21, 1129–1148, 1985.
5. Hansen, P. C., *Rank-deficient and Discrete Ill-posed Problems: Numerical Aspects of Linear Inversion*, SIAM, 1997.
6. Paige, C. C. and M. A. Saunders, "LSQR: An algorithm for sparse linear equations and sparse least squares," *ACM Transactions on Mathematical Software*, Vol. 8, No. 1, 43–71, 1982.
7. Saunders, M., "zlsqrmodule.f90," Jun. 29, 2013, Online Available: http://web.stanford.edu/group/SOL/software/lsqr/f90/zlsqr.zip.

Cascades of π Circuits Modeled by Independent Matrix Equations for Each Infinitesimal Unit

A. J. Prado[1], L. S. Lessa[2], R. C. Monzani[3], L. F. Bovolato[2],
J. Pissolato Filho[3], E. Assunção[2], and M. C. M. Teixeira[2]

[1]Telecommunication Engineering Department, Campus of S. J. Boa Vista
Univ. Estadual Paulista — UNESP, Brazil
[2]Electrical Engineering Department, Campus of Ilha Solteira
Universidade Estadual Paulista — UNESP, Brazil
[3]Electrical Engineering Department
The State University of Campinas — UNICAMP, Brazil

Abstract— A modified numeric procedure is applied to analyse the application of π circuits for representing distributed parameters. Numeric oscillations, which are associated usually with digital simulations associated with π circuits, are decreased. It is shown that these numeric oscillations, or Gibb's oscillations, are not related only to the mentioned associations. They are created by the application of the specific numeric integration methods for solving linear systems that describe the associations of π circuits. If the state equations are determined for each π circuit, then the proposed changes of the numeric routine for solving systems with π circuits lead to results with little influence on the numerical oscillations. This is confirmed using comparisons with results obtained from the Laplace transform and ATP software.

1. INTRODUCTION

For simulating transient phenomena and wave propagation in electrical power systems, digital programs and numerical tools are useful. This is because tests in actual systems can be impossible, for example, in actual transmission lines [1], or very difficult, because the results have very high frequencies, for example, during signal propagation in integrated circuits. For infinitesimal representation of systems with distributed parameters, lumped elements can be applied, using structures of π circuits [2–7]. With a great number of these infinitesimal units, it can provide good representations of these systems. There can be problems caused by numeric integration methods [8–10]: numerical oscillations. These numerical oscillations, called Gibb's oscillations, are produced by numeric integration methods related to associations of π circuits [1–10]. The cascade of π circuits is included in numeric routines as a space state matrix generated from the π circuit's state variables [2–7]. The order of the mentioned matrix depends on the number of π circuits applied. Applying n π circuits, it is necessary to have a $2n$-order matrix in the numeric routine. The increase of the order of the mentioned matrix is not related directly to a corresponding reduction of Gibb's oscillations [2–7, 10, 18, 19]. Searching for a simple representation of the cascade of π circuits, each unit is modelled individually [18, 19]. The influence of adjacent π circuit units are included by the differential relations among the state variables. Thus, the Gibb's oscillations are decreased significantly. The proposed numeric routine is more accurate than the numeric routine based on the application of only one matrix for representing the dynamics of π circuits [20, 21].

2. ANALYSES OF A CASCADE OF π CIRCUITS

A cascade of π circuits can be used for mono-phase representations of transmission lines. One unit of π circuit can be considered an infinitesimal unit of a line representation. The unit of π circuit is a first order filter [2–7]. For infinitesimal transmission line representations, the length of influence of the each π circuit unit on the voltage and current is introduced by an infinitesimal distance (Δx). The mentioned cascade is described as a linear system solved numerically [2–7, 10, 18, 19]:

$$\dot{x} = Ax + Bu \tag{1}$$

In (1), A is the matrix associated with the electrical system, B is the matrix or vector related to the sources, x is the vector of the state variables, and u is the vector of the inputs. If the cascade of π circuits is opened at the receiving end terminal, the structure of matrix A is as shown in (2)

for a voltage source connected to the sending end terminal. The matrix A is calculated by [2–7]:

$$A = \begin{bmatrix} 1/L & -R/L & 0 & \cdots & \cdots & 0 \\ 0 & 1/C & -G/C & -1/C & 0 & \cdots & \vdots \\ 0 & 0 & 1/L & -R/L & -1/L & 0 & \vdots \\ \vdots & \ddots & \ddots & \ddots & \ddots & \ddots & \vdots \\ \vdots & \ddots & \ddots & \ddots & \ddots & \ddots & 0 \\ \vdots & \ddots & \ddots & 0 & 1/L & -R/L & -1/L \\ 0 & \cdots & \cdots & \cdots & 0 & 2/C & -G/C \end{bmatrix} \qquad (2)$$

The elements in (2) are determined from [2, 3]:

$$R = \frac{R' \cdot d}{n} \quad L = \frac{L' \cdot d}{n} \quad C = \frac{C' \cdot d}{n} \quad G = \frac{G' \cdot d}{n} \qquad (3)$$

Calculating the eigenvalues of matrix A, it is obtained that:

$$\lambda = \begin{bmatrix} -\frac{G}{C} & -\frac{R}{L} + \frac{2}{\lambda_1 LC} & -\frac{G}{C} + \frac{1}{\lambda_2 LC} & \cdots & A_{kk} + \frac{1}{\lambda_{k-1} LC} & \cdots & -\frac{R}{L} + \frac{1}{\lambda_{n-1} LC} & -\frac{G}{C} + \frac{2}{\lambda_n LC} \end{bmatrix}^T \qquad (4)$$

$$k = 4, \ldots, 2n - 1 \quad \rightarrow \quad \text{If } k \text{ is even, } A_{kk} = -\frac{R}{L}. \quad \text{If } k \text{ is odd, } A_{kk} = -\frac{G}{C}.$$

Because the R, L, G, and C values are positive and real, the λ_1 value is real and negative. Based on the λ_1 value, each λ_k value depends on the previous eigenvalue and it is also real and negative. From (4) and (2), all eigenvalues of matrix A are real and negative. So, the linear system in (1) is a stable system. If Heun's method is used to simulate the wave propagation of a voltage step through the cascade of π circuits, the obtained results are as shown in Figs. 2–7 and based on [2]:

$$x(k + 1) = \left[I - \frac{\Delta t}{2} A \right]^{-1} \left\{ \left[I + \frac{\Delta t}{2} A \right] x(k) + \frac{\Delta t}{2} \left[u(k + 1) + u(k) \right] \right\}$$

$$x = \begin{bmatrix} i_1 & v_1 & i_2 & v_2 & \cdots & i_n & v_n \end{bmatrix}^T \qquad (5)$$

In (5), Δt is the time step of the trapezoidal rule, $x(k)$ is the known values of the state variables, and $x(k + 1)$ represents the new values of the state variables that are calculated from $x(k)$. The u vector has non-null elements for those points where the sources are connected. For the obtained results, the values of the line parameters are [2, 3]: $R' = 0.05\,\Omega/\text{km}$, $L' = 1\,\text{mH/km}$, $G' = 0.556\,\mu\text{S/km}$, and $C' = 11.11\,\text{nF/km}$. The other values are: $d = 5\,\text{km}$, $t_{\text{MAX}} = 60\,\text{ms}$ and $\Delta t = 50\,\text{ns}$.

Analyzing the results shown in this section (Figs. 1–2), it is observed that the changes in the number of π circuits and the time steps cannot modify the overvoltage value of the simulations performed. There are no modifications in the voltage peak values reached after voltage damping. With an increase of the number of π circuits or a decrease in the time step, the voltage peak values are about *2.03 pu*. The proceedings checked in this section can only modify the frequency of the Gibb's oscillations.
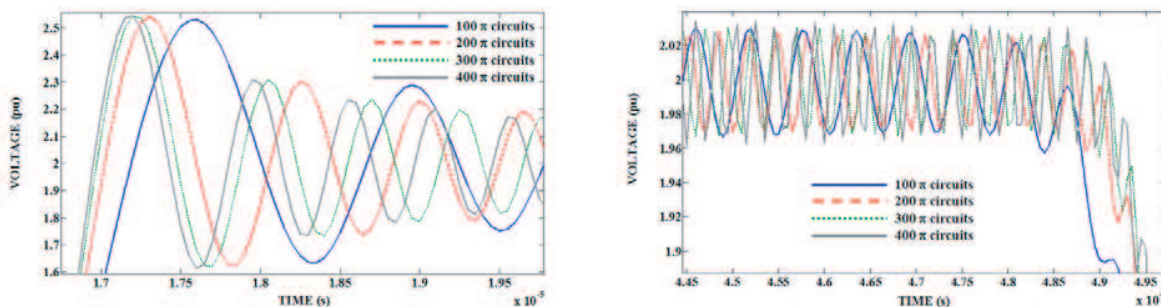

Figure 1: Voltage step propagation for different quantities of circuits using the state equation for the cascade of π circuits.
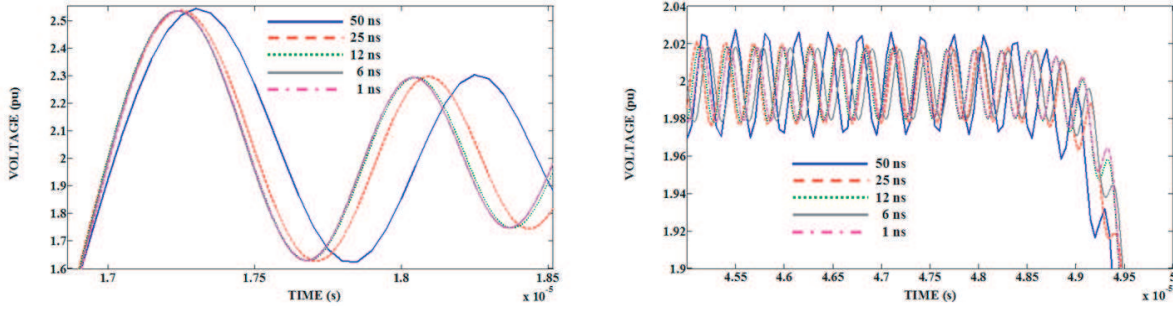
Figure 2: Voltage step propagation for different time steps using the state equation for the entire cascade of π circuits.

3. ROUTINE FOR ANALYSES OF EACH π CIRCUIT

The characteristic π circuits, shown in Fig. 3, are applied for all π circuits of the cascade. Only the first and the last π circuits are different of the other π circuits. From the second to the penultimate π circuits, the related state equation is given in (6) and its elements are in given in (7).

$$\dot{x}_j = A_\pi \cdot x_j + D i_{j+1} + E v_{j-1}, \quad j = 2, \ldots, n-1 \tag{6}$$

$$A_\pi = \begin{bmatrix} -R/L & -1/L \\ 1/C & -G/C \end{bmatrix} \quad E = \begin{bmatrix} 1/L \\ 0 \end{bmatrix} \quad D = \begin{bmatrix} 0 \\ -1/C \end{bmatrix} \quad x_j = \begin{bmatrix} i_j \\ v_j \end{bmatrix} \tag{7}$$

Applying the trapezoidal rule, it is obtained that:

$$x_j(k+1) = x_j(k) + \frac{\Delta t}{2} \left[\dot{x}_j(k+1) + \dot{x}_j(k) \right] \tag{8}$$

Both the vectors for x_j for different times are given in (9); there are two unknown values. One of these unknown values is the term $v_{j-1}(k)$ that has just changed into $v_{j-1}(k+1)$ for the previous π circuit. The term $i_{j+1}(k+1)$ cannot be determined without the actualisation of $v_j(k)$ and $i_j(k)$.

$$\dot{x}_j(k+1) = A_\pi \cdot x_j(k+1) + D i_{j+1}(k+1) + E v_{j-1}(k+1) \quad \dot{x}_j(k) = A_\pi \cdot x_j(k) + D i_{j+1}(k) + E v_{j-1}(k) \tag{9}$$

For the $v_{j-1}(k)$ and $i_{j+1}(k+1)$ unknown values, it is used:

$$\frac{di_j}{dt} = \frac{1}{L} v_{j-1} - \frac{R}{L} i_j - \frac{1}{L} v_j \rightarrow v_{j-1} = L \frac{di_j}{dt} + R i_j + v_j \tag{10}$$

For calculating the term $i_{j+1}(k+1)$, it is used:

$$\frac{\Delta i_j}{\Delta t} \cong \frac{di_j}{dt} = \frac{1}{L} v_{j-1} - \frac{R}{L} i_j - \frac{1}{L} v_j \tag{11}$$

Based on (12), the term $i_{j+1}(k+1)$ is:

$$i_{j+1}(k+1) = i_{j+1}(k) + \Delta i_{j+1}(k) \cong i_{j+1}(k) + \frac{\Delta t}{L} v_{j-1}(k) - \frac{R \Delta t}{L} i_{j+1}(k) - \frac{\Delta t}{L} v_{j+1}(k)$$

$$= \frac{\Delta t}{L} v_{j-1}(k) + \left(1 - \frac{R \Delta t}{L} \right) i_{j+1}(k) - \frac{\Delta t}{L} v_{j+1}(k) \tag{12}$$
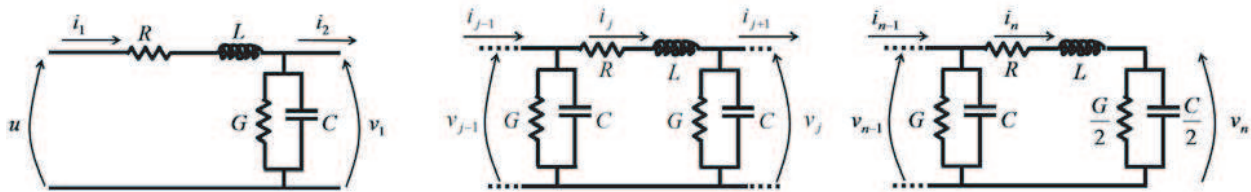

Figure 3: Structure of characteristic π circuits.

The relations in (11) and (12) are true when Δt is very small. With very small Δt, the next relation is:

$$v_{j-1}(k) \cong L\frac{i_j(k+1) - i_j(k)}{\Delta t} + Ri_j(k) + v_j(k) \tag{13}$$

Introducing (14) and (15) in (11), it is obtained that:

$$x_j(k+1) = M_5\{M_6x_j(k) + M_7x_{j-1}(k+1) + M_3x_{j+1}(k) + M_4[u_{CH}(k+1) + u_{CH}(k)]\} \tag{14}$$

In (14), the matrices are:

$$M_5 = \left[I - \frac{\Delta t}{2}A_{CH3}\right]^{-1} \quad M_6 = \left[I + \frac{\Delta t}{2}A_{CH2}\right] \quad M_7 = \frac{\Delta t}{2}E \quad M_3 = \frac{\Delta t}{2}D_{CH1} \quad M_4 = \frac{\Delta t}{2}B_{CH1} \tag{15}$$

The modified A matrices are:

$$A_{CH2} = \begin{bmatrix} -1/\Delta t & 0 \\ 1/C & -1/C \cdot (G + \Delta t/L) \end{bmatrix} \quad A_{CH3} = \begin{bmatrix} -R/L + 1/\Delta t & -1/L \\ 1/C & -G/C \end{bmatrix} \tag{16}$$

The other matrices and vectors are:

$$B_{CH1} = \begin{bmatrix} 1/L & 0 \\ 0 & 1/C \end{bmatrix} \quad u_{CH} = \begin{bmatrix} u_j \\ i_{Fj} \end{bmatrix} \quad D_{CH1} = -1/C \cdot \begin{bmatrix} 0 & 0 \\ 2 - R\Delta t/ & -\Delta t/L \end{bmatrix} \tag{17}$$

For the first and the last units, it is obtained that:

$$\dot{x}_1 = A_\pi \cdot x_1 + B_{1\pi}u + Di_2 \quad \dot{x}_n = A_{n\pi} \cdot x_n + Ev_{n-1} \tag{18}$$

Applying Heun's method, it is obtained that:

$$\begin{aligned} x_1(k+1) &= M_1\{M_2x_1(k) + M_3x_2(k) + M_4[u_{CH}(k+1) + u_{CH}(k)]\} \\ x_n(k+1) &= M_8\{M_9x_n(k) + M_7x_{n-1}(k+1) + M_4[u_{CH}(k+1) + u_{CH}(k)]\} \end{aligned} \tag{19}$$

In (19), the unknown elements are:

$$M_1 = \left[I - \frac{\Delta t}{2}A_\pi\right]^{-1} \quad M_2 = \left[I + \frac{\Delta t}{2}A_{CH1}\right] \quad M_8 = \left[I - \frac{\Delta t}{2}A_{CH5}\right]^{-1} \quad M_9 = \left[I + \frac{\Delta t}{2}A_{CH4}\right] \tag{20}$$

The new A matrices are given in (21). In the case of the A_π and $A_{n\pi}$ matrices, the eigenvalues shown in the vector forms are in (22). The determined eigenvalues are always real and negative values. Each linear system related to the corresponding π circuit unit is a stable system.

$$\begin{aligned} A_{CH1} &= \begin{bmatrix} -R/L & -1/L \\ 1/C & -1/C \cdot (G + \Delta t/L) \end{bmatrix} \quad A_{CH4} = \begin{bmatrix} -1/\Delta t & 0 \\ 2/C & -G/C \end{bmatrix} \\ A_{CH5} &= \begin{bmatrix} -R/L + 1/\Delta t & -1/L \\ 1/C & -G/C \end{bmatrix} \end{aligned} \tag{21}$$

$$\lambda_{A\pi} = \begin{bmatrix} -\frac{R}{L} \\ -\frac{1}{RC}(RG+1) \end{bmatrix} \quad \lambda_{An\pi} = \begin{bmatrix} -\frac{R}{L} \\ -\frac{1}{RC}(RG+2) \end{bmatrix} \tag{22}$$

In Fig. 4, the flowchart for applying numerically the proposal carried out in this section is presented.

In Figs. 5–6, the results obtained with the equations proposed in this section and summarised in the flowchart of Fig. 4 are shown. Compared with Figs. 1–2, it can be seen that the curve for 333π circuits does not have numerical oscillations. It can be observed for an application of 333π circuits that the overvoltage is reduced significantly from about 25% to about 2.5%. The curves for 200 and 300π circuits present lower overvoltage values than the corresponding curves in Figs. 1–2. Similarly, the voltage damping values for the curves of 200 and 300π circuits are faster than the corresponding curves.

For the results obtained in this section, there are limits to the numerical stability related to the number of π circuits and the time step. Considering a time step of 50.0481 ns, the mentioned limit is 333π circuits. Also, using 333π circuits with higher time steps than the considered time step, gives inadequate results. Numerical stability is associated with the relation between the number of π circuits and the time step that leads to the lowest overvoltage and the fastest voltage damping for the results shown in this section. The time step of 50 ns is suggested for teaching power system transients with the use of a personal computer [2].
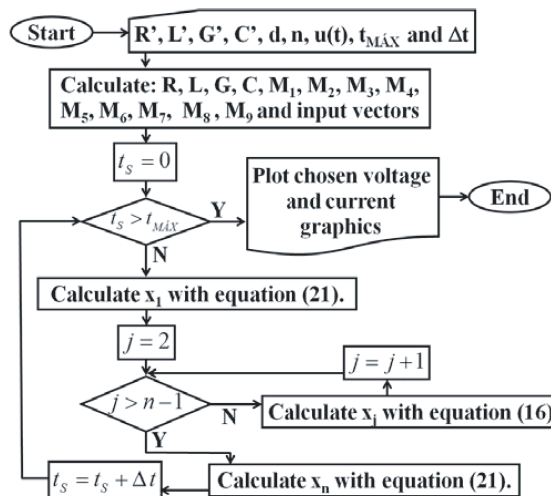
Figure 4: Flowchart of the proposed numeric routine.
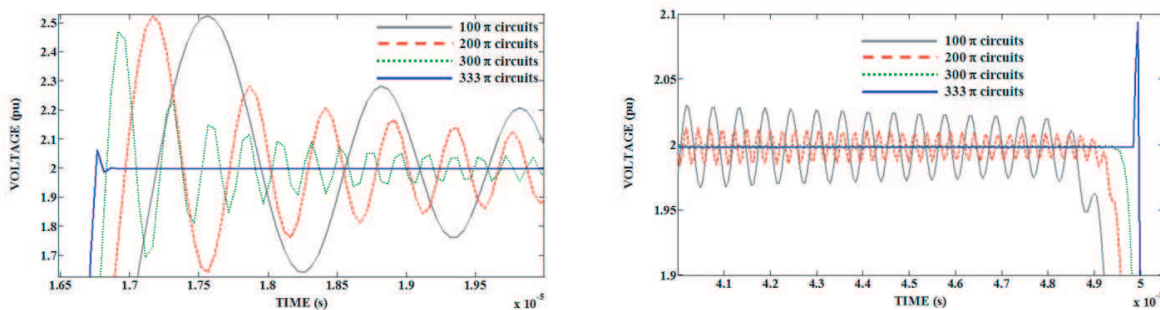
Figure 5: The wave propagation voltage step for different quantities of π circuits using state equations for each π circuit.
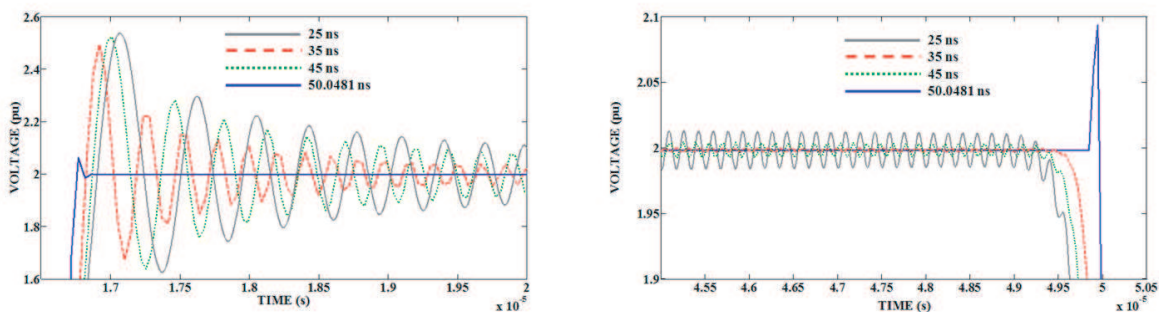
Figure 6: Wave propagation voltage step for different time steps using state equations for each π circuit.

4. CONCLUSION

A modified numeric routine for the application of the trapezoidal integration, or Heun's method for modelling associations of π circuits is presented and analyzed. This numeric routine is applied to simulate the propagation of wave and electromagnetic phenomena through a cascade of π circuits. The proposed changes in the numeric application are based on 2-order matrices for representing each π circuit unit. An important characteristic of the applied 2-order matrices is that these matrices do not have null elements. The results are investigated for a mono-phase representation of a transmission line that is connected to a voltage step input. Analyzing the obtained voltage output, the proposed numeric routine leads to results showing that the numeric oscillations are decreased. Comparing the proposed numeric routine with the unmodified routine used previously for this type of simulation, the reduction in the peaks of the numeric oscillations is about ten times. The previous unmodified numeric routine uses only one $2n$-order matrix to represent the entire cascade with $n\pi$

circuits. This implies that for a specific instant of the simulation, all variables are determined using relations between the $2n$-matrices and the inverse $2n$-order matrices. Therefore, the main change is the method of the application of the numeric integration. Using the same numeric integration method applied to the unmodified numeric routine, the overshot values are only about 3% higher than the voltage output for the proposed numeric routine. This is a decrease of about ten times in these undesirable numeric oscillations. These oscillations are damped in only three time steps.

ACKNOWLEDGMENT

REFERENCES

1. Dommel, H. W., *Electromagnetic Transients Program — Rule Book*, Oregon, 1984.
2. Nelms, R. M., G. B. Sheble, S. R. Newton, and L. L. Grigsby, "Using a personal computer to teach power system transients," *IEEE Trans. on Power Systems*, Vol. 4, No. 3, 1293–1294, Aug. 1989.
3. Nelms, R. M., S. R. Newton, G. B. Sheble, and L. L. Grigsby, "Simulation of transmission line transients using a personal computer," *IEEE Conference Record of the 1988 Eighteenth Power Modulator Symposium*, 229–232, Hilton Head, South Carolina, USA, Jun. 20–22, 1998.
4. Mamis, M. S., "Computation of electromagnetic transients on transmission lines with nonlinear components," *IEE Proc. Generation, Transmission and Distribution*, Vol. 150, No. 2, 200–204, Mar. 2003.
5. Mamis, M. S. and M. Koksal, "Transient analysis of nonuniform lossy transmission lines with frequency dependent parameters," *Electric Power Systems Research*, Vol. 52, No. 3, 223–228, Dec. 1999.
6. Mamis, M. S. and M. Koksal, "Solution of eigenproblems for state-space transient analysis of transmission lines," *Electric Power Systems Research*, Vol. 55, No. 1, 7–14, Jul. 2000.
7. Mamis, M. S. and M. E. Meral, "State-space modeling and analysis of fault arcs," *Electric Power Systems Research*, Vol. 76, No. 1–3, 46–51, Sep. 2005.
8. Macías, J. A. R., A. G. Expósito, and A. B. Soler, "A comparison of techniques for state-space transient analysis of transmission lines," *IEEE Trans. on Power Delivery*, Vol. 20, No. 2, 894–903, Apr. 2005.
9. Macías, J. A. R., A. G. Expósito, and A. B. Soler, "Correction to 'A comparison of techniques for state-space transient analysis of transmission lines,'" *IEEE Trans. on Power Delivery*, Vol. 20, No. 3, 2358, Jul. 2005.
10. Prado, A. J., S. Kurokawa, J. Pissolato Filho, L. F. Bovolato, and E. C. M. Costa, *Phase-mode Transformation Matrix Application for Transmission Line and Electromagnetic Transient Analyses*, Nova Science Publisher, Inc., Hauppauge, NY, 2011.
11. Morched, A., B. Gustavsen, and M. Tartibi, "A universal model for accurate calculation of electromagnetic transients on overhead lines and underground cables," *IEEE Trans. on Power Delivery*, Vol. 14, No. 3, 1032–1038, Jul. 1999.
12. Brandão Faria, J. A., "Overhead three-phase transmission lines — Non-diagonalizable situations," *IEEE Trans. on Power Delivery*, Vol. 3, No. 4, Oct. 1988.
13. Brandão Faria, J. A. and J. Briceño Mendez, "Modal analysis of untransposed bilateral three-phase lines — A perturbation approach," *IEEE Trans. on Power Delivery*, Vol. 12, No. 1, Jan. 1997.
14. Brandão Faria, J. A. and J. Briceño Mendez, "On the modal analysis of asymmetrical three-phase transmission lines using standard transformation matrices," *IEEE Trans. on Power Delivery*, Vol. 12, No. 4, Oct. 1997
15. Wedepohl, L. M., H. V. Nguyen, and G. D. Irwin, "Frequency-dependent transformation matrices for untransposed transmission lines using Newton-Raphson method," *IEEE Trans. on Power Systems*, Vol. 11, No. 3, 1538–1546, Aug. 1996.
16. Nguyen, T. T. and H. Y. Chan, "Evaluation of modal transformation matrices for overhead transmission lines and underground cables by optimization method," *IEEE Trans. on Power Delivery*, Vol. 17, No. 1, Jan. 2002.
17. Marti, J. R., "Accurate modelling of frequency-dependent transmission lines in electromagnetic transients simulations," *IEEE Trans. on PAS*, Vol. 101, 147–155, Jan. 1982.

18. Monzani, R. C., A. J. Prado, S. Kurokawa, L. F. Bovolato, and J. Pissolato Filho, "Using a low complexity numeric routine for solving electromagnetic transient simulations," *Matlab — A Fundamental Tool for Scientific Computing and Engineering Applications*, 463–484, InTech-Open Access Publisher, Rijeka, Croatia, 2012, DOI 10.5772/48507.

19. Lessa, L. S., A. J. Prado, S. Kurokawa, L. F. Bovolato, and J. Pissolato Filho, "The MatLab software application for electrical engineering simulations and power system analyses," *Mat-Lab — A Fundamental Tool for Scientific Computing and Engineering Applications*, 433–462, InTech-Open Access Publisher, Rijeka, Croatia, 2012, DOI 10.5772/48555.

20. Moreno, P. and A. Ramirez, "Implementation of the numerical Laplace transform: A review," *IEEE Trans. on Power Delivery*, Vol. 23, No. 4, Oct. 2008.

21. Prikler, L. and H. K. Hoidalen, *ATPDraw Version 3.5 — Users' Manual*, Trondheim, Norway, Aug. 2002.

22. Dommel, H. W., *EMTP Theory Book*, 2nd Edition, Vancouver, Apr. 1996.

23. Martí, J. R. and J. Lin, "Supression of numerical oscillations in the EMTP," *IEEE Trans. on Power Systems*, Vol. 4, No. 2, May 1989.

24. Lin, J. and J. R. Martí, "Implementation of the CDA procedure in the EMTP," *IEEE Trans. on Power Systems*, Vol. 5, No. 2, May 1990.

Whistler Modes Guided by Enhanced Density Ducts in a Nonresonant Magnetoplasma

O. M. Ostafiychuk, **V. A. Es'kin**, and **A. V. Kudrin**

University of Nizhny Novgorod, Russia

Abstract— Guidance of azimuthally symmetric waves by cylindrical density ducts in a magnetoplasma in the nonresonant region of the whistler frequency range is investigated. It is demonstrated that eigenmodes existing at the studied frequencies in ducts with enhanced density admit simplified description that makes analysis of the features of their guided propagation much easier. The results of calculation of the dispersion characteristics and field structures of the whistler modes supported by such ducts are reported.

1. INTRODUCTION

Investigation of the guided propagation of waves in the whistler frequency range in plasma channels (density ducts) in the presence of an external static magnetic field was performed in a large number of works (see [1, 2] and references therein). Whistler waves supported by such structures are intensely studied because of an important role that they play in many fundamental physical processes in the Earth's ionosphere and magnetosphere [1], as well as due to various applications including, in particular, use of the guiding properties of density ducts for controlling the characteristics of electromagnetic sources in a magnetoplasma [2], VLF diagnostics of the near-Earth space [3], etc. The overwhelming majority of the theoretical studies devoted to specific features of excitation and propagation of whistler waves in the presence of density ducts in a magnetoplasma deal with waves in the resonant region of the whistler range, which lies above the lower-hybrid resonance frequency ω_{LH} and allows the existence of quasi-electrostatic waves [4–6]. It was shown in those works that in this frequency region, the ducts whose density is lower than the background value can support eigenmodes of different kinds, whereas the ducts with enhanced density can support no more than one eigenmode with the volume-surface field structure (for each fixed value of the azimuthal index) and improper leaky modes. As to the waves with frequencies below ω_{LH}, their guided propagation in cylindrical density ducts has attracted little attention in the literature.

It is the purpose of this work to study the dispersion properties and field structures of eigenmodes of density ducts in the case where the angular frequency ω of the field lies in the nonresonant region

$$\Omega_H < \omega < \omega_{\text{LH}} \ll \omega_H \ll \omega_p \tag{1}$$

of the whistler range. Here, Ω_H is the ion gyrofrequency, and ω_H and ω_p are the gyrofrequency and the plasma frequency of electrons, respectively. Note that only an extraordinary wave having a closed refractive index surface is propagating in a magnetoplasma in the frequency range determined by inequalities (1). This circumstance leads to fundamental differences in the behavior of waves guided by the density ducts in this frequency interval compared with the case where the frequency ω lies in the resonant region of the whistler frequency range, in which the refractive index surface of the propagating extraordinary wave is open.

For simplicity, we limit our analysis to axisymmetric waves that are supported by cylindrical density ducts in range (1). Such guiding structures can appear in a magnetoplasma as a result of nonlinear interaction of the fields of electromagnetic sources with the surrounding (background) plasma medium. It should be noted that interest in specific features of the behavior of whistler waves in range (1) was stimulated in the past decade by a number of new experimental studies aimed at developing efficient methods of wave excitation in the indicated frequency interval [7].

2. MODES GUIDED BY A UNIFORM DENSITY DUCT

We consider an axisymmetric enhanced-density duct aligned with a uniform external magnetic field and surrounded by the cold collisionless background plasma. The external magnetic field $\mathbf{B}_0$ is assumed to be directed along the z axis of a cylindrical coordinate system (ρ, ϕ, z): $\mathbf{B}_0 = B_0 \mathbf{z}_0$. In the presence of such a duct, the electron number (plasma) density N is a function of only the radial cylindrical coordinate ρ: $N = N(\rho)$. The plasma is described by the dielectric permittivity tensor with nonzero elements $\varepsilon_{\rho\rho} = \varepsilon_{\phi\phi} = \varepsilon$, $\varepsilon_{\rho\phi} = -\varepsilon_{\phi\rho} = -ig$, and $\varepsilon_{zz} = \eta$. Expressions for

ε, g, and η can be found elsewhere [2]. Fields of axisymmetric modes supported by the duct (with the time dependence $\exp(i\omega t)$ dropped) can be represented as $\mathbf{E}(\mathbf{r}) = \mathbf{E}(\rho)\exp(-ik_0 pz)$ and $\mathbf{B}(\mathbf{r}) = \mathbf{B}(\rho)\exp(-ik_0 pz)$, where k_0 is the wave number in free space and p is the normalized (to k_0) propagation constant. In this case, the quantities $\mathbf{E}(\rho)$ and $\mathbf{B}(\rho)$ can conveniently be described by scalar functions $E_\phi(\rho)$ and $E_z(\rho)$ that obey the equations

$$\frac{d^2 E_\phi}{d\rho^2} + \frac{1}{\rho}\frac{dE_\phi}{d\rho} - \frac{E_\phi}{\rho^2} + k_0^2\left(\frac{g^2}{p^2 - \varepsilon} - p^2 + \varepsilon\right)E_\phi = \frac{k_0 pg}{p^2 - \varepsilon}\frac{dE_z}{d\rho}, \tag{2}$$

$$\frac{d^2 E_z}{d\rho^2} + \frac{1}{\rho}\frac{dE_z}{d\rho} + \frac{p^2}{(p^2 - \varepsilon)\varepsilon}\frac{d\varepsilon}{d\rho}\frac{dE_z}{d\rho} + k_0^2\frac{\eta}{\varepsilon}(\varepsilon - p^2)E_z = k_0\frac{p}{\varepsilon}(p^2 - \varepsilon)\frac{1}{\rho}\frac{d}{d\rho}\left(\frac{\rho g E_\phi}{p^2 - \varepsilon}\right). \tag{3}$$

Note that in the presence of a uniform duct, the distribution of plasma density over the radius is given by the expression $N(\rho) = N_a + (\tilde{N} - N_a)[1 - U(\rho - a)]$, where U is a Heaviside step function, a is the duct radius, $N_a = \text{const}$ is the background plasma density ($\rho > a$), and $\tilde{N} = \text{const}$ is the plasma density inside the duct ($\rho < a$). In what follows, the quantities referring to the region inside the duct will be denoted by the tilde, whereas the quantities referring to the outer region will be written without such a designation.

In the case of a uniform duct, the field components of the axisymmetric modes can be described by general expressions obtained in [2]. Outside the duct ($\rho > a$), expressions for the azimuthal and longitudinal electric-field components, which are solutions of Eqs. (2) and (3), can be written as follows:

$$E_\phi = i\sum_{k=1}^{2} C_k K_1(k_0 s_k \rho), \quad E_z = -\frac{i}{\eta a}\sum_{k=1}^{2} C_k n_k s_k K_0(k_0 s_k \rho), \tag{4}$$

where K_m is the mth-order modified Bessel function of the second kind, and C_1 and C_2 are constants. The quantities s_k and n_k are determined by the relations

$$s_k^2 = -q_k^2, \quad n_k = -\varepsilon[p^2 + q_k^2 + (g^2 - \varepsilon^2)\varepsilon^{-1}](pg)^{-1},$$

$$q_k = \left\{[\varepsilon^2 - g^2 + \varepsilon\eta - (\varepsilon + \eta)p^2 + (-1)^k R(p)](2\varepsilon)^{-1}\right\}^{1/2}, \tag{5}$$

$$R(p) = (\varepsilon - \eta)[(p^2 - P_b^2)(p^2 - P_c^2)]^{1/2},$$

$$P_{b,c} = \left\{\varepsilon - (\varepsilon + \eta)\frac{g^2}{(\varepsilon - \eta)^2} + \frac{2\chi_{b,c}}{(\varepsilon - \eta)^2}[\varepsilon g^2 \eta(g^2 - (\varepsilon - \eta)^2)]^{1/2}\right\}^{1/2}, \quad \chi_b = -\chi_c = -1.$$

Inside the duct ($\rho < a$), the azimuthal and longitudinal electric-field components are represented as

$$E_\phi = i\sum_{k=1}^{2} B_k J_1(k_0 q_k \rho), \quad E_z = \frac{i}{\tilde{\eta}}\sum_{k=1}^{2} B_k \tilde{n}_k q_k J_0(k_0 q_k \rho), \tag{6}$$

where J_m is the Bessel function of order m, B_1 and B_2 are constants, and the quantities q_k and $\tilde{n}_k$ can be obtained from the corresponding expressions for q_k and n_k in (5) by putting $\varepsilon = \tilde{\varepsilon}$, $g = \tilde{g}$, and $\eta = \tilde{\eta}$ (when doing this, the quantities P_b and P_c are replaced by the corresponding quantities $\tilde{P}_b$ and $\tilde{P}_c$, respectively).

The continuity condition for the tangential field components at $\rho = a$ yields a rigorous dispersion relation that allows determining the propagation constants p of the considered modes. Such a relation is rather cumbersome and can be analyzed only numerically. However, it admits an approximate analytical solution at $\Omega_H \ll \omega < \omega_{\mathrm{LH}}$. In this case, after some lengthy algebra we obtain the approximate dispersion relation

$$\frac{J_1(k_0 q_1 a)}{J_0(k_0 q_1 a)} = -\left(1 - \frac{\tilde{P}^2}{p s_1 \sqrt{u_{\mathrm{LH}} - 1}}\frac{K_1(k_0 s_1 a)}{K_0(k_0 s_1 a)}\right)^{-1}\frac{q_1 K_1(k_0 s_1 a)}{s_1 K_0(k_0 s_1 a)}, \tag{7}$$

where $u_{\mathrm{LH}} = \omega_{\mathrm{LH}}^2/\omega^2$ and $\tilde{P} = (\tilde{\varepsilon} - \tilde{g})^{1/2}$.

The dependences $p(\omega)$ satisfying the rigorous dispersion relation and approximate relation (7) are illustrated in Fig. 1(a). In this case, the duct supports the guided propagation only of the lowest
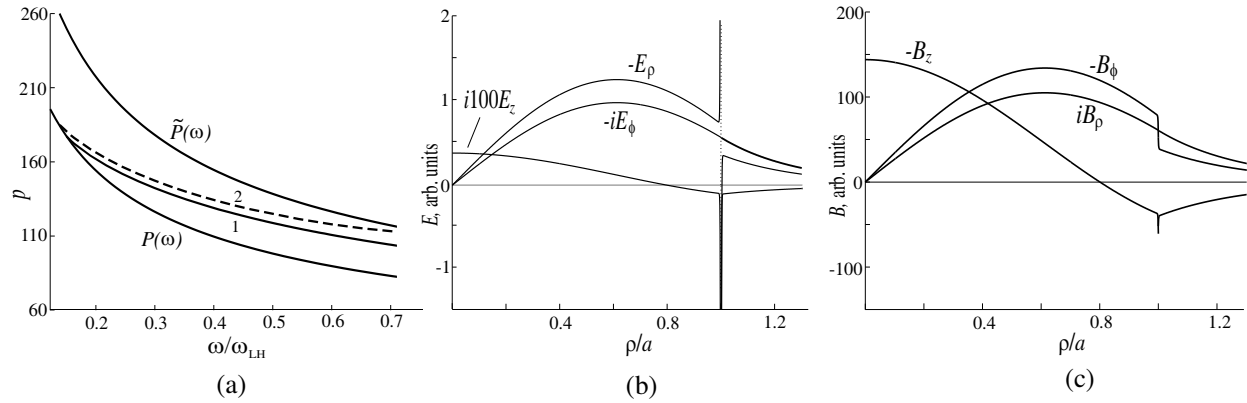
Figure 1: (a) Dispersion curves $P(\omega)$ of the lowest axisymmetric mode, which were calculated using the rigorous dispersion relation (curve 1) and approximate relation (7) (curve 2), and the dependences $\tilde{P}(\omega)$ and $P(\omega)$ for $\tilde{\omega}_p/\omega_{pa} = 1.41$, $\omega_{pa}/\omega_H = 4.5$, $\omega_H/\omega_{\mathrm{LH}} = 235$, and $\omega_{\mathrm{LH}} a/c = 5.25 \times 10^{-2}$. Transverse distributions of the electric (b) and magnetic (c) field components of this mode at $\omega/\omega_{\mathrm{LH}} = 0.68$.

eigenmode with the radial index $n = 1$. It is seen in the figure that the frequency dependences of the propagation constant obtained by rigorous and approximate methods are almost identical. The only exception is the vicinity of the lower hybrid resonance frequency ω_{LH}. When the frequency ω increases and approaches the lower hybrid resonance frequency, the accuracy of the approximate solution considerably deteriorates. With decreasing frequency, the mode propagation constant approaches the lower boundary $p = P(\omega) = (\varepsilon - g)^{1/2}$. After crossing this boundary, the mode ceases to be localized and becomes leaky.

The distributions of the field components of the lowest axisymmetric mode along the radial coordinate are illustrated in Figs. 1(b) and 1(c). The propagation constant of this mode $p = 104.87$. In this case, the quantities s_1 and s_2, which determine the field outside the duct, are real and the mode turns out to be localized. Inside the duct, q_1 is real, while q_2 is purely imaginary. The presence of the branches $q_2 = i\tilde{s}_2$ and s_2 leads to the appearance of sharp spikes in the components E_ρ and E_z and relatively fast changes in the components B_ϕ and B_z near the duct boundary. We emphasize that contribution of the components related to the presence of the branches $\tilde{s}_2$ and s_2 becomes evident only in close proximity to the duct boundary because of the large difference between the values of the transverse wave numbers q_1 and s_1 on the one hand, and $\tilde{s}_2$ and s_2 on the other hand. It can be seen in Figs. 1(b) and 1(c) that the lowest mode ($n = 1$) is characterized by the presence of one field oscillation over the radius, and the field structure is everywhere determined by the whistler component corresponding to the transverse wave numbers q_1 and s_1 and having quasi-TE polarization. In what follows, we will demonstrate that this circumstance allows one to substantially simplify the description of the fields of eigenmodes in the nonresonant region of the whistler frequency range, which appreciably facilitates their analysis in the case of a duct with a smooth variation in plasma density in the transverse direction.

3. MODES GUIDED BY A NONUNIFORM DENSITY DUCT

We now analyze the propagation of waves of the whistler range in a duct in which plasma density is described by a smooth function $N(\rho)$ monotonically decreasing from its maximum value $\tilde{N} = N(0)$ to the background value N_a with increasing cylindrical coordinate ρ. As in the preceding section, we will use the notations $\tilde{P}$ and P corresponding to the plasma densities $N = \tilde{N}$ and $N = N_a$, respectively.

Let us introduce the following notations:

$$\hat{q}_1^2 = \frac{g^2}{p^2 - \varepsilon} - p^2 + \varepsilon, \quad \hat{q}_2^2 = -\frac{\eta}{\varepsilon}(p^2 - \varepsilon), \quad \chi = (k_0 a p u^{1/2})^{-1}, \quad \xi = \rho/a. \tag{8}$$

Hereafter, a denotes the characteristic transverse scale of the plasma density drop in a nonuniform duct, while $\hat{q}_1$ and $\hat{q}_2$, in contrast to the corresponding quantities in the preceding section, are functions of the coordinate ρ. In new notations, Eqs. (2) and (3) for axisymmetric modes take the

form

$$\frac{d^2 E_\phi}{d\xi^2} + \frac{1}{\xi}\frac{dE_\phi}{d\xi} - \frac{E_\phi}{\xi^2} + (k_0 a\hat{q}_1)^2 E_\phi = k_0 ap\,\frac{g}{p^2 - \varepsilon}\frac{dE_z}{d\xi}, \tag{9}$$

$$\chi^2(1 - u_{\mathrm{LH}})\left(\frac{d^2 E_z}{d\xi^2} + \frac{1}{\xi}\frac{dE_z}{d\xi} + \frac{p^2}{(p^2 - \varepsilon)\varepsilon}\frac{d\varepsilon}{d\xi}\frac{dE_z}{d\xi}\right) - \frac{\varepsilon}{p^2\eta}\hat{q}_2^2 E_z = -\chi\,\frac{p^2 - \varepsilon}{g}\frac{1}{\xi}\frac{d}{d\xi}\left(\frac{\xi g E_\phi}{p^2 - \varepsilon}\right). \tag{10}$$

Allowing for the condition $P < p < \tilde{P}$ and the inequality $k_0 ap \geq 1$, which holds for the considered axisymmetric whistler modes in an enhanced-density duct, it can easily be verified that the following relations are satisfied in the case under consideration: $\chi \ll 1$, $\chi u_{\mathrm{LH}}^{1/2} \ll 1$, $p^2 \gg |\varepsilon|$, and $|\varepsilon\hat{q}_2^2/p^2\eta| \simeq 1$, which allows using the perturbation method for analysis of Eqs. (9) and (10). In zero-order perturbation theory ($\chi = 0$ and $\chi^2 u_{\mathrm{LH}} = 0$), we have

$$\frac{d^2 E_\phi}{d\rho^2} + \frac{1}{\rho}\frac{dE_\phi}{d\rho} - \frac{E_\phi}{\rho^2} + k_0^2\left(\frac{g^2}{p^2} - p^2\right)E_\phi = 0 \tag{11}$$

and $E_z = 0$. The nontrivial expression for the longitudinal component of the electric field is obtained from Eq. (10) in the next (first-order) approximation of the perturbation theory ($\chi \neq 0$ and $\chi^2(1 - u_{\mathrm{LH}}) \approx 0$) and has the form

$$E_z = -\frac{1}{k_0 p\eta}\frac{1}{\rho}\frac{d}{d\rho}(\rho g E_\phi). \tag{12}$$

In the zero-order approximation, other field components are expressed as

$$E_\rho = -igp^{-2}E_\phi, \quad B_\rho = -pE_\phi, \quad B_\phi = -igp^{-1}E_\phi, \quad B_z = \frac{i}{k_0\rho}\frac{d}{d\rho}(\rho E_\phi). \tag{13}$$

In the case of a weakly nonuniform cylindrical density duct, the density profile in the vicinity of the axis can be approximated by the quadratic law

$$N(\rho) = \tilde{N}\left(1 - \frac{\rho^2}{2a^2}\right). \tag{14}$$

In this case, in Eq. (11) one should put $g^2 \approx \tilde{g}^2\left(1 - \rho^2/a^2\right)$, where $\tilde{g} = g(0)$. The solution $E_\phi(\rho)$ of Eq. (11) must be finite everywhere and approach zero as ρ tends to infinity ($\rho \to \infty$). Let us seek the solution for the component E_ϕ in the form

$$E_\phi = \zeta^{1/2}f(\zeta)\exp\left(-\frac{\zeta}{2}\right),$$

where $\zeta = \rho^2 k_0 |\tilde{g}|/(pa)$. Substituting this representation into Eq. (11) yields the equation

$$\zeta f''(\zeta) + (2 - \zeta)f'(\zeta) + (n - 1)f(\zeta) = 0,$$

where $n = (\tilde{g}^2 - p^4)k_0 a/(4|\tilde{g}|p)$. Solution to this equation yields the function $E_\phi(\rho)$ satisfying all the above-mentioned conditions only if n is positive integer. As a result, we obtain the following dispersion relation for the propagation constant p:

$$p^4 + \frac{4n|\tilde{g}|}{k_0 a}p - \tilde{g}^2 = 0, \quad n = 1, 2, \ldots. \tag{15}$$

In this case, the solution $f(\zeta)$ is expressed in terms of a confluent hypergeometric function $\Phi(a, c; x)$: $f(\zeta) = \Phi(1 - n, 2; \zeta)$ [8]. Taking into account that the function $\Phi(-k, 1 + \alpha; x)$ for nonnegative integer k is reduced to the generalized Laguerre polynomials [8]

$$L_k^\alpha(x) = \frac{1}{k!}e^x x^{-\alpha}\frac{d^k}{dx^k}\left(e^{-x}x^{\alpha+k}\right),$$

the component E_ϕ of the field of the mode with the number n can be expressed in the form

$$E_\phi = E_0 \frac{\rho}{\rho_n} L_{n-1}^1 \left(\frac{\rho^2}{\rho_n^2} \right) \exp\left(-\frac{\rho^2}{2\rho_n^2} \right), \tag{16}$$

where E_0 is an arbitrary constant, $\rho_n = (p_n a/k_0 |\tilde{g}|)^{1/2}$ is the characteristic transverse scale of the field distribution of the nth mode over the radius, and p_n is the propagation constant which is the solution of Eq. (15). For the lowest mode, i.e., for $n = 1$, azimuthal component (16) is written as

$$E_\phi = E_0 \frac{\rho}{\rho_1} \exp\left(-\frac{\rho^2}{2\rho_1^2} \right). \tag{17}$$

All other components can be obtained from the azimuthal component of the electric field.

4. CONCLUSION

In this work, we have studied the dispersion properties and field structures of axisymmetric eigenmodes guided by density ducts in a magnetoplasma in the nonresonant region of the whistler frequency range. It is established that eigenmodes in this frequency region exist only in the ducts in which plasma density is higher than the background density. The possibility of a simplified description of these modes due to the extremely small value of the longitudinal component of their electric field inside and outside the duct is demonstrated. It is important that this possibility exists for both a sharp-walled uniform duct and a smooth-walled nonuniform duct. Obviously, such a simplified description of the modes should make analysis of the features of their excitation by electromagnetic sources much easier. This circumstance should be taken into account when solving the corresponding problems, in particular, when the source is located in the near-axis region of the duct.

REFERENCES

1. Helliwell, R. A., *Whistlers and Related Ionospheric Phenomena*, Dover, Mineola, 2006.
2. Kondrat'ev, I. G., A. V. Kudrin, and T. M. Zaboronkova, *Electrodynamics of Density Ducts in Magnetized Plasmas*, Gordon and Breach, Amsterdam, 1999.
3. Sazhin, S., M. Hayakava, and K. Bullough, "Whistler diagnostics of magnetospheric parameters: A review," *Ann. Geophys.*, Vol. 10, No. 5, 293–308, 1992.
4. Zaboronkova, T. M., A. V. Kudrin, M. Yu. Lyakh, and L. L. Popova, "Nonsymmetric whistler waves guided by cylindrical ducts with enhanced plasma density," *Radiophys. Quantum Electron.*, Vol. 45, No. 10, 764–783, 2002.
5. Es'kin, V. A., T. M. Zaboronkova, and A. V. Kudrin, "Whistler waves guided by ducts with enhanced density in a collisional magnetoplasma," *Radiophys. Quantum Electron.*, Vol. 51, No. 1, 28–44, 2008.
6. Bakharev, P. V., T. M. Zaboronkova, A. V. Kudrin, and C. Krafft, "Whistler waves guided by density depletion ducts in a magnetoplasma," *Plasma Phys. Rep.*, Vol. 36, No. 11, 919–930, 2010.
7. Karavaev, A. V., N. A. Gumerov, K. Papadopoulos, X. Shao, A. S. Sharma, W. Gekelman, A. Gigliotti, P. Pribyl, and S. Vincena, "Generation of whistler waves by a rotating magnetic field source," *Phys. Plasmas*, Vol. 17, No. 1, 012102, 2010.
8. Erdélyi, A., Ed., *Higher Transcendental Functions (Bateman Manuscript Project)*, McGraw-Hill, New York, 1953.

Hybrid TEM Wave Radiation from a Coaxial Waveguide with a Semi-infinite PEC Outer Cylinder and an Infinite Inner Cylinder Loaded with Partial Impedance

Kutlu Karayahşi[1], İsmail H. Tayyar[2], and Arif Dolma[3]

[1]Electrical & Electronics Engineering Department, Okan University
Tuzla Campus, Akfirat, Tuzla, Istanbul 34959, Turkey
[2]Mechatronic Engineering Department, Engineering Faculty
Karabük University, Balıklarkayası, Mevkii, Karabük, TR 78050, Turkey
[3]Electronics & Communications Engineering Department, KOU Engineering Faculty
Kocaeli University, Building B, Umuttepe Campus Kocaeli, TR 41380, Turkey

Abstract— In this work, the radiation of a hybrid TEM mode from a coaxial waveguide with an infinitely thin semi infinite outer cylinder made of perfect electric conductor and an infinite inner cylinder lying along axial direction which has piecewise surface impedance has been analyzed through the Wiener-Hopf technique in conjunction with the mode matching method.

1. INTRODUCTION

The aim of this work is to analyze the radiation of a hybrid TEM mode from a coaxial waveguide with an infinitely thin semi infinite outer cylinder made of perfect electric conductor and an infinite inner cylinder lying along axial direction which has piecewise surface impedance as shown in Figure 1. Being a very good model for long monopole antennas or traveling wave antennas, the excitation of such structures with TE, TM and TEM modes have been analyzed extensively [1–7]. In this work, Wiener-Hopf technique in conjunction with the mode-matching method has been implemented to the radiation problem of a TM_{00} (Hybrid TEM) mode wave travelling inside the coaxial structure shown in Figure 1. By expanding the scattered field into a series of normal modes in the waveguide region and applying Fourier transform else where one gets a modified Wiener-Hopf equation. The solution involves three sets of infinite expansion coefficients satisfying three sets of infinite linear algebraic equations. The numerical results showing the effects of physical parameters have been given graphically. A time dependence $e^{-i\omega t}$ with ω being the angular frequency is assumed and suppressed throughout.
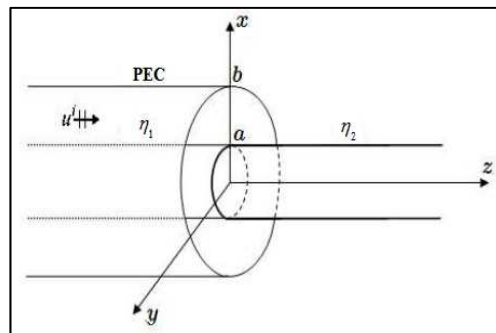
Figure 1: Geometry of the problem.

2. ANALYSIS

The waveguide analyzed here is defined by two coaxial cylinders. The inner cylinder is defined as $\rho = a$, $\phi \in (-\pi, \pi)$, $z \in (-\infty, \infty)$ while the outer cylinder is defined $\rho = b$, $\phi \in (-\pi, \pi)$, $z \in (-\infty, 0)$ where (ρ, ϕ, z) are cylindrical coordinates. The outer cylinder is infinitely thin and made of perfect electrical conductor and the inner conductor has the surface impedance $Z_1 = \eta_1 Z_0$ where $z < 0$ and $Z_2 = \eta_2 Z_0$ where $z > 0$. Here, Z_0 denotes the impedance of free space. The incident TM_{00}

(Hybrid TEM) mode has the angular frequency ω and propagates in the $+z$ direction and it is given as $H_\rho = 0$, $H_\phi = u_i$, $H_z = 0$. Total field can be written as shown below.

$$u^T (\rho, z) = \begin{cases} u_1 (\rho, z), & \rho > b, & z \in (-\infty, \infty) \\ u_2 (\rho, z), & \rho \in (a, b), & z > b \\ u^i (\rho, z) + u_3 (\rho, z), & \rho \in (a, b), & z < b \end{cases} \tag{1}$$

$u_n(\rho, z)$ and $u^i(\rho, z)$ are solutions of the Helmholtz equation shown below.

$$\left[\frac{1}{\rho} \frac{\partial}{\partial \rho} \left(\rho \frac{\partial}{\partial \rho} \right) + \frac{\partial^2}{\partial z^2} + k^2 - \frac{1}{\rho^2} \right] u_n (\rho, z) = 0, \quad n = 1, 2, 3 \tag{2}$$

where k is the propagation constant which is assumed to have a small imaginary part corresponding of slightly lossy medium. The field terms in Equation (1) are subject to the following boundary and continuity conditions.

$$u_{1,3} (b, z) + b \frac{\partial u_{1,3} (b, z)}{\partial \rho} = 0, \quad z < 0, \tag{3}$$

$$(1 + ika\eta_{1,2}) u_{3,2} (a, z) + a \frac{\partial u_{3,2} (a, z)}{\partial \rho} = 0, \quad z < 0, \tag{4}$$

$$u_2 (b, z) = u_1 (b, z), \quad z > 0, \tag{5a}$$

$$\frac{\partial u_2 (b, z)}{\partial \rho} = \frac{\partial u_1 (b, z)}{\partial \rho}, \quad z > 0 \tag{5b}$$

$$u^i (\rho, 0) + u_3 (\rho, 0) = u_2 (\rho, 0), \quad \rho \in (a, b), \tag{6a}$$

$$\frac{\partial u^i (\rho, 0)}{\partial z} + \frac{\partial u_3 (\rho, 0)}{\partial z} = \frac{\partial u_2 (\rho, 0)}{\partial z}, \quad \rho \in (a, b) \tag{6b}$$

In order to find a single solution for the mixed boundary value problem defined with Equations (2) and (3)–(6), the edge and radiation conditions shown below are also needed to be considered.

$$u^T (b, z) = O \left(|z|^{1/2} \right), \quad |z| \to 0, \tag{7a}$$

$$u_1 (\rho, z) = O \left(\frac{e^{ik|\rho|}}{\rho} \right), \quad |\rho| \to \infty \tag{7b}$$

The Wiener-Hopf equation shown in (8) can be obtained by applying Fourier transformation is to (2) for $u_1(\rho, z)$ and $u_2(\rho, z)$ and using (3), (4), (5a), and (5b)

$$\frac{1}{N (\alpha) M (\alpha)} P^+ (\alpha) - \frac{F^- (b, \alpha)}{ik\eta_2} = -b \sum_{m=0}^{\infty} \frac{[f_m - i\alpha g_m] [J_m Y_1 (K_m b) - Y_m J_1 (K_m b)]}{\alpha^2 - \alpha_m^2} \tag{8}$$

$$M (\alpha) = K (\alpha) [J (\alpha) Y_0 [K (\alpha) b] - Y (\alpha) J_0 [K (\alpha) b]], \tag{9a}$$

$$N (\alpha) = \frac{H_0^1 (Kb)}{H_1^1 (Kb) M_0 (\alpha) + H_0^1 (Kb) M_1 (\alpha)} \tag{9b}$$

$$J (\alpha) = ik\eta_2 J_1 [K (\alpha) a] + K (\alpha) J_0 [K (\alpha) a], \tag{10a}$$

$$Y (\alpha) = ik\eta_2 Y_1 [K (\alpha) a] + K (\alpha) Y_0 [K (\alpha) a] \tag{10b}$$

$$M_j (\alpha) = J (\alpha) Y_j (Kb) - Y (\alpha) J_j (Kb), \quad j = 0, 1 \tag{11}$$

$$P^+ (\alpha) = G^+ (b, \alpha) + b\dot{G}^+ (b, \alpha) = F^+ (b, \alpha) + b\dot{F}^+ (b, \alpha), \tag{12a}$$

$$P^+ (\alpha_m) = -\frac{\pi}{2} K_m b [f_m - i\alpha_m g_m] \Delta_m \tag{12b}$$

Here, $(\dot{\ })$ denotes derivation in terms of ρ.

$$F^{\pm}(\rho,\alpha) = \pm \int_0^{\pm\infty} u_1(\rho,z) e^{i\alpha z} dz, \tag{13a}$$

$$G^+(\rho,\alpha) = \int_0^{\infty} u_2(\rho,z) e^{i\alpha z} dz \tag{13b}$$

$$\begin{bmatrix} f_m \\ g_m \end{bmatrix} = \frac{1}{\Delta_m} \int_a^b \begin{bmatrix} f(\rho) \\ g(\rho) \end{bmatrix} [J_0(K_m b) Y_1(K_m \rho) - J_1(K_m \rho) Y_0(K_m b)] \rho d\rho \tag{14}$$

$$f(\rho) = \frac{\partial}{\partial z} u_2(\rho,0), \tag{15a}$$

$$g(\rho) = u_2(\rho,0) \tag{15b}$$

$$\begin{bmatrix} f(\rho) \\ g(\rho) \end{bmatrix} = \sum_{m=0}^{\infty} \begin{bmatrix} f_m \\ g_m \end{bmatrix} [J_0(K_m b) Y_1(K_m \rho) - J_1(K_m \rho) Y_0(K_m b)] \tag{16}$$

$$\Delta_m = \frac{b^2}{2} \left(\frac{2}{\pi K_m b} \right)^2 - \frac{a^2}{2} \left[1 + \frac{ik\eta_2}{K_m^2 a} (2 + ik\eta_2 a) \right] \tilde{L}_1^2, \tag{17a}$$

$$\tilde{L}_1 = J_0(K_m b) Y_1(K_m a) - J_1(K_m a) Y_0(K_m b) \tag{17b}$$

$K(\alpha) = \sqrt{k^2 - \alpha^2}$ is the square root function defined on the complex α-plane and $K_m = K(\alpha_m)$. Where,

$$M(\alpha_m) = 0, Im(\alpha_m) > Im(-k), \quad m = 0,1,2,\ldots \tag{18}$$

3. THE SOLUTION OF THE WIENER-HOPF EQUATION

By applying the Wiener-Hopf procedure to (8), we obtain (19).

$$\frac{P^+(\alpha)}{V^+(\alpha)} = b \sum_{m=0}^{\infty} \frac{[f_m - i\alpha_m g_m][J_m Y_1(K_m b) - Y_m J_1(K_m b)] N^+(\alpha_m) M^+(\alpha_m)}{2\alpha_m(\alpha + \alpha_m)}, \tag{19a}$$

$$V(\alpha) = M(\alpha) N(\alpha) = V^+(\alpha) V^-(\alpha) \tag{19b}$$

$V^+(\alpha)$ and $V^-(\alpha)$ which are regular and don't have zeros in the regions $\text{Im}(\alpha) < \text{Im}(k)$ and $\text{Im}(\alpha) > \text{Im}(k)$ respectively. $V^+(\alpha)$ is obtained as below using the procedures explained in [9].

$$V^+(\alpha) = \sqrt{V(0)} e^{\left\{ \frac{i\alpha(b-a)}{\pi} \left[1 - C - \ln\left(\frac{2\pi}{k(b-a)} \right) + i\frac{\pi}{2} \right] + \frac{K(\alpha)(b-a)}{\pi} \ln\left(\frac{\alpha + iK(\alpha)}{k} \right) - \frac{1}{2} i(b-a)K(\alpha) + q(\alpha) \right\}}$$
$$\prod_{l=1}^{L} \left(\frac{\beta_l - \alpha}{\beta_l + \alpha} \right)^{1/2} \prod_{m=0}^{\infty} \left(1 + \frac{\alpha}{\alpha_m} \right) e^{\left(\frac{i\alpha(b-a)}{m\pi} \right)} \tag{20}$$

$$q(\alpha) = \frac{1}{2} P \int_0^{\infty} K_w(w) \ln\left[\frac{\sqrt{k^2 - w^2} + \alpha}{\sqrt{k^2 - w^2} - \alpha} \right] dw, \tag{21a}$$

$$K_w(w) = \frac{(b-a)}{\pi} + \frac{1}{2\pi i} \left[B_w(w) + B_w(we^{i\pi}) \right] \tag{21b}$$

$$B_w(w) = \frac{bH_1^{(1)}(wb)}{H_0^{(1)}(wb)} + \frac{\left[H_1^{(1)}(wb) - H_0^{(1)}(wb) \right] \begin{bmatrix} T_{00}(w) & T_{01}(w) \\ T_{10}(w) & T_{11}(w) \end{bmatrix} \begin{bmatrix} ik\eta a \\ -\left(\frac{i2k\eta}{w} + a \right) \end{bmatrix}}{\left[H_1^{(1)}(wb) - H_0^{(1)}(wb) \right] \begin{bmatrix} T_{00}(w) & T_{01}(w) \\ T_{10}(w) & T_{11}(w) \end{bmatrix} \begin{bmatrix} w \\ ik\eta \end{bmatrix}} \tag{22}$$

$$T_{ij}(w) = Y_i(wb) J_j(wa) - Y_j(wa) J_i(wb), \quad i,j = 0,1 \tag{23}$$

C in (20) is Euler constant which is $C = 0.57721\ldots$. $\pm\beta_l$ are the roots of $N(\alpha)$. P in (21a) signifies that Cauchy principle value of the integral has been considered.

Let the axially symmetric TM$_{00}$ mode incident field be represented by [1]

$$u^i = \left[J_1(\xi_0\rho) - \frac{J_0(\xi_0 b)}{Y_0(\xi_0 b)} Y_1(\xi_0\rho) \right] e^{i\beta_0 z}, \tag{24}$$

where β_0 is the propagation constant for dominant mode related to ξ_0 by the equation $\beta_n = \sqrt{k^2 - \xi_n^2}$, $n = 0, 1, 2, \ldots$ with $n = 0$. ξ_n is determined by the characteristic equation

$$\frac{ik\eta_1 \left[J_1(\xi_n a) Y_0(\xi b) - J_0(\xi_n b) Y_1(\xi_n a) \right] + \xi \left[J_0(\xi_n a) Y_0(\xi_n b) - J_0(\xi_n b) Y_0(\xi_n a) \right]}{Y_0(\xi_n b)} = 0 \tag{25}$$

Size of the waveguide is chosen such that only the one real root of the equation will be allowed. This signifies the dominant mode. The important point to be noted is that only the inductive guiding surface ($\eta_1 = iX_1$) may support the TM$_{00}$ mode. In the waveguide region the scattered field $u_3(\rho, z)$ can be expanded into a series of normal modes as

$$u_3(\rho, z) = c_0 \left[J_1(\xi_0\rho) - \frac{J_0(\xi_0 b)}{Y_0(\xi_0 b)} Y_1(\xi_0\rho) \right] e^{-i\beta_0 z} + \sum_{n=1}^{\infty} c_n \left[J_1(\xi_n\rho) - \frac{J_0(\xi_n b)}{Y_0(\xi_n b)} Y_1(\xi_n\rho) \right] e^{-i\beta_n z} \tag{26}$$

The first term of the right side of (26) describes the reflected field for the dominant mode.

The unknown coefficients f_m, g_m and c_n appearing in (12b) and (26), respectively are to be determined trough the following matching conditions derived from continuity relations (6a), (6b)

$$\Delta_m g_m = (c_0 + 1) I_0^{(1)} + \sum_{n=1}^{\infty} c_n I_n^{(1)}, \tag{27a}$$

$$\Delta_m f_m = i\beta_0 (1 - c_0) I_m^{(1)} - \sum_{n=1}^{\infty} i\beta_n c_n I_n^{(1)} \tag{27b}$$

$$-\frac{\pi K_m b}{2} [f_m - i\alpha_m g_m] \Delta_m = N^+(\alpha_m) M^+(\alpha_m) b \sum_{n=0}^{\infty} \frac{[f_n - i\alpha_n g_n] N^+(\alpha_n) M^+(\alpha_n)}{2\alpha_n (\alpha_m + \alpha_n)} I_n^{(2)},$$
$$m = 0, 1, 2, \ldots \tag{28}$$

with

$$I_n^{(1)} = \int_a^b \left[J_1(\xi_n\rho) - \frac{J_0(\xi_n b)}{Y_0(\xi_n b)} Y_1(\xi_n\rho) \right] [J_0(K_m b) Y_1(K_m\rho) - J_1(K_m\rho) Y_0(K_m b)] \rho \, d\rho \tag{29}$$

$$I_n^{(2)} = J_n Y_1(K_n b) - Y_n J_1(K_n b), \tag{30}$$

where $Y_n = Y(\alpha_n)$, $J_n = J(\alpha_n)$. (27a), (27b) (28)–(30) form an infinite system of linear algebraic equations which is used to calculate the unknown coefficients.

4. SCATTERED FIELDS AND NUMERICAL RESULTS

The radiated field $u_1(\rho, z)$ can be obtained by evaluating the following integral

$$u_1(\rho, z) = \int_L \frac{P^+(\alpha)}{bK(\alpha) H_0^{(1)}[K(\alpha) b]} H_1^{(1)}[K(\alpha)\rho] e^{-i\alpha z} d\alpha \tag{31}$$

The evaluation of the above integral by using steepest descent path method gives rise to the far field asymptotic expression of $u_1(\rho, z)$ as follows:

$$u_1(r, \theta) = H(\theta) \frac{e^{ikr}}{kr}, \quad H(\theta) = -\frac{1}{\pi b \sin\theta} \frac{F^+(-k\cos\theta)}{H_0^{(1)}[kb\sin\theta]} \tag{32}$$

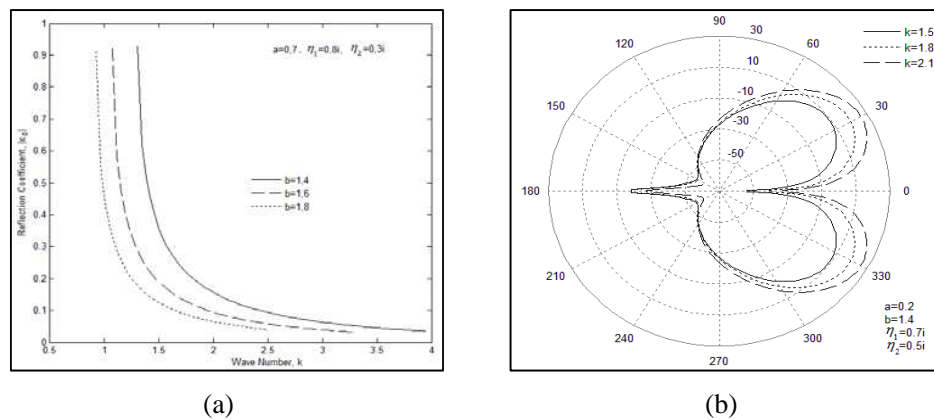Here r and θ denote spherical coordinates defined by $\rho = r\sin\theta$, $z = r\cos\theta$.

Figure 2: (a) Variation of the amplitude of the reflection coefficient $|c_0|$ against k for different values of outer radius b. (b) Variation of the $20 \log |u_1|$ versus observation angle for different values of k.

The coefficient c_0 corresponds to the amplitude of the reflected field is obtained by numerical calculation of the infinite system of linear algebraic Equations (27)–(30). Figure 2(a) shows the variation of the amplitude of the reflection coefficient $|c_0|$, against the wave number for three different values of b while $a = 0.7$, $\eta_1 = 0.8i$, $\eta_2 = 0.3i$. It is seen that the amplitude of the reflection coefficient decreases rapidly with increasing values of the frequency. Figure 2(b) shows the variation of the amplitude of the radiated field, $20 \log |u_1|$ against observation angle for three different values of wave number k while $a = 0.2$, $b = 1.4$, $\eta_1 = 0.7$, $\eta_2 = 0.5i$. It is observed that the amplitude of the radiated field increases especially observation angle θ between $(0°, 60°)$ degrees with increasing values of the frequency.

REFERENCES

1. Vijayaraghavan, S. and R. K. Arora, "Scattering of a shielded surface wave in a coaxial waveguide by a wall impedance discontinuity (correspondence)," *Trans. Microwave Theory Tech.*, Vol. 19, No. 8, 736–739, Aug. 1971.

2. Bird, T. S., "TE$_{11}$ mode excitation of flanged circular coaxial waveguides with an extended centre conductor," *IEEE Trans. Antennas and Propagat.*, Vol. 35, 1358–1366, 1987.

3. Bird, T. S., "Exact solution of open-ended coaxial waveguide with centre conductor of infinite extent and applications," *IEE Proceedings H*, Vol. 134, No. 5, 1987.

4. Saoudy, S. A. and B. Sinha, "Wiener-Hopf type analysis of dielectric-coated dipole antenna in relatively dense medium," *IEEE Trans. Antennas and Propagat.*, Vol. 39, No. 8, 1057–1061, Aug. 1991.

5. Hacıvelioğlu, F. and A. Büyükaksoy, "Analysis of a coaxial waveguide with finite-length impedance loadings in the inner and outer conductors," *Hindawi Publishing Corporation Mathematical Problems in Engineering*, Vol. 2009, Article ID 473616, 18 Pages, 2009, Doi: 10.1155/2009/473616.

6. Hacıvelioğlu, F. and A. Büyükaksoy, "Scattering of the TEM mode at the junction of perfectly conducting and impedance coaxial waveguides," *Electrical Engineering*, Vol. 92, Nos. 4–5, 2010.

7. Tayyar, I. H. and A. Büyükaksoy, "A Wiener-Hopf analysis of the coaxial waveguide radiator," *2011 International Conference on Electromagnetics in Advanced Applications (ICEAA)*, 580–583, Sep. 12–16, 2011.

8. Sneddon, I. H., *The Use of Integral Transforms*, McGraw-Hill, New York, 1972.

9. Mittra, R. and S. W. Lee, *Analytical Techniques in the Theory of Guided Waves*, McMillan, New York, 1971.

One Way Speed of Light and Why Nothing Can Be Faster Than Light

V. N. Matveev and O. V. Matvejev

Homo Sapiens Publishers, Vilnius, Lithuania

Abstract— The problematic nature of synchronizing clocks consists of the use of the condition of the equality of the speed of light in opposite directions for clock synchronization in the STR, while the experimental verification of this equation is considered impossible in principle. Einstein, by alluding to the impossibility of measuring velocity in one direction without arbitrary assumptions, assumed that the speed of light propagation in a vacuum from point A to point B is equal to the speed of light passing from B to A. Does nature not permit us to measure the speed of light in one direction without arbitrary assumptions? Did S. Marinov and his followers measure the one way speed?

In the paper method and device for measuring the speed of light in a single direction without arbitrary assumptions are discussed.

A possible cause of the boundedness of the velocity of material objects is demonstrated without reference to the provisions of the special theory of relativity. A condition is formulated on the basis of which the assumption of the movement of material objects at any arbitrarily prescribed velocities proves to be self-contradictory in instances when the arbitrarily prescribed velocities of the objects exceed a certain value. This condition consists of the existence of massles signals and particles that are propagated in space and inside material objects at a velocity greater than any prescribed velocity of the material objects and particles that do have mass.

1. INTRODUCTION

The problematic nature of synchronizing clocks consists of the use of the condition of the equality of the speed of light in opposite directions for clock synchronization in the STR, while the experimental verification of this equation is considered impossible in principle. In order to measure the speed of light from point A to point B, then from point B to point A, and then to compare these speeds, it is necessary to have synchronously running clocks at points A and B. However, in the STR it is only possible to synchronize the clocks at points A and B using the Einstein method by assuming that these velocities are equal even before they are measured. Naturally, after this assumption is made, they also become equal based on the measurement results.

It is also not possible to measure velocity by synchronizing a pair of clocks at point A, then moving one of them to point B, since the result of the synchronization and measurement of the speeds of light from point A to point B and back, v_{AB} and v_{BA}, respectively, is dependent upon the speed at which the clocks are transported from one point to the other.

It is frequently said that Rømer measured the speed of light in one direction. It may seem strange, but Rømer velocity is also the velocity obtained under the tacit assumption of the equality of the speeds of light in opposite directions. The fact of the matter is that Rømer and Cassini were speculating about the movement of Jupiter's satellites, automatically assuming that the observers' space was isotropic. The Australian physicist L. Karlov [1] showed that Rømer actually measured the speed of light by implicitly making the assumption of the equality of the speeds of light back and forth.

Poincare examined the proposition of the equality of the speed of light from A to B and the speed from B to A, and this proposition in particular became the principal postulate of Einstein's 1905 work [2], although it was not presented in the form of a postulate, but rather in the form of a "definition", which preceded two Einsteinian principals that are often called postulates. Later Einstein called this "definition" an assumption, during which he noted that it pertains not only to the speed of light, but also to velocity in general.

It is often said that the equality of the speeds back and forth is obvious, since space is isotropic, and that inequality is unobvious. This is not the case. The fact that light requires more time to move from point A to point B than to move from B to A is also obvious if, for example, point A is located in the stern and point B in the bow of a spacecraft that is moving relative to us and we track the process of light movement from A to B and back not from within, but rather from without. In principle, both the equality and the inequality of this craft's light propagation times from point A

to point B and back can be found from a host of other reference systems that are in motion relative to this craft, even if the clocks of these systems have been synchronized using Einstein's method. In this vein, what is the basis on which the clock inside the craft is synchronized without allowance for the objective results of the observation of light behavior inside the craft obtained from different reference systems outside the craft?

During the 1960s and 1970s, references were often encountered in abstract journals to foreign works in which versions of the special theory of relativity based on the proposition of the inequality of the speeds of light in opposite directions were examined. These versions were called ε-STR and consistently described everything that the STR describes. In truth, most of them were more "ponderous" and less convenient than Einstein's version, since they violated the requirement of the immutability of the mathematical form of notation of laws in different reference systems. Most of the works of these authors were not opposed to Einstein's version, but rather demonstrated the consistency of an untraditional approach. The authors of these works attempted, by disrupting the mathematical beauty of the STR, to uncover its physical content and to clear up the enigma of the speed of light in one direction. Why nature does not permit us to measure the speed of light in one direction without arbitrary assumptions! Is this randomness or something deeper? The developers of the alternative theories did not answer this question.

2. ONE WAY SPEED OF LIGHT. DEVICE AND METHOD FOR MEASURING IT

And yet, a method does exist for measuring the speed of light in a single direction without arbitrary assumptions. This method was proposed by S. Marinov and implemented by S. Marinov himself and his followers [3–5]. Here we consider a method similar to the Marinov's method and a device for measuring the speed of light in one direction and analyze the features associated with this measurement.

The essence of this method and the means for implementing it consist of the following.

Imagine a long cylindrical elastic rod, S, to the edge, A, of the cylindrical surface of which a great number of strokes evenly arranged around the periphery is applied. At a certain moment in time, the rod is set into rotation around the axis of the cylindrical surface, for which purpose torque is applied to end A of the rod. After an angular spin rate of equaling ω_0 is achieved, the predetermined angular velocity of end A is rigorously maintained.

Let's assume a sensor is located alongside rod end A that records the passage of the strokes near it and simultaneously generates pulses that proceed to a counter. The pulse counter transmits data concerning the number of pulses reaching it to a device that performs the function of a clock after the constancy of the angular velocity of rod end A is established, converting the number of pulses received by the counter into a time reading.

Let us further assume that precisely the same instruments as near end A, including a pulse counter and a clock, are installed at the other end of rod S — end B, and that precisely the same strokes as on end A are located on the cylindrical surface of end B. During the initial period of time, when the rod is rotating at an increasing rate, the angular velocity of end B is less than that of end A due to a delay in torque transmission. If a straight guide line is applied along the generatrix of the rod's cylindrical surface over its entire length before the rod is set into a state of rotation, the guide line on the cylindrical surface of the rod takes on a helical shape during this period of time. When the angular acceleration of end A is sufficiently low, only a poorly expressed helicity (a quite large helix pitch) that does not lead to extreme rod deformation can be achieved. After a certain amount of time, the angular velocity of end B becomes constant and equals ω_0. Under steady-state conditions, it cannot be otherwise, since the difference in the angular velocities of the ends would lead to gradual "twisting" and to rod breakage. We will assume that there are no residual strains in the freely rotating rod and that no external braking forces act on it (the rod is rotating in a vacuum, or in the ideal case, in a state of weightlessness). Under these conditions, the clocks on the ends of the freely rotating rod with a straightened guide line run synchronously.

In confirming this, we proceed on the basis of the fact that if the pulse counters installed on both ends of the rods are zeroed out before end A starts to spin, both ends must then make an identical number of revolutions by the time the helix disappears. For this reason, the counter guide lines must transfer identical numbers to the clocks when helicity is absent, and the clocks must provide identical readings.

Clocks synchronized in this way can be used to measure the speed of light in a single direction — from end A to end B of a rod or vice versa. Clock synchronicity does not require arbitrary assumptions concerning the nature of the speeds of light in opposite directions.

If the postulate concerning the equality of the speeds of light in opposite directions proposed in the special theory of relativity is true in the physical sense, the result of the measurement of the one-way speed of light by the clocks must then be the acquisition of a velocity value that equals the constant c. Due to the equality of inertial frames of reference, such an experimental result must not be dependent upon the selection of the inertial frame of reference within which an experiment is conducted.

In the Lorentz ether theory, physical ether time and physical ether simultaneity are absolute. If the device described above is at rest in the ether, then the straight guide line on the cylindrical surface of a rod after it is set into a state of free rotation must remain straight due to ether space anisotropy and due to rod symmetry. On the other hand, since physical simultaneity in the ether theory is absolute, a straight guide line on a rotating rod that is simultaneously recorded in one inertial frame of reference must also remain straight in another inertial frame of reference. Furthermore, guide line straightness on all similar rods at rest or in motion in the ether at different velocities must be retained in all inertial frames of reference. But absolute ether simultaneity leads to the inequality of the speeds of light in opposite directions in inertial systems that are in motion in the ether. For this reason, the speeds of light measured by the aforementioned clocks located on the ends of a rotating rod in opposite directions must be different if the rotating shaft is moving through the ether in the axial direction.

3. WHY NOTHING CAN BE FASTER THAN LIGHT

We will presume to postulate a condition during the satisfaction of which the fact of the finiteness of velocity becomes obvious and stops contradicting everyday common sense, while the possibility of a boundless increase in the velocity of tangible objects fully emerges beyond the framework of everyday common sense.

This condition is as follows: "*Massles signals and particles that are always present in material objects are propagated at a velocity, V, that is unattainable for physical objects and particles that do have mass, continuously initiate interactions and processes in these bodies*".

The condition does not contain a limitation of the velocity of tangible objects, but also does not contradict it. As we will demonstrate further on, this limitation proves to be a consequence, not a requirement of the condition. However, while observing the condition and temporarily skirting the prohibitions of the special theory of relativity, let us *a priori* assume the existence of velocities of solid physical bodies and particles that equal any prescribed values. Here, in order to satisfy the requirement of the unattainability of the velocity of massless interaction signals and carrier particles by these bodies and particles that is contained in the condition, we will presume that any prescribed postulated velocity, v, in all our speculations is negligible as compared to the postulated velocity, V.

Can we, by satisfying the condition cited above, conceptually dispatch a free-moving signal or solid body to point A, located a distance of L from a certain material body at rest (in our reference system), at a predetermined velocity and bring it back in such a way that they almost instantaneously fly to and fro, traversing a distance of $2L$ in this instance?

At first glance, we can — after all, we are able to assign the body any v velocity, and according to the condition we formulated, the V velocity of a signal is much greater. But before we rush to judgment, can we pause to ponder the content of the concept of "instantaneously"?

What does "instantaneously" mean?

In the metrological sense, "instantaneously" means a zero variation in the readings of arbitrarily accurately running clock between the times when a body or signal is dispatched and it returns. In the physical sense, "instantaneously" means that no processes and variations occurred between these times — even at the microlevel. The dispatch time and the return time must merge together in this instance. After all, if any processes and variations occurred in a body between these times, then by occurring in time, the processes and variations required a specific amount of time. This means that the times are separated by a time interval to which the arbitrarily accurately running clock must react by a change in their readings.

We now wonder is it possible for an arbitrarily fast-moving body or signal to traverse a distance of $2L$ while no variations occur in a body at rest?

No, this is not possible if the condition we formulated is valid, and there are interaction signals and carrier particles in the body at rest that are propagated at a velocity of V and that initiate events.

Let us remember that everything changes at the microlevel in material bodies, without stopping

for even the tiniest period of time. Interaction signals and carrier particles that exchange the elements of material bodies are responsible for many processes and events in these bodies.

Being found in material bodies in a state of motion at a velocity of V according to the condition we formulated, interaction signals and carrier particles initiate the accomplishment of events. If the average distance, λ, between material body elements interacting in a certain way is considerably less than the entire $2L$ path, then when a (massless) signal moving to point A and back covers a total of a small part of the path it is traversing, which equals λ, each of the event-initiating interaction signals and carrier particles of a specific type present in a body at rest produces an interaction in the mean statistical sense. However, during the time of travel of a signal to point A and back, and its traversal of a distance of $2L$, $2L/\lambda$ times more events of a given type are accomplished in a body at rest than when traversing a short distance equaling λ. But if there are interactions in a body, the body then changes in time, and arbitrarily accurately running clock must react to these changes by way of a variation in readings.

4. CONCLUSION

A method for measuring the speed of light in a single direction without arbitrary assumptions is discussed. Such a method was implemented in Marinov's experiment and is considered by his followers.

Clock, synchronized by the proposed method can be used to measure the speed of light in one direction. If the postulate concerning the equality of the speeds of light in opposite directions proposed in the special theory of relativity is true in the physical sense, the result of the measurement of the one-way speed of light by the clocks must then be the acquisition of a velocity value that equals the constant c. If ether exists, then the speeds of light measured by the clocks located on the ends of a rotating rod in opposite directions must be different if the rotating shaft is moving through the ether in the axial direction.

We initially examined the conditions under which the velocity of material bodies has a limited nature based on the example of the model (the simulation of the special theory of relativity) described in references [6–8]. We later departed from this model and made the transition to the examination of the question independent of it. However, the considerations set forth in the aforementioned works in particular impelled us toward the logical solution of the problem of the finiteness of velocity and made it possible to answer the questions arising during the resolution of this problem.

REFERENCES

1. Karlov, L., "Does Rømer's method yield a unidirectional speed of light?," *Australian Journal of Physics*, Vol. 23, No. 3, 243–253, 1970.
2. Einstein, A., "On the electrodynamics of moving bodies," *Annals of Physics*, Vol. IV, No. 17, 891–921, 1905.
3. Marinov, S., *Found. Phys.*, Vol. 8(1/2), 137–156, 1978.
4. Ahmed, Md. F., B. Quin, S. Sargoitchev, and A. D. Staufer, "To re-consider the one-way speed of light using Fizeau-type-coupled-slotted-disks," http://arxiv.org/abs/1103.6086.
5. Ahmed, Md. F., B. Quin, S. Pagiatakis, and A. D. Staufer, "Results of a one-way experiment to test the isotropy of the speed of light," http://arxiv.org/abs/1310.1171.
6. Matveev, V. N. and O. V. Matvejev, "Simulation of Kinematics of special theory of relativity," http://arxiv.org/abs/1201.1828.
7. Matveev, V. N. and O. V. Matvejev, "Simulations of relativistic effects, relativistic time and the constancy of light velocity," L. R. Amoroso, L. H. Kauffman, P. Rowlands (eds.), *The Physics of Reality: Space, Time, Matter, Cosmos: World Scientific, The VIII-th Symposium Honoring Mathematical Physicist Jean-Pierre Vigier*, 100–106, Covent Garden, London, UK, Aug. 15–18, 2012; 2013.
8. Matveev, V. N. and O. V. Matvejev, *An Entertaining Simulation of the Special Theory of Relativity Using Methods of Classical Physics*, LIBROKOM Book House, Moscow, 2012.

Experimental and Numerical Analyses of Leakage Flux Distribution in Core-type Voltage Transformers

Fevzi Kentli[1], İsmail Bozkurt[2], and Nevzat Onat[2]

[1]Faculty of Technology, Marmara University, Turkey
[2]Vocational School of Technical Studies, Marmara University, Turkey

Abstract— This study is based on leakage magnetic flux analysis of a core type transformer. The distributions that obtained experimentally were compared with two-dimensional FDM and FEM calculation results to verify. The experiment set includes a voltage transformer and measurement coils that are used to determine leakage flux distribution around of transformer iron leg. With the solution of the matrix created by measuring the induced voltage, polynomial mathematical equations were obtained. Then flux values have been calculated in accordance with the numerical methods. In order to compare the results, plotting of the flux distribution is the best solution. For this purpose, total flux lines was determined. In addition, the difference between the smallest and largest value of the vector potential is also determined. The voltage (potential difference) vector is calculated by dividing the difference to flux lines. In the last step, the equipotential points were determined by adding to the minimum potential value. This process was repeated for eight different heights in the legs and two-dimensional coordinates of the equipotential point was determined at each height. By combining the same valuable points, flux distribution was obtained graphically. Finally, fluxes have been drawn in line with the measurement and calculation results, and have been compared with each other. As a result, leakage flux distribution of voltage transformer is obtained and it is observed that FEM calculates closer values to the measurements. According to the study results, the using of the measurements from several points taken with magnetic field probes in FEM model, can provide sufficient accuracy solutions.

1. INTRODUCTION

Magnetic flux measurement is a process that usually needs to be done during in service periods of machines. Especially in large power transformers, the measurement around the core during operation includes a variety of challenges. Since fluxes always complete their circuits by following the path of lowest magnetic resistance, refractions occur when the magnetic resistance of the path followed over the air becomes higher than the path over the metal sheet. Therefore, leakage fluxes are usually low, and they practically compose 5% of the useful flux. Despite their low value, leakage fluxes play a significant role in the operation of not only stationary-type machines but also rotating machines [1, 2]. Recognition of the flux distribution in machines is required for three reasons: 1) measurement of the inductances, 2) the forces applied to the coils, and 3) the additional losses that occur in the coils and steel parts. The finite different (FDM) and the finite element (FEM) methods [3–6] are the main approximation in this area. Among these methods, applications are the determination of losses [7, 8], magnetic flux, and circulating current analysis of new age amorphous modular transformers [9], superconducting high voltage transformers [10], and planar transformers [11] that are commonly used at low voltages, the computation of electromagnetic forces created by short-circuit faults [12], and in obtaining equivalent simulation models [13]. In addition, two-dimensional (2D) FEM is used in leakage flux analysis of electrical machines. In references [14–16], leakage flux analyses of mono-phase induction motor, transverse flux motor, and three-phase induction motor are realized with 2D FEM respectively. Reference [17] also investigates the effects of leakage fluxes on magnetic materials using 2D FEM. Khelil and Elleuch have proposed that the effects of the air gap on a magnetic-equivalent circuit can be determined by the FEM without the need for experimental measurements [18]. Similarly, in reference [19], the losses and distribution of current density in the conductors for a large air gap transformer were calculated by 3-D FEM. Hernandez et al. developed the Gaussian model for the magnetic flux analysis of transformers, using it to obtain the equivalent permeability and reluctance circuit, and compared the result with the FEM [20]. Hernandez and Arjona calculated efficiency, losses, impedance, magnetic flux density, and the magnetization current of a transformer using a hybrid FEM and knowledge-based system; the results are remarkably close to the values provided by the manufacturer [21]. Localized flux measurements in a wound core transformer are realized and extended by FEM to the point that

values are unknown in reference [22]. Leakage flux distribution in large power transformers was examined by Me and Zhang with 3-D FEM [23].

In this study, leakage magnetic flux distributions that were obtained using FEMM software has been compared with the results obtained by measurements. In the next section, the method that is used for drawing the flux lines is described. The third section involves the introduction about the test set and also includes an analysis of the outputs and calculation results. The last section consists of analyzing the obtained output.

2. DRAWING THE FLUX LINES

Taking the potential difference between the flux lines is a basis: If the differences between the flux lines, that is to say the increases (or decreases), are requested to be a certain value, the drawing starts from the lowest or highest value. The value of the next flux line is different from the previous flux line at a value equal to the amount of increase (or decrease). In this method, the total number of lines is equal to the amount of increase (or decrease) in the difference between the highest value and the lowest value. The potential value of the line, which will be drawn, is compared with the potential value of the two adjacent nodes of each element. After this comparison, the coordinate of the equipotent point can be calculated by utilizing the coordinates of the adjacent nodes. In this study, an equipotent line crossing over a triangular element was considered as in reference [24].

3. EXPERIMENTAL STUDIES

In experimental studies, the primary coil of transformer was supplied from a synchronous generator. Measurements have been performed at eight different heights (55 mm–125 mm) starting from the inner corner of the leg and at two different primary currents (2.1 A–4.1 A). There is not any device which measures the magnetic flux distribution directly. For this reason, measuring coils are used to realize this process. The magnetic field of a coil induced a voltage (U_{ind}) that can be expressed as:

$$U_{ind} = \frac{\omega \cdot B \cdot A \cdot N}{\sqrt{2}} \tag{1}$$

In this equation, B, A and N represent magnetic flux density (T), cross-section of the coil (m^2) and number of turns, respectively. ω is also angular velocity (Rad/s). Thus, flux density (B) can be calculated by measuring the induced coil voltage [25]. Figure 1 shows the perspective view of the transformer with measuring coils and the photo of experimental set.
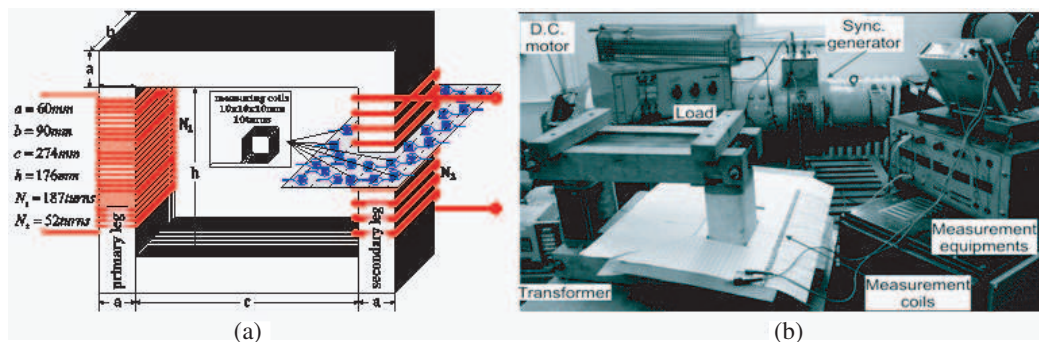

Figure 1: (a) Appearance of the transformer and measuring coils. (b) The photograph of the test set.

Superficial flux distribution in the secondary leg of the transformer has been drawn for eight different heights using FEMM software. For the drawing process, first the surface on which the flux distribution was divided into 3232 elements is shown in Figure 2. Then, equipotent points were calculated and superficial flux distributions were obtained by FEMM software and are also shown in Figure 2. Flux values and coordinates of a, b, c, and d points are given in Table 1.

Lastly, the flux distributions in the secondary leg of the experiment voltage transformer were drawn using these superficial flux distributions. A rectangular-lined central domain shown in the figures is the section where the secondary leg crosses. The flux distributions within this domain are the beneficial flux distributions. As for the flux distributions outside this domain, they show the leakage flux distributions. The coordinates of any point on the flux lines and the magnitudes belonging to the flux on that point can be determined using the computer program. Boundary
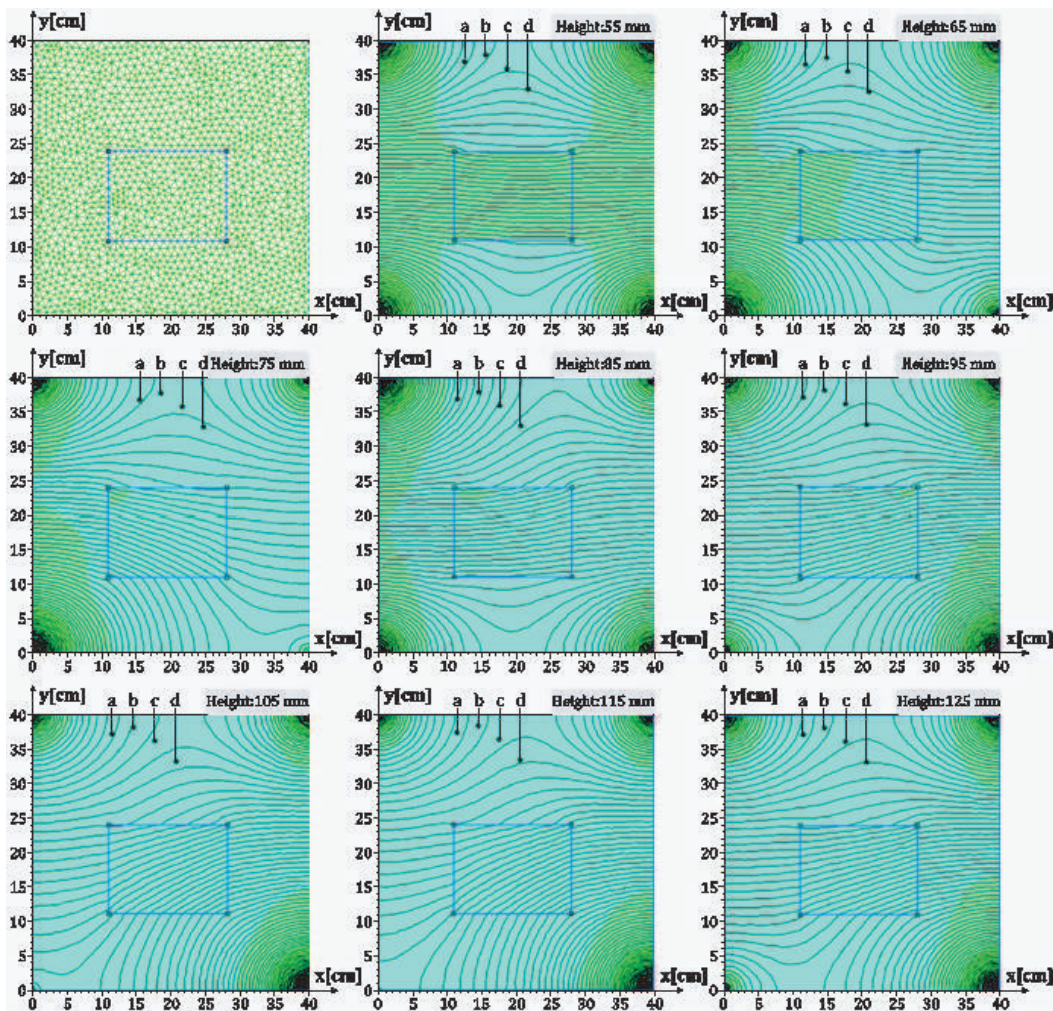
Figure 2: 3232 triangle finite elements for flux distribution measurement (top left) and surface flux distributions at eight different heights on the secondary leg.

Table 1: Flux values and coordinates of measurement points.

Point	Coordinates (x, y)	Flux values [x10^{-7} Wb]							
		55 mm	65 mm	75 mm	85 mm	95 mm	105 mm	115 mm	125 mm
a	(13.9-37.8)	0.2773	0.3516	0.4914	0.3679	0.2605	0.2225	0.2323	0.2141
b	(15.0-36.5)	0.2800	0.3556	0.4976	0.3724	0.2628	0.2244	0.2343	0.2158
c	(20.0-36.5)	0.2826	0.3578	0.5050	0.3816	0.2661	0.2276	0.2370	0.2186

values must be determined in order to calculate the potential value in each measuring coil in Figure 1 and to compare the measurement results. The measurement values and flux distributions drawn according to the two different flux values ($1.74 \cdot 10^{-7}$ Wb and $2.14 \cdot 10^{-7}$ Wb) using FEM and FDM are given in Figure 3 in order to compare them to one another. It suggests that at a height of 55 mm (from the leg), 0.4746 mV (or $2.14 \cdot 10^{-7}$ Wb flux value) is observed at a horizontal distance of 83 mm, 77 mm and 92 mm according to the measurement results, FDM, and FEM calculations, respectively. At a height of 95 mm, the same potential value is observed at a horizontal distance of 92 mm. Similarly, for $1.74 \cdot 10^{-7}$ Wb flux value, these results are measured as 55 mm, 110.24 mm, and 169.44 mm respectively.
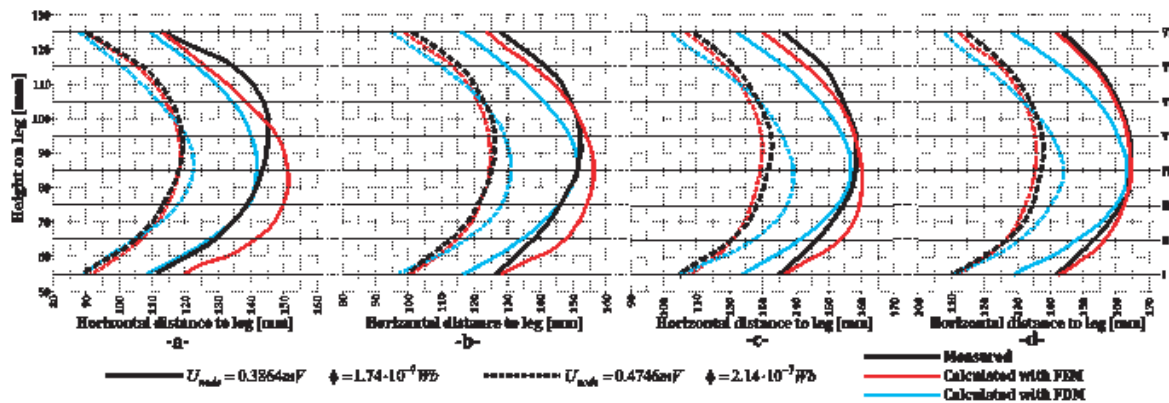
Figure 3: Comparison of the flux distributions for different horizontal distances from secondary leg of transformer.

4. CONCLUSION

This study is based on a comparison of flux distributions of a core type voltage transformer. The experimental set was established to measure real time flux components. Results of measurements and calculations obtained from the most useful numerical methods (FEM and FDM) were compared with each other. It shows that if a good imitation and definition is in place, numerical methods are superior in terms of accuracy in the detection of flux distributions.

As seen in Figure 3, FEM and FDM offer very close results for a network that contains an equal number of unknowns. Moreover, the numerical methods provide adequate close results in terms of the flux distributions compared to experimental measurements. Furthermore, flux distributions that were calculated using FEM and obtained from the measurement results were shown to be very close to each other (slopes nearly overlap). In the study, the results obtained using triangular elements and the approximation function of the first degree were found to be adequate, but the degree of the polynomial has not been increased accordingly. The accuracy rate can be increased by increasing the polynomial used in FEM. FEM can be more reliable depending on the sizes of the finite elements and the flexibility of the figures. Boundary conditions can be easily implemented, and an unlimited number and boundary conditions can be obtained. Thanks to the multifaceted and flexible structure of these methods, environment and field relations in complex structures as well as cause-effect relationships in different problems can be constantly calculated efficiently. The results obtained show that both numerical methods can be applied effectively and easily in determining leakage flux of voltage transformers. These methods can also be used for different transformer model in future investigations.

ACKNOWLEDGMENT

REFERENCES

1. Faghihi, F. and H. Heydari, "Reduction of leakage magnetic field in electromagnetic systems based on active shielding concept verified by eigenvalue analysis," *Progress In Electromagnetics Research*, Vol. 96, 217–236, 2009.
2. Thayalan, D. T. and J. H. Park, "Transformer flux leakage modeling and optimization of contactless power converter with an air gap of l cm for small power applications," *Proceedings of International Conference on Electrical Machines and Systems*, 1507–1512, Busan, Korea, October 2013.
3. Sadiku, M. N. O., *Numerical Techniques in Electromagnetics*, 2nd Edition, CRC Press, Boca Raton, 2001.
4. Hutton, D. V., *Fundamentals of Finite Element Analysis*, McGraw-Hill, NY, USA, 2004.
5. Szabo, B. and I. Babuska, *Introduction to Finite Element Analysis*, John Wiley & Sons Ltd., 2011.
6. Roylance, D., "Finite element analysis," Department of Materials Science and Engineering, Massachusetts Institute of Technology, Cambridge, February 28, 2001.

7. Basak, A., C. H. Yu, and G. Lloyd, "Efficient transformer design by computing core loss using a novel approach," *IEEE Trans. Magn.*, Vol. 30, No. 5, 3275–3278, 1994.

8. Ram, B. S., "Loss and current distribution in foil windings of transformers," *IEE Proc. Generat. Trans. Distrib.*, Vol. 145, No. 6, 709–716, 1998.

9. Tomczuk, B. and D. Koteras, "Magnetic flux distribution in the amorphous modular transformers," *J. Magn. Magn. Mater.*, Vol. 323, No. 32, 1611–1615, 2011.

10. Li, X., Q. Chen, J. Sun, Y. Zhang, and G. Long, "Analysis of magnetic field and circulating current for HTS transformer windings," *IEEE Trans. Appl. Supercond.*, Vol. 15, No. 3, 3808–3813, 2005.

11. Bai, F., Z.-X. Niu, Y.-J. Shi, and D.-F. Zhou, "Finite element analysis of high voltage planar transformer," *Proceedings of the 7th International Symposium on Antennas, Propagation & EM Theory*, 1–4, Guilin, China, 2006.

12. Ahn, H. M., J. Y. Lee, J. K. Kim, Y. H. Oh, S. Y. Jung, and S. C. Hahn, "Finite-element analysis of short-circuit electromagnetic force in power transformer," *IEEE Trans. Ind. Appl.*, Vol. 47, No. 3, 126–1272, 2011.

13. Mohammed, O. A., Z. Liu, S. Liu, and N. Y. Abed, "Finite-element-based nonlinear physical model of iron-core transformers for dynamic simulations," *IEEE Trans. Magn.*, Vol. 42, No. 4, 1027–1030, 2006.

14. Kumar, A., S. Marwaha, A. Marwaha, and N. S. Kalsi, "Magnetic field analysis of induction motor for optimal cooling duct design," *Simulat. Model. Pract. Theor.*, Vol. 18, No. 2, 157–164, 2010.

15. Wang, X., J. Du, N. Ren, Z. Liu, and R. Tang, "Optimization of stator structure of transverse flux motor," *Proceedings of 19th International Workshop on Rare Earth Permanent Magnets & Their Applications*, 466–470, Amsterdam, Netherlands, 2006,

16. Widyan, M. S. and R. E. Hanitsch, "High-power density radial-flux permanent-magnet sinusoidal three-phase three-slot four-pole electrical generator," *Int. J. Electr. Power Energ. Syst.*, Vol. 43, No. 1, 1221–1227, 2012.

17. Zakaria, Z., M. S. B. Mansor, A. H. Jahidin, M. S. Z. Azlan, and R. A. Rahim, "Simulation of magnetic flux leakage (MFL) analysis using FEMM software," *Proceedings of IEEE Symposium on Industrial Electronics and Applications*, 481–486, Penang, Malaysia, 2010.

18. Khelil, M. and M. Elleuch, "Modeling of the air-gaps of overlapped joints in three-phase transformer iron core for using by FEM," *Proceedings of the 6th International Multi-Conference on Systems, Signals and Devices, SSD '09*, 1–9, Djerba, Tunusia, March 2009.

19. Sibué, J. R., J. P. Ferrieux, G. Meunier, and R. Périot, "Modeling of losses and current density distribution in conductors of a large air-gap transformer using homogenization and 3-D FEM," *IEEE Trans. Magn.*, Vol. 48, No. 2, 763–766, 2012.

20. Hernandez, I., F. Leon, J. M. Canedo, and J. C. Olivares-Galvan, "Modeling transformer core joints using Gaussian models for the magnetic flux density and permeability," *IET Electr. Power Appl.*, Vol. 4, No. 9, 761–771, 2010.

21. Hernandez, C. and M. A. Arjona, "Design of distribution transformers based on a knowledge-based system and 2D finite elements," *Finite Elem. Anal. Des.*, Vol. 43, No. 8, 659–665, 2007.

22. Loizos, G., T. D. Kefalas, A. G. Kladas, and A. T. Souflaris, "Flux distribution analysis in three-phase Si-Fe wound transformer cores," *IEEE Trans. Magn.*, Vol. 46, No. 2, 594–597, 2010.

23. Ma, X. and D. Zhang, "Computation of leakage flux and magnetic force in transformer by using field-circuit coupled finite element method," *Proceedings of the Power and Energy Engineering Conference (APPEEC)*, 1–4, Chengdu, Asia-Pacific, March 2010.

24. Kentli, F., İ. Bozkurt, and N. Onat, "FDM based flux distribution analysis method for electrical machines," *Prz. Elektrotechniczn.*, Vol. 89, No. 5, 6–10, 2013.

25. Tandler, D., "Messung Niederfrequenter Elektrischer und Magnetischer Felder," *Proceedings of the EMVU-Kongress*, 1–32, Germany, March 1995.

Multi-layer Transmission of Spoof Surface Plasmon Polaritons

Bai Cao Pan, **Zui Tao**, **and Tie Jun Cui**

State Key Laboratory of Millimetre Waves, School of Information Science and Engineering
Southeast University, Nanjing 210096, China

Abstract— Spoof surface plasmon polaritons (SSPPs) show a low-pass transmission property with a remarkable stop frequency due to the asymptotic property of the dispersion relationship. A series of SSPPs waveguides and their applications have been reported such as high efficiency transmission, ultra-thin waveguides and active device researches. However, in order to show more potential in combining with the traditional integrated circuits and achieve new-type plasmonic circuits, the SSPPs signal needs to be transmitted between multiple layers efficiently. Here, we propose a method to transmit such surface modes from one side of the substrate to the other side efficiently. In our design, a metallic hole inlayed inside the substrate is used to connect the traditional corrugated metallic strip waveguide on both sides of the substrate. The metallic hole could provide a decoupling effect near the transition parts between the two waveguide on different sides since the electromagnetic field distribution is remained. The simulation results show that our design could transmit the SSPPs wave from the top layer of the medium to the bottom layer without significant loss. On the other hand, through the modulation of the position of the metallic hole, a series of absorption peaks during the transmission frequency band appears because of the coupling in the superposition section of the two waveguides. It's simulated that such design could provide a broadband high-efficient multi-layer transmission with a controllable absorption and such absorption is only related to the superposition area of the corrugated metallic strip. Based on our design, SSPPs with ultra-short wavelength and high-confinement property are able to play a more important role in the plasmonic integrated circuits.

Surface plasmon polaritons (SPPs) are propagating surface modes along the interface of metal and medium with the normal component of the field decaying exponentially in the near-infrared and light frequency [1]. Such surface modes show a great confinement and much shorter wavelength property, which have been researched in a variety of areas and applications such as overcoming the diffraction limit [2], high-resolution imaging [3, 4], electromagnetically induced transparency (EIT) [5], photovoltaic improvement [6] and biosensing [7]. In 2004, Pendry et al. proposed a SPPs-like phenomenon on the surfaces perforated by holes [8]. On such basis, spoof SPPs have been designed and experimental observed both on terahertz and microwave frequency [9, 10]. In 2004, a high-efficient broadband Spoof SPPs waveguide based on ultrathin corrugated metallic strip was reported [11]. The design contains an excitation part of coplanar waveguide, a momentum matching part with gradually altering grooves and a Spoof SPP transmission part. Such waveguide provides a perfect broadband transmission property with rare loss which shows great potential for the SPP waveguide to be used in the plasmonic circuit and system applications.

Up to now, more and more applications of Spoof SPPs have been reported such as the tunable SPP filter [12] and the active circuit [13]. In order to use the Spoof SPPs in a wider area, it's of importance to combine the SPP devices and the traditional circuits. However, the traditional chip system is based on the multi-layer circuits. The transmission property of SPPs among different layers needs to be researched. In this paper, we proposed the well transmission between different layers with a metallic hole connecting the two parts of SPP waveguide. And we give the simulation results indicating that by modulating the location of the hole and the overlapping part, the waveguide could provide not only the efficient transmission but also some tunable rejecting peaks. The multi-layer transmission has great potential in applications of complex plasmonic system.

The schematic structure of the Spoof SPP waveguide is shown in Fig. 1(a). As is fully discussed in Ma's broadband highly efficient SPP waveguide, Spoof SPP modes are highly confined along such corrugated waveguide and mainly oscillate around the grooves with the component of the field inside the waveguide surface. At the transition part of a double-layer transmission where the field couples from the top side to the bottom side of the medium, the normal component of the electric field would be strengthened when the sickness of the medium gets thick, which would reduce the transmission efficiency.

Figure 2(a) shows the comparison of the transmission with and without the metallic hole when the sickness of the substrate is 0.8 mm. From the figure we can surely observed that the transmission
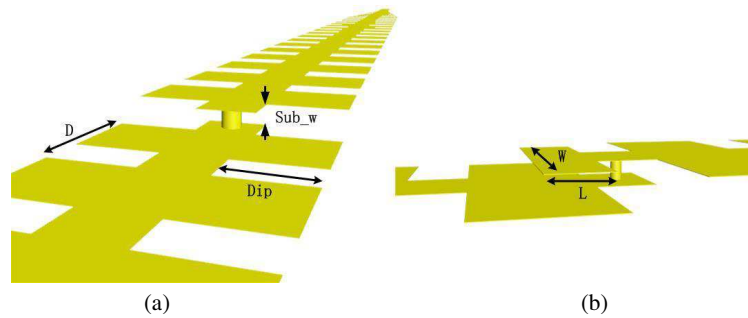
Figure 1: (a) The schematic structure of the double-layer spoof SPP waveguide. (b) The Spoof SPP waveguide with an overlapping part.

efficiency is improved when the metallic hole is added especially in high frequency band. And the cut-off effect is much better with a more cliffy falling edge.

Moreover, when the waveguides on both sides of the medium have an overlapping part instead of directly connected by the metallic hole, as is shown in Fig. 1(b), a strong resonance mode would be excited. By modulating the sizes of the overlapping rectangular patch, we could control the absorption frequency caused by the resonance. Fig. 2(b) exhibits the transmission coefficient under different width of the patch w. We can obviously observe that a distinguish rejection appears within the transmission with the efficiency over -18 dB and the rejection shifts to a lower frequency with the width of the patch increasing. Such controlment could also be achieved through the modulation of the length of the overlapping L.
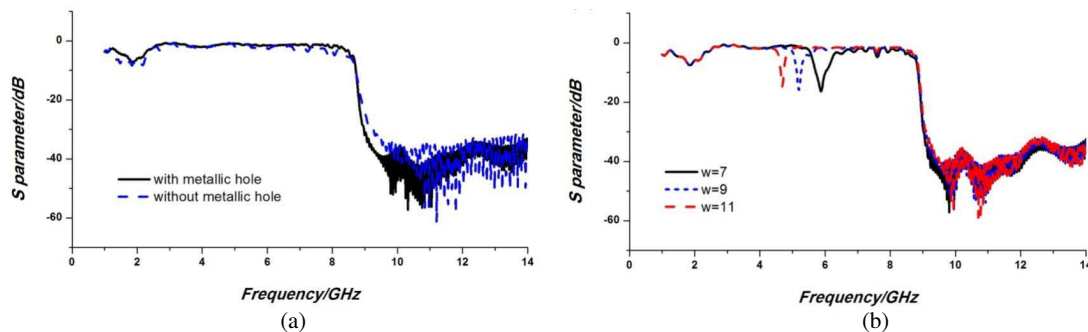

Figure 2: (a) The comparison of transmission with and without the metallic hole. (b) The absorption properties when the widths of the overlapping patch are $w = 7$ mm, 9 mm and 11 mm.

We proposed a method to realize the highly efficient transmission between different layers, and achieve a controllable absorption property by adding an overlapping corrugated unit at the transition part of the SPP waveguide. The metallic hole we add between the SPP waveguides on both sides of the medium helps to increase the efficiency especially with a thicker medium. Such design has great potential in the multi-layer plasmonic circuits and systems.

REFERENCES

1. Maier, S. A., *Plasmonics: Fundamentals and Applications: Fundamentals and Applications*, Springer Science & Business Media, 2007.

2. Gramotnev, D. K. and S. I. Bozhevolnyi, "Plasmonics beyond the diffraction limit," *Nat. Photonics*, Vol. 4, No. 2, 83–91, 2010.

3. Fang, N., H. Lee, C. Sun, and X. Zhang, "Sub-diffraction-limited optical imaging with a silver superlens," *Science*, Vol. 308, No. 5721, 534–537, 2005.

4. Wei, F. and Z. Liu, "Plasmonic structured illumination microscopy," *Nano Letters*, Vol. 10, No. 7, 2531–2536, 2010.

5. Han, Z. and S. I. Bozhevolnyi, "Plasmon-induced transparency with detuned ultracompact Fabry-Perot resonators in integrated plasmonic devices," *Opt. Express*, Vol. 19, No. 4, 3251–3257, 2011.

6. Atwater, H. A. and A.Polman, "Plasmonics for improved photovoltaic devices," *Nature Materials*, Vol. 9, No. 3, 205–213,2010.

7. Kabashin, A. V., P. Evans, S. Pastkovsky, et al., "Plasmonic nanorod metamaterials for biosensing," *Nature materials*, Vol. 8, No. 11, 867–871, 2009.

8. Pendry, J. B., L. Martin-Moreno, and F. J. Garcia-Vidal, "Mimicking surface plasmons with structured surfaces," *Science*, Vol. 305, No. 5685, 847–848, 2004.

9. Williams, C. R., S. R. Andrews, S. A. Maier, A. I. Fernández-Domínguez, L. Martín-Moreno, and F. J. García-Vidal, "Highly confined guiding of terahertz surface plasmonpolaritons on structured metal surfaces," *Nat. Photonics*, Vol. 2, No. 3, 175–179, 2008.

10. Shen, X., T. J. Cui, D. Martin-Cano, and F. J. Garcia-Vidal, "Conformal surface plasmons propagating on ultrathin and flexible films," *Proc. Natl. Acad. Sci. U. S. A.*, Vol. 110, No. 1, 40–45, 2013.

11. Ma, H. F., X. Shen, Q. Cheng, W. X. Jiang, and T. J. Cui, "Broadband and high-efficiency conversion from guided waves to spoof surface plasmon polaritons," *Laser Photon. Rev.*, Vol. 8, No. 1, 146–151, 2014.

12. Pan, B. C., Z. Liao, J. Zhao, and T. J. Cui, "Controlling rejections of spoof surface plasmonpolaritons using metamaterial particles," *Optics Express*, Vol. 22, No. 11, 13940–13950, 2014.

13. Zhang, H. C., S. Liu, X. Shen, et al., "Broadband amplification of spoof surface plasmonpolaritons at microwave frequencies," *Laser & Photon. Rev.*, Vol. 9, No. 1, 83–90, 2015.

Analysis of EM Shielding Effectiveness of CNT Films Based on TEM Cell Electric and Magnetic Coupling Fields

Jung-Yeol Park[1], **Jin-A Choi**[1], **Jae-Kyung Wee**[1], **Inchae Song**[1], **and Soon-Il Yeo**[2]

[1]School of Electronic Engineering, Soongsil University, Korea
[2]Electronics and Telecommunications Research Institute, Korea

Abstract— In this paper, we evaluated the electromagnetic (EM) shielding effectiveness (SE) of various carbon nanotubes (CNTs)-based films which were prepared with deposited carbon densities and thicknesses of the CNTs. The test environment based on a transverse electromagnetic (TEM) cell was adapted for (1) a comparison of the standard American society for testing and materials (ASTM) test and the near-field test using electric and magnetic field probes and (2) the differences of CNT SE on the electric field and magnetic field according to near end or far-end tests by the rotations of a microstrip patch antenna as a DUT. In addition, (3) the effect of CNTs composites and their thickness on the SE is investigated with TEM cell electric and magnetic field coupling to the DUT.

1. INTRODUCTION

The electromagnetic interference (EMI) of high speed circuits is becoming a cause of malfunction in electronic devices due to the rapid increase in operating frequencies. Therefore, the shielding material used to prevent EMI has become an issue, and its shielding ability has been usually presented with standardized procedures ASTM D 4935-99 for analyzing the characteristics of shielding materials [1]. The near-field SE of ASTM methods based on far-field tests may be calculated for magnetic sources for electrically thin specimens. However, their validity and applicability have not been established for shielding effectiveness (SE) in the near-field between chips because near-field is directly influenced by the E-field and H-field. A lot of research has been carried out about the evaluation method of SE for near-field but a standardized method has not been presented. In this paper, we present the evaluation method of near-field SE using a TEM cell according to the standardized procedures IEC 61967-2 [2] and IEC 62132-2 [3] for the analysis of EM emission of integrated circuits. The newly devised near-field test located CNTs with deposited carbon densities and thicknesses of CNT between the TEM Cell and the patch antenna, and measured by the current direction of the patch antenna as an EM radiated source. This method can also predict the SE of an E-field and H-field by using the H-field's cancelation, according to current direction [4]. Also, the SE on the CNT films for measuring the point of near-field probe (Langer EMV-Technik RF1) is different because the shielding material in the near-field region isn't uniformly measured on all sides by locating the GND contact [5]. Finally, a comparison of the proposed near-field test and far-field test will evaluate the range of use of CNT films by frequency.

2. MEASUREMENT RESULTS

The SE analysis of standardized ASTM 4935-99 procedures were measured and presented with various deposited carbon densities and thicknesses of carbon nanotube (CNT) films as shown in Figure 1 and Figure 2. For SE tests, the manufactured CNTs, having the densities of 2%, 5%, 10% and the thicknesses of 0.3 mm, 1 mm and 2 mm, were measured from 50 MHz to 1.5 GHz. The measure of SE is given as the Equation (1),

$$\text{SE [dB]} = \text{P1 [dBm]} - \text{P2 [dBm]}, \tag{1}$$

where P1 is the input power and P2 is the output power. The SE measurements have different values according to fabricated conditions because their electric conductivity had different levels of densities and thicknesses.

Figure 3(a) shows the test environment of the near-field and its measured coupling between the TEM cell septum and the patch antenna. The TEM cell used in this work was a product of FCC-TEM-JM3. The patch antenna was composed of a 2-layer PCB and the test was repeated four times at angles 0, 90, 180, and 270 degrees between the antenna pattern and the TEM cell septum. The frequency domain measurements were performed by a two-port vector network analyzer (VNA) up to the frequency of 1 GHz.

Figure 3(b) shows the angle-dependent coupling factors when the patch antenna is positioned with respect to the TEM Cell septum because the inductive coupling was affected according to the different angle directions.

Figure 4 shows SE measurements according to densities, thicknesses and directions of the DUT. The SE results were calculated with the equations as follows, SE [dB] = Coupling factor without CNT film [dBm] − Coupling factor with CNT film [dBm].

The SE levels as a function of density changes decreased by increasing frequency and depended on CNT contained percentages (2, 5, or 10%) because of the low CNT percentage having a relatively low electrical conductivity. Also these results show that SE of over 100 MHz didn't shield the EM source by densities. In contrast, SE by thicknesses increased by increasing frequency, except for the thickness of 0.3 mm because inductive coupling at a higher frequency was shielded. But Figures 4(a) and (b) can be properly taken into account in regards to the densities and thicknesses of the CNT films. Figure 4(c) shows SE according to DUT direction. The measured SE of CNT films at 0 and 180 degrees were lower levels than those of 90 and 270 degrees. The four-rotated test results could be explained as CNT films not effectively preventing magnetic fields in low frequencies, but CNT films could reduce electric fields.
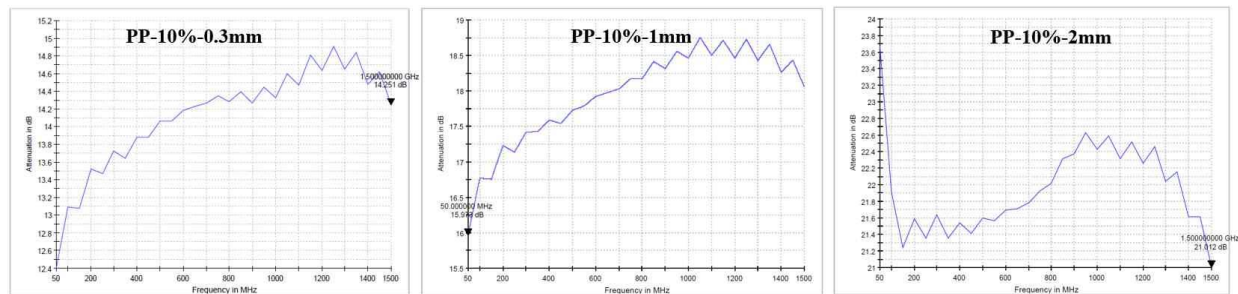

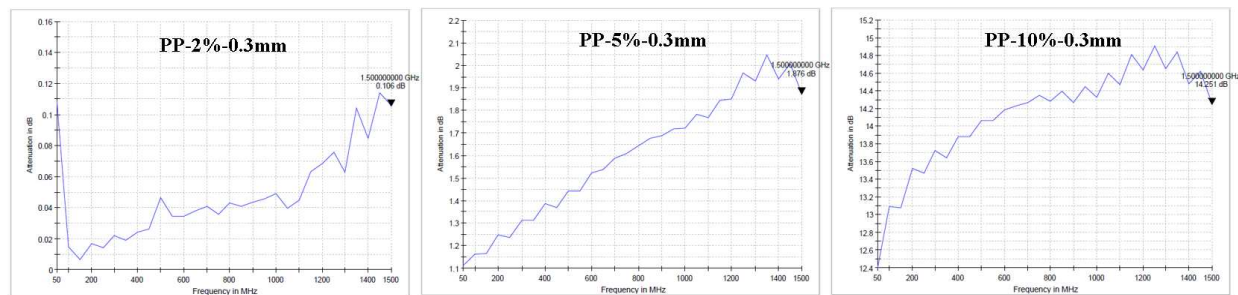Figure 1: Measured SEs of ASTM on various CNT films by thicknesses.

Figure 2: Measured SEs of ASTM on various CNT films by densities.
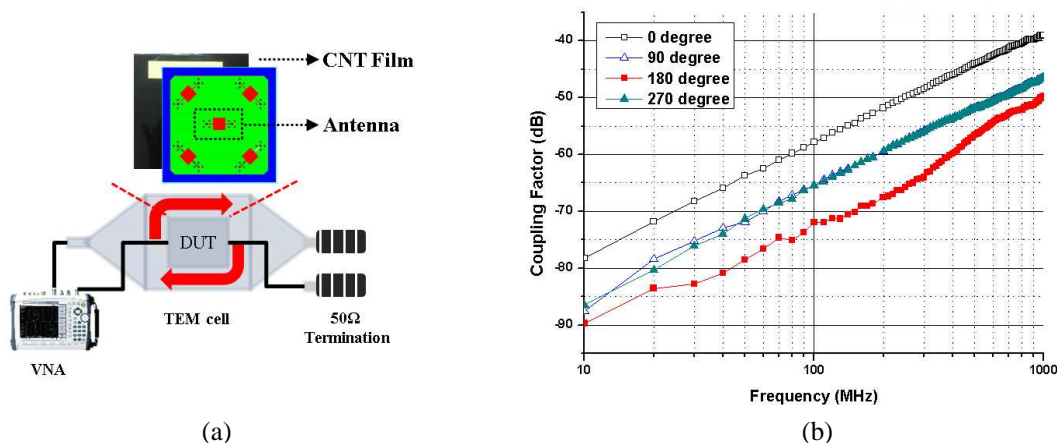

Figure 3: (a) Near field test environment and (b) coupling factor by DUT direction without CNT film.
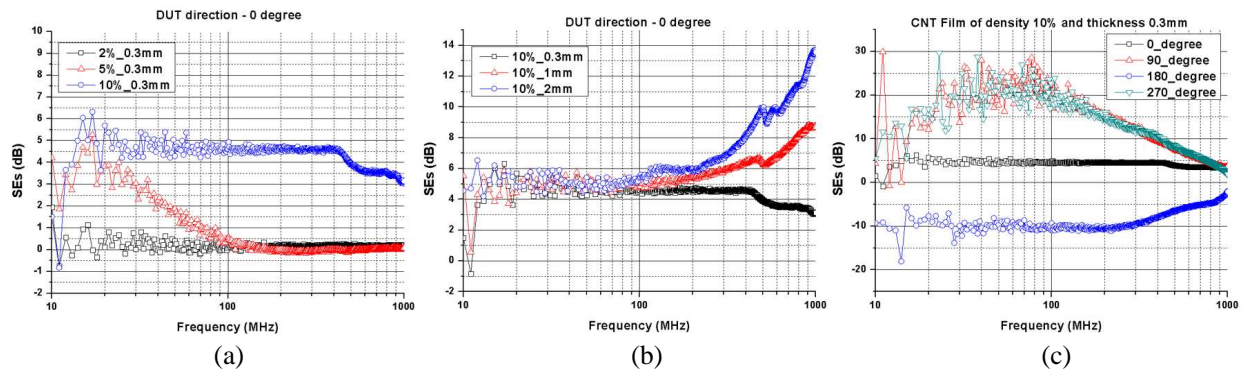
Figure 4: Shielding effectiveness according to (a) densities, (b) thicknesses, and (c) DUT direction.
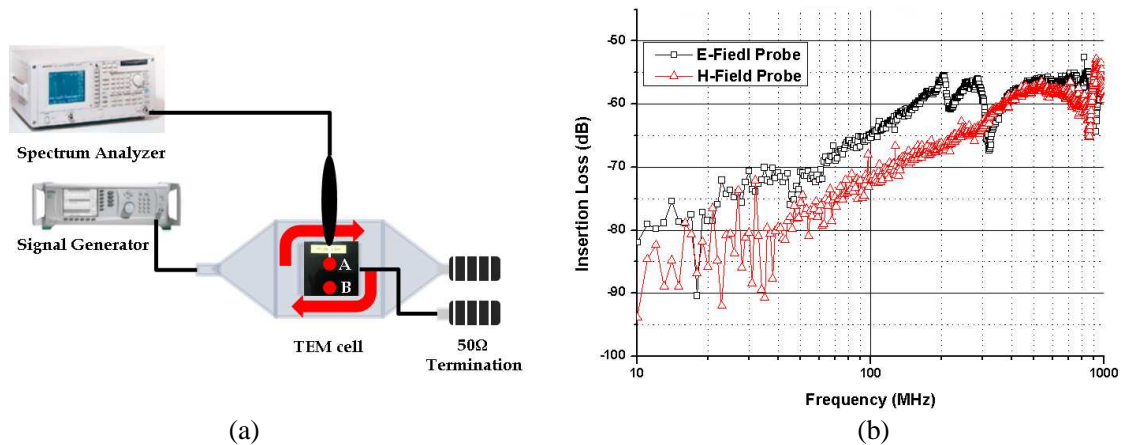

Figure 5: (a) Near field measurement environment based on TEM cell and (b) insertion loss of near field probe without CNT films.
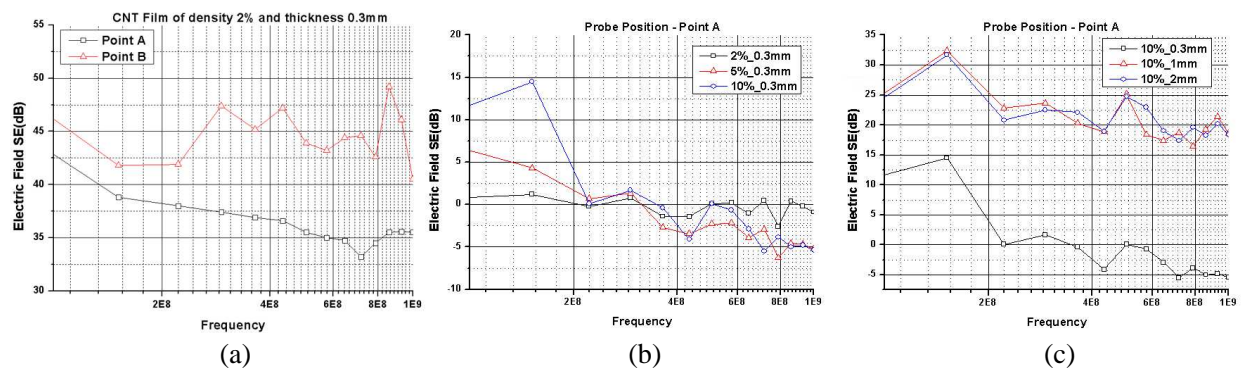

Figure 6: Electric Field SEs using near field measurement by: (a) probe position, (b) densities, and (c) thicknesses of CNT films.

Figure 5 shows the near-field test environment using a near-field probe and the insertion loss of commercial antennas. Insertion loss was measured for evaluation by a sensitivity of the height of the E-field and H-field. The test method of insertion loss was performed by using a VNA on the septum of a TEM cell and had a height of 2.5 mm from the near-field probe to the top wall of the TEM cell. The test results showed a difference of about 5 dB between the E-field probe and H-field probe below 400 MHz. The E-field SE results decreased by increasing frequency, as shown in Figure 6, because the CNT films didn't effectively shield the capacitive coupling in the high frequency. Also, E-field SE as a function of probe positions showed different results in Figure 6(a). Prior analysis of SE by probe position measured E-field intensity without CNT films at two points. The test results were almost the same value, but SE with CNT film presents different curves in
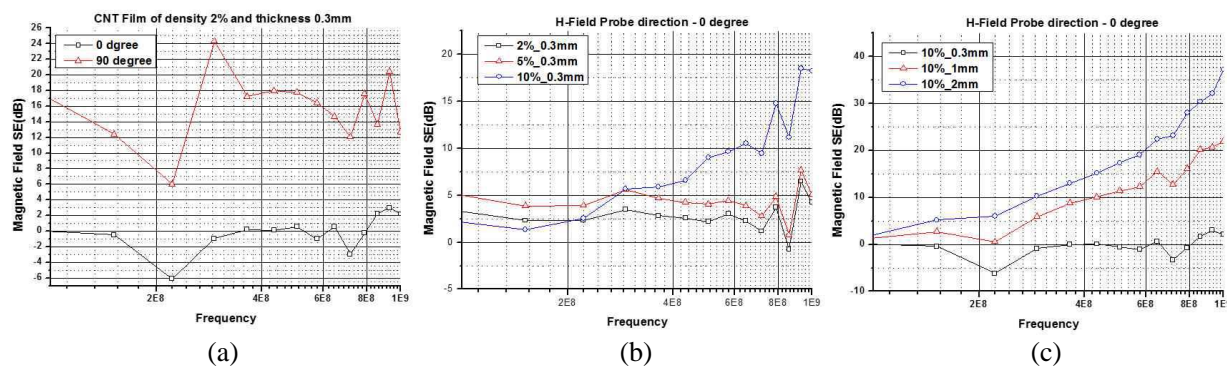
Figure 7: Magnetic Field SEs using near field measurement by: (a) probe direction, (b) densities, and (c) thicknesses of CNT films.

probe position because the resistance and capacitance on CNT film was changed by probe positions.

Figure 7 shows measured SE with the H-field probe. The measured H-field SE was not shielded at the lower frequency because magnetic field cancelation didn't happen between the TEM cell septum and the CNT, which imperceptibly flowed the eddy current on CNT films due to low conductivity.

The test environment based on a TEM cell was adapted for a comparison of the standard ASTM test and the near-field test, which used the electric and magnetic coupling fields of CNT films' SE on an electric field and magnetic field. The SE results of a far-field test as shown in Figure 1 can be explained as those of the electric field shielding effects, however the SE of magnetic field shielding had a relatively lower shielding effect, or negative shield effect, depending on angle characteristics.

3. CONCLUSION

Generally, the analysis of the SE of shielding material has been standardized in test environments based on far-field testing. But far-field tests are not suitable between chips in near-field situations. In this paper, we proposed a near-field test to predict the SE of CNTs. The near-field test used a coupling between the TEM Cell septum and the patch antenna. In order to analyze the SE of CNT films for the near-field test, the measurements for the CNT with deposited carbon densities and thicknesses of the CNTs, the direction of the patch antenna and the probe position on the CNT were measured. The measured results found the appropriate densities and thicknesses of CNTs. Regardless of the densities of the CNTs, the SE results were almost the same; but the SE by thicknesses changed without 0.3 mm of thickness. Also, the tests with 0 or 180 degree angles showed different results between ASTM tests and the near-field test. The measured SE of CNT at 0 and 180 degrees were at much lower levels than those of 90 and 270 degrees because the eddy currents on CNT films gave an additional magnetic coupling effect. The 4 rotated test results could be explained as CNTs not effectively preventing magnetic fields, but CNTs could reduce electric fields. Also, SE in the near-field test by the position of an E-field probe increased the closer to the ground of the TEM Cell. These results show that the placement of a semiconductor package using a CNT film is important.

REFERENCES

1. ASTM D 4935-99, "Standard test method for measuring the electromagnetic shielding effectiveness for planar materials," 1999.

2. "Integrated circuits measurement of electromagnetic emissions Part 2: Measurement of radiated emissions, TEM cell and wideband TEM cell method," 1st Edition, IEC 61967-2, 2005.

3. "Integrated circuits — Measurement of electromagnetic immunity — Part 2: Measurement of radiated immunity, TEM cell and wideband TEM cell method," 1st Edition, IEC 62132-2, 2010.

4. Mandic, T., R. Gillon, and B. Nauwelaers, "Characterizing the TEM cell electric and magnetic field coupling to PCB transmission lines," *IEEE Transactions on Electromagnetic Compatibility*, Vol. 54, No. 5, Oct. 2012.

5. Wee, J.-K., Y.-J. Park, H.-S. Min, D.-H. Cho, M.-H. Seung, and H.-S. Park, "Modeling the substrate effect in interconnect line characteristics of high-speed VLSI circuits," *IEEE Transaction on Microwave Theory And Techniques*, Vol. 46, No. 10, Oct. 1998.

Thermal Imaging of RF Induced Heat Loss in a Microwave Metamaterial Absorber

K. Ozden[1], O. M. Yucedag[2], A. Ozer[2], H. Bayrak[2], H. Isik[3], and H. Kocer[2]

[1]Defense Sciences Institute, Turkish Military Academy Ankara, Turkey
[2]Department of Electrical Engineering, Turkish Military Academy Ankara, Turkey
[3]Department of Mechanical Engineering, Turkish Military Academy Ankara, Turkey

Abstract— Metamaterial absorbers (MAs) play an important role in stealth technology in microwave bands. Although MAs absorb incident RF power, they usually convert it into the heat which might be a disadvantage for counter-measurement against remote thermal imaging systems. In this study, we present the design, simulation, fabrication and RF/thermal imaging of a narrowband MA in the microwave region. The MA consists of a two dimensional periodic array of a well-known metallic split ring resonator (SRR) and a ground plane separated by a dielectric layer. For horizontally and vertically polarized illumination cases, thermal imaging of the MA is carried out using a commercial thermal imager which has a longwave infrared sensor between 8–12 μm wavelengths. Surface temperature map of the MAs are extracted from the recorded thermal images. It is shown that a slight temperature difference happens with respect to the ambient temperature for the MA of the near-perfect absorption whereas the MA of the near-zero absorption has zero temperature difference. Physical mechanisms of the RF absorption and the RF induced heat loss are explained using further electromagnetic numerical simulations.

1. INTRODUCTION

Metamaterials are manmade structures which have novel features such as backward wave propagation, negative refractive index and phase velocity. Metamaterials with these properties are used in many practical applications such as super lenses [1], antennas [2], sensors [3] and perfect absorbers [4, 5]. The matematerial based perfect absorbers have attracted a great deal of interest in stealth technology in recent years. Metamaterial absorbers (MAs) consist of periodic conductive and insulator layers which are responsible for producing negative permittivity (ε) and permeability (μ) at resonance frequency. These artificial structures can be utilized as a radar absorbing material (RAM) in microwave bands.

Although metamaterials were theoretically investigated by a Russian physicist V. Veselago in 1968 [6], studies on MAs are not going too far back. The first metamaterial based absorption experiments were held by Landy et al. [4] in 2008. Initially, narrow bandwith perfect absorption was achieved. After that, most of the researches were concentrated on obtaining the polarization-insensitive [7], wide-angle [8], multi-band [9] and broadband absorption [10] using the MAs.

In this study, we present the design, simulation, fabrication and RF/thermal imaging of a narrowband-polarization sensitive MA in the microwave region. The MA consists of a two dimensional periodic array of a well-known metallic split ring resonator (SRR) proposed by Pendry et al. [11] and a ground plane separated by a dielectric layer. By adjusting the dimensions, the SRR is optimized to have resonance at 4.75 GHz. Measurements of the MA was held in uncontrolled room. It is observed that the RF simulation results are in good agreement with the measurements such that near-perfect absorption occurs at 4.75 GHz when the incident electric field vector is perpendicular to the SRR gaps. On the other hand, near-zero absorption is obtained when the incident electric field vector is parallel to the gaps. To better understand the mechanism of the RF absorption, the electric field distribution, magnetic field distribution and current distribution are simulated at on-resonance (4.75 GHz) and off-resonance (4.00 GHz) frequencies. It is seen that MA absorbs incident RF power at resonance frequency. The incident RF power is neither reflected nor transmitted but is turned into heat and get absorbed. While it might be an advantage to use MAs against microwave radars, it might be a disadvantage for counter-measurement against remote thermal imaging systems in infrared region. So, thermal imaging of the MA is carried out using a commercial thermal imager which has a longwave infrared sensor between 8-12 μm wavelengths. Surface temperature map of the MA is extracted from the recorded thermal images. It is shown that a slight temperature difference occurs for the MA of the near-perfect absorption whereas the MA of the near-zero absorption case has zero temperature difference.

2. DESIGN, SIMULATION AND MEASUREMENT OF THE METAMATERIAL ABSORBER

The proposed MA consists of two metallic layers separated by dielectric. The first metallic layer is the SRR and the second one is metallic continuous ground plane. The SRR consists of two concentric rings separated by a gap. A schematic drawing of the SRR can be seen in Fig. 1(a). Both rings have splits at the opposite sides. These metallic layers are selected as copper which has 35 μm thickness and its frequency independent conductivity (σ) is 5.8×10^7 S/m. The dielectric material is epoxy glass cloth laminate (FR4) which has 1.6 mm thickness and its relative dielectric permittivity (ε_r) is 3.85 and the loss tangent ($\tan \delta$) is 0.02. The geometrical parameters of the SRR are defined as follows: L is the length and width of the unit cell, d is the width of the splits, g is the gap between the rings, w is the width of both copper rings and r is the radius of the outer ring. The proposed SRR has the dimensions, in millimeters, of: $L = 10$, $d = 0.50$, $g = 0.56$, $r = 3.55$ and $w = 1.20$.

We have utilized a commercial electromagnetic solver, CST Microwave Studio, which is based on the finite integration technique. In the simulation setup, MA is illuminated by a horizontally polarized plane wave in 3–6 GHz frequency band. The plane wave propagates along $-z$ direction and the direction of the electric field vector is along the x-axis. Periodic type boundary conditions are applied along x and y-axes as shown in Fig. 1(b). MA structure which consists of 300 SRRs (i.e., 15 along x-axis and 20 along y-axis) is fabricated using printed circuit board (PCB) technique as shown in Fig. 1(c).
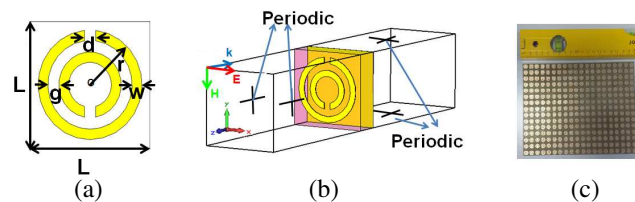

Figure 1: (a) Front view. (b) Perspective view of the simulation. (c) Photograph of the fabricated MA sample.

In the experimental setup, as shown in Fig. 2(a), a vector network analyzer (Rohde & Schwarz ZNB 8, 9 kHz–8.5 GHz), a pair of standard gain pyramidal horns antennas (ARRA 187-862) and a thermal imager (FLIR T650sc) are used. The distance between the horn antennas is set at 34 cm to prevent the near fields effects on the reflection and the MA is located 60 cm away from the antennas. The two horn antennas serving as the source and receiver are connected to the network analyzer by using low loss exible cables in order to measure the reflection coefficient.
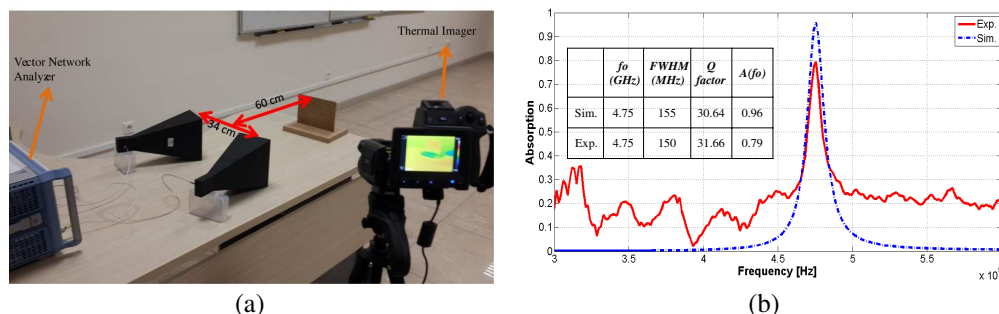

Figure 2: (a) The experimental setup. (b) Simulated and measured absorption of the MA structure.

We experimentally verified the behavior of the absorber by measuring the reflectance. In order to measure standard reflection response, the back plane of the MA which is completely metallic is measured at the first phase. In the second phase, the reflection coefficient is measured by using surface of the MA which includes SRR units. The frequency dependent absorption $A(f)$ of a material is related to its transmission $T(f)$ and reflection $R(f)$ by $A(f) = 1 - T(f) - R(f)$. Here, $R(f) = |S_{11}(f)|^2$ and $T(f) = |S_{21}(f)|^2$ where $S_{11}(f)$ and $S_{21}(f)$ are reflection and transmission coefficients, respectively. $T(f)$ is zero due to the presence of the continuous copper ground plane. Thus, the total absorption is calculated only by the reflection. In order to achieve the maximum

absorption, the reflection should be minimized. The frequency characteristic of the absorption is presented in Fig. 2(b). It is noted that the reflection of the absorber drops to a minimum at 4.75 GHz denoting impedance matching with the free space. We obtained simulated and measured values of 96% and 80% at 4.75 GHz, respectively. These results show that the RF simulation results are in good agreement with the measurements such that near-perfect absorption occurs at 4.75 GHz when the incident electric field vector is perpendicular to the SRR gaps. On the other hand, near-zero absorption is obtained when the incident electric field vector is parallel to the gaps. The quality-factor can be calculated from the resonance spectra in Fig. 2(b) by the following equation:

$$Q = \frac{f_0}{\Delta f_{FWHM}} \tag{1}$$

Here, f_0 is the resonance frequency and Δf_{FWHM} is its half maximum width. The Q-factor from the simulation and experimental results using Eq. (1) was found to be approximately 30.64 and 31.66, respectively.

3. ABSORBTION MECHANISM OF THE METAMATERIAL ABSORBER

Physical mechanisms of the RF absorption and the RF induced heat loss are investigated using further electromagnetic numerical simulations and thermal imaging measurement. Experiments are carried out to explore the absorbing characteristics for different polarizations of normal incident EM waves at on-resonance (4.75 GHz) and off-resonance (4.00 GHz) frequencies.

For the on-resonance and horizontal polarization case, the electric field is strongly concentrated at the outer ring split as shown in Fig. 3(a-i). However, relatively low electric field distribution is observed at the outer split region for the case of off-resonance as seen in Fig. 3(a-ii). As expected, there is negligible electric field distribution in vertical polarization case shown in Fig. 3(a-iii) and Fig. 3(a-iv), respectively.
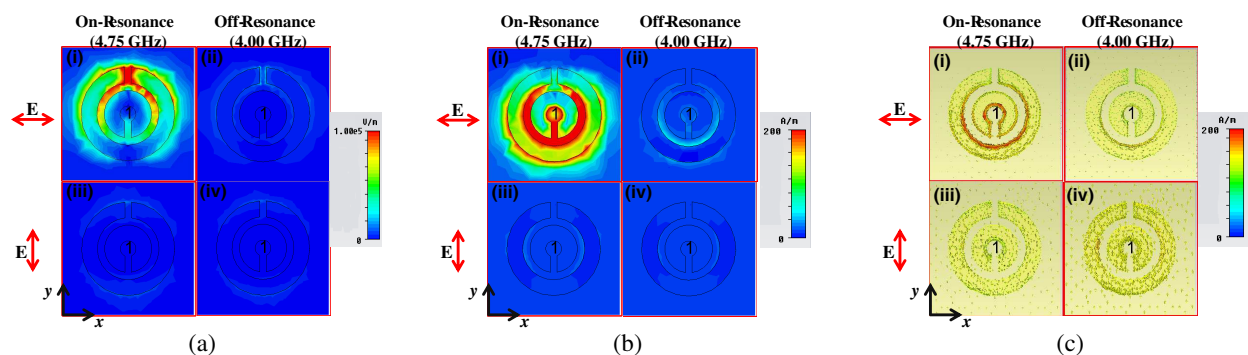

Figure 3: (a) Electric field distribution of the MA, $|E|$ field. (b) Magnetic field distribution of the MA, $|H|$ field. (c) Surface current distributions on the front side of the MA.

It can be observed that for the case of on-resonance and horizontal polarization, the magnetic field component is coupled to the gap and inner split as seen in Fig. 3(b-i). In case of off-resonance, relatively low magnetic field distribution is also observed at the gap region as shown in Fig. 3(b-ii). While the MA is illuminated by a vertical polarized plane wave, there is negligible magnetic field distribution as illustrated in Fig. 3(b-iii) and Fig. 3(b-iv), respectively.

Subsequently, the surface current distribution is investigated, as shown in Fig. 3(c). When the incident field is horizontally polarized, for the case of on-resonance, it is observed that the current distribution mainly focuses on the bottom side of the outer ring as seen in Fig. 3(c-i). For the case of off-resonance, the current distribution which is relatively lower than on-resonance case, is also observed as shown in Fig. 3(c-ii). When the MA is illuminated by vertically polarized field, the current is not induced over a specific part of the SRR for onand off-resonance cases as illustrated in Fig. 3(b-iii) and Fig. 3(b-iv), respectively.

The MA is illuminated by RF radiation (its frequency is between 4.74 and 4.76 GHz and power is 30 dBm) from the Vector Network Analyzer. Thermal imager is located with an angle of 10 degree to prevent the metallic reflection. Using the thermal imager, surface temperature measurement is taken before the RF power was applied. Then, the remote surface temperature is measured in the 5 minute intervals in the case of on- and off-resonances. Later, the measurements are repeated

for the vertically polarized plane wave. The heat loss induced remote temperature measurements are obtained by calculating average tempereture of MA with ThermalCAM Researcher program as shown in Fig. 4. It is shown that a slight temperature difference ($\Delta T = 0.6°\text{C}$) happens with respect to the ambient temperature for the MA of the near-perfect absorption whereas the MA of the near-zero absorption has zero temperature ($\Delta T = 0°\text{C}$) difference.
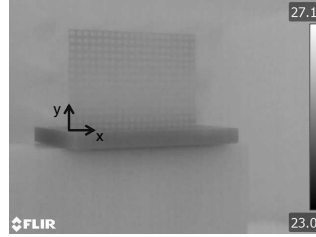

Figure 4: Thermal image of the MA.

4. CONCLUSION

In this paper, we presented the design, simulation, fabrication and RF/thermal imaging measurement of a MA having narrowband absorption resonance in the microwave region. The fabricated MA exhibits absorption peak at 4.75 GHz which is in good agreement with the simulated result. Effect of the RF induced heat loss over the front surface of the MA is investigated. Based on the remote temperature measurements using thermal imager, a slight temperature difference is observed for the MA of near-perfect absorption. Depending on these results, it is possible to say that, temperature difference of MA is linked to the RF power absorption. So, in stealth applications, the thermal effect of MAs have to be considered against remote thermal sensing systems in infrared region.

REFERENCES

1. Fang, N., H. Lee, C. Sun, and X. Zhang, "Subdiffraction-limited optical imaging with a silver superlens," *Science*, Vol. 308, No. 5721, 534–537, 2005.
2. Si, L. M. and X. Lv, "CPW-FED multi-band omni-directional planar microstrip antenna using composite metamaterial resonators for wireless communications," *Progress In Electromagnetics Research*, Vol. 83, 133–146, 2008.
3. Liu, N., M. Mesch, T. Weiss, M. Hentschel, and H. Giessen, "Infrared perfect absorber and its application as plasmonic sensor," *Nano Lett.*, Vol. 10, No. 7, 2342–2348, 2010.
4. Landy, I. N., S. Sajuyigbe, J. J. Mock, D. R. Smith, and W. J. Padilla, "Perfect metamaterial absorber," *Phys. Rev. Lett.*, Vol. 100, No. 20, 207402, 2008.
5. Li, L., Y. Yang, and C. H. Liang, "A wideangle polarization-insensitive ultra-thin metamaterial absorber with three resonant modes," *J. Appl. Phys.*, Vol. 110, 063702, 2011.
6. Veselago, V. G., "The electrodynamics of substances with simultaneously negative values of ε and μ," *Sov. Phys. Uspekhi*, Vol. 10, 509–514, 1968.
7. Zhu, B., Z. Wang, C. Huang, Y. Feng, J. Zhao, and T. Jiang, "Polarization insensitive metamaterial absorber with wide incident angle," *Progress In Electromagnetics Research*, Vol. 101, 231–239, 2011.
8. He, X. J., Y. Wang, T. L. Gui, and Q. Wu, "Dual-band terahertz metamaterial absorber with polarization insensitivity and wide angle," *Progress In Electromagnetics Research*, Vol. 115, 381–397, 2011.
9. Bian, B. R., S. B. Liu, S. Y. Wang, X. K. Kong, H. F. Zhang, B. Ma, and H. Yang, "Novel tripleband polarization-insensitive wide-angle ultra-thin microwave metamaterial absorber," *J. Appl. Phys.*, Vol. 114, No. 19, 194511, 2013.
10. Wang, B. Y., S. B. Liu, B. R. Bian, Z. W. Mao, X. C. Liu, B. Ma, and L. Chen, "A novel ultrathin and broadband microwave metamaterial absorber," *J. Appl. Phys.*, Vol. 116, 094504, 2014.
11. Pendry, J. B., A. J. Holden, D. J. Robbins, and W. J. Stewart, "Magnetism from conductors and enhanced nonlinear phenomena," *IEEE Trans. Microw. Theory Tech.*, Vol. 47, 2075–2084, 1999.

Analog Multiplexer with an Improved High Linearity Bootstrapped Switch for Multi-channel Neural Signal Recording

Feng Yuan[1], Zhi-Gong Wang[2], Xiao-Ying Lü[2], and Yu-Feng Guo[1]

[1]College of Electronic Science and Engineering
Nanjing University of Posts and Telecommunications, Nanjing 210023, China
[2]Southeast University, Nanjing, China

Abstract— An analog integrated multiplexer and a bootstrapped switch for the interface of multi-channel neural signal recording system is presented. The bootstrapped switch is improved to suit the specific environment, which satisfies the requirements of constant clock feed-through, constant charge injection, and compensation for body-effect Simulation results show a higher linearity comparing the proposed switch with the conventional bootstrapped switches. Under typical-case conditions the switch maintains about $-107\,\mathrm{dB}$ THD for an input signal with the frequency range of $1\,\mathrm{kHz}{\sim}10\,\mathrm{kHz}$.

1. INTRODUCTION

The acquisition of neural signals has received significant interest from the neuroscience research community very recently, as it has been thought that neural signals can be the key to study functional mapping of the brain. The advent of micro-electrode arrays acquiring electric signals from neurons has driven the need for electronics which is used to amplify, filter, and digitize neural signals. Since the number of the electrodes should be affirmatively much larger than the number of recording channels, the multiplexer is necessary in such systems. Taking into account our special application, the multiplexer here is expected to have the following characteristics:

- High linearity.
- Low power consumption.
- Low noise.

Meanwhile, another important requirement in many systems where analog multiplexer are used is for the ON resistance of the closed switch to remain constant when either or both the analog input and the supply voltages change. The ON resistance of a MOS transistor when used as a switch changes with variations in the amplitude of the analog signal and the supply voltages.

This paper is organized as follows: Section 2 presents a description on the structure of the multiplexer. In Section 3, certain issues related with the design of bootstrapped switch are introduced and an improved high linearity bootstrapped switch for multi-channel neural signal recording is presented. Simulation results are shown in Section 4. Finally, conclusions are drawn in Section 5.

2. MULTIPLEXER ARCHITECTURE

An analog integrated multiplexer is an indispensable element for the input analog interface of multi-channel neural signal recording system. The block diagram of the analogue multiplexer is shown in Fig. 1.

The multiplexer contains N input channels and an extra channel which is added as a reference to cancel the offset and the cross-talk. Each channel consists of hold switch, sample switch, a storage capacitor and necessary buffers. The multiplexing function is implemented by a simple array of hold and sample switches controlled by a control module.

3. SWITCH DESIGN

Considerable attention is paid to low distortion performance of the multiplexer as it is the importance part delivering the amplified neural signals to the analog to digital converters. However, most switches in multiplexers suffer from the distortion of passing signals from the non-ideality of the MOS transistor [1].

3.1. Non-linearity Source of the MOSFET Switch

The following are some effects producing deviation which degrading the linearity and the resolution:
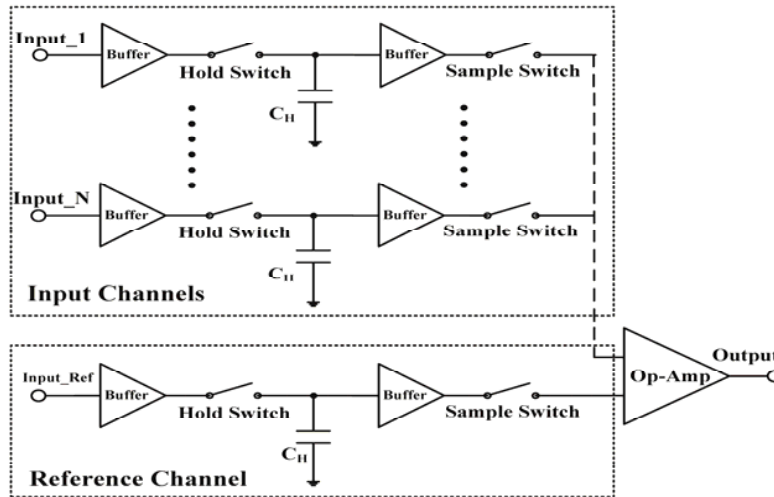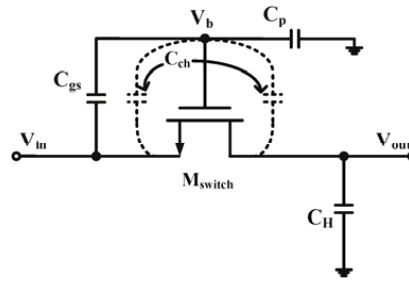
Figure 1: Block diagram of analogue multiplexer.

Figure 2: The model of a MOSFET switch.

3.1.1. Threshold Voltage Variation

A CMOS transistor used as a switch has a non-zero on-resistance. The on-resistance can be approximated as:

$$R_{on} = \frac{\partial V_{ds}}{\partial I_d} = \frac{1}{\mu C_{ox} \frac{W}{L} (V_{gs} - V_{TH} - V_{ds})} \tag{1}$$

This means that the on-resistance becomes signal dependent.

3.1.2. The Parasitic Capacitance

As Fig. 2 shows, both the generation of the inverter layer under the gate and the total equivalent capacitance C_{gs} (the sum of all capacitance between gate-source), C_p (the parasitic capacitance between the gate-ground) will significantly reduce the gate voltage. This charge leakage effect can be formulated by:

$$V_{gs} = \frac{C_{gs}}{C_{gs} + C_{ch} + C_p} V_b - \frac{C_p}{C_{gs} + C_{ch} + C_p} V_{in} \tag{2}$$

V_{gs} is the practical voltage between the gate and source. C_{ch} is the equivalent capacitance of the inverter layer.

3.1.3. Charge Injection

The charge that has been build up in inverter layer of the channel will be divided between the source and drain side when a transistor turns off. In the worst case, all the charges are injected into the output node which is approximated with Formula (3):

$$\Delta V_{ci} = \frac{WLC_{ox}}{C_H} (V_{gs} - V_{TH}) \tag{3}$$

Here, C_H is the total capacitance on the output terminal.

3.1.4. Clock Feed-through

The parasitic capacitance between the gate-source or gate-drain will feed-through the clock signal to the output node which can be approximated as:

$$\Delta V_{cf} = (V_{gs,on} - V_{gs,off}) \frac{C_g d}{C_{gd} + C_H} \tag{4}$$

3.2. Bootstrapped Switch

Bootstrapped switch is attractive as a circuit technique to deal with the aforementioned non-linearity sources which is widely employed for low-voltage, high-linearity applications [2–12]. The main idea behind this technique is to keep the gate-to-source voltage of a transistor constant to be constant. A high linearity bootstrapped switch is proposed here which is improved in body effect, charge leakage, charge injection and clock feed-through. As shown in Fig. 3, the proposed bootstrapped switch works on two phases in which the M_{sw} is turned on and off.

3.2.1. Phase "off" (φ_2)

During the phase "off", the M_{sw} is turned off. The two capacitors C_{b1} and C_{b2} are charged by a pair of complementary power supply V_{DD} and V_{SS}. The M_{n2} controlled by gate-voltage $\overline{CLK}$ and M_{p4} by CLK connect the C_{b1} to V_{SS} and V_{DD}. Simultaneously, M_{p6} with the gate-voltage CLK clamps the gate-voltage of M_{p3} to V_{DD} and keeps it in "off" state which isolates the drain of M_{p4} from V_{SS}. Both M_{p3} and M_{n1} are in off-state during this phase. Analogously, C_{b2} is connected to V_{DD} and V_{SS} by M_{p8} and M_{p10} which are in on-state. At the end of this phase, the gate voltage of M_{sw} is pre-set on a low input-dependent level by a path composed of M_{n13} and M_{n15} to keep the clock feed-through a constant throughout the switching period of φ_2 to φ_1.

3.2.2. Phase "on" (φ_1)

During the phase "on", the CLK goes high and M_{n9} is excited to be on-state which provide a path for the charged capacitor C_{b1} acting as a battery to pump charge onto the gate of M_{sw}. The increased gate-voltage turns on the M_{sw} and M_{n1}. Specifically, the voltage across the gate and source of the M_{sw} is a constant offset setting by C_{b1} regardless of the variable input signal. Moreover, M_{n5} and M_{n7} provide a path for C_{b2} to compensate the threshold voltage variation and eliminate the non-linearity of body effect.

4. RESULTS

The switch is simulated in the $0.5\,\mu\mathrm{m}$ CMOS technology using BSIM3v3 device model. The transistor level simulations are done in Cadence Virtuoso Analog Design Environment. The dynamic performance of the bootstrapped switch is depicted in Fig. 5. The results for HD2 and HD3 are illustrated in Fig. 6.

As Table 1 shows, some design of bootstrapped switches presented by other articles are compared with the one proposed here. The calculations of total harmonic distortion were carried out by
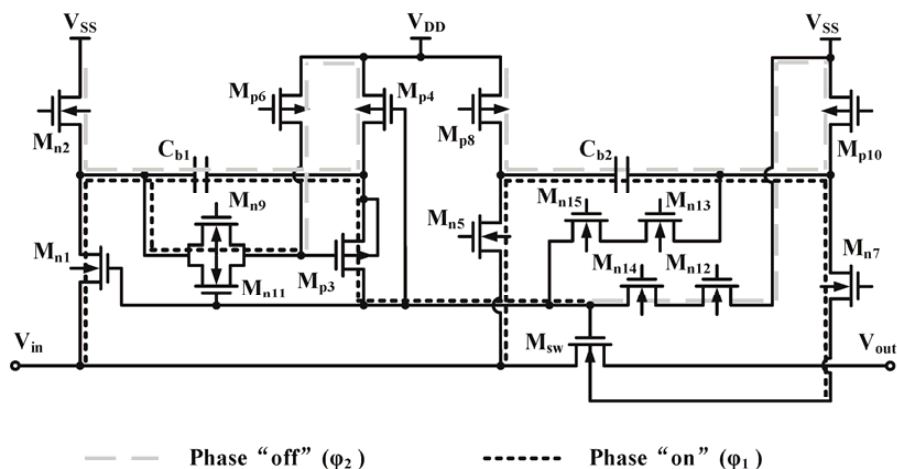

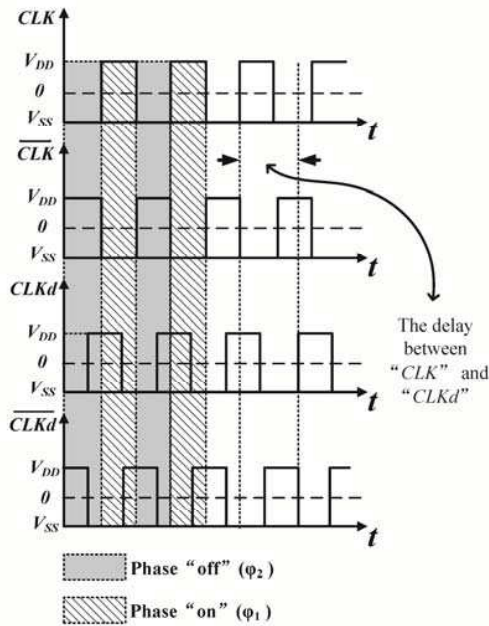Figure 3: The schematic of the proposed bootstrapped switch.

Figure 4: Time-domain switching scheme for the operation of the proposed bootstrapped switch.
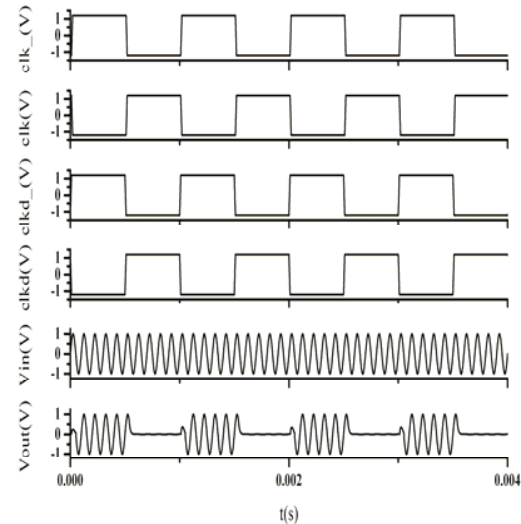
Figure 5: Simulated switch behavior with a dynamically changing input signal.

Table 1: Comparison of the harmonic distortion.

	THD	THD2	THD3
Conventional @ $f_s = 100\,\mathrm{MHz}$	$-85.3\,\mathrm{dB}$	$-85.2\,\mathrm{dB}$	$-106\,\mathrm{dB}$
Ref. [8] @ $f_s = 300\,\mathrm{MHz}$	$-84.1\,\mathrm{dB}$	$-87.9\,\mathrm{dB}$	$-105.9\,\mathrm{dB}$
Ref. [10] @ $f_s = 100\,\mathrm{MHz}$	$-101\,\mathrm{dB}$	$-102\,\mathrm{dB}$	$-115.4\,\mathrm{dB}$
Ref. [12] @ $f_s = 125\,\mathrm{MHz}$	$-105\,\mathrm{dB}$	$-110\,\mathrm{dB}$	$-115\,\mathrm{dB}$
Proposed @ $f_s = 10\,\mathrm{MHz}$	$-107\,\mathrm{dB}$	$-113\,\mathrm{dB}$	$-116\,\mathrm{dB}$

using the calculator option "THD" of Cadence Analog Design Environment. The range of values of input signal frequencies was from 1 kHz to 10 kHz.

5. CONCLUSIONS

In this article, a bootstrapped switch is proposed which has improvement in the requirements of constant clock feed-through, constant charge injection, and compensation for body-effect. Meanwhile, the switch remains the practicability for less increase in complexity. An exemplary 4-channels analog multiplexer is constructed based on the proposed bootstrapped switch for verifying the effectiveness of the optimization. As the simulation results show, a higher linearity comparing with the switch in other work is achieved in the proposed bootstrapped switches.

REFERENCES

1. Razavi, B., *Design of Analog CMOS Integrated Circuits*, 1st Edition, McGraw-Hill, 2000.
2. Abo, A. M. and P. R. Gray, "A 1.5-V, 10-bit, 14.3-MS/s CMOS pipeline analog-to-digital converter," *IEEE J. Solid-State Circuits*, Vol. 34, No. 5, 599–606, May 1999.
3. Dessouky, M. and A. Kaiser, "Input switch configuration suitable for rail-to-rail operation of switched-opamp circuits," *Electron. Lett.*, Vol. 35, No. 1, 8–10, Jan. 1999.
4. Steensgaard, J., "Bootstrapped low-voltage analog switches," *Proc. ISCAS*, Vol. 2, 1129–1132, 1999.
5. Waltari, M. and K. Halonen, "Bootstrapped switch without bulk effect in standard CMOS technology," *Electron. Lett.*, Vol. 38, No. 12, 555–557, 2002.

6. Dessouky, M. and A. Kaiser, "Very low-voltage digital audio modulator with 88-dB dynamic range using local switch bootstrapping," *IEEE Journal Solid-State Circuits*, Vol. 36, No. 3, 349–355, Mar. 2001.

7. Fayomi, C. J. B., G. W. Roberts, and M. Sawan, "Low-voltage CMOS analog bootstrapped switch for sample-and-hold circuit: Design and chip characterization," *Proc. IEEE Int. Symp. on Circuits and Systems*, Vol. 3, 2200–2203, May 2005.

8. Yang, C. Y. and C. C. Hung, "A low-voltage low-distortion MOS sampling switch," *Proc. IEEE Int. Symp. on Circuits and Systems*, Vol. 4, 3131–3134, May 2005.

9. Cornelissens, K. and M. Steyaert, "A novel bootstrapped switch design, applied in a 400 MHz clocked $\Delta\Sigma$ ADC," *13th IEEE International Conference on Electronics, Circuits and Systems, ICECS'06*, 1156–1159, 2006.

10. Wang, L., J. Ren, W. Yin, T. Chen, and J. Xu, "A high-speed high-resolution low-distortion CMOS bootstrapped switch," *IEEE ISCAS 2007*, 1721–1724, May 2007.

11. Pan, H., et al., "A 3.3-v 12-b 50-MS/s A/D converter in 0.6-µm CMOS with over 80-dB SFDR," *IEEE JSSC*, Vol. 35, No. 12, 1769–1780, Dec. 2000.

12. Chen, H., L. He, et al., "A high-performance bootstrap switch for low voltage switched-capacitor circuits," *2014 IEEE International Symposium on Radio-Frequency Integration Technology (RFIT)*, 1–3, 2014.